

AD-782 310

ANTENNAS FOR AVIONICS

Advisory Group for Aerospace Research
and Development
Paris, France

June 1974

DISTRIBUTED BY:

NTIS

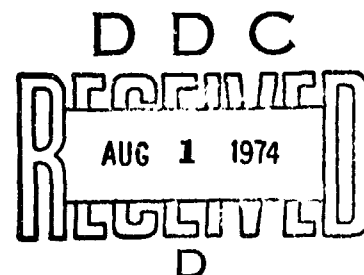
National Technical Information Service
U. S. DEPARTMENT OF COMMERCE
5285 Port Royal Road, Springfield Va. 22151

AD-782310

NORTH ATLANTIC TREATY ORGANISATION
ADVISORY GROUP FOR AEROSPACE RESEARCH AND DEVELOPMENT
(ORGANISATION DU TRAITE DE L'ATLANTIQUE NORD)

AGARD Conference Proceedings No.139

ANTENNAS FOR AVIONICS



Reproduced by
NATIONAL TECHNICAL
INFORMATION SERVICE
U S Department of Commerce
Springfield VA 22151

DISTRIBUTION STATEMENT A

Approved for public release;
Distribution Unlimited

Copies of papers presented at the 26th meeting of the Avionics Panel Symposium held
in Munich, Germany, 26-30 November 1973.

THE MISSION OF AGARD

The mission of AGARD is to bring together the leading personalities of the NATO nations in the fields of science and technology relating to aerospace for the following purposes:

- Exchanging of scientific and technical information;
 - Continuously stimulating advances in the aerospace sciences relevant to strengthening the common defence posture;
 - Improving the co-operation among member nations in aerospace research and development;
 - Providing scientific and technical advice and assistance to the North Atlantic Military Committee in the field of aerospace research and development;
 - Rendering scientific and technical assistance, as requested, to other NATO bodies and to member nations in connection with research and development problems in the aerospace field;
 - Providing assistance to member nations for the purpose of increasing their scientific and technical potential;
- Recommending effective ways for the member nations to use their research and development capabilities for the common benefit of the NATO community.

The highest authority within AGARD is the National Delegates Board consisting of officially appointed senior representatives from each member nation. The mission of AGARD is carried out through the Panels which are composed of experts appointed by the National Delegates, the Consultant and Exchange Program and the Aerospace Applications Studies Program. The results of AGARD work are reported to the member nations and the NATO Authorities through the AGARD series of publications of which this is one.

Participation in AGARD activities is by invitation only and is normally limited to citizens of the NATO nations.

The content of this publication has been reproduced directly from material supplied by AGARD or the author.

Published June 1974

621.396.67:629.7.066:629.7.05



*Printed by Technical Editing and Reproduction Ltd
Harford House, 7-9 Charlotte St, London. W1P 1HD*

PROGRAM AND MEETING OFFICIALS

PROGRAM CHAIRMAN

Mr W.T.Blackband
Procurement Executive
Ministry of Defence
Farnborough, Hants
UK

AVIONICS PANEL CHAIRMAN

Dr I Gabelman
Chief Scientist
Rome Air Development Center
Griffiss Air Force Base
New York 13440
USA

HOST COORDINATORS

Dr H.Leysieffer
NZL Wv Ort und Mess
Siemens AG
8 Munchen 70
Hofmannstrasse 51
Germany

Dr Ing. M.Vogel
Deutsche Forschungs-und Versuchsanstalt
für Luft und Raumfahrt e.v.
Institut für Flugfunk und Mikrowellen
8031 Oberpfaffenhofen
Post Wessling/obb
Germany

AVIONICS PANEL EXECUTIVE

Dr N.R.Ogg
AGARD

EDITOR'S FOREWORD

The Avionics Panel of AGARD has held two previous symposia on the subject of radio antennas: "Signal Processing Array" and "Radio Antennas for Aircraft and Aerospace Vehicles". These each led to a printed volume of Conference Proceedings.*

During the last few years there have been many developments in avionics and it has become increasingly apparent that in many cases the deciding factor determining whether or not a proposed radio system is feasible is the realisability of the antennas required. For this reason it is necessary that avionics engineers should look carefully at the latest developments in antenna science.

With this in mind the Avionics Panel held a Symposium on the subject of "Antennas for Avionics" in Munich from 26 to 30 November 1973. The present volume includes the full texts of the papers presented in shortened versions at this meeting together with a record of the subsequent discussions.

In reading this volume of Proceedings the avionics engineer will be able to welcome many old friends such as the subject of HF antennas for aircraft. Three papers (7, 8 and 33) bear on this subject and I expect that after a further decade of research the problems of HF antennas in aircraft will still be unresolved. In fact it will be surprising if the problems have not worsened because of the growing importance for military purposes of small helicopters in which more and more metal is replaced by plastic and more and more antennas are fitted. For such vehicles it is becoming increasingly difficult to install wire antennas of sufficient length and to find sufficient metal structure to excite. Probably the biggest step forward in the design of HF aeriels would follow the development of a process whereby corrosion could be prevented without impairing the radio-frequency conductivity between adjacent sheets of the fuselage thus making the best use of the metal available as a counterpoise.

One of the new aspects of the study of avionics antennas is their application to the Aerosat systems, either on the aircraft, on the satellite or on the ground. The four papers (18, 19, 20 and 21) on the subject of antennas for aircraft installation in Aerosat systems reflect the difference in the designs of military and civil projects forced upon the engineers by the present frequency allocations. There is no doubt that the choice of the L-band frequency of 1600 MHz for the Civil Aerosat system does not suit the convenience of the antenna engineers concerned but results from the present allocation of frequencies.

Two other papers (22 and 43) are concerned with the design of the antennas to be carried on the satellite of the system. The first describes a planar array which gives a circularly polarised beam by the interaction of longitudinal and transverse slots cut in the broad face of a high order mode waveguide. The second discusses a stepped reflector antenna for the generation of a beam which is a good approximation to a sector in shape with low side lobes. This antenna was not designed primarily for Aerosat systems, but may well have applications in this field if the links from satellite to fixed ground station are moved into the higher microwave bands.

The large dish antennas used for the ground to satellite link have much in common with those used for deep space communications. Three papers (29, 30 and 31) refer to such large dish antennas. Two of these have Cassegrain feeds while one is Gregorian. Among the factors discussed are dichroic sub-reflectors, toroidal aperture distribution and the design of dual mode horns.

In parallel with the development of large dish antennas has gone the study of array technology. Two papers (11 and 34) discuss methods of thinning arrays in order to minimise the cost for a given performance. This process of thinning not only diminishes the cost by reducing the numbers of array elements, but also by simplifying the feeder system which may contain costly phase changers and circulators. This is a most important line of development because the biggest problem facing the would be designer of a large phased array is finding someone to pay for it.

Another paper (32) discusses the optimisation of the design of antennas used for Precision Approach Radars. In these applications the required scan coverage is very limited and advantage of this fact can be taken in the design procedure so that the number of feed elements and the complexity of the feeder system can be minimised. Several classes of such antennas are described and compared in terms of the element use factor.

The design of antennas for Airborne Early Warning radars is discussed in Paper 12. This subject is an interesting example of the manner in which the choice of optimum frequency for an avionic system is often dominated by considerations of antenna performance.

The number of antennas on aircraft seems to be ever increasing. Over the last few years there have been attempts made to make combined antennas which can be used simultaneously by more than one system at a time. A number of these are commercially available but they have not at present made much impact on the problem.

* "Signal Processing Arrays" and "Radio Antennas for Aircraft and Aerospace Vehicles". Both edited by W.T. Blackband and published by Technivision, Maidenhead, England.

There are of course difficulties in the use of combined antennas, these are chiefly:

- (a) the mutual interference between the systems,
- (b) differences in coverage which demand differing sites on the aircraft.

Where the required coverages of two antennas are markedly different there is little that the antenna engineer can do, for instance it would not be possible to choose a site suitable both for a radio-altimeter antenna looking towards the ground and an Aerosat antenna looking towards the sky. However the effects of mutual interference can be minimised by careful antenna design. Here one has to distinguish between interference on the fundamental frequencies and those on difference frequencies of various orders. Interference on the fundamental frequencies must be reduced by careful antenna feed design whereby the signals at two fundamental frequencies are fed to separate parts with minimum mutual coupling between them. This can be helped in some cases by feeding one signal at a minimum in the standing wave pattern of the other, or by simple high pass or low pass filters built into the antenna structure. In many cases this filtering will need to be supplemented by additional filters. When this is the case these should be sited as close to the antenna as possible so that the unwanted signals do not pass into the feeder system. Interference at difference frequencies raises the old question of how to minimise intermodulation products. So far avionics engineers have not had as much experience in this field as have their naval colleagues, however this problem must be faced. At present research into the control of non-linearity at metallic junctions is making progress but at present the best advice is to avoid any but welded joints in the antenna and to avoid siting the antenna near a join in the aircraft skin.

The problem of reducing the number of aircraft antenna by the development of combined units is one which must receive attention if the development of avionics systems is to progress; and the attention of antenna engineers should be drawn to it as one of the most important problems facing the profession.

I would like to thank all those whose efforts in support of the Symposium were so generous. The response to the Call for Papers was very pleasing but it posed the problem of selecting 43 out of the 85 synopses submitted. This called for a judgement of Solomon as the synopses were of excellent promise. It was with regret that so many good papers could not be accepted particularly as they would have provided the material of a good level symposium on their own. Seeing that there has been this enthusiasm for this Antenna Symposium it is hoped that the Avionics Panel will be able to hold another in a few years time.

W.T.BLACKBAND
Programme Chairman and Editor
8 March 1974

CONTENTS

	Page
PROGRAM AND MEETING OFFICIALS	iii
EDITOR'S FOREWORD	iv
	Reference
 <u>SESSION I</u>	
CONFORMAL ARRAYS FOR AIRCRAFT by J.Provencher, J.Boyns and A.Hessel	1
PATTERNS AND POLARISATIONS OF SIMULTANEOUSLY EXCITED PLANAR ARRAYS ON A CONFORMAL SURFACE by J.K.Hsiao and A.G.Cha	2
DESIGN OF PERIODICALLY MODULATED TRI-PLATE ANTENNAS by F.Laursen	3
 <u>SESSION II</u>	
HIGH EFFICIENCY ANTENNAS FOR AIRBORNE RADAR by R.W.Forrester and A.J.Lait	4
SHF HIGH POWER AIRBORNE COMMUNICATIONS ANTENNA by J.P.Grabowski and F.L.Lanphear	5
PROBLEMES D'ANTENNES POSES PAR LE PASSAGE EN BANDE S DES TELEMESURES par M.Nicolas et C.Mast	6
 <u>SESSION III</u>	
RADIATION CHARACTERISTICS OF HF NOTCH AERIALS INSTALLED IN SMALL AIRCRAFT by N.A.D.Pavey	7
HF ANTENNA SYSTEMS FOR SMALL AIRPLANES AND HELICOPTERS by R.E.Deasy	8
VERY SLIM, HIGH GAIN PRINTED CIRCUIT MICROWAVE ANTENNA FOR AIRBORNE BLIND LANDING AID by W.Hersch	9
POLYROD AERIALS FOR AVIONIC APPLICATIONS by M.Scorer and A.M.Smith	10
 <u>SESSION IV</u>	
LINEAR PHASED ARRAY FOR YAW STABILISATION by D.S.Hicks	11
AEW RADAR ANTENNAS by T.L. ap Rhys and G.A.Andrews, Jr	12
AIRBORNE LOW-VHF ANTENNAS by C.E.Cooper	13

SESSION V

- TE₁₁ CIRCULAR WAVEGUIDE FERRITE PHASERS OPTIMIZATION
by A.M.Duputz and A.C.Priou 14
- A CROSSED-SLOT BELT ARRAY ANTENNA FOR SATELLITE APPLICATION
by R.Breithaupt, B.Clark and D.Waung 15
- CROSS-POLARISED RADIATION FROM SATELLITE REFLECTOR ANTENNAS
by A.W.Rudge, T.Pratt and A.Fer 16
- PROBLEMS OF LONG LINEAR ARRAYS IN HELICOPTER BLADES
by R.H.J.Cary 17

SESSION VI

- SYSTEME D'ANTENNES A COMMUTATION REALISANT UNE COUVERTURE AVION
AUX NORMES AEROSAT
par C.Ancona et P.Froidure 18
- A LINEAR ARRAY OF BLADE ANTENNAS AS AN AIRCRAFT ANTENNA FOR
SATELLITE COMMUNICATION
by O.B.M.Pietersen, J.P.B.Vreeburg and F.Klinker 19
- UHF LINEAR PHASED ARRAYS FOR AERONAUTICAL SATELLITE COMMUNICATIONS
by H.L.Werstiuk, J.D.Lambert, L.A.Maynard and J.H.Chinnick 20

SESSION VII

- A COMPARISON OF TWO L-BAND AIRCRAFT ANTENNAS FOR AERONAUTICAL
SATELLITE APPLICATIONS
by R.G.Bland and J.M.Clark 21
- CIRCULARLY POLARIZED L-BAND PLANAR ARRAY FOR AERONAUTICAL
SATELLITE USE
by B.Palumbo and S.Cosentino 22
- UPPER L-BAND TELEMETRY AERIALS FOR ROCKETS AND MISSILES
by J.Mahoney 23
- ELECTRONICALLY SCANNED TACAN ANTENNA AS AN ENROUTE AND TERMINAL
NAVIGATIONAL AID
by E.J.Christopher 24

SESSION VIII

- ANALYSIS OF FINITE ARRAYS OF RECTANGULAR APERTURES ON CONDUCTING
DIELECTRIC COATED CYLINDERS
by J.Vogt 25
- ANTENNES HYPERFREQUENCE POUR MISSILES HYPERSONIQUES
par C.Pouit 26
- Paper 27 withdrawn

SESSION IX

- THE DESIGN OF WIDE BAND NOTCH AERIALS AND SOME APPLICATIONS TO
AVIONICS
by G.Bagley 28

SESSION IX (Continued)

DUAL FREQUENCY DICHROIC FEED PERFORMANCE by D.A.Bathker	29
EMPLOYMENT OF NEARFIELD CASSEGRAIN ANTENNAS WITH HIGH FREQUENCY AND LOW SIDELOBES TAKING THE INTELSAT-GROUNDSTATIONS AND THE GERMAN HELIOS-TELECOMMANDSTATION AS EXAMPLES by U.Leupelt and W.Rebhan	30
DEVELOPMENT OF AN S-BAND DUAL MODE HORN FOR TELEMETRY RECEPTION BY THE 100 m EFFELSBERG RADIO TELESCOPE by W.Hess and B.Liesenkötter	31

SESSION X

ARRAY AND REFLECTOR TECHNIQUES FOR AIRPORT PRECISION APPROACH RADARS by K.J.Mailloux and P.Blacksmith	32
NOTES ON THE RADIATION PATTERNS OF HF AERIALS INSTALLED ON HELICOPTERS by W.T.Blackband	33
RADIATION CHARACTERISTICS OF THINNED ARRAY ANTENNAS by W.Söntgerath	34

SESSION XI

IN-FLIGHT MEASUREMENT OF AIRCRAFT ANTENNAE RADIATION PATTERNS by H.Bothe	35
DYNAMIC MEASUREMENT OF AVIONIC ANTENNAS by I.D.Olin and E.E.Maine, Jr	36
AN IMPROVED MEASURING TECHNIQUE FOR INVESTIGATIONS OF THE NEARFIELD REGION OF ANTENNAS by R.Anders	37
DETERMINATION OF THE MOVEMENT OF THE APPARENT PHASE CENTRES OF AIRCRAFT ANTENNAS FOR CALIBRATING THE ZDBS INTERFEROMETER by A.Schrott and S.Modabber	38

SESSION XII

OFF-BORESIGHT ANGLE ESTIMATION WITH A PHASE COMPARISON MONOPULSE SYSTEM by W.Sander	39
Paper 40 withdrawn	

SESSION XIII

ROLL PLANE ANALYSIS OF ON-AIRCRAFT ANTENNAS by W.D.Burnside, R.J.Marhefka and C.L.Yu	41
INVESTIGATION OF CHARACTERISTICS AND PRACTICAL IMPLEMENTATION OF ARBITRARILY POLARIZED RADIATORS IN SLOT ARRAYS by J.S.Ajioka, D.M.Joe, R.Tang and N.S.Wong	42
STEPPED REFLECTOR ANTENNA WITH A SECTOR SHAPED MAIN BEAM by H.Thielen	43

CONFORMAL ARRAYS FOR AIRCRAFT*

by

J. Provencher
J. Boyns
Naval Electronics Laboratory Center
San Diego, California 92152
and
A. Hessel
Polytechnic Institute of New York
Farmingdale, N. Y., 11735
U.S.A.

SUMMARY

Present and future requirements for wideband, multi-function antennas for many applications offer attractive potential uses for circular symmetric and multi-frequency arrays. Rigorous analytical techniques are not available to investigate Non Planar array characteristics and experimental techniques can be used to simulate scanning of non planar arrays. Planar phased arrays received considerable attention over the past twenty years, and although significant advances have been made, their widespread use in systems has not been achieved. A major factor that limits their use is high cost; and for aircraft, the lack of small, lightweight components.

One approach which is aimed at solving several of these problems is a conformal multifrequency array, using Microwave Integrated Circuit (MIC) techniques.

This paper describes some design considerations involved with the multifrequency conformal array. Among these are:

1. Element pattern effects in non planar arrays,
2. Multifrequency array techniques, and
3. MIC components and cost considerations.

The element patterns of conical arrays are examined to determine if behavior is similar to known element patterns for the cylindrical or planar arrays, and a conical sector experimental array is used to simulate selected "scanned" beam positions to determine array behavior, i.e., beamwidth, scan limits, polarization and side lobe level. The concept of the multi-frequency array has been shown to be feasible, and the use of the interlacing technique with the conformal array allows more flexibility due to the larger element spacings possible. These features, combined with MIC hybrid matrix techniques for multiple beams; diode phasors and hybrid drivers for beam steering; and flush mounted radiating elements provide the system designer with a versatile antenna system.

Prototype arrays designed at wavelengths of 30cm, 10cm, 7cm and 3cm are described. The arrays have potential application for satellite communications, IFF and navigation. Experimental and calculated array patterns, element patterns and polarization data are given, and factors affecting cost are also discussed.

INTRODUCTION

The increasing requirements for high data rate and multiple beam antennas for aircraft, coupled with a limited space available on the vehicle, and the requirement for arrays of wide frequency bandwidth has led to a revival of the techniques used several decades ago for circular and cylindrical arrays.

Recent developments in circular arrays have increased the interest in and desirability of taking advantage of the inherent broadband capability of circular symmetric geometries. This interest has led to more rigorous theoretical approaches for solutions of the problems involved in the determination of useful amplitude and phase distributions, and reduction in the complexities of the feeding structures. The limited space available on ships, aircraft and missiles has prompted development of radiating structures for more efficient use of vehicle space. In addition, the aerodynamic requirements and non planar surfaces present attractive potential applications of flush mounted non planar or conformal arrays. For the purposes of this paper, a conformal array will include cylindrical, conical or any non planar array.

For certain applications, the use of the circular symmetric array has some advantages, especially where single rings are used to form multi-dimensional arrays for narrow beams in the vertical plane.

*This work was partially supported by the Naval Ship Systems Command and the Naval Air Systems Command.

In contrast to the linear or planar array, the radiated beam in the azimuthal plane of the circular symmetric array does not change with scan angle, and changes very slightly when phase scanned over small scan angles. In general, the amplitude and phase distributions required to produce given beam shapes for the circular symmetric arrays are more complicated than those required for planar arrays.

The usual method for steering the beam of circular arrays in azimuth is to commute the excitation distribution. This usually involves complex switching networks. With a space feed approach the amplitude can be commuted by steering the source feed beam. Using a combination of source beam commutation and fine phase steering, azimuth beam steering can be simplified. In addition, multiple beams are also possible by illuminating non-overlapping sectors of the aperture with multiple source beams. An advantage of the circular array is the independence of the beam steering or azimuth beam stepping with arc spacing. Since the beam is stepped, rather than phase scanned (as in a linear or planar array), the restrictions on element spacing with scan angle are not as severe. There is not, however, complete freedom in the selection of the spacing. For example, undesired radiation lobes appear at azimuth angles on the order of 100° and are a function of element spacing, angle of arc, and radius, as shown in Figure 1. The effects of spacing on element patterns is an important design factor in non planar arrays.

A recent theory (Sureau, J.C. and Hessel, A., 1971) and another approach (Munger, A.D., et al., 1971) can be used to predict the behavior of circular array element patterns and gives considerable insight into the behavior of a uniformly spaced circular symmetric array of waveguide-fed apertures in a large conducting cylinder. No comparable theory is available to predict the behavior of element patterns on a conical surface, although recent experiments at the Naval Electronics Laboratory Center (NELC), San Diego, using waveguide elements in conical configurations, indicate that the element pattern behavior is similar to that of the cylindrical array. Present efforts at NELC, and several contractual efforts are aimed towards a mathematical theory for the conical configurations and extension of these techniques to the ogive and cigar-shaped geometries.

Previously reported analytical and experimental investigations of the element and array pattern behavior of large conical array sectors using dipole elements are not adequate to completely predict array behavior, but give some insight into the behavior of the conical array. (Boyns, J.E., and Munger, A.D., 1971). The concept of the projected distribution can yield acceptable patterns in the absence of a rigorous mathematical theory.

The technique of interlacing several waveguide aperture arrays into the same physical has been demonstrated for cylindrical surfaces. (Provencher, J.H. and Boyns, J.E., 1971) Experiments have shown that the interaction between several arrays, operating simultaneously at close proximity, can be reduced to tolerable levels. The excitation of several arrays in the same area poses problems as to the choice of feed device as well as the radiating element. The use of dielectric materials to reduce the size of the waveguides is one approach to the problem. Another technique makes use of copper clad dielectric waveguides operating in the TEM mode feeding a printed dipole. A third method uses a printed cavity-backed spiral for wide frequency bandwidth and circular polarization.

The selection of the proper method of excitation, radiating element and other components required for the array is dependent not only upon performance, but is also a function of cost. The restrictions on space, weight and structure require the consideration of ultimate cost of reproduction of prototype units in the early design stages. The elimination of interconnections between phase shifter, radiating element and feed system can be readily accomplished using Microwave Integrated Circuit (MIC) techniques. In addition, these devices can be mass produced, possess high reliability and occupy a low volume. Some basic advantages of the multi-frequency conformal array are:

1. The radiating elements can be flush mounted to conform to the non planar surface;
2. Fewer components are required due to larger element spacings possible with the curved array, and in addition,
3. More space is available between elements to interlace arrays at other frequencies.

These advantages, when combined with the MIC components can provide multi-frequency arrays and simultaneous beam operation.

ARRAY DESIGN CONSIDERATIONS

Aperture design of conformal arrays requires knowledge of the performance of its typical elements in regard to gain, phase and polarization patterns. This implies that coupling coefficients can be

calculated or measured. Since with existing theories, the coefficients cannot be calculated; experimental techniques to measure element patterns are used. This data can then be used with the projected distribution concept.

This approach assumes a reasonable distribution followed by pattern analysis to show that the distribution chosen yields no undesirable characteristics. A cylindrical array is known to consist of a product of the pattern of a single constituent ring array with that of a linear array along the cylinder axis excited by the ring-to-ring distribution. Since the pattern of a ring array varies slowly in elevation, the vertical pattern of the complete antenna can be controlled by using a ring-to-ring distribution of the form normally used for linear arrays. It is reasonable to use the same type of distribution along the vertical arrays of a conical antenna provided that the cone angle is not too large and modifications to the distribution are made to account for a varying radius. This projection technique must take into account both element patterns and apparent element density when viewed as in Figure 2. The projected element density shown in the figure is proportional to the secant of the angle from the main beam direction.

When the element pattern is of the form

$$g(\theta, \phi) = f(\theta) \cos \phi \quad -\pi/2 < \phi < \pi/2$$

$$= 0 \quad \text{elsewhere,} \quad (1)$$

then the element density and pattern effects cancel, and the required distribution on the arc has a magnitude equal to that at the equivalent point on the linear aperture. The phase excitation is then chosen to be cophasal in the main beam direction. These techniques have been demonstrated by computer simulation, and have been verified experimentally at NELC. The array sector is shown in Figure 3 and has 700 dipole elements and a mean radius on the order of 17 wavelengths, and a cone angle of 30°. Computed patterns of the conical array and a cylindrical array of similar parameters are given in Figure 4 for elevation scan angles, θ_0 , of 0° and 60°. Both arrays used a staggered configuration as shown in Figure 5, and the pattern behavior of the conical array at 60° is improved over the cylindrical array in terms of beamwidth and gain. A more complete report on this work will appear in the special issue of IEEE Transactions on Antennas and Propagation to be published in January, 1974.

The techniques discussed are not adequate to fully determine the conformal array parameters required although acceptable data can be obtained. However more rigorous theories are being examined under Navy sponsorship at Polytechnic Institute of New York and Hughes Aircraft.

The theoretical determination of the far field pattern of an antenna is predicated on the knowledge of the aperture distribution. In the array case, this requires the knowledge of the relevant mutual coupling parameters, which for the case of aperture elements takes the form of the mutual admittance coefficients Y_{ij} . The mutual admittance Y_{12} between two "single mode" aperture elements in a conformal array in Figure 5 is given by the relation

$$V_{12} = \int_{\rho}^P [\hat{n}(r) \times E_2(r)] \cdot H_1(r) dS / V_1 V_2. \quad (2)$$

Here E_2 is the electric field in the aperture (2), \hat{n} , the local normal to the array surface, H_1 the magnetic field due to aperture A_1 in the location of aperture A_2 when the latter is short circuited, and V_1, V_2 are the respective amplitudes of the two aperture modes.

The magnetic field $H_1(r)$ is given by

$$H_1(r) = \int_{\rho}^P \underline{G}(r, r') \cdot [E_1(r') \times \hat{n}(r')] dS' \quad (3)$$

where the dyadic Green's function $\underline{G}(r, r')$ represents the magnetic field at r due to a unity magnetic current element at r' on the conformal array surface.

If the latter is not separable, i. e., it is not a constant coordinate surface of a frame in which Maxwell's equations separate, then the exact form of $\underline{G}(r, r')$ is not known. Even when the surface is separable, but the radii of curvature are electrically large, modal procedures which can be applied, are poorly convergent. These difficulties are overcome by recourse to the Geometric Theory of Diffraction.

In several papers, (Levy, 1959) (Keller, J. B., 1962), a generalized concept of surface (creeping) rays for arbitrary, convex conducting surfaces was given. It postulates, in accordance with Fermat's principle, propagation of electromagnetic waves along surface ray trajectories that are geodesics of the surface. Typical surface ray trajectories are shown in Figure 6. The theory assigns to each point on the ray path a field amplitude, phase and polarization. Once these are known at a point on the ray trajectory, they may be traced along the ray path, i. e., they may be calculated via the formula

$$U[P(s)] = U(P_0)D(s) \exp\left\{-\int_{P_0}^P \alpha[\rho(s)]ds\right\} \exp\left\{-j\int_{P_0}^P \beta[\rho(s)]ds\right\} \quad (4)$$

where $U(P)$ is any field component in the local, ray (geodesic) coordinate system (e.g. along the local binormal). In (4) $\rho(s)$ is the principal radius of curvature of the surface at a point s along the ray path; $D(s)$ is the ray divergence coefficient and $\beta \approx k$ the free space wave number. Thus, the value of a typical ray field component at P is given in terms of its starting value at P_0 , a ray divergence factor $D(s)$, which accounts for the energy spreading when the rays are not parallel, and an exponential decay along with a phase delay along the ray travel path. The latter are integrals of the attenuation and propagation constants corresponding to a local conduction cylinder with radius of curvature equal to the local principal radius of curvature.

The derivations and details have been omitted, and much work is still required. However, these techniques appear promising and could lead to realizable solutions for many nonplanar configurations.

Although the conical array is only one of several conformal arrays, the knowledge to be gained from the study of this geometry lends itself to the possible solution of other configurations. For example, in Figure 7(A), the conical end fire and broadside array parameters must be determined using different mathematical techniques i.e., ray techniques and modal methods. However, once a theory has been established and verified, extension to the ogive of Figure 7(B) is accomplished only by calculation of a new set of coupling coefficients for the particular geometry.

CONFORMAL ELEMENT PATTERNS

A necessary set of parameters for the aperture design of a conformal array can be obtained from the element pattern. Extensive experimental parametric studies are expensive and time consuming, but are required at the present time due to the lack of a basic theory. The studies to be discussed are part of a parallel study with the Polytechnic Institute of New York to verify expected theoretical results. Previous theoretical results, (Hessel, 1970) for circular and cylindrical array element patterns were verified at NELC. (Provencher, 1971) (Hessel, 1972)

The element pattern of elements arrayed on a circular, symmetric array exhibits large changes in shape and gain as the interelement spacing approaches 1λ . This effect is caused by interference from creeping waves which are radiated as a result of the periodicity of elements. Figure 8 shows the various wave contributions. These significant differences from the planar array theory were predicted by the non planar theory. The element pattern behavior was strongly affected by the spacing of its neighboring elements along the curve. This is illustrated in Figure 9 for a single ring array with a radius of 13 wavelengths and element spacings, a , of 0.58 and 0.78 wavelengths. The pattern beamwidth decreases substantially, as shown in the figure for the respective wavelengths. A corresponding increase in gain is also predicted. For example, when $a = 0.52\lambda$, the gain is increased more than 2 dB over that of the isolated pattern, as shown in the calculated composite patterns of Figure 10 (A). Measured patterns in Figure 10(B) for the same array show a marked similarity to those calculated. The HPBW is about 6° and the peak gain is about 5 dB higher than that of the isolated element pattern. This compares with 7 dB for the calculated values for an array of infinite slits.

Similar results were also obtained for a cylindrical array with a radius of 26 wavelengths and for element spacings of 0.54 and 0.79 wavelengths. These results are given in Figure 11 which compares calculated patterns assuming an infinite array in the Z direction in 11(A) with corresponding measured patterns given in 11(B). The split beam for $a/\lambda = 0.79$ is due to an out-of-phase condition for the creeping waves on the cylinder.

Since the conical array can be considered as a stack of ring arrays, it is assumed that the observed element pattern characteristics of the circular or cylindrical array will also be evident for the conical configuration. Preliminary measurements tend to confirm this assumption as shown in Figure 12. These patterns indicate behavior similar to that observed for the waveguide arrays described. This experimental array shown in Figure 13 has a mean radius of 16 wavelengths, a mean element spacing of 0.6 wavelengths and consists of 44 linear arrays in azimuth with 11 elements in the slant plane. The cone angle is 20° .

MULTIFREQUENCY TECHNIQUES

The feasibility of integrating several functions at different frequencies into the same aperture has been reported (Boyns, J.E., and Provencher, J.H., 1972) for both non planar and planar geometries. Consideration of the constraints imposed on array element spacings suggest a multiple, periodic configuration and/or a tapered or non cylindrical type of structure. One requirement is that the element-to-element spacing to suppress grating lobes, (i.e., $a < \lambda$) must be satisfied for the highest operating frequency. In addition, the spacing limitations discussed for curved arrays, (i.e., $a < 0.8\lambda$) dictate a truncated conical or an ogive surface if the several arrays are not interlaced. Both of these techniques are illustrated in Figure 14. Combination of the two techniques into a single multi-frequency array are also possible.

Mutual coupling between the various arrays must be considered in the design of the overall array. Coupling measurements made on the three band array shown in Figure 15 confirmed assumptions that mutual coupling levels are tolerable for many applications.

The array consists of two vertically polarized elements in the 30 cm band; 64 horizontally polarized elements in the 10 cm band; and 120 vertically polarized elements in the 5 cm band.

The elements are arrayed on a sector of cylinder 5m in diameter. The feed systems provided a uniform distribution and phase correction for aperture curvature in the design of the power dividers. Since this array is on a large radius curved surface, the results are a good approximation to the planar array.

Coupling levels are generally lower for non planar waveguide arrays due to radius of curvature and larger element spacings. Coupling between the arrays can be reduced by orientation of the elements to take advantage of different linear polarizations. Higher frequency energy is coupled into the lower frequency waveguides as higher order modes and can be suppressed by means of mode filters. Coupling effects between interlaced dipole arrays have also been examined and since the dipole radiator does not possess good cut-off characteristics, their use in the multifrequency interlaced array is severely restricted. However, limited success has been achieved using a combination of printed dipoles and waveguide elements in a three band planar array. Similar techniques are feasible for non planar arrays.

ARRAY IMPLEMENTATION

The demand placed on the antenna array due to space and weight restrictions on an aircraft implies small, light and highly reliable components. The (MIC) techniques are well developed for the lower microwave frequencies and have been shown to have high reliability. These techniques yield components that are amenable to modular concepts. Figure 16 shows a typical MIC module for use as a module for an array with four simultaneous beams in one plane and switched (step scan) in the other plane. The simultaneous beams are provided by means of a 4-port hybrid matrix and are switched using diode switches.

The array is steered in the other plane using ferrite or diode phase shifters. The MIC module consists of four dipole elements, a four port hybrid matrix and the matrix switching network. These components are printed on alumina substrates and occupy an area of 8 square inches. The circuits are highly reproducible and relatively inexpensive to fabricate. The hybrid matrix has also been reproduced on alumina for 8 and 16 beam arrays.

One advantage of this technique is that connections between components become an integral part of the module, and interconnecting fittings are eliminated. This results in lower losses and tends to increase reliability. A disadvantage of present techniques is that MIC devices exhibit relatively high losses at the higher frequencies. However, this is a trade-off factor which must be considered along with space, weight and reliability. For some applications, the losses are tolerable. The various trade-offs that can be made are dependent upon component cost. In general, array antennas have not received widespread use. The one single factor for this situation is the high cost of the components which are required. Considerable effort has been expended to reduce fabrication costs and limited success has been achieved. The MIC modular techniques hold promise for cost reductions by minimizing interconnections, reducing component size, and reducing human operations required for fabrication. Once the basic configuration has been determined, etching techniques can be used to produce many identical units with close tolerances. The power handling capability of the devices can present a limitation when a small number of units are used in an array, however, improvements in materials and the application of small power sources at each radiating element increase the possibility of successful, useful conformal arrays.

REFERENCES

- BOYNS, J.E., 1969, "Interlacing of Multi-Frequency, Multi-Function Integrated Arrays," NELC Technical Report 1674
- BOYNS, J.E., and MUNGER, A.D., Sept 1971, "Cylindrical and Conical Array Investigations", 1971 International Symposium on Antennas and Propagation, Sendai, Japan
- BOYNS, J.E. and PROVENCHER, J.H., 1972, "Experimental Results of a Multi-Frequency Array Antenna", IEEE Trans. Antennas and Propagation, Vol. AP-20
- HESEL, A. June 1970, "Mutual Coupling Effects in Circular Arrays on Cylindrical Surfaces", Proc. 1970 Phased Array Antenna Symposium, Polytechnic Institute of Brooklyn, Farmingdale, N.Y. June 2-5, 1970
- HESEL, A., 1972, "Mutual Coupling Effects in Circular Arrays on Cylindrical Surfaces--Aperture Design Implications and Analysis", Phased Array Antennas, Artech House, Dedham, Mass.
- KELLER, J.B., Feb, 1972, "Geometric Theory of Diffraction," J. Opt. Soc. America
- LEVY, B.R., and KELLER, J.B., 1959, "Diffraction by a Smooth Object." Communication on Pure and Applied Mathematics, Vol. XII
- MUNGER, A.D., and PROVENCHER, J.H., and GLADMAN, B.R., Jan 1971, "Mutual Coupling on a Cylindrical Array of Waveguide Elements", IEEE Trans. Antennas and Propagation, Vol. AP-19
- PROVENCHER, J.H., June, 1971, "Element Gain Patterns in Large Circular Arrays on Conducting Cylinders", M.S. Thesis, Polytechnic Institute of Brooklyn, N.Y.
- PROVENCHER, J.H., and BOYNS, J.E., Aug 1971, "Multi-Frequency Multi-Function Antennas", Proc. European Microwave Conference, Stockholm, Sweden
- SUREAU, J.C., and HESSEL, A., Jan 1971, "Element Patterns for Circular Arrays of Waveguide-Fed Axial Slits on Large Conducting Cylinders", IEEE Trans. Antennas and Propagation, Vol. AP-19

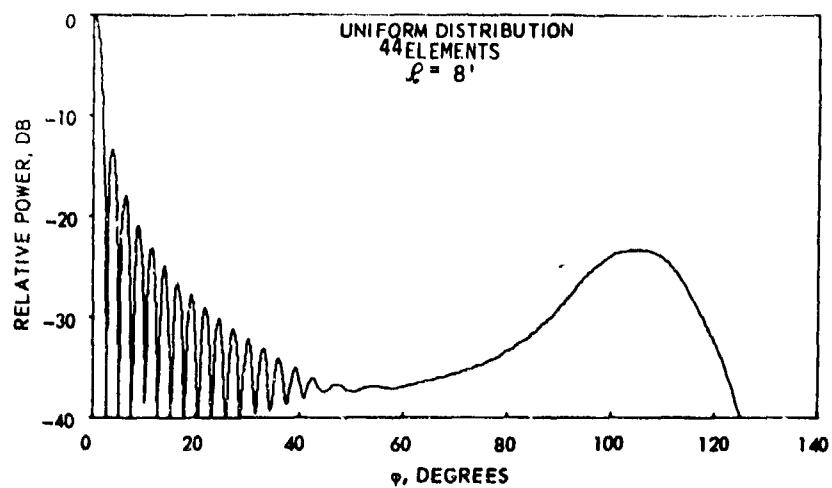


Fig.1 Cylindrical array azimuth radiation pattern, 44 elements, $f = 3.2$ GHz, radius = 26.3 wavelengths

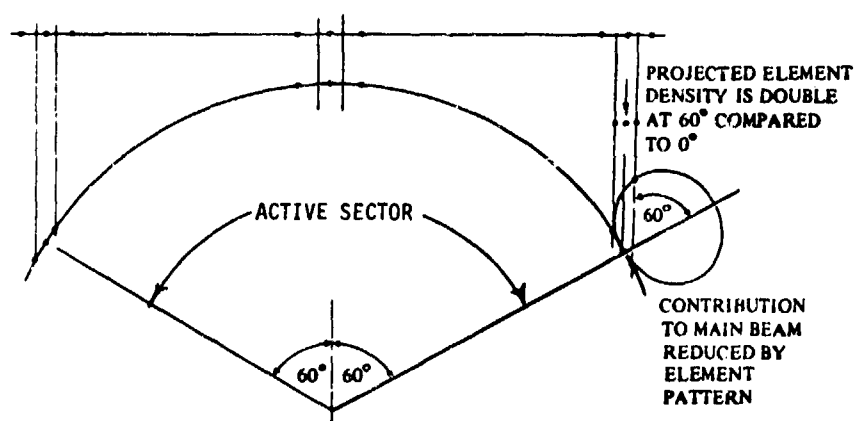


Fig.2 Projected element density, active sector = 120° , $f = 12.0$ GHz, waveguide elements, measured

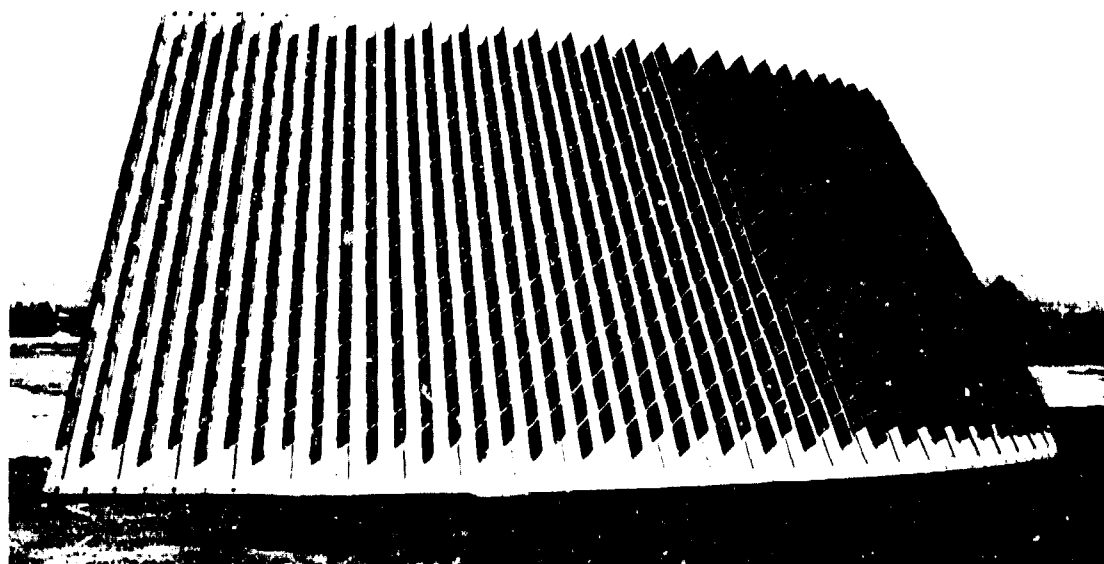
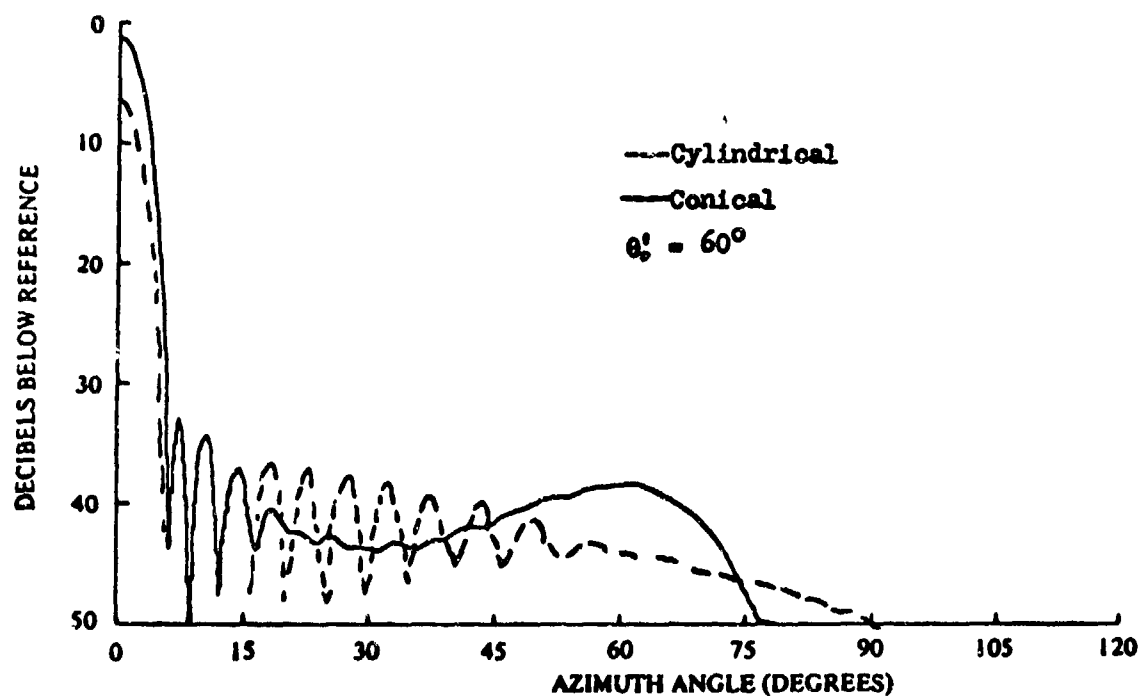


Fig.3 Conical array sector, mean radius = 17 wavelengths, 700 dipole elements, cone angle = 25°

(A)



(B)

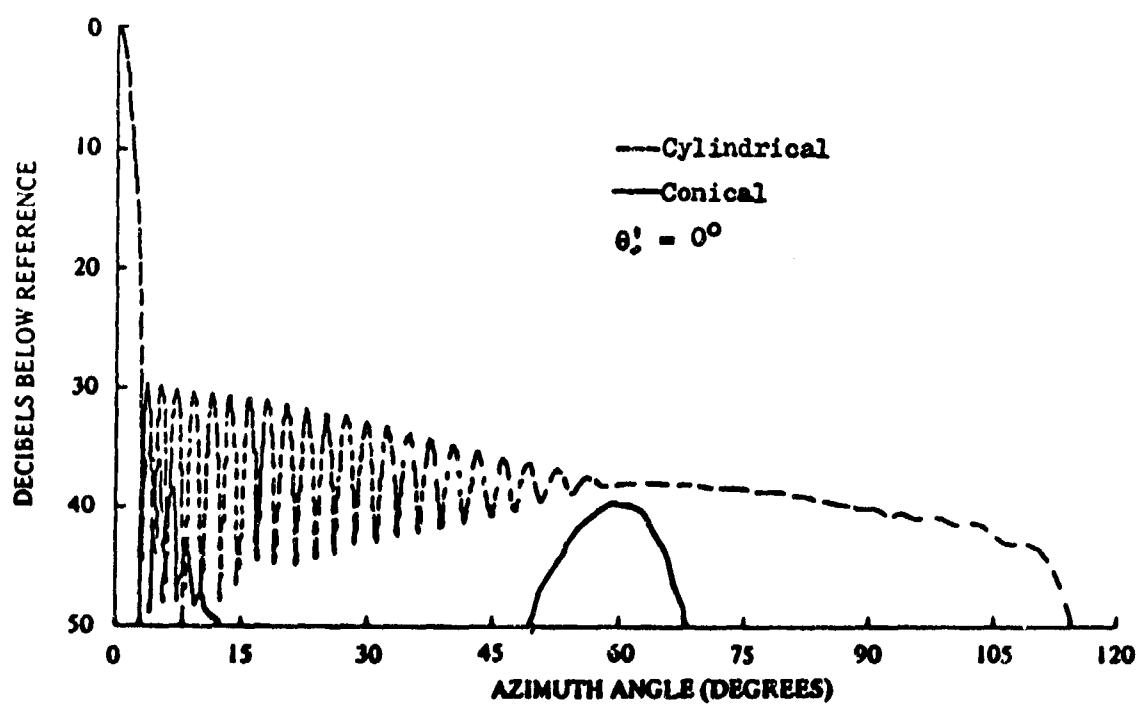


Fig.4 Conical and cylindrical array elevation patterns, $\phi = 0$, $\theta_0' = 0^\circ, 60^\circ$ calculated, mean radius = 26.3 wavelengths

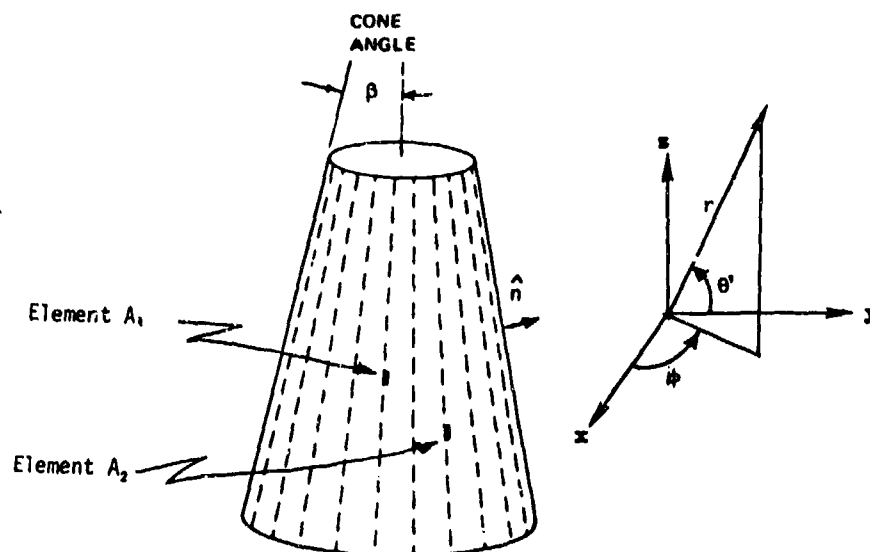


Fig.5 Coordinate system and staggered element configuration for conical array

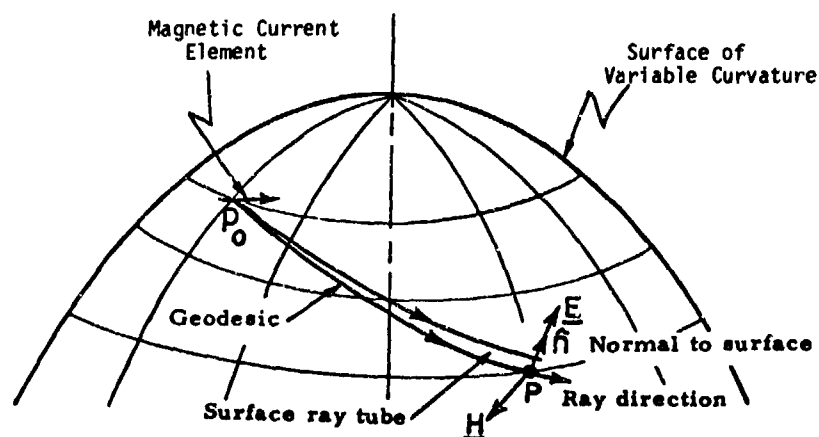


Fig.6 Surface ray trajectories

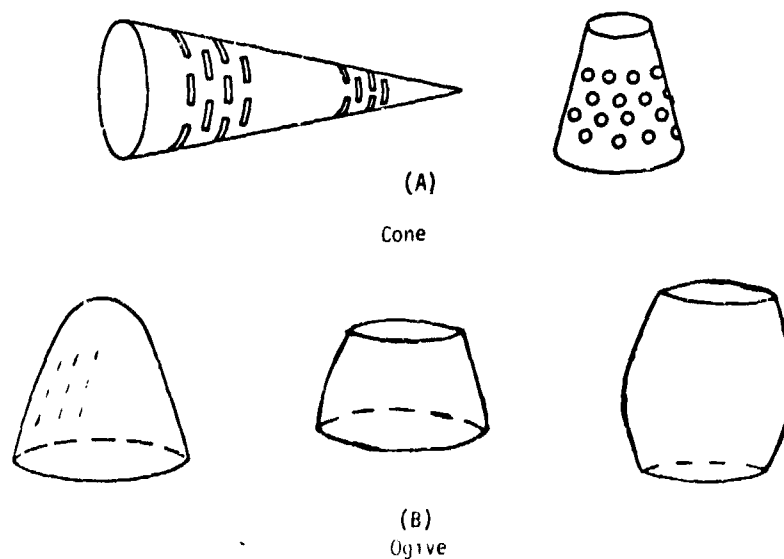


Fig.7 Non planar array geometries

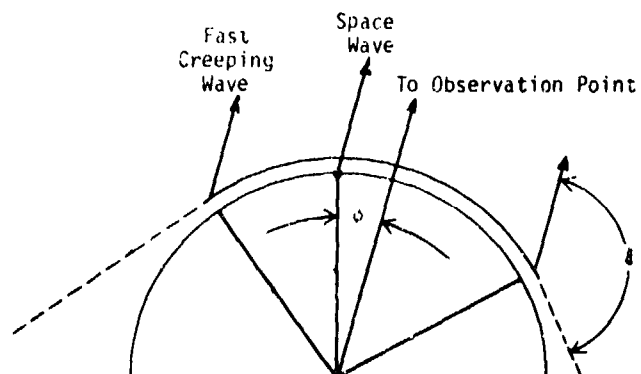


Fig.8 Wave contributions for non planar array, waveguide elements

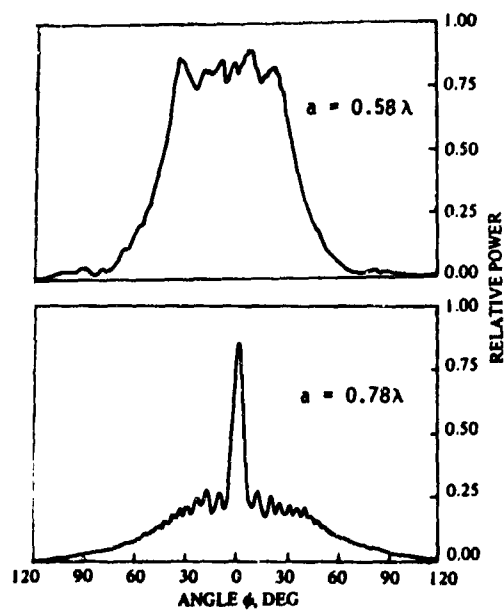
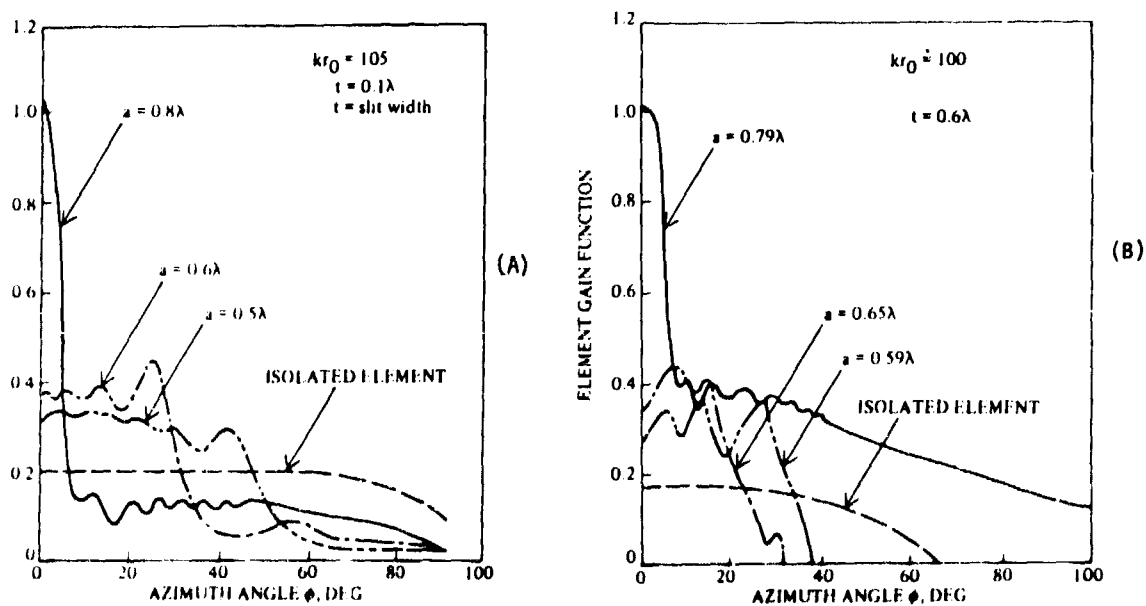
Fig.9 Circular array element patterns, radius = 13 wavelengths, $a = 0.58\lambda$, 0.78λ , in azimuth, measured

Fig.10 Circular array element gain function, radius = 13 wavelengths; (A) calculated, (B) measured

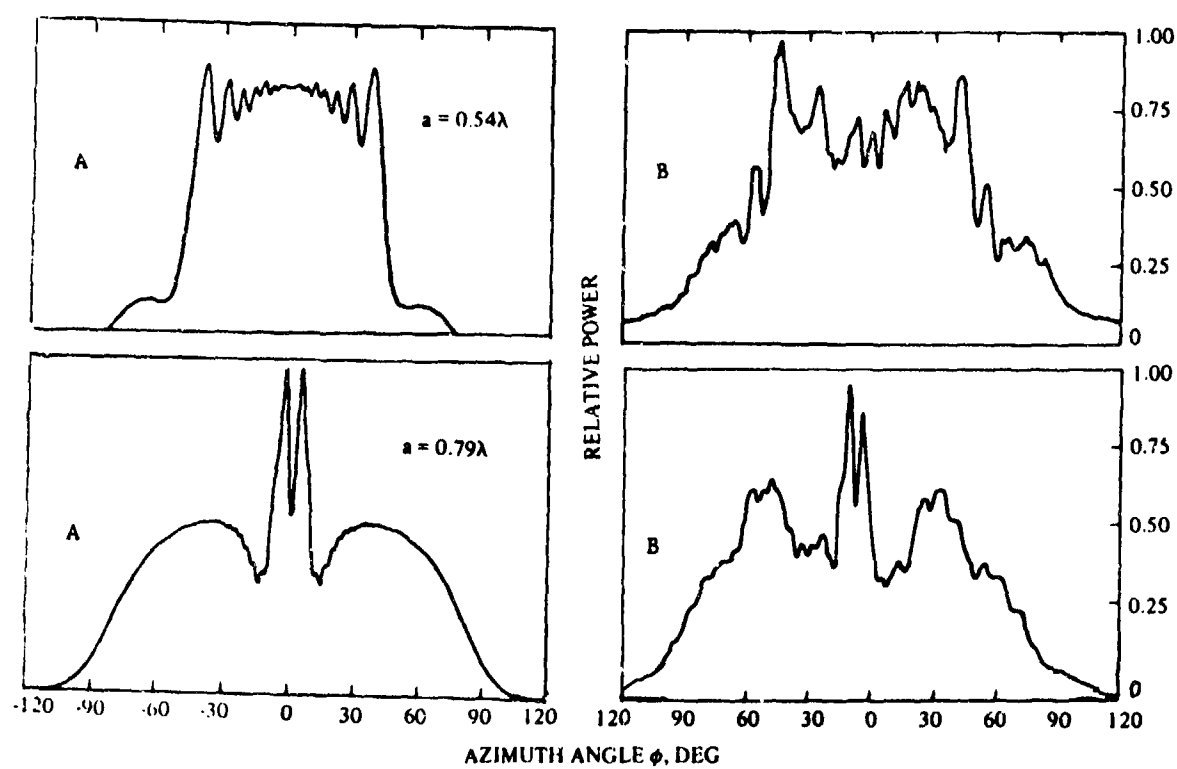


Fig.11 Cylindrical array element patterns, radius = 26 wavelengths, $a = 0.54\lambda$, 0.79λ ;
(A) calculated, (B) measured

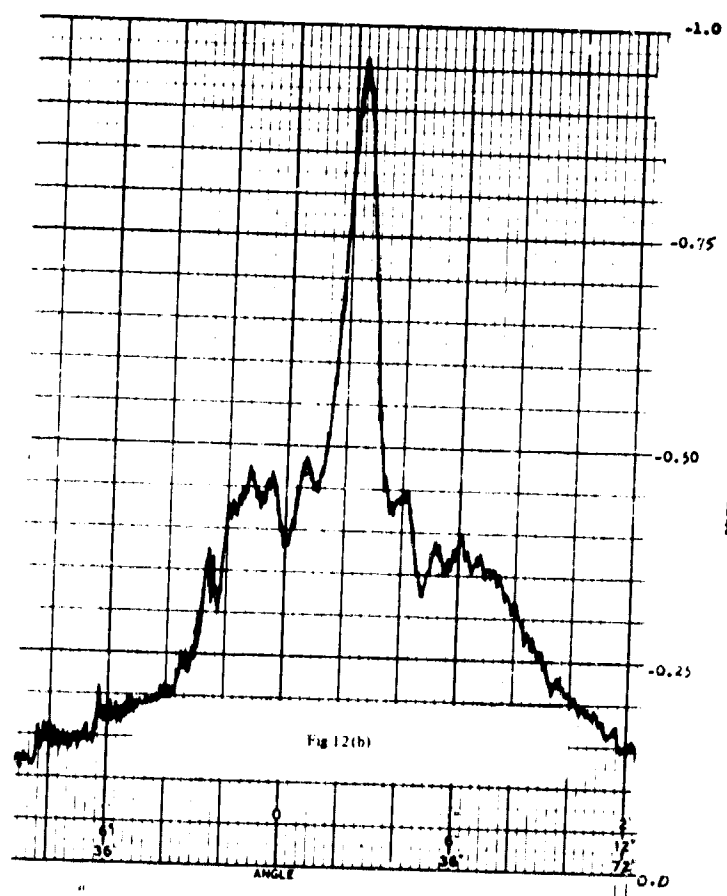
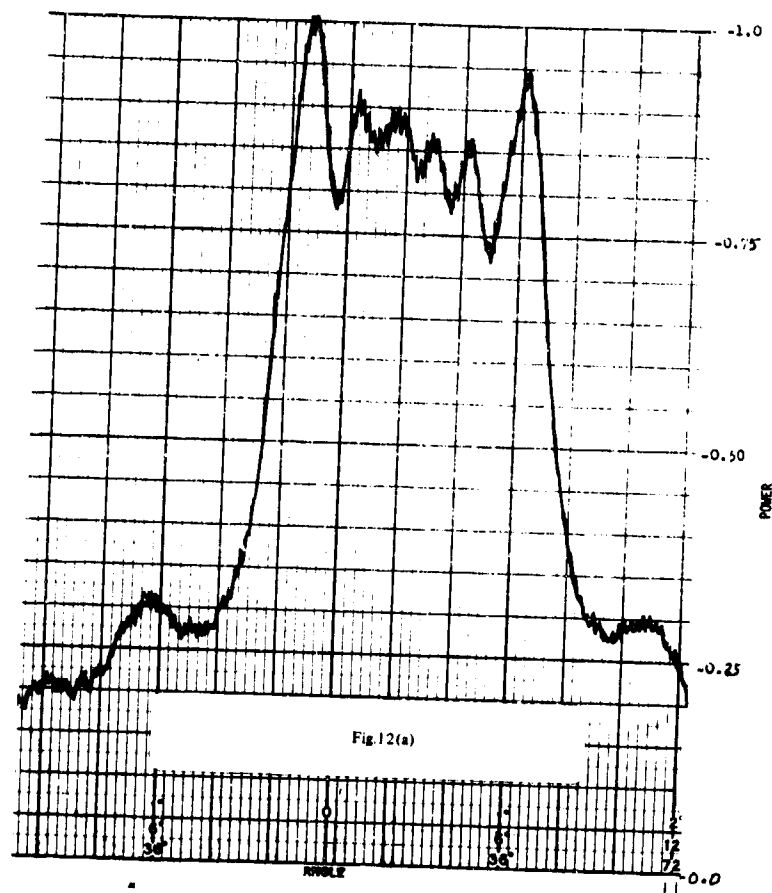


Fig 12 Conical array element patterns, measured, $a = 0.63\lambda$, 0.79λ , azimuth mean radius = 16 wavelengths, $\beta = 20^\circ$



Fig.13 Conical array, 484 waveguide elements, 44×11 , mean radius = 16 wavelength
mean element spacing = 0.6λ , $\beta = 20^\circ$

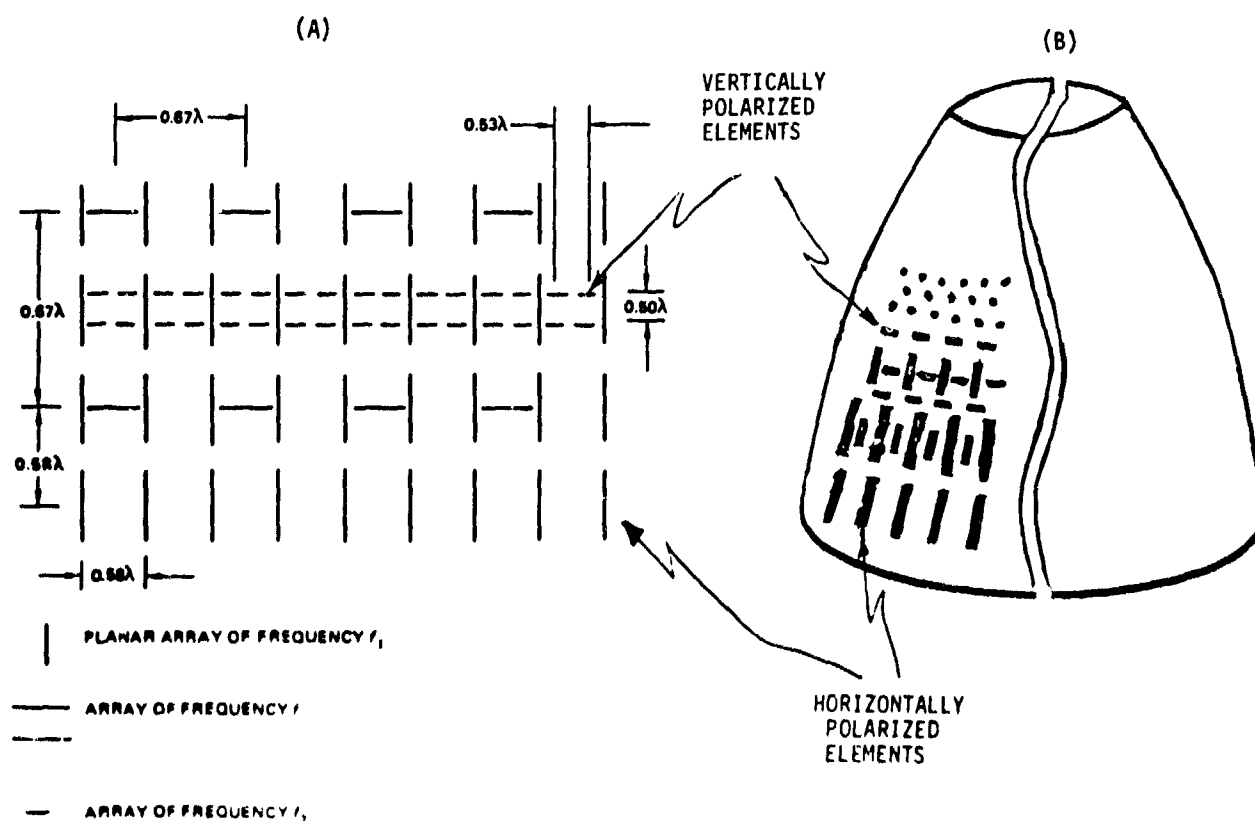


Fig.14 Multifrequency arrays: (A) interlacing elements, (B) non cylindrical configuration

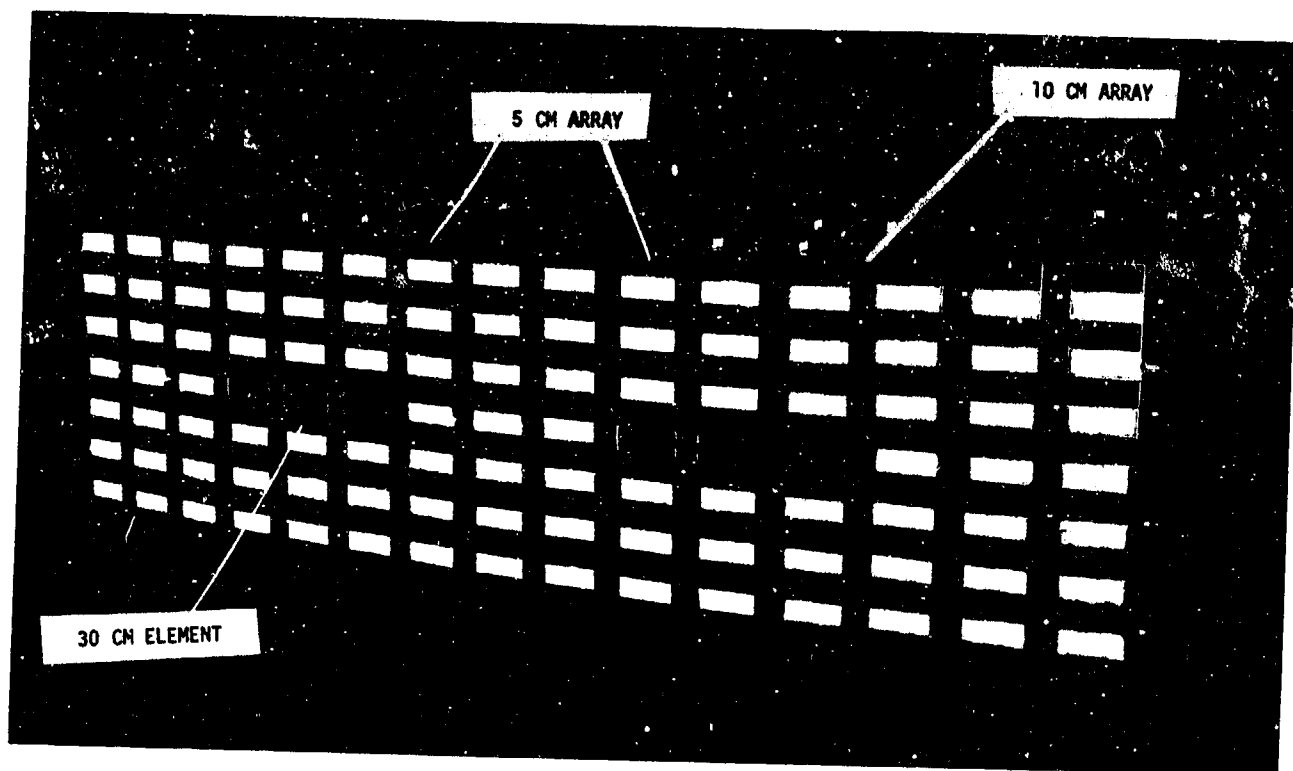


Fig.15 Three band multifrequency array, radius = 26 wavelengths, 30 cm band, 10 cm band, 5 cm band. Interlaced configuration

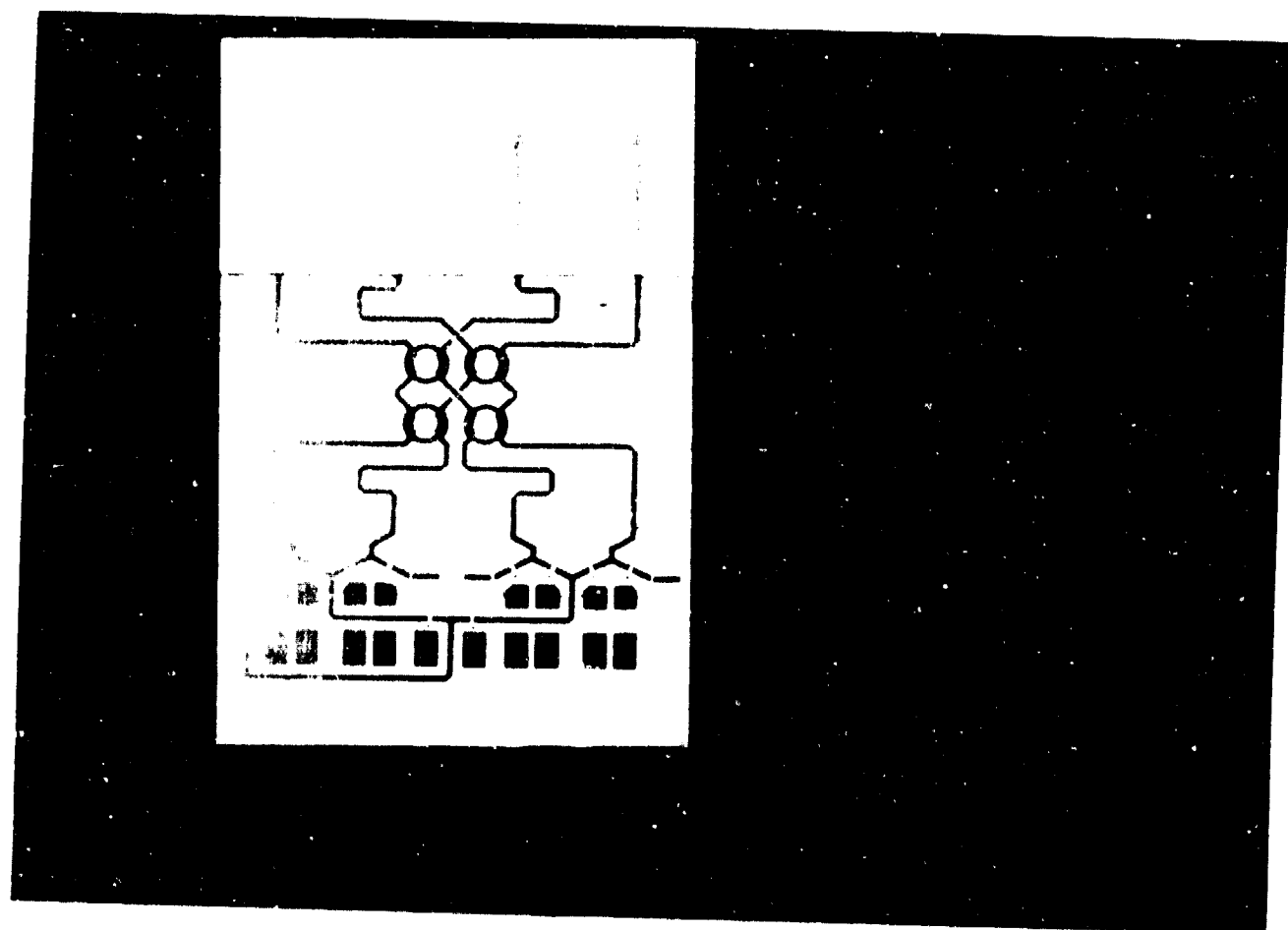


Fig.16 Typical MIC module

DISCUSSION

R.H.J. Gary: Have you considered a choke system to reduce creeping waves? Have you measured cross-polarization on conical arrays? What material and thickness do you use for covering the antenna and will this not have an effect on coupling and performance.

A.D. Munger: 1. No. It might be possible but I think it is better to start with good element design and proper spacing.

2. Yes. We have both measured it and computed it. The cross-polarization varies with Θ -scan angle, and with the percent sector of the array that is activated. For a 60-70 degree arc, I think 15-20 dB is a typical number. The situation is helped somewhat by the fact that the cross-polarizations from the symmetrical halves of the aperture are anti-phased.

3. We have not used nor analysed the effect of a dielectric covering. J.C. Sureau solved this problem for an infinite cylindrical array, I think in a recent I.E.E.E.-GAP issue. Also, a paper later in this conference (J. Vogt (Paper 25)) deals with the problem for finite number of elements on the cylinder.

R. Reitzig: Following up your slides what strikes me is that the element pattern is more strongly deteriorated due to mutual coupling for larger element spacing although I would have expected a decreasing effect of mutual coupling on the element pattern with larger element spacing within the conformal array.

A.D. Munger: If you measure the power coupled by a singly excited element into an adjacent, it is indeed larger for more closely spaced elements. However, it is the effect of the coupling with which we are concerned and this is determined by the phases as well as amplitude of the coupling and the way in which coupling effects from several elements either reinforce or cancel.

To get a feeling for the element pattern behaviour as a function of spacing, we can probably use analogy with a linear or planar array. We know that in a planar array, the scanning is limited when the element spacing is too great due to the grating lobe in invisible space nearing the boundary of real space. The narrowing of the element pattern on the circular array limits the "scan" in the sense that the angular portion that can be excited is reduced to those elements that can contribute to the beam.

G. Borgiotti: The creeping wave approach requires the solution of a very complex transverse resonance equation. This is practically impossible for complicated multimodal elements. The modal approach is the only one leading at the present state of the art to numerically manageable solutions (See for example Borgiotti and Balzano, I.E.E.E. GAP Sept. 1973).

A. Hessel: Professor Borgiotti's point of view is narrow. It is true that the modal analysis is straight forward in the cases when it applies, i.e. in a planar, cylindrical, spherical and conical geometry. But already for spheroidal or paraboloidal surfaces the modal approach breaks down because these geometries are no longer vector (e.g. TE, TM) separable. Even in a separable geometry, i.e., for conical arrays, modal techniques are poorly convergent when the elements are in remote locations from the tip.

To overcome these difficulties, one resorts to the Geometrical Theory of Diffraction which permits handling of mutual coupling in arrays on conducting curved surfaces with large radii of curvature in a non-separable geometry. This method utilizes the guided waves (creeping waves) of the unperforated conducting array surface for calculation of mutual admittance coefficients. The size of the array of multimode elements that can be accommodated in this manner, however, is limited by the maximum size of the mutual admittance matrix that in practice can be inverted on a digital computer.

At this point the "useless" roots of the complex transverse resonance equation become useful. Instead of employing the element by element approach, one considers the variation of curvature of a uniformly spaced conformal array as a perturbation of a cylindrical array with all its elements match-terminated. In this form the mutual coupling takes place via guided waves (creeping waves) of a locally cylindrical match terminated array. These guided waves automatically take into account the presence of the neighbouring elements and the coupling between them. The variation of curvature is then taken into account by using the phase integral method. The method is described in ref. (1) and a paper showing an application of this approach to a conformal array of slits on a parabolic cylinder surface is in preparation.

The difficulties of solution of complex resonance equations are exaggerated by Borgiotti. Since the approximate location of the complex roots is always known the computation problem is not very difficult, providing that, of course, one pays proper attention to the radiation condition.

(1) J. Shapira, L.B. Felsen and A. Hessel: Ray analysis of conformal antenna arrays, to be published in the I.E.E.E. trans. on Antennas and Propagation, Special Issue on Conformal Arrays (to appear Jan. 1974).

PATTERNS AND POLARIZATIONS OF SIMULTANEOUSLY EXCITED PLANAR ARRAYS ON A CONFORMAL SURFACE

by

J. K. Hsiao and A. G. Cha
 Radar Division
 Naval Research Laboratory
 Washington, D. C., USA 20375

SUMMARY

A conformal array on a surface of small curvature can be approximated by a number of planar arrays, several of which may be excited simultaneously so as to achieve a performance similar to that of a conformal array. Since the main beam of a planar array can be steered to any direction in visible space, several arrays, each oriented in a different direction, can be steered cooperatively to form a single beam in a desired direction. A general formulation of the radiated field of such an array of arrays is developed with the aid of formulas which relate the components into which a vector is resolved in one orthogonal coordinate system with those into which the same vector is resolved in a second orthogonal coordinate system. This formulation does not involve the integration of the current source but is solely dependent upon the knowledge of the far field expressions of elementary radiators. Using this formulation, it can be shown that within each array, the conventional row and column phase setting can be used, although each array requires an additional phase shift to compensate for the phase difference caused by its position on the curved surface. As examples, the radiation patterns and polarizations of multiple arrays of short dipoles are studied using the present formulation. A comparison of the multiple planar array with the conventional conformal array is also presented.

I. INTRODUCTION

In recent years, considerable interest has been shown in conformal arrays. This type of array has a variety of potential uses. For example on an airplane or a missile, due to the limitation of available space, it is often difficult to install a large-size conventional antenna. However a conformal array can be fitted onto the surface of part of the vehicle body, and the installation of such a flush-mounted antenna need not interfere with the operation of the vehicle. Furthermore because part of the vehicle body forms the ground plane of the antenna, the electrical interference problem should be minimized. However, in general, conformal arrays suffer several drawbacks. First, the phasing of such arrays is very difficult. Except for a few particular cases, there is no available approach for phasing such an array. Second, the switching of the beam of such an array becomes exceedingly complicated. Moreover, the complexity of the switching network usually introduces very high losses in the system and hence degrades its performance.

It is conceivable that, on a surface of small curvature, one may approximate this conformal array by a number of planar arrays, several of which may be excited simultaneously so as to achieve performance similar to that of a conformal array. Since the main beam of a planar array can be steered to any direction in real space, several planar arrays, each oriented in a different direction, can be steered cooperatively to form a single beam in a desired direction. With such an arrangement, the problem of array phasing is greatly eased. Within each array, the conventional row and column phase setting can be used, although each array requires an additional phase shift to compensate for the phase difference caused by its position on the curved surface. However, this correction is much simpler than that required for a conventional conformal array in which each element requires this compensating phase setting. Furthermore, the switching is greatly simplified as it involves only a few planar arrays as compared to the usual conformal array, in which one must switch radiating power among a large number of elements.

The problem was formulated in an earlier report (Hsiao, J. K., 1972) for multiple planar arrays of vertical dipoles which might be used to approximate a conformal array of vertical dipoles on a cylindrical surface. It was shown that a composite array pattern function can be defined such that the far field is the product of the element radiation pattern and the composite array pattern function. Numerical examples for this kind of composite array were also presented and properties of the far field were discussed. The analysis in the earlier report is strictly valid only when the element pattern of each planar array in the composite array is similarly polarized. The present report deals with the general case where the polarization of the far field of each planar array may be different. The radiation pattern and polarization characteristics are studied again using arrays of short dipoles.

II. SIMULTANEOUSLY EXCITED PLANAR ARRAYS OF ANTENNAS

In analyzing the field of a system of simultaneously excited planar arrays of antennas, it is convenient to write the field expressions in coordinate variables of different coordinate systems. Figures (1) and (2) illustrate these various coordinate systems. Figure (1) shows the position of each planar array relative to the origin of the unprimed coordinate system. Figure 2 shows the lattice structure of the l -th planar array and its radiators. One primed coordinate system is assigned to each planar array, e.g., (x_l, y_l, z_l) for the l -th planar array. One double primed coordinate system is also assigned to the radiators of a planar array, e.g., (x_l', y_l', z_l') for the radiators of the l -th planar array. The primed coordinate systems are useful since the array pattern functions for the planar arrays are known in terms of the primed coordinate variables (θ_l', ϕ_l') . The double primed coordinate systems are useful since the element pattern of the radiators of the l -th planar array may be known in a different coordinate system than the primed coordinates (θ_l', ϕ_l') .

The far field of a system of simultaneously excited planar arrays of antennas may be written, omitting the time phase factor $e^{j\omega t}$, as

$$\vec{E} = \sum_{l=1}^L \vec{E}_l = \sum_{l=1}^L \left\{ \bar{e}_l(\theta_l'', \varphi_l'') \cdot \sum_{m,n} A_{lmn} e^{jk(\bar{R}_l + \bar{R}_{lmn}) \cdot \hat{R}} \right\} \quad (1)$$

where

$$\bar{R}_{lmn}' = m \bar{u}_l'' + N \bar{v}_l' \quad (2)$$

where

L = the number of planar arrays

E_l = the electric field due to the l -th planar array

$\bar{e}_l(\theta_l'', \varphi_l'')$ = the element pattern of the l -th planar array

k = free space wave number

A_{lmn} = complex excitation coefficient of the radiating element at the point $\bar{R}_l + \bar{R}_{lmn}'$

\hat{R} = unit radial vector

In spherical coordinates,

$$\hat{R} = (\sin \theta \cos \varphi, \sin \theta \sin \varphi, \cos \theta) \quad (3)$$

For maximum radiation in a certain direction (θ_0, φ_0) , the conventional row and column phase setting can be used within each array to steer the beam in that direction. In addition to aligning the main beam spatially, one must also be sure that each E_l is in time phase in the direction (θ_0, φ_0) . This condition can be met if

$$A_{lmn} = Q_l Q_{lmn} e^{-jk(\bar{R}_l + \bar{R}_{lmn}) \cdot \hat{R}_0} \quad (4)$$

where

$$\hat{R}_0 = (\sin \theta_0 \cos \varphi_0, \sin \theta_0 \sin \varphi_0, \cos \theta_0) \quad (5)$$

and Q_l and Q_{lmn} are constants to be specified very soon. Substituting (4) in (1),

$$\begin{aligned} \vec{E} &= \sum_{l=1}^L Q_l \bar{e}_l(\theta_l'', \varphi_l'') e^{jk\bar{R}_l \cdot (\hat{R} - \hat{R}_0)} \\ &= \sum_{l=1}^L Q_l \bar{e}_l(\theta_l'', \varphi_l'') e^{jk\bar{R}_l \cdot (\hat{R} - \hat{R}_0)} \left[\sum_{mn} Q_{lmn} e^{jk\bar{R}_{lmn}' \cdot (\hat{R} - \hat{R}_0)} \right] \\ &= \sum_{l=1}^L Q_l \bar{e}_l(\theta_l'', \varphi_l'') e^{jk\bar{R}_l \cdot (\hat{R} - \hat{R}_0)} f_l(\theta_l', \varphi_l') \end{aligned} \quad (6)$$

where

$$f_l(\theta_l', \varphi_l') = \sum_{mn} Q_{lmn} e^{jk\bar{R}_{lmn}' \cdot (\hat{R} - \hat{R}_0)} \quad (7)$$

Note $f_l(\theta_l', \varphi_l')$ is simply the array factor for the l -th planar array phased to have maximum radiation in the direction \hat{R}_0 . The complex constant Q_l 's may be set to certain convenient values that would cancel out any phase differences of the E_l 's in the direction \hat{R}_0 . For instance, Q_l 's may be set in the following way

$$Q_l = (-) \text{ phase of } \left[\bar{e}_l(\theta_l'', \varphi_l'') f_l(\theta_l', \varphi_l') \right] \text{ in the direction } \hat{R}_0 \quad (8)$$

The constant Q_{lmn} is simply the amplitude of the excitation coefficient of the element with the indices l, m, n . Each element pattern $\bar{e}_l(\theta_l'', \varphi_l'')$ is assumed to be known in the form

$$\bar{e}_l(\theta_l'', \varphi_l'') = \bar{e}_{\theta_l''}(\theta_l'', \varphi_l'') \hat{\theta}_l'' + \bar{e}_{\varphi_l''}(\theta_l'', \varphi_l'') \hat{\varphi}_l'' \quad (9)$$

Two problems would have to be solved before Eq. (6) can be used. First, one must decompose each set of unit vectors $(\hat{\theta}_l'', \hat{\varphi}_l'')$ in terms of the unit vectors $\hat{\theta}$ and $\hat{\varphi}$ in order to perform the vector addition of the fields \bar{E}_l 's. Second, the double primed and primed coordinate variables $\theta_l'', \varphi_l'', \theta_l', \varphi_l'$ etc. must be expressed as functions of the unprimed coordinate variables θ and φ .

III. TRANSFORMATIONS OF COORDINATE SYSTEMS

The problem of coordinates transformation is in expressing a vector function \bar{V} known in the primed coordinate variables and unit vectors in terms of the unprimed coordinate variables and unit vectors. That is, \bar{V} is known in the form

$$\bar{V} = V_{\theta'} (\theta', \varphi') \hat{\theta}' + V_{\varphi'} (\theta', \varphi') \hat{\varphi}' \quad (10)$$

where $V_{\theta'}$ and $V_{\varphi'}$ denote two functions of θ' and φ' .

We are interested in finding \bar{V} in the form

$$\bar{V} = V_{\theta} (\theta, \varphi) \hat{\theta} + V_{\varphi} (\theta, \varphi) \hat{\varphi} \quad (11)$$

where V_{θ} and V_{φ} denote two functions of θ and φ . Note we have confined ourselves to the discussion of radiation fields. Thus, the vector has no radial component and is independent of the radius variable R .

In the following paragraphs, we will be dealing with a class of matrices known as real orthogonal matrices. These matrices transform a vector from one orthogonal coordinate system to a second orthogonal coordinate system in the three dimensional Euclidean space. That is, if (α, β, γ) and $(\alpha', \beta', \gamma')$ are the two sets of unit vectors of two orthogonal coordinate systems, then the components of a vector \bar{V} in the two coordinate systems are related by an orthogonal matrix $|D|$,

$$|V| = |D| \cdot |V'| \quad (12)$$

where $|V|$ and $|V'|$ are the column matrix representations of the vector \bar{V} in the two coordinate systems,

$$|V| = \begin{pmatrix} V_{\alpha} \\ V_{\beta} \\ V_{\gamma} \end{pmatrix} \quad (13)$$

$$|V'| = \begin{pmatrix} V_{\alpha'} \\ V_{\beta'} \\ V_{\gamma'} \end{pmatrix} \quad (14)$$

Real orthogonal matrices have two useful properties. First, the inverse $|D|^{-1}$ of a real orthogonal matrix $|D|$ is the transpose $|D|^T$ of $|D|$, or

$$|D|^{-1} = |D|^T \quad (15)$$

Second, the product of real orthogonal matrices is a real orthogonal matrix. These properties will be utilized in later discussions.

Coordinate transformations involve either a linear translation or a change of orientation of the coordinate system. Refer to Fig. 1. The only translations involved in the present problem are in moving the origins of the primed coordinate systems back to the common reference point, the origin of the unprimed coordinates. For the far field, the only effect of this translation is in introducing the phase factor $e^{jkR_0} (R - R_0)$ in Eq. (6). The functional dependence of a field vector \bar{V} on the coordinate variables and unit vectors is not altered by coordinate translations. This is illustrated in Fig. 3 where, for clarity, the translation \bar{R}_0 between the two coordinate systems is assumed to be in the x-y plane. Let P be the field observation point, then it can be seen if the field point P is truly at infinity, one would have

$$\begin{cases} R' = R - \bar{R}' \cdot \hat{R} \\ \theta' = \theta \\ \varphi' = \varphi \end{cases} \quad (16)$$

and

$$\begin{cases} \hat{R}' = \hat{R} \\ \hat{\theta}' = \hat{\theta} \\ \hat{\varphi}' = \hat{\varphi} \end{cases} \quad (17)$$

The field vector \bar{V} in terms of $\theta, \varphi, \hat{\theta}, \hat{\varphi}$ can be obtained by substitution of (16) and (17) in (10). Since \bar{V} is independent of R' , it is obvious that the functions V_{θ} and V_{φ} in (11) are identical to the functions $V_{\theta'}$ and $V_{\varphi'}$ on (10). For example, the radiation field of a short dipole, lying along the z' -axis and at the origin of the primed coordinate system in Fig. 3, is given by

$$\bar{E} = E_0 (t, R') \sin \theta' \hat{\theta}' \quad (18)$$

$$E_0(t, R') = \frac{j\omega I S e^{j\omega(t - \frac{R'}{C})}}{4\pi\epsilon_0 C^2 R'}$$

where I and S are the current and length of the dipole.

(19)

Substituting (16), (17) in (18), (19) and using the far field approximation $R' = R$ for the denominator of (19),

$$\vec{E} = \left[E_0(t, R) \sin \theta \hat{\theta} \right] e^{jk\vec{R} \cdot \vec{R}} \quad (20)$$

Note the factor inside the square bracket of (20) has an identical form as that of (18).

From the above discussion, we conclude that with the inclusion of the exponential factor $e^{jk\vec{R} \cdot \vec{R}}$, the translation \vec{R}_0 has no other effect on Eq. (6) and will be ignored in later discussions.

The second transformation is one in which the orientation of the coordinate system is changed. The transformation formula has been set up in classical mechanics problems using matrices. Three independent parameters are needed to specify the orientation of a rigid body. These are known as Eulerian angles. The transformation is described by the three angles as explained in the following paragraphs.

The change of the orientation of the coordinate system is accomplished by three successive rotations about the three coordinate axes. These rotations are shown in Fig. 4. The first rotation is for an angle ξ_y about the y-axis. The orthogonal matrix between the primed and the unprimed coordinate systems for this rotation is

$$|A| = \begin{vmatrix} \cos \xi_y & 0 & \sin \xi_y \\ 0 & 1 & 0 \\ -\sin \xi_y & 0 & \cos \xi_y \end{vmatrix} \quad (21)$$

The second rotation is for an angle ξ_z about the z-axis. The orthogonal matrix for this rotation is

$$|B| = \begin{vmatrix} \cos \xi_z & -\sin \xi_z & 0 \\ \sin \xi_z & \cos \xi_z & 0 \\ 0 & 0 & 1 \end{vmatrix} \quad (22)$$

The third rotation is for an angle ξ_x about the x-axis.

$$|C| = \begin{vmatrix} 1 & 0 & 0 \\ 0 & \cos \xi_x & -\sin \xi_x \\ 0 & \sin \xi_x & \cos \xi_x \end{vmatrix} \quad (23)$$

In all three rotations the angle of rotation is positive when the rotation is counterclockwise with respect to the axis of rotation. The overall transformation may be written as

$$|D| = |C| |B| |A|. \quad (24)$$

One should note here that the order of matrix multiplication is not commutative; thus the sequence of these transformations is not interchangeable.

Note the matrices $|A|$, $|B|$, $|C|$, $|D|$ are real orthogonal. Thus

$$|D|^{-1} = |D|^T \quad (25)$$

Multiplying Eq. (12) by $|D|^{-1}$, one obtains

$$|V'| = |D|^{-1} \cdot |V| \quad (26)$$

Using $|D|$ and $|D|^T$, a vector decomposed in one rectangular coordinate system may be re-decomposed in a different rectangular coordinate system. To treat radiation fields, however, one would also have to deal with components in spherical coordinates. The spherical coordinate components and the rectangular coordinate components of a vector are also related by real orthogonal matrices.

$$\begin{vmatrix} V_r \\ V_\theta \\ V_\phi \end{vmatrix} = |D_{RP}| \cdot \begin{vmatrix} V_x \\ V_y \\ V_z \end{vmatrix} \quad (27)$$

$$\begin{vmatrix} v_x \\ v_y \\ v_z \end{vmatrix} = |D_{PR}| \begin{vmatrix} v_r \\ v_\theta \\ v_\varphi \end{vmatrix} \quad (28)$$

where

$$|D_{PR}| = \begin{vmatrix} \sin \theta \cos \varphi & \cos \theta \cos \varphi & -\sin \varphi \\ \sin \theta \sin \varphi & \cos \theta \sin \varphi & \cos \varphi \\ \cos \theta & -\sin \theta & 0 \end{vmatrix} \quad (29)$$

$$|D_{RP}| = |D_{PR}|^{-1} = |D_{PR}|^T \quad (30)$$

Substituting (27), (28) in (12), and if \bar{V} is the radiation field in (10), we obtain

$$\begin{vmatrix} v_R \\ v_\theta \\ v_\varphi \end{vmatrix} = |D_{RP}| \cdot |D| \cdot |D'_{PR}| \cdot \begin{vmatrix} 0 \\ v_{\theta'}(\theta', \varphi') \\ v_{\varphi'}(\theta', \varphi') \end{vmatrix} \quad (31)$$

where $|D'_{PR}|$ is given by Eq. (29), with (θ', φ') replacing (θ, φ) . It is used since the first transformation is from the primed polar coordinates to the primed rectangular coordinates. Equations (6) and (7) can now be rewritten in the matrix form with the aid of (31) and (12) respectively,

$$\begin{vmatrix} E_R(\theta, \varphi) \\ E_\theta(\theta, \varphi) \\ E_\varphi(\theta, \varphi) \end{vmatrix} = \sum_{\ell} a_{\ell} e^{jk\bar{R}_{\ell} \cdot (\hat{R} - \hat{R}_0)} f_{\ell}(\theta_{\ell}, \varphi_{\ell}) |D_{2\ell}| |D'_{PR}| \begin{vmatrix} 0 \\ e''_{\theta\ell}(\theta''_{\ell}, \varphi''_{\ell}) \\ e''_{\varphi\ell}(\theta''_{\ell}, \varphi''_{\ell}) \end{vmatrix} \quad (32)$$

$$f_{\ell}(\theta_{\ell}, \varphi_{\ell}) = \sum_{mn} a_{mn} e^{jk(|D_{1\ell}| \cdot |\bar{R}'_{\ell mn}|) \cdot (\hat{R} - \hat{R}_0)} \quad (33)$$

where $|\bar{R}'_{\ell mn}|$ is the matrix of $R'_{\ell mn}$ in $(x_{\ell}, y_{\ell}, z_{\ell})$ coordinates. The matrix $D_{2\ell}$ is the transformation matrix from $(x'_{\ell}, y'_{\ell}, z'_{\ell})$ to (x, y, z) and $D_{1\ell}$ is the transformation matrix from $(x_{\ell}, y_{\ell}, z_{\ell})$ to (x, y, z) . Equations (32) and (33) give the formal solution of the radiation field of multiple planar arrays, assuming the double primed and primed coordinate variables $\theta''_{\ell}, \varphi''_{\ell}, \theta'_{\ell}, \varphi'_{\ell}$, etc are functions of the unprimed polar coordinate variables θ and φ .

Next, we consider relations between coordinate variables under coordinate transformations. The relations between rectangular coordinate variables are obtained by substituting the position vector \bar{R} for the vector \bar{V} in (26).

$$|R'| = |D|^{-1} |R| \quad (34)$$

where

$$|R'| = \begin{vmatrix} x' \\ y' \\ z' \end{vmatrix} \quad (35)$$

$$|R| = \begin{vmatrix} x \\ y \\ z \end{vmatrix} \quad (36)$$

The relations between polar coordinate variables are found by substituting

$$\begin{vmatrix} x \\ y \\ z \end{vmatrix} = \begin{vmatrix} \sin \theta \cos \varphi \\ \sin \theta \sin \varphi \\ \cos \theta \end{vmatrix} \quad (37)$$

and

$$\begin{vmatrix} x' \\ y' \\ z' \end{vmatrix} = \begin{vmatrix} \sin \theta' \cos \varphi' \\ \sin \theta' \sin \varphi' \\ \cos \theta' \end{vmatrix} \quad (38)$$

in (34) and solving for θ' and φ' .

Using the three Eulerian angles, it can be shown that

$$\theta' = \cos^{-1} Z'(\theta, \varphi) \quad (39)$$

$$\varphi' = \tan^{-1} \frac{Y'(\theta, \varphi)}{X'(\theta, \varphi)} \quad (40)$$

$$X'(\theta, \varphi) = \sin \theta \cos \varphi \cos \xi_y \cos \xi_z + \sin \theta \sin \varphi \sin \xi_z + \cos \theta \sin \xi_y \cos \xi_z \quad (41)$$

$$Y'(\theta, \varphi) = -\sin \theta \cos \varphi (\cos \xi_y \sin \xi_z \cos \xi_x + \sin \xi_y \sin \xi_x) + \sin \theta \sin \varphi \cos \xi_z \cos \xi_x - \cos \theta (\sin \xi_y \sin \xi_z \cos \xi_x - \cos \xi_y \sin \xi_x) \quad (42)$$

$$Z'(\theta, \varphi) = \sin \theta \cos \varphi (\cos \xi_y \sin \xi_z \sin \xi_x - \sin \xi_y \cos \xi_x) - \sin \theta \sin \varphi \cos \xi_z \sin \xi_x + \cos \theta (\sin \xi_y \sin \xi_z \sin \xi_x + \cos \xi_y \cos \xi_x) \quad (43)$$

The ambiguity in the value of the arc tangent function in Eq. (40) is resolved by applying the same set of rules that one uses to determine the value of $\tan^{-1}(y/x)$ where x and y are the rectangular coordinate variables.

IV. THE RADIATION FIELD OF A HORIZONTAL SHORT DIPOLE

In Fig. 5a, let z be the elevation axis, then the dipole lying along the x -axis may be referred to as a horizontal dipole. The far field of a dipole is commonly known in the coordinate system in Fig. 5b and is given by Eqs. (18) and (19). The far field of the horizontal dipole may be obtained from Eq. (18) using coordinate transformation formulas. The primed rectangular coordinate system in Fig. 5b is obtained from the unprimed rectangular coordinate system in Fig. 5a by a simple rotation of -90 degrees about the y -axis. From (21), using the Eulerian parameter $\xi_y = 90$ degrees,

$$|D| = |A| = \begin{vmatrix} 0 & 0 & 1 \\ 0 & 1 & 0 \\ -1 & 0 & 0 \end{vmatrix} \quad (44)$$

The relations between the rectangular coordinate variables are from (34)

$$\begin{aligned} x' &= -z \\ y' &= y \\ z' &= x \end{aligned} \quad (45)$$

The relations between the polar coordinate variables can be obtained from (45).

$$\begin{aligned} \cos \theta' &= \frac{z'}{R'} = \frac{x}{R} = \sin \theta \cos \varphi \\ \sin \theta' &= \sqrt{1 - \sin^2 \theta \cos^2 \varphi} \\ \cos \varphi' &= \frac{x'}{R' \sin \theta'} = \frac{-\cos \theta}{\sqrt{1 - \sin^2 \theta \cos^2 \varphi}} \\ \sin \varphi' &= \frac{y'}{R' \sin \theta'} = \frac{\sin \theta \sin \varphi}{\sqrt{1 - \sin^2 \theta \cos^2 \varphi}} \end{aligned} \quad (46)$$

The matrix form for \vec{E} in the primed polar coordinates is

$$\begin{vmatrix} E_{r'} \\ E_{\theta'} \\ E_{\varphi'} \end{vmatrix} = \begin{vmatrix} 0 \\ E_0(t) \sin \theta' \\ 0 \end{vmatrix} \quad (47)$$

Carrying out the successive matrix multiplication in (31) using (29), (30), (44), (47)

$$\begin{vmatrix} E_r \\ E_\theta \\ E_\varphi \end{vmatrix} = \begin{vmatrix} -\sin \theta \cos \varphi \sin \theta' + \sin \theta \sin \varphi \cos \theta' \sin \varphi' - \cos \theta \cos \theta' \cos \varphi' \\ -\cos \theta \cos \varphi \sin \theta' + \cos \theta \sin \varphi \cos \theta' \sin \varphi' + \sin \theta \cos \theta' \cos \varphi' \\ \sin \varphi \sin \theta' + \cos \varphi \cos \theta' \sin \varphi' \end{vmatrix} \quad (48)$$

If we now substitute (46) in the above expression to get rid of the primed coordinate variables, we obtain

$$\begin{vmatrix} E_r \\ E_\theta \\ E_\varphi \end{vmatrix} = \begin{vmatrix} 0 \\ -E_0(t) \cos \theta \cos \varphi \\ E_0(t) \sin \varphi \end{vmatrix} \quad (49)$$

or

$$\vec{E} = E_0(t) (-\cos \theta \cos \varphi \hat{\theta} + \sin \varphi \hat{\varphi}) \quad (50)$$

V. PLANAR ARRAYS OF SHORT DIPOLES

In this section, we will consider using planar arrays of short dipoles to approximate a confor-mal array of short dipoles on a cylindrical surface. The geometry of the problem is shown in Fig. 1. The elements of the l -th array are symmetrically placed about the reference point θ_l . The elements are short dipoles either in the direction of x_l -axis or z_l -axis of Fig. 2. Using the element pattern functions in (50) and (18), the double primed coordinates are obviously the same and the primed coordinates for both these cases. The Eulerian parameters between the (x, y, z) coordinates and the (x_l, y_l, z_l) coordinates are $\xi_{xl} = 0$, $\xi_{yl} = 0$, $\xi_{zl} = -[(l-1)\frac{2\pi}{L} + \frac{\pi}{2}]$.

$$|D| = \begin{vmatrix} \cos \xi_{zl} & -\sin \xi_{zl} & 0 \\ \sin \xi_{zl} & \cos \xi_{zl} & 0 \\ 0 & 0 & 1 \end{vmatrix} \quad (51)$$

It is easy to see that, for this simple rotation, the following relations hold for any far field expressions.

$$\begin{aligned} \theta_l' &= \theta \\ \varphi_l' &= \varphi - \xi_{zl} \\ \hat{\theta}_l' &= \hat{\theta} \\ \hat{\varphi}_l' &= \hat{\varphi} \end{aligned} \quad (53)$$

Since the vectors $\hat{\theta}_l'$ and $\hat{\varphi}_l'$ are identical to $\hat{\theta}$ and $\hat{\varphi}$, one can use Eq. (6) in place of Eq. (32) for the vector addition process. Thus

$$\vec{E} = \sum_l \alpha_l [\epsilon_{\theta\theta}(\theta_l', \varphi_l') \hat{\theta}_l' + \epsilon_{\theta\varphi}(\theta_l', \varphi_l') \hat{\varphi}_l'] e^{jk\vec{R}_l \cdot (\vec{R} - \vec{R}_0)} \cdot \epsilon_l(\theta_l', \varphi_l') \quad (54)$$

The excitation coefficients are assumed to have uniform magnitude of one. The array pattern function $f_l(\theta, \varphi)$ is obtained from Eq. (33) as

$$f_l(\theta, \varphi) = \sum_{m=-M}^M \sum_{n=-N}^N e^{jk(|D|^T \cdot |\vec{R}'_{lmn}|) \cdot |\vec{R} - \vec{R}_0|} \quad (55)$$

where

$$|\vec{R}'_{lmn}| = \begin{vmatrix} m d_x \\ 0 \\ n d_z \end{vmatrix} \quad (56)$$

Carrying out the matrix multiplication and rearranging terms, it can be shown

$$f_l(\theta, \varphi) = f_{xl}(\theta, \varphi) f_{zl}(\theta, \varphi) \quad (57)$$

where

$$f_{xl}(\theta, \varphi) = 1 + 2 \sum_{m=1}^M \cos m k d_x [\sin \theta \cos (\varphi - \xi_{zl}) - \sin \theta_0 \cos (\varphi_0 - \xi_{zl})] \quad (58)$$

$$f_{zl}(\theta, \varphi) = 1 + 2 \sum_{n=1}^N \cos n k d_z (\cos \theta - \cos \theta_0) \quad (59)$$

Substituting (18), (52), (53) in (54), the radiation field for a system of planar arrays of vertical short dipoles is

$$\vec{E} = E_0(t) \sin \theta \left[\sum_{l=1}^L e^{jk\vec{R}_l \cdot (\vec{R} - \vec{R}_0)} f_l(\theta_l, \varphi_l) \right] \hat{\theta} \quad (60)$$

Substituting (50), (52), (53) in (54), the radiation field of planar arrays of horizontal dipoles is

$$\begin{aligned} E = E_0(t) & \left[\sum_l \left[1 - \cos \theta \cos (\varphi - \varphi_{zl}) \right] e^{jk\vec{R}_l \cdot (\vec{R} - \vec{R}_0)} f_l(\theta, \varphi) \right] \hat{\theta} \\ & + E_0(t) \left[\sum_l \sin (\varphi - \varphi_{zl}) e^{jk\vec{R}_l \cdot (\vec{R} - \vec{R}_0)} f_l(\theta, \varphi) \right] \hat{\varphi} \end{aligned} \quad (61)$$

In obtaining both (60) and (61), the complex constants Q_l in (6) were set equal to one.

VI. NUMERICAL CALCULATIONS

For the multiple planar arrays of vertical dipoles, one can define a composite array function $A(\theta, \varphi)$.

$$A(\theta, \varphi) = \sum_{l=1}^L e^{jk\vec{R}_l \cdot (\vec{R} - \vec{R}_0)} f_l(\theta_l, \varphi_l) \quad (62)$$

The radiation field is then, from (60),

$$\vec{E} = [E_0(t) \sin \theta \hat{\theta}] A(\theta, \varphi) \quad (63)$$

This composite array function was calculated for different parameters in an earlier report (Hsiao, J. K., 1972).

In the case of multiple planar arrays of horizontal dipoles, the far field can not be factored into the product of an array function and an element pattern function, as can be seen from Eq. (61). This is characteristic of multiple planar arrays where the element polarization differs from one array to another. The radiation pattern and the polarization of the multiple planar arrays shown in Fig. 1 were calculated for both cases. Each planar array is assumed to be a linear array in the direction of the x'_l -axis. In one case, the elements of the arrays are short dipoles lying parallel to the z -axis and Eq. (62) was used to calculate the array pattern function of the composite array. In another case, the elements of the arrays are short dipoles lying parallel to the x'_l -axis of each array and the far field components E_θ and E_φ were calculated using Eq. (61). Note if there are more than two elements along the z' -axis, the only modification to the present calculation would be to multiply the radiation field by the factor $f_{zl}(\theta, \varphi)$ in Eq. (54). It is obvious that $f_{zl}(\theta, \varphi)$ is simply the array factor of a linear array in the direction of the z -axis.

The following parameters were used:

Aperture length along x'_l -axis - 10λ

Element spacing = 0.4λ

Number of elements of each array = 23

$(\theta_0, \varphi_0) = (90^\circ, 0^\circ)$

Note there is no element at either end of each aperture. Figure 6 shows the array pattern function vs. the angle φ in the x - y plane for multiple arrays of vertical dipoles when the planar arrays 1, 2 and 3 in Fig. 1 are excited simultaneously. Figure 7a shows E_φ vs. the angle φ in the x - y plane when only the planar array No. 2 is active. Figure 7b shows the same when the three planar arrays 1, 2 and 3 are active. Note the improvement in the directivity of the composite array by having three active planar arrays as compared with just one active array. The half power beamwidth is about 6° in Fig. 7a and about 2° in Fig. 7b. The more interesting comparison is between Fig. 7b and Fig. 7c, which shows E_φ vs. φ in the x - y plane for a conformal array of 76 equally spaced horizontal, tangential, short dipoles on the arc ABCD (Fig. 1). In both Figs. 7b and 7c, the half power beamwidth is two degrees and the side-lobe level is -13 dB. Patterns were also calculated for the conformal array and the multiple planar arrays for scanning angles $\varphi_0 = 10^\circ, 20^\circ, 30^\circ$ in the x - y plane. In all instances, the beamwidth and the side-lobe level are the same as in Figs. 7b and 7c. It is, therefore, concluded that the performance of a conformal array on a cylindrical surface can be closely matched by a small number of multiple planar arrays, having roughly the same total number of elements and occupying roughly the same space.

So far, we have ignored the other component E_θ . This is because $E_\theta = 0$ in the x - y plane ($\theta = 90^\circ$), as can be seen from Eq. (61). The far field is thus horizontally polarized in the x - y plane. The cross polarized component E_θ becomes more important at large elevation angles (smaller θ). It can also be seen from Eq. (61) that E_θ is always in phase with E_φ if $f_l(\theta, \varphi)$ is real, or if each planar array is symmetrically excited relative to the array center element. The exact value of the cross polarized field E_θ depends on $\theta, \varphi, \theta_0$ and φ_0 for a given composite array and can be calculated from Eq. (61). For example, Fig. 8 shows the two components E_θ and E_φ on the conical surface $\theta = 80^\circ$ for the multiple planar arrays used in calculating Fig. 7b.

VII. CONCLUSIONS

It has been demonstrated that the radiation characteristics of a conformal array on a cylindrical surface can be closely matched by a number of planar arrays approximating the cylindrical surface. It is expected that the same technique will be applicable to many other types of conformal surfaces. The phase setting and switching problems of the multiple planar arrays are considerably simpler than those encountered with the conventional conformal array. As a result, the multiple planar arrays would have less complicated switching network and lower losses than a conventional conformal array. It is also worth noting that the present formulation based on vector decomposition also provides a very efficient numeric algorithm for calculating the far field of many complex radiating structures. Using this approach, the structures are broken down into pieces and are treated as arrays of elementary radiators. The computation efficiency of the present approach results from making use of known pattern functions of elementary sources. In this way, the time-consuming numerical integrations and differentiations that one normally encounters in far field calculations are greatly alleviated.

REFERENCES

- [1] J. K. Hsiao, "Approximation of a Conformal Array with Multiple Simultaneously Excited Planar Arrays," NRL Report 7442, July 1972.
- [2] H. Goldstein, *Classical Mechanics*, Ch. 4, Cambridge, Mass., Addison-Wesley, 1950, pp. 93-142.
- [3] R. C. Hansen, editor, *Microwave Scanning Antennas*, Vol. 2, New York, Academic Press, 1966.
- [4] H. L. Knudsen, "Radiation from Ring Quasi-Arrays," IRE Trans. Antennas Propagation AP-4, 452-472 (July 1956).
- [5] W. W. Lee and Y. T. Lo, "On the Pattern Function of Circular Arc Arrays," IEEE Trans. Antennas Propagation AP-13, 649-650 (July 1965).

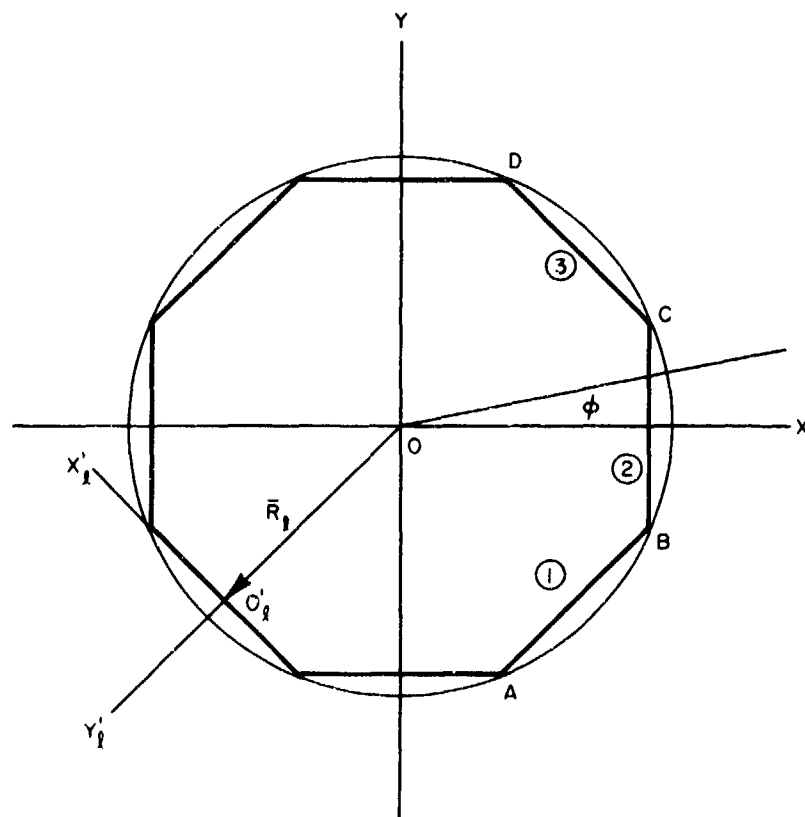


Figure 1. Geometry of multiple planar arrays of antennas.

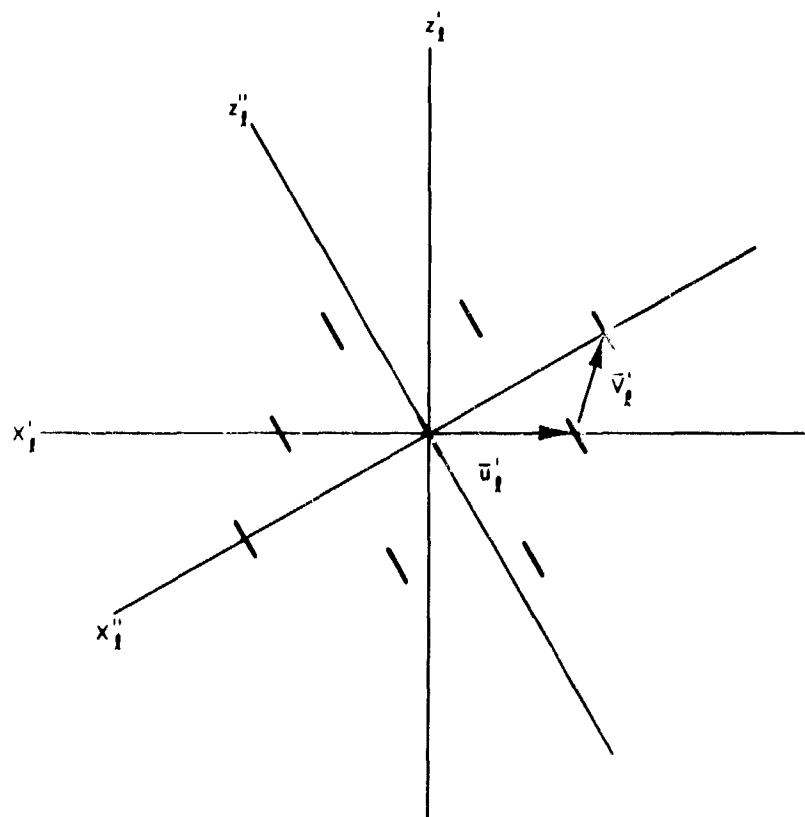


Figure 2. A planar array of short dipoles.

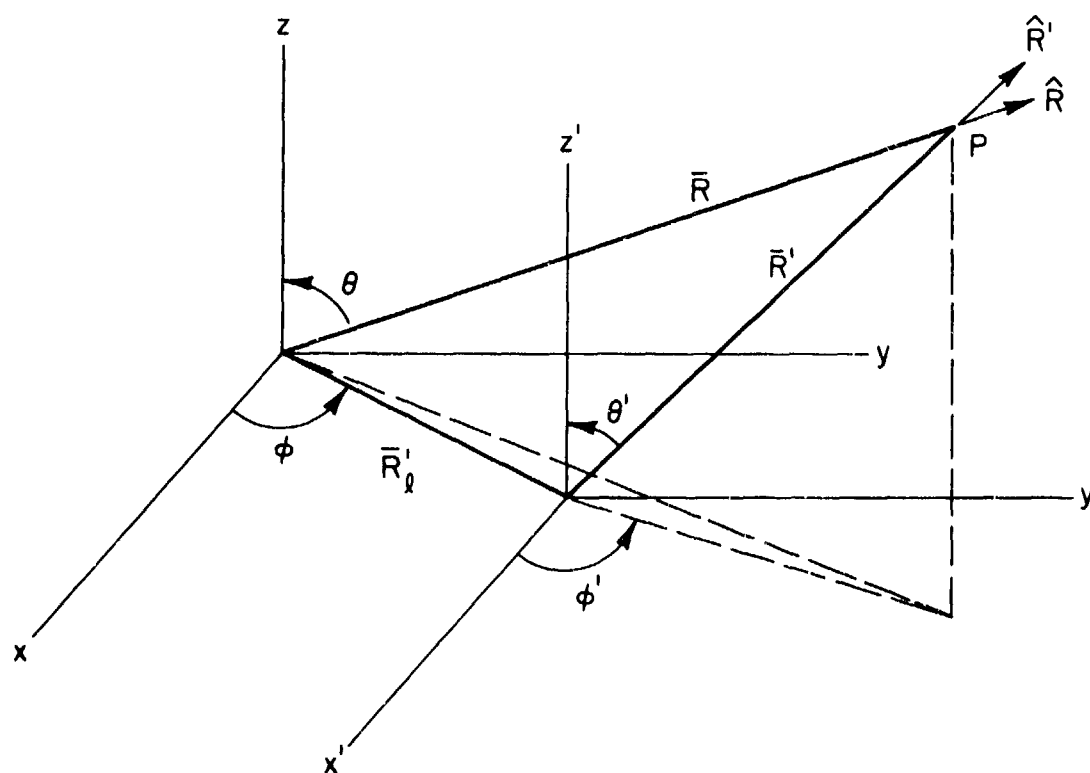
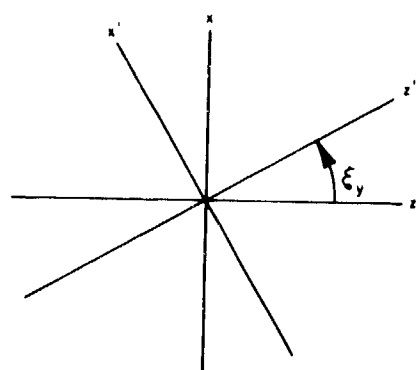
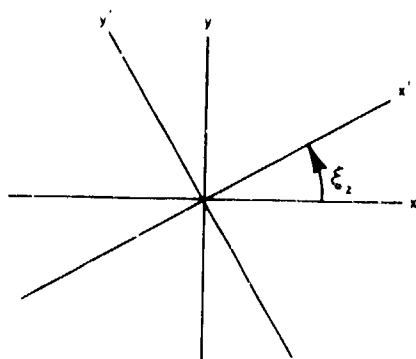


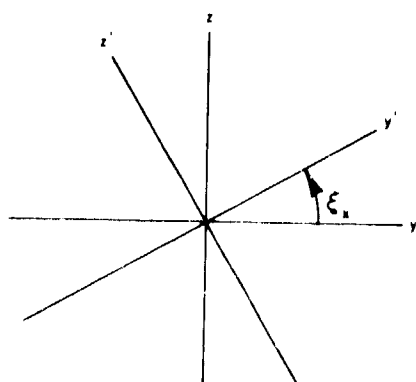
Figure 3. Translation of a coordinate system.



(a)

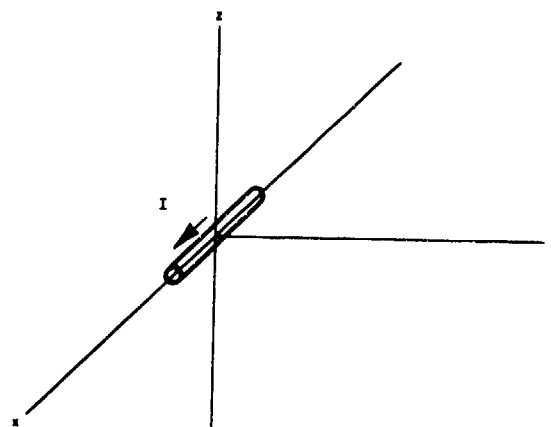


(b)

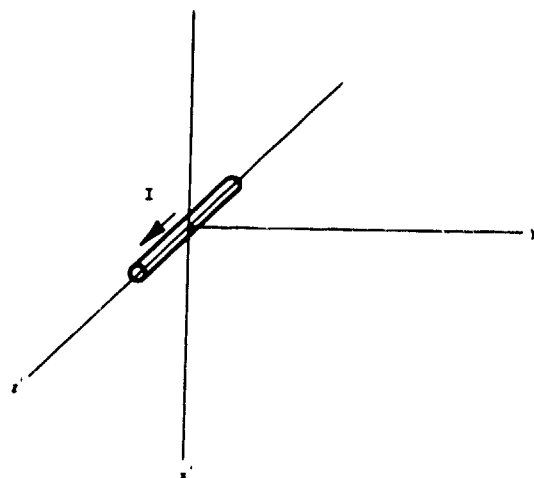


(c)

Figure 4. Rotations of coordinate systems.



(a)



(b)

Figure 5. A short dipole in two coordinate systems.

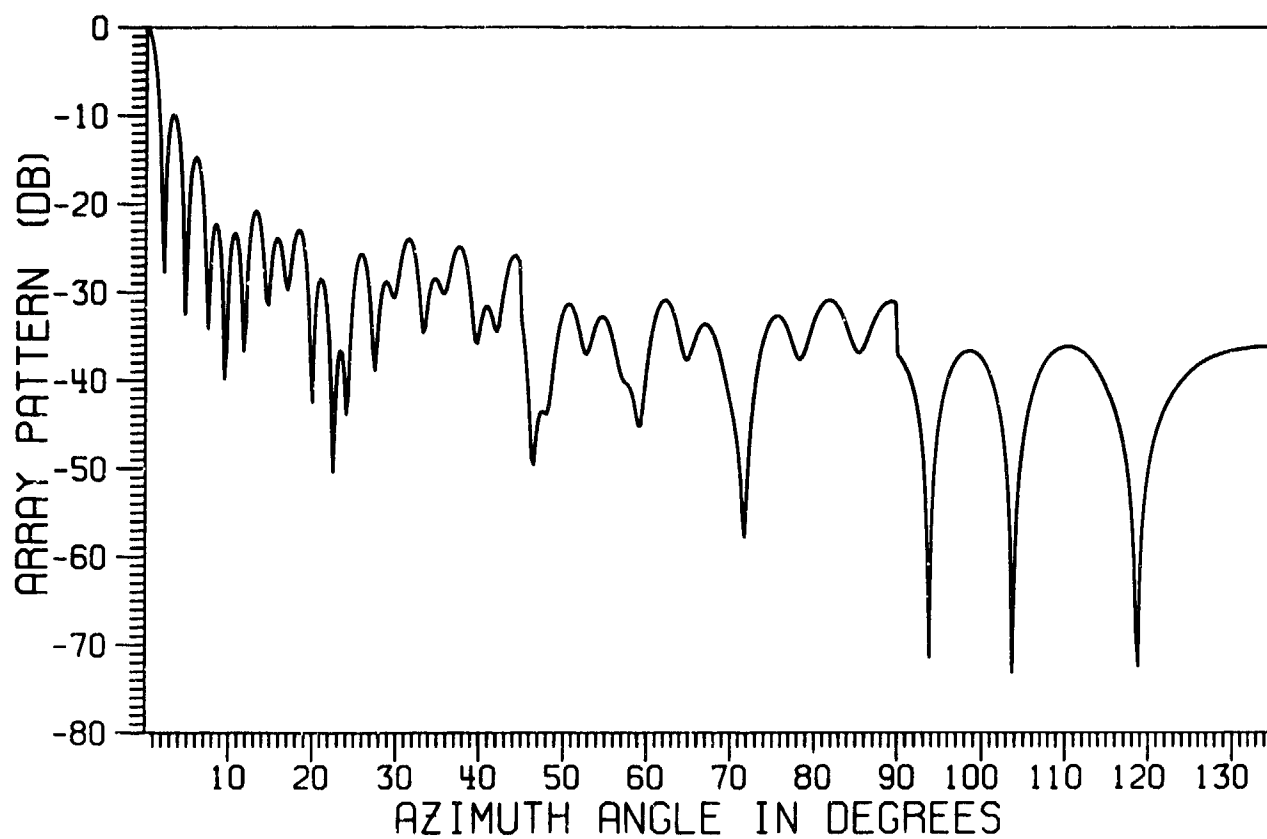


Figure 6. Composite array pattern function for the multiple arrays of Fig. 1, vertical dipole case.

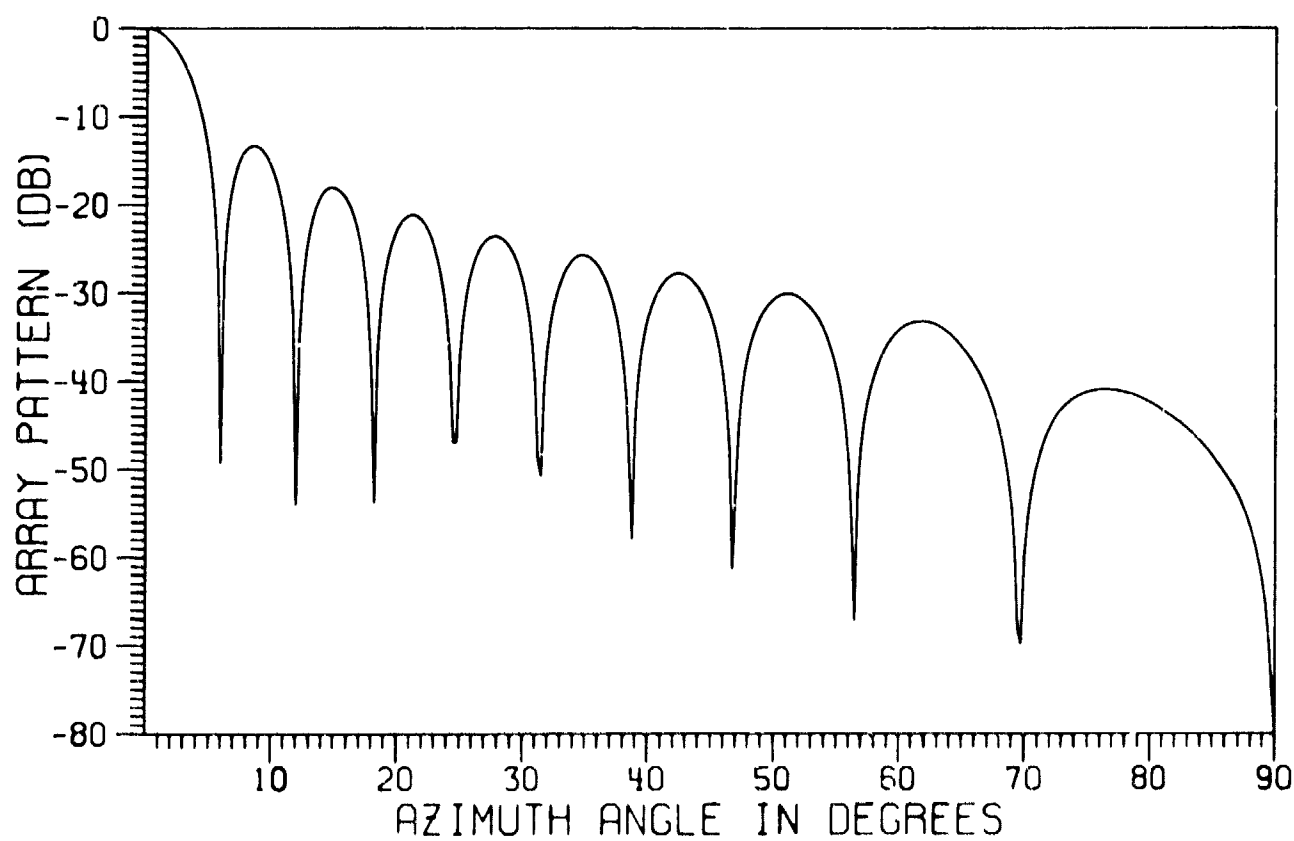


Figure 7(a)

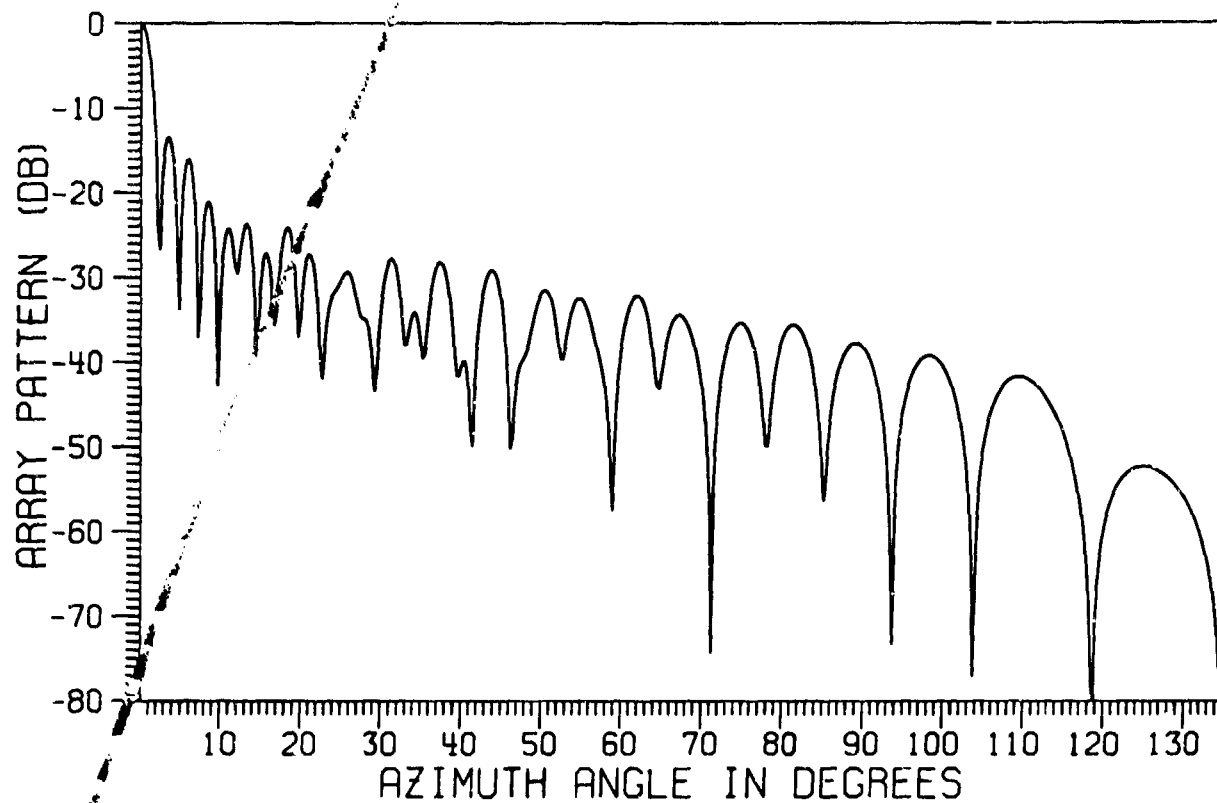


Figure 7(b)

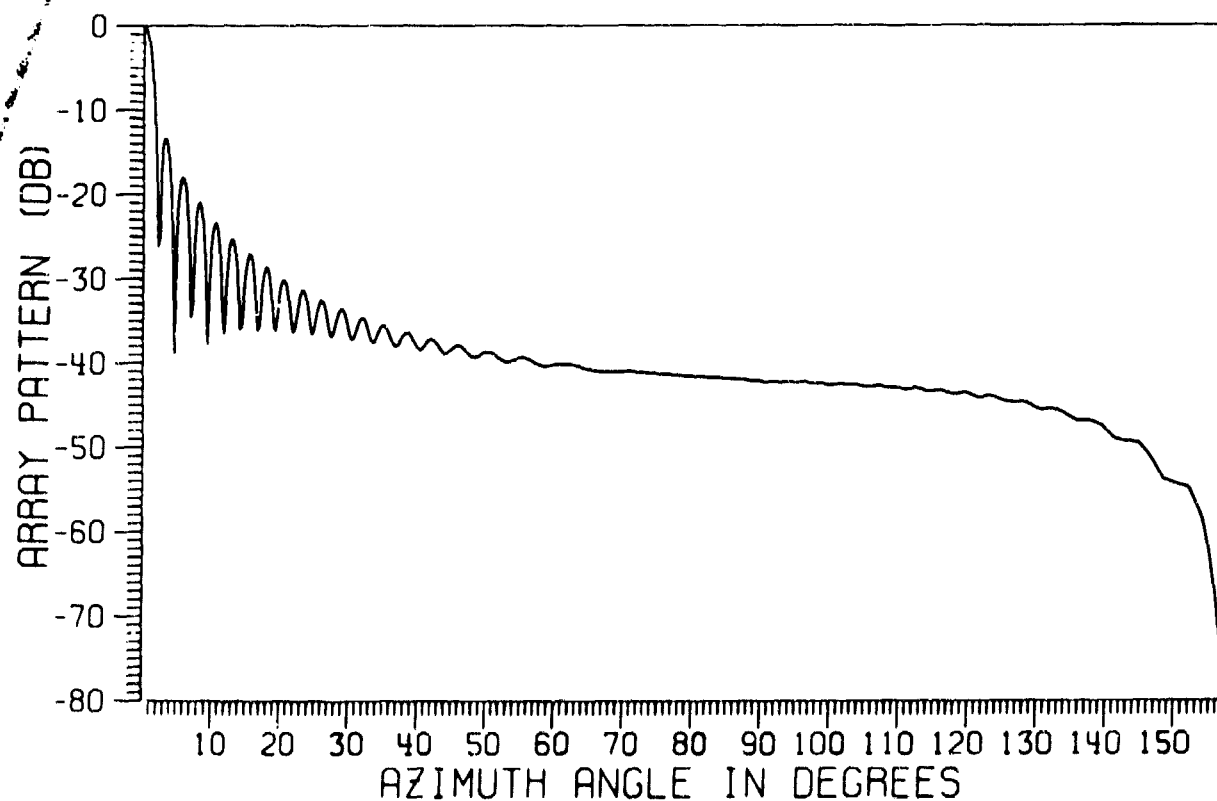


Figure 7(c)

Figure 7. Far field patterns of the multiple arrays of Fig. 1, horizontal dipole case. (a) Planar array No. 2 is active. (b) Planar arrays 1, 2, 3 are active. (c) A conformal array of 76 active elements on the arc ABCD.

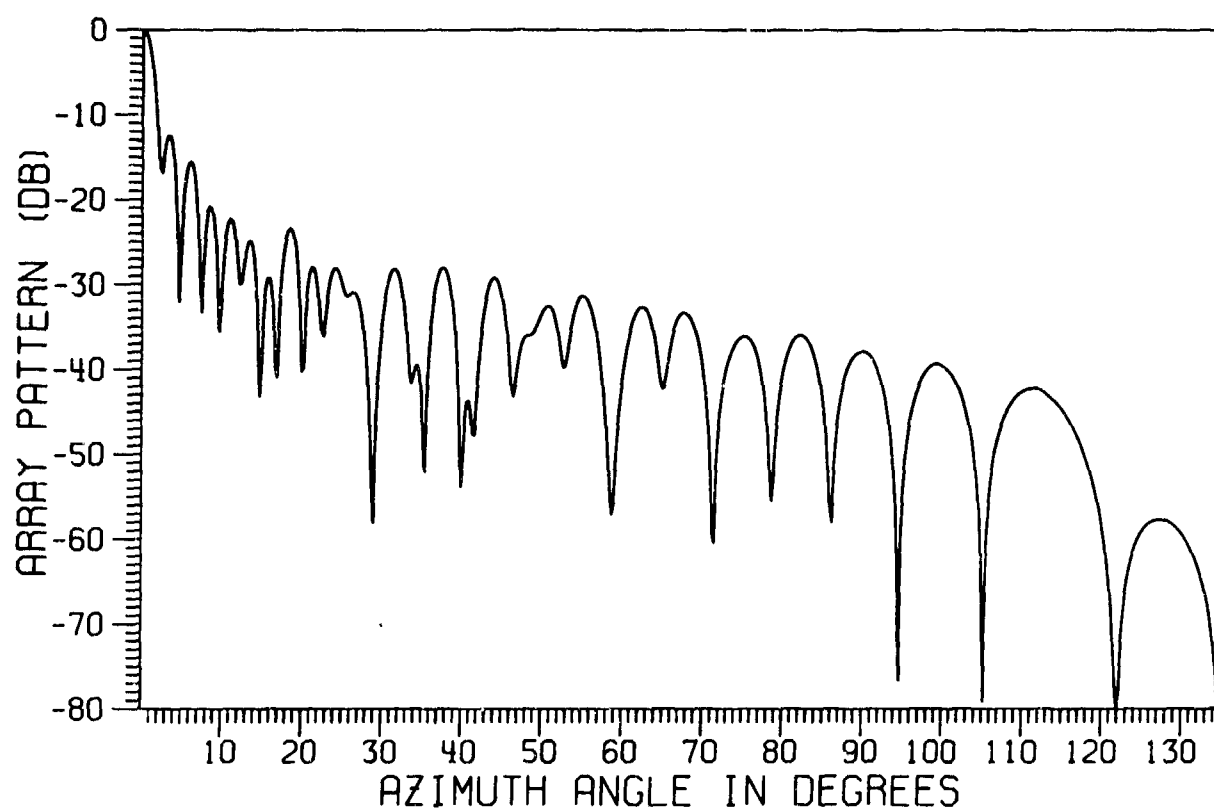


Figure 8(a)

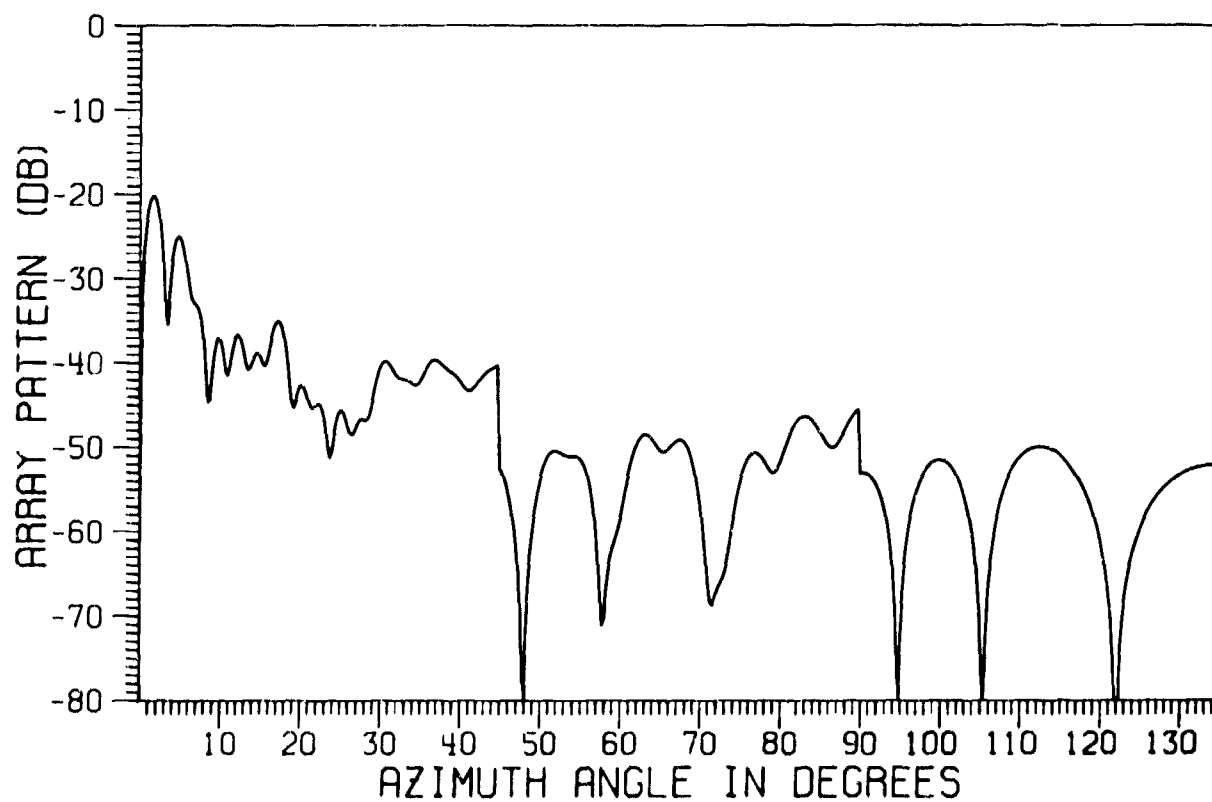


Figure 8(b)

Figure 8. Far field patterns on the conical surface $\theta = 80^\circ$ for the multiple arrays in Fig. 1. Planar arrays 1, 2, 3 are active. (a) E_ϕ . (b) E_θ .

DISCUSSION

S. Cornbleet: Would not the application of the constraint of having a single polarization reduce the matrix analysis from that of using all three Euler angles to two, or in the case of the simple cylindrical arrays - one.

J.K. Hsiao: I do not think that polarization has anything to do with co-ordinate system transformation. Furthermore due to the different orientations of the many elements, in general, a conformal array introduces other polarizations, even if each element has a single polarization.

R.H.-J. Cary: What are the advantages of the octagonal planar array system, against a conformal cylindrical array.

J.K. Hsiao: For a very large cylindrical array, the switching of radiating power between elements is very difficult and complicated. By the use of a few planar arrays, this problem can be avoided.

DESIGN OF PERIODICALLY MODULATED TRI-PLATE ANTENNAS

by

Finn Laursen

TERMA ELEKTRONISK INDUSTRI A/S
12, Haslegaardsvej
8210 Aarhus
Denmark

Summary

A new configuration of periodically modulated traveling-wave tri-plate antennas has been developed. The physical complexity of this new configuration implies that sufficiently accurate design data are extremely difficult to predict by any known analytical methods.

Three different measuring methods to achieve experimental design data are discussed. The far-field method, which has been further developed during this investigation, the near-field method, and the insertion loss method. The most appropriate combination of the three methods is used to find the design data. An X-band antenna array is designed and discussed. The new structure is mechanically simple, it has good impedance characteristics, allows good control of the aperture illumination, and radiates a linear polarized field with a very low cross-polarized component.

Introduction

Reducing size, weight, and physical complexity of antennas with large radiating apertures is an important objective in antenna engineering. Another essential factor can be the ease with which the antenna structure can be built to fit curved contours such as the fuselage of airplanes.

The stripline antennas might contribute to achieve these things. A new configuration of a periodically modulated traveling wave stripline antenna is described. The physical complexity of this configuration implies that sufficiently accurate design data are extremely difficult to predict by any known analytical methods for which reason it is important to develop experimental measurement methods. Design data are extracted from the measured results, and an X-band antenna array formed by line source radiating elements is designed.

Radiating Structure

Different periodically modulated structures have been investigated to find a structure with the following features:

- The power radiated per unit length should be sufficient to allow a low power waste in the load.
- The radiated field should be linear polarized with a low cross-polarized component.
- The attenuation factor should be frequency independent to allow frequency scanning.
- The configuration should be compact.

The structure chosen which will be dealt with in the following is a tri-plate antenna with a zigzag or trapezoidal modulation of the strip and a longitudinal slot in the top plate, fig. 1.

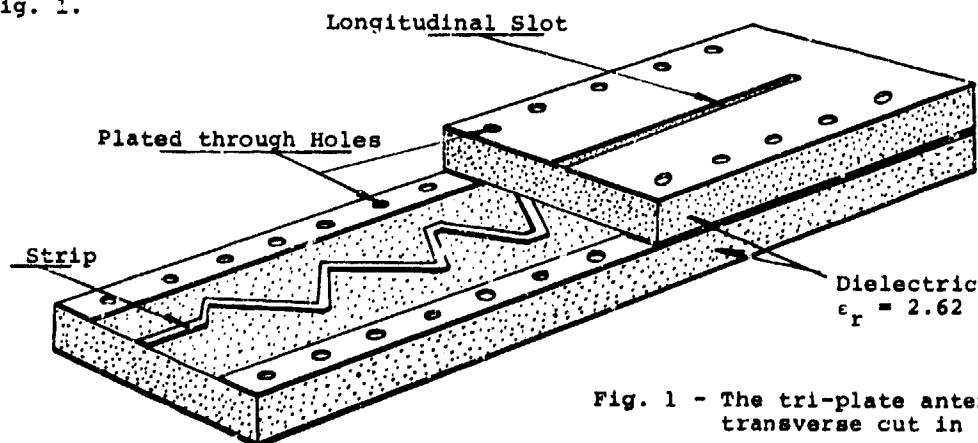


Fig. 1 - The tri-plate antenna with a transverse cut in the upper plate.

Measurement Methods

The traveling wave guided by a periodic structure is, in its fast wave region, characterized by a complex propagation constant $\gamma = \alpha + j\beta$, composed of attenuation constant α and phase constant β . The value of these two real constants must be known before a line source of optimum radiation characteristics can be designed.

The following three different methods of measuring α and β are discussed:

- 1) The far-field method (Jacobsen J., 1970)
- 2) The near-field method (Jacobsen J., 1970)
- 3) The insertion loss method (Montgomery C.G., 1948)

The Test Structures:

The value of the attenuation constant is a function of the centerstrip inclination angle ϕ (fig. 2).

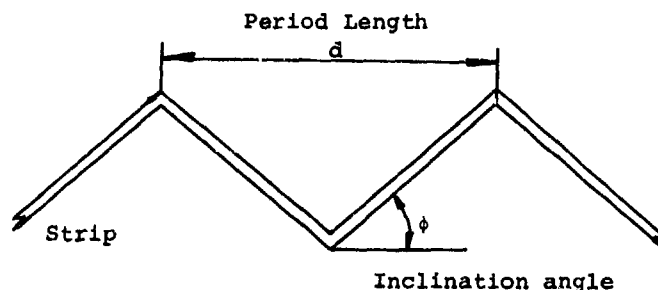


Fig. 2.

A section of a zigzag strip with the period length d , and the inclination angle ϕ .

Various test structures, each having a constant inclination angle, have been designed for measurements in the X-band. The test structures are about ten wavelengths long and mounted with SMA connectors at both ends.

The Far-field Method:

The guided wave launched at the excitation at one end of the structure is, as far as the structure is terminated by a short circuit, composed of an incident and a reflected traveling-wave. Each wave produces a single mainbeam. The ratio between the two mainbeams is equal to the attenuation of the guided wave over the total length of the structure. If this ratio is A dB then the attenuation constant is determined by Eq(1) (Jacobsen J., 1970)

$$A \approx 20 \log \exp(-\alpha L) \quad (1)$$

where L is the length of the structure.

The angle between the two mainlobes is twice the squint angle and this relation is used to determine the phase constant β Eq(2) (Jacobsen J., 1970).

$$\beta = K_0 \sin \theta_m \quad (2)$$

where θ_m = squint angle.

A typical radiation pattern is shown in fig. 3.

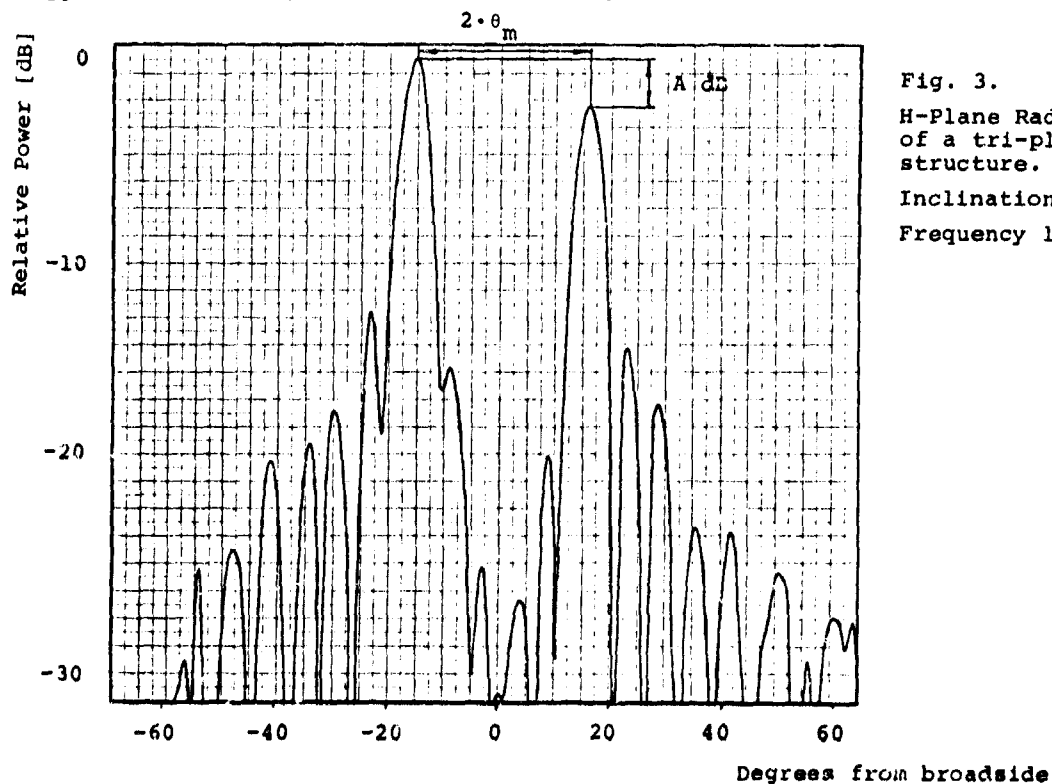


Fig. 3.

H-Plane Radiation Pattern of a tri-plate test structure.

Inclination angle $\phi = 10^\circ$

Frequency 11.4 GHz.

If the attenuation constant is so high that sidelobes associated with the incident wave will have essential influence on the level of the mainbeam associated with the reflected wave then the far-field method described by Jacobsen J. fails. The far-field method used in this investigation has been improved. The short circuit termination is replaced by a movable short circuit. This short circuit can shift the phase of the reflected mainbeam relative to the radiation pattern from the incident wave. Sum and difference pattern is achieved by moving the short circuit and the reflected mainbeam level can be calculated.

The Near-field Method:

If the attenuation constant is so high that even the improved far-field method fails then the attenuation constant and the phase constant can be determined by the near-field method. Only the attenuation constant has in this investigation been measured by the near-field method. The phase constant or the squint angle can be measured by the far-field method even for high figures of attenuation.

The attenuation per unit length is constant for constant inclination angle which means that the incident wave will decay exponentially from the excitation point. The field is measured at discrete points along the structure, the measurement distance from the structure to the probe is about 5 mm (determined by experiments). The measured attenuation points are fitted with a straight line and the attenuation constant is determined from the slope of this. A typical result is shown in fig. 4.

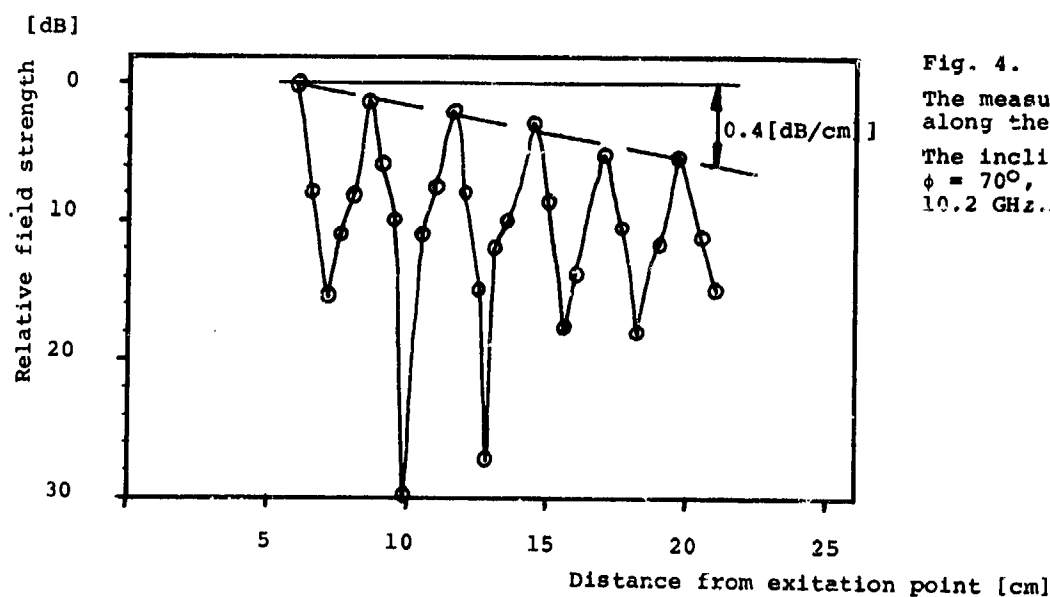


Fig. 4.
The measured field points along the structure.
The inclination angle $\phi = 70^\circ$, the frequency = 10.2 GHz.

The method is more inaccurate than the far-field method and considerably more tedious.

Insertion Loss:

This method is old and well known but will only give the attenuation constant and can therefore not be used alone.

The measured results from the test structures have been prepared and plotted in k - β (Brillouin) diagrams and k - α diagrams, and design curves have been extracted from these, fig. 5a-b.

Design curves for tri-plate line source antennas. Frequency 10.5 GHz, squint angle $\phi = 5^\circ$.

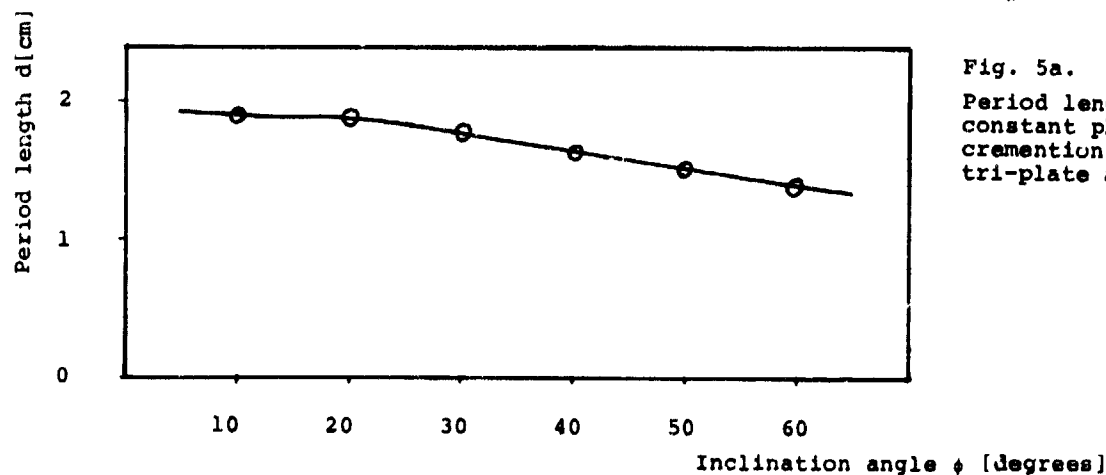


Fig. 5a.
Period length for constant phase incrementation for the tri-plate antenna.

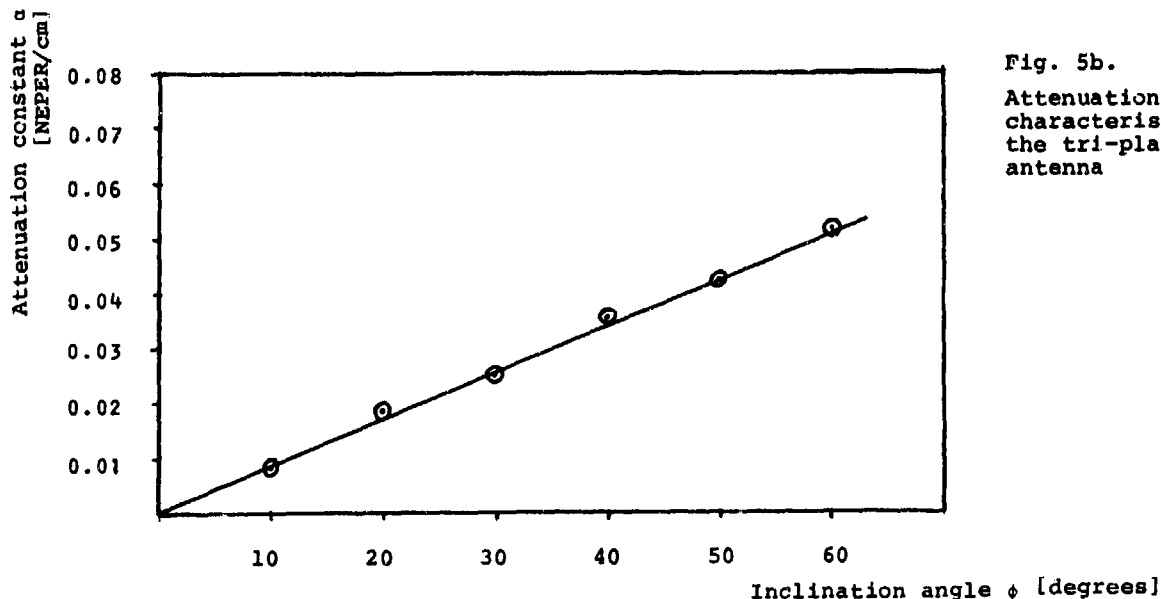


Fig. 5b.
Attenuation
characteristic of
the tri-plate
antenna

X-Band Antenna Array

An X-band antenna array composed of eight periodically modulated line sources has been designed. The amplitude distribution on each line source has been shaped to obtain low sidelobes and the attenuation constant along the line source is computed from the relation Eq(3) (Rotman and Karas, 1959).

$$2\alpha(z) = \frac{A^2}{\int_z^L A^2 dz + \frac{P(L)}{P(0)-P(L)} \int_0^L A^2 dz} \quad [\text{Nepers/unit length}] \quad (3)$$

where α = attenuation constant
 z = distance from load along the line source
 A = amplitude distribution
 $P(L)$ = power dissipated in load
 $P(0)$ = power at input

The value of the inclination angle ϕ corresponding to the attenuation constant α is found in the design curve fig. 5b.

Each element is terminated by a tapered resistance card load.

The feed system for the array is a T-junction power divider designed to deliver equal power and phase signals to each line source. A radome covers the antenna aperture.

Examples of an VSWR plot are shown in fig. 6, and H- and E-plan radiation patterns in figs 7 and 8.

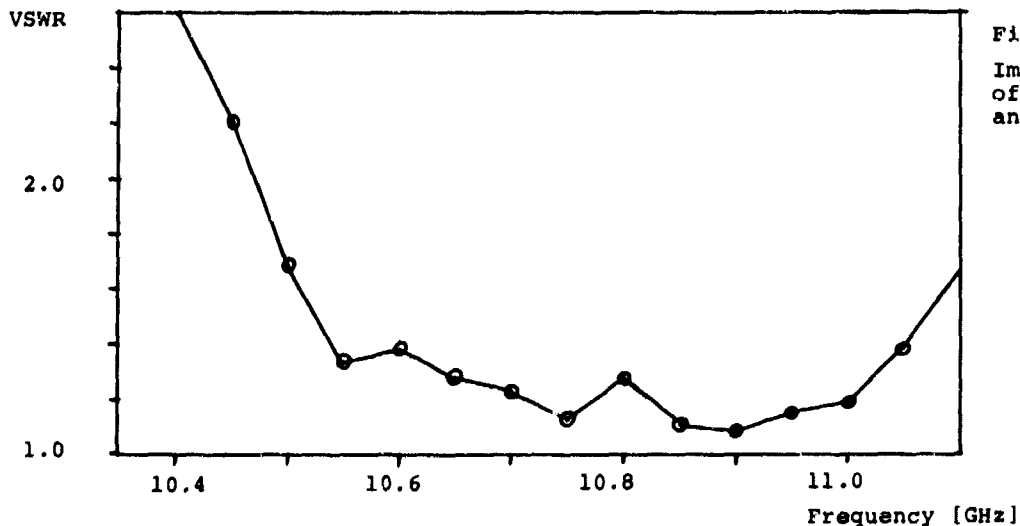


Fig. 6.
Impedance plot
of the tri-plate
antenna array.

Fig. 7 - H-plan radiation pattern for tri-plate antenna array
Frequency 10.5 GHz

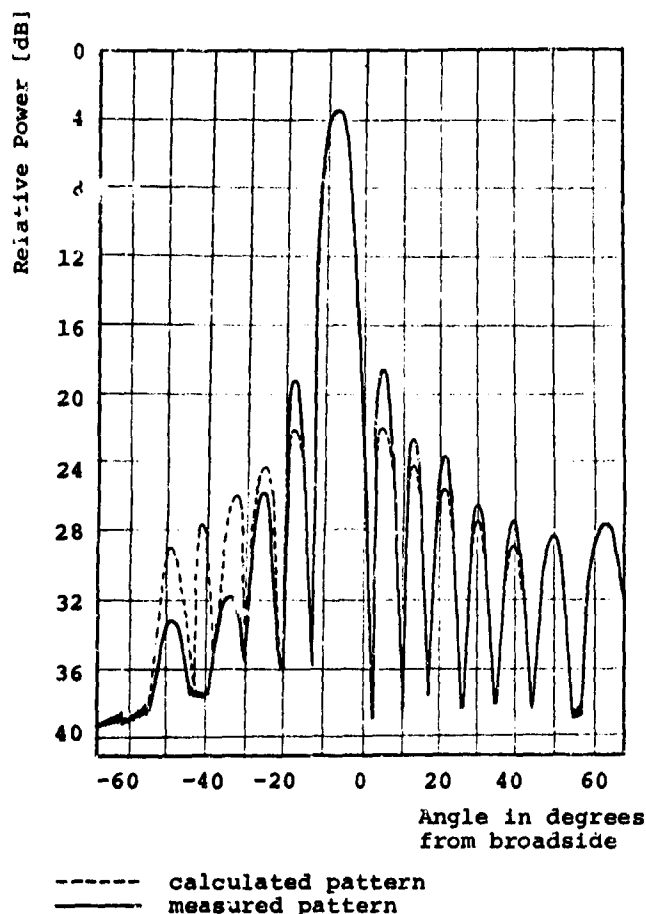
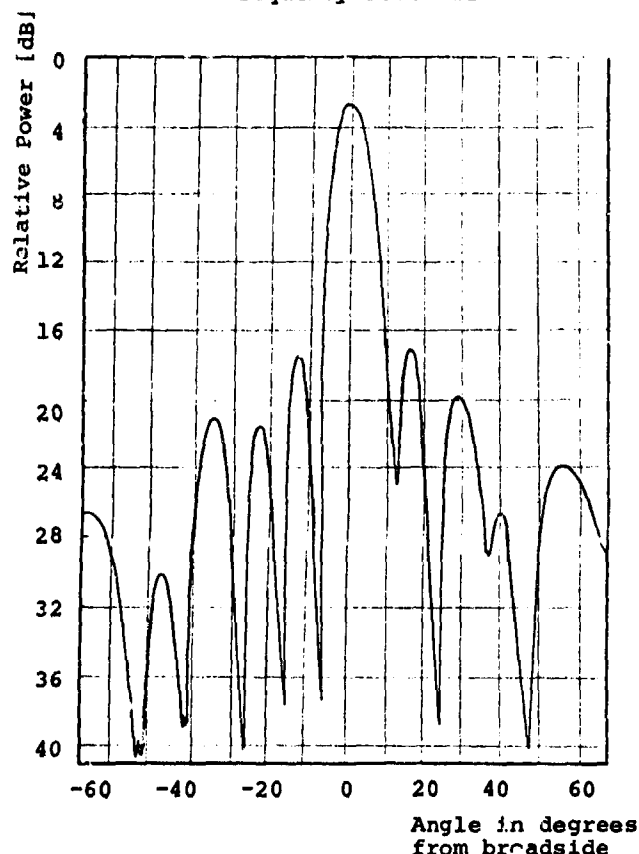


Fig. 8 - E-plan radiation pattern for tri-plate antenna array
Frequency 10.5 GHz



The radiation patterns agree well with the predicted patterns, and the VSWR plot shows very good impedance characteristic.

Conclusion

A new microwave line source configuration with excellent properties has been introduced. The design data for this structure have been achieved by using the improved far-field measurement method supplemented at extremely high attenuation constant by the near-field and the insertion loss methods.

The X-band antenna array predicted from the design curves shows that the predicted and measured performances agree very well. The cross-polarized component is at least 30 dB below the level of the principal field.

The very accurate control of the field amplitude as well as the phase along the aperture of the line source will make this structure very suitable for design of shaped beam antennas. Furthermore the broad-band impedance and radiation pattern characteristic are properties necessary for frequency scanning antennas.

Further results are hoped to be ready before the oral presentation.

References:

1. A. Hessel
"On the Influence of Complex Poles on the Radiation Pattern of Leaky-Wave Antennas", IEEE Trans. Antennas and Propagation (Communications), Vol. AP-10, Sept. 1962, pp 646-647.
2. J. Jacobsen
"Analytical, Numerical, and Experimental Investigation of Guided Waves on a Periodically Strip-Loaded Dielectric Slab", IEEE Trans. Antennas and Propagation, Vol. AP-18, May 1970, pp 379-388.
3. C.G. Montgomery
"Technique of Microwave Measurements", MIT Radiation Laboratory Series Vol. 11, McGraw-Hill Book Company Inc., New York, 1948.
4. Walter Rotman and Nicholas Karas
"Printed Circuit Radiators", Microwave Journal, August 1959, pp 29 - 33.

DISCUSSION

A. BRUNNER: You showed the frequency bandwidth in respect to the impedance. Can you tell us something about the frequency dependance of the sidelobes? In which frequency bandwidth can you for instance hold a sidelobe level of say 20dB?

F. LAURSEN: The first sidelobe level was designed to be 18dB and the measurement value was shown to be nearly 15dB. The antenna radiation has been measured through the band from 9 GHz to 12 GHz. The sidelobe level which was measured to be 15dB at the design frequency did not rise above 14dB within the 9-12 GHz band.

J.R. MARK: We have developed a very similar antenna. It differs in that the central conductor follows a "sinusoidally" perturbed path and the slot in this case was of variable width. What width slot was used in your antenna and was its width constant.

F. LAURSEN: The slot width of the described model was constant and equal to about 0.1 cm.

J. THRAVES: Would you indicate the type of radome that you used? How far away from the aerial was it? Did it affect the attenuation and phase change along the array? Was the spacing critical?

F. LAURSEN: The radome used for the antenna is a 5 cm. thick PVC foam block -1.05 covered by a 0.5 mm. thick glass reinforced polyester skin.

It does not influence the attenuation nor the phase constants, and the spacing was not found to be critical.

J. JACOBSEN: 1. Dielectric losses are important for the efficiency. In the actual antenna the dielectric losses plus copper losses amounts to approximately 2dB.

2. If the antenna is covered by a dielectric layer (radome) this effects the phase constant and the leakage rate. However this could be taken into account in the design.

F. LAURSEN: The relation between the two main loss factors, conductor and dielectric is:-

conductor = 30%, dielectric 70%

J. SNIEDER: What is the efficiency of the radiating structure? How much power is absorbed in the terminating load?

F. LAURSEN: The radiating structure which is nearly 25 cm. long does have a residual power at the load of between 10-15%.

This can be achieved even for shorter structures if the longitudinal slot in the top plate is widened.

R.H.J. CARY: Have you a comment on temperative effects on the performance of the antenna due to changes of attenuation and dielectric constant?

F. LAURSEN: The only change in antenna performance due to changes of temperative is a small change in the loss in the structure (conductor and dielectric). For the material used this change is very small.

HIGH EFFICIENCY ANTENNAS FOR AIRBORNE RADAR

R.W. Forrester and A.J. Lait,
Senior Design Engineers,
FERRANTI LIMITED,
Silverknowes, Ferry Road,
Edinburgh, EH4 4AD,
United Kingdom.

SUMMARY

Consideration is given to several antenna types which are suitable for use in airborne radars, and their advantages and disadvantages discussed. Several important antenna properties are efficiency, side-lobe level, scanning rate, weight, cost, etc. In this paper the emphasis is concentrated on methods which give a high antenna efficiency, whilst trying to maintain as many of the other properties as possible.

An experimental Cassegrain antenna has been designed and built. This employs energy redistribution techniques to give a high antenna efficiency, whilst retaining a reasonable sidelobe level. A measured efficiency of 70% was obtained at the design frequency, which only dropped to 65% at 500 MHz above design frequency. The antenna gave good sum and difference patterns over a 2 GHz band in X-band.

1. INTRODUCTION.

There are several different types of antenna which are suitable for use with airborne radars. These types each have their own advantages and disadvantages, which will depend to some extent on the role of the radar. The main roles are Airborne Interception, Ground Mapping, Terrain Avoidance and Terrain Following. In all these cases there will be a requirement for high efficiency and for low sidelobe level, combined with the need to scan the antenna beam, either electrically or mechanically, in one or two planes.

Let us consider the attributes of the different types of antennas. Those described here range from relatively simple antennas to much more sophisticated and expensive ones, the list is not intended to be comprehensive but rather to illustrate and compare representative types.

i) Front-Fed Reflector Antenna.

This is the simplest and cheapest of the antenna types under consideration. The feed may consist of a single channel, e.g. in a weather radar, or may have multiple apertures giving monopulse operation in one or two planes. The use of a front-feed with single-plane monopulse will give good performance when the split is in the E-plane of the aperture. Splitting in the H-plane will generally be much less efficient unless a multimode feed is used, or the antenna employs phase comparison between two halves of the aperture which are independently illuminated by the two halves of the feed. These comments also apply to the case of the two-plane monopulse system. The use of a multimode feed for a front-fed reflector will tend to increase the size and complexity of the feed. This will add to the aperture blockage, thus degrading the efficiency and sidelobe levels. The increased weight forward of the mounting points will require the use of stronger feed supports, thus increasing the weight and inertia of the antenna. It is possible that in some cases, an offset feed can be used, thus eliminating the blockage and easing the feed mounting problems. However, whilst this solution is available in ground-based radars, most airborne radar environments preclude this solution.

A front-fed antenna with a single-plane simple monopulse feed can give an efficiency of the order of 50-55%, with a sidelobe level not worse than 20 dB. A typical bandwidth will be at least 10%. The use of a multimode feed will give monopulse operation in both planes, and probably increase the antenna efficiency slightly at the centre of the frequency band, because of the lower spillover achievable with this type of feed. It will however have a lower bandwidth because of dephasing between the modes in the feed. The intermediate stage of a feed supporting a single sum mode and a single difference mode will behave more like the simpler feed, whilst giving the ability to track in both planes.

ii) Cassegrain Antenna.

Under this section, the Cassegrain antenna will be considered to be the normal one with a parabolic main reflector and a hyperbolic subreflector. The two main types are those with conventional metal reflecting surfaces, such as the minimum blockage Cassegrain, and those with a polarisation twisting main reflector and gridded subreflector. The former type has a blockage level which is very high for the small antennas normally used in airborne radar, with a diameter up to say 1 metre, whereas for large antennas such as are used for satellite communications, the blockage is relatively small. On the other hand, the polarisation twisting reflector is a relatively complicated structure and needs to be manufactured to a high degree of accuracy. This manufacture can be achieved without too much difficulty for small reflectors, where wire grids can be laid up directly on the reflector surface. For larger reflectors, this technique soon becomes impractical, and resort must be made to the use of wires embedded in fibreglass cloth, or similar material, which must be specially produced to give the desired wire spacing. Thus there is a fairly well marked dividing line between the use of twisting Cassegrains for small antennas, and the use of conventional surfaces for larger antennas. This will occur around 1½ metres diameter at X-band.

The main advantages of the Cassegrain antenna are that the feed projects through the reflector from the rear, and that the main reflector may have a longer focal length because of the use of the two reflector system. The rear feed cuts down the amount of feed blockage to that of the feed aperture, since there is no blockage from a support structure. The comparator structure for obtaining the sum and difference signals may be situated either in the feed stem, or conveniently folded back along the rear surface of the main reflector. This also reduces the inertia of the antenna since the inertia of the subreflector and its supports will normally be less than that of a front feed, and will certainly be less for antennas of equivalent focal length. The longer focal length available means that the antenna may be designed to have a low level of cross-polarisation, again improving the efficiency.

The comments in the earlier section on the use of simple or multimode feeds apply equally to the

Cassegrain antenna. The full multimode feed will give a better efficiency, and considerably improve the difference patterns.

The efficiency of a twisting Cassegrain will generally be slightly higher than the comparable front-fed antenna. The bandwidth will usually be limited by the design of the twist-reflector (except when a multimode feed is used, in which case this will probably limit the bandwidth), being dictated by the acceptable level of cross-polarisation due to imperfect twisting. This cross-polarisation will normally show up in the direction of the main beam, rather than in the 45 degree planes where the normal reflector cross-polarisation is at its maximum. The efficiency of a small Cassegrain with normal reflecting surfaces will generally be too low to be acceptable, whilst the sidelobe level will suffer even more from blockage than the efficiency.

iii) High Efficiency Cassegrain Antenna.

The conventional Cassegrain antenna uses the classical reflector shapes to satisfy the conditions which give a plane wavefront in the radiating aperture of the antenna. There is however an infinite family of surfaces which satisfy these conditions. By using the extra freedom of choice which this range gives, the designer may, within reason, produce almost any desired amplitude distribution in the radiating aperture, whilst retaining the plane wavefront. This process has been used (1), (2) mostly for large satellite communications antennas, where a uniform amplitude distribution is desirable. In a later section of this paper, an experimental antenna is described which uses these techniques to produce an illumination more suitable for a radar antenna. This antenna has good radiation patterns in both sum and difference channels, with a measured efficiency of 70% at the design frequency. This is a considerable improvement on the conventional Cassegrain.

iv) Flat Plate Antenna.

This antenna consists of a flat radiating surface which contains a large number of radiating slots. In a typical antenna the slots are cut in the broad faces of waveguides running in the plane of the aperture, the slots being separated by half a guide wavelength and displaced on alternating sides of the centreline, so that they radiate in phase. These waveguides will have some form of feeder network, which distributes the power to the waveguides. In many cases, the waveguides will be split in the centre by a short circuit so that the two half-waveguides can give monopulse information.

The amplitude distribution of this antenna is determined by the displacements of the slots. As with the high-efficiency Cassegrain, there is considerable scope for choice of a suitable illumination, such as a Taylor distribution. The feed network can be designed to have a fairly low loss, so that an efficiency of the order of 80% can be achieved at the centre of the frequency band.

For all except the very smallest flat plate antennas, the bandwidth is limited by the length of the slotted waveguides, as with the design of any other resonant array. This can be alleviated by subdividing the lengths of waveguide, and feeding them separately from a complex feeder network. A 20 slot antenna, with central short circuits, will have a bandwidth of about 5%. The bandwidth varies inversely with the number of slots, but can be improved by further subdivision with short circuits.

The efficiency of the antenna at the edge of the frequency band will be down considerably on the central efficiency, to say 65%. However, because the flat-plate antenna has very little depth (an X-band antenna may be 2½ to 5 cm. thick, including feeders and comparators), it will normally be possible to install a larger diameter of flat-plate than of Cassegrain in a given swept volume. Thus for a given available swept volume, the gain of a flat-plate antenna may be significantly higher than a Cassegrain antenna, even at the edge of the frequency band.

The main disadvantages of the flat-plate antenna are the low bandwidth, high cost, and difficulty of manufacture. The antenna, whether made from waveguides or sheet metal, must be made to waveguide tolerances, and joints must be well made, often in difficult positions, so that there is no high-power breakdown or leakage, and minimum gas leakage if the antenna is pressurised.

v) Phased array antenna.

The phased array antenna, which has been a subject of considerable interest in recent years may be considered to be in a different class from the other antennas discussed in this section, since its scan rate is several orders of magnitude faster than mechanically scanned antennas, whilst its gain is considerably lower.

There are two main types of phased arrays; those where the amplitude distribution is provided by some form of power divider network, and the phase shifters are transmission units, and those which are illuminated in the same way as a front-fed reflector, and use short-circuited phase shifters to reflect the energy so that it may be re-radiated.

With the conventional type of phased array, the use of a feeder network gives scope for choice of amplitude distribution. The feeder network is likely to be very complicated, especially if two-plane scanning is required. However, for many applications, it may be sufficient to use high-speed scanning in one plane, and mechanical scanning in the other plane, giving a raster scan. In this case a much simpler feeder network can be used, with distribution in the other plane by means of conventional arrays.

This type of antenna has considerable loss of power in both the feeder network and the phase shifter elements, these being typically at least 1 dB each. After aperture efficiency and other losses have been included, the total antenna efficiency may be of the order of 30%.

The reflect array may well be a better antenna when phase scanning is required in both planes. A multimode feed can be used to illuminate the array, thus minimising spillover loss. There is not much scope for choosing an efficient amplitude distribution, so that the overall efficiency will be considerably influenced by a low aperture efficiency. The phase shifter loss will again be at least 1 dB, at the present state of technology, so that an overall efficiency of about 30% may again be typical.

This antenna has the advantage that it does not require a complicated and expensive feeder network, so that the cost may be significantly less than a comparable transmission array, although considerably more expensive than the other antenna types considered. The presence of the front-feed does not have the same disadvantages as with the front-fed reflector, since it fits conveniently within radomes because the antenna is fixed, and the need to minimise antenna inertia no longer applies.

Although the phased arrays considered have efficiencies 3 or 4 dB down on the best antennas described earlier, the extremely high scanning rate may give sufficient systems advantage to outweigh the low gain. Thus the phased array, in its present state of development, does not qualify as a high efficiency antenna. Nevertheless, it is interesting to speculate what the future may hold for it.

2. HIGH EFFICIENCY CASSEGRAIN ANTENNAS.

i) Reflector Design.

The conventional Cassegrain antenna uses the classical reflector shapes (parabolic main reflector and hyperbolic sub-reflector) to produce a plane wavefront in the radiating aperture, by ensuring that the path lengths from the phase centre of the feed to all points of the radiating aperture are equal. These reflector shapes are part of an infinity of surfaces which satisfy this condition. This gives an extra degree of freedom which is used to produce an arbitrary distribution.

This extra freedom has been used by Williams (1) and Claydon (2) to produce designs where the feed illumination has been converted to give an uniform amplitude distribution. This procedure has generally been applied to cases with large reflectors, using a minimum blockage sub-reflector and a single channel feed. Two designs are described in this paper which extend this procedure to produce an illumination more suitable for a radar antenna. The distribution used is a raised cosine-squared distribution with an edge taper of $14\frac{1}{2}$ dB, which has a theoretical aperture efficiency of 89%, and sidelobe level of 27 dB. This distribution is virtually identical to a 27 dB Taylor distribution for a circular aperture.

The mechanism for the energy redistribution may be seen by reference to figure 1. The shape of the sub-reflector tends to be more sharply curved than usual in its central area, bending round to a much flatter profile at the edge. As a result some of the energy from the central part of the feed pattern is forced to the outer part of the aperture. This process is even more marked when an uniform distribution is being produced.

Referring again to figure 1 for the appropriate symbols, the relevant equations are

$$dr/d\theta = r \tan \frac{1}{2}(\theta + \phi) \quad (1)$$

$$dy/dx = - \tan \frac{1}{2}\phi \quad (2)$$

$$r = C + y - (x - r \sin \theta) / \sin \phi \quad (3)$$

where C is a constant

$$dx/d\theta = A f(\theta) \sin \theta / (x f(x)) \quad (4)$$

where $F(\theta)$ is the radiation pattern of the feed, $f(x)$ is the desired amplitude distribution and

$$A = \frac{\int_0^x x f(x) dx}{\int_0^\theta F(\theta) \sin \theta d\theta}$$

is the constant which ensures conservation of energy.

Equations (1) and (2) are the conditions for optical reflection at the surfaces of the two reflectors, equation (3) is the condition for equal lengths along all paths from the feed phase centre to the radiating aperture plane (taken for mathematical simplicity as the plane through the vertex of the main reflector) and equation (4) is the condition that the energy in a section of the aperture is equal to the energy in the corresponding section of the feed pattern, the constant A ensuring that the total energy in the radiating aperture is equal to the total energy in that part of the feed pattern which is used.

The feed is a multimode horn, with uniform illumination in the E-plane and a combination of HO1 and HO3 modes in H-plane, chosen to give a good approximation to a circularly symmetrical feed pattern. The E-plane shape of the pattern is used for the function $F(\theta)$ because this gives a simpler mathematical representation than the H-plane shape. A large feed angle has been chosen, which gives a large subreflector, but reduces the total depth of the antenna. There is still a certain amount of freedom to choose the position of the reflectors and the feed. The feed phase centre was chosen fairly well forward of the main reflector to allow space for the modulator section and the first level of couplers (the second level can be folded back along the rear surface of the reflector to give an improved package). With all these factors specified, the subreflector position was then chosen, from examination of the resultant profiles, to minimise the total swept volume by making the edges of the main and subreflectors equidistant from the proposed axis of rotation. The four equations, and the other values specified as above, are sufficient to produce the reflector profiles. The differential equations are solved numerically on a computer, using the Runge-Kutta technique. Extensions to the edges of the reflector profiles were calculated using a curve fitting technique. These were used to produce moulds sufficiently large that the reflectors could be manufactured oversize, and then cut to the required size.

ii) Feed Design.

The choice of suitable ratios of modes, and ratios of aperture dimensions is based on the results given by Hannan(3). The optimum values given in this paper are for the simple front-fed reflector of long focal length, where the obliquity factor is not included in the theoretical feed pattern. This method gives a unique relationship between the reflector size and the optimum feed size. This uniqueness is removed for the case of the Cassegrain, since the feed angle can be specified, and the subreflector is then specified. With the present reflector conditions, there is also further freedom to choose subreflector position (this is not available in the simple Cassegrain when the feed position and feed angle have been chosen). The chosen mode ratio between HO3 and HO1 of 0.4, together with appropriate aperture dimensions gives a good approximation to a circularly symmetrical beam, which can be used down to 20 dB below the peak, thus giving a very low spillover loss.

The design of the H-plane moding discontinuity, to give this mode ratio, used an extension of the method described by Drabowitch (4). It was found that some of the solutions, after initially converging with the first few modes, then became unstable with the addition of extra modes. The results of the stable part of the convergence were extrapolated to get the solutions. Shortly after this part of the feed design had been completed, papers were published by Masterman and Clarricots (5) and Lee et al (6) which gave explanations for this phenomenon, and indicated methods of solution based upon careful choice of the number of modes used in the various waveguide sections. As well as obtaining the appropriate mode ratio, the phases of the modes were obtained from the computation.

The output from the modulator has a smaller cross-section than the required aperture. A flare section is used to provide the transition. This section must have its length chosen so that the HO3 and HO1 modes are in phase at the aperture. The design of the flare was deliberately made shorter than required, and spacer pieces (with the same cross-section as the modulator end of the flare) introduced to make up the

length, thus enabling the correct phasing to be checked experimentally.

The four channels from the modulator feed through two levels of phase shifters and in-line 3 dB couplers to give signals to the sum channel and the two difference channels. This gives a very compact comparator package, with the first level in the feed stem forward of the reflector surface.

iii) Construction Details.

The feed stem and comparator network are milled from solid metal with covers added later. The E-plane 3 dB couplers are Double Slot Couplers designed at Ferranti by Brown and Ashforth, and the H-plane couplers are a modified version of the Riblet Coupler to allow easier machining. The flare section is separately machined, as are the spacers, and dowelled to the feed stem to give correct alignment at the modulator discontinuity.

The main reflector is a twistreflector, built to a corrected Hannan design. This was laid up on the mould, using fibreglass honeycomb for the core, and aluminium tape for the reflecting surface. A further layer of honeycomb was bonded to the rear surface to give extra strength. Experience of the completed structure indicated that this was probably not necessary, and that a fibreglass skin behind the reflecting surface would be sufficient. The subreflector is of A-sandwich construction, with a wire grid embedded in the skin nearest the feed. Metal sub-reflector supports were used for the experimental antenna. For a production version, a dielectric cone would be used.

The weight of the present antenna is about 10 pounds. With the removal of the rear layer of fibreglass honeycomb, and other manufacturing improvements such as the use of thinner walls in the feed, a weight of about 5 pounds should be achieved.

iv) Experimental Measurements and Results.

Radiation patterns of the feed were measured in both planes, with different numbers of spacers between the feed stem and the flare. Each spacer represented an extra 10 degrees of differential phase between the HO1 and HO3 modes. The elevation plane pattern (not the multimode plane) remained unchanged, whilst the azimuth plane beamwidth reached a maximum value when the two modes were in phase. The maximum beamwidth was achieved with a spacer setting within 1 spacer of the expected value. At this setting the beamwidths in the two planes were equal, and the beam gave a good approximation to circular symmetry and to the theoretical shape. This setting has been used in all later measurements with the multimode horn.

The twistreflector was initially tested by front-feeding it with a simple horn. As this reflector is a good approximation to a paraboloid for most of its radius, this gave good radiation patterns with twisted polarisation, with a low level of untwisted polarisation over the desired bandwidth, indicating that the twistreflector was well centred in frequency.

The complete Cassegrain antenna was then focussed with a simple horn (of the same beam shape) in place of the multimode horn. After focussing with the simple horn, the multimode horn was substituted. It was found that, at the design frequency of 9.25 GHz, the E-plane and H-plane phase centres of the feed were separated by about 2 cm., whilst at 9.75 GHz, the phase centres were coincident. The antenna was focussed so that the feed was placed midway between the azimuth plane best focus and the elevation plane best focus. No attempt has yet been made to redesign the feed to make the phase centres coincide at 9.25 GHz.

Gain measurements at this stage gave an efficiency only just over 60%. Investigation of this showed that the aperture illumination cut off about 3 cm. inside the edge of the main reflector. This suggested that the outer edge of the subreflector was not acting as a true reflector because the wires at the edges of the subreflector were not seeing short circuited terminations. To overcome this, a larger subreflector was made, taking advantage of the fact that the moulding tool had been made oversize. With this reflector in position the illumination came within 1 cm. of the edge of the main reflector, with the diameter of the subreflector 5 cm. greater than the original one. This improvement also showed when radiation patterns were taken of the subreflectors illuminated by the simple horn. The patterns with the original subreflector cut off sharply at too low an angle, whereas those with the larger subreflector gave much nearer the correct angle. These radiation patterns showed the general shape of the desired illumination, together with the ripple normally associated with subreflector patterns.

After refocussing with the larger sub-reflector, further radiation patterns were measured, and gain checks made. The efficiency at 9.25 GHz was now up to 70% and was as high as 65% at 9.75 GHz (with the antenna set to the mean focus position at 9.25 GHz). Figures 2-6 give a summary of the results from the radiation patterns taken at 0.25 GHz steps from 8.5 to 10.75 GHz. The difference channel levels have been corrected for mismatch loss, since the feed is at present unmatched. The feed at present has a VSWR ranging up to 2:1 in the sum and azimuth difference channels (up to 1.6:1 between 9 and 10 GHz), and up to 3:1 in the elevation difference channel. The levels presented in the diagrams are the mean results from the two sides of the patterns.

Good results have been obtained over the whole measured frequency band, with sum sidelobes better than 20 dB over most of the band. The azimuth difference patterns (generated by the HO2 mode in the feed) show the high level to be expected from the optimised difference pattern, and the elevation difference pattern is at the level consistent with a normal E-plane split. The low 3 dB beamwidths indicate the high efficiency achieved in the design. The results are best in the region of 9.75 GHz, indicating that the movement of the horn phase centres is probably the most significant factor affecting the bandwidth of the antenna.

Wide angle radiation patterns have been measured at 9.75 GHz. The far out sidelobe level (from 40 to 180 degrees each side of the main beam) was better than 52 dB down in both planes, for normal and cross polarisation. This level was achieved without recourse to the standard methods for reducing the effects of spillover, and is also somewhat aggravated by the use of metal struts to support the subreflector. The use of a dielectric cone to support the subreflector, and of spillover suppression should reduce the far out sidelobe level to 60 dB down on the main beam. The highest measured cross-polarisation in the principal planes was 30 dB down on the correct polarisation.

v) Improvement of Efficiency of an Existing Cassegrain Antenna.

A set of reflectors was designed for an existing Cassegrain antenna so that a test could be made to check how much improvement of efficiency can be achieved by the use of specially shaped reflectors. The existing feed was retained, but was allowed axial movement during the design process. Various sets of reflector profiles were tried, with the aim of retaining the existing main reflector if possible. A design was reached where the main reflector could be retained without introducing an unacceptable level of phase error. A new subreflector was manufactured to the chosen profile, using an oversize diameter as described in the previous section. The antenna has a twisting main reflector and gridded subreflector.

The antenna diameter is 48 cm.

Gain measurements were made for the existing antenna. The new subreflector was then introduced, and the antenna focussed with the feed in its new position. Good radiation patterns were obtained. The sidelobe levels were higher than with the original antenna, this being consistent with the use of a best-fit paraboloid instead of the correct shape for the main reflector. The 3 dB beamwidth with the new sub-reflector was considerably lower than before. The measured gain for the modified antenna was 31.1 dB at 8.95 GHz, giving an efficiency of 63%. This is $\frac{1}{2}$ dB better than the gain of the original antenna, and is a very good efficiency for such a small dual-plane monopulse antenna.

vi) Conclusions.

The two antenna designs reported above clearly indicate the improvement that can be made to the efficiency of a Cassegrain antenna by the use of specially shaped reflectors. This improvement is partly caused by the increase in aperture efficiency, and partly because more of the feed illumination can be usefully used. The use of more of the feed pattern improves the efficiency in this design because the reflectors redistribute it efficiently, whereas, with the classical reflector shapes, the use of too much of the feed pattern will give a high edge taper to the illumination and lower the overall efficiency.

The small antenna indicated that this technique works well, even for an aperture as small as 15 wavelengths, with an increase of gain of $\frac{1}{2}$ dB. The main antenna described gives an efficiency of 70% at the design frequency. The patterns obtained are good for a first prototype. The results from the reflectors, with both the simple and the multimode horn, are very close to the desired results, whilst the feed, apart from the need to control the phase centres and improve the matching, gives good results with a wide bandwidth.

The antenna is an improvement on the classical Cassegrain with no apparent disadvantages compared with it. Once the moulding tools have been made, it should not cost more to manufacture, whilst the weight is only marginally higher because a larger subreflector is used.

REFERENCES.

1. Williams, W.F. High Efficiency Antenna Reflector. Microwave Journal Vol.8 No.7 July 1965. pp. 79-82.
2. Claydon, B. A Study of the Performance of Cassegrain Aerials. The Marconi Review Vol. XXX No. 165 Second Quarter 1967. pp. 98-115.
3. Hannan, P.W. Optimum Feeds for All Three Modes of a Monopulse Antenna. IRE Trans-AP. September 1961. I:Theory pp. 444-454. II: Practice pp. 454-461.
4. Drabowitch, S. Théorie et Applications des Antennes Multimodes. Rev. Tech. CFTH. Nov. 1962. pp. 117-168.
5. Masterman, P.H. and Clarricoats, P.J.B. Computer Field-Matching Solution of Waveguide Transverse Discontinuities. Proc. IEE. Vol. 118. Jan. 1971 pp. 51-63.
6. Lee, S.W., Jones, W.R. and Campbell, J.J. Convergence of Numerical Solutions of Iris-Type Discontinuity Problems. IEEE Trans-MTT Vol. 19 No.6 June 1971. pp. 528 - 536.

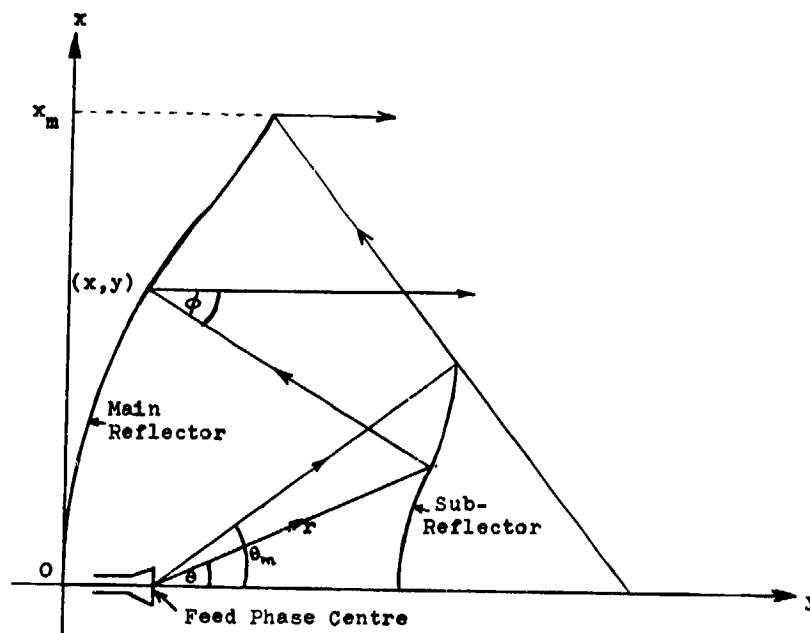


Fig.1. Geometry of Reflector System.

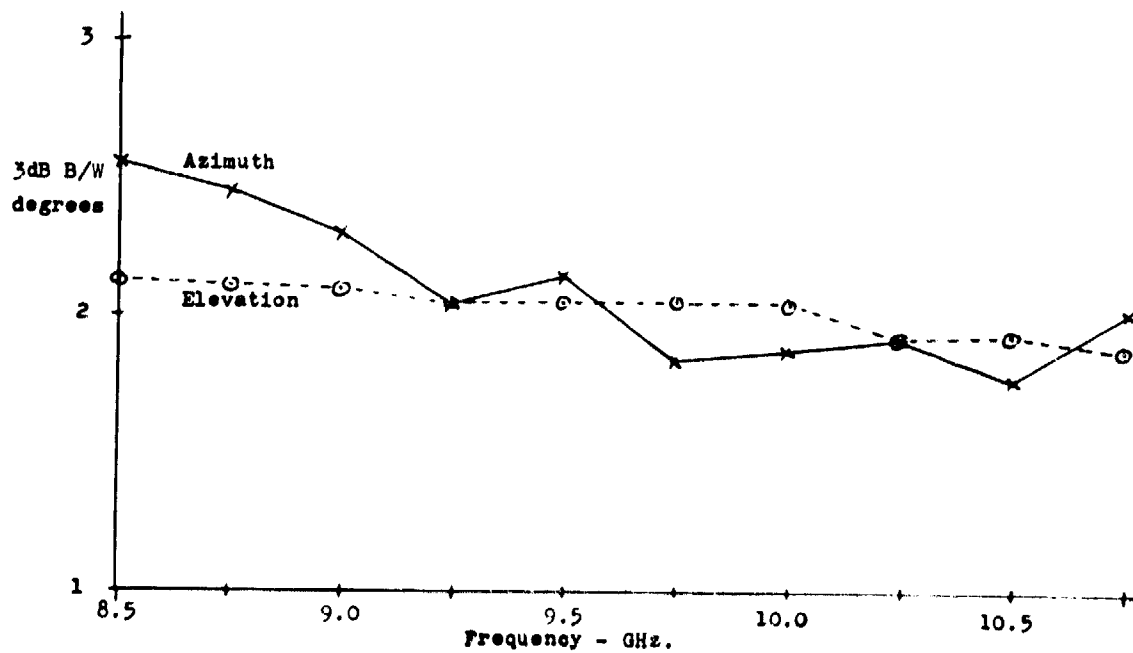


Fig.2. Sum Channel Beamwidths.

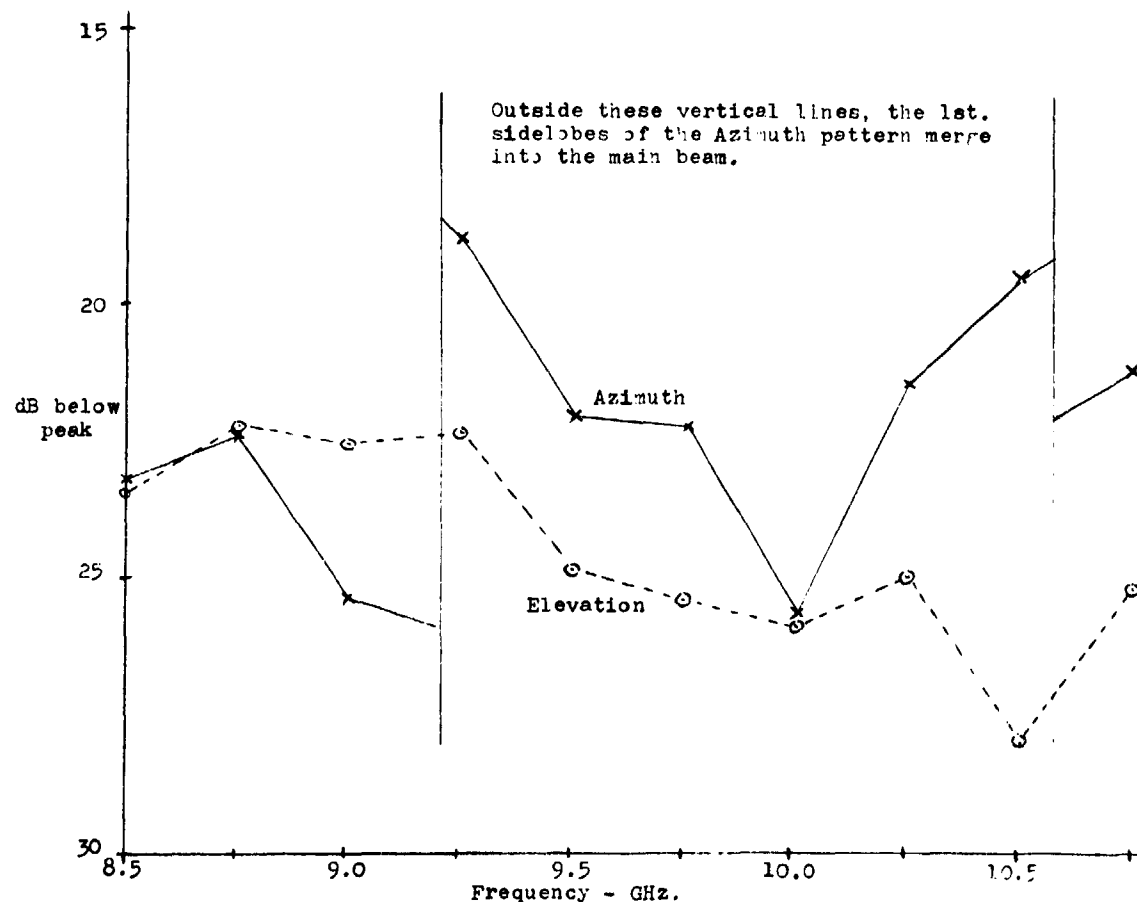


Fig.3. Level of Sum Channel Sidelobes.

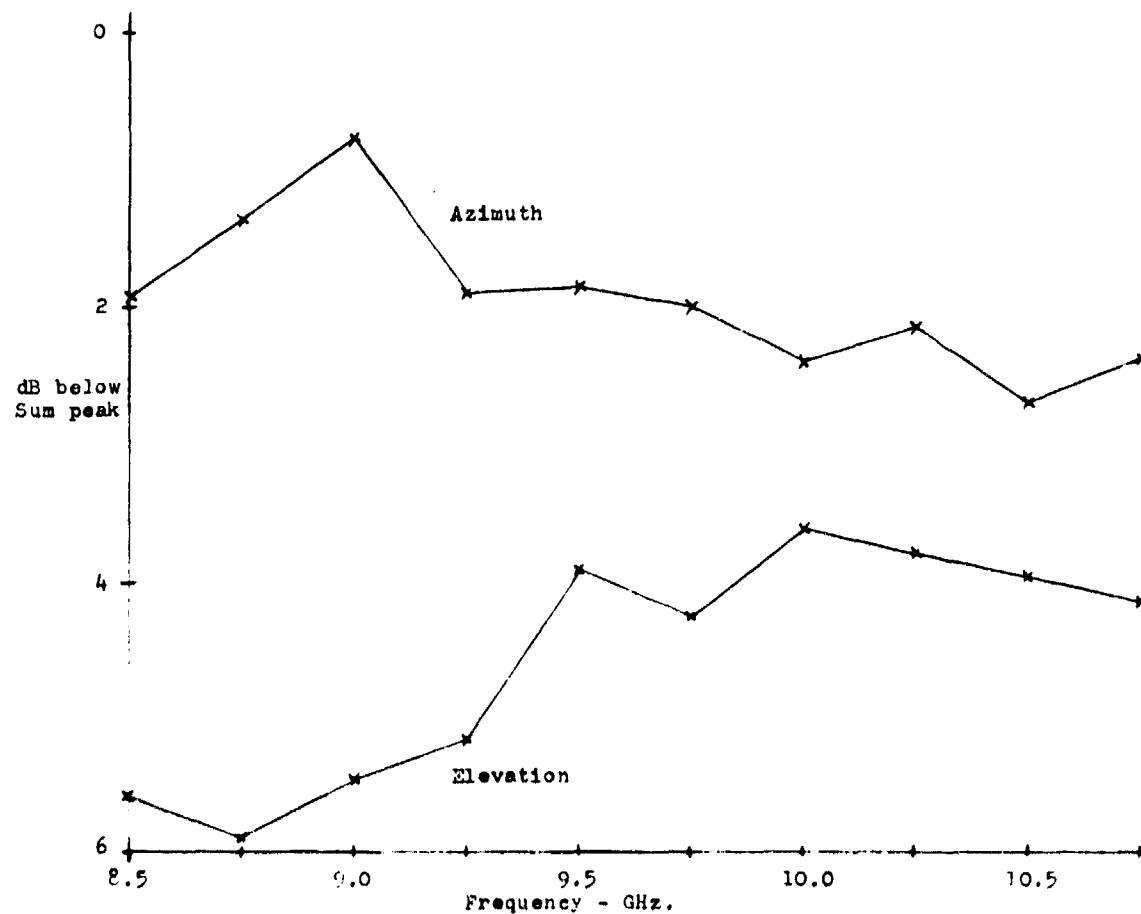


Fig.4. Level of Difference Channel Peaks.

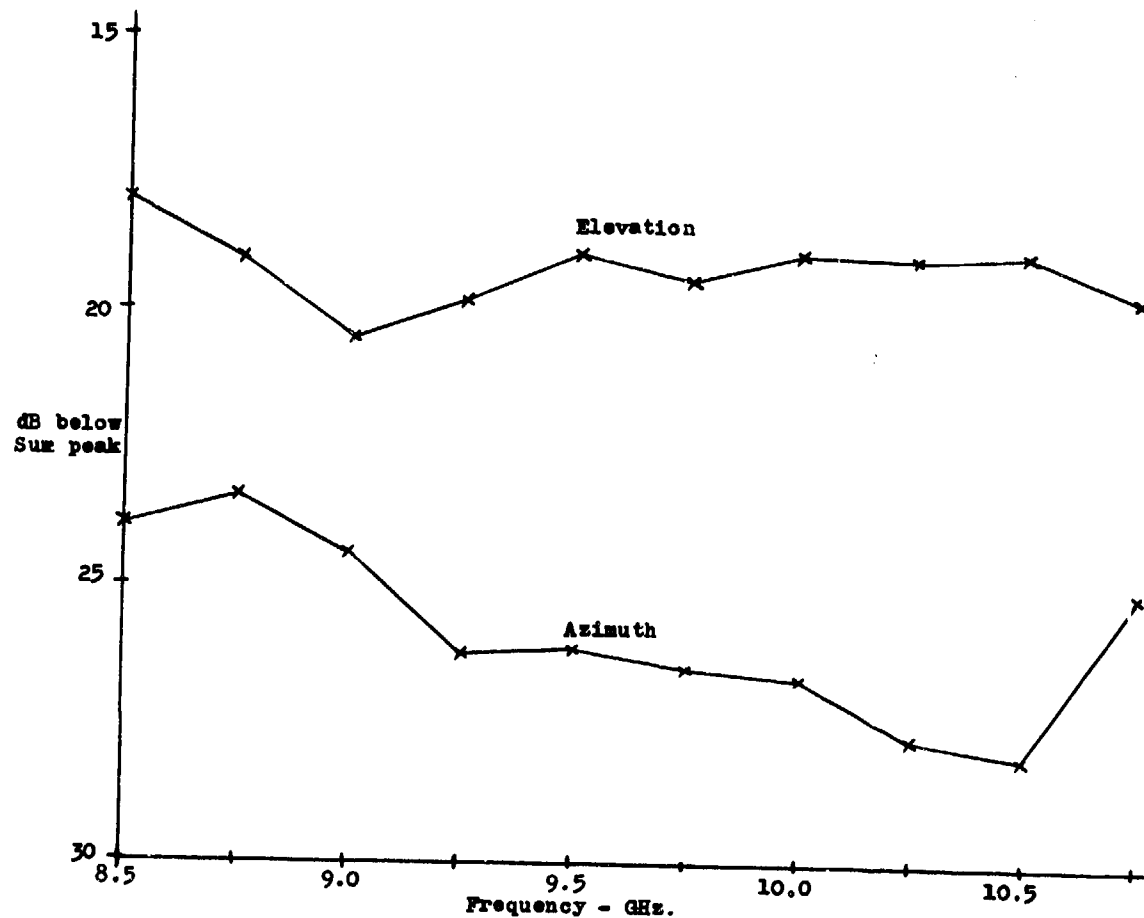


Fig. 5. Level of Difference Channel Sidelobes.

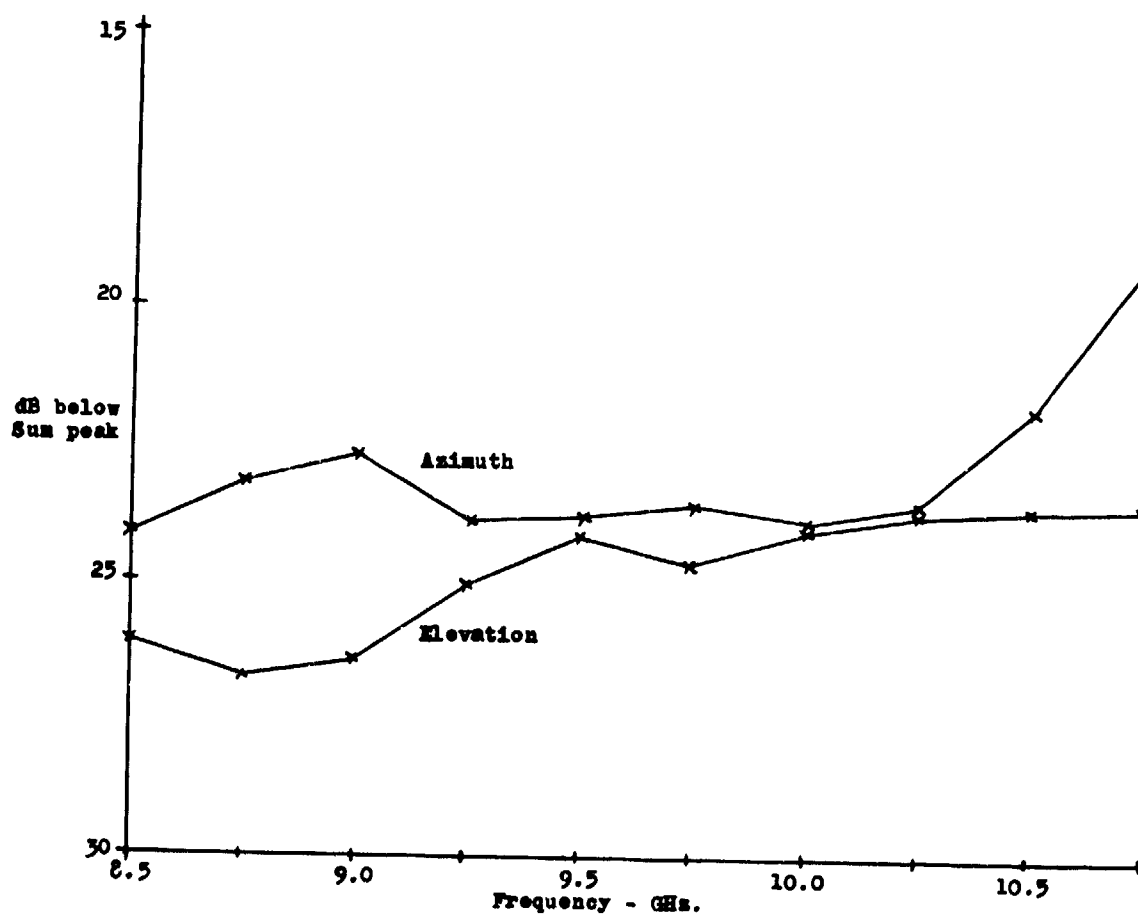


Fig. 6. Depth of Difference Channel Nulls.

DISCUSSION

M. VOGEL: What type of measurement did use to find out the aperture illumination cut-off inside the edge of the main reflector?

A.J. LAIT: Near field probe measurements using a small horn, were made. These were only approximate measurements, but they gave a good indication of the cut-off of the illumination. This measurement also indicated that the desired redistribution of the energy had been achieved.

T. KEATING: Does your efficiency value include I^2R losses, and to where do you reference the value?

A.J. LAIT: Yet it includes these losses, and the value is referred to the antenna input. The efficiency is calculated from the measured gain.

R.H.J. CARY: How do you measure efficiency?

A.J. LAIT: The gain of the antenna is measured by comparison with a standard gain horn. The efficiency is then calculated by comparing this gain with the gain of the uniform illumination across the total antenna aperture. This therefore includes the effect of all antenna losses, which may be resistive, aperture loss, spillover, cross-polarization, etc.

SHF HIGH POWER AIRBORNE COMMUNICATIONS ANTENNA

J. P. Grabowski
 F. L. Lanphear
 RCA Missile and Surface Radar Division
 Moorestown, New Jersey 08057

SUMMARY

The high power SHF antenna, which is mounted atop the fuselage of a KC-135 aircraft, is part of a link which permits communication between tactical terminals by means of a synchronous-altitude satellite. The antenna can acquire and track a satellite beacon signal, hold a stable line of sight for a short period of time, and is capable of being computer pointed. The antenna configuration was specifically designed for handling high CW power levels at X-band frequencies without the use of forced-air or liquid cooling.

A 32-inch Cassegrain antenna system was selected to provide a minimum antenna gain of 32.5 dB over a 6% transmit frequency band and a separate 6% receive frequency band. The antenna radiates a right-hand circularly polarized signal at a CW power level of 12.5 kW and simultaneously receives left-hand circularly polarized signals. Computations utilizing measured antenna patterns indicate the antenna noise temperature to be 84°K.

The feedhorn is a simple conical horn aperture operating in the dominant mode. A 2-mil H-film aperture window serves as the feed radome and pressure barrier. Compactness is achieved in the feed design by incorporating a circularly polarized dual-mode transducer which generates the required senses of circular polarization and at the same time provides the duplexing between the transmit and receive signals. The subreflector is only four wavelengths in diameter and includes a reflective disk at the hyperbola vertex to give a broadband impedance match and provide control of the transmit-receive isolation.

1. INTRODUCTION

The High Power SHF Antenna was designed to help evaluate a tactical satellite communications system which links tactical terminals by means of a synchronous-altitude satellite. The antenna is intended to be part of an airborne terminal communication system which can acquire and track* a satellite beacon signal, hold a stable line of sight for a short period of time with on-mount gyros, or be computer pointed. The antenna system selected for this application is a Cassegrain design which includes a 32-inch main reflector and a 6-inch subreflector which is servo controlled in azimuth and elevation to provide nearly complete hemispheric coverage.

This paper will discuss only the RF portions of the antenna subsystem. The antenna was developed and flown with a 2 kW average power system and then was redesigned to handle 12.5 kW. This latter configuration will be described.

2. HIGH POWER DESIGN

The existing 2 kW antenna system (Figures 1 and 2) was assessed for its suitability and limitations for handling the specified 12.5 kW of average transmitter power. With no additional cooling, the majority of the components used in the transmitter RF channel would reach excessive (425° F) or near excessive temperature. Highest temperatures would occur in the two transmit-channel rotary joints and in the feedhorn.

Two general approaches are available to reduce these temperature extremes: cooling and reduction of heat input.

2.1. Thermal Design

Cooling requires a design which more readily uses conduction, convection, and radiation without relying on liquid or forced air since the application is for an airborne system. These design considerations were assessed and optimized by computer methods.

A thermal model was established and verified by temperature data from the 2 kW SHF antenna system. As a result of this computer evaluation, the thermal efficiency of the RF system was increased by the following methods:

1. Improved conductive coupling between the RF components and the basic antenna structure. This permits the antenna to serve more efficiently as a thermal radiator.

* Tracking data is obtained by a slow mechanical movement of the main aperture which is platform stabilized for aircraft motion. Only a single receive channel is required.

2. The use of fins on the waveguide and the feedhorn.
3. The use of special paints that have a higher emissive value than the original system.

2.2. RF Design

The reduction of heat input by minimizing RF loss is doubly beneficial because 1) less thermal energy is to be dissipated, and 2) an increase in the radiated RF energy is achieved. Appreciable loss reduction is possible by taking full advantage of the microwave technology on surfaces, materials, waveguide modes, and component configuration.

In the transmit path the original aluminum WR112 waveguide was replaced with WR137 OFHC (oxygen-free high conductivity) copper waveguide with the exception of a 4-inch flexible waveguide section made of beryllium copper. The flexible waveguide solves mechanical tolerance and thermal expansion problems. Special considerations were applied to the flexible waveguide with regard to plating, jacketing, and external finish. Waveguide joints were minimized, including combination of the feedhorn and polarizer network. Where flanges were required, special Parker-type seals were used both to seal and to ensure maximum heat transfer across the flange.

Coating of the waveguide inner surfaces was investigated with the conclusion that in a dry, non-corrosive atmosphere, an uncoated surface was best. Tests were made on a temperature-cycled piece of waveguide having an uncoated inner surface, and no increase in loss was detected.

Figure 2 shows the losses in the original system as compared to the 12.5 kW system. The combination of reduced RF loss and increased thermal efficiency results in acceptable component temperatures under worst-case conditions.

3. COMPONENT DESIGN

The following paragraphs briefly describe the microwave components in the antenna subsystem, with special emphasis on the dual-channel rotary joint which proved to be a critical component in terms of the high power design.

3.1. Rotary Joints

Three rotary joints are required in the antenna system: 1) a high-power dual-channel azimuth, 2) a high-power elevation, and 3) a low-power elevation. In the conventional, coaxial, TEM-mode rotary joints, the greatest loss and thus highest temperatures occur at the center conductor where dissipation is most difficult. A logical solution is elimination of the center conductor. For the single-channel high-power elevation joint, the TM_{01} mode was used, where, without the center conductor, all the RF losses occur in the outer wall. This type of joint also has lower losses than the conventional TEM type as the TM_{01} mode is a lower loss mode. For the dual-channel azimuth joint, two decoupled modes in circular waveguide were used, the TM_{01} mode for the transmit channel and the circularly polarized TE_{11} mode for the receive channel. (A third channel, the opposite-sense circularly polarized TE_{11} mode was unused and terminated.) This design approach has the following advantages:

1. The cross coupling between the transmit and receive channels is independent of impedance mismatches in either channel. Theoretically the modes are completely decoupled; actually 35 to 40 dB is attained.
2. Since the TM_{01} mode has no phase variation with rotation, the line stretching effect is eliminated in the transmit channel.
3. Reflections caused by minor fabrication imperfections are absorbed in the resistive load terminating the third channel.
4. Reduction in loss for both channels is obtained over an equivalent TEM rotary joint.
5. Ease of thermal dissipation of the heat generated is achieved.

A block diagram of the rotary joint parts is shown in Figures 3 and 4. The non-rotating section consists of a mode exciter and a polarizer. The exciter is a waveguide junction in which the TM_{01} mode and two orthogonal TE_{11} modes are launched in circular waveguide. The transmitter is connected to the TM_{01} mode port and the receiver to the TE_{11} mode port. The polarizer converts the orthogonal TE_{11} modes into a circularly polarized TE_{11} mode at the rotating junction. The rotating section is identical to the non-rotating.

With this design a new type of rotary joint has been developed for dual channel applications with high average power capability and extremely low loss for both the transmit and receive channels.

The low power receive elevation rotary joint uses the conventional TEM design.

3.2. Feed and Radome

The feedhorn is a simple conical horn aperture operating in the dominant mode. The 10-dB beamwidth is 100 degrees, which efficiently illuminates the subreflector and the antenna. The aperture window is 2-mil H-film which also serves as a pressure barrier. The H-film material maintains excellent electrical and physical properties over

a wide range of temperatures. The finned waveguide feed as seen in Figure 5 is well within the shadow of the subreflector and provides an efficient thermal path for the removal of heat.

3.3. Polarizer

The polarizer element is essentially a dual-mode transducer and a circular polarizer integrated into a single microwave component. It consists of two rectangular waveguide inputs with a common center wall which forms a sloping (20°) septum arrangement extending from the top to the bottom waveguide wall. The output of the polarizer is a single, square, waveguide channel capable of supporting circular polarization. A sketch of the polarizer is shown in Figure 6. Linearly polarized signals from the transmitter pass through the polarizer and emerge as right-hand circularly polarized signals. Conversely, left-hand circularly polarized signals are received by the antenna, and as they pass through the polarizer the signals are simultaneously combined into a linearly polarized signal and directed to the receive channel.

3.4. Subreflector

The subreflector is a four-wavelength hyperbola which includes a vertex matching plate. The purpose of the vertex plate is to reduce the mismatch of the subreflector to the feedhorn. These reflections, which are approximately 14 dB down from the transmitted signal, degrade the inherent isolation between the transmit and receive channels. Since "duplexing" is achieved by the polarization characteristics of the antenna, all reflections from the subreflector which re-enter the feed end up in the receive channel. There are various ways in which the subreflector can be matched; however, the 16% bandwidth requires the matching element to be placed at the source of the mismatch. The disadvantage of the vertex plate is an increase in the antenna pattern first sidelobe levels from 18 dB to 15 dB.

4. PERFORMANCE

Except for the thermal analysis, all of the following data and results were obtained from a completely assembled end-item antenna. The thermal data was obtained by a computer analysis of a thermal model of the antenna, requiring inputs from insertion loss measurements and high power tests of the various microwave components. Accurate insertion loss measurements were made with the use of a HP-8540A Network Analyzer. In addition, high power tests which measured heat dissipation of the various components were evaluated against the measured insertion losses and good correlation was obtained. Table I summarizes the antenna performance.

4.1. Thermal Analysis

Table II shows the calculated temperatures of the 2-kW system components if used at 12.5 kW. Also shown in Table II are the 12.5-kW system component resultant temperatures for the condition of: 1) the aircraft at sea level, operating in the sun with no wind (the worst case), and 2) at 45,000 feet altitude, all based upon computer analysis. Figure 7 shows the location of the components listed in the table. A limiting temperature value is stipulated to be 425°F for no appreciable strength loss of aluminum alloys.

High power RF tests were performed on the feedhorn-polarizer, elevation rotary joint, and the dual-channel azimuth rotary joint to evaluate the design for RF breakdown and heat dissipation. These tests were performed at 10 kW CW, with the results extrapolated to 12.5 kW CW (10 kW CW being the maximum power available, since the final transmitter was not yet developed). The components were found to be free of RF breakdown when operated to the point of full temperature stabilization.

4.2. Pattern Data

A contour pattern of the antenna is shown in Figure 8. The symmetry of the main beam can be seen along with the sidelobe structure which is at a maximum in the 45° planes. These sidelobes are the result of the quadripod support for the subreflector. The first sidelobes occur at an angle of 5 degrees from boresight and vary between 14 and 16 dB over the frequency band. The second sidelobe varies between 24 and 30 dB. The 3-dB beamwidth is 3 degrees and is consistent with the antenna gain. Sidelobes and beamwidth data are shown in Figure 9.

4.3. Gain

The antenna gain at center frequency was calculated to be 33.8 dB. This value results from an antenna efficiency calculation of 55%. Measured gain values of 33.25 dB were obtained at the input to the dual channel rotary joint. The microwave losses amount to 0.4 dB, and when added to the measured gain values result in an antenna gain of 33.65 dB. Gain values are shown in Figure 9.

4.4. Axial Ratio

The axial ratio of the antenna is almost entirely a function of the polarizer performance. As can be seen from Figure 9, the axial ratio is less than 1.0 dB across the complete operating frequency band.

4.5. Isolation

The isolation between the transmit and receive channels is achieved by the tuning disk at the vertex of the subreflector. The disk diameter and location have been experimentally developed to yield the best overall isolation

characteristics. The measured values all exceed the requirement of 20 dB. Figure 10 shows the effectiveness of the disk on the transmit-receive isolation.

4.6. Antenna Noise Temperature

The antenna noise temperature, in degrees K, is calculated from the expression

$$T_A' = \frac{T_A}{L_A} + T_t \left(1 - \frac{1}{L_A}\right)$$

where

T_A is the antenna noise temperature due to the pattern.

L_A is the microwave losses.

T_t is the thermal temperature of the antenna = 290°K.

T_A is first determined by dividing the antenna pattern into sectors and multiplying the temperature of the source which the sector is directed at by the percentage of energy contained in each sector. The sum of the individual temperature contributions yields the antenna temperature due to external sources. Table III shows the pattern breakdown and calculation of T_A for an elevation angle of 7.5 degrees. From the table, T_A is 53.4°K.

The microwave losses have been measured at 0.6 dB maximum and the resultant computation of T_A' gives an antenna noise temperature of 83.6°K.

5. CONCLUSION

A successful modification has been accomplished to an existing airborne antenna which required an increase in the average power-handling capabilities from 2 kW to 12.5 kW at X band. The basic design of the antenna and microwave layout was unchanged and all of the original specifications were met or exceeded. The modified design resorted to neither liquid nor forced-air cooling to dissipate the additional heat load. Instead, acceptable component temperatures were achieved by reducing the RF insertion loss and increasing the thermal efficiency. Finally, a new dual-channel rotary joint was developed for this program, featuring extremely low loss in both the transmit and receive channels.

6. REFERENCES

Weber, H. E., October 1969, "Aircraft to Satellite SHF Communications," Microwave Journal, V. 12.

Woodward, O. M., December 1970, "A Dual-Channel Rotary Joint for High Average Power Operation," IEEE Transactions on MTT.

7. ACKNOWLEDGEMENTS

The work reported was carried out under the sponsorship of the Air Force Avionics Laboratory, Wright Patterson AFB, Ohio, contracts F33615-69-C-1601 and F19628-67-C-0428. The guidance and assistance of Harold E. Weber of the Avionics Laboratory is gratefully acknowledged; his contributions were a significant factor to the success of both programs.

It is also a pleasure to acknowledge the contributions and leadership of W. C. Wilkinson of RCA in Moorestown, New Jersey to the above mentioned programs.

TABLE I. ANTENNA PERFORMANCE

Parameter	Specified Value	Measured Value
Frequency	7.25 - 8.4 GHz	7.25 - 8.4 GHz
Gain	> 32 dB	> 32.5 dB
Polarization	Xmit RHCP, Rcv LHCP	Xmit RHCP, Rcv LHCP
Axial Ratio	< 3 dB	< 1.0 dB
Beam Shape	Symmetrical	Symmetrical
Sidelobes	< -12 dB	< -14 dB
VSWR	< 1.5	< 1.35
Losses	< 0.6 dB	< 0.5 dB
Power Handling	12.5 kW avg.	12.5 kW avg.
Isolation	20 dB	> 20 dB
Antenna Noise Temperature	92°K	83.6°K

TABLE II. COMPONENT TEMPERATURE, ASSOCIATED DISSIPATION AND CONDITION

Component Dissipation - watts (724 watts total)			
Gyros	6.5	Finned Waveguide	50.0*
Az Motor	1.0	El Rotary Joint	83.0*
El Motor	30.0	Long Waveguide	60.0*
Slip Ring	2.0	Az Rotary Joint	112.0*
El Synchro	1.5	Feedhorn	10.0*
Az Synchro	1.0	Polarizer	50.0*
* at 75°F, with loss (dB) linearly varying to a 30% increase at 400°F.			
Assumed Conditions			
	A	B	
Radome RF Heating, watts	375	375	
Ambient Temperature °F	100	-40	
Altitude, ft	S. L.	45,000	
Cabin Temperature °F	90	70	
Cabin Pressure Altitude	S. L.	8,000	
Aircraft Airspeed (Knots)	0	200	
Radome Thermal Resistance, °F/BTU/HR	0.011	0.011	
Radome Thermal Absorbance	0.9	0.9	
Radome Thermal Emissivity	0.8	0.8	
Temperatures °F for the Assumed Conditions			
Location (see Figure 7)	2 kW Components	A	B
A Radome Apex		243	191
B Radome Air	338	209	115
C Feed/Polarizer	610	304	272
D Transmit Elevation RJ	620	362	322
E Transmit Waveguide	450	390	321
F Az Rotary Joint	800	264	208
G Az Rotary Joint		237	195
H Az Rotary Joint		257	247
I Receive Waveguide		230	165
J Receive Waveguide		235	179
K Gyros		240	170
L El Motor		243	185
M Az Motor		221	171

TABLE III. ANTENNA TEMPERATURE DUE TO THE PATTERN

Pattern Section	Percent of Energy	Temperature Source (°K)	Contribution (°K)
Main Beam -3.5° to +3.5°	61.5	20	12.3
Sidelobes up +3.5° to +8°	6.53	11	0.718
Sidelobes down -3.5° to -8°	6.53	60	3.92
Sidelobes up +8° to +30°	3.04	6	0.18
Sidelobes down -8° to -30°	3.04	290	8.81
Sidelobes up +30° to +60°	5.4	4	0.216
Sidelobes down -30° to -60°	5.4	290	15.65
Sidelobes up +60° to 90°	3.92	2	0.0784
Sidelobes down -60° to -90°	3.92	290	11.35
Backlobes up +90° to +180°	0.4	5.5	0.0022
Backlobes down -90° to -180°	0.4	290	<u>0.156</u>
TOTAL			53.4°K

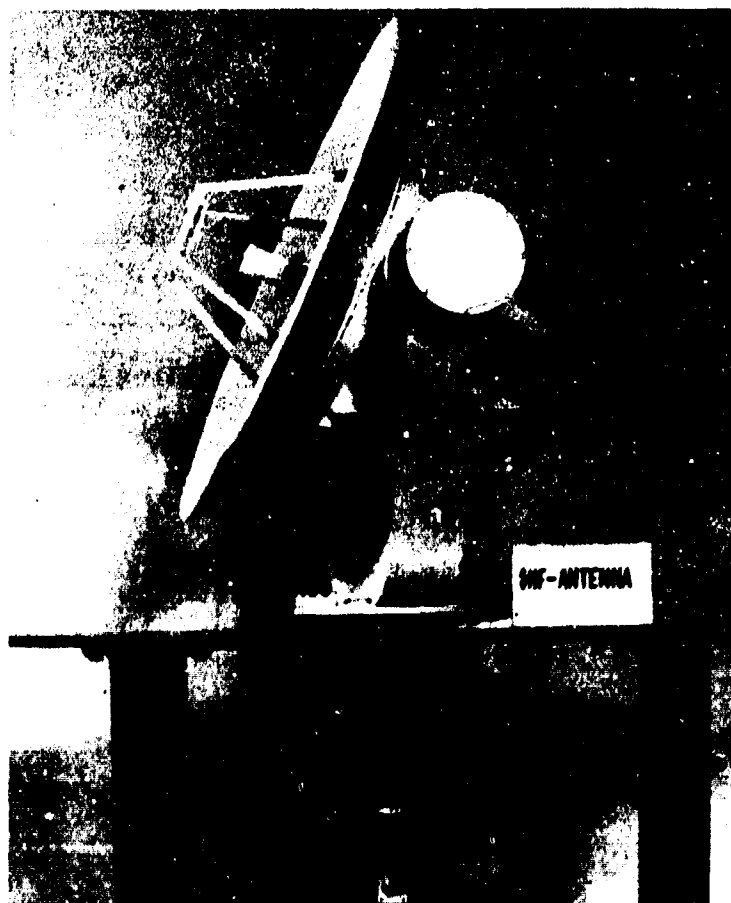


Figure 1. SHF High Power Airborne Communications Antenna

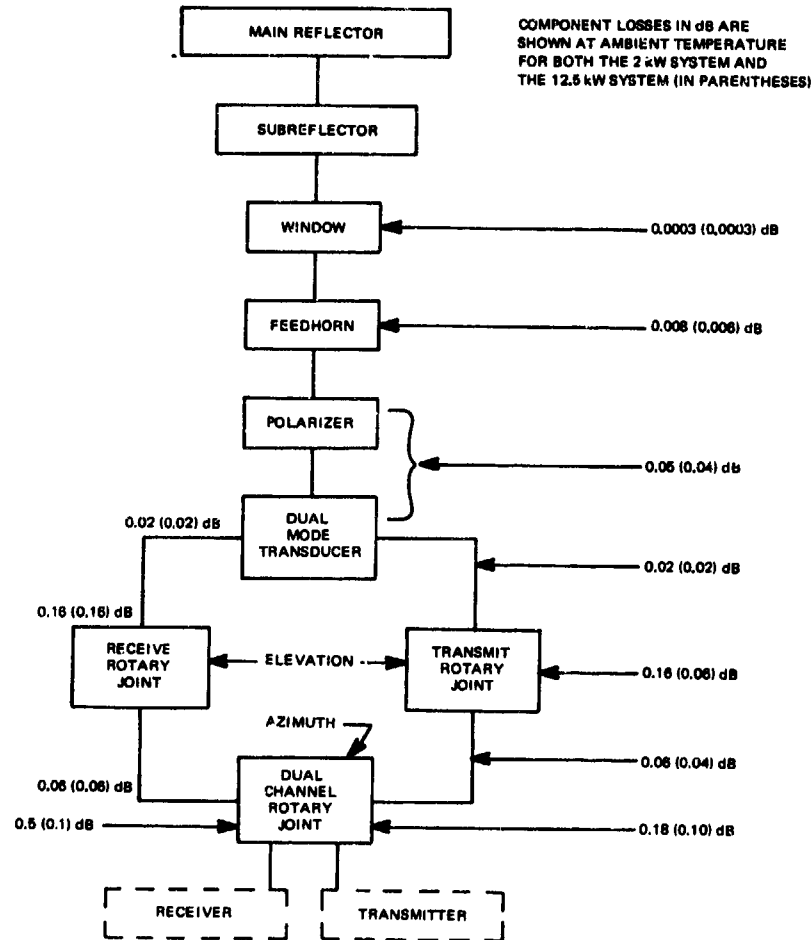


Figure 2. SHF Antenna Block Diagram

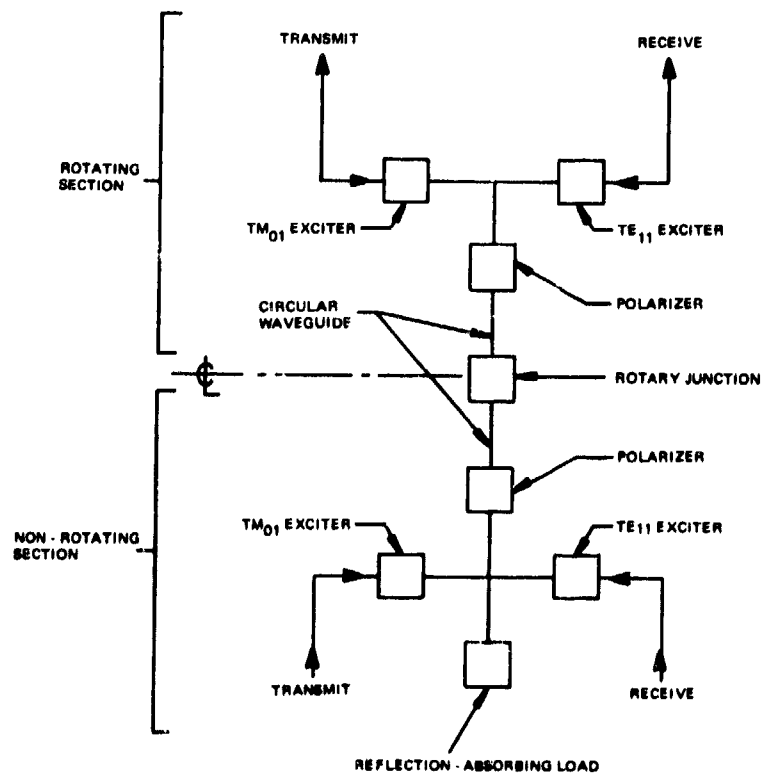


Figure 3. Block Diagram of Dual Channel Rotary Joint

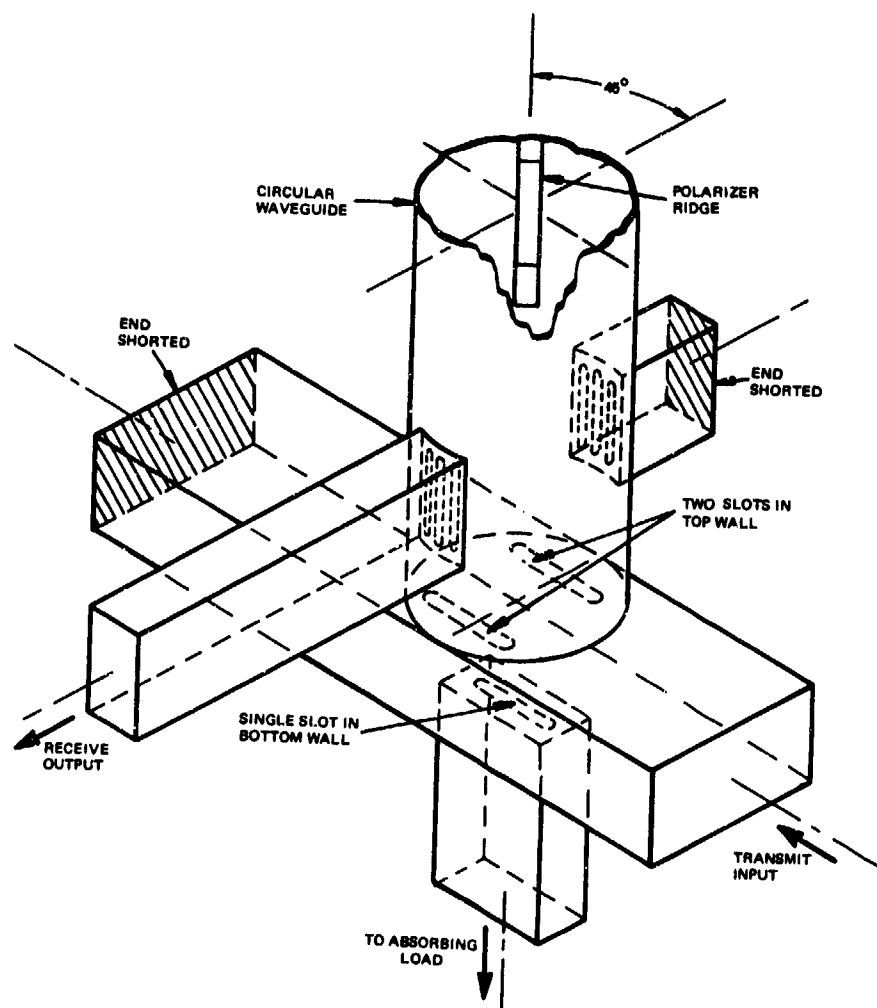


Figure 4. Multimode Exciter and Polarizer



Figure 5. Feedhorn

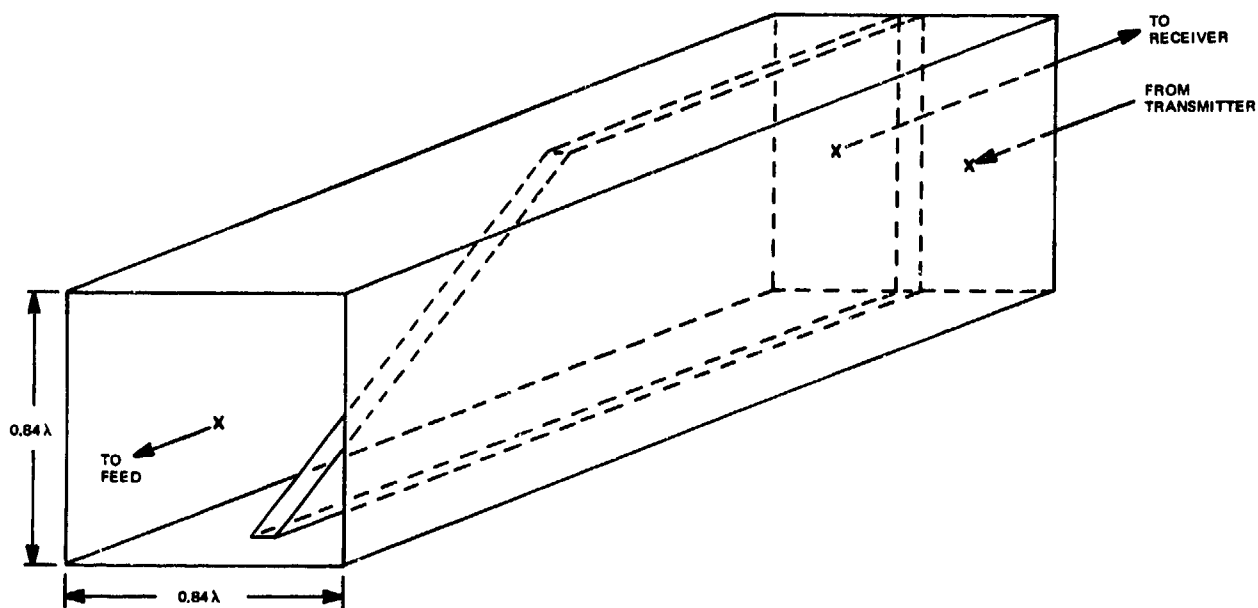


Figure 6. Basic Construction of Dual Mode Polarizer

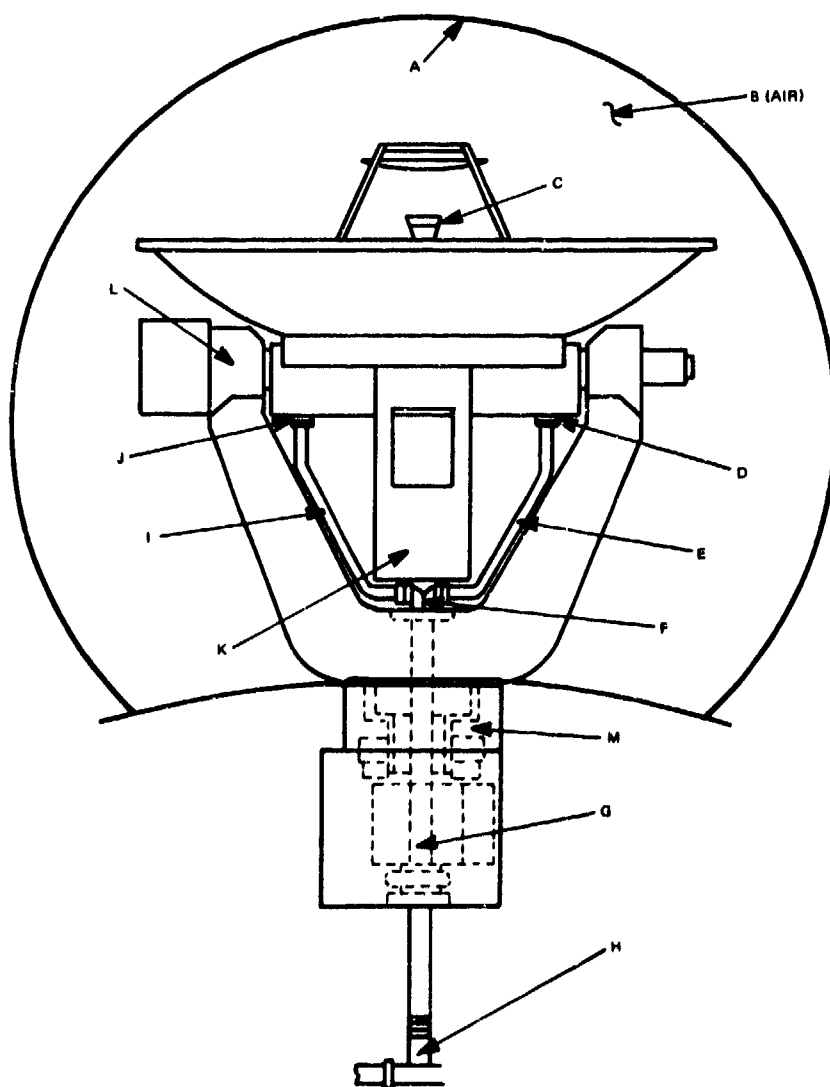


Figure 7. Thermocouple Location for Thermal Analysis of Antenna

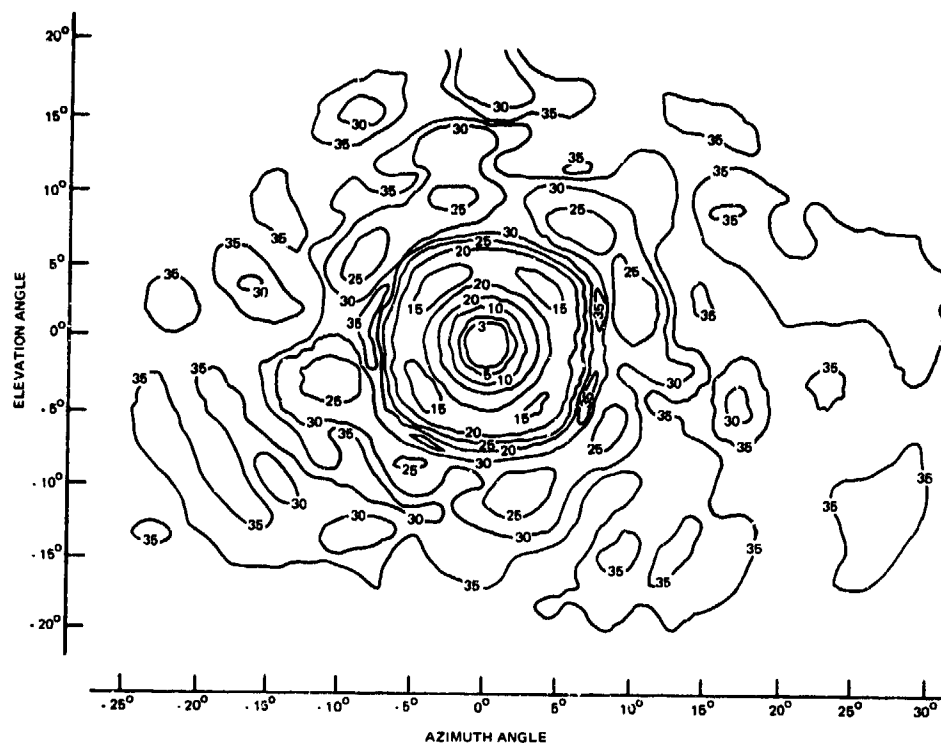


Figure 8. SHF Antenna Contour Pattern

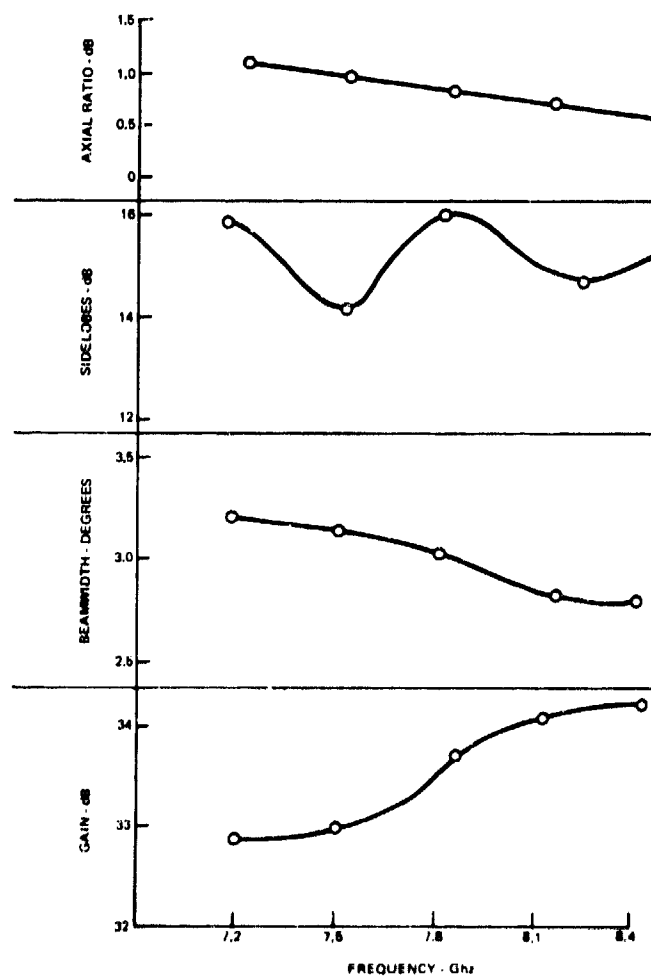


Figure 9. Measured Data, SHF Antenna

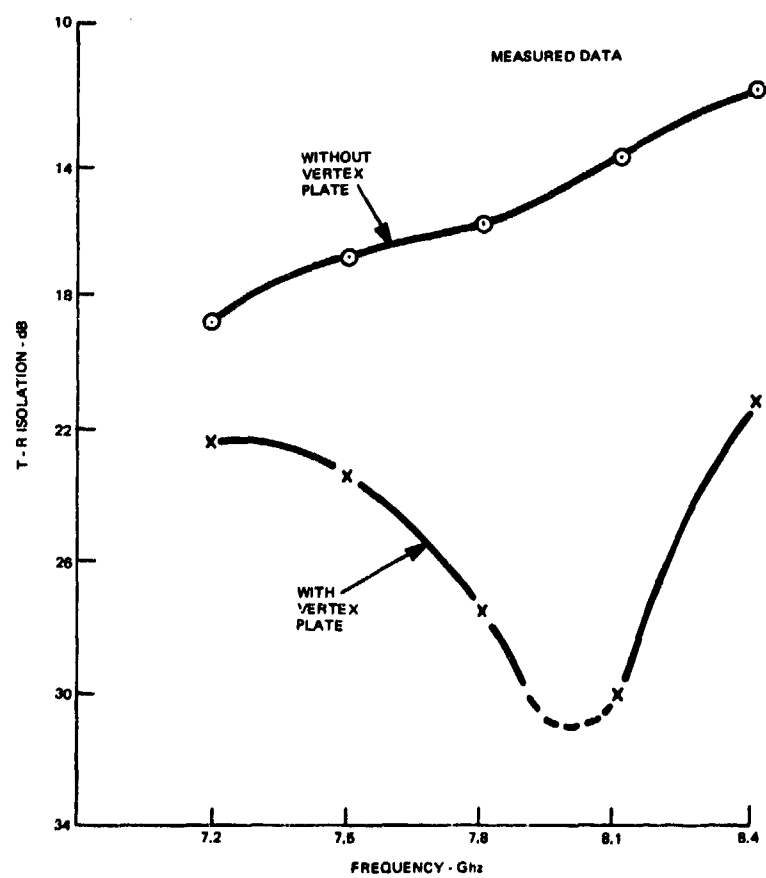


Figure 10. SHF Transmit-Receive Isolation

DISCUSSION

M. VOGEL: Even for high isolation between transmit and receive channels, many watts of cw power will leak into the receive channel. Does this pose any problems?

F.P. GRABOWSKI: During transmission, energy coupled from the transmit channel to the receive channel is reflected back towards the feed horn by filters protecting the receivers. This coupled energy is reradiated by the feed in the opposite sense circular polarization which has a slight degrading effect on the axial ratio of the transmitted signal. Measured transmit axial ratios with the receiver part short circuited are less than 1.5dB.

PROBLEMES D'ANTENNES POSES PAR LE PASSAGE EN BANDE S

DES TELEMESURES

M. NICOLAS et C. MAST
ELECMA, 22 Quai Galliéni,
92150 SURESNES - FRANCE

RESUME.-

Le passage en bande S des télémessures nécessite par l'encombrement de la bande VHF pose de nouveaux problèmes pour les antennes sol et bord. Au sol, une augmentation de gain est nécessaire ; l'étroitesse des faisceaux impose une poursuite plus précise. A bord, le rayonnement est très perturbé par le corps de l'engin et sa rotation éventuelle.

On décrit les principes retenus pour des antennes sol, bande S, à poursuite automatique, et on donne des exemples de réalisation. Les antennes sont du type réflecteur parabolique et source monopulse. Les signaux d'écartométrie sont traités de façon à fournir un signal composite analogue à celui délivré par un dispositif de balayage conique. Le récepteur de poursuite est ainsi particulièrement simple.

On donne également un exemple d'antenne sol recevant simultanément les deux bandes, S et VHF.

Enfin, on décrit une antenne d'engin, constituée d'un réseau circulaire de fentes rayonnantes, fournissant un diagramme indépendant de la rotation.

1.- INTRODUCTION.-

Les télémessures pour les essais d'avions et d'engins abandonnent progressivement la bande 215-260 MHz au profit de la bande S (2300 MHz). Cette évolution est imposée par l'encombrement croissant de la bande VHF. Elle permet de plus une augmentation du volume d'informations transmises.

Le passage en bande S pose de nouveaux problèmes, autant pour les antennes sol de réception que pour les antennes bord.

2.- PROBLEMES POSES PAR LE PASSAGE EN BANDE S.-

Une augmentation de fréquence toutes choses égales d'ailleurs, entraîne une dégradation des bilans de liaison. Ceci doit être compensé par une augmentation du gain des antennes et, notamment, de l'antenne de réception au sol. Celle-ci est donc d'assez grandes dimensions, et doit, par ailleurs, être réalisée avec une meilleure précision mécanique, du fait de la réduction de la longueur d'onde.

L'antenne sol ayant un gain plus élevé, sa directivité est plus grande, de sorte que son pointage dans la direction de l'avion ou de l'engin doit être réalisé avec une meilleure précision et que l'acquisition angulaire est plus difficile à effectuer. Un système de poursuite automatique évolué s'avère indispensable. D'autre part, compte tenu de la réduction de la longueur d'onde, le respect des conditions de phase impose une réalisation plus précise des circuits d'écartométrie. L'augmentation de la précision de poursuite présente toutefois un avantage : l'antenne de télémessure pourra éventuellement fournir des éléments de trajectographie.

En ce qui concerne les antennes bord, la longueur d'onde utilisée étant généralement très inférieure aux dimensions des engins, le diagramme obtenu est essentiellement variable en fonction de l'implantation de l'antenne. Le problème est d'obtenir un diagramme aussi régulier que possible, assurant un gain sensiblement constant dans la direction de l'antenne de réception. Un cas particulièrement fréquent et difficile est celui des engins en rotation.

Enfin, le passage de la bande VHF à la bande S s'effectuant progressivement, il est nécessaire de pouvoir assurer, pendant plusieurs années, l'utilisation simultanée des deux bandes. Ceci a conduit, notamment, à la réalisation d'antennes sol recevant les deux bandes de fréquence.

3.- PRINCIPES RETENUS POUR LES ANTENNES SOL : EXEMPLES DE REALISATION.-

Le gain élevé exigé des antennes de réception au sol en bande S a conduit à utiliser des réflecteurs paraboliques de grandes dimensions. Les figures 1, 2 et 3 montrent des exemples de réalisation :

- . CYCLOPE II (figure 1) est dotée d'un réflecteur de 18 mètres de diamètre.
Le gain maximal en bande S est de 48 dB.
- . ANTARES I (figure 2) est dotée d'un réflecteur de 4 mètres de diamètre.
Le gain maximal en bande S est de 35 dB.
- . ANTARES II (figure 3) est dotée d'un réflecteur de 2 mètres de diamètre.
Le gain maximal en bande S est de 24 dB.

../

La source primaire est composée de quatre éléments identiques, disposés en losange, permettant d'élaborer les signaux d'écartométrie, différence site ΔS , différence gisement ΔG , et somme Σ nécessaires à la poursuite automatique de l'engin. Le système retenu consiste à moduler le signal Σ par les signaux ΔS et ΔG affectés d'une modulation de phase périodique. On obtient ainsi, par un procédé statique, l'équivalent d'un balayage cône qui serait obtenu par rotation d'une source primaire unique autour de l'axe du réflecteur. Par rapport à un monopulse d'amplitude classique, cette solution présente l'avantage de ne nécessiter qu'une seule chaîne de réception de poursuite, au lieu de trois. Par rapport au balayage cône obtenu par rotation de la source primaire (solution adoptée dans une version antérieure de CYCLOPE II), les problèmes mécaniques sont éliminés, et notamment, le joint tournant qui contribue en général fortement à limiter la fiabilité de l'ensemble.

La figure 4 donne le principe du système d'écartométrie. Les deux signaux différence ΔS et ΔG sont modulés en phase, 0 - π , par deux signaux à 500 Hertz en quadrature de phase, puis additionnés au signal somme Σ , prélevé après préamplification. On obtient ainsi un signal composite, analogue à celui que fournirait un balayage cône, dont on extrait les informations erreur site et erreur gisement par détection synchrone à l'aide des signaux de référence de modulation site et gisement.

Les modulateurs 0 - π réalisés en circuit triplaqué, utilisent des longueurs de ligne et des commutateurs à diodes P. I. N.

Les éléments rayonnants sont du type "dipôle croisé", permettant la réception simultanée en polarisation circulaire droite et gauche. Ils sont placés en avant d'un plan réflecteur, derrière lequel est situé l'ensemble des circuits hyperfréquences en bande S et, notamment, les circuits d'écartométrie.

Le tableau ci-dessous donne les principales caractéristiques de différents modèles d'antenne sol en bande S qui ont été réalisés par ELECMA :

TYPE D'ANTENNE	CYCLOPE II	ANTARES I	ANTARES II
Diamètre du réflecteur parabolique	18 m	4 m	2 m
Gain	48 dB	35 dB	27 dB
Rapport d'ondes stationnaires dans la bande 2180-2310 MHz	< 1,5	< 1,5	< 1,5
Largeur à 3 dB du lobe principal	0,45°	2,3°	5°
Niveau des lobes secondaires par rapport au lobe principal	< -15 dB	< -20 dB	< -17 dB
Taux d'ellipticité (polarisation circulaire droite et gauche)	< 3 dB	< 3 dB	< 3 dB
Précision de poursuite (erreur quadratique moyenne)	0,2°	0,2°	0,25°
Domaine d'acquisition	1°	4,5°	10°

La largeur de bande des éléments rayonnants est suffisante pour permettre éventuellement la réception, à l'aide d'antennes de types ANTARES, de la bande 1750-1860 MHz, quelquefois utilisée simultanément avec la bande 2180-2310 MHz.

L'antenne CYCLOPE II permet de recevoir également la bande VHF 215-260 MHz.

4.- RECEPTION SIMULTANEE DES BANDES S et VHF.-

L'antenne CYCLOPE II permet la réception des signaux de télémétrie dans les deux bandes 2180-2310 MHz et 215-260 MHz, la poursuite automatique s'effectuant sur l'une ou l'autre des bandes de fréquence.

Ceci est obtenu en utilisant une source primaire constituée de quatre éléments en bande VHF (figure 5). Les éléments rayonnants sont du type dipôle croisé, permettant la réception en polarisation circulaire droite et gauche. Les quatre dipôles fonctionnant dans la bande S sont disposés aux sommets d'un carré et placés devant un réflecteur plan de 200 mm de diamètre. Les quatre dipôles fonctionnant en

bande VHF, également disposés aux sommets d'un carré, entourent la source en bande S ; ils sont placés devant un réflecteur plan de 1,80 mètre de diamètre. Les plans réflecteurs des deux sources sont séparés afin d'obtenir un centre de phase aussi voisin que possible du foyer du réflecteur parabolique dans les deux bandes de fréquences ; on évite ainsi les pertes de gain par défocalisation. Il est à noter qu'une solution de type Cassegrain, qui a été envisagée, n'offre pas d'intérêt car les conditions géométriques correspondant aux deux bandes sont trop différentes pour pouvoir donner lieu à un compromis valable. Dans la solution adoptée (sources primaires au foyer du réflecteur parabolique), le point critique est le masque important créé par la source en bande VHF, qui détériore les performances en bande S, notamment le niveau des lobes secondaires.

Le système d'écartométrie est identique dans les deux bandes. Il fonctionne selon le principe de pseudo balayage cône décrit au paragraphe 3.

Le tableau ci-dessous récapitule les principales performances de l'antenne CYCLOPE II dans les deux bandes de fréquence :

Bande de Fréquence	215 - 260 MHz (bande VHF)	2180 - 2310 MHz (bande S)
Gain	28 dB	48 dB
Rapport d'ondes stationnaires	< 2	< 1,5
Largeur à 3 dB du lobe principal	5°	0,45°
Précision de poursuite (erreur quadratique moyenne)	0,3°	0,2°
Domaine d'acquisition	10°	1°
Niveau des lobes secondaires par rapport au lobe principal	< -13 dB	< -15 dB

5.- ANTENNE BORD : exemple d'antenne à caractéristiques indépendantes de la rotation.

ELECMA a effectué, sur marché D.R.M.E., une étude théorique et expérimentale d'une antenne embarquée sur engin dont les caractéristiques de rayonnement sont insensibles à la rotation.

L'antenne consiste en un réseau circulaire de sources rayonnantes alimentées en équiphase et équiamplitude. Le choix du type d'élément rayonnant a été fait en fonction des conditions suivantes :

- . l'antenne doit présenter une épaisseur très faible afin de pouvoir être plaquée à la peau de l'engin,
- . le diagramme de rayonnement obtenu doit être quasiment omnidirectionnel, avec un trou aussi réduit que possible dans l'axe de l'engin.

Il est apparu que le type d'élément rayonnant le mieux adapté était une fente taillée sur l'une des faces d'une ligne triplée, disposée symétriquement au ruban central de la ligne. La fente a une longueur d'environ $\lambda/2$ et une largeur de $\lambda/10$ (λ étant la longueur d'onde) et fonctionne en mode résonnant.

L'antenne étant implantée sur une partie cylindrique de l'engin, les fentes peuvent être disposées selon les génératrices du cylindre, ou perpendiculairement aux génératrices. Il apparaît que la disposition perpendiculaire aux génératrices est préférable car elle fournit un diagramme de rayonnement présentant un trou moins important dans l'axe de l'engin.

Le nombre d'éléments rayonnants constituant l'antenne est fonction du diamètre du corps de l'engin et du taux d'ondulation que l'on tolère sur le diagramme de rayonnement dans un plan perpendiculaire à l'axe de l'engin. A diamètre donné, le taux d'ondulation est d'autant plus faible que le nombre d'éléments est grand.

Les principales caractéristiques d'une antenne de ce type en bande S seraient par exemple les suivantes :

- . bande de fréquence : 2188 - 2230 MHz
- . puissance admissible : 15 W
- . rapport d'ondes stationnaires : ≈ 2

- . cône de silence dans l'axe de l'engin : 10° à -10 dB
- . taux d'ondulation : $\leq \pm 3$ dB
- . polarisation rectiligne.
- . épaisseur maximale de l'antenne : 10 mm
- . implantation sur un engin d'un diamètre de 550 mm (environ 4 longueurs d'onde).

Pour obtenir un taux d'ondulation inférieur à 3 dB, compte tenu du diamètre de l'engin, il faut au minimum 15 éléments rayonnants. Pour des raisons de commodité d'alimentation, on choisit plutôt 16 éléments. Les 16 éléments, qui sont des fentes sur ligne triplaque à diélectrique verre téflon, sont alimentées en parallèle au moyen d'un répartiteur de puissance, également réalisé en technologie triplaque.

Si la longueur de la partie cylindrique du corps de l'engin sur laquelle est implantée l'antenne est supérieure à environ 8 longueurs d'onde (1100 mm), l'antenne étant située au milieu, le diagramme et notamment la largeur du cône de silence dans l'axe de l'engin ne dépendent pratiquement pas de la forme des extrémités du cylindre.

Les résultats théoriques ont été vérifiés à l'aide d'une maquette de 200 mm de diamètre, l'antenne comportant 8 éléments rayonnants (figure 6). Les diagrammes de rayonnement relevés dans un plan passant par l'axe de l'engin et dans un plan perpendiculaire à l'axe sont donnés figures 7 et 8.



FIG. 1 : ANTENNE CYCLOPE II

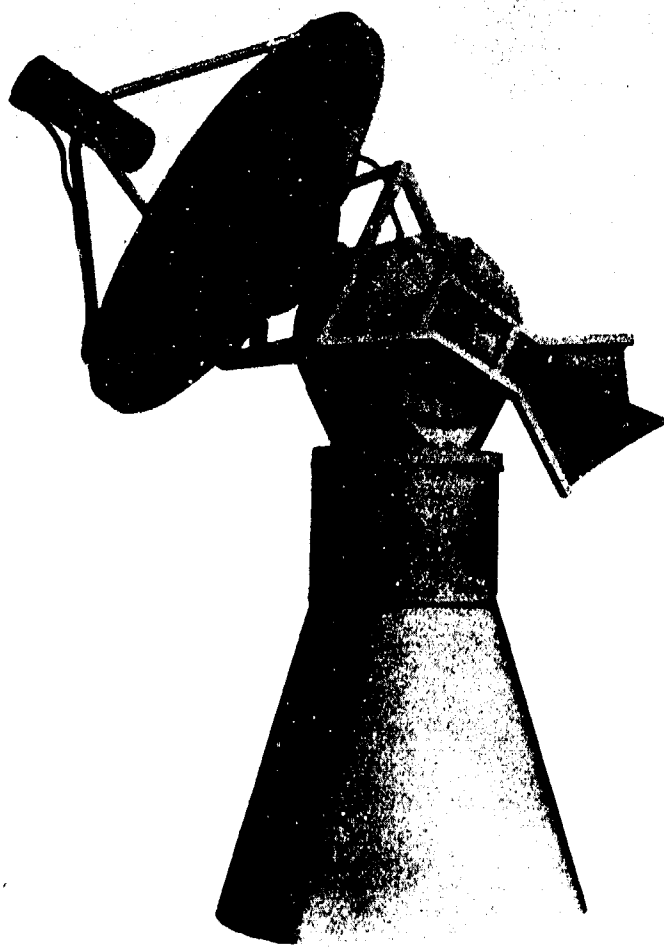


FIG. 2 : ANTENNE ANTARES I

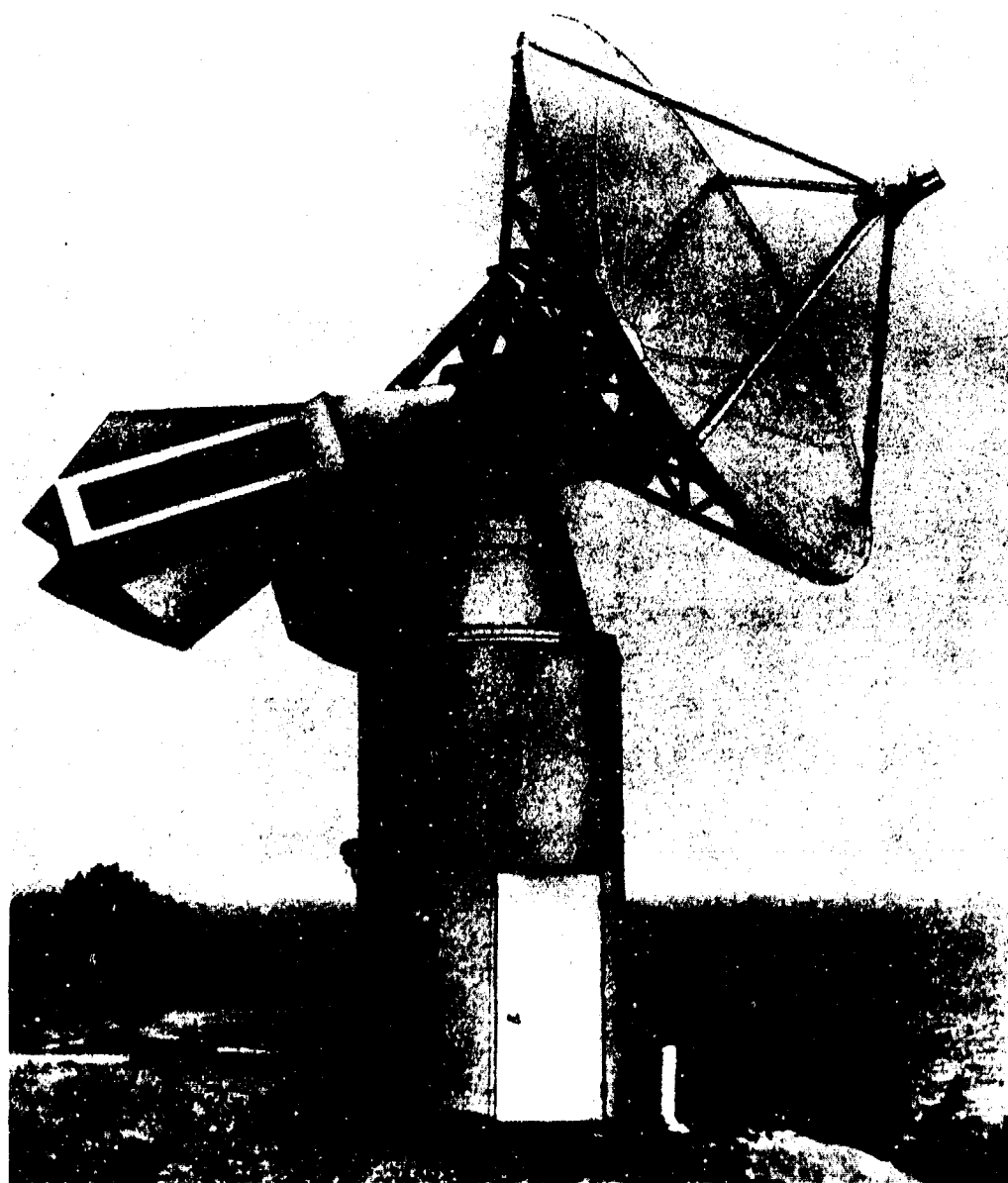


FIG. 3 : ANTENNE ANTARES II

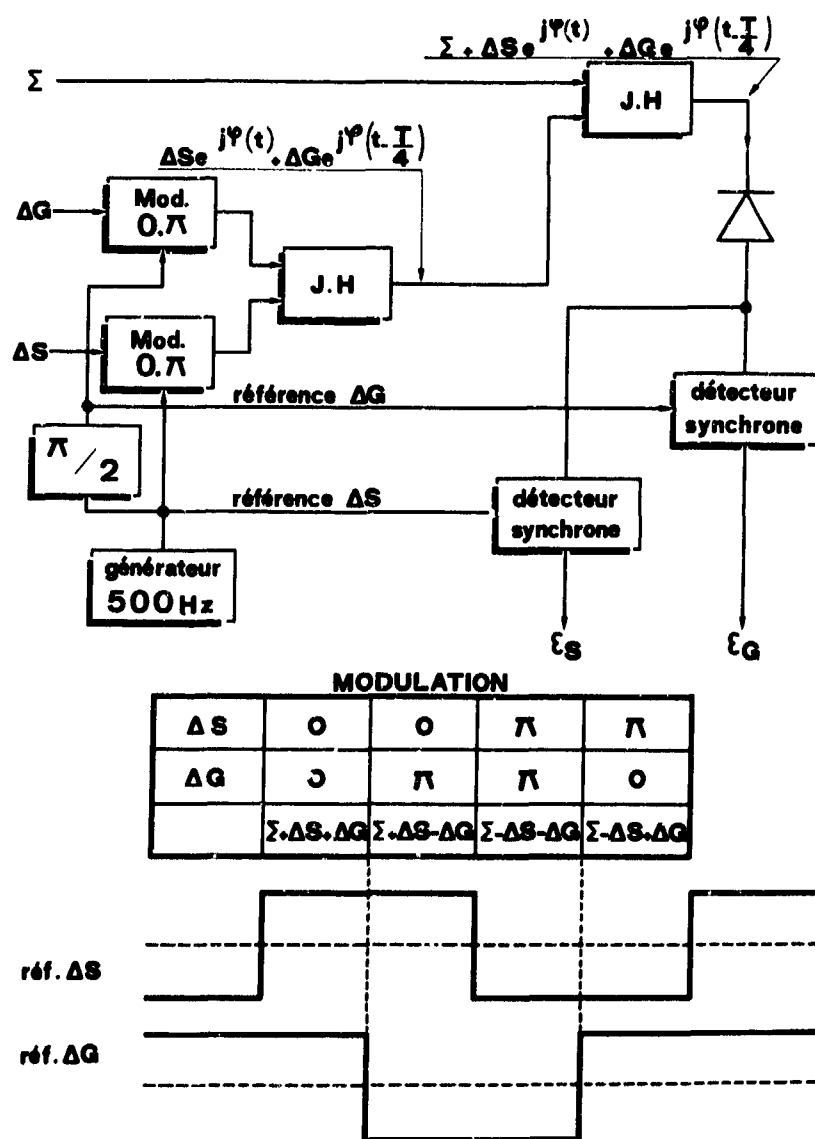


FIG. 4 : PRINCIPE DU SYSTEME D'ECARTOMETRIE

SOURCE CYCLOPE II

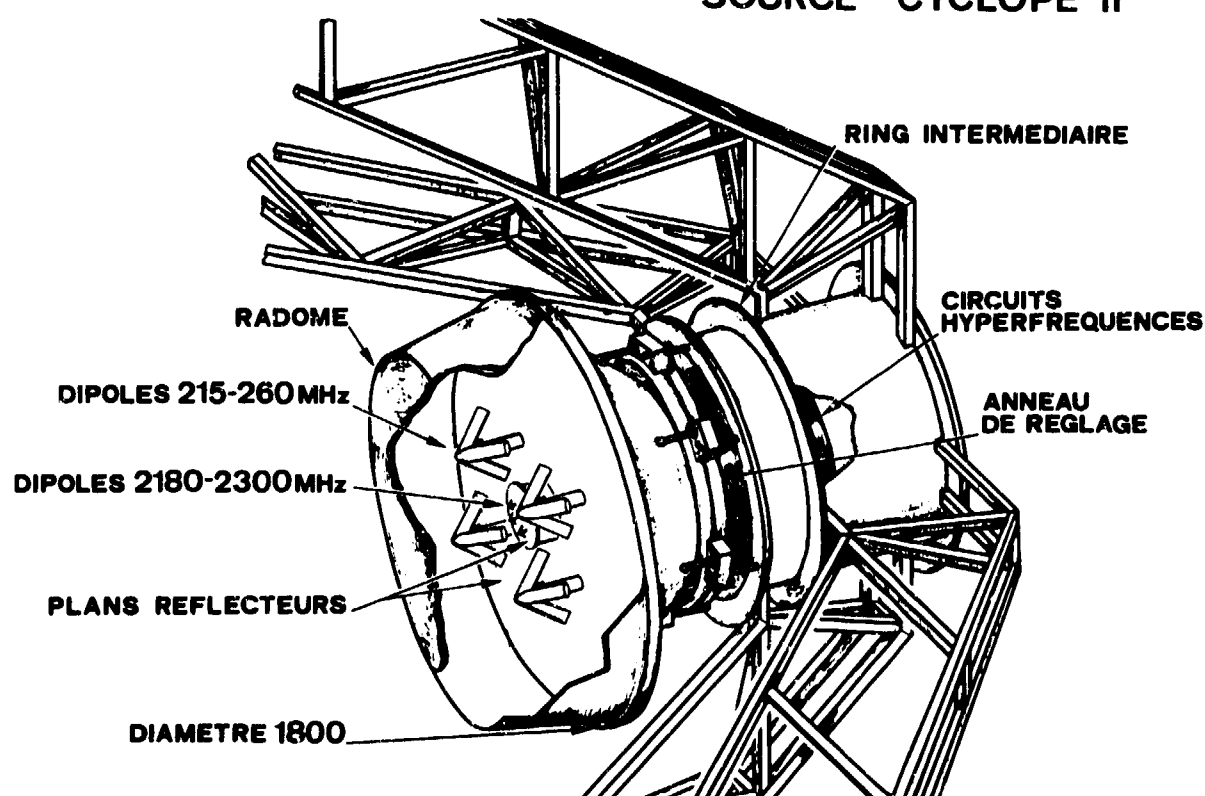


FIG. 5 : SOURCE BI-BANDE DE L'ANTENNE CYCLOPE II

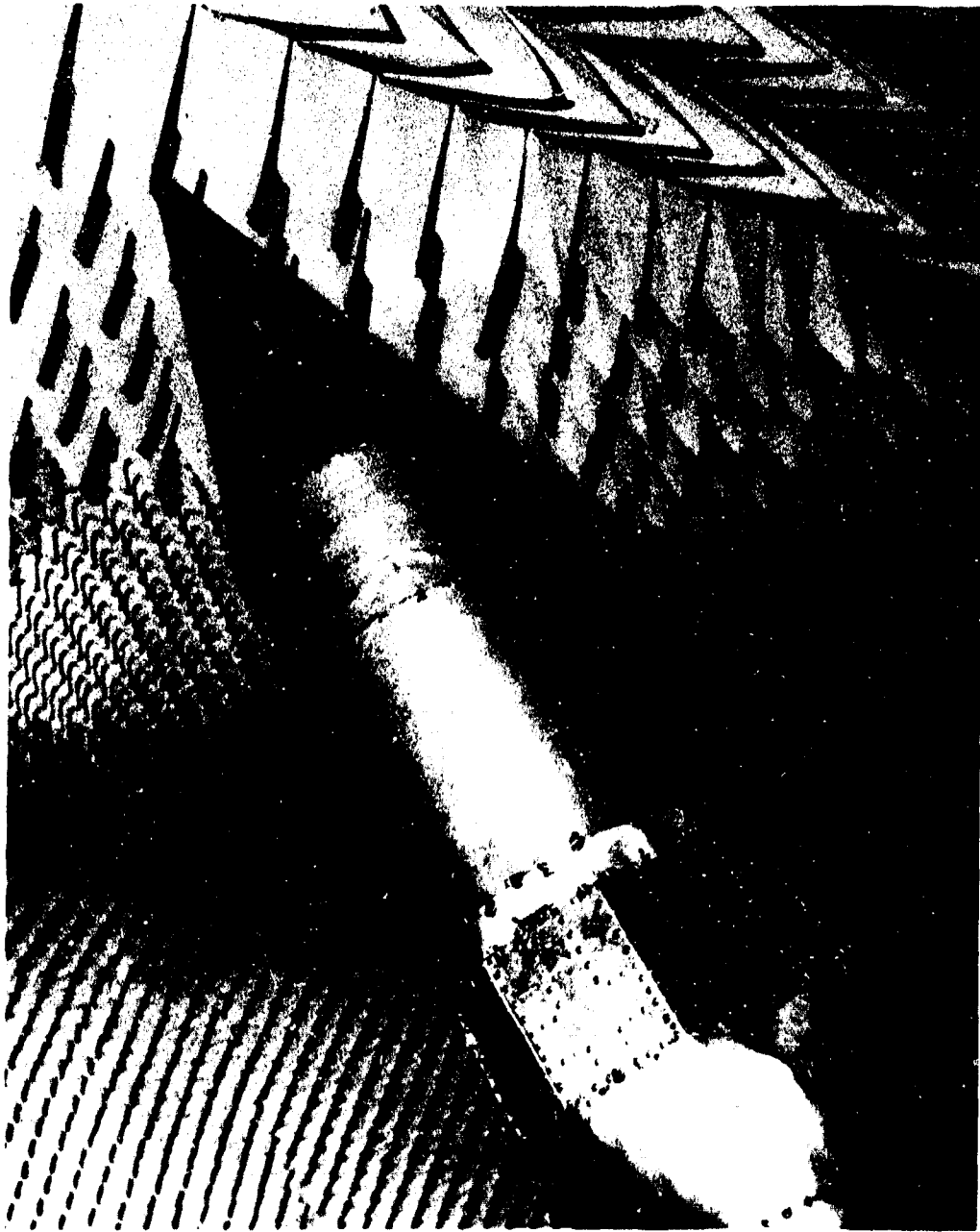


FIG. 6 : MAQUETTE D'ANTENNE ENGIN

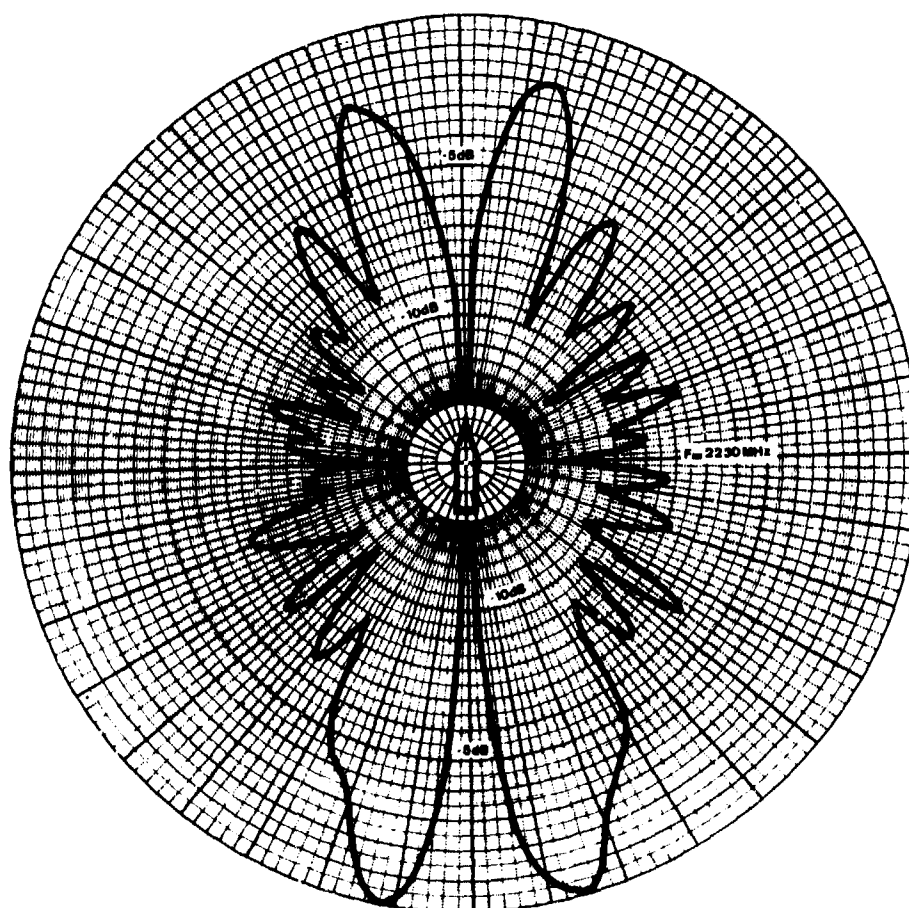


FIG. 7 : DIAGRAMME DE RAYONNEMENT DANS UN PLAN PASSANT PAR
L'AXE DE L'ENGIN.

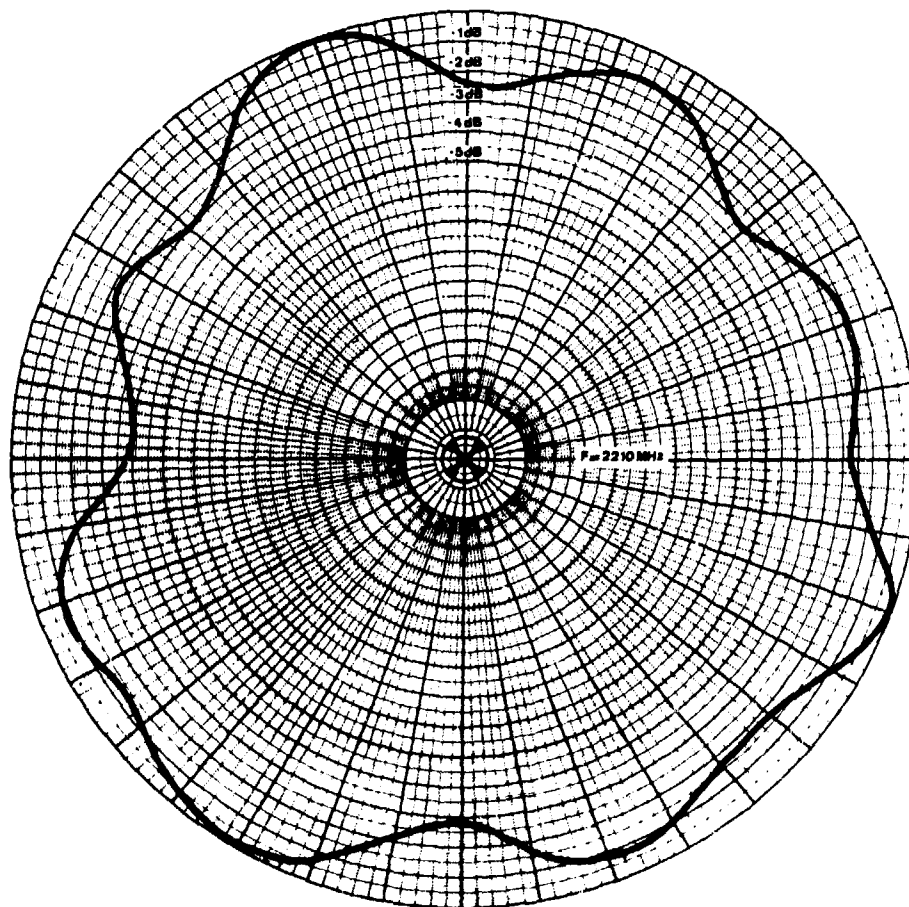


FIG. 8 : DIAGRAMME DE RAYONNEMENT DANS UN PLAN PERPENDICULAIRE
A L'AXE DE L'ENGIN

DISCUSSION

J.F. GOBERT: 1. Est il possible de poursuivre l'engin a partir du sol quand la polarisation varie?

2. Pourriez vous utiliser un mode de poursuite automatique, par exemple du type "diversité"?

C. MAS: La polarisation de l'onde reçue varie effectivement dans le temps, en fonction notamment de l'attitude de l'engin. Les antennes au sol présentées permettant la réception dans les deux polarisations circulaires inverses. La réception du signal de télémessure (voie "somme") se fait systématiquement en diversité de polarisation. La poursuite automatique est effectuée dans l'une ou l'autre des polarisations, par commutation. Actuellement, cette commutation ne se fait pas de façon automatique, mais en passant en effet être envisagé.

RADIATION CHARACTERISTICS OF HF NOTCH AERIALS INSTALLED IN SMALL AIRCRAFT

by

N. A. D. Pavey
Royal Aircraft Establishment
Farnborough Hants
England

SUMMARY

The radiation characteristics of HF notch aerials in small aircraft are analysed for the band 2 to 10 MHz. Radiation occurs in two main modes; a magnetic dipole mode resulting from the high local RF currents flowing around the notch, and an electric dipole mode resulting from longitudinal RF currents in the fuselage.

A procedure is given for the estimation of the radiation efficiency of an aircraft notch aerial. It is shown that high radiation efficiencies may be realised at frequencies near the aircraft electrical resonance, typically 10 MHz, but that a rapid reduction of radiation efficiency occurs at lower frequencies. A radiation efficiency of less than 0.1% at 2 MHz is to be expected for many aircraft notch aerials.

1. INTRODUCTION

HF notch aerials and allied aerials which are contained physically within the aircraft structure are usually much more attractive to aircraft designers than alternative possibilities. For example wire aerials have the disadvantages of an exterior structure, while insulated tail-cap aerials present awkward high-voltage insulation problems.

Early work on the application of notch aerials to HF communications systems in military aircraft was carried out at RAE by CARY, R.H.J., 1952 and JOHNSON, W.A., 1955, and a subsequent paper by TANNER, R.L., 1958 is an important contribution to the understanding of radiation from aircraft-installed notch aerials. A prime objective at that time was the realisation of high radiation efficiencies, usually several tens of per cent. Tanner showed that in practical aircraft installations such efficiencies may be achieved only if strong coupling exists between the notch and the airframe, ie the predominant source of radiation is the RF current distribution over the whole aircraft. Furthermore he showed that adequate notch/airframe coupling could be achieved at HF using a large notch aerial at a good site on a large aircraft. More recently HF notch aerials have been employed in small aircraft; Fig 1 illustrates a typical tail-fin installation. It has been realised for some years that such installations offered low radiation efficiencies at the low end of the HF band, but little basic work appears to have been carried out on the problem. It is the purpose of this paper to examine radiation mechanisms and to establish a procedure whereby reasonable estimates of the achievable radiation efficiency may be obtained from a knowledge of the notch and airframe geometries.

As part of a more general study, radiation patterns of scale models of small aircraft with tail-fin notches have been measured; Fig 2 is a typical example at the low end of the HF band. Two radiation modes may be identified, both of which contribute significantly to the total radiation. The vertically polarised mode is characteristic of a magnetic dipole, and is attributed to the high RF current which exists in the immediate vicinity of the notch. The horizontally polarised mode is characteristic of an electric dipole and is attributed to longitudinal RF currents in the aircraft fuselage. The simple nature of these observed radiation characteristics suggests that by making simplifying assumptions about the electrical characteristics of the notch and airframe it should be possible to arrive at analytical expressions which give approximate values of radiation resistance. This is the approach adopted in the following text.

2. PROPERTIES OF A NOTCH AERIAL IN A SEMI-INFINITE SHEET

2.1. General comments

The impedance characteristics of a notch aerial in a thin, perfectly conducting, semi-infinite sheet are derived in the following sections. In such a lossless system the resistive component of the notch impedance is its series radiation resistance. The chosen method of analysis is to apply Babinet's principle to equivalent dipole radiators, the properties of which have been investigated extensively.

Provided that there are some constraints on notch geometry, this analysis leads to simple equations which enable the general properties of notch aerials to be understood readily. The effects of notch shape and structure thickness are discussed subsequently.

2.2. Properties of dipole radiators

Information on the impedance properties of dipole radiators (Fig 3) is employed extensively in this paper. A general equation for the impedance at the centre of a dipole is too complicated to be useful here, but a great simplification may be effected (CARTER, F.S., 1932) for lossless electrically small dipoles of limited thickness (say a total length of not more than a quarter-wavelength and a length-to-diameter ratio of not less than 10:1). Thus:

$$z_1 = r_1 + jx_1 \quad (1)$$

$$= 20(ka)^2 - j120F_1/ka \quad (2)$$

where r_1 = radiation resistance

x_1 = reactance

$k = 2\pi/\lambda$

$2a$ = dipole length

d = dipole diameter

λ = wavelength

$F_1 = \log 4a/d-1$

Tables of aerial impedance are available for thick dipoles (KING, R.W.P., 1971). Examination of Eq (2) shows that the equivalent circuit of an electrically small lossless dipole is a resistance whose value is proportional to the square of its electrical length in series with a capacitance of fixed value. The value of F_1 is determined only by the dipole geometry; for a length/diameter ratio of 10, $F_1 = 2.0$. From Eq (1)

$$|x_1|/r_1 = 6F_1/(ka)^3 \quad (3)$$

Regarding the dipole as an electric circuit element, this quantity may be regarded as its Q factor, and the strong dependence on wavelength may be noted. As an illustrative example, for a dipole which is $\lambda/10$ long a Q factor of over 300 is obtained. Generally, for electrically small aeriels

$$|x_1|/r_1 \gg 1 \quad (4)$$

A planar dipole (Fig 3b) of negligible thickness and width w may be treated as an equivalent cylindrical dipole of effective diameter $w/2$ (JASIK, H., 1964).

2.3. Properties of electrically small slot aeriels

Babinet's principle (BOOKER, H.L., 1946) may be employed to determine the admittance of a slot in a thin, perfectly conducting, infinite sheet (Fig 4a) from the impedance of its complementary planar dipole (Fig 3b), and the following expression is obtained:

$$(r_1 + jx_1)/(g_2 + jb_2) = Z_w^2/4 \quad (5)$$

where g_2 = shunt radiation conductance of slot

b_2 = shunt susceptance of slot

Z_w = wave impedance of free space
= 377 ohm.

Equation real and imaginary parts

$$r_1/g_2 = x_1/b_2 = Z_w^2/4 \quad (6)$$

Inspection of Eqs (5) and (6) and reference to Eq (1) shows that an electrically small slot, compared with a half-wave slot, possesses a low shunt radiation conductance and a high negative shunt susceptance. The equivalent circuit (Fig 4b) is a lossy inductance.

2.4. Properties of electrically small notch aeriels

Suppose that a thin cut is made in the infinite sheet containing the slot, perpendicular to the slot major axis, so that the slot and feed are bisected. Since no electric current flow lines have been intercepted there is negligible perturbation of the aerial system and consequently negligible perturbation of its radiation pattern and impedance properties.

Let one half of the aerial system be removed, leaving a notch aerial in a semi-infinite sheet (Fig 5a). It is to be expected that the radiation patterns of the notch aerial will be considerably different from those of the slot, due to the removal of a major conducting boundary containing a radiator. However, apart from minor fringing field effects at the feed points, it appears reasonable to assume that the removal of the half-sheet will not result in a radical redistribution of the current in the remaining half-sheet. Assuming that for practical purposes the sheet current distribution around the notch is negligibly different from that of the corresponding slot, the admittance of the notch is taken to be half that of the slot. Further discussion on this point is given in later sections of this paper.

Referring to Eq (5)

$$y = g + jb = \frac{1}{2}(g_2 + jb_2) = 2(r_1 + jx_1)/Z_w^2 \quad (7)$$

where g = radiation conductance of notch aerial
 b = susceptance of notch aerial.

Provided that the length-to-width ratio (a/w in Fig 4(a)) is not too small, and from the discussion in section 2.2 this would mean a/w not less than 2.5, the values given in Eq (1) may be substituted in

Eq (5). Equating real parts and imaginary parts,

$$g = 2x_1/Z_w^2 = 40(ka)^2/Z_w^2 \quad (8)$$

$$b = -2x_1/Z_w^2 = -240F/kaZ_w^2 \quad (9)$$

where $w/2$ has been substituted for d (see section 2.2) and

$$F = \log 8a/w - 1 \quad (10)$$

As a particular example, for $a/w = 2.5$, $F = 2.0$, giving

$$b = 480/kaZ_w^2 \quad (11)$$

As in the case of the electrically small slot, an electrically small notch regarded as a circuit element is a lossy inductance. A useful parameter is the Q factor, which is given by

$$Q = |b/g| = 6F/(ka)^3 \quad (12)$$

This may be compared with Eq (3) for a dipole, and as before and it may be noted that Q is proportional to $(\lambda/a)^3$. As an illustrative example, put $a/w = 2.5$, $a = 1m$ and $\lambda = 100m$, which gives a Q factor of $5 \cdot 10^4$ for a lossless notch.

A very important parameter is the equivalent series radiation resistance which is given by

$$r = g/b^2 \quad (13)$$

with negligible error. From Eqs (6), (7), (8) and (11)

$$r = (ka)^4 Z_w^2 / 1440F^2 \quad (14)$$

$$= 1.54 \cdot 10^5 a^4 / \lambda^4 F^2 \quad (15)$$

If $F = 2$ as before, then

$$r = 3.85 \cdot 10^4 (a/\lambda)^4 \quad (16)$$

The fourth-power law dependence of the radiation resistance on frequency may be noted, compared with the square-law dependence for a dipole (Eq (2)).

2.5. Current loop model of a notch aerial

The series radiation resistance of an electrically small single turn loop aerial in free space is given by:-

$$r_3 = 320\pi^4 A_3^2 / \lambda^4 \quad (17)$$

where r_3 = loop radiation resistance

A_3 = loop area.

The form of Eq (17) is very similar to that of Eq (15), which suggests that from the radiation resistance aspect a notch may be treated as a current loop having an equivalent area A_4 which is determined by the notch geometry. Thus

$$A_4 = 2.23 a^2 / F \quad (18)$$

Taking the same illustrative example as before, putting $a/w = 2.5$ and $F = 2$.

$$A_4 = 1.15 a^2 \quad (19)$$

or

$$A_4 = 2.8A \quad (20)$$

where A is the area of the notch.

This result is intuitively satisfying. When a notch aerial in a thin sheet is excited, current circulates around the notch and there is a close similarity with the loop aerial case. Moreover since the currents flow outside the cut-out area it is to be expected that an equivalent loop would be larger than the notch cut-out. It may also be noted that the effective radiating area of an electrically small notch aerial is invariant with frequency.

2.6. Notch aerial in a thick sheet

In practical aircraft installations notch aeriels are cut into aerofoil sections which may be of considerable thickness. To analyse such cases it is firstly necessary to determine the general properties of a notch cut in a semi-infinite sheet of finite thickness.

Consider such a notch fed at its extremities with an RF power source. Current will flow both externally on the surface of the sheet and around the internal surface of the notch. It is reasonable to suppose that the RF current distribution on the surface of the sheet is not perturbed significantly by the current on the inner surface of the notch. Accordingly the total admittance of a notch in a thick sheet is taken to be the sum of the admittance of a similar notch in a thin sheet and the admittance presented by the inner surface of the thick notch. Thus

$$G_5 + jB_5 = G + jB + G_4 + jB_4 \quad (21)$$

where $G_5 + jB_5$ = admittance of thick notch

$G_4 + jB_4$ = admittance of inner surface of thick notch.

The equivalent series radiation resistance r_5 is given by

$$r_5 = (G + G_4) / (b + b_4)^2 \quad (22)$$

As an illustrative example of the effects of the sheet thickness, let $b = b_4$, so that the internal and external notch RF currents are equal for practical purposes. The effective radiating area of the internal RF current cannot exceed the side-projected area of the notch (and is likely to be somewhat less when screening effects are considered). For the case considered in 2.5, ($a/w = 2.5$), we have from Eq (13),

$$\frac{r_5}{r} = \frac{(G + G_4)}{G} \cdot \frac{b^2}{(b + b_4)^2} \quad (23)$$

$$\text{or} \quad \frac{r_5}{r} \approx 0.278 \quad (24)$$

since radiation conductance is proportional to (effective radiating area)². It may be seen in this case that there is a drastic reduction in radiation resistance (a factor of 3.6), corresponding to a new value of effective radiating area of 1.5A. It is evident that the thickness of the structure supporting the notch should be kept to a minimum.

In practical notch aerial systems the inductance L may be measured. Then from Eqs (8) and (13),

$$r_5 = 40 (ka)^2 (\omega L)^2 / Z_w^2 \quad (25)$$

As an illustrative example, measurements which were made on an experimental notch aerial of 1 metre length and 0.4 metre width in a structure of approximately 15 cm thickness gave a notch inductance of approximately 0.7 microhenries (NEW, C. and SHARP, T.W., 1966). Substituting in Eq (25) and putting $\omega = 3.14 \times 10^8$ rad/sec,

$$r \approx 19,500 / \lambda^4 \text{ ohms} \quad (26)$$

and comparing with Eq (17) the effective area A_5 of an equivalent loop radiator r is

$$A_5 \approx 0.79 \text{ m}^2 \quad (27)$$

$$\text{or} \quad A_5 \approx 2.0 \text{ A} \quad (28)$$

where A is the side-projected area of the notch.

Compared with the theoretical value of 2.8A in Eq (20) for a similar notch in a thin sheet this shows a reduction in effective radiating area by a factor of 1.4. Thus this experimental evidence does indicate that the thickness of the structure is a significant factor in determining the effective radiating area of a notch aerial. It may be noted that at 2 MHz the radiation resistance of the notch aerial just considered is 38 microhms when radiating in a current loop mode.

3. PROPERTIES OF A NOTCH AERIAL IN A FINITE RECTANGULAR PLATE

3.1. Admittance characteristics

Consider the radiation characteristics of a thin lossless rectangular plate containing a notch aerial (see Fig 6); this may radiate in both magnetic and electric dipole modes and thus resembles the aircraft case. As a model of an aircraft it is over-simplified, but the analysis leads to simple expressions for radiation resistance which illustrate the dependence of radiation resistance on frequency which is to be expected from aircraft notch arials.

Applying the analytical treatment of TANNER, R.L., 1958 the admittance y_6 at the terminals of the notch is given by

$$y_6 = y + Ky_1 \quad (29)$$

where y = notch admittance

y_1 = admittance of rectangular sheet radiating in a dipole mode

K = a real dimensionless coupling factor.

Eq (29) states that the input admittance of the notch/plate combination is made up of two components. The first of these is simply the admittance of the notch from Eq (7), which is assumed to be affected only slightly by the limited size of the plate. The second term is the dipole admittance, as seen at the plane of the slot, multiplied by the coupling factor. For the aircraft notch aerials considered here the values of K are less than 0.1, and Tanner's results reduce to

$$K = 0.20 a/h \quad (30)$$

where a = slot length
 h = plate width.

3.2. Centrally sited notch in a rectangular plate

For a centrally sited notch aerial in a rectangular plate of length ℓ and width h , the impedance of the plate regarded as an electrically small dipole may be obtained from Eq (2), subject to the same constraints on length/width ratio. Putting the diameter of an equivalent cylindrical dipole equal to half the plate width,

$$z_1 = r_1 + jx_1 = 5 (k\ell)^2 - j240 F_2/k\ell \quad (31)$$

$$\text{where} \quad F_2 = \log 4\ell/h - 1 \quad (32)$$

The corresponding admittance y_1 is given by:

$$y_1 = 1/z_1 = 5\{(k\ell)^4 + j240 F_2 k\ell\} \div \{25 (k\ell)^6 + 240^2 F_2^2\} \quad (33)$$

For an electrically small plate the denominator term in $(k\ell)^6$ may be neglected so that Eq (33) becomes

$$y_1 = \frac{(k\ell)^4}{1.15 \cdot 10^4 F_2^2} + \frac{j k\ell}{240 F_2} \quad (34)$$

Fig 6b shows the equivalent circuit of the total radiating system; the admittance of this system may be determined from Eq (29) as follows:-

$$\begin{aligned} y_6 &= y + Ky_1 \\ &= \frac{40 (ka)^2}{Z_w^2} - \frac{j240 F}{ka Z_w^2} + \frac{K (k\ell)^4}{1.15 \cdot 10^4 F_2^2} + \frac{j K k\ell}{240 F_2} \end{aligned} \quad (35)$$

where y is obtained from Eqs (7) to (10). For frequencies well below the natural resonance of the airframe the last term of Eq (35) is negligibly small.

$$\text{Writing} \quad y_6 = g_6 + jb_6 \quad (36)$$

$$g_6 = \frac{40 (ka)^2}{Z_w^2} + \frac{K (k\ell)^4}{1.15 \cdot 10^4 F_2^2} \quad (37)$$

$$b_6 = 240F/ka Z_w^2 \quad (38)$$

An important parameter is the corresponding series radiation resistance r , which is given with negligible error by

$$r_6 = g_6/b_6^2 \quad (39)$$

$$= \frac{(ka)^4}{1440 F^2} - \frac{Kk^5 \ell^4}{6 \cdot 10^8 F^2 F_2^2} \quad (40)$$

The first term (which is identical with Eq 14) is the component of the radiation resistance due to the RF current circulating around the notch which radiates in a current loop mode, and its value has an r^4 dependence. The second term is the component of the radiation resistance due to the RF current flowing longitudinally in the rectangular plate and its value has an r^6 dependence; this radiates in an electric dipole mode.

As an illustrative example, put

$$\begin{aligned} a &= 1 \text{ metre} \\ F &= F_2 = 2.0 \\ \ell &= 15 \text{ metres} \\ K &= 0.067 \end{aligned}$$

Then

$$r_6 = \frac{3.84 \cdot 10^4}{\lambda^4} + \frac{3.96 \cdot 10^8}{\lambda^6} \quad (41)$$

Fig 7 shows these radiation resistances as a function of frequency. In the region of 2 MHz the current loop mode is predominant, while at 3.0 MHz the contributions of the two modes are equal; for higher frequencies the electric dipole mode is predominant. The very low values of radiation resistance may be noted.

3.3. Asymmetrical notch in a rectangular sheet

To analyse the case of a rectangular sheet containing an asymmetrically sited notch it is necessary to determine the impedance of the sheet regarded as a dipole which is driven at the site of the notch. An approximate method which is adequate for the purposes of this paper is as follows:-

Suppose that the notch is sited at a distance ℓ_1 from one end of the plate, and ℓ_2 from the other so that:

$$\ell = \ell_1 + \ell_2 \quad (42)$$

Consider next two dipoles of lengths $2\ell_1$ and $2\ell_2$ respectively. An approximate formula for the impedance of the asymmetrical dipole is that it is equal to the mean of the impedances of these two dipoles (KING, R.W.P., 1950).

Although the impedance is different from the symmetrical case, it is to be expected with an electrically small asymmetrical dipole that the radiation resistance will have a square law dependence with frequency and that the reactive component may be represented by a capacitor. Accordingly the general form of the impedance will be similar to Eq (35), leading to an equation for the radiation resistance which is of similar form to Eq (40).

4. AIRCRAFT HF NOTCH AERIALS

4.1. Estimation of radiation characteristics

A commonly employed notch aerial site is the base of the tail-fin (see Fig 1), and most of the following discussion refers to this case. A main objective is the determination of the radiation resistance referred to the notch terminals at frequencies near and below the first electrical resonance of the aircraft. The radiation efficiency may then be derived from a knowledge of the tuning unit characteristics.

The procedure is based on the discussion in Section 3 of this paper, and it is accordingly necessary to determine the following parameters.

- (i) The impedance which may be attributed to the notch radiating in a current loop mode.
- (ii) The impedance of the aircraft radiating in a longitudinal dipole mode as seen at the notch position.
- (iii) The notch/airframe coupling factor.

Initial rough estimates of these parameters may be made from a knowledge of the notch and airframe geometries. More accurate information may be obtained from impedance and radiation field measurements on a mock-up notch, by impedance and radiation pattern measurements on a scale model and by computer modelling. It is planned to report separately on experimental techniques.

4.2. An illustrative example

The example chosen is shown in Figs 1 and 8, and the following values have been chosen as typical.

Notch inductance $L = 0.6 \mu\text{H}$
 Effective radiating area of notch $A = 0.5 \text{ m}^2$
 Notch/airframe coupling factor $K = 0.05$

The notch impedance is given by

$$Z = 320 \pi^4 A^2 / \lambda^4 + j\omega L \quad (43)$$

Referring to Fig 8, a visual estimate has been made of equivalent monopoles which represent the electrical properties of the aircraft structure fore and aft of the notch. The impedance of the airframe is taken to be the sum of the impedances of these monopoles, which have been calculated using King's tables. Fig 9 shows the radiation resistance and reactance terms of the airframe impedance.

Fig 10 shows the radiation resistance terms as seen at the notch terminals; the reactive term is dominated by the notch inductive reactance. Assuming that the resistive losses in the aerial system are predominantly conductor losses, they may be expected to follow an approximate \sqrt{f} law, and a typical value at 2 MHz is 0.05 ohms. Using this data the radiation efficiency as a function of frequency is given in Fig 11.

5. DISCUSSION

Starting with a knowledge of the aircraft and notch geometries, it is believed that the foregoing treatment offers a means of obtaining rough quantitative estimates of the radiation characteristics which are useful for initial design purposes. The accuracy of these estimates may be improved by employing data obtained from mock-ups and models. Clearly many of the simplifying assumptions need more rigorous justification, and more experimental evidence is needed; nevertheless experimental results to date are in reasonable agreement with the predictions.

Radiation has been shown to occur in two main modes; a magnetic dipole mode resulting from the high local RF currents flowing around the notch, and an electric dipole mode resulting from longitudinal RF currents in the fuselage. At frequencies near the natural electrical resonance of the airframe high radiation efficiencies are possible. However the combination of the notch aerial and the electrically small airframe results in a rapid reduction of radiation efficiency at lower frequencies. With typical sizes of notch in current use, radiation efficiencies of less than 0.1% at 2 MHz are to be expected.

6. REFERENCES

- BOOKER, H.L., 1946, "Slot aeriels and their relation to complementary wire aeriels (Babinet's Principle)", JIEE No 4 Pt IIIa.
- CARTER, P.S., 1932, "Circuit relations in radiating systems and applications to antenna problems", Proc IRE Vol 20.
- CARY, R.H.J., 1952, "The slot aerial and its application to aircraft", Proc. IEE Vol 99 Pt III.
- JASIK, H., 1961, "Antenna Engineering Handbook", McGraw-Hill, 1961.
- JOHNSON, W.A., 1955, "The notch aerial and some applications to aircraft radio installations", Proc IEE Vol 102 Pt B.
- KING, R.W.P., 1950, "Asymmetrically driven antennas and the sleeve dipole", Proc IRE Vol 38.
- KING, R.W.P., 1971, "Tables of antenna characteristics", IFI/Plenum.
- NEW, C. and
SHARP, T.W., 1966, "HF suppressed aeriels for aircraft", AGARD Conf. Proc No 15. Radio Antennas for Aircraft and Aerospace Vehicles.
- TANNER, R.L., 1958, "Shunt and notch-fed HF aircraft antennas", Trans. IRE AP-6.

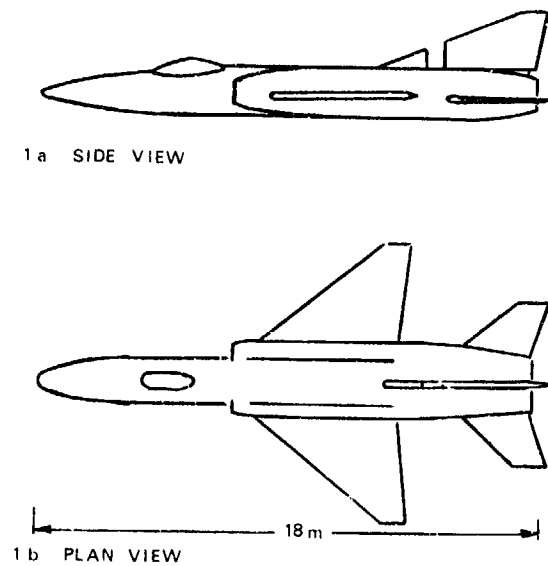


Fig.1 Aircraft with tail-fin notch aerial

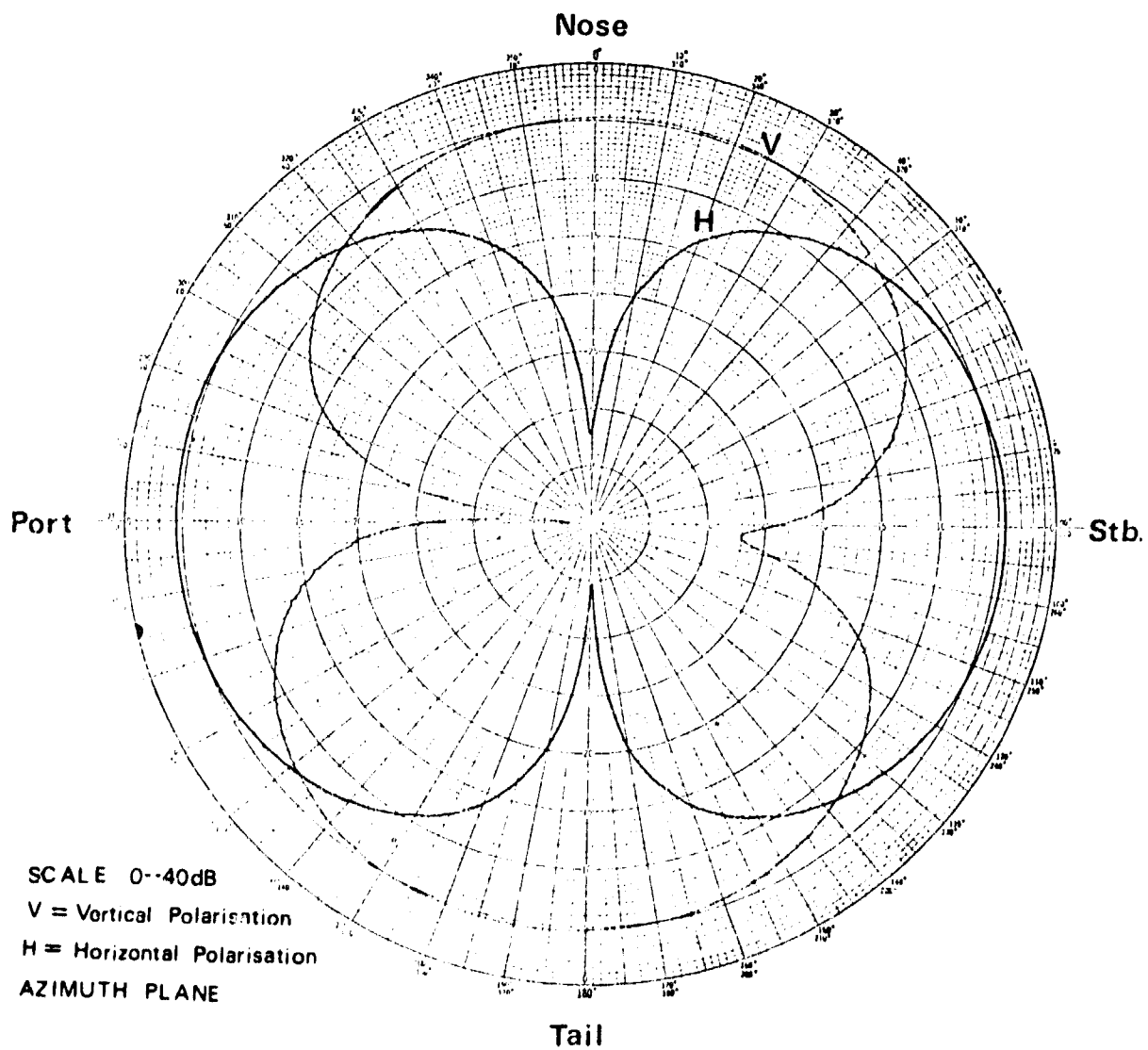
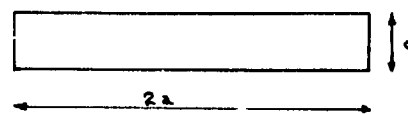
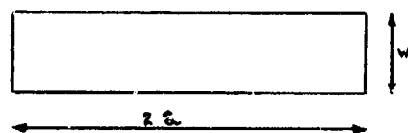


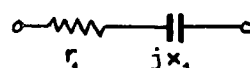
Fig.2 Radiation patterns of scale model of aircraft with tail-fin notch



3a Cylindrical dipole



3b Planar dipole



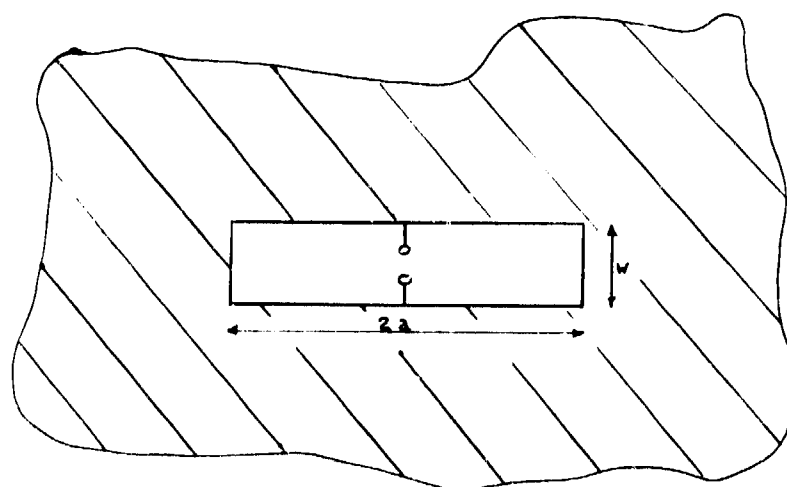
$$r_i = 20(ka)^2$$

$$x_i = -120(\log 4a/d - 1)/ka \quad \text{for 3a}$$

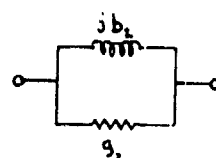
$$x_i = -120(\log 8a/w - 1)/ka \quad \text{for 3b}$$

3c Equivalent circuits

Fig.3 Electrically small dipole aerials

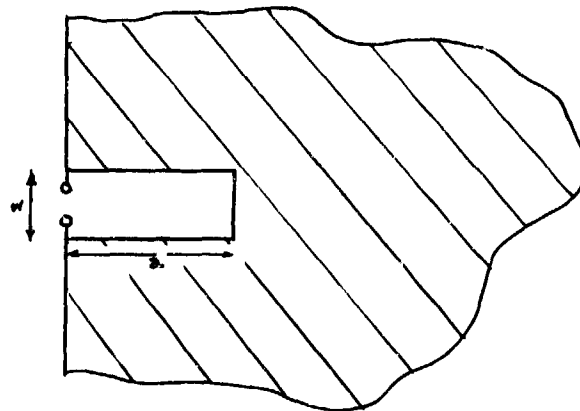


4a Slot aerial in infinite thin sheet

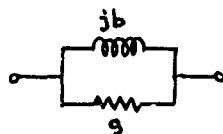


4b Equivalent circuit

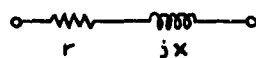
Fig.4 Electrically small slot aerial



5a Notch aerial in semi-infinite thin sheet



5b Equivalent shunt circuit

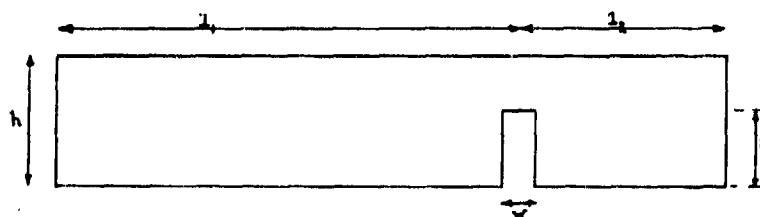


$$r = (ka)^4 Z_w^2 / 1440 (\log 8a/w - 1)^2$$

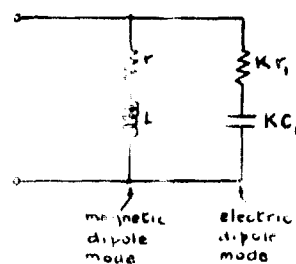
$$x = ka Z_w^2 / 240 (\log 8a/w - 1)$$

5c Equivalent series circuit

Fig.5 Electrically small notch aerial

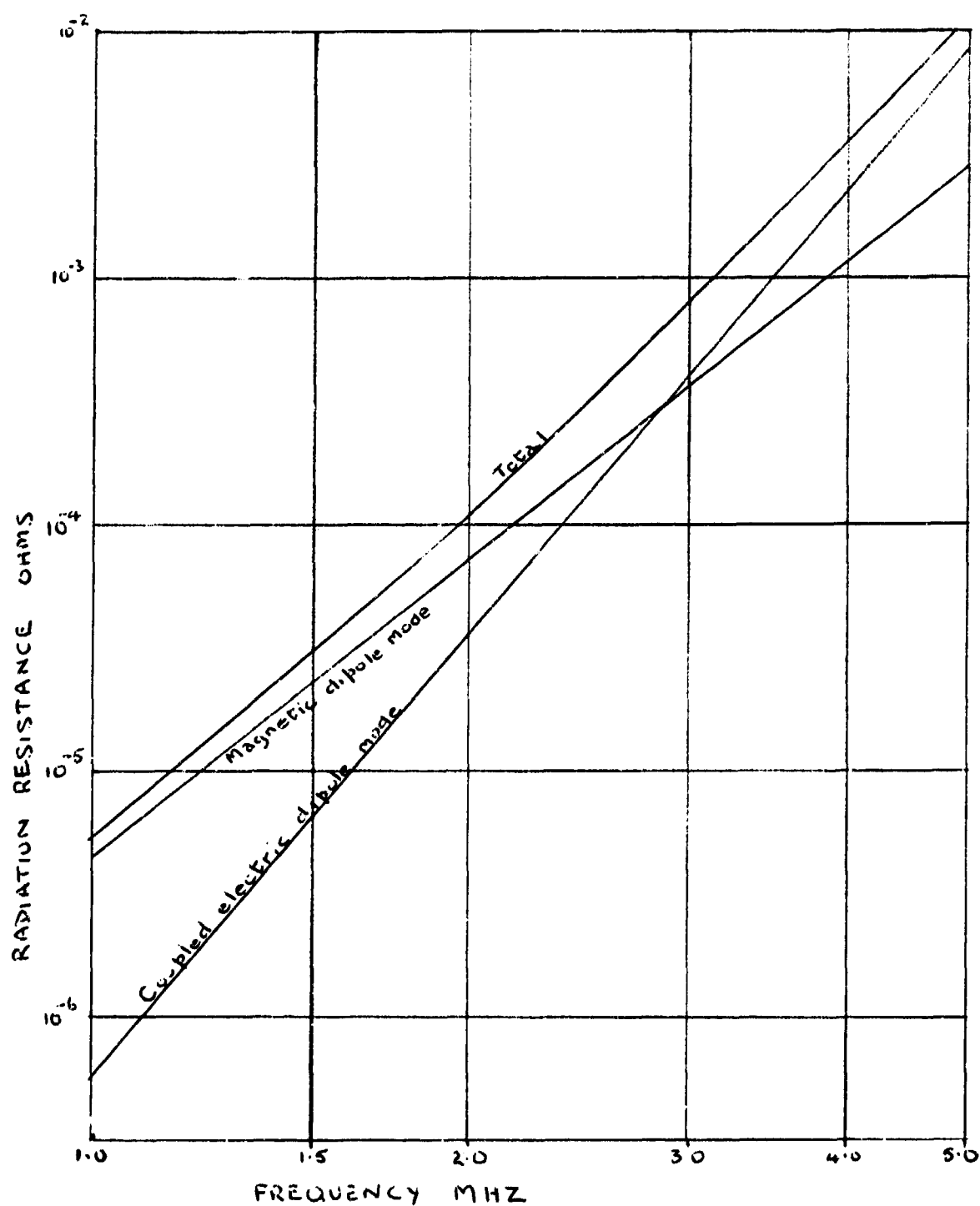


6a NOTCH AERIAL IN RECTANGULAR PLATE



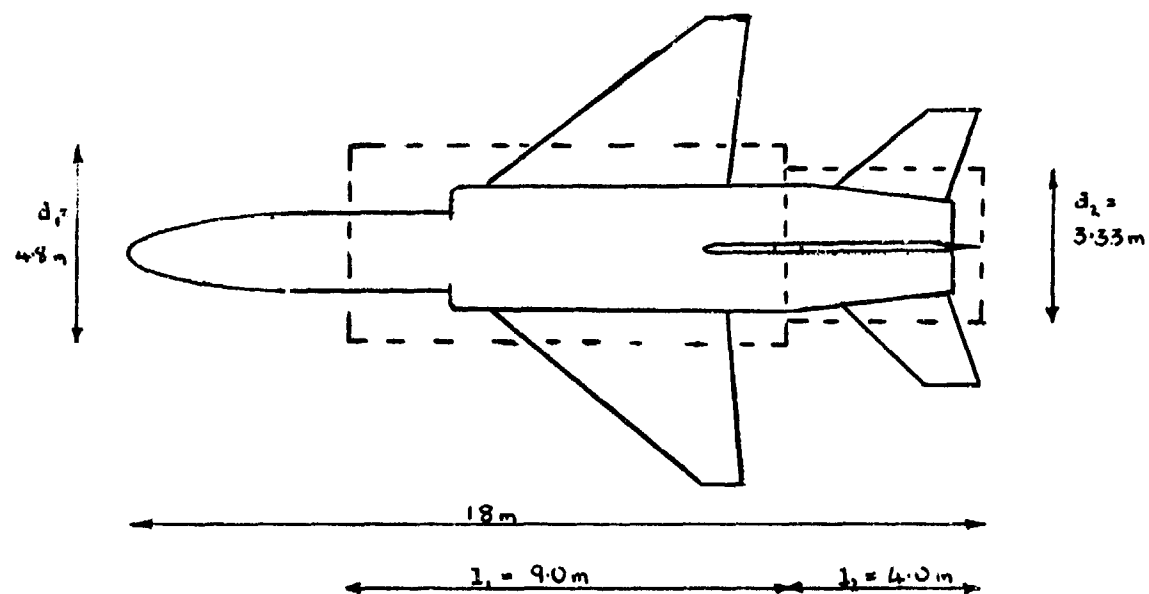
6b EQUIVALENT CIRCUIT OF ELECTRICALLY SMALL STRUCTURE

Fig.6 Notch aerial in a rectangular plate

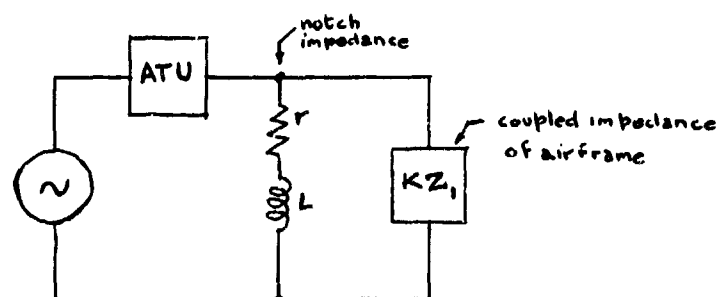


DATA OBTAINED FROM EQ(41) - CENTRAL NOTCH

Fig.7 Radiation resistance of notch aerial in rectangular plate



8a DIPOLE EQUIVALENT OF AIRFRAME



8b EQUIVALENT CIRCUIT OF NOTCH AERIAL SYSTEM

Fig.8 Electrical equivalent of aircraft-installed notch aerial

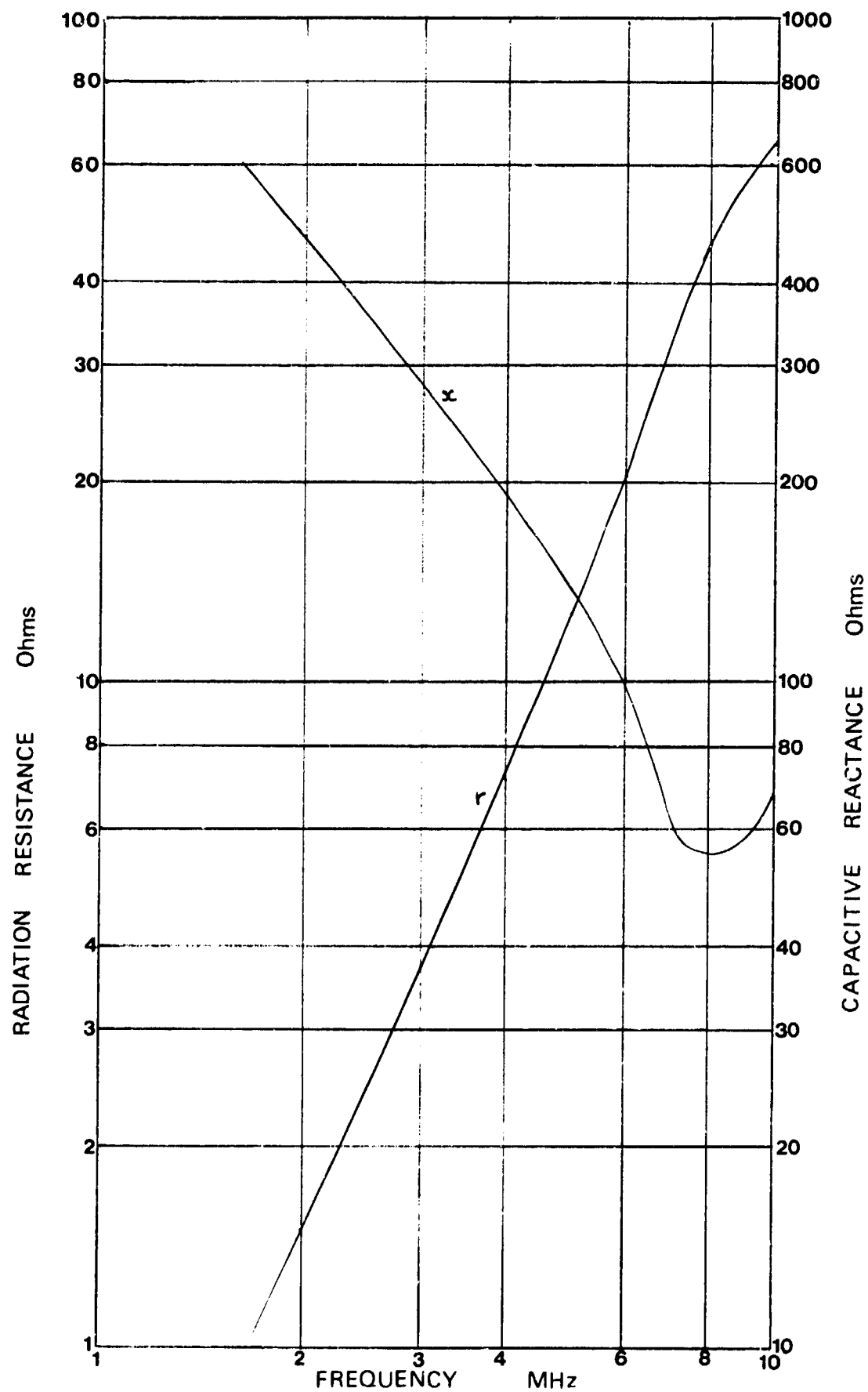


Fig.9 Impedance of airframe at notch position

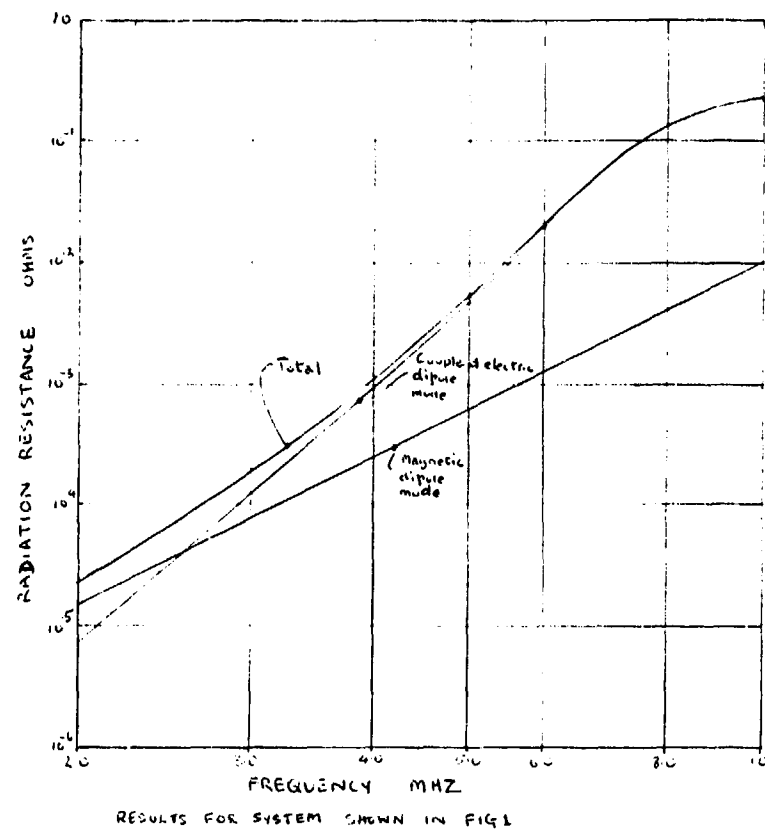


Fig. 10 Radiation resistance of aircraft-installed notch aerial system

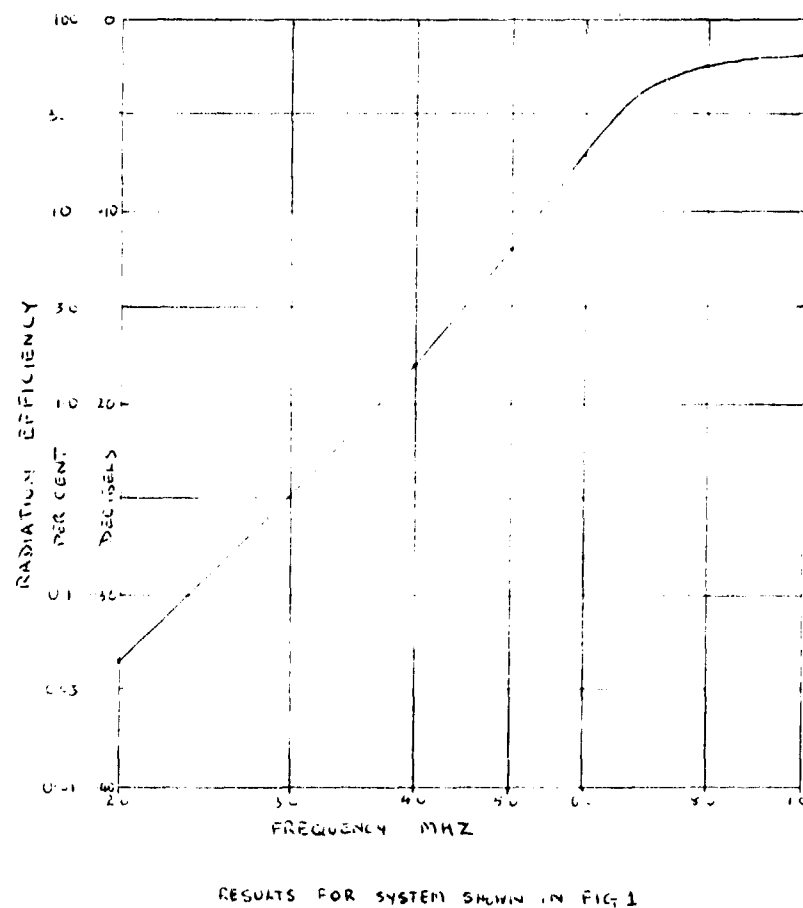


Fig. 11 Radiation efficiency of aircraft-installed notch aerial system

DISCUSSION

J. THRAVES: Would you comment on the efficiency of the choice of your notch position with regards to the excitation of body currents (electric dipole mode) in the aircraft? Which positions are good and which are bad in this respect?

N.A.D. PAVEY: Ideally the notch should be cut as deeply as possible into the body of the aircraft and should be sited near its electrical centre. The base of the tail fin is a reasonable choice where the tail fin is large. Notches near the wing roots are to be preferred where the tail fin is small, but in this case the direct radiation from the notch is horizontally polarized. There are usually serious aircraft structural constraints on the size and siting of the notch.

HF ANTENNA SYSTEMS FOR SMALL AIRPLANES AND HELICOPTERS

R.E. Deasy
Antenna Coupler/Filter Group Head
Telecommunications Equipment Division
Collins Radio Company
Cedar Rapids, Iowa 52406
USA

SUMMARY

Basic information is presented to help antenna designers and installers provide optimum hf antenna systems on small airplanes and helicopters. This paper covers many of the most typical problems faced when installing an hf system on a small aircraft. It is based on experience related to the use of automatic antenna couplers in a great variety of installations. Discussion involves practical antenna installation considerations rather than detailed antenna theory.

Wire, shunt/notch, and tuned monopole types of antennas and associated antenna couplers are discussed. Important details related to the selection, installation, and successful operation of these antenna systems are given. Typical antenna location, size, and configuration are related to aircraft characteristics.

Three common forms of wire antennas (long wire, inverted V, and short grounded wire) are illustrated. Techniques such as rf grounding, bonding, and shielding to eliminate RFI are discussed in detail. Shielded antenna feedline techniques (including efficiency considerations) are shown. Voltage-altitude design considerations are given.

Shunt and notch type antennas are illustrated and general details of location, size, and construction are discussed. A typical installation is detailed showing RFI considerations.

A tuned monopole (with load wire) antenna is discussed for applications on small airplanes and helicopters. Typical installation guidelines are given along with details showing RFI considerations.

1. INTRODUCTION

The installation of a good hf antenna system on a small helicopter or airplane can present some difficult problems. Basic aircraft characteristics (such as speed and size) usually present practical limitations which determine the types of hf antenna systems that can be used. Antenna designers must recognize the many restrictions placed on the antenna and be knowledgeable in many approaches to antenna solutions. Every new design seems to require some unique solutions. This paper describes solutions to many of the problems associated with the installation of hf antenna systems on typical small aircraft. It is written from the viewpoint of the antenna coupler engineer (at Collins Radio Company), and is based on the experience gained from many such installations using automatic antenna couplers on all types of aircraft.

Large, slow aircraft can use standard long-wire antennas that generally require relatively little design consideration. On fast jet aircraft, wire antennas must be designed to be very strong, and many mechanical problems must be solved for safe and reliable operation. In the past, probe and tail cap antennas were designed for large jet aircraft to replace wires. Today, shunt, or notch, type antennas are being used on virtually all new designs where wires cannot be tolerated. On small, slow aircraft, wire antennas are still being used in a great variety of configurations.

But, what about the average small airplane or helicopter? What is the best possible (optimum) antenna system configuration for these aircraft? Ideally, the antenna solution should be included while the airframe is being designed, but quite often due to cost, schedule, or lack of interest, the hf antenna is given low priority. The aircraft designer usually wants the smallest possible antenna that can be tuned and system efficiency is too often forgotten. The antenna designer must understand antenna systems well enough to bring together an optimum antenna and antenna coupler combination that is acceptable to the aircraft designer.

The antenna system discussions that follow are believed to present working solutions to many of the problems associated with installations on small aircraft. Of course, these solutions may also be applied to larger aircraft. The antenna coupler group at Collins Radio Company endorses the types of antenna systems shown. This material is also intended to help the antenna designer, or installer, to better understand the capabilities of various types of antenna couplers and the main points concerned with their use. The choice of antenna type, size, and configuration is often a practical compromise based to a large extent on what equipment is available. It is obviously important that new antennas be made compatible with available antenna couplers. The Collins 548S 100-watt hf pa coupler and accessories are used to illustrate how a standard production unit can be designed to be universal and work efficiently with virtually any kind of antenna.

Basic types of small aircraft hf antennas and associated couplers are discussed and examples are given. Important installation details such as rf bonding, high-voltage considerations, and vibration are covered. The presentation of the material should provide valuable information to the hf antenna designer and systems engineer.

2. HF ANTENNA SYSTEMS

The hf antenna system is defined in the paper to consist of the following parts:

- a. Antenna coupler
- b. Rf feedline (all rf connections between coupler and antenna)
- c. Antenna (portion of system that excites the aircraft)

In an optimized system, all of these parts are considered to be important.

The antenna coupler provides accurate and efficient impedance matching between the radio and the antenna. An existing antenna coupler can usually be found for almost any type of antenna installation. There are some unique situations that involve very special, or state-of-the-art design, but these should be considered as special cases. The antenna coupler must of course be selected to tune the antenna over the desired operating frequency range (assumed to be 2 to 30 MHz in this paper).

The antenna coupler must provide a good 50-ohm load (1.3 to 1 vswr or better is considered sufficient) for good, reliable transmitter performance. This low vswr requirement becomes more important with the use of solid-state power amplifiers because it is related directly to distortion and power output design. In systems where the antenna impedance can change during operation, the coupler should have the ability to automatically accurately retune during transmitting. When tuned, the coupler also provides a good impedance match from the antenna to the receiver.

Examples of successful antenna coupler installations are discussed in the sections on antenna types.

The rf feedline connects the antenna to the coupler. Both the direct connection and the rf ground current return path must be considered in feedline designs. Efficiency is an important consideration, but the feedline also performs the important function of eliminating hf interference with other systems on the aircraft. Examples are given showing rf feedline techniques.

The hf antenna on a small aircraft basically excites the airframe to produce (or absorb) desired radiation of hf energy. This is especially true at the lower hf frequencies where the antenna is much shorter than the signal wavelength. Proper location of the antenna on the airframe, such as shown in the examples, will yield desirable radiation patterns.

The antenna can be considered as a complex transmission line in relation with the airframe. From the viewpoint of the antenna coupler designer, the complex impedance of the antenna indicates how well it couples to the airframe. Input reactance is mostly related to antenna dimensions (size, spacing, and shape). Input resistance is a close function of how well the antenna couples to the airframe. Aircraft electrical resonances show up as input resistance peaks. In general as antenna spacing to the airframe increases, antenna effectiveness also increases.

The antenna system designer should recognize the different antenna coupler configurations for different antenna types (as illustrated in the antenna discussions). Three general categories of hf antennas for small aircraft are covered. These are as follows: Wire antennas (open end or grounded end), shunt (or notch), and tuned monopole with load wire.

Experience has shown that hf antenna performance does not lend itself to a completely theoretical analysis (because of complex coupling to airframe). A full scale tuning and communicating test of the system is the real proof of performance. The material that is presented is intended to point out guidelines and techniques found to be necessary for successful hf antenna systems. It is not a detailed discussion in antenna theory.

3. WIRE ANTENNAS

The wire antenna is the most widely used and perhaps best understood type of hf antenna. Because of low cost and ease of installation, the wire antenna should as a general rule be considered for new installations before approaching other, more complicated types of antennas. On high-speed jet aircraft, safety aspects and drag effects of the wire antenna must be weighed against antenna costs.

An example of an optimized wire antenna system on a Collins Radio Company aircraft (a turboprop Gulfstream I) is shown in figure 1. The important features of this antenna system will be discussed in order that they may be applied to other similar installations. Note that the antenna coupler, shielded rf feedline, and lightning arrester, are located at the top right of the radio bay (shown in bottom photo of figure 1). The performance of this antenna system is excellent.

Wire antennas are used in a great variety of sizes and shapes but for this discussion only three general wire configurations will be covered (see figure 2). Experience with these types of wire antennas (or slight variations) has shown they will produce good communication results. Wire types are as follows:

- a. Straight long-wire antenna (more than 8 meters long)
- b. Inverted V-wire antenna (approximately 6 to 8 meters long)
- c. Short grounded-wire antenna (less than 6 meters long)

Rules for the use of these antennas will be given together with discussions of important system features.

3.1 Straight Long-Wire Antenna

The top mounted straight long wire (shown in figure 1 and at the top of figure 2) is considered to be the best wire antenna configuration. It requires the antenna coupler to be located at the forward end of the wire near the top of the aircraft (note coupler feedpoint in figure 2). The Collins airplane shown has a 14-meter wire in this configuration and has an insulator at the rear end (open end). General rules for installing this type of wire are as follows:

- a. Position the wire as close as possible to longitudinal (top view) centerline of aircraft for best antenna pattern (and minimum wind drag).
- b. Space rear end of wire as far as possible above fuselage (side view) for maximum vertical antenna component and antenna pattern.
- c. Use low capacitance feedthrough insulator or mast at coupler feedpoint for maximum coupler efficiency.
- d. Wire length should be 8 meters or longer for good coupler and antenna efficiency (or consider using the inverted V wire configuration). If length is greater than approximately 14 meters, there appears to be little difference between performance of open or grounded end wire configuration.
- e. Use lightning arrester where possible (read lightning protection literature).
- f. Use static drain resistor (usually provided in antenna coupler) for open ended wire antennas.
- g. The rf feedline between the coupler and antenna feedpoint must provide good rf grounding and shielding to eliminate rf interference problems (see figure 3). It must be as short as possible for maximum efficiency (coax feedline efficiency is critical, see figure 4).
- h. Use good high-voltage practices around connection to antenna (eliminate sharp edges and provide adequate spacings).
- i. Mechanical design of the antenna must be verified for safety of aircraft.

The rf feedline should always be made as short as possible inside the aircraft. The design of the rf feedline is usually related to how close the antenna coupler is to other electronics equipment on the aircraft. The coupler shown in figure 1 is located in a large electronics bay so extensive grounding and shielding are required. Figure 3 (top part) illustrates the design technique used on the Collins airplane (and on other similar installations). The coaxial type of shielding around the antenna lead (feed wire) and the lightning arrester confines the rf ground return currents inside the shielded feedline. Otherwise, ground currents will flow all around the inside of the aircraft in returning to the coupler. The shield also eliminates direct radiation from the feed wire. In many installations the techniques shown in the bottom of figure 3 are adequate. The ground strap should be close to the feed wire to approximate a low impedance ground plane for the antenna feed wire. The length to width ratio of the ground strap should not be greater than 5.

Rf feedline efficiency is generally not a problem if line length is kept short (in the order of 0.3 meter). If solid dielectric coax line is used, coax length has a large effect on efficiency. Figure 4 shows how coax line efficiency varies with line length when used with a typical 8-meter wire antenna. Efficiency will improve if the antenna is longer (Collins antenna is 14 meters long and efficiency of C.3-meter line

is approximately 75 percent at 2 MHz worse case). If a long coax is required, use a low-loss high-impedance type. Large diameter air dielectric coax is available for high-voltage applications. If the antenna coupler is used with vibration isolators, flexible feedline connections that do not interfere with isolators are required.

3.1.1 High Voltage Design

As antenna length is decreased, the antenna coupler must generate higher voltages to deliver power to the open wire. Depending on coupler efficiency, the highest voltages will occur near 2 MHz. The antenna system must be designed to handle the peak voltages that occur with peak transmitter power at the maximum operating altitude of the aircraft. High-voltage design is too complex to be adequately covered in this paper, but some general rules will be given. At Collins, high-voltage designs use the following procedures:

- a. Use purchased components rated for operation at maximum peak and average operating voltages.
- b. Design to eliminate sharp edges and points on high-voltage circuits and nearby ground circuits.
- c. Provide adequate spacing between high-voltage circuits and ground.
- d. Perform tests at limit conditions of voltage, altitude, and power to verify arcing or corona does not occur.

As a general rule a spacing (across air) of 25 mm, with no sharp edges or points present, will handle approximately 10,000 peak volts at 30,000 feet (9,144 meters) altitude. A safety factor of at least 50 percent on spacing should be used. Most high-voltage test problems are solved by eliminating sharpness on mechanical parts rather than increasing spacing.

Figure 5 gives a simplified illustration of the effect of altitude on breakdown voltage (based on Collins Technical Report, CTR-143, 1955). The curves should be considered only as guides for general information.

3.2 Inverted V-Wire Antenna

When it is not possible to install at least 8 meters of wire in the straight configuration, the inverted V open wire antenna as shown in the middle of figure 2 should be considered. The inverted V also allows the antenna coupler to be installed in the aircraft tail or rear electronics bay. In small aircraft, there is often no forward space for the antenna coupler, so the inverted V is gaining popularity in its usage.

The typical inverted V-wire is approximately 8 meters long with a 2-meter vertical section followed by a 6-meter horizontal section as illustrated. The wire should be spaced at least 0.3 meter from the aircraft skin at the two insulators. Locate the tail insulator as high as possible on the tail. The feedthrough at the coupler feedpoint must be rated for 10,000-peak volts when a 400-watt pep radio is used. The coupler feedpoint should be approximately 1 meter forward of the base of the aircraft tail and near the top of the aircraft. The general rules given for the straight wire installation should be used where applicable for the inverted V-wire installation. Wire length should be at least 6 meters long.

Impedance data measured on several inverted V-wire installations indicates good coupling to the airframe. Aircraft dimensional resonances appear in antenna impedance superimposed on wire dimensional resonances indicating that the wire is exciting the airframe.

3.3 Short Grounded-Wire Antenna

The short grounded-wire antenna shown on the bottom of figure 2 has been used where a minimum length wire antenna is desired. This type of wire antenna is really a simplified version of a shunt-fed antenna discussed in paragraph 4. Two features leading to the use of the short grounded-wire antenna are as follows:

- a. Minimum wire length achieves minimum drag and breakage problems on high speed aircraft.
- b. Grounded configuration eliminates the high voltages associated with a very short open wire and allows use at high altitudes.

The main disadvantage of this current fed type of antenna is low efficiency at the lower operating frequencies due to high power losses in the wire. Use a large diameter wire with low loss resistance to minimize wire losses. Use low loss ground connections and rf feedline connection to the coupler.

The wire should be grounded as high up as possible on the aircraft tail to minimize radiation pattern nulls in the fore and aft direction of the aircraft.

Apply the general rules given for the straight long-wire installation (design for high currents rather than for high voltages). If operation performance must be improved, consider using the shunt feed rod configuration in paragraph 4.

4. SHUNT/NOTCH ANTENNAS

Shunt and notch type hf antennas are becoming increasingly popular on modern high speed or streamlined aircraft. Figure 6 shows a variety of configurations used for this type of antenna. Figure 7 shows general details of the shunt/notch antenna configuration. The word "shunt" will be used here in reference to both shunt and notch configurations since the basic difference between the two is the ratio of length to width of the cutout (dielectric) portion of the aircraft (as shown in figure 7).

The shunt (shunt feed) antenna is best described as a kind of transmission line that uses one part of the aircraft (fin or wing) to feed the rest. It can be located at various points on an airframe, but since it functions as a type of inductive coupling it should be located at a point of low impedance or high current. The current in the shunt feed loop induces current in the airframe, so the airframe, or a limited portion of it, acts as the antenna. The coupler feedpoint should always be located at the end of the shunt feed which is closest to the center of the aircraft.

The design of the antenna first involves finding a suitable location for the dielectric area, and then arranging the dimensions of the shunt feed and dielectric area to provide an antenna that can be efficiently matched to 50 ohms with a relatively simple antenna coupler. Collins has developed several useful guidelines to consider when designing a shunt antenna. They include the following:

- a. **Antenna Location** - The first choice should be at the root of the tail fin as shown in most of the configurations in figure 6. An alternate is at a wing root; however, vertically polarized signals are reduced. Keep the antenna close to fin or wing root for maximum coupling to aircraft.
- b. **Location of Antenna Tuner** - The tuner should be connected to the shunt feed at the end near the tail or wing root to provide maximum efficiency. Proper rf grounding and shielding will eliminate rf interference.
- c. **Dielectric Section** - The dielectric material used to fill the opening below the shunt feed should be a good grade of fiber glass or equivalent. The surface must be sealed to prevent arcing due to moisture and other contamination, and the metal fasteners used must be spaced enough to prevent arcing and corona.

Experience with a variety of antennas (as shown in figure 6) indicates that exact sizes and shapes of the dielectric areas are not critical design parameters. The dielectric area (see figure 7) should always be as deep as possible for maximum coupling to the aircraft. Efficiency can be considered proportional to dielectric area.

- d. **Shunt Feed** - Since rf current of over 50 amperes (with a 400-watt radio) is typical near 2 MHz, the shunt feed and all joints or connections must be designed to have very low rf resistance. Sharp edges must be avoided near the feed end where the highest voltages (typically 3000 to 5000 volts peak) occur. The shunt feed is typically about 2.5 meters long with a dielectric depth of about 0.2 meter at the feedline end.
- e. **Antenna Impedance** - To avoid the need for a complicated antenna tuner, the antenna impedance at 2.0 MHz should be no less than $+j17$ ohms, and should have parallel resonance between 20 and 30 MHz. Series resonance should be avoided completely so the antenna reactance gets no closer to resonance than $-j100$ ohms at 30 MHz, and an antenna's greatest R_p should be less than 20,000 ohms to achieve good coupling. Typically, a shunt (or large notch) antenna will fall within these parameters.
- f. **Lossy Materials** - Since high rf current is present all around the dielectric area, no magnetic materials or materials of low conductivity or high dissipation should be located in or near this area.

Figures 7 and 8 show details of shunt feed antenna installations. Note the provisions for locating the antenna coupler inside the aircraft skin. The Collins 548S-3 PA Coupler and 641D-1 Capacitor (shown in figure 8) illustrate how the high antenna currents can be kept outside the aircraft skin. The capacitor resonates the inductance of the antenna producing a large current flowing around the rim of the dielectric area (also see bottom of figure 7). The rf coax feeding the resonant circuit does not have to carry the high antenna currents. Apply the same general rules given for installations in paragraph 3.1.

4.1 Shunt/Notch Comparison To Probe Type Antenna

Shunt/notch antennas are considered to have many advantages over the older style probe and cap type antennas. These are the following:

- a. Weight - No lightning arrester required. Nothing external to aircraft. Small lightweight antenna tuner.
- b. Wind Resistance - Nothing external to aircraft.
- c. Antenna Voltage - Maximum voltage is less than half that of probe antenna.
- d. Tuner Efficiency - Typically 70 percent minimum compared with 20 percent minimum for a probe.
- e. Tuner Accessibility - Can be located inside cabin near fin or wing root.
- f. Environment - Coupler does not have to be located at fin or wing tip in high vibration area.

Performance of a good shunt/notch type antenna system is comparable to that for a probe or cap type system. Dual ARINC systems for commercial airlines (such as Collins 490S-1 coupler) are approximately half the complexity, size, and weight of comparable probe and cap type systems.

5. TUNED MONOPOLE HF ANTENNA

A tuned hf monopole (with load wire) antenna system is presented as an optimum solution for helicopters and other small aircraft where a good long wire is not practical. Figures 9 and 10 show system configuration and installation details of the Collins 437R-2 Antenna System. This miniature monopole is a tunable loading coil that series resonates an approximately 3 to 4 meters long load wire. The theory of this antenna is covered in a 1966 AGARD paper "Recent Developments in HF Helicopter Antennas" by J. D. Cosgrove and R. C. Fenwick of Collins Radio Company. The section from this paper concerning optimum antenna system configuration follows:

The theory and patterns presented show that the optimum antenna configuration for small or medium size helicopters is an open-ended wire antenna, which usually must be side mounted. Since sky-wave is favored regardless of the configuration, it remains to maximize the surface wave radiation. Generalized recommendations for an optimum antenna configuration are as follows:

- a. Spacing of the wire from the fuselage should be as great as practicable.
- b. The horizontal portion of the wire should be as far below the fuselage as practicable, or above the fuselage if rotor modulation can be tolerated.
- c. A tunable loading coil should be inserted in the wire and adjusted so that the input impedance is near resonance at each operating frequency.

The latter recommendation requires further elaboration. The inclusion of the tunable loading coil increases the vertically polarized radiation typically by one to two dB due to its effect on the wire current distribution. The major contribution is the lower matching loss compared to what would be obtained with a reasonable size coil inside the fuselage. Whether the coil is placed in the horizontal or vertical portion of the wire makes little difference. Horizontal coil placement gives slightly greater gain when airborne, as shown by scale model gain measurements, and less aerodynamic drag; vertical placement gives greater gain on the ground and is less susceptible to physical damage. In most cases, vertical coil placement is the best compromise.

In 1963, a number of antenna systems were tested by Collins Radio Company and the US Marine Corps on an actual helicopter to determine the best configuration suitable for helicopter use. The results of these tests showed that a vertically mounted tunable loading coil with a short open-ended wire antenna was superior to other types (that is, wires, fans, shunts, etc). These tests also showed that vibration and rotor modulation are of major concern in hf SSB communications.

It should be noted that the tunable loading coil does not make use of any new or unusual principle in its operation as can be seen in the preceding theoretical discussions. The usefulness of the tunable loading coil lies in the fact that it is a practical approach toward producing vertically polarized signals at low (2 to 6 MHz) hf frequencies. Its effectiveness is directly dependent on the use of an antenna coupler and the antenna/antenna coupler system interface, which allows its use with conventional hf SSB transceivers.

One of the key decisions made during the early study phase was to use a tunable loading coil as an extension of the tuning capability of a general purpose antenna coupler. This method was preferred over the solution of placing all the tuning elements in the tunable loading coil, the reasons for which were as follows:

- a. Typically, airborne SSB transceivers require a 1.3:1 swr (50 ohms) or less at their output terminals to achieve rated performance. This means that the antenna circuit must be tuned accurately. Precise tuning elements are required. To place these elements in the severe vibrational environment of the tunable loading coil outside of the helicopter would impose difficult design restrictions.
- b. Since the loading coil should be mounted as far from the fuselage as possible, it is mandatory that weight be kept to a minimum.
- c. A tunable loading coil that is operated (slaved) by an antenna coupler can be produced as an accessory item. Since the antenna coupler is general purpose, it can be produced at a high rate thus lowering the overall cost of the system.
- d. If the tunable load coil is damaged, the coupler can tune the remaining portion, thus maintaining communications.
- e. The antenna coupler can be used on larger aircraft using fixed wire antennas or at fixed stations using whips or wires. The use of this common coupler reduces inventory, logistics support, and maintenance requirements.

Figures 9 and 10 show how the 437R-2 system conforms well to the general recommendations of the 1966 paper.

Methods of choosing the mounting location of the 437R-2 and load wire for best performance are outlined in figure 9. Top mounting should be used if possible. On helicopters, the 437R-2 must be located on the bottom of the aircraft (as shown) to eliminate rotor blade modulation problems. Rigid support of the wire is required to eliminate vibration induced movement that can detune the high Q antenna. The wire that extends back toward the tail of the aircraft is necessary for optimum efficiency and to provide excitation for horizontally polarized signals. Radiating characteristics of the antenna system are improved as the distances from the wire to the aircraft skin are increased.

The system pictorial drawing (figure 10) shows that provisions for very adequate rf bonding and grounding are inherent in this design. The rf line between the 548S mount (990C-6) is coaxially shielded (including connectors) to effectively eliminate rf interference inside the aircraft. Mounting vibration isolators have rf bypass straps to the mounting shelf, which serves as a good rf ground when bonded to the inside of the aircraft skin near the 437R-2.

Special rf feedline considerations are used with the 437R-2. High impedance (95 ohms) coax is used to reduce losses and minimize stray shunt capacity. The end of the load wire is normally open circuited, but in some installations a series L-C network (load termination) is used to control the impedance near 30 MHz to optimize efficiency.

The same general rules given for antenna installation in paragraph 3.1 should be followed along with those given here.

6. CONCLUSION

A variety of hf antenna systems have been discussed in applications for small aircraft. This information is intended to provide practical background information to the antenna designer or installer and help achieve better understanding of optimized antenna systems. Knowledge of different types of antenna systems is just a starting point toward antenna design. Each different application will present some unique problems. The final result is the tested proof of performance and successful hf communication.

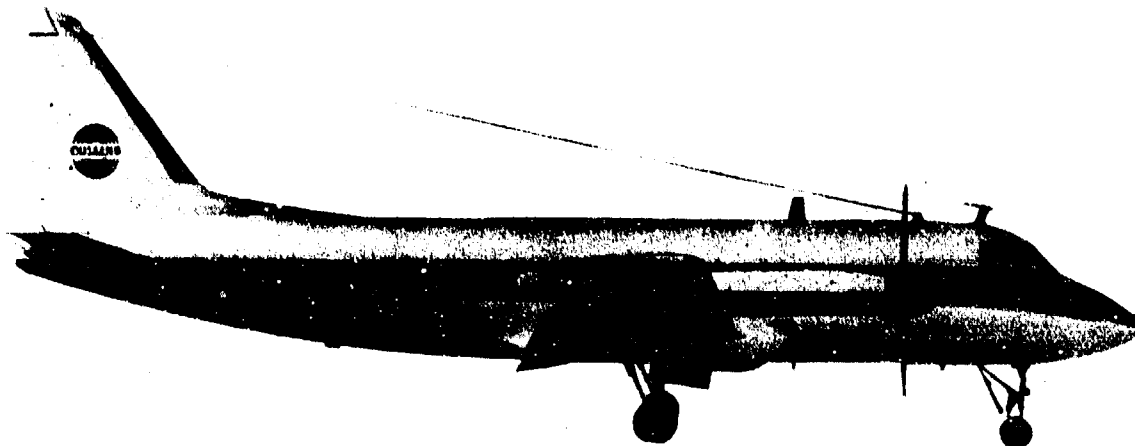
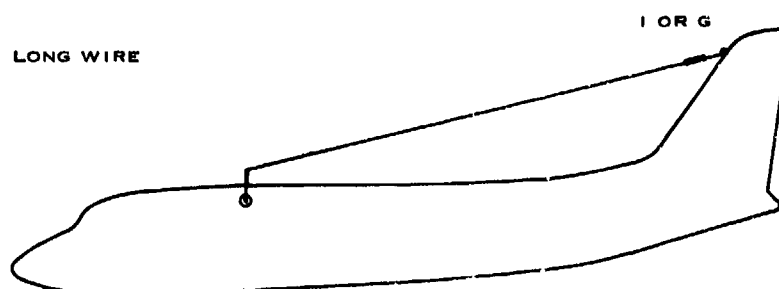


Figure 1. Long-Wire Antenna on Collins Airplane and Radio Bay.



INVERTED V WIRE



SHORT GROUNDED WIRE



⊙ COUPLER FEED POINT (MAST OR FEED THRU)
I INSULATOR
G GROUND

Figure 2. Wire Antenna Types.

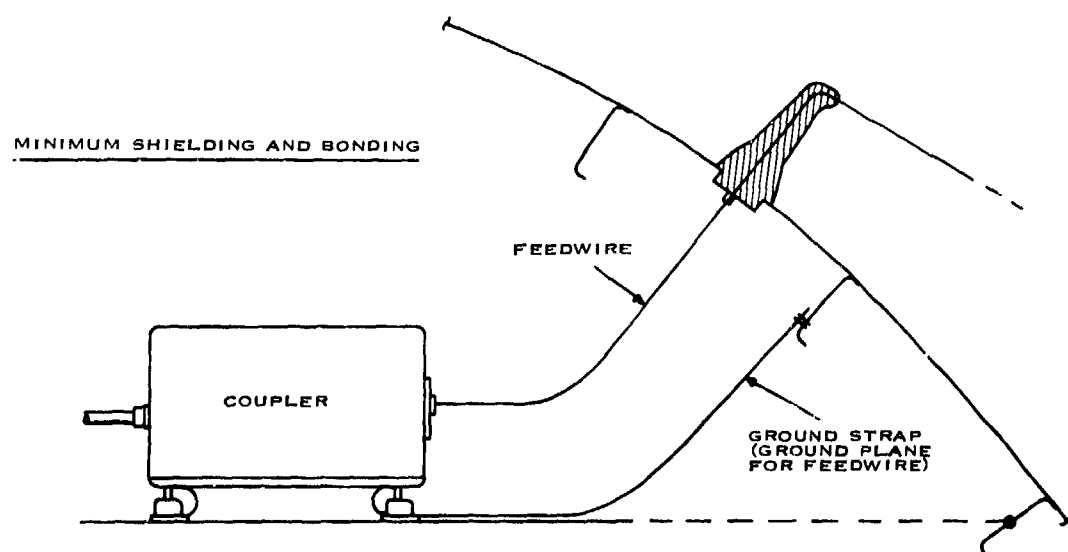
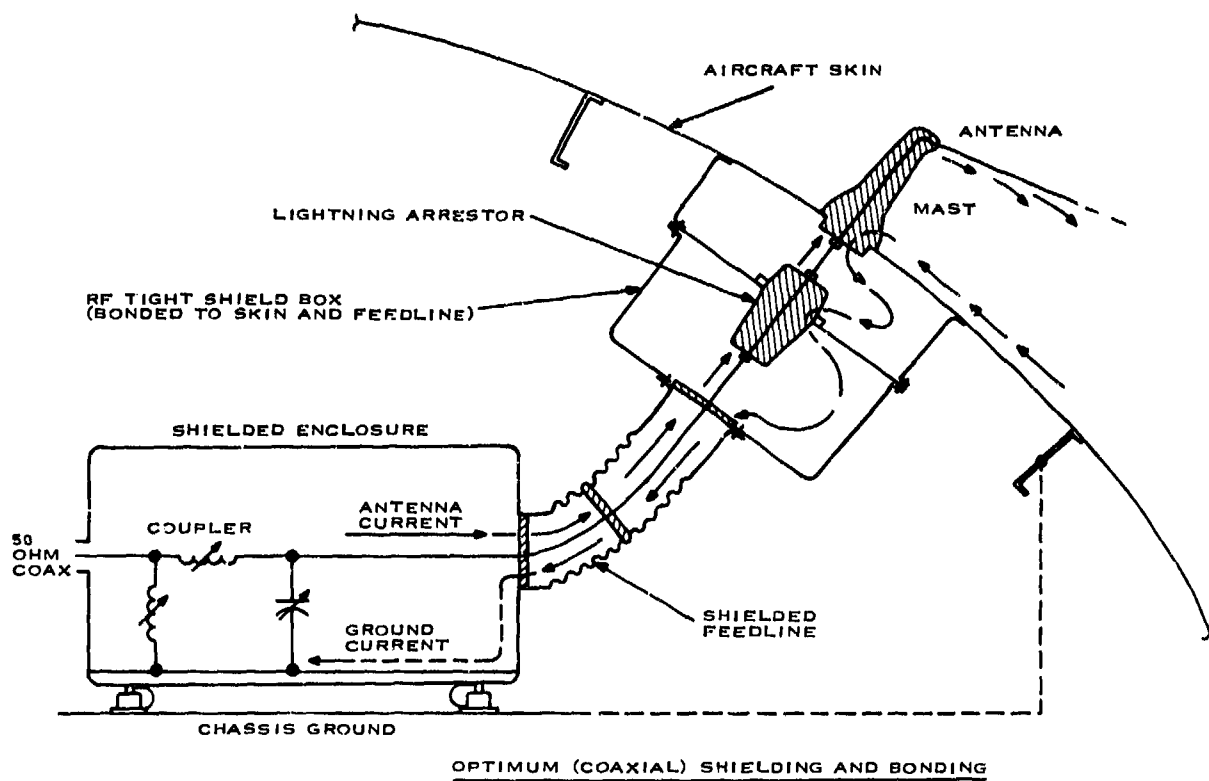


Figure 3. Wire Antenna/Coupler Shielding and Bonding Techniques.

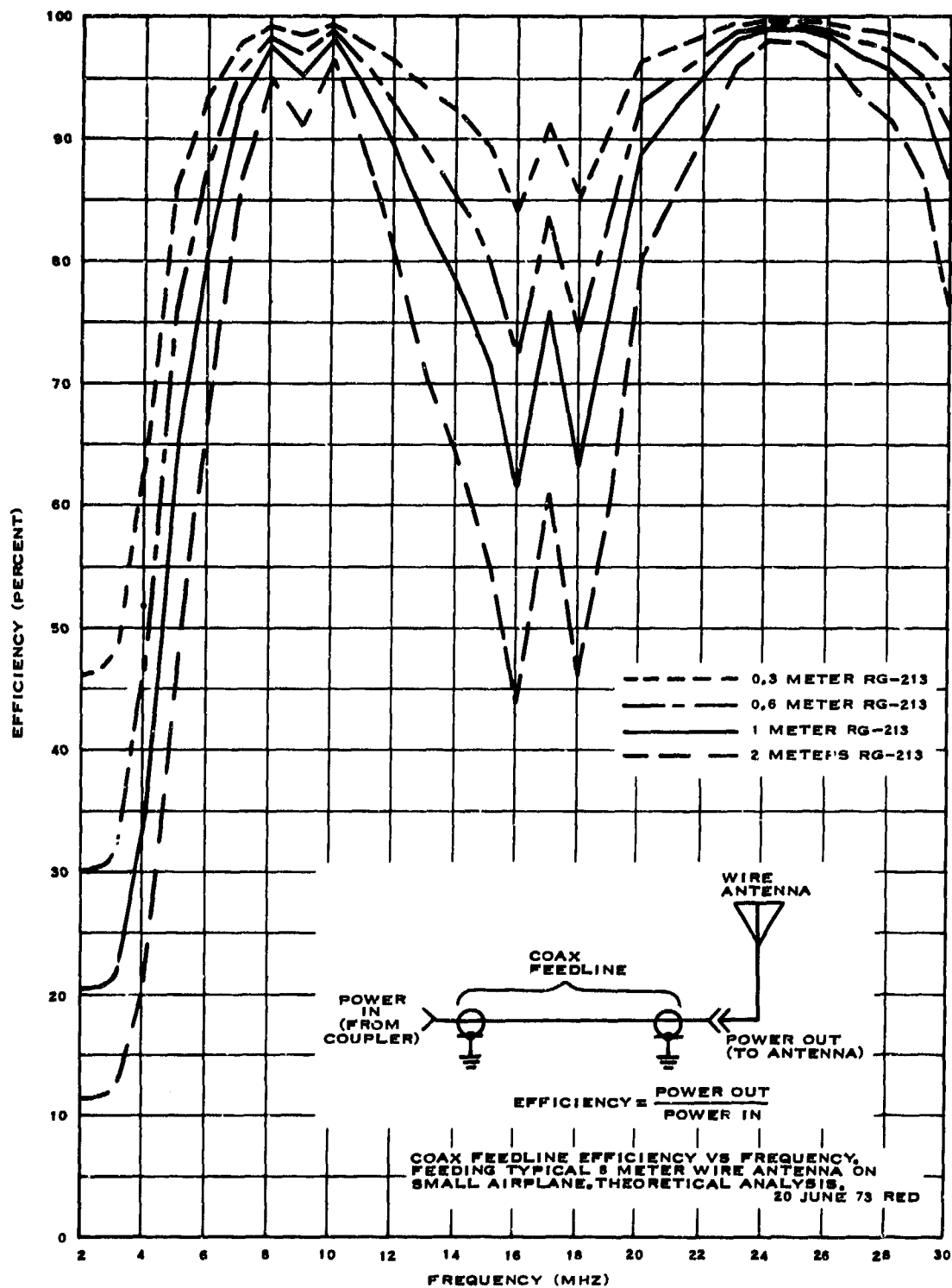


Figure 4. Wire Antenna - Typical Coax Feedline Efficiency.

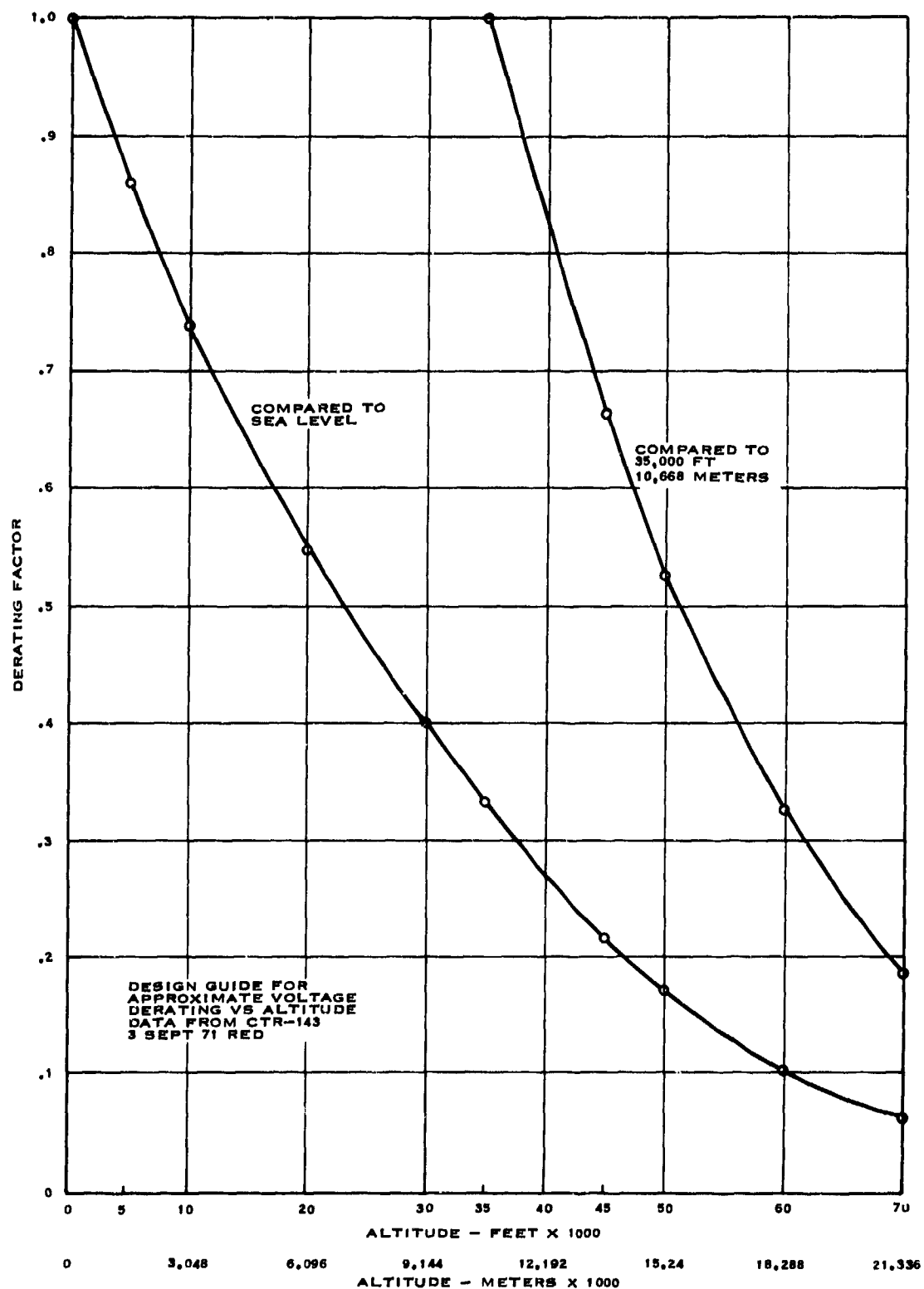
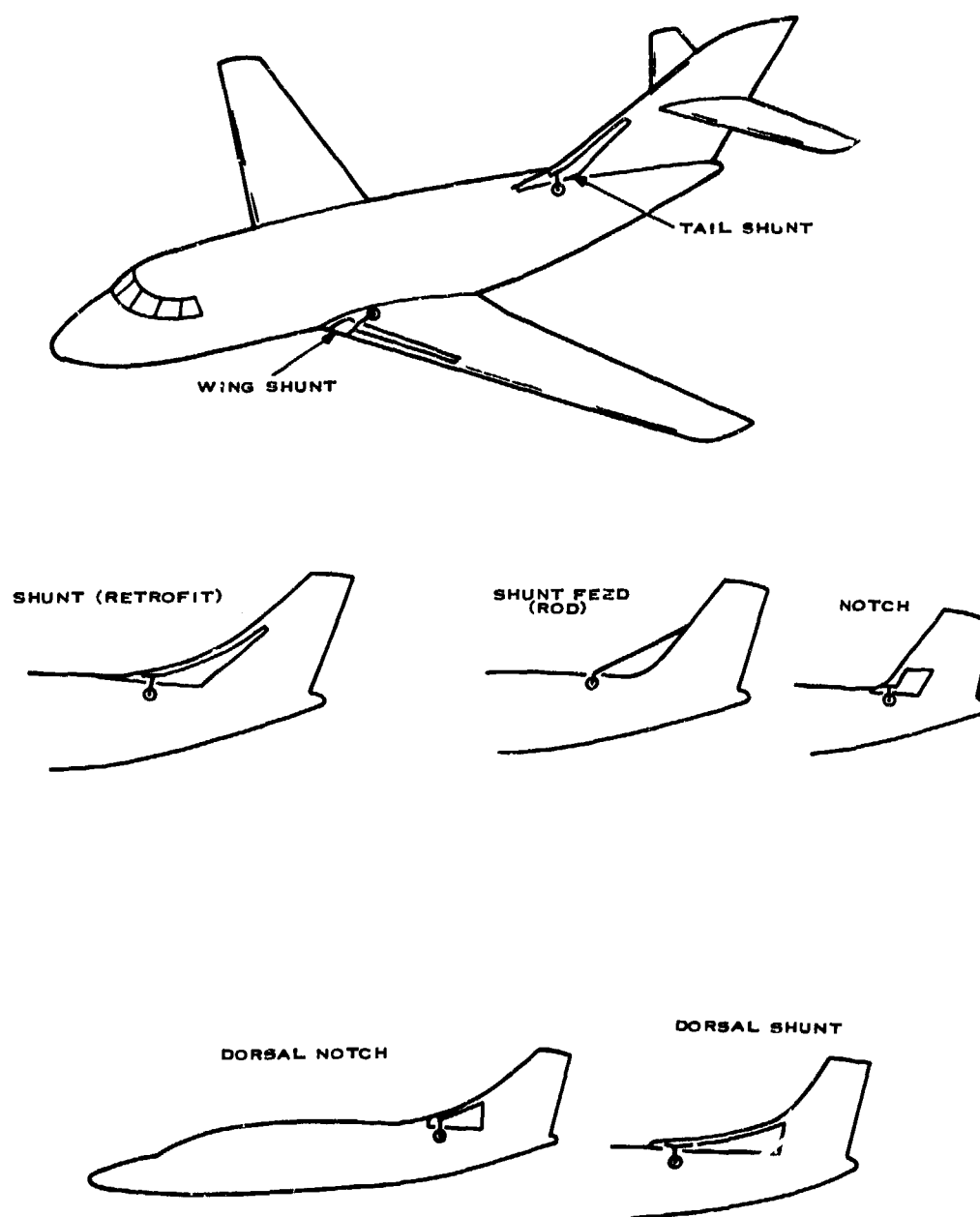


Figure 5. Typical Altitude Voltage Derating Curve.



⊙ COUPLER FEED POINT (HIGH CURRENT-HIGH VOLTAGE FEED THRU)

Figure 6. Shunt/Notch Antenna Types.

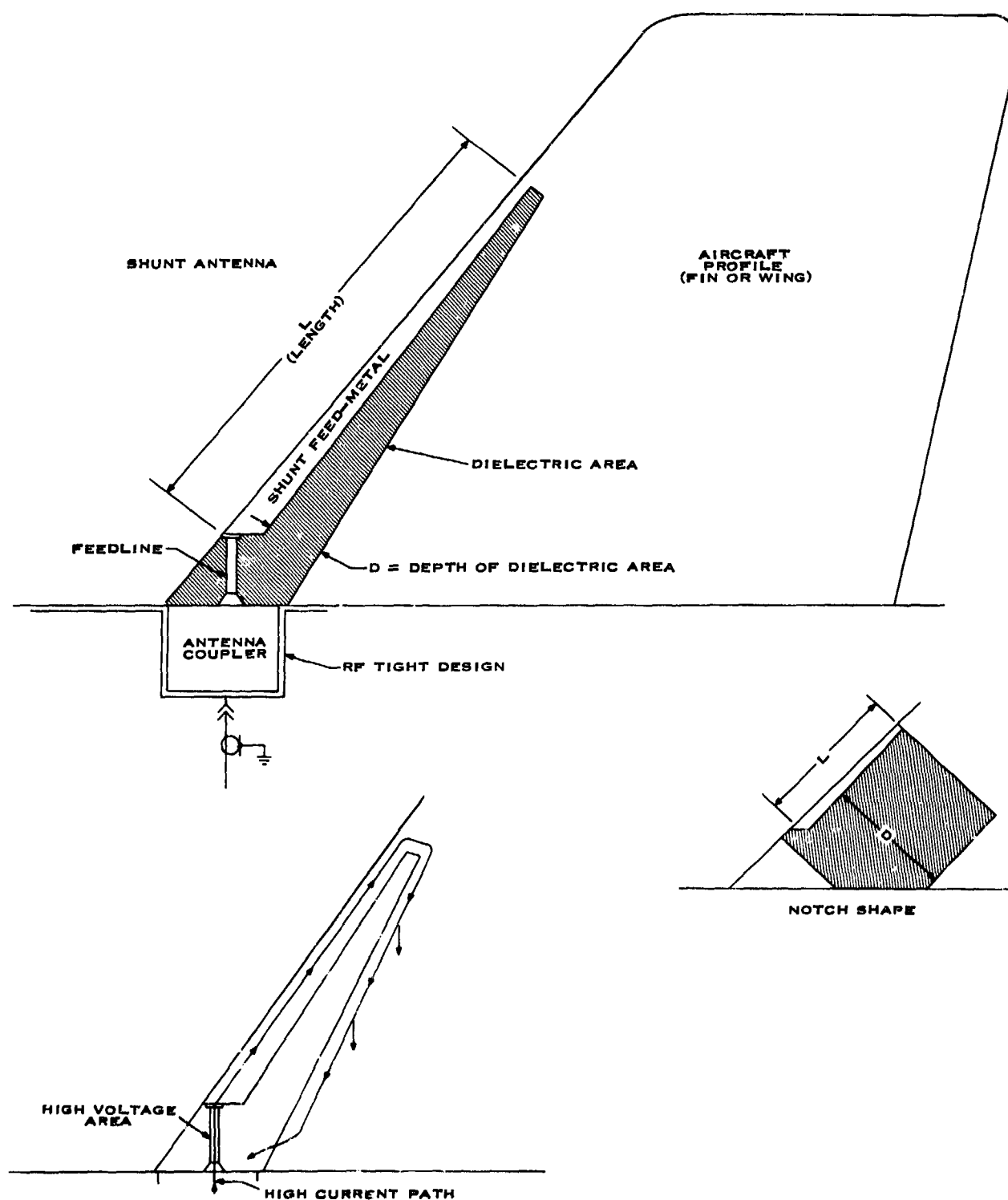


Figure 7. Shunt/Notch Antenna Details.

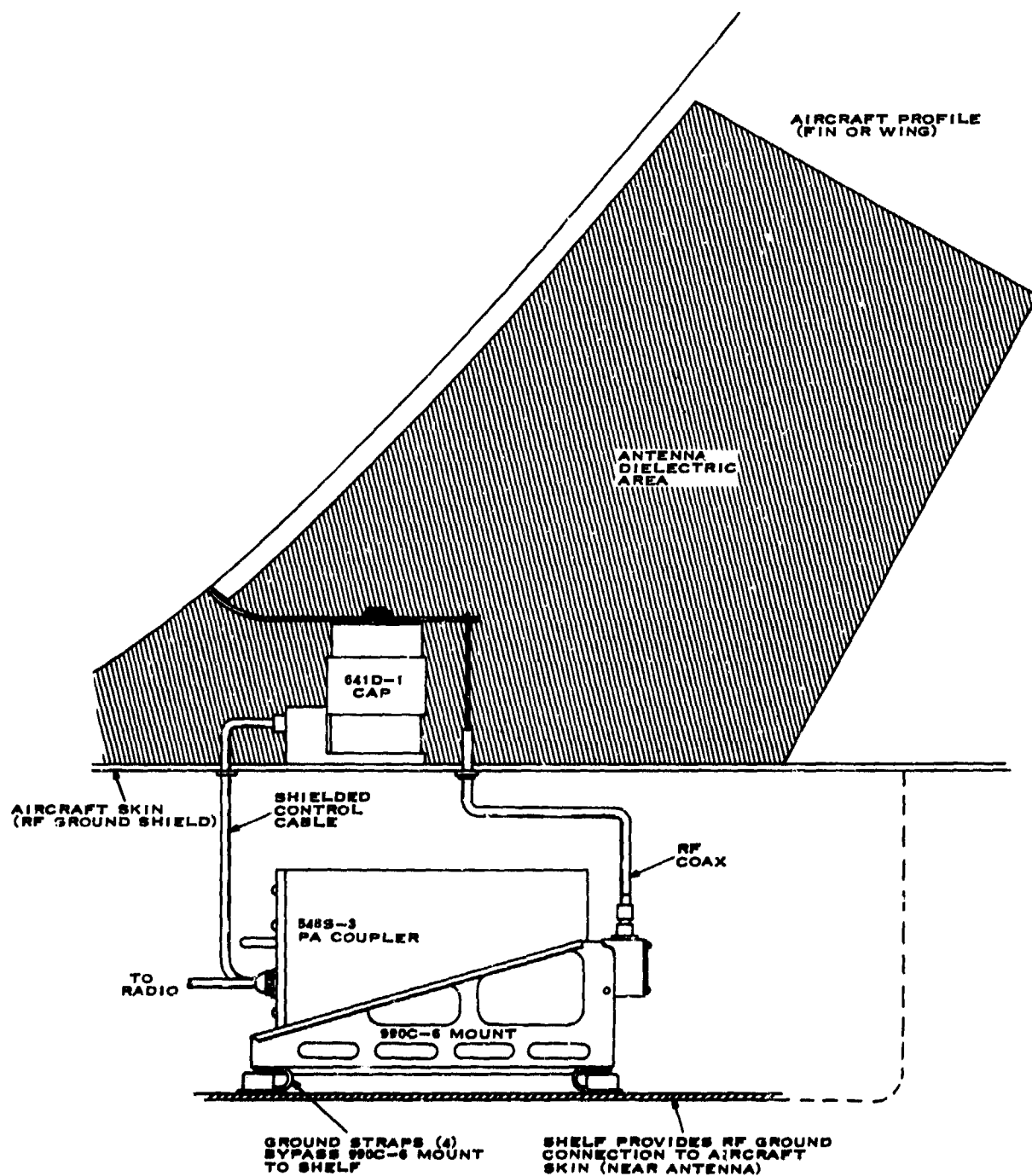
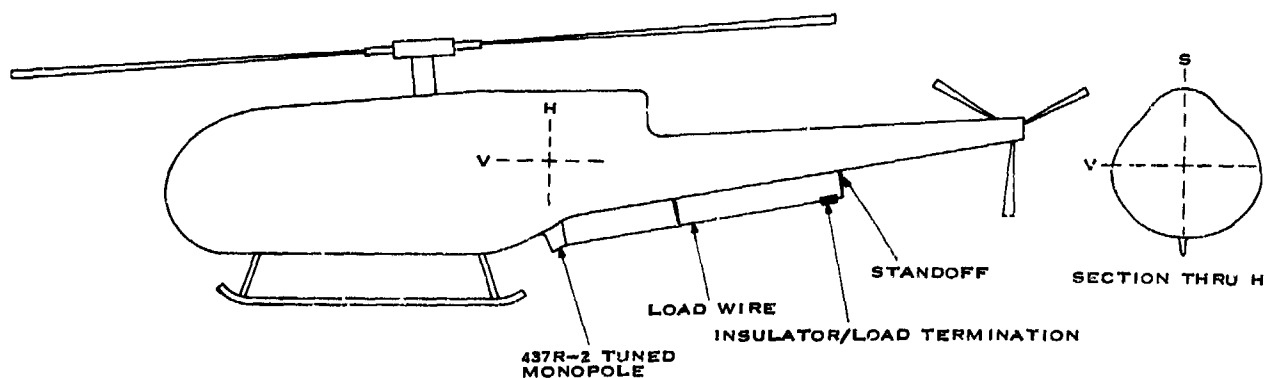


Figure 8. Shunt/Notch Antenna - Typical Installation With Collina 548S and 641D.



1. MOUNT THE 437R-2:
 - CLOSE AS POSSIBLE TO HORIZONTAL CENTER OF AIRCRAFT (H) AND SIDE TO SIDE CENTER (S)
 - AS FAR AS PRACTICAL ABOVE OR BELOW VERTICAL CENTER OF AIRCRAFT (V) (ON HELICOPTER MOUNT ON BOTTOM ONLY-AWAY FROM MAIN ROTOR)
2. LOAD WIRE
 - LENGTH 10 TO 15 FEET (3.05 TO 4.07 M)
 - SPACE AS FAR AS POSSIBLE FROM AIRCRAFT SKIN (MINIMUM OF 1 FOOT (0.3M) AT END). USE 10,000 VOLT STANDOFFS AND INSULATOR/LOAD TERMINATION (SEE INSTRUCTION BOOK)
 - KEEP TIGHT TO PREVENT MOVEMENT FROM WIND AND VIBRATION
 - ROUTE IN RELATIVELY STRAIGHT LINE TOWARD REAR OF AIRCRAFT

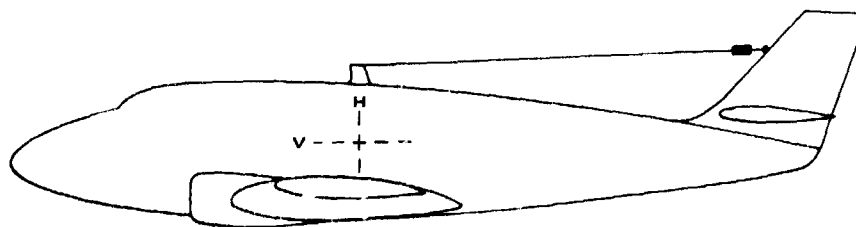


Figure 9. Tuned Monopole Antenna Types (Collins 437R-2).

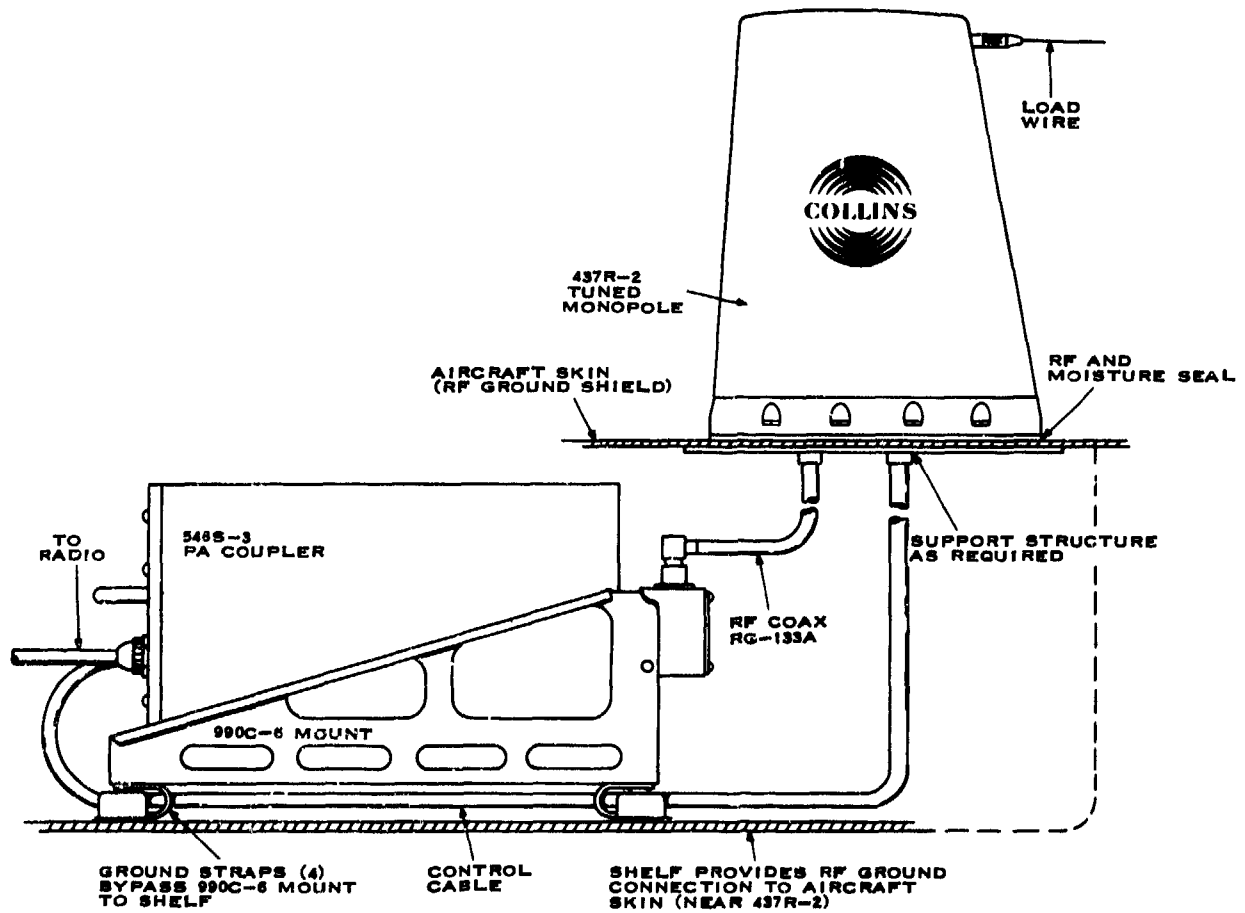


Figure 10. Tuned Monopole Antenna - Typical Installation With Collins 548S and 437R-2.

DISCUSSION

C.E.COOPER: The V-antenna described is assymetric - it could be fed at either extreme, or at the apex point, possibly with some physical rearrangement. Is there known to be particular merit for any feed point?

2. The monopole loading system for a helicopter antenna shows a load termination at the extreme aft end of the wire. What if anything is needed aft of this unit in order to make it work?

R.E.DEASY: 1. There is better vertically polarized radiation when fed from the aft extremity, since the higher currents then flow in the near vertical section.

2. The load termination is an insulator for most installations. On some helicopters, a series L-C circuit resonating just above 30 MHz is used in order to improve the tuning efficiency near 30 MHz.

VERY SLIM, HIGH GAIN
PRINTED CIRCUIT MICROWAVE ANTENNA
FOR AIRBORNE BLIND LANDING AID

By: W.Hersch Ph.D. B.Sc.(Eng.) M.I.E.E.
(MEL Equipment Company Ltd.)

S U M M A R Y

A very slim stripline microwave antenna designed for C - Band consists basically of two selectively etched POLYGUIDE boards. The integral radiating elements are 2 stacked dipoles, backed by a reflector, yielding a cardioid shaped beam approximately 40 degrees wide. An aerodynamically shaped radome and the use of high temperature materials makes this antenna suitable for all supersonic aircraft.

Antennas used for navigational purposes and in particular antennas for Blind Landing Aids must exhibit a carefully controlled polar diagram. In one Blind Landing System known as MADGE (Microwave Airborne Digital Guidance Equipment), which uses vertical polarisation, the beamwidth in elevation need only be wide enough to accommodate the variation in pitch of the aircraft during the approach phase, typically ± 20 degrees, whereas omnidirectional cover is required in the azimuth plane.

At microwave frequencies, no single antenna can provide omnidirectional cover due to obscuration by the fuselage and hence 2 antennas are employed, one fore and one aft, which are alternately connected to the transmitter/receiver.

By way of explanation, Figure 1 shows schematically a coaxial cable-fed version of the basic configuration. The equivalent arrangement in stripline is illustrated in the exploded view of Figure 2. The outsides of the two copper clad POLYGUIDE boards are here selectively etched so that the two halves of each dipole are integrally formed on separate panels. The stripline feeder including the power splitter and quarter wave matching sections are produced by photo etching on the inside.

The two panels are held together by rivets, spaced in such a way that they form chokes thus suppressing radiation resulting from unbalanced parallel plate modes. The centrally placed load in the 4th arm of the power splitter has only to absorb reflected power due to asymmetry between the two dipoles and in a well balanced assembly may be omitted altogether. It becomes thus possible to design a physically short antenna and yet to maintain a 10 : 1 cord ratio stipulated for supersonic aircraft.

None of the microwave components are highly frequency sensitive and hence a match of 1.5 : 1 can readily be maintained over a 5% frequency band. The complete assembly is normally enclosed in an aerodynamically shaped radome which, because of the inherent slimness of stripline, results in a blade like appearance, see Figure 3.

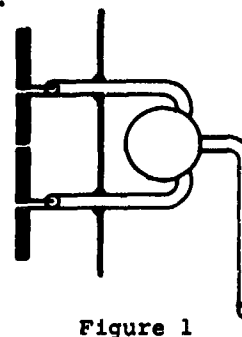


Figure 1

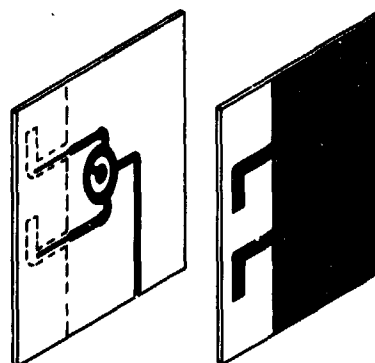


Figure 2

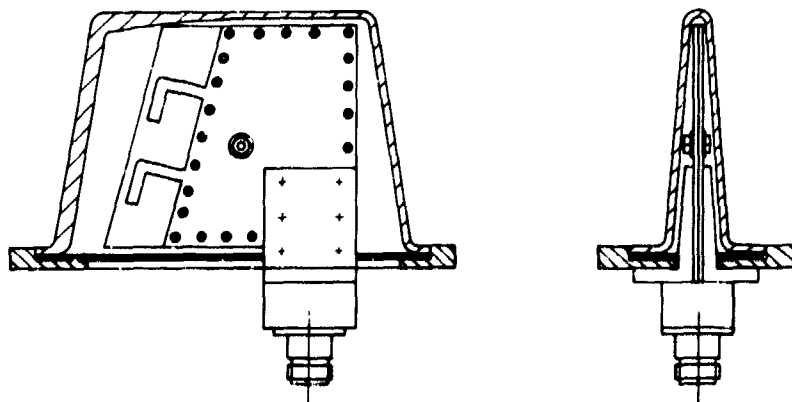


Figure 3

A typical free space radiation pattern is shown in familiar polar coordinates in Figures 4 and 5.

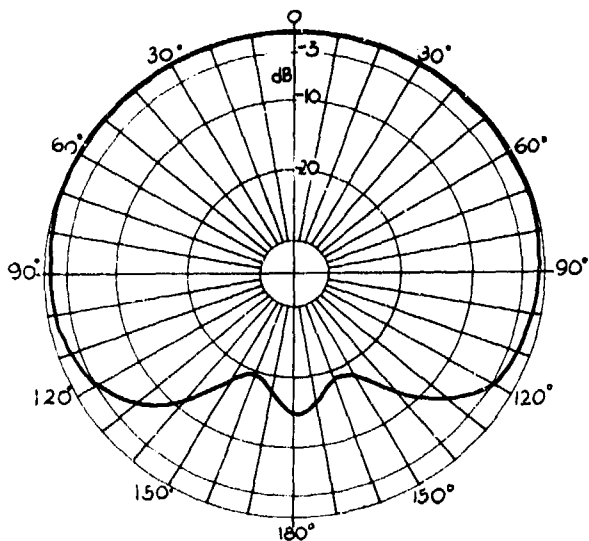


Figure 4 (Azimuth)

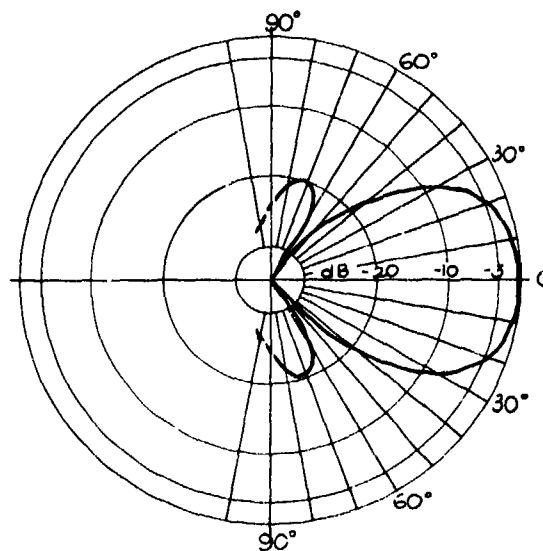


Figure 5 (Elevation)

The azimuth pattern can be modified within limits by enlarging the reflecting edge of the stripline assembly. For instance, the addition of metal strips 4 mm wide, bonded to the outside, will reduce the azimuth beamwidth from ± 120 degrees to ± 80 degrees, with a corresponding increase in gain in the forward direction of 1 dB, as illustrated in the X - Y plot, Fig. 6 in which the enlarged scale demonstrates the effect of small changes more clearly.

The elevation pattern, perfectly smooth when measured under 'free space' conditions, can suffer fluctuations typically of the order of ± 4 dB due to reflection from the fuselage, but careful siting of the antenna, where this is possible, can considerably minimise the effect.

Since various types of aircraft are going to be equipped with the MADGE Blind Landing Aid, 3 slightly different versions of the antenna have been produced with upward beam tilts of 0° , 14° and 28° , to cater for installation conditions typically encountered in practice.

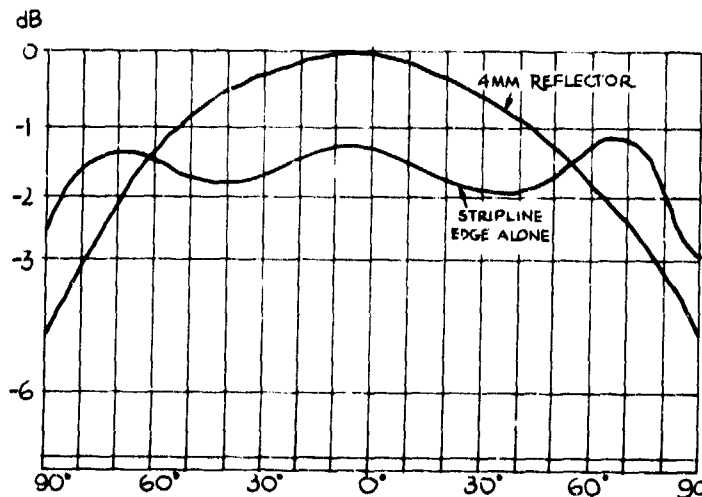


Figure 6

POLYROD AERIALS FOR AVIONIC APPLICATIONS

by

M. Scorer
A.M. Smith
Marconi-Elliott Avionic Systems Ltd
Elstree Way
Borehamwood
Hertfordshire
WD6 1RX
England

SUMMARY

This paper investigates the effect of adding rectangular dielectric slabs, having cross sections of the order of tens of square wavelengths, to the aperture of an aerial with a view to increasing its gain. A theory has been developed to describe the performance of such an aerial and has been verified experimentally. Theoretical and experimental curves of gain enhancement versus slab length for slabs having various dielectric constants are presented. Hybrid slabs, comprising sections of different dielectric constants, have been designed according to the theory and show improved performance over slabs of constant dielectric constant. Slabs excited by feeds whose apertures have cross sections smaller than the slab cross section have also been examined.

1. INTRODUCTION

In most airborne radar applications the gain that can be obtained from the aerial is at a premium, and with conventional reflector or planar array aerials a large cross-sectional area is needed to achieve high gain. In practice, sufficient space to accommodate these aerials is not always available in the parts of an aircraft, such as the nose and tail, in which the aerial and its associated equipment must be installed. This paper describes a composite aerial in which a dielectric slab is mounted in front of a conventional aerial to enhance its gain. The composite aerial can have a variety of sizes and shapes to suit the space available. However, this paper is principally concerned with the case where the cross-section of the aerial is rectangular and several tens of square wavelengths in area. It will be shown that for the type of avionic application envisaged, the required dielectric constant is low (around 1.1) and so the aerial can be made from lightweight natural dielectric foams or an artificial dielectric if extreme lightness is required.

The dielectric slab achieves gain enhancement in two ways. Firstly, energy from the feed is coupled into a surface wave mode which propagates along the slab and is radiated from its free end. This surface wave mode has a field distribution which can extend beyond the boundaries of the slab and hence form a radiating aperture which is larger than the feed aperture. In addition, energy is radiated directly from the feed/slab interface and beats with the radiation from the free end of the slab.

Conventional dielectric aerials which have a cross section which is small compared to a wavelength and which use relatively high dielectric constant material have been extensively studied. However, in the case where the basic aerial has a cross section of several square wavelengths, no information has hitherto been available concerning the optimisation of parameters such as dielectric constant and geometry. The aim of this paper is to establish a model which is capable of furnishing such design information.

2. TWO APERTURE MODEL

The behaviour of a dielectric enhanced aerial can be described by utilising a two aperture model (COLLIN, R.E., 1969, GALLETT, I.N.L., 1973). This model assumes that some of the energy is radiated from the feed/slab interface and the remainder is launched into a surface wave which is propagated along the slab and is radiated from its free end. The radiation pattern of the composite aerial is determined by the vector addition of the radiation from the two ends of the slab.

In order to utilise this model it is necessary to determine the propagation characteristics of the surface wave and to determine the forms of the effective aperture distribution at the free end of the slab, and at the feed/slab interface.

The first part of the theoretical analysis solves the electromagnetic boundary problem. In the case of slabs with circular or elliptical cross section, the propagation constants can be found analytically (JAMES, J.R., 1967, YEH, C., 1962) but for slabs of rectangular cross section the Point Matching Technique has to be used. (JAMES, J.R., 1972, GALLETT, I.N.L., 1972) and (BATES, R.H.T., JAMES, J.R.,

GALLET, I.N.L., MILLAR, R.F., 1973). Solution of the resulting transcendental equation yields the propagation constants for the various modes. Typical mode charts for rectangular slabs are shown in Figure 1. The parameter β is the phase constant for the surface wave and takes account of both the dielectric constant and the guiding effects of the slabs. The mode designations are those used by (MARCATELLI, E.A.J., 1969) and by (GOELL, J.E., 1969) and are classified according to the symmetry properties of the electric field. The mode nomenclature is such that the superscript denotes the direction of the electric vector and the subscripts give the number of regions of power concentration in the x and y directions. The lowest order hybrid modes which have plane wave fronts are of importance in the practical work. These are the E_{11}^x and the E_{11}^y modes which are illustrated in Figure 2. The density distributions of these modes are approximately Gaussian in form and consequently the radiation from the free end of the slab (which we will call the termination radiation) also has approximately Gaussian form. Previous workers have usually assumed that the direct radiation from the feed/slab interface may be assumed to be derived from an aperture distribution which has an identical form to that of the feed but which is reduced in amplitude. However, a more realistic model assumes that the distribution at the feed/slab interface is the difference between the original feeder distribution and that of the E_{11}^x or E_{11}^y mode which is propagated on the dielectric slab. This distribution may be either predominantly negative or predominantly positive depending on the relative amplitudes and forms of the surface wave and feed distributions. Thus, in some cases there will be a 180° phase shift between the two apertures and in other cases a 0° phase shift.

Before the complete radiation pattern of the dielectric enhanced aerial can be calculated, the relative amplitudes of the radiation from each of the two apertures must be determined. These have been ascertained empirically by fitting to the measured result for one particular case. The deduced amplitudes may then be used to calculate a generalised family of results.

An important property in assessing a dielectric enhanced aerial is the amount of gain enhancement obtained. This is defined as the difference between the gain of the combined feed and dielectric slab and that of the feed alone. Curves of gain enhancement have been calculated, using the above theory, for slabs of various dielectric constants and are presented in Figure 4.

To achieve a significant amount of gain enhancement from a dielectric slab aerial the two radiating apertures have to be correctly phased to give constructive interference. The particular case examined of a rectangular horn of aperture $9.5 \lambda_0$ by $2.4 \lambda_0$ is found to have an inherent 180° phase difference between the termination aperture and feed/slab aperture. The separation of the apertures i.e. the length of slab, therefore has to be adjusted to give another 180° of phase so that the maximum gain enhancement may be obtained. This basic result of the model has been used to design uniform and non-uniform dielectric constant slab aerials to give an optimised performance.

3. EXPERIMENTAL INVESTIGATION

The experiments involved measurements of the gain and far field radiation patterns of various dielectric enhanced aerials. In some cases it was necessary to measure both the phase and amplitude of the radiation pattern.

The simplest experiments involved measuring the variation in gain when slabs having differing dielectric constants and lengths were mounted in front of a horn aerial whose aperture was $9.5 \lambda_0$ by $2.4 \lambda_0$. The experimental arrangement is illustrated in Figure 3. In each case the overall aerial gain was measured as the length of the slab was increased up to a maximum of $50 \lambda_0$, and for the higher dielectric constant slabs, sufficient length was available to show an approximately sinusoidal gain variation. The measured results are shown in Figure 4 where they are compared with the theoretical curves which were obtained in the manner previously outlined. The periodicities and amplitudes of the theoretical and measured results are in good agreement which not only endorses the two-aperture model but confirms that the calculated values of β are in close correspondence with the assumed nominal values of the permittivity of the dielectric material.

In the case where the slab had a dielectric constant of 1.1, results were obtained with the electric vector parallel to both the long and the short sides of the slab corresponding to the slab supporting the E_{11}^x and E_{11}^y modes respectively. These are presented in Figure 5 from which it can be seen that the E_{11}^x mode gave a peak gain enhancement of about 3.3dB whereas the E_{11}^y mode gave a peak enhancement of about 2dB.

The two-aperture model was examined in more detail by separating the contributions of the two apertures using the method of (ZUCKER and STROM, J.A., 1970). This method involved measuring the phase and amplitude of the radiation from the composite aerial in the far field as the separation of the two apertures was varied. It was assumed that as the length of the dielectric slab was varied, thereby

altering the separation of the two apertures, the contribution from the feed/slab aperture remained constant while that from the termination aperture was constant in amplitude but varied in phase. The vector addition of these two signals results in a circle centred on the junction of the two vectors having a radius equal to the amplitude of the termination aperture vector.

Measurements were made on a rectangular slab of dielectric constant 1.1 fed by a horn. These measurements were made at 1° scan angles up to 20° off boresight for each slab length as the latter was reduced in steps of $1.56 \lambda_0$. Both polarisations were used i.e. with the electric vector parallel to both the long and short sides, and the aerial was scanned in both the E and H planes resulting in four sets of measurements. For each set of measurements polar plots were drawn to allow the contributions from the two apertures to be separated. A typical plot is shown in Figure 6. The radiation patterns of each aperture obtained from this measurement are presented in Figures 7 - 10 as curves A and B. The pattern which was obtained without the slab in front of the horn is shown in the figures as curve C. From the model outlined earlier, the feed/slab radiation pattern may also be obtained by differencing the measured horn and derived termination patterns (curve C - curve A) and this result is shown as curve D. The two curves for the feed/slab radiation pattern are in good agreement.

The two-aperture model enables the length of the slab to be chosen so that the radiation from the two apertures adds in phase to produce gain enhancement. This model has been used to design hybrid slabs composed of several different dielectric constant materials of uniform cross section. The objective was to obtain a slab onto which the energy from the horn could be launched efficiently while retaining a high gain termination radiation pattern. The former requires the field of the surface wave to be confined within the horn aperture dimensions i.e. for the slab to have a high dielectric constant, whereas the latter necessitates a large virtual aperture i.e. a low dielectric constant slab.

In order to investigate the effects of hybrid slabs a reference aerial was selected which comprised a $10.9 \lambda_0$ long slab of dielectric constant 1.1. This slab length was chosen so that constructive interference between the two apertures occurred. A two component hybrid slab ($\epsilon = 1.1, 1.2$) was designed by choosing the lengths of the individual sections so that constructive interference of the radiation from the two apertures was obtained. The slab was constrained to have an overall length of $10.9 \lambda_0$. The E and H plane radiation patterns of the resulting aerial are shown in Figure 11 together with the radiation patterns of the reference aerial. When these patterns are compared with those of the reference aerial (which has the same form of termination pattern) it is seen that the H plane sidelobes have been reduced to -17.6dB compared with -10.6dB. The gain enhancement has also been slightly reduced (2.6dB compared with 3.25dB) due to a slight increase in the H plane beamwidth. The E plane pattern is unaffected.

A hybrid slab composed of more component sections would have less abrupt junction discontinuities which might therefore cause less radiation from the junctions and hence lower the sidelobe levels still further. Consequently a 3-component hybrid slab ($\epsilon = 1.2, 1.14, 1.1$) whose overall length was also $10.9 \lambda_0$ was evaluated. The lengths of its sections were chosen so that constructive interference occurred between the two apertures. The resulting E and H plane radiation patterns are shown in Figure 12. In this case the H plane sidelobes were reduced to -18.2dB but the H plane beamwidth improved to give a gain enhancement of 3dB. The E plane pattern was again unaffected.

A further 3-component hybrid slab which was also constrained to a length of $10.9 \lambda_0$ was investigated. This had a termination section having a lower dielectric constant than the previous slab (1.04 as compared with 1.1) and would therefore be expected to have a larger virtual aperture and increased gain. The dielectric constants of the remaining sections were unaltered so that the launching conditions were unchanged but the lengths of the sections had to be adjusted to give constructive interference again. However, the measured results showed a slight decrease in gain (0.4dB). This is probably due to the greater discontinuity occurring at the last junction resulting in increased sidelobes.

Finally, a 7-component hybrid slab ($\epsilon = 1.4, 1.3, 1.2, 1.14, 1.1, 1.04$ and 1.02) with an overall length of $10.9 \lambda_0$ was again designed to give constructive interference between the two apertures. The E and H plane radiation patterns of this structure are shown in Figure 13. The H planes have been further reduced to about -23dB but once again the H plane beamwidth has increased resulting in a slightly reduced gain enhancement of 2.5dB. The E plane is still unaffected.

In summary the use of a hybrid dielectric constant slab instead of a uniform one, reduces the H plane sidelobe level. The improvement in sidelobe level increases with the number of sections used and with a seven section slab the sidelobe level was -23dB which compares with -10.6dB for a uniform slab.

3.1 Reduced Height Feeds

In most avionic applications the aerial housing will have a curved cross section and there is a possibility of using a similarly curved dielectric slab to enhance the gain. However, feeding such an aperture with a plane wave often presents engineering difficulties and there tend to be advantages if the shaped slab can be fed by a smaller rectangular cross sectioned feed. This section considers whether the

use of such a rectangular feed significantly impairs the performance of the composite aerial.

Some experiments were conducted on the effect of reducing the height of the horn feeding a rectangular cross sectioned slab to examine the effects on the gain of the composite aerial.

The measurements were made using a slotted waveguide array with an associated horn which flared out to an aperture approximately $30 \lambda_0$ by $3 \lambda_0$. The array had a -18dB cosine taper across its larger dimension and its E vector was parallel to this direction. The height of the horn could be reduced in stages down to $1.5 \lambda_0$. This feed was used to excite the E_{11}^x mode on a rectangular cross section slab of dielectric constant 1.08 whose length could be increased in stages up to a maximum of $16 \lambda_0$.

Table 1 summarises the results for the case when the feed occupied half the height of the slab. It can be seen that when the slab was $7.8 \lambda_0$ long and the feed occupied half the height of the slab the gain of the composite aerial was reduced by 3.3dB compared with that obtained with a full size feed. When the slab length was increased to $15.6 \lambda_0$, the sacrifice in gain with the half height feed was reduced to 1.6dB. This probably represents the best that can be achieved with this dielectric constant slab as $15.6 \lambda_0$ is approaching the correct length for constructive interference between the radiation from the termination and feed/slab interface apertures.

Height of Feed Horn	SLAB LENGTH					
	$7.8 \lambda_0$ Length	$9.3 \lambda_0$ Length	$10.9 \lambda_0$ Length	$12.5 \lambda_0$ Length	$14 \lambda_0$ Length	$15.6 \lambda_0$ Length
$1.5 \lambda_0$	25.7dB	26.8dB	27.1dB	28.3dB	28.9dB	29.0dB
$3 \lambda_0$	29.0dB	29.4dB	29.8dB	30.2dB	30.6dB	30.6dB

TABLE I

Comparison of the total gain of dielectric enhanced horn with full and half height feeds.

4. CONCLUSIONS

A two aperture model has been developed which describes the performance of a dielectric enhanced aerial and has been verified experimentally by far field phase and amplitude measurements. Theoretical and experimental curves of gain enhancement versus slab length have been obtained and show good agreement, providing further endorsement of the two aperture model and confirming that the calculated values of β are in close correspondence with the assumed nominal values of permittivity.

In the case of the E_{11}^y mode of propagation the optimum permittivity is less than 1.1 for slabs having lengths greater than $5 \lambda_0$ and with cross sections $9.5 \lambda_0$ by $2.4 \lambda_0$ resulting in gain enhancements in excess of 0.5dB. However, it has been found that, for a slab of dielectric constant 1.1, use of the E_{11}^x mode of propagation can give a gain enhancement which is up to 2dB greater than that obtained for the E_{11}^y mode of propagation.

The sidelobe performance of dielectric enhanced aerials can be substantially improved by the use of hybrid slabs and these may be designed using the theory which has been developed.

We conclude therefore that a model has been established which is capable of describing the performance of a dielectric enhanced aerial and can furnish the necessary design information.

REFERENCES

1. Collin, R.E. and Zucker F.J. "Antenna Theory" Part II, Inter-University Electronics Series, Vol. 7, Chapter 21. "Surface Wave Antennas" pp 298-348, 1969.
2. Gallett I.N.L., Graham R, James J.R., Scorer M. and Smith A.M. "Gain Enhancement of Microwave Linear Arrays with Dielectric Slab Attachments", 1973 European Microwave Conference (to be published).
3. James J.R. "Theoretical Investigation of Cylindrical Dielectric Rod Antennas". Proc. IEE, Vol. 114, No. 3, pp 309-319, March 1967.
4. Yeh C. "Elliptical Dielectric Waveguides", J. Applied Physics, Vol. 33, No. 11, pp 3235-3243, November 1962.
5. James J.R. and Gallett I.N.L. "Point Matched Solutions for Propagating Modes on Arbitrarily shaped Dielectric Rods". The Radio & Electronic Engineer, Vol. 42, No. 3., pp 103-113, March 1972.
6. Bates R.H.T., James J.R., Gallett I.N.L. and Millar R.F. "An Overview of Point Matching". The Radio and Electronic Engineer, 43 No. 3, pp 193-199, March 1973.
7. Marcatelli E.A.J. "Dielectric Rectangular Waveguide and Directional Coupler for Integrated Optics". Bell Systems Technical Journal, September 1969, pp 2071-2102.
8. Goell J.E. "A Circular-Harmonic Computer Analysis of Rectangular Dielectric Waveguides". Bell Systems Technical Journal, September 1969, pp 2133-2160.
9. Zucker and Strom J.A. "Experimental Resolution of Surfacewave Antenna Radiation into Feed and Terminal Patterns". IEE Transaction on Antennas and Propagation. May 1970, pp 420-422.

ACKNOWLEDGEMENT

This paper reports work carried out with the support of the Procurement Executive, Ministry of Defence.

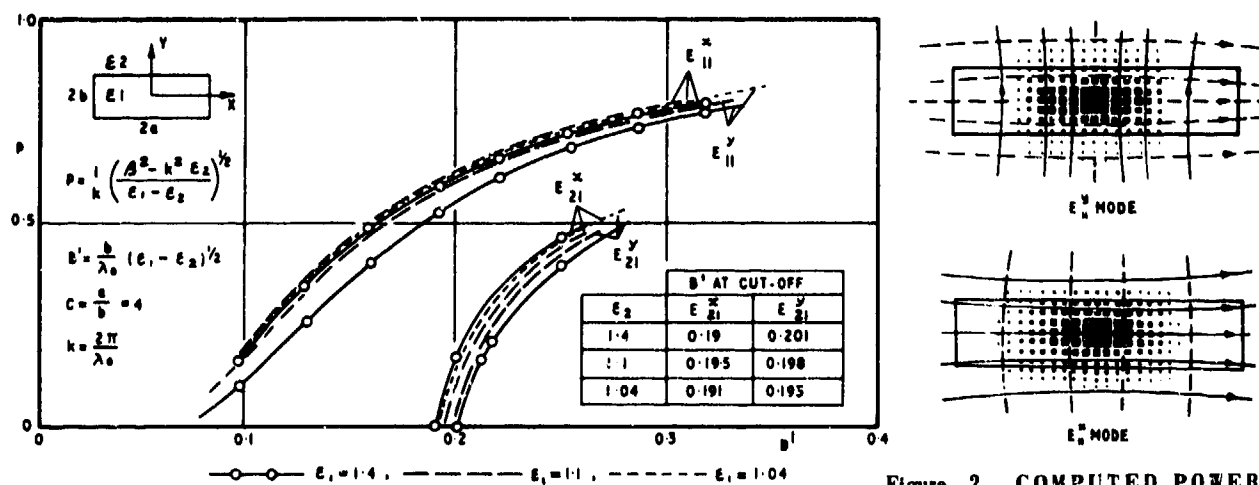


Figure 2 COMPUTED POWER AND FIELD PLOTS

Figure 1. MODE CHART SHOWING VARIATION OF β WITH ϵ_1 FOR $\epsilon_2 = 1$

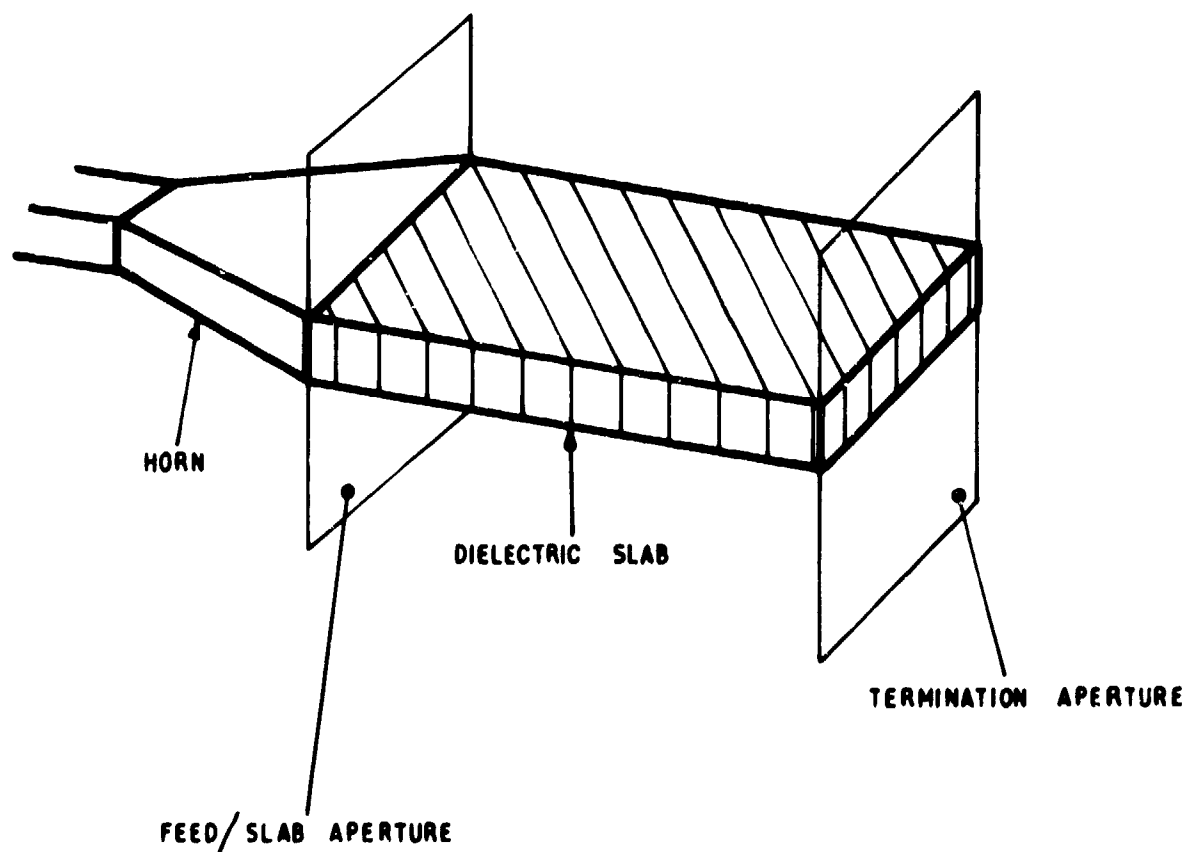


Figure 3. EXPERIMENTAL ARRANGEMENT

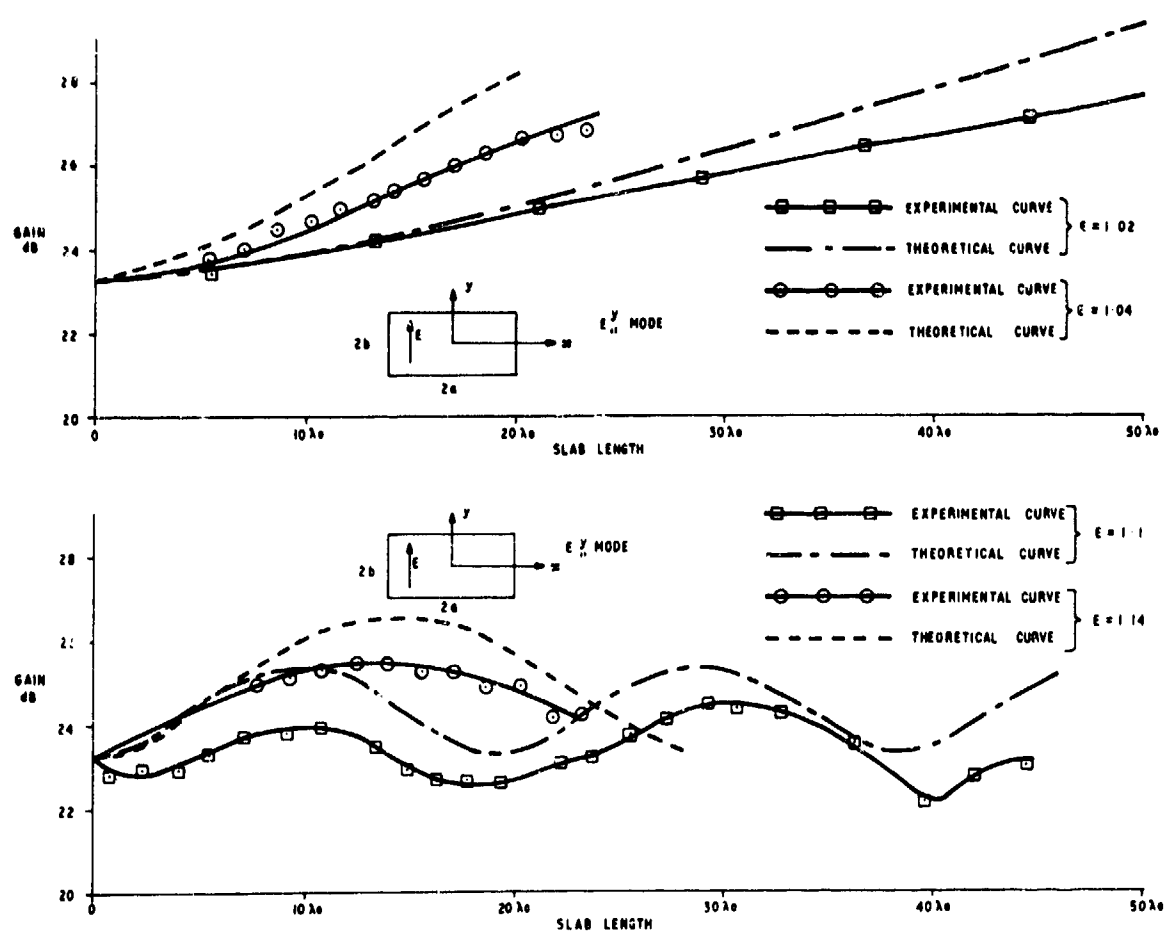
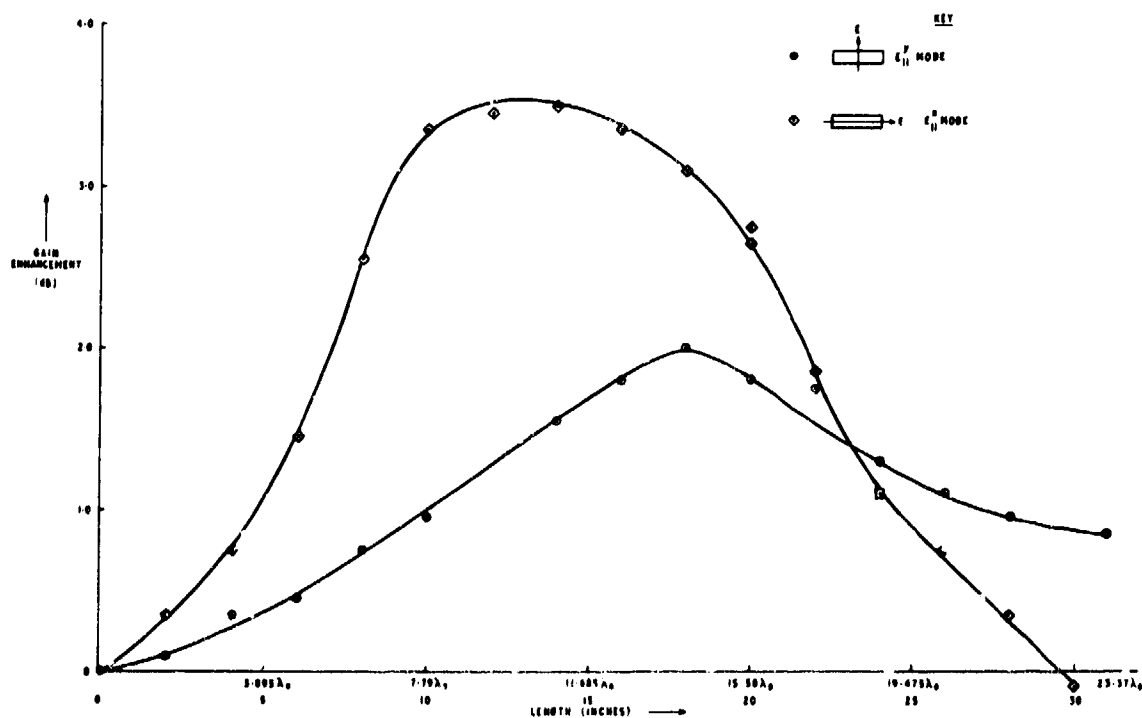
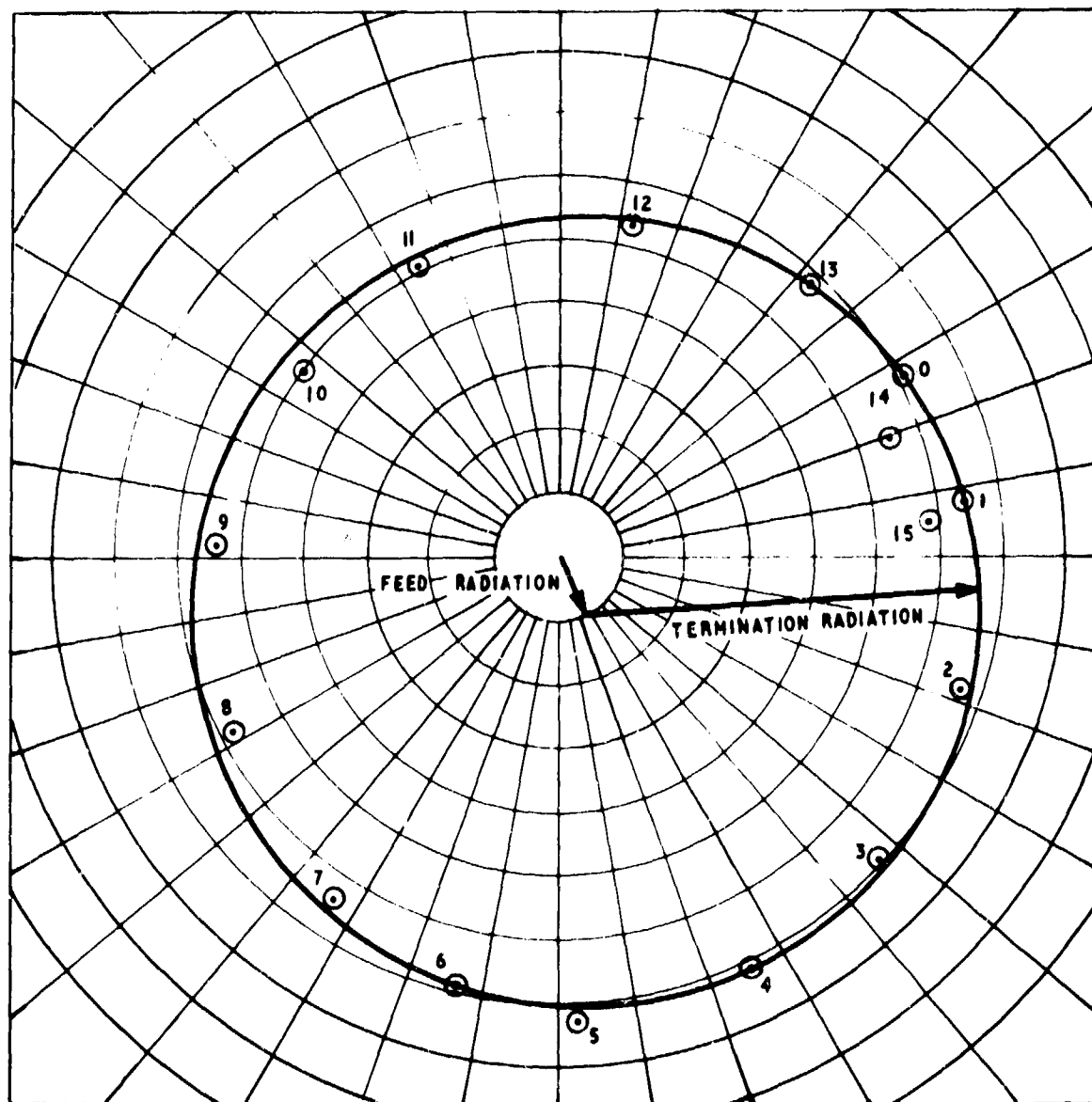


Figure 4. VARIATION OF AERIAL GAIN WITH LENGTH OF SLAB

Figure 5. VARIATION OF GAIN ENHANCEMENT WITH LENGTH FOR THE $\epsilon = 1.1$ DIELECTRIC SLAB



SCAN ANGLE 6°

NUMBERS SHOW THE LENGTH OF SLAB IN UNITS OF 1.56λ

Figure 6. FAR FIELD PHASE AND AMPLITUDE PLOT OF THE DIELECTRIC ENHANCED HORN

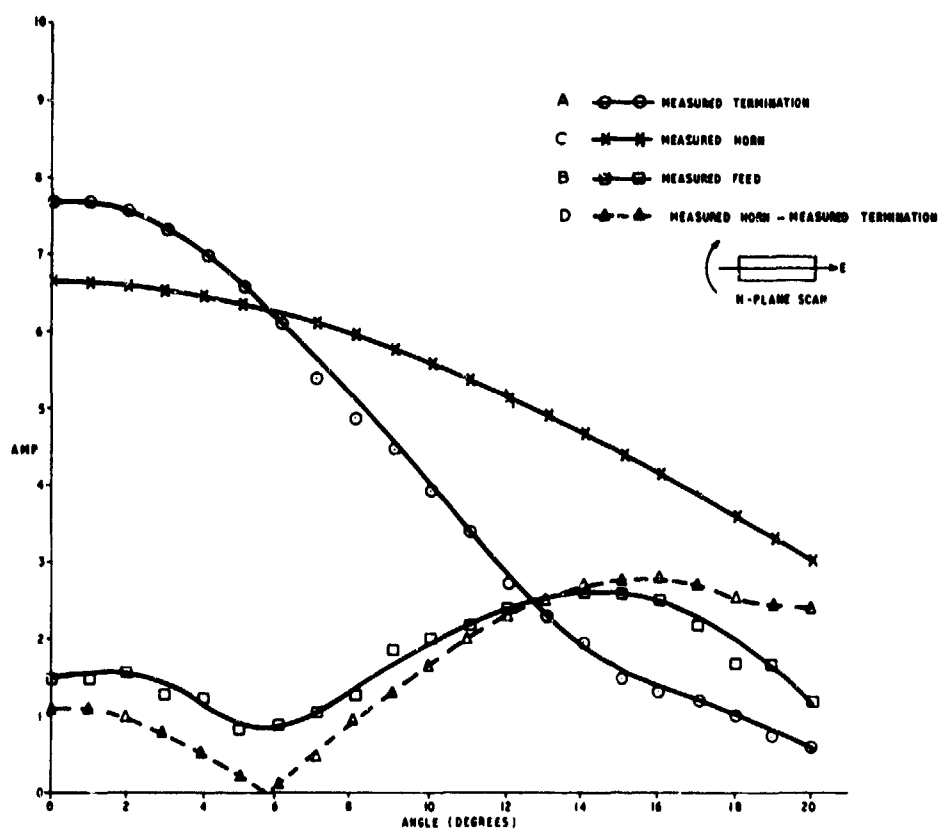


Figure 7. SEPARATED RADIATION PATTERNS OF THE TWO APERTURES FOR THE E_{11}^x MODE, H-PLANE

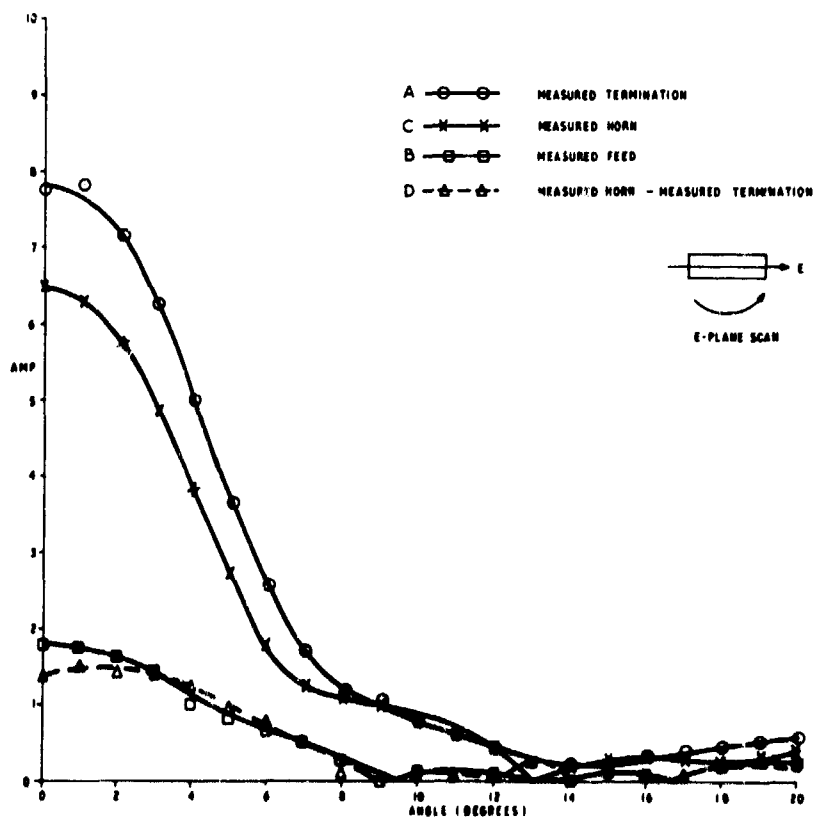


Figure 8. SEPARATED RADIATION PATTERNS OF THE TWO APERTURES FOR THE E_{11}^x MODE, E-PLANE

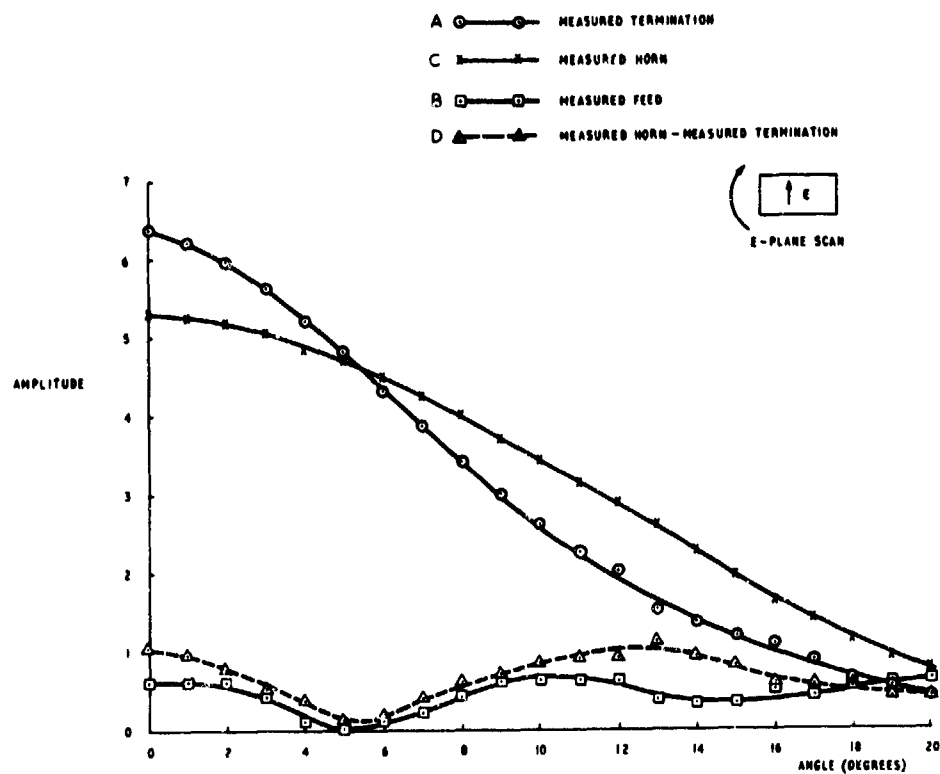


Figure 9. SEPARATED RADIATION PATTERNS OF THE TWO APERTURES FOR THE E_{11}^y MODE, E-PLANE

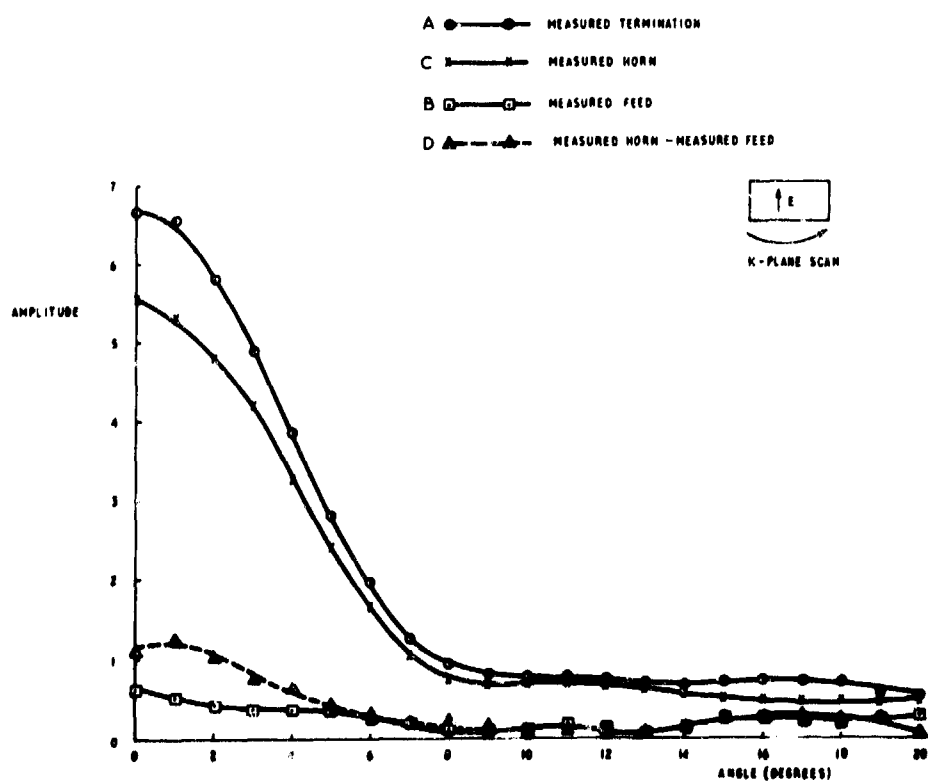


Figure 10. SEPARATED RADIATION PATTERNS OF THE TWO APERTURES FOR THE E_{11}^y MODE, H-PLANE

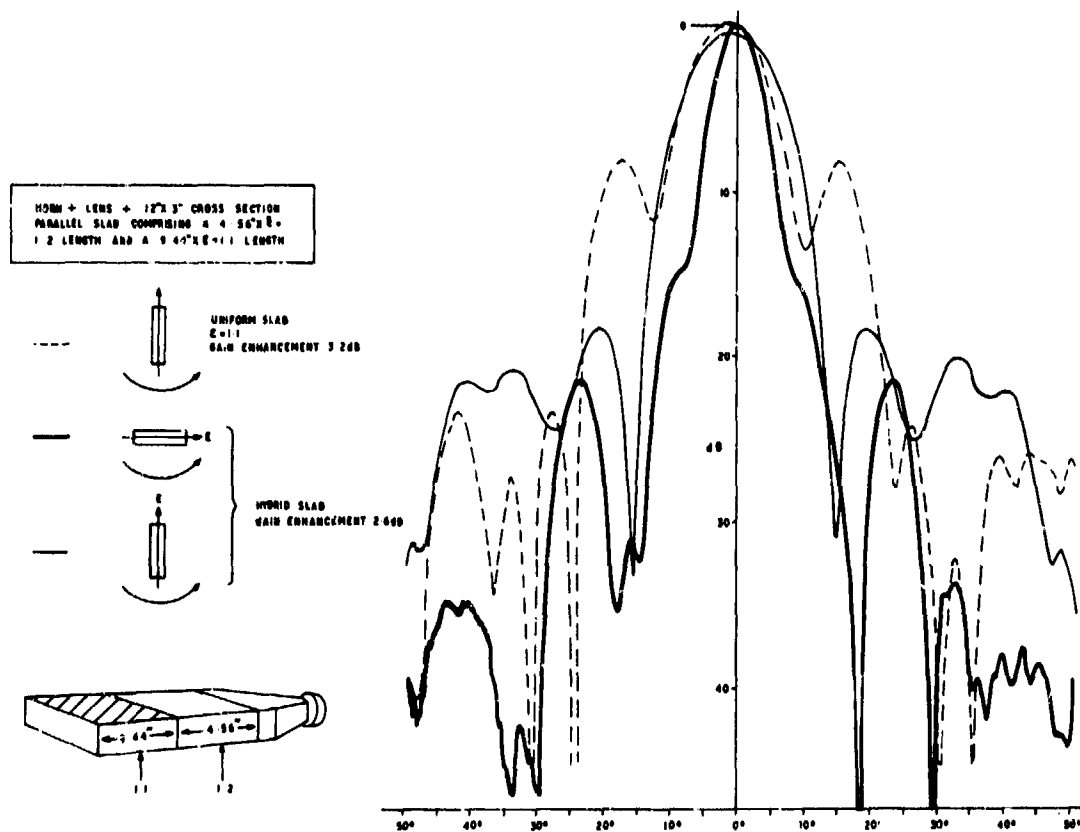


Figure 11. E AND H PLANE RADIATION PATTERNS OF A TWO COMPONENT HYBRID SLAB ($\epsilon = 1.2$ and 1.1)

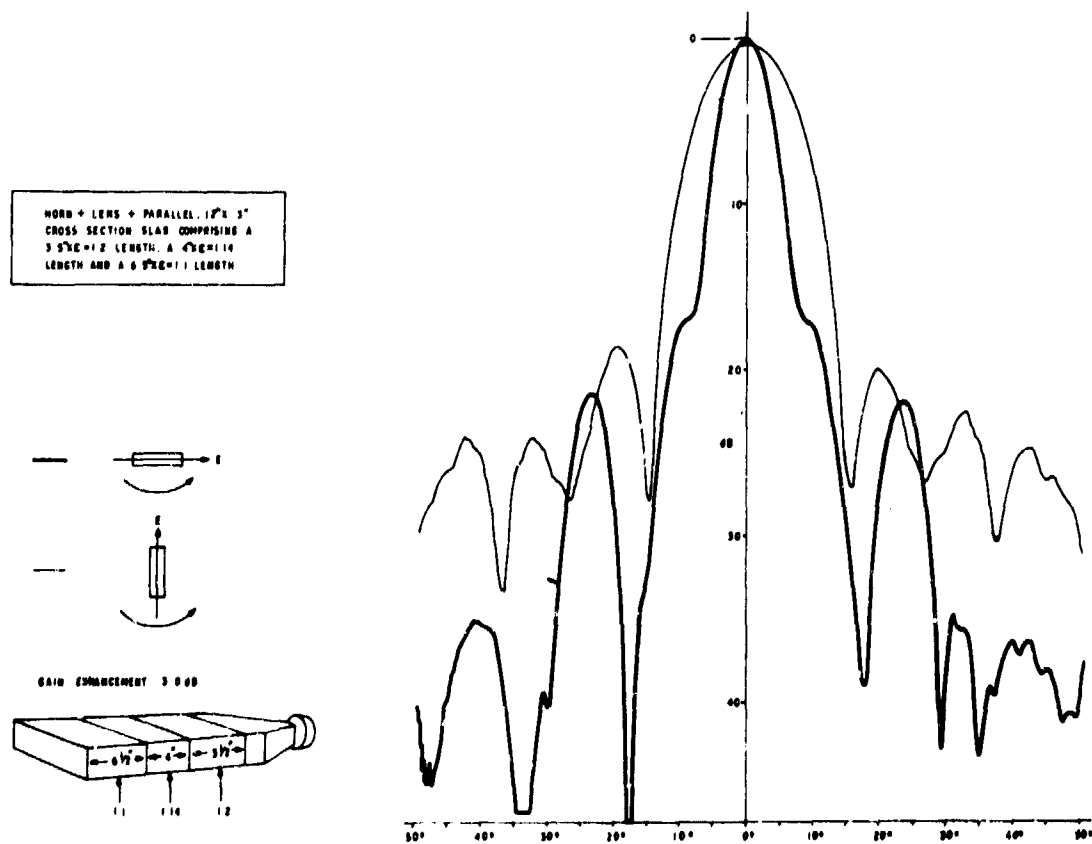


Figure 12. E AND H PLANE RADIATION PATTERNS OF A THREE COMPONENT HYBRID SLAB ($\epsilon = 1.2, 1.14$ and 1.1)

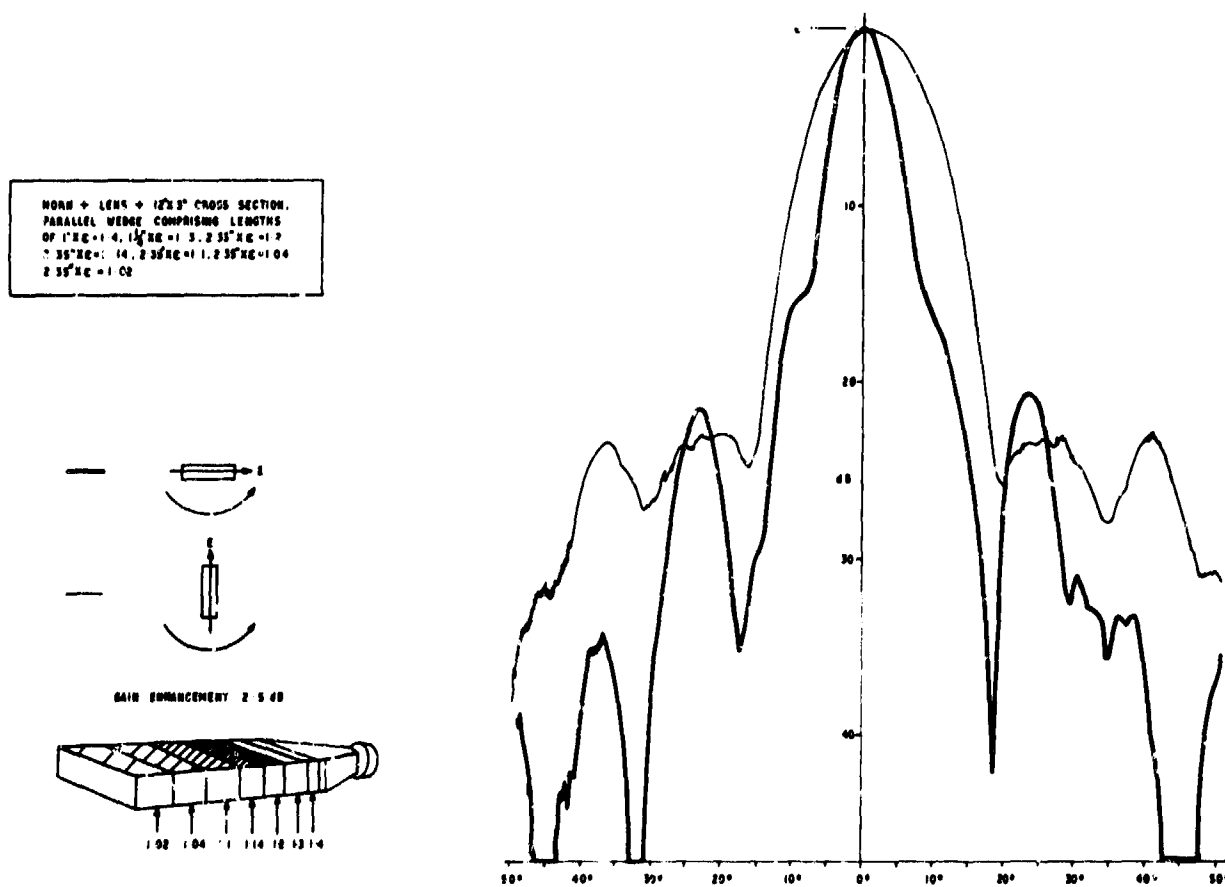


Figure 13. E AND H PLANE RADIATION PATTERNS OF A SEVEN COMPONENT
HYBRID SLAB (1.4, 1.3, 1.2, 1.14, 1.1, 1.04, and 1.02)

DISCUSSION

T.W. BAZIRE: Did the measured increase in gain correlate with the measured reduction in beam widths (i.e. were there dielectric losses?).

A.M. SMITH: The correlation was good which indicated that the losses were negligible.

S. CORNBLETT: Does not the reduction in dielectric constant agree with that of the normal tapering of polyrods?

A.M. SMITH: The principle behind the normal tapering of polyrods is to achieve good launching efficiency while maintaining a high gain radiating aperture which are opposing requirements solved by tapering the diameter of the rod so that it does not radiate along its length. We chose our high dielectric constant launch section and low dielectric constant termination section to achieve the same effects and also the lengths of the individual sections were chosen so that construction interference occurred at the termination aperture between the wave inside the rod and the free space radiated from the launch aperture. This latter condition also affects the gain in the type of polyrod we considered (dimensions $> \lambda$).

We have made hybrid rods with sections having identical effective refraction indices both by varying dielectric constants and stepping the cross sectional size. The latter gave completely different radiation patterns to the former.

We do not know the explanation for this phenomenon. It could be that the internal radiating aperture at the termination end of the rod is a different function of the dimensions and dielectric constant than the effective refraction index. If so, making the latter equal in the two cases would not ensure equal gain from the aperture.

LINEAR PHASED ARRAY FOR YAW STABILISATION

by

D S Hicks

Royal Radar Establishment, Malvern, England

SUMMARY

The theoretical performance of a linear digital phased array with both equal and unequal inter-element spacing has been investigated with the aid of a computer program written in ALGOL 68R. Three aeriels have been studied. The first is a conventional linear phased array in which each element consists of a waveguide horn. The elements are placed side by side to form a "fully filled" aperture. The other two arrays consist of identical waveguide horn elements but the spacing is not equal. Two arbitrarily chosen spacing laws were studied each of which had an exponential form.

The loss in gain due to phase quantization has been calculated and the effects of the unequal inter-element spacing law on gain and beamwidth is estimated. The beam pointing error, the beam granularity and the magnitude of the peak sidelobes are presented here for the three arrays. It is shown that some reduction in the number of elements required to fabricate an array may be achieved if the inter-element spacing is not made equal, and also the magnitude of the grating lobes may be significantly reduced if the spacing law is chosen correctly. Lastly a simple means by which a static split system may be achieved is discussed and some simulation program results presented.

1 INTRODUCTION

In the small volumes available for the installation of equipment in a modern high speed aircraft it may be difficult or even impossible to achieve a fully motion-compensated aerial by mechanical techniques. One method by which a fully stabilised aerial may be achieved is to utilise a linear digital phased array scanning in the horizontal plane to give yaw stabilisation, whilst a mechanical system is used to stabilise the aerial in the other planes.

This paper will only consider the linear digital phased array required to obtain yaw stabilisation and the economies that can be made in phase shifters when certain operating limits are exploited. The two principal operating limits which can be exploited in this application are:-

- 1) The array is linear and scanning is required in only one plane
- 2) The scan angle is limited to small angles.

The cost and complexity of a digital phased array is determined by:

- a) The number of elements with active phase shifters in their feed systems
- b) The number of bits per phase shifter

The number of elements, and therefore the number of phase shifters, assuming each element requires at least one is determined by the array aperture, the signal frequency, and the maximum scan angle required before grating lobes are encountered. These factors are usually set by prior operating requirements. The number of elements (determined by considering these factors) can be reduced by a small percentage if the far field radiation pattern of the elements is taken into account and used to reduce grating lobes that occur at large angles from the broadside position. Reduction beyond this number of elements is impossible if the inter-element spacing is made equal. A method by which further reductions can be achieved is to destroy, fully or partially, the periodicity of the far field radiation pattern by spacing the elements unequal distances apart.

Ultimately the performance of a digital phased array depends on the number of 'bits' per phase shifter available for beam steering. The number of bits is constrained at the lower end by the beam pointing errors and the phase quantization sidelobes that can be tolerated, and at the higher end by the insertion losses and the limitations of present technology. The present practical constraints in the number of bits per phase shifter is between one and four.

2 THE ARRAY

The general diagram of the array is shown in FIG 2.1. The non dispersive feed system can take the form of an optical, a reactive corporate or a matched corporate type of feed. This is required to minimise beam squinting over a 2% bandwidth.

The array is to be approximately 3.5 ft (1.07M) long and the maximum scan required is $\pm 10^\circ$ about the broadside position with a maximum one-way sidelobe level of -15 dB over this range. The maximum beam pointing error is to be less than 0.2° over the scan range. Estimations based on Millers¹ results indicate that three or four bits (8 or 16 phase steps) would be adequate to meet the initial specifications.

3 AN ARRAY WITH EQUAL INTER-ELEMENT SPACING

If the inter-element spacing is equal, and no amplitude taper is applied across the array aperture, then the maximum inter-element spacing before grating lobes appear in real space is given by:-

$$d = \frac{\lambda}{1 + |\sin \psi_m|} \quad \dots\dots\dots 3.1$$

where,

$$\begin{aligned}\lambda &= \text{signal wavelength} \\ \psi_m &= \text{maximum scan angle}\end{aligned}$$

If the radiating elements are anisotropic and their far field radiation pattern is taken into account some degree of grating lobe suppression can be obtained, permitting d to be increased. The minimum number of isotropic elements required to fabricate an array 3.5 ft long at 10 GHz and avoid grating lobes when the beam is scanned $\pm 10^\circ$, is 42. If the elements are, say, waveguide horns the number of elements can be reduced to approximately 36, (assuming the aperture is filled) because the far field element radiation pattern will suppress the grating lobe that appears $\mp 59^\circ$.

The initial simulation program results obtained from the proposed 36 element linear array confirms that the grating lobes will be suppressed by the element radiation pattern. The element pattern is a reasonable approximation to the radiation from a small waveguide horn in an infinite array environment (FIG 3.1). The effect of varying the number of bits per phase shifter on sidelobe performance and beam pointing error is reported in section 5.

4 AN ARRAY WITH EXPONENTIAL INTER-ELEMENT SPACING

The angular periodicity of the far field radiation pattern can be destroyed if the elements are not placed at equal increments along the aperture. If the periodicity is destroyed in this way the number of elements can be reduced as grating lobes will no longer be a problem. Spacing the elements in unequal increments along the aperture will result however in an array with an aperture which is not fully filled. As the array becomes less filled ie thinned, the mean side lobe level will increase and therefore the amount by which the number of elements may be reduced is limited.

Calculations were done on arrays with an inter-element spacing law of the form:-

$$d_{(n,n+1)} = A + B \exp(\alpha n), (n = 1, 2, 3 - \text{etc}) \dots\dots\dots 4.1$$

where

$$\begin{aligned}n &= \text{number of elements from the array centre (+ re integer)} \\ A, B \text{ and } \alpha &= \text{constants} \\ d_{(n,n+1)} &= \text{spacing between the } n\text{th and } (n+1)\text{th element}\end{aligned}$$

This type of law was chosen because there are indications in the current literature² that an attenuated flat grating plateau would result. No theoretical analysis has been done to choose values that would optimise the array performance and therefore the choice of values is empirical. Ten different inter-element spacing laws, all of the form given by equation 4.1 were considered initially (Table 4.1). These values were chosen because they resulted in an array approximately 3.5 ft long with between 26 and 32 elements. Computer simulation runs were done and two distributions were chosen for further investigation because of their superior sidelobe performance. The two arrays chosen for further study are:

- 1) 30 element array with inter-element spacing defined by

$$d_{(n,n+1)} = 0.05 + 0.05 \exp(0.05n) \text{ ft} \dots\dots\dots 4.2$$

- 2) 28 element array with inter-element spacing defined by

$$d_{(n,n+1)} = 0.05 + 0.02 \exp(0.15n) \text{ ft} \dots\dots\dots 4.3$$

The simulation program results obtained from considering these arrays is reported in section 5. The radiating elements are identical to those considered in section 3 and the assumed far field radiation pattern is shown in FIG 3.1.

5 SIMULATION PROGRAM RESULTS

5.1 VARIATION OF BEAM WIDTH WITH SCAN ANGLE

The theory of scanned arrays predicts that the beamwidth will increase as the beam is scanned such that,

$$\theta_s = \theta_0 \sec \psi \dots\dots\dots 5.1.1$$

where

$$\begin{aligned}\psi &= \text{scan angle} \\ \theta_0 &= \text{Beamwidth in the broadside position} \\ \theta_s &= \text{Beamwidth at the scan angle } \psi\end{aligned}$$

The increase in beamwidth with scan angle expressed in equation 5.1.1 has been proved for equally spaced arrays by several workers^{3,4}. Results determined in this study have proved that equation 5.1.1 also applies to arrays with unequal inter-element spacing. The graphs of beamwidth against scan angle are shown in FIG 5.1.1 for the 36 element array defined in section 3 and in FIGS 5.1.2 and 5.1.3 for the unequally spaced arrays defined in section 4. Very good agreement with equation 5.1.1 was obtained in all cases. However, as the scan angle was increased above 30° the assumed element far field radiation pattern displaced the actual beam centre and equation 5.1.1 became inaccurate for larger scan angles than 30° .

5.2 LOSS OF GAIN DUE TO PHASE QUANTIZATION

The loss of gain due to phase quantization up to a scan angle of 10° was calculated for each of the three arrays. The calculations were done for three and four bit phase shifters in the case of the 36 element array and for four 'bit' phase shifters in the case of the arrays with the unequal inter-element spacing laws (FIG 5.2.1, 5.2.2, 5.2.3 and 5.2.4). The loss in gain varies in all cases in a random way as the scan angle is changed. However, the results agree essentially with those obtained by Summers³ for a particular array with equal inter-element spacing, in that the losses are all of the order predicted by Miller¹.

5.3 BEAM POINTING ERROR

The beam pointing accuracy is essentially a function of the number of 'bits' available to steer the beam. Closely linked with beam pointing accuracy is beam granularity. Granularity is defined as the smallest realisable increment between adjacent beam positions and is caused by the finite number of phase steps available to scan the beam. Naturally the beam granularity decreases as the number of bits is increased.

The beam pointing accuracy of the array is presented in tables 5.3.1, 5.3.2, 5.3.3 and 5.3.4. Tables 5.3.3 and 5.3.4 have included in them calculations on identical array which have equal inter-element spacing for comparison. The errors in all four cases are essentially random with both positive and negative errors occurring with approximately equal frequency. The peak errors are generally greater than those obtained by Summers³, who used an optical feed to destroy the periodicity of the phase errors that occur with digital phase shifters. However the results show Miller's¹ statistical estimation to be pessimistic by approximately a factor of 1.3. It is of interest to note that the results obtained with unequally spaced arrays are slightly inferior to those obtained with equally spaced arrays. It was determined that no mechanism inherent in the characteristics of space tapered arrays caused this effect, but rather the angle of scan chosen for these measurements were unfortunate. Other scan angles gave lower magnitudes of error and we therefore conclude that the RMS beam pointing error is a function of the number of 'bits' per phase shifter and not a function of the element spacing law.

5.4 BEAM GRANULARITY

The beam granularity was estimated by scanning the main beam in 0.075° steps. The array is steered from the centre. The feed system is cophasal and it is expected that the granularity will be largest near the broadside position because the end phase shifters cannot reset until the demanded scan angle is large enough. The results of the beam granularity measurements done on the four arrays are shown in tables 5.4.1 and 5.4.2. The granularity of the equally spaced 4 'bit' array is largest close to the broadside position being approximately 0.1° , but then decreases to approximately 0.075° for demanded scan angles greater than 0.5° . The unequally spaced element arrays appear slightly less granular about the broadside position but the average is similar to that of the equally spaced array.

5.5 EFFECTS OF SPACE TAPER ON GAIN AND BEAMWIDTH

As no phase randomizing feeds are used the beam in the broadside position will be identical to that of a non-scanning array. It is therefore possible to investigate the effects of space tapering without scanning effects interfering with the measurement.

As expected the gain of the arrays with the exponential spacing law was unaffected by changes in the spacing law. The unequal spacing law did, however give rise to a change in the 3 dB beamwidth of when compared with that of an array of equal length and a similar number of elements but with equal inter-element spacing. To investigate the effect on beamwidth of varying the exponential term in equation 4.1 the aerial aperture was allowed to vary. The constants A and B were kept at constant values while α was allowed to vary with both positive and negative values. A graph of α against the difference in beamwidth of a similar equal spaced array is plotted in FIG 5.5.1. The graph is essentially linear for small values of $|\alpha|$, but the change in beamwidth is not so great for large values of $|\alpha|$, and hence the graph tends to become non-linear. These non-linear portions of the graph may be explained thus. As α becomes more negative the exponential term becomes less significant and the inter-element spacing approaches A as α approaches minus infinity giving rise to no change in beamwidth. As α becomes very large the beamwidth approaches a Dirac delta function and the significance of the exponential law will decrease rapidly as α approaches infinity. The effect that causes a change in beamwidth when the elements of an array are spacially tapered has not been theoretically investigated. Such an investigation may however, prove necessary as this effect will have to be taken into account when designing aerials with an inter-element spacing law of this type.

5.6 SIDELobe PERFORMANCE

Results of the sidelobe performance calculations for the three arrays are presented here as histograms. (FIGS 5.6.1, 5.6.2 and 5.6.3). They have each been drawn in two sections; the total sidelobe performance when scanning to 10° , and the sidelobe performance when scanning to 5.5° . This has been done to separate those sidelobes that are due to grating lobes when the scan angle nears 10° from the sidelobes due to the array factor and phase quantization which would not normally contain contributions from grating lobes, ie when the scan angle is small.

The 36 element array when scanned to $\pm 10^\circ$ does not, as predicted, contain contributions from grating lobes, however there are large sidelobes occurring very close to main beam (FIG 5.6.4). These sidelobes are due to the periodic nature of the array equation and in the absence of the assumed element far field radiation pattern would decrease according to a $\sin x/x$ law. These sidelobes can be decreased in the normal way by introducing an amplitude taper across the array aperture, although a corresponding reduction in the gain of the array is inevitable. The results presented here are for arrays utilising four bit phase shifters. The results obtained from the 36 element array using three bit phase shifters have not been included. They do, however, indicate that unless some form of phase randomizing feed is used the peak sidelobes due to phase quantization when three bit phase shifters are used will be approximately

-13 dB as compared with -19 dB in the case of four bit phase shifters. Reducing the number of elements increases the mean sidelobe level, which is also a function of the number of bits, thus it was decided that to obtain the desired sidelobe performance four bit phase shifters would have to be used.

The main reason for choosing spaced tapered arrays for further study is the likelihood of obtaining a better sidelobe performance for a given number of elements. Because the inter-element spacing is no longer equal the periodicity of the far field radiation pattern equation is lost either fully or partially. Therefore substantial reduction of grating lobes will result if the spacing is chosen correctly.

In FIG 5.6.2 it can be seen that a number of large sidelobes appear between the scan angles of 5.5° and 10° whilst from FIG 5.6.3 relatively few large sidelobes are caused by the increase in scan angle, therefore it appears that equation 4.3 results in an array with superior grating lobe suppression than equation 4.2. The effect of flattening the grating lobe can be further illustrated by referring to FIG 5.6.5 and 5.6.6 which are computer drawn representations of the far field radiation patterns of the arrays. For comparison the far field radiation pattern of identical arrays with equal inter-element spacing are included. (FIGS 5.6.7 and 5.6.8.)

It can be seen from FIGS 5.6.5, 5.6.6, 5.6.7 and 5.6.8 that the effect of unequal spacing is to spread the grating lobe over a greater angle whilst reducing its magnitude and widening the main beam.

6 SIMPLE STATIC SPLIT SYSTEM

In certain applications a static split type of aerial may be required. In non-scanning linear arrays a switching system is used to convert the array from a cophasally fed array to an array which has one half of its aperture fed in antiphase to the other, thus giving a static split array. When digital phase shifters are used to steer the beam the static split can be achieved without mechanical switching by simply adding (or subtracting) the most significant bit (180°) to either half of the array. Computer drawn far field radiation patterns of arrays whose left hand elements are fed 180° in advance of the right hand elements are shown in FIG 6.1a and 6.1b. These patterns are derived from arrays whose spacing laws are defined by equations 4.2 and 4.3. The actual choice of array depends on the application and thus exercise was done simply to demonstrate the ease in which such a far field characteristic can be achieved from any linear digital phased array.

CONCLUSIONS

The initial requirement of a $\pm 10^\circ$ scan range set the minimum number of isotropic elements required to fabricate a 3.5ft long array at 42. It has been shown that the relatively small scan angle and the elements far field radiation pattern allowed this number to be reduced to 36, whilst still avoiding large secondary (grating) lobes appearing in real space. Further reduction in the number of elements was achieved by considering arrays with unequal inter-element spacing. Calculations performed on the two unequally spaced arrays defined by equations 4.2 and 4.3 have shown that grating lobes may be reduced by 6 dB if this type of exponential spacing law is used. The 28 element array whose spacing law is defined by equation 4.3 gives a superior sidelobe performance to the 30 element array whose spacing law is defined by equation 4.2. The losses due to phase quantization, the beam pointing error, and the beam granularity have been found to be independent of the inter-element spacing law and are essentially a function of the number of bits per phase shifter.

However the sidelobe performance of the arrays may be improved in two ways.

- 1) The array is fed with an amplitude tapered signal
- 2) The array is fed via a phase randomizing network

The first of which is a long established method of tailoring radiation characteristics, the second method however will reduce the peak sidelobes due to the periodicity of the phase errors that occur with digital phase shifters. The randomizing network usually takes the form of an optical feed⁵, which also gives an excellent non-dispersive feed. The optical feed has been investigated thoroughly by other workers and the reader is referred to the references for detailed discussions.

The 3 dB beamwidth has been found to be a function of the spacing law and has been found to vary as the exponential constant, α , is varied for a given array aperture. This effect will have to be taken into account when designing an array of this type. A theoretical analysis of the effect cannot be found by the author in the literature and a detailed analysis would possibly be a useful exercise for future work.

Contributed by permission of the Director REE. Copyright Controller H.B.M.C.O.

REFERENCES

- 1 Miller C J, Minimizing the effects of Phase Quantization error, in an electronically scanned array. Proceedings of Symposium on Electronically Scanned Array Techniques and Applications. Technical Documentary Report No RADC-TDR-64-225, VOL 1, JULY 1964, PAGES 17-38.
- 2 Yen J L, Chow Y L, 'On Large Nonuniformly Spaced Arrays', Canadian Journal of Physics VOL 41, NO 1, JANUARY 1963.
- 3 Summers J E, Calculated Performance of a 25 Element Linear and a 2500 Element Planar Digital Phased Array, Unpublished MOD (PE) Work; November 1971.
- 4 Skolnik M I, Radar Handbook, McGraw Hill 1970, PAGES 11-41 - 11-42.
- 5 Sciambi A F, The effect of the Aperture Illumination on the Circular Aperture Antenna Pattern Characteristics, Microwave Journal, VOL 8, NO 8, AUGUST 1965.

TABLE 4.1 INITIAL ARRAYS PROPOSED FOR INVESTIGATION

NO ELEMENTS	A ft	B ft	α	LENGTH ft
34	0.055	0.020	+0.100	3.4966
34	0.075	0.075	-0.125	3.5241
30	0.075	0.003	+0.300	3.6986
30	0.000	0.100	+0.025	3.4946
30	0.050	0.050	+0.050	3.5786
30	0.040	0.100	-0.025	3.5931
28	0.050	0.020	+0.150	3.4966
28	0.100	0.050	-0.090	3.4823
26	0.040	0.050	+0.100	3.4881
26	0.100	0.070	-0.100	3.5002

TABLE 5.3.1 BEAM POINTING ERRORS OF 36 ELEMENT ARRAY 3 'BITS'

SCAN REGION DEG	RMS (BEAMWIDTHS)	PEAK (BEAMWIDTHS)	PEAK (MILLER) (BEAMWIDTHS)
0.0- 0.5	0.037	0.071	0.098
5.0- 5.5	0.034	0.064	0.098
9.5-10.0	0.035	0.065	0.098

TABLE 5.3.2 BEAM POINTING ERRORS OF 36 ELEMENT ARRAY 4 'BITS'

SCAN REGION DEG	RMS (BEAMWIDTHS)	PEAK (BEAMWIDTHS)	PEAK (MILLER) (BEAMWIDTHS)
0.0- 0.5	0.014	0.034	0.049
5.0- 5.5	0.013	0.028	0.049
9.5-10.0	0.011	0.018	0.049

TABLE 5.3.3 BEAM POINTING ERRORS OF ARRAY DEFINED BY EQUATION 4.1

SCAN REGION DEG	4 BIT. 30 ELEMENTS SPACE TAPERED ARRAY (EQUATION 4.1)		4 BIT. 30 ELEMENTS EQUAL INTER-ELEMENT SPACING	
	BEAM POINTING ERROR (BEAMWIDTHS)		BEAM POINTING ERROR (BEAMWIDTHS)	
	PEAK	RMS	PEAK	RMS
0.0- 0.5	0.038907	0.02092	0.036813	0.018816
5.0- 5.5	0.038867	0.02349	0.013856	0.006355
9.5-10.0	0.017516	0.00775	0.013295	0.011870

TABLE 5.3.4 BEAM POINTING ERRORS OF ARRAY DEFINED BY EQUATION 4.2

SCAN REGION DEG	4 BIT. 28 ELEMENT, SPACE TAPERED ARRAY (EQUATION 4.2)		4 BIT. 28 ELEMENTS EQUAL INTER-ELEMENT SPACING	
	BEAM POINTING ERROR (BEAMWIDTHS)		BEAM POINTING ERROR (BEAMWIDTHS)	
	PEAK	RMS	PEAK	RMS
0.0- 0.5	0.046025	0.021903	0.043783	0.0215789
5.0- 5.5	0.019334	0.011376	0.010129	0.005281
9.5-10.0	0.024313	0.01280	0.038306	0.018876

TABLE 5.4.1 GRANULARITY OF 36 ELEMENT ARRAY

NO OF PHASE BITS	LENGTH OF REGIONS WHERE THE MAIN BEAM REMAINED STATIONARY (DEGREES)			EXPECTED AVERAGE GRANULARITY
	0°-0.5° SCAN	5.0°-5.5° SCAN	9.5-10° SCAN	
3	0.2	0.2	0.2	0.15
4	0.1	0.075	0.075	0.07

TABLE 5.4.2 GRANULARITY OF ARRAY WITH UNEQUAL & INTER-ELEMENT SPACING (4 BITS)

SPACING LAW EQUATION	LENGTH OF REGION WHERE THE MAIN BEAM REMAINED STATIONERY (DEGREES)		
	0°-0.5° SCAN	5.0°-5.5° SCAN	9.5°-10° SCAN
4.2	0.075	0.075	0.075
4.3	0.075	0.075	0.075

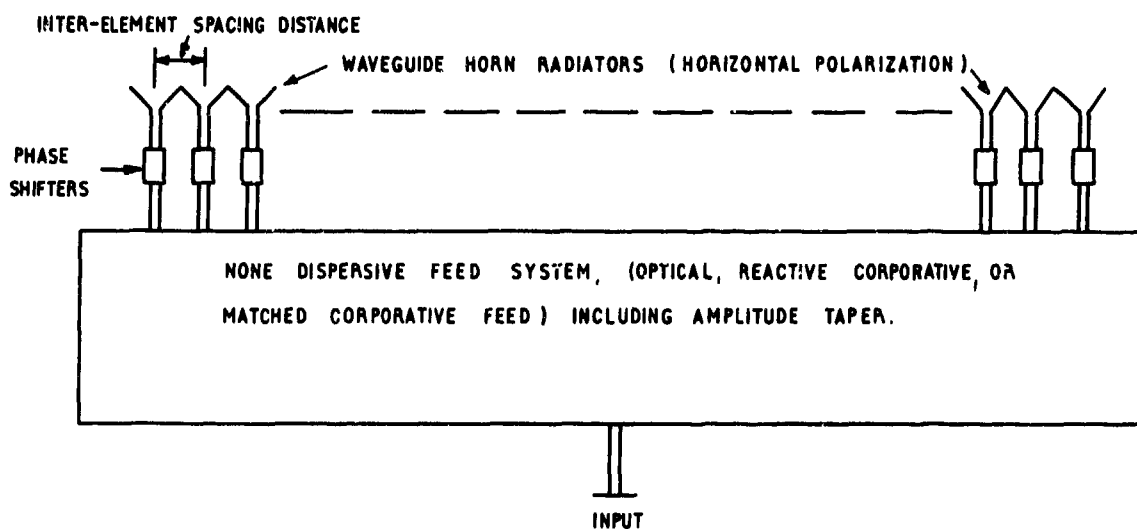


Fig.2.1 General diagram of the array

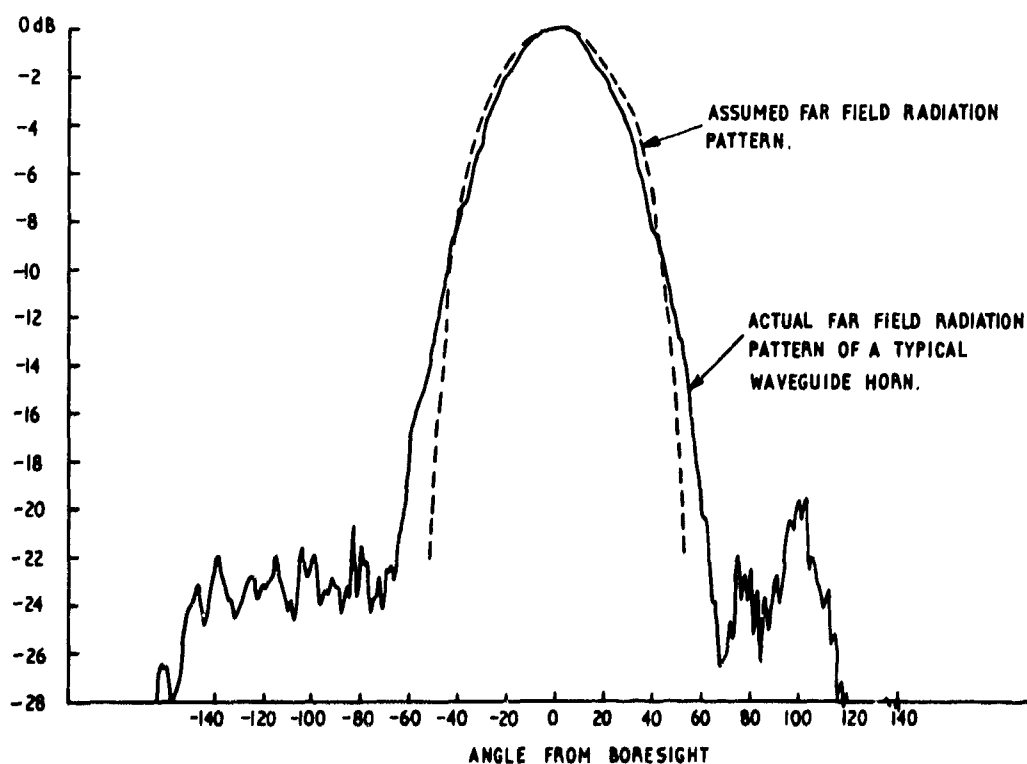


Fig.3.1 Actual and assumed element far field radiation pattern. (E plane)

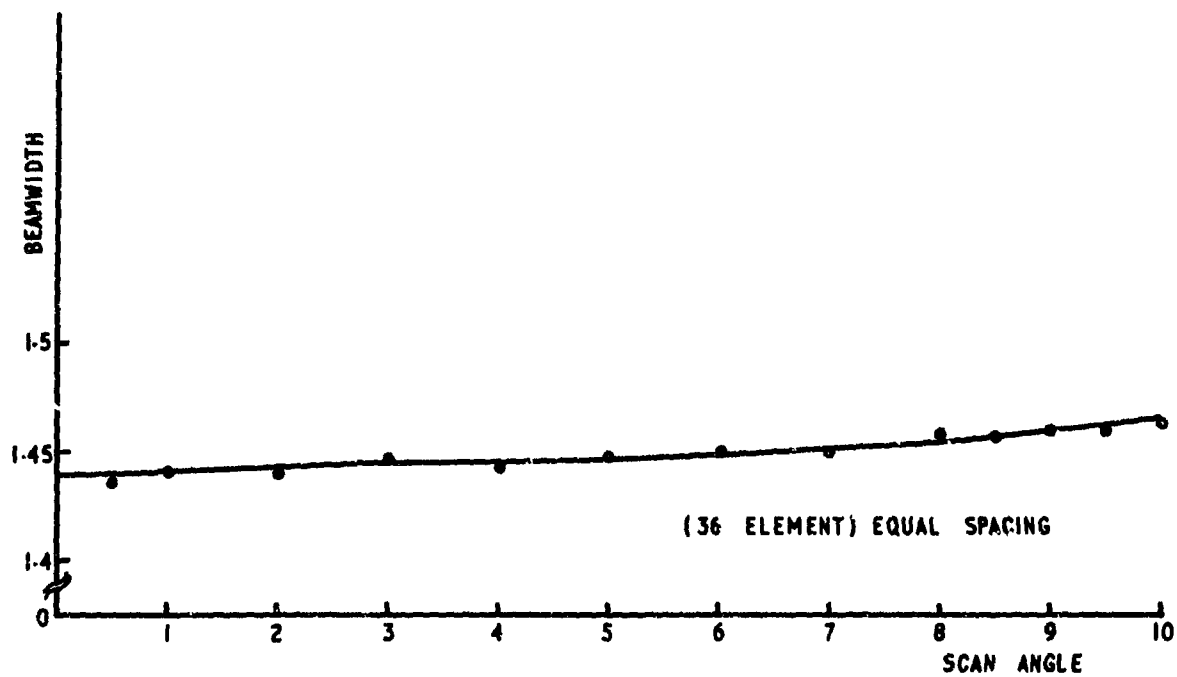


Fig.5.1.1 Scan angle against beamwidth

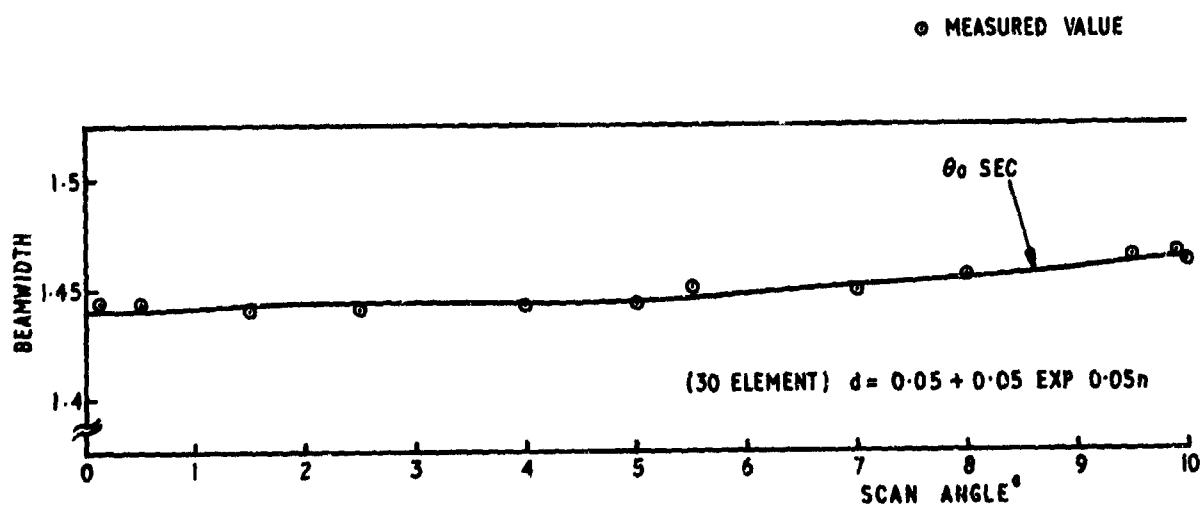


Fig.5.1.2 Scan angle against beamwidth

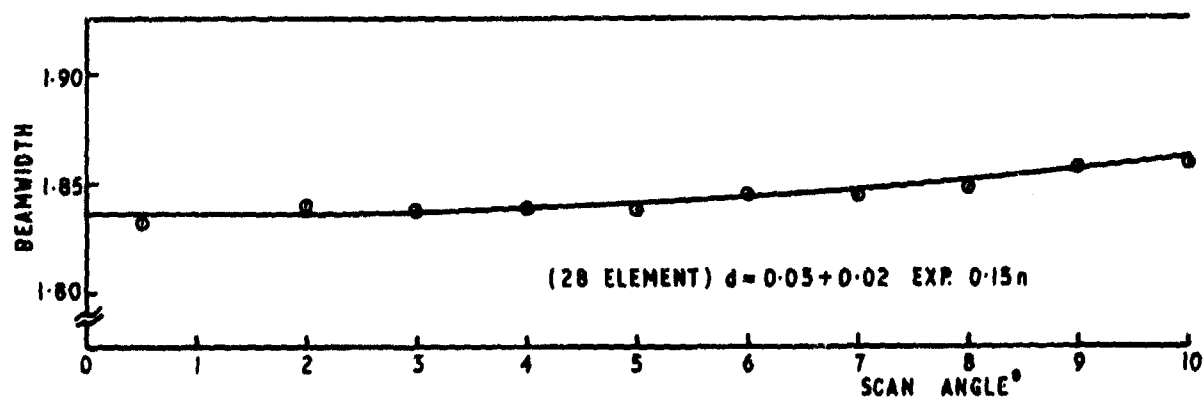


Fig.5.1.3 Scan angle against beamwidth

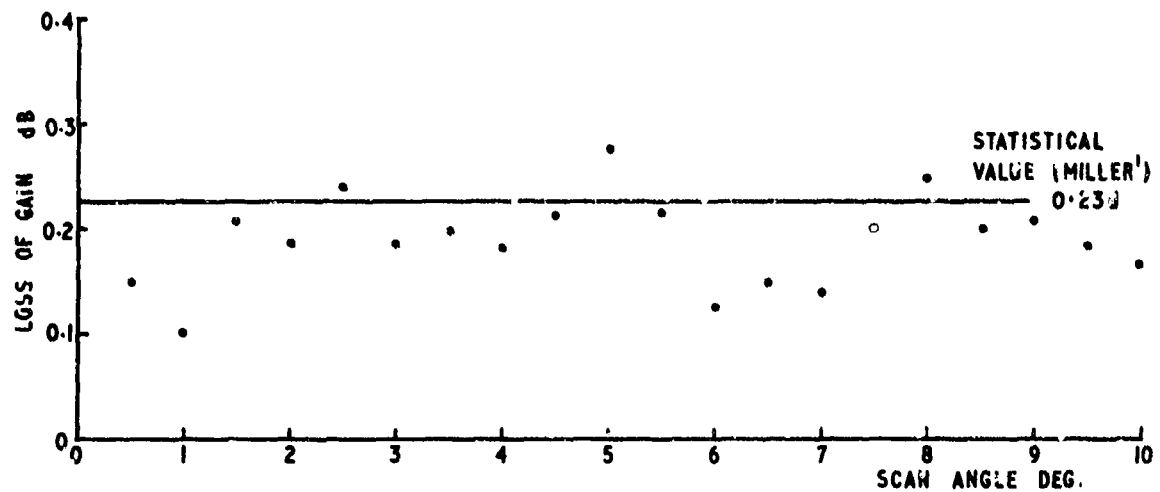


Fig. 5.2.1 Loss of gain due to phase quantization of the 36 element array (3 bits)

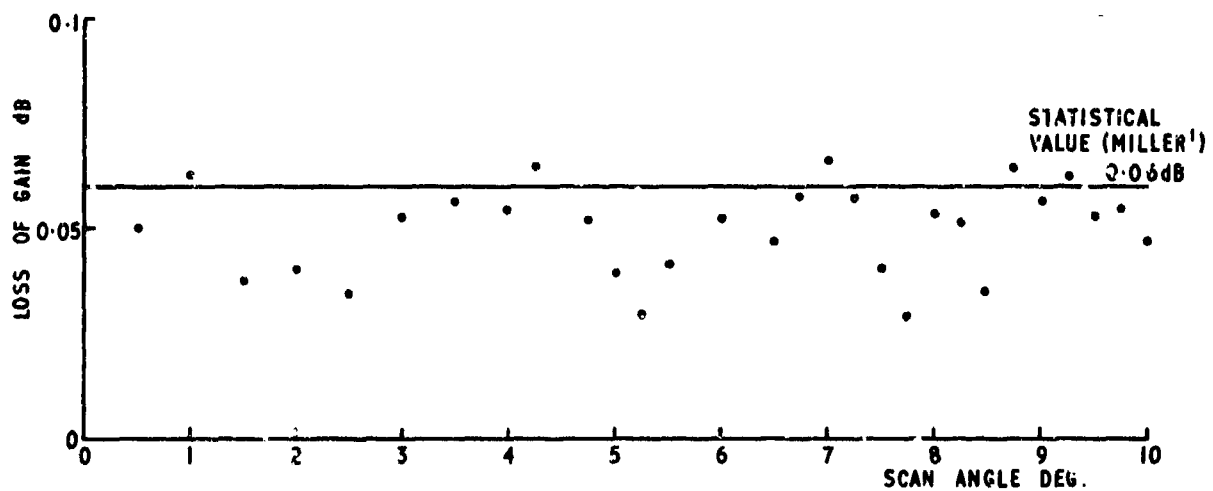


Fig. 5.2.2 Loss of gain due to phase quantization of the 36 element array (4 bits)

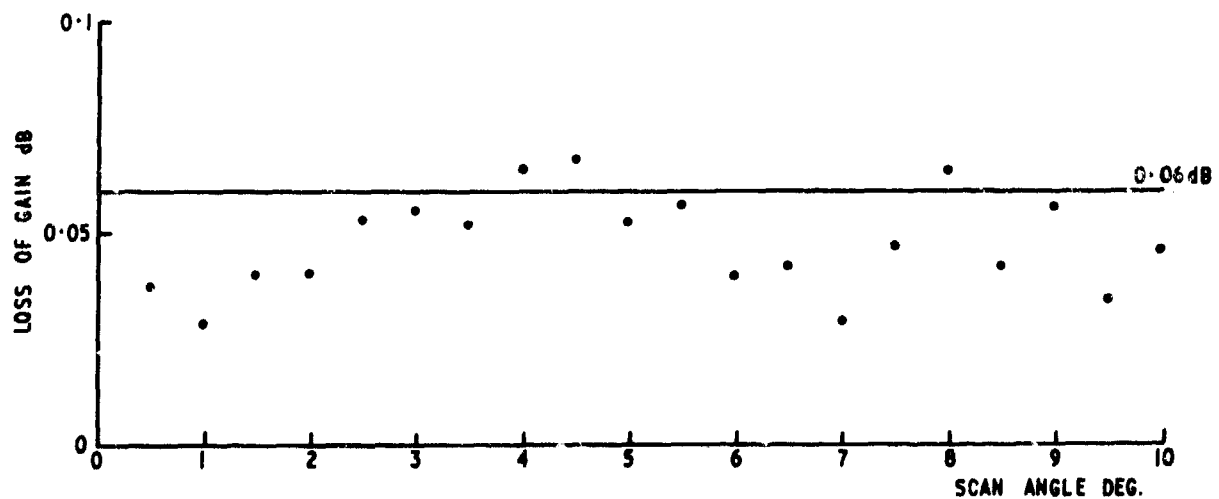


Fig. 5.2.3 Loss of gain due to phase quantization of the array defined by Equation 4.2

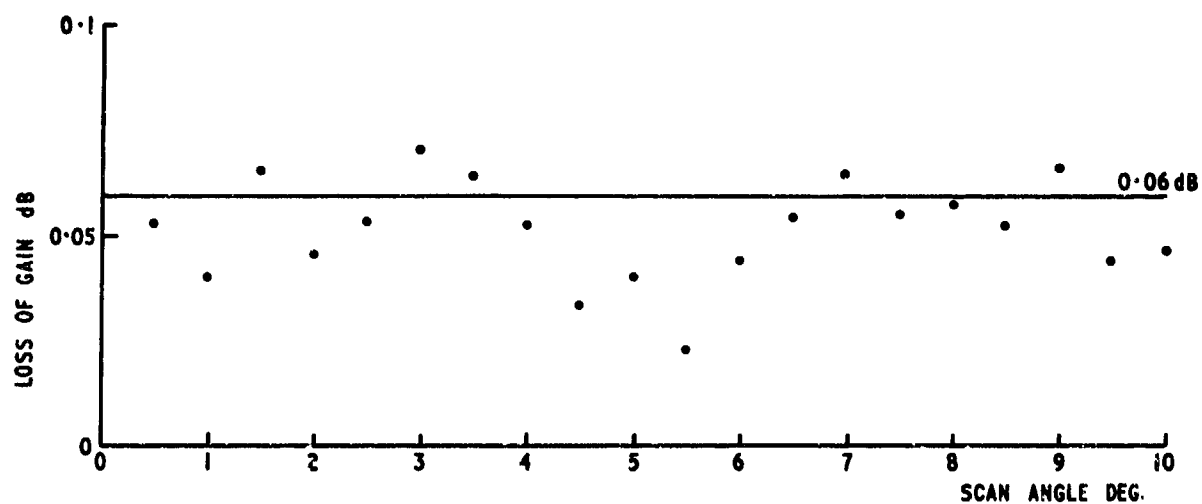


Fig.5.2.4 Loss of gain due to phase quantization of the array defined by Equation 4.3

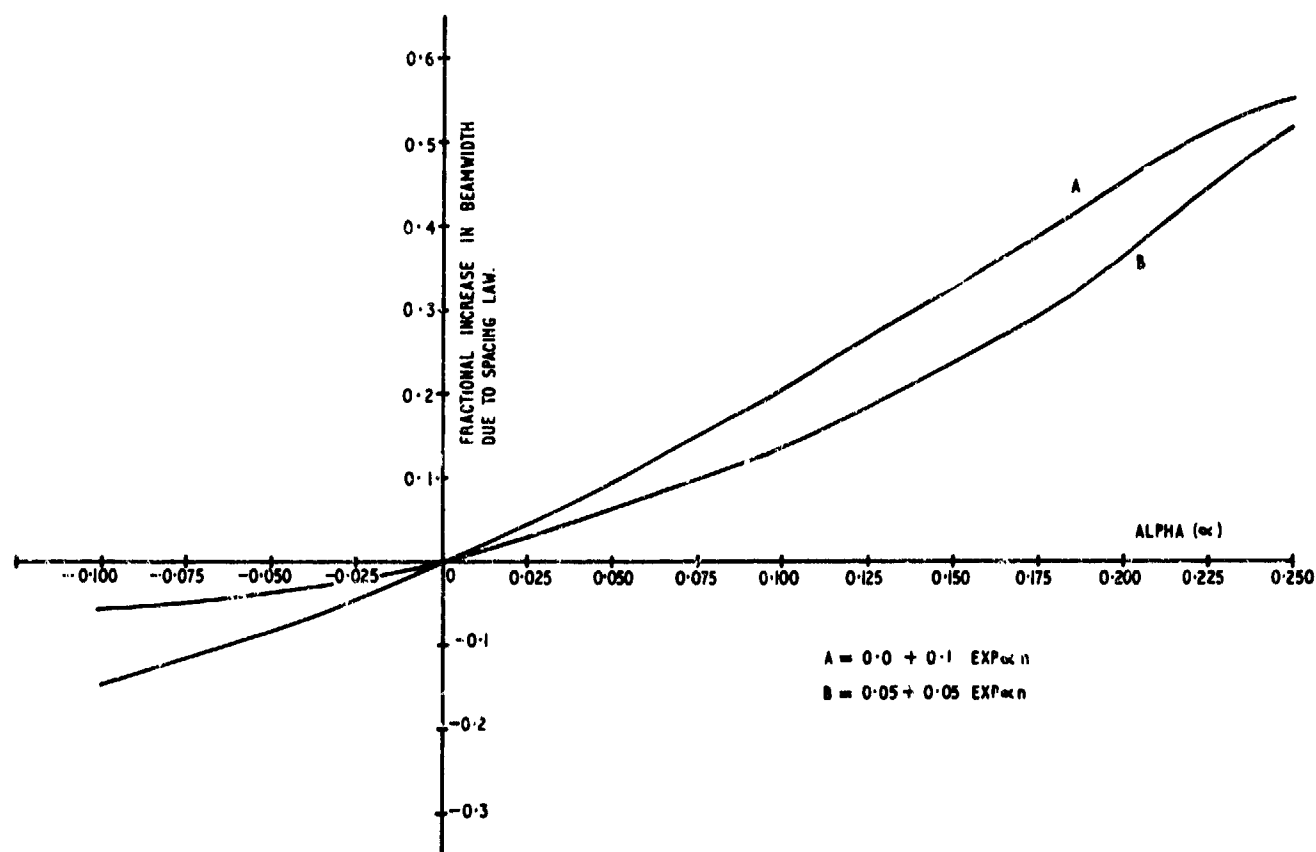


Fig.5.5.1 The increase in beam width against alpha (aperture not fixed)

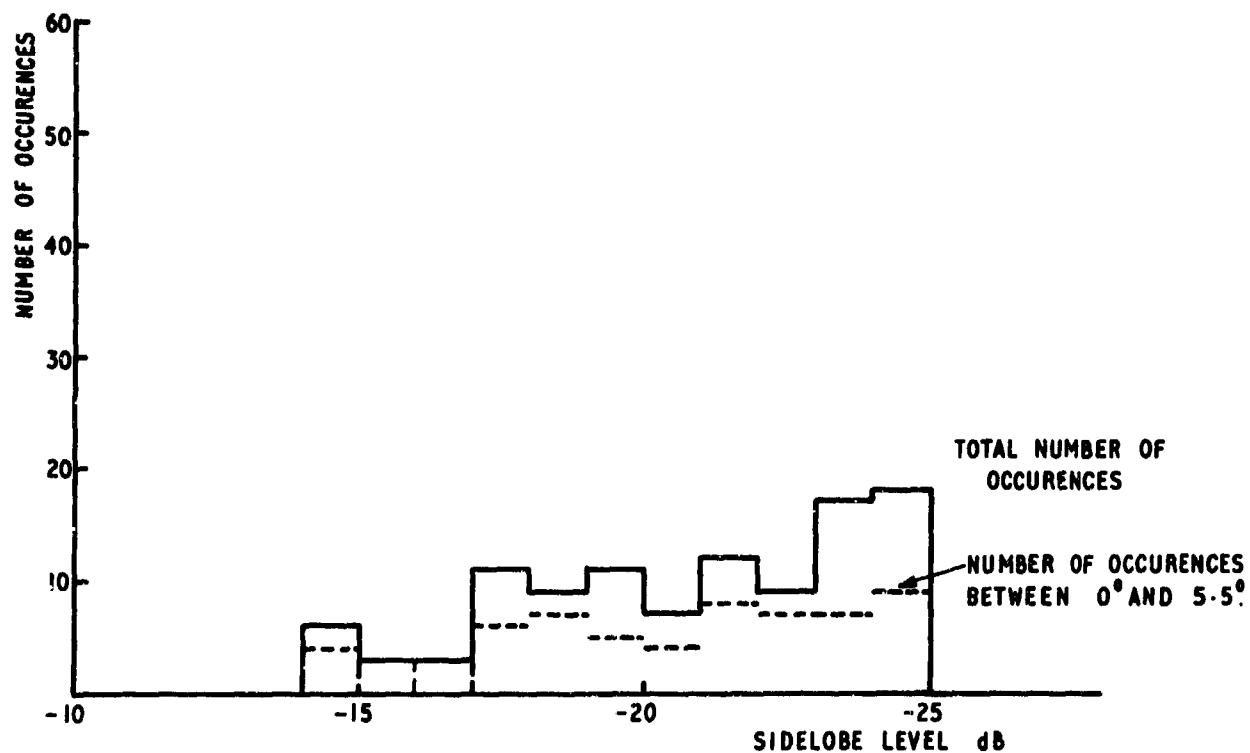


Fig.5.6.1 Side lobe histogram; 36 elements, equal inter-element spacing

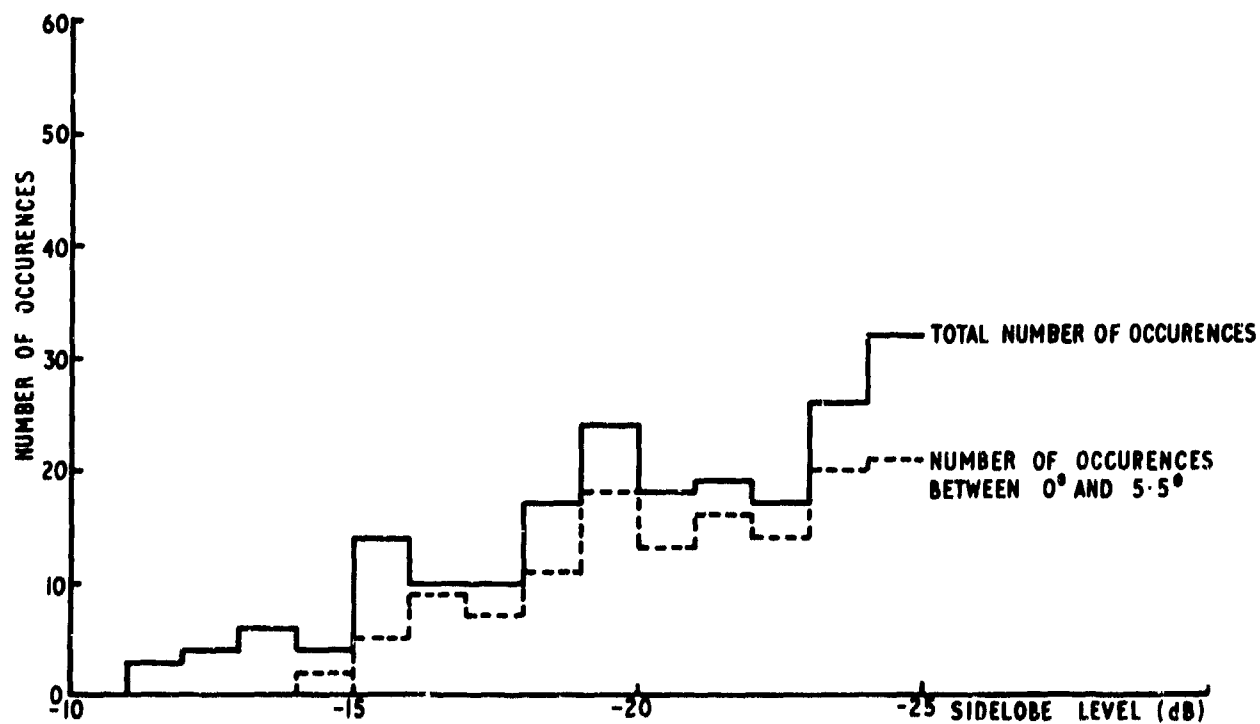


Fig.5.6.2 Side lobe histogram; 30 elements, spacing defined by Equation 4.2

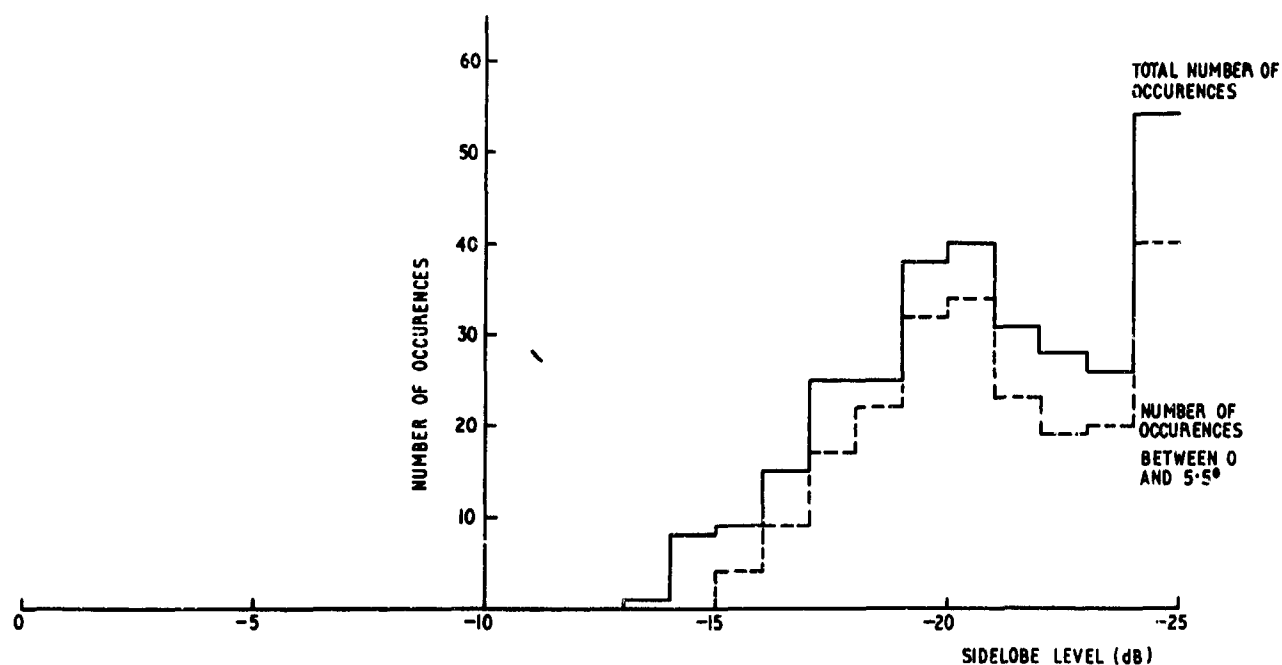


Fig.5.6.3 Side lobe histogram; 28 elements, spacing defined by Equation 4.3

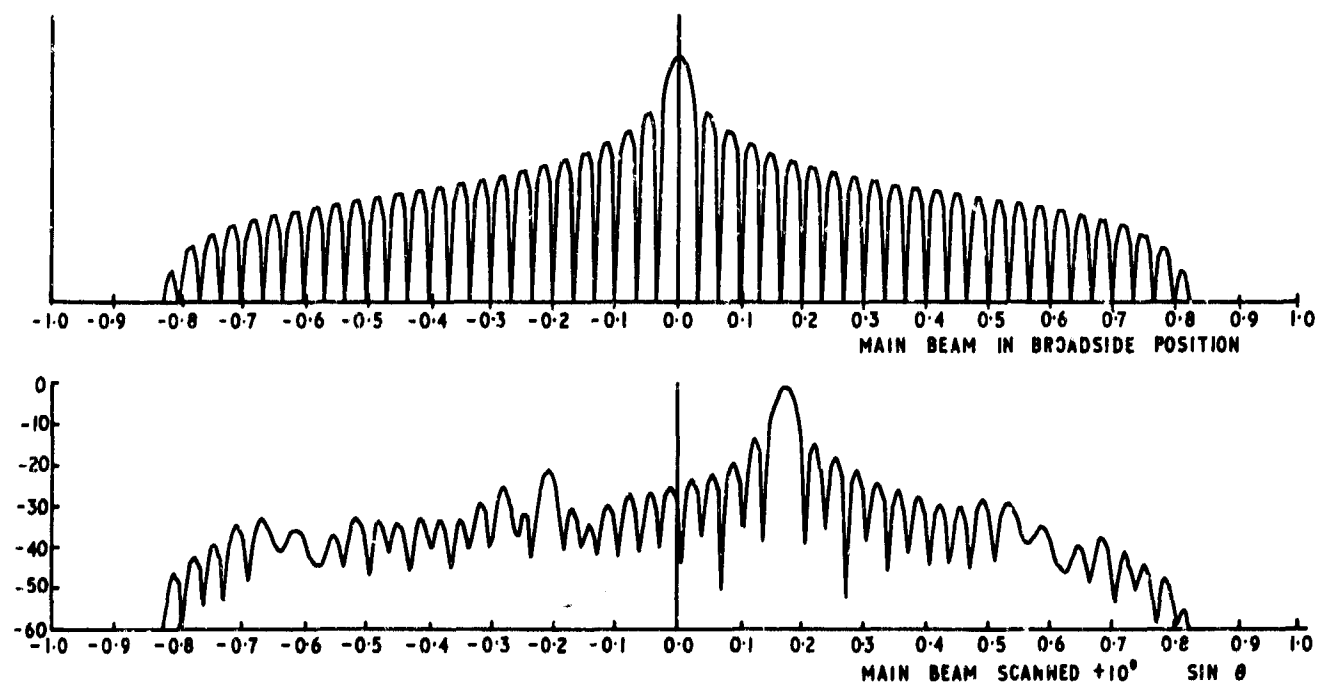


Fig.5.6.4 Far field radiation pattern of a 36 element array with equal inter-element spacing

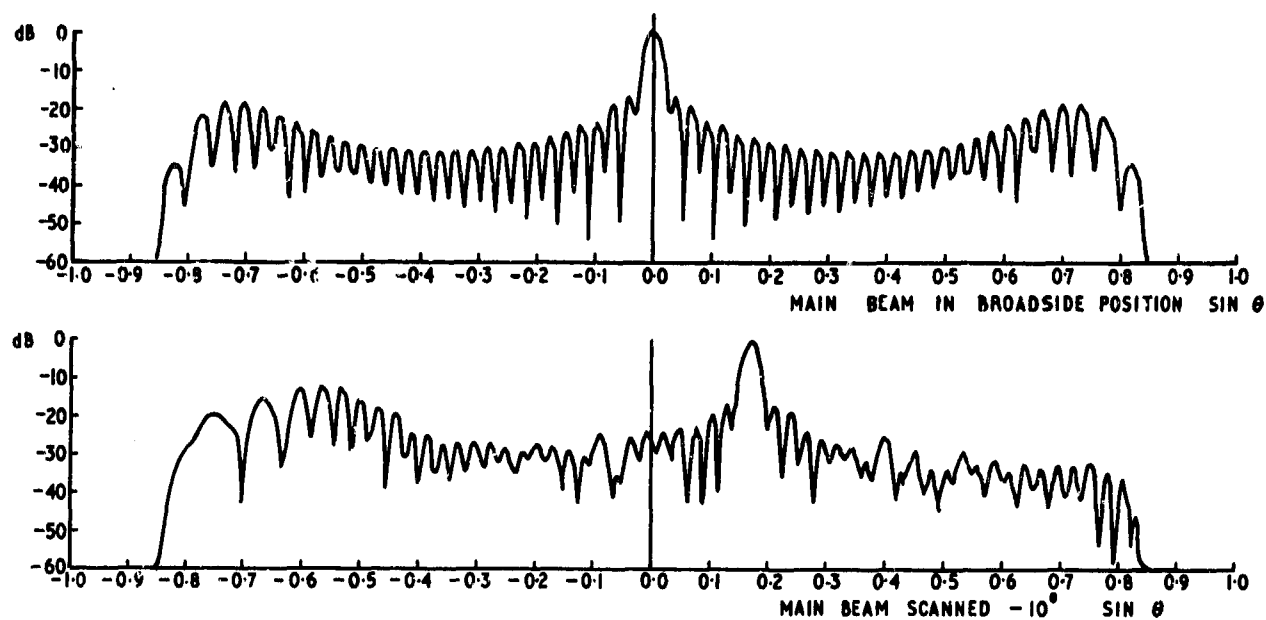


Fig.5.6.5 Far field radiation pattern of a 30 element array with spacing law defined by Equation 4.2

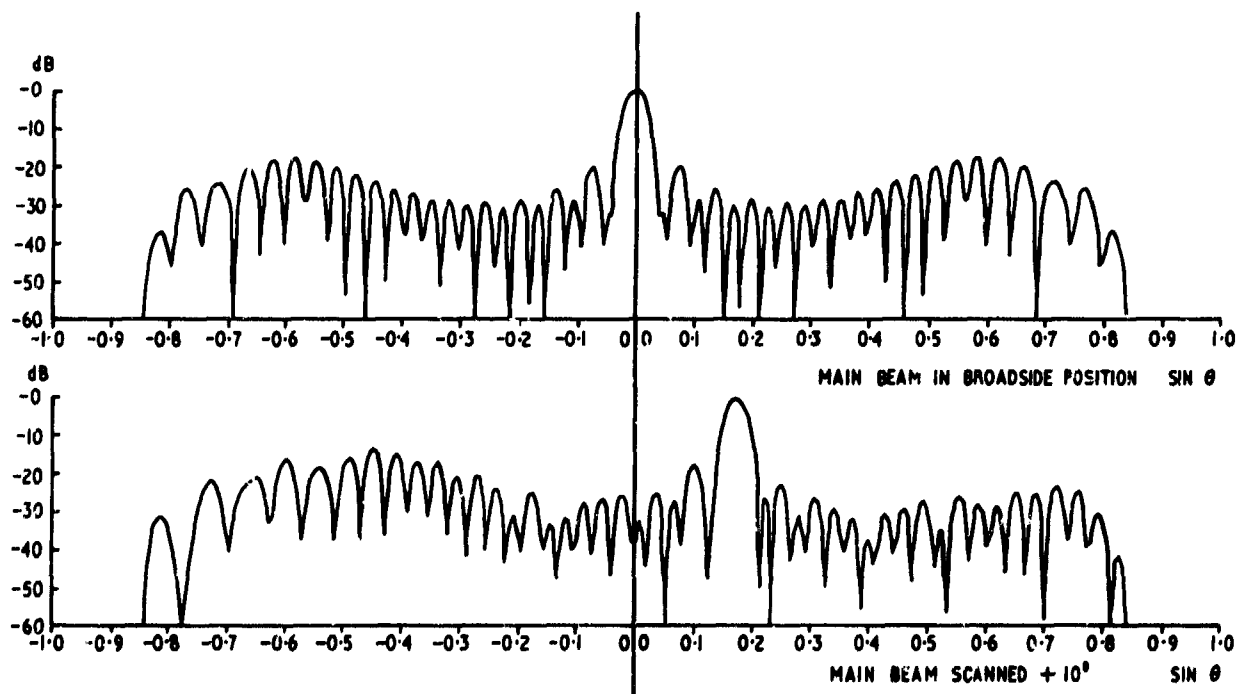


Fig.5.6.6 Far field radiation pattern of a 28 element array with spacing law defined by Equation 4.3

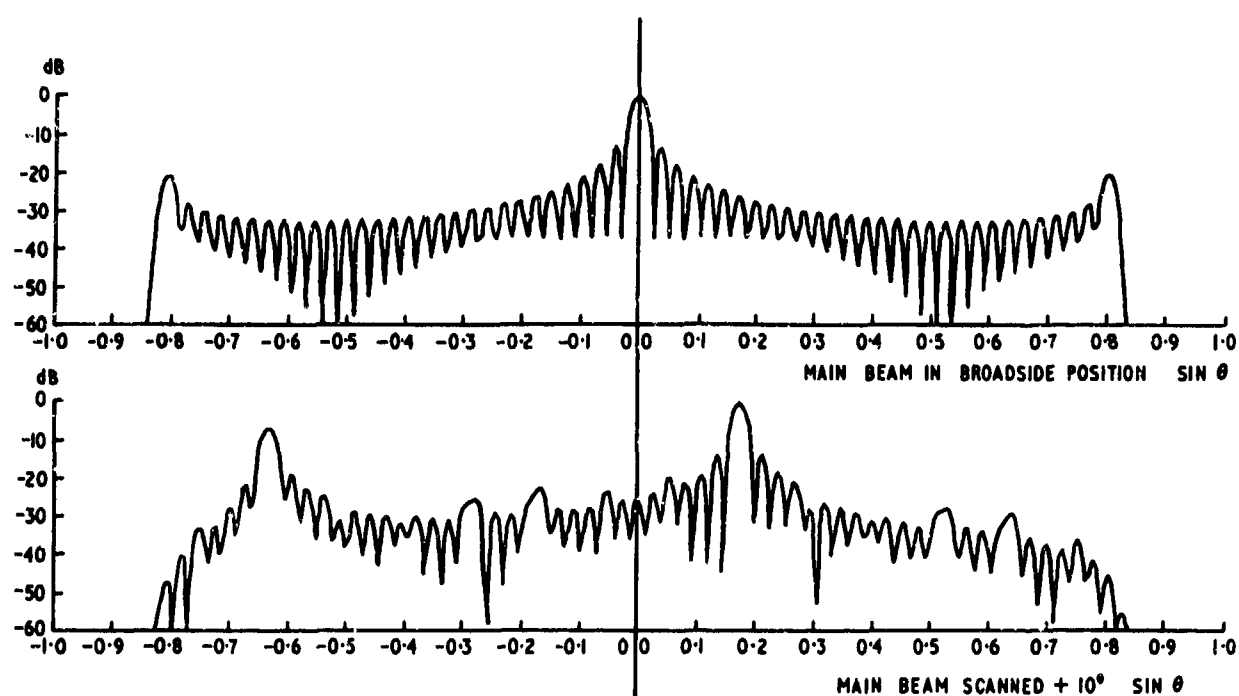


Fig.5.6.7 Far field radiation pattern of a 30 element array with equal inter-element spacing, and of identical length to the array defined by Equation 4.2

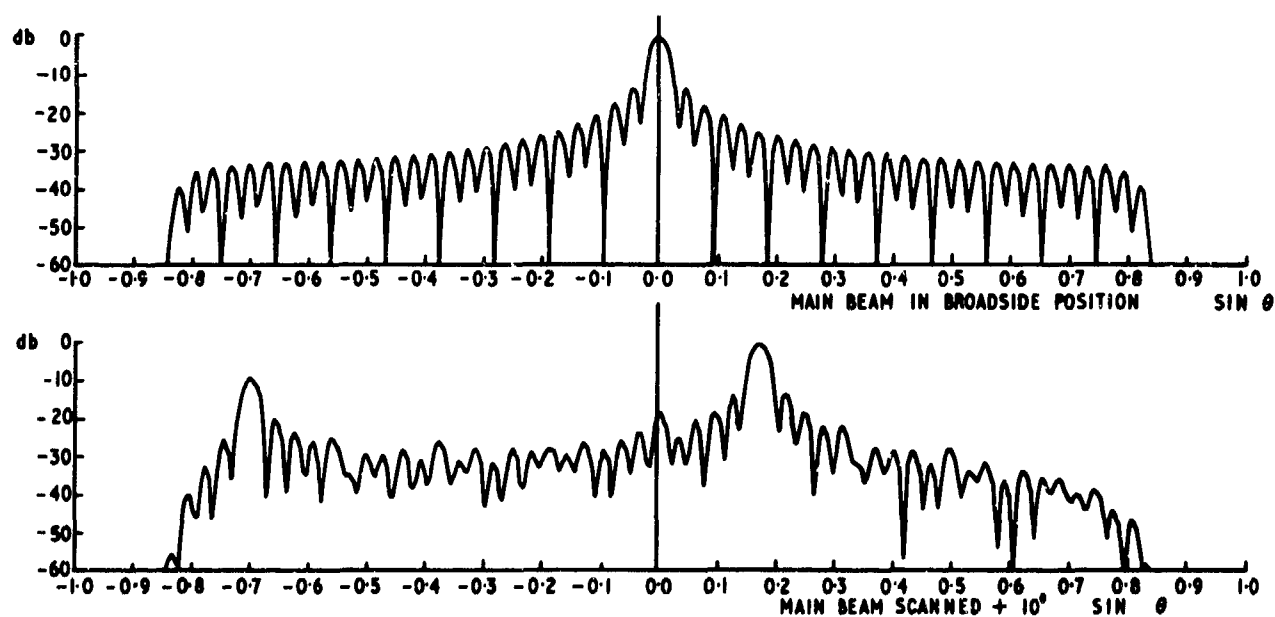


Fig.5.6.8 Far field radiation pattern of a 28 element array with equal inter-element spacing and of identical length to the array defined by Equation 4.3

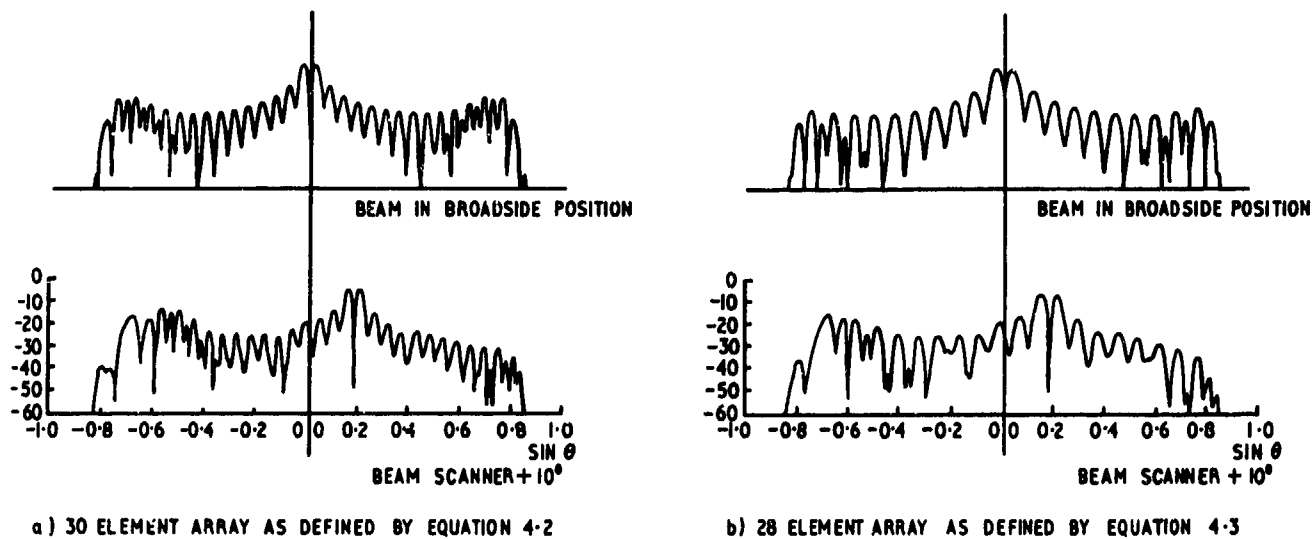


Fig.6.1 Static split far field radiation pattern

AEW RADAR ANTENNAS

by

Tomos Llewelyn ap Rhys
 Grealie Anderson Andrews, Jr.
 Electronics Engineer
 Naval Research Laboratory
 Code 5360
 Washington, D. C. 20375

ABSTRACT

The environment in which Airborne Early Warning (AEW) radars must be able to operate, in the future, presents some severe problems to the designer in many important respects. These include the need to operate over land, the need to detect very small targets ($<1\text{m}^2$) at long range and the need to be able to operate in the presence of jamming.

It is shown that the single most important factor influencing the ability of the AEW radar system to operate in this future environment is the antenna's sidelobe performance. In general, this sidelobe performance is dominated by the airframe on which it is mounted. Careful design is needed, considering both aerodynamic as well as electrical aspects, before an overall optimal system configuration can be determined.

Once the antenna sidelobe performance has reached an acceptable level, it is then found that the next limitation is that due to errors in the compensation of platform motion. Recent advances in digital processing technique offer many advantages in connection with moving-target indication (MTI) but these can only be realized when the platform-motion compensation is sufficiently accurate. The various system considerations governing this performance are discussed and the requirements reflecting on the antenna performance described in detail.

1. Introduction

A paper¹ was presented to the Eighth Symposium of the Avionics Panel in 1964 which dealt with some of the basic considerations in the design of an airborne early-warning radar, with particular reference to that used on the E-2A carrier-based system. This used a low prf mainly because of its feature of unambiguous range. It is of interest here to examine the applicability of this type of technology to a larger aircraft, specifically a modified Lockheed Electra turbo-prop, designated as the P-3 by the U.S. Navy.

Of great importance in such a radar is the detection performance and this is largely determined by that of its AMTI sub-system. This, in turn, is critically dependent on the effectiveness of the platform motion compensation. What is in mind is a system in which the velocity components normal to the antenna aperture are corrected by some variant of TACCAR* and these components parallel to the antenna aperture by some technique similar to DPCA**.

It is of interest to determine what are the ultimate bounds on the detection performance of such a system preparatory to quantifying their effects and establishing an optimal design. It is well known that certain types of terrain give rise to large clutter returns which can effectively mask the returns from small targets and prevent their detection. Coherent integration, multiple-delay cancellation and improved system characteristics can be used to improve the detection performance, but each exacts a price in system-cost so that the problem reduces to one of determining the improvement in performance and its associated cost in hardware for each addition. It is shown below that the antenna sidelobe performance has a crucial effect on the system performance, in general, and determines the lowest operating frequency that can be used.

2. AMTI Considerations

MTI improvement factor is defined as the ratio of the output signal-to-clutter ratio to the input signal-to-clutter ratio. It has been derived in Ref. 2 for single, double, and triple-delay cancellers and elsewhere for an n-stage MTI (Ref. 3). Figure 1 shows the MTI improvement factor (I_n) as a function of the ratio of the clutter spectral width (σ_c) to the pulse repetition frequency (PRF). The system characteristics which limit the MTI improvement factor can be related to an effective clutter spectral width and to a shift in the mean of the spectrum. The total clutter spectral width is given by taking the square root of the sum of the squares of all the individual spectral widths. This assumes statistical independence between the individual contributions.

*TACCAR is an acronym for Time Average Clutter Coherent Radar, A system developed by Lincoln Laboratory of MIT. By general usage TACCAR now refers to the technique which was the special feature of that system.

**DPCA is the acronym for Displaced Phase Center Antenna, a technique which simulates electronically the motion of the antenna aperture in its own plane.

The achievable MTI improvement factor for an operating AEW system is limited by the internal motion of the clutter itself and also by system considerations. Specifically, these limitations arise from:

1. Platform motion
2. Antenna sidelobe levels
3. Antenna scanning modulation
4. System stability

To determine the relative importance of each of these contributions, they are considered separately and illustrated in Fig. 1.

A typical value for the spectral width due to internal motion of overland clutter is 0.2 meters/second (Ref. 4, Chapter 17). Figure 1 shows that the MTI improvement factor for this condition is 40 dB for a single canceller, 78 dB for a double canceller, and 114 dB for a triple canceller. If the system were limited by internal motion then all practical requirements could be met easily by the use of a double canceller.

Platform motion can be resolved into two components, one parallel to the antenna aperture and one perpendicular to the antenna aperture. These components have the effect of both spreading the spectrum of the clutter returns and shifting the mean of the spectrum. The relationship for the spreading of the spectrum is given in Ref. 4, Chapter 18. Using typical parameters (a platform velocity of 300 knots, an aperture of 25 feet and a prf of 300 Hz), Fig. 1 shows that the MTI improvement factor is about 15 dB for a single canceller, 25 dB for a double canceller and 35 dB for a triple canceller with the antenna aperture parallel to the velocity vector. For this case, many practical requirements cannot be met with either a single, double or triple canceller. Rather than go to higher order cancellers, other processing techniques should be employed.

With the antenna aperture perpendicular to the velocity vector, the dominant effect is the shifting of the mean of the clutter spectrum. The mean of the doppler spectrum is determined by the platform velocity and the transmitted frequency and generally requires compensation for successful MTI operation.

Since the antenna sidelobes essentially cover 360° , the doppler shifts received through the sidelobes range from $-v_p$ (v_p is the platform velocity) to $+v_p$. This doppler spread can cover the entire MTI ambiguous frequency band. As a result, these sidelobe returns are not cancelled and the MTI improvement factor is limited by the integrated mainlobe-to-sidelobe ratio. This is the ratio of the integrated energy entering the system through the mainlobe to that entering through the sidelobes for the two-way antenna pattern.

The effect of antenna scanning modulation on the clutter spectral width is given in Ref. 2. It is affected by the antenna scanning, the antenna aperture, the transmitter frequency, and the PRF. Most requirements can be met without compensation for this effect.

System stability is greatly simplified by digital processing which allows one clock to control the entire system including the MTI delays. However, the pulse-to-pulse phase instability of the transmitter is not eliminated by digital processing, so that the performance of the system could be limited by the transmitter stability. Excluding the transmitter, a clock stability of 10^{-8} is within the state of the art. The corresponding MTI improvement factor (referring to Fig. 1) is 22 dB for an single canceller, 42 dB for double canceller, and 62 dB for a triple canceller. Again, most requirements can be met with one or other of these cancellers.

The conclusion is that the factors which limit the improvement factor are antenna sidelobes and platform motion.

It has been seen that unless a correction is made for the shift in the mean of the clutter spectrum, then MTI is impossible. TACCAR makes this correction by phase-locking the system to the clutter returns. A phase-lock loop is gated on at a selected range interval. The time constant of this phase-lock loop must be large compared with the interpulse period in order to maintain pulse-to-pulse coherency needed for successful MTI action. This results in a single correction for all ranges. However, the average doppler changes with range since the angle of arrival varies with range for an aircraft flying at some altitude above the earth's surface.

The effect of this incomplete correction results in a smaller MTI improvement factor. This decrease in the improvement factor is derived elsewhere (Ref. 3). It is a function of the ratio of the correction error and the clutter spectral width. For a typical set of parameters, these losses due to TACCAR are illustrated by Fig. 2 when the antenna is pointed in the direction of the aircraft velocity vector.

DPCA is a technique that compensates for the component of aircraft velocity parallel to the antenna aperture. This is accomplished by either physically or electrically displacing the phase center of the antenna in the direction opposite to the velocity component. A detailed discussion of DPCA, on which the following is based, is given elsewhere (Ref. 5).

A single canceller MTI can be almost perfectly compensated by DPCA with essentially no loss. It can be shown (Ref. 5) that for double, triple or higher-order cancellers, only the first canceller is compensated. This results in an imperfect compensation so that the effects of platform motion are not completely eliminated. This is illustrated in Fig. 3 for a typical set of parameters.

The MTI improvement factor for a single canceller with DPCA coincides with the perfectly compensated curve. The improvement factors for double and triple cancellers are much less than the perfectly compensated curves.

If the system stability can be increased from 10^{-8} to 10^{-9} , then the improvement factor will be limited by scanning modulation. From Fig. 3, a UHF system is limited by scanning modulation and DPCA losses when the antenna is pointed broadside to about 30 dB for a single canceller, 50 dB for a double canceller and 62 dB for a triple canceller.

The use of coherent integration can ease the requirements on the AMTI (Ref. 6). This technique corresponds to doppler filtering as used in a pulsed-doppler radar, except that for a low-PRF radar only a very limited number of pulses can be integrated before the return from a moving target moves out of the range cell. Typically sixteen pulses can be integrated. This corresponds to a theoretical integration gain of 12 dB for a perfectly coherent signal in "white" noise. However, neither of these conditions applies. First, a perfectly coherent signal (or target return) implies that the doppler of the return is such that its frequency is at the center of one of the filters in the bank of filters formed by the coherent integration. Second, the clutter residue from the MTI is not "white". The problem then is to determine how much gain in signal-to-clutter ratio can be expected from this technique.

The integration of 16 pulses with no weighting provides 16 contiguous filters covering the frequency band from zero to the pulse repetition frequency. With no weighting, the filters have a $(\sin x)/x$ frequency response. Since the doppler of the target returns are not known, they are assumed to have a uniform probability of occurring anywhere in a particular filter between the cross-over points of adjacent filters. Averaging the signal gain over this band results in a loss in coherent integration gain of about 1.1 dB for "white" noise. If weighting functions are used to get some desired filter sidelobe level additional losses occur depending on the weighting function. Therefore, a net gain of about 10 dB could be expected for "white" noise.

Since the clutter residue from the antenna sidelobes cover all frequencies in the band from zero to the pulse repetition frequency, this 10 dB gain can be applied to this residue as well as other components of the clutter residue. Reference 6 shows that the improvement factor achieved against mainlobe clutter (which is not white) is much more than 10 dB. It is typically about 24 dB depending somewhat on the type of MTI used.

As will be shown below, the antenna sidelobes can be reduced when the transmitter frequency is increased. However, this solution affects the doppler processing. Over land, at L-band with a system stability factor of 10^{-9} the effects of internal motion, scanning modulation, and system stability are illustrated by Figs. 3 and 4. Referring to these figures it can be seen that the effect of scanning modulation dominates the other effects. For a double canceller these limitations are about 25 dB for scanning modulation and TACCAR losses (antenna at $+90^\circ$). If the TACCAR losses and the DPCA losses could be eliminated, then the limitation to the MTI improvement factor caused by scanning modulation at L-band is about 55 dB for a triple canceller (see Fig. 4). Reduction of these losses, are discussed in Refs. 3 and 5, consist of making TACCAR corrections at additional points in range and applying a DPCA correction to all cancellers.

In summary, to insure adequate performance, a typical set of system specifications would be:

1. Integrated mainlobe-to-sidelobe ratio - 60 dB (two-way)
2. System stability factor - 10^{-9} (pulse-to-pulse)
3. Transmitter stability factor - 10^{-9} (pulse to pulse)
4. Triple canceller MTI
5. 16-pulse coherent integration
6. TACCAR correction at 3 points in range
7. DPCA correction of all 3 cancellers

3. Antenna Considerations

It is helpful (Ref. 4) to separate the improvement factor associated with the antenna (I_A) into two parts -- that due to the energy entering through the sidelobes (I_{SL}) and that due to imperfect platform motion compensation over the mainlobe (I_{DPCA}).

$$1/I_A = 1/I_{SL} + 1/I_{DPCA}$$

The improvement factor determined by the energy entering through the sidelobes is equal to the integrated mainlobe-to-sidelobe ratio.

$$I_{SL} = \int_{-\pi}^{\pi} E^4(\theta) d\theta / \int_{SL} E^4(\theta) d\theta$$

Consequently it is directly related to the antenna performance when the antenna is mounted on the aircraft and is independent of other system factors. The mainlobe-to-sidelobe ratio is a quality factor for the antenna when used in this type of radar.

The improvement factor associated with the motion compensation over the arc corresponding with the beamwidth of the mainlobe is dependent on the shape of the sum and difference mainlobe patterns but also on the signal processing used. It is susceptible to improvement by the use of higher-order cancellation and motion compensation and so, in principle, its influence on system performance can be made negligible.

In general, when a large radar antenna is mounted on an aircraft, there is a deterioration in performance. This becomes evident in increased sidelobe levels resulting in decreased values of mainlobe-to-sidelobe ratio and also in distortion of the mainlobe patterns resulting in poor compensation of the velocity components parallel to the antenna aperture. These effects arise from the presence of the aircraft structure close to the antenna. Three ways in which the antenna field can be perturbed are (a) blockage

of the antenna aperture by parts of the aircraft such as the wings and tails, (b) scattering from surfaces such as the tops of the wings, and (c) excitation of currents in the aircraft's surface by the near fields of the antenna. All three of these sources of pattern perturbation tend to decrease in effect with increasing frequency whereas it is advantageous otherwise to decrease the operating frequency. Consequently, for optimal design, it is necessary to determine the lowest frequency at which the aircraft perturbations will permit the required improvement factor to be achieved.

A great deal depends on the aircraft design. To minimize blockage and scattering the wing-tips, nose and tail should be so located that their depression angles from the horizontal plane through the antenna should be as large as possible. To minimize direct excitation by the near-fields of the antennas, the distance of the antenna from the nearest conducting surface, expressed in wavelengths, must be maximized.

The P-3 aircraft (see Fig. 5) is an attractive candidate for such an AEW platform, except for the effect of its large tail which bisects the antenna beam as it sweeps around the rear of the aircraft.

In Fig. 5 is pictured a P-3 with a rotodome antenna mounted on it. Such an antenna consists of an antenna array and corporate feed integrated with a radome, the whole structure being rotated mechanically as one unit. Possible frequencies of operation being considered for this system are UHF and L-band.

4. Scale-Model Experiments

A scale-factor of 1/7 was chosen for these experiments. This conveniently put the scale-model frequencies into S-band and X-band. Three scale-model antennas were procured: a ten-element array antenna and a twelve-element array antenna, both operating at S-band and therefore corresponding to full-scale UHF antennas, and a slotted-waveguide array antenna operating at X-band, and therefore corresponding to a full-scale L-band antenna.

A schematic diagram of the ten-element array antenna is shown in Fig. 6. It can be seen that symmetrically placed elements are taken to hybrid couplers, the outputs of which are summed in separate networks to give sum- and difference-pattern output ports. The element weights were chosen to give Dolph-Chebyshev sum patterns, with a peak sidelobe level of -32 dB. The elements themselves are Yagi arrays split in the vertical plane so that the antenna could be considered as a twenty-element array antenna, equally well. The elements are spaced a wavelength apart with grating lobes minimized by shaping of the element patterns.

A 1/7 scale-model of the P-3 aircraft was constructed for these tests and is shown in Fig. 7 mounted on the antenna range. This was a ground-range carefully levelled and cleared so that sidelobe levels can be measured accurately to -60 dB and usefully down to -80 dB. The measured data were recorded directly on magnetic tape to permit processing afterwards using a large-scale digital computer. In general, the antenna patterns were plotted to a convenient format and the integrated mainlobe-to-sidelobe ratio calculated and recorded at the same time. The results for an elevation angle of -20° are shown in Fig. 8. These are plotted on polar graph paper to show the effect of the aircraft geometry on the sidelobe performance. The effect of the tail can be seen to be large. Also shown is the free-space performance of the antenna. It can be seen that the performance did not deteriorate greatly when the antenna was mounted on the aircraft except over the tail. Also shown is the DPCA performance, assuming the use of a double canceller. It can be seen that this actually is inferior to the sidelobe performance near broadside. These same results are presented differently in Fig. 9. This makes clear the basic nature of the sidelobe limitation on the improvement factor.

The elevation characteristics of this model are shown in Fig. 10. The flat behavior is to be noted. The behavior over the nose (0°) is typical but that over the tail (180°) is still reasonably good.

The twelve-element array antenna was carefully designed for good sidelobe performance. Its mainlobe-to-sidelobe ratio in free space is some 10 dB better than that of the ten-element array antenna. It achieved this by reducing the spacing between elements so as to eliminate the grating lobes and by careful attention to the detailed design of the central elements. Its schematic diagram is shown in Fig. 11. It can be seen there that only the sum pattern is implemented in this antenna. A photographic view of this antenna is shown in Fig. 12.

The polar diagram measured for this experiment is shown in Fig. 13 to the same reference as that of Fig. 8. The free-space performance is now represented by the center point of the diagram. The general behavior is much improved except over the tail. This can be seen better in Fig. 14. There is now a larger discrepancy between free-space and on-aircraft performance indicating that direct excitation is now becoming a significant factor. If this could be suppressed, excellent performance could be achieved outside the tail region.

Figure 15 confirms the generally flat behavior available in elevation. This means that good performance can be maintained down to short-range.

The slotted-waveguide array was designed to a Dolph-Chebyshev characteristic with a peak sidelobe level of -46 dB. The free-space performance was measured to be somewhat inferior to this and with a mainlobe-to-sidelobe ratio some 20 dB superior to that of the ten-element array antenna. The schematic diagram of this array is shown in Fig. 16. It consists of eight waveguides (sticks) excited uniformly by a single manifold. A view of the completed antenna is shown in Fig. 17.

Some of the results obtained with this antenna are shown in Fig. 18. Characteristics for elevation angles of -2° , -8° , and -12° are shown. The effect of the wing can be observed in the characteristic for -12° and the effects of the nose and engine nacelles can be observed in varying degree in all cases. The effect of the tail is comparable to that observed in the UHF case except that it is restricted to a narrower sector because of the narrower antenna beam.

The elevation characteristics for this L-band experiment are shown in Fig. 19. It can be seen that the free-space performance of this antenna decreases quite rapidly with increasing depression angle. This has been traced to the presence of a two-peaked sidelobe at a wide angle, symmetrically placed around the azimuthal principal plane. The source of this sidelobe has been attributed to an error made in the construction of the manifold. The effect of this error is significant on the on-aircraft characteristics, particularly at the larger depression angles. The characteristics for the 100° look-angle is typical. This deterioration affects performance at the shorter ranges such as 20 miles or so.

Discussion

It was found useful to establish a theoretical background for these experiments by computing the antenna patterns of the various antennas in free space and also when mounted on the aircraft. This latter was done by establishing an aperture at a distance from the aircraft sufficient to clear all obstacles and then to compute the field in this aperture due to each element with suitable provision made for reflection and shadowing by the aircraft structure. These contributions were then summed and the Fourier Transform taken to determine the far-field pattern. It was found from the results of these computations that tolerances had to be met of about 5° in phase and 0.5 dB in amplitude for each element. Also, the major effects over the tail and nose are due to shadowing. Elsewhere at UHF, direction excitation by the near fields of the antenna was evident.

The most serious problem in this system is the poor performance over the tail. This occurs over a narrow sector and may not be to significant operationally. Two ways of dealing with this would be (a) to replace the metallic tail with a dielectric one designed to minimize blockage and reflection, (b) re-design the aerodynamic structure so that the tail does not intrude into the antenna beam. This would be done by adopting a multiple tail or by placing the rotodome on top of an elongated single tail. The latter approach involves too drastic a modification of the aerodynamic design, so that the multiple tail is preferred.

The best solution appears to be the adoption of a multiple-tail design with each component made from dielectric materials in such a way as to minimize reflection and shadowing. This should be sufficient to bring the performance up to an appropriate level.

Conclusions

The detection performance achievable with a low-prf airborne radar is limited by direct excitation of the aircraft at UHF. This limitation is no longer a factor at L-band but care must be taken to minimize reflection and scattering.

References

1. "Radar Techniques for Detection, Tracking and Navigation," Ed. W. T. Blackband, Gordon and Breach Science Publishers, Chapter 12.
2. Barton, D.K., "Radar System Analysis," Prentice-Hall, Englewood Cliffs, N. J., 1964
3. Andrews, G. A., "Airborne Motion Compensation Techniques, Evaluation of TACCAR," NRL Report 7407, April 12, 1972.
4. Skolnik, M. I., "Radar Handbook," McGraw-Hill, N. Y., 1970.
5. Andrews, G. A., "Airborne Motion Compensation Techniques, Evaluation of DPCA," NRL Report 7426, July 20, 1972.
6. Andrews, G. A., "Performance of Cascaded MTI and Coherent Integration Filters in a Clutter Environment," NRL Report 7533, March 27, 1973.

Acknowledgements

This work was supported under Airtask A360-5333/058B/3F12-141-601 under the direction of Naval Air Systems Command. The assistance is acknowledged of Mr. J. Tyskiewicz (Naval Air Systems Command), Mr. D. L. Ringwalt, Mr. F. M. Staudaher, Mr. Carl Olson (NRL), Mr. D. Lloyd (RCA), Mr. B Sichelstiel, Mr. K. Ramsey and Mr. R. Vogelsang (Westinghouse Electric Corporation).

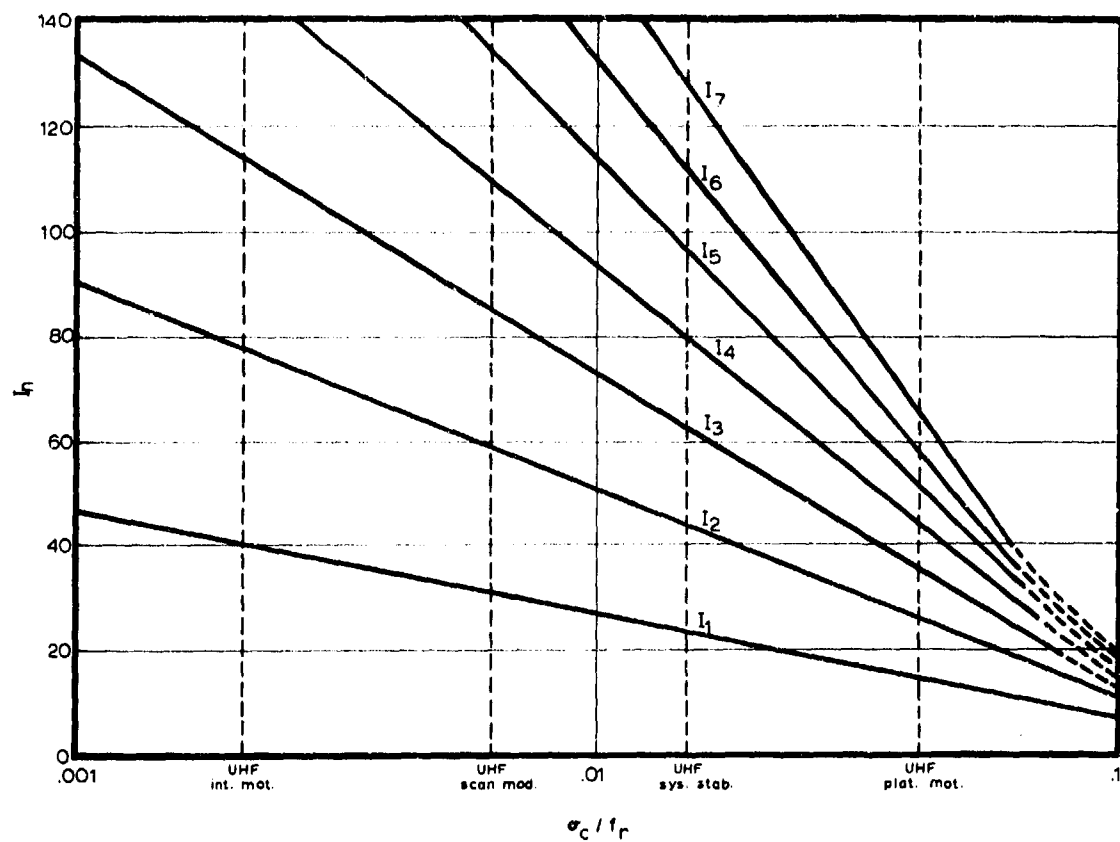


Fig. 1 MTI improvement factor (I_n) . n = number of delays

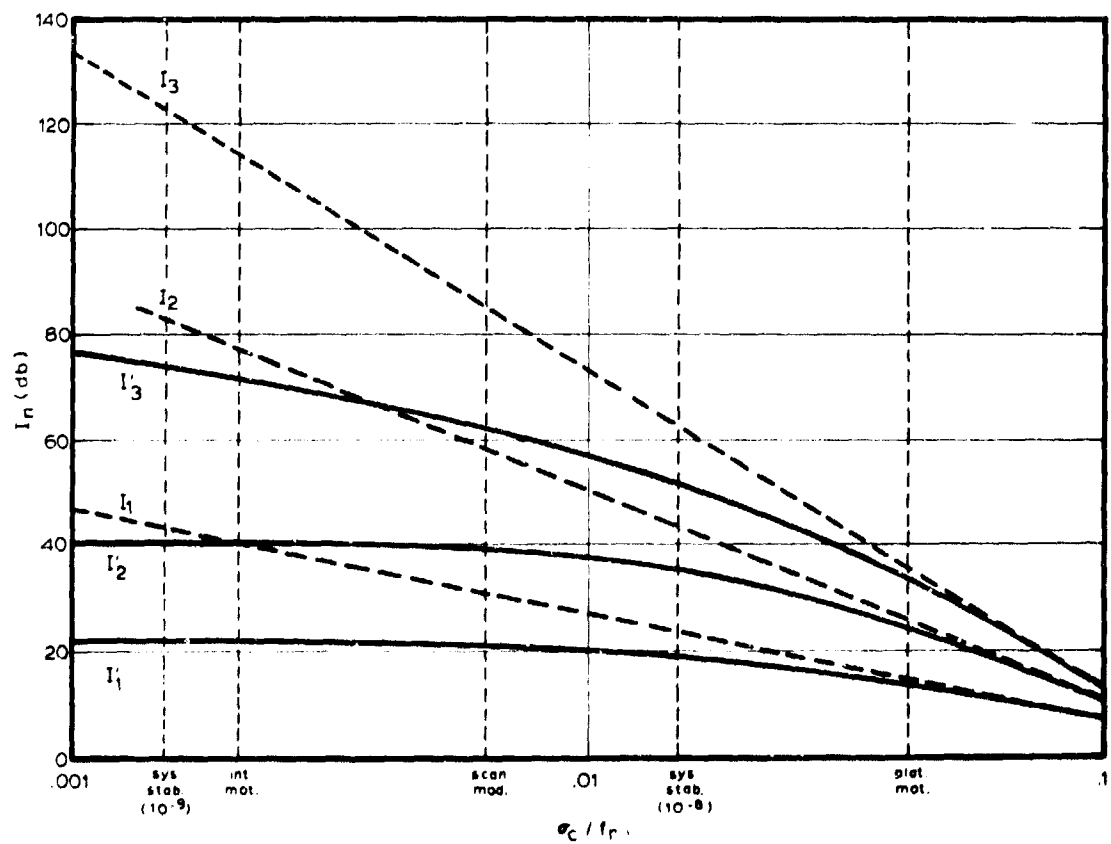


Fig. 2 MTI improvement factor with no platform motion (I_n) and with platform motion and taccar losses at UHF (I'_n) . n = number of delays

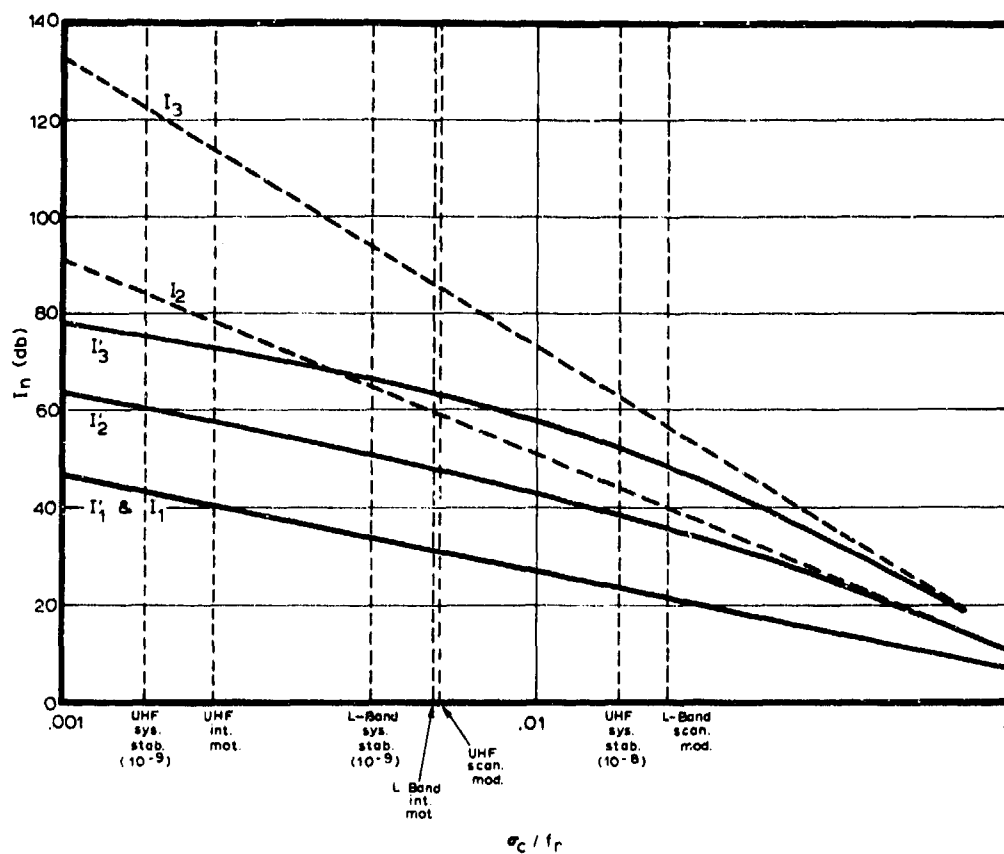


Fig. 3 MTI improvement factor with no platform motion (I_n) and with platform motion and DPCA losses (I'_n). n = number of delays

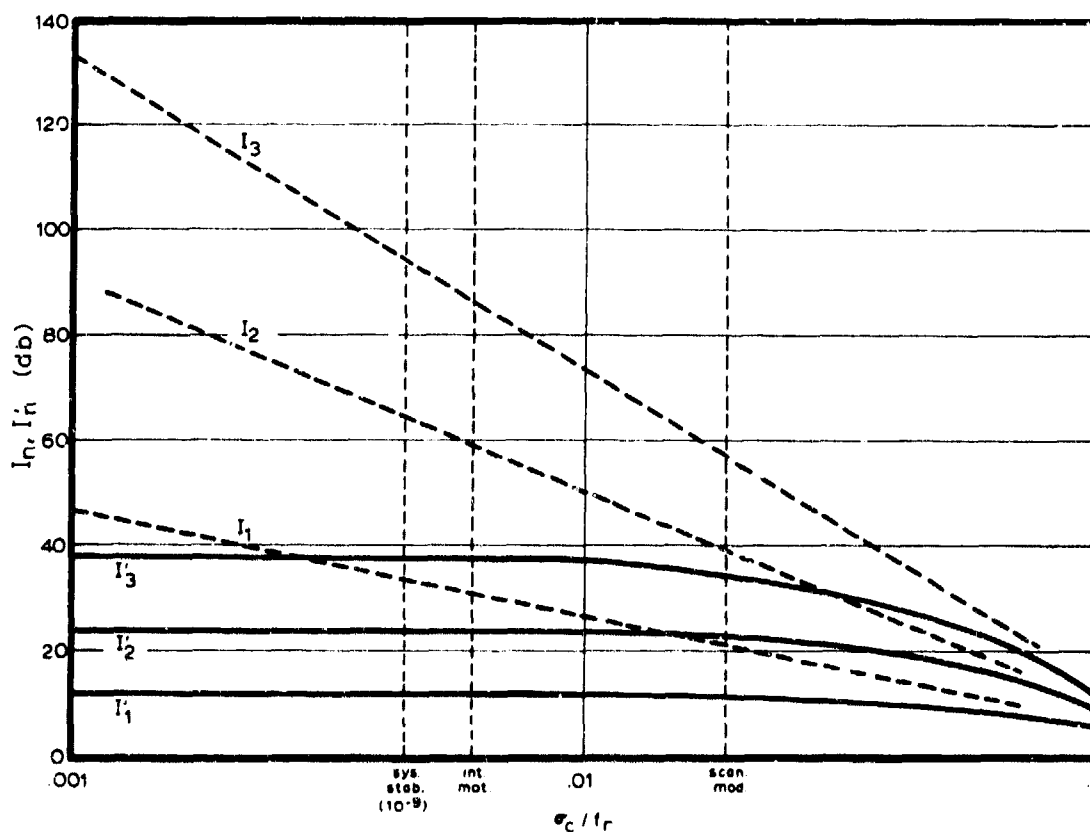


Fig. 4 MTI improvement factor with no platform motion (I_n) and with platform motion and taccar losses at L-band (I'_n). n = number of delays

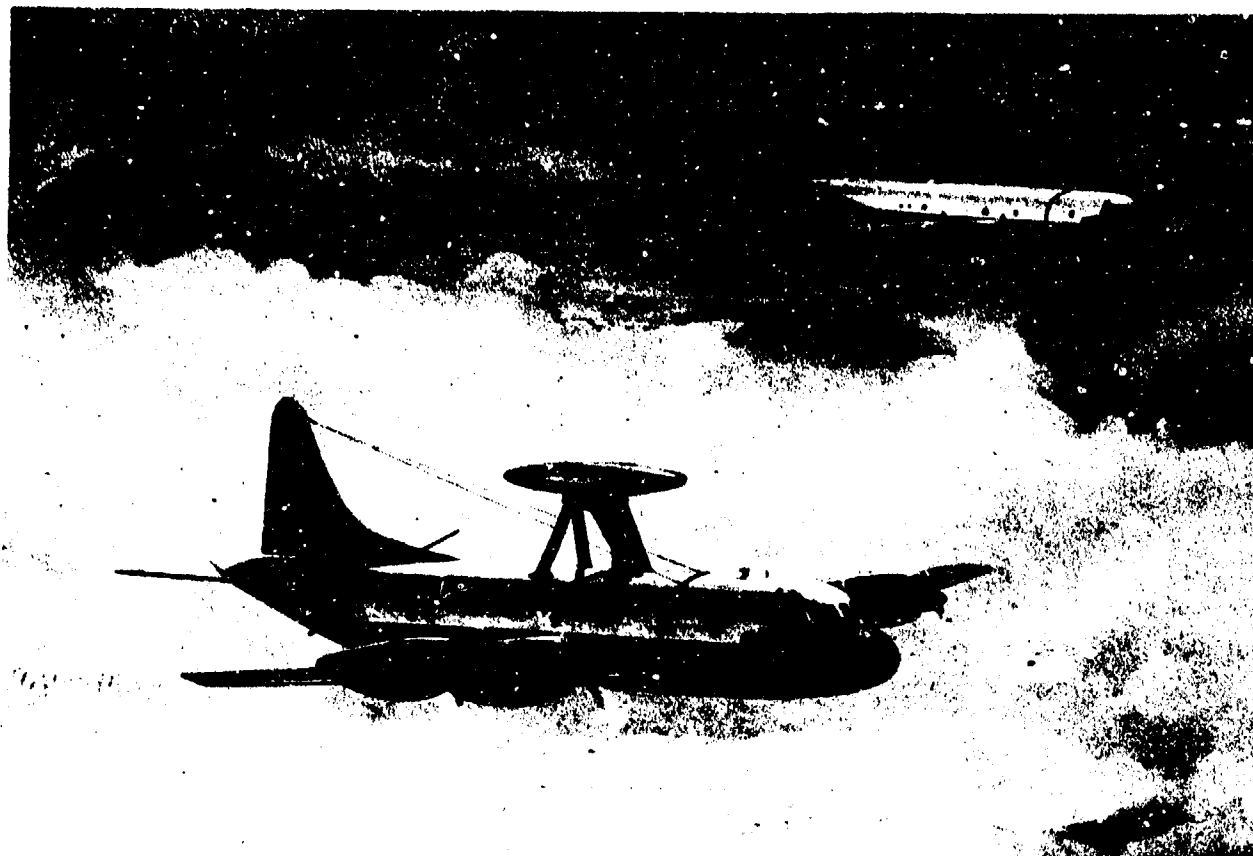


Fig.5 The P-3 aircraft

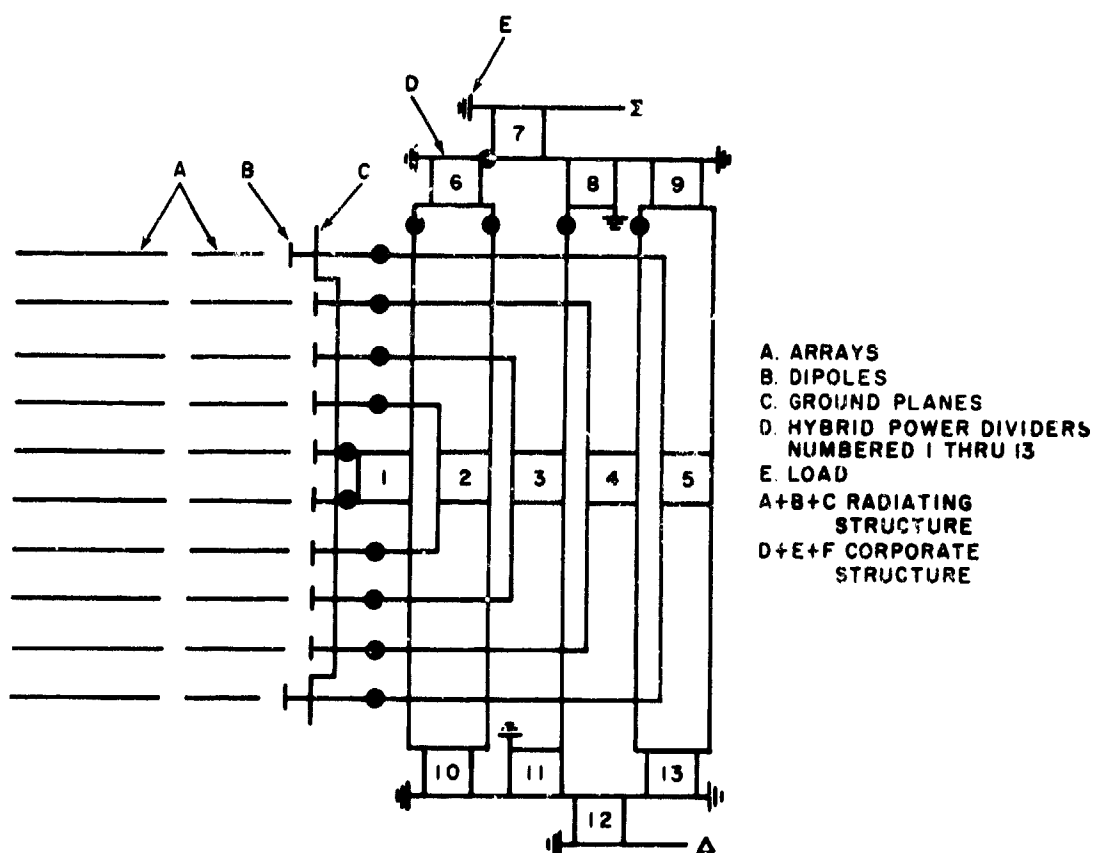


Fig.6 Schematic of the ten-element array



Fig.7 The scale-model of the P-3

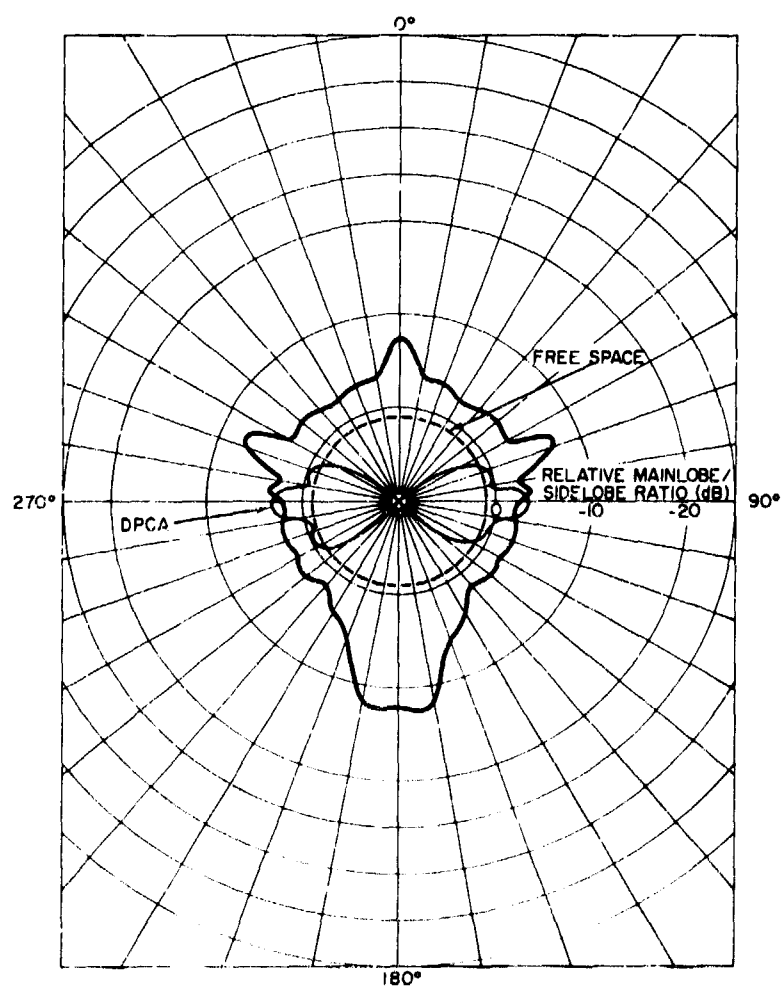


Fig.8 Antenna characteristics (-2°) ten-element array

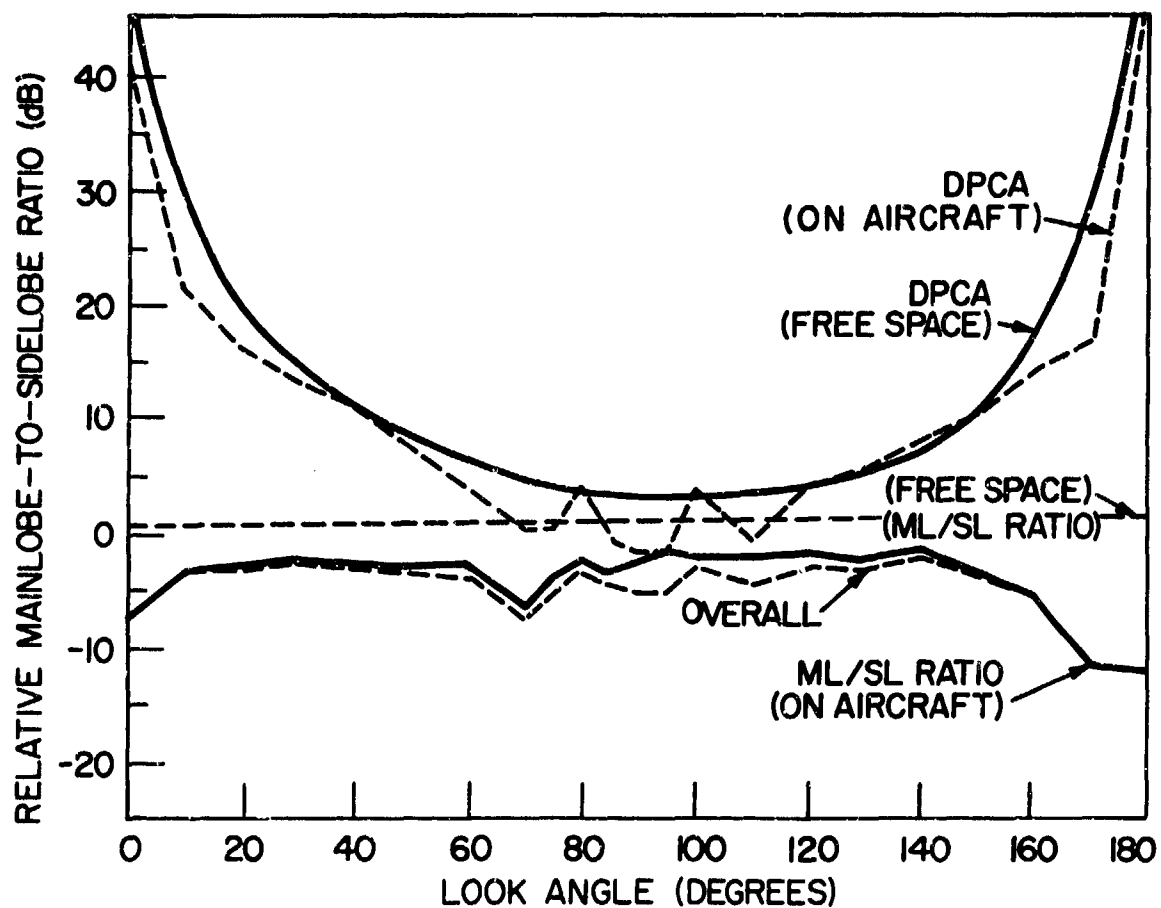


Fig.9 Antenna characteristics: ten-element array

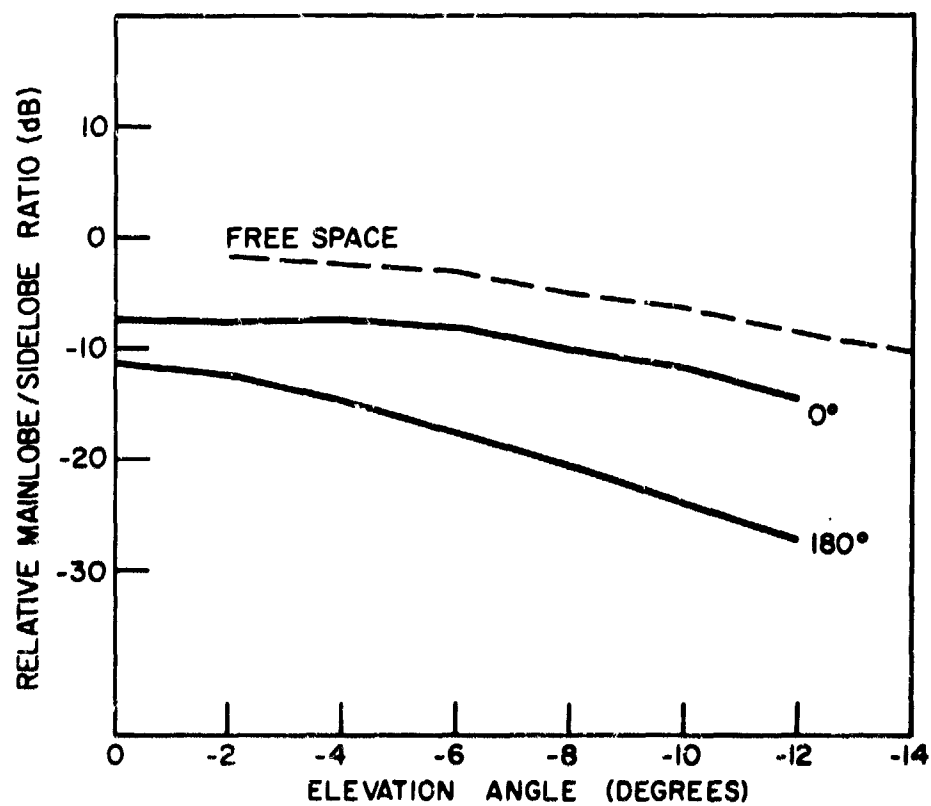


Fig.10 Elevation characteristics: ten-element antenna

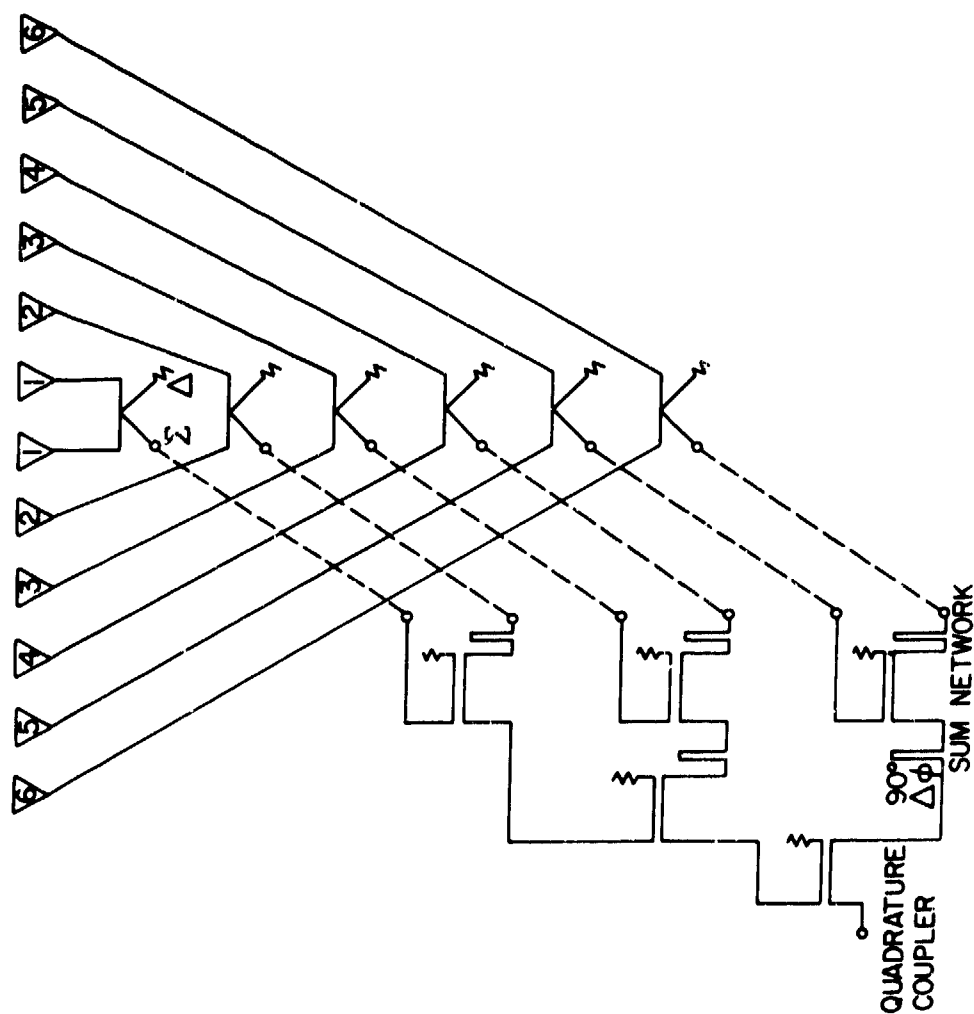


Fig.11 Schematic diagram of the twelve-element antenna

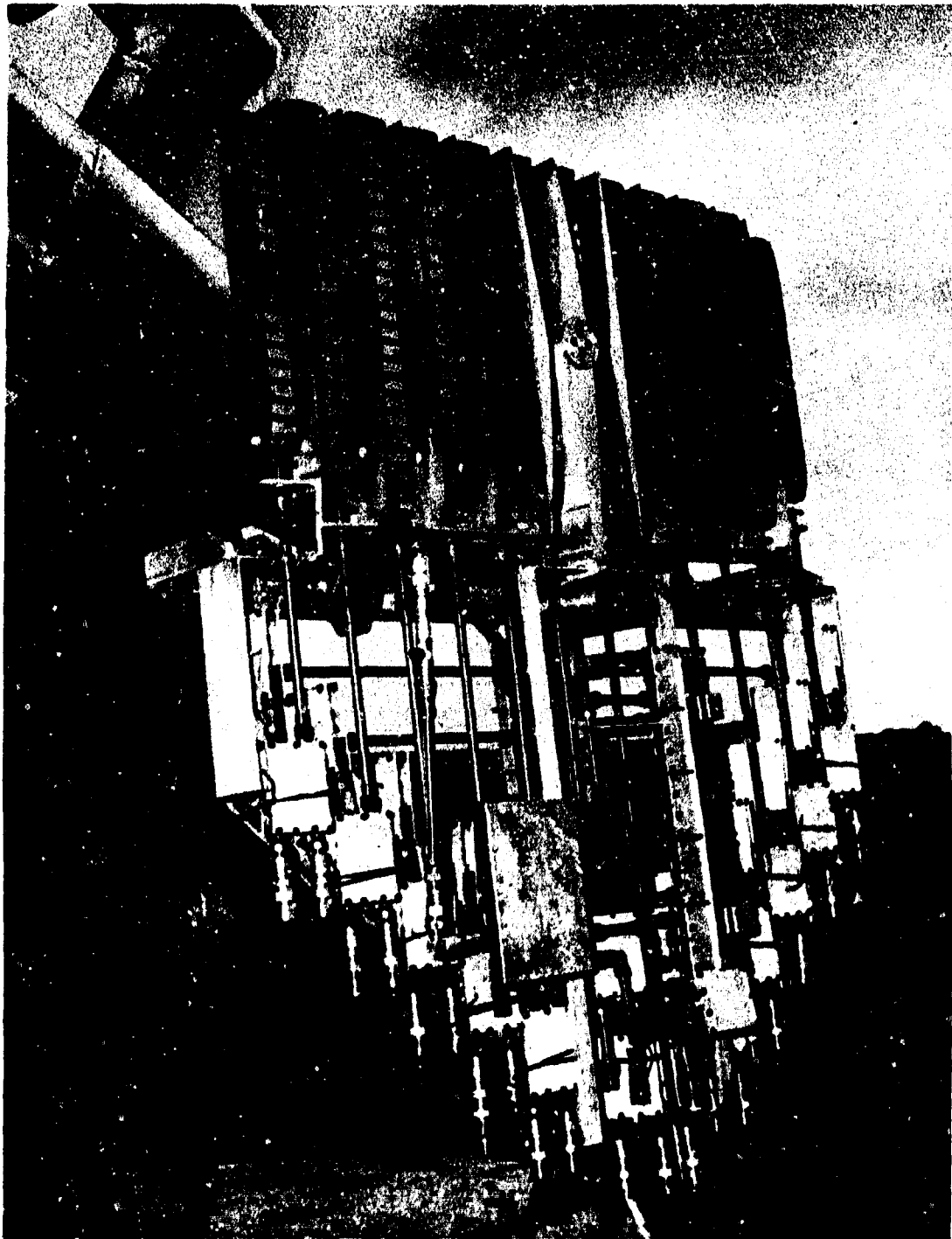


Fig.12 The twelve-element antenna

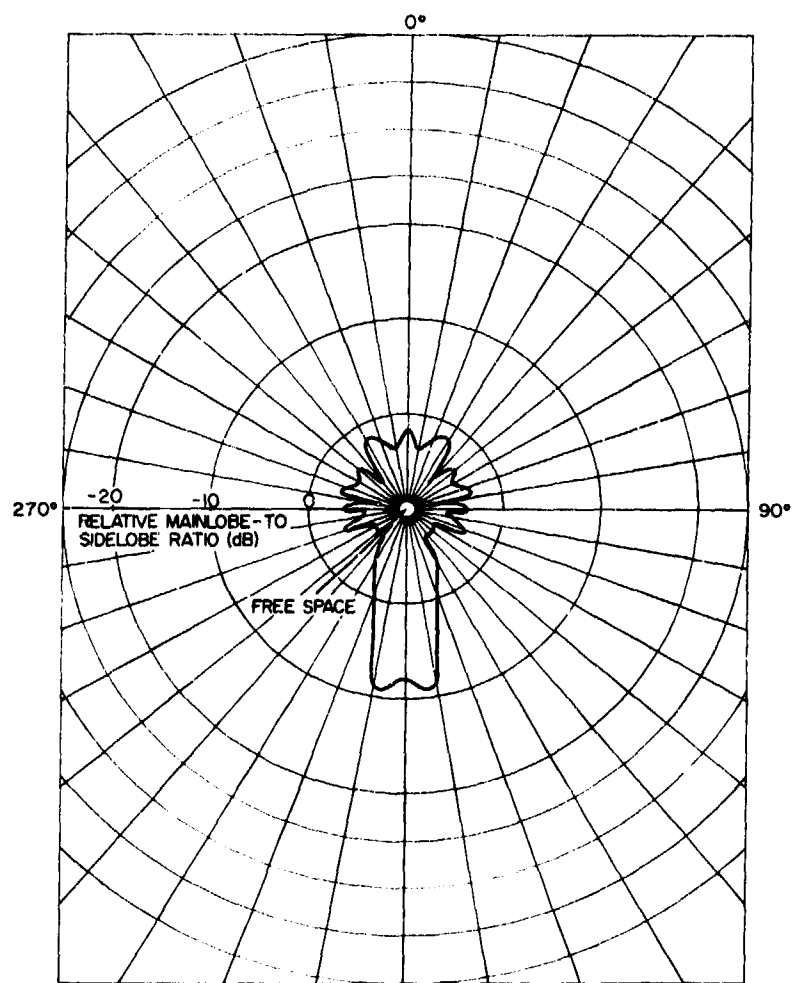


Fig.13 Sidelobe characteristic (-2°) twelve-element array

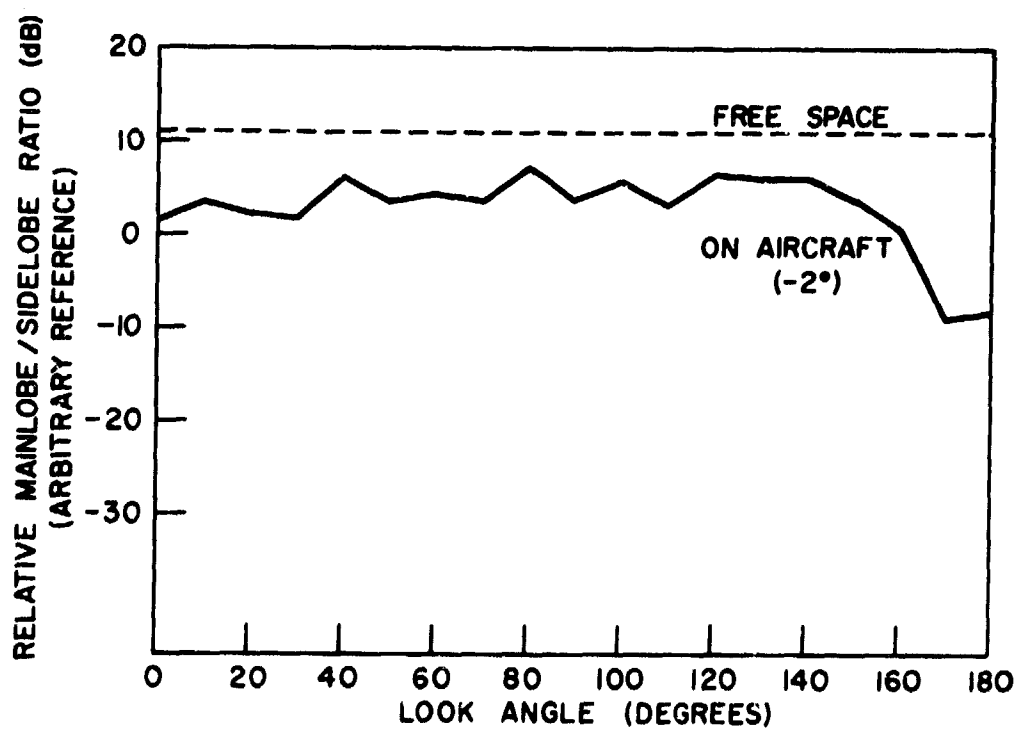


Fig.14 Antenna characteristics: twelve-element array

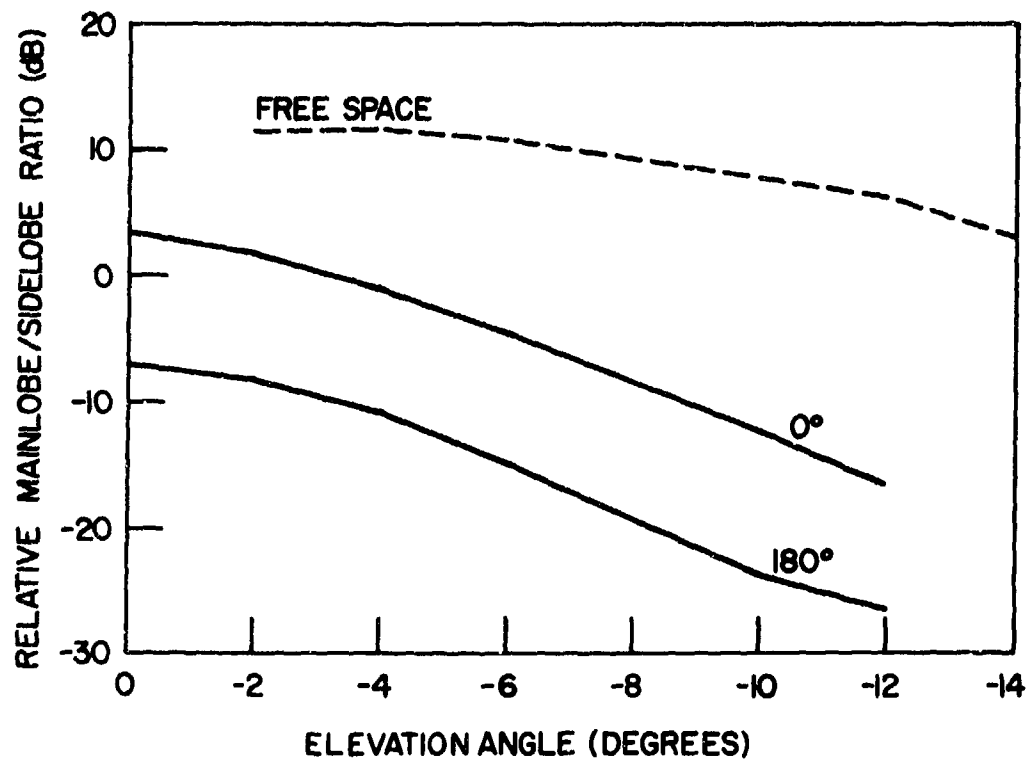


Fig.15 Elevation characteristics: twelve-element antenna

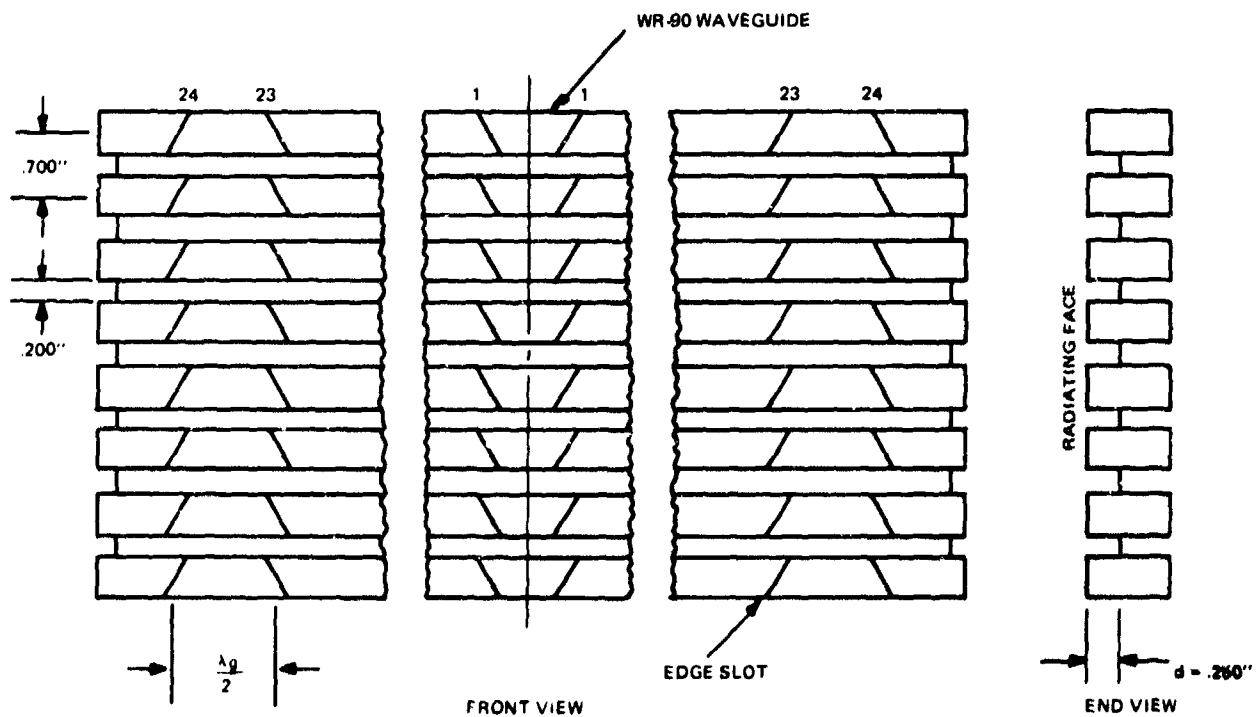


Fig.16 Schematic diagram of the slotted-waveguide antenna

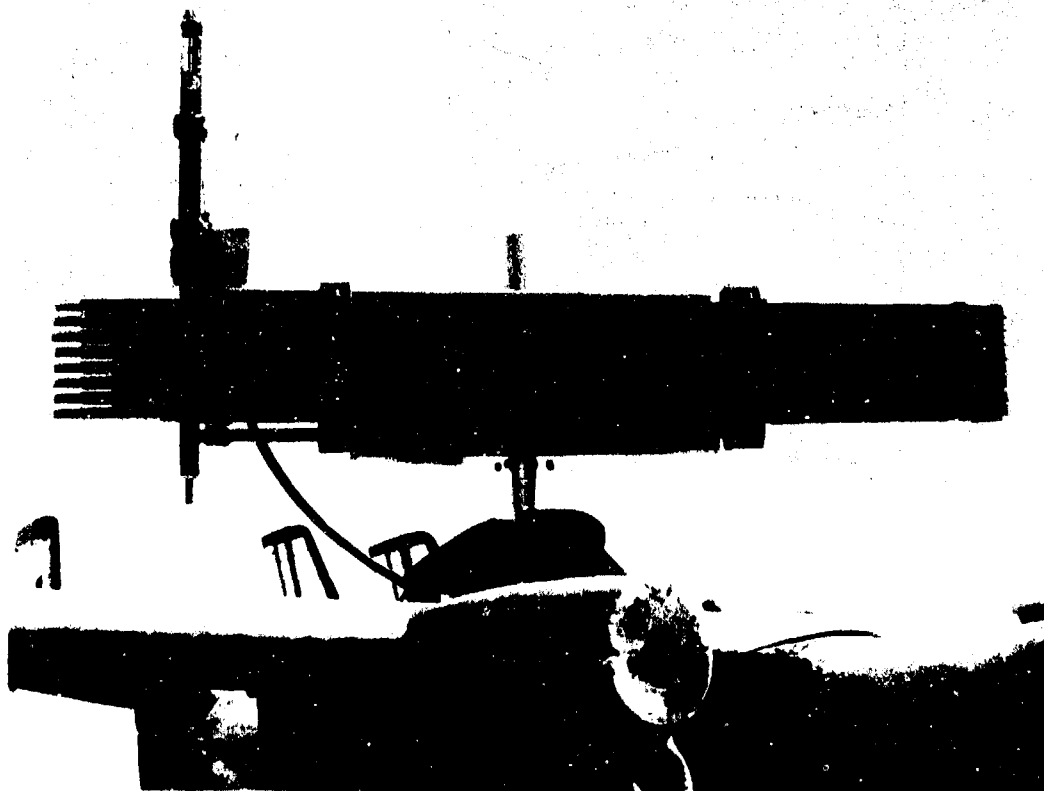


Fig.17 The slotted-waveguide array antenna

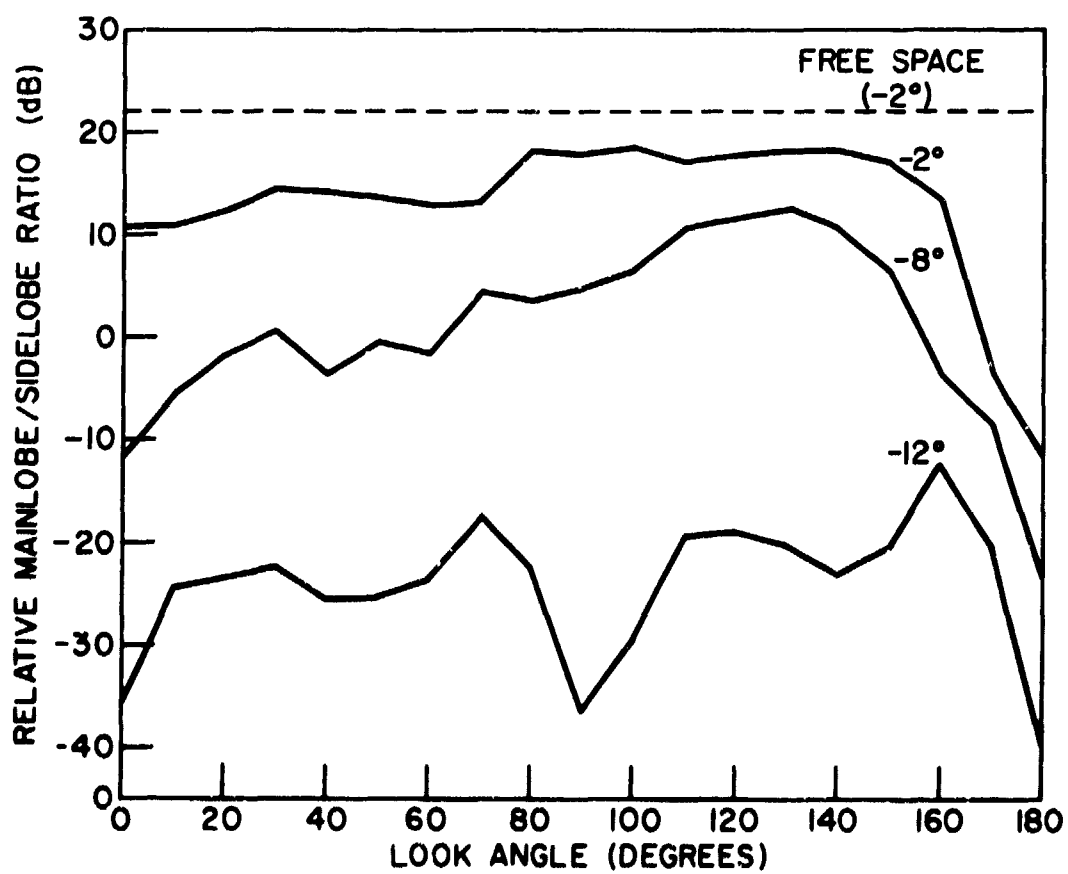


Fig.18 Sidelobe characteristics: slotted-waveguide array

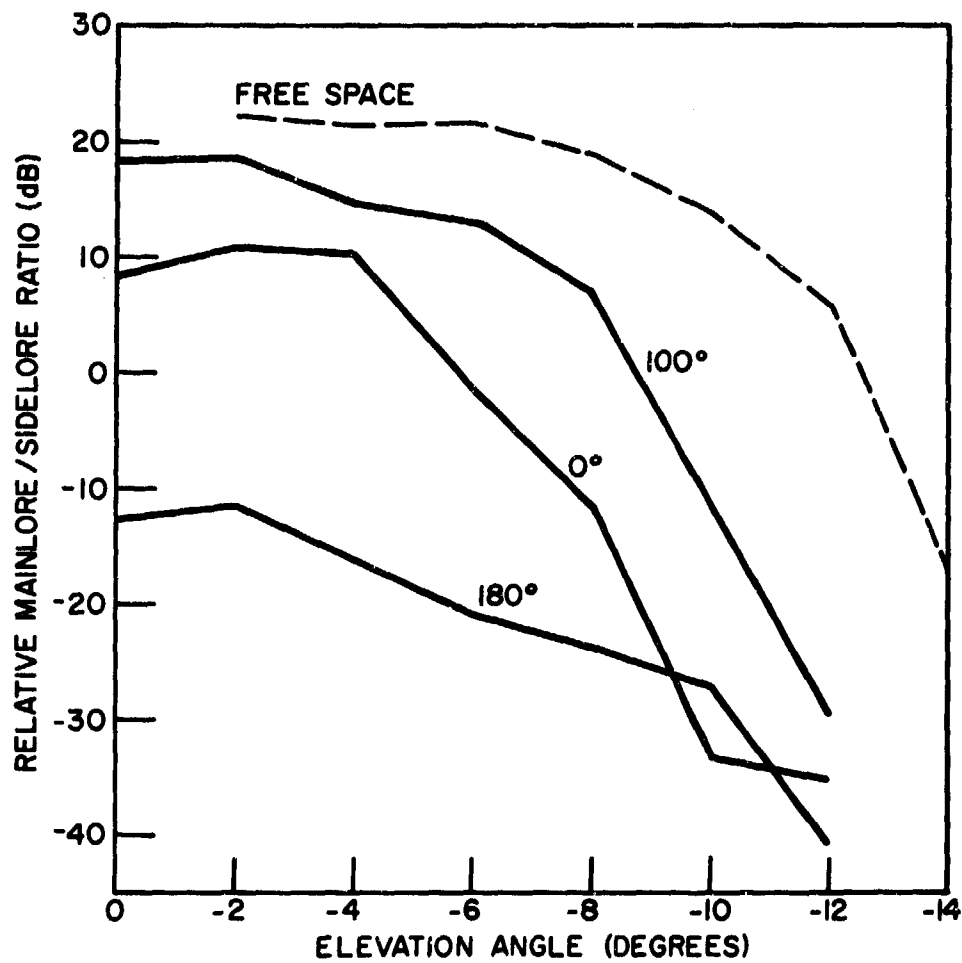


Fig.19 Elevation characteristics: slotted-waveguide array

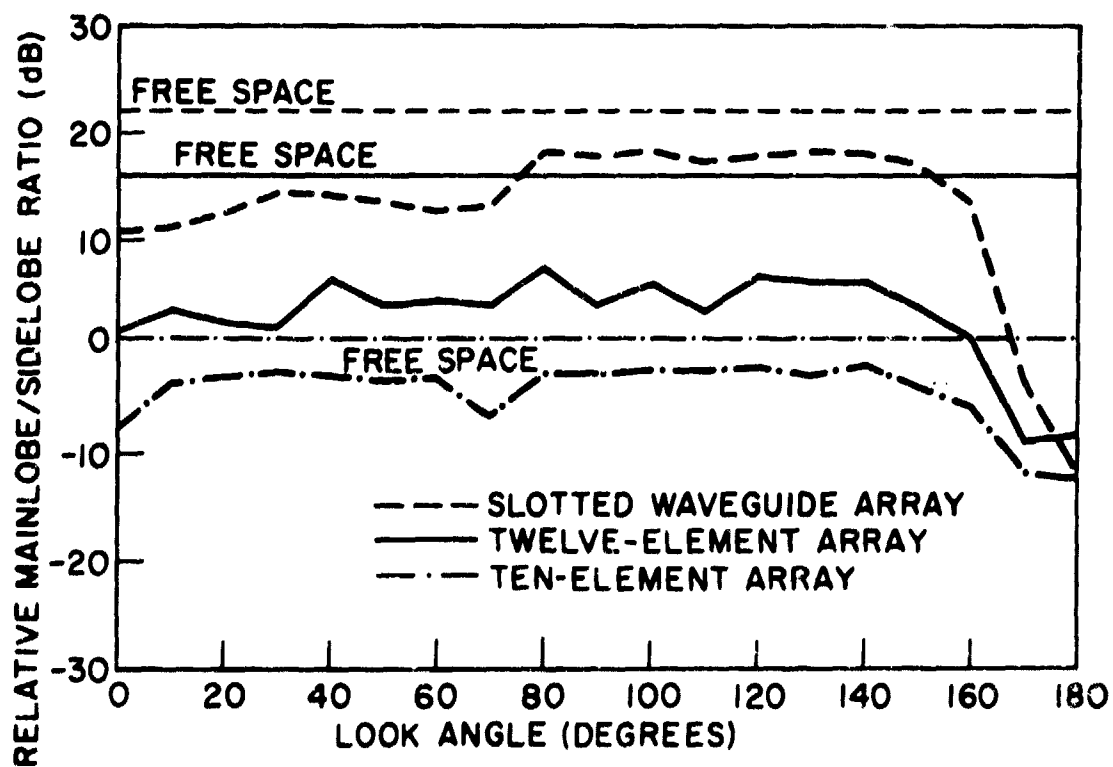


Fig.20 Comparison of sidelobe characteristics

DISCUSSION

J. THRAVES: Would you indicate the side lobe levels that you have achieved on the different aerial systems you have described.

In particular with the L Band slot arrays does the mentioned level of 40dB also include the inevitable cross-polarized level obtained with the use of such slots. What means was used to control them?

T.L. AP RHYS: In the azimuthal principal plane, the 10-element antenna patterns show a peak sidelobe level of 23dB for the main polarization and 34dB for the cross-polarization.

The corresponding figures for the 12 element antenna are 30dB and 32dB.

For the slot antenna mentioned in the paper, the sidelobe level is generally about 42dB except for a couple of sidelobes which have a peak level of 36dB. The cross-polarized pattern shows two lobes symmetrically placed at $\pm 50^\circ$ with respect to boresight at the same level of 36dB.

Some control of the cross-polarized energy was achieved by adjusting the depth of the grooves between the waveguide sticks. It is believed that this energy could be much reduced by a more careful construction of the antennas manifold, but this was not pursued because the performance was adequate for the experiment of interest.

A.M. SMITH: What type of radome structure was used? How was it designed to overcome the high and varying incident angles near the tip?

Was the rotodome tilted with respect to the aircraft axes and if so, what effect did this have on the aerial pattern, assuming that it was desirable to keep the radar beam horizontal so that the beam passes asymmetrically through the radome tip.

T.L. AP RHYS: The aerial position is fixed with respect to the radome thus easing the design problems. Initially there were troubles with radome effects on aerial patterns but these had been overcome. It was now possible to design radomes with exceptional performance using sandwich construction.

J. JACOBSEN: What effect on the cross-polarization had the random spacing of the waveguides? And how did you know that this effect was caused by the random spacing?

T.L. AP RHYS: An error made in the construction of the manifold resulted in a systematic error in the horizontal placement of the waveguide radiating sticks. This resulted in corresponding slots falling out of line and so reducing the effectiveness of the geometrical cancellation scheme. This showed up as increased cross-polarization lobes at $\pm 50^\circ$ in azimuth with respect to boresight.

The use of a computer simulation developed for this antenna confirmed that this systematic error was the source of this increased cross-polarization. This was still small and did not effect the results of the experiment.

R.H.J. CARY: What were the effects of propeller modulation and the high tail structure, and could they be improved?

T.L. AP RHYS: Propeller modulation effects were not measured. However, the geometry of the system is such as to minimise them. A final design would have to balance the aerodynamic advantages of propellers against their electronic disadvantages of limiting the performance in the forward aspect. It is believed that this limit would permit satisfactory detection performance.

The current tail design is unsatisfactory. A great improvement could be obtained by retaining the present aerodynamic tail design but replacing its present conventional construction by one using dielectric materials such as to make it transparent at the operating frequency. Alternatively the single tail could be replaced by a multiple tail of reduced height but this would require extensive wind-tunnel tests.

AIRBORNE LOW-VHF ANTENNAS

by

Charles E. Cooper
Managing Director
Chelton (Electrostatics) Ltd.
Marlow
Bucks. SL7 1LR
England.

SUMMARY

This paper principally describes a blade type antenna design for airborne transmission and reception, with variants covering major sections of the overall frequency band from 26 to 100 MHz. The first version, covering 30-76 MHz is shown in Figure 1, with internal construction 'ghosted' in.

It uses miniature high-vacuum relays to tune via pre-selection of up to six binary-related inductors, providing up to sixty four tuning combinations, with individual band widths varying from about 0.5 to 5.0 MHz. The relays are remotely controlled either manually or automatically, and the retune process can be virtually instantaneous upon both 'receive' and 'ready to transmit' modes, without having to be incepted by any period of transmission.

Incorporation of a variable - tuning system was compelled by the specified combination of total frequency coverage and maximum allowable dimensions for the antenna. However, experimental investigations into the practical limits of broadbanding produced an antenna design fixed-tuned to cover 38 to 46 MHz, which is briefly described.

The paper also provides brief description of a wideband VHF homing antenna which is now in process of field trials for Gazelle helicopters. The system is principally unusual in its use of antenna elements formed out of transparent metallic-film depositions upon the acrylic canopy of the helicopter.

Production of the wideband T/R antenna system resulted from a new specification requirement for coverage of the total band 30-76 MHz, or preferably 30-100 MHz, within dimensional and other characteristics permitting interchangeable fitment on aircraft types ranging from helicopters to supersonic fighters. In practice, this restricted size and shape more or less to that currently in use for blade antennas covering some 108-156 MHz.

Basic design proved to be dominated by the further specification requirement that the complete T/R system maintains total radio silence during possibly frequent changes in frequency of 'receive' or 'readiness to transmit'. Apparently, currently available location equipment can produce a 'fix' on transmissions lasting only a small fraction of a second.

This radio-silence requirement prevented retune-control of the antenna by the conventional process used in H.F. equipment, whereby phase and magnitude relationships of antenna input voltage and current are sensed, amplified, and used for servo-drive to antenna tuning-matching circuits. The sensing and retune process requires a transmission period of a few seconds upwards, even for 'reception' only, unless this latter can tolerate loss of sensitivity arising from antenna mistune.

The antenna had therefore either to be retuned by the selection of pre-determined settings, or be broadbanded to cover the full frequency range at a single fixed - tuned setting.

The more recent of VHF broadband blade antennas have achieved coverage of some 100-162 MHz, i.e. a ratio of upper to lower frequency $f_2/f_1 = 1.62$, where the blade height is equivalent to some $\lambda/8$ at the lowest frequency f_1 . For the required low-VHF band antenna, 30-76 MHz at least, $f_2/f_1 = 2.5$, where a similar dimension now represents only some $\lambda/26$. Clearly not the most hopeful situation!

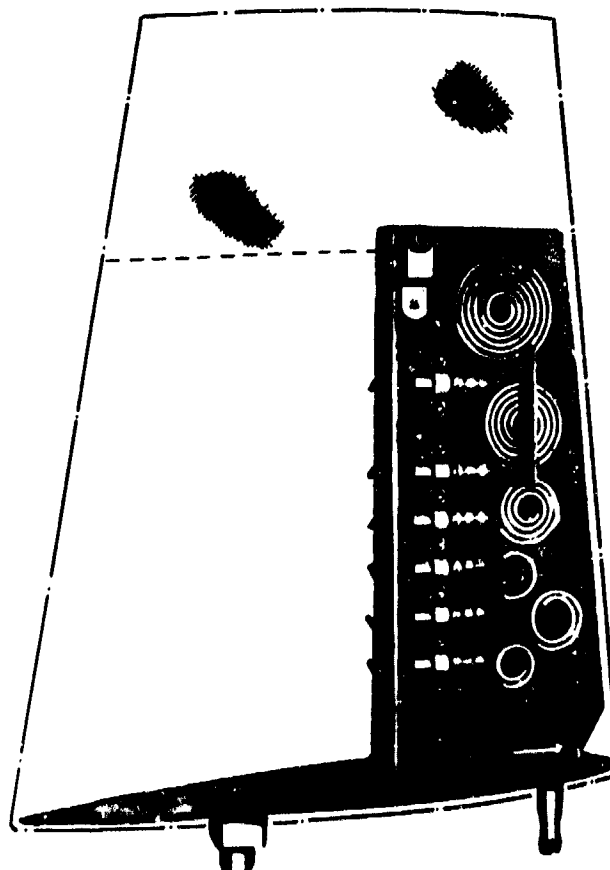


Fig.1

Nevertheless, initial investigations were made into the possibilities for extending existing broadband techniques. Although not achieving the desired aim, these investigations did produce a design covering 38-46 MHz, in fulfilment of an alternative requirement. Figs. 2 and 3 show respectively the antenna blade and its circuitry essentials.



Fig. 2

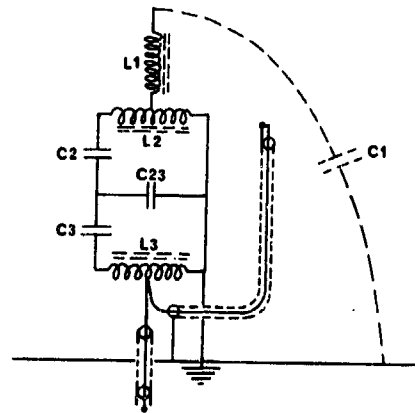


Fig. 3

Radiation is principally via the elevated stray capacitance $C1$ to ground of the tubing section on top of the glass-fibre blade. The length of this tube is an insignificant fraction of a wavelength within the band covered, and vertically polarised radiation has an azimuthal pattern which is very substantially circular.

Radiating capacitance $C1$ is resonated by high 'Q' inductor $L1$. A part of $L1$ is common with a second resonant circuit $L2/C2-C23$, $C23$ being common with a third resonant circuit $L3/C3-C23$. The terminal connection is tapped across a part of $L3$, via a short coaxial line section, with a short-circuited stub in shunt.

Figure 4 shows overall response in terms of V.S.W.R. relative to 50 ohms. at the terminal connector. V.S.W.R. rises very rapidly for frequencies outside the passband, and the experimentally - achieved design gave no indication of possible extension to cover 30-76 MHz or more, since the triple-tuned circuit gave only moderate advantage over what had previously been achieved using only two fixed-tuned circuits.

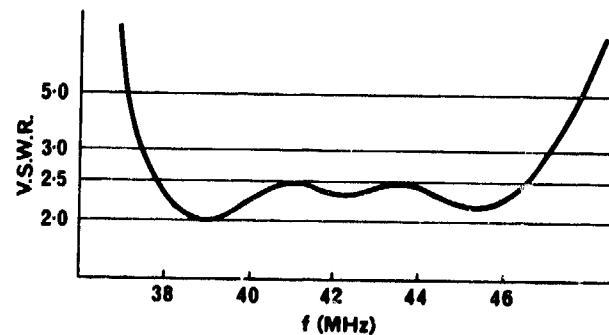


Fig. 4

Design effort was next directed at variable - tuning of one circuit only out of the twin-tuned arrangement, as shown in Fig. 5A, which can be redrawn as 5B to show it more clearly as a conventional band pass arrangement. This is tightly coupled by the fact of the whole of one tuning inductor ($L2$) being common to both the fixed tuned circuit $C1/L1+L2$ and the variably tuned circuit $L2/C2+C12$. Control of matching to the line is achieved by varying the ratio of $C2$ to $C12$.

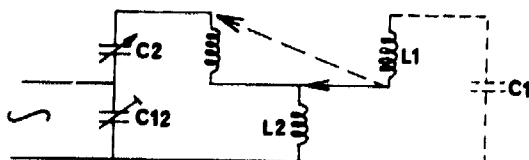


Fig. 5B

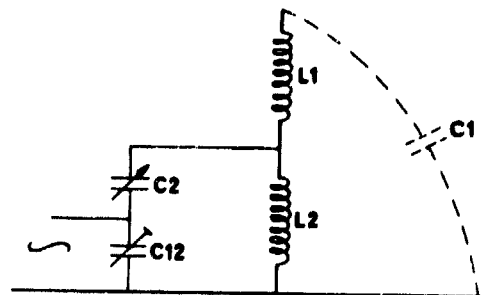


Fig. 5A

Radiation is, as before, from the elevated capacitance $C1$, and the circuitry objective is to achieve effective radiation by considerable voltage magnification across $C1$. The voltages appearing across $C2/C12/L2$ are very much lower, thereby simplifying the problems of providing for variable tuning in a device which must accept the severe environment of external fitment on high-speed aircraft.

Nevertheless, the arrangement became abandoned in favour of the reversed arrangement of Figure 6, where the high-voltage radiating circuit is variably tuned by the inductor series L1-1 to L1-6 inclusive. The arrangements for providing and controlling change of total inductance value became the essential basis of the wide-range antenna design, of which the first variant is shown in Fig.1, using a mesh plate form for the radiating capacitance C1.

In Fig.6, the inductor series L1-1/6 comprises six printed circuit coils having inductance values in an approximately binary relationship. Departure from exact binary is due to mutual inductance between them, and because the stray inductance of interconnections is comparable in value to the smallest of the discrete inductors. Shorting-out from 0 to 6 coils provides a total of 64 combinations at constant increments, except for the strays.

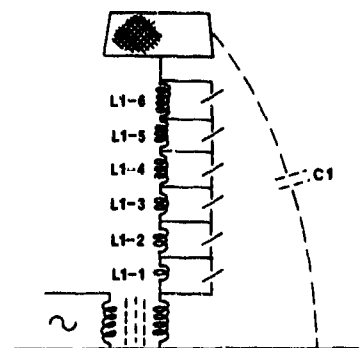


Fig.6

Six of the possible inductance combinations will each, of course, be that of a single coil only, when virtually the full resonant-magnified voltage appears across that coil and its switching. When coils are shorted out of circuit, their switching must carry the full R.F. current of the resonant circuit, and needs to have extremely low contact resistance in order not to become comparable with the quite low radiation resistance of C1.

This combination of switching requirements is met in remarkably small dimensions by the high-vacuum relay illustrated in Fig.7 (approx. full-size). The switching rod (r) pivots from a diaphragm (d) which forms one contact lead-out (C1), and which is also the seal between vacuum chamber (v) and the operating solenoid (s) and armature (a). A ceramic bead (b) provides low-capacitance isolation between the switching and operating parts of the rod. The vacuum chamber uses ceramic insulators (I1/I2), sealed to the lead-out contacts (C1/2/3). Although as shown it is a changeover device, in the antenna C1&2/C3 are used only as an open/closed contact pair.

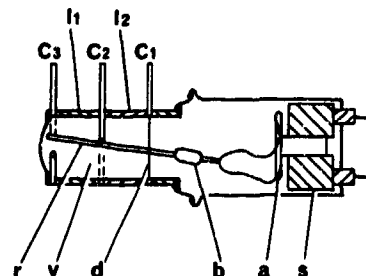


Fig.7

The plate radiator is provided by a fine mesh of stainless steel wires, moulded into the outer surface of the upper part of the glass-fibre shell which houses antenna circuitry. The moulding process leaves all wire intersections just exposed at the glass-fibre surface, to minimise radio-noise problems arising from redistribution of static charges acquired during high-speed flight.

A requirement for this plate to have maximum effective height has to balance against the need for its capacitance C1 to be substantial compared with non-radiating stray capacitances associated with the inductor series and their switching relays. This was experimentally compromised by mesh extending over the upper third of the shell, producing C1 about 10 pf at an effective height of about 0.3 metre.

With the inductance values (all 6 coils in circuit) necessary to tune C1 to 30 MHz, the circuit strays of capacitance and inductance initially produced an upper frequency limit of 75 MHz, with all coils shorted-out of circuit. However, in a later version, reduction of (particularly) the inductance strays allowed frequency range to extend up to 100 MHz, as currently available.

The inductance-variation method used was found to provide a useful bonus, whereby it proved possible to couple between terminal and the antenna circuit via a ferrite-cored wideband transformer of fixed ratio. This arises because change in Q value of the series resonant circuit C1/L1-1/6 is of such form as to balance changes in the radiation resistance R_r of C1.

Fig.8 shows change of Q with change of inductor combination selected, in the absence of radiation from C1. As set for low-frequency operation, overall Q is high, since the discrete high-Q inductance is large compared to the stray inductance, which has low Q value. This low Q predominates when the discrete inductors are all or most shorted out of circuit for operation towards the upper frequency limit.

The general form of Q variation, as averaged between the two dotted curves, is subject to cyclic variations, with Q peaking at each frequency tuned by a single inductor. For the next frequency above each such condition, all the smaller inductors will come into circuit in place of the single larger one, with an appreciable fall in overall Q. For tuning to 30 MHz, where high Q is essential, the two smallest inductors are therefore excluded from use.

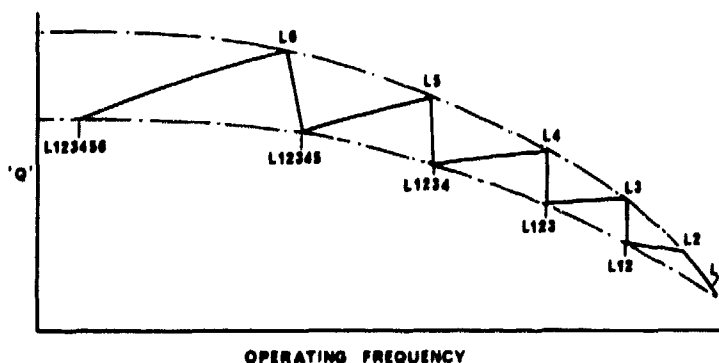


Fig.8

Figure 9 shows the measured overall response of an early version of the antenna, in terms of passband $f/\Delta f$ for V.S.W.R. 3.0 : 1 maximum, against the central frequencies tuned by each different coil combination. The dotted slopes mark bandwidths of 1,2,3,4,5 and 10 MHz (overall) respectively. As can be seen, inclusion of the two smallest coils to tune to 30 MHz reduces bandwidth marginally below 1 MHz.

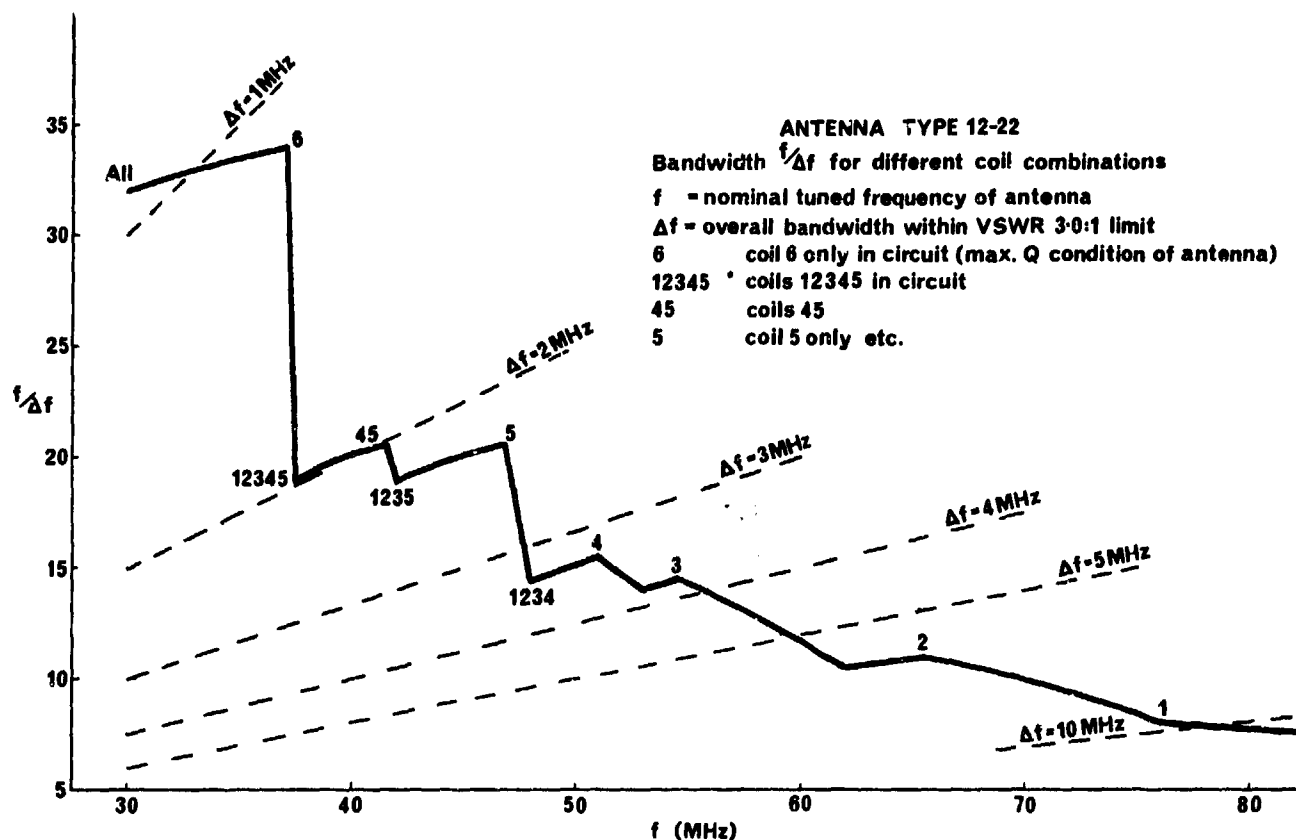


Fig.9

Since it was not intended to use frequency-setting information finer than 1 MHz steps, a later design increased certain inductor values in order to tune down to 30.5 MHz (central frequency) by coil combination 3456 only. This then maintained at least 1 MHz bandwidth from 30 to 40 MHz, 2MHz from 40 to at least 50 MHz, and rising to 15 MHz overall bandwidth for the upper-frequency limit condition, where all coils are shorted out to tune by stray inductance alone. Above 40 MHz, therefore, there is an increasing redundancy of coil combinations if the 1 MHz frequency-setting steps are maintained.

The antenna was intended for fitment onto a variety of different aircraft, producing possible considerable variation in effective ground plane area, or even in grounded metalwork relatively near to the mesh plate radiator.

Figure 10 curve A shows the shift of resonant frequency resulting from change of flat ground plane size, from 8ft.x4ft. down to 4ft.x2ft., i.e. one quarter of the area. Curve B shows the very reasonable compensation resulting from addition of a small ($3\frac{1}{2}$ "x1 $\frac{1}{2}$ "") horizontal plate upon the antenna top. However, the existence of redundant coil combinations makes it possible alternatively to correct for ground plane size within the antenna control circuitry, and provision for this has been incorporated into certain control units.

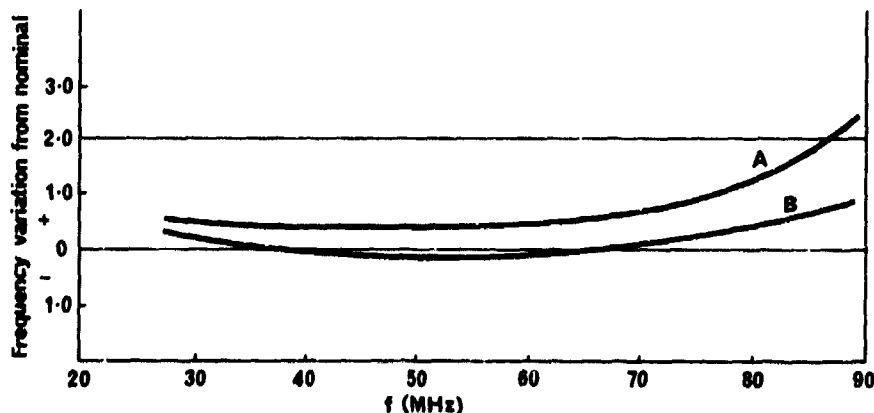


Fig.10

Antenna retune via the relays requires a nominal 28 volts D.C., with some 30-35 m/a per relay, i.e. 200 m/a maximum total. Relays are so arranged that, when energised, they short-out the inductors, so that failure of either operating solenoid or power supply leaves the antenna tuned below, rather than above the intended frequency, which has some marginal benefit. The inductor board and control terminal assembly incorporate shunt diodes and filtercoons to prevent unwanted transfer of signals in either direction between antenna circuit and the tuning control lines.

Remote-control retune of the antenna can be achieved by one of the following methods:

- A manually operated rotary switch unit, which must be reset separately from the T/R retune control(s). The switch unit has 30 positions, covering the total frequency range in 1 MHz steps up to 40 MHz, thereafter including some greater bandwidths per step.
- Where associated with newly-developed T/R equipments, by incorporation of additional contacts onto the frequency-control switching of the T/R, for simultaneous control of both.
- With existing equipments, by automatically following any retune of the T/R, via a solid-state 'logic' or 'code' converter operating from the same D.C. potentials as are used to control frequency setting of the T/R. The principal function of this converter unit is to change the code of the particular T/R into the near-binary code necessary for antenna control.

Only D.C. potentials exist at either input or output terminals of the logic converter, which may be positioned anywhere between antenna and T/R unit, although adjacent to the latter is the usual position. The converter unit operates to follow any change in frequency of either 'receive' or 'readiness to transmit', without the process needing to be incepted by any period of full or partial transmission power, hence operating in total 'radio silence'.

Each type of logic converter comprises the following 3 basic units, plus a stabilised and filtered power supply operating from the aircraft nominal 28 volt D.C. line.

- The input isolating stages. There is one isolator for each information line, to prevent any loading which might possibly affect T/R frequency control. As examples, the Arinc Code 410 uses 10 lines for units and (all) tens of MHz, whereas the code for ARC 54 and ARC 131 needs only 6 lines for units and tens of MHz from 30 to 75 MHz. The above two codes use only on-off information per line; as an alternative example, ARC 114 code uses 5 potential steps per line to control from 30 to 75 MHz by only 3 lines (in all cases, plus ground).
- The code converter stage. In original designs, these units included a multi-pin programming plug and socket, allowing a limited degree of code conversion variation by plug interchange. This was principally intended to provide for adjustment to suit the effects of differing ground plane characteristics. However, any requirement for such adjustment has proved too marginal to justify the complication, and the programming facility has been omitted from most later designs. Recent design of these converter stage units has been based upon use of 'Read-only memory' units (ROMS), which are fixed-programmed by a master controlled burn-out process.
- Power amplifier stages. There is one of these for each relay (normally six), providing adequate current reserve to ensure relay closure, each incorporating a resistive limiter to prevent damage in the event of an accidental short-circuit. These stages are unchanged throughout the range of converter variants.

Figure 11 represents logic converter type 7-4, for use with the special 5 line coding system of ARC 44 T/R. This converter still includes the programming plug facility, to allow for modified versions of the ARC 44 covering different frequency bands, either 30-56 or 26-52 MHz. To suit this latter range, the antenna capacitance plate has been supplemented by a top tubing section (similar to that on the antenna shown in Fig.2). This extends the lower frequency limit down to 24 MHz, but restricts upper frequency to very little above the required 52 MHz.

This particular logic converter, as well as some others, incorporates delay into the input stages, whereby the converter is held inoperative until the input information has remained unchanged for about $1\frac{1}{2}$ seconds. This prevents chatter, and hence needless wear of the very fast-acting relays in following every frequency-setting passed through when the T/R changes from one frequency to another. Antenna retune is completed in only milliseconds after the $1\frac{1}{2}$ second delay period, whilst remaining functional to whatever extent the mistune is acceptable. Certain T/R equipments, such as Marconi AD 1400, incorporate an 'inhibit' line which substitutes for converter delay circuitry.

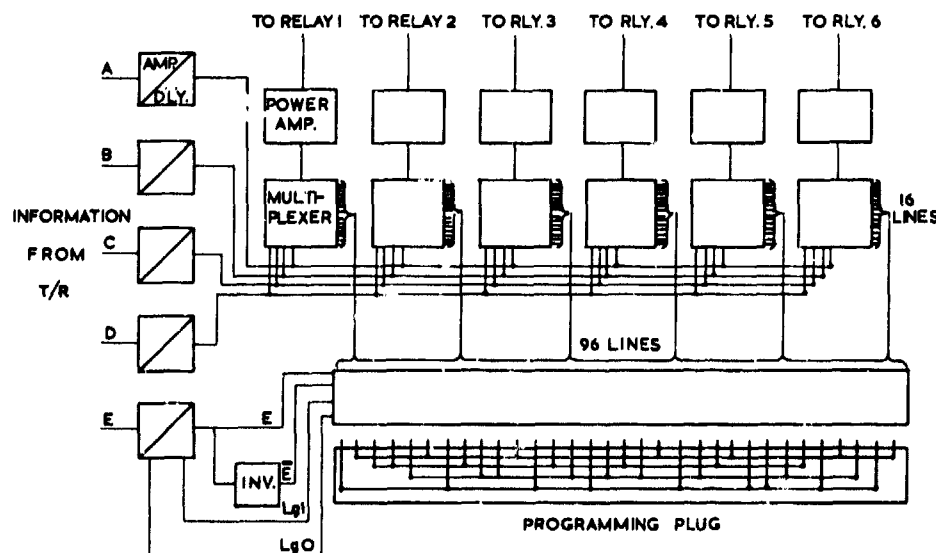


Fig. 11

There have been several special applications of the inductance-tuned antenna system described, each using the basic assembly board of coils, relays, transformer and filters as shown in Fig.12.

In one of these applications, the tuning assembly has been mounted within the glass-fibre tailcap of a helicopter, with the radiating capacitance formed of aluminium foil bonded-on to the inner surface of the tailcap. The plate area is set to produce the correct tuning capacitance to the ground metalwork at the base of the tailfin.

With this configuration, the capacitance paths are considerably longer, equivalent to greater effective height than with the blade antenna (Fig.1) as normally mounted over a relatively flat fuselage area. This increased effective height markedly improves bandwidth near the low-frequency end of the band.

In another application, there is a requirement for the normal transmission/reception on any selected frequency to be supplemented by simultaneous reception only on a fixed-frequency 'guard' channel. This has been achieved by an additional capacitance plate part-way up the antenna housing of Fig.1, fixed-resonated and coupled via the same ferrite-cored transformer to the single terminal connector. Sensitivity on the guard channel is rather low, but acceptable.

An antenna system very different from those described above has been evolved to cover the same frequency band of 30-76 MHz for 'homing' reception on helicopters.

For this function, variably-tuned antenna systems are not practicable, and it has proved difficult to obtain an adequate combination of bearing discrimination and signal sensitivity from a single-pattern antenna system. The practice has therefore become one of rapid left-right switching (or 'lobing') of two complementary patterns. These may derive either from two separate antenna systems, or more commonly from one in which all parts of the antenna contribute equally to both patterns.

The achievement of acceptable homing patterns generally compels placement of the antennas at the extreme forward end of the helicopter, and clear of conducting projections. As with all aircraft usage, dimensional limitations produce a preference for unipole antennas, but these are particularly susceptible to the irregular shape and erratic skin conductivity typical of helicopters.

Dipole systems have a somewhat lesser dependence on the nature of nearby metalwork, but for the frequency band 30-76 MHz, the necessary dipole dimensions are generally objectionable within the pilot's field of view, or else create other operational problems. Fig.13 shows a dipole self-resonant at about the band centre frequency, fitted onto the front of a Gazelle helicopter. Two such dipoles, left-right spaced at about $\lambda/6$, have their outputs combined after phase-shifting to produce approximately cardioid patterns, lobing-switched for homing purposes. Some, at least, of the operational objections are self-evident.

In order to provide a better alternative, experiments have been conducted using antenna elements formed of metallic film sufficiently thin to be effectively transparent, and so able to be placed directly upon the perspex canopy. The acceptable levels of light loss and scatter have been found to be determined principally at the observable junctions of conductive and non-conductive areas; by so arranging element shape that these junctions appear as true verticals, it has been found possible to gain acceptance of gold film depositions producing conductivity of about 1/10 MHO per square.

The gold film material is first deposited onto a thin acrylic (perspex) sub-strate, complete with fully conductive termination strips, which are of such size and position that opacity is acceptable. The sub-strate also carries a connecting length of transmission line formed by two thin wires embedded into grooves. The assembly is then autoclave-bonded onto the inner surface of the perspex canopy, and the bonded-in transmission line connected to a moulded perspex socket-block also bonded directly on to the canopy.

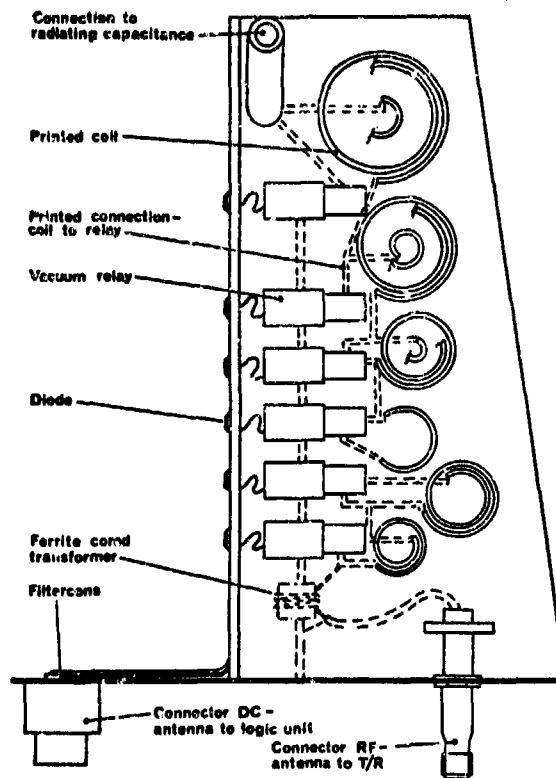


Fig.12

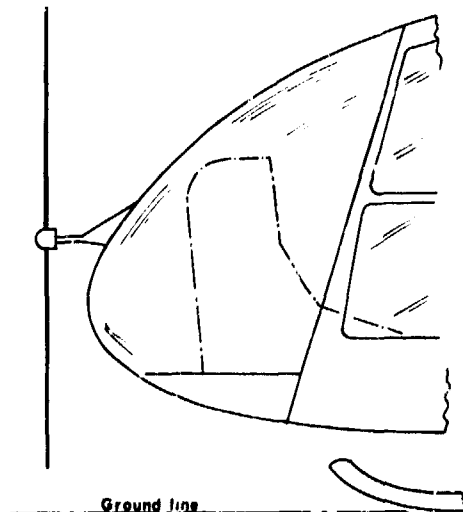
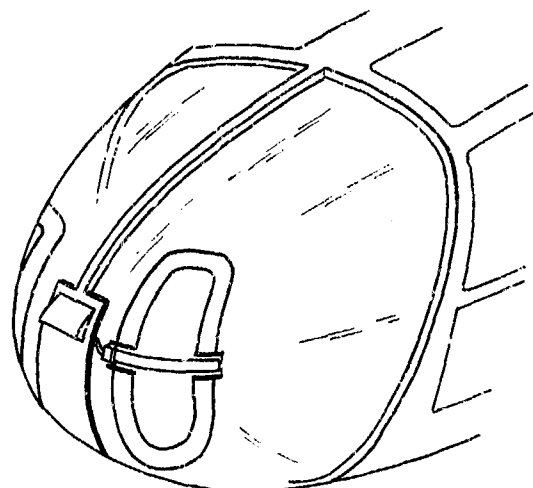


Fig.13

Investigations into a practical antenna system were initially based upon a single loop of horizontal form, split for the insertion of resistive termination at one end and signal coupling at the other, to produce left-right cardioid patterns by reversal switching of termination and coupling positions.

The investigations then became associated with Gazelle helicopters, on which the perspex canopy is vertically spanned by supporting metalwork at the centre. This compelled change to a system of two separate loops, now of vertical form, and shaped to appear as vertical opacity-boundaries upon the double-curved canopy, when viewed from the pilot's position. In Fig.14 the film conductive areas are illustrated much more densely than in reality.

Intent was to interconnect the two separate loops for combined function as a single loop, producing combined left-right patterns by termination switching as for the single horizontal loop. However, this arrangement was found to complicate optimisation of the loop configurations, and was temporarily abandoned in favour of treating each loop as a self-complete system, then merely switching over from one loop to the other.



Gold film loops on Gazelle

Fig.14

Each loop is therefore split for fixed insertion of a termination resistor and signal coupling. Within the configuration shown in Fig.14, the 1/10 MHO per-square film-conductivity produces, for each complete loop, a resistive value of some 300 ohms, the terminating resistor and transmission line impedance being of similar values. The bonded-on socket connects via a short length of flexible twin-wire transmission line to a balun, for conversion to 50 ohms unbalanced (co-axial).

Fig.15A shows the patterns achievable at 30,35,50,60 and 70 MHz, with the complementary pattern (left-right reversed) for 30 MHz also included. In all cases, sensitivity has been normalised to the forward direction 0°. Disappearance of the sideways-looking null at the lower frequencies is of no consequence, except insofar as this diminishes rate of change up to about 30° on either side of the true forward bearing. The 30 MHz pattern shown does in fact provide a sufficient bearing discrimination, but does not yet include the almost inevitable deterioration with aircraft mounting.

The patterns of Fig.15A are all for zero elevation angle; Fig.15B shows the 50 MHz pattern at increasing angles of elevation. Although sensitivity diminishes, the pattern remains gratifyingly acceptable.

This antenna system is currently being investigated under flight service conditions.

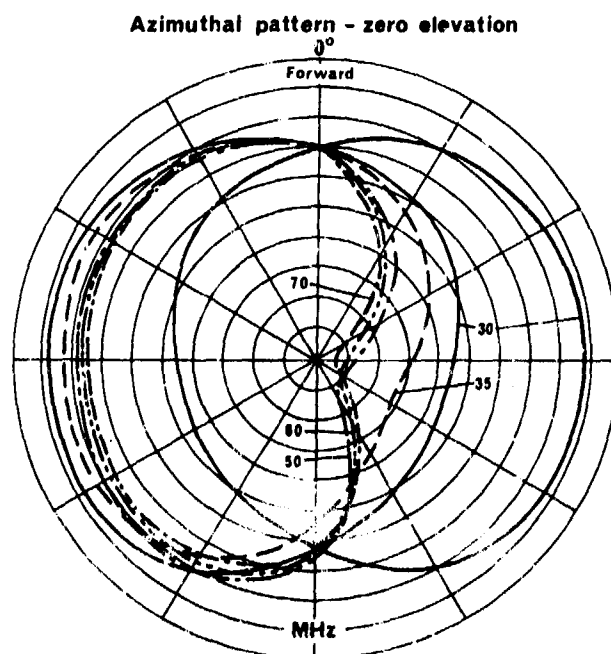


Fig.15A

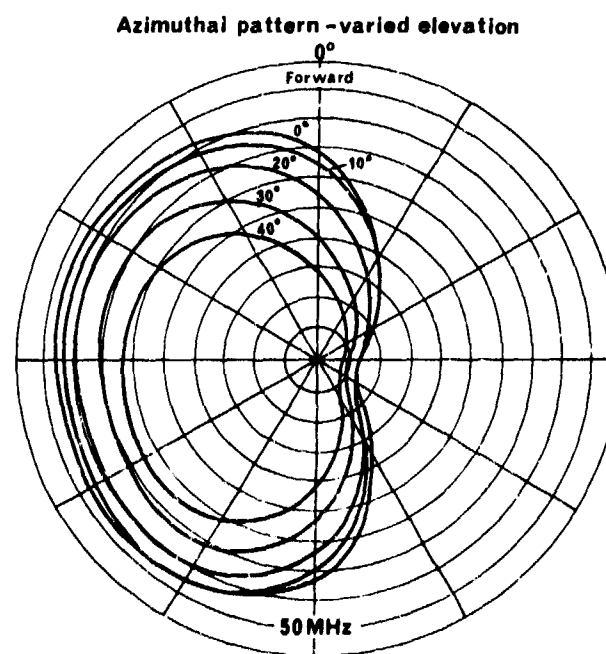


Fig.15B

DISCUSSION

R. DEASY: Please comment on the efficiency of the tuneable antenna and on the insertion loss versus mismatch loss for the tuned condition.

C.E. COOPER: Efficiency is variable depending on the Q of the inductors actually used for tuning at each frequency. The Q of the coil has a large effect on the frequency band width for any given setting of the tuner.

R.A. BURBERRY: Could you please comment on the gain of the blade aerial compared with for example a resonant monopole.

C.E. COOPER: Comparing a series of self-resonant dipoles with the blade antenna switched to each frequency, the blade gain is down compared with the dipoles by some 1-2dB at the high frequency end of the band, increasing to some 6-7dB at the low frequency end.

However, comparing a single dipole self-resonant at about the centre of the overall range covered by the blade antenna with the blade antenna switched to follow the operating frequency, dipole and blade become equal a few MHz off the dipole resonant frequency, and for greater deviation in frequency, the blade antenna shows higher gain than the dipole.

M.H. MATTES: I would like to comment that with the development of airborne antennas they are becoming more and more sophisticated and complicated. Although there is no doubt that these antennas have improved performance compared with simpler ones, they give rise to problems for those who measure antenna radiation patterns using aircraft models. For such work scaled antenna models are required and the problem arises of including within the model the circuitry which is used within the full sized antenna. Sometimes this proves impossible.

C.E. COOPER: In general, the point is accepted. However, in the case of the two communications antennas described the radiating function is simply that of a capacitance plate, involving no difficulty if scaled representation. The two different tuning coupling systems used, although physically contained within the antenna housings, are not substantially radiative. Consequently, in these instances, there is no requirement for them to be represented in scale.

TE₁₁ CIRCULAR WAVEGUIDE
FERRITE PHASERS OPTIMIZATION

Mrs A.M. DUPUTZ and A.C. PRIOU

IEEE member

ONERA-CERT Laboratoire du DERMO
 BP 4025 TOULOUSE CEDEX - FRANCE

SUMMARY

An exact analytical and numerical method has been elaborated for the complete determination of the propagating modes in a reduced size circular TE₁₁ waveguide partially or fully filled with a lossy axially partially magnetized ferrite rod.

We are presenting some computed results at 17 GHz and 9.5 GHz which allow for optimization of circular polarised phasers such as Dual Plode Phasers (D.M.P.) or Polarization Insensitive Phasers P.I.P.

1. INTRODUCTION

The electromagnetic propagation of waves in circular waveguides containing a gyromagnetic medium has been the object of many studies for the last twenty years (KALES M.L. 1953, Van TRIER A.A. th.M. 1953, CLARRICATS, P.J.B. 1957, 1959 ; WALDRONRA 1958, 1960-1963).

The purpose of this study is to determine the best choice of materials and the well suited geometry for reduced space ferrite phasers widely used in electronically scanned antenna systems.

In this paper after a short review of the analysis study of propagation in loaded TE₁₁ circular waveguides we present the numerical results obtained in KU and X band for two particular structures :

- 1) a fully filled ferrite waveguide
- 2) a partially loaded ferrite waveguide

in the two cases the ferrite is axially magnetized.

2. GENERAL TREATMENT

The analytical calculation of the propagating modes in these two structures is based on a theoretical model using the following hypothesis :

- Structure infinite along the propagating direction or finite with no terminal reflections,
- Perfectly conducting waveguide walls,
- Polycrystalline ferrite material biased by an uniform static magnetic field,
- Lossy, dispersive and homogeneous dielectric and ferrite materials,
- Linear behavior.

2.1. Analytical treatment

In these conditions, the propagation constants are obtained by solving a general equation $F(\Gamma) = 0$ with $\Gamma = \alpha + j\beta$. This equation corresponds to the determinant of the boundary conditions system. It is transcendental involving complex BESSEL functions. The analytical study was first presented at a seminar in FRANCE (DUPUTZ A.M. and PRIOU A.C. 1972).

2.2. Numerical analysis

A general method has been investigated to find a numerical solution of $F(\Gamma) = 0$ by computing (DELFOUR A., PRIOU A., GARDIOL F, CHICAGO 1972). We then count the propagating modes and characterize them as follows :

- Insertion loss and phase shift per unit length,
- Spatial field configuration and polarization state,
- Power flow distribution in any section,
- Distribution of the absorbed power in the materials.

2.3. Materials characterization

This general treatment was applied in the case of a partially magnetized ferrite. The evolution of the real parts of the permeability tensor elements μ' , K' and μ'_z is given with the RADO, GREEN SANDY and PATTON formulae (RADO GT 1953, GREEN J.J. SANDY F. and PATTON - 1971) and is represented in Figure 1 versus the internal H_i magnetic field :

$$\mu' = \mu'_i + (1 - \mu'_i) \frac{\text{th}(1,25(M/M_s)^2)}{\text{th}(1,25)}$$

$$\mu'_z = \mu'_i (1 - (M/M_s)^{5/2}) \quad K' = -\gamma M/\omega$$

μ'_i is the real part of the initial permeability ($H_i = 0$).

But, actually, we don't know the imaginary parts μ'' , K'' and μ''_z for the ferrite used. These elements had to be measured.

However, in our general computer program involving both the dielectric and magnetic losses in the ferrite, we have used the qualitative features set up by GREEN, SANDY and PATTON (GREEN J.J., SANDY F., PATTON C.E. 1971). They conclude that, when $\frac{\omega_M}{M} < 0,75$, we can describe the loss of the partially magnetized state by a single parameter μ''_i , value of μ'' in the demagnetized state. We let then :

$$\mu'' = \mu''_z = \mu''_i \quad ; \quad K'' = 0 \text{ in the range : } 0 \text{ to } 50 \text{ oe.}$$

3. GEOMETRICAL OPTIMIZATION IN KU BAND

3.1. Partially loaded waveguide

A ferrite rod (radius b) is located on the axis of a reduced size circular waveguide (inner radius $a = 3 \text{ mm}$). The ferrite rod is surrounded by quartz dielectric ($\epsilon = 3,8$; $\text{tg}\delta = 2 \times 10^{-4}$). The TE_{11} mode is then the only propagating mode in the quartz loaded waveguide.

The L.T.T. 6108 nickel ferrite characteristics are :

$$M_s = 0,46 \text{ T} ; \epsilon_f = 12,6 ; \text{tg}\delta = 3,8 \times 10^{-4} ; \mu'_i = 0,85 ; \\ \mu''_i = 6 \times 10^{-3}$$

The signal frequency $f = (17 \pm 0,5) \text{ GHz}$.

Moreover the "Lignes Télégraphiques et Téléphoniques" Firm (L.T.T.) has provided us the hysteresis loop and the first magnetization curve for each ferrite.

3.1.1. $b = 1,6 \text{ mm}$ variable frequency and static field

We note the following for the two fundamental rotative modes :

- There is an increase of the attenuation constants α^+ and α^- with the frequency (Fig.2). The absorption losses of the negative rotative mode are greater than those of the positive rotative mode.

In the same figure, we have sketched the curve $\alpha = \alpha^+ + \alpha^-$ which represents the attenuation constant of a transmission P.I.P. element. If the latter has a 2 l length, the insertion loss is equal to $\alpha \text{ l}$: α remains almost constant, about $0,4 \text{ db/cm}$ in the magnetic field range from zero to 50 oe .

- The maximum value of the differential phase shift $\Delta\beta = \Delta\beta^- + \Delta\beta^+$ is equal to 100 deg/cm in the considered bandwidth (Fig.3). $\Delta\beta \text{ l}$ is then the phase shift of circularly or linearly polarized wave propagating through the 2 l length P.I.P. element.

We note, also, an appreciable dispersion over the bandwidth (16,5 to 17,5 GHz).

3.1.2. - $f = 17$ GHz ; $H_i = 50$ oe ; b variable ($0,33 < \frac{b}{a} < 0,66$)

We notice the following for the two fundamental rotative modes :

- There is a regular increase of the absorption losses versus the filling factor $\frac{b}{a}$ (Fig. 4). The attenuation constant α for the P.I.P. structure goes from 0,14 db/cm when $b = 1$ mm, to 0,54 db/cm when $b = 2$ mm.

- There is a regular increase of the relative phase shift versus b/a , the increase being more important for the negative mode (Fig. 5).

The differential phase shift has a very flat maximum for $b = 1,7$ mm and $\Delta \beta_{\max} = 111$ deg/cm.

- The figure of merit for the P.I.P. structure, defined by (Fig. 6) :

$$m = \frac{\Delta \beta_{\max}}{\alpha_{\max}} = \frac{\Delta \beta}{\alpha} H_i = 50 \text{ oe.}$$

increases when b is varying from 1 mm to 1,7 mm, and then decreases. We have $m_{\max} = 34,2$ rd/Np.

The electromagnetic field patterns and polarization state are given in a D.R.M.E. final report (DUPUTZ A.M., PRIOU A. 1972). The knowledge of the field components allows us to determine the radial distribution of the power flow per unit area through the section $z = 0$ (Fig. 7) and of the absorbed power in the materials per unit length (Fig. 8).

We therefore see that when the applied magnetic field increases, the power flow concentration in the ferrite increases for the negative rotative mode, and decreases for the positive one. This is in complete agreement with the behavior of the propagation constants :

$$\alpha^+ < \alpha^i < \alpha^-, \quad \beta^+ < \beta^i < \beta^- \quad \text{where} \quad \Gamma^i = \alpha^i + j \beta^i$$

is the propagation constant for $H_i = 0$.

The measurements were made by the L.T.T. Firm with a transmission P.I.P. element involving two ferrite rods of length $l = 3,8$ cm.

For the theoretical device, we calculated a phase shift of 360° and insertion loss of about 1,02db. While the L.T.T. Firm found for the experimental device 360° of phase shift and 0,8 to 0,9 db of insertion loss. The slight difference between these results occurs probably from the rough approximation we have made for μ'' , μ_z and K .

3.2. Fully filled waveguide (with L.T.T. 6108 ferrite, radius $a = 3$ mm)

The figures 9 and 10 show the variation of attenuation constants α^+ and α^- and relative phase shifts $\Delta \beta^+$ and $\Delta \beta^-$ versus H_i field for the two fundamental rotative modes. The differential phase shift is smaller than in the previous structure and the maximum phase shift is reached for a weak field ($f = 17$ GHz, $H_i = 12,50$ oe, $\Delta \beta_{\max} = 46,8$ deg/cm, $m = 9,59$ rd/Np).

However, this structure offers a very good figure of merit, especially for the negative rotative mode. At 17 GHz we obtain : $m^+ = -81,7$ and $m^- = 298,4$. Then, it is the most convenient structure for making a circularly polarized phaser such a Dual Mode Phaser.

The manufacturer will have to make a choice :

- He realises a good power handling capability device by using the positive rotative mode though less efficient in phase shift.

- Or, he utilizes the negative rotative mode for a lower average power handling device (Fig. 12).

Finally, in Fig.11, we give the radial distribution of the incident power flow.

4. OPTIMIZATION IN X BAND

4.1. Purposes of the optimization

The purpose of our study in that band is to determine the best dielectric ferrite couple for the inhomogeneously loaded waveguide and the best geometrical definition such that the considered phasers fulfil at the following criteria :

- monomode propagation, fundamental mode
- maximum figure of merit
- low dispersion of the phase characteristics around the central frequency $f = 9,5$ GHz.

The exact frequency range extends from 9.3 to 9.7 GHz. The properties of a first selection of dielectrics and ferrite are given in table I.

In order to analyze the influence of various geometrical and physical parameters on the behavior of the phasers we consider :

- 1) a waveguide of variable radius "a" fully filled by each ferrite
- 2) a waveguide of fixed radius loaded by various ferrite dielectric combinations ; the variable is then the radius "b" ie the filling factor b/a .

4.2. Optimization results

By using the same computer programme as in part 3 we obtain the following main results.

We observe that the initial attenuation ($H_i = 0$) of a circularly polarized wave in a ferrite loaded waveguide increases quasi linearly with the magnetic loss tangent μ''/μ' of the ferrite (Fig. 13) The L.T.T. 6301-2 ferrite is the least lossy and as a result of its high saturation magnetization value ($M_s = 0,24T$) we can conclude that it will be the best ferrite for making a phase shifter. On the other hand, the 6101 ferrite characterized by high magnetic loss max be excluded :

- we notice in addition that if the radius "a" increases the attenuation decreases. However when approaching the cut-off region, the propagation of a second mode sets in. We have then to choose a value of the normalized radius $a/\lambda_0 = af/c$ giving only the propagation of the fundamental mode and we limit the study to this mode.

- figure 14 shows the effects of both the radius "a" and the frequency on the maximum phase shift $\Delta \beta_{\max} = \beta_{\max} - \beta_i$ in case of a L.T.T. 6301-2 ferrite loaded waveguide for three types of operation (anticounterclockwise and counterclockwise circular polarizations and polarization insensitive working).

The dotted line drawn indicates that the maximum value of $\Delta \beta$ corresponds to a H_i value lower than 50 oe. Beyond the value $a = 8$ mm two modes can propagate. Figure 15 to 17 represent the figure of merit $m = \Delta \beta_{\max} / \alpha_{\max}$ versus a/λ_0 for a ferrite fully filled waveguide. We deduce the optimum radius for each type of operation.

The analysis of a dielectric plus L.T.T. 6301-2 ferrite loaded waveguide yields to the following conclusions :

- when the radius "a" is greater than 6 mm, many higher order modes can propagate even if we use a low permittivity dielectric such SiO_2 .

- for a radius $a = 6$ mm, the dielectric must have a permittivity lower than that of the ferrite to obtain a single mode.

Figures 18 to 20 allow us to determine the optimum filling factor for each dielectric materials. In tables II and III we present the optimal characteristics of the reapocal phasers working at 9.5 GHz and using a maximum internal DC magnetic field of 50 oe.

5. CONCLUSION

We have proposed examples of a general method for the theoretical ferrite phasers optimization which permits from a first selection of dielectrics and ferrites to determine the best choice of materials and the well suited geometry of the device.

ACKNOWLEDGMENT

This work was supported by the "Direction des Recherches et Moyens d'Essais" from the French Army Ministry. The authors would like to express thanks to Miss A.M. DE ROBERT, B. GIMONET and A. DELFOUR who helped us for the numeral analysis of the problem.

LIST OF REFERENCES

- KALES M.L. 1953 "Modes in waveguides containing ferrites" - J. Applied Physics 24.N°5 p.604
- VAN TRIER, A.A.Th.M. 1953 "Guided electromagnetic waves in anisotropic media" Appl. Scien. Research Sect B Vol.3 p.305
- CLARRICOATS PJB 1957 " Some properties of circular waveguides containing ferrites" - Proc IEE Vol.104 Part B p.286
- CLARRICOATS PJB 1959 " A perturbation method for circular waveguides containing ferrites" - Proc IEE paper n°1796 E
- WALDRON R.A. 1958 "Electromagnetic wave propagation in cylindrical waveguide containing gyromagnetic media" - J. British I.R.E. Vol.18 Part I-II-III
- WALDRON R.A. 1960 "Features of cylindrical waveguides containing gyromagnetic media" - J. British I.R.E. Vol.20 p.695
- WALDRON R.A. and Mrs BOWE D.J. - 1963
"Loss properties of cylindrical waveguides containing gyromagnetic media" - J. British I.R.E. Vol.25 p.231
- DUPUTZ A.M. and PRIOU A. - 1972
"Etude théorique des guides TE_{11} complètement ou partiellement remplis de ferrites" - Séminaire International sur les ferrites - Mars 1972 Toulouse
- DELFOUR A., PRIOU A., GARDIOL F. 1972
"A method for the determination of all the propagating modes in a loaded waveguide structure"
IEEE-GMTT - CHICAGO 1972
- RADO G.T. - 1953 "Theory of the microwave permeability tensor and Faraday effect in a non saturated ferromagnetic material"
Physi. Review Vol.89 p.529
- GREEN J.J., SANDY F., PATTON C.E. - 1971
"Microwave properties of partially magnetized ferrites"
IEEE-GMTT 1971
- DUPUTZ A.M. and PRIOU A. - 1972
Final report DRME 71-34 130-00480 75-01
"Comportement des ferrites en grande puissance"

TABLE I

Type	Composition	FERRITES						DIELECTRICS		
		Ms(T)	ΔH Gs	ϵf	$\operatorname{tg} \delta f$	$\mu'1$	$\mu''1$	Composition	ϵd	$\operatorname{tg} \delta d$
6101	NiZnCr	0,242	23	10,9	$0,5 \times 10^{-3}$	0,78	10^{-2}	SiO ₂	3,8	2×10^{-4}
6301	MgMn	0,203	3	12,6	$0,5 \times 10^{-3}$	0,77	$2,9 \times 10^{-3}$	BaO	6,4	4×10^{-4}
6301-1	MgMn	0,223	3,6	12,7	$0,3 \times 10^{-3}$	0,73	6×10^{-4}	Al ₂ O ₃	9,4	5×10^{-4}
6301-2	MgMn	0,240	3,3	13,1	$0,2 \times 10^{-3}$	0,69	5×10^{-4}	TiO ₂ - 2%O	15	2×10^{-4}
6307	MgMnTiNi	0,179	7	13,7	$0,3 \times 10^{-3}$	0,82	$1,5 \times 10^{-3}$	BaTiO ₃	35	4×10^{-4}
								TiO ₂	85	$4,5 \times 10^{-4}$

TABLE II

Type of operation	Waveguide fully filled with L.T.T. 6301.2 ferrite - $f = 9,5$ GHz							
	a optimum (mm)	a/ λ optimum	$\Delta \beta_{\max}$ (deg/cm)	α_{\max} (db/cm)	m (deg/db)	length for $\Delta \beta_{\max}=360^\circ$ (cm)	insertion losses	dispersion (deg/GHz)
Positive mode	6	0,19	- 49,5	0,034	1440	7,27	0,247	2
Negative mode	8	0,25	+158,7	0,026	6100	2,27	0,059	3
Transmission P.I.P.	8	0,25	+160,7	0,065	2473	2,24x2=4,48	0,146	13

TABLE III

Type of operation	Waveguide containing a LTT 6301.2 ferrite rod surrounded by SiO ₂ - $f = 9,5$ GHz							
	a optimum	a/b optimum	b optimum (mm)	$\Delta \beta_{\max}$ (deg/cm)	α_{\max} (db/cm)	m (deg/db)	length for $\Delta \beta_{\max} = 360^\circ$	insertion losses for $\Delta \beta_{\max}=360^\circ$
Positive mode	6	0,80	4,8	- 54,3	0,024	2250	6,64	0,159
Negative mode	6	0,80	4,8	+157,8	0,025	6250	2,28	0,057
Transmission P.I.P.	6	0,60	3,6	+ 96,5	0,038	2445	3,73x2=7,46	0,143

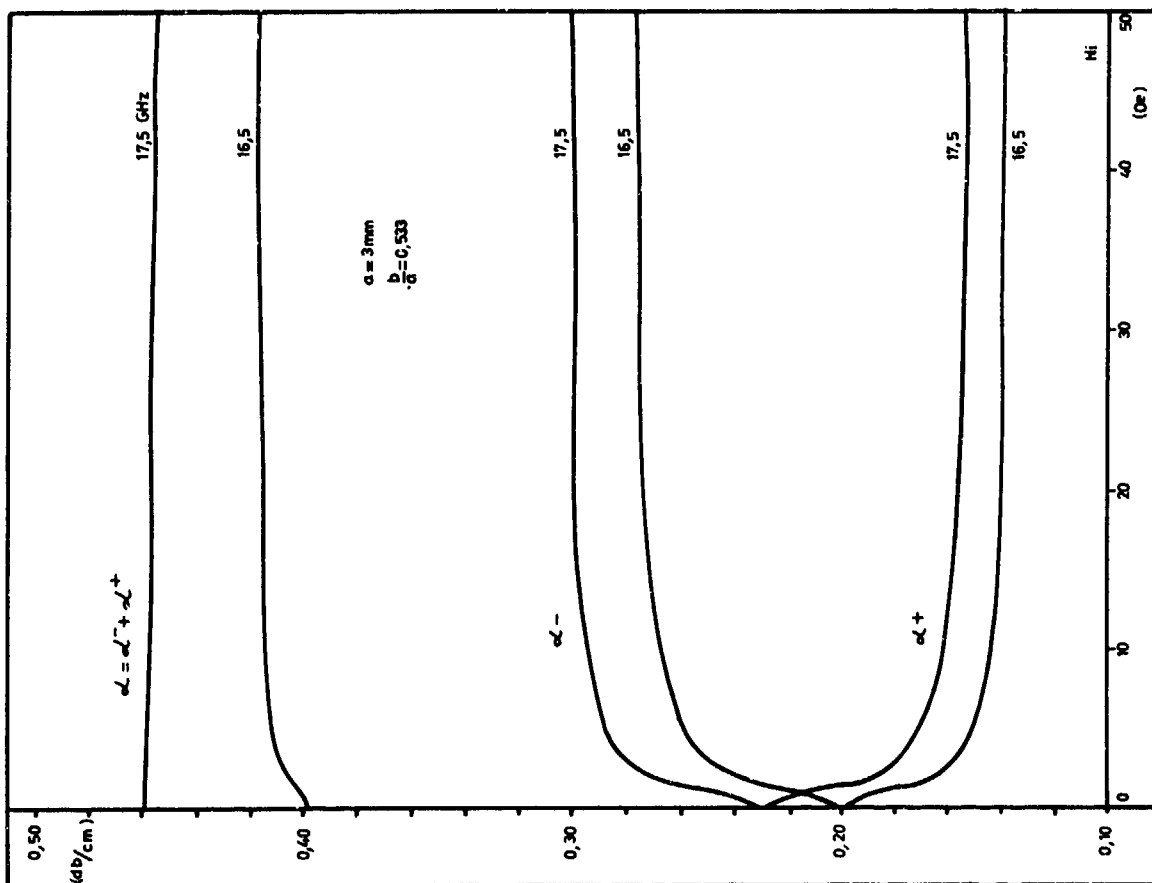


fig. 2: INSERTION LOSS PER UNIT LENGTH

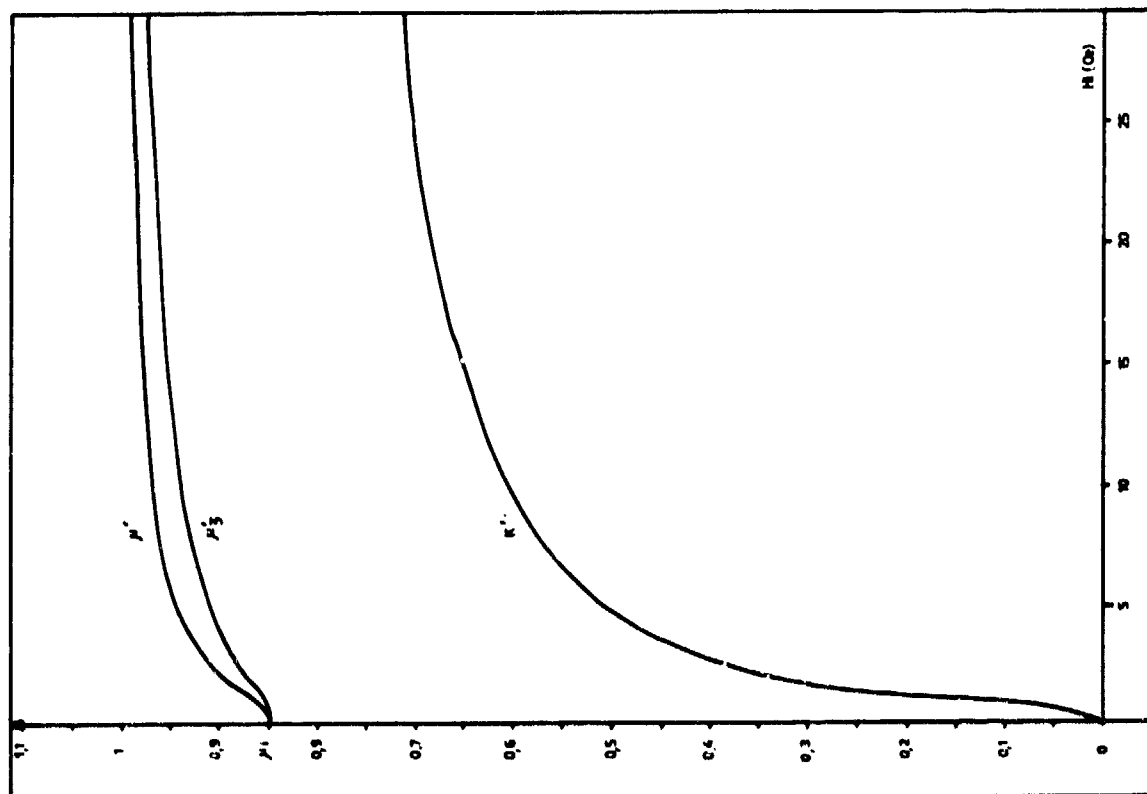


fig. 1: Evolution of the real parts of the LTT 6108 ferrite permeability tensor at 17 GHz

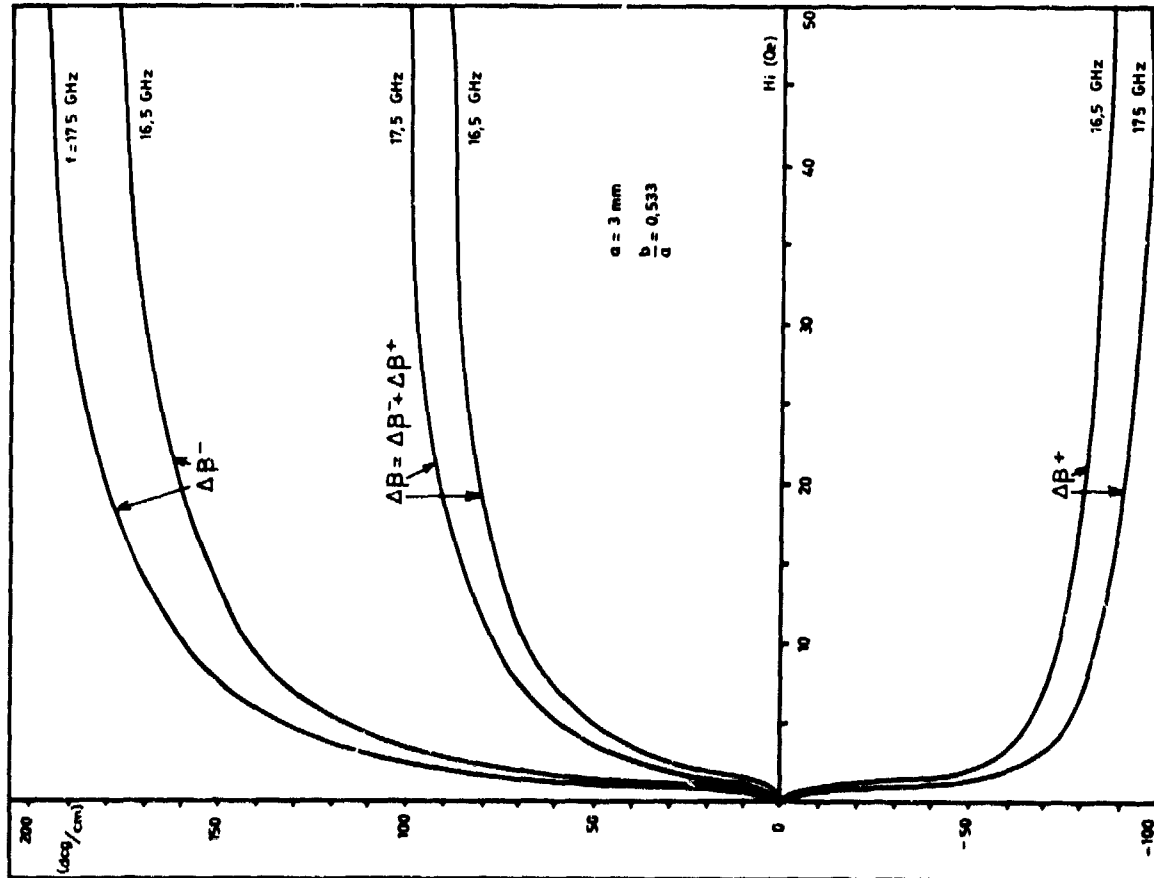


fig. 3: PHASE SHIFT PER UNIT LENGTH

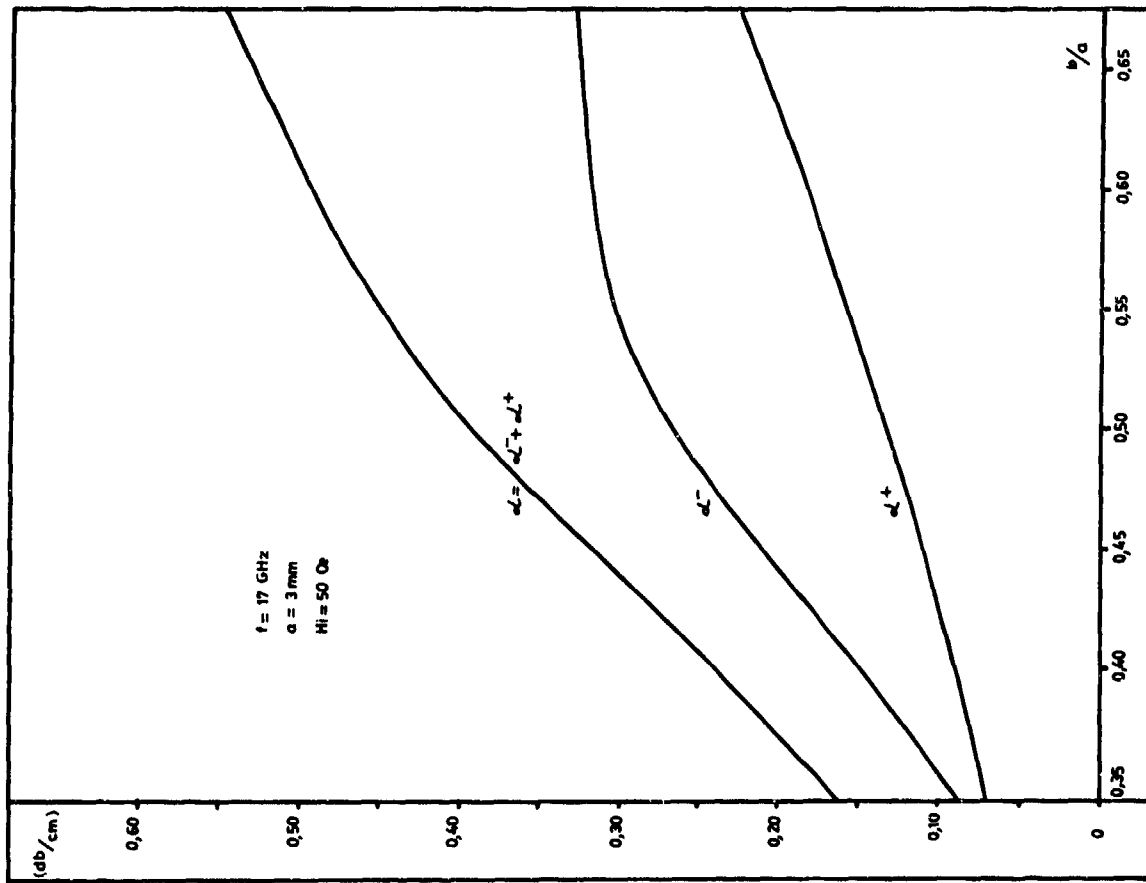


fig. 4: INSERTION LOSS PER UNIT LENGTH

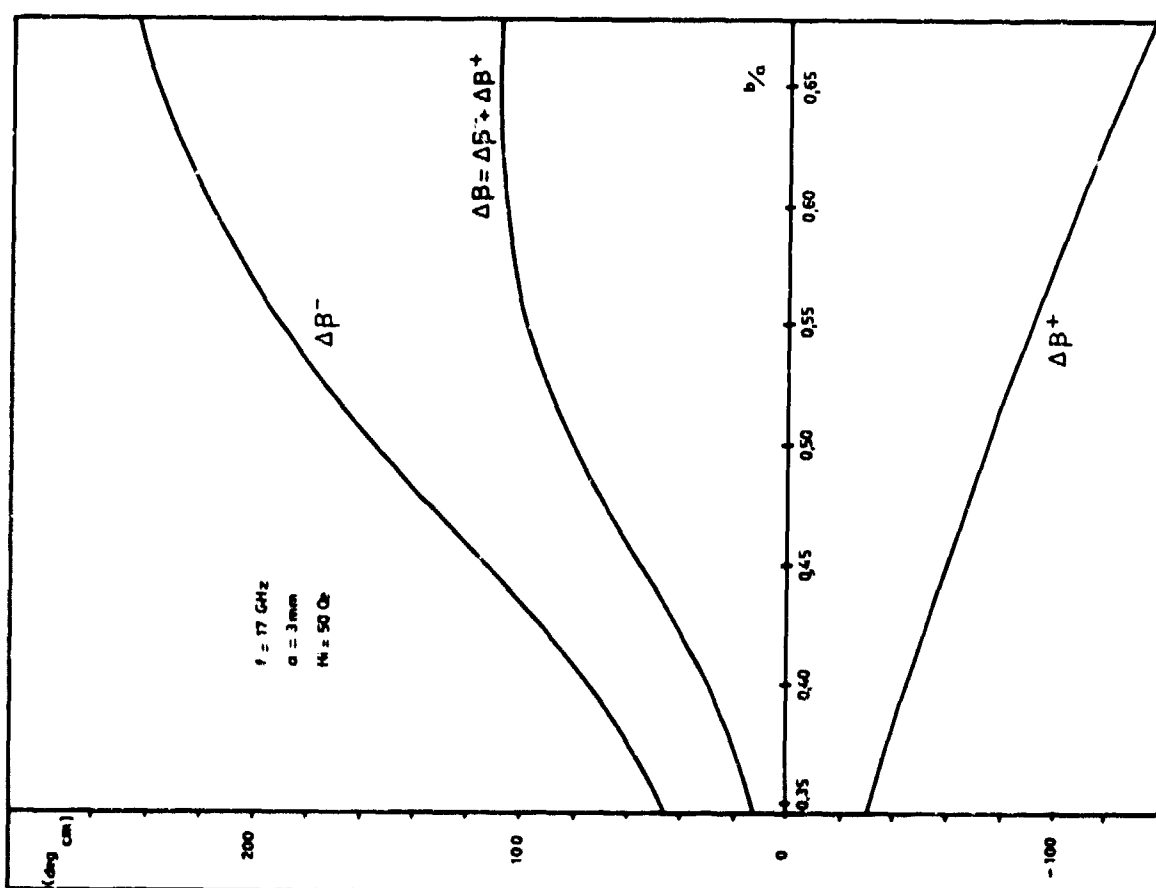


fig. 5: PHASE SHIFT PER UNIT LENGTH

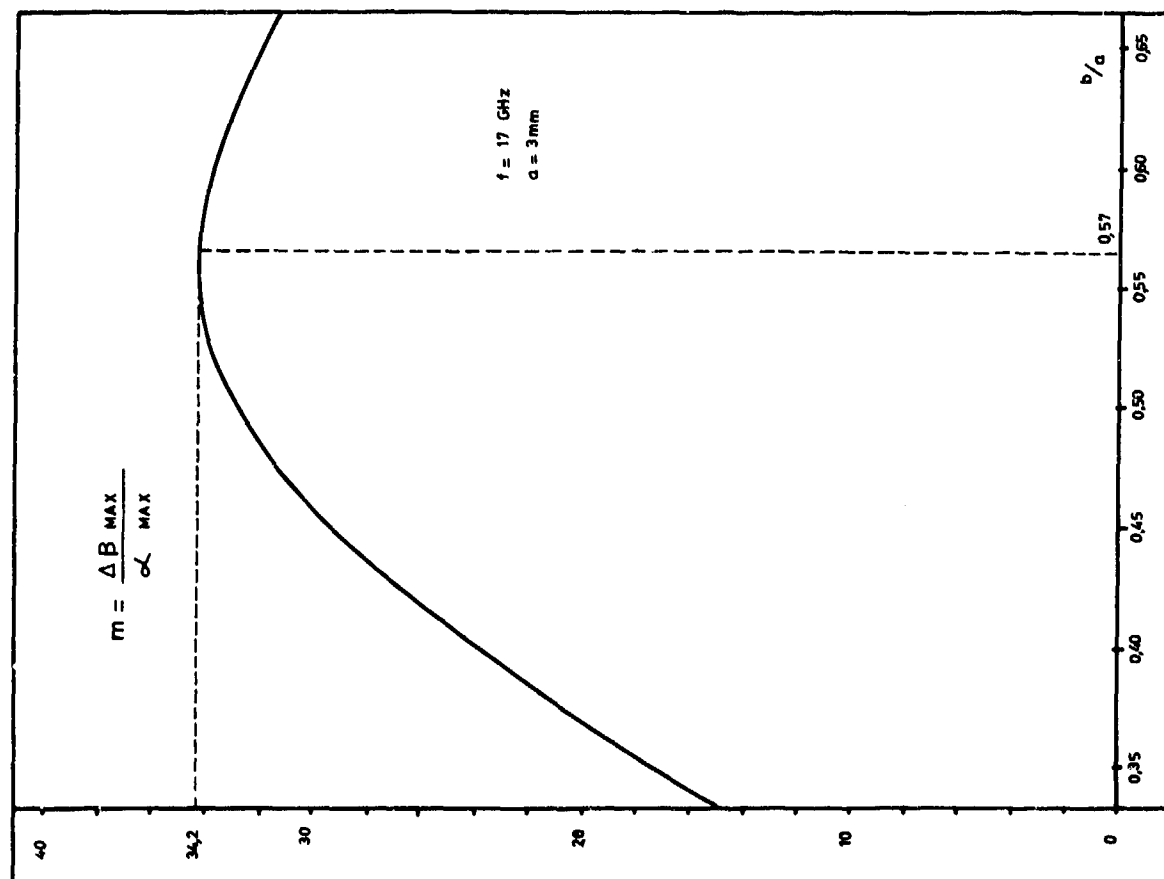
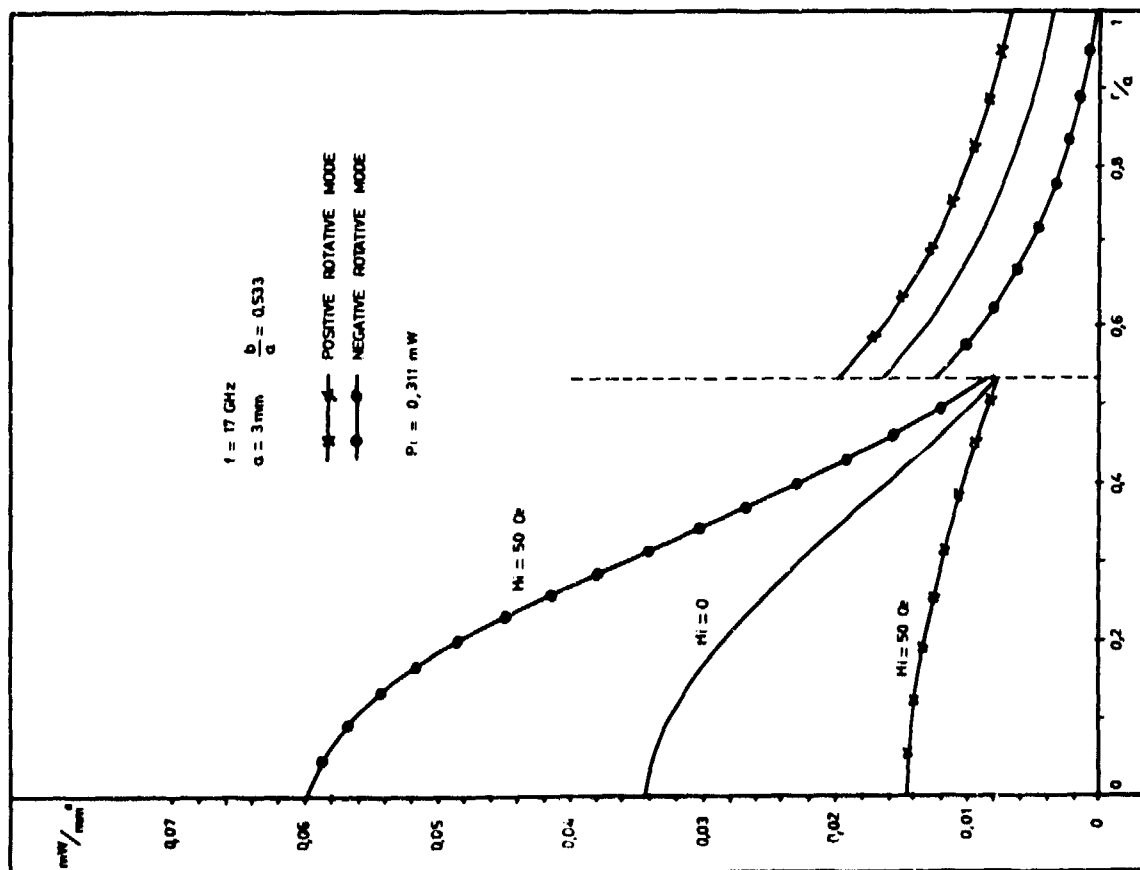
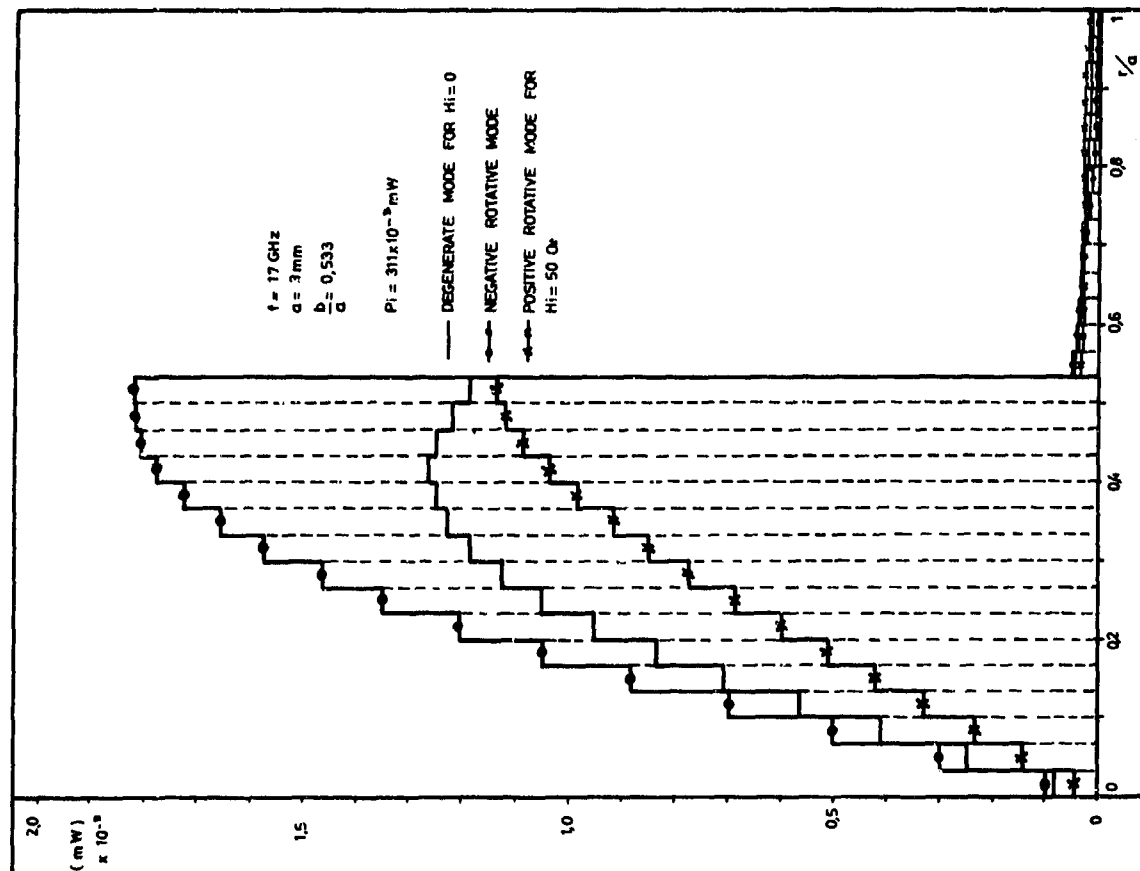


fig. 6: FIGURE OF MERIT OF THE P.I.P.

fig. 7 : POWER FLOW PER UNIT AREA THROUGH THE SECTION $z = 0$ fig. 8 : RADIAL DISTRIBUTION OF THE ABSORBED POWER BETWEEN THE SECTIONS $z=0$ AND $z=1 \text{ cm}$

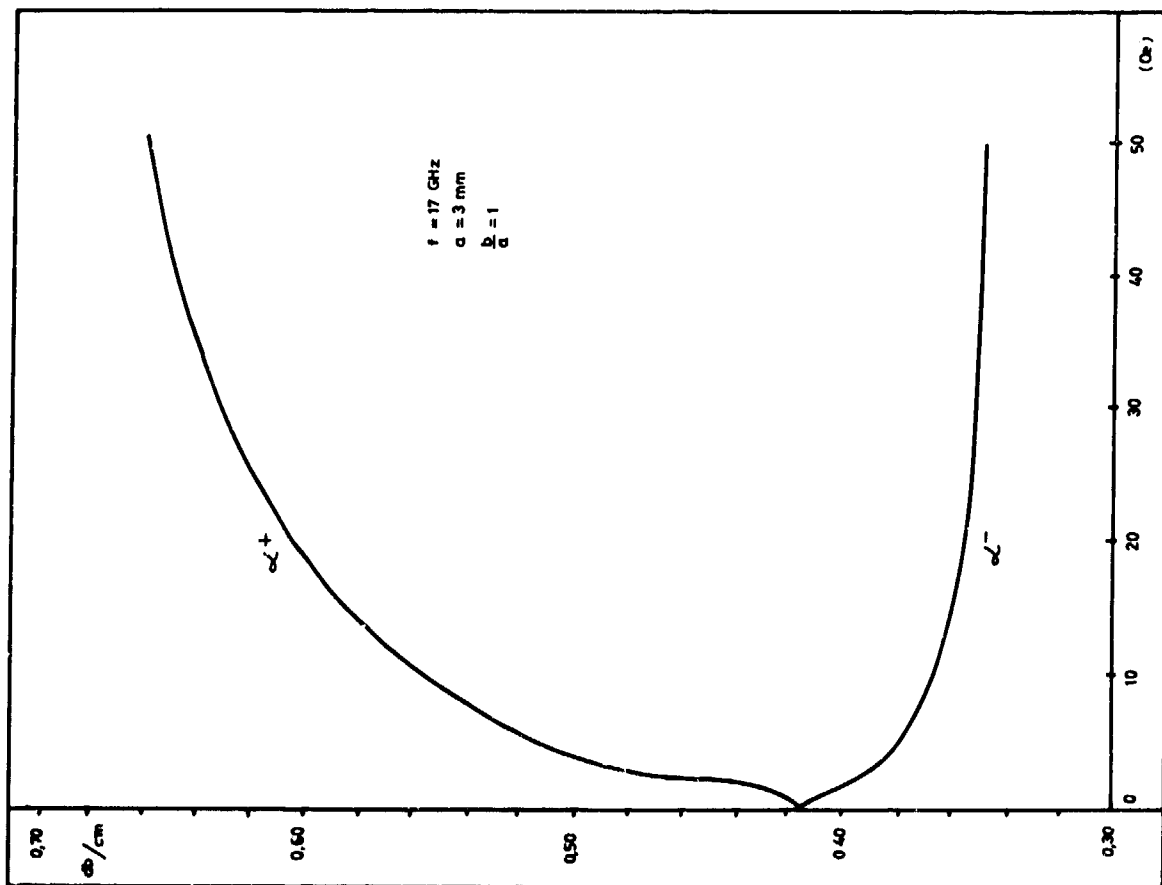


fig.9 : INSERTION LOSS PER UNIT LENGTH

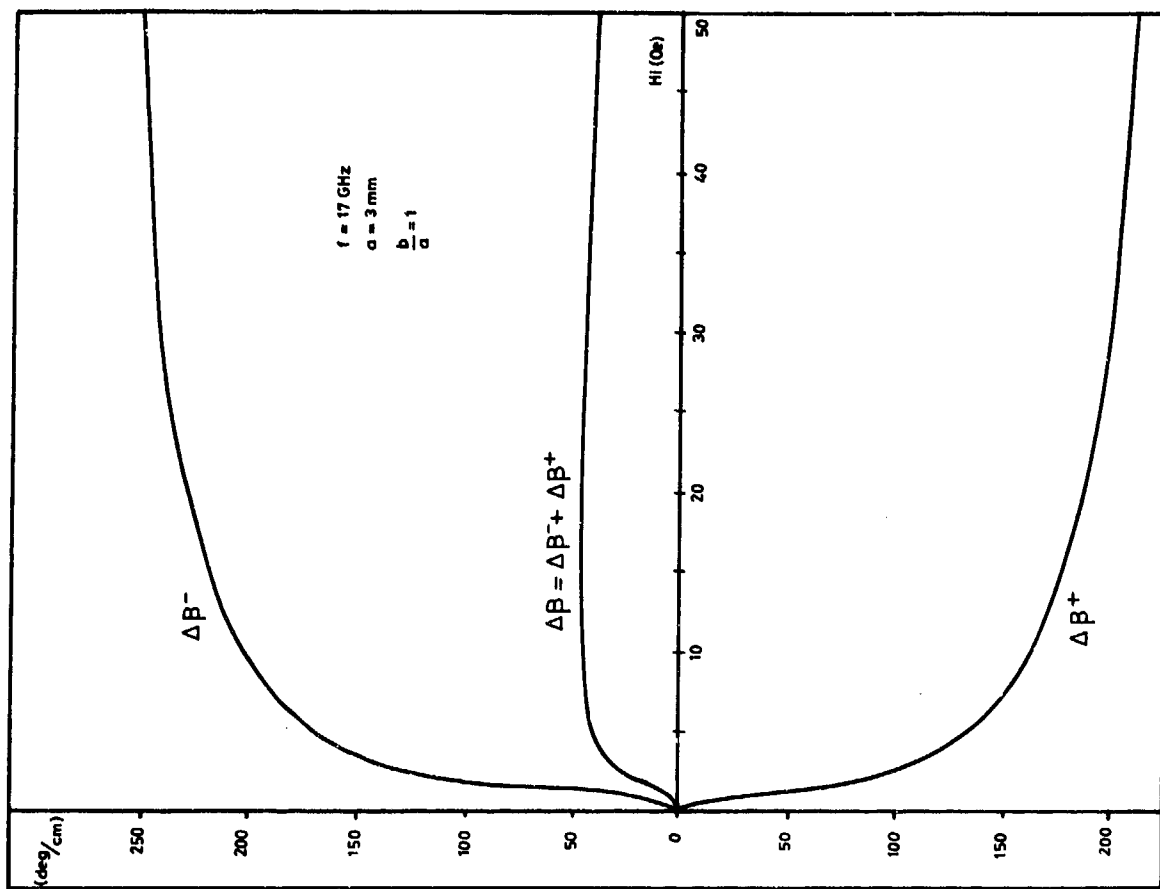


fig.10 : PHASE SHIFT PER UNIT LENGTH

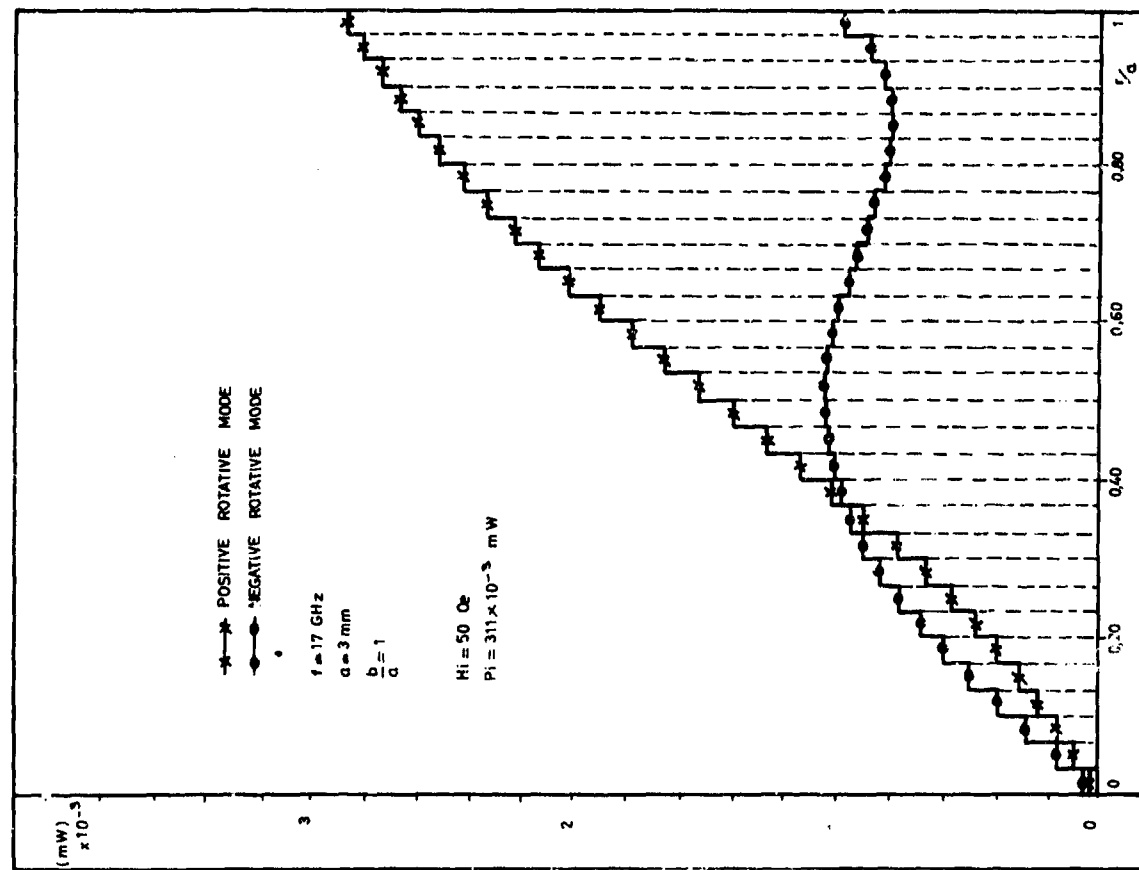


fig. 12: RADIAL DISTRIBUTION OF THE ABSORBED POWER BETWEEN THE SECTIONS $Z=0$ AND $Z=1 \text{ cm}$.

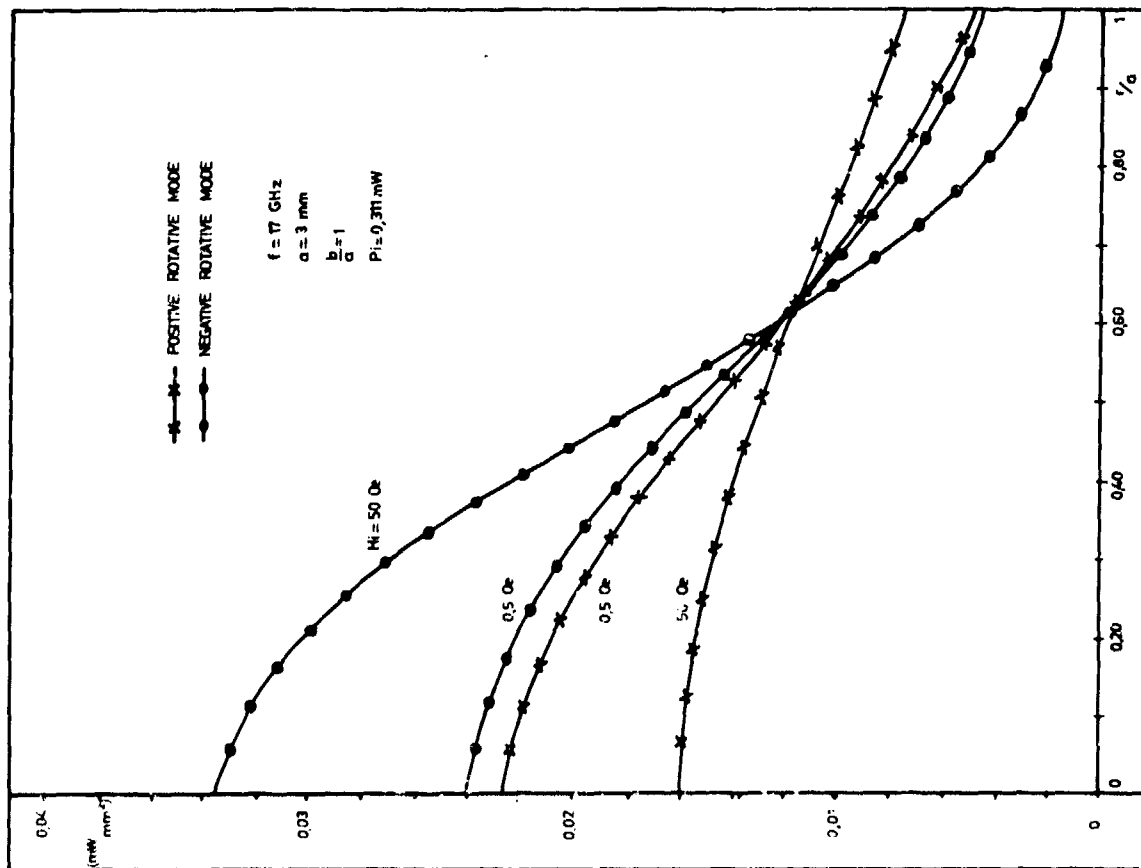


fig. 11: POWER FLOW PER UNIT AREA THROUGH THE SECTION $Z=0$

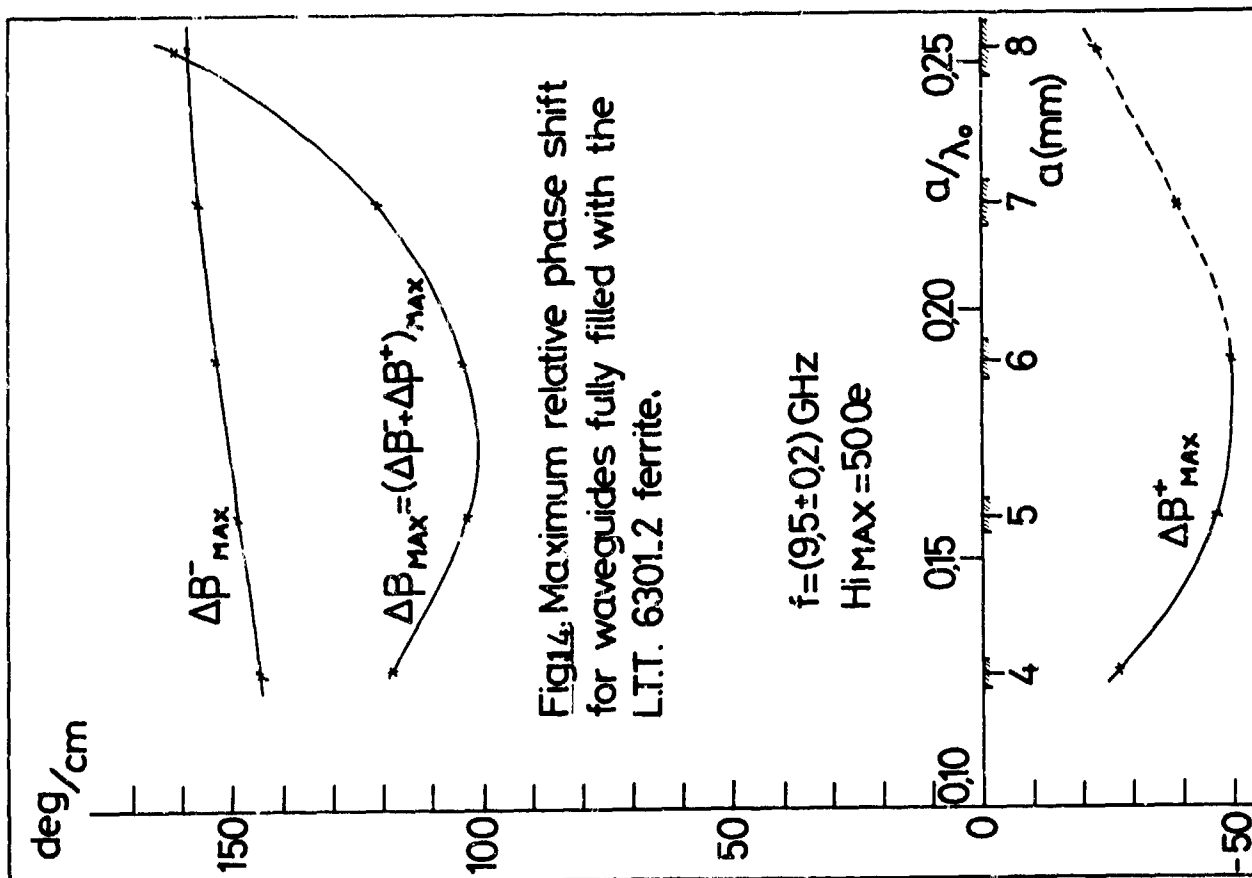
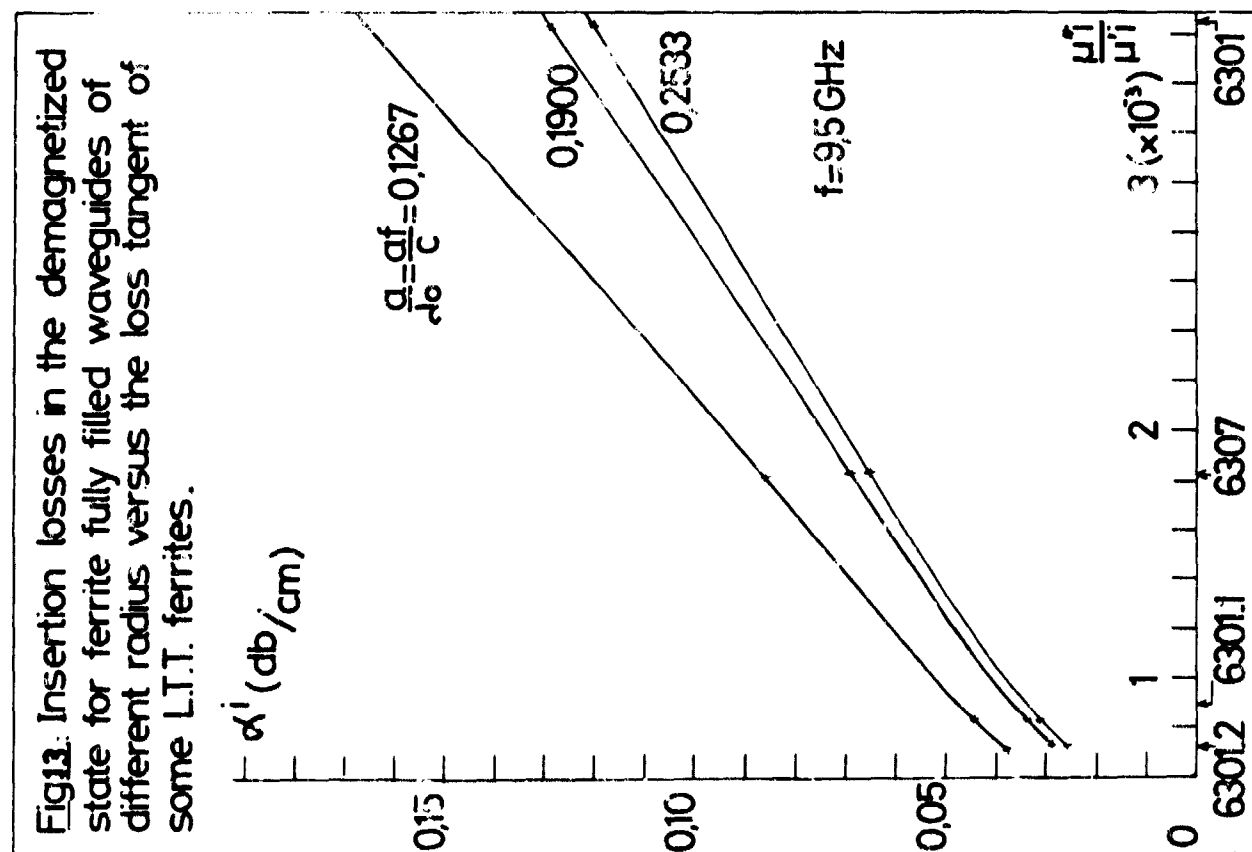


Fig.15. Circularly polarized phaser using the fundamental positive rotative mode in a ferrite fully filled waveguide section.

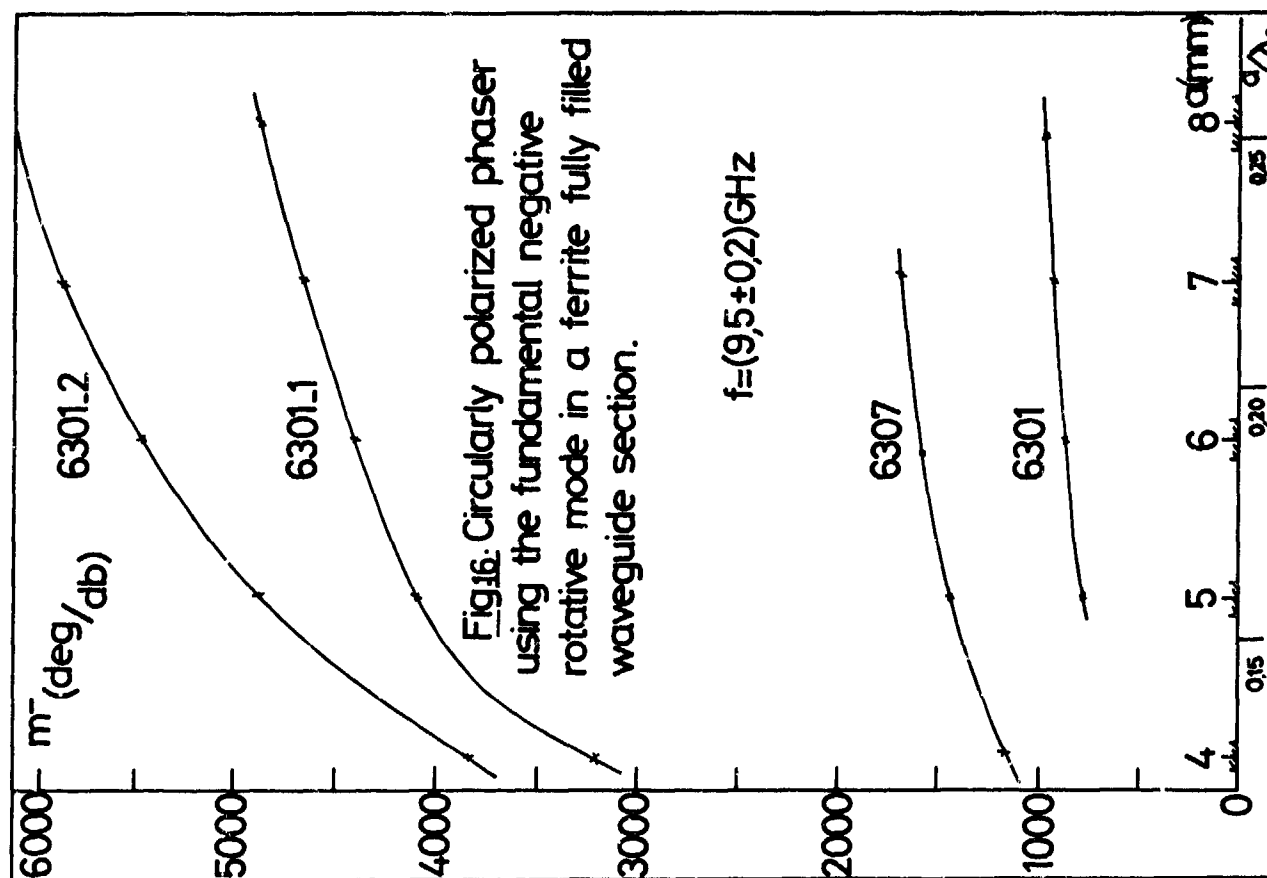
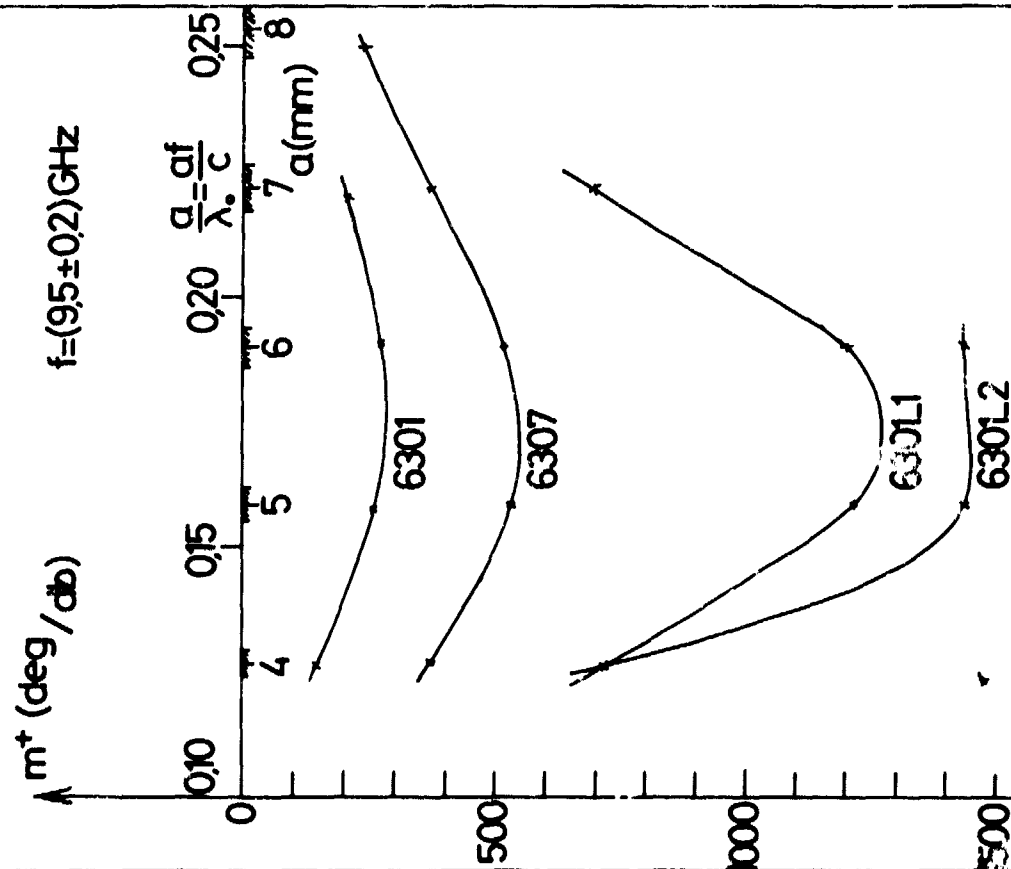
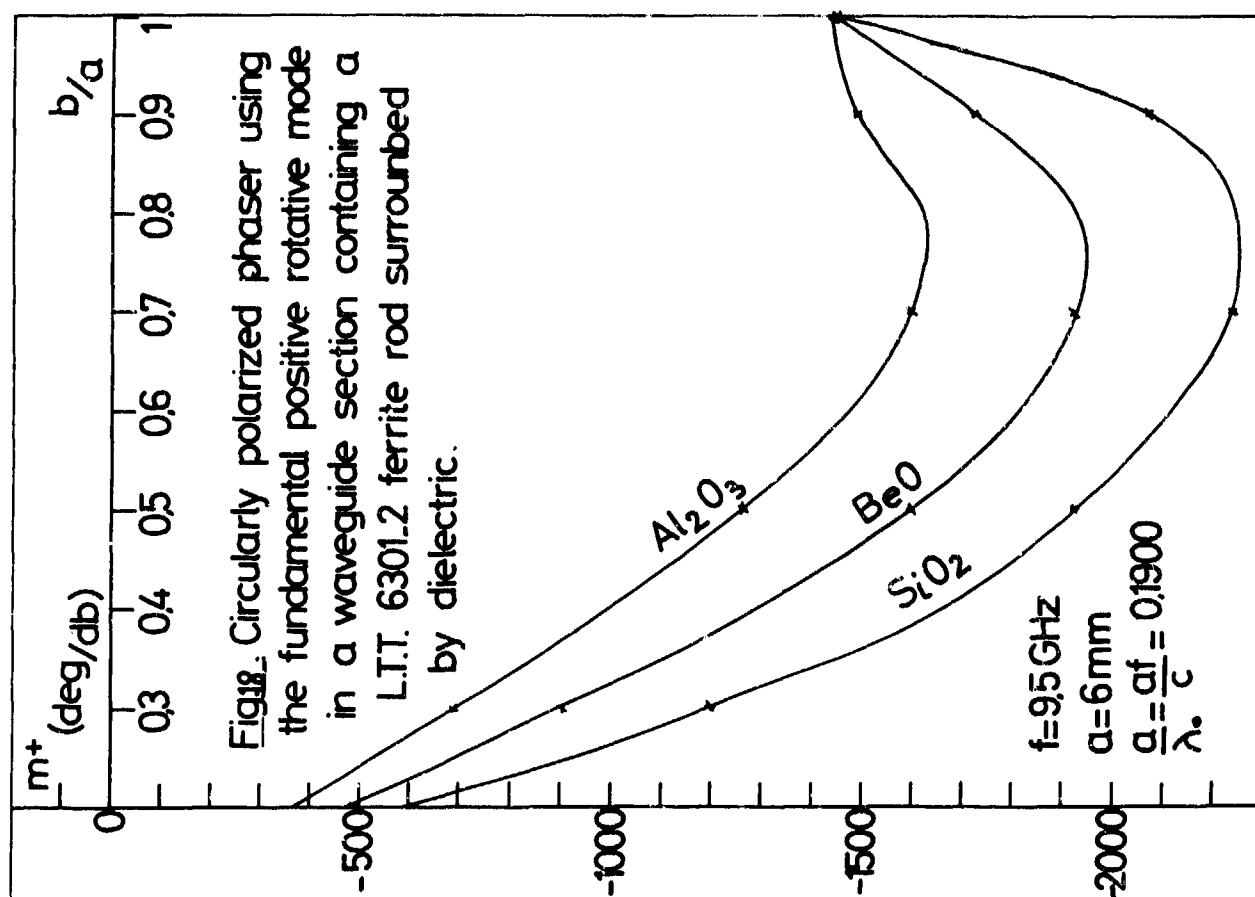
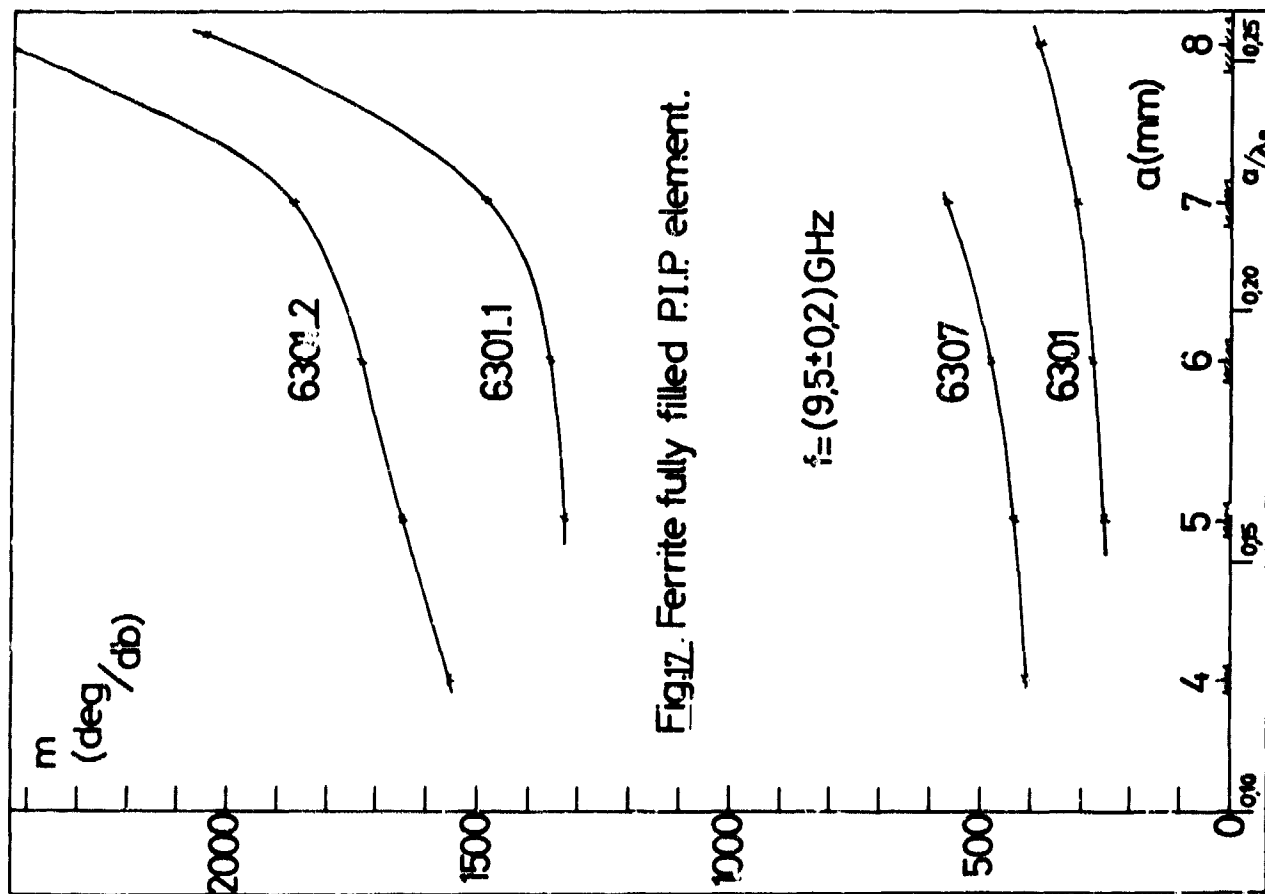
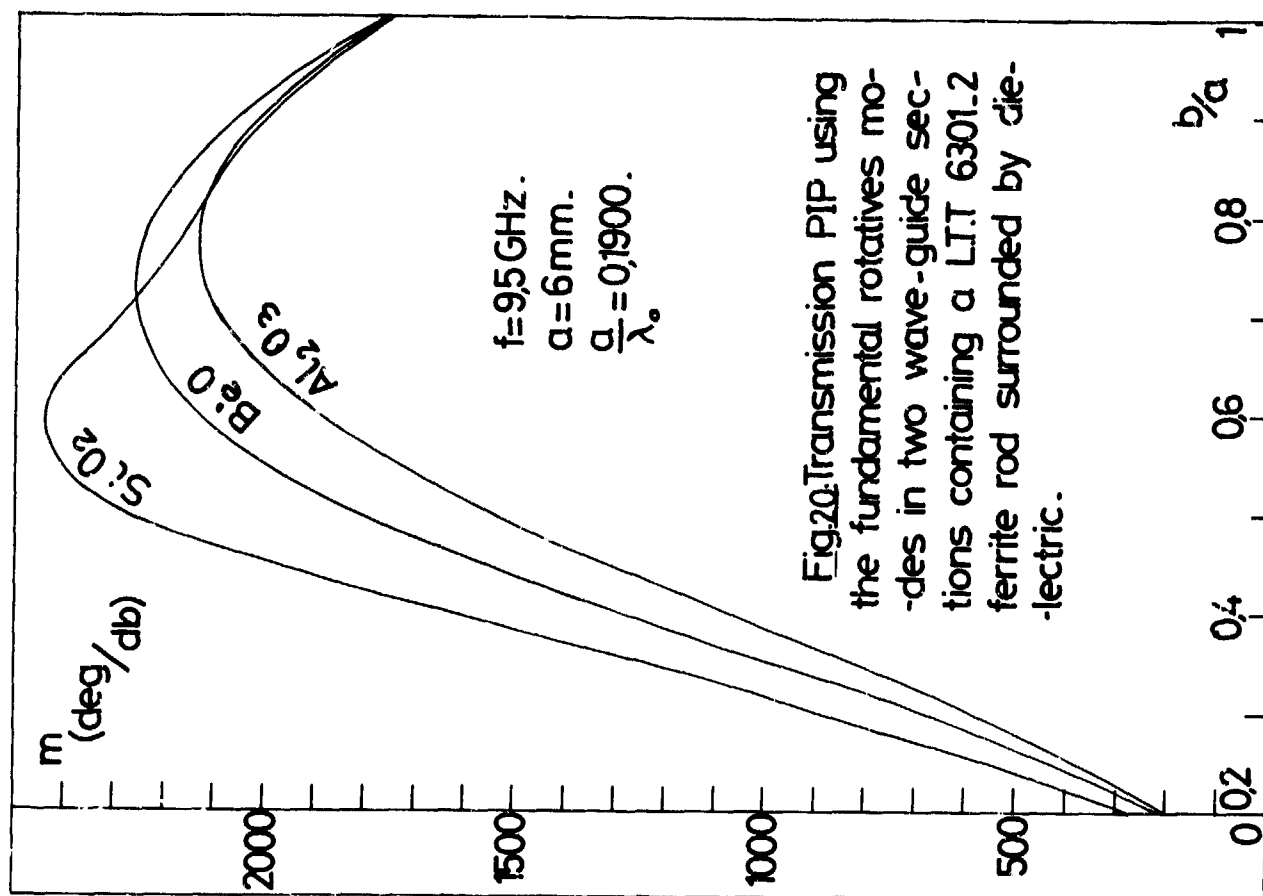
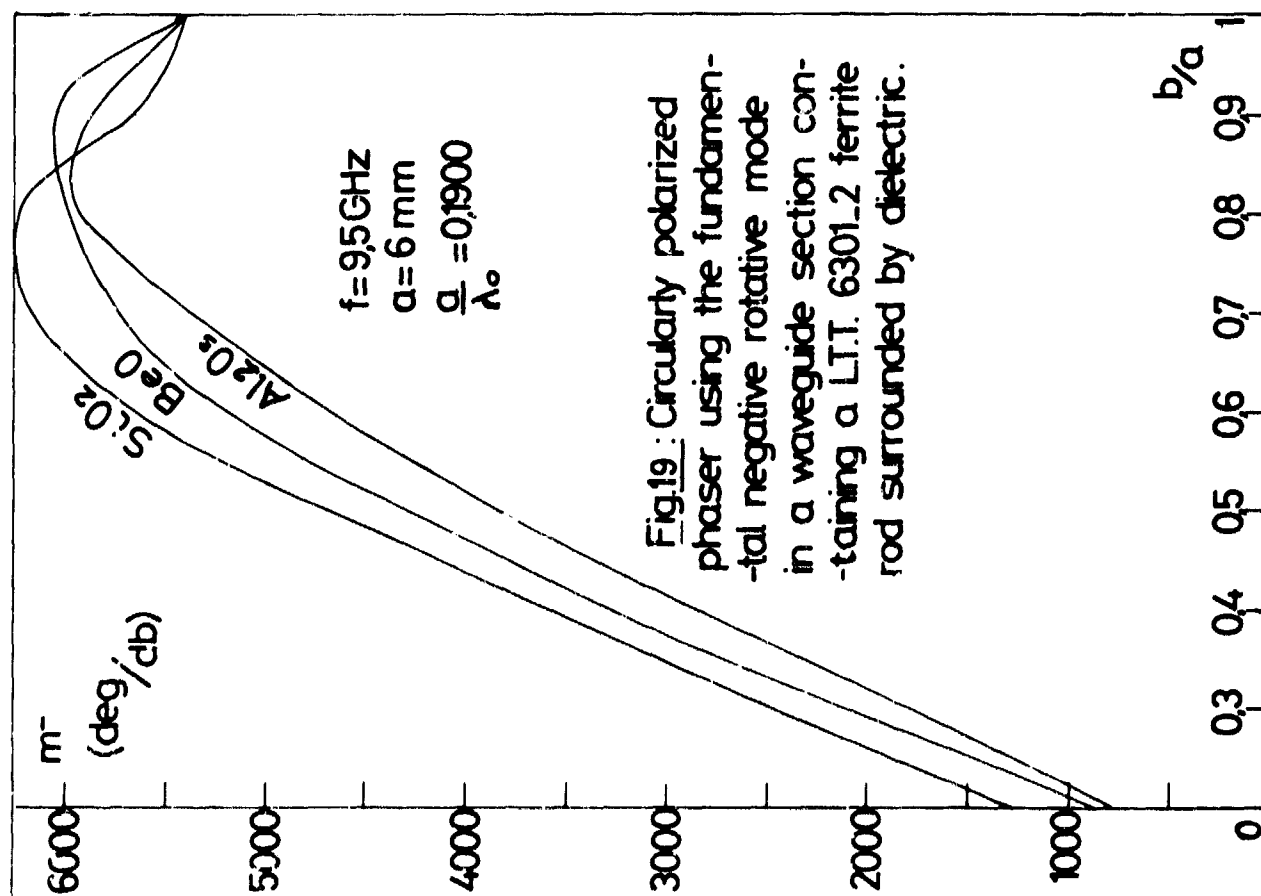


Fig.16. Circularly polarized phaser using the fundamental negative rotative mode in a ferrite fully filled waveguide section.





A CROSSED-SLOT BELT ARRAY ANTENNA FOR SATELLITE APPLICATION

R. Breithaupt, B. Clarke, D. Waung*
 Department of Communications
 Communications Research Centre
 P.O. Box 490, Station A
 Ottawa, Canada K1N 8T5

SUMMARY

A partially complete feasibility study of the design and fabrication of a fixed beam, circular-polarized belt array for possible use as a telemetry/command antenna (2 GHz) on a geostationary communications satellite, is described. This application requires a toroid-shaped coverage pattern for use when the satellite is not oriented on station.

The belt array of circular-polarized elements used is fed using travelling-wave excitation by a thin plated dielectric waveguide of .060 in. x 2.350 in. cross-section. After some measurements on round hole radiating elements, crossed slots with external dielectric loading were finally chosen. These elements were matched and characterized in terms of scattering parameters in an active array environment.

Measured performance of this array was less than expected due to significant effects of tolerance and placement of the external dielectric loading on individual elements. Subject to these element design limitations, a lightweight travelling-wave fed structure appears to offer a reasonable alternative to the usual parallel fed belt array, for this application.

1. INTRODUCTION

All synchronous geostationary communication satellites require a nearly omnidirectional telemetry and command (T&C) antenna for initial acquisition purposes during transfer orbit, or for occasions when the usual on-station spacecraft orientation is sufficiently perturbed. The normal requirement is for circular polarization, so that a polarization rotation capability is not imposed on the ground station. Therefore in choosing a T&C antenna for such an application, a basic choice exists between a single antenna system which has a cardioid-shaped pattern, and a two antenna system which has a moderate gain antenna for on-station operation plus a lower gain antenna with toroid-shaped coverage. An example of a spacecraft with this coverage requirement is the joint Canadian-U.S. Communications Technology Satellite (CTS), to be launched in late 1975. Nulls in this case are in the direction of the spacecraft front deck and apogee motor.

The purpose of this work is to examine the feasibility of a particular type of antenna which can provide the toroid-shaped coverage in a two-antenna system for spacecraft T&C at frequencies 2.1 and 2.3 GHz. A spacecraft configuration similar to that of CTS will be assumed throughout this paper and this is shown in Fig. 1. Such an antenna is usually thought of as a circular belt array of elements around the spacecraft body. For a CTS type of application, however, the spacecraft body is not circular-cylindrical, which introduces element phasing difficulty in producing a uniform far-field pattern in the plane of the belt. As a consequence, a logical location for this antenna would be around the lower end of the apogee motor skirt in the form of a circular belt of diameter about 44 in.

A basic choice between a parallel and a travelling-wave feed, or some combination thereof, must be made for the elements of this fixed-beam belt array. The parallel feed is usually chosen, as the bandwidth limitation then is simply that of the radiating elements. Cavity-backed spirals or crossed dipoles have been used as radiating elements, although microstrip elements now appear to offer the best compromise between electrical performance, light weight, and structural integrity.

The present study is being made to explore the advantages and limitations of a combined series-parallel feed using a plated solid-dielectric waveguide travelling-wave feed of reduced height and cross-section .060 in. x 2.35 in. This would be light weight and have good structural integrity, as for the microstrip case. Apertures placed in the appropriate location in the broad wall of the waveguide are used to provide the desired circular polarization. Two types of aperture were considered, the round hole which was found to radiate insufficient power, and the crossed slot with external dielectric loading, which is the configuration adopted in this application.

Following sections of this paper deal with the array element, array analysis, array design and measured results, respectively.

2. ARRAY ELEMENTS

2.1 Element Characterization

It is well known that an aperture, such as a round hole or crossed slot placed appropriately in the broad wall of a rectangular (dominant mode) waveguide will radiate circular polarization, and have directional properties^{1,2,3}.

The scattering matrix of such a radiator will normally contain one port for each propagating mode on either side of the waveguide feed, as well as one port for each expansion mode of the radiated field. In this case a simplifying assumption is made that the modal expansion of the radiation field consists of two orthogonal circular-polarized modes only. This simplification contains the implicit assumption that all elements see a similar environment, which implies a constant mutual coupling between elements.

* summer assistant

If the remaining four ports are numbered as in Fig. 2 then the scattering matrix S has the form shown in this Figure, which is appropriate for a directional coupler. The unknown complex coefficients A and B must then be determined for the element used. Conservation of energy, and the assumption of a lossless element require that $|A|^2 + |B|^2 = 1$. In order to measure A , define a reference plane for port 1 and 2 across the waveguide, centered on the element aperture. The reference plane chosen for radiated energy is not important except that it must be kept constant. Note that if LHC polarization for instance, is desired in the transmit case, then any energy incident on port 2 (i.e. a_2) will contaminate the desired polarization and make it elliptical. Therefore all element matching must be done on the feed side of each element unless polarization modification is desired. The port impedances are assumed normalized so that the net real power through a port is $(|a_n|^2 - |b_n|^2)/2$.

This array was designed using experimentally derived data for the radiating elements, as no analytical results appeared available, and because preliminary data could be more economically obtained experimentally. Three different measurements can be made to determine the four unknowns in A and B as a function of element parameters and frequency; these are transmission measurement, and near/far field measurements. Most of these were done in an active environment using an array of six identical matched elements spaced a guide wavelength apart. If the transmission coefficient $|A|$ is sufficiently small ($-20 \log |A|$ is > 1 dB say), then $|A|$ may be measured using near-field scan data or by a transmission loss measurement. $\arg(A)$ is obtained from near-field scan data for all cases. $|B|$ can be obtained as $|B| = (1 - |A|^2)^{1/2}$ or from far field pattern and gain measurement of the six element array. $\arg(B)$ can be measured by a phase comparison of different single elements. It is also possible to measure a combination of $\arg(A) + \arg(B)$ from the phase slope of an array of elements of continuously varying size.

2.2 Belt Waveguide

Since the radiating elements to be described are an intimate part of the waveguide feed itself, a very brief description of the waveguide used will be given here. Double-clad teflon/glass board (3M Co. K-6098-22) was used. This material was milled to 36.6 in. x 2.35 in. size, and the edges were electroless plated and electroplated to give approximately .001 in. copper on the side walls. This was operated in the dominant rectangular waveguide mode. A mean relative dielectric constant, as derived from guide wavelength at 2.20 GHz, was found to be 2.52. Waveguide loss was measured both by reflection and transmission methods, and found to be 1.67 dB/m. at 2.2 GHz, as compared to a theoretical value based on a 3M published $\tan \delta = .0018$, of 1.17 dB/m.

A two-step coaxial impedance transformer was incorporated in a 3 mm coax-wg transition, which had a VSWR of < 1.4 from 2.1 - 2.3 GHz the guide having a characteristic impedance of about 20 ohms, depending on the definition used. No attempt was made to optimize this transition in terms of weight, and it is shown in Fig. 3. A very simple resonant type of low power waveguide load was used in the final belt fabrication. This is also shown in Fig. 3 and consists of a narrow transverse slot in the waveguide partially filled with resistive sheet material. A non-protruding load is required for final belt assembly.

2.3 Round Hole Element

A round hole was initially thought to be a good candidate as a radiating element because of ease of fabrication. In the absence of published results for this element, it was characterized experimentally. This revealed that the maximum power radiated by a hole of maximum diameter ($d = 1.19$ in.) in the waveguide chosen, is 3%, which is too small for the moderately short array in question. The measured coupling characteristic is given in Fig. 4. The holes were placed in the waveguide at a transverse distance from one side of

$$x = \frac{a}{\pi} \tan^{-1} (\lambda g / 2a) \\ = .601 \text{ in.}$$

where λg is the guide wavelength at 2.20 GHz and a is the width of the waveguide.

This is the approximate location for circular polarization^{1,2}. The largest hole (diam. = 1.19 in.) had a VSWR of 2.5 and thus required matching. Far-field ellipticity (on axis) for small round holes was < 1 dB over 5% bandwidth when a $6\lambda \times 6\lambda$ ground plane was used, but deteriorated to 2 - 3 dB for large holes. Ellipticity was a strong function of the ground plane near the round hole. With no additional ground plane, ellipticity on axis was ~ 7 dB due to strong asymmetric diffraction effects of the waveguide edges. Typical E,H plane radiation patterns of the round hole on a $6\lambda \times 6\lambda$ ground plane are given in Fig. 5. A conical or pyramidal horn structure placed on the round hole element provided more directivity and better off-axis ellipticity.

It was evident that with a round hole in a drastically reduced-height waveguide the fields are restricted to the hole periphery with very little radiation as a consequence. In fact, the dielectric could be removed from a 1.19 in. diameter hole with no appreciable change in reflection or radiation.

2.4 Loaded Crossed Slot Elements

In conventional full height waveguide, one pair of crossed slots can couple more than 80% of waveguide energy into radiation. However, because of the reduced-height waveguide used here (characteristic impedance ~ 20 ohms), only slightly more energy was coupled out of a long crossed slot than from a round hole. However, by using external dielectric loading, at least 60% coupling into radiation may be achieved. The loading used consisted of Stycast (Emerson-Cuming) blocks 1 in. x 1 in. x .260 in., of $\epsilon_r = 16$. The measured coupling characteristic is given in Fig. 6. These elements, although nominally reflectionless had a mismatch increasing with slot dimension, to a maximum VSWR of 2.7, for a slot length of 1.250 in.

and as a consequence slots often required matching. A significant problem was experienced due to the large change of $\arg(A)$ with slot length. This is shown in Fig. 7, and required element spacing to be varied in order to maintain a constant phase slope of radiated field around the circular aperture. Loaded crossed-slot radiation patterns were very similar to those for the round hole. On-axis ellipticity is 2 - 3 dB and can be reduced by using matching in front of the element as suggested by Simmons⁽¹⁾. A good measurement of $\arg(B)$ alone was not made. However the phase slope of a number of matched loaded elements of smoothly varying slot length, spaced λ_g , was made and the variation of the resulting phase slope was measured. This slope is affected by both $\arg(A)$ and $\arg(B)$, and the phase change between n^{th} and $n+1^{\text{th}}$ element radiation is essentially $\arg(A_r) + \arg(B_{n+1}) - \arg(B_n)$. This was used to modify element spacing in order to produce a constant progressive phase change around the belt array. These elements are shown in Fig. 7.

3. ARRAY ANALYSIS

3.1 Analysis

It is trivial to write formulas for an array analysis which will produce equal power from each array element, in an N element array if no coupling or reflection is assumed. Assume that the scattering representation of Fig. 2 applies with A_n , B_n associated with the n^{th} element, and that for constant element spacing d , the choice of B_1 is arbitrary. In order for the radiated field amplitudes to be equal (in the absence of coupling)

$$|B_n| = |B_1| e^{-(n-1)\alpha d} \prod_{m=1}^{n-1} |A_m|$$

where α is the waveguide attenuation coefficient, and

$$|A_n| = (1 - |B_n|^2)^{1/2}$$

In order to calculate the phase of the radiated field of the n^{th} element, it is necessary to define a spacing d_n which follows each element. By starting at the feed end, radiated fields associated with each element (i.e. b_{4n} in Fig. 2 representation) may be calculated. Power lost in transmission loss P_{TX} and that to the load P_L will be

$$P_L = |b_{2N}|^2 / 2$$

$$P_{TX} = \sum_{n=1}^{N-1} |b_{2n}|^2 (1 - e^{-2\alpha d_n}) / 2$$

The far-field pattern in the plane of the belt may be found easily by summing contributions from all elements. For the case of N elements spaced equally an angle θ_g apart on a circular array of radius R , where energy is assumed not to propagate across the belt, the far field $E(\theta)$ is simply

$$E(\theta) = \sum_{n=1}^N f(\phi) b_{4n} e^{-i\beta_0 R(1 - \cos \phi)}$$

sum for $\pi/2 > \phi > 3\pi/2$ only

where β_0 is the free space propagation constant, and

$$\phi = (n-1)\theta_g - \theta.$$

$f(\phi)$ is the element radiation pattern, and θ is the far-field observation angle, $\theta = 0$ at $n = 1$.

For the present case $f(\phi) \sim \cos \phi$ for $\pi/2 > \phi > 3\pi/2$. This formula for $E(\theta)$ requires some modification when unequal spacing is used.

In choosing a combined series-parallel feed arrangement, one must find a solution which has adequate bandwidth and acceptable far-field ripple in the plane of the belt. A series feed on a belt array has the additional constraint of requiring no discontinuity in phase slope between the first and N^{th} elements. This imposes an interdependence between number of elements N , element spacing d_n , radius R , and frequency f . Most parallel-fed belt arrays excite all elements on the belt in the same phase. This is possible on a belt array but a linear phase progression around the belt extends the possibility of reducing element spacing and thus far field ripple also. In addition, since a number of frequencies exist which provide a continuous phase slope around the belt array, dual frequency operation may be possible (i.e. in this case 2.1 and 2.3 GHz is desirable).

In order to choose a feed arrangement, a program was written which examines either a one point, two point, or four point series-fed belt. In the case of the four-point feed for example, each of four identical series-fed belts covers one quarter of the circumference and these must be fed in parallel

with $0, \pi/2, \pi, 3\pi/2, 2\pi$ relative phases. The operation of this program and some calculated results are presented in the following section.

3.2 Calculations

A program was written so that one, two and four point series feeds could be examined from a ripple and bandwidth point of view. The operation of this program is as follows:

- a) Choose number of series feed points (e.g. 4).
- b) Choose a nominal spacing (e.g. $.8\lambda_g$) and nominal radius (e.g. 23 in.).
- c) At a design frequency of 2.20 GHz, the program will then choose a number of elements divisible by four, a constant element spacing, and a radius consistent with progressive phasing around the belt, assuming $\arg(A) = \arg(B) = 0$. These will be close to the nominal values requested.
- d) Choose a value for B_1 .
- e) The program calculates fractional power lost in the transmission line and load and prints out element phases and amplitudes (b_{4n}) at 2.20 GHz.
- f) Choose a frequency for far-field calculation of ripple in the plane of the belt.
- g) The program prints new element amplitude and phase, the worst ripple in each of the four quadrants around the belt, and prints pattern if desired. Return to f) if desired.

Results from this program are plotted in Fig. 8 for one, two and four point feed designs. In a CTS type application, bandwidth of ± 10 MHz is required at both the telemetry and command frequencies, so it is evident from Fig. 8 that a single point feed is not appropriate. A four point feed should suffice, provided random variations in elements are not large and that excess transmission line phase shift due to temperature variation is small.

An interactive, iterative array design program was also written for a four point feed, which does not assume constant spacing, or $\arg(A) = \arg(B) = 0$. This program operates as follows:

- a) Choose a nominal spacing and nominal radius as before.
- b) The program computes the number of elements N , an interim radius R , a temporary constant spacing based on $\arg(A) = \arg(B) = 0$ (temporarily assumed), at a design frequency 2.20 GHz.
- c) Choose a value for B_1 .
- d) Power to the load, and power lost in the transmission line is calculated. If power to the load is unacceptable, go back to c).
- e) $|A_n|, |B_n|$ for $n = 1$ (1) $N/4$ are printed out and the operator is asked for the corresponding $\arg(A_n), \arg(B_n)$ as found experimentally.
- f) A (new) spacing d_n is computed so that the radiated field maintains a constant progressive phase shift per element, and a new set of $|A'_n|, |B'_n|$ required is calculated and printed.
- g) The operator is asked for a new set of $\arg(A'_n), \arg(B'_n)$ corresponding to $|A'_n|, |B'_n|$. If the new set of angles is not sufficiently close to the previous set, go to f).
- h) A final radius is calculated on the basis of the final d_n set, and the element spacings are printed.
- i) Far field in the plane of the array is calculated at any desired frequency and worst ripple in each quadrant is printed. The pattern is plotted if desired, and i) can be repeated as desired.

4. ARRAY DESIGN AND FABRICATION

4.1 Design

A preliminary four-point feed design has been fabricated and partially tested. The table of design data for each of the four nine-element arrays is given as follows:

$N = 36$
 $P_L = 17.1\%$
 $P_{TX} = 17.3\%$

$\lambda_g = 4.862 \text{ in. at } 2.20 \text{ GHz}$
 nominal spacing $= .75 \lambda_g = 3.646 \text{ in.}$

Element No.	$ B_n $	Slot Length (in.)	Spacing (in.)
1	.270	.981	3.833
2	.286	.995	3.803
3	.304	1.010	3.769
4	.325	1.025	3.728
5	.351	1.043	3.676
6	.382	1.066	3.609
7	.421	1.090	3.515
8	.473	1.121	3.370
9	.547	1.158	3.601

The belt was fabricated using an input coaxial connector and load as shown in Fig. 3, on a 36.6 in. long waveguide. Each element was individually matched to ~ 20 dB return loss by means of shorting posts on the feed side of the waveguide. The load end of each waveguide is clamped under the input transition of the following waveguide array, when mounted on a 3 ft. wide circular cylinder for test as a belt. Dielectric loading elements were cut with a diamond saw, from 1 in. x 1 in. Styrocast rod material, and bent to the approximate belt curvature by heating. This particular dielectric material would be unsuitable for space application. All tests were made with a nylon string holding the dielectric blocks down, but conductive epoxy would be used for permanent placement.

4.2 Measurement

Results from a near-field measurement of the nine-element preliminary design are shown in Fig. 9. This shows a linear phase progression of 52.5° per element and a ± 2 dB amplitude taper. Unfortunately, placement of the dielectric blocks on this array is critical, and the amplitude distribution can vary by a further ± 2 dB, with corresponding changes in the phase slope. These near-field measurements were made using a manual HP network analyzer in a small anechoic chamber, with the nine-element array segment held flat on a 3 ft. x 3 ft. ground plane. The probe used was a balanced loop of $\sim .75$ in. diameter, held $\sim .3$ in. above the dielectric loading blocks. A transmission/reflection test indicated that 22% power went to the load, as compared with the design value of 17%. All measurements were made with belt array segments taped to the aluminum ground plane, using aluminum tape purported to have a conductive adhesive.

Near-field measurements were also made on the assembled belt array, as shown in Fig. 10, except that the edges of the belt were taped to the ground plane. The four-way power splitter used was a ratrace plus two hybrids, which gave the required $0, \pi/2, \pi, 3\pi/2$ phases at a level of 6.5 dB below the input. The resulting amplitude and phase at 2.20 GHz are shown in Fig. 11. The amplitude variation now is increased to ± 4.5 dB but phase is fairly linear around the belt except for a phase jump between segments no. 1 and 4.

Finally, a preliminary far-field pattern in the plane of the belt is shown in Fig. 12. A gain calibration is also noted on this Figure. The maximum ripple shown here is not acceptable, indicating that better phase/amplitude control at each element is required. All of the above far-field measurements were made using the CRC 500 ft. protected range facility. The transmit antenna was nominally RHC polarized, with approximately 3 dB ellipticity. Polarization ellipticity was measured by rotating a linear-polarized transmit antenna, and was found to deteriorate to 10 dB at occasional points in the plane of the belt. Ellipticity of individual element radiators will be considerably improved by partial matching on each side of the element as suggested by Simmons¹. The amplitude distribution around the array was significantly affected by the hand-cut slots (tolerance $\sim \pm .005$ in.) and by placement of the high dielectric blocks. Further tests will be made on a version having etched slots and more reliable element loading.

5. CONCLUSION

A combined parallel-series fed array as described above is attractive in terms of lack of feed complexity and structural integrity, although greater element directivity is desirable. Calculated performance of this array using a reduced-height waveguide structure indicates suitability for narrow bandwidth applications. The predicted performance has not been achieved in this initial prototype because of shortcomings in the element design and fabrication, which will be improved.

6. REFERENCES

- ¹ SIMMONS, A.J., 1957, "Circularly Polarized Slot Radiators", IRE Trans. Antennas and Propagation, AP-5, No. 1, pp. 31-36.
- ² SANGSTER, A.J. and HAWKINS, D.C., 1972, "Scattering Parameters of an Arbitrarily Shaped Aperture in a Waveguide", IEE Summary M30 submitted to IEE Library, 29 Feb. 1972.
- ³ SANGSTER, A.J. and HAWKINS, D.C., 1971, "Arbitrarily Located Resonant Slots in Waveguide: Exact Condition for Circular Polarization", Electronics Letters, Vol. 7, No. 25, pp. 741-742.
- ⁴ HOWELL, J.Q., 1972, "Microstrip Antennas", Program Digest of 1972 IEEE G-AP Symposium, 11-14 Dec., 1972, Williamsburg.

7. ACKNOWLEDGEMENT

The authors are indebted to J.G. Dumoulin for performing many of the measurements.

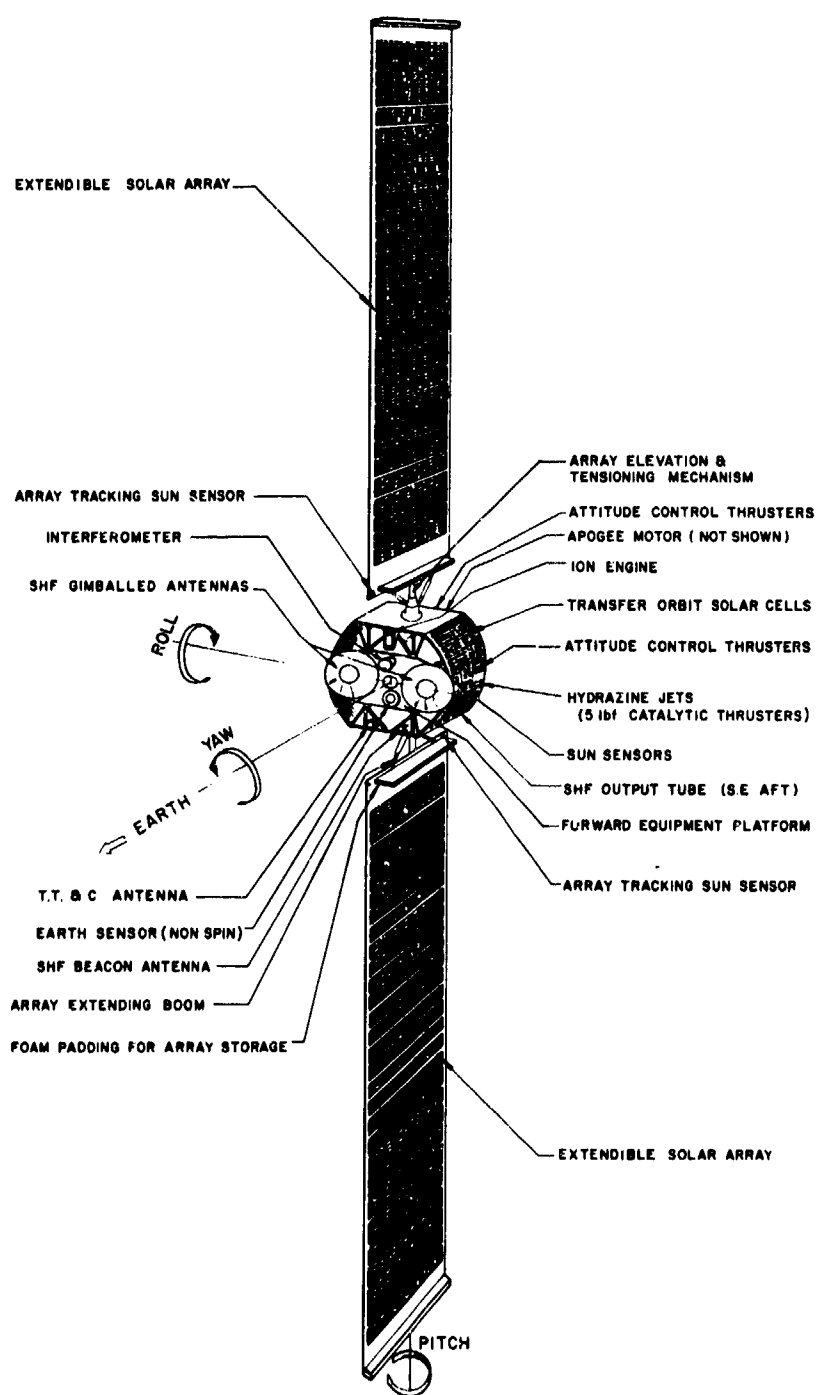


Fig.1 CTS Spacecraft Configuration

circular polarized radiation

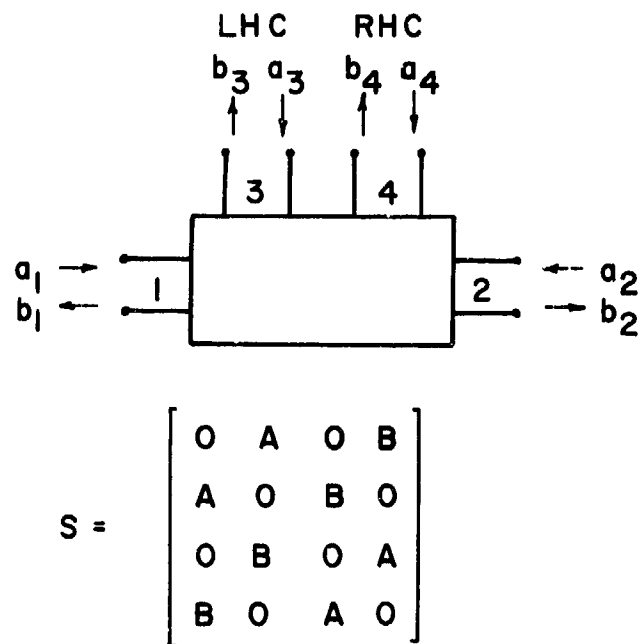
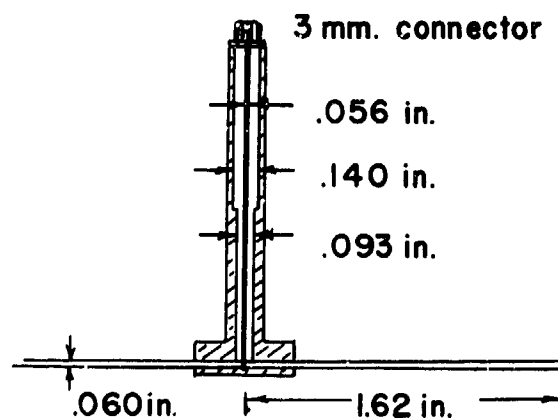
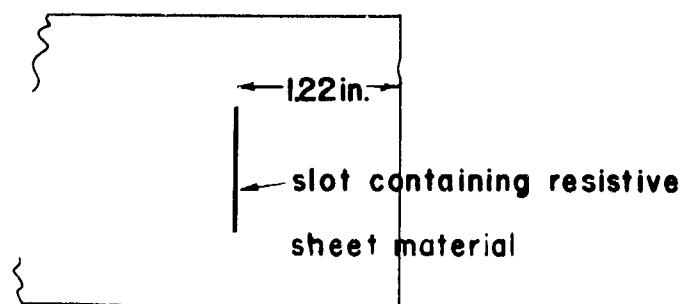


Fig.2 Simplified Element Scattering Matrix



(a) TRANSITION



(b) LOAD

Fig.3 Waveguide Transition and Load

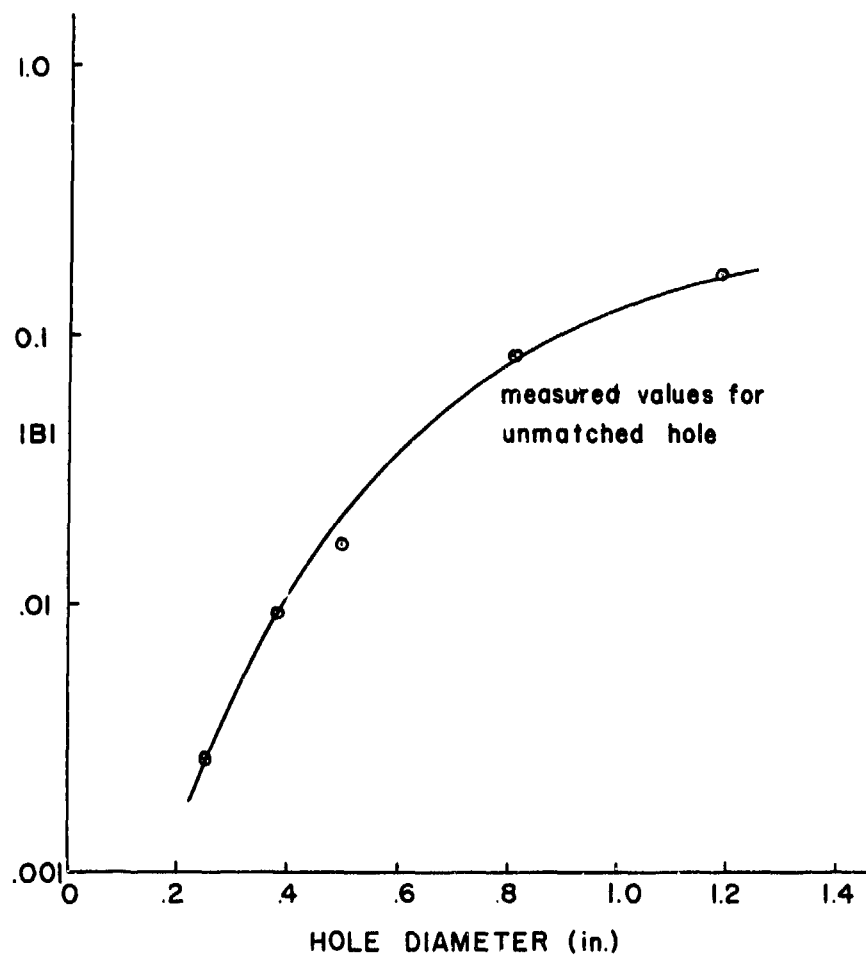


Fig.4 Round Hole Coupling Characteristic

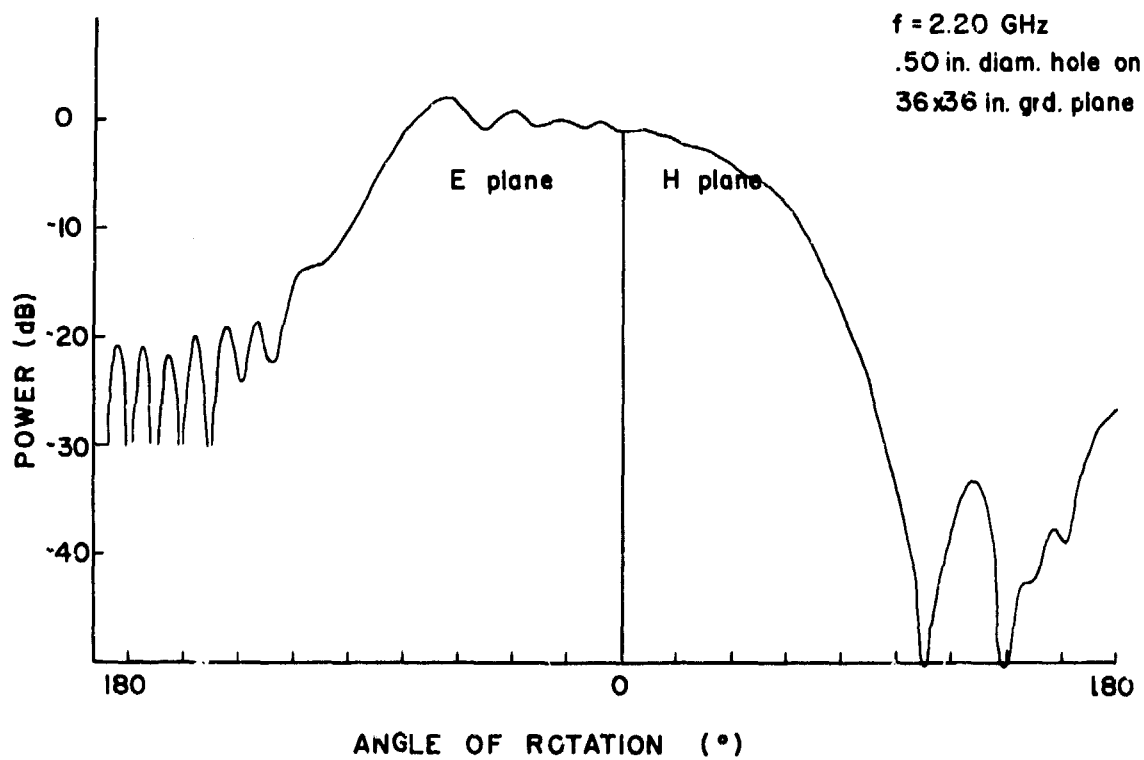


Fig.5 Round Hole Radiation Patterns

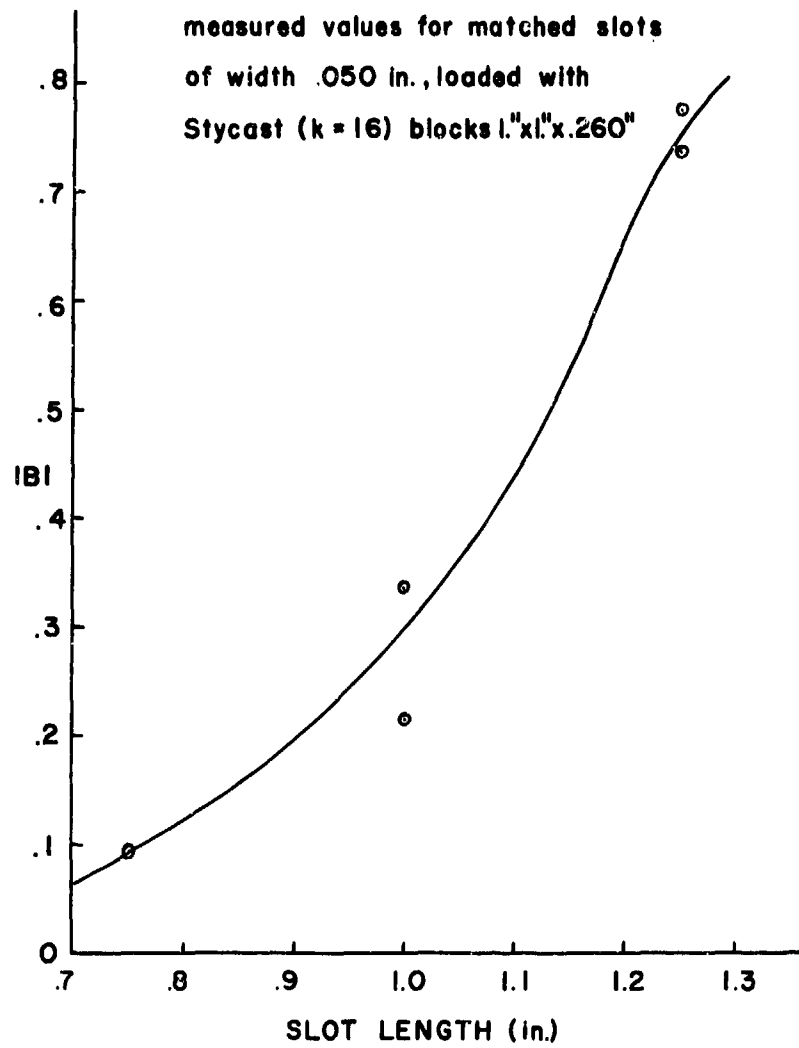


Fig.6 Crossed Slot Coupling Characteristic



Fig.7 Loaded Crossed Slot Elements (photo)

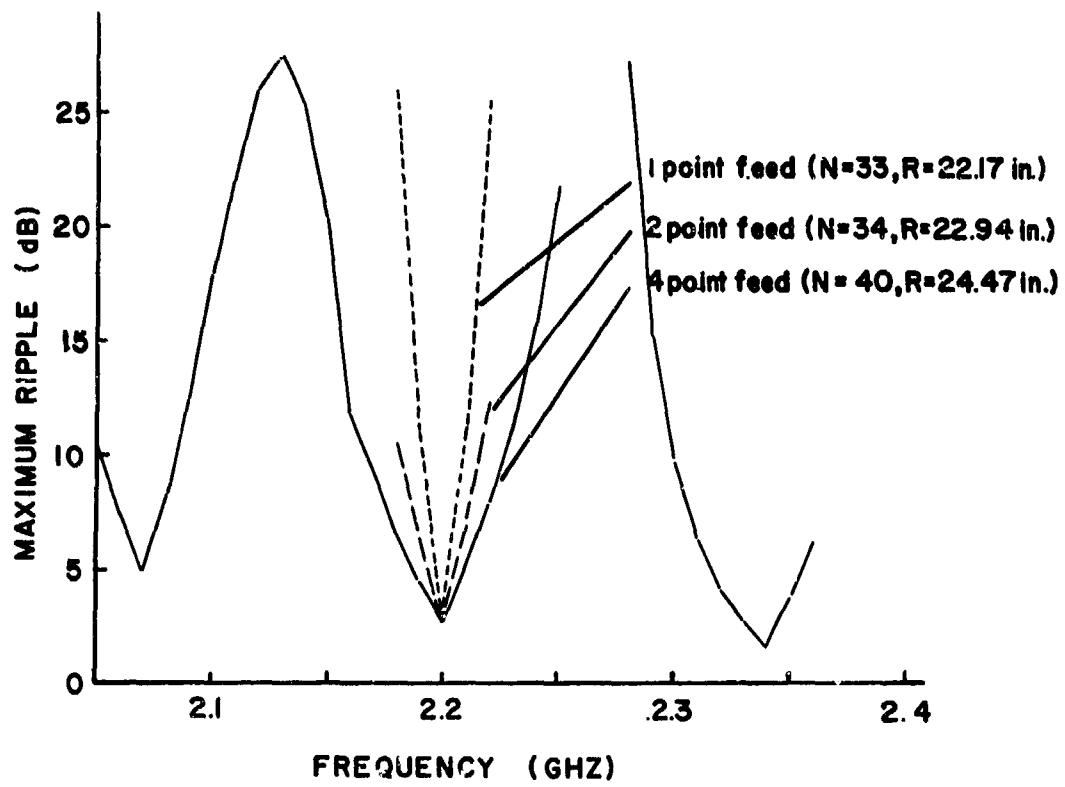


Fig.8 Feed Design-Bandwidth and Ripple

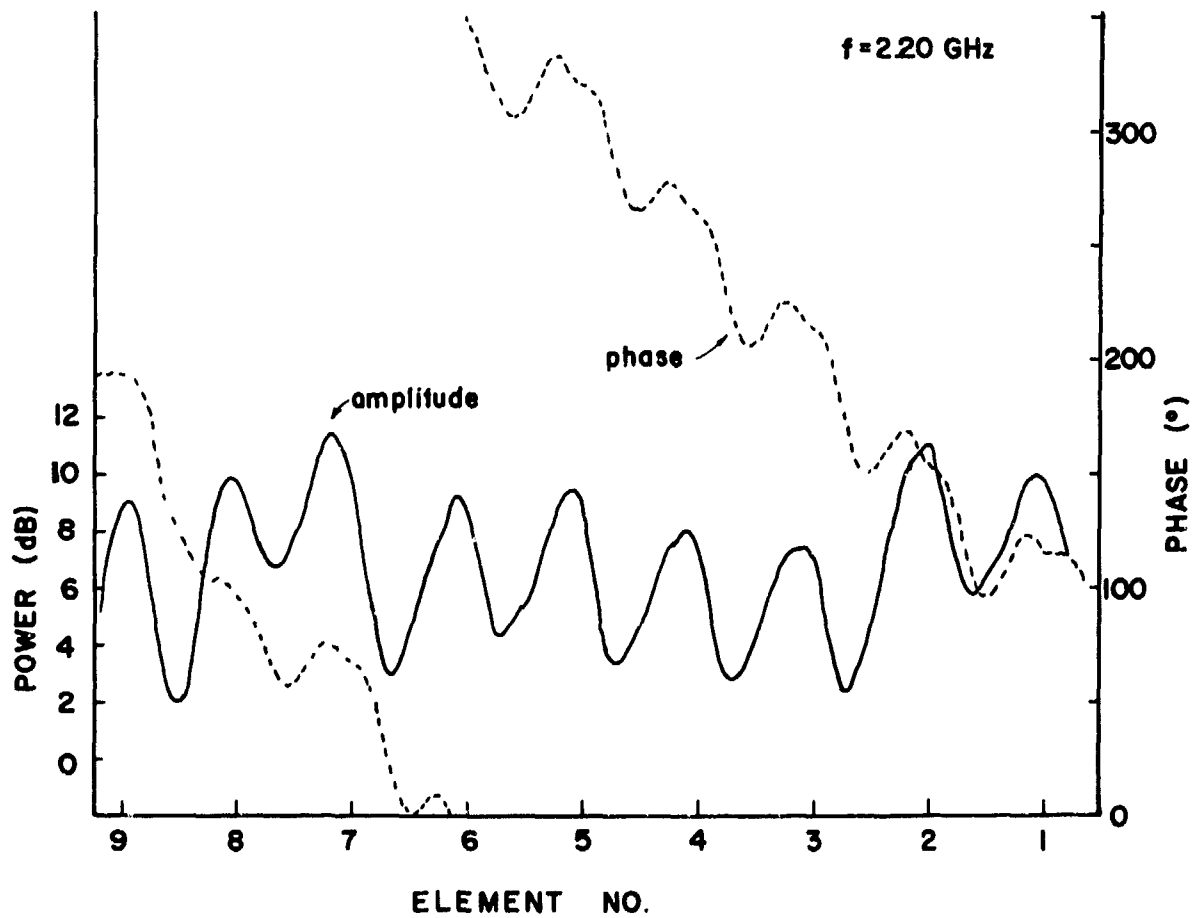


Fig.9 Measured Nine Element Array Aperture Distribution

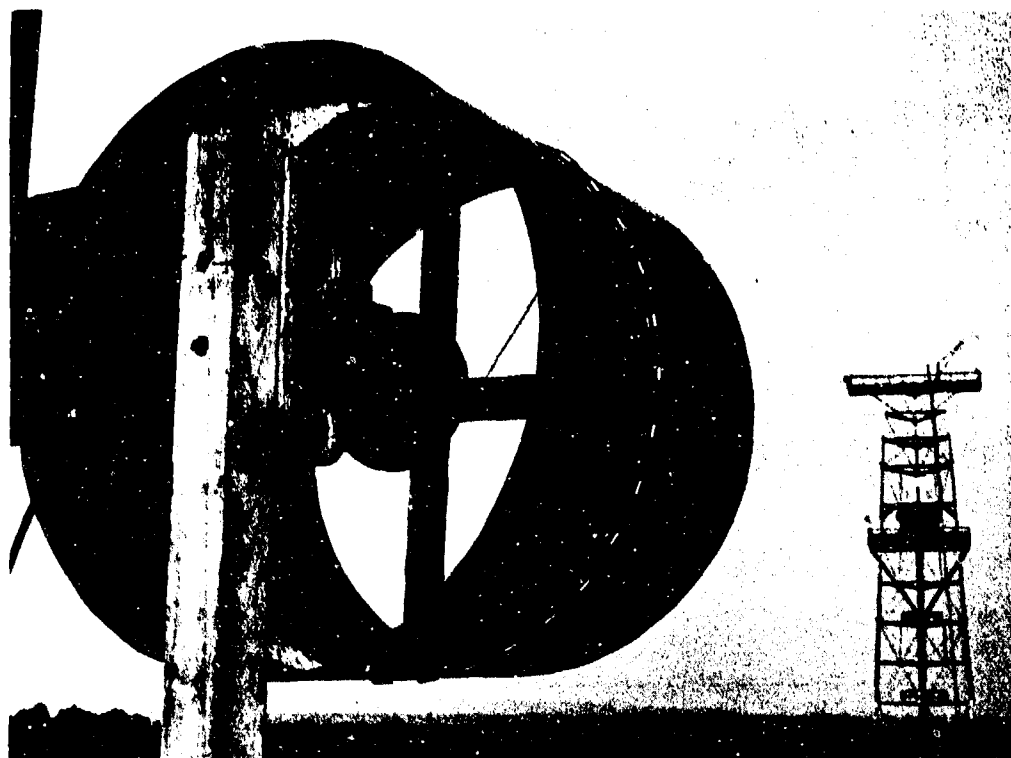


Fig.10 Belt Array on Test Cylinder (photo)

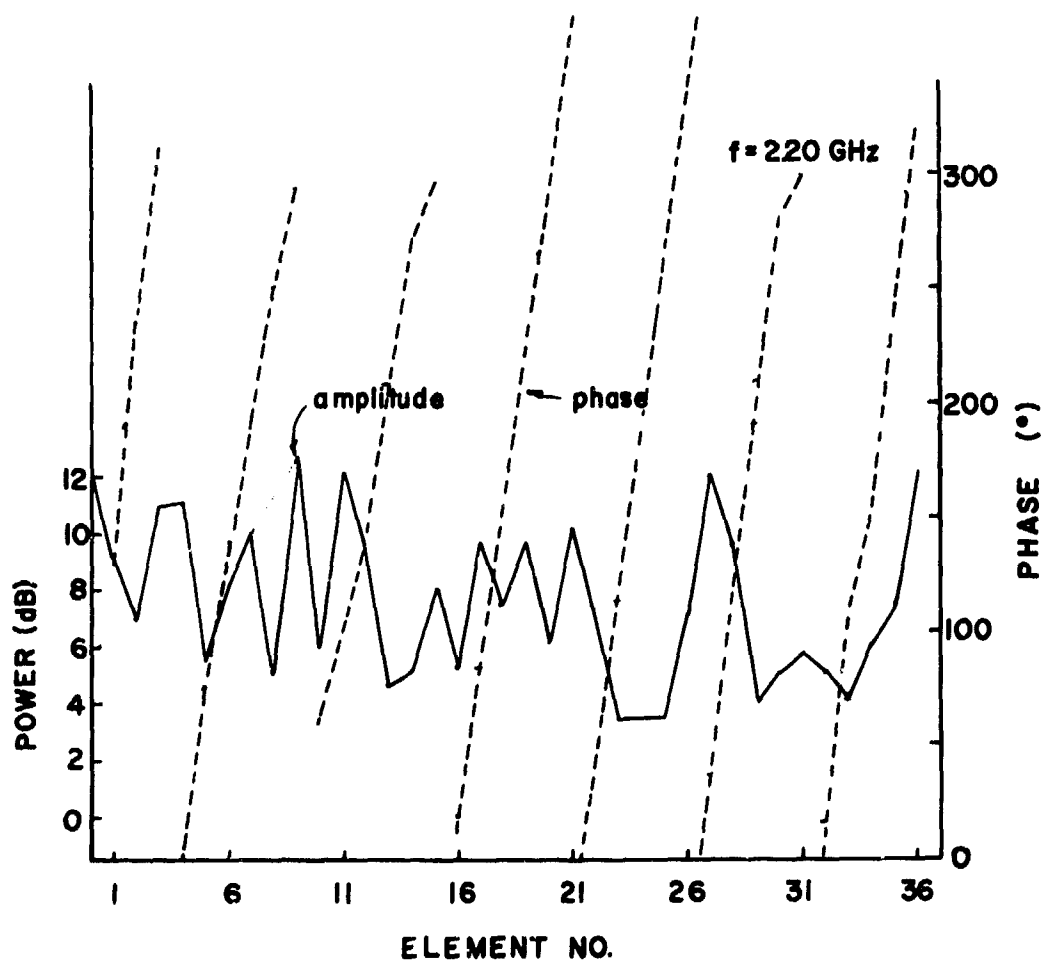


Fig.11 Measured Belt Aperture Distribution

DISCUSSION

- J.K. HSIAU: 1. How do you find the impedance of the crossed slot?
2. How do you locate your slot during your design procedure.

R. BREITHAUPT: 1. The impedance as such is not determined. Rather the element was characterized in terms of scattering matrix parameters A and B of Fig. 2. This information is available analytically for the crossed slot not externally loaded, but was found experimentally (no analytical results available) for the round hole and loaded crossed slot described here.

2. This is approximately the point in the broad wall where orthogonal magnetic field components are of equal amplitude, and is discussed at length in references 1, 2, and 3 quoted in the paper.

- J.F. GOBERT: 1. Do you think you can improve the polarization decoupling?
2. What problems does the undesired polarization give in meeting the operational requirement?

R. BREITHAUPT: 1. Yes, the radiated polarization purity may be improved in each element by partial element matching on either side of the radiating element. Polarization purity is related to energy incident on both parts 1 and 2 as shown in Fig. 2 of the paper.

2. Cross polarized radiation causes trouble only in so far as energy is lost from the nominal polarization. No use is made of cross-polarized telemetry/command signals in this system.

CROSS-POLARISED RADIATION FROM SATELLITE REFLECTOR ANTENNAS

A. W. Rudge, T. Pratt, A. Fer
Electronic & Electrical Engineering Department
University of Birmingham,
Birmingham B15 2TT
England.

SUMMARY

The limited RF spectrum which is available for satellite communication systems has led to increased interest in the use of dual-polarised and orthogonally-polarised multiple-beam antennas. Since an accurate knowledge of the antenna sidelobes and cross-polarised radiation is necessary to ensure adequate isolation between RF channels, this paper examines some available techniques which can be employed to predict the vector fields of reflector antennas. While the differences between the techniques are found to be comparatively unimportant in practical satellite antenna problems, the problem of providing an adequate description of the antenna primary-feed radiation is found to be a critical factor. Results for predicted and measured cross-polarised radiation fields are presented.

1. INTRODUCTION

The pressure on the available electromagnetic spectrum for satellite communication systems has led to considerable interest in the use of dual-polarised antennas, and multiple-beam antennas with orthogonally polarised beams, as a means of achieving frequency re-use. In the design of such antennas attention must be directed not only upon the polarisation purity in the main beam, or beams, of the antenna, but also upon the possibility of generating cross-polarised sidelobes which may result in interference between widely separated beams. Thus the satellite antenna has become one of the most critical components in future satellite communication systems.

Satellite antennas based upon the use of parabolic reflecting surfaces have proved to have many attractive features, and are a popular choice in providing narrow beams with acceptable sidelobe characteristics. The cross-polarisation characteristics of these antennas must be accurately known if they are to be applied in a dual-polarised or multiple-beam configuration, but comparatively little material has been published in the literature regarding their cross-polarised radiation.

This paper comprises a summary of the results of two related research projects in progress at the University of Birmingham. Both projects are basically concerned with prediction of the principal and cross-polarised field components radiated by parabolic reflector antennas. Of the two projects, one has concentrated on a study of parabolic reflector antenna depolarisation, with a view to clarifying its definition, causes, and means of minimising its effects. This study has also been concerned with the comparison and evaluation of a number of techniques which can be employed to predict the antenna depolarisation without the aid of large-scale numerical integration. The second project, which has been carried out under a contract with the European Space Research Organisation, has been concerned with the extension, modification and operation of a large-scale computer program, capable of predicting radiation fields - including cross-polarised components - for a wide range of reflector and primary-feed configurations.

This paper examines some fundamental techniques for the prediction of reflector radiation patterns, and presents results for calculated and measured cross-polarisation patterns of a typical front fed paraboloidal reflector antenna. The problem of obtaining an adequate description of the primary feed is discussed in some detail since this has been found to be a critical area in the prediction of cross-polarised radiation.

2. BASIC TECHNIQUES FOR MODELLING

A number of well established techniques exist which provide predictions of the vector radiation fields scattered from parabolic reflectors. These basic techniques are well described in texts, (Silver, 8, 1949; Collin and Zucker, 1969; Rusch and Potter, 1970), and a variety of applications have been reported in the literature. The best known of these techniques are probably those based upon variations of the 'aperture field' and 'current-distribution' methods. In practical applications both methods make use of the physical-optics approximation, which essentially demands that the reflector surface be large relative to the operating wavelength.

To provide a unified approach, the aperture-field and current-distribution methods can be considered as two examples of an application of the field-equivalence principle. Applying this principle, any radiating antenna can be replaced by a set of equivalent sources, located on an arbitrary surface, which encloses all of the sources of radiation. The equivalent sources on the surface are defined such that the electromagnetic fields anywhere outside the surface are identical to those excited by the radiating antenna. The equivalent sources may take the form of either an electric or magnetic current distribution, or some combination of both, over the defined surface. These current sources are related in a direct fashion to the tangential electric and magnetic fields which exist at the same surface with the antenna radiating (Collin and Zucker, 1969). Since a knowledge of either the tangential electric or magnetic fields (or their associated currents) over a closed surface is sufficient to determine the fields scattered

by the reflector antenna, then with reference to Figure 1 we can postulate the following mathematically equivalent models:

- a) The electric current distribution on surface 2 (electric-current method)
- b) The tangential electric-fields over surface 1 (aperture-field method)
- c) The electric and magnetic fields over surface 1
- d) The electric and magnetic fields over surface 2

Applying the physical-optics approximation to each of these models, we assume that on surface areas directly illuminated by the primary source, the tangential electric and magnetic fields and their associated currents are those that would be present if the fields were reflected optically. On shadowed regions the fields and currents are assumed to be zero. To satisfy Maxwell's equations at the boundary between the illuminated and non-illuminated regions, a line distribution of electric and magnetic charges can be introduced along the boundary curve in each of the above cases. The net effect of this boundary charge distribution is to ensure that the predicted radiation fields satisfy the radiation conditions and thus do not include a radiated field component in the direction of propagation (Silver, S.1949).

2.1 Comparison of techniques

The mathematical expressions for the radiated field components predicted by each of the postulated models have been derived. These expressions have been programmed and their predictions compared for a number of primary-feed and reflector combinations. The conclusions drawn from the study are summarised below.

All of the techniques provided similar predictions for the principally polarised (co-polar) fields over the main lobe and the first four or five sidelobes. At wide angles from the boresight only the combined electromagnetic techniques (c and d) were in agreement. The disagreement between the methods at wide angles tends to increase with increasing reflector curvature. For the cross-polar radiation again only c and d were in agreement. The peak value of the cross-polarised radiation normally occurs close to the boresight, and, in general, the techniques differ with regard to their respective predictions of cross-polar radiation introduced by the reflector curvature, as distinct from the cross-polar component originating in the primary feed radiation.

In practice, the differences between the predicted fields are less serious than these results suggest. At wide angles, the co-polar component of the radiation tends to be dominated by secondary effects, such as aperture blocking, edge diffraction, and primary feed spillover. These effects mask the differences between the predicted fields, and discussions of relative accuracies become irrelevant. Similarly, in the majority of cases the cross-polar component which is predicted due to the reflector curvature is very small and is swamped by the component due to the primary feed. For example, for a reflector with $F/\rho = 0.25$, fed by a realistic primary feed illumination, the peak cross-polar level predicted as a result of reflector curvature will typically occur some 50 dB below the peak of the co-polar field, and this level will reduce still further as the F/ρ ratio is increased. Since the primary feed illumination can result in an antenna pattern with cross-polar peaks only 15 dB below the co-polar peak, and typically results in cross-polar lobes 20 to 40 dB down, it appears reasonable to conclude that the contribution due to the reflector is of secondary importance in such cases.

In dealing with satellite reflector antennas we are chiefly interested in radiation within a comparatively narrow cone of angles about the antenna boresight, over a dynamic range of, perhaps, 50-60 dB. In this region, there is little significant variation between the predictions obtained by the various methods, and the techniques which are the most convenient, in a computational sense, can be employed. On this basis, methods (b) and (c) are superior.

2.2 Co-polar and cross-polar radiation

A number of definitions of cross-polarisation are commonly employed in the literature. Three of these definitions have been considered by Ludwig (Ludwig, A.C. 1973), and the authors are in agreement with his conclusion that the most useful definition is the one which provides predictions in a form which corresponds directly to the field distributions obtained from standard measurement practice (Silver, S.1949). The co-polar field is defined as that which would be measured on a conventional antenna range with the polarisation of the distant antenna initially aligned with that of the test antenna, on boresight. This polarisation is then retained while the test antenna is rotated through a set of 'field cuts' in the usual way to build up a complete measured radiation pattern. If the polarisation of either the test antenna or the source antenna is then rotated through 90° , and the radiation pattern measurements repeated, the recorded measurements correspond to the cross-polar field.

If the test antenna has its principal polarisation aligned with the y axis then the co-polar (E_p) and cross-polar (E_q) components of the radiated field are related to the usual spherical co-ordinate^p field components (E_θ, E_ϕ) by the following

$$E_p(\theta, \phi) = E_\theta(\theta, \phi) \sin \phi + E_\phi(\theta, \phi) \cos \phi \quad (1a)$$

$$E_q(\theta, \phi) = E_\theta(\theta, \phi) \cos \phi - E_\phi(\theta, \phi) \sin \phi \quad (1b)$$

3. A SIMPLE RADIATION MODEL

If a far field point is defined in terms of the spherical coordinate system (r, ψ, ϕ) shown in Figure 2, then using method (b), the normalised co-polar (E_{pn}) and cross-polar (E_{qn}) field components of a

paraboloidal reflector antenna can be expressed as (Rudge and Shirazi, 1973)

$$E_{pn} = \frac{\cos^2 \psi/2}{F_p(0,0)} [F_p(\psi, \phi) (1 - \tan^2 \psi/2 \cos 2\phi) + F_q(\psi, \phi) \tan^2 \psi/2 \sin 2\phi] \quad (2a)$$

$$E_{qn} = \frac{\cos^2 \psi/2}{F_q(0,0)} [F_q(\psi, \phi) (1 + \tan^2 \psi/2 \cos 2\phi) + F_p(\psi, \phi) \tan^2 \psi/2 \sin 2\phi] \quad (2b)$$

where F and F are the two-dimensional Fourier transforms of the co-polar and cross-polar components of the tangential electric field in the reflector aperture-plane (ϵ_p, ϵ_q) . The transform functions can be expressed as integrals in terms of the primary angular co-ordinates $q(\theta, \phi)$ in figure 2 as:

$$F_i(\psi, \phi) = \int_0^{2\pi} \int_0^{\theta^*} \epsilon_i(\theta, \phi) \exp[-jk R(\theta, \phi)] p^2(\theta) \sin \theta d\theta d\phi \quad (3)$$

where i is either p or q ; θ^* is the maximum angle subtended at the focus, F is the reflector focal length, $k = 2\pi/\lambda$, λ is the wavelength and,

$$p(\theta) = 2F/(1 + \cos \theta) \quad (4)$$

$$R(\theta, \phi) = 2kF \tan \theta/2 \sin \psi \cos(\phi + \phi) \quad (5)$$

When the primary-feed is located at the geometric focus with its principal electric vector aligned with the y axis, then the functions ϵ_p, ϵ_q are given by:

$$\epsilon_p = \frac{1}{p} (A_\phi(\theta, \phi) \cos \phi + A_\theta(\theta, \phi) \sin \phi) \exp(-jk2F) \quad (6a)$$

$$\epsilon_q = \frac{1}{p} (A_\phi(\theta, \phi) \sin \phi - A_\theta(\theta, \phi) \cos \phi) \exp(-jk2F) \quad (6b)$$

where A_θ, A_ϕ are the normalised spherical co-ordinate components of the primary-feed radiation.

If, for multiple-beam purposes, the primary-feed is offset a small distance from the geometric focus, the amplitude of the incident field at the reflector will be little affected. However, the movement of the feed phase centre will be very significant and can be accounted for by a compensatory phase term $\exp jk\Delta_2$, which will appear as a multiplying factor in equations 6. If Δ_t and Δ_z are small offset distances, in the transverse and axial directions respectively, and ϕ_0 (measured to the x axis) denotes the plane of the offset, then:

$$R_2 = \Delta_t \sin \theta \cos(\phi - \phi_0) + \Delta_z \cos \theta \quad (7)$$

Aperture-blocking effects due to the presence of the primary-feed and its supporting structure can be accounted for in an approximate fashion by applying the conventional shadow-diffraction technique in both of the scalar integral functions F_p, F_q . Aperture-blocking due to a central obstruction results in very significant changes in the sidelobe structure of the co-polar radiated field, but the cross-polar field has been found to be comparatively insensitive to this effect.

3.1 Computation of the model

Computation of the model can be made simple for reflector antennas with primary-feed illuminations where A_θ and A_ϕ are functions only of θ . In these cases, the outer integration of equation 3 can be carried out analytically and the single integral form which remains can readily be evaluated by a digital computer. Primary-feeds which satisfy this criterion include the electric dipole, the magnetic dipole, the TE_{11} mode circular waveguide and conical horn radiators, and idealised feeds which generate no cross-polarisation such as the Huygen source. For cases not satisfying this criterion it may prove necessary to compute the two-dimensional integrals, and this process can become costly in terms of computer time. A one-dimensional Romberg technique (Rudge and Shirazi, 1973) which involves the use of trapezoidal-rule integration, with successive interval-halving and a system of extrapolation to remove increasing orders of error, has been found very suitable for this application. The interval-halving process is repeated until a pre-set accuracy criterion is reached. Hence the number of iterations required to compute the integral is automatically minimised for the accuracy specified.

4. CURRENT DISTRIBUTION TECHNIQUES

In principle, a general approach to the problem of calculating the field at a distance from a conducting body, upon which an electromagnetic wave is incident, may be made by an exact application of the electric current distribution technique. Once the surface current is known the prediction of the distant fields is comparatively trivial. However, an exact solution involves the solution of coupled integral equations and is practicable numerically only when the body has dimensions of the order of the wavelength. For smooth conducting bodies which are very large relative to the wavelength the physical optics approx-

imation is commonly invoked. In terms of an incident magnetic field (\vec{H}) the approximate surface current (\vec{K}) is taken to be

$$\vec{K} = 2\vec{a}_n \times \vec{H} \quad (8)$$

where \vec{a}_n is a unit normal to the surface. In fact the physical optics approximation neglects an oscillatory component of the reflector surface current which becomes negligibly small for large reflectors.

Within the constraints imposed by the physical optics approximation, the fields scattered from an arbitrary reflecting surface can be determined providing the surface unit normal and the incident vector field can be defined at all points on the reflector. Then, for an incident magnetic field \vec{H} , the scattered electric field \vec{E}_s at a large distance r is given by, (Silver, 1949),

$$\vec{E}_s = \frac{1}{r} (\vec{I} \cdot \vec{a}_\psi + \vec{I} \cdot \vec{a}_\phi) \exp(-jkr) \quad (9)$$

where

$$\vec{I} = \frac{-j\eta_0}{\lambda} \int_S (\vec{a}_n \times \vec{H}) \exp(jk\vec{\rho} \cdot \vec{a}_r) dS \quad (10)$$

and \vec{a}_ψ , \vec{a}_ϕ and \vec{a}_r denote unit vectors in the ψ , ϕ and r directions respectively, while $\vec{\rho}$ is a vector from the geometric focus to a point on the reflector and η_0 is the impedance of free space.

4.1 A Large Scale Computer Program

Based on an arbitrary reflecting surface approach a computer program has been written at the Jet Propulsion Laboratory in California (Ludwig 1970) to calculate the far-field radiation patterns of asymmetrical reflectors. This program has been extended at the University of Birmingham to deal with offset and distorted reflectors and has been used to study cross-polar radiation from a variety of reflector antennas. Although the approach is general with respect to the antenna geometry it is extremely difficult to specify an arbitrary reflector system with an arbitrary incident field, and, in practice some restrictions must be placed on the descriptions of the surface and feed to keep the input data to the program within bounds. Hence, sub-programs are used to generate surface and feed data for configurations corresponding to useful antenna systems.

Aperture-blocking by feed systems and supports are again accounted for, in an approximate fashion, by removing from the integration the surface current elements which are shadowed. This has the effect of reducing the surface currents to zero in the shadowed regions while retaining the power radiated by the feed in those directions, thus accounting for both power loss and aperture efficiency effects.

Since the program includes a double integration process which may involve up to 7000 points on the scattering surface, a number of computational techniques have been developed and incorporated into the program to reduce the time and storage requirements. To define the incident magnetic field at the reflecting surface the program accepts either the far-field radiation pattern of the feed or a spherical harmonic expansion of the field at the surface of the reflector. By matching the far-field radiation of a feed system to a set of spherical waves at infinity, expressions for the near-field radiation can be determined. This is a useful facility in dual reflector systems where the main reflector may be located in the near-field region of the sub-reflector.

When the primary-feed radiation has the general form,

$$\vec{E}(\theta, \phi) = A_\theta(\theta) \sin \phi \vec{a}_\theta + A_\phi(\theta) \cos \phi \vec{a}_\phi \quad (11)$$

which implies a circular symmetry where A_θ and A_ϕ are independent of ϕ , then measurements of the complex co-polar component of the feed radiation in the principal E and H planes are sufficient to completely characterise the feed. The program accepts this measured data directly, however, it should be noted that rectangular feeds do not satisfy this condition and such radiators require measurements of the complex co-polar and cross-polar radiation in several planes.

Within the program, the reflecting surface is described in terms of Fourier expansion coefficients such that,

$$\rho(\theta, \phi) = \sum_{m=0}^M a_m(\theta) \cos m\phi + b_m(\theta) \sin m\phi \quad (12)$$

$$\frac{\partial \rho}{\partial \theta}(\theta, \phi) = \sum_{m=0}^M \frac{\partial a_m}{\partial \theta}(\theta) \cos m\phi + \frac{\partial b_m}{\partial \theta}(\theta) \sin m\phi \quad (13)$$

$$\frac{\partial \rho}{\partial \phi}(\theta, \phi) = \sum_{m=0}^M -m a_m(\theta) \sin m\phi + m b_m(\theta) \cos m\phi \quad (14)$$

The value of M may be chosen to allow for tilting and distortion of the reflector and a compromise between generality and practicality has to be made. With $M=2$ a tilt of up to 10° in the reflector can be accommodated. Offset feed systems can thus be treated by calculating the relevant coefficients of a tilted paraboloid. An example is shown in Figure 3 where a contour map of the magnitude of the co-polar and cross-polar field is shown for a paraboloidal reflector fed by an offset feed.

5. THE PRIMARY-FEED PROBLEM

Similar theoretical models to those described above can be developed without difficulty using the other techniques discussed in section 2. In every case, however, it is necessary to specify accurately the primary-feed radiation fields. The authors have found that this aspect of the modelling raises more difficulties than any differences encountered between the basic techniques. Although approximate expressions can be found in the literature, giving the radiation fields from simple feeds, a considerable disparity has been observed between the cross-polar components of these models.

For a symmetrical paraboloid the maximum level of the cross-polar field occurs in the diagonal planes when $\phi = m\pi/4$ and n is an integer. In Figure 4, curve 1 shows the measured cross-polar radiation pattern in the diagonal plane for a paraboloid with a diameter (D) of 38λ and a focal-length (F) of 15.2λ . The reflector is fed by a rectangular TE_{10} mode horn with aperture dimensions of $0.91\lambda \times 1.1\lambda$. Superimposed upon this distribution are the predicted fields using five rectangular horn primary-feed models. All but one of the models are based upon the assumption of a TE_{10} mode electric field in the horn mouth and are essentially derived from one of the forms of the equivalence principle discussed in section 2. The exception (curve 5) is based upon measured data. The derivation of the purely theoretical models can be summarized as follows:

- (i) Curve 2: Using horn-aperture tangential electric field only (Rudge and Shirazi, 1973, p36)
- (ii) Curve 3: Horn-aperture tangential electric and magnetic fields related by waveguide mode impedance (Silver, S, 1949, p343)
- (iii) No curve shown: Horn-aperture tangential electric and magnetic fields related by free-space impedance (Collin and Zucker, 1969, p637)
- (iv) Curve 4: A synthesized model obtained by interpolating between the principal E and H plane fields obtained from method (i) assuming a dependence of the form shown in equation (11).

Although all of the models agree essentially with regard to the co-polar radiation from the antenna, the differences in the predicted cross-polar fields are obviously significant. Method (i) appears to give the best result while method (iii) produces a very low level of cross-polarisation which is below the scale of figure 3. Curve 5 is based upon measurements of the primary-feed co-polar radiation in the principal E and H planes. This data is provided as input to the large scale program which interpolates between the 'measured' fields assuming that the radiation fields satisfy equation (11)

Similar problems exist with other primary-feed types and since the overall cross-polar radiation level, in practical cases, is very largely dependent upon the primary-feed radiation, the predictions can have little meaning unless there is considerable confidence in the expressions used.

6. CONCLUSIONS

Several methods of predicting the vector radiation from reflector antennas have been examined. Although the predictions obtained from these methods do have inherent differences it has been found that the discrepancies are very small for practical satellite antenna problems. A large scale program of the type described here has obvious advantages with regard to the generality of the scattering surface which can be treated. However for many applications involving well defined reflecting surfaces the comparative simplicity and low computational cost of the aperture fields methods are very attractive. A more serious shortcoming in the prediction techniques has been found to be that of obtaining an accurate description of the primary-feed radiation. Although measured radiation patterns of the primary-feed can be utilized as an alternative to the purely analytical approach, interpolation between the complex co-polar principal-plane fields will not, in general, be sufficient for primary-feeds which do not exhibit circular symmetry.

7. REFERENCES

- Collin, R.E., and Zucker, F.J., 1969: 'Antenna Theory, Part I' McGraw Hill, N.Y.
- Ludwig, A.C., 1970: 'Calculation of scattered patterns of asymmetrical reflectors' J.P.L. Tech Rept. No. 32-1430, Pasadena, USA.
- Ludwig, A.C., 1973: 'The definition of cross-polarisation', IEEE Trans, AP-21, 1, pp 116-119.
- Rudge, A.W., and Shirazi, M., 1973: 'Multiple beam antennas', Final report on ESRO/ESTEC Contract No. 1725/72 PP, University of Birmingham U.K.
- Rusch, W.V.T., and Potter, P.D., 1970: 'Analysis of reflector antennas', Academic Press,
- Silver, S. (Ed), 1949: 'Microwave antenna theory and design' Vol 12, MIT Radiation Lab. Series, McGraw-Hill, N.Y.

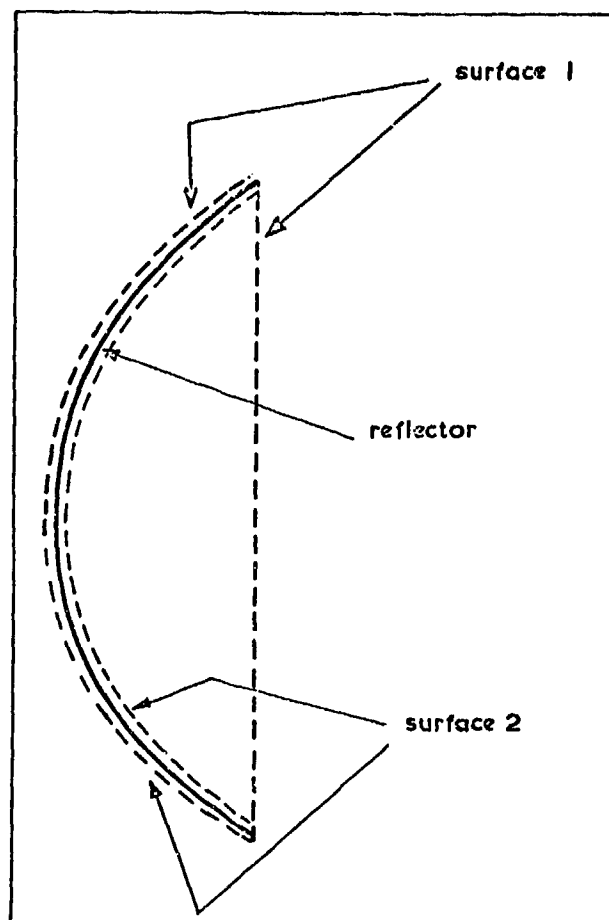


Figure 1 Surfaces of integration

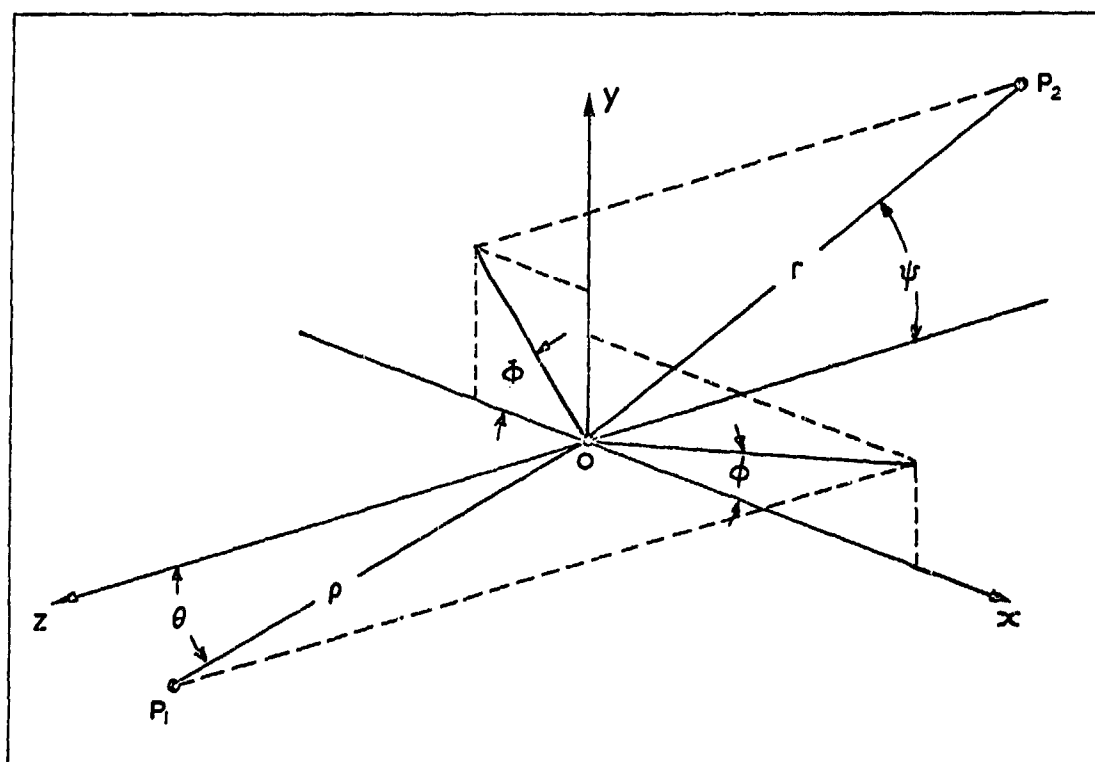


Figure 2 Co-ordinate systems. O is the geometric focus, P_1 is a point on the reflector and P_2 a far-field point

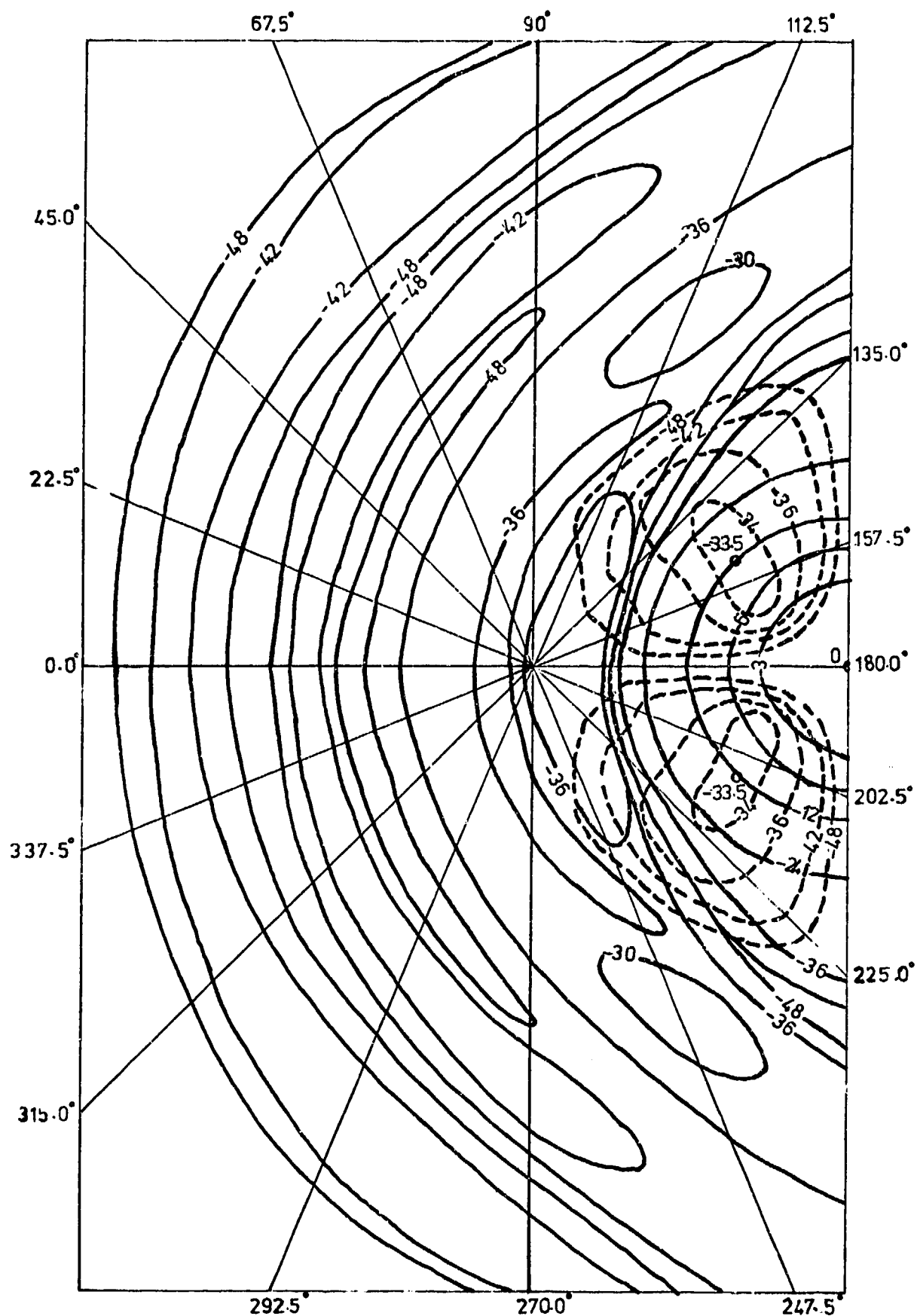


Figure 3

Contour map showing field magnitude for a paraboloidal reflector in dB with $D = 38\lambda$, $F = 15.2\lambda$ fed by a rectangular horn offset 1.0 wavelength from focus; Co-polar — ; cross-polar - - -

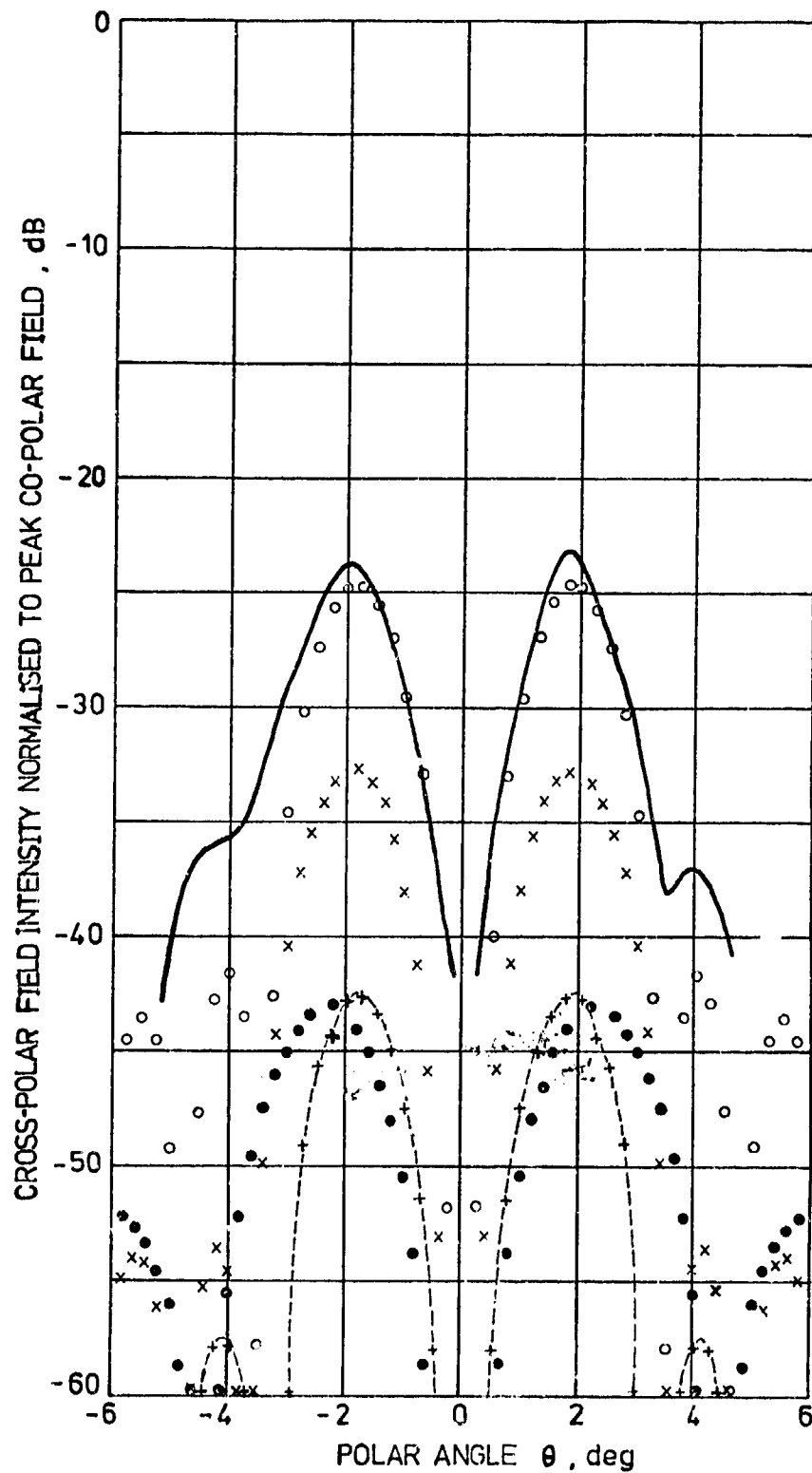


Figure 4 Measured and predicted cross-polar radiation in diagonal plane for paraboloid fed by a rectangular horn

—	Curve 1;	measured cross-polar field
o o o o	Curve 2;	feed case (i)
+ - - +	Curve 3;	feed case (ii)
x x x x	Curve 4;	feed case (iv)
. . . .	Curve 5;	feed radiation interpolated from measured data

DISCUSSION

T.L. AP RHYS: My own experience leads me to support the Author in his comments on the power of the physical-optics approach in a large range of problems. This has been generally underestimated. I believe.

In my own work, I found it necessary to use the FFT algorithm to reduce my computing time to a useful level. Has the Author considered using this technique and can he indicate the time that he needs in order to compute a pattern?

A.W. RUDGE: We have not carried out a detailed comparison of Fast Fourier Transform techniques with the Ramberg method. A superficial comparison was made and the conclusion reached that the FFT approach did not offer any significant advantage over the Ramberg method, and was probably inferior in that the Ramberg method automatically minimises the number of integrand evaluations for each calculation. Using the Ramberg method any two vector components (co-polar and cross-polar) at a given field point typically require an overall time of between 1 and 2 seconds to compute. These times are for an ICL 1906A machine.

W.D. BURNSIDE: I felt that Dr. Rudge made an excellent study of the physical-optic solution for various reflections. However, to complete this topic, I feel that the geometrical theory of diffraction (GTD) can be used with equivalent accuracy for additional side lobes, spillover and back lobes. In fact, the equivalent current approach has been applied very successfully to this type of problem. If he is not aware of this work perhaps he could contact Dr. Walter D. Burnside, 1320 Kinnear Rd., Columbus, Ohio 43212, U.S.A.

A.W. RUDGE: In our work on reflector antennas for satellites we have been largely concerned with details of the antenna vector radiation within a moderate sized cone of angles about the antenna boresight. Within this region we believe that the physical-optics techniques offer significant advantages over the other methods which are presently available. For predictions of wide-angle radiation, the accuracy of the physical-optics techniques is perhaps questionable and these methods certainly demand considerable computational effort in this region. It is in this region where I would expect the application of the GTD theory to be most profitable. I am aware of the excellent GTD work carried out at Ohio State University in the past and would be interested in obtaining further details of their present activities.

G. RIES: Please comment on the influence of the reflector on the cross-polarisation. How does this depend upon the F/D ratio?

A.W. RUDGE: The current distribution method predicts a cross-polarised component of radiated field which arises due to axially directed currents on the reflector. The magnitude of this radiation is inversely proportional to the reflector F/D ratio. However with a practical illumination taper on the reflector, these components typically have peak values which are -40 to 50dB below the peak of the co-polar beam and in this sense the dependence upon the F/D ratio is relatively unimportant. Indirectly the F/D parameter has a more significant effect in that it governs the angle subtended by the reflector at the primary feed point. Smaller F/D ratios imply larger subtended angles and difficulties are often encountered in achieving low levels of cross-polar radiation from the primary feed over these larger angular ranges.

PROBLEMS OF LONG LINEAR ARRAYS IN HELICOPTER BLADES

R H J Cary
Royal Radar Establishment, Malvern, UK

SUMMARY

Helicopter blades offer sites for the inclusion of long microwave antennas to give narrow azimuthal beams scanned by the rotation of the blades.

The variation of blade attitude as it rotates is such that it may lag, lead, bend in vertical and horizontal planes and twist, and in consequence places limits on the practical length of a linear array. The choice of location for antennas, either in the front or trailing edge, or out or inboard is discussed. Certain advantages accrue from a design where the antenna is located near the centre of gravity of the blade section, and radiating rearwards through the trailing edge, which requires to be of dielectric material. The length of the section of the trailing edge can be employed as a dielectric tapered slab antenna to shape the beam in the vertical plane and give more gain and direct the beam in a given direction. Theoretical discussion of the mechanism of this antenna and the choice of permittivity for the dielectric slab is discussed. High permittivity materials are not necessary, as those of low permittivity (1.15 - 1.5) have theoretically and experimentally given a considerable improvement in gain. While no accurate theory of the tapered dielectric slab antenna exists, the method of estimating an equivalent shorter uniform length for the section's tapered shape and calculating the theoretical radiation pattern of the launcher and end radiations, has indicated useful results in predicting experimental results obtained with microwave antennas in the dielectric tapered trailing section of the helicopter blade.

In practice a beam along the trailing blade axis is not necessarily required but needs to be modified to cover angles somewhat off this axis, due to the variation of the angle of the blade axis as it rotates. Methods to produce this off-set beam are shown.

The weight of a conventional dielectric slab antenna would tend to be unacceptable and the use of artificial dielectric materials has been considered to solve this problem. The design of an X band antenna waveguide feed and the dielectric core and skin etc of a tapered rear section of a helicopter blade is given.

1 INTRODUCTION

An increase in azimuth resolution and all round look capability may be required which are not provided by a conventional radar installation within the nose of a helicopter. Solutions which may give this requirement are, a scanning antenna mounted off the hub of the helicopter rotating above the blades, or a scanning antenna hung underneath the fuselage and clear of its landing gear, or an antenna housed within the helicopter blades. This paper concerns itself with the antenna installation in blades, which offer the opportunity of inclusion of long microwave antennas to give narrow azimuthal beams scanned by the rotation of the blades. High resolution and all round coverage suitable for navigation, mapping, search, landing aid, etc are possibilities with this antenna system. Among its disadvantages are that the scanning speed is tied to the speed of blade rotation, which if high can limit the range with such narrow beams.

The usual arrangement is for a number of blades to be supported and rotated from a central hub of the helicopter. The blades consist usually of a central metallic spar section which cannot be modified, with front and trailing sections which are mainly of aerodynamic shapes and offer the possibility of installation of antennas. This may be accomplished by either extra dielectric fairings added to the leading edge or for the front or trailing sections to be partly or wholly of dielectric material, within which the antennas are housed.

2 AVAILABLE AZIMUTH APERTURE

The widest aperture available would be one which employed an antenna system across the whole diameter of the blades. It is conceivable that an antenna in the leading edge of one blade and in the trailing edge of one opposite could be installed. There would be problems of making the antenna aperture continuous through the central hub region or to tolerate a gap in the middle of the antenna aperture resulting in deterioration of side lobe pattern in the azimuth pattern. Since the blades usually bend in the horizontal plane and if to maintain the azimuth beam, the conventional maximum criterion of a quarter-wave departure from linearity is adhered to, it is likely that an installation employing the full diameter of the blades would be limited to the longer wavelengths. Due to the flexing of the blades in the horizontal plane, at the shorter microwavelengths it may be found that only a limited part of the blade length may meet the antenna linearity requirements.

3 L AND S BAND DESIGNS

At L band (30 cm) wavelengths, the usual criterion for maximum departure of a linear array from linearity would be 7.5 cm (quarter-wave, and similarly for S band (10 cm) would be 2.5 cm. With these tolerances on linearity it may be likely that the blades bending movement in the azimuth plane may possibly permit near the whole of a blade to be utilised or even the whole diameter to be considered.

The antenna array at L or S band could be a conventional linear array of radiators such as horizontal dipoles located on or within the blade to minimise drag, and giving horizontal polarisation. An arrangement, Fig 1, would be to space the dipoles near 3.75 cm (eighth-wave at L Band) or 1.25 cm (eighth-wave at S Band) from any metal surfaces, installed in a dielectric fairing on the front edge and on or in a dielectric trailing section. The dipoles to save weight could be metal imprints on or within the dielectric. Since X Band antennas in dielectric fairings on the leading edge and within the trailing edge have been installed, and the same techniques could be employed for L or S Band antenna installation. The feed to the antenna components could be by coaxial cable or stripline, and would be

of waveguide which would be too large to incorporate within the blade. If the whole diameter is attempted to be used, the minimising of the centre gap in the aperture between the opposite blades would be essential to ensure low azimuth sidelobes. A typical gap between blades could be an eighth of the aperture in length. It would appear possible to reduce the gap by extending the antennas in a fairing closer inboard from the blades towards the hub.

4 X, K_u AND K_a BAND DESIGNS

4.1 ANTENNA LENGTH

The length of antenna which can be accommodated within the blade is not usually the same for each waveband due to the non-linear movement of the blades, and the quarter-wave criterion. In consequence the full resolution improvement by going to higher frequencies does not always materialise. Before being able to determine the antenna length considerable knowledge has to be ascertained as to the blades motion, deflections etc through its range of speed, climb, attitude, loads etc. This can be an expensive and difficult task before knowledge of the blades behaviour is available to assess the possible sites for lengths of antenna at various wavebands. A study on the information gathered from flight investigation of a particular helicopter indicated that the maximum lengths for each waveband were:-

X Band:- 4.3m, K_u Band:- 3.3m, K_a Band:- 2.3m

The 1.8 to 1 ratio of X to K_a band antenna lengths showed that the 4:1 wavelength ratio gave only a limited improvement in resolution.

The choice of the operational waveband will have to take this possible length of antenna into account and the resulting gain set against other factors in the operational performance equations. Additional to the usual radar parameters to be considered, is a scanning factor which arises because the transmit and receive beams except at zero range do not coincide. As the speed of rotation of the helicopter blade is high, typically 1800°/sec, a narrow beamwidth is soon traversed, and the narrower the beamwidth, and the greater the range, the larger the scanning loss. Thus the advantage of a narrower beamwidth at the shorter wavelengths is somewhat offset.

The type of antennas at these X K_u K_a wavebands are typically slotted linear waveguide arrays; strip line feeds with long antennas usually possess too large a loss to be considered. The slotted waveguides can conveniently be housed within the blade. At the shorter wavelengths the smaller waveguides have installation advantages of space, but their attenuation is increased, and as the transmitter-receiver will usually be located in the helicopter proper, the length of feed to the antenna can be appreciable and combined with the antenna length loss, can favour the longer wavelength. Further the smaller the waveguide the more critical it is to damage and tolerance errors. Thus many factors have to be considered in the choice of wavelength, much will depend upon the behaviour of the helicopter blade, operational requirement and ease of installation. Helicopter blade antenna designs and installations have mainly settled in X or K_u bands.

In the study for the longest linear length of blade for an antenna it may in some cases be that the longest linear length is towards the far end of the blade. Installation of an antenna in the end section of the blade has the disadvantage of increased outboard weight and increased loss and weight due to the longer feed to the radiating antenna. Usually a reasonable length of antenna can be found in the inboard section of the blade which does not have such disadvantages, and it may on balance be preferable to have a somewhat shorter antenna inboard than a longer one outboard. Where a helicopter has more than four blades a degree of screening from an adjacent blade may have to be considered.

The extension of the length of an antenna by incorporating phase correcting elements along its length to maintain linearity of phase front may be considered. Sensing devices of the variation of the blade shape with different angles of rotation, loads, etc would be required to provide information to adjust the phase shifters. This method of obtaining a longer antenna appears to present problems of control, installation and disadvantages in weight complexity and cost and would have to be set against the simpler installation of the shorter antenna with no phase shifters.

4.2 ANTENNA SITE IN BLADE SECTION

The section of the blade consists of three parts, the main spar and fore and aft sections. The main spar is usually not considered suitable for modification but both fore and aft sections have been utilised for inclusion of end-fed long linear waveguide arrays.

4.2.1 ANTENNA WITHIN THE FORWARD SECTION

Forward of the main spar is a metallic aerodynamic shaped section which contains the balance weights, located behind the leading edge. One installation (Ref 1) machined a rectangular section in the leading edge into which the linear end-fed waveguide was located, Fig 2(a). A dielectric cover over the waveguide preserved the original contour of the blade. This method introduced structural problems and would be costly to manufacture and would suffer from erosion in service.

4.2.2 ANTENNA EXTERNAL TO LEADING EDGE

Due to the complexity of installing the waveguide array within the leading edge, installations have been made externally on the leading edge. Ref 2. A dielectric fairing is contoured on to the leading edge and contains the antenna. Fig 2(b). The advantage of this is that the installation is relatively simple and does not interfere with the blade proper apart from balancing. One disadvantage is that it has some loss of performance aerodynamically and while tending to give more lift, does give some more drag and loss of range. The other disadvantage is the erosion of the dielectric cover which needs periodic attention.

4.2.3 ANTENNA WITHIN THE TRAILING EDGE SECTION

The trailing edge was also a site available for a linear end-fed waveguide array to be installed, by making the trailing section of dielectric. Ref 1, Fig 2(c). This antenna may function with a very stiff blade, but this site would offer difficulties with a less stiff blade which bends in the azimuth plane. Typical of such blades are those where the rear section consists of individual pockets along the length of the blade, the gaps between which open and close as the blade bends. The site in the trailing edge is furthest from the centre of gravity and any additional weight will have the maximum effect requiring the maximum counter balance. The support of the waveguide near the trailing edge requires extra support structure with additional weight, and counter-balancing.

4.2.4 ANTENNA WITHIN THE AFT BLADE SECTION

Locating the antenna close to the main spar in the rear section has the advantage of being near the centre of gravity. Fig 2(d). It does require the rear fairing to be made of dielectric material which is not necessarily a disadvantage, as it can permit the inclusion of elements to narrow the radiation in the vertical plane as required, which is not available by either antenna in the leading or trailing edges, thereby increasing the gain.

4.3 RADIATION PATTERNS

4.3.1 AZIMUTH PATTERNS

The azimuth patterns can be derived from the end-fed slotted non-resonant waveguide arrays. The aperture distribution along the length of the antenna is chosen to suit the gain, beamwidth, and sidelobe requirements. The resultant beam from the non-resonant slotted array will have a slight squint from the normal to waveguide axis, except in the case of the Holey array Ref 1 where the array of holes give a large squint and loss of effective aperture as a result.

In the case of the installation of the antenna aft of the spar, there is space usually to install either broad face or edge slotted waveguides to suit either vertical or horizontal polarisation requirements.

4.3.2 THE VERTICAL PATTERN

Antennas located in the leading or trailing edges have very limited aperture and the patterns in the vertical plane are similar to that of the basic waveguide slightly modified by the dielectric cover. Consequently beamwidths at X Band of such installations have been of the order of 80° . At K_u band with some directivity possible, give near 50° .

The blade as it rotates, varies its axis in the vertical plane according to the load and its angle in the azimuth plane. On some helicopters this variation could be of the order of 20° . Thus to ensure coverage, a fairly wide beam is required in the vertical plane, and the very broad beams in the leading trailing edge installations more than achieve this.

4.3.3 ANTENNAS TO GIVE VERTICAL PATTERN GAIN

With the antenna source located aft of the main spar, by virtue of the broad width of the section at this point, and the available length of the trailing section, this site offers the opportunity of designing the vertical pattern to give increased gain.

The construction of the trailing section, is usually a tapered metallic honeycomb core with thin metallic skins, both of which may be replaced by dielectric material. Fig 2(d). The dielectric skins are typically 0.4mm thick of glass fibre-resin of permittivity near 4 and the core of Nomex type honeycomb of permittivity near 1.05.

The waveguide source located aft of the main spar radiates in the direction along the blade axis and will feed through the honeycomb and the skins before finally radiating. The honeycomb by virtue of its shape and permittivity greater than 1 will tend to behave possibly like a polyrod type antenna. The skins due to the higher permittivity of 4 will cause reflections particularly as some of the angles of incidence are very high being near 84° .

4.3.4 ANTENNAS OF TUNED ELEMENTS TO CONTROL THE VERTICAL PATTERN

Among antennas which may be installed in the trailing sections are those which employ tuned director elements. Fig 3. The inclusion of tuned elements on the surface of the skins was not thought to be practical due to possible changes in their tuning, due to surface painting, contamination, erosion, humidity pick-up and possible damage. The inclusion of tuned elements within the blade at X_{K_u} or K_a band appeared to present problems of installation of very small precise elements in exact positions within the blade. The nearest approach to this was a solution to horizontal polarisation which divided the honeycomb into upper and lower layers between which was disposed a Nomex sheet on which were printed the metal elements. Difficulty of control of the glue line and exact positioning of the honeycomb on to the centre sheet arose which detuned the radiators in an unpredictable manner, led to the abandonment of this solution particularly as it was not favoured by the aircraft manufacturer, who was not enthusiastic to cut the honeycomb to insert the sheet of tuned elements.

4.3.5 ANTENNAS OF UNTUNED ELEMENTS TO CONTROL THE VERTICAL PATTERN

The site of the source aft of the main spar and the tapered section lends the configuration to be studied possible as a polyrod or rather a dielectric tapered slab antenna, which behaves in a somewhat different manner. The basic action of the polyrod is discussed prior to summarising results of a theoretical study of the slab type antenna.

4.3.5.1 THEORETICAL DISCUSSION OF BEAM SHAPING BY DIELECTRIC TAPERED SLAB

The dielectric rod antenna has been extensively studied by Ref 3-7. The early simple explanation of the dielectric material giving a phase delay to the radiation and collimating as a lens did concur with some experimental results with short lengths of material, but not in general, particularly with longer lengths of dielectric. The other simple explanation by ray tracing and considering transmission and reflection at the boundaries of the dielectric material was also not tenable, since for instance a material of low permittivity, where the amplitude of reflection is negligible, would permit the waves to escape, whereas, it is now known that a portion of the launched radiation is trapped as a surface wave. The advent of surface wave theory has thus helped to explain the mechanism of the polyrod. A review of theories by Ref 3-7 has helped explain the action. Consider a dielectric rod, it will channel electromagnetic waves in a similar manner to metal waveguides, the main difference is that some of the channelled power flows also outside the guide. The resultant surface waves flow on both sides of the dielectric boundary. For dense materials only a small fraction flows outside, whereas for low permittivity materials the majority is external. Ref 8. The launching of the wave in the dielectric rod from a source is not necessarily complete, the result is that some radiation takes place at the feed to the dielectric and the rest from the dielectric material. It is well established (Ref 8) that if the dielectric material is a rod or slab of uniform thickness there is essentially no radiation once the wave is launched in the dielectric material until the wave reaches the discontinuity at the end where it radiates with some reflection taking place. There are waves which continually leak radiation as they travel along the rod but these are only weakly excited. (Ref 7). Thus the final field pattern is mainly the result of two radiating sources, one at the launcher and one at the far end of the uniform dielectric rod or slab. The percentage power of the two radiations is determined by the efficiency of the launching.

When the launcher aperture is small, the aperture of the radiation of the end of the dielectric rod or slab is generally of greater extent and can thereby beam the radiation. James Ref 8-10 has shown that by calculating the ultimate aperture of the surface wave at the end of the uniform dielectric rod or slab and combining it with that of the launcher, the gain and far field pattern can be predicted.

No accurate design data exists for the tapered rod or slab dielectric which can leak radiation along its length, though recent papers suggest methods to attempt to solve this problem, Ref 8, 9. James suggests that the tapered dielectric may be regarded as a number of infinite steps each of which produce an impedance discontinuity which causes, at each step, a loosening of the field within the dielectric and the surface wave to be more external, and a degree of radiation to take place. Thus the tapered dielectric material resultant far field is a combination of the radiation from the launcher, the radiation from individual points down the tapered dielectric and the surface wave aperture at the end of the taper. An experiment combined with theory (Ref 8) of an 8.8 wavelength long perspex ($\epsilon = 2.56$) tapered section rod from .7 to .3 wavelength indicated however that this taper gave little radiation from its length, and the far field could be forecast by considering the launching and end radiation. Fig 4. A long dielectric slab of the same cross-section and material as that of Fig 4 was found experimentally by the author to give a much wider beamwidth in the plane perpendicular to the slab axis, indicating the information gained from a similar section polyrod is not necessarily applicable to a tapered dielectric slab.

As regard the helicopter blade tapered dielectric material, the question arises, though it may be possible to consider a material of $\epsilon = 2.56$, what was likely to be the most suitable permittivity for the configuration and was there in fact a wide choice likely to give directivity.

Due to the complexity of the tapered helicopter's blades dielectric section and difficulties of theoretically computing its performance, Callett and James (Ref 11) have suggested that a guide to obtaining theoretically the radiation patterns of the helicopter blade, would be obtained by an approximate method of assuming the tapered section as of a mean uniform dielectric slab. Fig 5(a). Computed patterns for the launching horn and dielectric slab have been made for various permittivities Ref 10. The patterns in the vertical plane are shown in Fig 5(b), and indicated that for the dimensions concerned the gain falls off with the higher permittivities. The theoretical results indicate that the addition of the dielectric slab can give a gain near 4dB over the horn launcher and 7dB over the waveguide alone. In this configuration the gain can be obtained with a low permittivity slab material resulting in the minimum weight increase and modification to the helicopter blade.

Experimental vertical patterns and relative gain for a length of slab antenna with sectional dimensions as the tapered helicopter blade shape, with various permittivities are shown in Fig 6(a) and 6(b) and indicated also that a low permittivity of near 1.3 gave the greatest gain.

Another experiment with a fixed longitudinal length of slab antenna, variation of the length of the dielectric tapered section, for a particular permittivity indicated that gain is sensitive to length of the tapered section. Fig 6(c). The gain curves in some cases have marked ripples, particularly the 1.75 permittivity, where the reaction between launcher and tapered dielectric radiations is most severe. Thus it would appear that the optimum conditions for gain of a particular dielectric shaped tapered slab will depend on its length, and a corresponding suitable dielectric, and an efficient launching system. The maximum gain appears to be at least that which would be from the equivalent aperture of the square root of the sectional length of the dielectric, as for conventional and fire arrays. The gain obtained by the addition of the dielectric slab decreases with increase in launcher aperture. (For a two wavelength aperture 3 dB and for one of four, near 0 dB).

Comparison of the theoretical estimate and the practical results showed a similar permittivity between 1.2 to 1.35 as giving best gain. However exact correlation would not be expected, since the theoretical method assumes the tapered shape to be equivalent to a shorter uniform length, and a suitable phase relation is given to the launcher and end radiation.

5 AN X BAND DESIGN STUDY OF VERTICAL PATTERN GAIN

5.1 THE REQUIREMENT

The trailing edge of the blades of a particular helicopter changed its axis as it rotated, from near 0° to 25° down. Thus the radiation if beamed along the trailing edge blade axis would radiate

downwards nearly all the time, whereas it was always required to radiate horizontally. Thus the beam would be required to radiate up to 25° above the blade axis as well as along the blade axis, a coverage of 25° . The launcher waveguide is positioned in the blade where the width is near 1.1 wavelengths and its polarisation was horizontal. The sectional length of dielectric tapered trailing section was near 5.5 wavelength (Fig 7(a)). Thus the problem was to raise the beam above the blade axis to cover the 25° of blade axis variation and to narrow the beam to give more gain.

5.2 DIELECTRIC ANTENNA WITH PERMITTIVITY NEAR 2.2

As the beam was required to be directed upwards to cover 25° , an application of the dielectric antenna design would be to arrange for the axis of a suitable dielectric to lie at an angle of say $12\frac{1}{2}^\circ$ within the blade. To obtain the longest sectional length of tapered dielectric the waveguide source is confined in the lower portion of the blade and fed from the waveguide to a short .4 wavelength metal horn enclosing a dielectric constant material near 2.2 of length 3.8 wavelengths.

Calculation from theory showed that this would give a beamwidth near 44° , neglecting the effect of the honeycomb and the skins. An experimental model with a suitable dielectric of polythene gave a vertical pattern as in Fig 7(b) with a beamwidth near 40° , similar to that forecast theoretically. The experimental model using polythene would have resulted in a considerable weight increase in the blade. To minimise the weight problem an artificial dielectric consisting of layers of short dipoles closely spaced within a lightweight foam giving a permittivity near 2.2 and loss tangent 0.01 (Fig 7(c)) was used to replace the polythene and achieved similar patterns. The construction of the blade with this foam still gave an undesirable weight increase and a difficult construction of skin, honeycomb, artificial dielectric and foam, to manufacture. Further the positioning of the waveguide located near the lower metal dielectric joint which was a high stress region was not favoured by the blade structural designer.

5.3 DIELECTRIC ANTENNA WITH LOW PERMITTIVITY

The theoretical studies of dielectric slabs has shown that beam directivity can also be obtained with quite low permittivities provided the launching of the waves is efficient. This has been confirmed by experiment and considerable gain has been achieved along the blade axis. In the case of the dimensions of the model, and pattern measurements Figs 5 and 6 a permittivity near 1.25 would give most gain.

Considering the X Band blade model to achieve this efficiency, the waveguide source needs to be within a metallic horn of the optimum aperture width offered by the blade ie 1.1 wavelengths. The horn is provided by the metallic surfaces of the blades, and the rear spar, and encloses the waveguide feeding the dielectric fairing. The required permittivity of 1.2 to 1.3 can be obtained with negligible weight increase by using the form of artificial dielectric consisting of metal imprints on the honeycomb material, or on thin dielectric material laid in the honeycomb cells as required. A design as Fig 8 gave a beamwidth of near 24° radiating along the blade axis.

The requirement of radiating at an angle above the blade axis was achieved by extending the side of the horn feed under the blade. Fig 9(a). The exact mechanism of this is not clear. The extension may have acted as a reflecting earth plane or it may have caused an asymmetry and phase difference in the surface waves on the upper and lower surface of the blade.

The pattern resulting from this arrangement shown in Fig 9(b) gave suitable coverage in the horizontal plane independent of blade angle in the vertical plane.

A pattern obtained with a lower permittivity near 1.08 is shown in Fig 9(b).

6 A K_u BAND DESIGN STUDY OF VERTICAL PATTERN

At K_u band the available aperture at the waveguide source was near 2 wavelengths and the length of the dielectric available was near 11 wavelengths. Fig 10(a). By designing the waveguide into a horn of 2 wavelengths aperture a beamwidth near 30° is obtained. With an artificial dielectric of permittivity 1.25 a narrow beam of 13° width is obtainable on blade axis and with a permittivity of 1.07 19° beamwidth. A beam directed up off blade axis by 13° , with a permittivity 1.2, a 18° beamwidth was obtained.

While these beams gave considerable gain, they were possibly embarrassingly narrow in the helicopter under study. To exploit the gain, a design which attempted to maintain a relatively narrow beam pointing at the desired vertical angle incorporated a double source. By control of power and phase in each waveguide, the beam could be maintained at a particular angle in the horizontal plane, independent of blade axis movement. Fig 10(b).

7 MECHANICAL DESIGN FOR X BAND MODEL

7.1 WAVEGUIDE

Weight being important, in an X Band design special Duraluminium waveguide was used which had the advantage of maximum strength to weight ratio. The shape of the guide is near rectangular with all corners radiused. The rounding of the waveguide was recommended to relieve, at the corners, any sharp stresses being transferred to a similarly shaped tube in which it was located. Fig 11(a).

The waveguide is held at the inboard position and rests in a tube in which it is free to elongate due to forces as the blade rotates. The freedom of movement of the waveguide longitudinally envisaged the minimum stress put on to the main spar.

Conventional edge slots were chosen as this suited the application, though broad slots would also have been practical. Though slots weakened the waveguide, it was calculated this was preferable to using radiating round holes which squint the beam to such an extent that considerable aperture is lost.

The waveguide lies in a glass fibre tube of 0.15 mm thickness. At the front face of the tube the thickness is reduced to 0.075 mm to reduce the material in direct contact with the slots, which have to be tuned in conjunction with the tube and whole blade section. Fig 11(a).

7.2 CORE

The dielectric support material within the trailing edge is Nomex honeycomb, in which may be located as necessary, metal imprints of shortened dipoles on Nomex sheet.

7.3 SKINS

The skins in the trailing edge are of dielectric resin-glass fibre 0.38 mm thick. Matching the skin may be achieved by wires as inductances in the skin for perpendicular polarisation as arises from horizontal polarisation. The wires lying longitudinally along the blade spaced 12mm apart and of 0.1mm diameter. The wires are laid between the two layers of glass cloth forming the skin. Various methods to match vertical and circular polarisation are outlined in Ref 12.

7.4 METALLIC SURFACES

The forward metallic skin is jointed to the dielectric skin as convenient to the manufacturer. The joints may be at the positions as required by the metallic launching horn and the metallic earth plane, or if nearer the main spar, thin wires set in the dielectric skins to simulate the horn and earthing plane are necessary. Fig 11(a).

7.5 BLADE POCKETS

Since some blade designs, as for instance in the helicopter under study, have considerable flexing, the trailing edge sections are normally made in short lengths, called pockets. Fig 11(b). Between each pocket is a flexible joint which compresses and stretches in both planes as required by the movement of the blade. It is important that the joints between these pockets are not such that they produce regular discontinuities across the aperture. By making the pockets of different sizes the regular pattern is broken, and by using the minimum amount of jointing material which has to be dielectric, minimum degradation of the azimuth patterns and sidelobes can result.

7.6 ANTENNA FEED

From the blade antenna to the centre hub, the waveguide system has to provide components capable of following the blade actuations of pitch, twisting, lag, lead etc. These elements have to operate in an environment of vibration buffeting and weather, and need to be designed accordingly. Fig 12.

From the centre hub to the transmitter receiver compartment within the helicopter, the waveguide has to incorporate a rotating joint system. The waveguide may on some helicopters be able to run down the centre of the hub and through the gear box and have a simple rotating joint system. If this is not possible the waveguide run would be external and a split waveguide "round the hub" rotating joint required.

8 CONCLUSIONS

Various sites have been considered for long antennas from L to K_a Band in helicopter blades and the overcoming of problems that arise have been discussed.

At the shorter microwavelengths (X K K_a), a site aft of the main spar in a dielectric trailing section has the advantage of being near to the centre of gravity. It has been shown theoretically and experimentally that an antenna radiation if launched efficiently into the dielectric section, whose permittivity is suitably chosen can permit a control of its vertical pattern to be made, with improved directivity and gain. High permittivity materials are not necessary as those of low permittivity (1.15 - 1.5) have given considerably improved gain.

While no accurate theory of the tapered dielectric slab antenna exists, the method of estimating an equivalent shorter uniform length for the tapered shape (Ref 11) and calculating the theoretical radiation pattern of the launcher and end radiations, have been useful in predicting the experimental results obtained with microwave antennas in the dielectric tapered trailing section of the helicopter blade.

Methods have been found to radiate the beam off axis to maintain the radiation in the horizontal plane, while the helicopter blade performs its various movements as it rotates.

To minimise weight the antenna may be constructed of lightweight waveguide, with the use of artificial dielectric materials in the blade's dielectric honeycomb, to give the required permittivity for the dielectric slab, and thin wires can be used to match the dielectric skins, and metallic foil or thin wires used to simulate the horn and its extension, as necessary.

9 REFERENCES

- Ref 1 Lockheed Electronics Coy. Plainfield N.J. "Rotor Blade Multi-Function Helicopter Radar Systems".
- Ref 2 Stolinski, J, Upton H, Witzke C. "Military Test Results on the Helicopter Multi-function System". 28th National Forum of American Helicopter Society Washington May 1972.
- Ref 3 Kiely D G. "Dielectric Aerials". Methven Monograph London 1953.
- Ref 4 Zucker J F. "Surface and leaky-wave antennas". Antenna Engineering Handbook Chapter 16, McGraw-Hill New York 1961.

- Ref 5 Brown J and Spector J O. "The radiating properties of and fire aeriels". Proc Instn Elect Engrs 104B pp 27-34 1957.
- Ref 6 James J R. Theoretical investigation of cylindrical dielectric-rod antennas. Proc Instn Elect Engrs 114 pp 309-19 1967.
- Ref 7 Bach Anderson "Metallic and Dielectric Antennas". Polyteknisk Forlag Denmark 1970.
- Ref 8 James J R. "Engineering Approach to the design of Tapered Dielectric Rod and Horn Antennas". The Radio and Electronic Engineer, Vol 42 No 6, June 1972.
- Ref 9 Balling, P. "Radiation from the dielectric wedge" Laboratory of Electromagnetic Theory LD 20b. The technical University of Denmark-Lyngby December 1971.
- Ref 10 Gallett, I N L et al. "Gain Enhancement of Microwave Linear Arrays with Dielectric Slab Attachments". European Microwave Conference Brussels September 1973.
- Ref 11 James J R and Gallett I. "Gain Enhancement of Helicopter Blade Antennas by Dielectric Inserts". Tech. Note RT 58 Royal Military College of Science Swindon UK May 1973.
- Ref 12 Cary, R H J. "Some experimental results of dielectric and metallic loading of radomes. Proc of 11th Electromagnetic Window Symposium, Georgia Institute of Technology, Atlanta, USA. August 1972.

"Contributed by permission of the Director of RRE. Copyright Controller HBMSO."

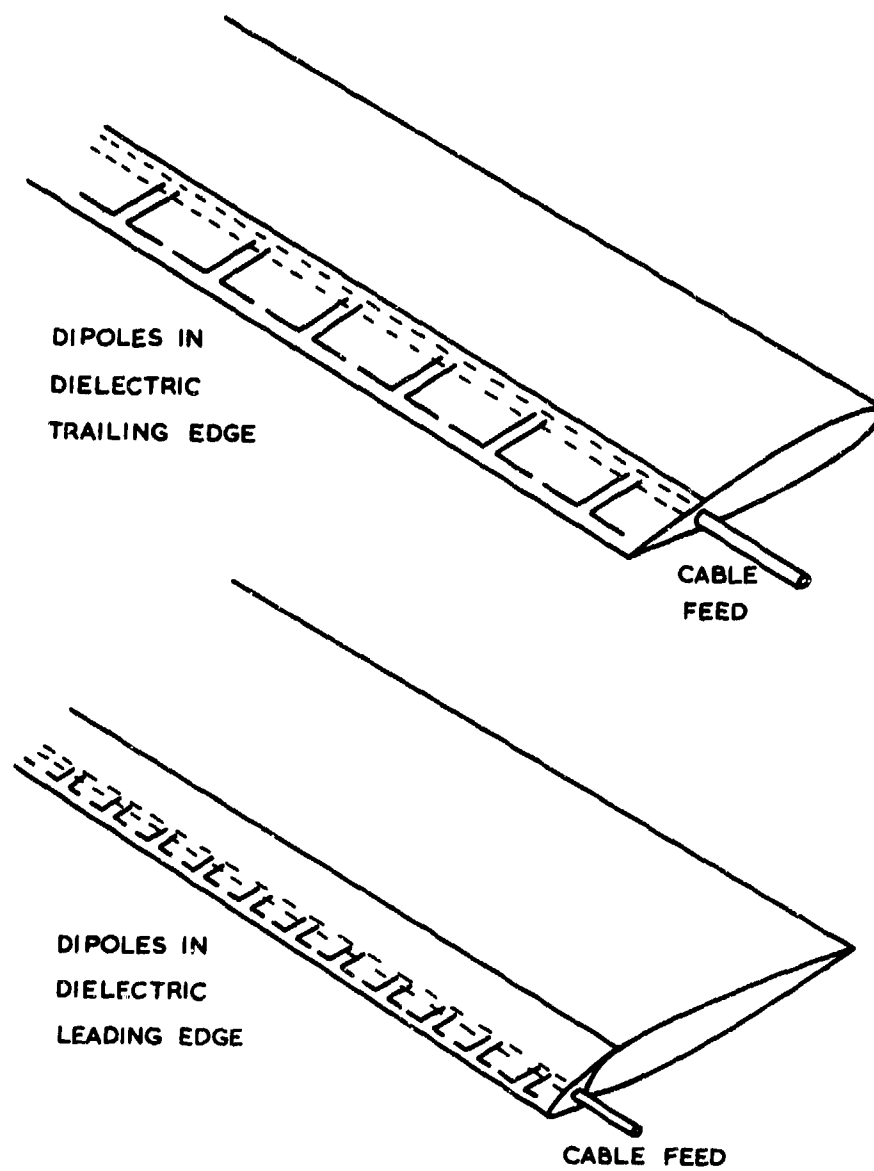


Fig.1 L or S band antenna in helicopter blade

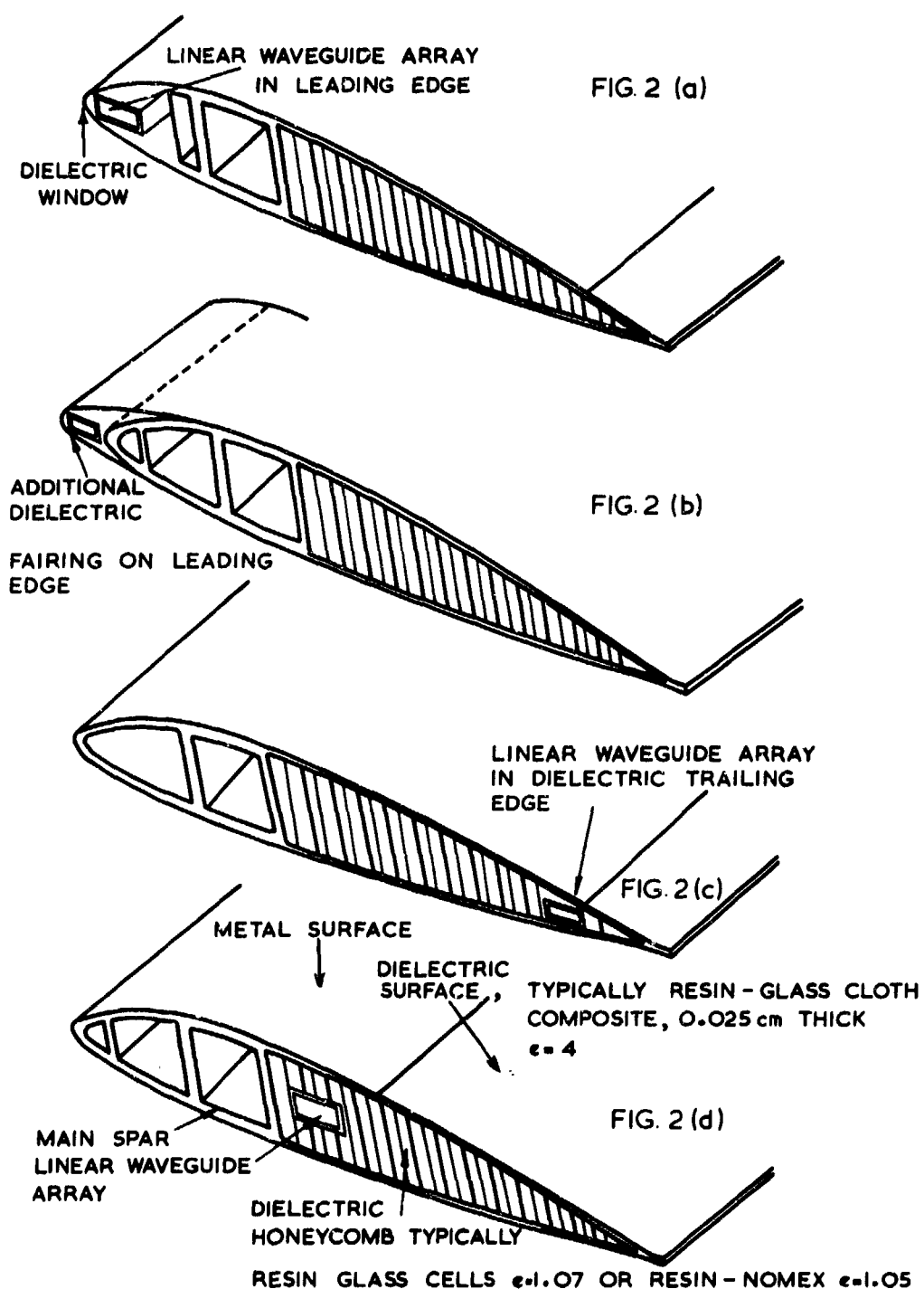
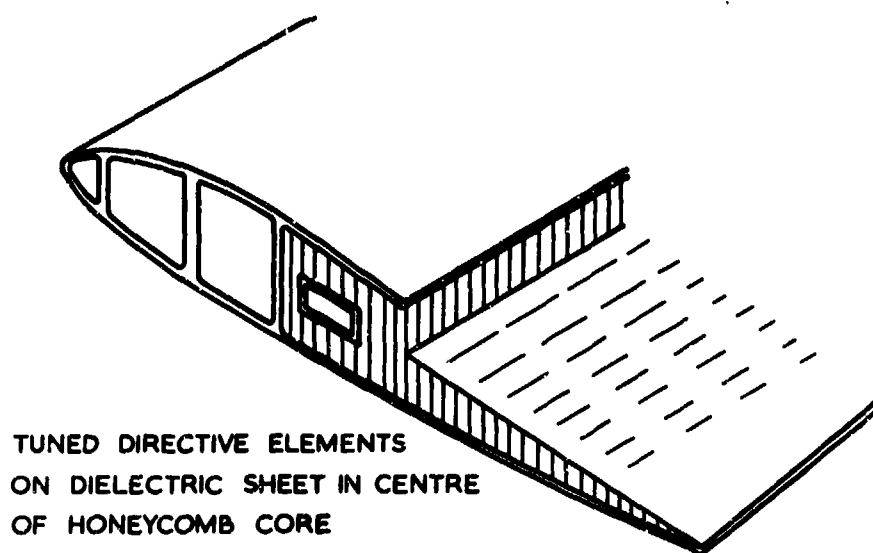
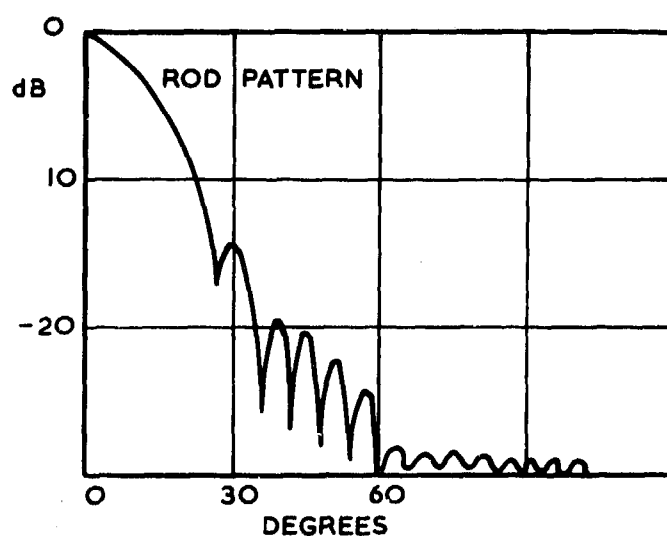


Fig.2 Sites of linear arrays in blade



TUNED DIRECTIVE ELEMENTS
ON DIELECTRIC SHEET IN CENTRE
OF HONEYCOMB CORE

Fig.3 Tuned directive elements to beam radiation



ROD BEAMWIDTH 24° (REF 8)

EXPERIMENTAL SLAB, BEAMWIDTH:- 50 & LOW GAIN
OF SAME SECTION.

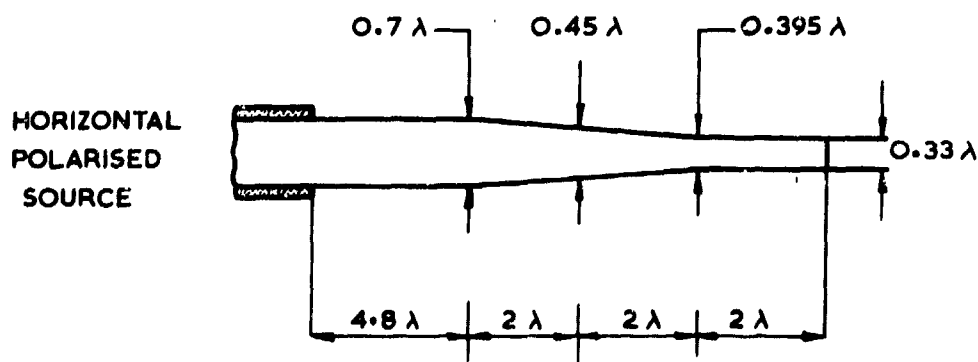


Fig.4 H plane radiation of dielectric rod antenna

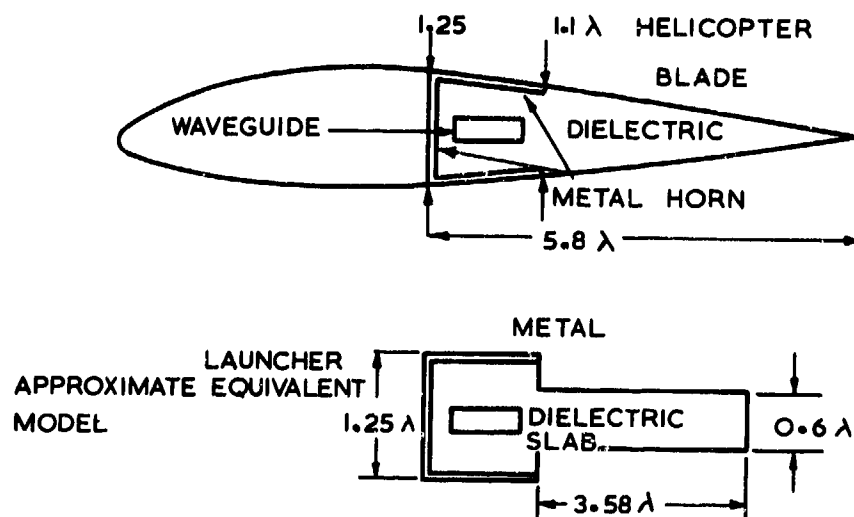


Fig.5(a) Helicopter blade antenna and approximate model

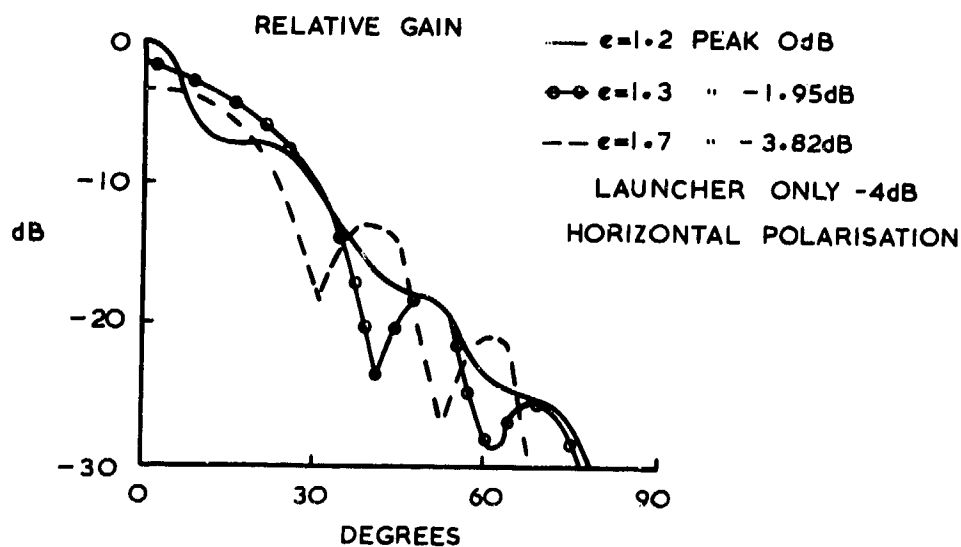


Fig.5(b) Vertical patterns of model antenna with various permittivities (theoretical)

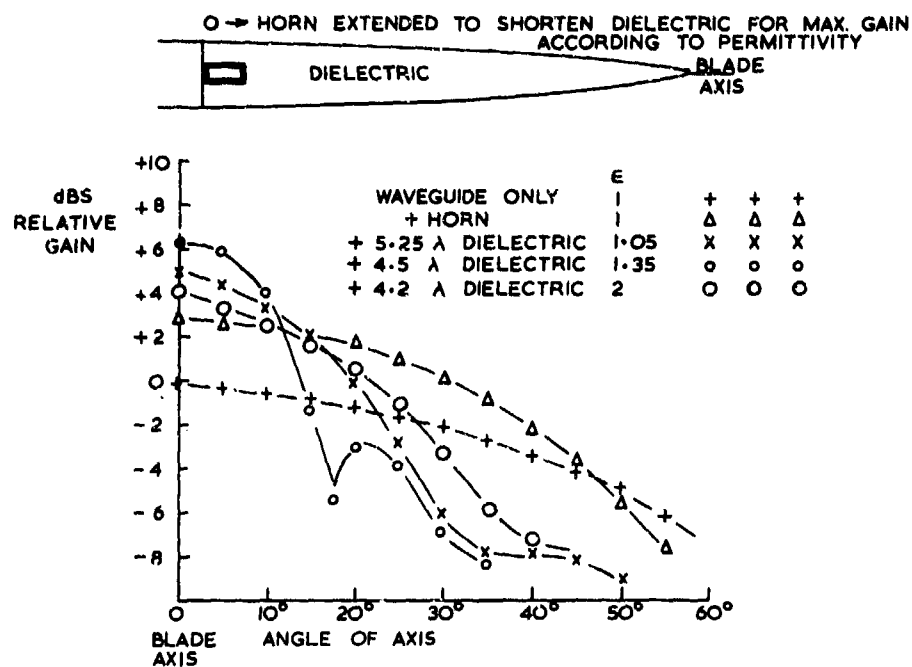


Fig.6(a) Radiation diagram off blade axis for various permittivities with dielectric length altered for maximum gain - H plane

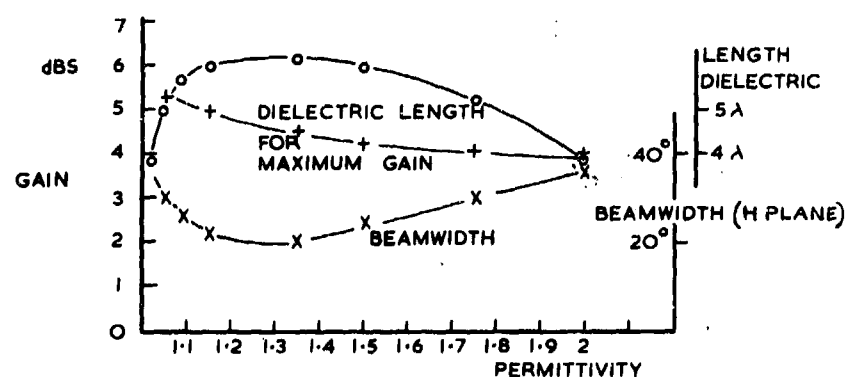


Fig.6(b) Variation of dielectric length for maximum gain and minimum beamwidth with various permittivities

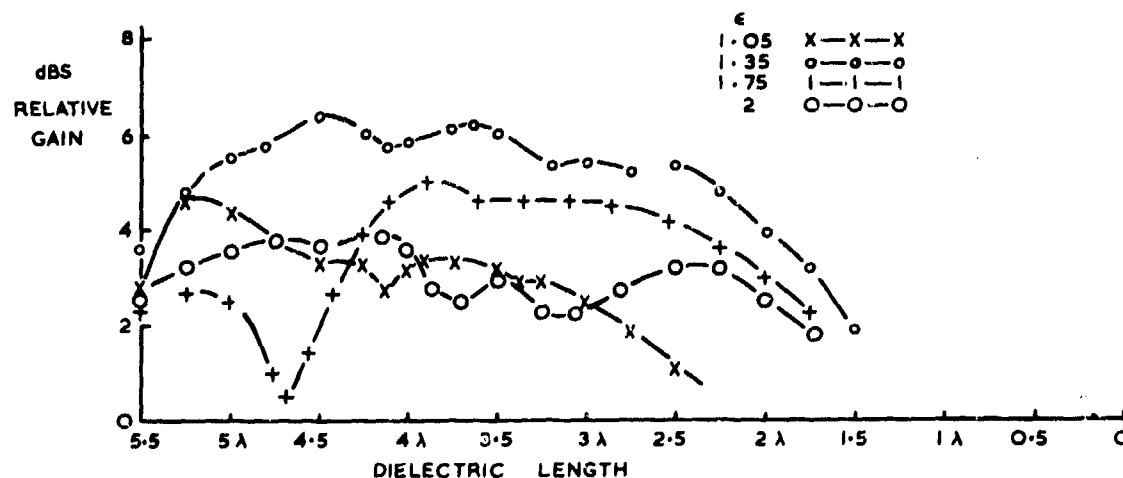


Fig.6(c) Gain versus dielectric length for various permittivities

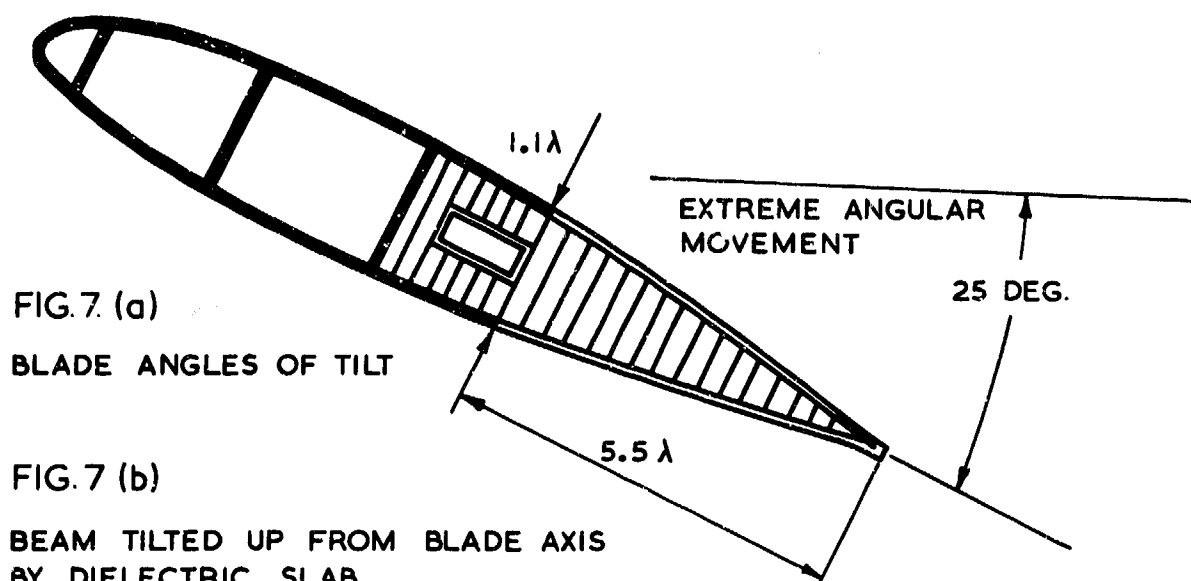


FIG. 7 (b)

BEAM TILTED UP FROM BLADE AXIS
BY DIELECTRIC SLAB

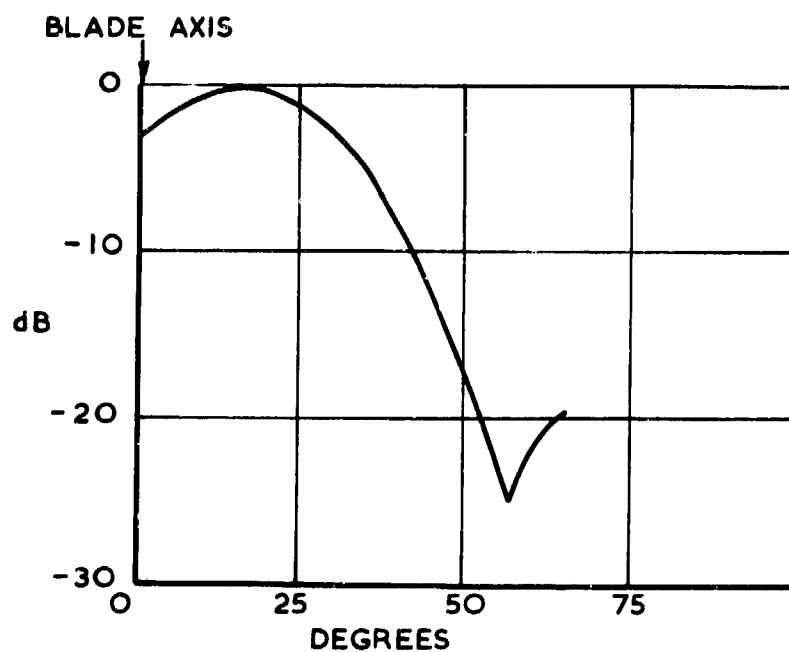
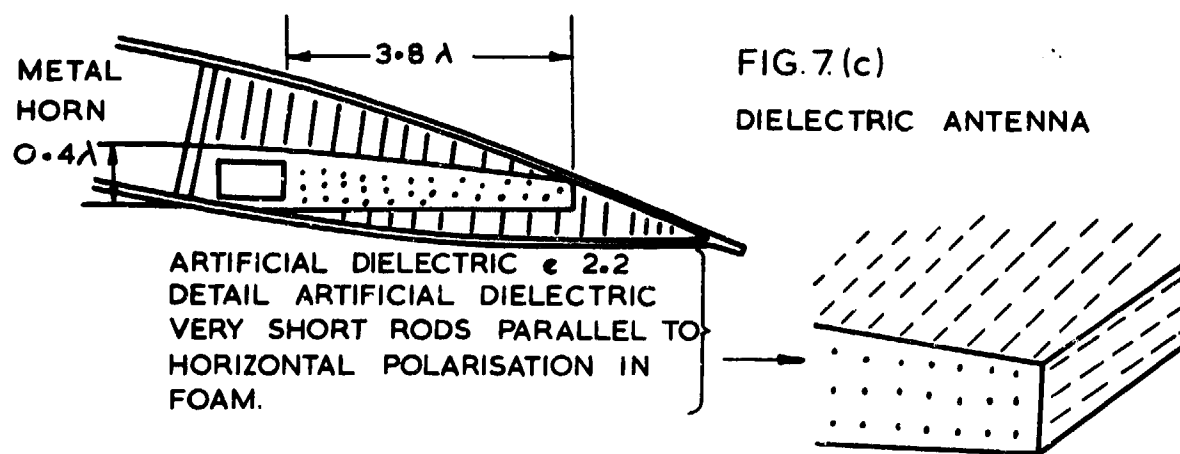
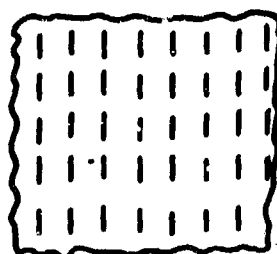


FIG. 7 (d)

Fig. 7 Beam tilt by artificial dielectric $\epsilon = 2.2$

ARTIFICIAL DIELECTRIC IN CELLULAR STRUCTURES

DIPOLES



LAYERS OF METALLIC DIPOLES

LAYER SPACING 7mm

DIPOLE SIZE 4mm

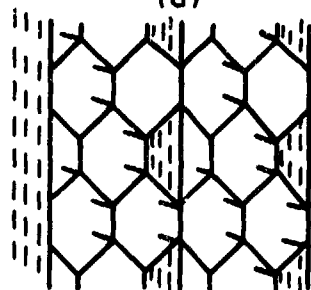
DIPOLE SPACING 7mm

 $\epsilon = 1.3$ LOSS TANGENT 0.003
(X BAND)

SHEETS WITH METAL IMPRINTS PLACED IN CELLS

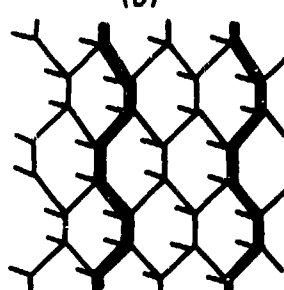
IN HONEYCOMB JOINTS

(a)



IN HONEYCOMB JOINTS

(b)



IN CELLS

(c)

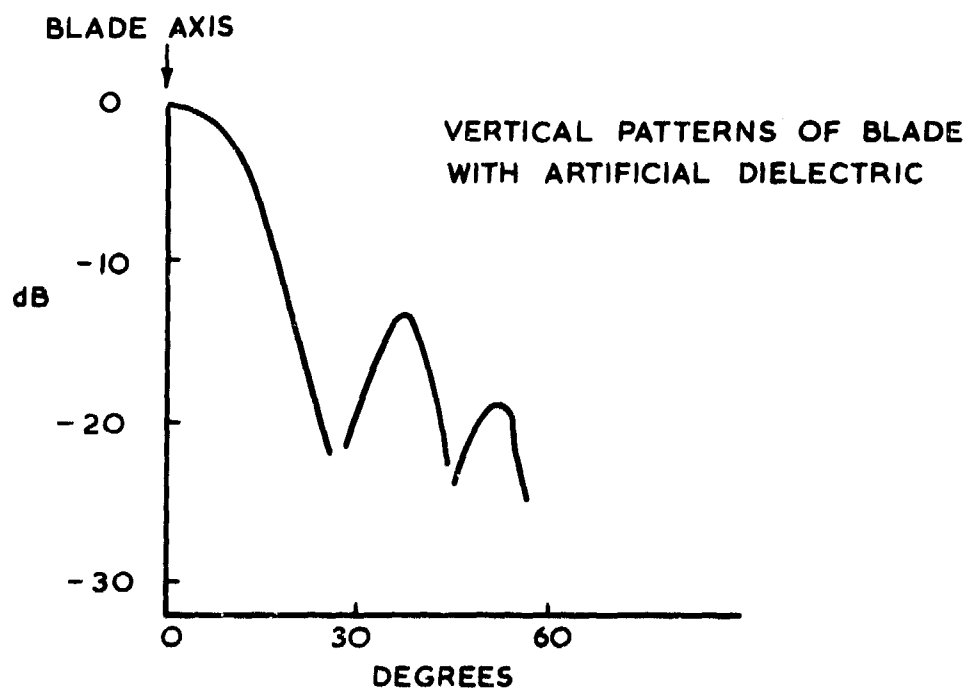
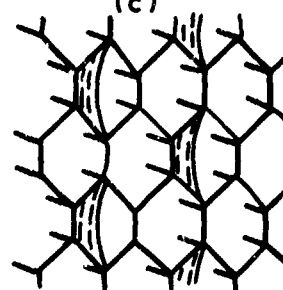


Fig.8 Blade antenna with artificial dielectric

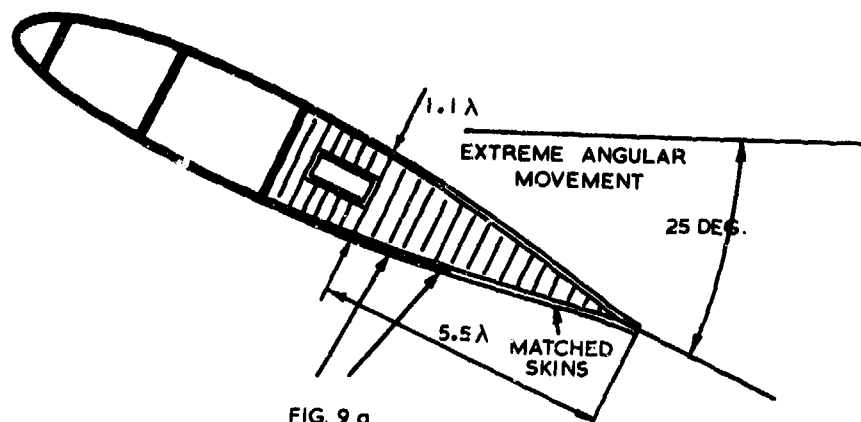


FIG. 9 a.
EARTH PLANE EXTENSION TO TILT BEAM

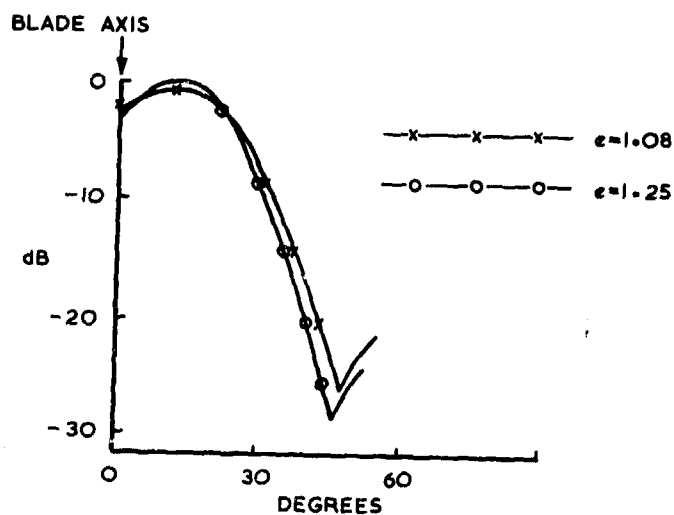
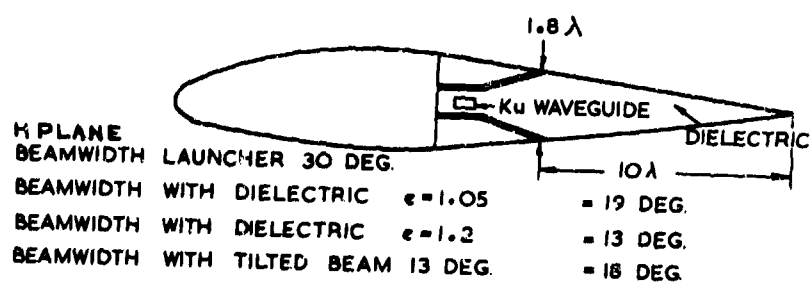
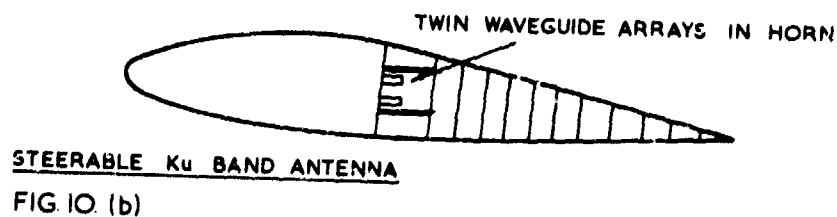


FIG. 9 b.
VERTICAL PATTERNS OF PLANE EXTENSION TO TILT BEAM

Fig.9 Tilted beam with earth plane extension



Ku BAND BEAMWIDTH
FIG. 10. (a)



STEERABLE Ku BAND ANTENNA
FIG. 10. (b)

Fig.10 Ku band antenna

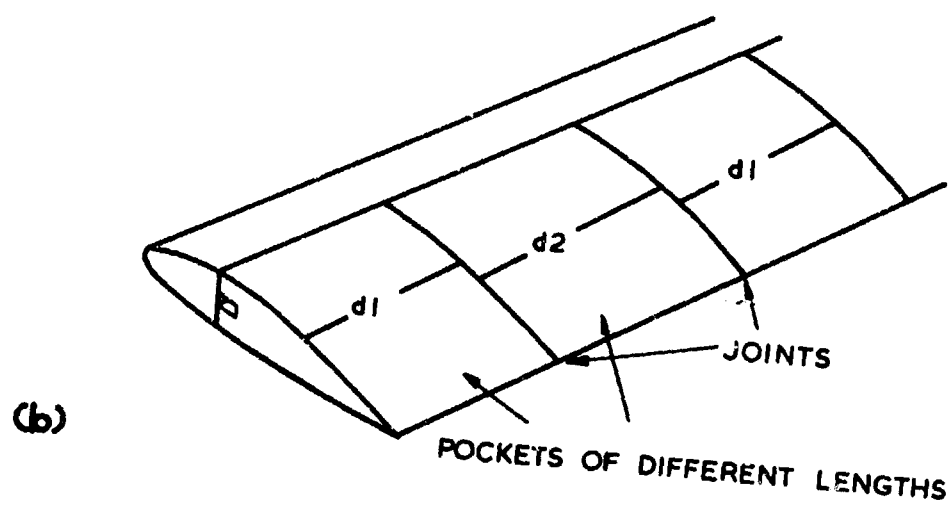
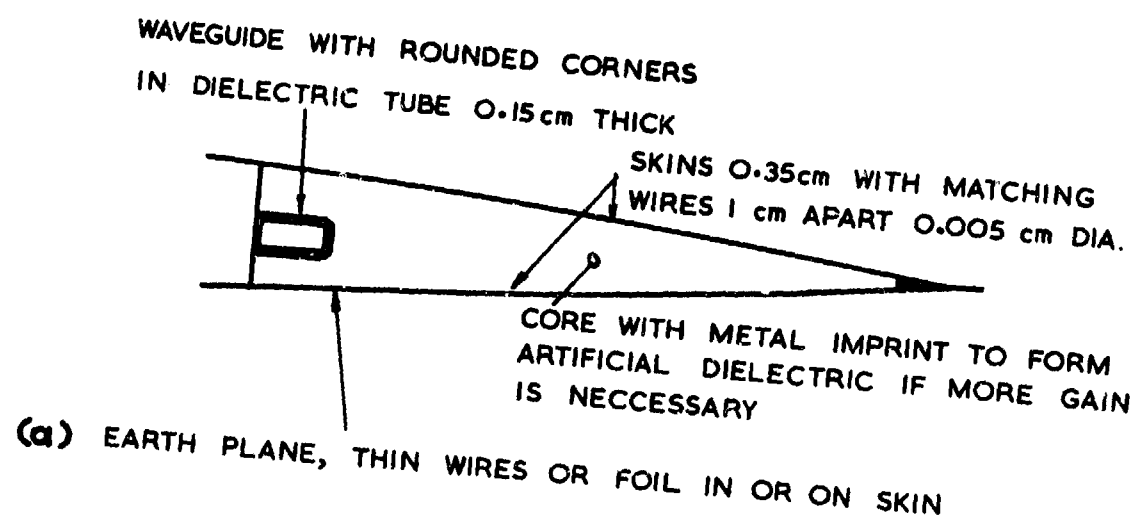


Fig. 11 Mechanical details of X band antenna

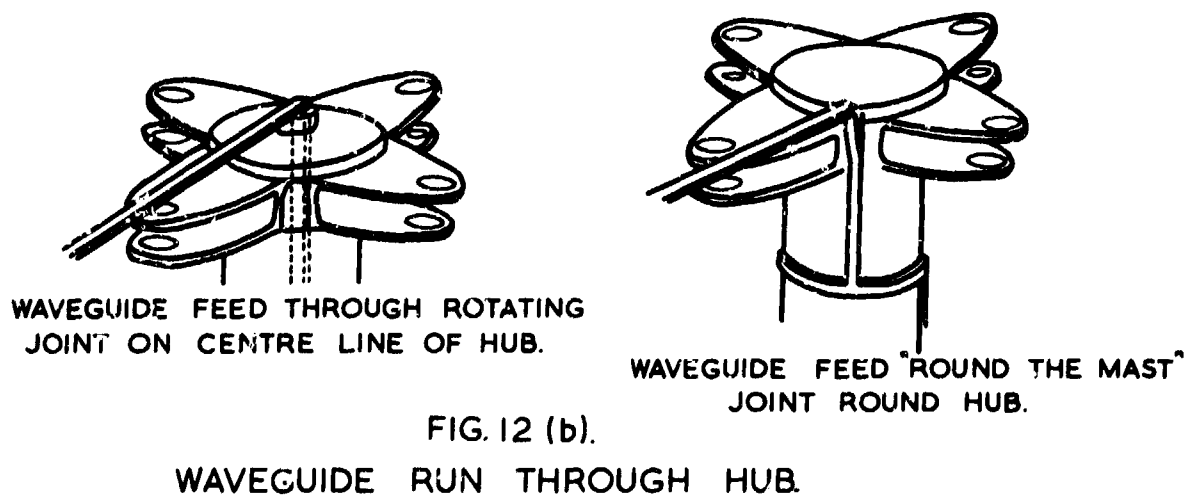
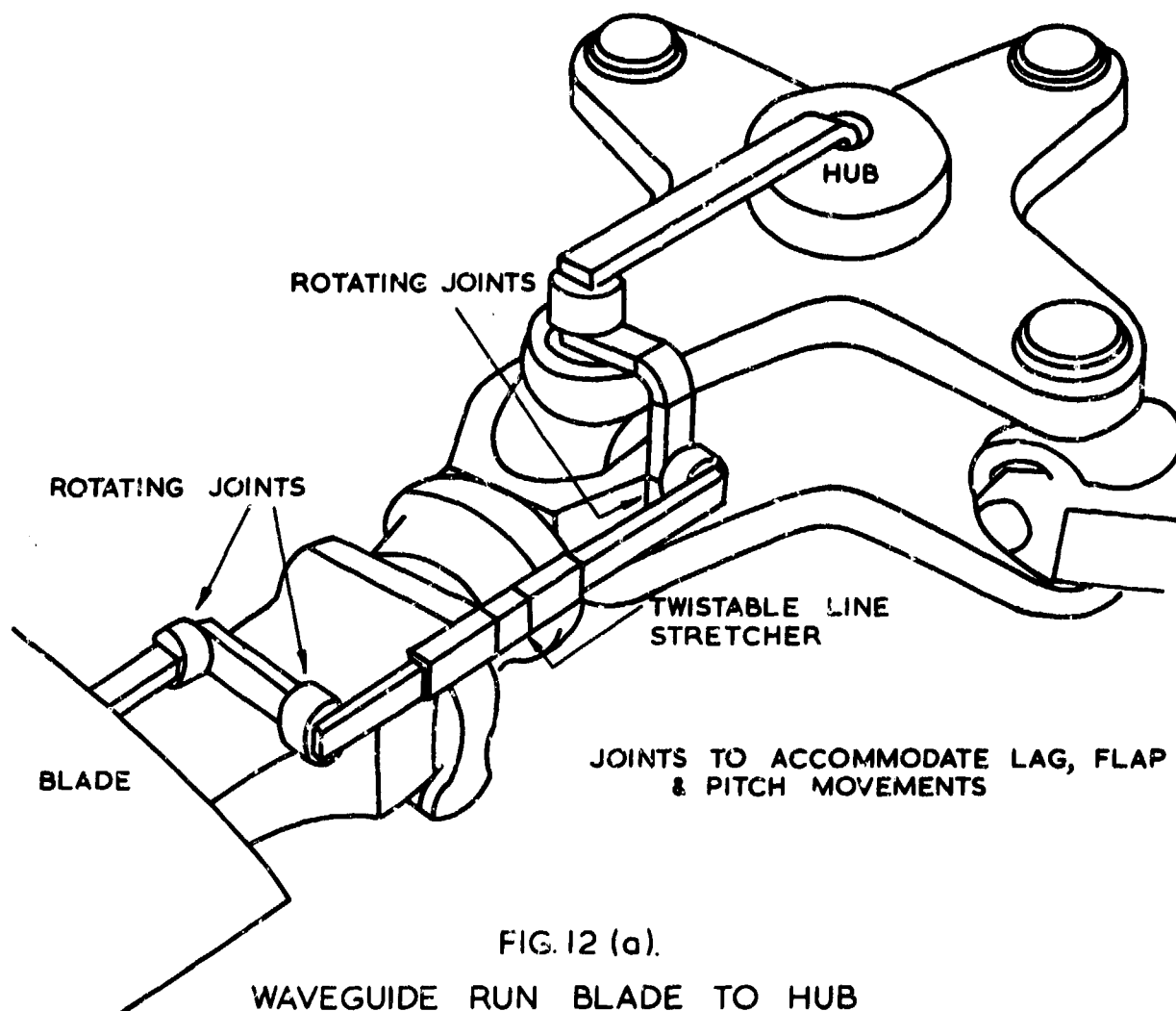


Fig.12 Waveguide feed to blade

DISCUSSION

J.F. GOBERT: Did you consider the possibility of frequency scanning; for example to keep the beam in a given direction independently of the blade rotation?

R.H.J. GARY: The blades rotate at nearly 200 r.p.m. but not in a perfectly circular motion. The lag and lead angle is measured mechanically and is fed to the radar rotating display so that the beam pointing is truly recorded. We have not used frequency shift to squint the beam in order to compensate for this lag and lead angle of the blade. I do not consider it possible to keep the beam in a given direction continuously, for instance for communication. The antenna is mainly on all round look device.

C. ANCONA: What is the opinion of the pilots about flying with such "electromagnetic" blades?

R.H.J. GARY: The integration of the waveguide inside the blade has needed considerable testing to be mechanically satisfactory. As a precaution a limit of 200 hours is placed on the antenna, but this will be extended to the full life of the blades as experience is gained. The pilot is happy with the safety factors and should be pleased to have such a high resolution radar map.

T.W. BAZIRE: Increased gain would be achieved by reducing the vertical beamwidth, but this would require control of beam direction in elevation to compensate for varying tilt of the blade. Have methods of achieving such control been considered?

R.H.J. GARY: A vertical stack of two waveguides within the blades has been considered, with a phase shifter in one guide feed to move the beam in the vertical plane, but it is more complex and when more confidence in the system is gained perhaps this method will be used.

J. VAN BLADEL: Was the Doppler effect of any significance in the operational use of the helicopter borne systems? What are typical rotational speeds for the antenna elements?

R.H.J. GARY: The typical speed is 150-200 r.p.m. This speed limits the range of a radar system with very narrow beamwidths, but the Doppler effect is not significant unless one is interested in M.T.I.

SYSTEME D'ANTENNES A COMMUTATION REALISANT UNE COUVERTURE AVION AUX NORMES AEROSAT

par

C. ANCONA et P. FROIDURE
STAREC : 12 avenue Carnot
91300 MASSY - FRANCE

RESUME :

Les projets de satellites aéronautiques nécessitent à bord d'avion des systèmes d'antennes qui assurent une couverture hémisphérique avec un gain minimum donné.

Trois types de solutions sont envisageables ; les réseaux à balayage électronique, les solutions à orientation mécanique et les systèmes d'antennes commutables que nous aborderons ici.

On examine dans la première partie de l'exposé quelques aspects théoriques de ce problème. On met d'abord en évidence les relations entre la couverture angulaire souhaitée, le gain dans l'axe de l'antenne assurant cette couverture, et le gain minimum dans la zone angulaire considérée (gain marginal).

Ces relations sont traduites sous forme d'un réseau de courbes permettant, soit d'optimiser le gain marginal, soit d'effectuer un compromis adéquat pour miniaturiser l'antenne, ou au contraire, pour l'agrandir et améliorer ainsi sa protection contre les trajets multiples. Les hypothèses faites sont celles de diagrammes de révolution à profil classique (non formé).

On examine ensuite, l'association optimale de n diagrammes de révolution du type décrit ($3 \leq n \leq 8$) en vue d'obtenir le pourcentage maximum d'angle solide couvert par rapport à l'hémisphère limité à des sites de 10° . Les résultats obtenus sont présentés sous la forme de courbes permettant de déterminer, à partir du nombre d'antennes supposées orientées de façon optimale, et de la couverture individuelle de chaque antenne, le pourcentage total de couverture qui peut être assuré.

La seconde partie de l'exposé concerne deux exemples de réalisation utilisant les résultats théoriques généraux exposés dans la première partie, exemples pour lesquels on a choisi d'utiliser respectivement 4 et 6 antennes.

Après avoir présenté les diagrammes de rayonnement de l'antenne élémentaire proposée (dipôles croisés dans une cavité cylindrique), on met en évidence les couvertures respectives obtenues sous forme de courbes iso-gain. On souligne les caractéristiques opérationnelles pour les principales routes aériennes en radio-communication (un seul satellite) et en localisation (deux satellites) y compris la protection contre les trajets multiples ("multipath"), et l'on présente un exemple d'implantation à bord d'avion.

On conclut en soulignant les possibilités offertes par l'utilisation d'antennes commutables quand le gain marginal désiré est modéré ($g \approx 4$ dB).

I. INTRODUCTION

Les projets de satellites aéronautiques nécessitent à bord d'avion, des systèmes d'antennes qui assurent une couverture hémisphérique limitée à un site de 10° en général, avec un gain minimum donné.

Trois types de solutions sont envisageables : les réseaux à balayage électronique, les solutions à orientation mécanique et les systèmes d'antennes commutables, que nous aborderons ici.

Le principe d'un système d'antenne commutable assurant une couverture hémisphérique consiste à implanter sur l'avion un certain nombre d'antennes, chacune assurant la liaison dans une portion de l'hémisphère (fig. 1).

Parmi les caractéristiques définissant ce type de solution, deux présentent une importance particulière : ce sont le nombre d'antennes élémentaires nécessaires et le gain minimum assuré dans la couverture.

Ces deux caractéristiques sont liées l'une à l'autre ; en effet, un gain minimum élevé dans toute la couverture ne pourra être obtenu qu'au prix d'un nombre important d'antennes élémentaires ; inversement, il est théoriquement impossible d'assurer un gain minimum supérieur à 3 dB à l'aide d'une antenne unique.

Dans le but d'éclairer le compromis à réaliser entre le nombre d'antennes élémentaires que l'on voudrait le plus petit possible, et le gain minimum assuré dans la couverture que l'on désire maximiser, nous allons examiner tout d'abord le cas d'une antenne élémentaire assurant une portion de la couverture totale. Pour cette antenne, supposée de révolution, nous dégagerons les relations entre la couverture angulaire souhaitée, le gain net dans l'axe de l'antenne, et le gain minimum net dans toute la couverture (gain marginal). Nous examinerons ensuite l'association géométrique optimale de plusieurs antennes identiques.

La seconde partie de l'exposé montrera deux exemples de réalisation possible optimisée à l'aide des résultats généraux exposés en première partie, ainsi qu'un exemple d'implantation à bord d'avion.

II. OPTIMISATION DES COUVERTURES ANGULAIRES

II.1. Analyse des caractéristiques de l'antenne élémentaire

Sur la figure 2, nous présentons les diagrammes relatifs de plusieurs antennes de gains différents; on constate que la couverture angulaire dans laquelle le gain est supérieur ou égal à 0 dB varie, et passe par un maximum pour une certaine valeur du gain dans l'axe.

Pour étudier de façon plus précise ce problème, nous ferons les hypothèses suivantes :

- 1) La forme du diagramme de rayonnement exprimé en dB d'une antenne au voisinage du maximum est assimilable à un arc de parabole.
- 2) Le gain maximum d'une antenne est égal, à une constante près, à la directivité du lobe sectoriel de révolution ayant pour largeur la largeur à 3 dB du diagramme de rayonnement de l'antenne considérée.

En appelant :

Θ_x : la largeur angulaire à X dB de gain net du lobe principal d'une antenne.

G_m : le gain maximum net par rapport à l'isotrope de cette antenne (en décibels).

α : la largeur à 3 dB du lobe principal de cette antenne.

Les hypothèses ci-dessus conduisent alors à la formule suivante :

$$\frac{(\Theta_x)^2}{(\alpha)^2} = \frac{G_m - X}{3} \quad (1)$$

qui traduit l'allure parabolique du diagramme de rayonnement :

$$\begin{aligned} \text{et } G_m &= 10 \log_{10} \left(\frac{4 \pi}{2 \pi (1 - \cos \alpha/2)} \right) - A \\ &= 10 \log_{10} \left(\frac{2}{1 - \cos \alpha/2} \right) - A \quad (2) \end{aligned}$$

où A est une constante liée au rendement de l'antenne aux pertes par désadaptation, par taux d'ellipticité, etc... dont la valeur est estimée à 2 dB.

En éliminant α entre les formules (1) et (2), nous avons tracé un réseau de courbes donnant la largeur utile Θ_x du lobe de l'antenne à X dB de gain net, en fonction du gain maximum net G_m en considérant X comme un paramètre.

On constate que chacune des courbes de ce réseau (fig. 3) présente un maximum : ainsi la couverture angulaire maximum que l'on peut réaliser avec un gain de 4 dB net ($X = 4$ dB) est de l'ordre de 80° ; pour un gain net de 7 dB, la couverture angulaire maximum est de 60° environ et tombe à 40° environ pour un gain net de 10 dB.

Notons enfin que l'aérien assurant la couverture angulaire maximum avec un gain net donné est celui qui présente un gain maximum supérieur de 4,3 dB au gain demandé dans la zone à couvrir.

Par exemple, l'antenne élémentaire qui assurera la couverture angulaire la plus large avec 4 dB de gain net dans toute la couverture sera celle qui présente un gain maximum net de $4 + 4,3 = 8,3$ dB.

Ce résultat est en parfait accord avec les travaux de J.W. DUCAN (Réf.1); c'est une propriété intrinsèque du lobe à 4,3 dB qui apparaît ainsi comme une valeur remarquable. Il ne s'applique cependant rigoureusement qu'aux antennes de révolution ayant un diagramme de rayonnement d'allure parabolique.

Signalons qu'il n'est pas toujours nécessaire d'adopter les solutions optima représentées sur la figure 3. On peut être conduit à s'en écarter quitte à augmenter leur nombre, soit pour avoir des antennes élémentaires de plus petites dimensions, soit pour admettre des antennes plus grandes en vue d'améliorer la protection contre les trajets multiples.

II.2. Association géométrique optimale de plusieurs couvertures angulaires de révolution identiques

La couverture angulaire de l'aérien élémentaire étant connue, se pose alors la question du pourcentage maximum de couverture réalisable par rapport à la zone à couvrir pour un nombre donné d'aériens élémentaires identiques.

II.2.1. Principe du calcul de l'optimum de la couverture

Ce calcul d'optimum est purement géométrique; il revient à se donner n cônes de largeurs angulaires Θ_x et à rechercher l'arrangement de ces cônes conduisant à la meilleure couverture.

En fait, si on se limite à $n \leq 8$, l'ensemble des configurations intéressantes se ramène à deux groupes. L'un où les n lobes sont pointés au même angle d'élévation et équidistants en azimut, l'autre déduit du précédent en rajoutant un lobe au zénith.

Pour chacune de ces deux configurations, et chacune des valeurs de ($n \leq 3$ à 8), nous avons calculé le pourcentage de couverture obtenu pour différentes valeurs de l'angle Θ entre le zénith et l'axe du cône.

La fig. 4 représente un exemple du résultat des calculs, effectués dans le cas d'un cône au zénith entouré de 5 cônes latéraux.

Sur les axes ox et oy , nous avons porté respectivement l'angle au sommet des cônes (Θ_x) et l'angle de l'axe de ces cônes avec le zénith (Θ); sur l'axe vertical est porté le pourcentage de couverture correspondant.

On constate que le pourcentage de couverture croît avec l'angle au sommet Θ_x des cônes et passe par un maximum en fonction de Θ .

A chaque angle au sommet des cônes Θ_x correspond donc une valeur maximum de couverture réalisable; la fig. 5 présente le réseau donnant ces valeurs maximum en fonction de l'angle au sommet des cônes. Le nombre n de cônes (ou lobes circulaires) étant pris comme paramètre. La configuration correspondant à la figure 5 ne comporte pas de lobe au zénith.

La figure 6 donne un réseau de courbes analogue dans le cas de la configuration comportant un lobe au zénith.

L'examen des courbes données aux figures 5 et 6 permet de déduire les largeurs utiles de lobe permettant une couverture totale de l'hémisphère à l'exclusion des sites inférieurs à 10° , en fonction des nombres de lobes et de leur arrangement. Ces valeurs sont reportées dans le tableau ci-dessous.

LARGEUR UTILE DE LOBE ASSURANT UNE COUVERTURE A 100 %						
NOMBRE DE LOBES	:	:	:	:	:	:
ARRANGEMENT	:	:	:	:	:	:
	4	5	6	7	8	
sans lobe au Zénith	98°	90°	88°	86°	84°	
Avec un lobe au Zénith	100°	88°	76°	68°	64°	

Ayant montré précédemment (fig.3) qu'une antenne élémentaire ne peut pas assurer un gain net supérieur à 7 dB dans un lobe dépassant 60° de largeur, nous concluons qu'il est impossible avec les hypothèses faites d'assurer une couverture avion à 100 % aux normes AEROSAT avec un gain minimum de 7 dB avec un nombre d'antennes commutables limité à 8.

III. APPLICATION A LA DEFINITION D'UN SYSTEME D'ANTENNES

Nous venons de voir que la réalisation d'une couverture avion à 7 dB de gain net avec un nombre raisonnable ($n \leq 8$) d'antennes commutables de dimensions acceptables, est impossible, nous nous attacherons donc à la réalisation d'une couverture à gain plus faible soit + 4 dB de gain net.

Le réseau de courbes présenté à la figure 3 montre que l'antenne réalisant une couverture optimum à + 4 dB de gain net à un gain maximum net voisin de 8 dB.

L'aérien que nous avons retenu (figure 7) se présente comme une cavité cylindrique de diamètre 140 mm environ et de 60 mm de profondeur fermée par un radôme plan. Dans cette cavité sont implantés deux dipôles symétriques orthogonaux, alimentés à l'aide d'un coupleur 3 dB.

Les performances de cette antenne dont le diagramme de rayonnement est donné à la figure 8 sont les suivantes :

- gain maximum net (toutes pertes comprises) 8 dB
- largeur utile du lobe à + 4 dB de gain net 80°
- Taux d'ellipticité ≤ 2 dB

En reportant le lobe utile de 80° sur les figures 5 et 6, on peut dresser le tableau ci-dessous donnant en fonction du nombre d'antennes, la couverture maximum réalisable, pour les deux types de configuration :

NOMBRE D'ANTENNES	:	:	:	:	:	:	:
	:	:	:	:	:	:	:
CONFIGURATION	:	3	4	5	6	7	8
	:	:	:	:	:	:	:
sans lobe au Zénith	:	81 %	93 %	97 %	98,5 %	99,5 %	100 %
avec lobe au Zénith	:		83 %	98 %	100 %	100 %	100 %

On constate que jusqu'à quatre antennes, la configuration sans lobe au zénith est plus intéressante. Nous la considérerons comme la solution minimum au problème posé.

La couverture à 100 % est réalisable à l'aide de six antennes dont une au zénith; cette configuration conduit à un pointage des antennes latérales plus bas sur l'horizon, donc à une protection contre le multipath plus faible; pour cette raison nous lui avons préféré la configuration sans antenne au zénith qui conduit à un pourcentage de couverture maximum de 98,5 % mais assure une meilleure protection contre "les trajets multiples".

Sur les figures 9 et 10, nous présentons sous forme de courbes iso-gain, les couvertures obtenues avec quatre antennes, et six antennes.

En vue de préciser les caractéristiques opérationnelles de ces couvertures en radiocommunication (liaison avec un seul satellite) et en radiolocalisation (liaison simultanée avec deux satellites), nous avons superposé aux courbes iso-gain, les directions sous lesquelles les deux satellites sont vus de l'avion pour un certain nombre de vols représentatifs, dont quelques uns sont représentés à la figure 11.

Le tableau ci-après résume les principales caractéristiques opérationnelles des couvertures obtenues avec 4 et 6 antennes.

Nombre d'antennes	4	6
Pourcentage de couverture à + 4 dB	94 %	99 %
Protection contre le multipath à - 10° de site	3,3 à 4 dB	3,6 à 3,9 dB
Fonctionnement en radiocommunication :		
Pourcentage de vols (sur 15 vols) assurés :		
totalelement à : + 7 dB de gain net	-	67 %
+ 4 dB de gain net	100 %	100 %
Fonctionnement en radiolocalisation (x)		
Pourcentage de vols (sur 15 vols) assurés :		
totalelement avec :		
- 7 dB sur 2 satellites	0 %	0 %
- 7 dB sur 1 satellite et 4 dB sur l'autre :	0 %	20 %
- 4 dB sur 2 satellites	0 %	40 %
- 4 dB sur 1 satellite et 1 dB sur l'autre :	87 %	100 %
(x) Les deux satellites étant stabilisés :	sur l'Atlantique	par 20°
Ouest et 60° Ouest.		

Le tableau ci-dessus montre qu'une couverture avion en bande L, réalisée grâce à 6 antennes fixes commutables, permet d'assurer constamment le fonctionnement en radiocommunication avec au moins 4 dB de gain net et en radiolocalisation avec au moins 4 dB de gain net sur un satellite de 1 dB sur l'autre; en outre, dans environ 70 % des vols considérés la radiocommunication est assurée avec + 7 dB de gain pendant toute la durée du vol.

La figure 12 donne un exemple d'implantation sur un avion rapide, les aériens étant entièrement encastrés, deux étant situés à droite et deux à gauche de l'avion dans la partie supérieure du fuselage.

Sur la même figure, nous présentons un exemple d'implantation sur avion subsonique des six aériens groupés sous un radome profilé faiblement saillant placé sur le dessus du fuselage. Cette implantation a l'avantage d'éviter des percages importants dans la structure et donc un affaiblissement de celle-ci.

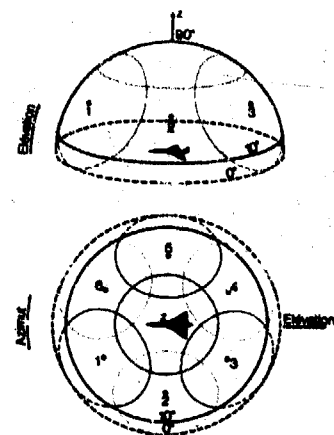
Notons que pour les deux exemples ci-dessus, l'implantation des antennes dans le fuselage au-dessus des ailes, devrait conduire à une amélioration de la protection contre les multitrajets.

REFERENCES :

- 1 - L.W. DUNCAN - Maximum Off-Axis Gain of Pencils beams - Proceedings of the IEEE- Oct. 1969 - p. 1791.
- 2 - J.A. BIJVOET - Documentation Results Program SADAH - Edité par l'ESRO - Mai 1971 - n° ATCS/445/JAB/EG.

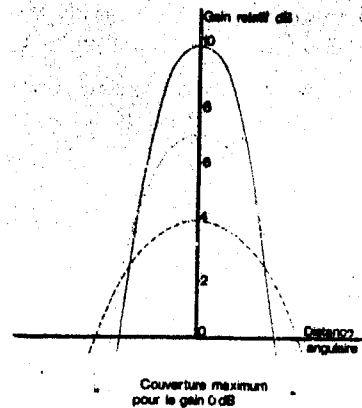
REMERCIEMENTS :

Les auteurs veulent ici remercier le Service Technique de la Navigation Aérienne qui a autorisé cette publication et en particulier Monsieur BOMONT qui est à l'origine de cette étude.



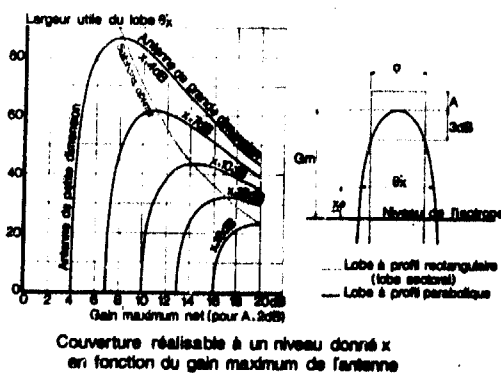
Principe de couverture avion
réalisée à l'aide d'antennes commutables

figure 1



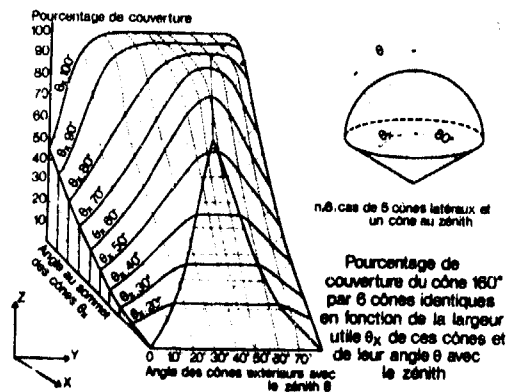
Gain relatif et ouverture
pour différents types d'antennes

figure 2



Couverture réalisable à un niveau donné x
en fonction du gain maximum de l'antenne

figure 3



n=5, cas de 5 cônes latéraux et
un cône au zénith

Pourcentage de
couverture du cône 180°
par 6 cônes identiques
en fonction de la largeur
utile θ_x de ces cônes et
de leur angle θ avec
le zénith

figure 4

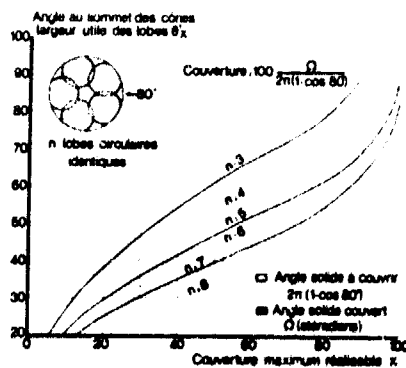


figure 5

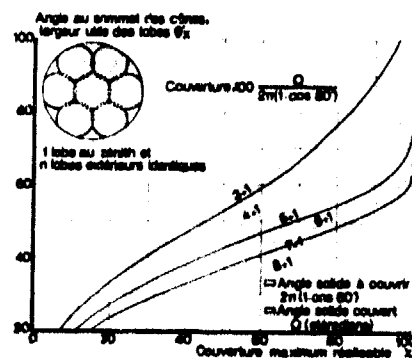
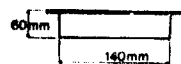
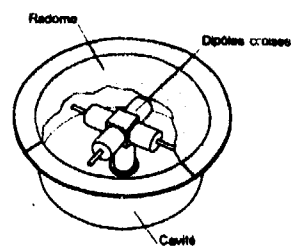
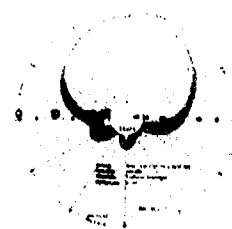


figure 6



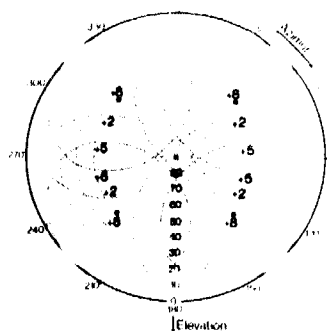
Dimensions approximatives à 1550MHz

Aérien encastré bande L



Aérien encastré bande L
Diagramme de rayonnement
(Polarisation linéaire tournante)

figure 7

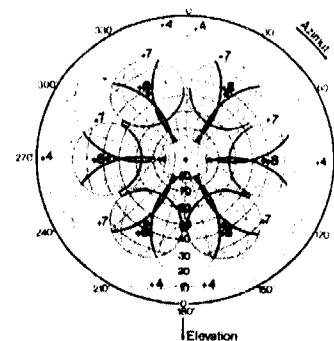


Couverture réalisée 94%

Caractéristiques de l'antenne élémentaire
Diamètre 90mm env
Profondeur 60mm env
Gain net au maximum Gm 18dB
Lobe utile à -1dB de gain net 0-4
Pointage optimum en élévation 40,2

4 antennes dipôles croisés

figure 9

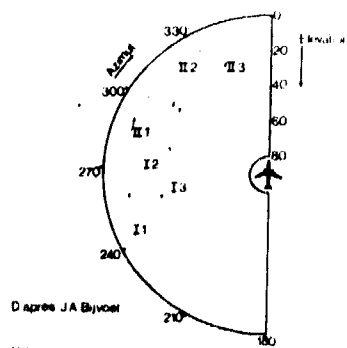


Couverture à -4dB 90%
Couverture à -7dB env 57%

Caractéristiques de l'antenne élémentaire
Diamètre 140mm env
Profondeur 70mm env
Gain net au maximum Gm 8dB
Lobe utile à -4dB 0-4
Lobe utile à -7dB 0-7
Pointage optimum en élévation 43,2

6 antennes dipôles croisés

figure 10



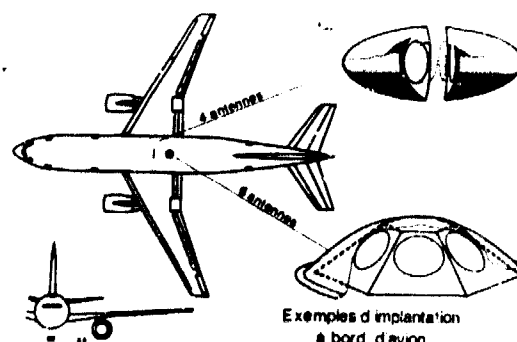
D'après J.A. Blyvoet

Voie subsonique schéma Atlantique nord

- I1 satellite géostationnaire 20 ouest
- I2 satellite géostationnaire 60 ouest
- I3 Amsterdam New York latitudes moyennes
- I4 Amsterdam New York latitudes maximums
- I5 Amsterdam New York latitudes minimums

Trajectoires des satellites
dans le trièdre avion

figure 11



Exemples d'implantation
à bord d'avion

figure 12

DISCUSSION

R. REITZIG: For simultaneous contact to two satellites there are instances in which two antennas have to be operated simultaneously. Doesn't this give severe interference problems.

P. FROIDURE: The beamwidth at +1dB of gain for the antenna chosen is about 100°; also there is such an overlap of antenna diagrams that it is always possible to find one of the six antennas on which the gain is at least +4dB towards one satellite and simultaneously +1dB towards the other satellite (at least for all the considered aircraft paths)

A LINEAR ARRAY OF BLADE ANTENNAS AS AN
AIRCRAFT ANTENNA FOR SATELLITE COMMUNICATION

O.B.M. Pietersen, J.P.B. Vreeburg, F. Klinker
National Aerospace Laboratory NLR
Amsterdam, The Netherlands

SUMMARY

In a ground-satellite-aircraft communication system the aircraft antenna is a critical part since it has to meet the typical environmental requirements and possess a rather high gain. This paper describes a suitable antenna system, installed on a Fokker Friendship aircraft. It consists of a linear array of blade antennas, a power division and phase shifting network in coax technique and a manual controlled beam selector/indicator. The design of the array is based on a mathematical model that has been constructed from theoretical considerations and experimental results. Mutual coupling effects are accounted for by using scattering coefficients. With the aid of a computer the spacings between the antennas were determined in such a way that a nearly constant directivity in the yaw plane of the aircraft could be expected.

The performance of the array was evaluated in several flights in which radiation patterns were measured in the receive and the transmit mode. From these measurements it is concluded that with the linear phased array of eight blade antennas a gain of 10 dB can be achieved. The antenna coverage in the yaw plane equals 360° , in the pitch and roll plane 25° .

1. INTRODUCTION

With the advancement of (geostationary) communication satellites the number of applications of such satellites is steadily increasing. A particular class of applications concerns the communication (including surveillance and navigation) to mobile users in parts of the globe that are otherwise rather inaccessible. An important example of such a mobile user is an aircraft over an ocean.

In a ground-satellite-aircraft communication system the aircraft antenna is a critical part because it has to meet the demands imposed by the aircraft environment and at the same time possess a rather high gain. If the antenna is placed outside the skin of the aircraft it should be able to withstand the loads (e.g. vibration) that are generated by the high speed airflow around the aircraft, even when it is covered by ice (icing conditions). Also, the disturbances in the airflow that are caused by a protruding antenna should not degrade the stability and flying characteristics of the aircraft. If the antenna is inside the skin, it usually requires an appreciable amount of space. Also, the dielectric cover that is flush with the contour of the aircraft will degrade the electromagnetic signal and, may be more important, the load carrying ability of the aircraft skin.

The gain required of an aircraft antenna for satellite communication, depends on the frequency and bandwidth of the electromagnetic signals and on the characteristics of aircraft and satellite equipment. However, increases in gain will lower the requirements, and hence the costs, of the equipment. Depending on the purpose and use of the communication system an optimum antenna gain at the current state-of-the-art may be defined. Among the candidate antenna systems with a gain of up to about 10 dB, linear arrays of simple and cheap antennas appear to be reasonable choices. This paper contains a discussion of the characteristics and performance of a linear array of 8 blade antennas which has been installed on top of a Fokker F-27 aircraft and used for voice communication in the lower UHF region via the geostationary LES-6 satellite.

2. DESCRIPTION OF THE ARRAY

The antenna system consists of a linear array of eight UHF blade antennas, a power division and phase-shifting network with associated control logic, and a beam selector with indicator. The applicable phase-shifts and mutual distances between the elements obtained from prediction of the achievable antenna patterns. In the mathematical model used for this prediction the incorporation of the actual scattering coefficients is essential. Therefore these coefficients were measured on a (partial) mock-up of the aircraft. The array was optimized in such a way that the antenna system possesses a nearly constant directivity over 360° in the yaw plane and meets the absolute gain requirements derived from the power budget calculation. The elements are not uniformly spaced; towards the ends of the array the blade antennas are spaced more closely than at the array center.

The power division is accomplished by hybrid T's. The phase-shifting is obtained by inserting different lengths of coaxial cable between hybrids and the array elements. It was possible to use the same coaxial lines for both the transmit and the receive mode of the antenna although the applied frequencies were some 50 MHz apart. The lengths of the coaxial phase shifters were optimized for the receive frequency because the satellite-to-aircraft link was recognized as the most demanding one in the system. Only the control logic for the phase shifters had to be specialized for either mode. The manual control of the beam direction is achieved by comparing the aircraft heading and the satellite position. In twelve steps the full 360° of the yaw plane are covered.

3. DESIGN

3.1. Number of elements

Power budget calculations for the up and down links of the aircraft satellite system showed that the highest demand on the aircraft antenna is a gain of about 10 dB in the down link (i.e. aircraft receiving). Comparison of the geometrical array factors for linear phased arrays indicates that a gain of 10 dB should be obtainable with 8 blade antennas. Besides, selection of an array of this size is attractive in view of power division considerations.

Additional justification for the selection of 8 elements is provided by the fact that a similar array developed by the Canadian Armed Forces consists of 9 elements and has been reported to work satisfactorily (Lambert, J.D. et al, 1969).

3.2. Array theory and verification

In order to predict the performance of the linear array, a theory was derived and tested. A full description of the theory and of the experimental results for a linear array of three blade antennas is given in an earlier publication (Vreeburg, J.P.B. et al, 1971). The experimental results were obtained with the array installed on a mock-up of its immediate electrical environment on an F-27 aircraft. It was found that the measured radiation patterns agreed well with the patterns predicted by the theory. For example, the sidelobe levels were predicted with an average accuracy of 1.5 dB as compared to 2.0 dB for the geometrical array factor.

In the derivation of the employed theory two important assumptions have been made. First, each antenna in the array radiates the same pattern, and second, the contribution of each antenna to the total field is determined by the phase and amplitude of the antenna current at a specific location on that antenna. In the sequel this location will be referred to as the phase center of the antenna.

The first assumption implies that there is no electromagnetic coupling between the antennas. However, by the second assumption, the mutual effects can be accounted for in an integrated form by their influence on the locations of and the conditions at the phase centers of the antennas.

Although the phase center has been defined, it is still impossible to determine its location without knowledge of the current distribution on the antenna. Therefore, it is assumed that the current distribution on the antenna is rather simply related to the current distribution in the feeding line. Then the phase center can be defined sensibly in the coaxial line of each antenna. Experiments that corroborate this assumption are given by Angelakos, D.J., 1951.

The current distributions in the feeding lines are determined from the excitation waves and the measured self and mutual scattering coefficients of the antennas in the array. Thus, when a location in a feeding line has been chosen the phase and amplitude of the current at that location are known.

Two different definitions of the phase center locations were tried and checked experimentally for the 8-element array. The first definition puts the phase center at a location of maximum current in the line on the expectation that large currents in the feeding line will correspond to large antenna currents. The second definition locates the phase centers at some suitably chosen constant distance from the antennas. This distance is determined by matching selected measured radiation patterns to theoretical patterns, using the pattern of a single antenna without neighbouring elements as the element radiation pattern.

The results obtained by the use of the two different definitions were compared with measurements on a linear array of three blade antennas (Vreeburg, J.P.B. et al, 1971). Each definition gave about equally accurate results although the pattern predicted by one definition was different from the pattern predicted by the other.

After the geometry of the 8-element linear array had been finalised, the theoretical radiation patterns, predicted by the different definition of the phase centers, were compared with measured patterns. It now appeared that the assumption of a phase center at a constant distance from the antenna in the line gave better results than the alternative definition of the phase center as the location of maximum current.

3.3. Choice of configuration and excitations

The selection criteria were:

- (1) uniformity of the directivity over the scan range, i.e. the composite radiation pattern for all excitations should be approximately circular in the azimuth plane,
- (2) the number of main beams required to fulfil criteria (1) at the two frequencies should not be very large, i.e. successive beams should overlap efficiently,
- (3) insensitivity to small errors in spacing and excitation, i.e. small changes in the geometry or excitation should give only a small degradation in overall performance,
- (4) the total length of the array must not exceed the available installation space on the fairing.

After an equidistant 8-element array had been installed on the mock-up of the F-27 aircraft, the scattering coefficients were measured and empirical functions were determined that gave close representations of the measured coefficients. These functions were used to calculate the performance of different array geometries for a range of excitations.

The "best" choice of array geometry was found to possess the following spacings between the successive elements (in meters): 0,54 - 0,56 - 0,62 - 0,62 - 0,62 - 0,56 - 0,54.

Finally, by a try-and-error procedure, using computations and pattern measurements, a satisfactory aggregate of beam directions and their corresponding excitations was obtained.

4. CONSTRUCTION

The 8-element blade antenna array has been installed on top of the F-27 Troopship by means of a fairing between the cockpit and the wing. The total length on the fairing available for installation of the array was 4.77 m. A picture of the installed array on the aircraft is given in figure 1.

The method of using a fairing rather than installing the blades directly on the aircraft was chosen because:

- 1) the antenna cables could be guided through the fairing and brought into the interior of the aircraft through an existing hatch of the pressurized cabin,
- 2) the installation could be prepared largely independent of the aircraft so that actual installation time was minimal,
- 3) remodification of the aircraft after the experiments would be easy because the pressurized cabin hull had not been pierced.

A possible disadvantage of the fairing could be degradation of the antenna radiation patterns due to the influence of its geometry and/or unsatisfactory electrical connection to the fuselage. Therefore the fairing was simulated on the mock-up of the F-27 and its effects investigated. No adverse influences of the chosen fairing geometry on the antenna characteristics were found.

The influence of the protruding parts of the antenna system on the flight characteristics of the aircraft had been estimated to be minor. In order to check this estimate, a test flight with the aircraft was carried out after installation of the fairing with antennas. The results of this flight accorded with the expectations; no appreciable deterioration of aircraft performance has been observed.

5. EXPERIMENTS

5.1. Background information

The experimental program to test the array antenna performance should be interpreted in view of the aim of the antenna development. This aim is to show the feasibility of a linear array antenna for satellite communication in the lower UHF region.

If for each beam excitation the full three-dimensional radiation pattern of the array were known, one would have complete information about the antenna. A very extensive test program is required to collect this information and a large part thereof (e.g. the detailed sidelobe structures) would not be necessary to demonstrate antenna feasibility. Thus, only the most important parts of the different radiation patterns have been measured.

The experimental program has been carried out with three systems, viz.:

- airborne station: RNI4F F-27 Friendship
- groundstation: Physics Laboratory RVO/TNO, The Hague
- satellite: LES-6.

The geostationary LES-6 satellite is visible from the Netherlands at an azimuth angle of 234° (magnetic north = 0°) and an elevation angle of 18° . The satellite contains a repeater that receives at a frequency of about 302 MHz and transmits at 249 MHz.

5.2. Pattern measurements

The overall system configurations during the recording of the radiation patterns at the transmit frequency and at the receive frequency of the array, is given in figure 2.

It is known that the signal transmitted by the LES-6 satellite exhibits a fading of up to 6 dB with a period of about 6 seconds. This fading is related to the spin rate of the satellite. Because these amplitude variations are superimposed on the radiation pattern, the recording of the field strength must be at a sufficiently low rate so that the spin fading contribution can be recognized and subsequently eliminated.

Radiation patterns with the array in the receive mode have been recorded in the aircraft. The groundstation transmitted a constant signal to the satellite and monitored the satellite output signal so that the recordings made in the aircraft could be corrected for variations in satellite output power.

To obtain the "azimuth" radiation patterns a full turn was flown in approximately 12 minutes at a speed of about 160 knots. The bank-angle was kept as small as possible.

Points of the radiation pattern in the pitch-plane were measured while the aircraft climbed or descended at a constant pitch angle during half a minute. During these manoeuvres the course was kept constant at 234° or 54° and the constant pitch angle was chosen between -15° and $+15^{\circ}$.

In the transmit mode, a constant signal was generated in the aircraft and transmitted to the satellite. The output signal from the satellite repeater was recorded at the groundstation. At the same time, heading information was sent from the aircraft to the groundstation via a line-of-sight VHF link.

Gain measurements have been carried out in the transmit mode for the two endfire beams. The gain was determined by comparing the satellite output power when illuminated by both a known up-link signal and by the signal from the array.

Recording equipment in the aircraft consisted of a photopanel recorder, a galvanometer recorder and an x-y recorder. The photopanel recorder was used mainly for registration of the flight parameters which included the various angles that fix the attitude of the aircraft. The galvanometer recorder registered the field strength, aircraft heading, time and beam number. These recordings were the most accurate and have been used to construct the radiation pattern figures. The x-y recorder was used to obtain quick-look information. Correlation between the photopanel and galvanometer recorders was obtained by time synchronization.

At the groundstation information was recorded on x-y recorders. Again, time synchronization allowed to correlate the recordings in the aircraft and the groundstation.

6. RESULTS

6.1. Power patterns at 249 MHz (Receive mode)

The aircraft heading and the field strength were input simultaneously in the x-y recorder onboard the aircraft in order to have an immediate check on the (approximate) correctness of the data. Figures 3 and 4 contain photographs of radiation patterns that were recorded in flight by the x-y recorder. Notice the pronounced effect of the satellite spin fading on the patterns.

The patterns recorded during level flight do not represent the directivity of the antenna in a horizontal plane. Because the satellite is viewed under an angle of 18° , the radiation pattern is measured parallel to the surface of a cone with an apex angle of 36° . Figure 5 contains an envelope of all main beams recorded in level flights for the array in the receive mode and hence gives an accurate indication of the coverage of the antenna. The information presented in figure 5 has been recorded on the galvanometer recorder during a number of flights.

Figure 6 shows the power pattern in the vertical symmetry plane (pitch plane). Pitch angle information was obtained from the photopanel recorder, the field strength from the galvanometer recorder. Correlation between these recordings was obtained from time synchronization.

6.2. Power patterns at 302 MHz (Transmit mode)

The field strength measurements were recorded on an x-y recorder at the groundstation. The power transmitted from the aircraft to the satellite was held constant at 50 Watt. Heading information from the aircraft was transmitted via a VHF link between aircraft and groundstation. The results are given in polar form in figure 7 and are seen to be similar to the patterns in the receive mode.

No data were taken of the transmit power pattern in the pitch plane of the aircraft because pitch angle information could not readily be transmitted over the VHF link to the groundstation.

6.3. Multipath effects

From the measurements taken during rectilinear flights with constant climb or descent rates some conclusions about multipath effects can be drawn. Figure 8 shows photographs of the galvanometer recordings for aircraft pitch angles of $+10^\circ$ and -10° which were obtained for the determination of the array pitch plane patterns in the receive mode. The low frequency component in the field strength recording is caused by the spin fading of the satellite (in this case about 5 dB maximum). The high frequency component in the signal is due to multipath fading. The mechanism involved is as follows.

During climb or descent of the aircraft, its height above the ground varies and thereby the difference between the path lengths of the direct and ground-reflected rays from the satellite to the aircraft. Hence the phase difference between these two signals will vary which appears on the recording as an amplitude modulation of the sum signal. The beat frequency of the sum of the two rays will be (see Figure 9)

$$f = 0.62 \frac{V}{\lambda} \sin \alpha$$

where V represents the aircraft speed and α the pitch angle.

The formula shows that f increases with $\sin \alpha$. This effect shows clearly on the left hand side of figure 8 and corresponds to the transition of the aircraft from horizontal flight to a 10° dive. The dependence of f on V is also apparent in the recording because during climb (dive) with constant pitch f decreases (increases) with V .

Near the end of the 10° climb, the beat frequency is about 5 Hz which corresponds to an aircraft speed of 55 m/sec. This speed (107 knots) accorded with the measured aircraft speed at that moment hence one must conclude that the observed effects are indeed due to multipath fading.

The amplitude of the multipath fading depends on the shape of the antenna radiation pattern and the reflection coefficient of the earth. For a dielectric constant between 5 and 20 (land), angle of incidence of 18° and vertical polarization, the reflection coefficient will be less than 0.15 (Klinker, F. and Pietersen, O.B.M., 1970). This value corresponds to a fading of 3.2 dB if the radiation pattern does not discriminate between the direct and the reflected ray. The maximum multipath fading observed on any of the pitch plane pattern recordings was about 2.5 dB.

7. CONCLUSION

The experimental results presented in this paper show that for an F-27 type aircraft a linear array of 8 blade antennas constitutes a feasible satcom antenna when gains of about 10 dB are required at elevation angles between 5° and 30° .

The range of elevation angles is somewhat arbitrary because it depends on the particular blade antennas that are used. However, when the quoted range applies, the antenna will be operable in about 44 % of the coverage area of the geostationary satellite. Outside this area the gain of the antenna will not suffice to allow satcom during level flight.

The measured results are corroborated by the experiences gained during voice communication tests. It has been observed that intelligible communication between groundstation and aircraft could be maintained during level flight for all aircraft headings.

8. REFERENCES

- Angelakos, D.J., 1951, "Current and charge distributions on antennas and open-wire lines", J. Appl. Phys. 22, 7, 910-915.
- Klinker, F. and Pietersen, O.B.M., 1970, "Experimental evaluation of possible antenna test range locations at the NLR site", NLR Memo WE-70-053 (In Dutch).
- Lambert, J.D., Maynard, L.A. and Werstiuk, B.L., 1969, "A UHF airborne satellite communication system", Proc. 5th TACSATCOM Symp., Livorno, Italy.
- Vreeburg, J.P.B., Pietersen, O.B.M. and Klinker F., 1971, "Design of a linear array of blade antennas for aircraft-satellite communication", IEE Conf. Publ. 77, 176-185.

9. ACKNOWLEDGEMENT

This work has been carried out under contract with the Royal Netherlands Air Force.

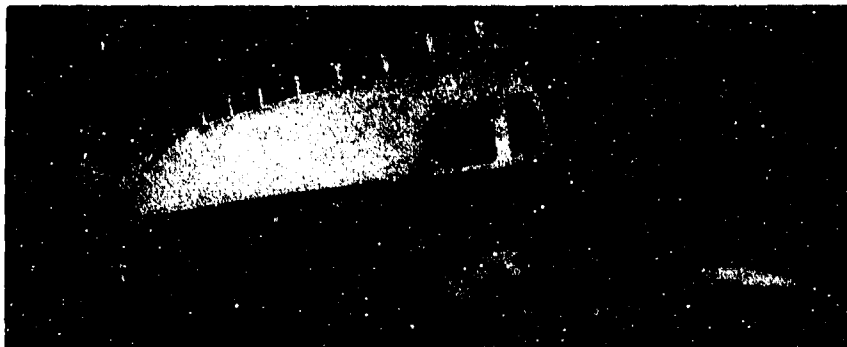
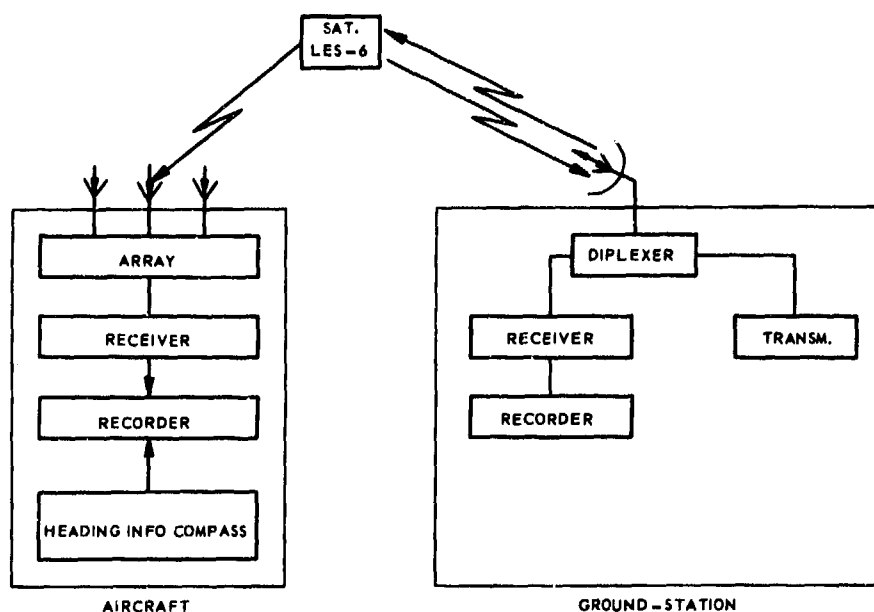
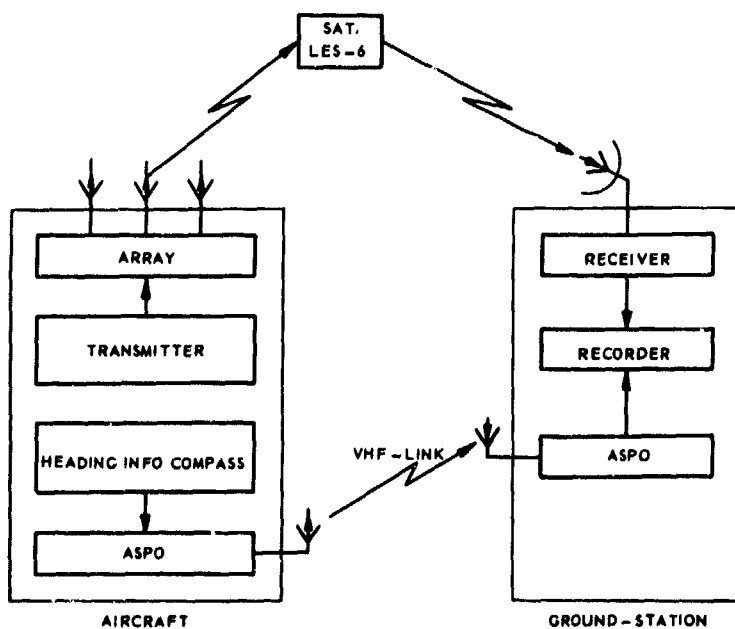


Figure 1: Blade antenna array installed on top of the aircraft.



RECEIVE-MODE PATTERNS



TRANSMIT-MODE PATTERNS

Figure 2: System configurations for the recording of radiation patterns.

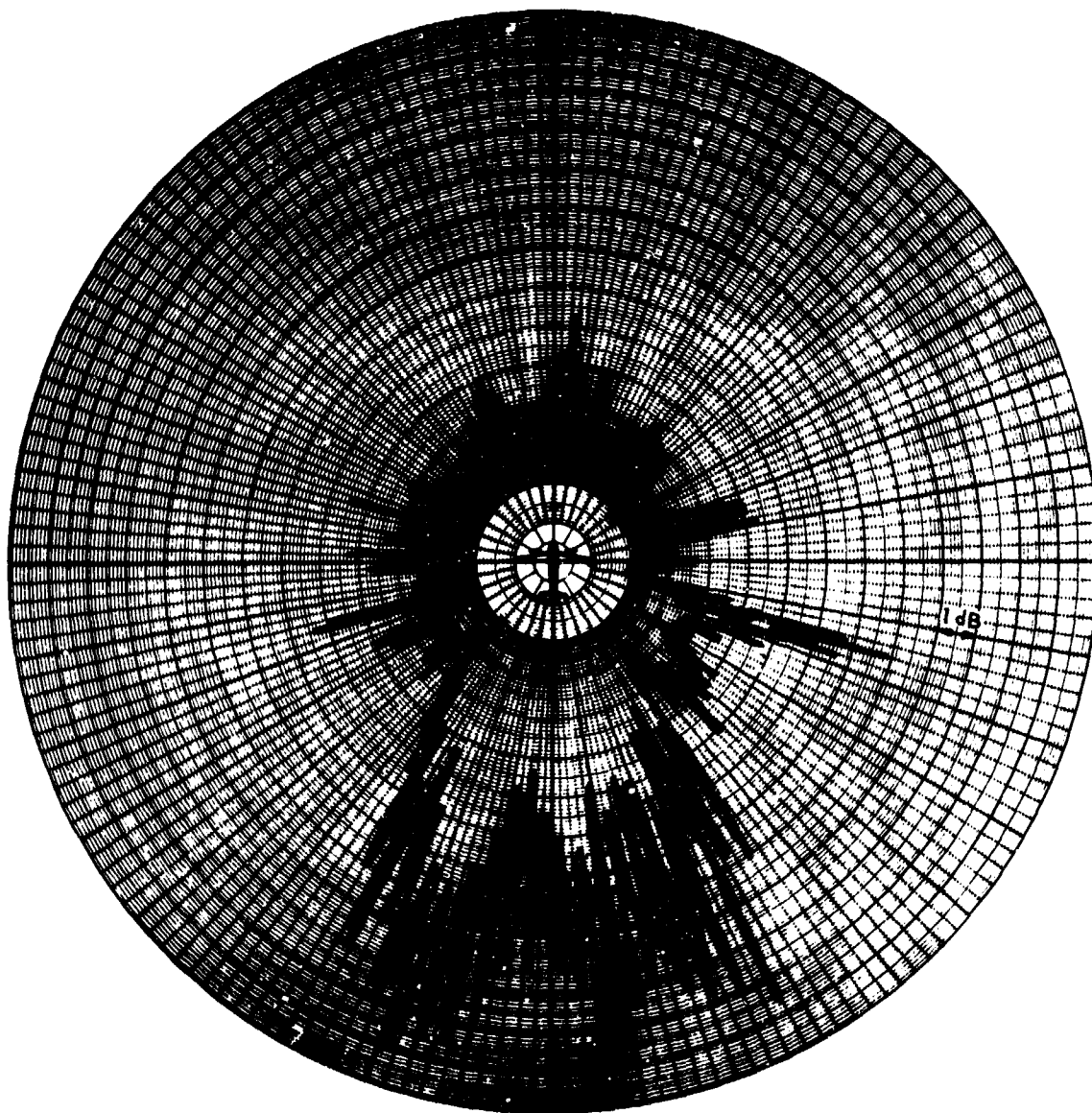


Figure 3: Inflight recording of an endfire radiation pattern (receive mode).

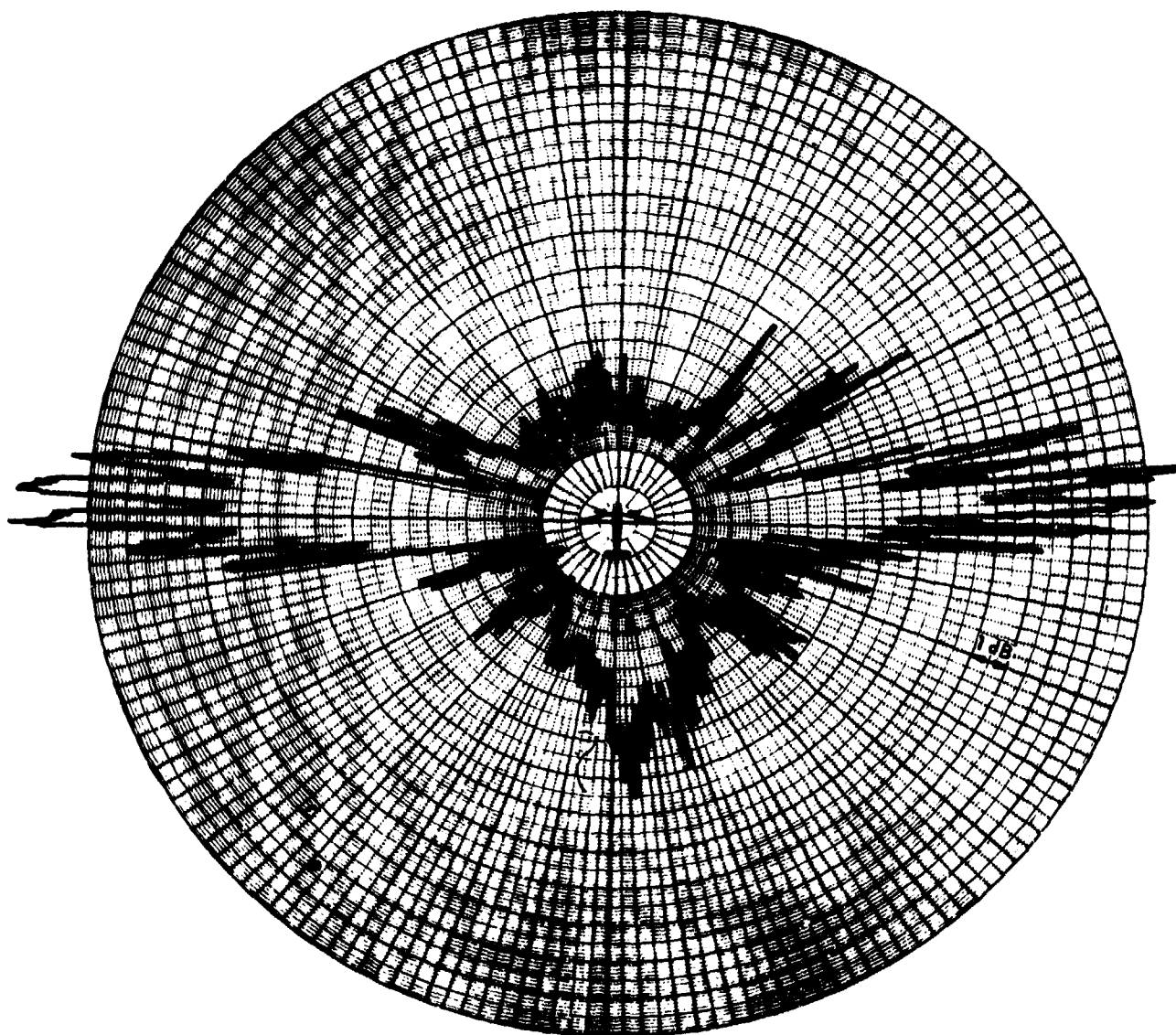


Figure 4: Inflight recording of the near broadside radiation pattern (receive mode).

FREQUENCY : 249.1 MHz

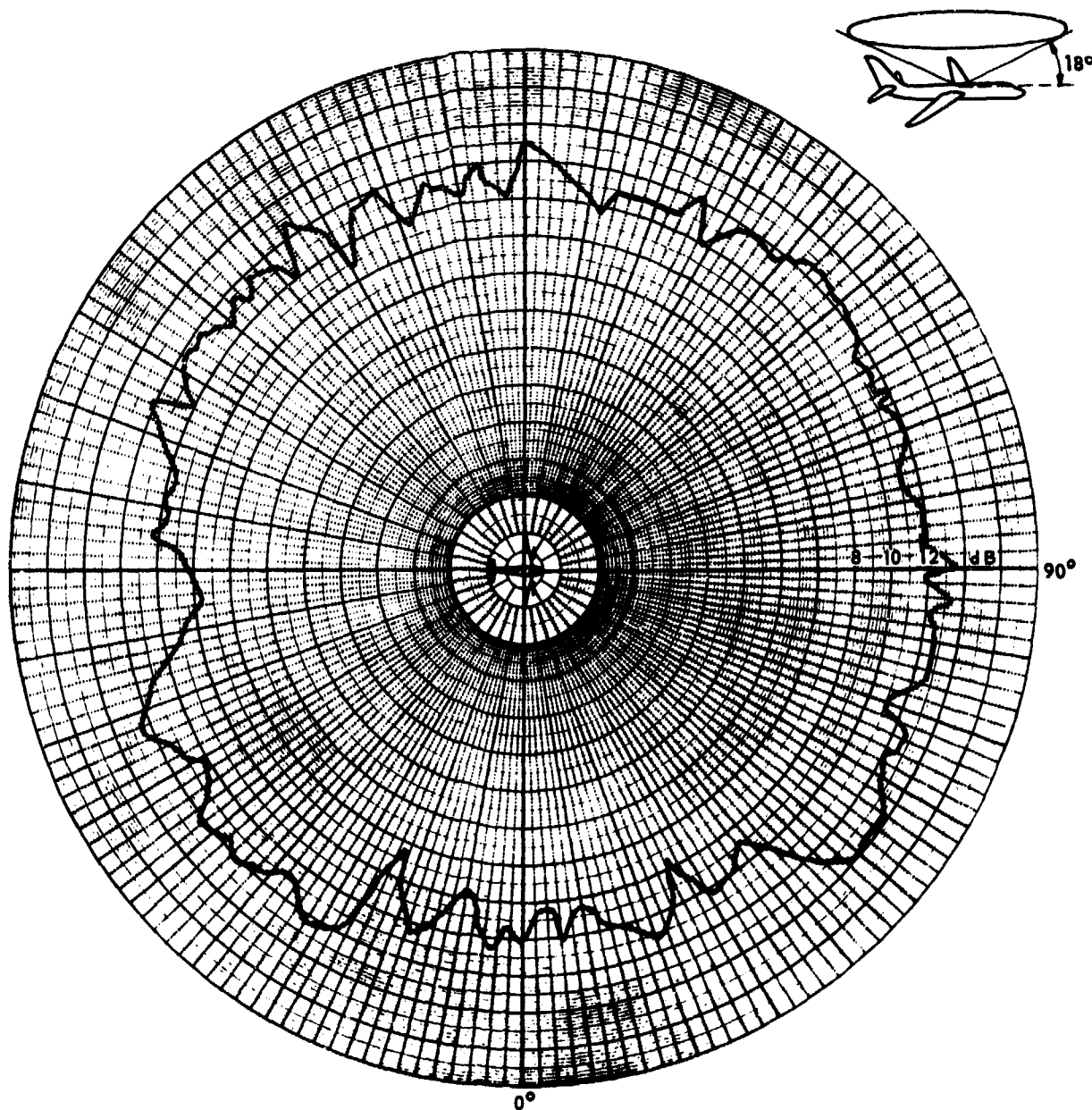


Figure 5: Composite power pattern of the array in the receive mode.

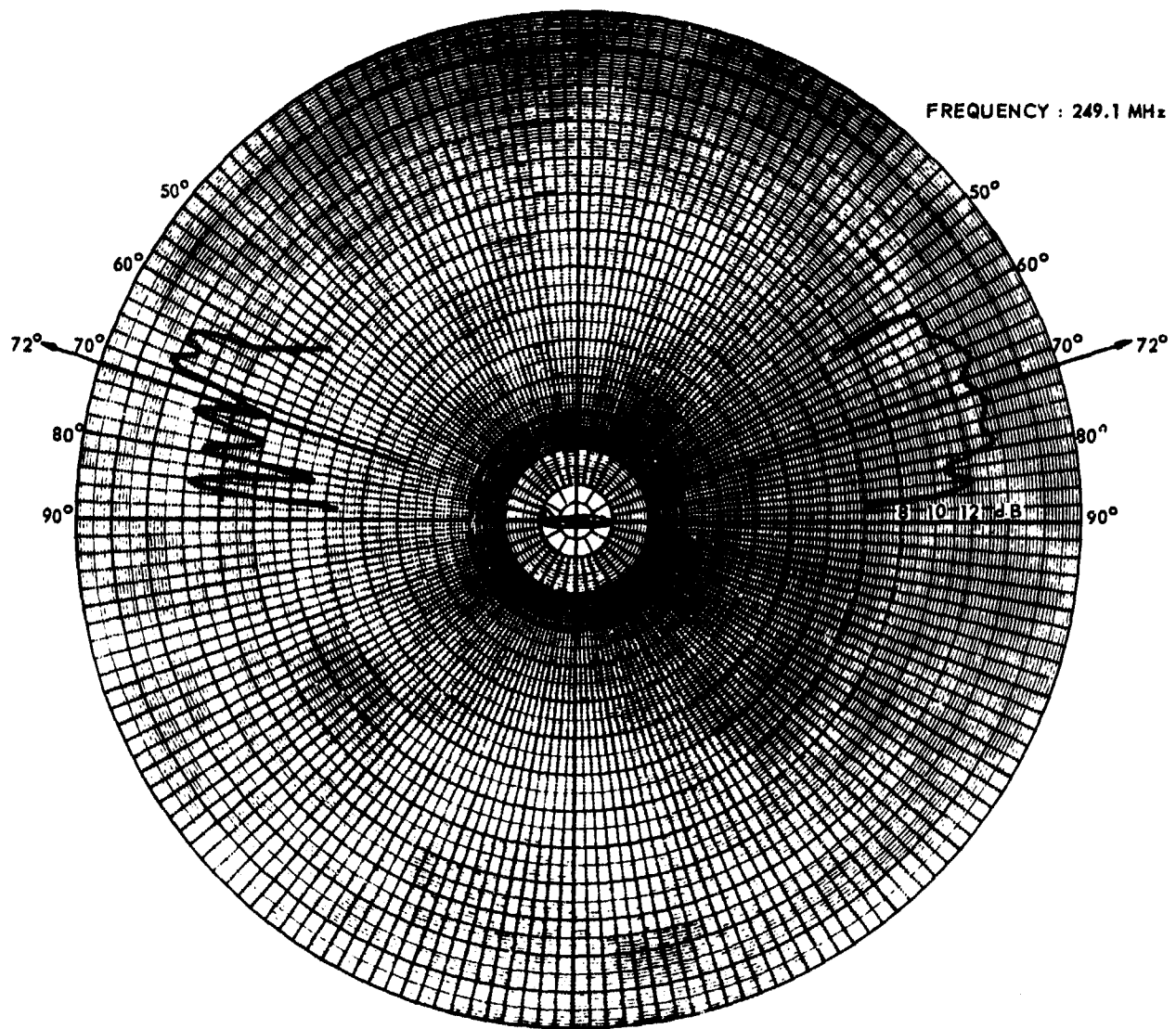


Figure 6: Pitch plane power pattern of the array in the receive mode.

FREQUENCY : 302.5 MHz

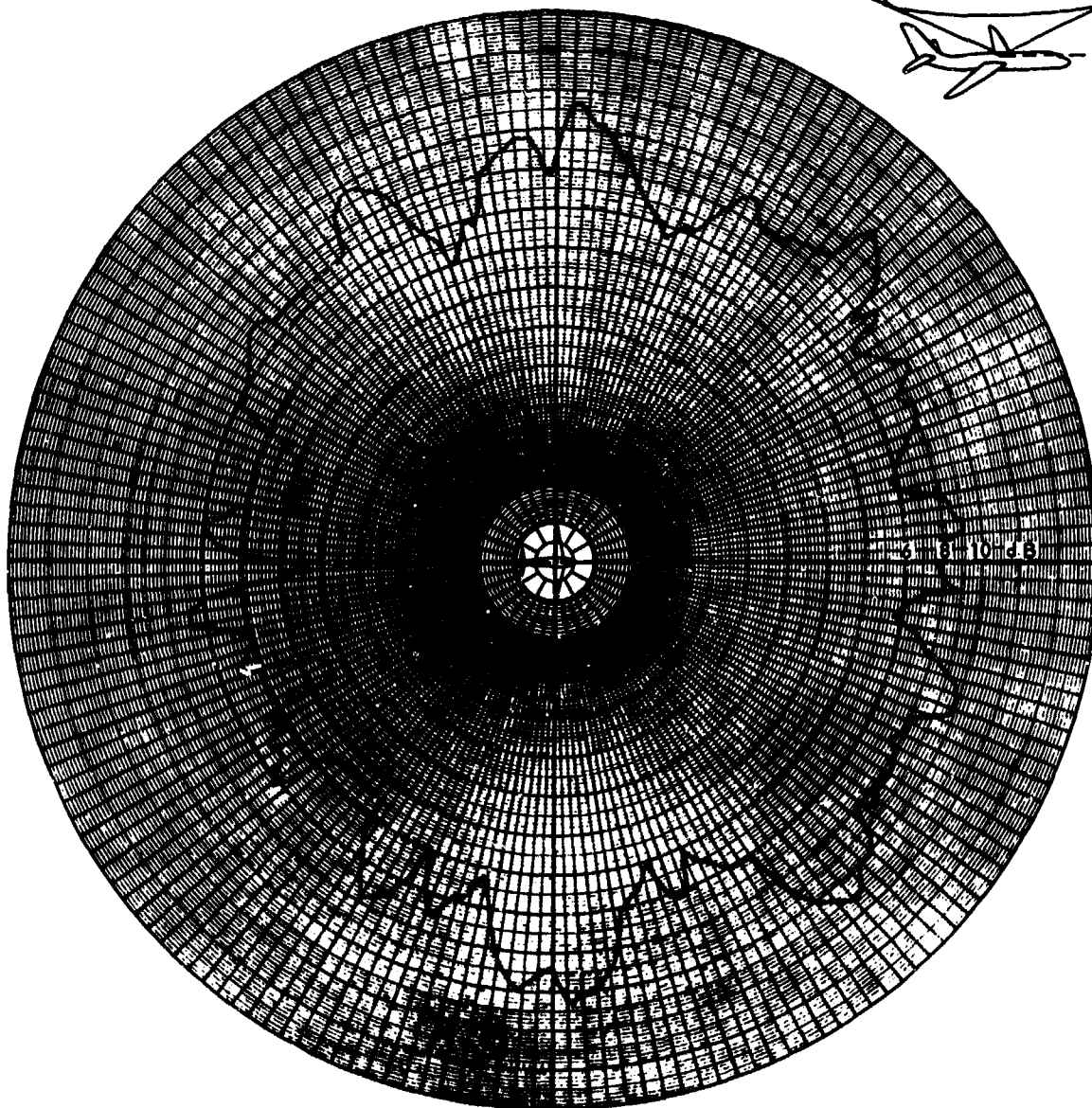
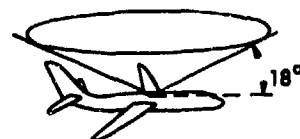


Figure 7: Composite power pattern of the array in the transmit mode.

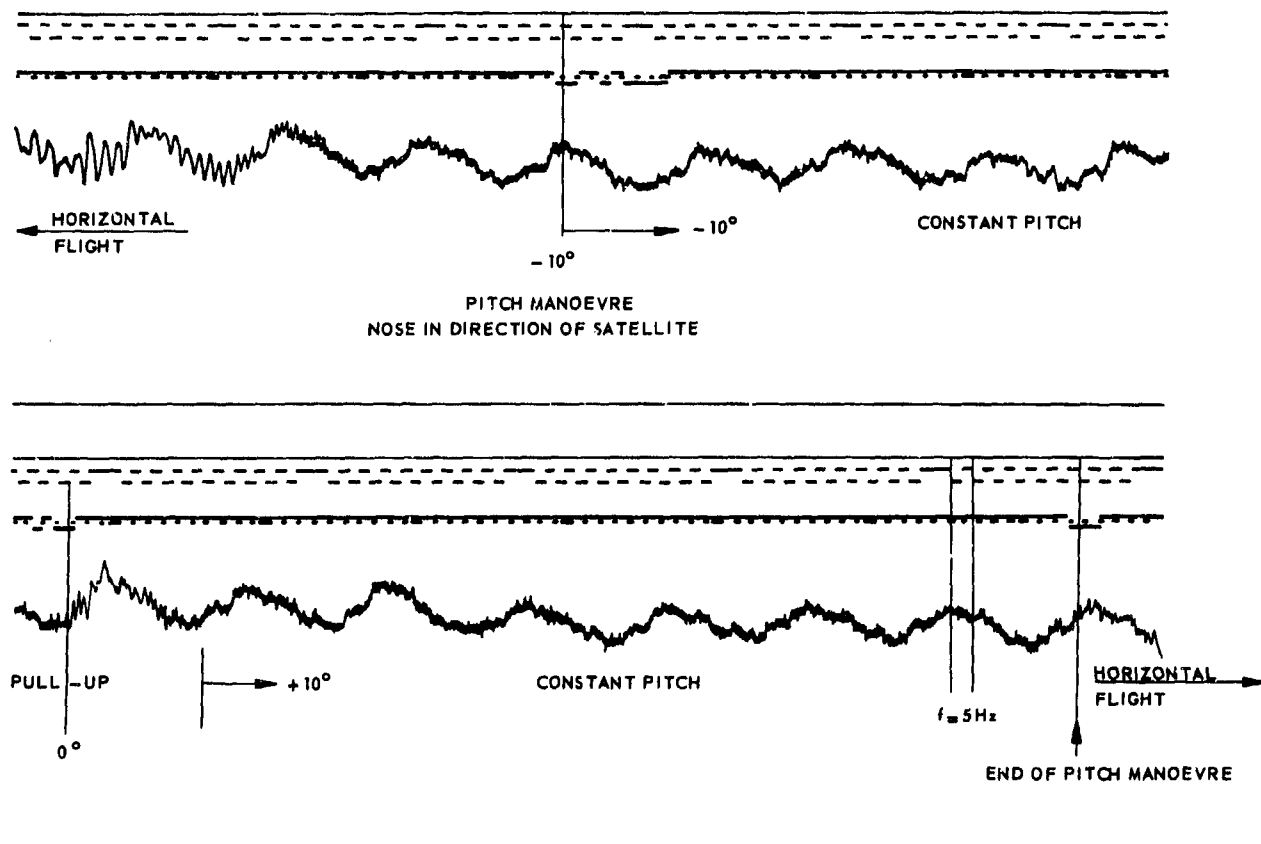


Figure 8: Recording of the field strength showing multipath fading during pitch manoeuvres.

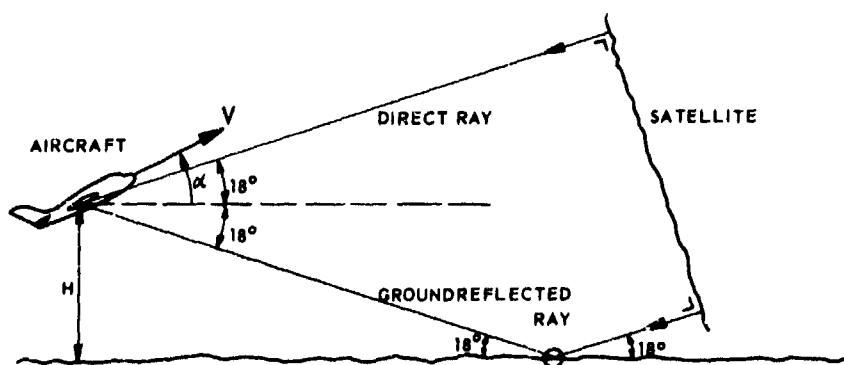


Figure 9: Multipath fading due to earth reflections.

DISCUSSION

R. REITZIG: For aircraft satellite communication one usually employs circular polarization. Your blade antenna, however, uses linear polarization which incorporates a 3dB gain loss. What are the particular advantages of your blade radiators?

O.B. PIETERSEN: The main reason for use of the vertical polarized blades was the commercial availability of these radiators. Further, the maximum directivity of the blade on top of the aircraft is just in the direction of the satellite (about 18 degrees elevation angle, looking from Western Europe) The positioning of circular polarized elements (e.g. crossed slots), with the full advantage of 3dB more gain should require two linear arrays at both sides of the aircraft.

UHF LINEAR PHASED ARRAYS FOR AERONAUTICAL SATELLITE COMMUNICATIONS

by

H.L. Werstiuk, J.D. Lambert, L.A. Maynard and J.H. Chinnick
 Communications Research Centre,
 Department of Communications.
 P.O. Box 490, Station "A",
 Ottawa, Canada,
 K1N 8T5

SUMMARY

An ultra-high frequency phased array antenna has been developed at the Communications Research Centre (CRC) and test flown on a Canadian Forces C-47 Dakota and a C-130 Hercules. Successful voice communications were achieved with the aircraft terminals via the Lincoln Experimental Satellite LES-6 at 300 MHz. The prototype antenna system consists of nine blade antenna elements mounted along the top of the aircraft fuselage. The antenna is electronically scanned and generates a series of symmetrical conical fan beams. The electronics necessary to control the array scan are relatively simple because of the single dimension of the array and the insensitivity of the patterns to large phase errors at each element. This paper describes the techniques used to construct the phased array, and some of the test results obtained. Two methods developed to provide automatic tracking for the array are also described.

CRC has sponsored contracts with the Canadian Marconi Co. to adapt the phased array design for operation at 1500 MHz. Results of the experimental hardware development for this antenna system are discussed. It is intended that this antenna system will satisfy the communication and position-determination requirements of aeronautical satellite systems.

1. INTRODUCTION

In the design of satellite systems for aeronautical applications, the gain of the mobile station antenna is an important variable used in performing studies of cost effectiveness. Increasing the antenna gain of a station allows the system designer to allocate the available satellite power either to support more communications services or to improve the quality of these services.

However, satellite communication antennas on-board aircraft pose a serious design problem. The provision of an aircraft antenna with gain higher than that of an omnidirectional antenna introduces problems involving the optimization of gain, coverage, and multipath rejection. Because of these difficulties, a major concern in aeronautical satellite system design is the development and evaluation of suitable antennas for aircraft. The selected antenna system should be economical, reliable, and easily installed.

This paper describes the initial design and development of a linear phased array undertaken at CRC in the period 1968-1972. It also describes contract work which is presently being carried out by the Canadian Marconi Co. to adapt this array for operation near 1500 MHz. The latter development is expected to result in an antenna system capable of satisfying the communication and position-determination requirements for proposed aeronautical applications.

2. SELECTION OF AN ANTENNA

Many different types of antennas have been proposed (References 1-4) for airborne use with satellites but basically they fall in one of two groups:

a) Low-Gain Antennas (0-4 dB)

Three or more omnidirectional antennas are installed in advantageous locations on the aircraft fuselage, (e.g., one top-mounted and two side-mounted). The use of multiple antennas partially overcomes the gaps in coverage experienced with a single-location omnidirectional antenna.

b) High-Gain Antennas (8-10 dB)

Proposals to achieve these gains involve the use of linear and planar phased arrays, either in single or multiple-location installations on the aircraft.

The airborne antenna development program at the Communications Research Centre has been concerned with UHF antenna design in the high-gain category. A phased array was chosen for the development program because it has two unique advantages over other antennas:

- 1) It is composed of small, mechanically simple, streamlined elements which can be located with some flexibility on the aircraft fuselage. This feature is particularly useful since specific fuselage structures tend to limit the available positions for antenna mounting.
- 2) High-speed, electronic beam steering can be used, since there are no mechanical time constants to restrict the rate of scan.

A linear phased array was selected because it has several advantages over more complex, multi-dimensional arrays. For example:

- 1) The single dimension of the array results in considerable simplification of the electronics required to control the array.

- 2) The rotational symmetry of the patterns about the aircraft fore-and-aft axis means that aircraft roll will not affect the beam position required to access the satellite. Hence, any automatic tracking system for the phased array need consider only aircraft pitch and yaw.
- 3) The array patterns and gain are relatively insensitive to phase errors at each element of the array. This permits use of a simplified two-bit phase shifter.

3. 300 MHz PROTOTYPE ARRAY

3.1 Design Considerations

The antenna patterns for a linear array of isotropic elements were initially predicted with the aid of a computer in order to study the effects of parameter changes. The predicted patterns were shown to have rotational symmetry about the array axis (Fig. 1) so that the beams formed sections of cones. Thus one parameter, the cone angle, completely specified a beam direction with respect to the aircraft. The patterns shown were calculated for a linear array of isotropic elements. The use of non-isotropic elements (e.g., blades) modifies the amplitude of the patterns, but the desired beam directions remain the same.

The thickness or angular width of these cones varies from 40° along the axis of the array to 9° in the broadside direction, measured to the -1.5 dB points. It was determined that the entire azimuth-elevation hemisphere could be scanned with 27 different beam directions (or cone angles) assuming overlap at the 1.5 dB points for adjacent beam lobes. It was further determined that the scan requirements could still be achieved using 90° phase quantization at each element instead of a unique phase shift for each beam direction. These simplifications result in a considerable reduction in the complexity of the array electronics.

The actual array was constructed using nine standard UHF monopole Blade antennas mounted near the top centerline of the aircraft fuselage (Fig. 2). The blades were spaced at approximately half-wavelength intervals, so that, at 300 MHz, the total array length was about five metres. As shown in Fig. 3, the blades are connected to a Phased Array Driver (PAD), which contains the phase shifters and logic required to steer the antenna. Pointing directions for the antenna are fed to the PAD from a Phased Array Tracker (PAT), which contains electronics for automatically steering the array as the aircraft manoeuvres.

3.2 Phased Array Driver

The PAD unit controls the electrical phase of the signals propagating to and from the antenna elements. As shown in Fig. 4, it contains phase shifters, a power divider/combiner, and associated digital control circuits.

Each of the antenna elements is connected to the PAD with an equal length of coaxial cable. The center element in the array is considered to be the reference element, and the other eight are equipped with phase shifters. The signal at each of the elements is capable of being independently phased at 0° , $\pm 90^\circ$ and 180° with respect to the signal at the reference element. This quadrature phase shifting is achieved by means of four-position PIN diode switches which are in turn controlled by digital-driver circuitry and a phase-selector matrix. The selector matrix decodes a desired antenna direction into a set of positions for the phase switches. The resulting phase shifts at the individual elements have the effect of reinforcing an in-phase signal in the desired beam direction.

Pointing directions for the antenna are fed to the selector matrix from a control unit which is located at the operator's position. When controlling the antenna manually, the operator must know both the aircraft heading and the satellite position in order that he can select the array beam which will access the satellite.

In its prototype form, the PAD is not capable of simultaneous phasing for both transmit and receive signals, which have a 50 MHz frequency separation.

3.3 Phased Array Tracking

There are several automatic beam steering techniques which can be employed with an airborne phased array. These include:

1. Direct tracking from the aircraft navigational instruments. The tracker must be updated with satellite position every few degrees of aircraft position change.
2. Scan-tracking over array beam positions. A full or partial scan is triggered by a preset signal strength threshold and programmed to select the beam producing the maximum signal strength.
3. Scan-tracking over all possible phase combinations of the elements. This is the exhaustive search technique and would suffer from time limitations.
4. Hill climbing on the received signal strength by adaptive adjustment of array phasing.

Initially, the first of these tracking techniques was implemented. A system was developed which accepted satellite azimuth and elevation inputs from the operator and used the aircraft gyrosyn compass system to steer the antenna automatically as the aircraft manoeuvred.

As shown in Fig. 5, the three-phase signal from the aircraft compass system passed through a synchro-differential transformer which subtracted satellite azimuth from aircraft heading to determine the required beam-azimuth for the antenna. The resulting information was converted to a seven bit

digital signal, and gated into one of a series of beam-selector matrices by the elevation control. The beam-selector matrix used the beam-azimuth signal to select the correct antenna beam number for the phased array driver.

The major limitation with this tracking method was that operator input was needed to orient the antenna before communications could take place. Clearly, a "hands-off" beam pointing scheme was required which would simplify the operation of the airborne terminal, making it a "push-to-talk" radio like the other systems in the aircraft.

A second tracking method, the "scanning" tracker, was therefore selected for evaluation. It was designed to maintain satellite acquisition by periodically searching through all antenna positions for the one which provided maximum received signal strength. One complete search required 250 ms when operated with a beacon receiver having an integration time constant of 6 ms. This results in a break in voice communications of approximately one syllable each time a search took place.

Figure 6 is a block diagram of the scanning tracker. The Central Processing Unit (CPU) is essentially a hard-wired, 64 instruction computer and is responsible for all timing and sequencing events. A description of the operating sequence follows: A scan is initiated by the control unit. The CPU responds by forcing the array driver and the radio equipment into the receive mode. It then begins to steer the array beam sequentially through the entire hemisphere, pausing on each beam position long enough to store the received beacon level into an analog memory unit for that particular beam. The CPU then sweeps the D/A converter output downward until at least one of the analog comparators senses a match with its analog memory unit output. This is the signal for the CPU to discontinue the D/A scan, adjust the gating circuits, and poll the comparators. When the appropriate comparator number has been identified, the gating circuits are again adjusted to allow the selected number to be passed on to the PAD as the selected beam. The CPU then releases the array driver and radio equipment from the forced receive mode and returns to standby, awaiting another trigger from the control unit or the search mode control logic.

The scanning tracker and the compass-input tracker were designed to be easily interchangeable. They use the same cabling and the same power source in the aircraft.

3.4 Performance of the Prototype Array

A number of test flights were conducted in the period 1968 to 1971 to determine the extent of agreement between theoretical and actual array patterns. The measured data from the tests were used to make up more accurate antenna pointing charts and to adjust the automatic tracking devices used with the antenna system. Two installations were evaluated; one on a C-47 aircraft, and the other on a C-130 aircraft.

Figure 7 shows a typical plot of a measured array beam pattern compared with the theoretical plot calculated for an array of isotropic elements. The greater gain of the measured pattern is due to the non-isotropic nature of the blades which form the array elements.

Figure 8 is an overlay of the plots of theoretical array coverage for all directions from the aircraft, at 30° elevation. The variation in the width of the beams from the broadside to the fore-and-aft axis can be observed. A corresponding plot of measured patterns for the C-47 installation is shown in Fig. 9. Using the 9½ dB gain circle as a reference, this composite plot for the C-47 shows no significant null for any beam azimuth. Figure 10 is a composite plot of measured patterns for the C-130 installation. A noticeable degradation is evident toward the rear of the aircraft, and it is accounted for by the high wing and pronounced vertical stabilizer of the C-130. A five degree error in pointing accuracy is estimated for the measurements due to the effects of compass system inaccuracies.

During the test and demonstration phase of this antenna development program, both the C-47 and C-130 terminals participated in a variety of missions. Successful communications from the aircraft were maintained during flights over the Canadian Arctic, the North Atlantic and South America. Aircraft-to-aircraft voice communications via satellite were also demonstrated. The C-130 participated in a multi-terminal demonstration to the NATO Communications and Electronics Board in Brussels, September 1970.

3.5 Summary of the 300 MHz Prototype Array

The significant characteristics of the array are summarized in Table 1.

TABLE 1
300 Mhz Array Characteristics

Number of antenna elements:	9
Nominal Gain:	9.5 dB over circularly polarized isotropic
System Operating Frequency:	Tx 300 MHz Rx 250 MHz
Phased Array Driver:	Size: 19 cm x 19 cm x 30 cm Weight: 11 Kg
Phased Array Tracker:	Size: 19 cm x 19 cm x 30 cm Weight: 11 Kg

All control of the phased array antenna system and associated radio equipment is accomplished by compact control units installed on the flight deck. All other functional equipment is installed as near as possible to the antenna array.

Figure 11 illustrates a typical configuration of the complete set of phased array electronics. The tracking unit shown uses a compass system input. Interconnections between the units are normally made through a wiring harness installed in the aircraft. Antenna connections are made to the RF connectors shown on the phased array driver unit.

4. L-BAND PHASED ARRAY DEVELOPMENT

CRC, in cooperation with the Ministry of Transport and the Department of Industry Trade and Commerce, has sponsored contracts with the Canadian Marconi Company to develop a linear phased array for L-Band frequencies. The L-Band array will be a candidate antenna for use with the proposed international aeronautical satellite system. It will operate in the frequency band 1540 to 1660 MHz, and is an extension of the original 300 MHz array developed by CRC. The factor of five increase in frequency allows a radically different physical design of the system from that described for operation at 300 MHz.

4.1 L-Band Antenna Structure

An outline of the antenna structure is shown in Fig. 12. There are three connectors used on the antenna unit: an RF array input connector, an RF single element connection, and a multi-pin connector for the diode switch drivers. These connectors must pass through the surface of the fuselage. The unit is attached using 16 mounting screws which fasten to a base plate mounted on the aircraft fuselage. Each element within the radome area will be structurally independent, removing the need to have any "fill" material under the radome.

Figure 13 shows the array unit with the radome removed. Each element contains its own phase shifter network, and is fed by a microstrip board which combines the functions of the RF power divider and power distribution network. The individual phase shift modules also contain the power-splitting and balun functions for the radiating elements.

4.2 Phase Shifter

There are several ways in which PIN diodes may be used to switch phase between discrete states. A hybrid technique is employed which obtains a transmission phase shift by the transformation of a reflection phase shift through a 3 dB coupler. Two such shifters are required in cascade. The microstrip layout for the cascaded phase shifters and balun transformer is shown in Fig. 14. The main advantage of this approach is that only four PIN diodes are required to achieve the four phase states. The transmission medium for the phase shifter is a high dielectric-constant microstrip.

4.3 Power Splitter

The basic requirement for the feed is to divide the power 9 ways equally in amplitude and phase. It must also, however, provide isolation among the elements to ensure reasonably accurate power splitting, since small differences in impedance among the elements can cause serious power division errors resulting in pattern distortion. The power splitter selected has an isolated corporate feed with one isolated 1/9 - 8/9 Wilkinson power divider for the center element and seven 2-way Wilkinson isolated power dividers for the remaining elements. Figure 15 shows a schematic of this circuit. The power splitter is contained in the base unit of the antenna structure.

4.4 The Radiating Element

Table 2 details some of the performance criteria involved in the design of a radiating element.

TABLE 2

Desirable Electrical Requirements of a Radiating Element

- | | |
|-----|---|
| (a) | Maximization of gain at elevation angles greater than 10 degrees. |
| (b) | Minimization of gain at elevation angles less than 10 degrees, to reduce multipath effects. |
| (c) | Right-hand-circular polarization for all elevation angles greater than 0 degrees. |
| (d) | Input reflection coefficient of -20 dB or better. |
| (e) | Negligible mutual coupling (-30 dB) between elements. |

A cross-drooping-dipole element has been designed that approximates the requirements of Table 2. Figure 16 shows the type of pattern which can be achieved with this element. Note that this is a plot of directivity as measured by a circularly-polarized receiving antenna. This element has an acceptable circularity (axial ratio ≤ 6 dB) except at the 45 degree elevation angle direction where the axial ratio deteriorates to greater than 12 dB. Since this direction corresponds to a pattern maximum, the loss due to non-circularity is not important.

Figure 17 shows a prototype phase shifter and radiating element. Based on work to date, the design parameters for the array unit are given in Table 3.

TABLE 3

Design Goal for the Aerosat L-Band Aircraft Antenna Unit

1	Centre Frequency:	1.6 GHz
2	Bandwidth:	± 60 MHz
3	Gain, Nominal*:	10 dB
4	Gain, Min over $\pm 80^\circ$ * from Vertical:	6.2 dB
5	Receive Noise Factor:	1.3 dB
6	Power, Max:	200W
7	Input Impedance:	50 ohms
8	VSWR:	1.5:1
9	Dimensions:	Length 100 cm x height 10 cm x width 11.5 cm (less mounting flange)
10	Weight:	5.7 kg
11	Cross-section Profile:	77 sq. cm (less mounting flange)
12	MTBF (calculated use factor 4):	22,000 hours operating

* Includes losses due to phase and beam quantization, sidelobe radiation, lobe degradation, PIN diode series resistance losses, and element interaction losses.

5. CONCLUSIONS

The experience gained with the 300 MHz array development suggests that a linear phased array is easier to mount and, because of its simplicity, is potentially more reliable than other high-gain airborne antenna systems. The simple external mounting arrangement for the L-Band array module, in particular, means that its installation on existing aircraft will not be a serious problem. A preliminary estimate of \$4000.00 has been quoted as the cost of the L-Band array, complete with the necessary electronics. This is expected to compare favorably with the cost of other proposed antenna systems.

6. ACKNOWLEDGEMENT

This work was sponsored, in part, by the Defence Research Board, Department of National Defence, Canada.

7. REFERENCES

1. B. Dorier, "The Aircraft Antenna of the Dioscures System. Application of Electronically Phased Arrays to Aeronautical Navigation Using Satellites," L'Onde Electrique, vol. 51, no. 6, pp. 479-85, June 1971 (in French).
2. "L-Band and VHF Hemispherical Coverage Antennas for Satellite Communication," Technical Proposal D6-24782, Boeing Airplane Company, Renton, Washington.
3. Fraser and Williams, "An Airborne Phased Array for Use in an ATC Satellite System in L-Band," IEEE Conference Publication No. 77, p. 188, 1971.
4. British Aircraft Corporation Brochure H ESS/SS 313, British Aircraft Corporation, Box 77, Bristol BS99 7AR.

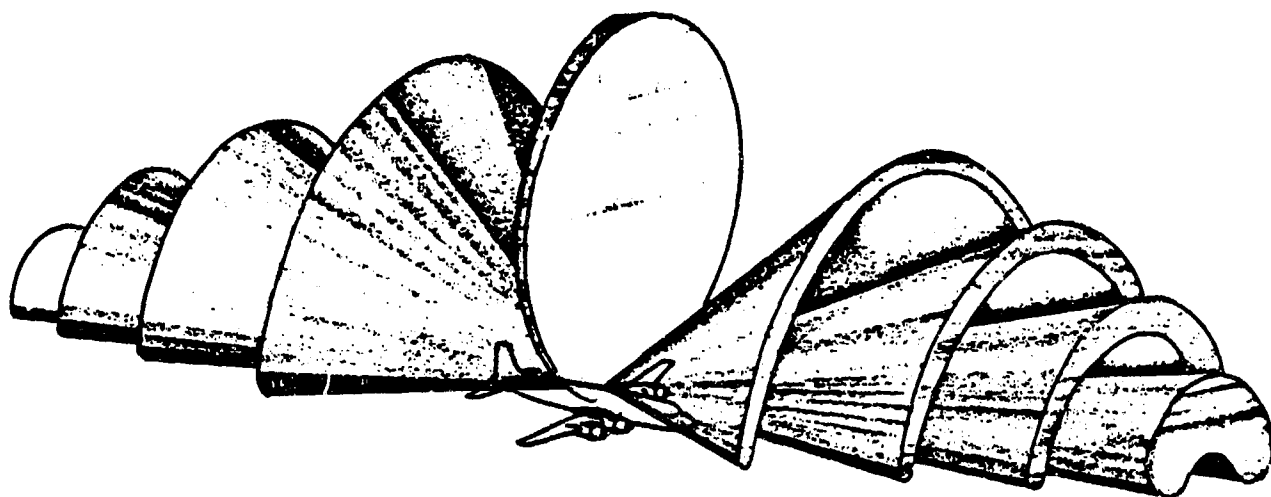


Fig.1 Some typical radiation patterns of a linear phased-array

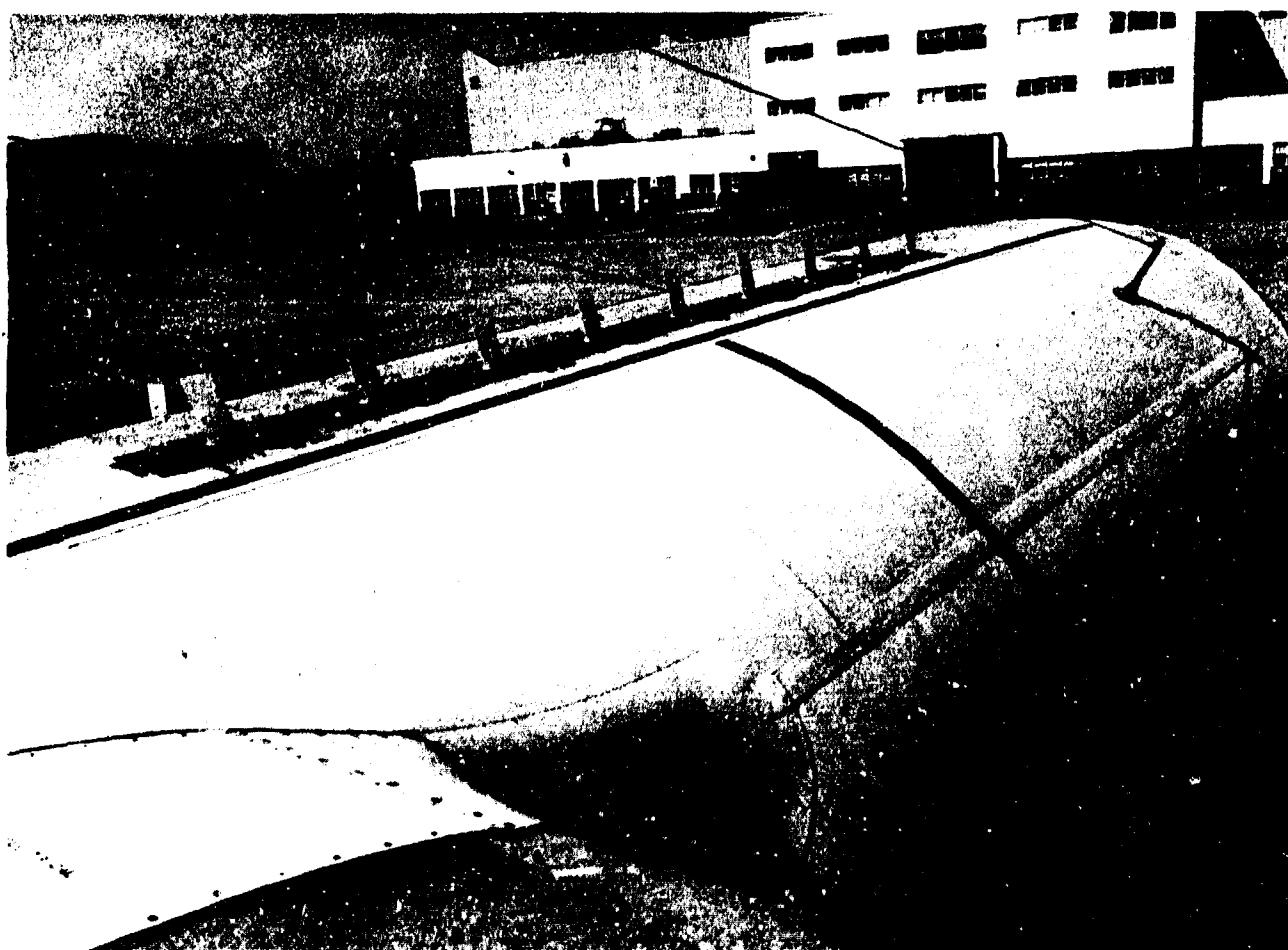


Fig.2 UHF array mounted on a C-130 aircraft

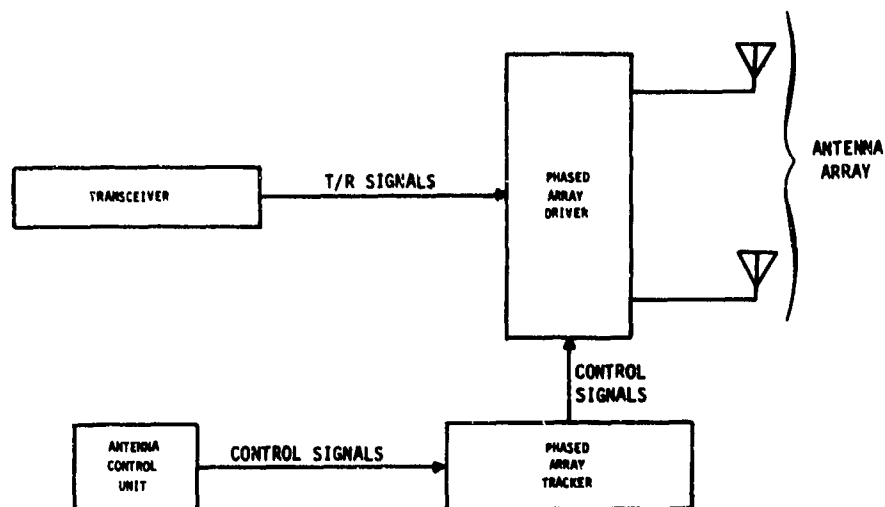


Fig.3 Block diagram of phased array system

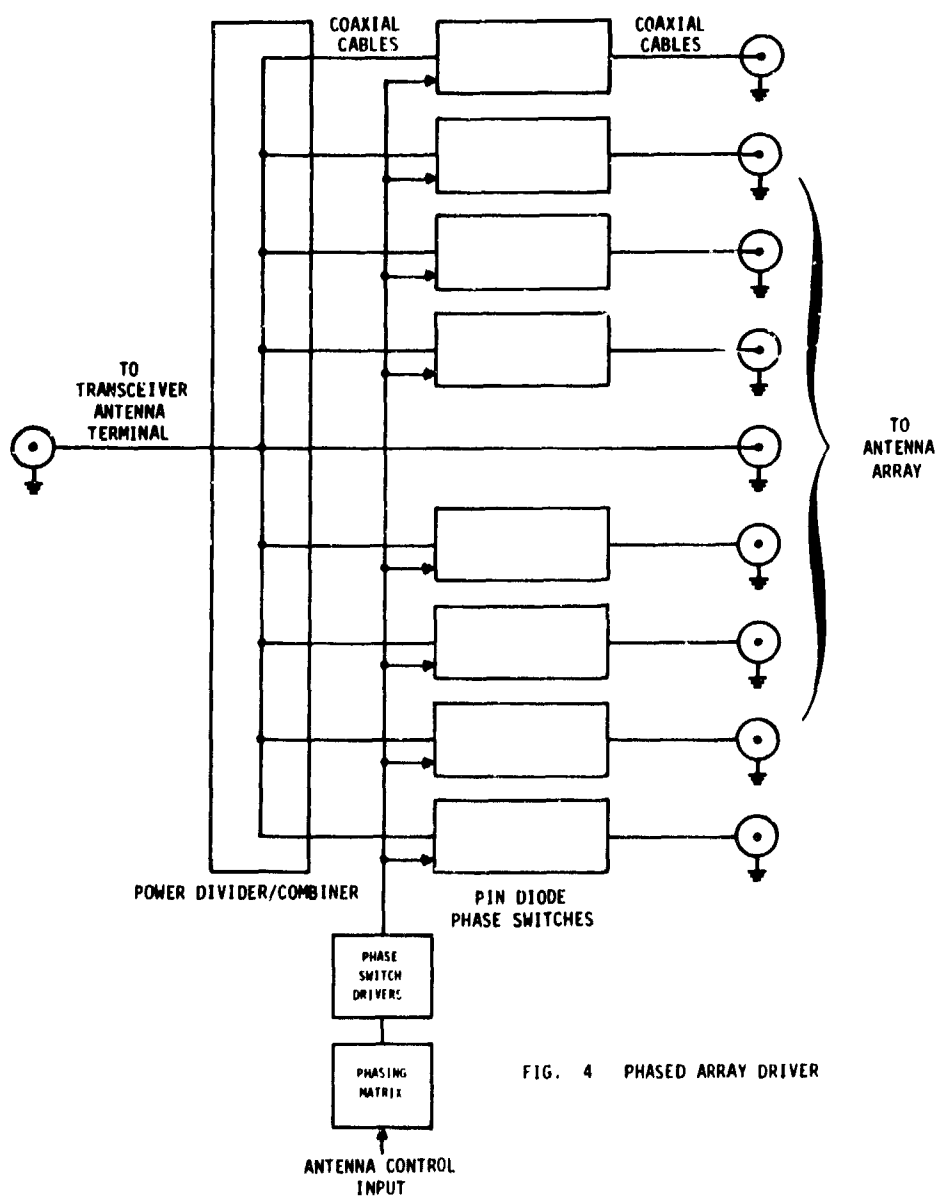


Fig.4 Phased array driver

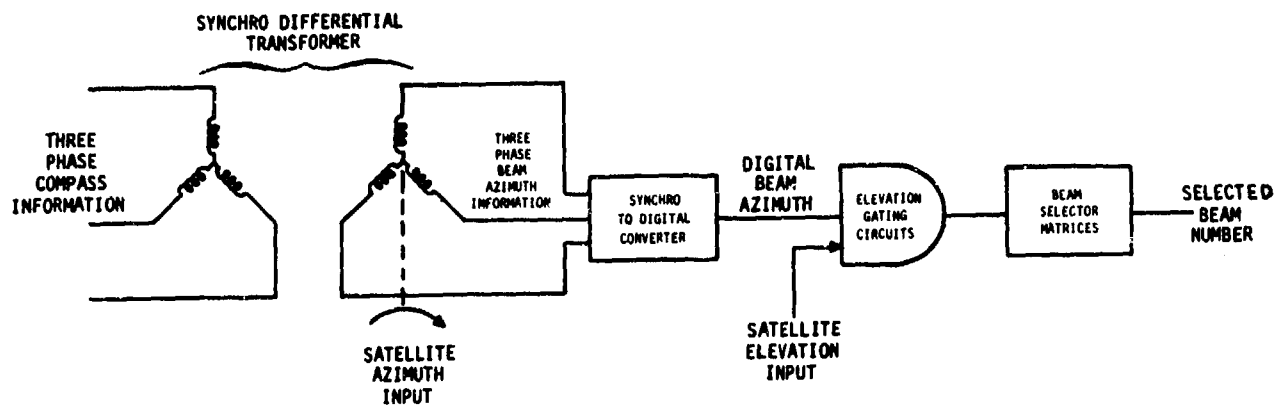


Fig.5 Compass driven phased array tracker

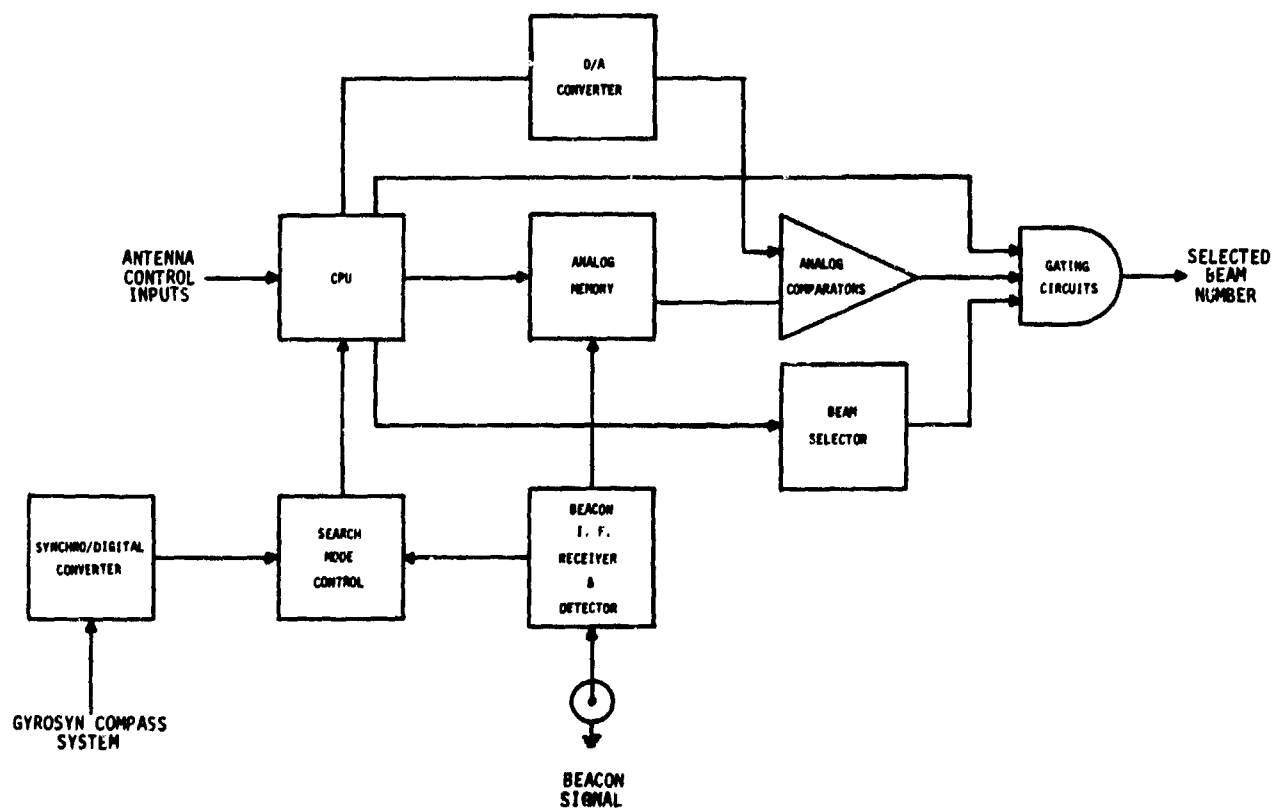


Fig.6 Scanning phased array tracker

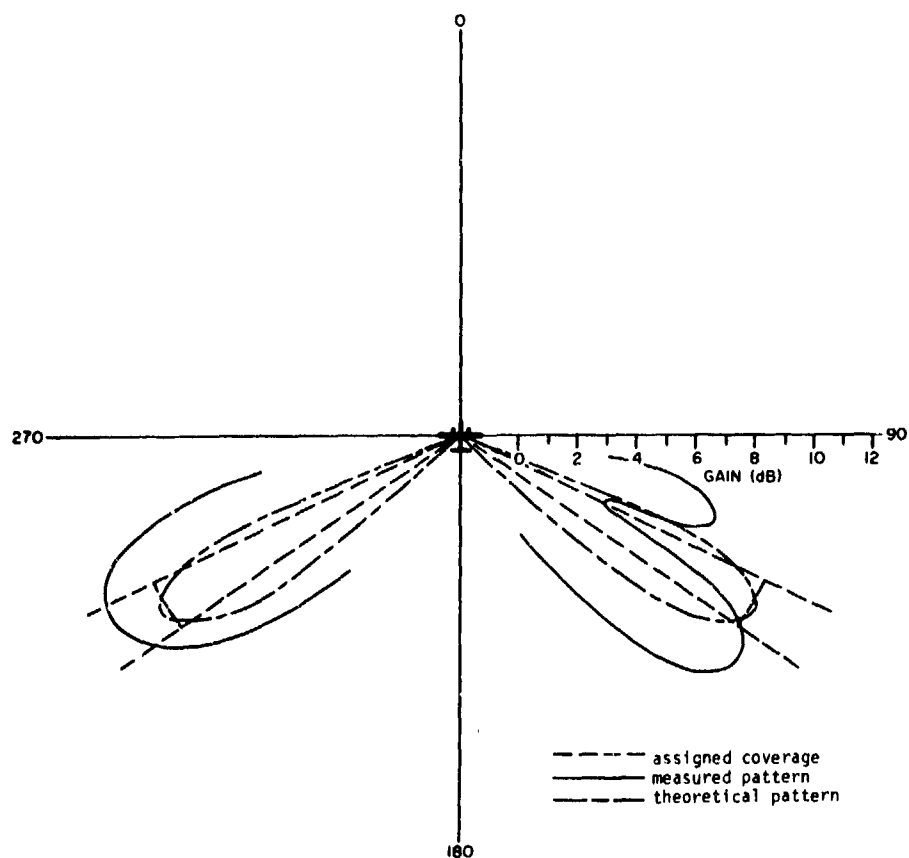


Fig. 7 Receive pattern of beam No. 19 (C-47 installation)

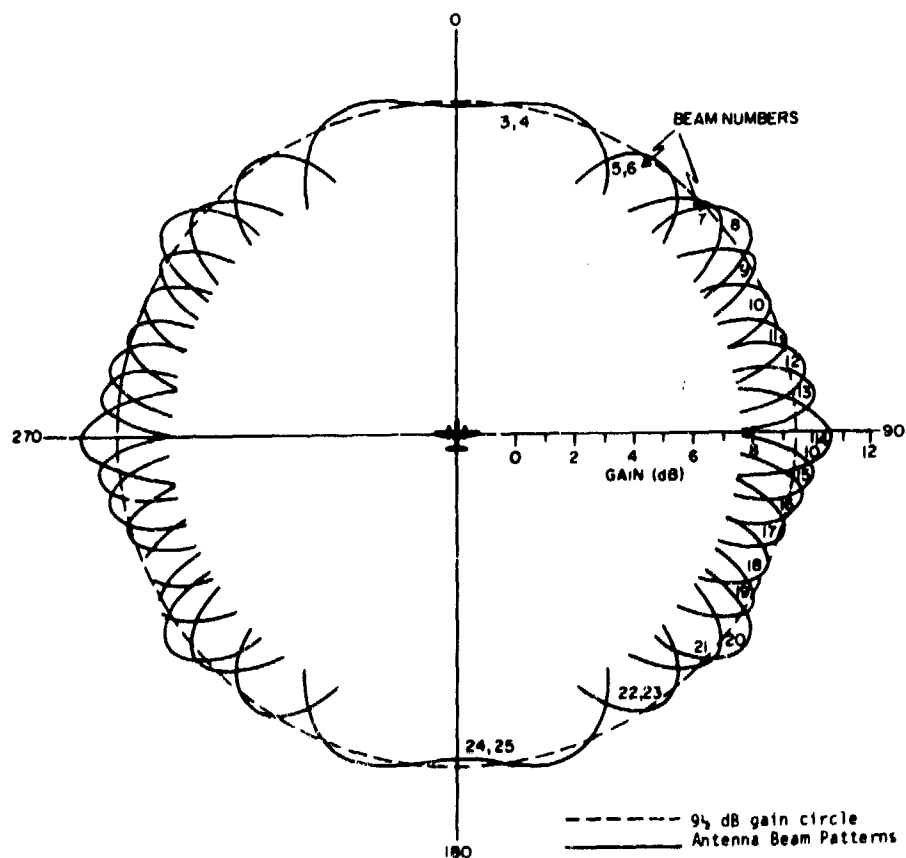


Fig. 8 Composite theoretical beam pattern for 30° elev. at RX freq.

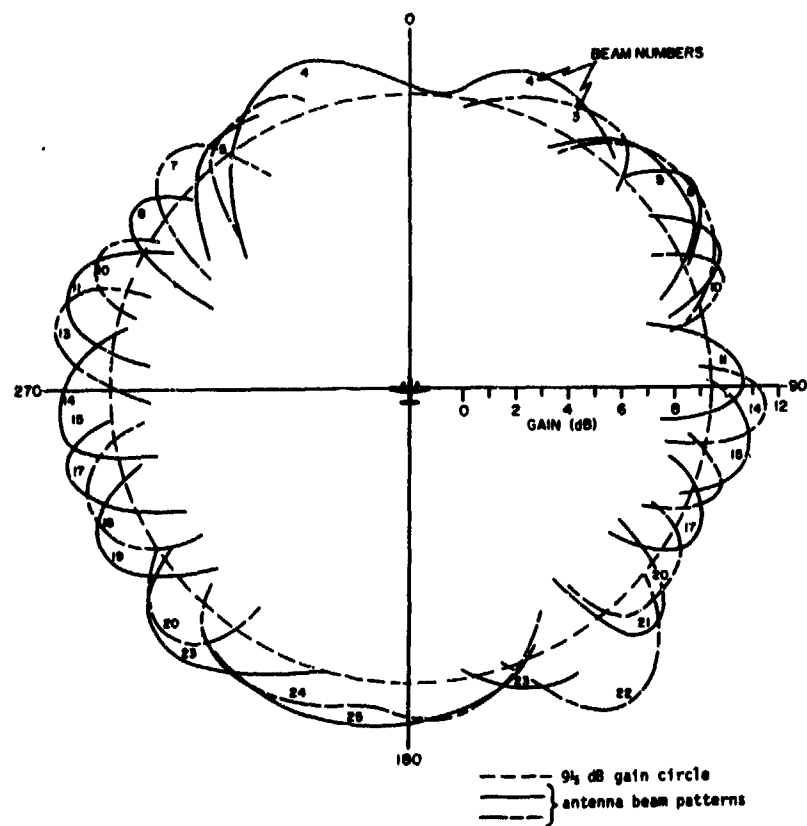


Fig.9 Composite measured beam patterns for 30° elev. at Rx. freq. (C-47 installation)

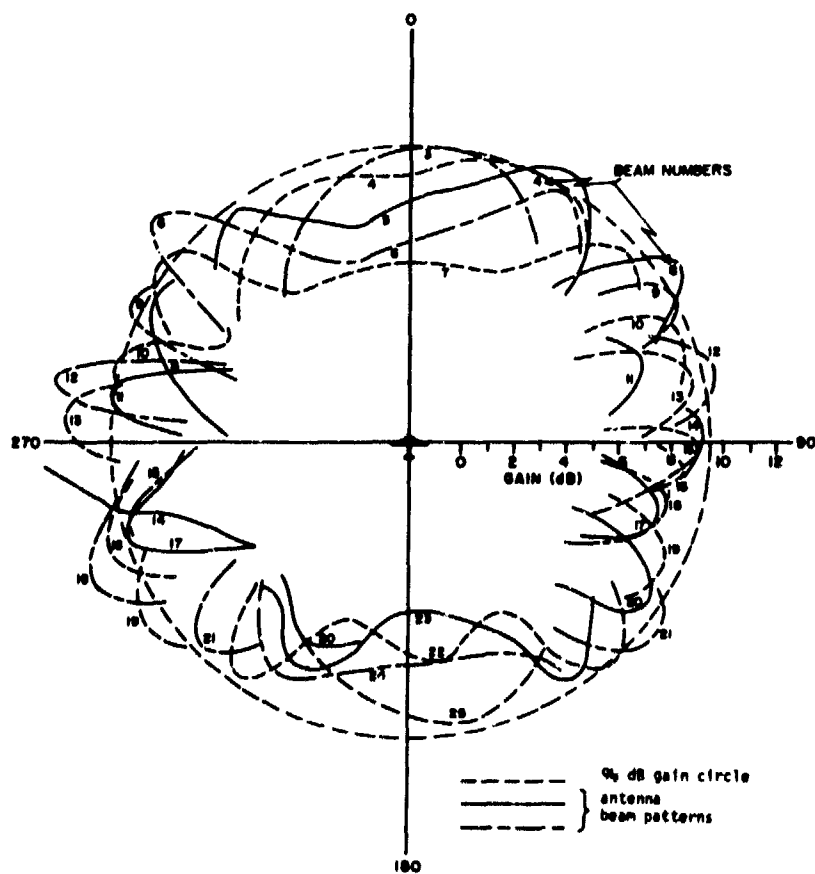
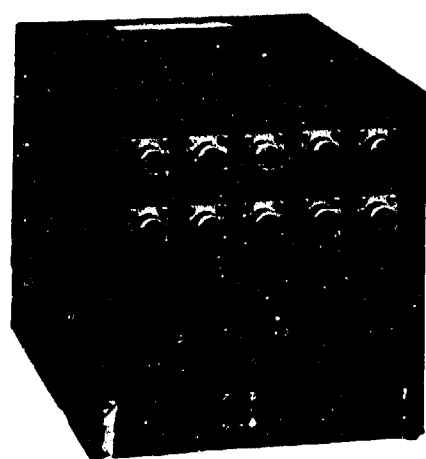
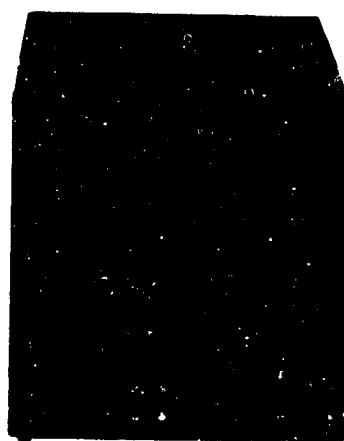


Fig.10 Composite measured beam patterns for 25° elev. at Rx. freq. (C-130 installation)



Phased Array Driver

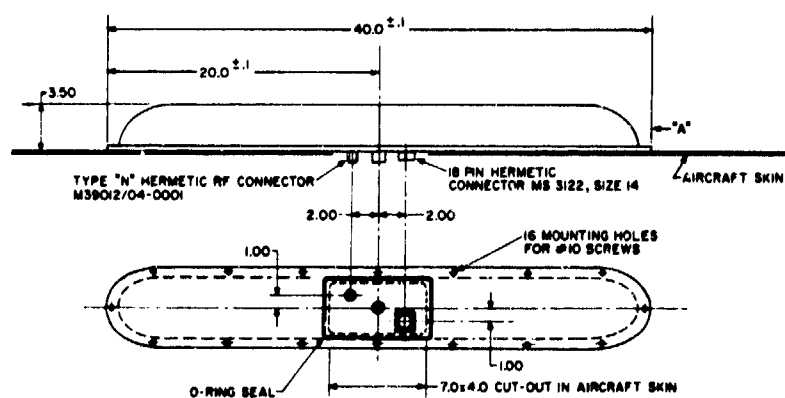


Phased Array Tracker



Antenna Control Unit

Fig.11 Complete phased array electronics



(all dimensions in inches)

Fig.12 Outline of L-band array structure

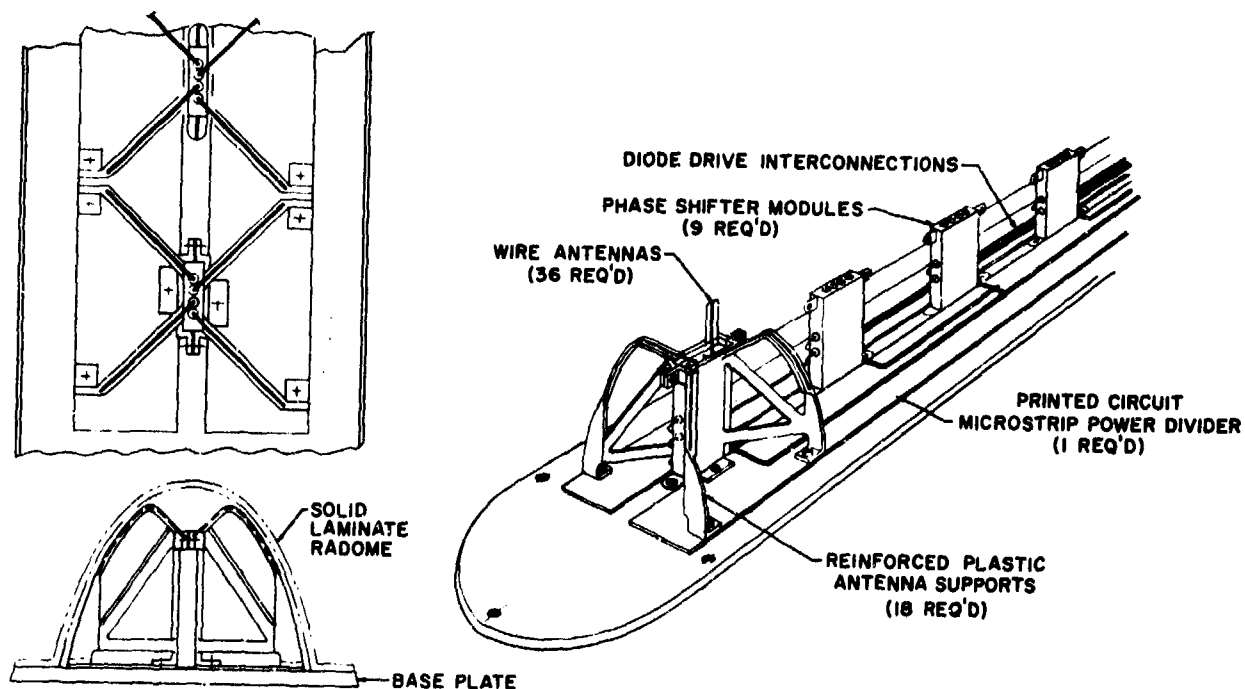


Fig. 13 Detailed schematic of L-band array showing phase shifter units and radiating elements.
Diagram supplied by Canadian Marconi Co.

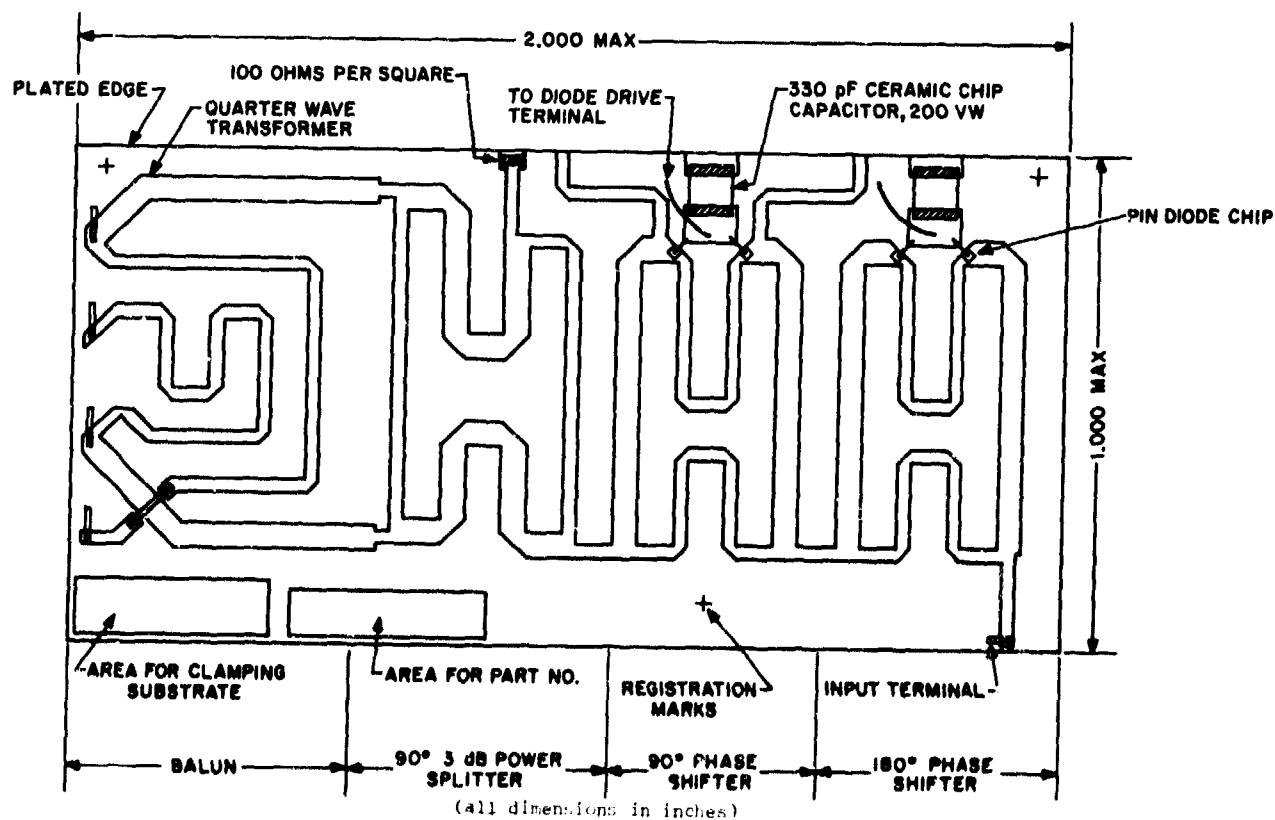


Fig. 14 Microstrip layout for phased shifter and Balun transformer as proposed by
Canadian Marconi Co.

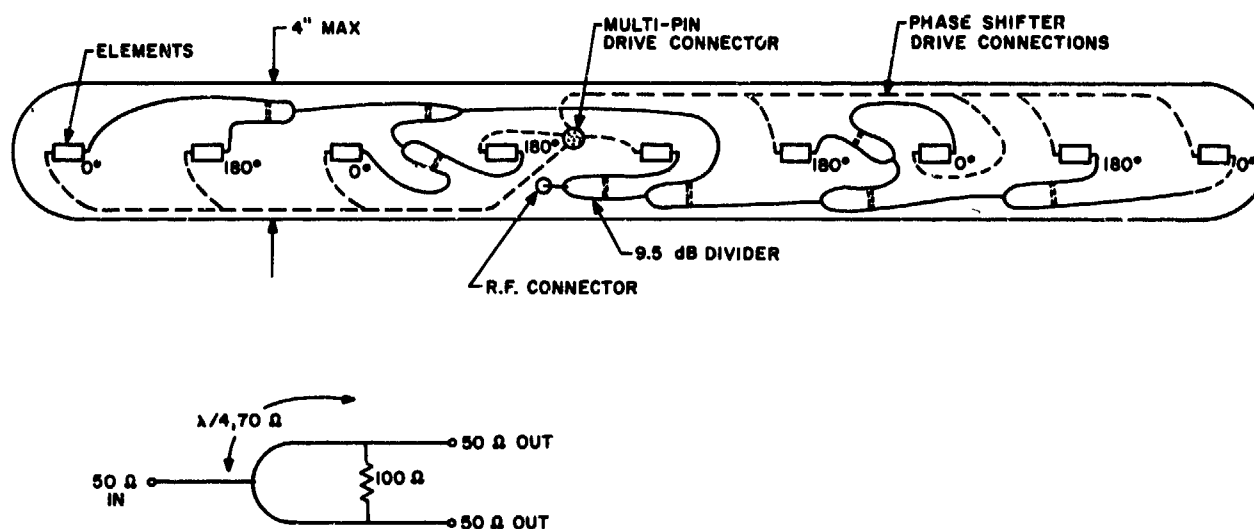


Fig.15 Layout of microstrip power splitter using seven 3 dB Wilkinson dividers and one 9.5 dB divider, as proposed by Canadian Marconi Co.

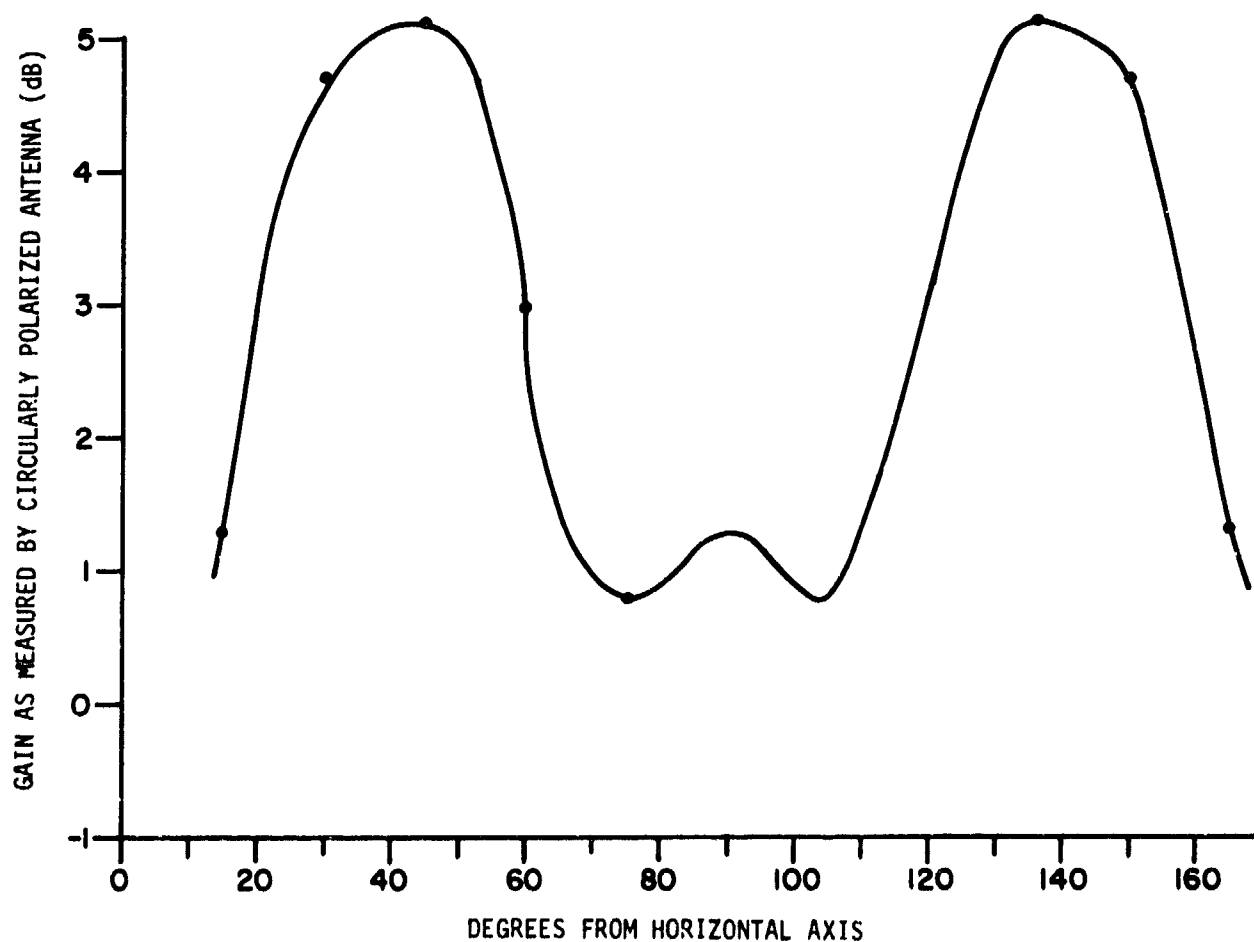


Fig.16 Radiation pattern typical of crossed-drooping-dipole element used in array

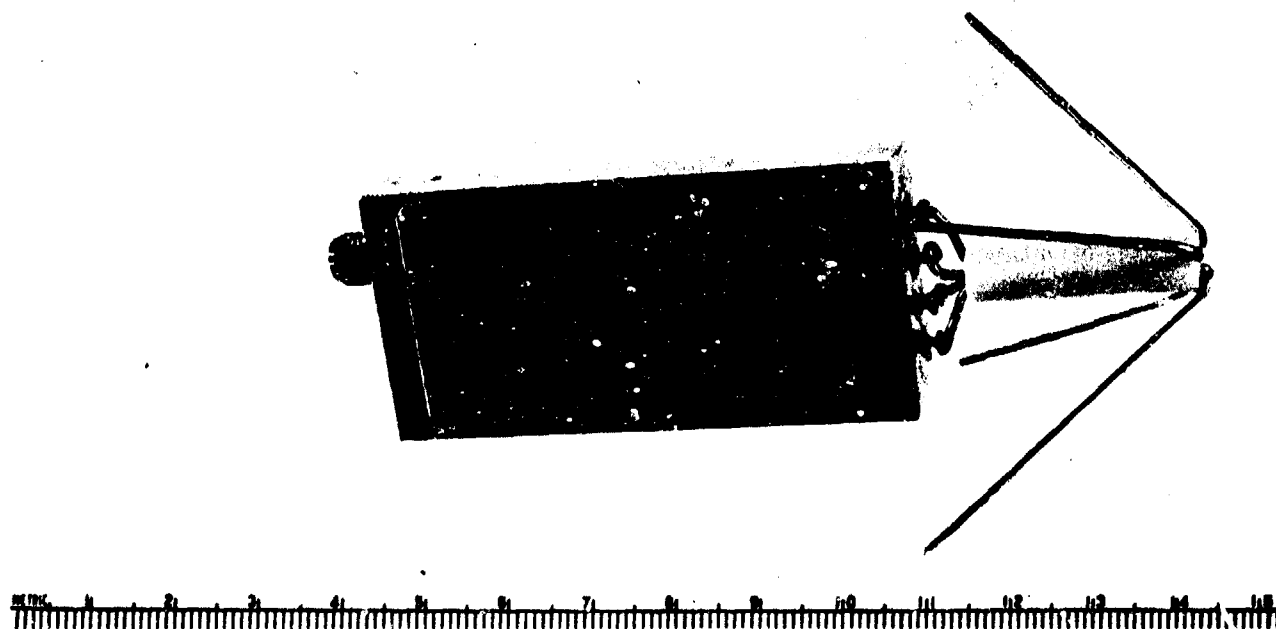


Fig.17 Prototype L-band radiating element and phase shifter

A COMPARISON OF TWO L-BAND AIRCRAFT ANTENNAS FOR
AERONAUTICAL SATELLITE APPLICATIONS

Robert G. Bland and John M. Clarke
Department of Transportation
Transportation Systems Center
Cambridge, Massachusetts 02142
U.S.A.

ABSTRACT

A comparison is made of the measured performance characteristics of two circularly polarized flush mounted L-band (1535-1660 MHz) aircraft antennas for aeronautical satellite applications. In order to facilitate radiation pattern measurements, the previously validated technique of using a scale model aircraft antenna was employed. One of the candidate antennas under comparison is a cavity backed dipole fed slot configuration. Measurements were conducted on a 1/10th scale model of a Convair 880 aircraft. The other antenna is an orthogonal-mode crossed-slot configuration. In this case measurements were conducted on a 1/20th scale model of a Boeing 707 aircraft which is almost identical in size to the Convair 880. The basic requirements of this class of antenna are to provide moderate gain of +4 dB above isotropic at L-band over the upper hemispheric region of the aircraft. Furthermore, there should be a sharp cutoff at the horizon with a minimum of gain in the lower hemisphere to enhance multipath signal rejection. The paper also discusses the results of a diversity combination techniques study for the two antennas under comparison. This study considers a switched multiple element system in which various fuselage placement and combination arrangements of elements are evaluated in order to meet the objectives stated.

1. INTRODUCTION

The performance characteristics of two different types of circularly polarized flush mounted L-band (1535-1660 MHz) aircraft antennas are compared. This effort was directed to the evaluation of low cost aircraft antennas providing hemispheric coverage with a smooth radiation pattern and a sharp decrease in gain outside the desired coverage region. From a literature search, two candidate antenna designs were selected for evaluation. These are: the cavity backed dipole fed slot antenna developed by the Diamond Antenna and Microwave Corporation (DICO) and the orthogonal-mode crossed-slot antenna developed by the Boeing Company. Scale model antenna radiation pattern test programs were conducted for each of these antennas. The techniques of using scale model antennas and a scale model of the vehicle to obtain pattern data had previously been validated on aircraft and missile programs.

In any antenna system, the local effects of the aircraft structure may cause pattern nulls which degrade signals in a communication link. The effects of signal fading due to earth and sea surface reflections (multipath) are also a function of the antenna gain pattern and polarization. Therefore, by careful design of the antenna and its location on the aircraft, the communications link performance can be greatly improved in the region of interest. These antennas have possible applications, either as a single element or a switched multiple element system, in an aircraft to satellite communications system such as the AEROSAT system.

The Airplane Coordinate System used for all pattern descriptions is shown in Figure 1. θ and ϕ are defined as follows:

- θ = Elevation angle in a standard spherical coordinate system measured from 0 degrees (zenith, directly above aircraft) to 180 degrees (nadir).
- ϕ = Azimuth angle in the equatorial plane of the standard spherical coordinate system. ϕ varies from 0 to 360 degrees. For conical cuts ϕ is projected into the equatorial plane.

Full size flight models of each of these antennas were used in actual flight tests to evaluate aircraft communications techniques, and these antennas were flush mounted. The cavity backed dipole antennas were low power units designed for receiving Right Hand circular polarized signals. The crossed slot antennas were designed for both receive and transmit (500 watts RF) modes; and provided terminals for both Right Hand Circular and Left Hand Circular polarization with polarization selection by external coaxial switching.

2. OBJECTIVES

The basic requirements of this class of antenna are to provide moderate gain of +4 dB above isotropic at the L-band frequencies (1535-1660 MHz) over the upper hemisphere of the aircraft with relatively small gain variations in this coverage region. The antenna should provide circular polarization with a high degree of circularity over the widest possible cone around zenith. Furthermore, there should be a sharp cutoff of 10dB in gain from $\theta = 80^\circ$ to $\theta = 100^\circ$, with a minimum of gain below the aircraft to provide rejection of multipath signals. This antenna would operate in aircraft to satellite communications systems. A low cost, rugged, reliable unit requiring no routine maintenance was required.

These performance objectives may be satisfied by a single element or several (2 to 4) elements spaced around the aircraft body employing simple switching for selecting the antenna receiving the maximum signal.

The data presented in this paper pertains to the performance characteristics of single elements, of each of the two designs, located at several places on the aircraft fuselage as illustrated by Figure 2. The influence of the aircraft surfaces, wings and stabilizers on the antenna patterns is indicated in the pattern plots. From this data, the feasibility of a simple, switched multiple element system can be determined.

Theory and Design

Cavity Backed Dipole Fed Slot Antenna

The cavity backed dipole fed slot antenna provides circular polarization to be realized in a rectangular slot by exciting a tilted dipole in the plane of the aperture of a cavity backed parasitic slot. This antenna produces an elliptical shaped pattern over the desired coverage region. A more directive pattern can be obtained by orienting the long dimension of the slot orthogonal to the longitudinal (roll) axis of the aircraft, rather than normal to this axis.

The theory of operation of a circularly polarized slot antenna is described by Wilkinson¹. An antenna design is discussed which allows circular polarization to be realized in a rectangular slot by placing a tilted parasitic dipole in the plane of the aperture. In addition, a reactive stub is connected at right angles to the dipole. This arrangement enables circular polarization to be realized without the complexity of 90° phase shifters and 2:1 power dividers in the antenna feed system. It was also shown that for UHF applications it was simpler to excite the dipole with the slot acting as the parasitic element. In this case the slot is backed up by a cavity which shunts a reactance across the aperture to correspond to the reactive stub employed with the parasitic dipole case. This latter configuration is employed in the DICO antenna configuration tested, and is illustrated by Figure 3. Theoretically either the slot or dipole may be used as the parasitic element.

Equations have been derived and combined to give the ratio of vertical to horizontal field vectors \bar{E}_y/\bar{E}_x along the axis normal to the radiating slot aperture. The magnitude of the ratio \bar{E}_y/\bar{E}_x for orthogonal axial fields, and also the phase angle ϕ of \bar{E}_y/\bar{E}_x between orthogonal axial fields for the slot dipole antenna are theoretically related to the dipole tilt angle ψ with reference to Figure 3 for different values of X_0 , the reactance of dipole plus termination. The resistance R_0 of the dipole in the presence of the slot is also a function of ψ and using measured values of R_0 at specific normalized frequencies for which the dipole is $\lambda/2$, the magnitude and phase angle of \bar{E}_y/\bar{E}_x can be calculated and plotted as a function of the tilt angle ψ .

NOTE: The ratio \bar{E}_y/\bar{E}_x can be interpreted as the ratio of the field components $\bar{E}_\theta/\bar{E}_\phi$ for a top center mounted antenna indicated on the coordinate system Figure 1. The conditions for circular polarization are:

$$\left| \frac{\bar{E}_y}{\bar{E}_x} \right| = 1, \quad \phi = \pm \pi/2$$

depending upon whether right-hand or left-hand circular polarization is employed. For a circularly polarized system, the multipath rejection is maximized by an aircraft antenna pattern that is nearly circularly polarized for the direct path and has a high axial ratio for the reflected-wave path. The axial ratio of the generalized polarization ellipse is defined as the ratio of the semimajor axis to the semiminor axis for the polarization ellipse. (Circular polarization is one particular case of elliptical polarization). The design and performance criteria also had to consider installation of the antenna element in a region relatively free from shadowing by the wings and stabilizers, namely on the dorsal region of the fuselage, with the radiating aperture pointed towards zenith.

Based upon the previously defined objectives, another criteria which resulted in the selection of this antenna element is the gross effect on the pattern of a flush mounted antenna due to the curvature of a cylindrical conducting body. In this case, we are concerned with the curvature of the aircraft fuselage which is effectively a curved ground plane. The curvature of the aircraft fuselage was determined from $c = ka = 2\pi a/\lambda$ where $k = 2\pi/\lambda$, a = cylinder radius and λ = wavelength at the operating frequency. In this equation, c is the circumference in wavelengths, and for the Convair 880, $c = 61.5$.

The equatorial plane radiation fields produced by a sinusoidal distribution of axial electric field on a metallic cylinder of radius (a) have been calculated by Knop and Battista². Radiation patterns in this plane are plotted (Figure 4) for cylinder size from $1 \leq c \leq 30$. From these patterns it can be seen that as the cylinder size increases the patterns sharpen, and in the limit of infinite cylinder radius (a) the patterns approach that from a slot on an infinite plane. For cylinders of size $c \geq 30$, which includes all large commercial aircraft, the patterns are identical within 0.5 dB for angles off the axis of ± 65 degrees. Because of the large curvature of the Convair 880 fuselage, it was expected that lower hemisphere coverage would be reduced. Lower gain below the aircraft would reduce multipath signals from earth reflections.

Measured data from previous missile programs were reviewed and analyzed. The data indicated that a scale model operating at C-band could provide most of the required gain, polarization and coverage features. The data was obtained for two diametrically opposite antenna

elements on a missile cylindrical surface. Thus, the scale model technique was considered feasible for the aircraft application involving large cylinders (aircraft fuselage circumference). Analysis of the data resulted in an estimate of the coverage that could be obtained from a single flush mounted element at L-band.

The Diamond Antenna and Microwave Corporation (DICO), Winchester, Massachusetts, USA., developed a full scale L-band cavity backed dipole fed slot antenna and demonstrated near hemispherical coverage on a cylindrical ground plane. An extensive radiation pattern test program was initiated with DICO⁴ in 1971 to perform pattern measurements of 1/10th scale elements at several locations on a 1/10th scale model of a Convair 880 aircraft shown in Figure 2. The test frequency was 15.5 GHz, scaled up from 1550 MHz. The results of this scaled model antenna and aircraft pattern test program are summarized. The full size antenna is illustrated in Figure 8.

Orthogonal - Mode Crossed - Slot Antenna

The basic antenna consists of two orthogonal half-wave length slots fed in balance and in phase quadrature, thus providing a low-gain hemispherical coverage circularly polarized radiator. In this case the crossed-slot iris is the parasitic element. The crossed-slot feed is fabricated by etching slots on a 1/8 inch thick, 2 oz. copper clad Teflon-loaded fiberglass plate mounted in the antenna aperture. The slots are fed in balance and phase quadrature from a 90° ring hybrid circuit located within the antenna cavity. The antenna feed network is illustrated as connected to the radiating aperture shown in Figure 5. The balanced feed enables the individual slot impedances to track each other when both slots are fed. This impedance tracking is necessary to feed the slots in phase quadrature and achieve equal power division by means of a simple quadrature hybrid. The impedances of concern are those appearing at points 0' and 0'' in Figure 5. The impedance at these points is maintained at 50 ohms over the frequency band within a VSWR of 2:1. When a relative phase shift of 90° exists between the slots, the antenna will transmit (or receive) a purely circularly polarized field on the axis (boresight) of the antenna aperture. When port R is connected to the receiver and L is terminated in 50 ohms the radiated field is right-handed circularly (RHC) polarized. Alternately, port L may be connected to the receiver (or transmitter) for left-handed (LHC) polarization. A coaxial switch is shown in Figure 5 to facilitate the change from RHC to LHC polarization. An illustration of the orthogonal-mode crossed-slot antenna mounted on a section of curved ground plane is shown in Figure 6.

The principle of operation is illustrated by the electric field diagrams shown in Figure 7. Figures 7a and 7b show the idealized far field E-plane and H-plane patterns of the individual slots in the crossed-slot iris. Figure 7c shows the pattern which is obtained by superposition of the individual slot patterns. When the individual slot fields, symbolized by the electric field vectors E_a and E_b , are equal in magnitude and in phase quadrature, pure circular polarization (0 dB axial ratio) is obtained in the direction $\theta = 0^\circ$. As one moves off axis the circularity becomes poorer due to the increased axial ratio between the E-plane and H-plane fields. As the horizon is approached ($\theta = 90^\circ$) the polarization becomes nearly linear as the vertical, E-field component, is dominant.

Initial design of the antenna element was performed using a cylindrical ground plane many wavelengths in size. This gives an indication of the approximate radiation pattern of the antenna. However, for accurate evaluation and comparison of antenna performance in the presence of reflecting surfaces such as the wings, stabilizers and engine nacelles measurements are made on a true scale model of the aircraft. To verify that the performance of the scale model antenna is equivalent to the full size antenna, pattern tests on a cylindrical ground plane are performed with the scaled antenna in the same environment as the original tests on the full size antenna.

The Boeing Company, Seattle, Washington, USA, developed full scale flight worthy orthogonal-mode crossed-slot antennas and performed complete spherical scale model pattern measurements⁶ for two antenna locations (reference Figure 2) using a 1/20th scale model of a Boeing 707 aircraft which has an airframe almost identical in size and shape to the Convair 880. It was believed that the data would not be significantly affected by the small differences of the Boeing 707 from the Convair 880. The test frequency was 32.0 GHz scaled up from 1600 MHz. The initial development of this antenna design was performed by the Boeing Company in 1968 under a NASA sponsored SST/L-band Satellite Study Program⁷. The full size Boeing crossed-slot antenna is shown in Figure 8.

Performance

A discussion of the performance of each of the two antennas is presented followed by a comparison of the antennas and a discussion of applications. Figure 2 indicates the locations of the antennas on the aircraft where scale pattern measurements were taken namely; station 820 for the Boeing crossed-slot, and stations 803.5 and 940 for the DICO dipole fed slot. At each station antennas were located at two places: top centerline and 35° off the top centerline. The electrical characteristics of these antennas are summarized in Table 1.

The dipole fed slot antenna was tested at two stations over the wings to determine the effects of the wings on the pattern shape and the gain. The top centerline antenna at station 803.5 has a measured peak gain of +9.2 dB above a circularly polarized isotropic radiator and produced an elliptical shaped conical beam. This antenna has an efficiency of greater than 85% and provides relatively high peak gain for a broad beam radiator. As shown by the solid lines in Figure 9, the gain pattern orthogonal to the aircraft fuselage provides a beamwidth of 65° for a gain of +4 dBci and 100° ($\theta = \pm 50^\circ$) for a gain of 0 dB. At angles below $\theta = \pm 50^\circ$ the aircraft wings and horizontal and vertical stabilizers begin to cause pattern nulls and ripple which increases as θ increases. Of particular interest is the difference of the gain at $\theta = 80^\circ$ to $\theta = 100^\circ$ (elevation of 10° above the horizon to 10° below the horizon) and the gain below the aircraft. The gain pattern cuts off sharply in the roll plane (refer to Figure 9) and less sharply in the pitch plane shown in Figure 10. In the roll plane the gain difference for $\theta = 80^\circ$ to $\theta = 100^\circ$ is 3 dB while the gain decreases another 12 dB at $\theta = 120^\circ$. Gain patterns for two conical cuts, $\theta = 40^\circ$ and 80° are shown in Figures 13 and 14 respectively. These patterns indicate the smooth circular pattern of near constant gain at narrow beamwidth and the elliptical pattern shape with numerous ripples and nulls near the aircraft wings and tail at wide beamwidth.

The dipole fed slot antenna located 35° off top centerline at station 803.5 suffers a decrease in peak gain to 7.8 dBci and some distortion in the uniformity of the beam pattern in the roll plane as shown in Figure 11. The gain at 65° beamwidth ($\theta = 2^\circ$ to 67°) is +4 dBci and at $\theta = 80^\circ$ the gain is +2 dBci. The gain cutoff from $\theta = 80^\circ$ to $\theta = 100^\circ$ is only 5 dB, however, at $\theta = 120^\circ$ the gain decreases another 20 dB. Thus, the multipath rejection is unacceptable at $\theta = 100^\circ$, but it is good below $\theta = 120^\circ$. Figures 15 and 16 illustrate the patterns for conical cuts of $\theta = 40^\circ$ and 80° respectively. These patterns indicate the gain profiles are relatively smooth and asymmetric in the direction the antenna aperture is facing. On the side opposite the antenna, the radiation decreases significantly with unmeasurable levels below $\theta = 100^\circ$ (10° below the horizon).

At station 940, top centerline location, the peak gain is 9.8 dBci, slightly greater than that for station 803.5. There is a sharp break up in the pitch plane pattern with a null just above the aircraft nose ($\theta = 83^\circ$) and a large peak directly off the nose ($\theta = 90^\circ$). In comparing the conical patterns at station 940 to those at station 803.5, it is found at $\theta = 110^\circ$ the lobes have more gain in the forward and aft directions for the antenna at station 940. From this data, it is clear that multipath signals received from below the aircraft are suppressed, by using the antenna at station 803.5. Thus, station 803.5 is the preferred location. Performance of the antenna at station 940, located 35° off centerline is not greatly different from the station 803.5, 35° antenna except the gain below the aircraft is significantly greater. This means the multipath rejection is less. From the data presented here and in the DICO report⁴ the dipole fed slot located at station 803.5 has superior performance to that at station 940. Therefore, no further consideration will be given to the antenna at station 940.

The Boeing crossed-slot antenna was tested at station 820 rather than 803.5 because this is the actual location of the antenna on the Convair 880 due to interference with existing equipment on the aircraft. The difference in these two locations does not cause any significant variations in the measured pattern data because the distance is small relative to the size of the fuselage and to the distance to the wings and stabilizers. The measured gain of the crossed-slot was +5.0 dBci at the top centerline ($\theta = 0^\circ$) and +6.4 dBci at the starboard side ($\theta = 35^\circ$) off centerline. The wing structures at the 35° position cause a focusing effect on the pattern resulting in larger lobes and higher gain. The efficiency of this antenna was measured as 87%. Gain of +4 dBci is achieved over a beamwidth of 55° , while 0 dBci gain is provided over 150° beamwidth. The Boeing patterns in Figure 9 and 10 indicate the smoothness in the roll and pitch planes. The gain decreases approximately 7 dB from $\theta = 80^\circ$ to $\theta = 100^\circ$ but the difference between peak gain at $\theta = 0^\circ$ and that at $\theta = 100^\circ$ is only 15 dB. This antenna is best suited for the top centerline location because at the 35° position the multipath rejection is not acceptable and some pattern distortion occurs due to the wings. These patterns are shown in Figures 11 and 12.

The circularly polarized orthogonal-mode crossed-slot antenna is intended to serve as an upper hemisphere coverage antenna. From the radiation patterns⁶, the top centerline location provides a gain equal to or greater than isotropic for approximately 90% of the coverage sector of $\theta = 0^\circ$ to $\theta = +80^\circ$. In addition, the coverage below the horizon decreases rapidly below the 100° conic ($\theta = 100^\circ$), providing good multipath rejection. Due to the low peak gain, this antenna has a rather narrow beamwidth at +4 dBci. It should be noted the scale patterns on top centerline compare very well with those obtained for the full size production antenna when tested on a 4 foot by 4 foot ground plane.

The discussion thus far has focused on a single element antenna to provide hemispheric beamwidth and moderate gain (0 to +4 dB) with good multipath rejection outside the desired coverage region. We have shown that the Boeing crossed-slot comes close to meeting the minimum gain of 0 dBci. Upon examination of the data we can see that the DICO dipole fed slot provides a higher gain of +4 dBci and could provide the beamwidth, minimum of 160° ($\theta = +80^\circ$), by using two or three elements appropriately spaced around the fuselage. These would be electrically or manually switch selected to direct the desired beam toward the satellite in an aeronautical communications system. The beamwidth of these antennas in the pitch plane indicates two satellites could be in the field of vision simultaneously for surveillance functions for most azimuth angles (aircraft headings).

It should be noted that the "initial" goal of this evaluation program was to find an antenna providing 0 dBci gain over 160° beamwidth in the upper hemisphere. During the performance of these test programs the AEROSAT system definition was initiated and requirements developed which called for a minimum of +4 dBci over the same beamwidth. We believe the antennas discussed have promise of fulfilling that requirement at a relatively low cost. The feasibility of multiple elements has been demonstrated in follow-on work performed by Texas Instruments Inc., Dallas, Texas, involving diversity techniques and combination studies using the Boeing crossed-slot and DICO dipole fed slot antennas. Two pair (four elements) of the DICO antennas employing switch selection of sum and difference patterns provides a minimum of +4 dBci over the hemispheric region above $\theta = 80^\circ$. Each pair of elements is located on the side of the aircraft fuselage, 55° down from zenith at station 803.5. The two elements in a pair are separated by $0.75s/\lambda$. The sum and difference patterns generated by computer from the scale model pattern are shown in Figure 18. Performance of the crossed-slot antenna in the same configuration is shown in Figure 17 for comparison. This data is in process of being published as a US Department of Transportation contractor's report⁸.

CONCLUSIONS

The antennas discussed are applicable to the future L-band aeronautical satellite ATC systems being planned. These are low cost antennas (approximately \$500.00 per unit in quantity) capable of satisfying digital communications and surveillance requirements with one or two elements and will satisfy the minimum quality voice communications requirements with 3 or 4 elements in combination. Additional work is required to provide field testing and evaluation of these antennas. Both the DICO and Boeing antennas described were tested and evaluated in communications tests performed with a Convair 880 aircraft and balloons in 1971 in the USA and in France in Cooperation with ERSO⁹. Future antenna tests are planned by the US Department of Transportation using the NASA ATS-F satellite in 1974 and 1975.

REFERENCES

1. Wilkinson, E.J., "A Circularly Polarized Slot Antenna", Microwave Journal, Vol. 4, No. 3, March 1961.
2. Kraus, John D., "Antennas", McGraw-Hill, Electrical and Electronic Engineering Series, McGraw-Hill Book Company, Inc., 1950.
3. Knop, C.M., Battista, A.R., "Calculated Equatorial Plane Radiation Patterns Produced by a Circumferential Slot on a Cylinder", Institute of Radio Engineers (IEEE) Transactions on Antennas and Propagation (pp 498, 499), September 1961.
4. McCabe, W.J., "A Scale Model Aircraft and Antenna Pattern Test Program", Final Report on Contract No. DOT/TSC-167, October 1971, Diamond Antenna and Microwave Corporation, 33 River Street, Winchester, MA., USA.
5. Clarke, J.M., McCabe, W.J., "L-Band Aircraft Antenna Patterns for AEROSAT Systems", Twenty-Second Annual Symposium, USAF, Antenna Research and Development Program, University of Illinois, Monticello, Illinois, USA, October 1972.
6. Olsson, T., Stapleton, B.P., "L-Band Orthogonal-Mode Crossed-Slot Antenna and VHF Crossed-Loop Antenna," Final Report No. DOT-TSC-NASA-72-2, August 1972, Boeing Company, P.O. Box 3707, Seattle, Washington, 98124, USA.
7. Kiskaddon, W.V., Carman, D.M., "Experimental L-Band SST Satellite Communications/Surveillance Terminal Study", Vol. 4, Aircraft Antenna Studies, Prepared Under Contract No. NAS 12-621, November 1968, Boeing Commercial Airplane Division, Renton, Washington, USA.
8. Fuller, J.A., Jones, A.S., "Final Report on Diversity Combination Techniques Study", Contract No. DOT-TSC-550, August 1973, Texas Instruments Inc., P.O. Box 6015, Dallas, Texas, USA.
9. "Ballons Used in AEROSAT Tests", Aviation Week and Space Technology, Vol. 94, No. 25, June 21, 1971.

ACKNOWLEDGEMENTS

The Authors wish to recognize the contributions made to this paper by the following persons:

Mr. W.J. McCabe of the Diamond Antenna and Microwave Corporation,
Messrs. T. Olsson and B.P. Stapleton of the Boeing Company, and
Mr. J.A. Fuller and Dr. A.S. Jones of Texas Instruments Inc.

The data provided to the US Department of Transportation by these individuals was very helpful in the preparation of this paper.

TABLE 1 ANTENNA ELECTRICAL CHARACTERISTICS

ANTENNA TYPE	MANUFACTURER	STATION LOCATION	TEST FREQUENCY	POWER DIVISION PORTS 1 & 2	ISOLATION BETWEEN SLOTS	ANTENNA AT TOP CENTERLINE			ANTENNA 35° FROM TOP CENTERLINE	
						PEAK GAIN	INPUT VSWR	AXIAL RATIO	PEAK GAIN	INPUT VSWR
Cavity Backed Dipole Fed Slot	Diamond Antenna and Microwave Corp. (DICO)	STA. 803.5	15.5 GHz	NA	NA	9.2 dBCi Max.	1.70:1 Max.	($\phi=0^\circ-90^\circ$) 2dB, $\theta=0^\circ$, $\phi=0^\circ$ 3.5dB, $\theta=\pm 40^\circ$, $\phi=60^\circ$ 7.0dB, $\theta=\pm 40^\circ$, $\phi=60^\circ$ 5.5dB, $\theta=\pm 40^\circ$, $\phi=90^\circ$	7.8 dBCi Max.	1.50:1 Max.
Cavity Backed Orthogonal-Mode Crossed-Slot	Boeing Co.	STA. 940	15.5 GHz	NA	NA	9.8 dBCi	1.70:1 Max.	SAME	8.2 dB	1.6:1 Max.
		STA. 820	32.0 GHz	Equal within 0.3 dB	19 dB min. (1540 MHz)	5.0 dBCi Max.	1.50:1 Max.	($\phi=0^\circ-360^\circ$) 1dB, $\theta=0^\circ$, $\phi=\pm 40^\circ$	6.4 dBCi Max.	1.50:1 Max.

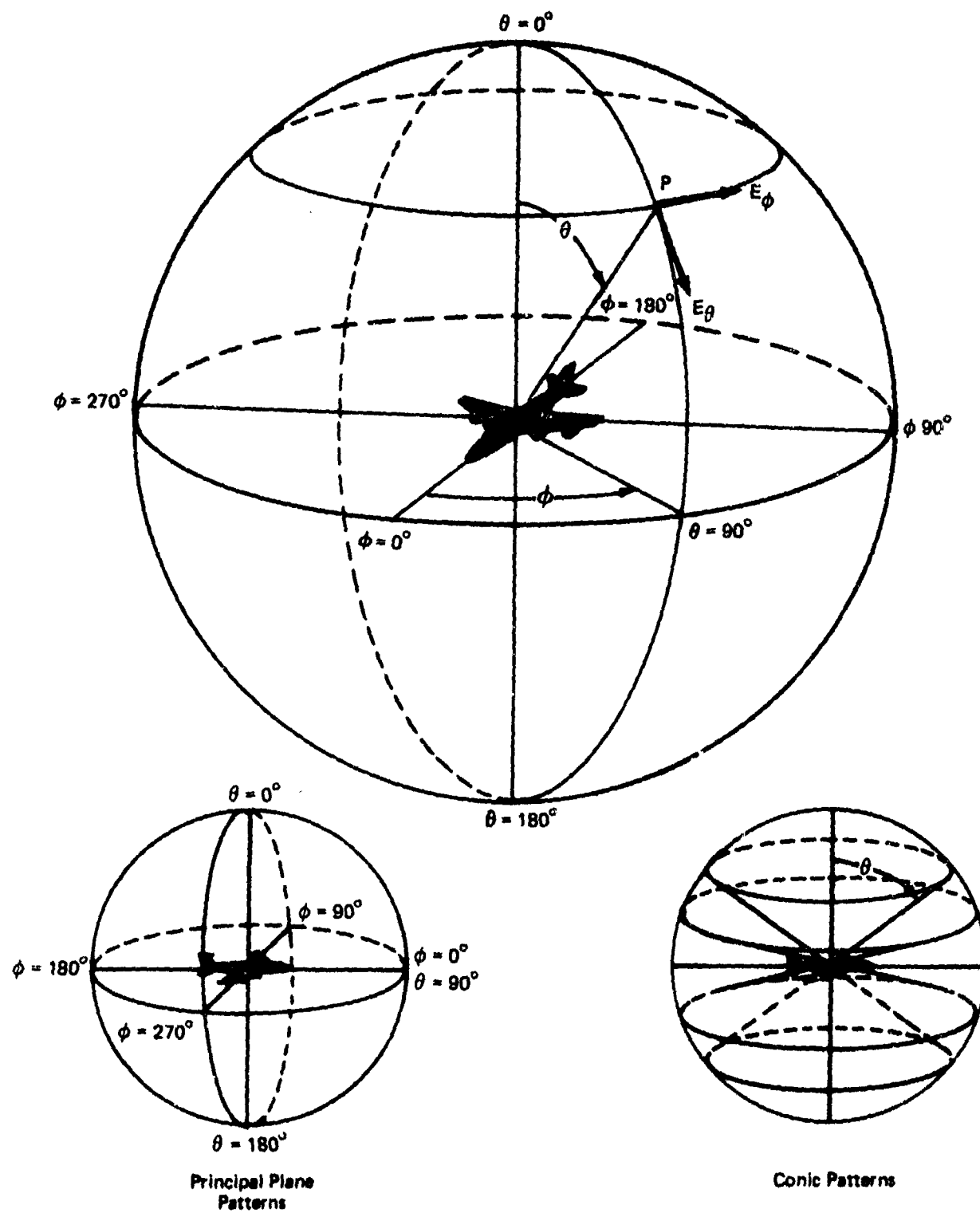
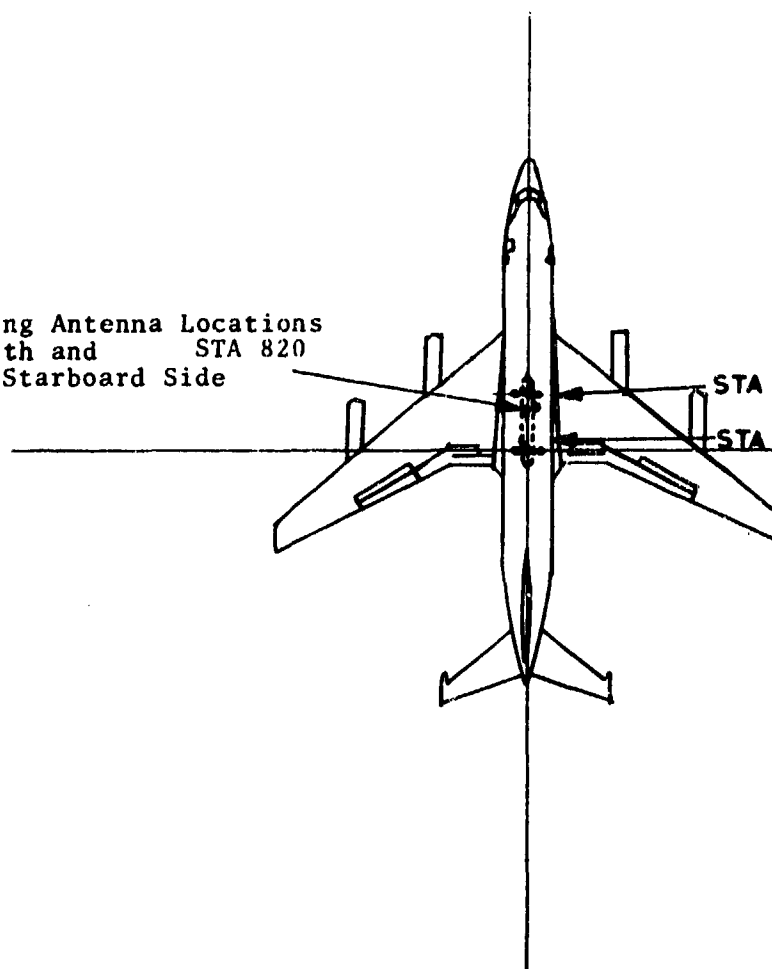


Figure 1. Airplane Coordinate System

Boeing Antenna Locations
Zenith and STA 820
35° Starboard Side



DICO Antenna Locations

Zenith and both

STA 803.5 \pm 35° From Zenith

STA 940 Zenith and both
 \pm 35° From Zenith

Figure 2. Antenna Element Locations

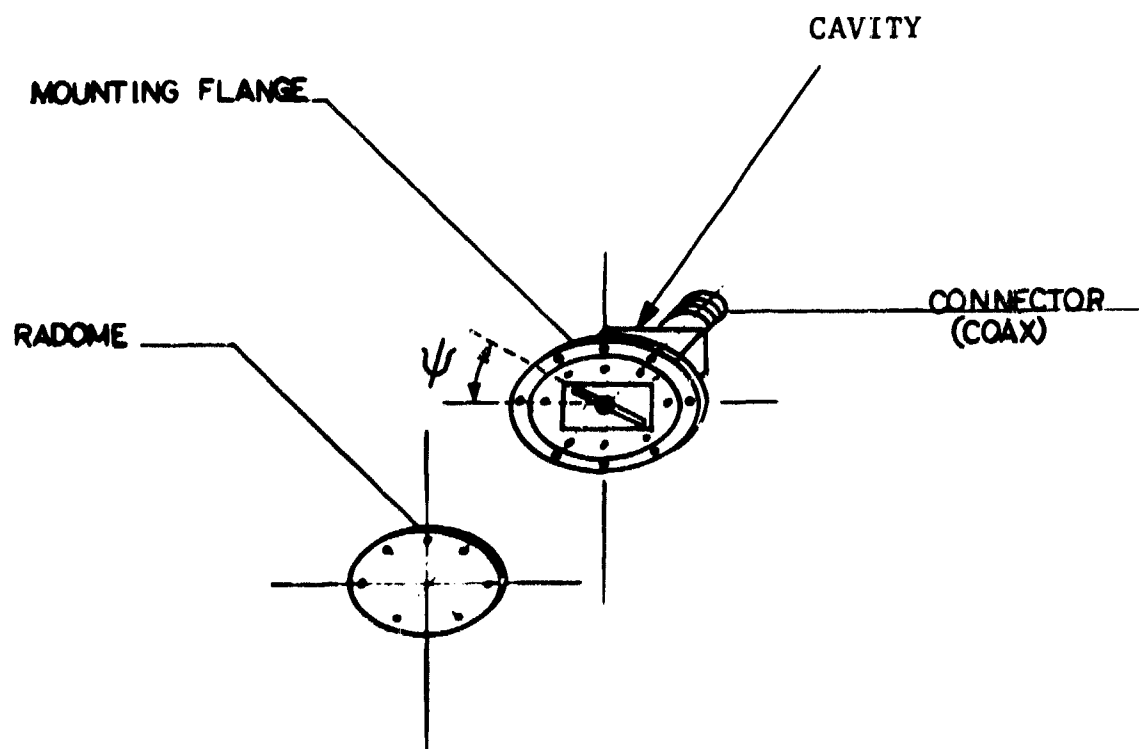


Figure 3. DICO. Antenna Element Description Dipole Slot

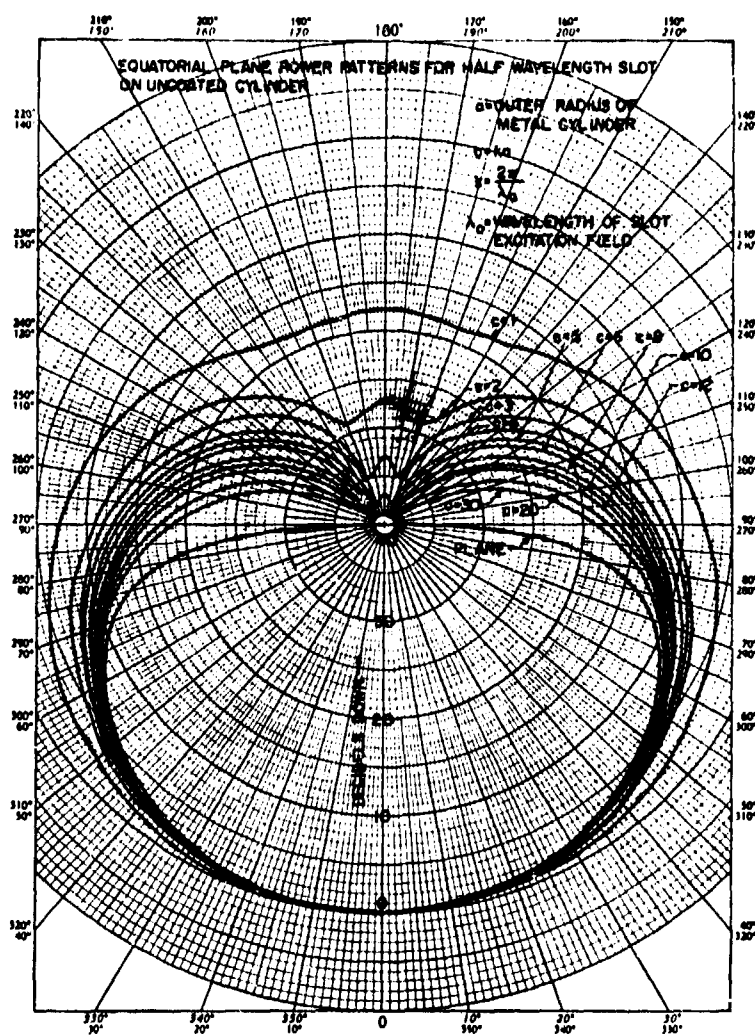


Figure 4. Equatorial Plane Power Patterns

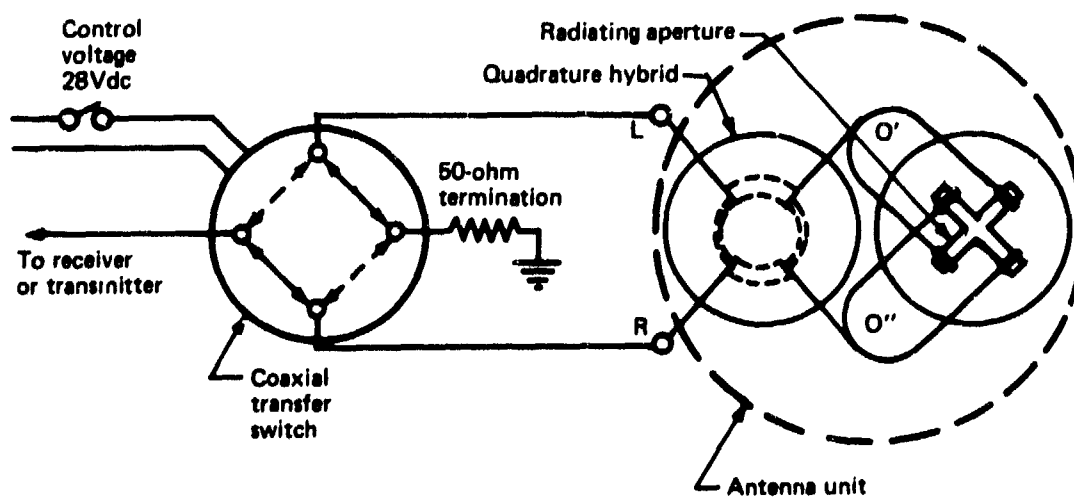


Figure 5. Antenna Feed Network and External Control Circuit

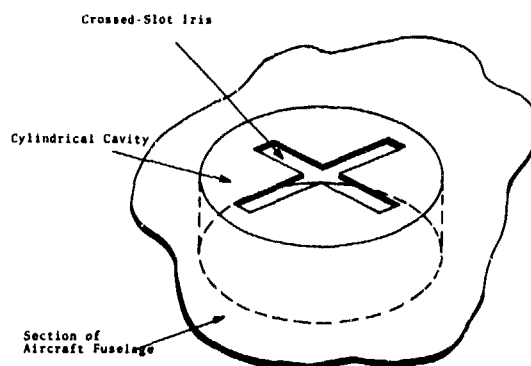


Figure 6. Boeing Cavity-Backed Orthogonal Slots

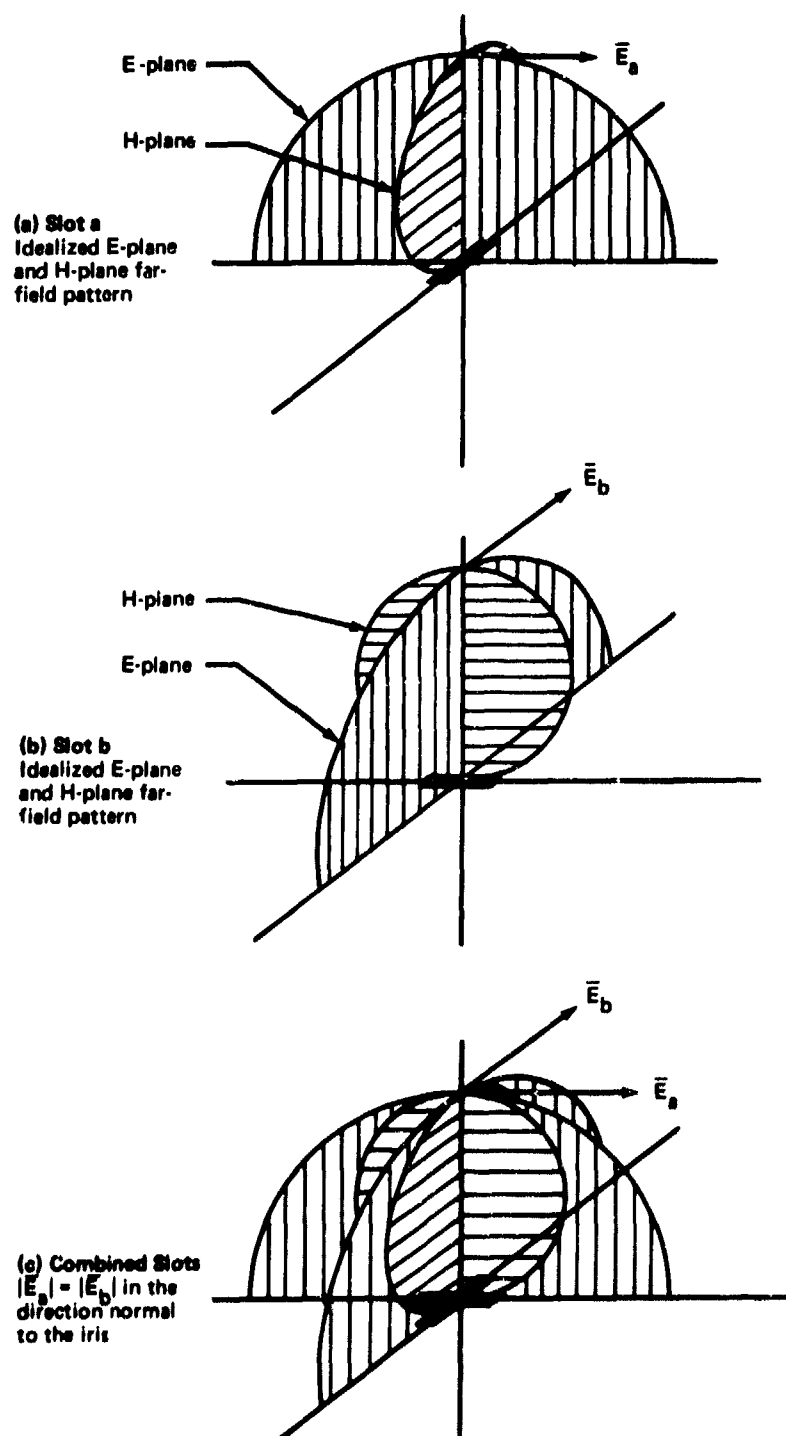
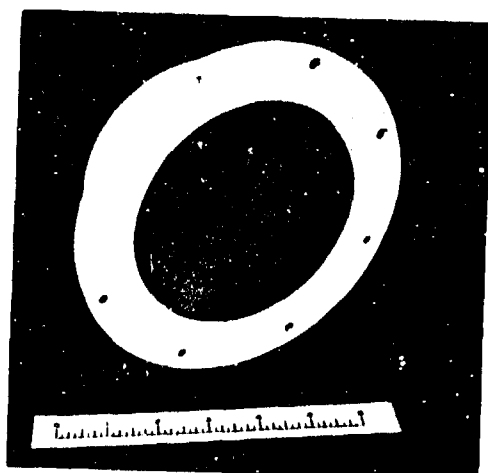
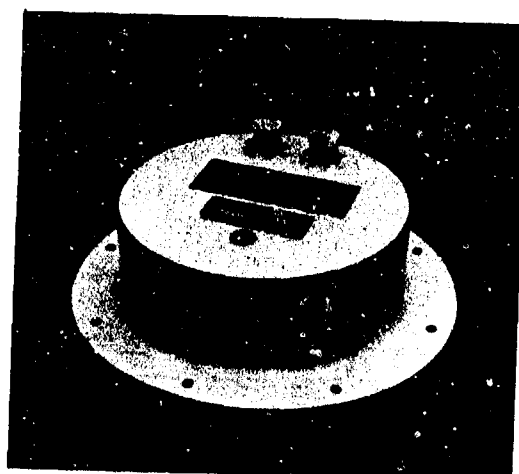


Figure 7. Idealized E-Plane and H-Plane Far-Field Patterns From a Crossed-Slot Iris in a Horizontal Ground Plane

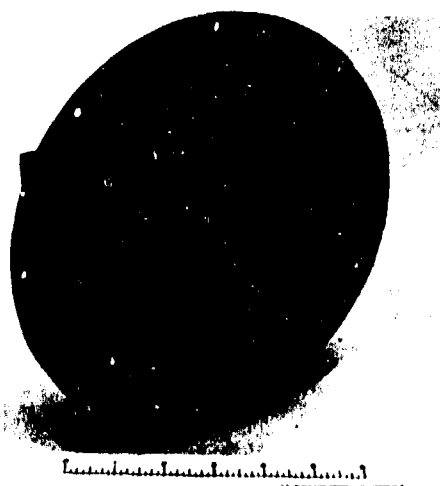


FRONT

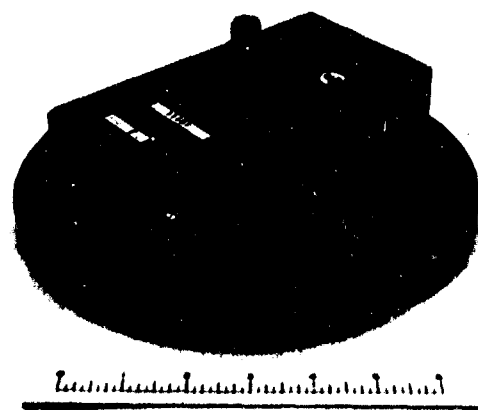


REAR

BOEING



FRONT



REAR

DICO

Figure 8. Full Size Antennas

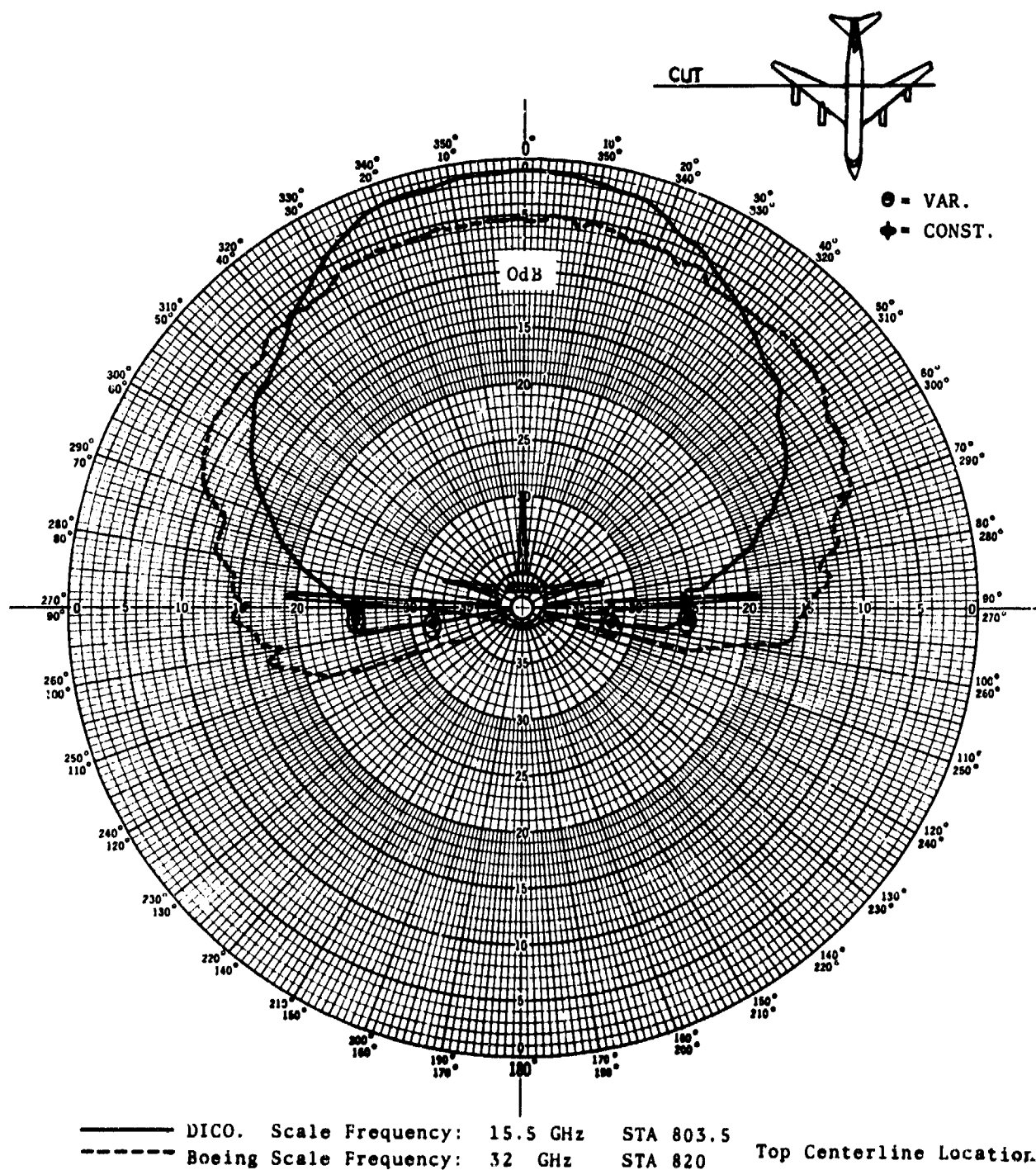


Figure 9. Antenna Roll Plane Patterns

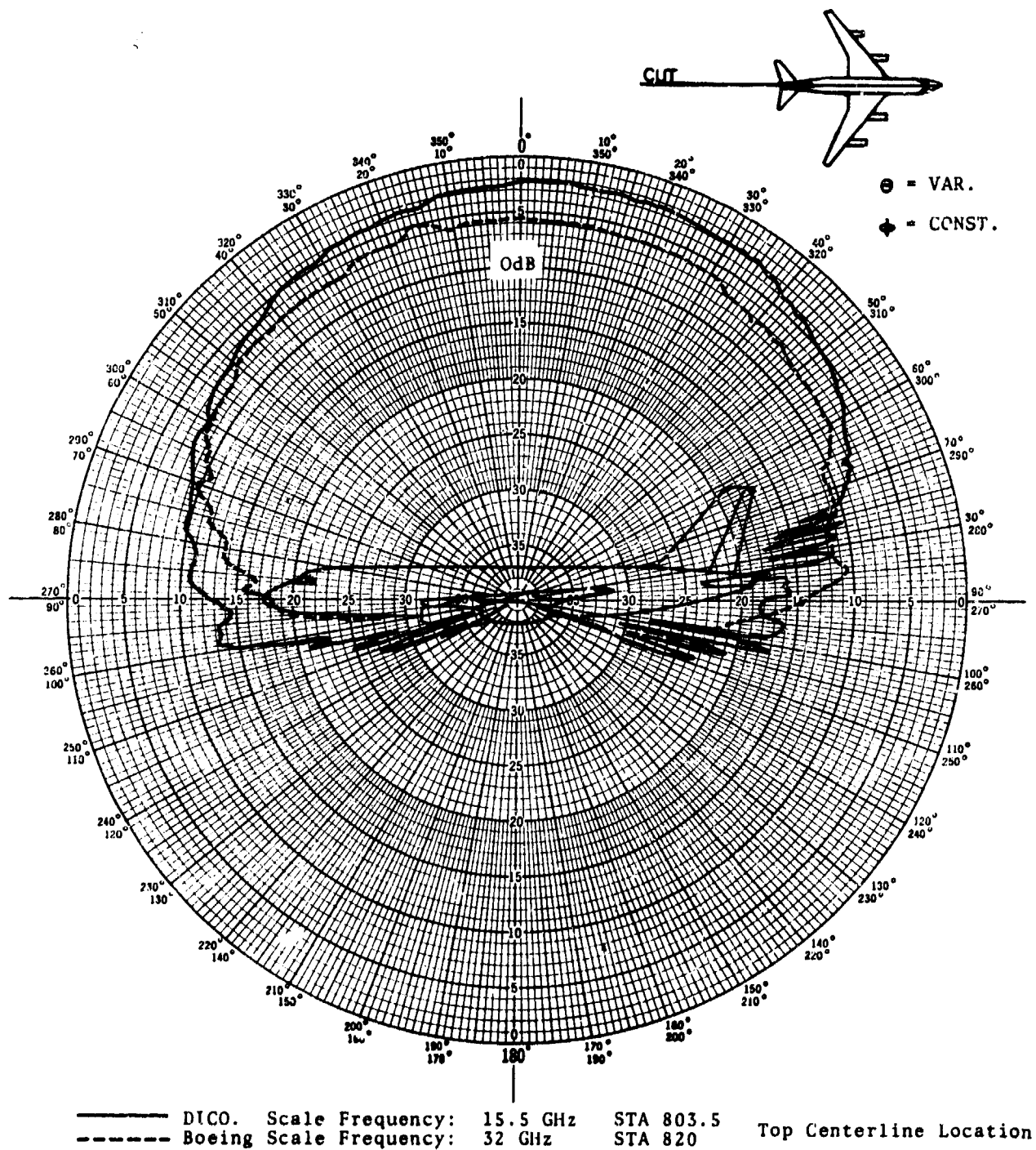


Figure 10. Antenna Pitch Plane Patterns

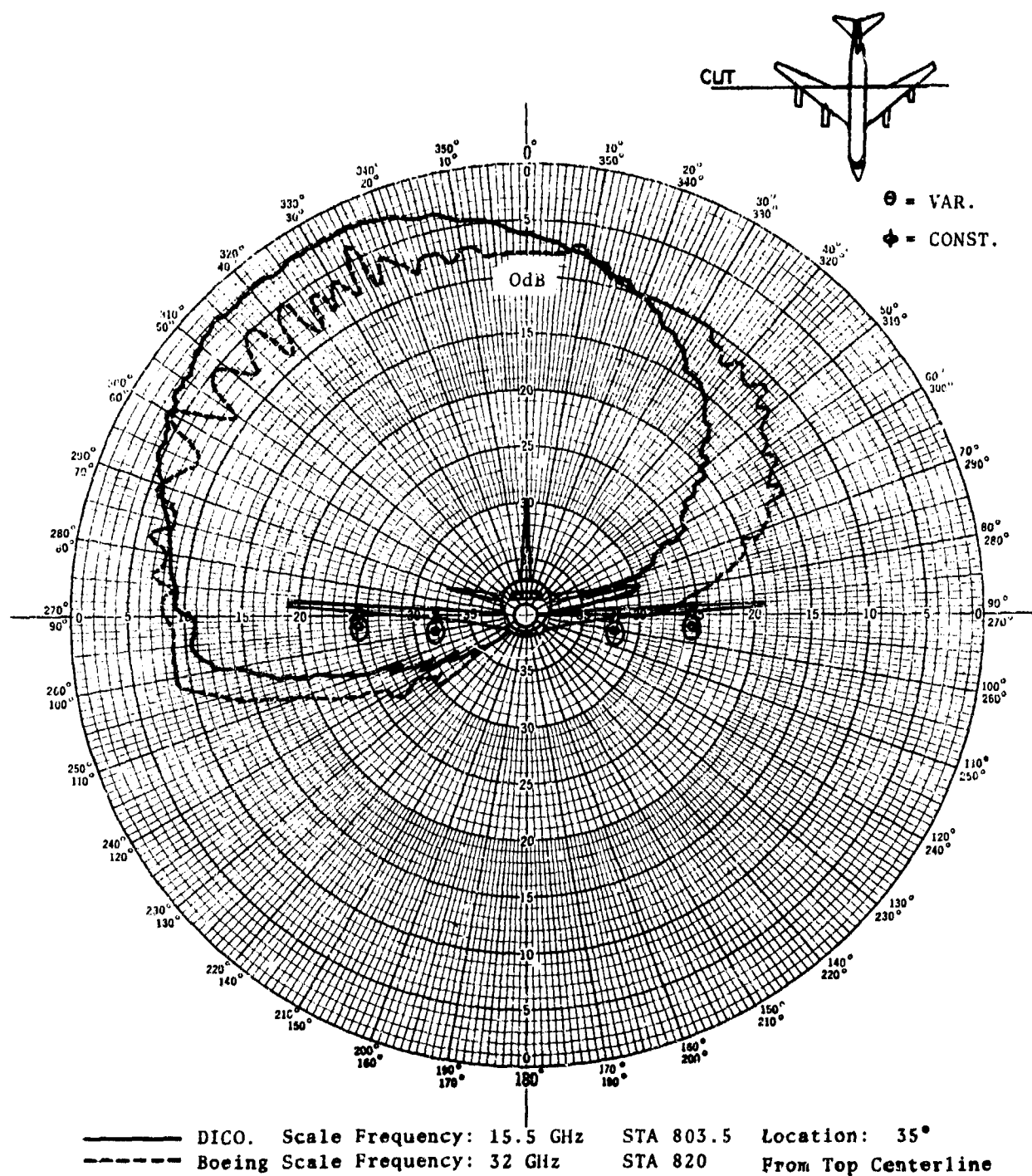


Figure 11. Antenna Roll Plane Patterns

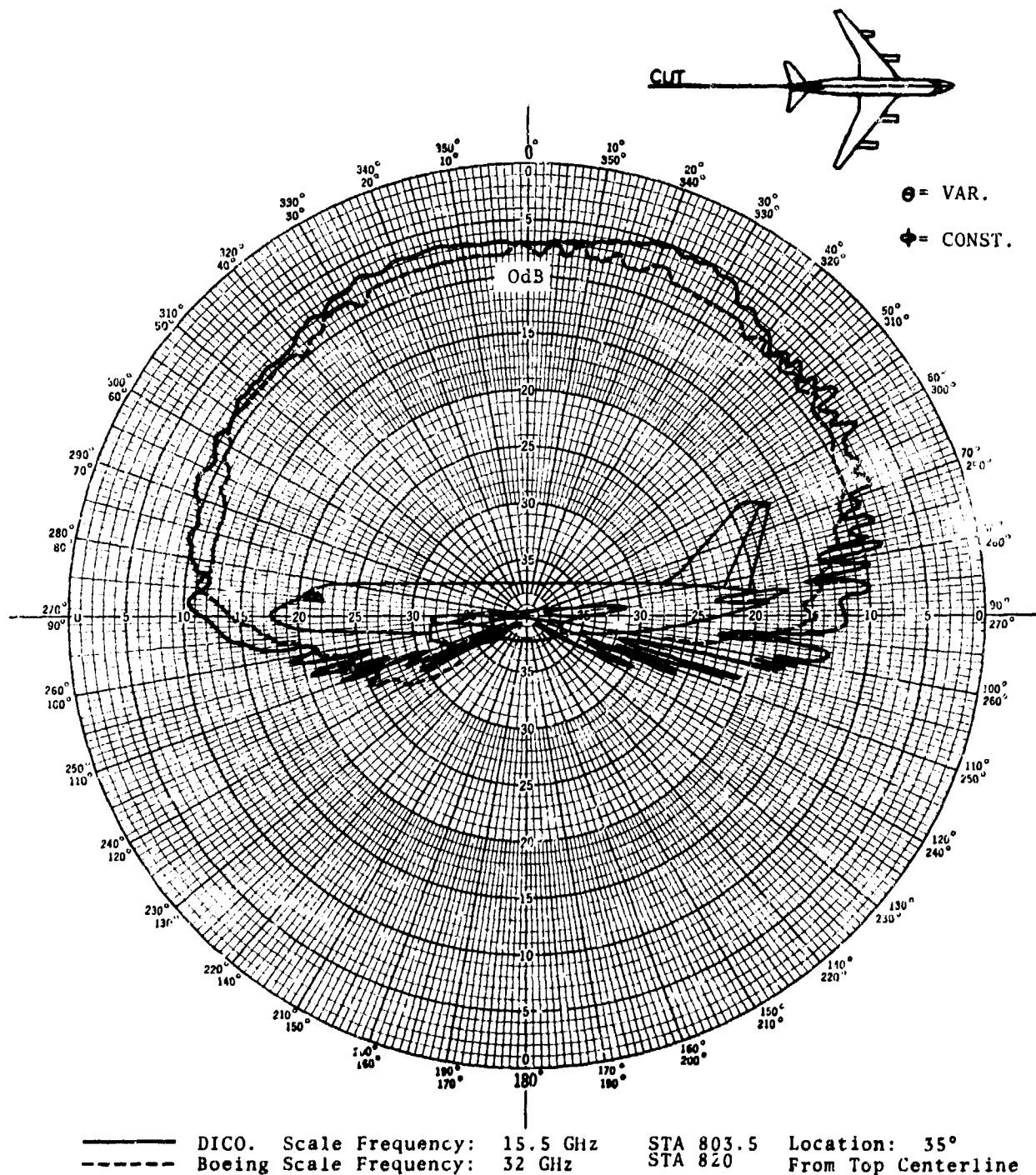
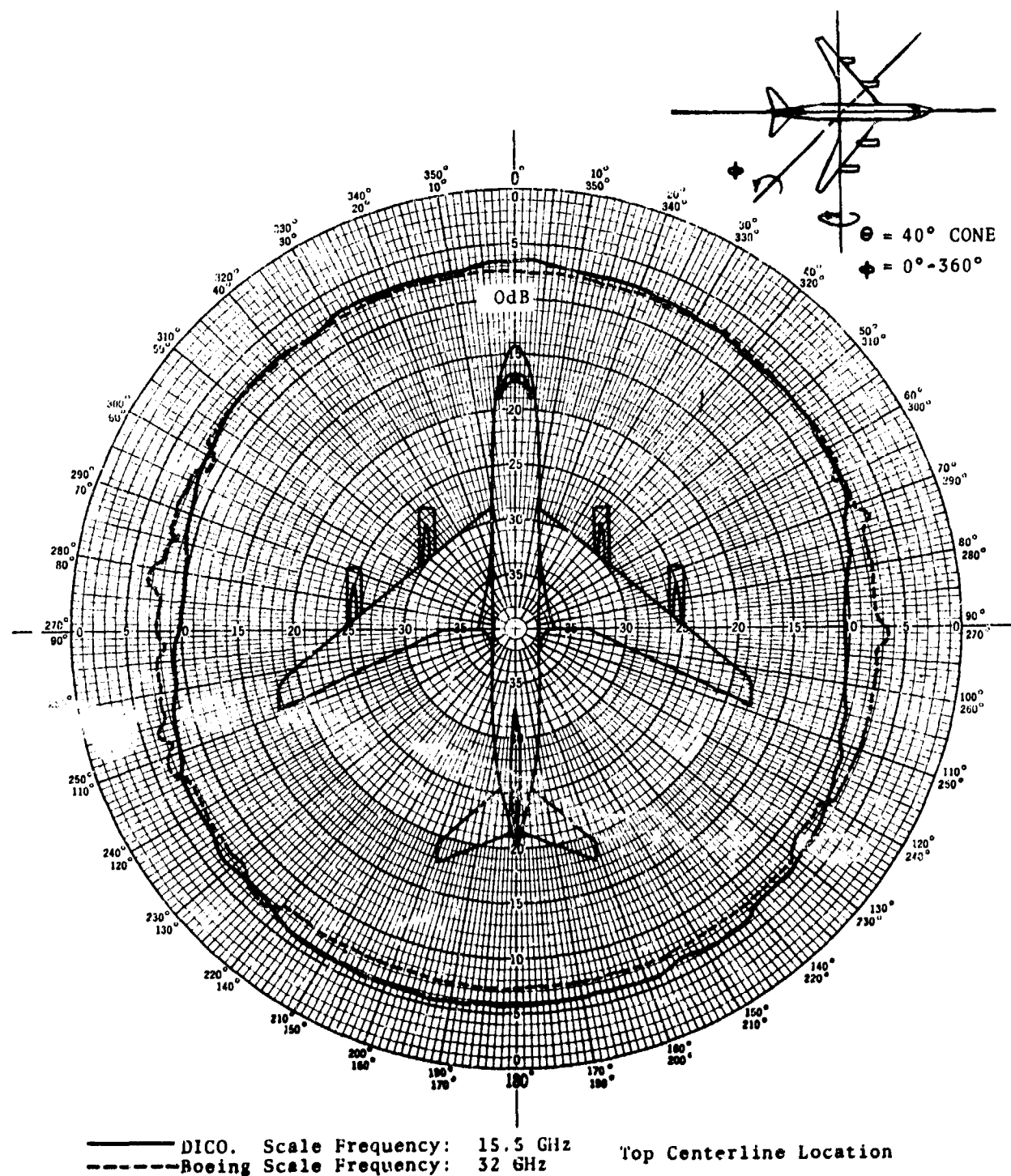
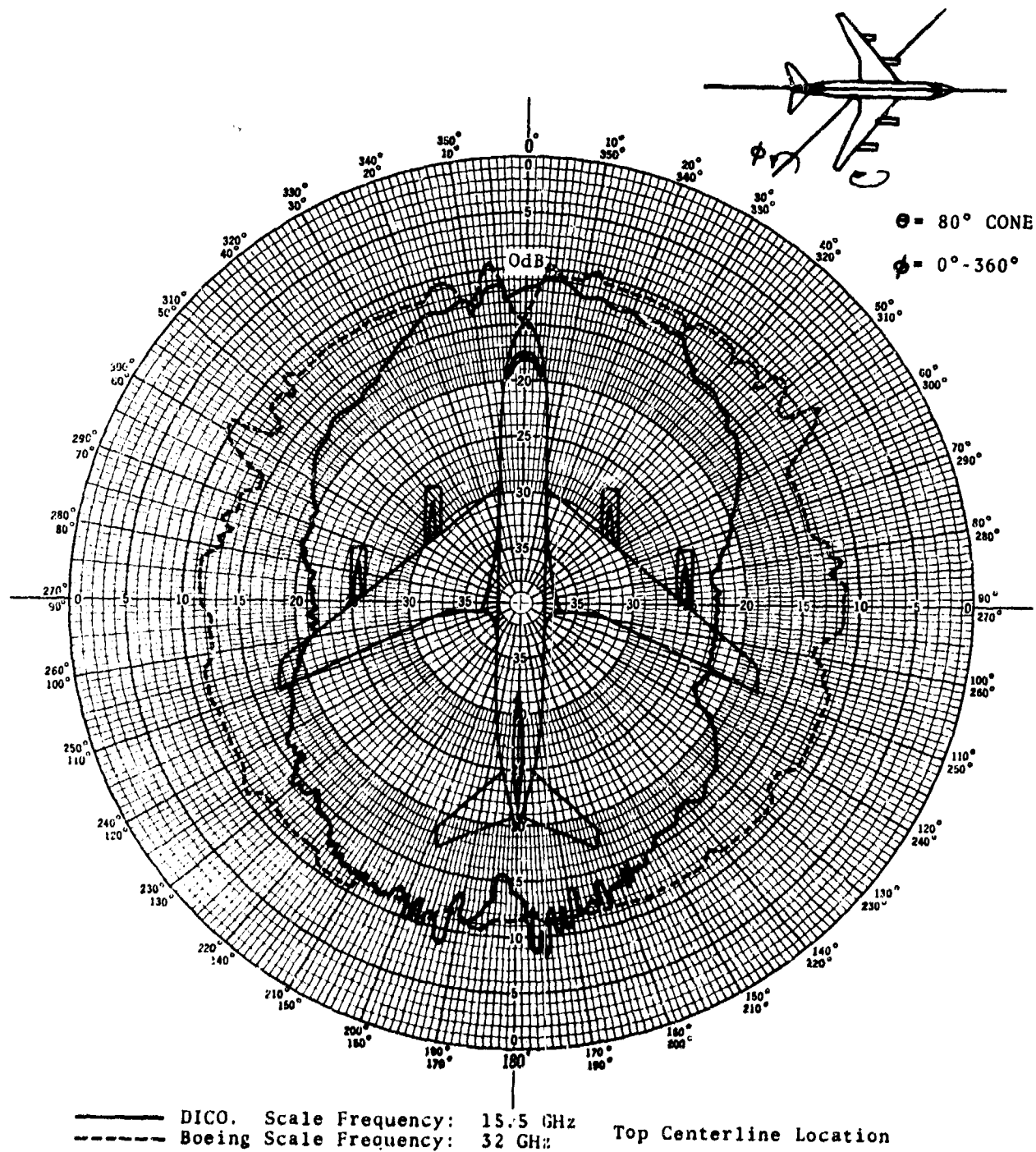
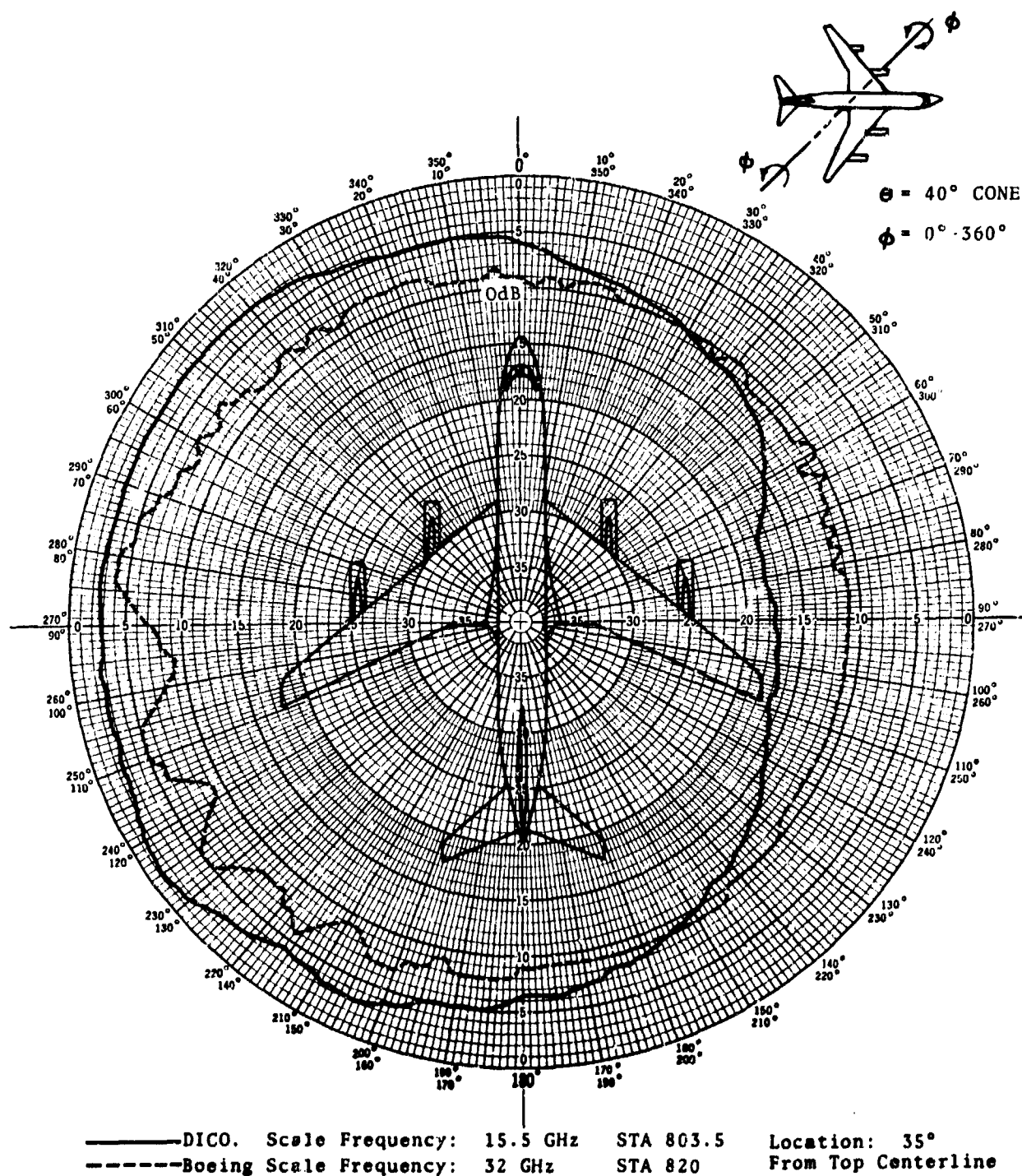
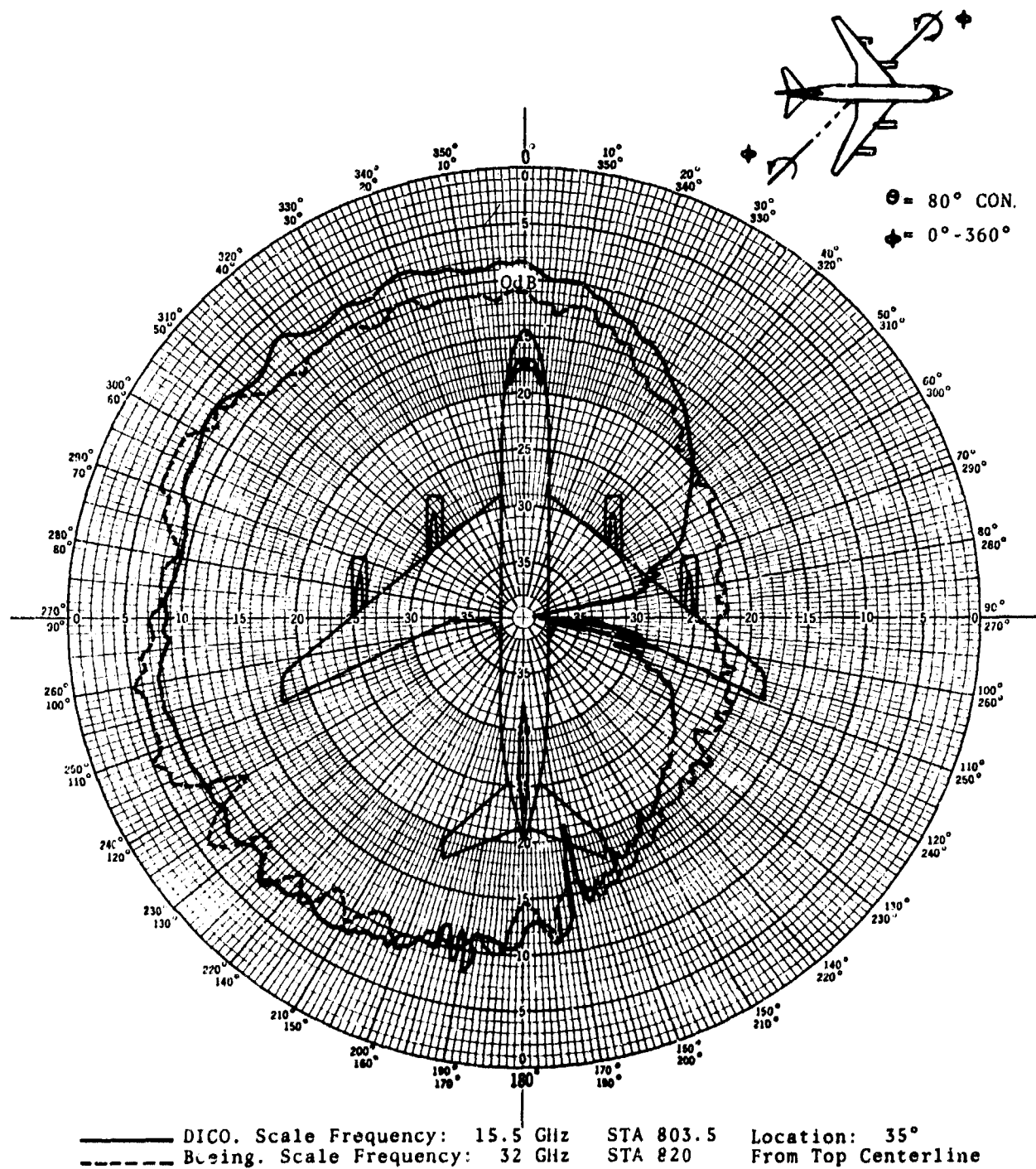


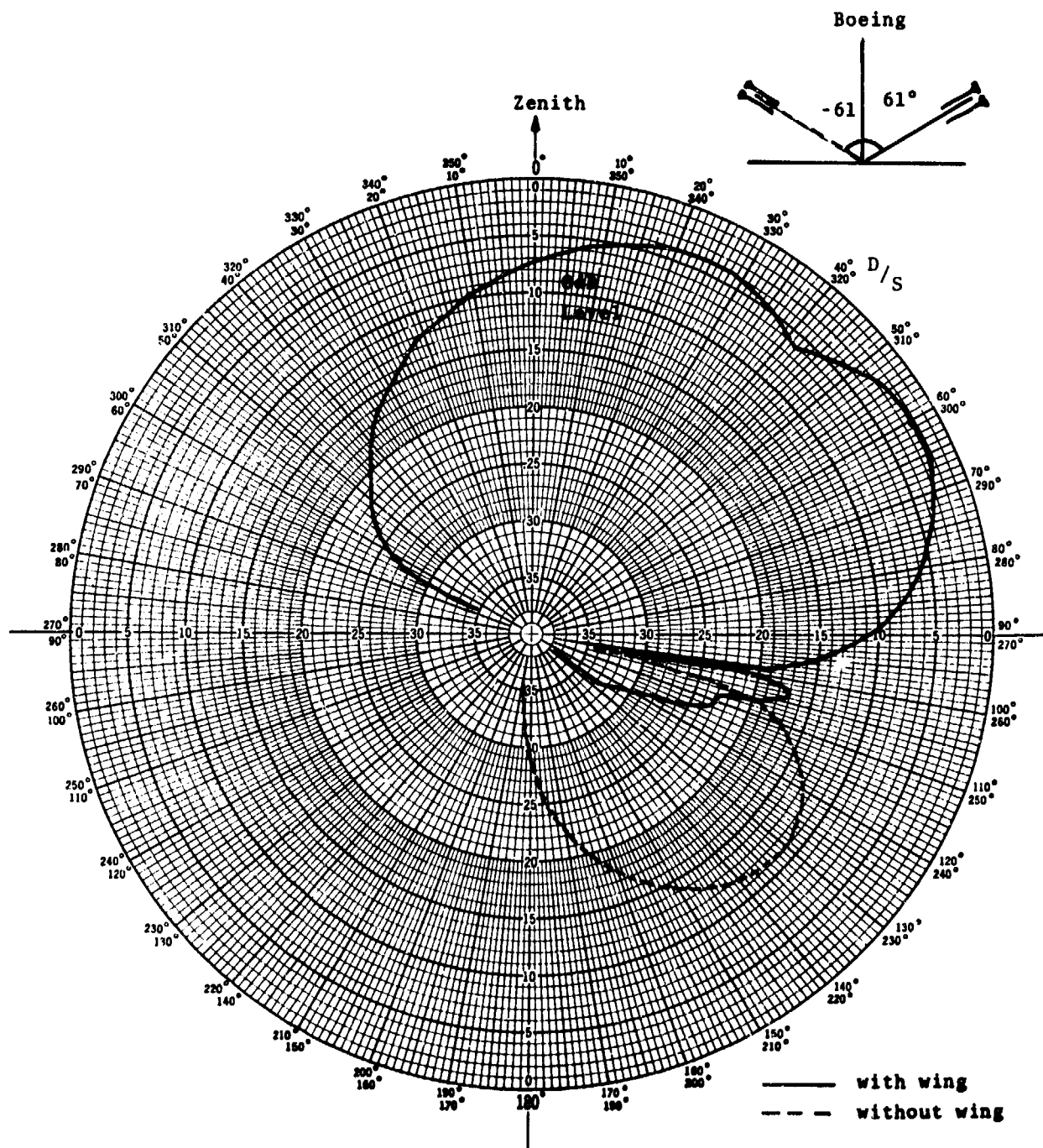
Figure 12. Antenna Pitch Plane Patterns

Figure 13. Antenna Conical Patterns ($\theta=40^\circ$)

Figure 14. Antenna Conical Patterns ($\theta=80^\circ$)

Figure 15. Antenna Conical Patterns ($\theta=40^\circ$)

Figure 16. Antenna Conical Patterns ($\theta=80^\circ$)



ANTENNA. Boeing; 2 element array, $s/\lambda = 0.75$ PATTERN NO:
 POLARIZATION: RH-C, Roll Plane CUT: ϕ $\theta = 0^\circ = \text{zenith}$
 FREQUENCY: 1.6 GHz DATE:
 REMARKS: Array boresight at 61° ;
 sum-difference switch at 41°

Figure 17. Boeing Composite Pattern

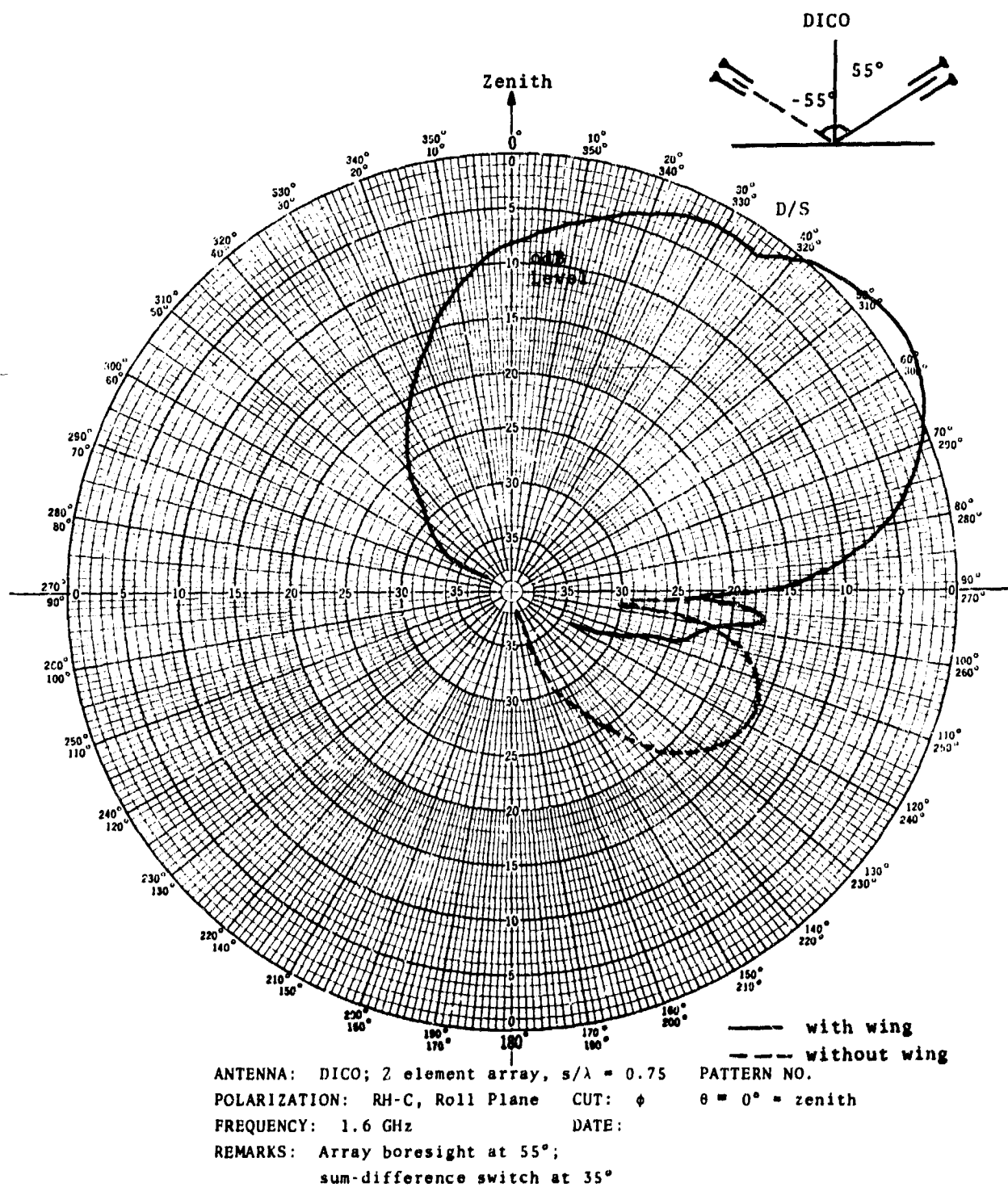


Figure 18. DICO Composite Pattern

DISCUSSION

W T BLACKBAND

The Authors' radiation patterns measured at 15.5 GHz have been of great interest to our antenna team at RAE Farnborough. We have made measurements of a similar system in which a slot-dipole antenna was sited on the shoulder of the fuselage of a Comet aircraft. These measurements were made at 1/10th scale with a working frequency of 15.5 GHz. As a cross check on the measurements made at RAE the radiation patterns were also measured on the MBB test range at Otterburn. The general agreement between the two sets of measurements was very pleasing. Because the geometry of the measurements at RAE was the same as that used by DICO it is possible to make a direct comparison between the two resulting sets of data.

In order to illustrate the comparison the curves of Figures 12 and 15 of the Authors' paper are reproduced here with the RAE data marked on with crosses. As will be seen there is excellent agreement between the positions of the crosses and the solid curve of the DICO results.

It should be noted that for the planes of measurement displayed in Figures 12 and 15 the radiation patterns would be expected to be independent of the wing geometry and for this reason it is not surprising that there is such good agreement between measurements made for a Comet and a Boeing 707. For a measurement plane such as that of Figure 11 for which wing reflections are important, there is good agreement between the DICO and RAE data at angles of elevation above about 10 to 20° but marked differences at lower angles of elevation or depression because of the differences of wing structure of the 2 mode aircraft.

It is pleasing at this Conference where prominence is being given to scale model techniques to see this good correlation between measurements made at sites 6000 miles apart.

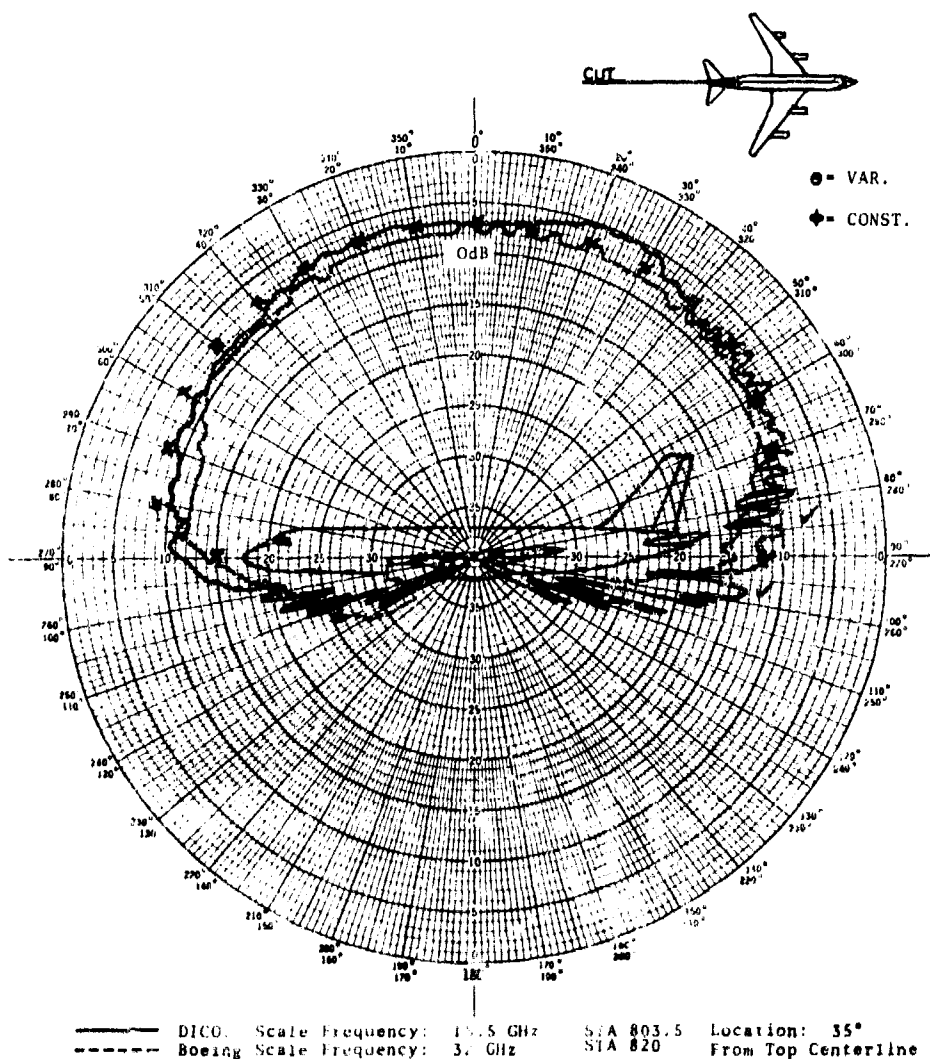
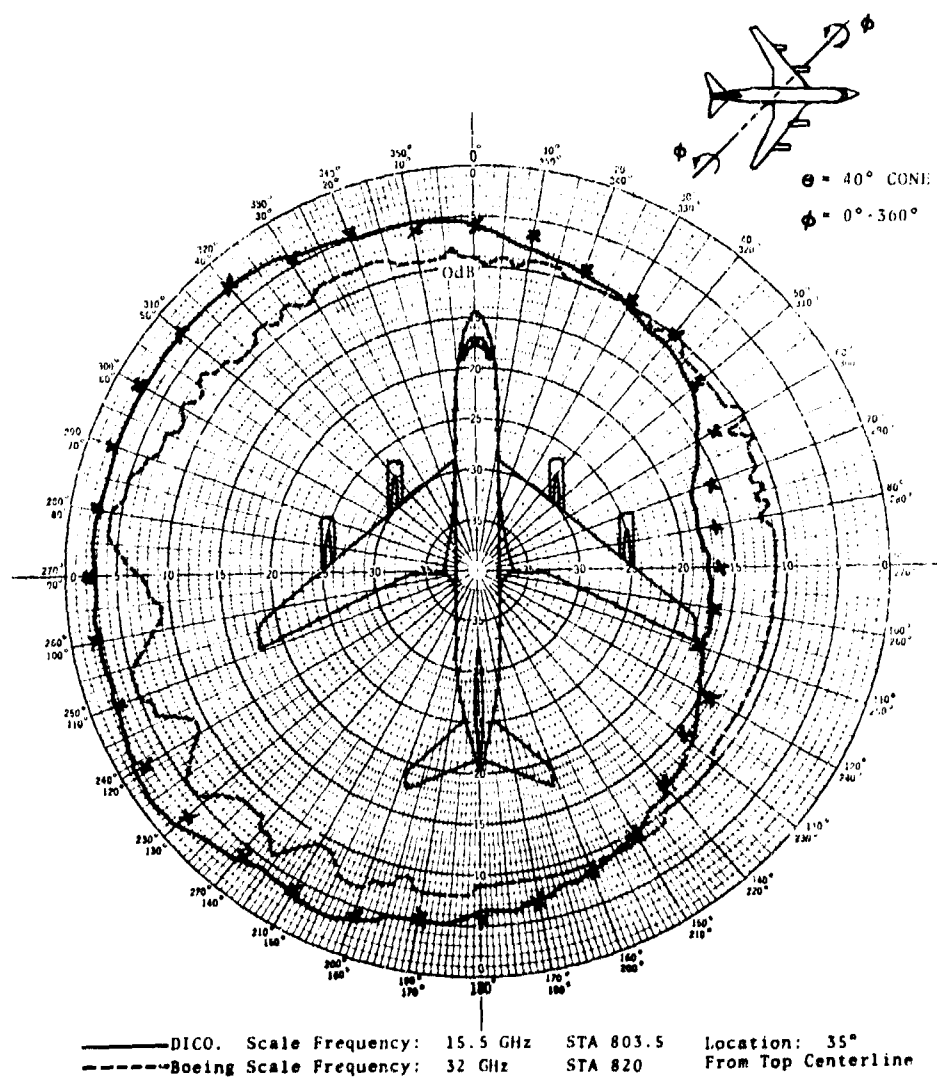


Figure 12. Antenna Pitch Plane Patterns
 with RAE measured data marked by crosses

Figure 15. Antenna Conical Patterns ($\theta=40^\circ$)

with RAE measured data marked by crosses

CIRCULARLY POLARIZED L-BAND PLANAR ARRAY FOR AERONAUTICAL SATELLITE USE

by

Benito Palumbo
Salvatore Cosentino
Antenna Section, R. & D. Division
SELENIA S.p.A.
Rome, Italy

SUMMARY

A circularly polarized L-Band planar array for aeronautical satellite use is presented. A simple trade-off is outlined among the several earth coverage antenna types mainly for what concerns the constraints on weight and size. From this trade-off a planar array, consisting of two interlaced arrays of transverse and longitudinal slots, appears the most attractive solution, mainly if wide operating bandwidths are not required. The design criteria for such an antenna are presented and the principal electrical critical areas together with the main technological and mechanical characteristics are discussed. The main results on an experimental work on transverse slots are reported with their implications on the antenna design criteria. Experimental results (radiation patterns, VSWR) on a breadboard and on the L-band model are presented.

1. INTRODUCTION

Earth coverage antennas for surveillance and communication are normally required for aeronautical satellite use. The allocated frequency band for aeronautical satellite service (1545-1645 MHz) creates some problems for antenna hardware from the point of view of weight, size and stiffness. If we take into account the usual constraints coming from the launchers capabilities and available room under the shrouds, low weight, compact and flat antenna configurations are preferable.

Use of circular polarization is mandatory, due to the variations of the aircraft attitude with respect to the satellite. The requirements on the circularity of the polarization are more stringent at the earth edge, since the aircraft sees the satellite at low elevation angles, where high ellipticity values, normally encountered in aircraft antennas far from the zenithal direction, can cause high polarization losses.

It is well known that the maximum edge gain corresponds to a gain about 4.2 dB below the peak at the edge of the coverage, with a normal gaussian beam shape. Higher minimum gain values can be obtained by means of proper beam shaping, with attendant size and weight increase of the antenna. The normal -3 dB beamwidth for an earth coverage antenna on board of a geostationary satellite is then 14.8°.

Many antenna configurations can be envisaged for obtaining an earth coverage beam. We can disregard solutions utilizing horns (in all possible geometries), lenses (constrained, artificial dielectric) mainly in view of weight and size problems.

A trade-off between reflector systems and arrays of low or medium gain radiating elements shows an higher merit figure for the latter. Arrays of crossed dipoles, spirals, helices require power dividing networks that are generally lossy and decrease the overall antenna efficiency. Waveguide fed slot arrays appear a better solution, mainly if wide operating bandwidths are not required. Preference is given to resonant type arrays, where the slots are spaced by an integer number of half guide wavelengths with an end short circuit.

Non resonant type arrays with an end load would decrease unacceptably the antenna efficiency, if we consider the limited number of slots of an earth coverage array.

2. GENERAL REMARKS

A planar array antenna appears a very attractive solution for the earth coverage antenna. Waveguide fed slot arrays have generally higher efficiencies. Circularly polarized slot arrays have been previously described (1).

An alternative approach is to make use of polarization converters in form of grids or printed circuits in front of a linearly polarized slot array. A dual frequency, opposite sense circularly polarized slot array has been also developed as a radiating element for a circular array (2). The use of broadwall transverse and longitudinal slots, fed by a common waveguide, to generate the circular polarization, when displaced by a quarter of guide wavelength, presents some problems. They are due mainly to the transverse slots that have to be spaced by a guide wavelength in order that the slot of the array radiate in phase. Use of guide loading (dielectric or corrugated surface of the waveguide bottom broad wall) is then required.

Besides, the radiated power from the slots is controlled with the displacement from the centre line of the broad wall of the feeding waveguide and the transverse slot in the displaced condition can extend beyond the broad wall edge, along the narrow guide wall. The arrangement of transverse and longitudinal slot arrays, to form two - dimensional arrays, becomes very difficult to be realized. A feeding technique of an array of waveguide fed, broad wall, longitudinal slot arrays with the removal of the contiguous separating guide narrow walls has been presented in (3). The slots are excited by an equivalent waveguide operating in the higher order mode TE_{no} , where n indicates the number of the equivalent virtual contiguous waveguides. The above described technique implies an alternate out-of-phase feeding of the contiguous virtual waveguides. In phase excitation of half-waveguide spaced transverse slots can be then obtained by feeding them alternately from two adjacent waveguides. In order to obtain the correct length for the required resistance and reactance values, part of the transverse slot can be extended over the broad wall of the adjacent waveguide. This affects the impedance characteristics of the slot. The effect can also be represented as an excitation from a waveguide operating in the TE_{20} mode, with the transverse slot displaced from the centre line of the broad wall of the equivalent waveguide. The above interpretation was reported in (4) for a possible improved version of the Surveyor antenna. Recently radiating properties of half-wave slots in a rectangular guide operating in the fundamental and TE_{20} modes have been reported (5).

The antenna consists therefore of two interlaced resonant arrays of longitudinal and transverse slots for the two orthogonal linear components of the circular polarization. The required 90° relative phase shift results from the one quarter wavelength spacing in the feeding waveguide. The above condition is met if the slots of the two types are resonant (about half wavelength) or if one set of the two is sufficiently far from the resonance conditions. It appears more convenient in the latter case to use non resonant transverse slots, by considering their flat behaviour of the resistance with the length (6). The longitudinal and transverse slots are cut on the broad wall of a rectangular waveguide, where a higher order mode TE_{no} propagates. It can be thought as consisting of n virtual waveguides, operating on the TE_{10} mode, side by side, with the common narrow walls removed.

The power dividing network for feeding the adjacent virtual waveguides can be of any type, provided they are alternately fed with 180° phase shift and proper power distribution. The corporate feeding network is a good solution; a more compact and efficient system consists of a main waveguide, slot coupled with the virtual waveguides carrying the radiating slots and orthogonal to the main waveguide. From the mechanical and electrical point of view the best coupling system appears to be that one consisting of longitudinal slots on the broad wall of the main guide, radiating into the region between the top and bottom plates of the waveguide with the radiating slots.

Each of the two above mentioned interlaced arrays is of resonant type, that is the radiating elements are fed in phase. Let us consider first the array of longitudinal slots that generate one of the two linear orthogonal components of the circular polarization. It consists of an array of arrays of slots on the broad walls of the virtual waveguides, where the in-phase excitation is obtained by means of half guide wavelength spacing between the slots and by alternating the sense of the slot displacement with respect to the virtual waveguide broad wall center line. If the half guide wavelength is sufficiently lower than the free space wavelength, grating lobes are not allowed. The slots are of resonant length and therefore equivalent to pure shunt resistance in the waveguide equivalent transmission line. A short circuit is positioned at a quarter guide-wavelength from the last longitudinal slot center according to the common resonant array technique (7)(8). The slots amplitude excitation is controlled by means of the displacement from the broad wall center line.

The transverse slot array generates the linear component orthogonal to that of the longitudinal slot array. Most of the above discussed considerations also apply, with the following differences:

- 1) the resonant transverse slot is equivalent to a pure series resistance
- 2) the end short circuit is positioned at a half guide-wavelength from the last transverse slot
- 3) no phase inversion is obtained by reversing the sense of displacement of the slot from the center line of the broad wall of each virtual waveguide.

In phase radiation from successive transverse slots, spaced by half guide wavelength to avoid grating lobes, can be obtained by feeding them alternately from adjacent virtual waveguides, that are themselves fed in antiphase. It is the same to say that the in-phase excitation is obtained by reversing the sense of slot displacement from the virtual common wall of adjacent waveguides and by spacing the slots by half guide wavelength.

An explanatory scheme of the basic concept of the antenna is shown in fig. 2.1.

3. DESIGN CRITERIA

3.1. General

Following the concepts presented in the preceeding paragraphs, the main design criteria for an aeronautical satellite, earth coverage antenna are below indicated:

- Good circularity of the polarization, with particularly stringent requirements at the earth coverage edge. A goal value of 2,5 dB maximum ellipticity at the edge is assumed.
- Gain level of 4,2 dB below the peak-at the edge of coverage, according to the optimum gain conditions, for normal gaussian beam shape.
- Minimum efficiency loss of the antenna system, by taking into account mechanical and thermal constraints.

With uniform illumination distribution on a linear or square array, the beamwidth values change with discrete steps by changing the slot number, at fixed spacing value. For a given beamwidth, the minimum number of slots is found where, decreasing the slot number, a beamwidth value equal or less than required is first obtained. If necessary, the correct beamwidth is then obtained by introducing a proper tapering in the illumination distribution. However, due to the chosen interlaced configuration of the two arrays in the plane parallel to the main feeding guide axis the longitudinal slot array consists of one equivalent linear array more than the number of the equivalent arrays of transverse slot. In the plane orthogonal to the main feeding waveguide axis, the phase center coincidence between the two arrays requires again that the number of longitudinal and transverse slots differ by one. Therefore the condition of minimum number of slots cannot be met in any of the two principal planes simultaneously for both the interlaced arrays. Compromise solutions must then be found. Equispacing of the slot centers along the two principal axes of the square grid, representing the planar array, minimizes the slot number, if beamwidth equalization in each plane and for each polarization is desired. The half waveguide spacing between successive slots in the virtual waveguide implies the following equation, where a is the virtual waveguide width and λ is the operating wavelength:

$$(3.1) \quad a = \frac{\lambda}{2 \sqrt{1 - \left(\frac{\lambda}{2a}\right)^2}}$$

With the chosen configuration and if the displacements from the center line are neglected in a first approximation, the minimum number of slots for a required beamwidth corresponds to

$$a = \frac{\lambda}{\sqrt{2}}$$

In this condition the slot spacings in the two principal planes are the same.

If constraints on the array size require that the number of slots along one or both the principal directions be less than the minimum required for the given beamwidth, square grid configuration of the slot array gives the minimum beamwidth spread. This is clearly shown in fig. 3.I, where the -3 db beamwidth variation for the two orthogonal linear polarizations in the principal planes is plotted in terms of spacing between the slots for a planar array with 4x6 transverse and 5x5 longitudinal slots.

It must be evidenced that the element factor plays a negligible role in determining the array -3 db beamwidth, for typical values of about 15°, as in the case of earth coverage from a geostationary orbit.

3.2. Longitudinal slot array

From the above considerations it turns out that the optimum configuration consists of 5x5 slot array, spaced by $\frac{\lambda}{\sqrt{2}}$ in the the two principal directions of the grid and excited with uniform amplitude and phase.

Use of reduced height waveguide is advisable in view of the smaller required displacements from the centre line of the broad wall of the virtual waveguide. The reduced height configuration is convenient also for the transverse slot array, where unacceptable slot overlapping and limited displacement are conflicting requirements that in our case find a compromise solution with half height feeding waveguide.

The longitudinal slots are resonant and their length is therefore approximately one half wavelength, with no dielectric loading of the exciting waveguide. They can be represented at the resonance as pure conductances in parallel to the feeding waveguide. Since the design of the longitudinal slot array must be performed in connection with that of the transverse slot array, the evaluation of the conductance distribution is presented together with the design of the interlaced array of transverse slots.

3.3. Transverse slot array

With reference to the choice of the longitudinal slot array two possible solutions can be envisaged for the interlaced array of transverse slots:

Solution A: $N-1$ slots in the direction parallel to the power dividing waveguide axis. This value is imposed by the antenna structure.

$N-1$ slots in the direction orthogonal to the above mentioned axis.

Solution B: $N-1$ slots in the direction parallel to the power dividing waveguide axis.

$N+1$ slots in the direction orthogonal to the above axis.

Both solutions meet the requirement that the two arrays have the same phase center. The solution B is preferable, since it allows to play with the distribution tapering to minimize the gain level difference between the two orthogonal linear polarizations and therefore the ellipticity at the edge of the coverage. The transverse slot array consists then of 4×6 slots fed in phase, but with proper amplitude distribution.

The determination of the proper taper, and therefore of the slot excitation coefficients, comes out from the beamwidth requirements.

In order to evaluate the resistances and conductances values, the following assumptions have to be made:

- 1) The sum of the power radiated by longitudinal and transverse slots of each virtual waveguide must be equal to the power entering into it,
- 2) The total power radiated by the longitudinal slots must be equal to the power radiated by the transverse ones,
- 3) The distribution of the resistance values of the transverse slot must correspond to same internal ratios calculated according to the required taper.

These assumptions allow to calculate the required set of resistance and conductance values. Moreover, it has to be pointed out that the transverse slots contribution in the external virtual waveguides is different from that relative to the inner waveguides. The first of the above indicated assumptions, which is a matching condition, leads to conductance values for the longitudinal slots in the external waveguides different from those in the internal ones. This means a slight deviation from the uniform amplitude distribution with some inverse taper. However the effects on the beam shape and the sidelobe level are still acceptable.

3.4. Feeding system

It consists of a resonant array of five slots cut on the broad wall of a rectangular waveguide operating in the fundamental mode.

The usual design criteria can be used for this array (8). It has to be pointed out that in this case the slots do not radiate in the free space but between two metallic planes. The conductance values are quite different from those relative to the condition of radiation in the free space.

However this effect can be properly taken into account (8).

3.5. Conductances and resistances practical realization

One of the most important problems in the design of the above described antenna is the evaluation and the practical realization of the proper conductance and resistance values of the slots and the determination of their resonant length.

The longitudinal slots can be thought cut on the broad wall of a waveguide operating in the fundamental mode, and a lot of theoretical and experimental data of conductance and resonant length are available (6).

The transverse slots in this application are in a new configuration, as they are extending partially on to the broad wall of the contiguous equivalent waveguide excited out of phase. In order to evaluate this effect it has been necessary to carry out a set of measurements on transverse slots on the broad wall of a waveguide operating in the TE_{20} mode. The results of these measurements are synthesized in the curves of Figg. 3-II, 3-III, 3-IV.

From the fig. 3-II one can obtain the resonant length as a function of the λ/λ_0 value of interest.

The fig. 3-III represents a characteristic curve from which one can derive the proper displacement value in order to have the required resistances values. The last curve (see fig. 3-IV) shows the dependence of the resonant length from the slot displacement.

4. RESISTANCE AND RESONANT FREQUENCY TESTS ON TRANSVERSE SLOTS

From the measurement of the reflection coefficient, the values of the normalized resistance and the resonant frequency of the transverse slots can be evaluated. The test have been performed by making use of the HP Network analyzer 8410-A in the configuration shown in fig. 4-I. At the end of the reference and test channels two identical sections of waveguide, terminated by sliding short circuits are connected to a folded magic-T, fed at the H input in order to excite the TE_{20} mode. The transverse slot under test is cut on the broad wall of the waveguide at the end of the test channel. The whole broad wall is removable and many values of slot lengths and displacements from the centre line can be examined. At each frequency the sliding short circuit is at half guide wavelength from the slot center, so that the equivalent transmission line can be considered as terminated only by the slot impedance.

The reference channel short circuit is in the same position of that in the test channel, so that the two channels can be considered identical when the slot is covered and doesn't radiate. The similarity of the two channels is verified during the calibration.

The network analyzer 8410-A is equipped with a phase gain indicator 8413-A which gives modulus and phase of the reflection coefficient. With the slot in the radiating condition, the reflection coefficient of the test channel changes, as measured at the H input of the folded magic-T. The frequency is changed, with the short circuit at one half guide wavelength from the center of the slot under test. The resonant frequency of the slot is found when there is no change of the phase ϕ of the reflection coefficient $\Gamma = |\Gamma| e^{j\phi}$ measured at the input of the test channel with the slot radiating and not radiating. This indicates that the slot impedance is purely resistive and therefore the slot is of resonant length. From the amplitude $|\Gamma|$ of the reflection coefficient the normalized resistance value r is found by the following equation ($r < 1$)

$$(4.1) \quad r = \frac{1 - |\Gamma|^2}{1 + |\Gamma|^2}$$

5. EXPERIMENTAL RESULTS

5.1. C-band breadboard.

A C-band model has been designed according to the above described design criteria. A photograph of the model is shown in fig. 5-I. The preliminary results on the model, where both transverse and longitudinal slots were of resonant length, showed that the mutual coupling effects were extremely important and deteriorated unacceptably the performances of the antenna. A study revealed that the negative effects were less and less relevant, when the transverse slot were brought out of resonance. It was decided to make use of not resonant transverse slot array, by taking advantage of the flat behaviour of the resistance with the slot length. The length was made sufficiently shorter than the resonant value, so that the reactive component of the slot impedance was near to zero and the insertion phase very small. The required 90° phase difference between the two linear components relative to the two interlaced arrays is so obtained. It must also be pointed out that a residual reactive component of the transverse slot impedance is useful to compensate the mutual coupling effects. Antenna VSWR and radiation patterns have been measured. It has been found that the antenna performances is good over a bandwidth wider than 2%. The input VSWR and radiation patterns, taken with a spinning linear source in the two principal planes, at the centre frequency, are shown in fig. 5-II. The radiation patterns in the two linear polarizations are superimposed over the ellipticity pattern. Separate contributions to the phase and amplitude errors of the circular polarization from the two interlaced arrays, linearly polarized, can be deducted.

An old X-band model built not in view of the use for the aeronautical satellite is shown in fig. 5-III. It had been realized mainly with the purpose of checking the feasibility of such a type of planar array some years ago.

5.3. L-band model.

A feasibility study of an aeronautical satellite earth coverage antenna has been undertaken in the frame of the work developed by the "Cosmos" Consortium of european aerospace industries, led for the Aerosat program by MBE, under an ESTEC contract. An L-band prototype has been developed to demonstrate the capabilities of the planar array antenna type for the aeronautical satellite use. The L-band model is not exactly scaled from the above described C-band breadboard, but it has been designed according to the outlined design criteria and the experimental results at C-band. The L-band prototype has not been fully optimized and further improvements in its performance can be expected.

The lightweight characteristics have been obtained by making use of a magnesium alloy power dividing waveguide and a paper nylon honeycomb structure with aluminum skins for the higher mode waveguide. The influence of the dielectric honeycomb structure can be taken into account and some data are available in the technical literature (10). The honeycomb electrical characteristics have been measured and the effect of the honeycomb on the transverse slot resistance and resonant length

has been experimentally verified during the program of measurements of the slot impedances. The VSWR results and typical measured radiation patterns in the two principal planes are shown in fig. 5-IV. The tests carried over a 2% relative frequency band have showed good electrical characteristics of the antenna. The performances do not deteriorate rapidly outside the above indicated band, but a graceful degradation of the ellipticity and gain over the earth coverage angular sector has been found. The minimum ellipticity characteristics of the antenna at the edge of the coverage are clearly evidenced.

A photograph of the array is shown in fig. 5-V.

6. CONCLUSIONS

The design criteria and the characteristics of a planar array for aeronautical satellite use have been shown. It appears that the solution of interlaced longitudinal and transverse slot arrays is attractive, if a lightweight, and compact structure has to be associated to good electrical characteristics. The intrinsic flexibility of the slot array design allows a solution tailored to the specific requirements. On the other hand the narrow operating bandwidth, decreasing with the increase of the number of the slots, and the discrete size variations, when the aperture has to be changed, have to be considered limitations in the use of the described array type.

REFERENCES

- (1) A. F. Seaton, G. A. Carnegis : "A novel polarized planar array for Surveyor".
IEEE Int. Conv. Rec. 1963 pt. 1, p. 2
- (2) B. Palumbo : "Dual polarized two-frequency slot array for a satellite electronically despun antenna".
European Microwave Conference, Sept. 1969
- (3) G. C. Mc Cormick : "A two-dimensional slotted array".
IRE Trans. on Ant. and Prop., Jan. 1958, pp. 26-39
- (4) -- : "Improved planar array beats Surveyor antenna in simplicity and cost".
Communications Designer's Digest, Feb. 70, p. 14
- (5) W. H. Kummer : "The properties of half-wave slots in two-mode rectangular waveguide".
IEEE Trans. A. P., March 1973 - pp. 202-206
- (6) Arthur A. Oliner : "The impedance properties of narrow radiating slots in the broad face of rectangular waveguide".
IRE Trans. on Ant. and Prop., Jan 1967 pp. 1 - 20
- (7) S. Silver : "Microwave Antenna Theory and Design".
Mc-Graw Hill Book Comp. Inc. 1949 - pp. 313-316
- (8) R.E. Collin - Zucker : "Antenna theory".
Mc Graw Hill Book Comp. - 1969 - Part I - Chap. 14
- (9) H. Gruenberg : "Theory of waveguide-fed slots radiating into parallel plate regions".
IRE Trans. on Ant. and Prop., August 1952
- (10) R.W. Larson and V.N. Powers : "Slots in dielectrically loaded waveguide".
Radio Science - Vol. I (New Series) - No. 1 - Jan. 1966, pp. 31 - 39

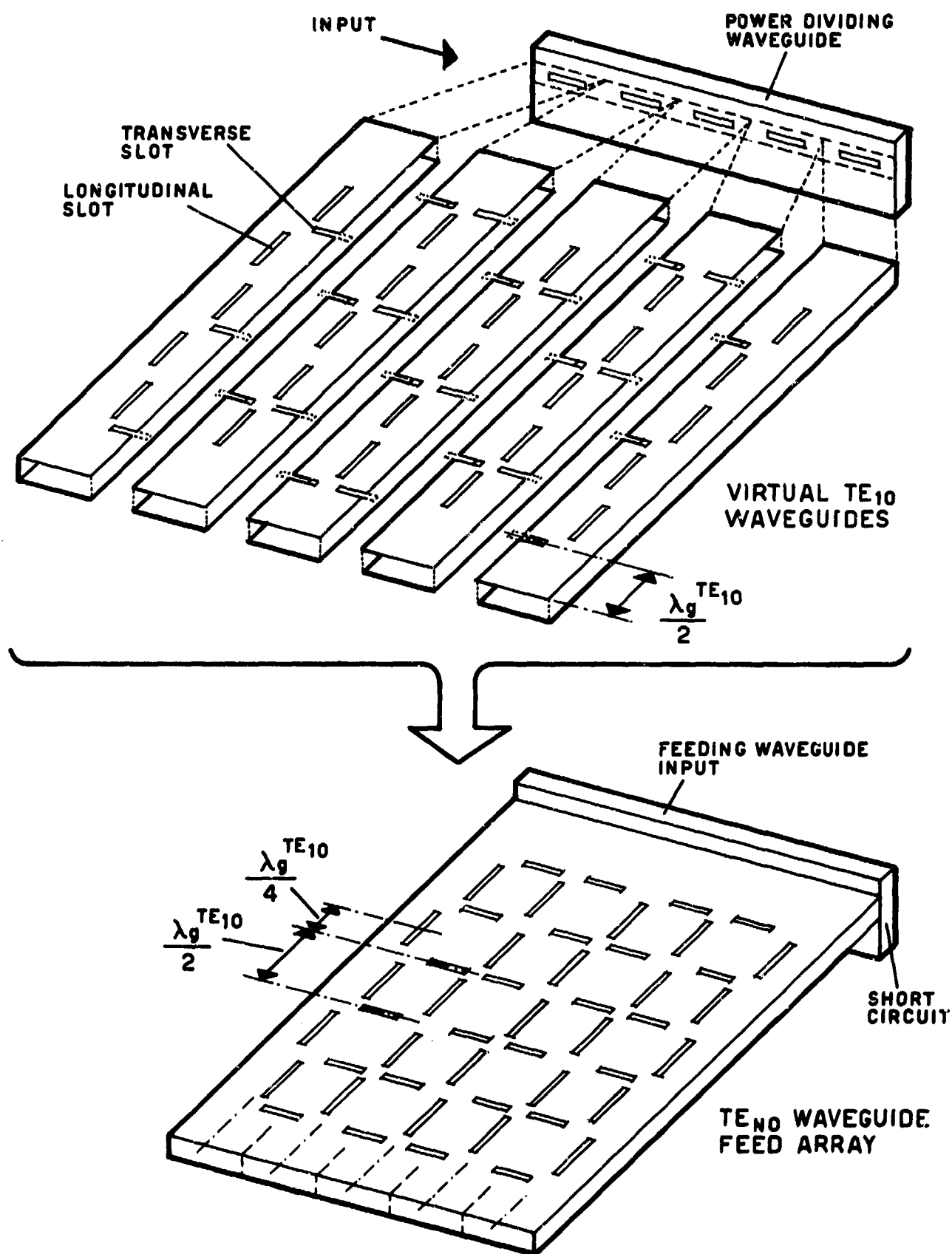


Figure 2-1

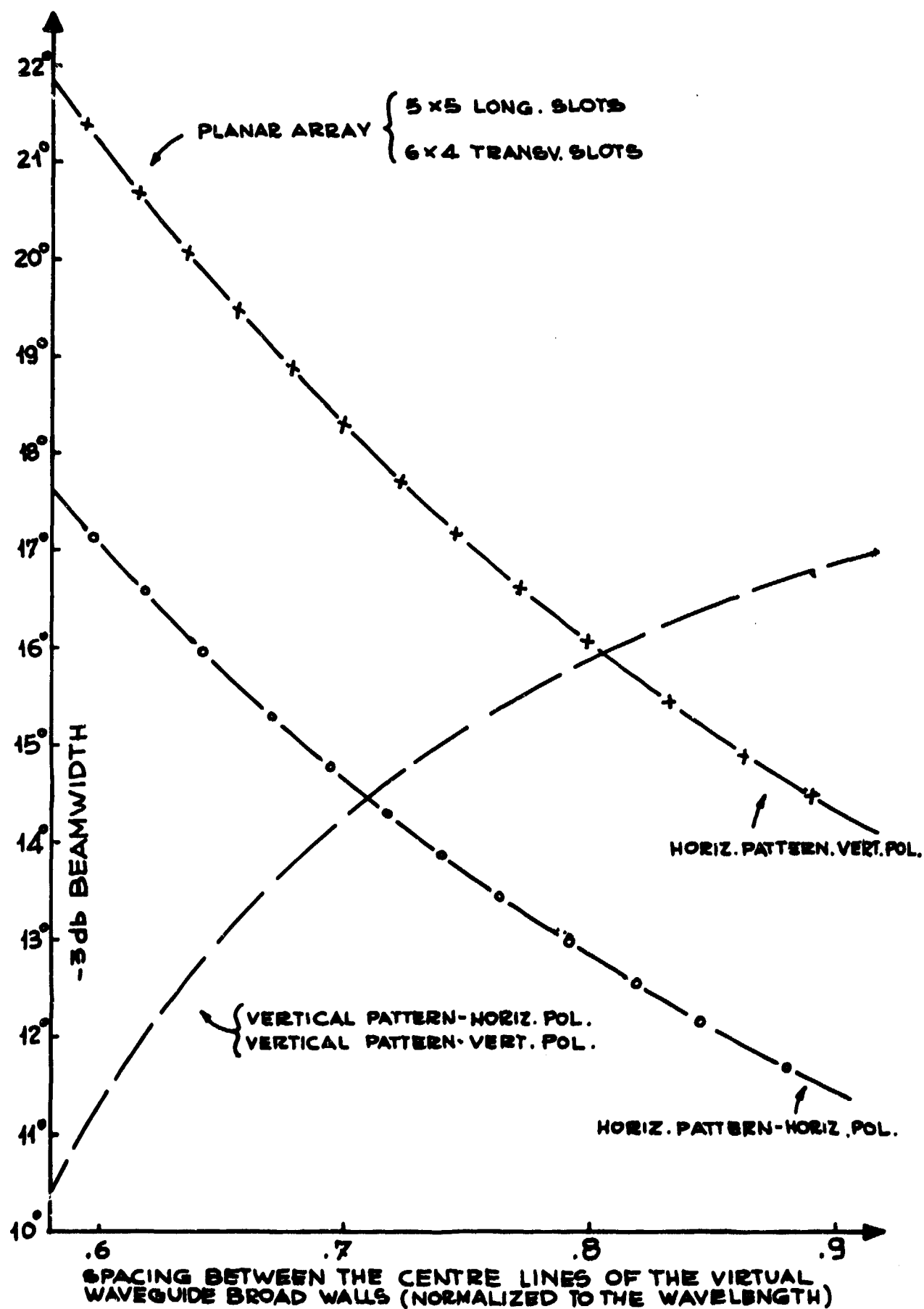


Figure 3-1

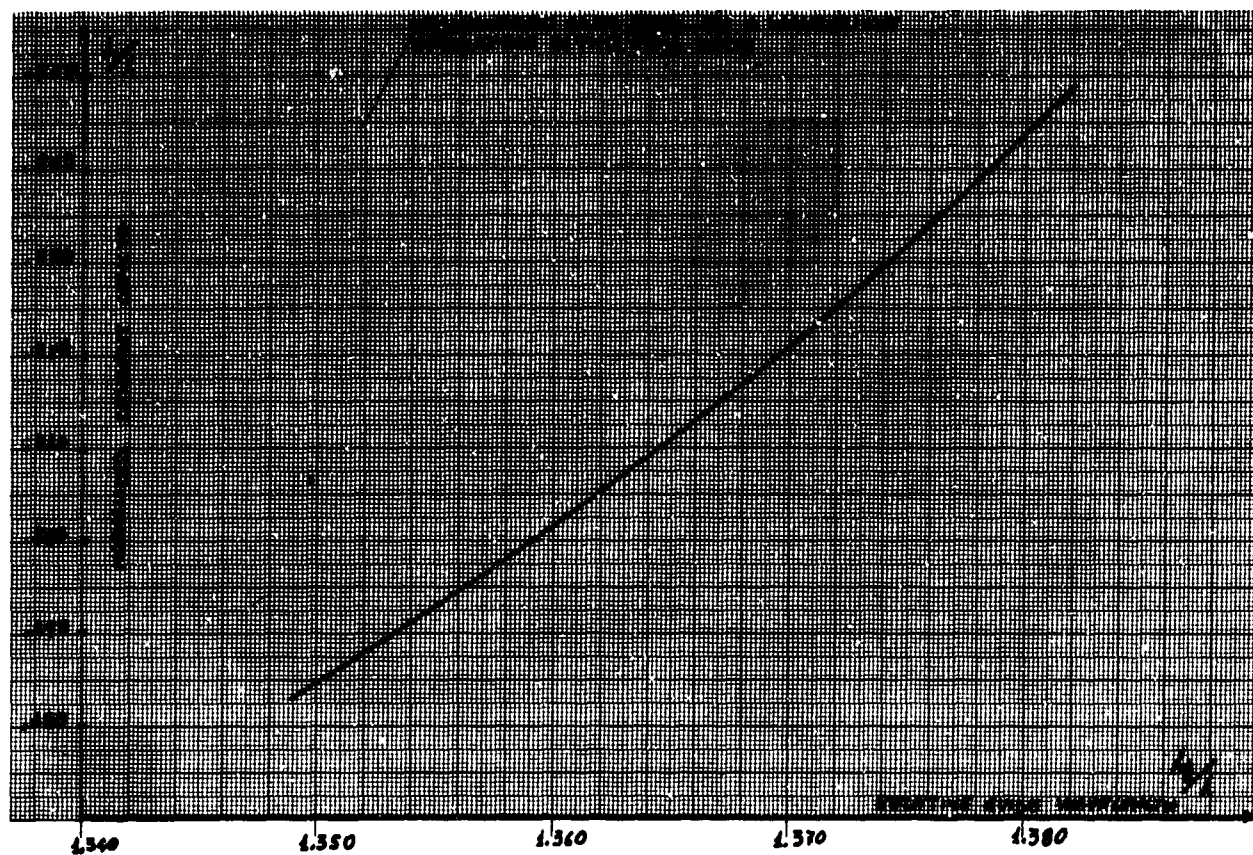


Figure 3-II

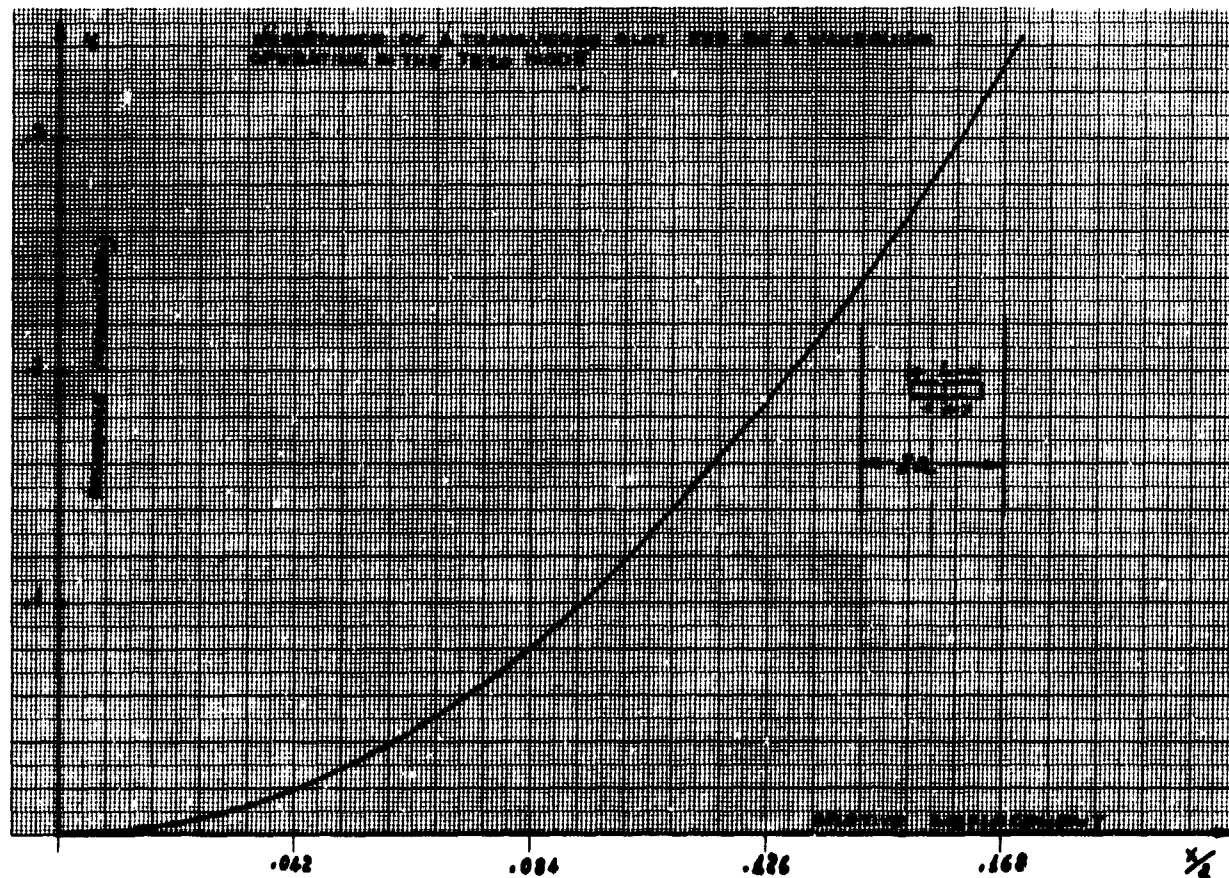


Figure 3-III

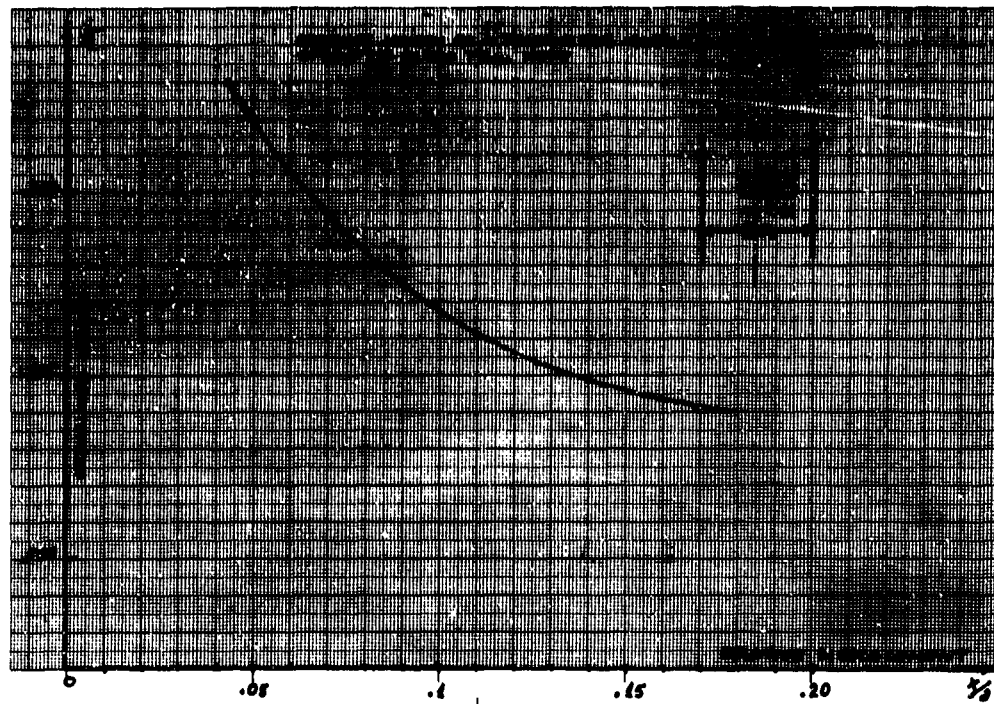


Figure 3-IV

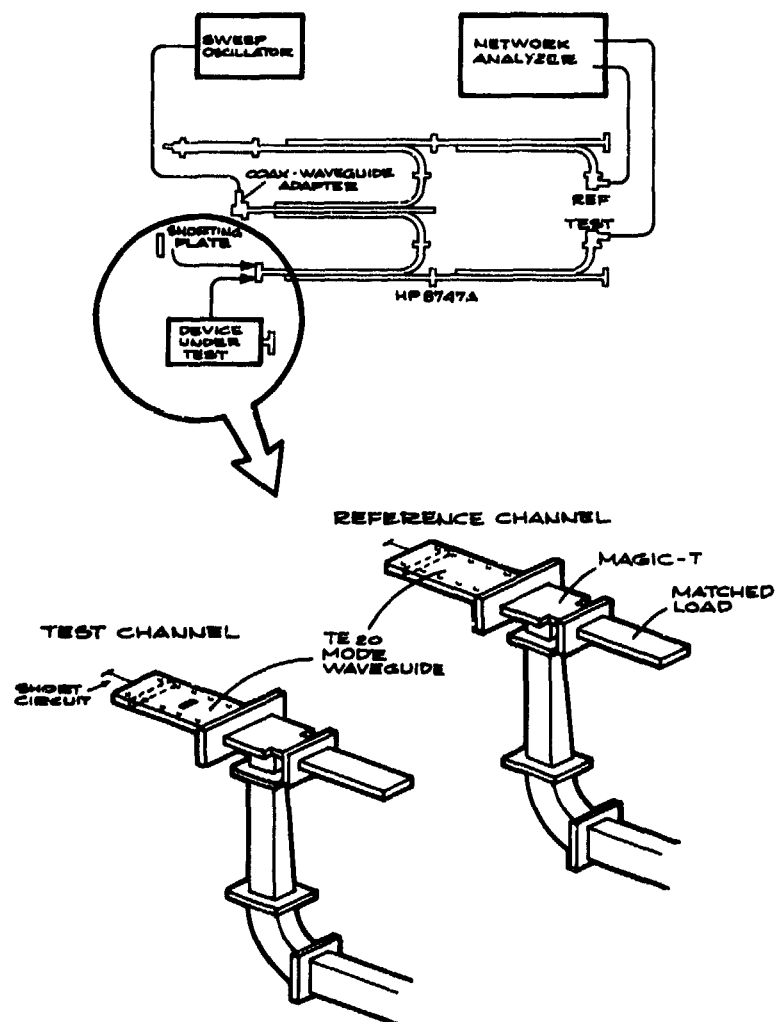


Figure 4-I



Figure 5-1

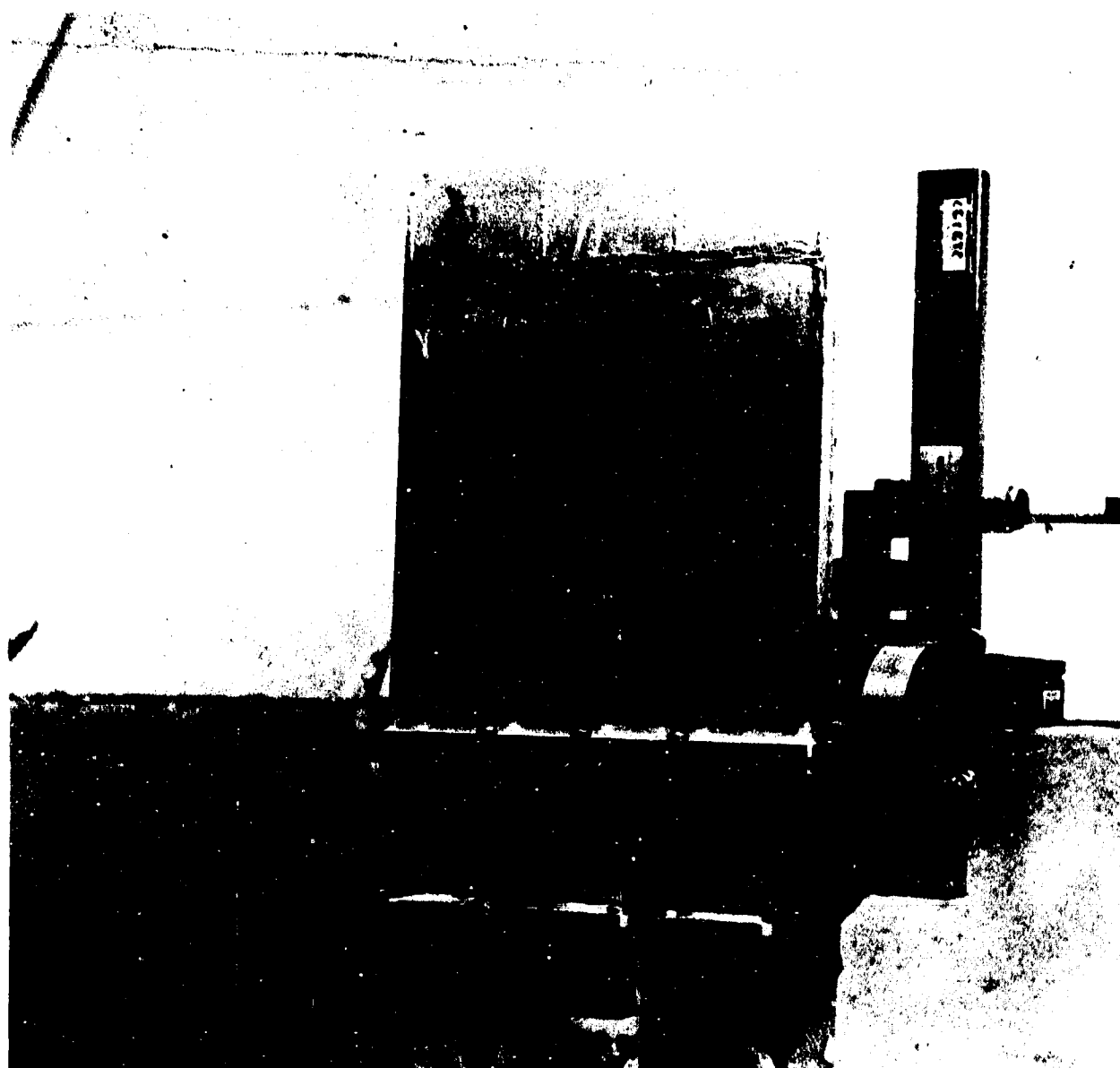


Figure 5-III

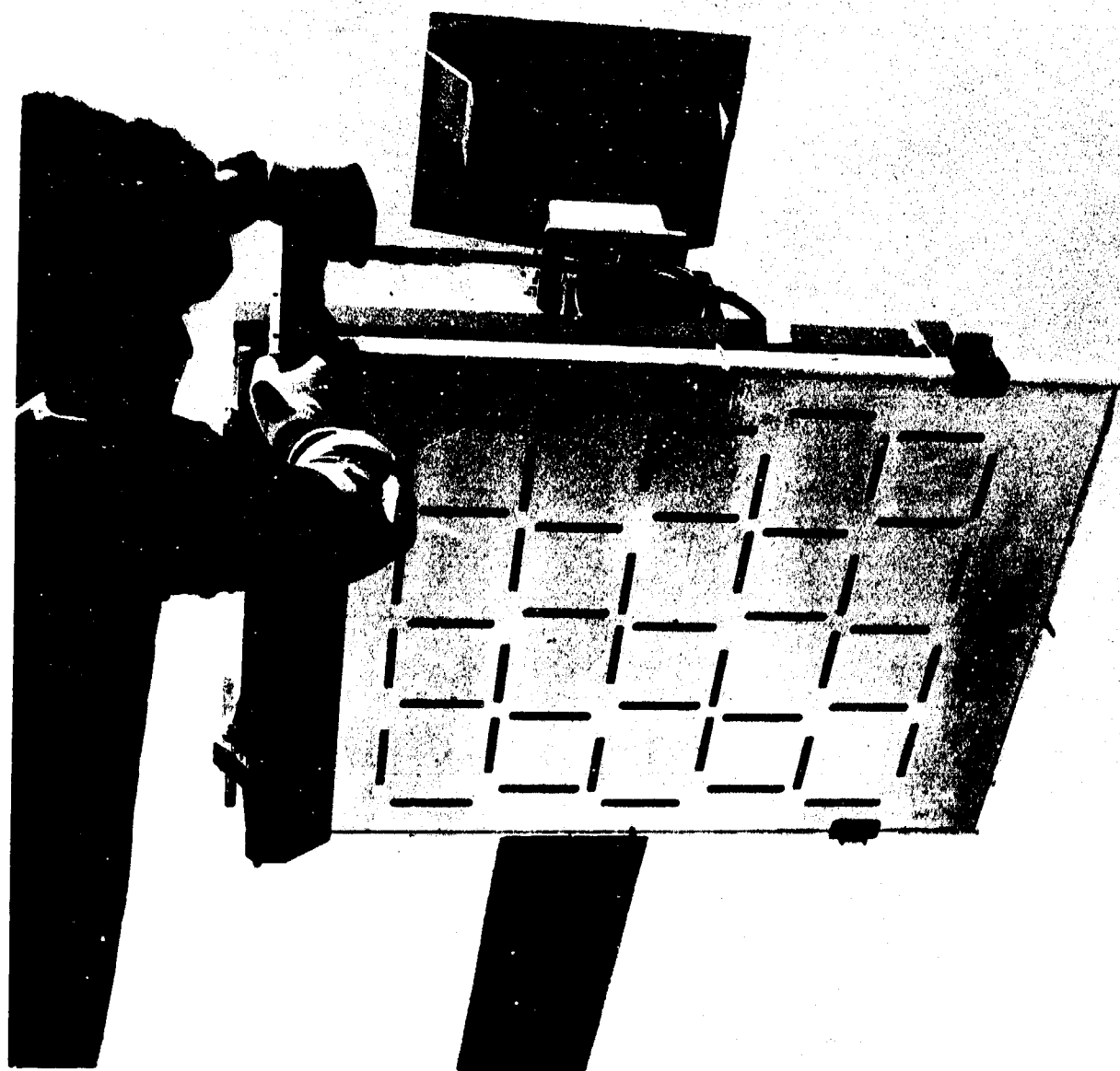


Figure 5-V

UPPER L-BAND TELEMETRY AERIALS FOR ROCKETS AND MISSILES

J. MAHONEY
E.M.I. Electronics Limited
Feltham, Middlesex
United Kingdom

SUMMARY

Future telemetry systems on missiles and rockets are likely to operate at Upper L-Band frequencies. The advantages to be gained and the problems likely to be encountered at these higher frequencies and the effects of change in the radiation pattern due to increased electrical spacing between individual aerials is given for a wide range of missile diameters. Methods of improving the radiation pattern coverage by altering the phase distribution to individual aerials and/or increasing the number of aerials are described. Effects caused by missile projections i.e. wings and tailfins and surrounding structures such as, launcher tubes and aircraft fuselage upon the radiation pattern are discussed.

A comparison between the performance of existing telemetry aerials operating at 450 MHz and various prototype Upper L-Band aerials is given. Problems relating to the working environmental conditions for a wide range of missile applications are described.

1. INTRODUCTION

In the United Kingdom telemetry systems on missiles and rockets have operated almost exclusively in the 400 to 500 MHz frequency band. Many aerial designs exist for use at these frequencies but due to congestion of frequency allocation in this band, it is anticipated that a move will be made towards the use of Upper L-Band frequencies typically, 1,400 to 1,500 MHz.

2. IMPLICATIONS OF CHANGE

The implications of the change in frequency can best be seen by stating the basic problem. If telemetry aerials operating at 450 MHz be replaced by aerials operating at 1,500 MHz, how does the radiation pattern of the missile change and does the missile geometry influence the change to a greater or lesser extent? The effects of increasing the r.f. frequency make themselves most obvious by virtue of the increased electrical spacing between individual aerials. This spacing can be defined in terms of the ratio of missile diameter or length to r.f. wavelength. It is better to express the spacing in terms of the missile diameter to r.f. wavelength ratio, because a small change in diameter will influence the radiation pattern more than a small change in missile length. A range of typical missile diameters is indicated in Table 1 which tabulates values of (D/λ) at both the old and the anticipated frequencies.

TABLE 1

Diameter D cm	(D/λ) at 450 MHz	(D/λ) at 1,500 MHz
5	0.075	0.25
11	0.165	0.55
19	0.285	0.95
20	0.300	1.00
35	0.525	1.75
45 (Skylark)	0.675	2.25
60	0.900	3.00
130	1.950	6.50

2.1 Polar Diagrams

The radiation pattern will be determined by the distribution of energy from the aerials mounted on the missile. Table 1 shows there is an overlap in values of D/λ at both the old and new frequencies. Therefore the patterns on the smaller diameter missiles at L-Band frequencies, should be similar to those obtained at the old frequencies on some of the larger diameter missiles. These patterns will however be modified by missile projections e.g. wings and tailfins, especially if the aerials are in close proximity to them.

2.2 Electrical Performance

The electrical performance of an aerial depends upon the size, shape and location of the aerial on the missile. The most commonly used aerials e.g. monopole, slot and notch, require a flat ground plane of at least 5λ in diameter for good impedance characteristics and polar diagram patterns. In practice this is seldom possible to arrange and a reduction in ground plane size will degrade the patterns, lower the V.S.W.R. and reduce the bandwidth of the aerial. The electrical performance of L-Band aerials will be improved due to the increased electrical size of the ground plane, and hence it will be easier to achieve a good impedance match on the smaller diameter missiles.

2.3 Mechanical Performance

From the mechanical point of view, the introduction of aeriels operating in the Upper L-Band frequency range offer distinct advantages. These advantages stem mainly from the possibility of achieving considerable reductions in the overall dimensions of aeriels at such short wavelengths. This in turn will lead to an all-round improvement in the aerodynamic and thermodynamic behaviour of individual aeriels under all conditions of flight. Further advantages can be envisaged in terms of increased reliability during subjection to a wide range of environmental conditions, and the ability to offer aeriels having minimal drag. One point that needs further consideration, however, is to what extent the aerodynamic advantages to be gained from using L-Band aeriels, are offset by the need for possibly a greater number of aeriels per missile to achieve adequate pattern coverage.

2.3.1 Aerodynamic and Thermodynamic Considerations

If we assume that the general upward trend in missile speeds will continue to rise at a similar rate in the future, then as a general rule, it would be true to say that the aerodynamic pressures and thermodynamic heating of externally mounted aeriels will also continue to rise. Therefore it is likely that certain existing aerial designs, and choice of materials, will need to be reconsidered in the very near future.

Studies on recent missiles have shown that aeriels operating in the UHF telemetry range having quarter wavelength spikes in the order of 17 cm. long with typical root diameters of 6 to 7 mm, would be aerodynamically unacceptable on small diameter missiles where the drag of external features often becomes significant. This has necessitated aerial designs having reduced spike diameters and greater sweepback, thereby reducing the drag to acceptable levels, but at the same time increasing the stress levels in the aerial and base assemblies, so requiring greater care in the selection of suitable materials.

On the question of thermodynamic heating, the point has now been reached where the use of certain materials such as epoxy resin adhesives, dielectrics, etc., is becoming marginal at elevated temperatures, particularly on aircraft-carried missiles where the aeriels can be subjected to high temperature 'soaks' for relatively long periods prior to launch. The dimensions of the L-Band aeriels will be reduced to approximately one third due to the shorter wavelength. Such aeriels with their lower, slender profiles will produce quite low aerodynamic drag even at high Mach numbers in the lower atmosphere.

Since telemetry aeriels are frequently located on the forward section of the missile, it is important that they should not trigger turbulent flow prematurely, and thus increase the friction drag component of the missile bodytube. Therefore, any reduction in aerial size would be beneficial in this respect, apart from reducing the pressure drag component acting on the aerial itself.

2.4 Effect of Surrounding Structures

If an aerial is sited close to a projection on a missile the radiated signal which illuminates the projection will be diffracted. Large currents may be induced in the projection and both of these effects will modify the radiation pattern. The degree of modification is dependant upon the size, shape and distance the projection is from the aerial. L-Band aeriels can be sited nearer to a missile projection than UHF aeriels, before their presence modifies the polar diagram pattern of the missile. The distance is expressed as a function of wavelength as explained in sub section 2.4.1. The impedance of the aerial is also affected but to a lesser extent.

2.4.1 Aeriels Close to Projections on a Missile

If a vertically polarised aerial e.g. blade or spike, is located not more than half a wavelength from, and parallel to, a fin of substantially the same dimensions, then large currents may be induced in the fin because the fin is grounded to the earth plane of the aerial. If the fin is longer than a quarter wavelength, the maximum radiation will be in the direction away from the fin and the fin acts as a reflector. If the fin is shorter than a quarter wavelength, the maximum radiation will be towards the fin and the fin acts as a director.

This characteristic could be used to provide a forward or rearward looking radiation pattern, although a distortion in the radiation pattern implies a gain in some direction since the total radiated power remains constant. The effects of diffraction upon the radiation pattern of an aerial in line and at a distance of 1λ and 10λ from a streamlined projection has been shown by (CARY, R.H.J., 1951). The effects are least when the aerial is most distant from the projection and when the latter has small dimensions. If the projection is normal to the aerial, instead of parallel to it, the disturbances are greatly reduced. The impedance of an aerial changes as the mutual coupling between the aerial and the fin increases.

2.4.2 Missile Mounted Under Aircraft Fuselage

The radiation pattern of the missile will be affected by the wings and fuselage of the aircraft, and is analogous to an aerial mounted on a cylinder above a shaped finite ground plane. The pattern will be modified by the dimensions and shape of the wings and fuselage, and also the distance the missile is from them. A theoretical analysis of the radiation pattern is difficult due to the shape of the aircraft and model measurements are necessary.

2.4.3 Missile Enclosed by Launcher Tube

Missiles are sometimes fired from launcher tubes attached to the fuselage and/or wings of an aircraft or alternatively from ground bases. The radiation pattern will be severely affected by the proximity of the metallic launching tube, and determined by the amount of radiation leaking from the partially or totally enclosed tube. Nulls in the radiation pattern can easily be 20 dB down from the free space condition, causing in the worst case, loss of transmission from the missile. The impedance of

the aerial is altered due to the increased capacitance between the spike tip or across the mouth of a slot aerial and the tube, causing a lower V.S.W.R. at the aerial input.

3. AERIAL SPECIFICATION

System requirements will determine whether a linearly or circularly polarised aerial is to be used. If the drag of an external aerial cannot be tolerated or alternatively if the gap between a missile and the launcher tube is small, then a suppressed aerial has to be fitted. Consideration must be given to the location and number of aerials required to provide adequate radiation pattern coverage for each missile. Much information can be obtained from the radiation patterns in three mutually perpendicular planes, commonly known as the principal radiation planes. The most important of these are the azimuth and the transverse elevation planes, and Fig.1 shows their disposition with respect to a missile. Radiation patterns in general should be omnidirectional in the transverse elevation plane with good rearward coverage in all other planes. (SCOTT, W.G. & SOO HOO, K.M., 1966) have demonstrated that the radiation pattern of an aerial without nulls must contain all polarisations from right hand circular, via linear to left hand circular. However, to take advantage of this result the ground receiving station must also respond to all polarisations. The missile may have to be roll stabilised if the stability of the missile affects the performance of the telemetry link from the missile to the receiving station.

To obtain maximum transfer of power between the transmitter or receiver and aerial, the impedance of the aerial should match the characteristic impedance of the feeder cable which connects them. The impedance should remain constant over the range of operating frequencies but is limited by the Standing Wave Ratio. The majority of telemetry aerials are matched to 50 ohms and the V.S.W.R. measured at the r.f. connector is greater than 0.8.

Most missile aerials operate under hostile environmental conditions. For example, if a missile travels to high altitudes then corona discharge may take place resulting in a subsequent reduction in signal strength received by the ground station. By reducing sharp corners and increasing element and base diameters the power (assuming same pressure) at which corona takes place is increased. Alternatively, the missile may travel close to the sea and sometimes through the crests of waves. In the latter condition the aerial would look like a partial short circuit resulting in an increase in reflected power which could upset the telemetry transmitter. Aerials are environmentally tested to British Standard 2G100 and other similar specifications. These tests include vibration, acceleration, climatic, water-proofness, salt corrosion, ice formation and compass safe distance.

4. REVIEW OF SUITABLE AERIAL DESIGNS

Missile aerials can be categorised as either external or suppressed aerials. External aerials protrude from the surface of the missile, whereas suppressed aerials are contoured and fit flush to the surface of the missile. Details of aerials that could be used for missile telemetry applications at Upper L-Band frequencies are shown in Table 2.

TABLE 2

Aerial type	Radiation Pattern	Polarisation	Typical Dimensions H - Height D - Diameter	Typical Bandwidth for a V.S.W.R. of 0.66
<u>External</u>				
Spike & Blade	Azimuth - omnidirectional	linear	H-5 cm D-0.4 cm	5% with stub compensation
Short Helical; Conical Helix Cylindrical Helix	Broad Beam	circular circular	H-1.34 cm D-0.5 cm H-0.8 cm D-0.5 cm	Under 1%
Equiangular; Planar Spiral Conical Spiral	Broad Beam	circular circular	D-28 cm H-16 cm D-8 cm	Large Large
Archimedean Planar Spiral	Broad Beam	circular	D-17 cm	Large
<u>Suppressed</u>				
Slot	Depends on missile diameter	linear	Length 10 cm Width 0.5 cm	4%
Crossed Slots when fed in phase quadrature	Depends on missile diameter	circular		4%
Notch	Broad Beam; depends on the size of the Missile projection	linear	Length 4 cm	6%

An analysis of the information in Table 2 reveals the following:

- (a) Each category contains a number of linearly and circularly polarised aeriels.
- (b) Short helical aeriels are essentially single frequency devices.
- (c) Spiral aeriels are generally too large to fit the smaller diameter missiles.
- (d) Slot aeriels would have to be contoured to suit the missile bodytube.

5. CALCULATION OF RADIATION PATTERNS

It is possible to calculate certain aspects of the expected patterns relatively easily, but other aspects present greater difficulty and require numerical techniques to achieve any success. The pattern aspect that can be computed easily demonstrates the distribution of energy around the missile diameter by aerial elements placed on an infinite cylinder. Solutions to the problem have been known for dipoles and slots for a long time, and (WAIT, J.R., 1959) includes a comprehensive survey of the available literature.

Computations have been carried out for a range of D/λ ratios using simple $\lambda/4$ monopoles, mounted radially on a cylinder of diameter D as illustrated in Figs. 2, 3 & 5.

5.1 Radiation Patterns of a Single Monopole Aerial

The patterns shown in Fig.2 indicate the gradual increase in the shadowing effect for an increase in missile diameter. The patterns also exhibit two complete nulls which are directly in line with the radiating element, and are due to the inability of such dipole like elements to radiate in directions along their own length.

Although for the smaller diameter sizes a reasonable distribution is obtained, for the larger sizes it is necessary to include more than one aerial to overcome the shadowing effect. This is summarised in Table 3 where the percentage of angles for which the level exceeds the average and (average - 10 dB) levels respectively is indicated. This average level must not be confused with the overall aerial gain since it only applies to the transverse elevation plane.

TABLE 3

D/λ	Percentage for which level is greater than:	
	average	average - 10 dB
0.063	57	87
0.25	56	82
0.67	65	85
1.83	51	88
3.08	50	83

Although Table 3 does show a trend of reduced coverage as diameter increases, it is not repeated in such an obvious manner at the -10 dB below average level. However, the accuracy of computation was not so great here. It is possible to fill the null directly in line with the aerial by using a raked spike aerial for instance, although this does not do the same on the opposite side of the missile and a shadow area still remains.

5.2 Radiation Patterns of Two Monopole Aeriels

In an attempt to improve the all round coverage a pair of simple monopole aeriels have often been used. For small diameter cylinders it is necessary that they be energised so that the contributions from each aerial add in phase as much as possible. This means in effect that they must be energised 180° out of phase, and since they point in opposite directions their contributions are finally brought back into phase. Fig.3 illustrates the resulting patterns for the range of D/λ previously used and Table 4 summarises the degree of coverage obtained.

TABLE 4

D/λ	Percentage for which level is greater than:	
	average	average - 10 dB
0.063	56	90
0.25	53	80
0.67	36	73
1.83	42	90
3.08	42	89

For the larger diameters there is a very obvious interference pattern in this plane and the coverage obtained is now no longer very dependent on the aerial phasing which could be allowed to take on any value as far as coverage in this plane is concerned.

A comparison of Table 4 with the previous one does not immediately show any significant improvement in the coverage obtained by using two aerials, except perhaps at the -10 dB below average level where there is a slight improvement. However, there is a more uniform distribution in general with two aerials since the angular sectors over which these levels fall below the specified level are smaller. A more significant improvement is obtained when raked aerials are used since the regions of low coverage are now improved on both sides of the missile.

5.3 Radiation Patterns of Four Monopole Aerials

Four simple spike aerials can be utilised on the smaller diameter missiles to produce almost perfect coverage in the sense indicated by (SCOTT, W.G., & SOO HOO, K.M., 1966). This is achieved by placing the four aerials uniformly around the diameter and energising them to produce circular polarisation of opposite hands along either direction of the cylinders longitudinal axis and linear polarisation in the transverse elevation plane. This is identical in effect to a turnstile aerial system. As the cylinder diameter is increased however, the transverse coverage worsens and breakup occurs due to increased aerial spacing.

Fig.4 illustrates the degree of coverage obtained with this arrangement as a function of cylinder diameter to r.f. wavelength. This figure plots the ripple in the transverse elevation plane i.e. ratio of maximum to minimum levels obtained around the cylinder. If a 10 dB ripple level is considered to be acceptable then the coverage obtained is satisfactory for all D/λ ratios up to 1.25 except for a small range of ratios between 0.55 and 0.9. The excessive ripple occurring at this diameter (i.e. $D = 0.7\lambda$), is due to the coincidence in angle of an interference null in this direction obtained between pairs of opposite aerials. Such nulls are also repeated at closer spacing as the diameter is increased. Fig.5 illustrates the patterns obtained for a range of D/λ ratios. The use of raked aerials as opposed to conventional monopoles will alter this picture and could possibly improve the coverage.

5.4 Radiation Patterns of More than Four Monopole Aerials

It is possible to extend the range of cylinder diameters up to which good coverage is obtainable by increasing the number of elementary radiators around the circumference. Some calculations have been made with 6 and 8 radiators which suggest that pattern ripple could be contained within less than 10 dB for all the diameters being considered (i.e. up to $D/\lambda = 3.08$ at least).

5.5 Effect of Missile Length

The theory used to compute the radiation pattern in directions around the cylinder, can be used to compute the pattern in other directions as shown by (WAIT, J.R., 1959 & SINCLAIR, G. 1951). Complete pattern calculations can be made but these only refer to aerials mounted on a plain cylinder of infinite length. In some cases, such calculations can be useful in predicting results but usually the finite length of the cylinder produces marked differences in the pattern.

A number of authors including (KUEHL, H.H., 1961 & BALANIS, C.A., 1970) have considered this problem using different mathematical techniques with various degrees of success. The usefulness of such solutions for a given missile configuration are not too clear at the present time, because the real problem is found when it is realised that missiles do not consist of perfect finite length cylinders. They have fins and wings etc., which have a pronounced effect on the pattern shape particularly in the rearward direction where telemetry reception is usually of most importance.

5.6 Electrical Resonances Caused by Discontinuity in Missile Airframes

It is very difficult to calculate the effects produced by a discontinuity in the missile airframe causing electrical resonances which affect the radiation pattern. For example, if a notch is cut into a wing which pivots about a central axis, the gap between the body of the missile and the root of the wing could produce an electrical resonance. The radiation pattern and the V.S.W.R. of the notch will be affected if the length of the gap from the leading and trailing edges of the wing to the pivot axis is approximately $\lambda/4$. These effects can easily be seen by making model radiation pattern measurements.

6. PROTOTYPE AERIAL DESIGNS AND EXPERIMENTAL RESULTS

The most generally used 450 MHz telemetry aerials are the spike, blade, notch and slot. These aerials are more attractive at 1,500 MHz due to their reduced dimensions and Figs. 6, 7, 8, 9 and 12 show prototype designs which are described below:

6.1 Spike Aerials

Fig.6 illustrates variations of the conventional $\lambda/4$ resonant spike aerial including dimensions for operation at both 450 and 1,500 MHz. These aerials combine simplicity with ruggedness and a vertical cylindrical spike can be tuned to cover a 5% bandwidth with a V.S.W.R. better than 0.66. The drag on a 1,500 MHz spike aerial is approximately 75% less than one operating at 450 MHz and can be further reduced by raking and tapering the spike. Raking the spike produces a marked increase in the H - plane radiation pattern and also a lower impedance and reduced bandwidth. These aerials can withstand high temperatures providing a stainless steel rod and good base insulators are used.

6.2 Notch Aerials

The notch or open ended slot has been described in detail by (JOHNSON, W.A., 1955). Using Babinet's principle a notch cut into a finite metallic sheet can be shown to have the same radiation pattern (except

for changes in polarisation) as a complementary monopole protruding from the edge of a complementary sheet. Notch aerials have been cut into the trailing edges of a missile tailfin and the radiation pattern produced is nearly omnidirectional in the azimuth plane and directional towards the rear of the missile in the fore and aft plane. The impedance at the mouth of the notch is very high, typically 1,000 Ω for a notch length of 0.2λ dielectric.

At 1,500 MHz the length of the notch is approximately 4 cm and the short circuited portion beyond the feed point in Fig.7 can be treated as compensating reactance, whilst further compensation can be obtained by adding parallel capacitance across the feed point or mouth of the notch. Bandwidths of 10% have been achieved for a V.S.W.R. of 0.5 and could be extended by varying the notch width to produce a tapered transmission line. Fig.8 shows a notch blade aerial which is capable of operating over nearly twice the frequency bandwidth of the spike aerial. The drag of the blade is slightly higher than that for the spike, although it is small when compared to other aerials operating at 450 MHz. The blade body can be produced in steel or light alloy as a casting or machining, and the notch loaded with a suitable dielectric material of a non-charring type.

6.3 Sleeve Aerial

Fig.9 shows a sleeve aerial which is new to missile work although it has been used successfully in communication and navigational systems on civil and military aircraft. It is a variant of the $\lambda/4$ resonant monopole in which the outer conductor, attached to the ground plane, surrounds part of the length of the inner radiating conductor. When the outer conductor is approximately $\lambda/8$ above the ground plane and the remaining inner conductor bent so that it is parallel to the ground plane, the impedance is approximately 50 ohms. The advantage of the sleeve aerial, with respect to the spike aerial, lies in its reduced height and increased bandwidth, typically 15% for a V.S.W.R. of 0.55 without stub compensation. Aerodynamically, this type of aerial has no great advantage over the blade or spike and the radiation pattern is similar.

6.4 Slot Aerial

The counterpart of the $\lambda/2$ dipole is the rectangular slot cut in a large metallic ground plane. The length of the slot is $\lambda/2$ and width simply related to the dipole cross-section. The radiation pattern is similar to that of the dipole but the radiation is horizontally polarised when that of the dipole is vertical. The impedance of a centre-fed slot radiating on both sides is 482 ohms, which is doubled when the radiation from one side is suppressed. Successful matching to 50 ohms can be achieved by a probe extending into the cavity behind the slot, or alternatively off-centre direct feeding can be used. The slot aerial is attractive at L-Band and higher frequencies because it offers:

- (a) A reduction in drag compared to external aerials.
- (b) Slot aperture under 10 cm long and narrow at 1,500 MHz.
- (c) If the cavity depth is reduced by dielectric loading, a stripline version of the aerial could be adhered to the surface of the missile.
- (d) The polarisation can be changed from linear to circular by using crossed slots, or by loading the slot with a parasitic dipole and feeding both elements in phase quadrature.

Longitudinal and circumferential slots cut into the surface of cylinders have been investigated by a number of authors including (WAIT, J.R., 1959 & SINCLAIR, G., 1951). A longitudinal slot cut into the surface of a horizontal cylinder produces a vertically polarised field which is essentially circular in the transverse elevation plane providing the D/λ ratio does not exceed 0.125. Increasing the diameter of the cylinder causes the pattern to gradually change in shape to a cardioid, although pronounced nulls occur behind the slot when $D/\lambda > 1$ as illustrated in Fig.10. Fig.10 also compares the radiation patterns between a longitudinal and circumferential slot aerial having the same D/λ ratio. The slot aerial has deep nulls in the radiation pattern at the narrow slot ends and to obtain good omnidirectional and rearward coverage two circumferential slots are generally used, although this arrangement is restricted to the medium and larger missile diameters. Fig.11 shows the pattern variation between two diametrically opposite circumferential slots fed in phase and in anti-phase. The radiation pattern in the other major planes depends mainly upon the length of the cylinder and can best be determined by using a scaled model. The bandwidth of a slot aerial is similar to a complementary dipole typically 8% for a V.S.W.R. of 0.5 which can be marginally improved by increasing the width of the slot, although the length to width ratio should remain approximately equal to three.

6.5 Printed Board Aerials

Several attempts have been made in recent years to manufacture inexpensive printed board telemetry aerials which can be attached to the outer surface of a missile. A new version of such an aerial described by (EBERSOL, E.T., 1973), has been designed to operate at L-Band frequencies. The aerial consists of a square metal plate supported by a dielectric substrate above a metallic ground plane and connection to a coaxial transmission line is made from the centre of one edge of the square as shown in Fig.12. A satisfactory performance is obtained when the sides of the square are $\lambda/2$ long measured in the dielectric material and the minimum size of the ground plane is 1.0λ . The aerial is linearly polarised with the electric vector perpendicular to the excited edge and typical radiation patterns are shown in Fig.13. The radiation mechanism of the aerial appears to be due to fringing fields present at both the excited and opposite edges. Successful attempts have been made to produce a circularly polarised aerial by feeding two adjacent edges in phase quadrature via a hybrid junction. The chief disadvantage of the aerial as presently utilised is due to the small available bandwidth typically not more than 5% for a V.S.W.R. of 0.4.

7. ACKNOWLEDGEMENTS

This paper reports work carried out with the support of the Procurement Executive, Ministry of Defence, and E.M.I. Electronics Limited. The author wishes to thank Mr.J. Thraves for many helpful discussions and suggestions.

8. REFERENCES

- BALANIS C.A., 1970, "Radiation characteristics of Current Elements near a Finite Length Cylinder". IEEE Trans. AP-18 p.352.
- CARY, R.H.J., 1951, "The Slot Aerial and its Application to Aircraft", Proc. IEE Vol 99 Part 3 p.187.
- EBERSOL E.T., 1973, "Antennas". Microwaves p.34.
- JOHNSON W.A., 1955, "The Notch Aerial and some Applications to Aircraft Radio Installation". Proc. IEE 102B p.211.
- KUEHL H.H., 1961, "Radiation from a Radial Dipole near a long Finite Circular Cylinder" IRE Trans. AP-9 p.546.
- SCOTT W.G. & SOO HOO K.M., 1966, "A Theorem on the Polarisation of Null Free Antennas". IEEE Trans. AP-14 p.587.
- SINCLAIR G., 1951, "The Patterns of Antennas Located near Cylinders of Elliptical Cross Section" Proc. IRE Vol 39 p.660.
- WAIT J.R., 1959, "Electromagnetic Radiation for Cylindrical Structures". Pergamon.

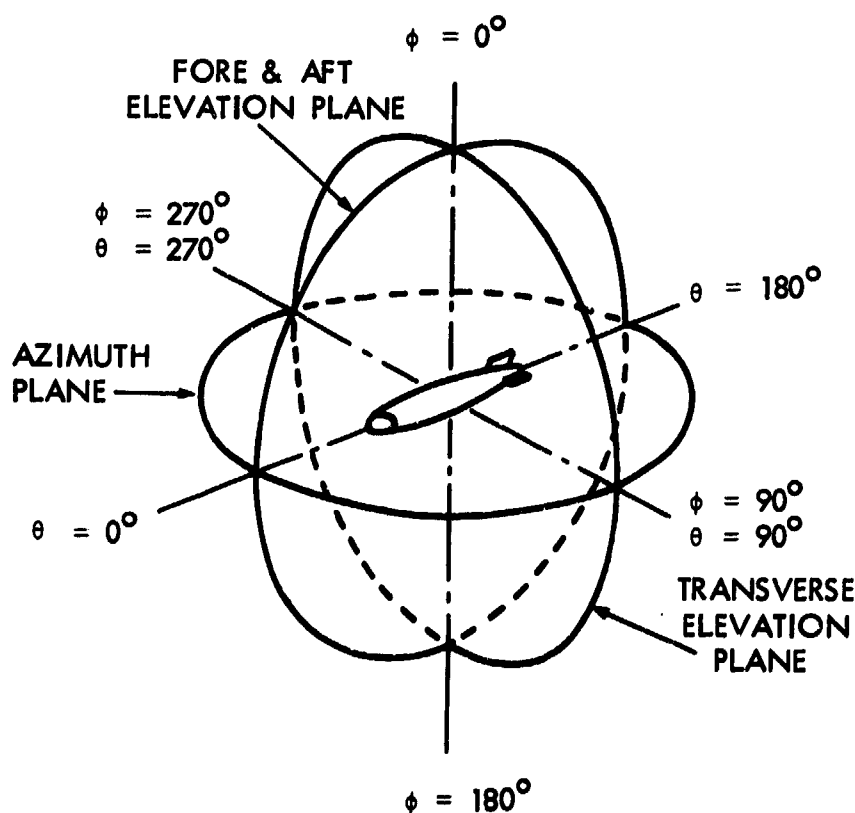


Fig.1. Principal Radiation Planes and Co-ordinate System For Telemetry Aerial Polar Diagrams.

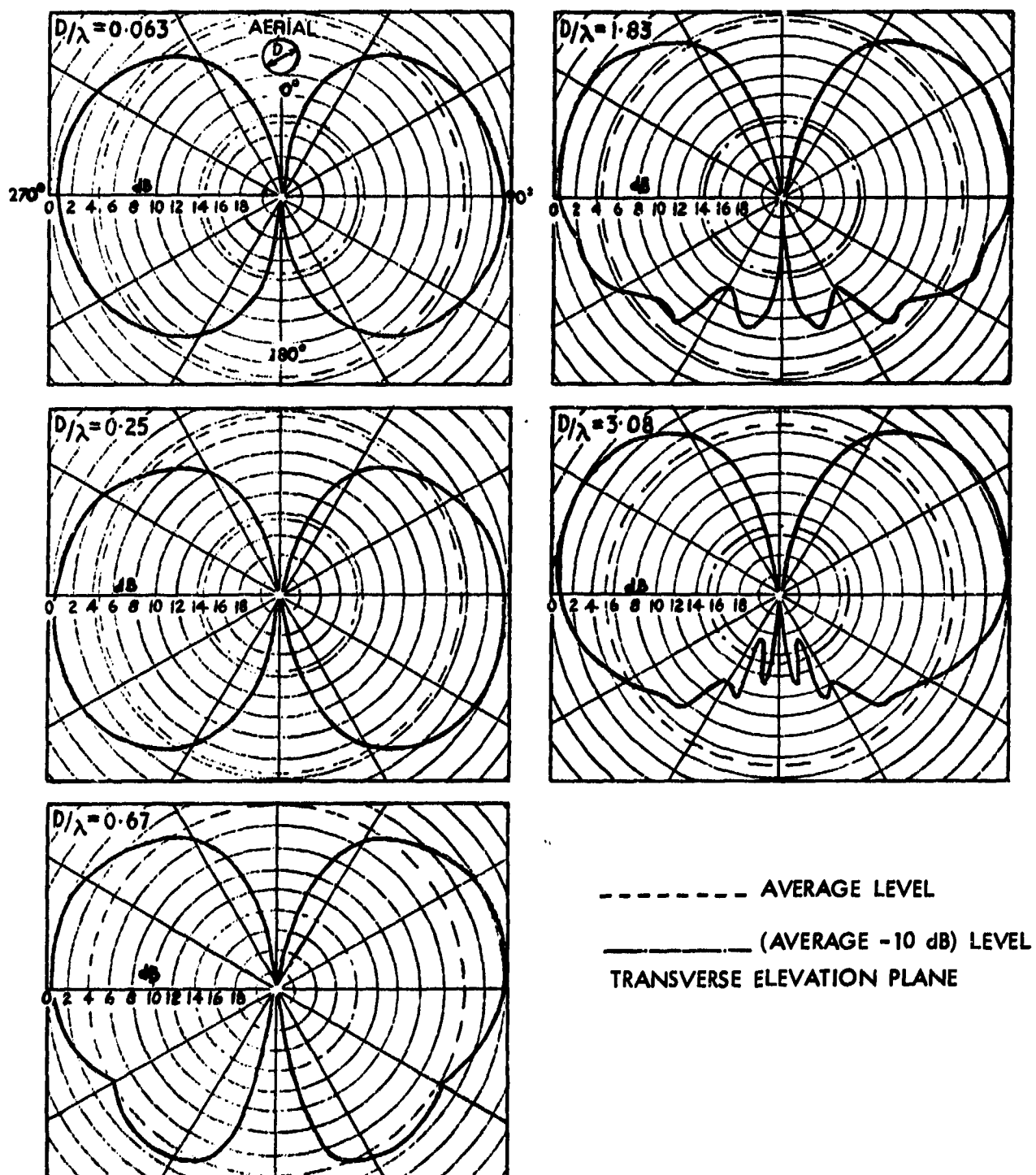


Fig.2. Computed Radiation Patterns of a Single Monopole Aerial Mounted on a Cylinder of Diameter D .

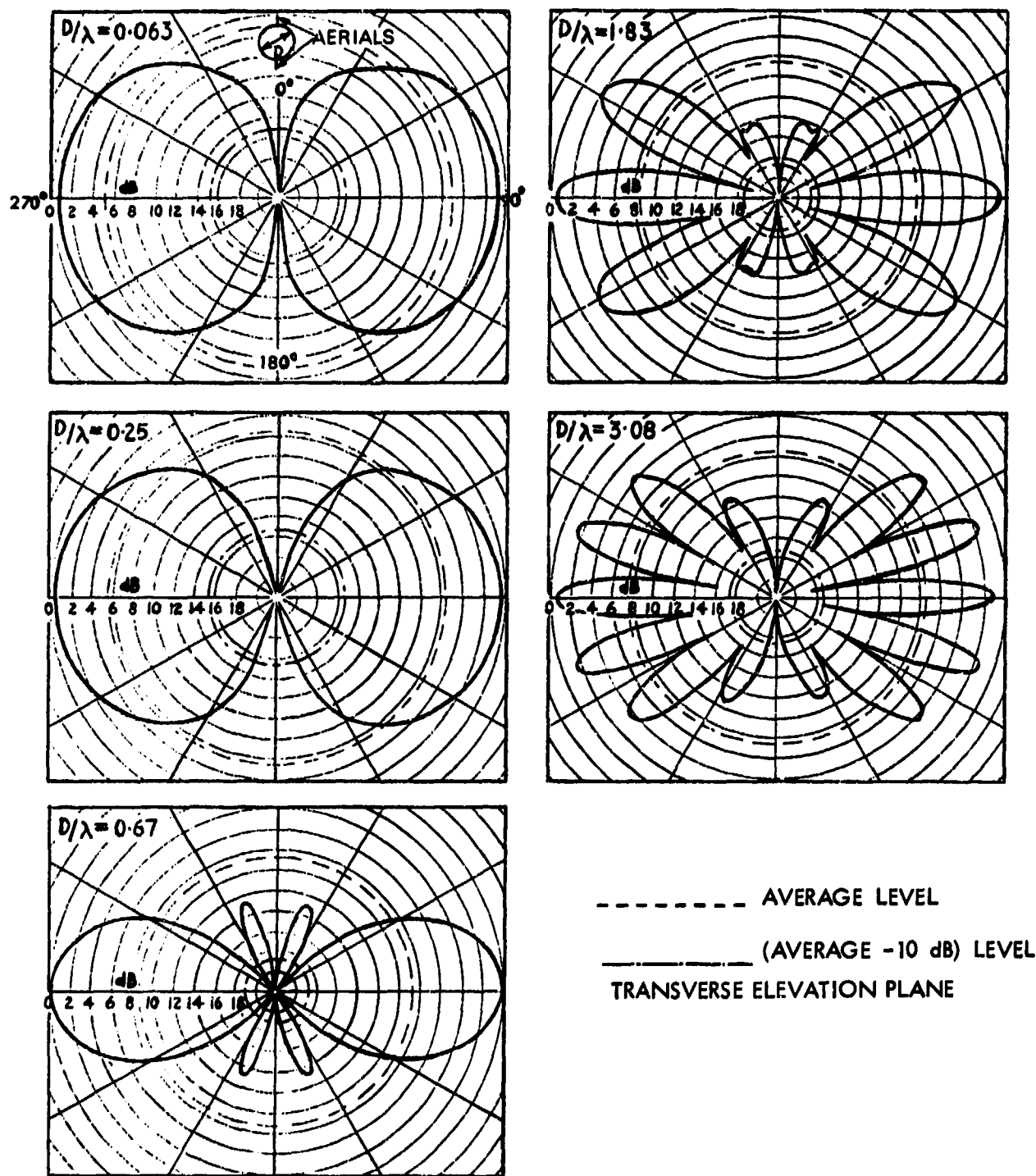


Fig.3. Computed Radiation Patterns of a Pair of Monopoles Fed in Anti-phase and diametrically Mounted on a Cylinder of Diameter D .

FOUR AERIALS MOUNTED ON
CYLINDER OF DIAMETER D

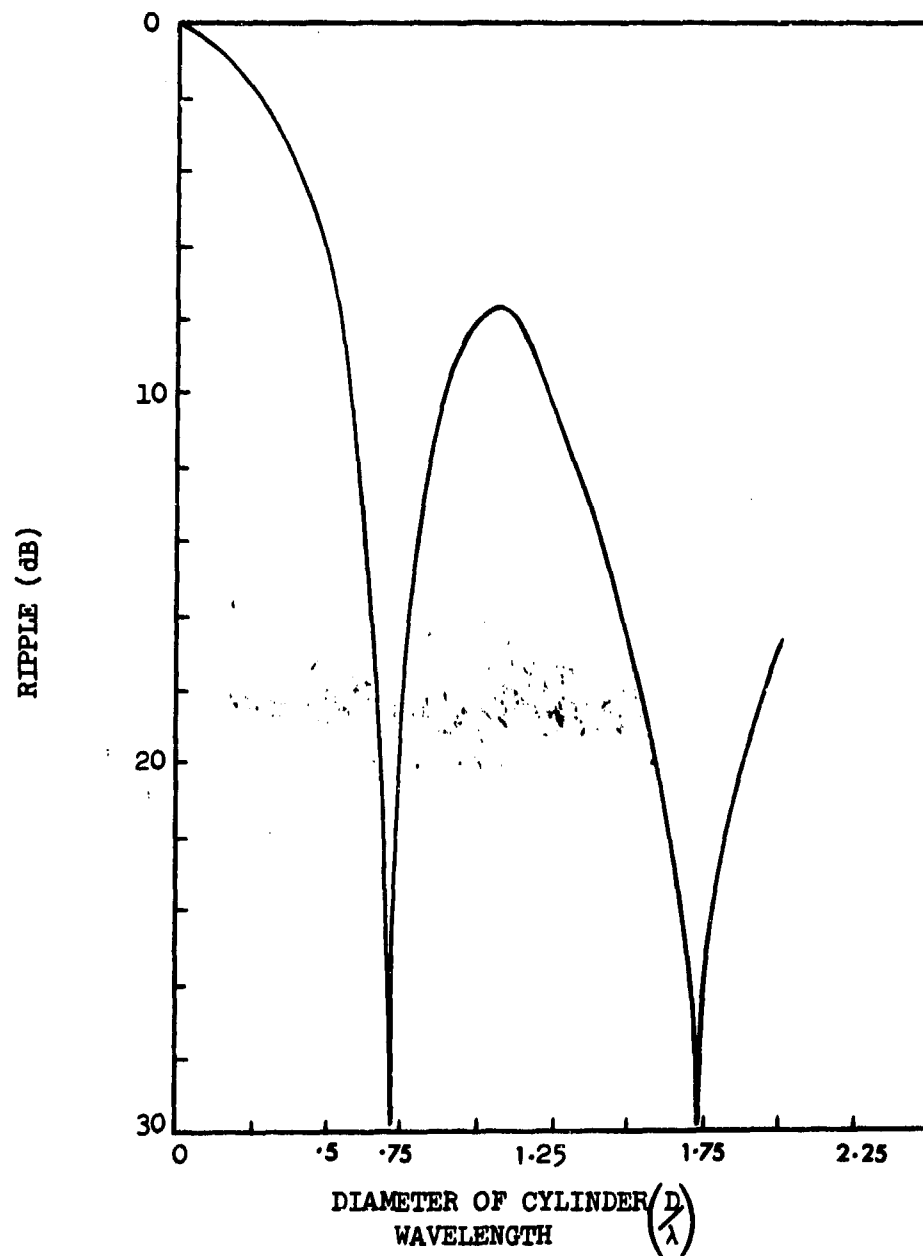
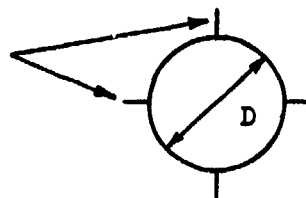


Fig.4. Computed Radiation Pattern Ripple in the Transverse Elevation Plane for various D/λ Ratios.

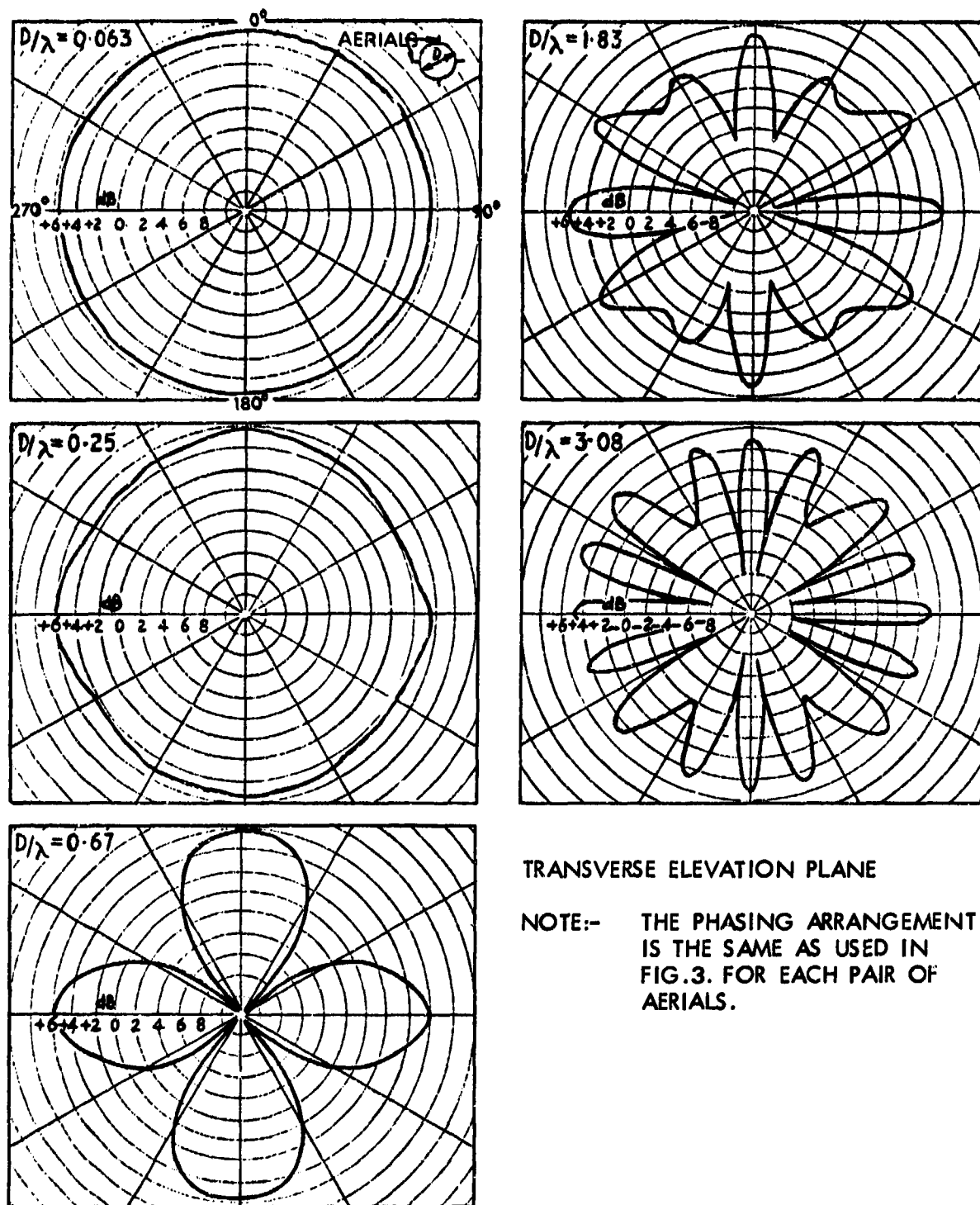


Fig. 5. Computed Radiation Patterns of Two pairs of Monopoles Fed in Phase Quadrature on a Cylinder of Diameter D .

FREQUENCY	CYLINDRICAL SPIKE	TAPERED RAKED SPIKE	BENT SPIKE
450 MHz	$h = 17 \text{ cm}$ $d = 0.6 \text{ cm}$	$h = 17 \text{ cm}$ $d_1 = 0.6 \text{ cm}$ $d_2 = 0.1 \text{ cm}$	$h_1 = 10 \text{ cm}$ $h_2 = 7 \text{ cm}$ $d = 0.6 \text{ cm}$
1500 MHz	$h = 5 \text{ cm}$ $d = 0.4 \text{ cm}$	$h = 5 \text{ cm}$ $d_1 = 0.4 \text{ cm}$ $d_2 = 0.08 \text{ cm}$	$h_1 = 3 \text{ cm}$ $h_2 = 2 \text{ cm}$ $d = 0.4 \text{ cm}$

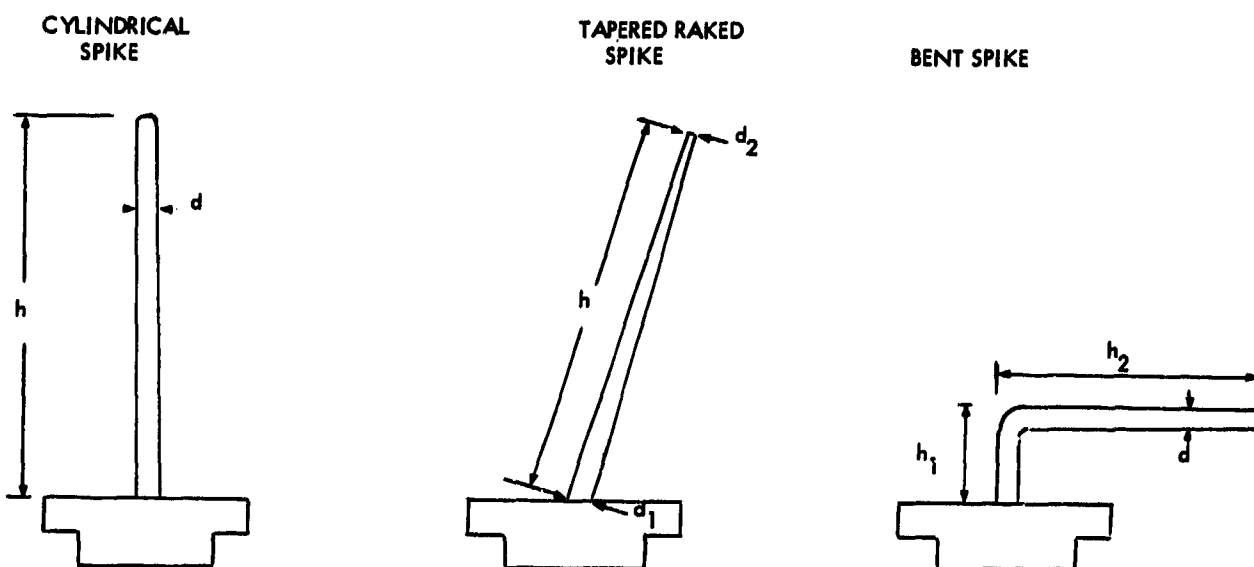
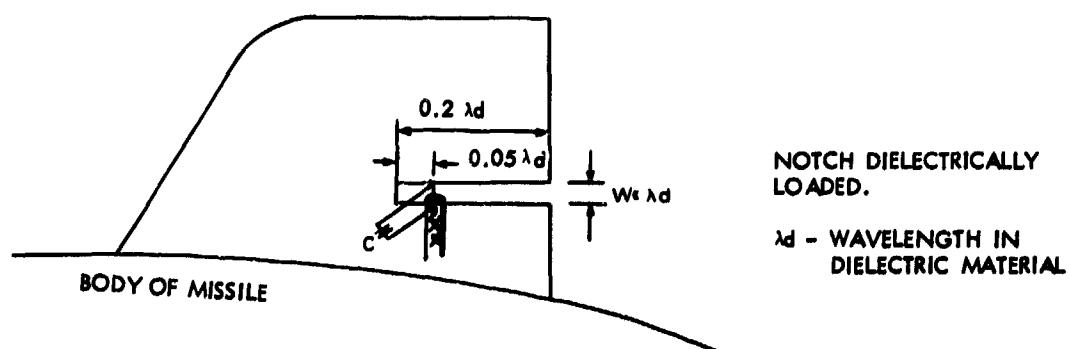
Fig. 6. $\lambda/4$ Resonant Spike Aerial.

Fig. 7. Notch Cut into the Trailing Edge of a Missile Tail Fin.

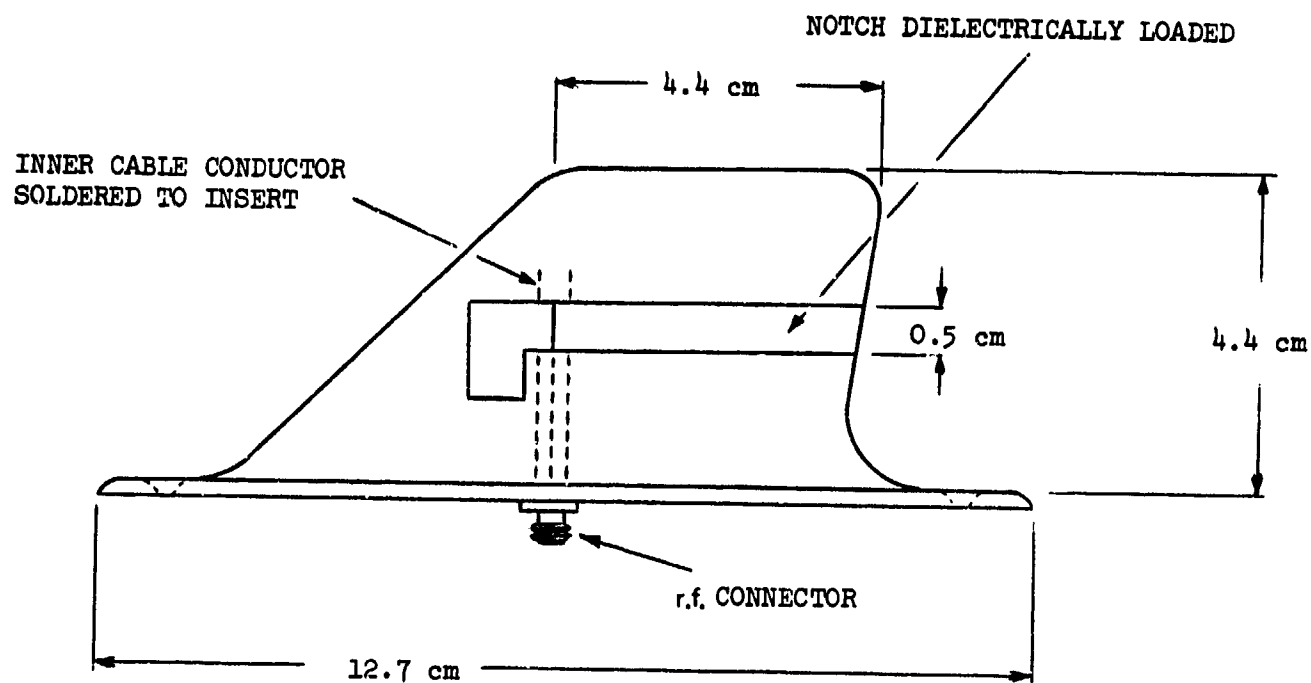


Fig.8. Upper L-Band Notch Blade Aerial.

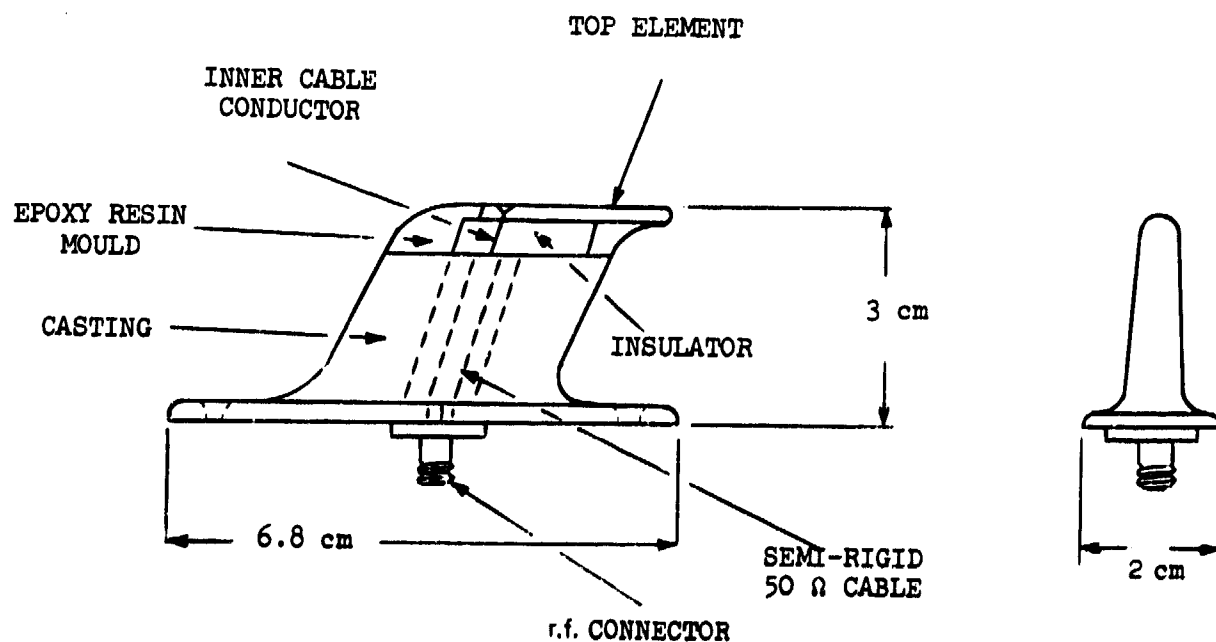


Fig.9. Upper L-Band Sleeve Aerial.

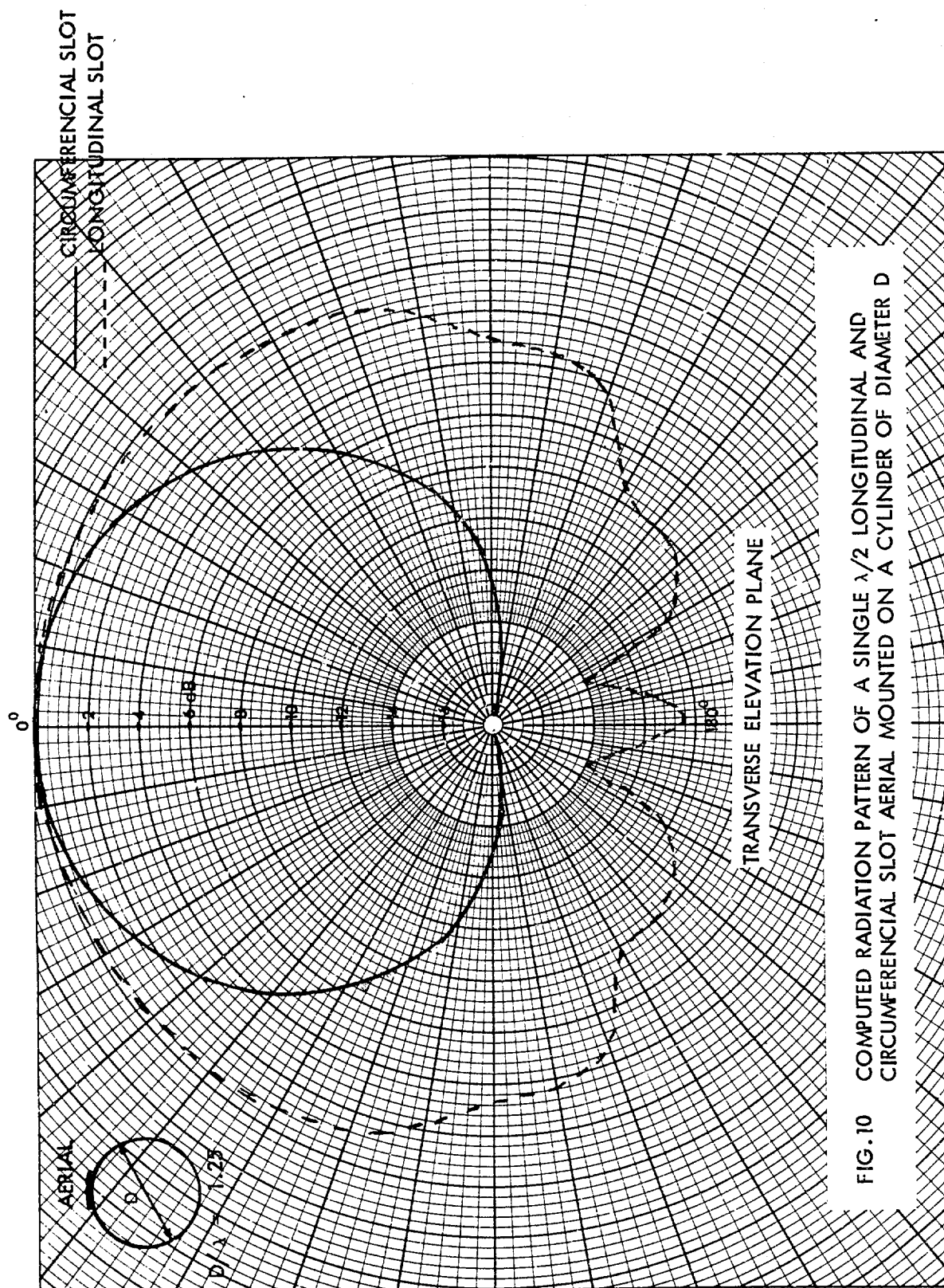
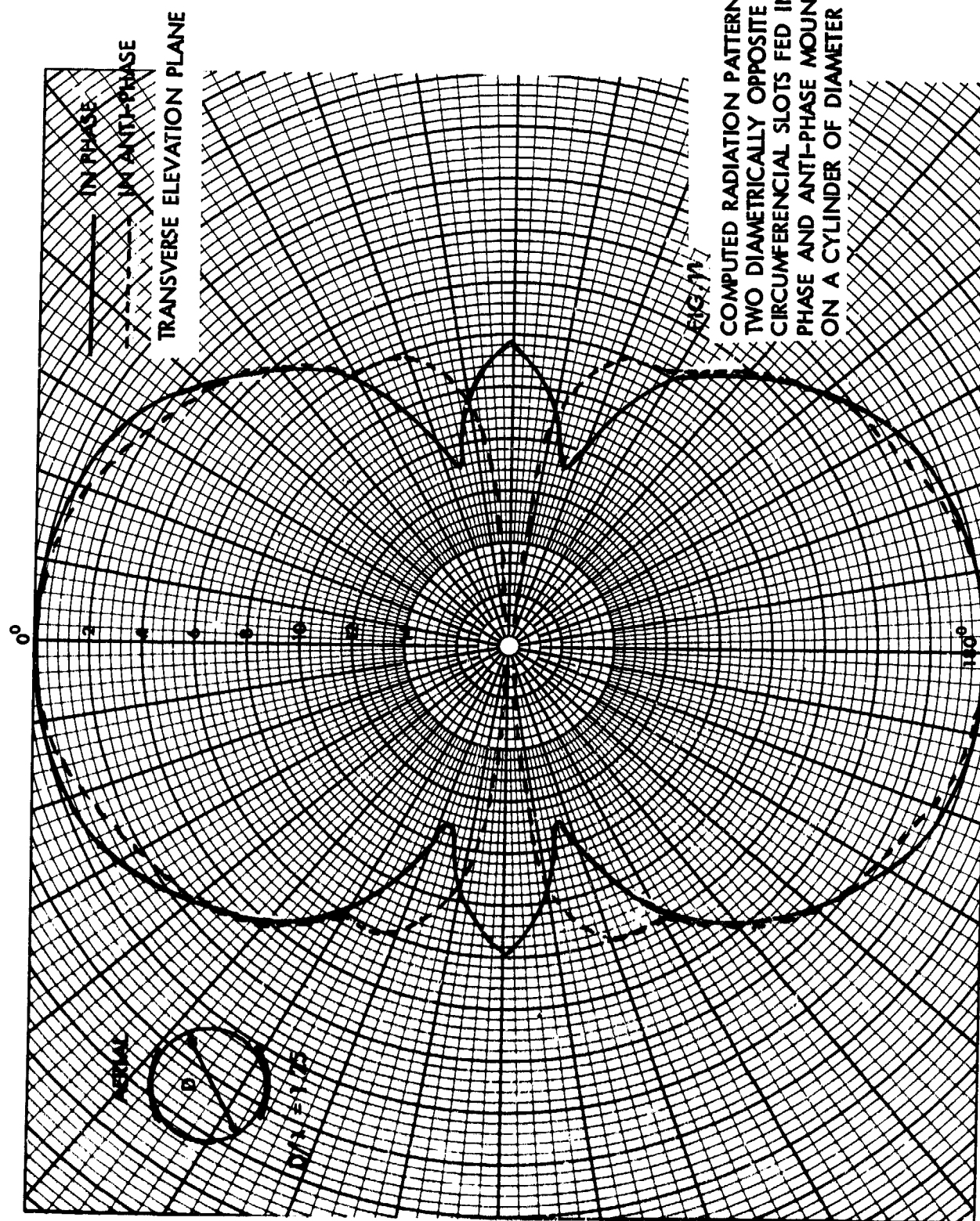


FIG. 10 COMPUTED RADIATION PATTERN OF A SINGLE $\lambda/2$ LONGITUDINAL AND CIRCUMFERENTIAL SLOT AERIAL MOUNTED ON A CYLINDER OF DIAMETER D



λ_d - WAVELENGTH IN
DIELECTRIC
SUBSTRATE

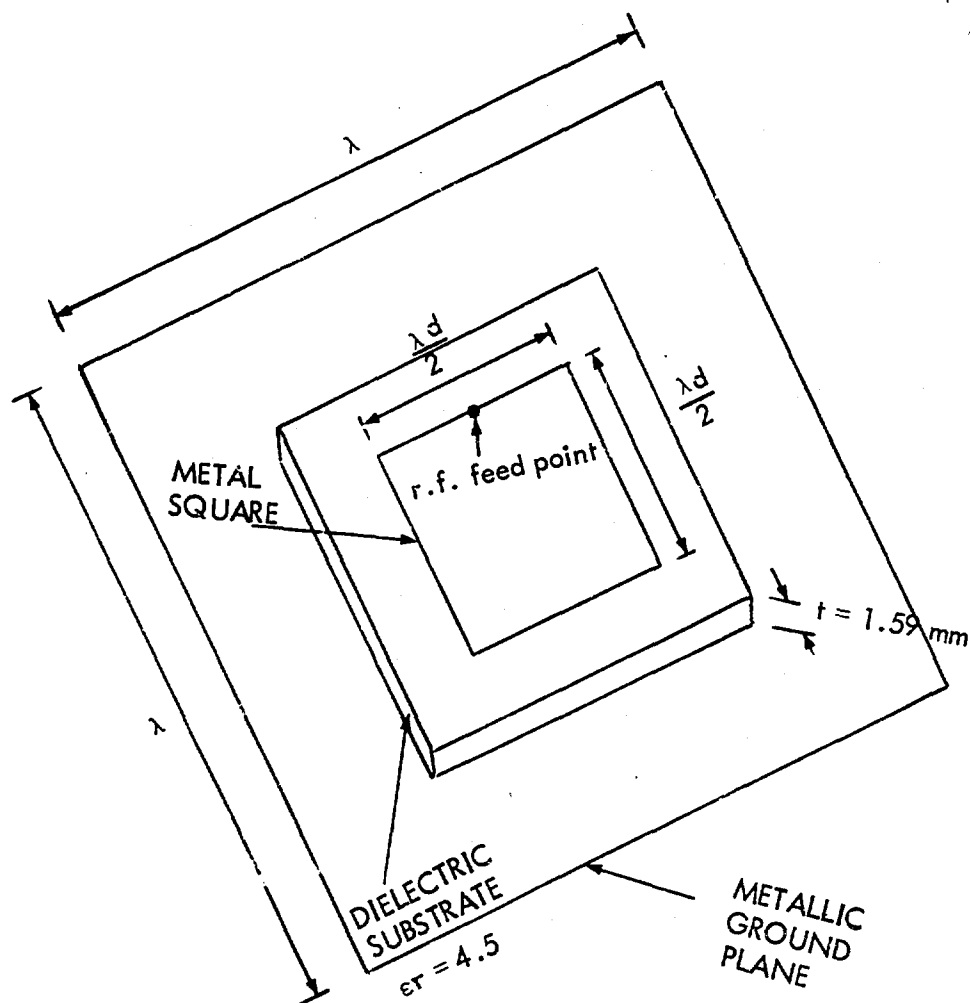


Fig.12. Upper L-Band Printed Board Aerial.

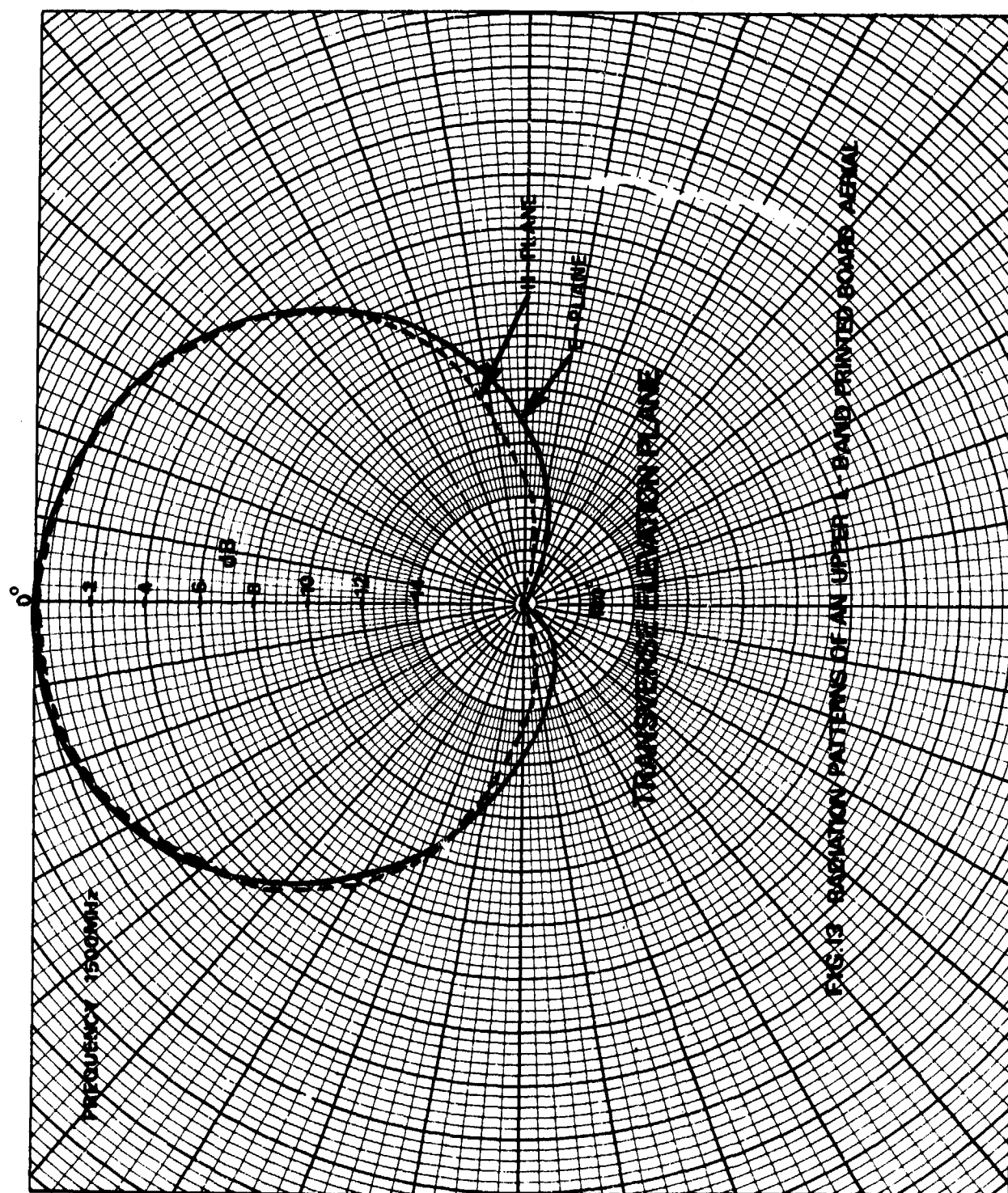


FIG. 13. RADIATION PATTERNS OF AN UPPER 1-BAND PRINTED BOARD AERIAL

ELECTRONICALLY SCANNED TACAN ANTENNA AS AN ENROUTE AND TERMINAL NAVIGATIONAL AID

Edward J. Christopher
Rome Air Development Center
Griffiss Air Force Base, New York 13441

SUMMARY

This paper describes the principles of operation of present mechanically rotated TACAN (Tactical Air Navigation) antenna systems and addresses their performance characteristics.

The manner in which these characteristics may be improved is addressed in an analysis of two (2) United States Air Force/Rome Air Development Center (RADC) contractual efforts which have resulted in the design, fabrication and test of two (2) experimental models of an electronically scanned TACAN antenna. RADC performed these efforts under the sponsorship of the AIMS/TRACALS System Program Office, Hanscom Field, Bedford, Massachusetts.

A TACAN antenna capable of providing full band operation and electronic scanning in a single radiating structure has been demonstrated. The array approach permits elevation pattern shaping. Through a combination of steep pattern slope at the horizon and low side lobes below the horizon, siting is less sensitive, i.e. bearing errors over the required spacial coverage of the TACAN system, which are introduced by the antenna environment, are minimized. There are no moving parts that require preventive maintenance and modular design should allow most repairs to be made in the field, reducing both mean time and mean cost to repair when compared with existing mechanical systems.

1. INTRODUCTION

TACAN is an air navigation system that provides to an aircraft its distance and bearing from a ground beacon within line of sight range. A brief explanation of TACAN system operation is given because a primary system function, that of providing bearing or azimuth information, is accomplished solely by the antenna subsystem. The key performance requirements of the antenna are critical to TACAN operation, and the TACAN function should be understood prior to discussion of the theory and design considerations of a cylindrical electronically scanned array for application to the TACAN system. Figure 1 illustrates the sequence of events involved between interrogation by the aircraft and the reply from the ground beacon transponder.

2. PERFORMANCE REQUIREMENTS

The purpose of the TACAN ground station is to transmit signals that enable an aircraft, equipped with multi-channel TACAN equipment, to fix its position relative to the ground station. The position is indicated as the distance in nautical miles of the aircraft from the ground station, and the magnetic bearing from the aircraft to the ground station. Because the system operates at ultra-high frequencies, transmission is limited to line of sight between the antenna of the TACAN ground station and the aircraft. A number of ground stations are necessary to cover a large geographical area; therefore, a multi-channel system is used. Each ground station is capable of receiving air-to-ground interrogations on any one of the two-hundred and fifty-two (252) assigned channels using one-hundred and twenty-six (126) frequencies from 1025 to 1150 MHz and each ground station can respond on any one of two-hundred and fifty-two (252) frequencies from 962 through 1215 MHz depending on channel assignment.

The basic elements of the ground station equipment comprises a radio beacon set; an antenna; power supplies, control, test, and monitor units. The ground station pulsed signal consists of distance measuring equipment (DME) replies, bearing reference signals, random pulses and station identification signals. The airborne equipment includes a multi-channel transceiver and visual bearing and distance indicators.

3. PRINCIPLE OF OPERATION

When the pilot selects a ground station, the airborne transmitter sends out distance interrogation pulses on the receiving channel frequency assigned to the ground station. As the pulses are received by the ground station, it triggers the transmitter, sending out reply pulses on its assigned transmitting channel. Timing circuits on the aircraft measure the time intervals between the interrogation and reply, and convert the time difference into a signal which operates the distance indicator.

Bearing information originates at the ground station and is multiplexed with the distance-measuring signals. The information derived at the aircraft is the compass heading (from magnetic north) from the aircraft to the ground station. The aircraft obtains this bearing by comparing the phase of two (2) modulated components imposed on the ground station transmitted signal output with the time occurrence of reference signal bursts also transmitted by the ground station. The ground antenna azimuth pattern, which is rotating, impresses this amplitude modulation on the pulse train of the transmitter, resulting in the signal-in-space from which bearing is derived.

Present ground beacon directional patterns are obtained from mechanically rotated antenna systems. (Greco, S.V., and Electrical Communications, 1956) Figure 2 provides diagrams of a mechanically rotated antenna system and radiation patterns. The system makes combined use of parasitic elements and a driven central antenna. Figure 2-A is the Limacon pattern obtained when energy from the central antenna strikes the 15 Hz parasitic element. Figure 2-B is the static 9-lobed pattern obtained when the 135 Hz parasitics intercept and reradiate energy from the central antenna. Figure 2-C is the resultant

pattern obtained due to the combined effects of the two (2) sets of parasitic elements. The composite pattern is mechanically rotated at 900 rpm.

Figure 3-A is a plot, in rectangular coordinates, of the cyclic variations in field strength of the radiated signal received by the aircraft as the antenna rotates. The composite azimuth pattern is shown in the polar plot of Figure 3-B.

In Figure 3-A the Limacon (15 Hz) pattern is represented as a sine wave in rectangular coordinates and the nine-lobed pattern superimposed on the Limacon is the ninth harmonic of the sine wave. Since the azimuth pattern rotation rate is one (1) full turn in 1/15th second, the radiation pattern of the antenna contains one (1) frequency component of the 15 Hz and a second frequency component, representing the ninth harmonic of the pattern's rotation, or 135 Hz. The complete signal radiated by the antenna contains both frequencies, and it is these two (2) frequencies which amplitude modulate the train of pulses transmitted by the ground station beacon in each azimuthal direction. The phase of these signals, with respect to the time occurrence of reference signal bursts, varies with azimuth.

To determine the aircraft bearing, the electrical phase of both the 15 Hz and 135 Hz signals must be measured. To measure the phase, fixed reference pulse bursts are transmitted during the rotation of the radiation pattern at specified instants. Separate reference signals are transmitted for the 15 Hz and 135 Hz waves. The reference signals are introduced into the pulse train whenever the reference group generator of the ground station is triggered by a pulse from the antenna control generator. The timing of the trigger is set to align the modulation to magnetic north. The north and auxiliary pulses are derived from and phased-locked with the 15 Hz and 135 Hz modulation. The time of arrival of these pulses relative to the zero-crossing of their respective modulating frequency waves is measured to find the aircraft bearing to the ground station.

Note in Figure 3 that the phase of the 15 Hz signal changes by 360 degrees as the aircraft flies one (1) orbit around the beacon. However, the aircraft receiver picks up not only the direct wave radiated by the antenna, but also waves reflected off large objects. Therefore, from the 15 Hz components of the wave, the aircraft obtains a compass heading to the ground station that indicates the direction of the ground station, but which may be several degrees in error.

This error is reduced by measuring the phase of the 135 Hz component of the wave. As the aircraft moves through 40 degrees of arc, the phase of the 135 Hz signal changes by 360 degrees. Thus, for every space degree change in bearing, there is a 9 degree change in phase. In other words, 1 degree of phase shift produces 1/9th degree change in azimuth indication at the aircraft. This reduces the 15 Hz bearing error ninefold. TACAN is basically a vernier system with coarse and fine information developed by the antenna used to provide azimuth bearing.

4. ANTENNA SYSTEM LIMITATIONS

The mechanically rotated TACAN antenna system is limited in vertical aperture since a large vertical aperture introduces mechanical rotation and wear problems. A limited aperture results in poor slope characteristics at the horizon intercept. This characteristic makes the antenna sensitive to both multipath and ground reflections which contribute to the formation of nulls in the vertical profile and errors in tracking accuracy due to distortion in the modulation side bands. To minimize the effects of ground reflections, a larger vertical aperture and improved phase and amplitude distribution is required. However a larger aperture introduces mechanical reliability problems when using the rotating parasitic approach.

A further limitation of the mechanical systems is that the geometry of the radiating elements restricts the achievable antenna bandwidth to half the TACAN frequency band. Therefore, two or more radiating structures are required to achieve full band coverage.

5. APPROACH

As a result of the limitations of the mechanical systems and with the increasing air traffic density problem it became evident that a more flexible antenna system was needed. Advancement in the state of the art in phased arrays showed much promise of employing a cylindrical electronically scanned array to provide the improved phase and amplitude distribution necessary to minimize the effects of ground reflections and to achieve all band coverage in a single radiating structure. However, an optimum solution had not been obtained to the problem of distributing the power in the azimuth plane to feed a cylindrical array with the correct phase and amplitude distribution and thereby provide the required azimuth Limacon and 9th harmonic pattern. Further, it had yet to be determined how this pattern would be rotated at a constant 900 rpm at all RF frequencies.

In March 1970, RADC under sponsorship of the AIMS/TRACALS System Program Office, Bedford, MA, awarded dual contracts to perform a study and investigation for the design of an all band electronically scanned cylindrical array compatible for use with the TACAN system. The contracts were awarded to the ITT Avionics Division Huxley, NJ and the RANTEC Division of the Emerson Electric Company, Calabasas, CA. Each contract consisted of two (2) phases, the first involved the study and design of a technique to meet the above needs. Phase II involved the fabrication and test of experimental models upon which the feasibility of the techniques developed under Phase I could be demonstrated. Prior to discussing the results of these efforts an analysis will be provided to better understand the limitations involved in the design of an electronically scanned TACAN antenna. (Hanratty, R.J., 1970)

5.1 Design Considerations

Several variables affect the 15 Hz and 135 Hz modulation characteristics. These include cylinder radius, array element density, element pattern, phase and amplitude modulation at each element and required elevation coverage. Figure 4 relates the amplitude modulation index to a factor, $\frac{R \cos \theta_{EL}}{A}$.

This factor defines the interrelationship between antenna radius (R), wavelength (λ), and elevation coverage (θ) when the radiating aperture is illuminated with amplitude modulation and a constant phase distribution. "Figure 4 shows the characteristic behavior of a cylindrical array as generated by computer simulation for a nine-lobed azimuth pattern using a modulation index of .35. The number of elements around the array was chosen to maintain circumferential spacings close to $.5\lambda$ for the various radii used. Note that for a given cylinder radius (R), increasing elevation angle (θ) corresponds to moving left along the curve and increasing frequency is indicated by movement to the right on the curve. This curve illustrates that if pattern lobing or modulation is to be larger than some design minimum only a limited range of antenna size, frequency, and elevation angle can be used. The modulation which is generated as the azimuth pattern is rotated is required to be between 12 and 30 per cent. It is also desirable to maintain the modulation index to as high an elevation angle as possible. Curves such as shown in Figure 4 allow these design requirements to be balanced and an optimum antenna radius to be chosen." (Shestag, L.N., 1970)

A far field amplitude modulation can also be generated by the rotating multilobed pattern when the radiating aperture is illuminated with phase modulation and a constant amplitude distribution. However, the use of pure phase modulation requires a cylinder of larger radius, to meet modulation specifications. To illustrate this, Table I which outlines the main objective of RADC's contractual requirements was prepared. To achieve the performance outlined in Table I a twelve (12) foot diameter cylindrical array would be needed if the aperture was phase modulated. If the aperture were illuminated with amplitude modulation, a five (5) foot diameter cylinder would be required. If consideration were given to illuminating the radiating aperture with a combination of phase and amplitude modulation a diameter intermediate to 5 and 12 feet would be required. Figure 5 represents the characteristic behavior of the particular cylindrical array required to meet the goals outlined in Table I. The shaded area bounds the limits within which the antenna system must be designed in order to achieve the desired frequency and elevation coverage, while maintaining a minimum cylinder radius. The shaded regions represent a cylinder of five (5) foot diameter. Therefore, to meet the bandwidth and elevation coverage outlined in Table I, a cylindrical array five (5) feet in diameter and which is excited with pure amplitude modulation is needed to provide the required TACAN performance characteristics over the complete frequency band, 960 to 1215 MHz.

The results of these considerations suggest that if nominal coverage at higher elevation angles, for example above 25 degrees, can be tolerated, a smaller diameter array, i.e., a diameter less than five (5) foot, capable of providing full band coverage and meeting most of the MIL-STD requirements can be achieved.

6. DATA ANALYSIS AND EVALUATION

The model's physical characteristics will now be described along with the modulation techniques employed. The anechoic chamber, field and flight test results are also provided.

The physical characteristics of the models are outlined in Table II. ITT's model is designated ESTA, for Electronically Scanned TACAN Antenna and the RANTEC model is referred to as the AT-100. The power requirement addressed in Table I refers to the AC power required to scan the modulated pattern and not the input RF power.

The Electronically Scanned TACAN Antenna (ESTA) consists of a cylindrical phased array of radiating elements capable of producing an omni-directional azimuth pattern, with a fundamental Limacon distribution and a 9th harmonic superimposed at nominal 20 per cent levels. The model shown in Figure 6 is 85 inches high, 65 inches in diameter and consists of 96 columns of 11 dipole elements each. This model uses digital modulation techniques for controlling radiating elements in place of the mechanically rotated parasitic elements previously used to modulate the bearing/distance pulsed RF transmission. Each vertical column radiates at a different amplitude and phase to generate the proper antenna pattern. RF energy enters the base of the array through an L-Band coaxial waveguide. A series of 64 digitally-controlled metal tabs in the waveguide, only one of which is shown in Figure 6, change the propagation mode at a 15 Hz rate, effectively modulating the RF at the desired coarse bearing signal rate. RF energy carrying the 15 Hz modulation waveform then goes through a 96:1 power divider and a distribution system to feed the 96 stacks of dipoles each one of which has a digital switch, located at the base of the vertical column, that turns on and partially off at the fine bearing modulation rate of 135 Hz.

Both digital controls are locked to a common clock to eliminate phase problems. The switching system actually steps a number of columns at one time to provide smooth rotation of the pattern in space.

After fabrication, the model was tested in the contractor's anechoic test chamber. Table III compares the results of these tests with the principal performance requirements.

The AT-100 model uses a cylindrical array to achieve all band TACAN coverage. The cylindrical array shown in Figure 7 is 96 inches high and 62 inches in diameter. It contains 36 columns of 12 elements each. The elements are wideband cavity radiators connected directly to the elevation beam shaping circuit. The circuit is a 12:1 power divider made up of two (2) 6:1 stripline networks that provide the correct phase and amplitude distribution to produce the required elevation pattern.

An analog modulator design has been selected. It is a split tee with a diode shunt on each output arm. Continuously varying the diode bias varies the ratio of power division between the two output ports. The modulation technique used is based on a characteristic of the TACAN azimuth modulation signal, which is: the sum of the voltages at diametrically opposite points on the antenna is a constant. There are 18 modulators feeding diametrically opposite columns of the array. The modulators operate such that when voltage is reduced on one side of the array in accordance with the modulation signal, it is added by the same amount to the opposite side of the array, thereby eliminating lossy downward modulation.*

*Patent Pending

The horizontal distribution network consists of four 3:1 power dividers and nine 2:1 power dividers to provide a distribution network from the beacon to feed the 18 modulators. The two (2) outputs on each of the 18 modulators provide the final inputs to the 36 columns. All power dividers are fabricated in stripline.

The electronic modulation generator provides all bias controls for the RF modulators and trigger signals to the beacon. This bias to the modulators is simultaneously varied at the 15 and 135 Hz rate to analog voltage modulators for rotating the composite radiation pattern (electronically) at 900 rpm.

The results of the anechoic test chamber measurements on the AT-100 are listed in Table IV.

As part of the contractual efforts reliability analysis were performed by both contractors. The analysis were based on a parts count approach using component failure rates taken primarily from MIL-HBK-217A "Reliability Stress and Failure Rates for Electronic Equipment". Tables V and VI constitute the definitions and the summarized information relative to the reliability analysis.

To better visualize the pattern coverage achieved, Figure 8, a measured elevation pattern taken at 1087 MHz has been plotted. It illustrates the high horizon slope, low negative (below horizon) side lobes, typically -16 dB across the frequency band and the excellent rejection to cross polarization, greater than -25 dB below the peak of the elevation beam. The two (2) dashed lines represent the limits within which the elevation coverage was to lie from the upper elevation 3 dB point to +50 degrees, to meet the requirements.

With the completion of the chamber tests, both models were field and flight tested at the United States Navy's Electronic Systems Test and Evaluation Facility (NESTEF) St. Inigoes, MD. The results of these tests have shown the following:

Closely verified the results of contractors' chamber tests;

Demonstrated that both models passed the azimuth accuracy requirements of Flight Inspection Manuals (AFM 55-8 and NAVAIR 16-1-1520) for enroute and approach radials.

7. SUMMARY

The performance limitations of mechanically rotated TACAN antennas, in particular operational bandwidth and sensitivity to ground reflections have been addressed. Design considerations have been described which considered the factors most pertinent to the achievement of all-band coverage in a single electronically scanned TACAN antenna.

As a result of the development efforts, two (2) experimental model TACAN antennas, each capable of providing all-band operation in a single electronically scanned radiating structure have been demonstrated. Such a system offers the following features:

a. The array approach permits controlled elevation pattern shaping to provide a combination of steep pattern slope at the horizon intercept and low below horizon side lobes thereby reducing site generated bearing errors and increasing accuracy of the system from an operational standpoint.

b. The absence of moving parts will reduce preventive maintenance requirements.

c. Modular design will allow most repairs to be made in the field thereby:

(1) Minimizing down time.

(2) Providing increased system availability.

(3) Reducing the meantime to repair and meancost to repair when compared with existing mechanical systems.

8. REFERENCES

Greco, S. V., "TACAN-Principles and Siting Criteria", September 1968.

"TACAN", Electrical Communications, Vol. 33 - 1956.

Hanratty, P. J., January 1970, "An Electronically Steered Array Antenna for TACAN", Proceedings of the NELC Conformal Array Antenna Conference.

Shestak, L. N., January 1970, "Scanning A Multi-Lobed Pattern With A Cylindrical Array", prepared for Conformal Array Antenna Conference.

ELECTRONICALLY SCANNED TACAN ANTENNA PERFORMANCE REQUIREMENTS

TABLE 1

FULL-BAND OPERATION 960 - 1215 MHz
 NONROTATING ANTENNA (ELECTRICALLY SCANNED)
PATTERN CHARACTERISTICS

SLOPE ON HORIZON	> .2 VOLT/DEG (NORMALIZED TO 1.0 V AT HORIZON)
GAIN	> 6 DB AT PEAK OF ELEVATION BEAM
ELEVATION COVERAGE	CSC θ IN VOLTAGE, WITHIN ± 2 DB, FROM UPPER 3 DB TO 50°
CROSS-POLARIZATION	AT LEAST -20 DB
SIDE LOBE LEVEL	BELOW HORIZON, MINIMUM OF -18 DB

EXPERIMENTAL MODELS PHYSICAL CHARACTERISTICS

TABLE 11

	ESTA	AT-100
Height	85 inches	96 inches
Weight	1050 pounds (Antenna and Electronics)	750 pounds (Antenna and Electronics)
Diameter	65 inches	62 inches
Scanning Modulator Power Requirements	less than 150 Watts	less than 150 Watts
Array Columns	96	36
Elements per Column	11 Dipole Elements	12 Radiating Cavity Elements

Both antennas achieved all-band coverage in a single radiating structure.

MEASURED TEST CHAMBER DATA "ESTA" MODEL

TABLE 111

RADC PERFORMANCE REQUIREMENTS	CONTRACTORS TEST CHAMBER DATA
Operational Bandwidth 960 - 1215 MHz	All Band Coverage Achieved
Slope Rate of Change of Signal Level Within $+2^\circ$ of Horizon .2 V/Degree When Normalized to 1 V at the Horizon	Varied Between .26 to .36 V/Degree Over the Frequency Band
Per Cent Modulation: Meet MIL-STD 291-B Requirements of $21\% \pm 9\%$, for 0° to $+50^\circ$ Elevation Angles Over the Full TACAN Frequency Band	15 Hz Sideband 0° to 50° Met MIL STD Requirements 135 Hz Sideband 0° to 40° Met MIL STD Requirements 135 Hz Sideband 40° to 50° From 960 to 1080 MHz Varied Between 5 to 10%
Phase Tracking (Bearing Accuracy) 15 Hz $\pm 3.0^\circ$ 135 Hz $\pm .3^\circ$ } Maximum	Peak of Pattern (6° Elevation) $\pm 4^\circ$ } Ave. \leftarrow 15 Hz $\rightarrow 9.8^\circ$ } Maximum Excursions $\pm .8^\circ$ } \leftarrow 135 Hz $\rightarrow 2.0^\circ$ }

MEASURED TEST CHAMBER DATA "AT-100" MODEL

TABLE 1V

RADC PERFORMANCE REQUIREMENTS	CONTRACTORS TEST CHAMBER DATA
Operational Bandwidth 960 - 1215 MHz	All Band Coverage Achieved
Slope Rate of Change of Signal Level Within $+2^\circ$ of Horizon .2 V/Degree When Normalized to 1 V at the Horizon	Varied Between .22 to .35 V/Degree Over the Frequency Band
Per Cent Modulation: Meet MIL STD 291-B Requirements of $21\% \pm 9\%$, for 0° to $+50^\circ$ Elevation Angles Over the Full TACAN Frequency Band	15 Hz Sideband 0° to 50° Met MIL STD Requirements 135 Hz Sideband 0° to 40° Met MIL STD Requirements 135 Hz Sideband 40° to 50° From 960 to 1080 MHz Varied Between 5 to 12%
Phase Tracking (Bearing Accuracy) 15 Hz $\pm 3.0^\circ$ 135 Hz $\pm .3^\circ$ } Maximum	Peak of Pattern (6° Elevation) $\pm .6^\circ$ } Ave. \leftarrow 15 Hz $\rightarrow + 6.0^\circ$ } Maximum Excursions $\pm .2^\circ$ } \leftarrow 135 Hz $\rightarrow + 1.0^\circ$ }

RELIABILITY FACTORS

TABLE V

<u>MEAN TIME BETWEEN FAILURE (MTBF)</u>	THE MEAN TIME BEFORE ANY FAILURE WILL OCCUR, THE FAILURE MAY OR MAY NOT ALARM THE MONITOR
<u>MTBF (WITH REDUNDANCY)</u>	THE MEAN TIME BEFORE ANY FAILURE WILL OCCUR USING REDUNDANT POWER SUPPLIES
<u>MTBF - SOFT FAILURE MODE (SFM)</u>	<u>SOFT FAILURE:</u> THE PRESENCE OF A FAILURE WHICH CONTINUES TO ALLOW THE SYSTEM TO OPERATE WITHIN SPEC BUT IN A DEGRADED MODE, i.e. NOT AT PEAK EFFICIENCY. <u>MTBF-SFM:</u> NUMBER OF HOURS SYSTEM WILL OPERATE, WITHIN SPEC, BEFORE CUMULATIVE SOFT FAILURES ALARM THE MONITOR.
<u>MTBF-SFM (WITH REDUNDANCY)</u>	MTBF-SFM WHEN REDUNDANT POWER SUPPLIES ARE AVAILABLE

PREDICTED RELIABILITY PERFORMANCE

TABLE VI

<u>ESTA</u>	<u>MTBF</u>	<u>AT-100</u>
(21.1K) 21.1Khrs (55K) 31.1Khrs	ANTENNA ASSEMBLY	(62.8K) 62.8Khrs
(15.2K)*1 12.6Khrs*2	CONTROL UNIT	(57K) 38.0Khrs
*2	SUB SYSTEM	(29.9K)*1 23.5Khrs
<u>(MTBF-SFM)</u>		
(107K) 107Khrs (55K) 37Khrs	ANTENNA ASSEMBLY	(128.7K) 128.7Khrs
(36.4K)*2 27.5Khrs	CONTROL UNIT	(57.0) 38.0Khrs
*3	SUB SYSTEM	(39.7K)*3 29.3Khrs

- *1 MTBF WITH REDUNDANT POWER SUPPLIES
 *2 COMPUTED BY RADC RELIABILITY BRANCH USING CONTRACTORS FAILURE RATES.
 *3 MTBF-SFM WITH REDUNDANT POWER SUPPLIES

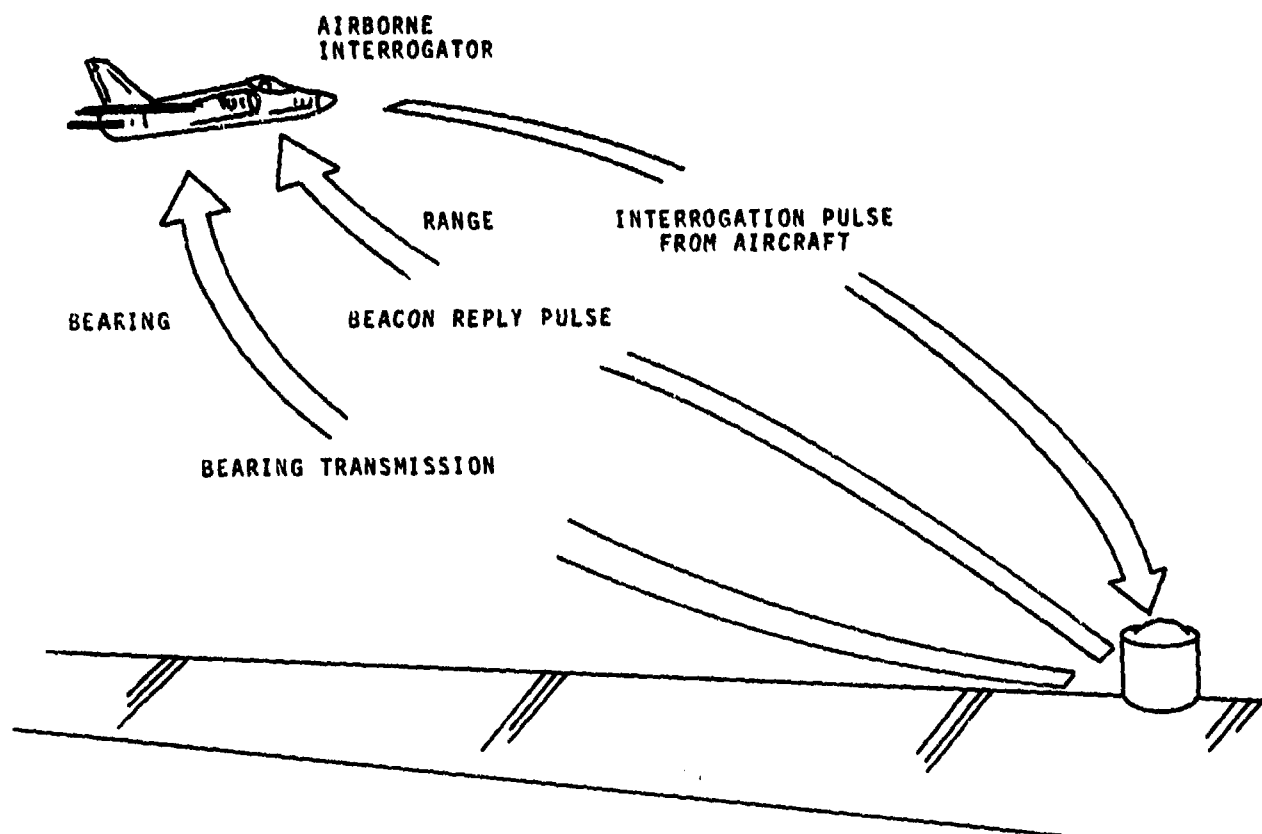


FIGURE 1 TACAN SYSTEM

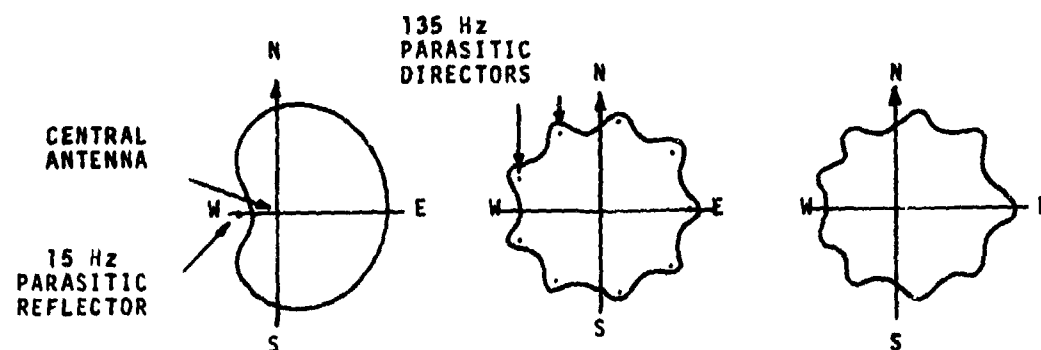


FIGURE 2-A

FIGURE 2-B

FIGURE 2-C

TACAN PATTERN CHARACTERISTICS

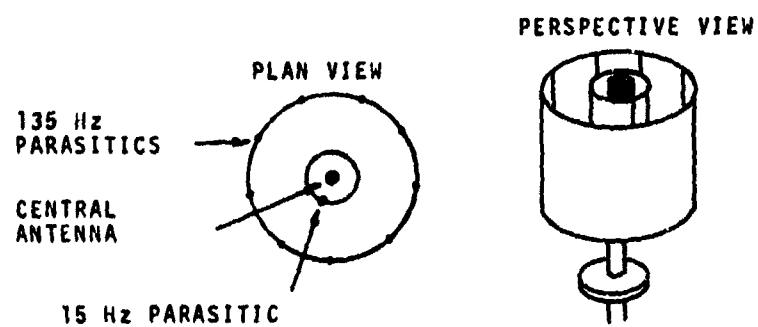


FIGURE 2 MECHANICALLY ROTATED TACAN ANTENNA

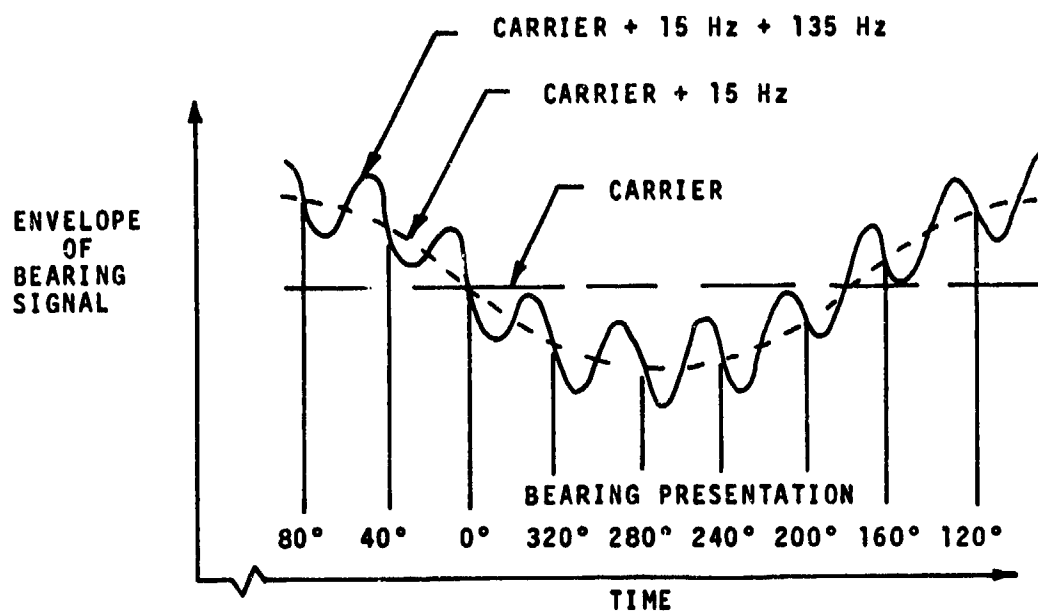


FIGURE 3A

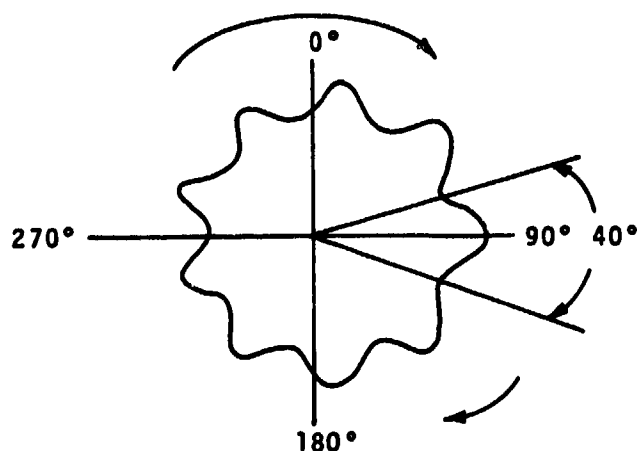


FIGURE 3B

FIGURE 3 COMPOSITE AZIMUTH PATTERN

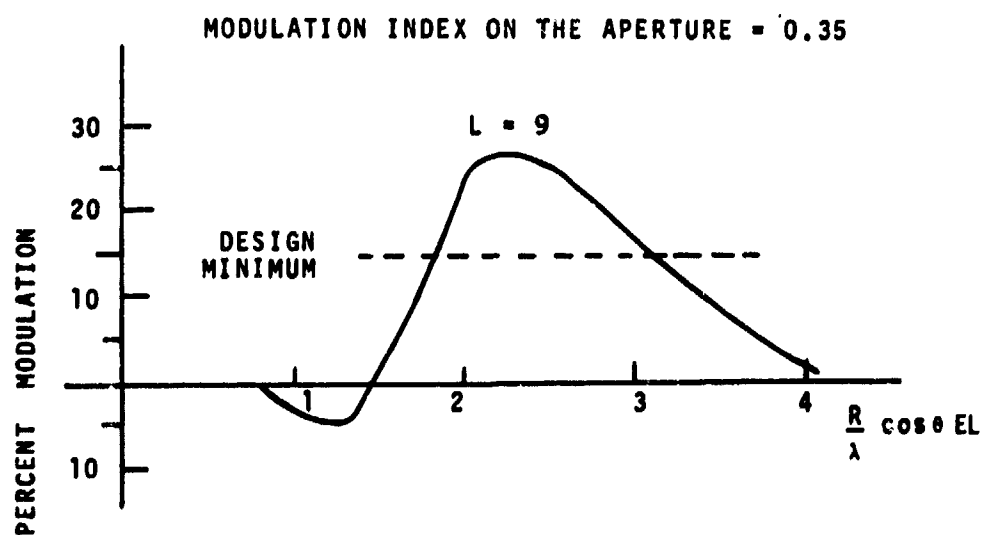


FIGURE 4 AMPLITUDE MODULATION CHARACTERISTICS

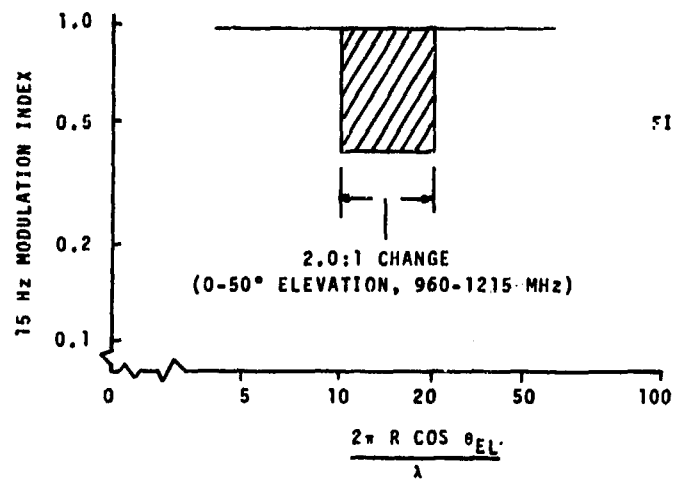


FIGURE 5A

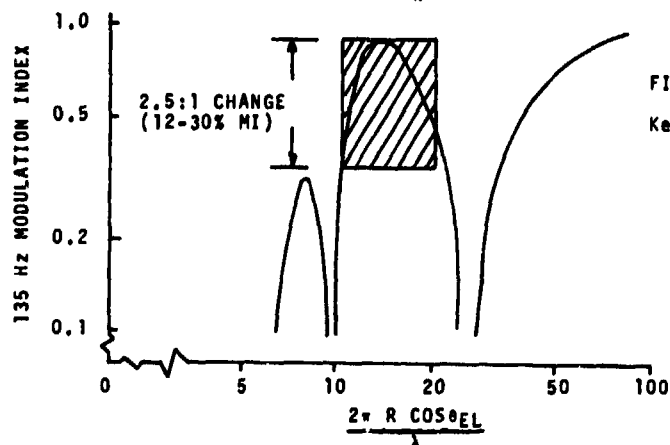


FIGURE 5B

Key:

R = RADIUS OF CYLINDRICAL
ARRAY

θ_{EL} = ELEVATION ANGLE TO
OBSERVATION POINT

λ = WAVELENGTH OF OPERATION

FIGURE 5 DESIGN CHARACTERISTICS

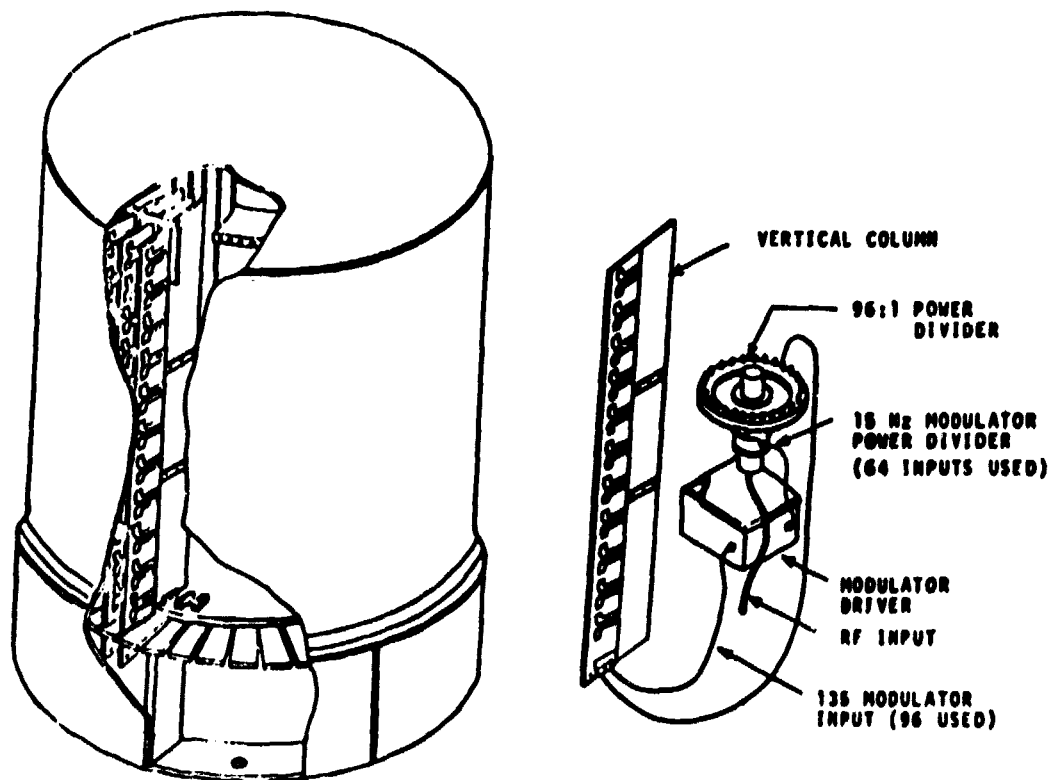


FIGURE 6 "ESTA" ANTENNA MODEL

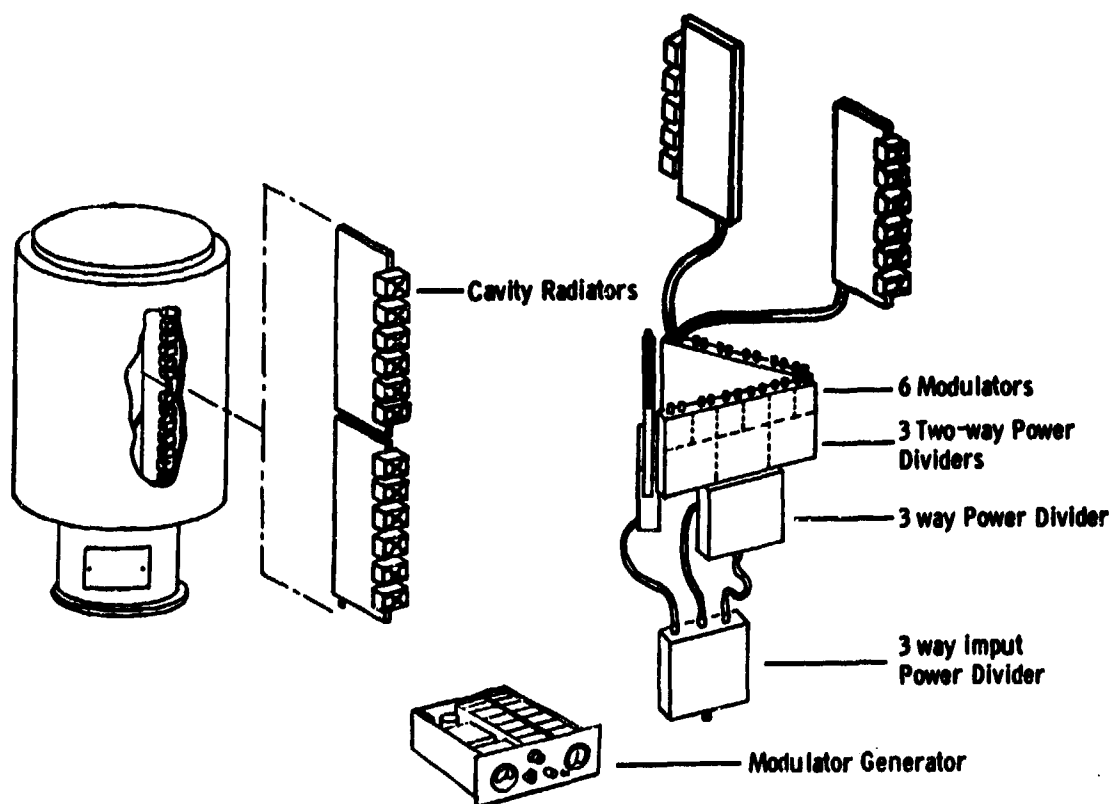


FIGURE 7 "AT-100" ANTENNA MODEL

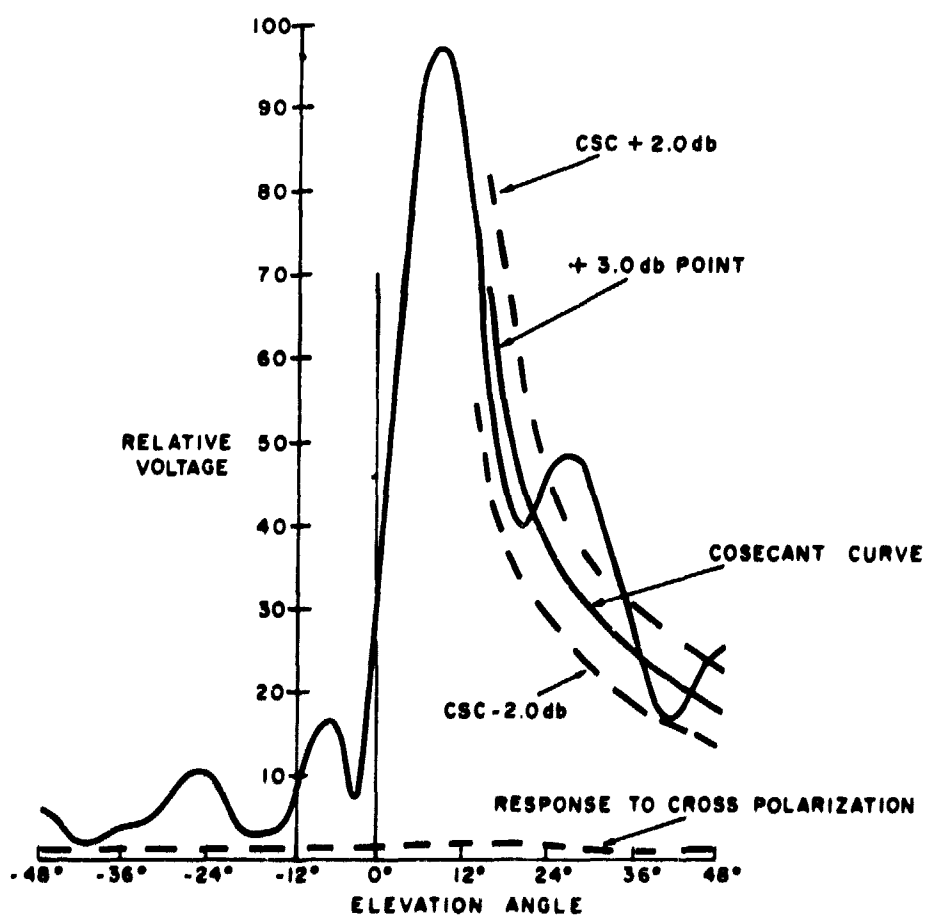


FIGURE 8 MEASURED ELEVATION PATTERN

ANALYSIS OF FINITE ARRAYS OF RECTANGULAR
APERTURES ON CONDUCTING DIELECTRIC COATED
CYLINDERS

J. Vogt
 AEG - TELEFUNKEN
 79 Ulm
 Germany

SUMMARY

The aim of the presented theory is to investigate the influence of mutual coupling and creeping waves on the performance of a phased array antenna, consisting of a finite number of apertures flush-mounted on the surface of an infinite conducting cylinder with a concentric dielectric covering. The numerical results show that mutual coupling effects are reduced due to the cylindrical structure of the surface, but are increased due to the dielectric covering.

1. INTRODUCTION

Recently there is an increasing interest in so-called conformal arrays, particularly in circular and cylindrical arrays. Flush-mounted antennas, for example apertures on cylinders, have ideal aerodynamic properties and become more and more used in airborne radiating systems.

In rockets and missiles one can save much place, if the radiating structure is built right into the radome or if it is placed near the radome wall. This integrated radome antenna concept is called "radant".

A simple approach to such a radant is the dielectric coated metallic cylinder with flush-mounted antennas. Beam scanning can be performed electronically. Because in a radant the radiators are located near or directly on the surface of the air- or spacecraft, the radiation patterns and the antenna near-field are substantially affected by this surface.

The purpose of the presented analysis is the investigation of such effects on the performance of antennas flush-mounted on the surface of a conducting dielectric coated cylinder.

The theory takes into account all electromagnetic interaction between the apertures and the effects due to the structure of the cylinder and the concentric coating.

In contrast to most of the recent publications, the array and the apertures are assumed to be finite.

2. MUTUAL COUPLING IN A FINITE ARRAY OF RECTANGULAR
 APERTURES ON A CONDUCTING DIELECTRIC COATED CYLINDER

2.1 Structure Geometry

The axis of the circular cylinder and the concentric electric coating is assumed to be the z axis of an xyz rectangular coordinate system. A $\varphi\psi z$ cylindrical coordinate system is associated with the xyz system in the usual manner. The metallic cylinder is assumed to be infinitely long and to have the outer radius a ; the concentric layer of homogeneous lossless dielectric has the outer radius b ($b \geq a$). The radiators in consideration are the open ends of the feeding rectangular TE-waveguides. The center of an aperture i is described by $(\varphi = \alpha, \psi = \psi_i, z = z_i)$. For simplicity it is supposed that all apertures are of equal dimensions $2h$ by $2d$, and that they are all oriented parallel to the z axis. The cylinder radius a is assumed to be large compared to the aperture width $2d$, therefore it is possible to consider the aperture planar with negligible error.

The waveguides are ideal; their dimensions are such that only the dominant mode is above cutoff.

2.2 The Electromagnetic Fields in the Regions $a \leq \rho \leq b$ and $\rho > b$

Following Wait [1], it is possible to synthesize a solution of the cylindrical wave equation in the region $a \leq \rho \leq b$ (region I) and the region outside the cylinder $\rho > b$ (region II) by superposition of the appropriate cylindrical Fourier transforms.

The expansions of the external fields in the two regions contain six unknown coefficients $A_\mu, B_\mu, C_\mu, D_\mu, E_\mu, F_\mu$ which can be determined by applying the following six tangential boundary conditions:

$$E_{\varphi I}(a, \varphi, z) = \begin{cases} E_{\varphi A} & \text{in the aperture,} \\ 0 & \text{outside the aperture.} \end{cases} \quad (1)$$

$$E_z I(a, \varphi, z) = \begin{cases} E_{zA} & \text{in the aperture,} \\ 0 & \text{outside the aperture.} \end{cases} \quad (2)$$

$$E_{\varphi I}(b, \varphi, z) = E_{\varphi II}(b, \varphi, z), \quad (3)$$

$$E_z I(b, \varphi, z) = E_z II(b, \varphi, z), \quad (4)$$

$$H_{\varphi I}(b, \varphi, z) = H_{\varphi II}(b, \varphi, z), \quad (5)$$

$$H_z I(b, \varphi, z) = H_z II(b, \varphi, z). \quad (6)$$

In (1), (2) \vec{E}_A is the transversal electric field in the aperture ("internal field") which may be expressed as a summation of all possible waveguide modes.

$$\vec{E}_A = \sum_p \vec{E}_A^p = \sum_p U^p \cdot \vec{r}^p. \quad (7)$$

The associated magnetic internal field is

$$\vec{H}_A = \sum_p \vec{H}_A^p = \sum_p I^p \cdot \vec{h}^p, \quad (8)$$

where the mode function $\vec{h}^p(\varphi, z)$ is orthogonal with respect to $\vec{r}^p(\varphi, z)$. The external field is by means of (1), (2) uniquely determined in terms of the tangential electric field on the cylinder surface.

2.3 Derivation of the Mutual Admittances

2.3.1 Mode Coupling in the Radiation Field of a Single Aperture

The internal complex power flowing through the feeding waveguide - in the following a single aperture is considered - is the sum of the powers of all individual modes without any coupling between the modes.

$$P = \frac{1}{2} \int_A (\vec{E}_A \times \vec{H}_A^*) \cdot d\vec{A}; \quad (9)$$

$$P = \frac{1}{2} \sum_p U^p \cdot I^{p*}; \quad (10)$$

$$P = \sum_p P^p. \quad (11)$$

This fact results from the boundary conditions in the waveguide and can be shown by means of the orthogonality of the vector mode functions \vec{r}^p and \vec{h}^p . Inside the waveguide there is no mutual coupling between the individual modes.

This does no longer hold true for the radiation fields outside the waveguide. In the external region $\rho > b$ a mutual coupling exists between the radiation field produced by a mode p and the radiation field produced by a mode q .

So the internal waveguide power of each mode, P^p , splits up into a pure self radiation power and into an infinite set of powers to maintain mutual coupling between the modes.

$$P_{int}^p = \sum_q P_{ext}^{pq}; p = 1, \dots, \infty. \quad (12)$$

Defining a complex mutual admittance

$$Y_{pq} = \frac{P_{ext}^{pq}}{\frac{1}{2} U^p U^q} \quad (13)$$

and using the result (10), expression (12) becomes

$$\sum_q Y_{pq} \cdot U^q = I^p; p = 1, \dots, \infty. \quad (14)$$

The coupling power P_{ext}^{pq} is produced by the electric radiation field \vec{E}^p due to the mode U^p together with the magnetic radiation field \vec{H}^q due to the mode U^q .

$$P_{ext}^{pq} = \frac{1}{2} \int_A (\vec{E}^p \times \vec{H}^{q*}) \cdot d\vec{A}; (A = \text{waveguide cross section}). \quad (15)$$

The integration in the $(\varphi = a, \varphi, z)$ space may be extended over the whole cylinder surface since $\vec{E}_{\text{tang}} = 0$ outside the aperture. This leads - using the orthogonality of the cylindrical Fourier transforms - to an integration in the so-called wave number space k_z (along z).

$$P_{ext}^{pq} = \frac{1}{2} \cdot a \cdot 4\pi^2 \sum_{\mu=-\infty}^{+\infty} \int_{-\infty}^{+\infty} (\vec{E}_{\varphi}^p \vec{H}_z^{q*}) dk_z. \quad (16)$$

In (16), the E_z -component was neglected for simplicity, because this component is usually very small compared to the E_{φ} component.

$\vec{E}_{\varphi}^p(\mu, k_z)$, $\vec{H}_z^q(\mu, k_z)$, are the Fourier transforms of $\vec{E}_{\varphi}^p(\varphi, z)$, $\vec{H}_z^q(\varphi, z)$, for fixed $\varphi = a$.

$$\vec{E}_{\varphi}^p = \underline{C}^p(\mu) \cdot \underline{D}^p(k_z), \quad (17)$$

$$\underline{C}^p(\mu) = \frac{1}{2\pi} \int_{-\varphi_0}^{+\varphi_0} \underline{U}^p(\varphi) e^{j\mu\varphi} d\varphi, \quad (18)$$

$$\underline{D}^p(k_z) = \frac{1}{2\pi} \int_{-h}^{+h} \underline{t}_2^p(z) e^{jk_z z} dz. \quad (19)$$

$$\underline{t}_2^p(\varphi, z) = \underline{t}_1^p(\varphi) \cdot \underline{t}_2^p(z). \quad (20)$$

Following Wait [1]

$$\vec{H}_z^q = \underline{C}^q(\mu) \cdot \underline{D}^q(k_z) \Lambda^2 [f(\mu, k_z) H_{\mu}^{(2)}(\Lambda a) + g(\mu, k_z) J_{\mu}(\Lambda a)]. \quad (21)$$

For an assumed harmonic time dependence $e^{j\omega t}$ the function Λ is given by

$$\Lambda = \begin{cases} +\sqrt{k_0^2 \epsilon_r - k_z^2} & ; k_z \leq k_0 \sqrt{\epsilon_r} \\ -j\sqrt{k_z^2 - k_0^2 \epsilon_r} & ; k_z > k_0 \sqrt{\epsilon_r} \end{cases} \quad (22)$$

The expressions $f(\mu, k_z)$, $g(\mu, k_z)$ refer to the coefficients b_{μ} , D_{μ} and depend only on the geometry of the cylinder resp. the dielectric layer.

With (17) and (21) the mode coupling (16) becomes

$$P_{ext}^{pq*} = \frac{1}{2} \cdot a \cdot 4\pi^2 \sum_{\mu=-\infty}^{+\infty} \underline{C}^{p*}(\mu) \underline{C}^q(\mu) \int_{-\infty}^{+\infty} \underline{D}^{p*}(k_z) \cdot \underline{D}^q(k_z) \Lambda^2 [f(\mu, k_z) H_{\mu}^{(2)}(\Lambda_1 a) + g(\mu, k_z) J_{\mu}(\Lambda_1 a)] dk_z. \quad (23)$$

The mutual admittance expression (13) for the mode coupling of a single aperture can be determined by means of (23).

2.3.2 Mutual Coupling in the Radiation Field of an Array of Apertures

Supplementary to (15) the expression of the mutual coupling comprises now the mode coupling p, q and - in addition to it the mutual coupling between the apertures, for instance the apertures i and k .

$$P_{ik}^{pq} = \frac{1}{2} \int_{A_i} (\vec{E}_i^p \times \vec{H}_k^{q*}) \cdot d\vec{A}_i; \quad (24)$$

where the integration is over the aperture i . H_k^{pq} is the magnetic radiation field of the aperture k (due to a mode q) measured on the aperture i .

With the transformations

$$\psi_i = \psi_k + \alpha_{ik}; z_i = z_k + \zeta_{ik}; \alpha_{ik} = \psi_i - \psi_k; \zeta_{ik} = \zeta_i - \zeta_k \quad (25)$$

and through (16), (17) with additional index i and (21) with index k the complex power (24) becomes

$$P_{ik}^{pq} = \frac{1}{2} \cdot a \cdot 4\pi^2 \sum_{\mu} e^{j\mu\alpha_{ik}} C_i^p(\mu) C_k^{q*}(\mu) \int_{-\infty}^{+\infty} D_i^p(k_z) D_k^{q*}(k_z) \Lambda^2 Z(\mu, k_z) e^{j\zeta_{ik} k_z} dk_z. \quad (26)$$

The mutual admittance is now defined by

$$Y_{ik}^{pq} = \frac{P_{ik}^{pq*}}{\frac{1}{2} U_i^{pq*} U_k^q}, \quad (27)$$

where P_{ik}^{pq} is given by (26). The system of N coupled apertures with M assumed modes is now described by

$$\sum_{k=1}^N \sum_{q=1}^M Y_{ik}^{pq} \cdot U_k^q = I_i^p; \quad p=1, \dots, M; \quad i=1, \dots, N. \quad (28)$$

If it is supposed that only the first mode ($p=1$) is above cutoff whereas the higher modes $p > 1$ do not propagate, the currents and voltages can be decomposed [3] into

$$U_k = U_k^+ + U_k^-; I_k = I_k^+ - I_k^- \quad (29)$$

where

$$I_k^+ = \frac{U_k^+}{Z_F}; \quad I_k^- = \frac{U_k^-}{Z_F} \quad (30)$$

and

$$I_k^p = -\frac{U_k^p}{Z_F^p}; \quad p > 1 \quad (31)$$

with

$$Z_F^p = \begin{cases} Z_F & p=1 \\ jX_F^p & p>1 \end{cases} \quad (32)$$

the characteristic waveguide impedance of the mode p .

(28) reduces now to

$$\sum_{k=1}^N \sum_{q=1}^M (Y_{ik}^{pq} + \delta_{ik}^{pq} \frac{1}{Z_F^p}) \cdot U_k^q = 2I_i^+ \cdot \delta^{p1} \quad (33)$$

where

$$p = 1, \dots, M$$

$$i = 1, \dots, N$$

$$\text{and } \delta_{ik}^{pq} = \begin{cases} 1; p=q; i=k \\ 0; \text{else.} \end{cases}$$

2.3.3 Example: Ring of Apertures on a Dielectric Coated Cylinder

Evaluating expression (26), (27) for a ring of axial apertures with $\zeta_{ik} = 0$ one finds for assumed TE_{m0} modes with uneven m the following mutual admittance expression:

$$Y_{ik}^{mn} = \frac{2ak_0}{Z_0(hk_0)^3 dk_0} \cdot \varphi_0^2 \cdot mn(-1)^{\frac{m-1}{2}} (-1)^{\frac{n-1}{2}} \cdot \sum_{\mu=0}^{\infty} \frac{\sin^2(\mu\varphi_0)}{(\mu\varphi_0)^2} \frac{\cos(\mu\alpha_{ik})}{(1+\delta_0^{\mu})} \cdot \int_0^{\infty} \frac{\cos^2(yk_0 h)}{((\frac{m\pi}{2hk_0})^2 - y^2)((\frac{n\pi}{2hk_0})^2 - y^2)} \cdot j\sqrt{\epsilon_r - y^2} \frac{\partial \mu(y)}{\partial y} dy. \quad (34)$$

where the complex functions $\underline{u}_\mu(y)$, $\underline{d}_\mu(y)$ are given explicitly by Knop [2]. For symmetry of the considered ring array with respect to the z axis, only the TE_{m0} modes with uneven m are possible.

2.4 Further Array Data

The mode voltages \underline{U}_k^g in (33) are readily computed by numerical methods. The \underline{U}_k^g represent the response of the array to a special excitation \underline{I}_k^g . All other parameters of the array can be calculated by means of the system response \underline{U}_k^g . The far field patterns may be derived from the rigorous field solution using the saddle-point method [1]. The array element gain function (all radiators are terminated except the element of interest) is computable through the array network data (active admittances, reflection coefficient) and the far field expression.

2.5 Numerical Results

Fig. 1 shows the E-plane gain function of a single aperture on a metallic cylinder with and without dielectric layer. The gain is referred to the matched isotropic radiator. The radius of the cylinder is $2\lambda_0$ (λ_0 = vacuum wavelength), the thickness of the layer is $0.1\lambda_0$. The rectangular aperture is of dimensions 0.72 by $0.16\lambda_0$ according to an angular width of 4.776° . The relative dielectric constant of the lossless layer is 2.1 . The one mode (TE_{10}) computation of the aperture admittance referred to the waveguide admittance yields the following results:

- a) $\underline{Y}_A = 0.45 + j 0.41$ for $\epsilon_r = 1$
- b) $\underline{Y}_A = 0.81 + j 1.06$ for $\epsilon_r = 2.1$

These data agree very well with measured data of apertures in an "infinite" perfectly conducting plane.

Fig. 2 refers to an array of 9 apertures of same dimensions as before. The apertures are parallel to the z axis with no axial separation ($\underline{z}_{jk} = 0$). The angular distance of the radiators is 8° . The apertures are terminated except the central aperture (no. 5) which is driven. The computed admittances of aperture no. 5 are

- a) $\underline{Y}_A = 0.44 + j 0.49$ for $\epsilon_r = 1$
- b) $\underline{Y}_A = 0.98 + j 1.17$ for $\epsilon_r = 2.1$

3. CONCLUSIONS

The presented theory describes the linear system of N coupled rectangular apertures on a dielectric coated perfectly conducting cylinder by means of a $N \cdot M$ quadratic admittance matrix where M is the number of assumed waveguide modes in the apertures. The matrix coefficients depend on the radius of the cylinder, the dimensions of the apertures, the vector mode functions, and the material and thickness of the dielectric layer. The theory takes into account all electromagnetic interaction between the apertures and all effects due to the cylindrical structure which is able to support axial and azimuthal surface waves.

Basing on the system response all interesting data of the array may be calculated.

4. REFERENCES

- [1] W a i t, F.R.:
"Electromagnetic Radiation From Cylindrical Structures"
New York; Pergamon Press, 1959
- [2] K n o p, C.M.:
"External Admittance of an Axial Slot on a Dielectric Coated Metal Cylinder"
Radio Science 8 (1968), 303-317
- [3] B r a n d, H.:
"Schaltungslehre linearer Mikrowellennetze"
Stuttgart; S. Hirzel Verlag, 1970

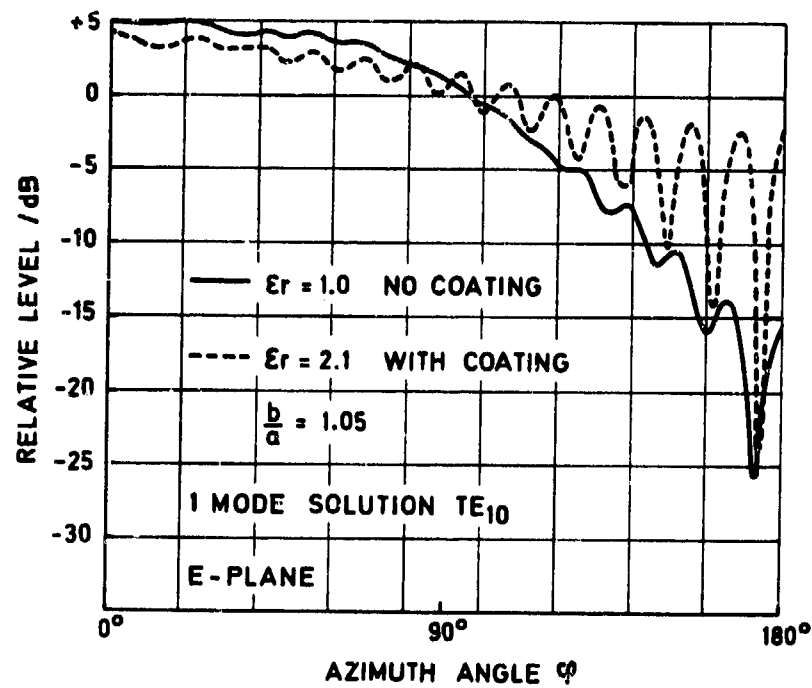


Figure 1: Gain function of a single aperture on a dielectric coated cylinder

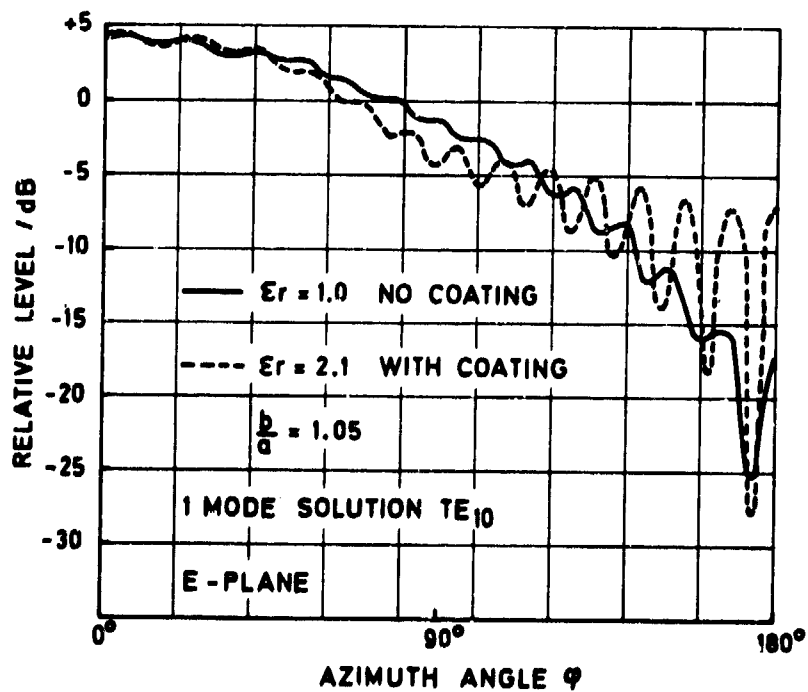


Figure 2: Element gain function of an array of 9 apertures on a dielectric coated cylinder

DISCUSSION

J. SNIELDER: The element pattern for waveguide apertures for an element distance of 0.5λ will display. The same flat curve with scan angle as has been shown. This is in contradiction with what has been mentioned by the speaker.

A drop is only found for element distance between 0.5λ and 1.0λ due to the appearance of the grating lobe in these cases.

J. VOGT: The remark on the element patterns was not restricted to the element distance shown in the figures but should be understood more generally. What I mentioned is true, however, for greater element distances also 1) However, for dipole antennas, our own investigations concerning a non-coated linear array of 17 halfwave-dipoles with a spacing of 0.25λ showed a notch in the central-element pattern (E-plane) of -5dB at an angle of about 60 degrees.

1) See for instance: G.V. Borgiotti Trans. on Antennas and Propagation AP-18, No. 1, Jan. 1970, Fig. 6.

ANTENNES HYPERFREQUENCE POUR MISSILES HYPERSONIQUES

par Christian POUIT
Office National d'Etudes et de Recherches Aérospatiales (ONERA)
92320 CHATILLON (France)

Résumé

Dans le cadre d'un programme d'essai en vol ayant pour but l'analyse des phénomènes physiques pendant la rentrée d'un missile hypersonique dans l'atmosphère, on a utilisé trois types d'antennes rayonnant dans les gammes de fréquences S, C et X. Le type d'antenne retenu (iris rectangulaire noyé dans l'alumine) a permis d'aboutir à la réalisation d'aériens satisfaisant aux conditions d'environnement particulièrement sévères tout en offrant un diagramme de rayonnement ouvert et uniforme, ce qui permet d'envoyer, par combinaison de ces aériens, d'obtenir un ensemble de diagrammes de rayonnement omnidirectionnel.

MICROWAVE ANTENNAS FOR HYPERSONIC MISSILES

Summary

Within a flight program aiming at analyzing physical phenomena during reentry of an hypersonic missile into the atmosphere, three types of antennas were used, radiating in the S, C and X frequency bands. The type of antenna chosen (rectangular iris embedded in alumina) allowed a design satisfying the particularly severe environment conditions while retaining a widely open radiation pattern, which permitted to obtain, by combination of these aeriens, an omnidirectional pattern set.

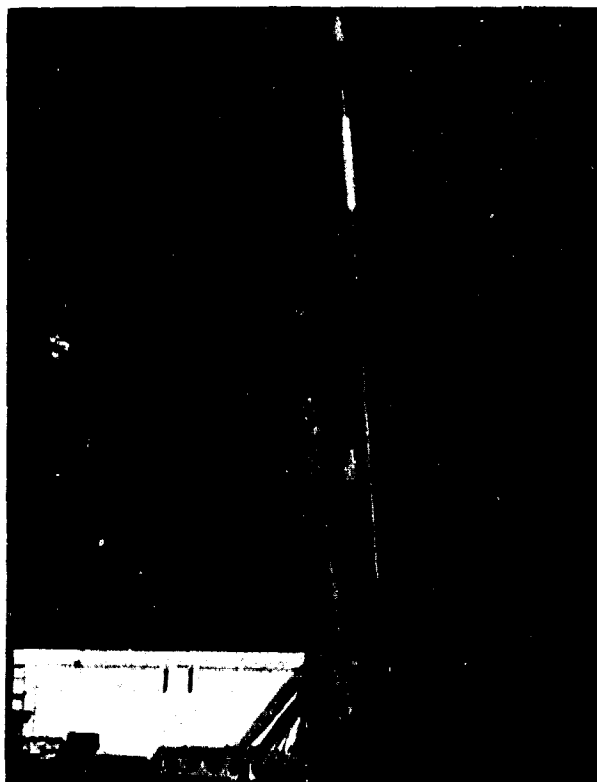
- - - - -

I - INTRODUCTION

Dans le cadre de l'étude des phénomènes électriques apparaissant au cours de la rentrée dans l'atmosphère des véhicules hypersoniques, l'ONERA a conçu et réalisé un programme d'expérimentation en vol dit opération "Electre". Ce programme a permis, en outre, de développer et d'essayer en vol des antennes hyperfréquences adaptées aux conditions de rayonnement à bord des engins les plus rapides.

Un tel domaine d'application impose en effet des contraintes tout à fait particulières aux antennes : miniaturisation, robustesse mécanique et tenue thermique sous un flux de chaleur très intense.

II - DESCRIPTION SOMMAIRE DU PLAN DE VOL DE LA POINTE DE RENTREE "ELECTRE" ET DES CONTRAINTES THERMIQUES IMPOSEES AUX ANTENNES.



La pointe Electre était propulsée par le lanceur Tibère à 3 étages (fig. 1), d'une masse de 4 600 kg et d'une longueur de 14 mètres.

Les deux premiers étages étaient mis à feu successivement pendant la montée ; ensuite le 3ème étage portant la charge scientifique était pointé à l'aide d'un pilote automatique pendant la phase balistique avant d'être mis en rotation et allumé. Lorsque la vitesse atteignait la valeur requise, la charge scientifique était séparée du propulseur pour effectuer un vol libre dans l'atmosphère. L'expérience scientifique proprement dite se déroulait pendant cette dernière phase entre les altitudes 60 et 20 km.

Du fait de l'échauffement cinétique du gaz atmosphérique, qui se trouvait porté à une température dépassant 6 000 °K, la surface de l'engin se trouvait soumise à un flux de chaleur, de l'ordre de 15 000 kJ/m², évacué vers l'intérieur par une structure en cuivre et en titane. La température dans le métal dépassait 1100 °K dans les parties les plus chaudes.

◀ fig.1 - Lanceur "Tibère"

III - L'ELEMENT RAYONNANT

Les contraintes aérodynamiques qui s'exercent sur un véhicule hypersonique imposent un profil très pur pour la structure. De ce fait, les antennes formant saillie sur la surface sont particulièrement déconseillées.

En effet, d'une part, le gaz comprimé en amont de la saillie provoquerait un accroissement local de la concentration électronique dans le plasma d'origine aérodynamique, phénomène nuisible à la propagation des ondes radioélectriques ; d'autre part, les filets fluides décollés de la paroi en aval de la saillie pourraient donner naissance à des tourbillons nuisibles à l'équilibre du vol de la pointe elle-même.

Par conséquent, si on exclut de plus l'utilisation d'un radôme très encombrant, on constate que l'antenne doit être soit imprimée sur la surface, soit encastrée dans la paroi du véhicule.



fig. 2 - Antenne en bande C avec sa fenêtre de protection en alumine.

Les antennes du type "ouverture rayonnante" encastrées dans la paroi paraissent être les mieux adaptées ; de plus, elles se prêtent bien à une analyse théorique détaillée du rayonnement [1] [3], ce qui est un avantage important dans le cas de l'expérience "Electre".

L'ouverture choisie ici est un iris rectangulaire de dimensions beaucoup plus petites que la longueur d'onde, qui est excité par l'intermédiaire d'une cavité parallélépipédique en alumine frittée de pureté supérieure à 99,5% (fig. 2).

La constante diélectrique relative de ce type d'alumine étant 9,5, les dimensions de la cavité et de l'iris sont réduites dans le rapport 1/3,1 par rapport à celles d'un montage équivalent où la propagation se ferait dans l'air.

La conductibilité thermique de l'alumine, qui est sensiblement la même que celle de l'acier, permet de propager les calories apportées par le gaz chaud extérieur sans que la température à l'intérieur de l'antenne ne dépasse les 1100 °K atteints dans les autres parties de la structure.

Grâce à cet échauffement limité, les facteurs de pertes diélectriques et ohmiques restent à un niveau faible, de l'ordre de 10^{-3} pour les fréquences comprises entre 1 et 10 GHz.

Les dimensions réduites de l'ouverture rayonnante permettent de simplifier l'étude théorique du rayonnement au travers de la couche de plasma inhomogène enveloppant la pointe. En effet, cette ouverture impose une répartition unique du champ dans le plan de séparation situé entre la cavité d'excitation et l'espace extérieur, de sorte que la matrice traduisant le couplage entre les modes électromagnétiques intérieurs et extérieurs à l'antenne est réduite à un seul terme.

IV - LES DISPOSITIFS D'ADAPTATION

Pour les besoins de l'expérience Electre, il était nécessaire de contrôler en vol avec précision les variations d'impédance des antennes, et de relier ces variations aux propriétés physiques du plasma. Ces mesures imposaient une adaptation d'impédance particulièrement soignée en régime de rayonnement libre.

IV-1.- Adaptation dans les bandes S et C (fig. 3).

La transition guide d'onde coaxiale en alumine C peut être déplacée en translation sur l'ouverture d'entrée de la cavité d'excitation B par action sur les vis pousseurs H. Cette translation agit sur le couplage entre les éléments B et C.

Un iris de couplage I obtenu par dépôt métallique obstruant partiellement l'ouverture d'entrée de la cavité B permet d'ajuster l'impédance réactive du couplage.

IV-2.- Adaptation en bande X (fig. 4).

Dans cette gamme de fréquence, les guides d'onde en alumine présentent des dimensions très petites qui rendent difficile la réalisation d'un couplage précis entre la transition guide d'onde coaxial et la cavité d'excitation ; c'est pourquoi on a remplacé l'alumine de la transition E par du fluorbearing, dont la constante diélectrique relative est 3.

Le fluorbearing présente des propriétés électriques semblables à celles du tétrafluoroéthylène dont il est dérivé, mais ses caractéristiques mécaniques et thermiques sont nettement améliorées ; en particulier, le faible coefficient de dilatation thermique permet d'éviter le fluage à l'intérieur d'un montage métallique tel qu'un guide d'onde, malgré un échauffement important.

La transition guide d'onde-coaxial est couplée à la cavité d'excitation en alumine B au moyen d'une seconde cavité en alumine C de très petites dimensions, insérée dans le remplissage en fluorbearing et appliquée contre la cavité d'excitation.

La cavité C est dimensionnée avec précision après plusieurs essais successifs pour réaliser l'accord électrique de l'antenne.

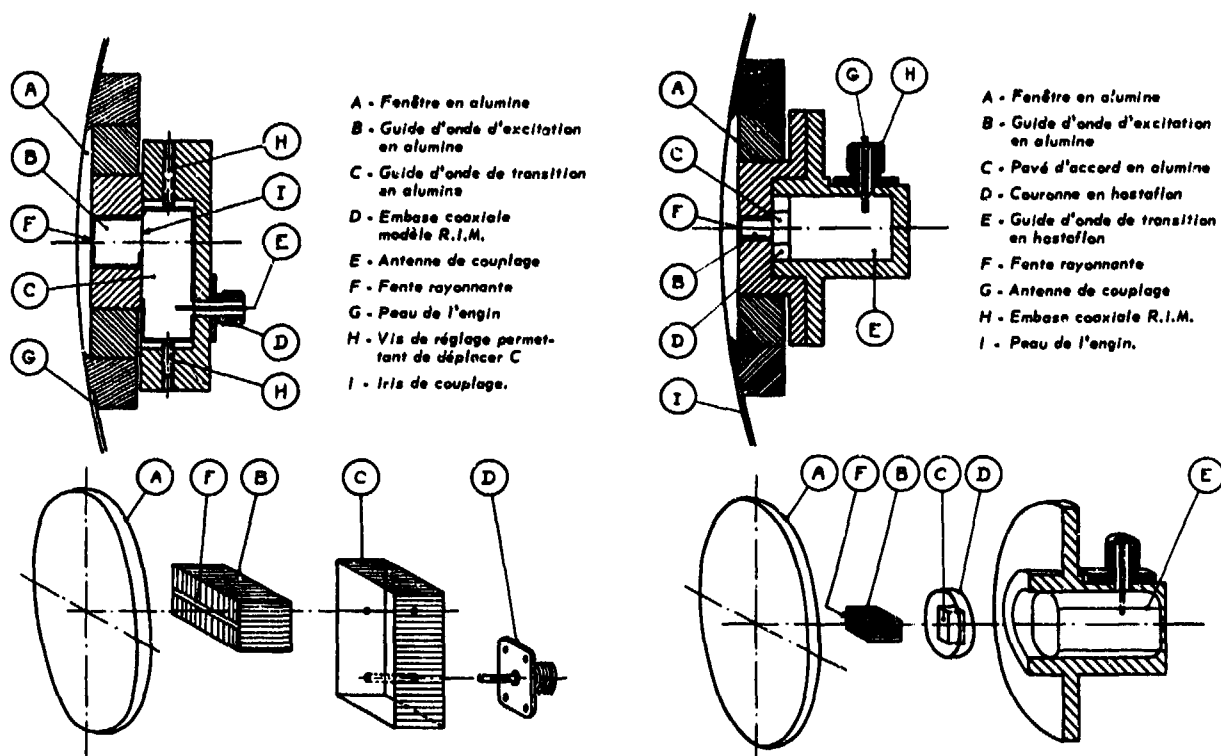


Fig. 3 - Schéma des antennes en bande S et C.

Fig. 4 - Schéma des antennes en bande X.

V - PERFORMANCES

Les principales caractéristiques électriques et mécaniques des antennes sont rassemblées sur la tableau I.

TABLEAU I - Performances obtenues

Bande de fréquence	S	C	X
Accord mécanique (MHz)	± 50	± 100	
Bande passante à 3 dB (MHz)	55	145	440
T.O.S. à froid	1,2	1,2	1,2
Dimensions (mm ³)	78 x 64 x 52	62 x 64 x 35	57 x 64 x 44
Masse sans la fenêtre en alumine (g)	550	310	220

Les pertes radioélectriques ont été évaluées à partir des résultats de mesures faites en vol avant la phase d'échauffement cinétique. En effet, du fait de la grande ouverture des diagrammes de rayonnement, ces mesures ne pouvaient être faites que dans un environnement totalement exempt de réflexions parasites.

Les essais thermiques ont été réalisés dans une tuyère de statoréacteur programmée de façon à reproduire les échauffements subis par un engin hypersonique, d'abord pendant la sortie, puis pendant la rentrée dans l'atmosphère à une vitesse dépassant Mach 15. Ces essais ont permis de constater que, pendant la période la plus intense de l'échauffement, la fenêtre en alumine protégeant

l'antenne prend une forme bombée vers l'extérieur, correspondant à un déplacement de 0,02 mm. Le petit espace vide apparaissant de ce fait entre l'iris rayonnant et la fenêtre de protection suffisait pour provoquer un désaccord électrique notable sur l'antenne. Ce défaut a pu être en partie corrigé au moyen d'un montage permettant de compenser les déformations mécaniques et d'assurer un contact permanent des surfaces entre elles. De cette façon, les taux d'ondes stationnaires mesurés sur les prises d'entrée des antennes dans les bandes S, C et X restaient inférieurs à 2 pendant les phases d'échauffement décrites précédemment. Les essais en vol ont confirmé largement ces résultats puisque les antennes embarquées fonctionnaient encore parfaitement en dessous de l'altitude 20 km, c'est-à-dire au delà de la durée exigée pour la réalisation du programme scientifique.

VI - REALISATION D'UN RAYONNEMENT OMNIDIRECTIONNEL

La forme exacte du diagramme de rayonnement d'une antenne encastrée dépend dans une large mesure de la forme et des dimensions extérieures de la structure qui la supporte. Toutefois, il apparaît que dans tous les cas où la surface en question est plane ou convexe, le rayonnement couvre une ouverture angulaire de 2π stéradians à - 10 dB. Cette propriété a été mise à profit pour réaliser un rayonnement omnidirectionnel à partir de deux éléments seulement, disposés sur une surface cylindrique et orientés dans des directions diamétralement opposées [2].

Une disposition du même type a permis de réaliser une liaison de télémesure en bande S entre la pointe Electre et le sol. Cette liaison était très peu affectée par les trous de champ qui, par ailleurs, sont inévitables mais qui, dans le cas présent, étaient réduits au minimum.

VII - CONCLUSION

Un nombre important d'antennes construites selon le modèle décrit ci-dessus ont équipé deux pointes scientifiques de l'opération Electre. La première a été lancée le 23 février 1971, la seconde le 12 mars 1972.

Ces deux vols, exécutés dans les conditions exactes de la rentrée dans l'atmosphère d'un engin balistique, ont prouvé les aptitudes des antennes en question tant pour fonctionner à bord d'un véhicule hypersonique que pour réaliser un rayonnement omnidirectionnel de bonne qualité.

-:- REFERENCES -:-

- [1] - GALEJS J. - Antennas in Inhomogeneous Media. Pergamon Press (1969).
- [2] - POUIT C. - Slot Aerial for 2300 MHz Omnidirectional Radiation. Communication présentée à la Conférence sur les antennes aérospatiales. IEE Londres - 8-10 juin 1971.
- [3] - POUIT C. - Etude théorique et Simulation en Soufflerie des Phénomènes électriques de la Rentrée.- La Recherche Aérospatiale n° 1972-4, p. 199-207.

THE DESIGN OF WIDE BAND NOTCH AERIALS AND SOME APPLICATIONS TO AVIONICS

George Bagley
 Royal Aircraft Establishment
 Farnborough, Hampshire
 United Kingdom

SUMMARY

This paper describes the experimental results obtained from notches of a variety of rectangular shapes cut in semi-infinite metal sections, and illustrates the various combinations of centre frequency and impedance bandwidth which can be obtained from a notch of fixed physical length. The results relate to a notch used in the self resonant mode, without any additional lumped reactance. The variables investigated (for a fixed length notch) are notch width, thickness of the section, and feed point position. It is possible to drive the notch either as a narrow band quarter wave radiator, or as a half wave radiator with a frequency bandwidth of 2.0:1. Several possible applications are discussed, including an omni-azimuthal horizontally polarised radiator with a band width of 3.0:1.

1. INTRODUCTION

Much of the previous work on the notch aerial has been confined to its application to specific problems. In the present case the properties of the notch were studied in general terms, and the information contained in this paper presents the results obtained at RAE by varying notch width, notch depth, and feed point position as defined in Figure 1.

2. EXPERIMENTAL NOTCH

Figure 1 shows the construction of the notch. Three pairs of rectangular metal boxes were made, with depths of 10cm, 7.5cm and 5cm. Each pair was bolted to the base through longitudinal slots allowing adjustment of notch width between zero and 10cm. The notch was fed by a 50 coaxial feeder, the outer of the feeder bonded to one face of the notch, and the inner conductor continued across the notch and connected to the opposite face. Each face of the notch carried a series of attachment points along its length at 2.5cm intervals, permitting stepped adjustment of the feed point along the notch.

3. EXPERIMENTAL NOTCH RESULTS

Figure 2 contains curves of voltage standing wave ratio (VSWR) versus frequency for combinations of a range of values of notch width, notch depth, and feed point position. Each block shows VSWR: frequency curves for fixed values of both notch width and notch depth, and six values of feed point position.

The effect of variation of notch width can be seen by examination of any set of curves on the same horizontal line, and that due to notch depth by comparison of similar values of feed point position in the same vertical column. Figure 3 is an enlargement of one block of Figure 2, and shows the effect of variation of feed point position on the VSWR: frequency characteristic. The generally accepted theory of a self resonant notch is that it can be considered as a lossy short circuited quarter wavelength transmission line. The impedance across the open end is a high resistive value, and is zero at the short circuit end. Therefore, by placing the feed point near the short circuit end of the notch, it should be possible to match into a 50 ohm feeder. The notch used in these experiments was quarter wavelength long at about 165 MHz. Referring to Figure 3, the topmost curve in the block is for a feed point 12.5 cm from the short circuit end of the notch, it is resonant at 165 MHz and the bandwidth is small. As the feed point is moved toward the open end of the notch, the bandwidth increases, but the operating frequency also shifts upwards such that in the maximum bandwidth position the centre frequency is of the order of 270-300 MHz, and the simple quarter wave resonance theory applies no longer.

The diagrams of Figures 2 and 3 show a broken horizontal line representing a VSWR of 2.5:1, this being taken as a reasonable maximum value, and the block in Figure 2 for a 5cm wide, 5cm deep notch shows an acceptable VSWR from 200 to 390 MHz with the feed point 32.5cm from the short circuit end. These physical dimensions appear to be optimum, within the limits of the results displayed in Figure 2. One point of interest is that the characteristic impedance of this particular notch which is square in cross section (5cm x 5cm), viewed as a parallel plate transmission line is approximately that of free space, - 120 Ω ohms.

4. NOTCH APPLICATIONS

One feature of the notch is that it can be built into non-structural parts of an aircraft to produce a dragless aerial, and the wide band characteristics which are now possible may make it more attractive to system designers. Among the problems of engineering a notch into an aircraft structure is the effect upon the impedance characteristic of radome material, and the geometry of the aerofoil section in which it is installed. If the characteristic impedance of the notch is maintained at 120 Ω , and its velocity ratio at 1.0, as far as possible, the engineered version is much more likely to attain the performance of the laboratory model. This point is illustrated in Figure 4.2. The aerofoil notch of Figure 4.2 has several disadvantages, because the cross section changes the characteristic impedance of the notch changes along its length. Furthermore, the dielectric cover for such a notch is in close contact with the edges, and will further affect the characteristic impedance and electrical length. The layout in Figure 4.1 is to be preferred. In this case the characteristic impedance is maintained constant throughout the length of the notch, and the notch is

faired back to the aerofoil in such a manner as to have a minimal effect upon the parallel plate notch section. The dielectric cover is removed from the immediate vicinity of the notch, and will have only a very minor effect upon it electrically.

There could be some advantage in siting components of the associated system adjacent to the notch, and comprising for example the transmitter power amplifier, and those parts of a receiver up to and including the mixer.

Figure 5 illustrates a model built at RAE in an attempt to produce horizontally polarised radiation over a wide band, and over a complete azimuth. The basis of the design is an 'ideal notch' scaled from the data given in Figure 2, cut in a metal disc. The axial tube is to provide a method of mounting. Detailed layout is given in Figure 6. The notch is fed two thirds of its length from the short circuit end. The triangular plate feed across the notch is an attempt to reduce the series inductance of the feed. Standing wave ratio measurements were carried out in the laboratory with the disc well clear of reflecting objects, and also with the disc mounted 15 and 20cm above a ground plane. The results are given in Figure 7. The solid curve was obtained with the aerial free standing. Points are also shown with the aerial mounted above a ground plane, and indicate that the proximity of the ground plane has only a slight effect upon the aerial impedance.

Figures 8, 9 and 10 show the field strength polar pattern in the plane of the disc for several frequencies. In each diagram there are two dips symmetrically disposed on the opposite side to the notch. This is to be expected, since it is only in this region that currents generated from the notch travelling in opposite directions round the edge of the disc are comparable in amplitude at any given point. In these diagrams 'horizontal polarisation' is polarised along a tangent to the disc. The 'vertical polarisation' recorded is certainly spurious, and should be disregarded. Throughout the frequency band there is good all round cover, horizontally polarised, with narrow 10-15dB dips at the rear.

If two discs are stacked on the same axis with a small angle between the two notches the depth of the dips is greatly reduced.

5. CONCLUSION

For a given set of notch dimensions it is possible to obtain bandwidths of 2.0:1 from a notch in a semi-infinite section. If bandwidth is not a primary consideration it is possible to shift the operating frequency of the notch by moving the feed point alone. From a similarly proportioned notch in a metal disc, a bandwidth of 3.0:1 may be obtained.

REFERENCES

1. G BAGLEY and J WHARF "Interim Report on the Wideband Notch Aerial" 1965
2. G BAGLEY "The Disc Aerial" 1970

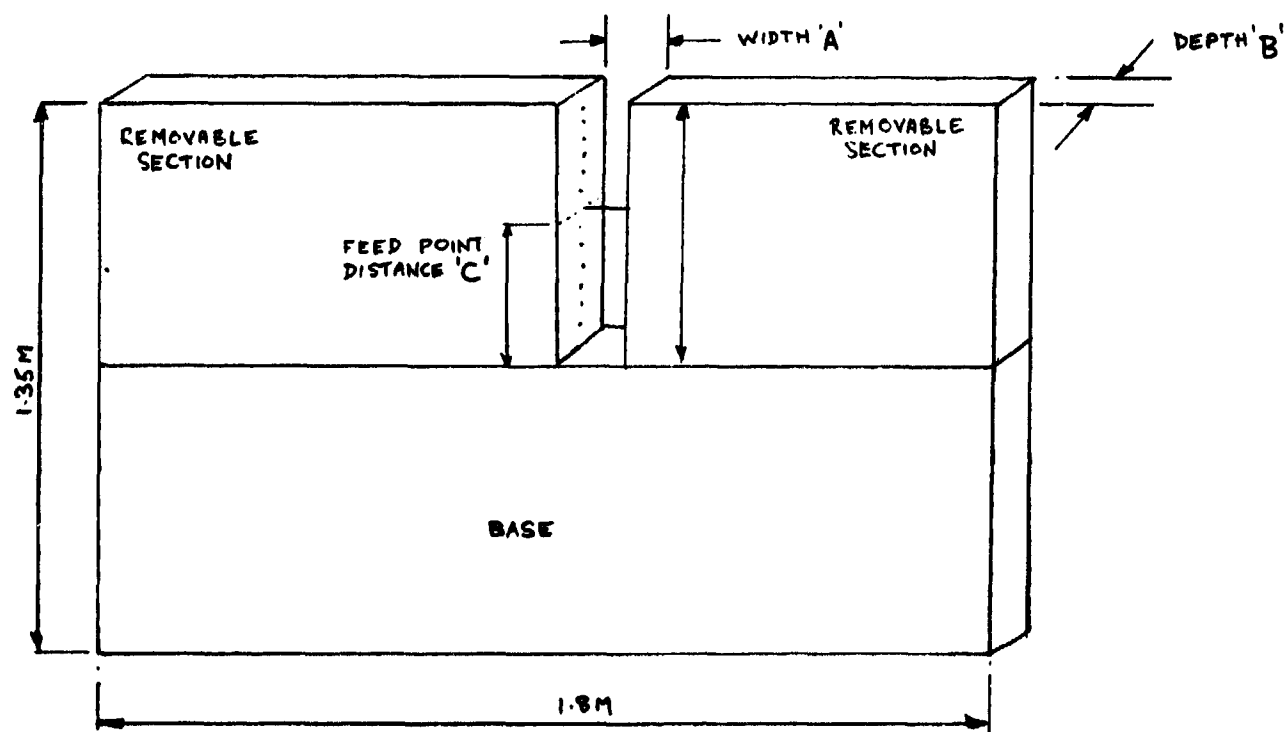


Fig.1 Experimental notch

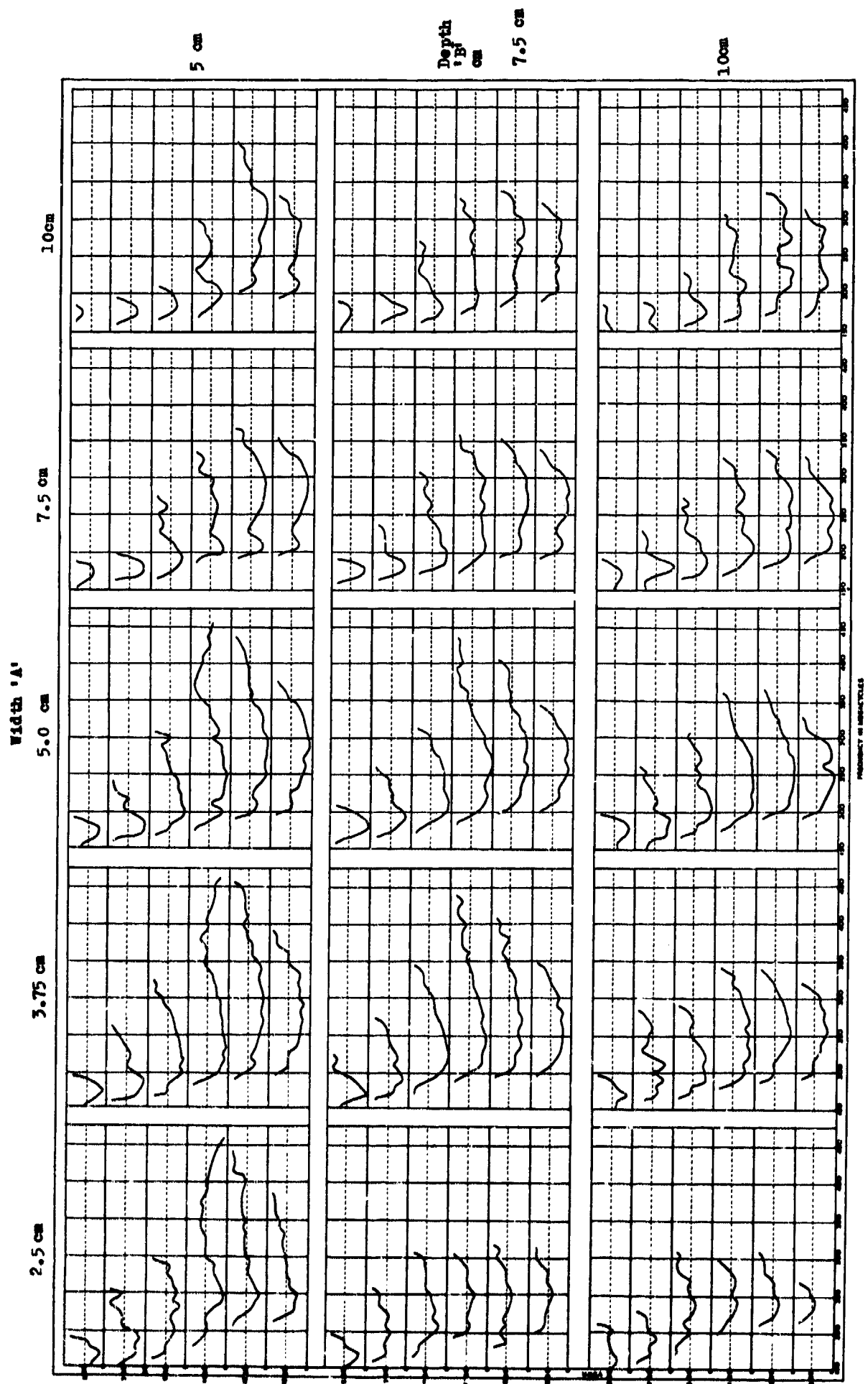


Fig.2 VSWR curves

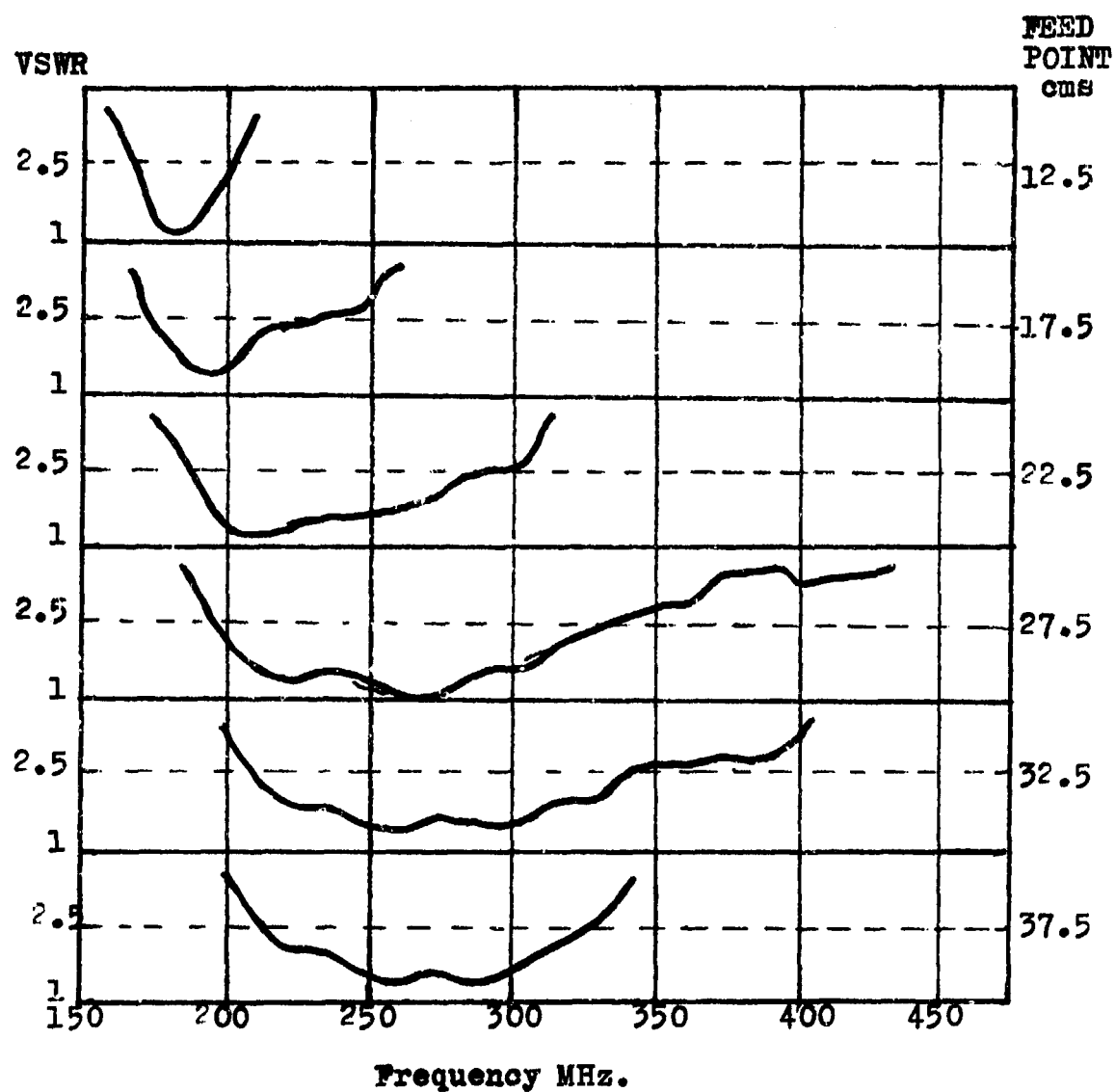
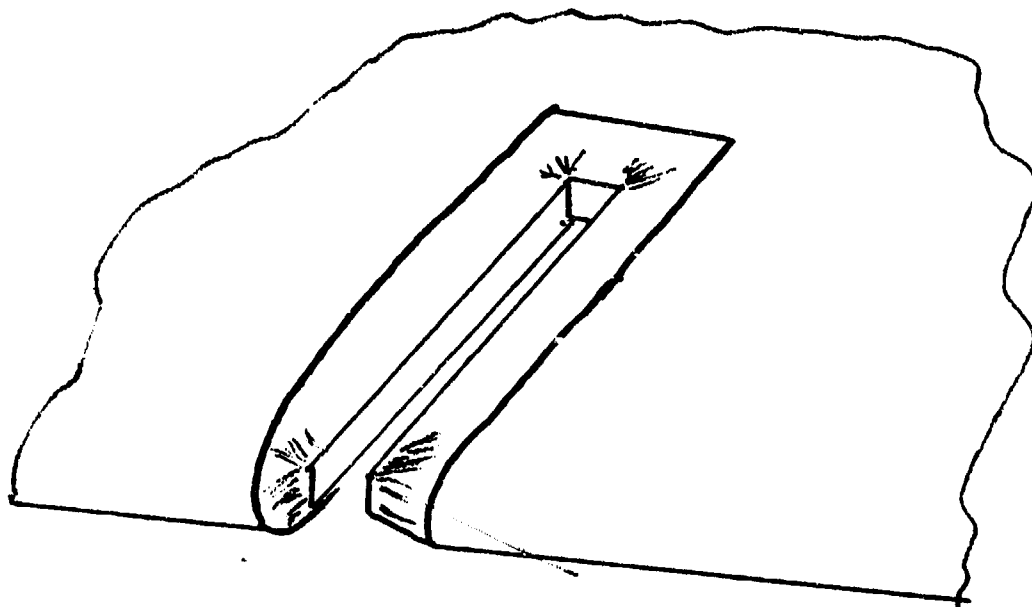
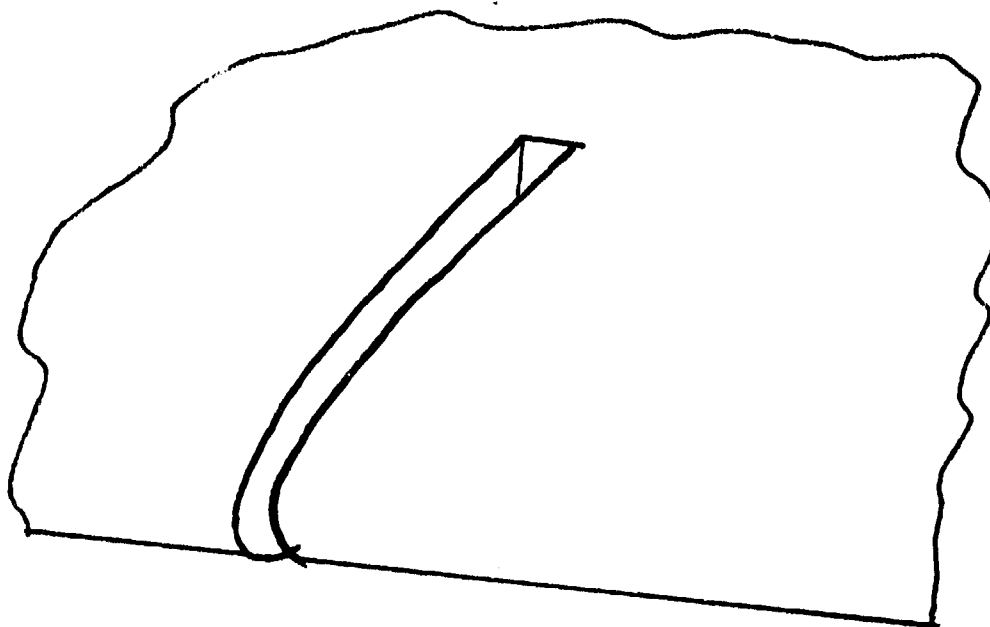


Fig.3 Enlarged block from Figure 2
A 5 cms B 5 cms C as shown



4.1 Parallel plate notch in an aerofoil



4.2 Aerofoil notch

Fig.4 Notches in aerofoils

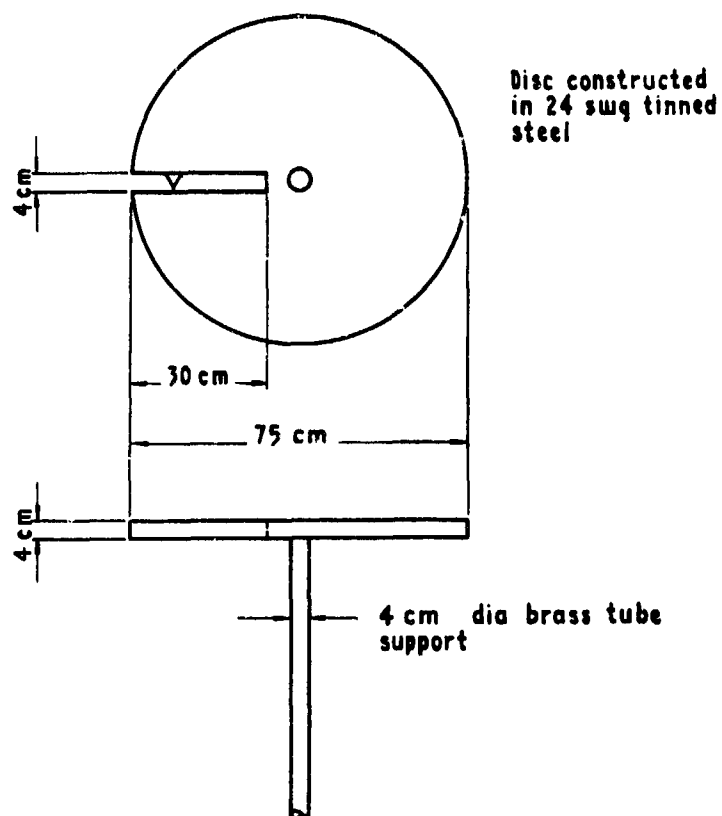


Fig.5 Disc aerial

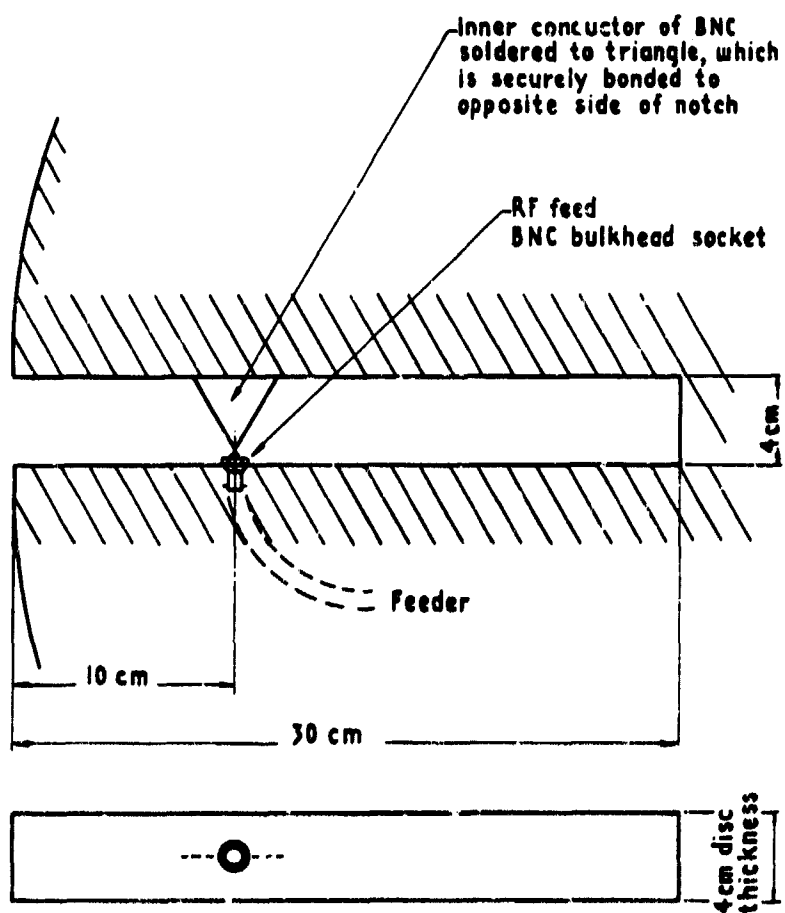


Fig.6 Notch details

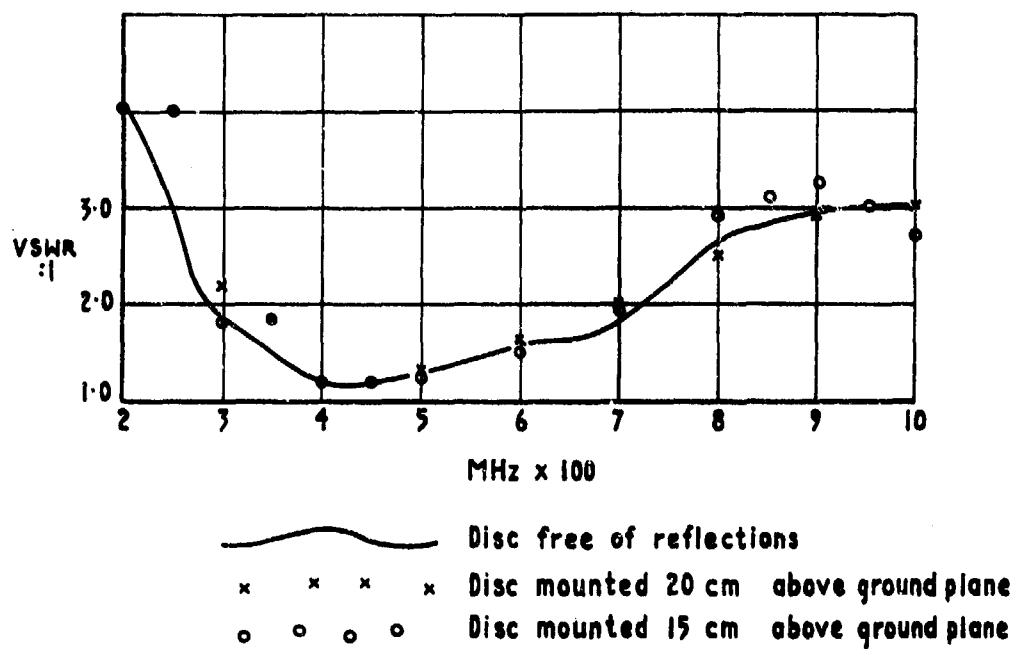


Fig.7 VSWR: frequency 200 MHz–1000 MHz

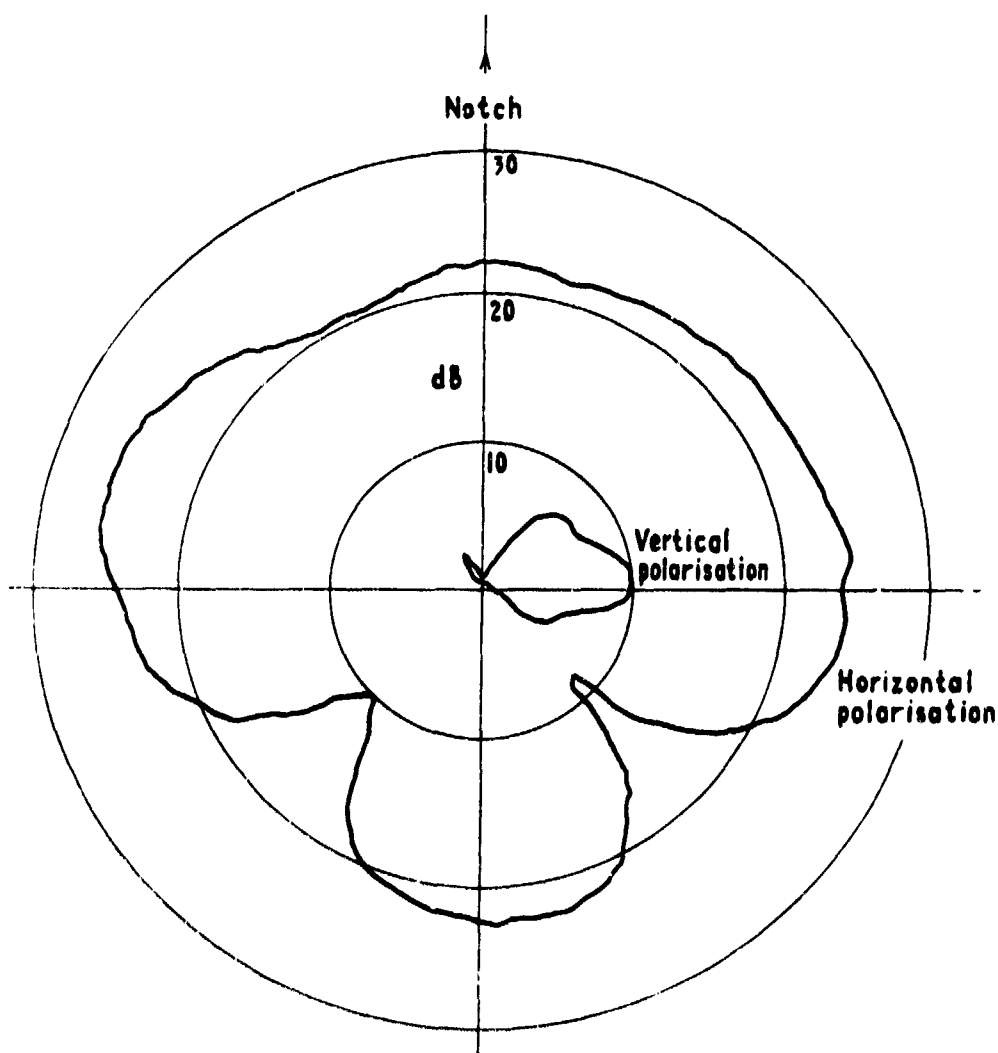


Fig.8 Azimuth plane pattern 250 MHz

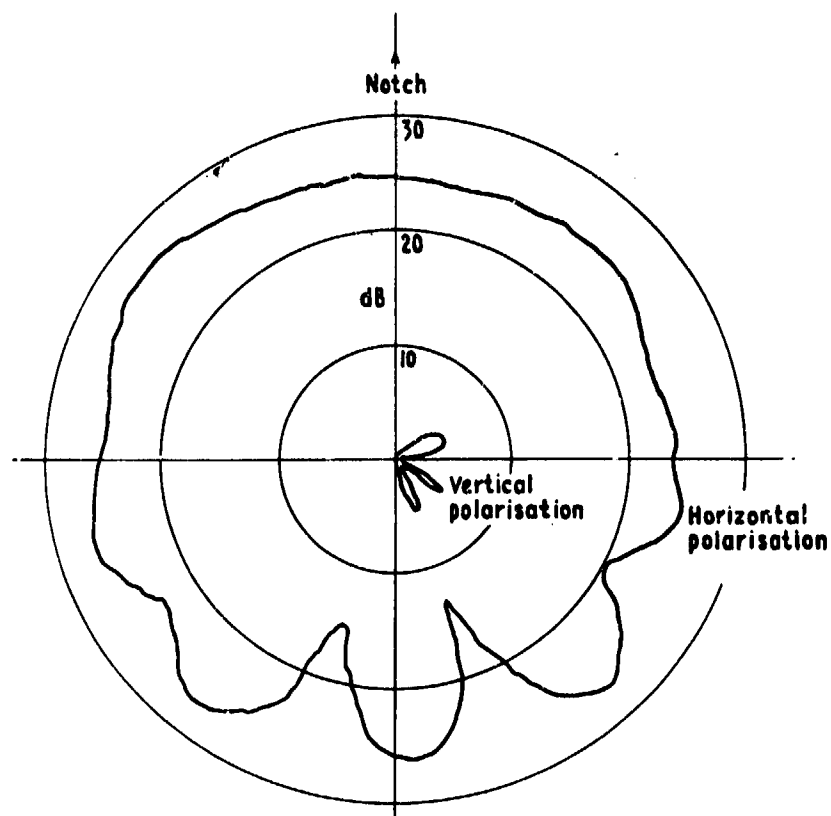


Fig.9 Azimuth plane pattern 550 MHz

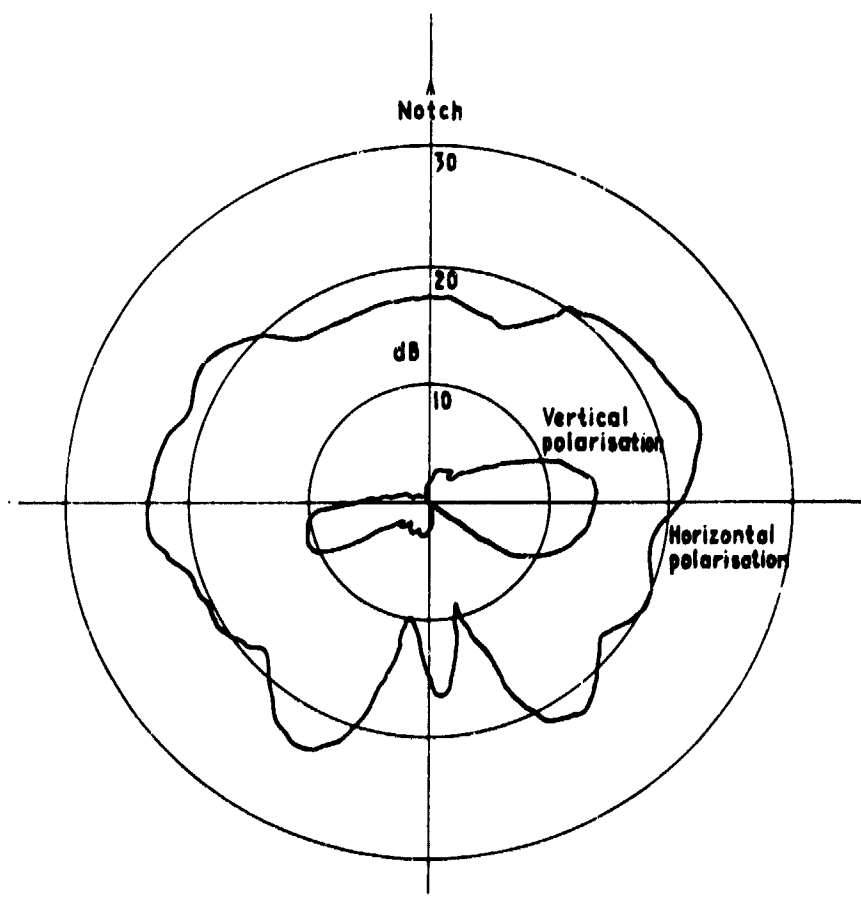


Fig.10 Azimuth plane pattern 750 MHz

DUAL FREQUENCY DICHROIC FEED PERFORMANCE

by

D. A. Bathker
 Jet Propulsion Laboratory
 California Institute of Technology
 4800 Oak Grove Drive
 Pasadena, California 91103
 USA

SUMMARY

The NASA Deep Space Net (DSN), under system management and technical direction of JPL, in support of the Viking Mars Project in 1976, and for science and technology demonstrations during the Mariner-Venus-Mercury mission in 1974, has developed and implemented a dual (S- and X-band) feed for large ground microwave antennas. This feed provides for a multiplicity of functions; very low noise listening capability at each downlink (spacecraft-to-earth) band as well as simultaneous diplexed very high cw power uplink (earth-to-spacecraft) at the S-band frequency.

This paper will stress total 64-m antenna system performance, in terms of gain, operating noise temperature and dual beam pointing or boresight coincidence. Because of the unique ability to fold or stow the dual band feed elements for single band operations, the performance definition between single and dual band operations will be reliable and accurate.

1. INTRODUCTION

In order to support both science and technology demonstration objectives, the United States Mariner-Venus-Mercury spacecraft, to flyby both Venus and Mercury in early 1974, carries both S- and X-band radio transmitters. Each spacecraft transmitter is coherent with the other and both transpond coherently given an earth-based S-band uplink. The ground antenna must therefore provide both S- and X-band downlink reception as well as simultaneous (diplexed) S-band uplink transmission.

The ground antenna dual band feed development and performance to be discussed here is a key item in the Mariner mission. Performance degradations of only a few percent in the receive gain to noise temperature ratio (G/T) would severely impact the overall telemetry capacity by requiring selection, by discrete step, of a reduced data rate. Further, the primary mission objectives are achievable using S-band only; X-band is a science and technology experiment in the 1974 context. A significant S-band performance degradation could not be tolerated, even at expense of limiting the X-band experiments.

The NASA/JPL 64-m dual band ground antenna feed development objectives were therefore to provide unaltered S-band low noise high efficiency reception (20K and 60% class) as well as not impact the very high cw power uplink (400 kW). A further goal of optimizing X-band reception was considered necessary since, following the 1974 demonstrations, follow on use of X-band provides the basis for accurate navigation and attractive high data rate links. It would be uneconomic to invest in technology not able to support those future objectives.

2. TRICONE

Prior to discussing the dual frequency feed it is necessary to review the NASA/JPL 64-m ground antenna TRICONE feed system (Stelzried, 1967). This system provides 5 selectable, single band feeds, housed within 3 Cassegrain feedcones (Fig. 1). Only one feed is functional, in the correct Cassegrain focus and total antenna boresight sense, at a given time. It should be recognized the functional feed operates without degradation to total antenna system pointing or G/T performance. Although defocused feeds have been employed as simultaneous squinted beams useful for background radiometry during mission directed S-band spacecraft tracking, they are not normally active. The functional feed is selected by rotating the asymmetric subreflector about an axis coincident with the boresight axis. The vertex of the subreflector, which is offset from the boresight axis thus describes a circle with a corresponding rotation of the Cassegrain focus (Fig. 2). Precision indexing allows the rotation to stop such that each feed, in turn, is perfectly boresighted. Finally, the TRICONE also houses, in addition to S-, X- and K-band front ends (masers, converters, and calibration equipments), three very high cw power transmitters. Complete descriptions, including operating performance, are available (Reid, 1972, 1973).

3. DICHROIC FEED CONCEPT

Approaches were sought to fulfill the dual band feed development objectives previously stated. Few, if any, approaches were found which, a priori, guaranteed the primary performance requirements. Furthermore, most known dual band feed methods suffered in the sense that secondary performance indices such as lack of arc susceptibility, lack of use of dielectric support and other transmitter power or receiver location considerations were not satisfied.



Figure No. 1 NASA/JPL 64-m Ground Antenna With Tricone Feeds

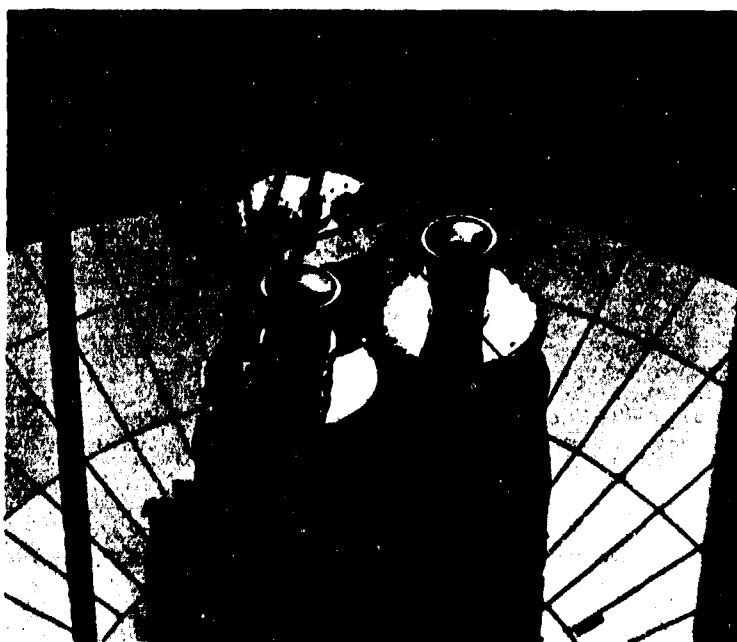


Figure No. 2 Detail of Tricone Feeds for S-, X- and K-Bands

The Reflex-Dichroic concept (Bathker, 1972) evolved around the recognition that a dichroic filter (transparent to short wavelengths but opaque to longer wavelengths) could probably be achieved with little impact, in the dissipation sense, to energy at either wavelength. This is so because a dichroic filter having the stated high/low, pass/reflect function is physically realizable in an all metallic structure. A second reflector, ellipsoidal in section, would be required to guide and refocus the longer wavelength, in order that the total system be compatible with use of existing but separate S- and X-band TRICONE feedcones (Fig. 3). Thus, an arrangement appeared conceptually possible which was all Cassegrain, with attendant potential of ultra low noise performance. As shown in Fig. 3, few if any questions regarding high power handling capacity are unanswered. Preliminary estimates, with consideration for the specific geometry employed, showed 2-m diameter reflectors were required and mechanical feasibility was rapidly established (Katow, 1971).

3.1 S-Band Design

Detailed RF optics design was complicated both by the asymmetric geometry and by the near range of both reflectors (Fig. 4). Previous work by Ludwig (Ludwig, 1969) provided the analytical basis with which, on an iterative basis, the S-band radiation emanating from F_s was, in large, duplicated with reference to F_s' . Because of the geometry and generous size of the dichroic reflector it was found the radiation from F_s' was nearly perfectly duplicated with reference to F_x . It should be appreciated both F_s and F_s' would, in the zero wavelength limit, be foci of an ellipse. Also shown in Fig. 4 are f_a , f_b , the geometric foci of the required ellipse, as modified by the near field behavior of this system, as determined by the near field asymmetric scattering iterations mentioned above.

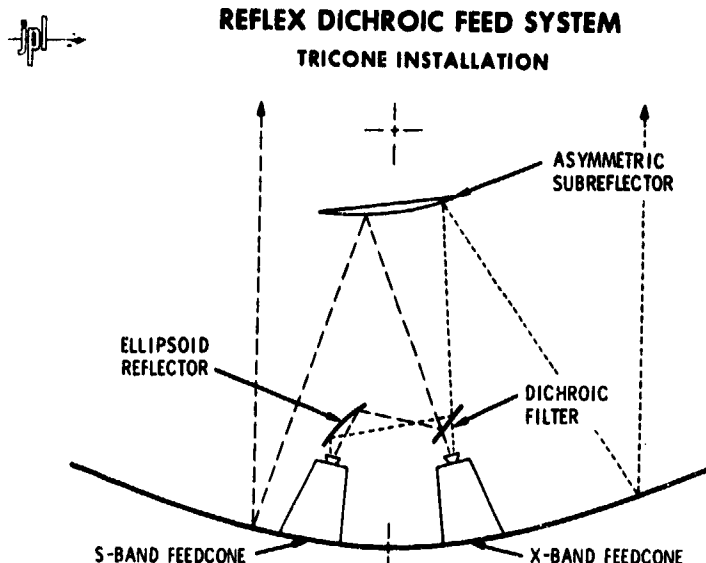


Figure No. 3 Conceptual Reflex-Dichroic Feed System

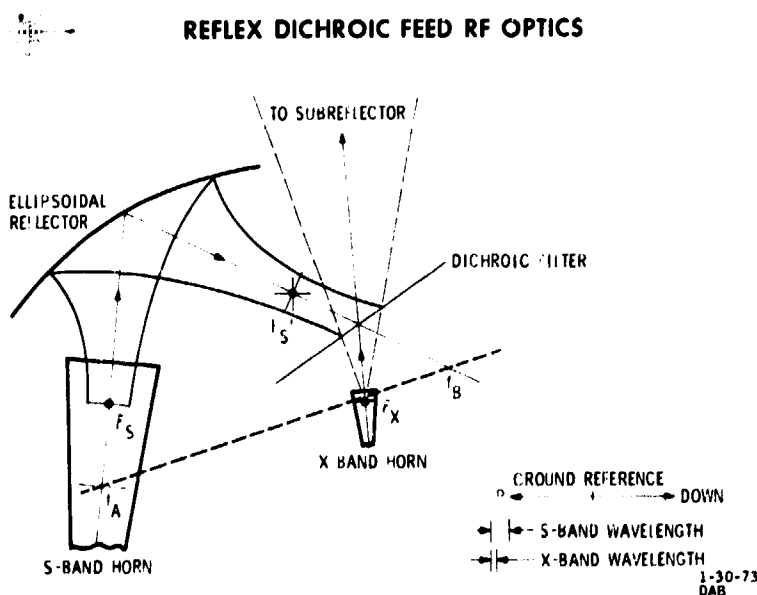


Figure No. 4 Detail of Reflex-Dichroic RF Optics

Because of the asymmetric geometry necessarily employed, the S-band reflex feed patterns do not exhibit the high level of symmetry as the corrugated waveguide feedhorn taken alone. Spherical wave techniques were used (Ludwig, 1970; Potter, 1967; Ludwig, 1971) as well as a new computer program (Potter, 1972), to predict overall S-band performance. Because this feed design was based on a series of computer programs, it was considered necessary to experimentally check the predictions. A 1/7 scale model program (Fig. 5) produced measured patterns, in both polarizations, essentially identical to those shown in Fig. 6. Also shown in Fig. 6 are the predicted scattered patterns of both the horn-ellipsoidal reflector, referenced to F_S , and the horn-ellipsoid and a flat plate (simulating an opaque dichroic filter) taken together, referenced to F_X .

Table 1 summarizes the predicted gain performance of the S-band reflex feed and compares that with previous TRICONE performance, itself a slightly asymmetric system. Table 1 illustrates the familiar trade-off in forward spillover and amplitude illumination loss, which is a function of feedhorn gain. In this case, the reduced forward spillover is a result of slightly higher gain for the horn/ellipsoid/flat plate patterns than for the horn alone. Additional design iterations with ellipsoid shape would have produced identical gains but were not considered necessary. Table 1 also shows the major penalty of asymmetric systems; radiated energy not contributing to forward antenna gain (M/I) and resultant cross polarization. In summary, the reflex system was expected to degrade S-band gain performance less than 0.06 dB, and negligibly impact the S-band noise temperature.

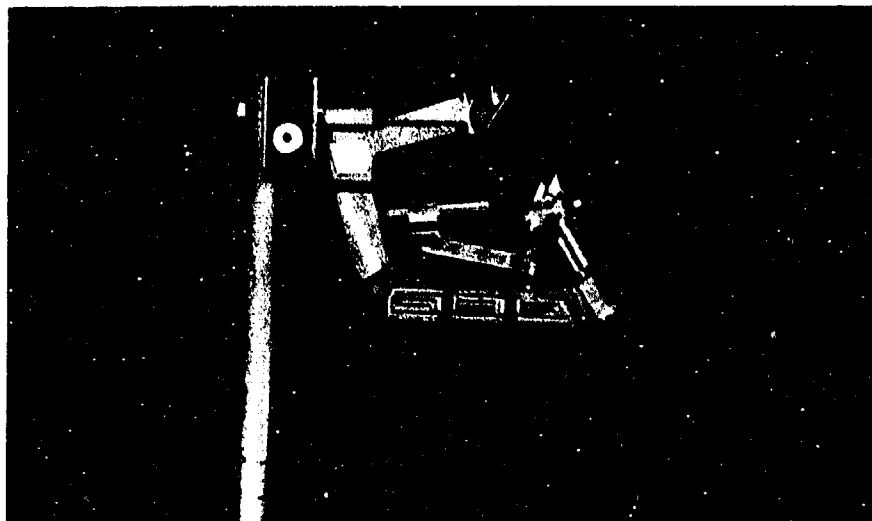


Figure No. 5 Scale Model Reflex-Dichroic Anechoic Chamber Test



COMPUTED AND MODEL PATTERNS

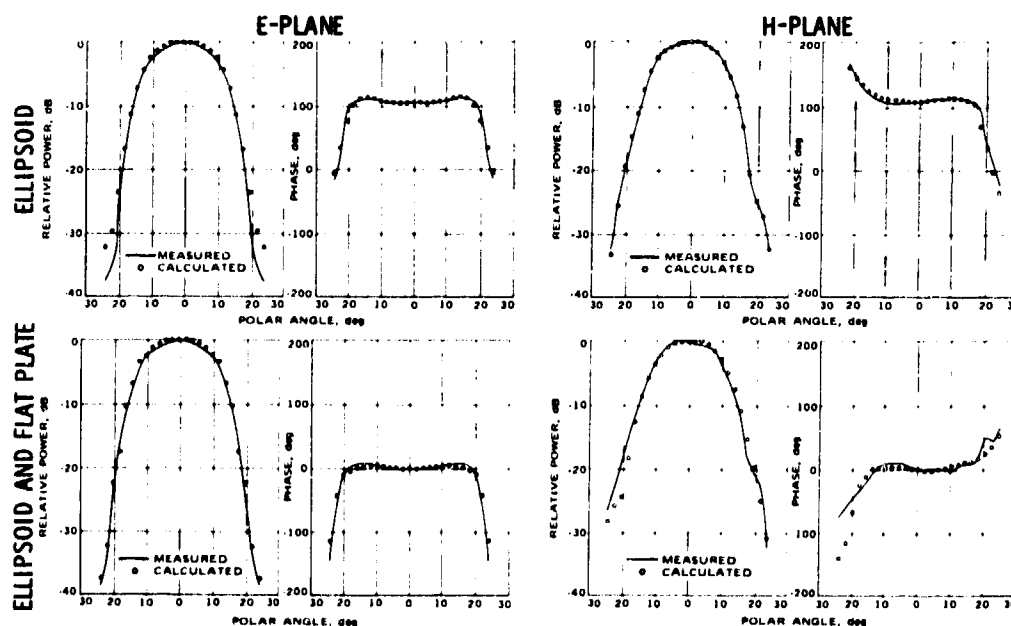


Figure No. 6 Calculated and Measured Model Low Band Patterns

TABLE 1
PREDICTED S-BAND GAIN PERFORMANCE
TRICONE AND REFLEX-TRICONE FEEDS

	TRICONE	REFLEX-TRICONE	NOTES
Forward Spillover	-0.247 dB	-0.133 dB	Due to asymmetric geometry
Rear Spillover	-0.011	-0.010	
Amplitude Illumination	-0.747	-0.840	
Phase Illumination	-0.088	-0.070	
Cross Polarization	-0.001	-0.005	
Myl Energy	-0.009	-0.089	
Central Blockage	-0.262	-0.260	
Quadripod Blockage	-0.580	-0.580	
Surface Tolerance	-0.093	-0.093	
Surface Tolerance	0	-0.010	
Resistivity	0	NEG.	Paraboloid/Subreflector 0.152 cm
Leakage	0	-0.003	Ellipsoid 0.051 cm
		NEG.	Dichroic
			Dichroic; relative to plane reflector
			Dichroic (-50 dB)
TOTALS	-2.038 dB	-2.093 dB	Net Loss, 0.055 dB

3.2 X-Band Design

Preliminary dichroic filter designs were based on discussions with and previous work by individuals at Ohio State University. That work was extended for circular polarization (Woo, 1971). These filters were physically ultra thin (0.4 mm), perforated with an array of reactively loaded close spaced slots. For this application the original filters were found inadequate in the dissipation loss sense, providing 0.3 dB loss at X-band for aluminum construction. 0.3 dB of ambient temperature dissipation, when added ahead of a 21K total operating noise temperature receive system results in a G/T degradation of 3 dB due to doubling the temperature term.

Intermediate filter designs increased bandwidth with attendant lower dissipation losses (2-4K) and thicker construction (3 mm). These intermediate designs also suffered from mechanical tolerance sensitivity problems as well as probable severe degradation due to paint, dirt and water droplet accumulation. Finally, due to the aspect ratio (3 mm thick, 1 m diameter), and the geometrical constraints, a difficult thermal distortion problem was identified. When illuminated with 400 kW S-band, with a beam diameter of approximately 40 cm, the thin filters invariably heated and became bowed, relative to S-band flatness requirements.

An excellent alternative to the thin thermal dependent type dichroic filters was proposed and developed by Potter (Potter, 1973). The solution was to obtain resonance by the simple means of a halfwave thick array of dominant mode cylindrical waveguide apertures. At X-band this construction is 3.6 cm thick with a calculated dissipation loss of 0.012 dB using aluminum (Fig. 7). Measurements proved an operating system noise temperature increase of 1.2K (0.02 dB), due to dissipation, with virtually no X-band pattern degradation. Bandwidth is approximately 100 MHz for the specific tilt angle and horn beamwidth (angular scan) employed.

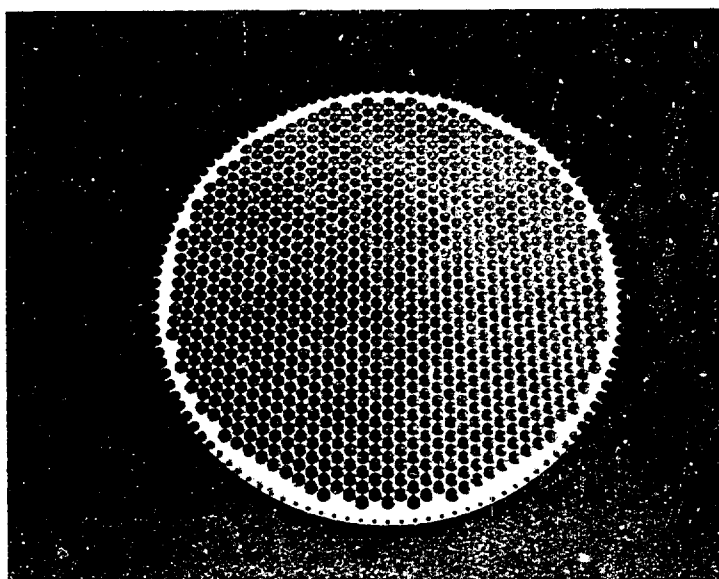


Figure No. 7 Halfwave Thick Dichroic Filter

Because the geometry shown in Fig. 4 tilts the dichroic filter at 30 degrees off normal to the X-band horn boresight, the E- and H-plane dichroic resonant frequencies are slightly split. Use of circular polarization results in different transmission phase shifts for orthogonal waves traversing the filter. The differential phase shift results in an on-axis X-band ellipticity of 1.8 dB which, accepting a perfectly circularly polarized antenna at the other end of a link, produces an additional 0.04 dB transmission loss. Another result of differential resonant frequencies for the tilted array is an approximate -18 dB reflection. This has two effects; an additional 0.04 dB reflection loss, and a slowly varying noise temperature term for the complete antenna, due to scatter, which is a function of elevation angle. The magnitude of this additional noise is 0.4 to 1.2K.

The total gain degradation at X-band is therefore 0.10 dB for a link employing circular polarization. The total noise temperature degradation is 1.6 to 2.4K. Accepting 2.0K as an average, and referenced to a base operating noise temperature of 21K, 0.4 dB is lost to noise, for a total G/T reduction of 0.5 dB. Prospects for largely eliminating the reflection and elliptical polarization loss appear bright. If accomplished, the overall degradation at X-band due to this technique appears limited at 0.02 dB gain and 0.25 dB temperature, for aluminum construction and a 21K base system temperature.

4. FULL SCALE REFLEX FEED MEASUREMENTS

A feature deemed necessary, at least for the prototype full scale feed, was mechanisms to allow rapid retraction or stowage of both dual band feed reflectors. By these means the rather small G/T degradations predicted could be accurately and reliably verified using radio star techniques. A further use of the mechanism on the ellipsoidal reflector is to permit precision closed loop S-band polarimetry previously employed (Stelzried, 1970). In this S-band only mode, full advantage of a very accurate polarimeter would not be compromised by increased cross polarization. A final use of the mechanism on the dichroic reflector is to allow a clear field of view for the K-band feed. Figure 8 shows a model TRICONE demonstrating the reflex dichroic feed elements extended and retracted.

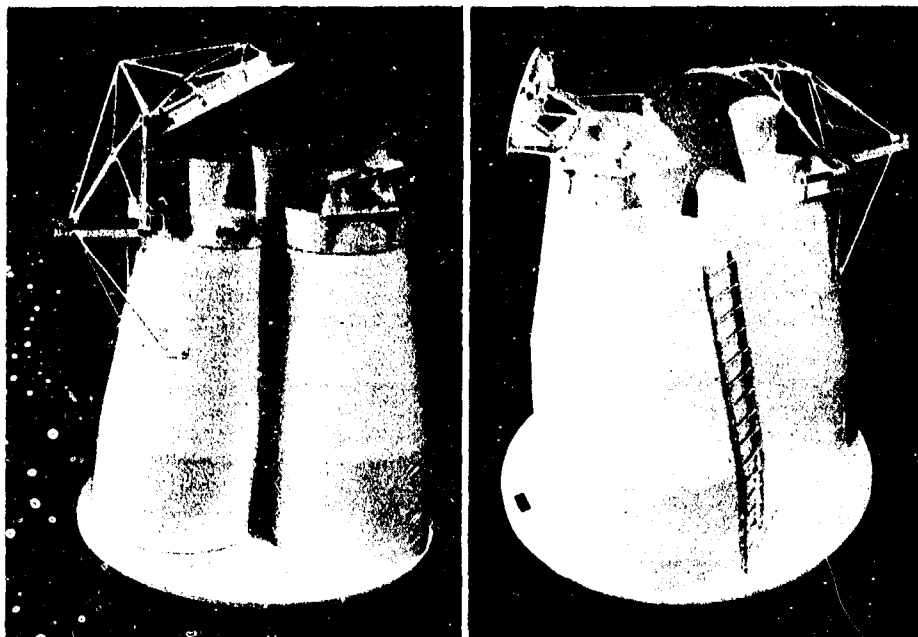


Figure No. 8 Reflex Dichroic Feed Elements Extended and Retracted

64-m antenna tests were conducted to include differential measures of the all important G/T at both bands, boresight coincidence or beam coaxiality, and high power transmission, at frequencies of 2.295, 8.415 and 2.115 GHz, respectively. Table 2 summarizes the measured performance of the full scale prototype dual band feed as installed at Goldstone, California, January 1973.

In Table 2 it is seen the measured S-band gain performance indicates improved performance (+0.01 dB), when pointing on the S-band beam peak. When allowance for 0.04 dB pointing loss is made, (discussed below) the S-band gain performance difference between reflex and non-reflex modes is difficult to distinguish (0.03 dB). Because of the reduced forward spillover and the TRICONE geometry, the S-band noise temperature performance is seen improved in Table 2. Most of this improvement is due to relative feedcone positions upon the TRICONE with respect to the ground, however, and is not attributed to the new feed. This is so because the S-band radiation, in the reflex mode, effectively emanates from Fx rather than Fs (Fig. 4). The X-band measured performance is in perfect agreement with predictions. The standard deviations in the gain difference determinations are approximately 0.02 dB and 0.10 dB, for S- and X-bands respectively. No deleterious thermal effects are observed with use of full uplink power.

TABLE 2
PREDICTED AND MEASURED PERFORMANCE SUMMARY
REFLEX DICHROIC FEED

	PREDICTED	MEASURED	NOTES
S-Band Gain	-0.055 dB	-0.03 dB	Measurement includes 0.045 dB Pointing Loss
S-Band Temperature	None	None 2.0K	Above 30 Degrees Elevation Angle Improvement Below 30 Degrees Elevation Angle
X-Band Gain	-0.10 dB -0.06 dB	-0.06 dB	Circular Polarization Random Polarization
X-Band Temperature	+1.6 to 2.4K	+1.5 to 2.3K	
Uplink cw Power	None	None	

Figure 9 is a view, facing the parabolic reflector, relative to local vertical, of the RF beam positions in space. Four beams are shown; the singular S- and X-band non-reflex beams (subreflector individually focussed and dual band reflectors stowed) and the simultaneous reflex beams (subreflector focussed to Fx and dual band reflectors functional). Several observations are worthwhile noting. The singular S- and X-band beams are offset 0.003 degree, typical of our experience with attained accuracy in feedhorn placement within the feedcones (± 6 mm) and TRICONE subreflector repeatability. Use of the dichroic reflector produces the noticeably lower X-band reflex beam (0.011 degree). This results from refraction through the relatively thick dichroic plate. The 30-60 degree characteristic seen in Fig. 9 is traceable to the TRICONE geometry (Fig. 8) with respect to local vertical. Upon first installation, the S-band reflex beam was found displaced 0.009 degree to the right of the non-reflex beam. This effect results from use of circular polarization in the presence of asymmetric geometry induced cross polarization mentioned above. Although not verified, it is predicted use of the opposite hand circular polarization would produce an S-band reflex beam peak displaced an equal amount to the left of the non-reflex beam.

Minor mechanical shimming subsequently moved the S-band reflex beam into the most advantageous location relative to the X-band reflex beam, as seen in Fig. 9, for the obvious reason of minimizing gain loss due to pointing. As shown in Fig. 9, when tracking on the X-band reflex beam peak, a gain loss of 0.045 dB is incurred at S-band. Within the limits imposed by the aforementioned S-band cross polarization induced beamshift, the present simple modification to the original mechanically determined alignment is the best possible in order to provide for future S-band polarization diversity in the reflex mode. The reason for the alignment modification was entirely traceable to the X-band refraction through the dichroic plate.

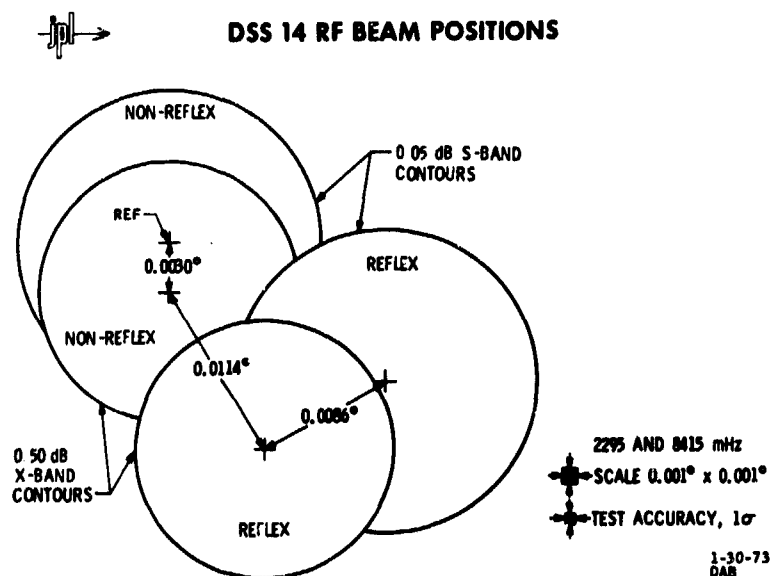


Figure No. 9 RF Beam Positions; Reflex Dichroic Elements Extended and Retracted

Figure 10 shows a simultaneous radio star drift scan using high resolution S- and X-band noise adding radiometers (Batelaan, 1970) as recorded on a 2 pen recorder. The high degree of coaxiality between the reflex beams is obvious. The expected half power beamwidths at each band is further verification of proper performance. Finally, Fig. 11 provides a view of the full scale reflex-dichroic feed installed and in the extended functional position on the NASA/JPL 64-m antenna at Goldstone, California

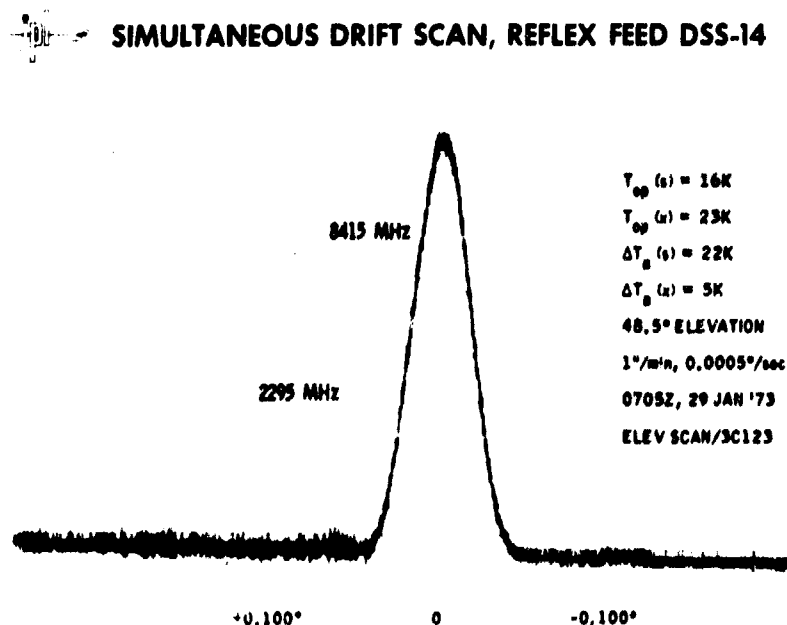


Figure No. 10 Radio Star Simultaneous Drift Scan



Figure No. 11 Full Scale Reflex Dichroic Feed Functional on 64-m Antenna

5. SUMMARY AND CONCLUSIONS

A dual band feed suitable for large ground microwave antennas has been described. In contrast with some solutions to the difficult problem of dual band feeding reflector antennas, the implementation described retains high G/T performance at both bands as well as not degrading very high cw power transmission at the longer wavelength.

Conceptually, the approach centers on an all-Cassegrain arrangement and use of an all metallic dichroic filter. A priori estimates of performance are possible and reliable, thereby minimizing risks. Present performance is obtained with minimal degradations, in G/T, of substantially less than 0.1 dB (low band) and 0.5 dB (high band). Possible improvement in high band performance to 0.25 dB is considered achievable with reasonable means.

Facility operating time and/or performance penalties are frequently experienced in providing rapid change or multiwavelength feeds for large ground antennas. Both radio/radar astronomy centers as well as deep space tracking installations share this common problem despite ever increasing technical and economic demands. The approaches described above (TRICONE, REFLEX DICHROIC FEED) yield significant capability and flexibility without undue performance penalties nor unrealistic reconfiguration times.

The ambitious objectives of the Mariner-Venus-Mercury project primary mission and experiments will undoubtedly be enhanced through use of the described additional capability.

6. ACKNOWLEDGEMENT

The reflex dichroic feed development reached the present state of perfection only through encouragement and support from NASA-Office of Tracking and Data Acquisition, the JPL Telecommunications management and the dedicated, consistent and innovative efforts of many engineers and technicians involved in the 3 year program.

- BATELAAN, P. D., GOLDSTEIN, R. M., and STELZRIED, C. T., "A Noise Adding Radiometer for Use in the DSN," Jet Propulsion Laboratory Space Programs Summary 37-65, Vol. II, pp. 66-69, September 30, 1970.
- BATHKER, D. A., BRUNSTEIN, S. A., and LUDWIG, A. C., "Dual Frequency Microwave Reflex Feed Patent Application," U.S. Patent Application SN-290022, NASA Case No. NPO-13091-1, Jet Propulsion Laboratory, September 18, 1972.
- KATOW, M. S., "S- and X-Band RF Feed System," Technical Report 32-1526, Vol. VI, pp. 139-141, Jet Propulsion Laboratory, Pasadena, California, December 15, 1971.
- LUDWIG, A. C., "Calculation of Scattered Patterns from Asymmetrical Reflectors," PhD Dissertation presented to the Faculty of the Graduate School, University of Southern California, June, 1969.
- LUDWIG, A. C., "Calculation of Scattered Patterns from Asymmetrical Reflectors," Technical Report 32-1430, Jet Propulsion Laboratory, Pasadena, California, February 15, 1970.
- LUDWIG, A. C., "Near-Field Far-Field Transformations Using Spherical-Wave Expansions," IEEE Transactions, Antennas and Propagation, Vol. AP-19, No. 2, pp. 214-220, March, 1971.
- POTTER, P. D., "Application of Spherical Wave Theory to Cassegrainian-Fed Paraboloids," IEEE Transactions, Antennas and Propagation, Vol. AP-15, No. 6, pp. 727-736, November, 1967.
- POTTER, P. D., "S- and X-Band RF Feed System," Technical Report 32-1526, Vol. VIII, pp. 53-60, Jet Propulsion Laboratory, Pasadena, California, April 15, 1972.
- POTTER, P. D., "S- and X-Band Feed System," Technical Report 32-1526, Vol. XV, pp. 54-62, Jet Propulsion Laboratory, Pasadena, California, June 15, 1973.
- REID, M. S., and BATHKER, D. A., "Low Noise Microwave Receiving Systems on a 64-m Antenna," 1972 IEEE-GMTT International Microwave Symposium, IEEE Catalog No. 72 CHO 612-2-MTT, pp. 17-19.
- REID, M. S., CLAUSS, R. C., BATHKER, D. A., and STELZRIED, C. T., "Low Noise Microwave Receiving Systems in a World Wide Network of Large Antennas," Proceedings IEEE - Special Issue, Radio and Radar Astronomy, September, 1973.
- STELZRIED, C. T., LEVY, G. S., and KATOW, M. S., "Multi-Feedcone for Cassegrain Antenna," Invention Report 30-1247, Jet Propulsion Laboratory, October 25, 1967. See also NASA Technical Brief 69-10269 and U.S. Patent No. 3,534,375.
- STELZRIED, C. T., "A Faraday Rotation Measurement of a 13-cm Signal in the Solar Corona," Technical Report 32-1401, Jet Propulsion Laboratory, Pasadena, California, July 15, 1970.
- WOO, R. T., "A Low-Loss Circularly Polarized Dichroic Plate," IEEE G-AP 1971 International Symposium Digest, pp. 149-152, IEEE Catalog No. 71C39-AP.

DISCUSSION

S. CORNBLEET: Could not the ellipticity effect at x-band have been overcome by using cells of square cross-section? In addition would not an all dielectric (multilayer) filter have been an advantage?

D.A. BATHKER: We view each cell as a single pole resonant filter, capable of transmission in each orthogonal polarisation. But the second order effect of having the array of cells tilted at 30° to the incident wave in fact produces two resonances, closely spaced in frequency. Presumably this is caused by the equivalent circuit elements (2 and susceptances separated by a length of transmission line slightly shorter than $\lambda_g/2$) being different for various incidence angles. I believe square cross section would still produce the resonance splitting. Very slightly rectangular, or elliptical cells rather than square and round, respectively, have been tried with success.

The selection of an all metallic realization of the filter was based on the high w. power we simultaneously transmit, as well as the desire to keep the insertion loss upon reception as low as possible for operating noise temperature minimisation. While a multilayer filter may well have advantage in other systems, I believe the single pole all metallic version is superb for our specific system.

J.R. MARK: The loss in gain due to cross polarisation was stated as $-.001$ dB & $.005$ dB for S-band tricone reflex tricone feeds. What are the corresponding levels of the cross polar lobes? Also what are the cross polar lobe levels for x-band operation?

D.A. BATHKER: This conference further demonstrates the keen interest in cross polar performance of late, judging from the numbers of papers either dealing with the topic or mentioning it, and with the many queries from the floor to various authors. Ignoring the well known diagonal plane cross polarization found in symmetric reflecting systems, we have dealt with the principal plane cross polar lobes, generated by the asymmetrical S-band feed. As in a hoghorn or horn reflector feed, principal plane cross polar lobes are generated in the mechanical symmetric plane. From calculation we obtain -21.5 dB relative to the peak of the main beam of the 64 m. aperture. The calculation ignores only the quadripod feed support. I estimate the feed support generated cross polarization is rather small at the near-in angles we are discussing here (0.1 degrees), and our confidence in the calculation is high. The given value is therefore considered the worst cross polar beam anywhere in the total pattern, using the reflex-tricone feed for the tricone taken alone, which is a slightly asymmetric system, the expected value, again calculated ignoring the feed support, is -28 dB, in the mechanical symmetric plane. At x-band we have dealt only with the axial cross polarization introduced by the dichroic plate, which arises due to different insertion phase shifts for orthogonal polarization. The differential phase shift is approximately 6 deg. yielding 1.8 dB axial ratio. Some additional information is available (JPL Technical report 32-1526, vol. XVII pp. 28-38, and 32-1526, vol. XV pp. 54-63.)

Employment of Nearfield Cassegrain Antennas with High Efficiency and Low Sidelobes, taking the Intelsat-Groundstations and the German Helios-Telecommandstation as Examples

by

Uwe Leupelt
Wolfgang Rebhan

Siemens AG, Zentrallaboratorium für Nachrichtentechnik, Lab 548,
D-8000 München 70, Hofmannstr. 51

Summary

A number of the large reflector antennas now employed by ground stations for satellite communications are constructed according to the nearfield Cassegrain technique. After a short description of the basic electrical principles involved as well as of the method of obtaining constant aperture illumination with the nearfield antenna also and thus optimizing efficiency by suitable shaping of the reflectors, a novel design for antennas of this type will be discussed. It allows the sidelobes of the radiation pattern to be reduced without excessively reducing gain. A special toroidal aperture illumination and a favorable arrangement of the subreflector supports are used for this purpose. The dimensions and design of the 28.5-m antennas already mentioned in connection with the Intelsat system will be discussed and the 30-m antenna now under construction for the German Helios telecommand station will be described as an example for the realization of an antenna with low sidelobes. After presenting typical electrical characteristics of the 28.5-m standard antenna we will give the radiation characteristics at higher frequencies and the cross-polarization properties with the aid of measured radiation patterns. Finally we will deal with prospects for possible improvements to further increase efficiency and to reduce spillover.

1. Electrical principles of high efficiency nearfield Cassegrain antennas

During the past decade a number of large Cassegrain antennas have been developed for satellite communications, primarily for transmitting the 4-GHz and 6-GHz frequency bands. Some of these antennas operate in accordance with the nearfield technique, in which the subreflector is located in the nearfield of the feed. This arrangement has certain advantages over a Cassegrain antenna with its subreflector in the farfield of the feed. The main advantages are the wider bandwidth, lower spillover losses at the reflector edges, the correspondingly lower sidelobes and lower noise temperature and last but not least the low back radiation of the antenna. The first antenna of this type was the 25-m antenna of the satellite ground station in Raisting erected in 1964 (Fig. 1). It has a deep parabolic reflector with an F/D of 0.25 and a horn reflector feed arranged at the apex of the main reflector. An approximately plane wave propagates between the aperture of the feed and the subreflector. Therefore the subreflector is approximately parabolic in shape. However, since the power carried by the primary wave is not distributed homogeneously over the cross section of the beam but is highly concentrated in the middle, an aperture illumination pattern tapered strongly toward the edges is obtained in the main reflector aperture. As we well know, the most uniform illumination pattern possible is desired to provide high efficiency and the associated high antenna gain. Thus even at the time mentioned we tried to influence the aperture illumination in this sense. We had a measure of success with concentric rings fixed at the subreflector, which transferred more energy to the poorly illuminated edge zones of the main reflector, but at the same time resulted in phase errors. The overall efficiency of the antenna was 53 % [1]. In the years that followed the method of aperture field synthesis by means of suitable shaping of both Cassegrain reflectors became well known, partly through the work of Galindo [2]. These principles were applied to the second and third nearfield Cassegrain antenna of the Raisting ground station, their diameter having been increased to 28.5 m, and to a similar antenna erected in the Netherlands, and provided an initial increase in antenna efficiency to 67 % (Raisting II) and a final increase to 70 % and 72 % (for Raisting III and Burum I respectively). Three conditions affect the profile of the reflectors: the reflection law at the subreflector, the same ray lengths between the primary wave and the antenna aperture, and the law of conservation of energy for ray beams. The energy law provides us with an integral equation describing the transfer of the primary field to the aperture field, and this integral equation can be solved directly for some simple illuminations such as uniform illumination. The desired contours are then obtained basically by interpolation and integrating the primary field distribution determined experimentally. Since the reflector shaping method which we have refined for nearfield Cassegrain antenna is also of significance for the problem of sidelobe suppression, it is outlined below: the primary wave which is required to be rotationally symmetrical is reflected at the subreflector roughly in accordance with the laws of optics and transformed to a secondary wave of certain intensity distribution according to the subreflector curvature. The field is intensified toward the edge zones of the main reflector or weakened toward the apex zone either by reducing the curvature of the subreflector in the edge zones or by increasing it at the center. The subreflector is much deeper than in the case of a paraboloid as a result of this change of profile. Since a reflector of arbitrary shape no longer has a focal point, the wave radiated from the subreflector is no longer spherical. The shape of the main reflector is also changed to compensate for resultant phase errors. Thus the depth of the main reflector is increased by the same amount as that of the subreflector, though the relative change is much less. The exact calculation makes allowance for the fact that any change in the profile of the main reflector also has a certain effect on the path losses of the secondary wave and thus the amplitude characteristic of the aperture distribution.

In order to make the aperture field synthesis method even more effective, future efforts will be directed toward the improvement of the feed or nearfield Cassegrain antennas, too, to provide an approximately rotationally-symmetrical primary field distribution. Some of the details on the design and experimental results of the antennas developed by Siemens for Intelsat ground stations have already been presented [3,4,5]. The overall efficiency of 70 to 72 % obtained by means of reflector shaping almost represents the theoretical optimum obtainable with antennas of this kind. The losses incurred are mainly due to unavoidable diffraction and shadowing effects.

2. Principle of an antenna with very low sidelobes

Along with gain, the sidelobe envelope is another important feature of a satellite ground antenna. Sidelobes which are directed at "hot zones" of the neighboring area increase the antenna's noise temperature. Sidelobes also pick up interference from other radiation sources and themselves act as a source of interference to other communications services such as radio relay links at higher transmitting powers. Our nearfield Cassegrain antennas which are designed for maximum gain have very high sidelobe attenuation in the rear hemisphere and in the bordering solid angle ranges of the front hemisphere.

In the solid angle ranges bordering onto the main lobe, however, the sidelobes are still relatively high as a result of the uniform illumination which is unfavorable in this respect. The first attempt to reduce the sidelobes in this range was made with the 30-m antenna of the German Helios telecommand station now under construction near Weilheim (frequency range 2.1 to 2.3 GHz). Fig. 2 shows the theoretical possibilities. Curve 1 is the sidelobe envelope curve obtained with uniform illumination. The slight variations are caused by the shadowing effect of the subreflector. Curve 2 shows the envelope curve for quadratic tapered aperture distribution. The effect of the subreflector having been ignored. The sidelobes are greatly reduced. Curve 3, which is a true representation of the antenna characteristic, is obtained if allowance is made for the influence of the subreflector. The wide humps are the sidelobes of the subreflector's interference radiation pattern. The presence of the subreflector almost completely offsets the reduction of the sidelobes, and for this reason other illumination patterns which are otherwise very favorable (e.g. Taylor illumination) do not make any great improvement in this case. As theoretical investigation has shown, the real cause of the high sidelobes is the sharp fall in the field at the edge of the subreflector. The sidelobe envelope curve 4 in Fig. 2 is obtained, for example, with the aid of a similarly uniform field taper, such as that towards the aperture edge. Although the influence of the subreflector is still noticeable, improvements in the sidelobe suppression of over 20 dB are evident. The first sidelobe is the only one which is not reduced. However, since the first sidelobes are never in the horizontal plane under actual operating conditions this is of no consequence. Fig. 2 also shows the torus-shaped illumination associated with envelope curve 4. The shape of the curve obeys the function

$$f(x) = 1 - x^2 + 2x \frac{x_M}{M} \cdot \ln x \quad (1)$$

where x is the radius referred to the antenna radius. x_M signifies the point of maximum illumination and is related to the normalized subreflector radius α according to the formula:

$$2x \frac{x_M}{M} = (\alpha^2 - 1)/\ln \alpha \quad (2)$$

The function is optimal in the following sense: the smoothest possible illumination characteristic is desired for reasons of realization and of the effect on the sidelobes. If the integral of the squared first derivatives of the aperture distribution taken across the aperture area is used to represent the degree of smoothness of the curve, a function giving the maximum aperture efficiency is obtainable for a given smoothness using the calculus of variations. This function contains a parameter which depends on the smoothness and which can be so determined that the curve is as smooth as possible. We obtain equation 1 for this parameter value. It serves as a basis for the design of the antenna of the Helios telecommand station. In spite of the improved sidelobe attenuation, the aperture efficiency of 80.5 % is markedly higher than the 74 % for the quadratic tapered aperture distribution.

The illumination is produced by suitable shaping of the Cassegrain reflectors. For calculation purposes the calculating method outlined above for the uniform illumination was extended in the following manner: the desired torus illumination is transformed return to the primary field along the ray paths of a reflector system computed for constant aperture distribution. There the measured primary field strength is divided by the transformed torus distribution afterwards the fictitious primary field obtained in this way is used to calculate new reflector contours for a uniform illumination pattern. The torus illumination is again transferred to the primary field along the rays of the new reflector system a.s.o. By using this iteration process which converges sufficiently when certain conditions are met it is possible to determine successive pairs of reflector contours which rapidly approach the correct contour. Fig. 3 shows the exact contours with associated secondary rays and the phase and amplitude distribution in the primary field determined from experimental values. Experiments were made with a model for 33 GHz to see whether the torus illumination could be realized. Fig. 4 shows the result of testing one half of the aperture with a probe (the curve marked by a thick line). The outer side of the circular maximum falls by about 20 dB while the inner side falls by about 15 dB. Slight interference variations, resulting

primarily from the spillover of the primary wave at the edges of the subreflector, make the response curve somewhat uneven and may be even more troublesome in other measuring planes of the field. The thin curve in Fig. 4 shows the intensity of the primary field measured in the aperture after the subreflector has been removed. We can see clearly the way in which the spillover fills the inner zero point of the torus illumination, with the result that the sidelobe level of the antenna rises. Further sources of interference to the aperture field are diffraction effects, reflector tolerances and especially the subreflector supports, which also raise the sidelobe level.

To reduce influences of the supports only two struts were used, both fixed in the main vertical plane of the antenna. The subreflector is tensioned perpendicular to this plane by means of thin ropes. The interference radiation caused by the supports is mainly concentrated in the plane defined by the guy ropes. Since the antenna is only operated at angles of elevation of over 10° , the interference due to the supports is greatly reduced in the horizontal plane, which is the one concerning us here. The interference in the plane of the supports is lower with torus illumination than with uniform illumination. In spite of the numerous sources of interference to the aperture illumination which have not yet been minimized, the maximum sidelobe level in the horizontal plane was shown to have decreased by approximately 5 dB throughout the antenna's operating elevation range when changing from uniform to torus illumination in experiments carried out with the 33-GHz model. The value of about 50 dB obtained for the sidelobe suppression is still considerably above the theoretical maximum, however. The total efficiency determined experimentally is around 50 % in the case of this not yet fully optimized antenna, putting it on a par with the efficiency of conventional parabolic antennas tapered down toward the edge of the aperture. Finally we would like to point out that the new principle of torus illumination is also applicable with other antennas whose apertures are partially obscured by interfering bodies.

3. Implementation and construction of nearfield antennas

Since satellite communications commenced in the early Sixties, approximately 90 antennas for so-called standard ground stations have been put into operation or are under construction in accordance with the ICSC (Interim Communications Satellite Committee) guidelines and in the framework of the world-wide Intelsat communications system. They are based on the experience gained with the first experimental stations. The Cassegrain antenna has become almost the universal standard type. The nearfield Cassegrain antenna accounts for about 15 % of this group. We ourselves employ a horn reflector with an aperture comparable in size to the diameter of the subreflector as a nearfield feed. (Fig. 5). It consists of a parabolic passive reflector illuminated by a conical horn with a circular cross-section. The apex of the horn and the focus of the passive reflector coincide; the axis of the horn is perpendicular to that of the paraboloid. The spherical wave from the horn is transformed to a plane wave. The energy radiated by the horn reflector remains concentrated in an approximately parallel ray beam over a wide frequency range in the nearfield. The performance of the antenna which to a large degree observes laws of geometrical optics is of decisive importance for the extremely broadband nature of the system.

This feed is so incorporated that the horn axis lies in the elevation axis and an RF rotary joint near the horn apex allows the equipment to be connected to be set up without regard to the antenna's elevation movements. A completely stationary equipment room is also made possible by bending the conical horn section downwards with the aid of an additional plane reflector and feeding the apex of the horn into a second RF rotary joint in the azimuth axis via a slightly curved circular waveguide (Raisting 2). The flare angle and length of this type of feed is adaptable within wide limits to the mechanical design of the antennas.

The standard antennas which we have designed up till now have a main reflector resembling a paraboloid with a diameter of 28.5 m and a depth-to-diameter ratio of approximately 0.26. The rms value of the main reflector profile is about 1 mm, and the ratio of the diameter of the subreflector to that of the main reflector is about 0.09. The subreflector is held in the plane of the main reflector by 4 short metal supports, oval in cross-section. Rear-heating protects the reflectors against the effects of the weather, while a dielectric window in the conical section of the feed prevents damp from penetrating. The reflectors are given a coating of lacquer which diffuses the energy it reflects so that they do not become warm on one side only.

The mechanical design of these antennas varies. The Raisting 2 and 3 antennas, for example, are so-called king-post systems, whereas the Raisting 1 and Burum 1 (Netherlands) models are wheel and track stations.

The nearfield Cassegrain method is also being used for the German Helios telecommand station now under construction. The station being built under the management of the DPVLR (Deutsche Forschungs- und Versuchsanstalt für Luft- und Raumfahrt). The Krupp company is responsible for the mechanical design and construction of the antenna. Fig. 6 shows a section through the wheel and track antenna which weighs 400 tons and employs the methods for improving sidelobe suppression described in section 2. A reflector with a diameter of around 30 m is used to provide the prescribed gain of at least 52 dB in the 2.11 to 2.12-GHz frequency range.

The horn reflector feed has a horn flare angle of 14° and a 2.3-m aperture. Its total length is 9.5 m. The subreflector diameter is 4.5 m. The ratio of the reflector's depth to its diameter is approximately 0.266. Reference has already been made to the special subreflector support configuration which is favourable with respect to side-lobe suppression. The rms value of the main reflector of ≤ 0.7 mm is very low for an S-Band antenna. The broadband feed and the high quality of the reflector make the system extremely flexible. It can be operated at frequencies of up to 10 GHz and more by exchanging waveguide components at the feed input.

For the time being only computer-controlled transmitting operation is being provided for the Helios project (maximum power 20 kW), but an expansion with receiving and autotracking equipment is possible. A universal polarizer operating on the principle of two mutually rotatable "quarter-wave plates" is connected to the feed to allow the polarization to be set as circular or as linear as required during the tracking of the polarization plane (Faraday effect). The system will commence operation after its completion in the Spring of 1974 in conjunction with the DSN-system of the NASA [6].

4. Electrical characteristics of the 28.5-m antenna for the standard ground stations

The main design criterion for the standard ground station is the input sensitivity which is defined as the ratio of the antenna gain to the system noise temperature. This so-called G/T value, referred to the preamplifier input, is fixed by ICSC at ≈ 40.7 dB/K at 4 GHz and 5° elevation. With the hitherto customary cooled amplifiers ($T_p = 20$ K) an antenna gain of ≥ 59 dB has been necessary, a figure which can be attained with reflector diameters of 27 to 30 m.

Typical electrical specifications of the 28.5-m antenna:

Gain at the feed input	60 dB at 4 GHz	63.5 dB at 6.2 GHz
Antenna efficiency at 3.7 to 4.2 GHz	0.7 to 0.72	
Antenna efficiency at 5.925 to 6.425 GHz	0.65 to 0.68	
Antenna noise temperature (4 GHz)		
5° elevation	36 ± 4 K	
90° elevation	8 to 10 K	
half power beamwidth 4 GHz	$\approx 0.16^\circ$	
half power beamwidth 6 GHz	$\approx 0.11^\circ$	
Attenuation of the 3.7 to 4.2 GHz	≈ 16 dB	
first sidelobes 5.925 to 6.425 GHz	≈ 15 dB	

These values refer to circular polarization.

The prescribed G/T value is met throughout the entire receiving range from 3.7 to 4.2 GHz and is considerably above specification in parts of it.

The first standard ground stations to be equipped with low-noise uncooled preamplifiers are being planned at present. The previous system temperatures of approximately 70 K (at a 5° angle of elevation) will then rise to approximately 100 to 110 K. The antenna diameter will increase to about 32 to 33 m for the same input sensitivity as before.

The antenna radiation patterns measured in the azimuth range demonstrate the favorable sidelobe suppression (Fig. 7). The isotropic level is reached at an angle of approximately 10° to 15° against the main direction of radiation. The attenuation for angles of more than $\pm 90^\circ$ is greater than 85 dB, apart from a few peaks. These discrete level increases are not real characteristics of the radiation pattern, however, nor are other peaks in the range from about the isotropic level onwards, but represent echoes from the surrounding area. During the radiation pattern measurement towards a satellite transmitter sending CW signals at very low angles of elevation the main beam scans hills, the terrain and other objects in the azimuth direction which are also illuminated by the test transmitter, and picks up energy which they scatter. Use of a pulse measuring method may make improvements in this respect.

The antenna always autotracks the satellite. The angular displacement information is derived from higher waveguide modes which are excited along with the fundamental mode in the horn reflector as the result of pointing errors. Since the tracking modes exist in the same feed as the communications signal, i.e. use the same aperture, the tracking is very sensitive. For the circular polarization used with the Intelsat system, for example, the E_{01} -wave which is additionally excited in the circular cross-section of the horn, when combined with the sum signal, can obtain all the tracking information alone. An additional wave mode such as the H_{21} - or H_{01} -mode is required in the case of linear polarization. The tracking modes are decoupled from the signal path via slits or pins. After suitable conversion they provide a difference signal which together with the sum signal provides the automatic control system signals for the antenna drive system. The tracking accuracy is approximately $\approx 0.01^\circ$.

5. Future applications and possible improvements

Measurements carried out on a standard 28.5-m antenna in the range from 3.7 to 15.5 GHz (Figs. 8 and 9) have shown the very broadband characteristic of the nearfield system with an horn reflector feed. The radiation patterns are very favorable at all the frequencies measured, and the half power beamwidth is almost a linear function of the frequency (0.16° at 4.0 GHz, approximately 0.06° at 13.0 GHz). An even wider frequency range is theoretically possible. Special demands on the broadband operation as may occur in research systems, radio surveillance stations or future communications systems, which operate with several separate frequency ranges simultaneously (e.g. 4/6 GHz and 12 GHz), can then be met quickly without altering the feed or the antenna, simply by replacing waveguide components.

With the so-called frequency-reuse technique the transmission capacity is doubled by simultaneously transmitting and receiving orthogonal signals of the same frequency (linearly or circularly polarized). Freedom from interference depends mainly on the cross-polarization decoupling attainable on the entire path, to which the ground antenna contributes significantly. The cross-polarization behavior of the nearfield antenna with asymmetrical horn reflector feed differs from that of the centrally-fed antenna. Since the line of symmetry of the horn reflector segment is parallel to the axis of elevation, the cross-polarization levels of the radiation patterns measured in the azimuth sections with linear polarization are much lower than those of the corresponding radiation patterns in the elevation planes, because theoretically the cross-components of the aperture field only rise with respect to the longitudinal horn axis. Fig. 10 takes as an example the measured values of a 28.5-m antenna to demonstrate these relationships (horn flare angle = 18°).

The differences between the cross-polarization maxima in the two pattern planes are about 10 to 15 dB. The maxima, referred to the maximum in the main direction of radiation in the azimuth pattern, reach values of -25 dB and fall to about ≤ -30 dB within a practical width of the main radiation pattern of, say, 1 dB, since there is always a well defined zero point of the cross-polarization in the main direction when the antenna is accurately adjusted.

The decoupling obtainable with circular polarization is additionally influenced by the inherent error of the used polarizers. This error, defined as axial ratio of the resultant elliptical polarization, corresponds to a component rotating in the opposite sense to the main direction of rotation which degrades the main channel accordingly. An axial ratio of 0.5 dB theoretically only permits a maximum decoupling value of 30 dB. However, such low axial ratios cannot be realized over broad frequency ranges (e.g. Intelsat) with the polarizers now available.

Reflections in the antenna system which cause the sense of rotation of the circular wave to change lead to additional interference. A maximum reflection coefficient of 3 % would be theoretically permissible for a decoupling value of 30 dB.

Thus it would appear that the decoupling should not fall far below 25 dB on a broadband basis with circular polarization.

Other points to be taken into consideration during operation are that the antenna used aboard the satellite has its own crosspolarization component, positional errors degrade the decoupling, and most important of all atmospheric effects have a considerable influence. In practice, decoupling values of less than 20 dB were measured with Intelsat antennas. Different delay times and, to a greater extent, scattering due to rain were responsible for these values, which would probably be too low for operation purposes.

Future improvements will mainly be directed towards the broadband symmetrization of the horn reflector characteristic by exciting additional wave-forming modes or hybrid modes in the feed. Thus large antennas should not only reduce cross-polarization but also improve efficiency by about 3 % or 4 %. In future increasing emphasis will be placed on sidelobe suppression. The horn reflector offers the possibility of reducing the spillover at the subreflector edge by slight focussing of the primary ray beam. For this purpose the paraboloid segment can be replaced by another suitable profile, such as an ellipsoid. Spillover values of ≤ 1 % can thus be obtained. Moreover, by suitably shaping the feed reflector asymmetries of the radiation pattern in the near-field can be reduced.

The authors are indebted to R.Bredow, G.Schindler and H.Thiere whose assistance in the work has been most valuable for the preparation of this paper. We also would like to express our thanks to the DFVLR for their sponsorship of the work on a low sidelobe Cassegrain antenna.

References:

- [1] Trentini G.v., Romeiser K.P., Jatsch W., Frequenz 19 (1965) p. 402
- [2] Galindo V., IEEE Trans., AP 12, July 1964, p. 403
- [3] Trentini G.v., Romeiser K.P., Reitzig R., Frequenz 22, 1968, p. 216
- [4] Romeiser K.P., Rebhan W., Leupelt U., NTF Bd. 45 (1972) p. 103
- [5] Leupelt U., Conf. Proc., Microwave 73, Brighton UK, p. 58
- [6] Ottl H., Holl H., Proc. Telem. Conf., Los Angeles 1972

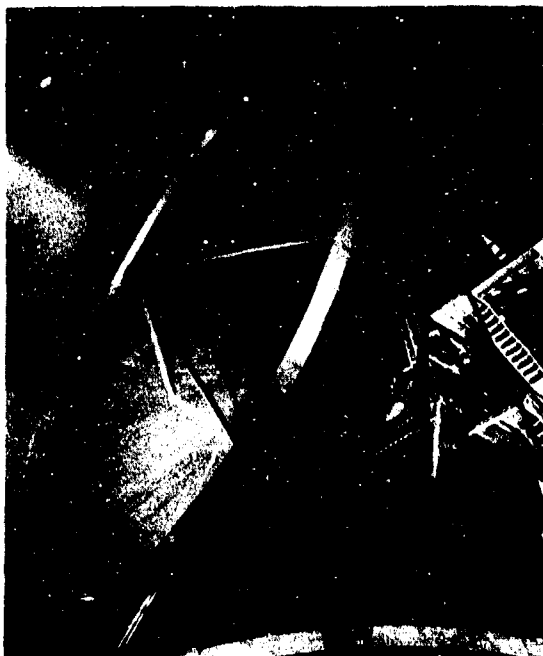


Fig.1 25 m nearfield Cassegrain antenna (Raisting 1)

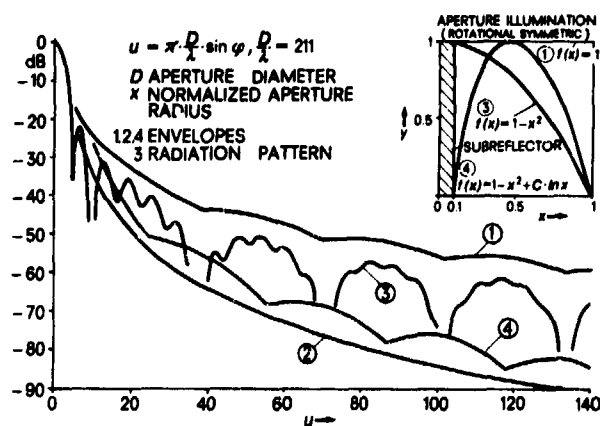


Fig.2 Calculated radiation patterns for different aperture illuminations

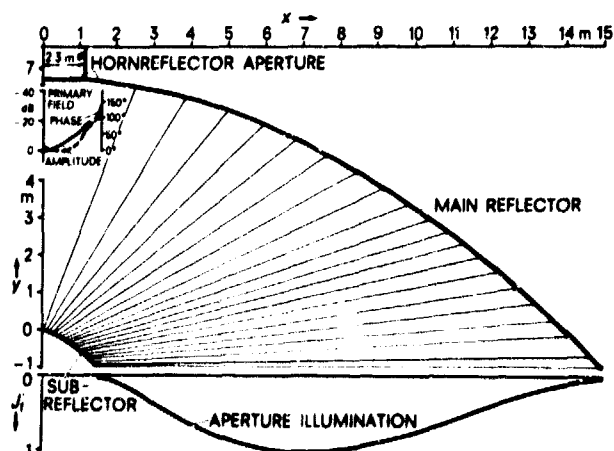


Fig.3 Cassegrain reflector system for a toroidal aperture illumination

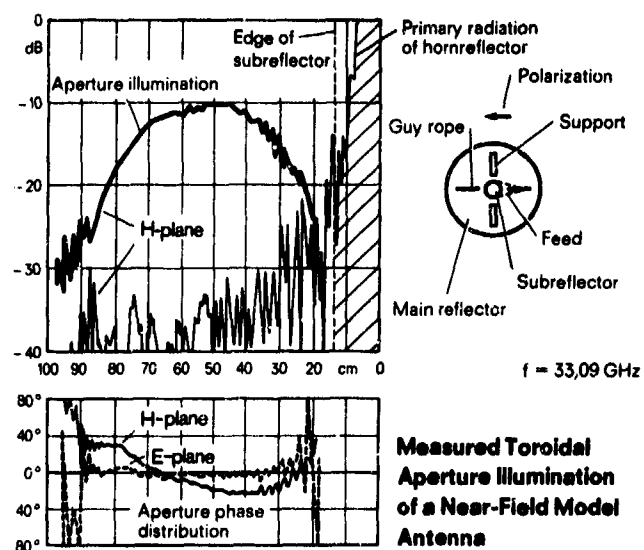


Fig.4 Measured toroidal aperture illumination (model)

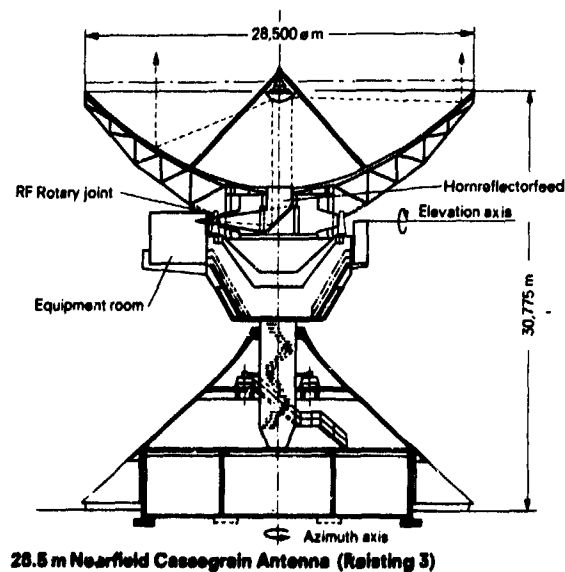


Fig.5 King-post type standard ground antenna (Raisting 3)

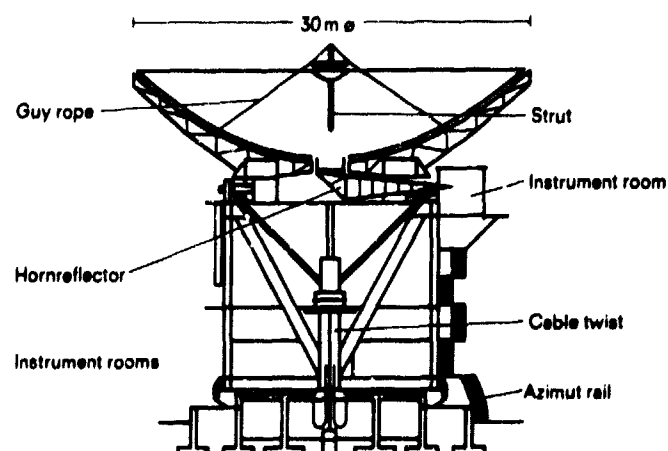


Fig.6 Wheel and track type low sidelobe antenna (Helios)

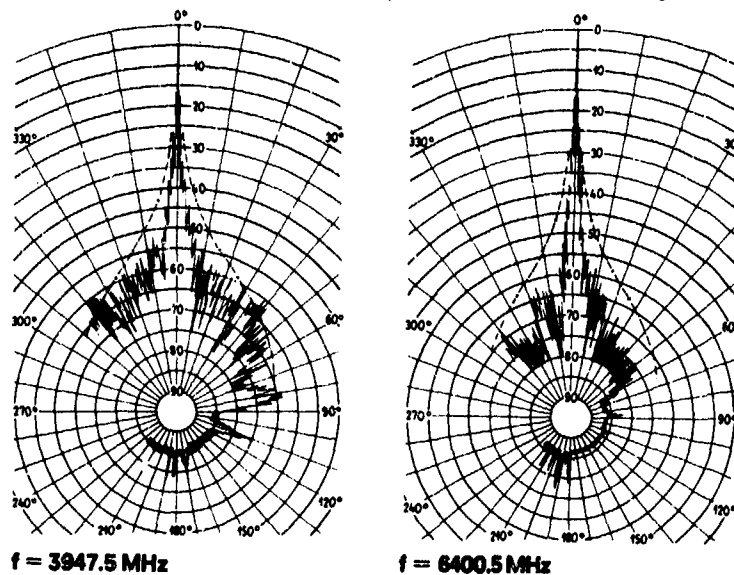
CIRCULAR POLARIZATION(DASHED LINES: $33 - 23 \log \varphi$ [dB])

Fig.7 Azimuth radiation patterns of the 28.5 m-antenna

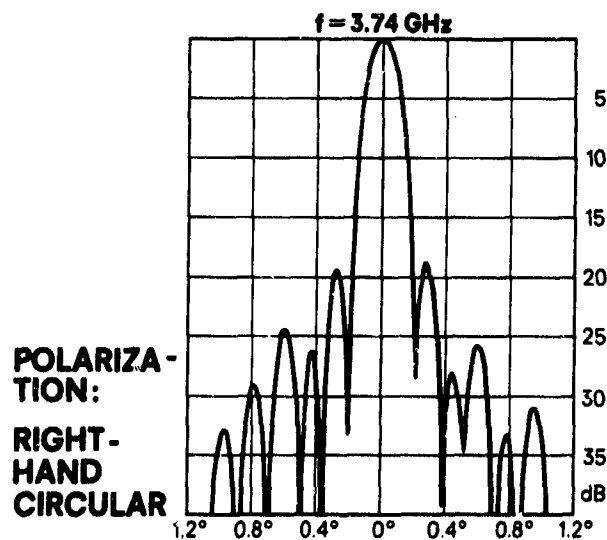


Fig.8(a) Radiation pattern of the 28.5 m-antenna

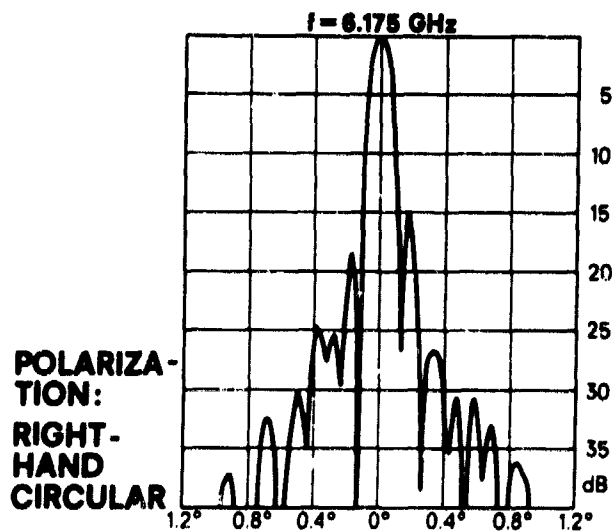


Fig.8(b) Radiation patterns of the 28.5 m-antenna

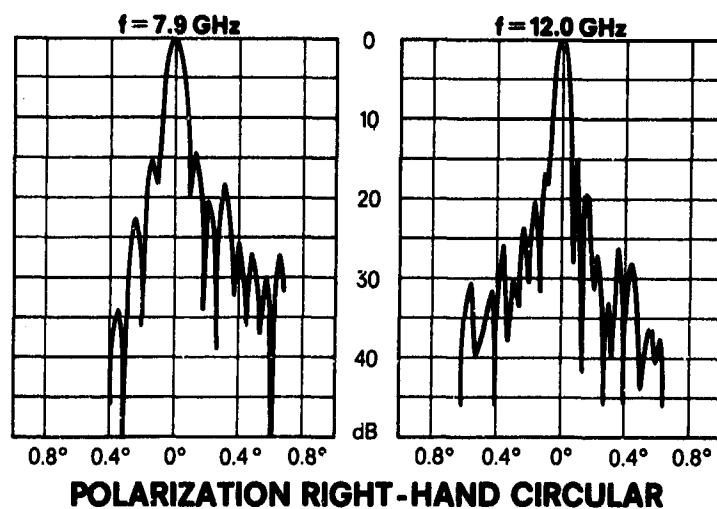


Fig.9(a) Radiation patterns of the 28.5 m-antenna at higher frequencies

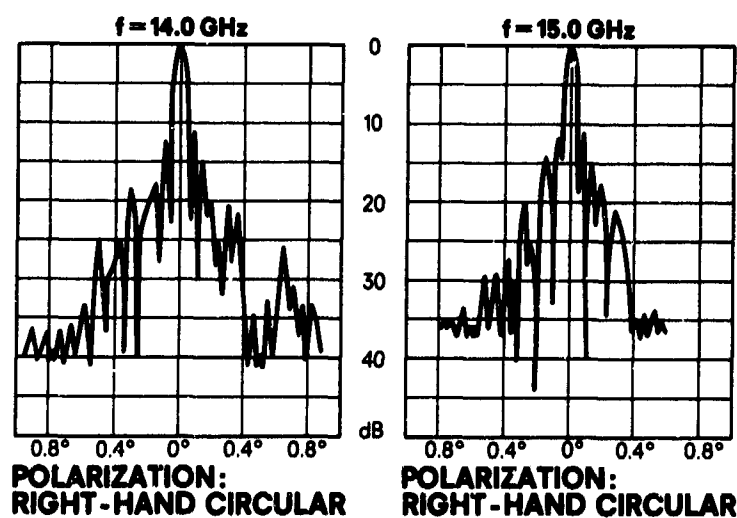


Fig.9(b) Radiation pattern of the 28.5 m-antenna at higher frequencies

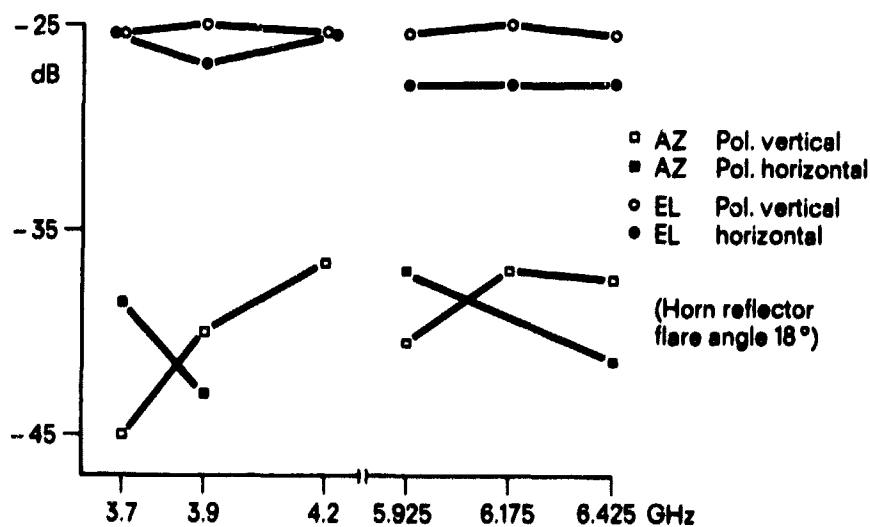


Fig.10 Maximum cross polarization levels of the 28.5 m-antenna

DISCUSSION

T. PRATT: In the Helios antenna, where torus illumination was used, what was the reduction of gain relative to the conventional near-uniform illumination? What was the improvement in G/T obtained by the torus illumination, with reduced gain and reduced far-out sidelobes?

How does its performance compare with that of the open Cassegrain antenna?

U. LEUFELT: Theoretically the directivity reduction, when taking a torus illumination as shown in Fig 2 instead of a uniform one, is from an efficiency of 99.9% to 80.5%, that is a reduction of 0.9 dB. If compared with the circularly polarised Raisting III antenna the gain reduction measured with the not yet fully optimised 33 GHz Helios model is about 1.5 dB which is an average value for horizontal and vertical polarisations. An unknown part of this reduction, however, is thought to be due to the smaller aperture of the Helios antenna when measured in wavelengths. With vertical polarisation the gain lies about 0.4 dB or a little more below that with horizontal polarisation due to the special strut configuration and the asymmetries of the primary field.

A special comparison with the open Cassegrain antenna was not made. Open Cassegrain antennas of such large diameters as discussed appear to be too expensive because of their more complicated structure, and they present difficult static and dynamic problems. For cases where the inner sidelobes are of minor interest compared with the outer ones, as was the case with the Helios antenna, it is thought that an open Cassegrain antenna has no better gain and sidelobe performance than has a rotationally symmetrical Cassegrain antenna.

G/T has not been measured. For the time being the Helios antenna is only used for transmission.

A.W. RUDGE: With regard to the cross-polarisation results presented; in which planes were these obtained?

Although the asymmetrical design of the feed may appear to produce the maximum cross-polarisation in one of the principle planes, have the authors examined the diagonal planes of the overall antenna radiation pattern in order to ensure that the levels in these planes are not greater than the results shown?

U. LEUFELT: The results were obtained in the main plane of the pattern. Measurements in the diagonal planes were not possible for technical reasons. The cross-polarisation of the horn reflector feed shows the highest possible level in the plane perpendicular to the horn-cone axis (transverse plane). This is due to the asymmetrical geometry of the horn reflector and is different from that of a straight conical horn.

D.A. BATHKER: In one view shown, referring to horizontal polarisation, the vertical struts blocking the aperture appeared to be wide while the horizontal ones were narrow, possibly being of dielectric ropes. My question is: Have overall system gain measurements been made to detect the gain loss difference due to wide compared with narrow struts? It is my opinion that struts or ropes (if metallic) of dimensions anywhere less than one wavelength (even if infinitely thin) will scatter effectively as though they are 0.5 to 1.0 wide, given parallel polarisation. For this reason I do not understand why thin struts are better than wide ones given parallel polarisation.

U. LEUFELT: It is well known that the scattering cross-section of conducting cylinders (e.g. ropes) depends on the orientation of the incident field vector with respect to the cylinder axis and is relatively greater with parallel than with orthogonal polarisation. If the diameter of the rope becomes very small compared with the wavelength, however, the resulting effective interference is accordingly much smaller than that of a strut of, say, one wavelength, even in the case of a parallel polarised E-field vector. No comparison gain measurements have been carried out on the model antenna with respect to the shadowing reduction gained by using thin metallic ropes instead of struts. The choice of these horizontal ropes, however, was not for reasons of gain, but mainly in order to optimise the sidelobe behaviour of the overall antenna pattern.

The part of the illumination obscured by the struts produces an interference pattern with high directivity and rapidly decreasing sidelobes in the main plane passing through the strut but is virtually spread in the plane perpendicular to this first plane.

Thus struts placed horizontally in the aperture basically influence the vertical radiation pattern whereas vertical struts affect the horizontal pattern. If the antenna has a certain angle of elevation, low sidelobes in the horizontal plane of the radiation pattern (as specified in our case) can be realized with two struts arranged perpendicular to the axis of elevation. Experimental farfield measurements using several support configurations have clearly confirmed this consideration.

DEVELOPMENT OF AN S-BAND DUAL MODE HORN FOR TELEMETRY RECEPTION BY THE 100 M EFFELSBERG RADIO TELESCOPE

by

W. Hess; B. Liesenkötter
MBB, Dynamics Division
Ottostrunn
Germany

SUMMARY

A Gregorian antenna system with 100 m paraboloid is being equipped with a dual mode horn feed in the secondary focus. This feed is intended to provide a favourable figure of merit of the antenna with respect to gain and noise temperature. The specified data made a horn of small flare angle and large length necessary. On the other hand the limited size of the apex cabin demanded length reduction by optimizing the horn feed zone.

In addition a directional coupler, integrated in the horn feed zone, was developed for special test purposes during operation later. All measurements during the development period as well as the qualification tests have been carried out on an X-band scaled model. The design of the original horn feed aimed in particular at cheapness, a short manufacturing period and a low weight. Thus a frame construction with non supporting inner horn structure was applied. Gain, spillover and noise temperature of the antenna system were calculated using a computer programme. The calculation was carried out by the Department of Electronic and Electrical Engineering, University of Birmingham.

1. INTRODUCTION

This dual mode horn was designed to operate in the secondary focus of a Gregorian system with 100 m paraboloid and elliptical subreflector. The antennasystem was equipped to effect the telemetry link with the Helios Solar probe to be launched in 1974.

The specified horn data were:

- frequency range 2.290...2.300 GHz
- overall antenna gain 65 dB
- as low noise temperature as possible (zenith)
- polarization-independent, rotationally symmetric main beam
- rather small horn sizes (due to the limited dimensions of the apex cabin) with respect to the electrical requirements

For special test purposes during operation later a directional coupler at the horn input had additionally to be developed.

2. DEVELOPMENT PERIOD

2.1 Selection of the principle

Preliminary experimental studies have been carried out on two Ku-band scaled horn models with equal geometric dimensions. One model was designed as a corrugated surface horn operating with the hybrid mode HE_{11} . The second model was a dual mode horn using both, the TE_{11} - and the TM_{11} modes. Both principles were compared with regard to beam equalization, sidelobe suppression, transmission loss and bandwidth property.

On account of the specified narrow-band characteristic and especially due to the relative simple structure the dual mode principle was selected for the feed horn. Thus, low price, a short manufacturing period as well as low weight could be realized.

2.2 Theoretical background and horn design

The dual mode technique utilizes a conical horn, excited in the throat region at both the dominant TE_{11} -mode and the higher order TM_{11} -mode (Potter, P.D., 1963). These two modes are then superposed with the appropriate relative amplitude and phase to effect a field distribution as shown in Fig. 1.

It can be seen that almost perfect circular symmetry of the electric field component is achieved and that the field at the edge of the horn aperture is nearly cancelled. This effect provides the following desirable features: sidelobe suppression, beam-width equalization in the E- and H-plane as well as phase center coincidence.

2.2.1 Mode generation by means of a step discontinuity

The TM_{11} mode excitation occurs by means of a step discontinuity which can be calculated from the assumption that for a rotationally symmetric field distribution in the aperture (see Fig. 1) a mode conversion coefficient of $c = 0.144$ is necessary (Reitzig, R., 1968). This means that the radiated power in the aperture must be divided into 87 % for the TE_{11} wave and 13 % for the TM_{11} wave. The diameter ratio at the discontinuity controls the conversion coefficient. In order to obtain the desired conversion the diameter ratio of the step discontinuity (see Fig. 2) should be theoretically $D_2/D_1 = 0.76$. This value had to be corrected to $D_2/D_1 = 0.82$ due to the dependence on the actual diameter D_1 and further mode conversion through the horn, as found later during experiments with an X-band scaled laboratory model. The actual diameters D_1 and D_2 were chosen so that only the TE_{11} mode can propagate in D_2 and TE_{11} , TM_{01} , TE_{21} , TE_{01} and TM_{11} in the oversized waveguide (D_1). TM_{01} , TE_{21} and TE_{01} however are not excited here because of the rotationally symmetric step. To realize that step discontinuity on the one hand and to connect the horn to a standard circular waveguide on the other hand it was necessary to form a proper transition zone with diameter D_2 . Matching could be carried out by cutting this transition to a quarter guide wave length and turning an additional inductance right next to the horn-waveguide connexion. The result was a polarization-independent VSWR of better than $s = 1.09$ in the specified frequency range.

Compared with the horn described by Potter (Potter, P.D., 1963) several sections of the horn feed zone could be eliminated. The "mode suppressor" was shortened to a quarter waveguide length and additionally redesigned as matching- and transition zone. The "tapered transition" could completely be omitted (see Fig. 2,3). Thus considerable length reduction was possible which had a positive effect on the horn flare angle and gain respectively, because of the limited overall horn length.

2.2.2 Phasing conditions in the horn

Another step of the horn design procedure is to determine the relative phase shift of TE_{11} and TM_{11} over the distance between TM_{11} excitation and the horn aperture. It is known that both modes must have their central fields in phase in the aperture to effect the dual mode characteristics:

$$\Delta\varphi = \sum_1^2 \Delta\varphi_i = 2n\pi \quad n = 0, 1, 2, \dots \quad (1)$$

Some small phase shifting effects in the transition between phasing section and cone as well as in the aperture will be neglected during the following calculation. There are three phasing components which effect the overall phase shift between the two modes TE_{11} and TM_{11}

$$\Delta\varphi = \Delta\varphi_{\text{cone}} + \Delta\varphi_{\text{step}} + \Delta\varphi_{\text{ph. section}} \quad (2)$$

The phase shift between TE_{11} and TM_{11} in the cone due to the different critical wavelengths may be calculated by integrating the cylindrical waveguide formula

$$\Delta\varphi_{\text{cone}} = \int_{z_1}^{z_2} B(z) dz \quad (3)$$

z is the direction of wave propagation; z_1 and z_2 are the cone edges; $B(z)$ = phase constant.

Carrying out the integration gives $\Delta\varphi_{\text{cone}} = 2.62\pi$

As to the second term, it is not possible to determine the phase shift $\Delta\varphi_{\text{step}}$ at the point of TM_{11} mode generation with low mathematical expense (Reitzig, R. 1968). We calculated $\Delta\varphi_{\text{cone}}$ and $\Delta\varphi_{\text{ph. section}}$ of several other dual mode horns according to the formulae of Eq (3) and Eq (4). Applying the results in Eq (2) the phase shift of the step was found to be approximately $\Delta\varphi_{\text{step}} = \pi/2$.

In order to get $\sum \Delta\varphi_i = 2n\pi$ (in our special application 4π) it is necessary to adjust the phasing section to $\Delta\varphi_{\text{ph. section}} = 0.88\pi$. From that value the length l of the phasing section can be calculated by the expression

$$l(B_{TE} - B_{TM}) = \Delta\varphi_{\text{ph. section}} \quad (4)$$

2.3 Measurement on a scaled model

By the aid of the above results it was possible to manufacture a scaled model operating in the X-band (see Fig. 4).

The dimensions were chosen in a way that both the geometric limits and the necessary relativly small flare angle were met. Thus maximum aperture efficiency was obtained.

2.3.1 Tests in the MBB anechoic chamber

The radiation pattern of the feed horn showed good conformity in the principal planes. Within the solid angle subtended by the subreflector, maximum deviation between the E- and H-plane of 0.3° was measured. Turning the horn feed around the axis through the phase center, an edge taper of about 10 dB was obtained.

No side lobes occurred within the dynamic range of 40 dB (see Fig. 5).

Gain measurement was carried out by the substitution method using a standard gain horn. A gain of approximately 27.5 dB was obtained.

Special attention was paid to the determination of the phase center. It is important to know its position exactly, for the horn feed phase center and the secondary focus of the Gregorian system shall be coincident. Because of the relative large horn aperture - the diameter is larger than 11 wavelengths - it was expected that the phase center would lie rather far behind the aperture.

The calculation for the location of the phase center can be carried out using the approximation formula (according to Bauer, K., 1955) for large apertures

$$d/\lambda = \frac{\sqrt{2\pi}}{45} \cdot \frac{a}{\lambda} \cdot \sqrt{\frac{l}{\lambda}} \quad (5)$$

where d = distance between phase center and aperture

a = aperture diameter

l = length of the cone

The calculated value was $d/\lambda = 20.8$

With the aid of phase pattern measurement the phase center could be determined experimentally (see Fig. 6). Turning the horn model around a point located 22 wavelengths behind the aperture a minimum phase deviation in the principal planes as well as the 45° -plane within the subtended angle of 14.7° was measured. It can be seen that mathematical determination and experimental work showed good conformance.

2.3.2 Further measurements

The noise temperature of the antenna system will be influenced by all ohmic losses of the circular wave guide system. Therefore the determination of the transmission loss should be carried out extremely carefully, and thus the Roberts-von Hippel method was used. The aperture was short-circuited and the rather high VSWR was measured with a slotted line and a receiver of better than -90 dBm sensitivity. Thus VSWR of more than 100 could be determined. The measured value of $s = 48$ indicated a transmission loss of $2\alpha = 0.175$ dB. Taking the scaling rules into consideration a transmission loss of $\alpha = 0.05$ dB for the original horn feed was found.

3. CALCULATION OF GAIN AND SPILLOVER

The overall antenna characteristic was determined using a computer programme of the University of Birmingham, U.K.. Primary feed patterns, measured in the actual distance of the horn aperture to the subreflector are used as input data. They represent the incident field at the subreflector. From that both, the far-field pattern of the subreflector and the near-field pattern at the main reflector surface have been calculated. With the far-field pattern the spillover and noise figure can be calculated, and with the near-field pattern an exact computation of the antenna's overall gain is possible. The computed on-axis gain of the antenna system was 65.64 dB and had to be reduced by losses due to strut blocking and surface errors.

The spillover is given by the addition of the spillover from the primary feed past the subreflector and the spillover from the subreflector past the main reflector.

Finally the antenna noise temperature was calculated using the spillover figure and well-known calculation methods.

4. DIRECTIONAL COUPLER

During later operation it is necessary to control the antenna polarization. The control signal comes from a directional coupler which couples the information into the primary feed. On account of further length reduction the directional coupler was integrated into the horn feed zone (see Fig. 2).

We tried to couple the energy with small probes directly out of the phasing section. The influence of the probes of the radiation properties and matching characteristics of the horn proved to be negligible on account of the high coupling attenuation of 60 dB. The problem was to find the correct distance of the probes to get a signal 90° out of phase from the two waves propagating in the phasing section with different guide wavelengths. The proper distance was empirically found to be 8.1 mm, a value between the TE_{11} - and TM_{11} guide wavelength.

The directional characteristics are then achieved by coupling the two signals into a rectangular waveguide with the appropriate dimensions in relation to the guide wavelength which must be four times the probe distance. Two transitions to coaxial terminals accomplish the directional coupler which has an overall length of about $1\lambda_0$.

5. CONSTRUCTION OF THE FINAL (FULL SCALE) HORN VERSION

The design of the final horn feed aimed in particular at cheapness, a short manufacturing period and a low weight. The dimensions of the horn are 1.5 m of diameter and 4.1 m of length. The conventional method of manufacturing a conical horn is to turn it from metal pieces; in our special case we had to use hammer forged aluminium-rings. Due to the limited lengths of those pieces and the necessary horn length of 4.1 m this method seemed not to be applicable because of the necessary high number of horn segments and fabrication expenditure.

In order to get a short manufacturing period it was decided to manufacture the horn according to the helling technique. The horn had to be divided into six segments in order to get it inside the apex cabin. Here the final assembling will be carried out. The feeder is designed as an aluminium frame work. It consists of six segments; two of them are shown in Fig. 7. Every segment consists of two flanges which are connected by thin walled tubes of aluminium. This structure is the supporting part of the horn. The electrical part of the horn, the cone, is formed of 1 mm thick sheet aluminium, the surface of which was sheltered against damage until assembling it in the segments. Thus, extremely high surface quality was achieved. The roundness in the aperture is better than 1 %.

Special attention was paid to the connection between the segments. The junctions of about 1/10 mm are joint by use of a special conducting glue. In addition the horn is covered by a supporting sheath for further stiffness and protection against mechanical hazards. The first and second horn segments are turned of brass because of the relative small conediameter. The next segment is manufactured as described above and is shown in Fig. 8. Here the mounting flange can be seen. This flange provides fitting the horn feed in the apex cabin.

REFERENCES

- Baur, K., 1955, "Das Phasenzentrum von Aperturstrahlern", A.E.Ü. 9 (1955)
- Ludwig, E.; Ries, G.; Zocher, E., 1969, "Verbesserter Hornerreger mit zwei Wellentypen für flache Parabolantennen", A.E.Ü. 23, (1969) 4
- Potter, P.D., 1963, "A New Horn Antenna with Suppressed Sidelobes and Equal Beamwidths", The Microwave Journal, June 1963
- Reitzig, R., 1968, "Änderungs- und Verbesserungsmöglichkeiten im Aufbau großer Cassegrain-antennen mit Hornparabolspeisung", Frequenz 22, (1968) 8

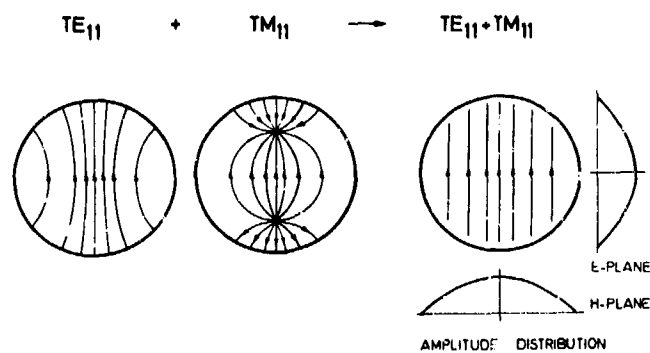
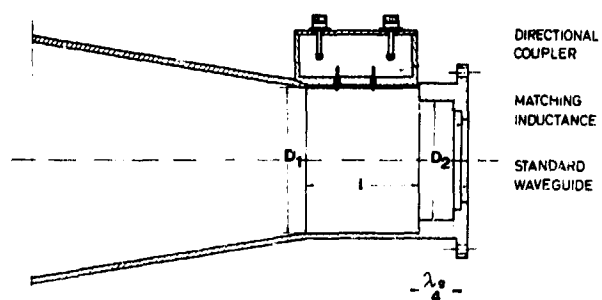
Fig.1 Superposition of TE_{11} and TM_{11} 

Fig.2 Horn feed zone



Fig.3 First horn segment

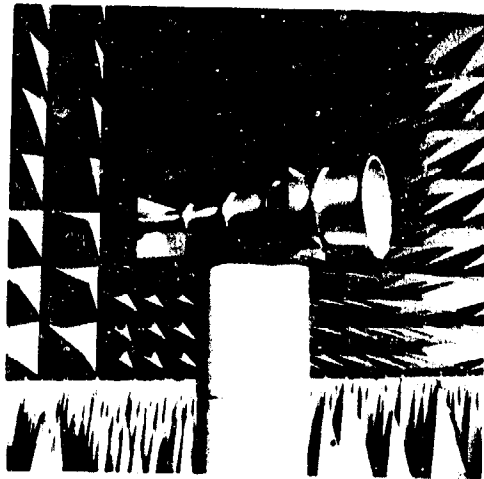


Fig.4 X-band scaled model in an anechoic chamber

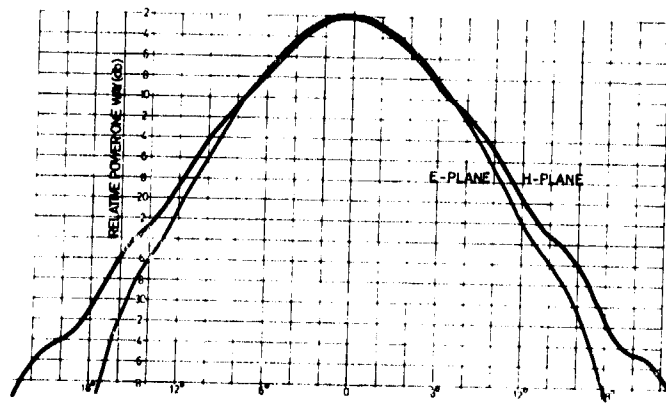


Fig.5 Amplitude pattern

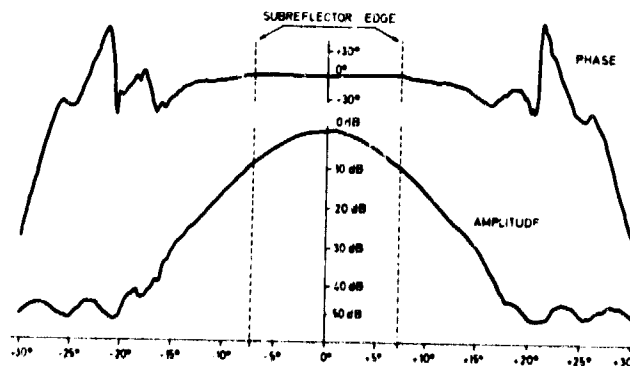


Fig.6 Phase- and amplitude pattern

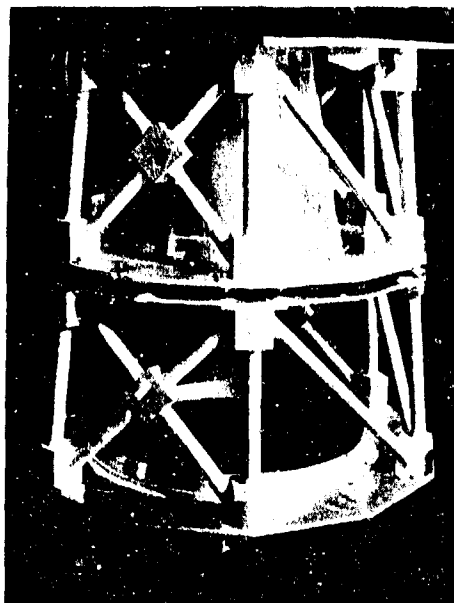


Fig.7 Aluminum frame work of two horn segments



Fig.8 Horn segment with mounting flange

DISCUSSION

R. REITZIG: In a Gregorian multiple reflector system the cross-polar component is increased. Could you comment on the magnitude of the cross-polarisation?

W. HESS: The magnitude of the cross-polarisation was not specified because the antenna was only required for a point-to-point system. Because of symmetry about the axis no cross-polarisation would be expected in the main direction of radiation.

ARRAY AND REFLECTOR
TECHNIQUES FOR AIRPORT PRECISION APPROACH RADARS

by

Robert J. Mailloux
and
Philipp Blacksmith
Air Force Cambridge Research Laboratories (AFSC)
Microwave Physics Laboratory
L. G. Hanscom Field, Bedford, Massachusetts 01730
U.S.A.

SUMMARY

Typical precision approach radar (PAR) antennas for Ground Control Approach (GCA) systems provide rapid electronic scanning over small scan sectors ranging between $\pm 4^\circ$ and $\pm 10^\circ$ in either plane of scan. These "limited scan" antennas are often required to have relatively high gain (40 to 50dB) and to conform to rigid sidelobe specifications (ideally -30dB) in order to minimize interference problems.

Conventional phased array technology would require an excessively large number of elements to perform this function because it takes no advantage of the very restricted scan coverage. Instead, a growing class of specialized antennas is being developed with reduced numbers of phase shifters and other cost-saving advantages made possible by the limited scan coverage.

This paper surveys the current state-of-the-art among array and array/reflector antennas for limited scan coverage, and introduces some new array techniques developed at AFCRL for this application. Other system parameters, such as frequency selection, will be discussed in light of their influence on antenna design requirements but the principle task addressed by the paper is to use the parameters of present PAR antenna systems to estimate the potential advantages of new technology.

Examples cited as new technology include the use of arrays to feed dual reflectors or lenses for improved aperture efficiency and reduced array size, and the AFCRL array techniques using large multimode apertures for grating lobe suppression and pattern control. Comparisons of these types of technology will be given for selected applications.

1. INTRODUCTION

Airport precision approach radar (PAR) antennas are highly directive pencil beam antennas requiring rapid electronic scan over small scan sectors or cones. Typical scan cones have half angles between 4° and 10° , and the antenna beamwidths are on the order of one half to one degree in either plane. Sidelobe specifications are stringent, with -30dB often set as a requirement for all beyond the first sidelobe, and -24 or -25dB first sidelobes. Frequency allotments for GCA systems usually place the PAR antenna at X-band, although S-band frequency allotments might offer better performance in rain. Any requirement for rapid scanning has traditionally been met by phased arrays with electronic beam steering, but the difficulty with PAR antennas is that they are so large that the phased arrays become too complex and costly to provide a viable solution. For 1° beamwidths, the aperture must be on the order of 60 wavelengths in diameter. Typical array apertures are spaced at most 0.9λ apart, and thus require at least 3500 phase shifters, while a 0.50° beam would require at least 14,000 phase shifters. At present day phase shifter prices these costs alone are excessive without further consideration of the power divider and circuit element costs. The costs are excessive because conventional array technology does not take advantage of the limited scan requirement, and is prohibited from doing so by the fact that regular periodic arrays have grating lobes for element spacings in excess of a wavelength. To fill this gap a growing class of specialized antennas is being developed with reduced numbers of phase shifters and other cost saving advantages made possible by the limited scan coverage. Chief among these are the reflector and lens type antennas, which take advantage of the magnification of such optical systems to illuminate large apertures with relatively small arrays. The special purpose array techniques discussed in this paper are designed especially to take advantage of the limited scan coverage by using large array elements and thus fewer phase shifters and accompanying reduced power divider requirements. This is accomplished in one case by using an aperiodic grid arrangement to prevent the formation of large grating lobes, and in another case by using multimode apertures to tailor array element patterns for grating lobe suppression.

This paper discusses a number of antenna techniques for satisfying the limited scan function. System requirements and special radar techniques have been excluded in order to concentrate on a practical comparison of the antenna techniques. Several of the antennas described are still in the development stage, and so it is difficult to assess their final impact on PAR antenna system selections. In describing these cases, an attempt has been made to outline areas of possible difficulties as well as the projected capabilities of the systems. Indeed, it should be emphasized that any comparison, however well intentioned, between a fully developed antenna and a new or proposed, but undemonstrated, technique is a little like comparing ones aspirations with ones accomplishments; it is difficult to be objective in such cases.

The coverage devoted to each technique discussed in the paper is intentionally uneven; new methods have been described in detail, while equally important systems are very briefly discussed if they are treated elsewhere. In addition, no attempt has been made to detail the history of limited scan antenna development from its early roots in mechanically displaced feeds for reflector and lens antennas. In this regard, in addition to the original research publications describing specific systems, there are several excellent survey references describing techniques pertinent to the limited scan application. (PATTON, W.T., 1972 and TANG, R., 1972)

2. PERTINENT CHARACTERISTICS FOR COMPARING PAR ANTENNAS

The gain, beamwidth, scanning and sidelobe characteristics mentioned in the introduction are the fundamental electromagnetic properties that the PAR antenna must provide. In addition to these there are many physical characteristics that, in the case of the large PAR structure, become equally important. Figure 1 shows a generalized limited scan antenna structure and serves to define some of the parameters referred to throughout the paper. The total length of the antenna (normalized to wavelength) is called f , and is a generalized focal length. The array (or primary) aperture diameter is d (wavelengths) and the final, or secondary aperture diameter is D (wavelengths). Throughout this paper all apertures are considered circular. One parameter of very great importance is the ratio f/D , which should be as short as possible for mechanical reasons, but which engineers often increase for electrical reasons. Another parameter of key importance is the optical magnification of the system D/d , which should be as large as possible to allow a very small array to feed a large final aperture. Neither of these factors describe the scanning capability of the system, but a common measure of this parameter is the number of half power beamwidths (NB) that the system scans. This beamwidth related parameter is meaningful for optical type systems, but breaks down as a description for array systems, and so a related parameter introduced by Patton (PATTON, W.T., 1972) and called the 'element use factor' will be used throughout this paper for comparison purposes. This factor is N/N_{\min} , where N is the actual number of phase shifters in the control array, and N_{\min} is a reasonable minimum number of control elements as defined by

$$N_{\min} = \left\{ \frac{\sin \theta_{\max}}{\sin \theta_{HP}} \right\}^2$$

where θ_{\max} is the maximum scan angle and θ_{HP} is the half power half beamwidth of the structure. This N_{\min} is therefore defined for a pencil beam system as approximately the square of the number of half power half beamwidths scanned, or $N_{\min} = 4N_B^2$. Its interpretation as an absolute minimum number of elements is open to question, but even in the case of the uniformly illuminated circular array of ideal but physically unrealizable array elements, the absolute minimum number is approximately 80% of the N_{\min} , and so it seems likely that this definition is a nearly optimum one for comparing various array and reflection or lens designs. A conventional phased array with a moderate taper and roughly circular aperture has an element use factor given by $0.23(W \sin \theta_{\max})^2$ for interelement spacing W (normalized to wavelength). This corresponds to factors 9.3 and 37 for 10° and 5° scan respectively when $W = 0.9$. Other techniques discussed in this paper have much smaller and relatively constant element use factors, and these numbers provide a direct comparison of the number of control circuits required by each system.

Another important factor for many applications is the aperture efficiency of the main limited scan aperture. This is so because many of the reflector or lens geometries require oversize reflectors because the feed structure illuminates only a spot on the main aperture, and that spot moves with scan angle. Aperture efficiencies for such structures can be of the order of 25% instead of the usual 55 to 60% for nonscanning reflectors, thus requiring double the aperture of these more efficient structures.

Finally, another electrical parameter is of importance, not because it affects performance, but because it deals with the complexity of the beam steering system for the array. This parameter is the type of steering or information necessary to steer the beam. The simplest type of steering is row and column steering with progressive phases in both planes. Certain antennas however require complex steering functions to be generated for off axis scan, and these result in slower beam steering or excessive computer scan data storage or both.

Each of the systems described in this paper will be compared on the basis of these parameters as well as on their electrical performance.

3. REFLECTOR AND LENS TECHNIQUES FOR LIMITED SCAN

The narrow beam, high gain requirements of PAR antennas, coupled with the need for scan over only a small angular sector lead quite naturally to the investigation of optical techniques, as embodied in lens and reflector geometries, for beam scanning. Indeed, nearly all limited scan antennas designed to date have been of optical design, and it seems likely that this will continue to be so for some time in the future. The following paragraphs describe some of the relevant studies of electronically scanned antenna systems for this application.

Winter (WINTER, C., 1968) describes an array feed for a parabola as shown in Figure 2. This technique achieved 7 beamwidths of scan with E-plane sidelobes approximately -15dB relative to the main beam in the E-plane, and approximately -10dB in the H-plane. The phase shifts required for achieving these scanned conditions were computed from geometrical optics. These were not progressive in either plane of scan and so row and column steering could not be used. The array consisted of 980 elements and so has an element use factor of approximately 5. The main reflector efficiency is low because the illuminated spot is allowed to move about on the main reflector to achieve scanning. This study is of great importance because of its timeliness and because it showed that reflectors could be scanned by a phased array without the accompanying coma lobes observed for offset feeds.

This preliminary work and other studies in limited scan reflector techniques has led to the development of structures with less aperture blockage and lower sidelobes. Notable among these is the PAR antenna of the TPN-19 GCA system. This antenna, shown in Figure 3, uses a hyperbolic main reflector and an offset phased array feed and uses a modified row and column steering technique with a convenient algorithm for off axis scanning. The antenna has 1.4° azimuthal beamwidth and 0.75° elevation beamwidth, and scans ± 10 beamwidths in elevation and ± 7.15 beamwidths in the azimuth plane. The array uses 824 phase shifters, and so has an element use factor of approximately 2.9. The first sidelobes are at the -22 to -24dB level in each plane, and further sidelobes are between -24 and -28dB with respect to the main beam. The system operates at X-band, over a 2% bandwidth and has a realized gain of 42dB on boresight and approximately 39dB at the scan limits. This realized gain is about 3.5dB below the

directive gain on boresight due to horn feed spillover, array face matching, and phase shifter losses. The main reflector size is about 9 ft by 11½ ft, corresponding to an aperture efficiency of approximately 30% at boresight. This low efficiency is due to the basic design concept of the system, for different parts of the main reflector are illuminated differently for various scan angles, and so an illuminated spot moves with scan.

Recent technological efforts have been concerned with developing systems for scanning over wider angles with pencil beams, and for providing these scanning capabilities with relatively small high efficiency primary apertures. Two recent studies (FITZGERALD, W.D., 1971a and 1971b) at Lincoln Laboratory have dealt with the quest for larger scan multiples (NB). One of these concerns a near field cassegrain antenna with main reflector and subreflector as confocal parabolas. The antenna, shown in Figure 4, is compact and has a generalized f/D of approximately 0.4, but the array size required was relatively large, with typical d/D ratios considered between 0.25 for a 400λ main reflector, and 0.35 for a 250λ main reflector. These computations show maximum NB of up to 17 with element use factors between 6 and 7. These relatively large element use factors are due to the fact that the array is only required to scan over a narrow range of angles, and so itself is a limited scan array. For this reason, element spacings greater than the 0.9λ assumed here can be used with proper precautions to maintain element efficiency (FITZGERALD, W.D., 1971a and TSANDOULAS, G.N., and FITZGERALD, W.D., 1972). The use of these oversized elements would reduce the element use factors for this approach to somewhere between 3 and 4. This array scheme also has the advantage of using linear phase control and since its generalized f/D ratio is short, can be mounted and moved conveniently. It has relatively high sidelobes, on the order of -13dB due to the inherent aperture blockage of the system.

The second approach investigated at Lincoln Laboratory was directed at this high sidelobe problem, and dealt with the offset - feed gregorian geometry shown in Figure 5. This technique, first proposed by Dudkovsky (DUDKOVSKY, E.A., 1962) has improved sidelobes due to decreased aperture blockage. The report describes a system with ½ beamwidth, scanning 14 beamwidths and with a relatively small array 45λ on a side. The element use factor is about 2.5 for this geometry, and this is mainly because the array is made to scan on the order of ±20°. Sidelobe levels for this antenna are on the order of -15 to -17dB for all scan angles. The structure has a generalized f/D of approximately 1.5, and so is awkward for pedestal mounting. The antenna has good aperture efficiency for all beam scan positions. The beam scanning requirements of this off axis feed imply the use of a combination of row and column steering and a beam steering algorithm for off axis scan.

Research sponsored by AFCRL has been concerned with providing scan coverage in excess of ten beamwidths but with minimum size final aperture and with reduced element use factors. These studies have sought increased main aperture efficiency by allowing movement of an illuminated one on a sub-aperture or by utilizing a beam forming matrix to produce a special sin μ/μ distribution at the main aperture. Studies at Raytheon (TANG, C.H., and WINTER, C.F., 1973) have included computer simulation of the array/lens structure shown in Figure 6. The structure consists of a planar feed of 437 elements arranged on a square grid spacing of 0.546λ. A 23-dB Gaussian type tapered amplitude excitation is employed to achieve the desired sidelobe level. The array is phased to focus to a small spot on the elliptical rear face of a lens containing 2617 passive elements arranged on a square grid of 0.5λ. The function of this lens is to transfer this spot to a region on the focal arc of a lens with spherical back face. This main lens is an equal path lens with two point correction (0, ±10°). This antenna is in the development stage and so it is difficult to predict sidelobe levels etc., but preliminary data shows some shouldering of the main beam and sidelobes at approximately the -16dB level for ±10° scan. The parametric features of this antenna are that at 65λ diameter, it forms a beam of approximately 1.2° for all scan angles, thus indicating efficient use of the scanned main aperture. In its present state of development, the antenna scans approximately 8½ beamwidths, and with 437 array elements this corresponds to an element use factor of about 1.5, the lowest of any of the optical techniques considered. The generalized f/D is at least 1.7, so the structure is quite long and bulky, but to compensate for this, the main aperture D is made nearly as small as possible because of its efficient illumination.

R. Tang (TANG, R., in preparation) and colleagues of Hughes Aircraft Company have investigated a variation of a technique described by Rudge and Withers (RUDGE, A.W., and WITHERS, M.J., 1971) who have shown that a Fourier transformer (Butler matrix) can be used to match the scanned beams of a reflector antenna. Tang and his colleagues have in addition developed a method of aperture distribution synthesis in which the antenna is viewed as a subarray system with each branch line of the corporate feed representing a subarray terminal. This antenna differs substantially from the Raytheon study because of its exploitation of the subarraying concept, and because the array itself is used quite differently. In this system too, a spot is moved along the focal arc of a main aperture (in this case an off axis reflector as shown in Figure 7). The array does not do the focusing however, and in fact it provides what is basically a linear phase front (except for phase corrections provided by the ferrite/diode phase shifters). The feed through lens focuses the energy from the feed array to form an approximate spot-type distribution across the reflector focal plane. As this distribution moves, the main array is scanned. This system can be viewed as one Fourier transform removed from the Raytheon work, in that here the array is progressively phased, and the feed through lens does the focusing to again form the moving distribution for scanning the main reflector.

The initial progressive phase shifts are shown here as produced by a multiple beam matrix, but alternatively could be a phased array. In this case the beam correcting phase shifts represent corrections to the progressive scan terms. Throughout this work, the amplitude distribution maintained across the array is reproduced at the main aperture and so good sidelobe control is possible. Preliminary studies have led to computed patterns with -26.5dB sidelobes for the on-axis beam, and -20.5 for the beam scanned 10 beamwidths. Gain reduction over the scan range is less than 2.5dB. The array lens and reflector system as presently conceived consists of 800 elements and scans the 0.8° pencil beam about 10 beamwidths corresponding to an element use factor of 2.0. The reflector aperture is 80λ and the generalized f/D ratio is approximately 1.5.

4. ARRAY TECHNIQUES FOR LIMITED SCAN

Conventional phased arrays can provide excellent sidelobe control and good wide-angle scan characteristics, but are in general too expensive for PAR limited scan applications because an excessive number of elements and phase shifters are required to fill the necessarily large radiating aperture. Phased arrays cannot in general be constructed with elements longer than a wavelength in the direction of either plane of scan because the resulting grating lobes absorb much of the power. In practice, arrays spaced a wavelength apart cannot be scanned more than a few degrees, and so the element spacing 0.9λ (MAILLOUX, R.J., 1972a and PHELAN, H.R., and HARRISON, J.L., 1973) will be used throughout this paper whenever comparisons are made to conventional array spacings for limited scan. Grating lobes can exist either because of an amplitude or phase taper in each element aperture which gives the array a scalloped aperture field distribution, or they can come about as the array is scanned because the single mode apertures can only stepwise approximate the linear phase taper which should be achieved for proper scanning of a phased array. Therefore, for elements longer than a wavelength in the scan plane, even if the power loss at broadside is tolerable, the main beam power decreases much too rapidly with scan for most applications because the grating lobes nearest broadside grow as they move toward the element pattern maximum.

If the angle of main beam scan is θ_0 , and the spacing between elements is W (normalized to wavelength), in the θ - plane, then grating lobes appear at the angles θ_n associated with

$$\sin \theta_n = \sin \theta_0 + \frac{n}{W}$$

for any positive or negative integer values of n which define a real angle θ_n . The size of the grating lobes when $\theta_0 = 0$ (broadside) depends upon the amount of amplitude and/or phase scalloping in the basic array elements. If there is no scalloping in one plane, as in the E-plane of an array of thin walled horn apertures, then the field pattern of an element in the array (the array element pattern) will have a null at each n/W point in $\sin \theta$, and all of the grating lobes will have zero amplitude. This is the optimum pattern achievable and it is also the narrowest element pattern achievable without resorting to superdirective apertures. When there is scalloping, as in the E-plane when the element size is less than the inter-element spacing, or in the H-plane of a horn array, then grating lobes will be present even for a beam at broadside. In either case, the lobes are present when the array is scanned away from broadside and special techniques must then be utilized to reduce them to tolerable levels.

4.1 APERIODIC ARRAYS

The occurrence of grating lobes is due to the periodic nature of conventional array lattices. The periodic structure leads to the formation of these ambiguous beams, but when this periodicity is removed by varying element spacings, the grating lobes can be effectively suppressed. One of the examples of the use of this type of system for limited scan application is the array investigated by W. Patton (PATTON, W.T., 1972). This structure, shown schematically in Figure 8, consists of a circular array of dipole subarrays arranged in an aperiodic fashion.

The elements have equal areas, and their size ultimately determines the maximum scan angle of the antenna at the element half power point, or approximately $\sin \theta_0 = 0.44/W$, where W is the normalized element width in any plane. This array is locally periodic, and so does have vestigial grating lobes, but these are considerably suppressed for a large array. Patton (PATTON, W.T., 1972) describes a 30 ft diameter array and a 10 ft diameter array at C-band. The 30 ft array consists of 1000 elements, instead of the approximately 27,000 elements needed to cover this area using conventional array technology. The subarray elements are excited by a combined optical and transmission line feed consisting of an optical power divider feeding a primary spherical array and providing monopulse beam options, and transmission line interconnections to the subarrays. The array is dually polarized and scans a 0.36° beam approximately 5° . Its element use factor is extremely low at 1.3. One disadvantage of this system is its relatively high losses due to gaps between the feed elements and the transmission line losses; these and other losses result in 5.94dB loss for the 10 ft model and in a projected 4.21dB loss for the 30 ft array. The transmission line interconnections may also make an X-band design somewhat less practical. Finally, the structure does have high average sidelobes at its maximum scan, when the main beam gain is reduced 3dB and the average sidelobes increased accordingly. Apart from these disadvantages however, this aperiodic array design is a major achievement in array technology; its peak sidelobes were measured at the -15dB level for the 10 ft diameter array, and are projected at -20.9dB for the 30 ft array, but the item of primary importance is the achievement of this extremely low element use factor (1.3) and the accompanying reduction in necessary phase shifters. This development also emphasizes the low generalized f/D ratio achievable with aperiodic array technology.

4.2 MULTI-MODE SCANNING TECHNIQUES

Recent AFRL studies have revealed that higher order odd modes can be used to allow the use of large aperture horns as elements of a limited scan array (MAILLOUX, R.J., 1972b and MAILLOUX, R.J., and FORBES, G.R., 1973). The technique is called odd mode scanning and is based upon the recognition that it is possible to choose an odd mode amplitude and phase so that the combined even and odd mode radiation pattern from any horn has a zero at the angle of the $(n-1)$ grating lobe nearest to broadside. The relative odd mode phase is fixed at $\pm 90^\circ$ with respect to the even mode phase. The (+) sign for scan on one side of broadside and the (-) sign for scan in the opposite direction, but except for the sign change this phase is constant with scan. The relative odd mode amplitude must increase monotonically with scan in order to move the zero of this combined active element pattern nearer to broadside in coincidence with the $(n-1)$ array grating lobe position. Figure 9 shows a comparison of a single mode element pattern with that of a horn with combined even and odd mode excitation. This figure demonstrates that although the principal effect of the superposition is to cancel the first grating lobe, in fact all of the nulls shift in the same direction and so tend to suppress other grating lobes for scan angles not too far from broadside. Another advantage of the technique displayed in these figures is that although the odd and even modes subtract at the $n-1$ grating lobe, they add together at the main beam, thereby providing

relatively constant gain with scan. This property is demonstrated in Figure 10.

A number of different circuits can be used for exciting the even and odd LSE modes; some are essentially power divider circuits used to supply signals to conventional monopulse horn geometries (MAILLOUX, R.J., 1972b) and these have the advantage of keeping even and odd modes separate for adjustment purposes. The simplest circuit, and likely the most practical one however is shown in Figure 11 for scanning in one plane. This figure shows an E-plane horn being excited by a dual mode waveguide section of length "L". The dual mode section is fed by two phase shifters with phase shifts different by the angle Δ . The phase shift η provides the beam control phase, and the difference Δ is used to excite an odd mode at the junction of the waveguide and the dual mode section. This junction is the dual mode equivalent of a 4-port magic tee hybrid. The odd mode amplitude is zero for $\Delta = 0$ and increases with the angle Δ up to 90° . The phase of this odd mode is constant (90° away from the even mode phase) except for a 180° shift as Δ goes from positive to negative. This relationship is not preserved throughout the horn however because the two modes propagate with a different phase constant, so the dual mode section length L is adjusted to give the required $\pm 90^\circ$ phase relationship at the horn face. The circuit therefore provides exactly the amplitude and phase control as required by the odd mode scanning technique. Two phase shifters are thus required per element for scanning in one plane, and the allowable element spacing is given by (MAILLOUX, R.J., and FORBES, G.R., 1973)

$$W \sin \theta_{\max} = 0.6$$

Elements can therefore be 3.5 wavelengths on a side for $\pm 10^\circ$ scan, 4.6 wavelengths for $\pm 7.5^\circ$ scan, corresponding to savings in phase shifters of 2 and 2.5 for one plane of scan. The phase controls required are the simple progressive terms for beam steering plus the difference term Δ which is the same for all elements but which does vary with scan angle.

As shown in Figure 9, the case of E-plane scan is ideally suited to the odd mode scanning technique because the array grating lobes lie in the element pattern nulls when the array is at broadside. The case of H-plane scan offers more difficulties because the widened element pattern has nulls beyond the grating lobe points for the array at broadside, and so energy is lost into these H-plane grating lobes. This problem has been solved by using a set of dielectric layers at the sides of each horn (TSANDOULAS, G.N., and FITZGERALD, W.D., 1972) to tailor the H-plane element pattern and move the nulls in to approximately the position of the broadside grating lobes. Using this design H-plane element patterns with appropriate scanning nulls have been designed and have achieved proper null scanning for grating lobe control with elements up to 4.6λ wide. The odd mode used to accompany the LSE10 mode for H-plane scan is the LSE20.

Figure 12 shows a circuit for exciting four modes (LSE10, LSE11, LSE20, LSE21) as required for scanning in two dimensions. This circuit, with phase shifts as noted on the figure, forms a separable aperture distribution at the horn face either for an unloaded horn or for one with dielectric wedges for H-plane control. The resulting element pattern is thus suitable for full two dimensional control using E-and H-plane difference phase terms as defined by the respective positions in direction cosine space. No cross product phase corrections are needed and again simple row and column phase control is sufficient. In this case the horns must be designed to maintain the proper phase relationship between all four modes.

Figure 13 shows a laboratory model of an array based upon this concept. The array is designed for E-plane scan $\pm 12^\circ$ and uses the odd mode power divider concept shown in Figure 11. Figures 14A and 14B show E-plane patterns of the array of Figure 1. In Figure 14A, the array is phased at broadside and the elements are excited with the central four at uniform amplitude, the second element in from each end of the array at -3dB amplitude, and the outer elements at -6dB amplitude. This taper should have first sidelobes at about -19dB, but due to cable and power divider phase errors the level is approximately -17dB. This figure shows grating lobes at approximately $\pm 19^\circ$ (-16dB) and also at $\pm 40^\circ$ (-26dB). These would be zero if the horn elements were perfect, and they can be reduced somewhat by using a dielectric lens to collimate the beam of each horn. Figure 14B shows two cases at the maximum scan angle $\pm 12^\circ$. The dashed curve in this figure shows the horn array radiation pattern without odd modes, and clearly indicates the impossibility of using such a design. In this case, the main beam gain is reduced over 5dB with respect to the broadside array and the grating lobe at -7° is larger than the main beam by 1.8dB. Other grating lobes are at tolerable levels. The solid curve of 14B shows that when each element is excited with an odd mode signal by changing the relative lengths, the offending grating lobe is reduced to approximately the -20dB level, and the main beam gain is increased to approximately -1.2dB with respect to the broadside case.

The array used for this experiment was not designed for wideband operation but does provide 18dB suppression of the $n=-1$ grating lobe over approximately 3% bandwidth, and 16dB suppression over a 4% band. It is expected that 10% can be achieved without excessive difficulty. A second E-plane horn element has been designed with 4.6λ aperture size and found to scan with approximately the same characteristics at the 2.9λ horn when viewed in W sin θ space. This horn was excited with a larger dual mode waveguide section, and so does have a bandwidth of about 6%.

The odd mode scanning technique described above results in a flat array face with periodic element spacings. The elements are highly efficient, being uniformly illuminated in the E-plane and very nearly so in the H-plane (because of the dielectric wedges designed to improve H-plane efficiency and null position). A study of the near and far sidelobes has revealed that these are of very different character, and that by using conventional aperture tapering procedures near sidelobe levels of -30dB or less can be achieved, and this level can be made as low as phase tolerances and array size will allow. The nulled grating lobe ($n=-1$) is suppressed 20 to 25dB for a small array (8 elements), but may be suppressed substantially more for larger arrays. The residual grating lobes at wider angles are unaffected by array amplitude tapering and remain the major limitation of the technique. This laboratory is now investigating the synthesis of stratified dielectric layer spatial filters for reduction of these far sidelobes. This technique shows good promise of success because lobes are already 12 to 15dB below the main beam and are at wide enough angles as compared with the main beam that they can be separated effectively by this means. With or without this filtering, the average energy in the sidelobes remains far below that of the aperiodic array schemes, for the odd mode technique typically incurs less than 1.5dB loss at the scan limit.

The element use factor is typically 2.5, and so compares quite favorably with many of the reflector or lens schemes. An additional positive factor is that the element spacings are quite large, and allow much more room than conventional arrays for mounting of phase shifters, cooling and adjusting or replacing individual members. The gain reduction with scan is minimal and the beamwidth variation is also minimal and is influenced only by the $\cos \theta$ projection factor. The structure can be excited by space feed or corporate feed geometries and the flat array face makes circular polarizers convenient if required. Of primary importance is that waveguide circuits can be used throughout, thus assuring extremely low loss operation. In addition, the structure can be made very short (in the sense of a generalized f/λ ratio) as compared with the optical structures, and comparable with aperiodic array techniques.

In summary, this method can provide moderate element use factors with many of the advantages of a conventional phased array for the limited scan application. Gain variation with scan is the best of any of the techniques considered, as is boresight gain. The major disadvantage of the technique at present is the relatively high far sidelobes; and it is anticipated that spatial filtering techniques will bring about a substantial improvement in this condition. Near sidelobes are lower than any of the optical techniques considered, and are at least as low as those of the aperiodic arrays.

5. CONCLUSION

This paper has described a number of techniques for limited antennas and has compared these for PAR application. Reflector and lens structures have advanced to a point at which low element use factors are achievable with sidelobes at approximately the -20dB range and good scanning characteristics. Aperiodic arrays have achieved the lowest element use factors with good peak sidelobe control, although with substantial average sidelobe levels. Finally, the multimode scanning technique shows promise of providing good element use factors with excellent efficiency and gain variation with scan. Successful application of this technique to PAR requirements will demand substantial improvements in far sidelobe control. Work in progress is addressed to providing this improved performance.

REFERENCES

1. Dudkovsky, E. A., (1962) 'A System for Exciting Large Parabolic Antennas', Russian Patent No. 146365.
2. Fitzgerald, W. D., (1971a) 'Limited Electronic Scanning With a Near Field Cassegrainian System' ESD-TR-71-271, Technical Report 484, Lincoln Laboratory.
3. Fitzgerald, W. D., (1971b) 'Limited Electronic Scanning With an Offset-Feed Near-Field Gregorian System' ESD-TR-71-272, Technical Report 486, Lincoln Laboratory.
4. Mailloux, R. J., (1972a) 'Surface Waves and Anomalous Wave Radiation Nulls on Phased Arrays of TEM Waveguides with Fences', IEEE Trans. AP-20, No. 2, pp160-166.
5. Mailloux, R. J., (1972b) 'Array Techniques for Limited Scan Application', AFCRL-72-0421 Physical Sciences Research Papers, No. 503.
6. Mailloux, R. J., and Forbes, G. R., (1973) 'An Array Technique with Grating-Lobe Suppression for Limited-Scan Application', IEEE Trans. AP-21, No. 5.
7. Phelen, H. R., and Harrison, J. L., (1973) 'Phased-Array Costs Cut by New Radiating Elements', Microwaves, Vol. 12, No. 1.
8. Patton, W. T., (1972) 'Limited Scan Arrays' in Phased Array Antennas, Proceedings of the 1970 Phased Array Antenna Symposium Edited by A. A. Oliner and G. H. Knittel, Aertech House, Inc., Dedham, MA, pp332-343.
9. Rudge, A. W., and Withers, M. J., (1971) 'New Techniques for Beam Steering with Fixed Parabolic Reflectors', Proc. IEEE, Vol. 58, No. 7, pp859-863.
10. Tang, R., (1972) 'Survey of Time-Delay Beam Steering Techniques', in Phased Array Antennas, Proceedings of the 1970 Phased Array Antenna Symposium, Edited by A. A. Oliner and G. H. Knittel, Aertech House, Inc., Dedham, MA., pp254-260.
11. Tang, C. H., and Winter, C. F., (1973) Final Report on Contract No. AF19628-72-C-0213.
12. Tang, R., (in Preparation) Final Report on Contract No. AF19628-73-C-0129.
13. Tsandoulas, G. N., and Fitzgerald, W. D., (1972) 'Aperture Efficiency Enhancement in Dielectrically Loaded Horns', IEEE Trans. AP-20, No. 1, pp69-74.
14. Winter, C., (1968) 'Phase Scanning Experiments with Two Reflector Antenna Systems', Proc. IEEE, Vol. 56, No. 11, pp1984-1999.

ACKNOWLEDGEMENTS

The authors thank C. H. Tang of Raytheon Corporation and R. Tang of Hughes Corporation for providing Figures 6 and 7, and W. P. Moland of the Air Force Electronics Systems Division (ESD) for Figure 3.

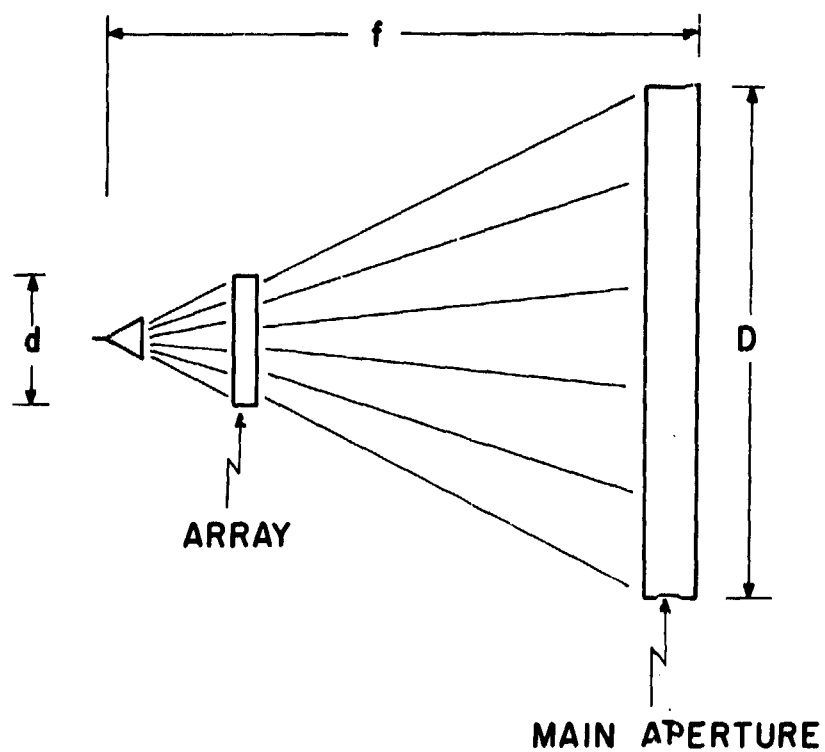


Fig.1 Generalized limited scan antenna geometry

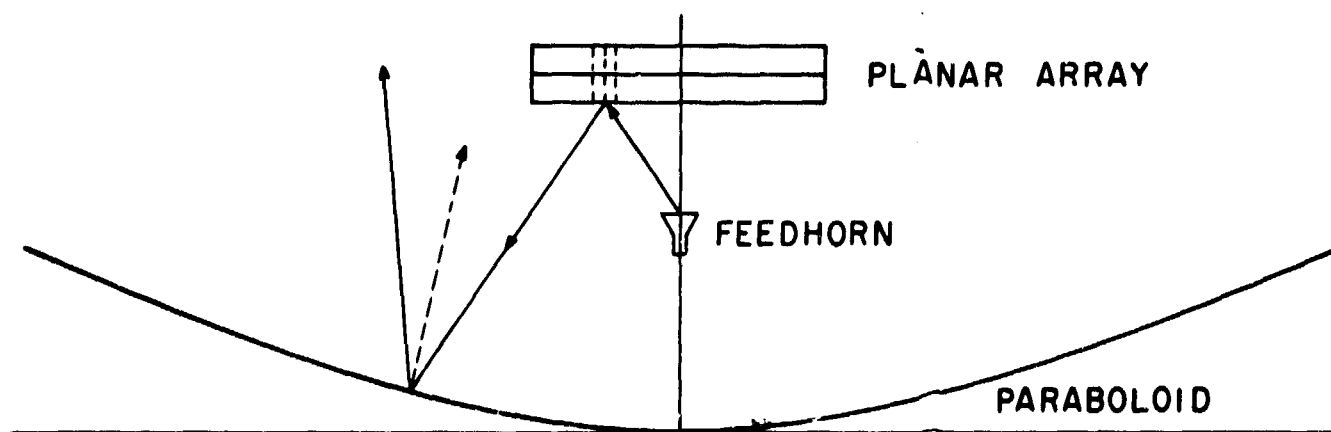


Fig.2 Planar array and paraboloid for limited scan

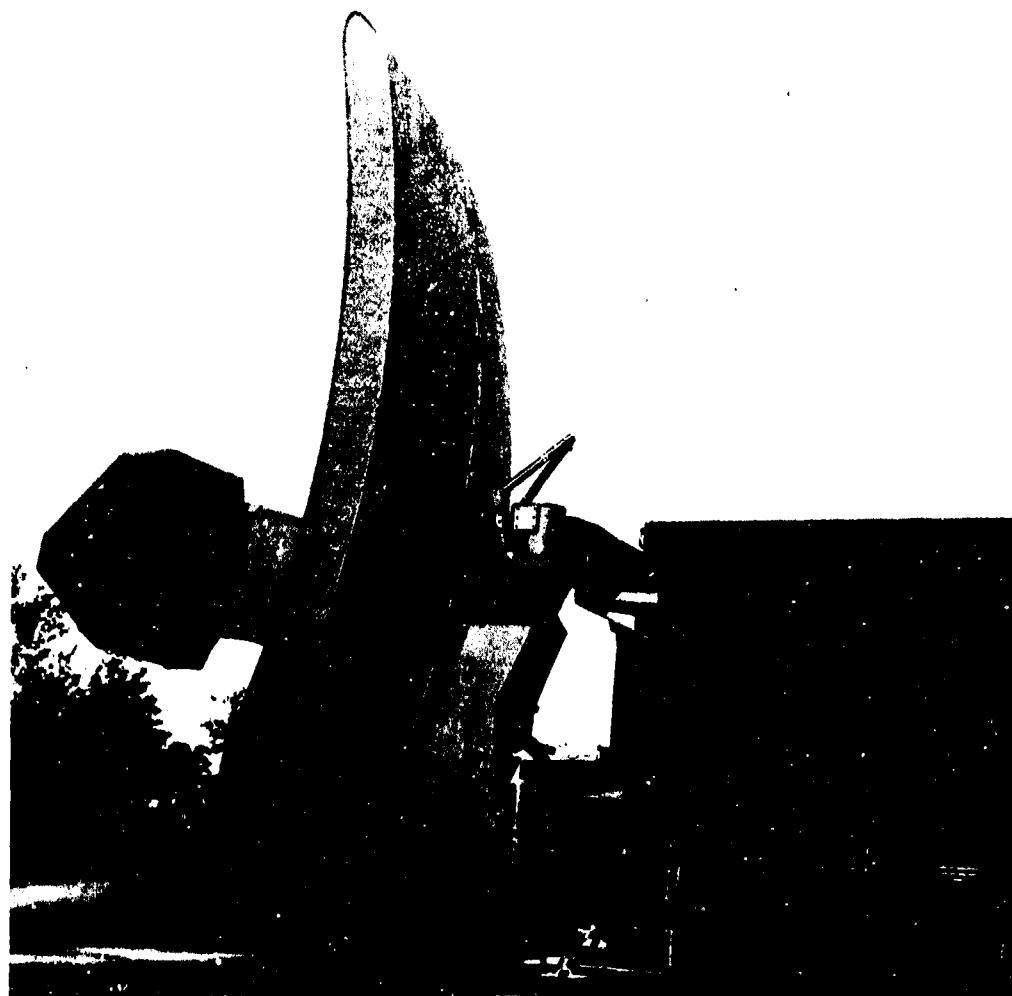


Fig.3 Precision approach radar antenna of AN/TPN-19

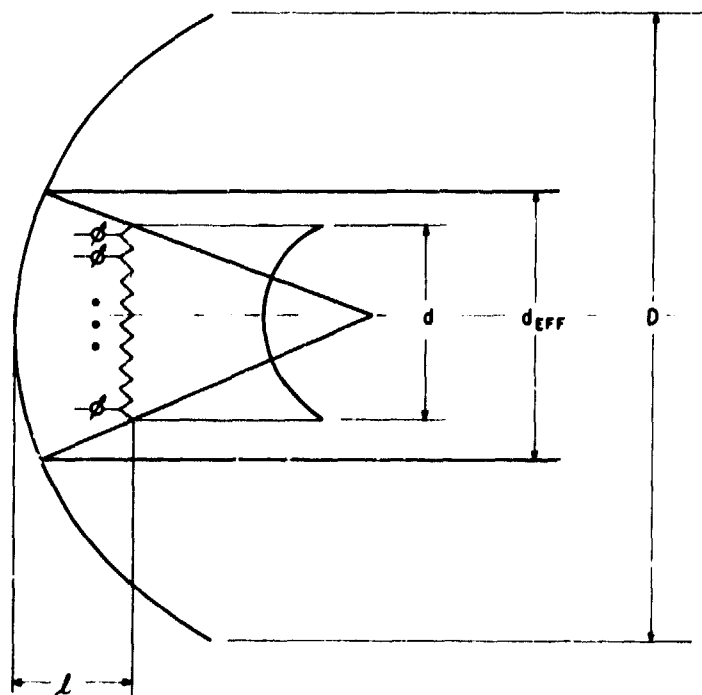


Fig.4 Near field Cassegrainian geometry

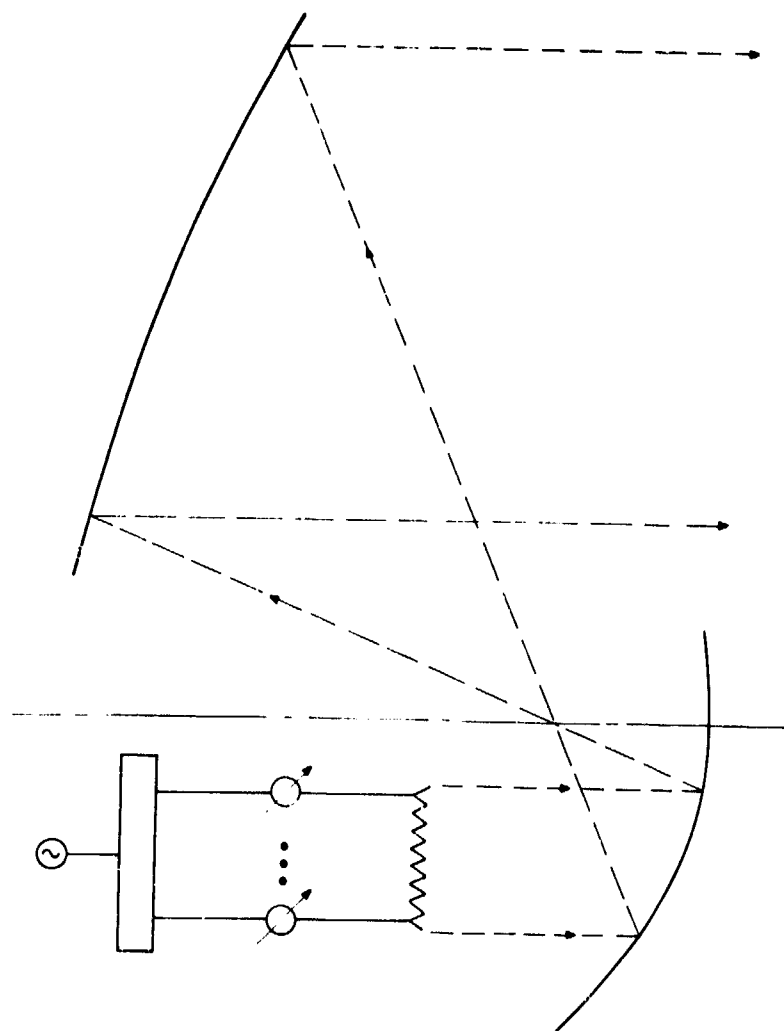


Fig.5 Offset-feed Gregorian geometry

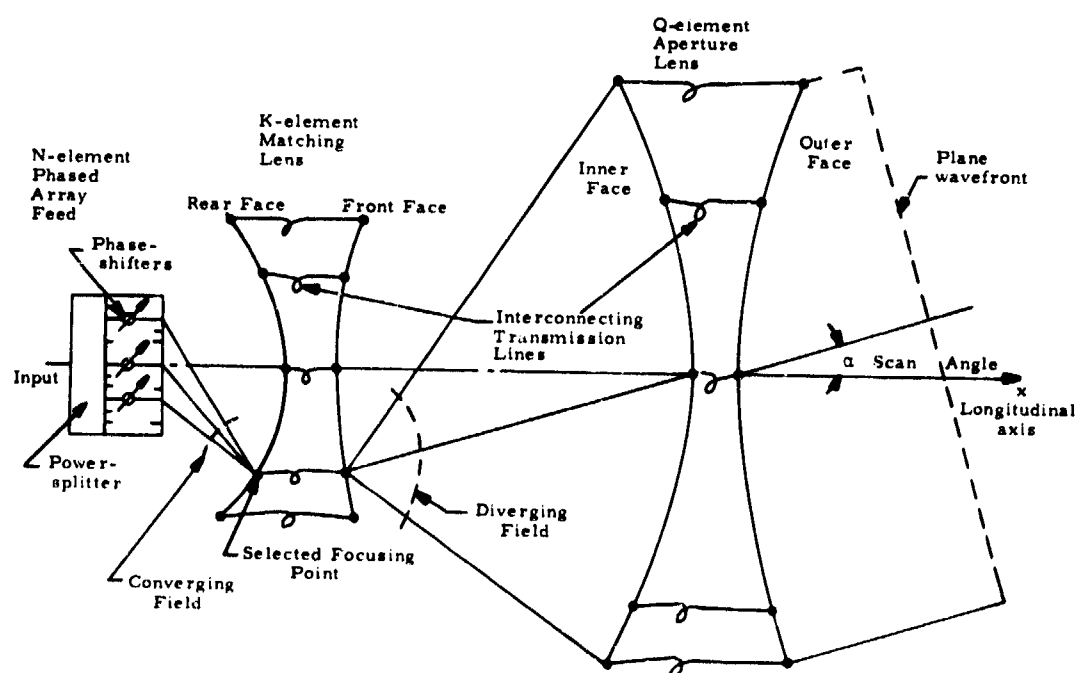
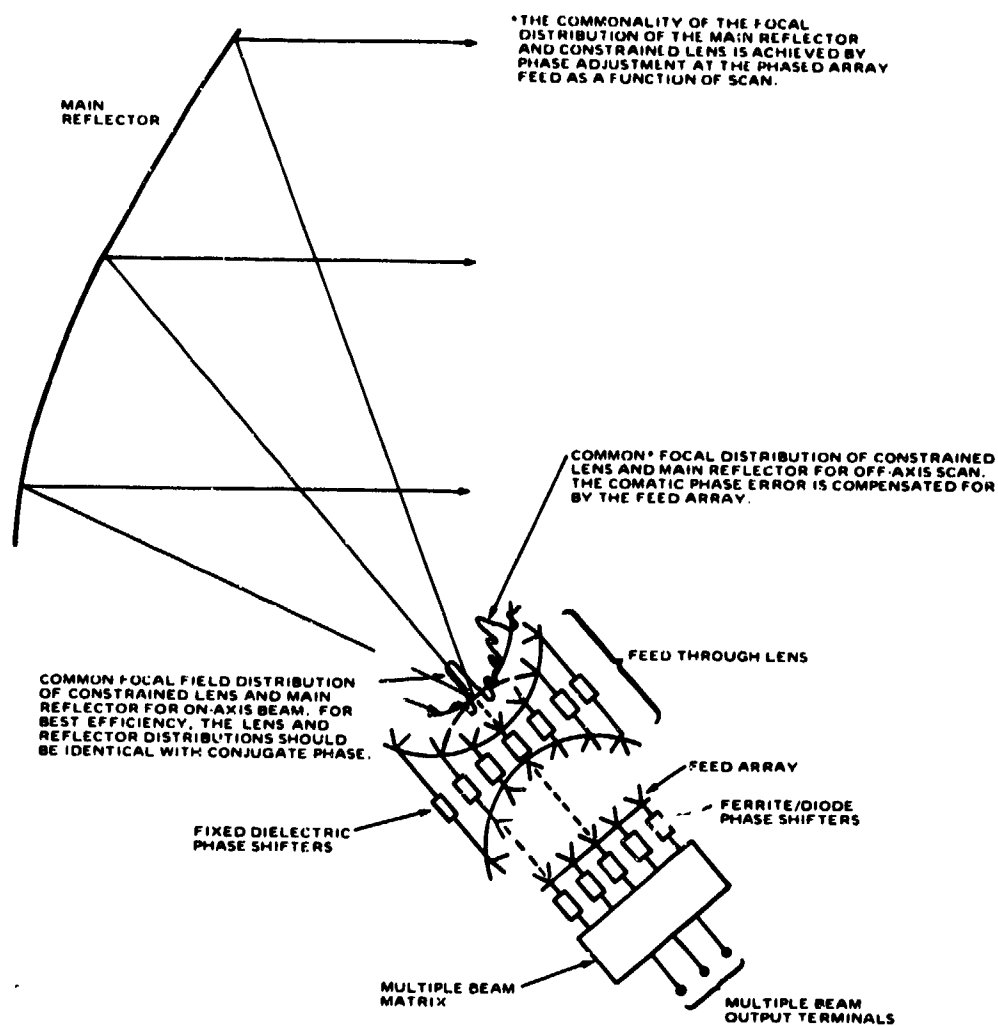


Fig.6 Dual lens limited scan concept (courtesy of C.H.Tang, Raytheon Co. Wayland, MA)



Single Reflector with Multiple Beam Constrained Lens

Fig.7 Reflector-lens limited scan concept (courtesy of R.Tang, Hughes Aircraft Co., Fullerton, CA)

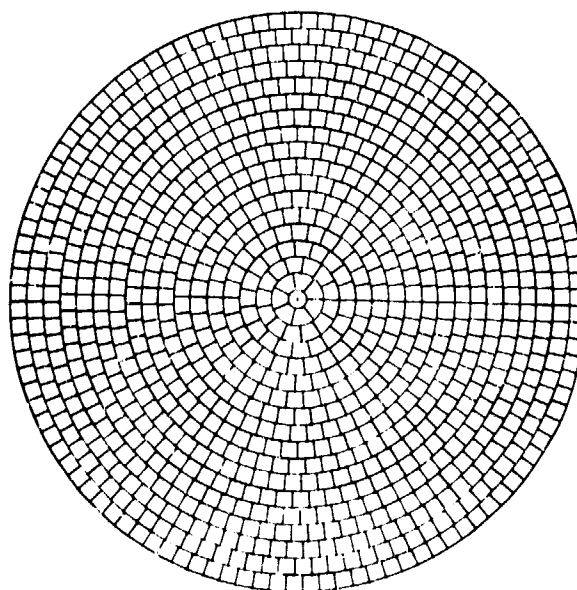


Fig.8 Aperiodic array for limited scan

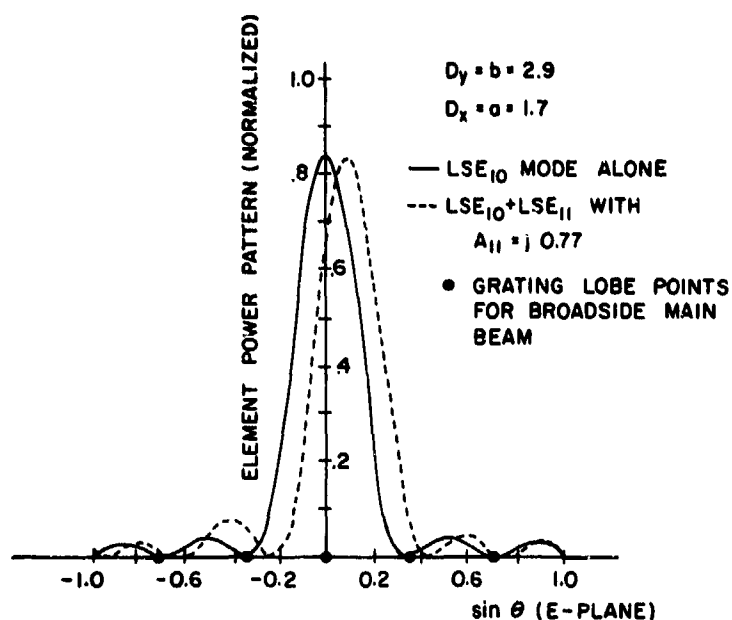


Fig.9 Array element patterns of fundamental mode ($A_1 = 0$) and of fundamental mode with odd mode ($A_1 = j0.77$) (2.9λ element separation in E-plane)

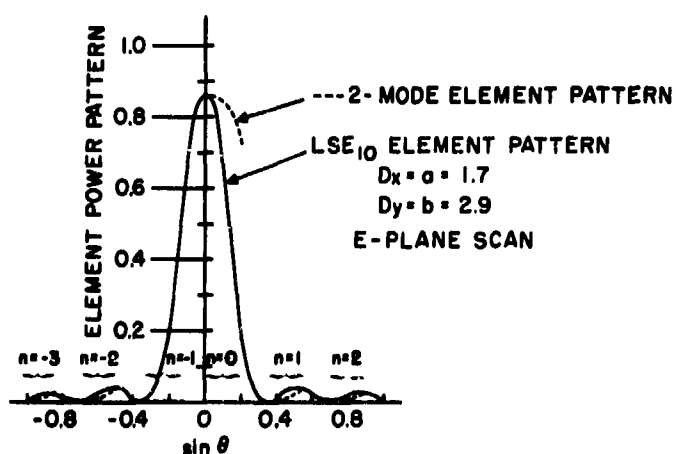


Fig.10 Active element pattern with odd mode chosen for $N = -1$ grating lobe cancellation

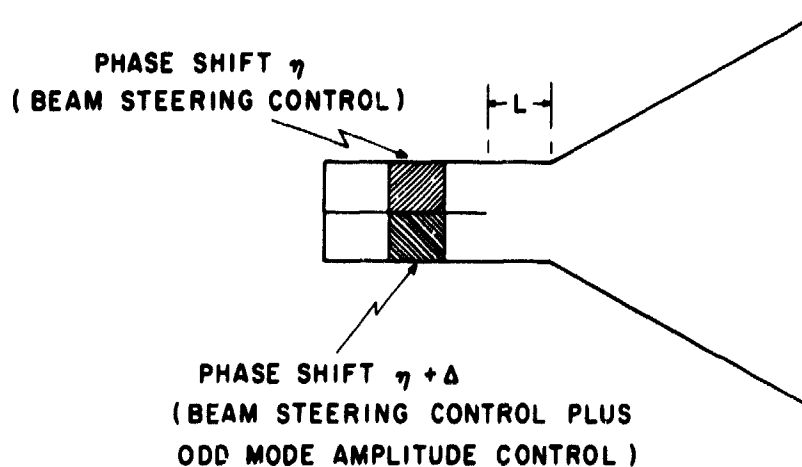


Fig.11 Even - odd mode power divider circuit for E-plane scanning

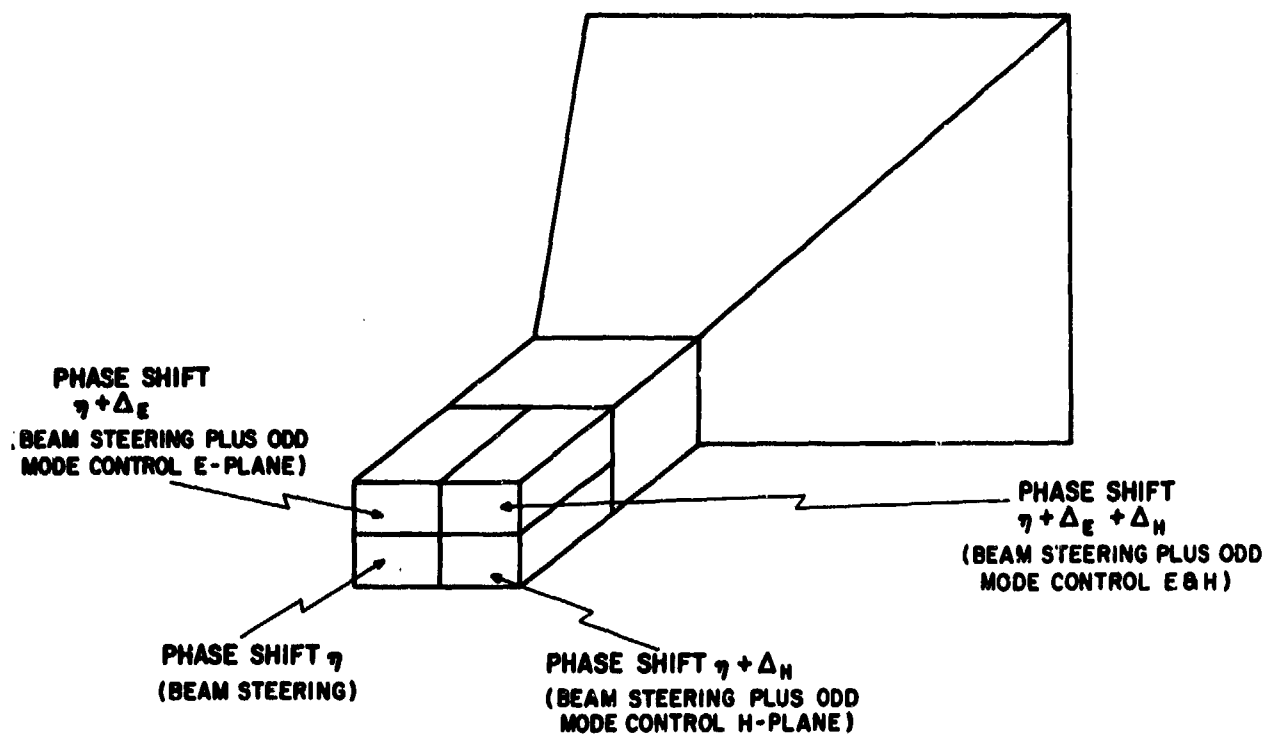
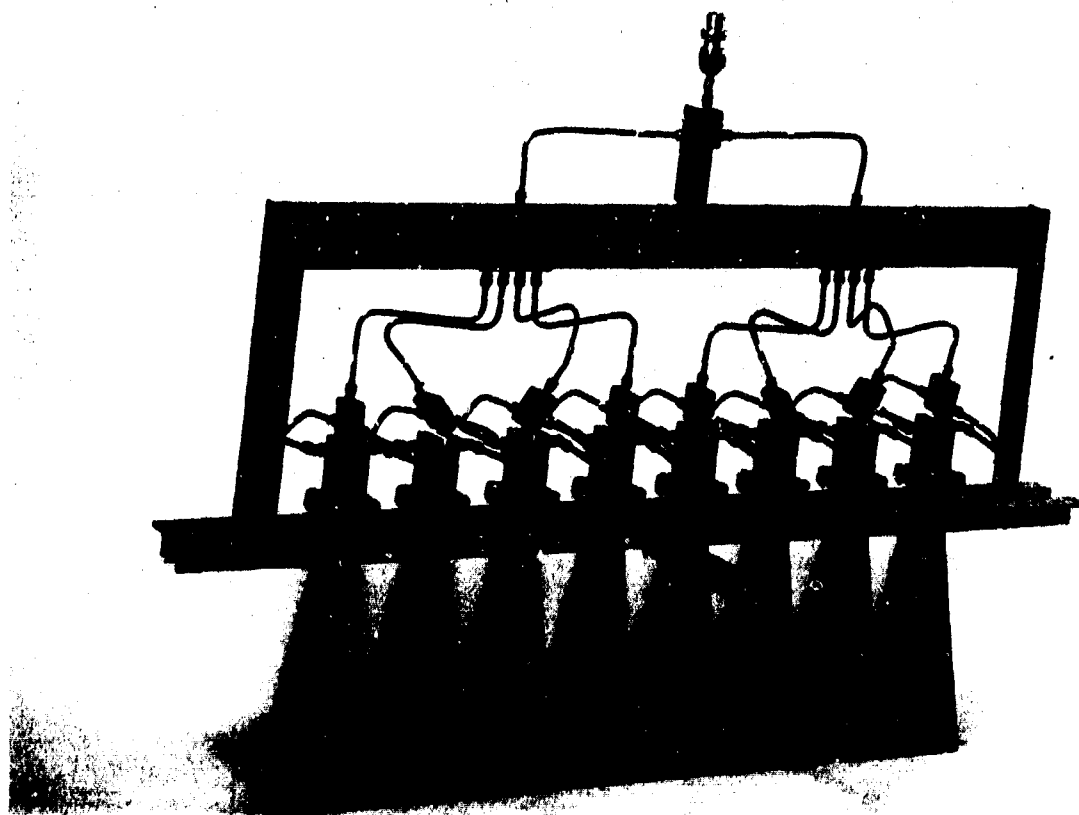


Fig.12 Four mode horn and power divider circuit

Fig.13 Prototype array for E-plane scan ($W = 3.01$)

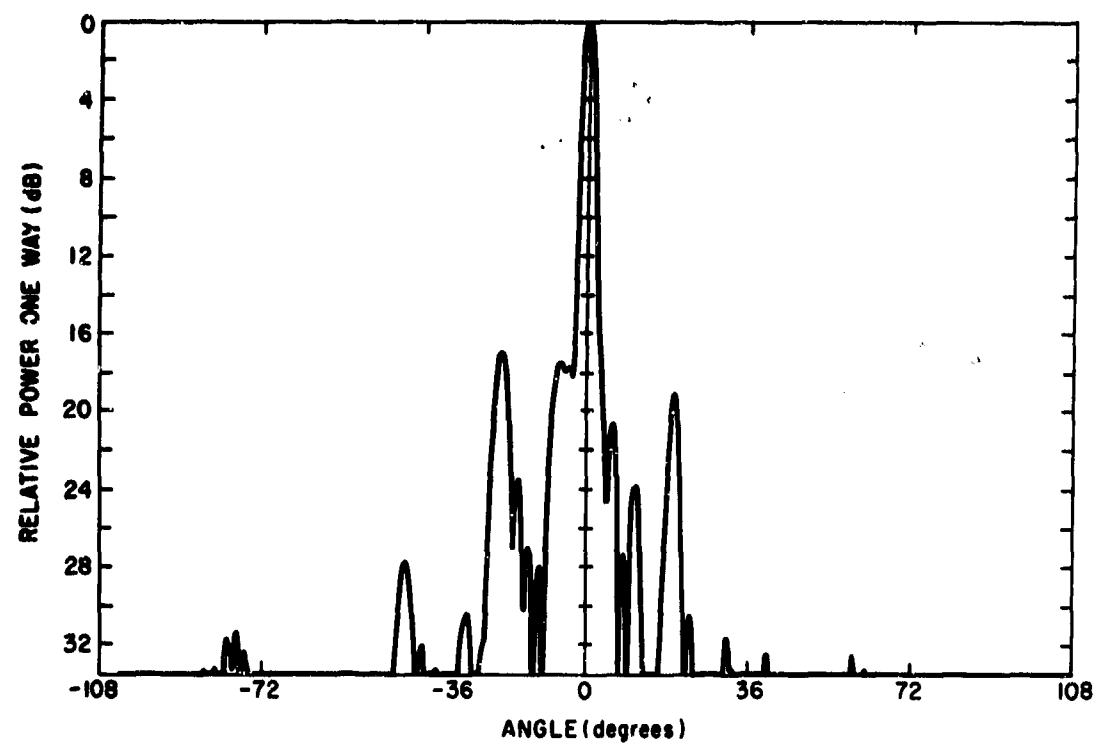


Fig.14(a) Array radiation pattern (broadside)

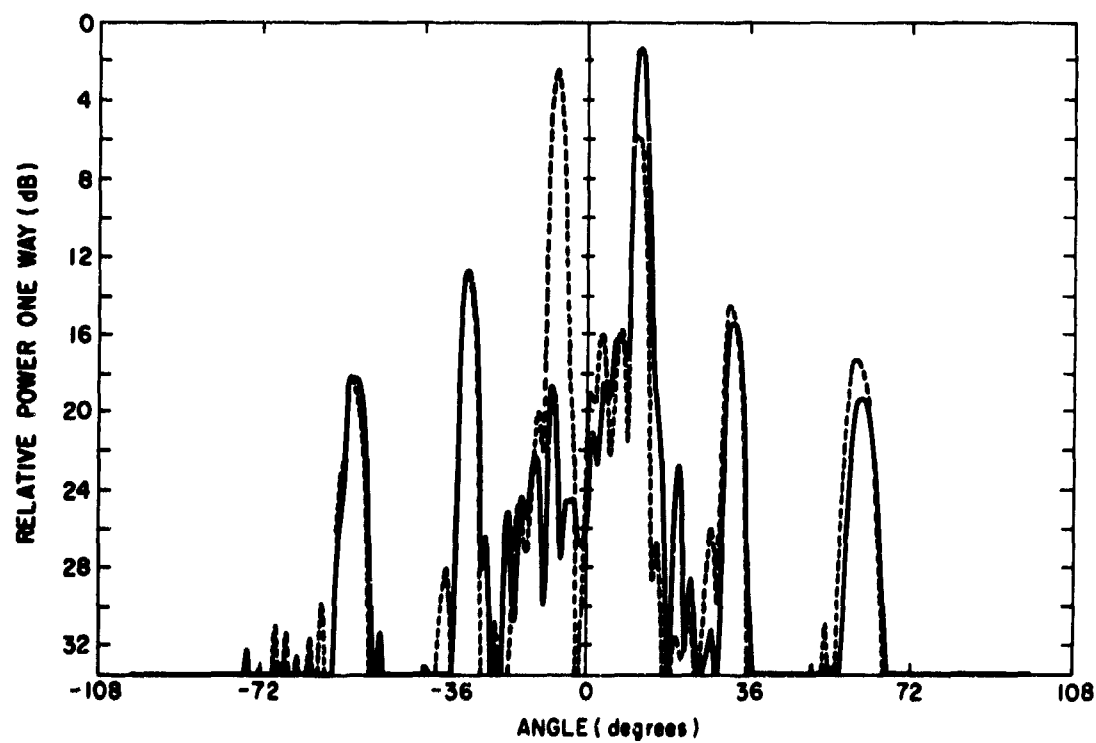


Fig.14(b) Array radiation patterns (12° scan)
 ——— with odd mode control
 - - - - - without odd mode control

DISCUSSION

R. REITZIG: In an array and reflector system with a lower number of elementary radiators and phase shifter units, the randomising effect of the multitude of phase shifters in a conventional phased array cannot be utilised. Therefore an increased accuracy in the phase shifters is required. Could you comment on this especially with respect to the technological impact on the phaseshifters.

R.J. MAILLOUX: Yes, you raise the point as to whether or not the search for techniques to reduce the number of array phase shifters might reach the stage of being counterproductive if the number of elements gets so small that very accurate phase shifters would be necessary. Obviously this would be the case if the arrays were not large in the first case; and indeed in such cases one would be better off to use conventional array technology. PAR antennas however are very large, and even with "element use factors" approaching unity, such arrays will have more than 400 to 500 elements. With such a large aperture, I do not expect that phase shifter tolerance will be a problem.

J.S. AJIOKA: Of the various limited scan techniques, you did not mention High Performance Space Feed (H.I.P.S.A.F.) of the Hughes Aircraft Co. Fullerton, Calif. sponsored by R.A.D.C. What's the possibility of rotating the parabolic sub-reflector of fig. 5 by 90° in a clockwise direction. With such a rotation the primary feed would point vertically downwards onto the sub-reflector. It seems that the off-axis aberrations with this change may cancel better because of symmetry.

A desirable geometry for a dual reflector system is to have the aperture distribution in the final (large) reflector to be stationary at the expense of distribution scanning over the smaller sub-reflector. This distribution scanning may be advantageous because this allows a greater degree of sub-reflector shaping (deviation from a paraboloid) for off axis aberration correction which is a function of scan, and since the distribution scans the sub-reflector, shape tailoring may be done to a greater degree. Do you know of work done along these lines? Since Hughes is working in this field, we are interested in the work of others, possibly unpublished.

R.J. MAILLOUX: I had no time to mention this in the oral presentation, but I have mentioned the overlapped sub-array technique in the text (page 32-3) and in the references (ref. 10). H.I.P.S.A.F. is of course, the first practical demonstration of this technique and was indeed successful. The work referred to on page 32-3 utilises this technique for synthesizing the sub-element pattern.

I should also note that we have conducted some overlapped array studies in-house at A.F.C.R.L.; and a report on this work is in preparation.

Your comment about rotating the sub-reflector 90° sounds reasonable, and I know of no other work along these lines.

NOTES ON THE RADIATION PATTERNS OF HF AERIALS INSTALLED ON HELICOPTERS

by

W T Blackhand
Royal Aircraft Establishment, Farnborough, England

SUMMARY

The fundamental modes of electrical oscillation of a helicopter are considered and their radiation patterns predicted. Scale model experiments have confirmed these predictions. Two modes of rotor modulation are possible. These have different characteristics, the first affecting signals at all azimuths while the effects of the other are most apparent near to minima in the radiation pattern.

1. INTRODUCTION

The basic radiation patterns for horizontally and vertically polarised radiation are discussed considering the helicopter structure as a resonator. The effects on these patterns of rotor rotation are predicted.

A series of measurements of the radiation patterns of a 1/20th scale "Whirlwind" helicopter have been made. These measured patterns illustrate and confirm the predictions made in the first part of the paper.

2. THE RADIO FREQUENCY RESONANCES OF THE HELICOPTER STRUCTURE

Two important resonances in the helicopter structure occur in the middle of the HF band. These are illustrated in Figure 1. The first, in which the current flow is shown by the continuous lines, is that in which the fuselage of the helicopter resonates as a dipole. This will occur at a frequency when the fuselage is about half a wavelength long (or a slightly lower frequency because the helicopter is a fat dipole). For a Whirlwind this would be at a frequency of about 10.5MHz while for a Wessex this would be at about 9.7MHz. This mode of resonance would lead to horizontally polarised radiation with the usual figure of eight radiation pattern of a dipole with, in the azimuthal plane, one lobe directed each side of the fuselage, and zeros end on fore and aft.

The second major resonance is one in which currents flow backwards and forwards from rotors to fuselage. The current pattern is shown in broken lines in Figure 1. The resonant frequency will be influenced to a certain extent by the form of the helicopter fuselage, but, to a first approximation it can be taken as that at which the rotor blades are a quarter of a wavelength long. The radiation of this current pattern is very simple - the radiations from horizontal currents on the rotors cancel as do to a first approximation those due to the forward and rearward parts of the helicopter. This leaves uncanceled the vertical currents on the rotor drive shaft and rotor tower. These currents approximate to those of a Hertzian doublet, and there is an omniazimuthal radiation of a vertically polarised signal with zeros above and below the helicopter. The resonant frequency for the mode in a Whirlwind would be about 9.3MHz and in a Wessex 8.4MHz approximately.

These two resonances dominate the distributions of current and consequently the radiation patterns in the midpart of the HF band.

3. THE RADIATION PATTERNS AT RESONANCE

The corresponding radiation patterns are shown in Figure 2 in which the continuous line shows the horizontally polarised dipole pattern of the first resonance and the dotted line shows the vertically polarised pattern of the second (rotor-fuselage) resonance. In this figure the dotted circle has been drawn outside the figure of eight for clarity, in practice their relative amplitudes would be governed by a variety of factors including the quality of electrical contact between the rotors and the fuselage.

The marked difference between the two radiation patterns shown in Figure 2 illustrates the importance of the direction of polarization in the evaluation of the utility of the radiation of an HF installation in a helicopter. Thus there is good omniazimuthal cover for vertical polarisation, but indifferent cover for the horizontal polarisation with nulls fore and aft. These nulls would seem to be inescapable for helicopter operation in the wavelength band dominated by the first mode.

It may be noted here that the Operational Requirement for an HF system ought to specify the direction of polarisation required, and that it will be fruitless to demand good forward or rearward cover with horizontal polarisation.

4. THE RADIATION PATTERNS AT OTHER FREQUENCIES

At frequencies above the resonant frequency the fuselage becomes a long dipole and the number of lobes in the pattern increases. Thus at double the first resonant frequency one might expect to have four lobes in the radiation pattern, however because of the gyronine form of the fuselage the splitting into four lobes occurs at a somewhat higher frequency. The vertically polarised component of the radiation will not be affected by the current distribution along the rotor blades or fuselage but only by the current on the central tower and rotor shaft. At the half wavelength resonance described above a maximum in the current standing wave pattern occurs on the central tower and rotor shaft and a relatively strong vertically polarised component is radiated. At about double this frequency the standing wave pattern will have changed so as to bring a minimum in place of the maximum and the vertically polarised radiation will be very much reduced.

As the frequency is lowered from the resonant frequency the horizontally polarised component keeps its figure of eight pattern with nulls fore and aft - it approaches that of a doublet.

At frequencies below the resonant frequency the current flowing in the rotor drive shaft and rotor tower will be very much less than at resonance and while its radiation will be omniasimuthal it will be at a low level and, as will be shown in Section 6, it can be masked by other sources of radiation.

5. ROTOR MODULATION

The rotation of the main rotor of the helicopter can produce an amplitude modulation of the signal transmitted in any given direction. There are two ways in which this modulation can arise.

Firstly the changing capacitance between the rotors and fuselage can alter the reactive load presented to the ATU and so modulate the amplitude. At operating frequencies close to the natural resonant frequency of airframe this amplitude change can be double humped with a marked modulation component at twice the frequency at which the rotors arms cross the tailboom. At frequencies much different from that of natural resonance the modulation will be single humped, the main component being at the frequency of rotor passes.

It is to be noted that this form of rotor modulation affects the signals equally in all directions and is independent of the azimuth of radiation. However there is another mechanism which gives a modulation concentrated in certain azimuths. This is illustrated in Figure 3.

Consider a helicopter with one rotor blade aligned with the fuselage. Because of the symmetry of the rotor system it would not affect the figure of eight horizontally polarised radiation pattern due to currents on the fuselage. Next consider the rotor system turned through a small angle from the fuselage axis. In this arrangement currents induced in the rotors are equivalent to those in a dipole making the same small angle with the axis. The combined effect of the currents in the fuselage considered as one dipole, and those in the rotors considered as another dipole, would be represented by an effective dipole making an angle with the fuselage lying between the fuselage and the rotor blade.

Thus as the rotor blade rotated it would swing the figure of eight radiation pattern about the fuselage axis through a small angle, θ . This is shown in Figure 3 where the solid and dotted lines show the limits of pattern swing. For an observer at A looking up towards O there is little change in received amplitude as the rotor turns as the rotor modulation is small. On the other hand for an observer at B there is a two to one variation in amplitude, while at C the signal would fall to zero and there would be 100% rotor modulation. It is to be noted that in contrast to the first form of rotor modulation which was independent of azimuth, the second form of modulation varies in depth with bearing, being deepest in the region of a dip in the radiation pattern.

As the rotors are horizontal in normal flight in general the second kind of rotor modulation, which is azimuth dependent, will be chiefly apparent on the horizontally polarised component of radiation, and not on the corresponding vertical component.

From the above discussion it would seem that the best precaution to take in order to limit rotor modulation of the first kind would be to ensure that the aerial system installed does not set up a high field in the regions through which the rotors pass. Experiments with a wire aerial run up the tail boom and left open circuited at the far end showed that this arrangement was very susceptible to rotor modulation - much more than when the same wire was short circuited at the upper end. This is because with the open wire there is a field concentration at the upper end in the region through which the rotors pass, while with the wire short circuited this field concentration is avoided.

In these notes there has not been any mention of the modulation effects of tail rotors. Such modulation does occur, particularly near the frequency where the rotor blades are a quarter wavelength long, but as in general, this frequency lies outside the HF band this phenomenon has been omitted from this discussion.

6. MEASURED RADIATION PATTERNS

It is not possible to measure the radiation patterns at resonance without having some mechanism for exciting the resonance. This mechanism in most cases will radiate on its own accord and so tend to mask the radiation of the basic resonance of the helicopter.

In order to check the predictions of the previous Sections a 1/20th scale model Whirlwind helicopter was used. This was fitted with a notch antenna out into the fairing between the cabin and the tail boom. This installed notch is illustrated in Figure 4. It was convenient to use the notch as the mechanism for exciting the currents in the helicopter fuselage because it acts as a loop antenna and so does not radiate energy with horizontal polarisation. For this reason the radiation patterns of the horizontally polarised component from the helicopter resonance will not be confused by any radiation from the notch. However, the notch will radiate with vertical polarisation a figure of eight pattern with lobes fore and aft and deep nulls to each side. It is to be expected that this radiation pattern will obscure the radiation pattern of the vertically polarised component from the helicopter resonance particularly at frequencies well away from the frequency of resonance.

The measured radiation patterns are shown in Figure 5. The three diagrams in the left hand column show the horizontal component of the radiation the upper at a measured frequency of 80MHz (scaled from 4MHz) which is well below resonance, the middle one at about the resonant frequency (206MHz scaled from 10.3MHz) and the lower one at twice the resonant frequency (400MHz scaled from 20MHz). From the foregoing discussion it is to be expected that these would not be affected by radiation from the notch and that they should agree with the predictions of Sections 3 and 4. This is seen to be the case. At the resonant frequency the radiation pattern is that of a dipole a figure of eight with nulls fore and aft. This is substantially unaltered at the lower frequency (It is not easy to distinguish between the

measured radiation patterns of a dipole and a Hertzian doublet). At twice the resonant frequency there are the beginnings of a breaking up into four lobes.

The diagram of the vertically polarised component are shown in the right hand column. As would be expected the radiation patterns are dominated by the fore and aft figure of eight of the notch radiation, particularly at the frequencies well below and well above the frequency of resonance. At the resonance frequency the radiation pattern is that of the expected omniazimuthal form with a distortion due to the figure of eight of the notch.

Thus the measured radiation patterns confirm the predictions made in Section 3 and 4 in particular demonstrating the expected presence of fore and aft nulls in the radiation pattern for the horizontally polarised component.

The importance of the resonance of the helicopter fuselage has been demonstrated by unpublished measurements of the effective radiated power of an HF installation in which a marked peak was demonstrated near to the frequency of fuselage resonance as a half wave dipole.

7. MEASURED ROTOR MODULATIONS

The two diagrams of Figure 6 show measured horizontal plane radiation patterns recorded as the rotors of the 1/20th scale model helicopter were rotated. Because the rotors were turned much faster than the model under test, the rotor modulation appears as a scalloping on the diagram. The depth of modulation can be read from the diagram using the marked dB scale (5dB between heavy lines). Both of these diagrams were recorded near the frequency of resonance where the modulation effects are most marked.

The upper diagram demonstrates the first kind of modulation described in Section 5, which appears of the same depth at all azimuths. As predicted this shows a marked double humping as the rotor arm brings the structure in and out of resonance.

The lower diagram demonstrates the second kind of modulation in which the modulation is much greater in the direction of the radiation minima than in other directions. It will be noted that in the rearward direction the modulation has a ratio of 25dB.

8. LIMITATIONS IN THE OPERATIONAL USE OF HF AERIALS ON HELICOPTERS

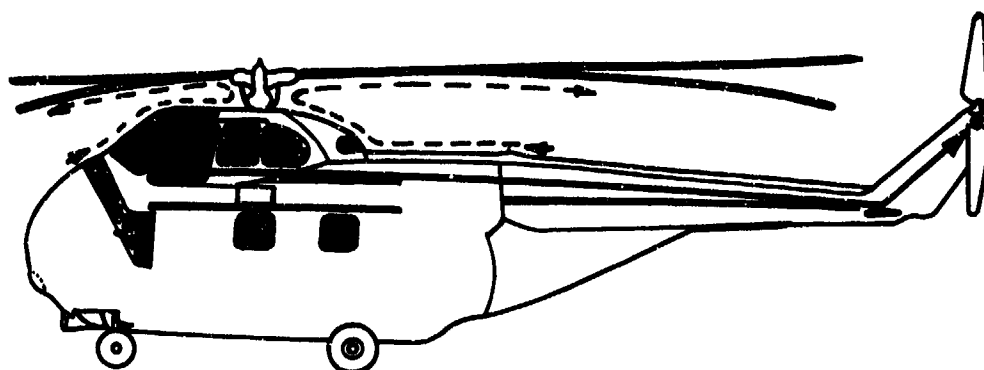
The radiation from a helicopter in the HF band is complex with both horizontally and vertically polarised components. The radiation patterns of these components are dissimilar and it is important to keep clearly in mind which component is being utilised in any given communication system.

The horizontally polarised component is radiated with a lobed pattern. These patterns are figure of eight for most of the frequency band. In this case the nulls are such that the signal level will be more than 10dB below that at the peak of the lobe for a sector 35° wide about each null. Operational planning must accept the inevitable fact that these nulls exist and that they extend to nose and tail.

Rotor modulation of the horizontally polarised radiation from helicopters can be extremely deep over narrow angular sectors but a fading ratio of 10dB is not unusual over a sector of say 30°. If there is plenty of power in hand the AGC can cope with this modulation as the frequency is low (in the band 10-20Hz). Unfortunately the depth of modulation is usually deepest in the directions of minima in the radiation pattern - that is in circumstances in which the AGC would not be in operation.

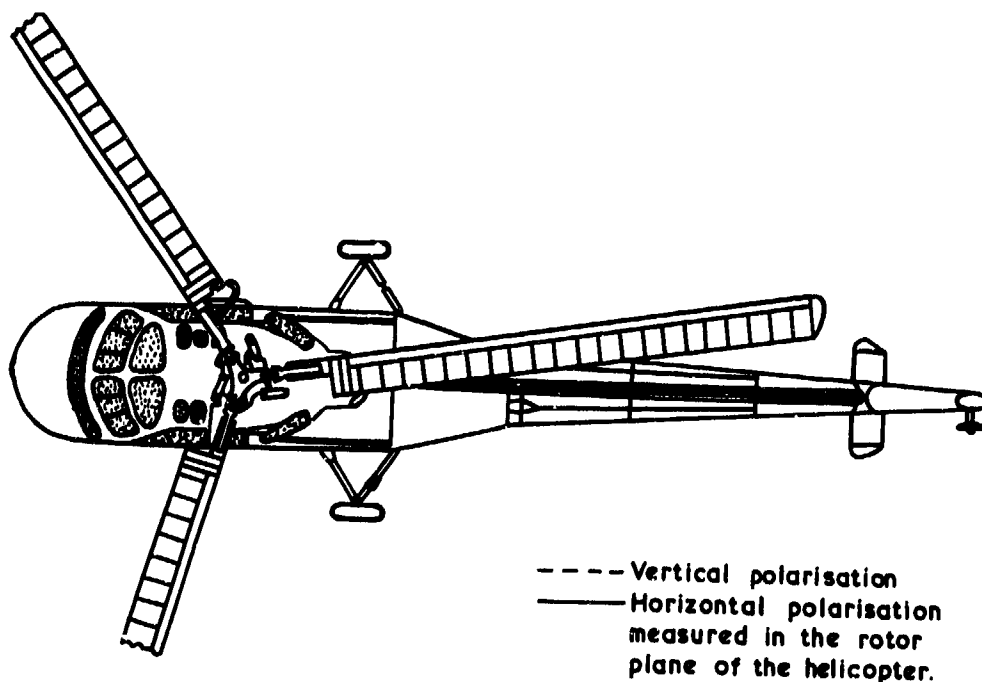
The vertically polarised component has a generally omniazimuthal configuration near resonance and so is but little affected by rotor modulation. At high and low frequencies nulls appear in the radiation pattern. They correspond in direction to the nulls of the notch aerial used in order to excite the helicopter fuselage.

The effects of the different radiation patterns and of rotor modulation on data link circuits require careful study. The use of polarisation diversity also requires consideration.



--- Vertical polarisation
 — Horizontal polarisation
 measured in the rotor
 plane of the helicopter

The two principal resonance modes in a helicopter



--- Vertical polarisation
 — Horizontal polarisation
 measured in the rotor
 plane of the helicopter.

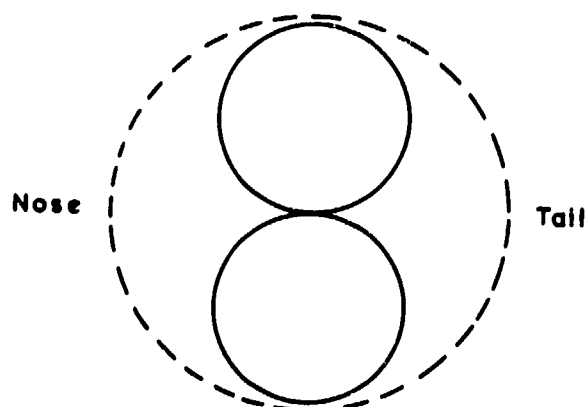


Fig.2 Radiation patterns of the principal modes

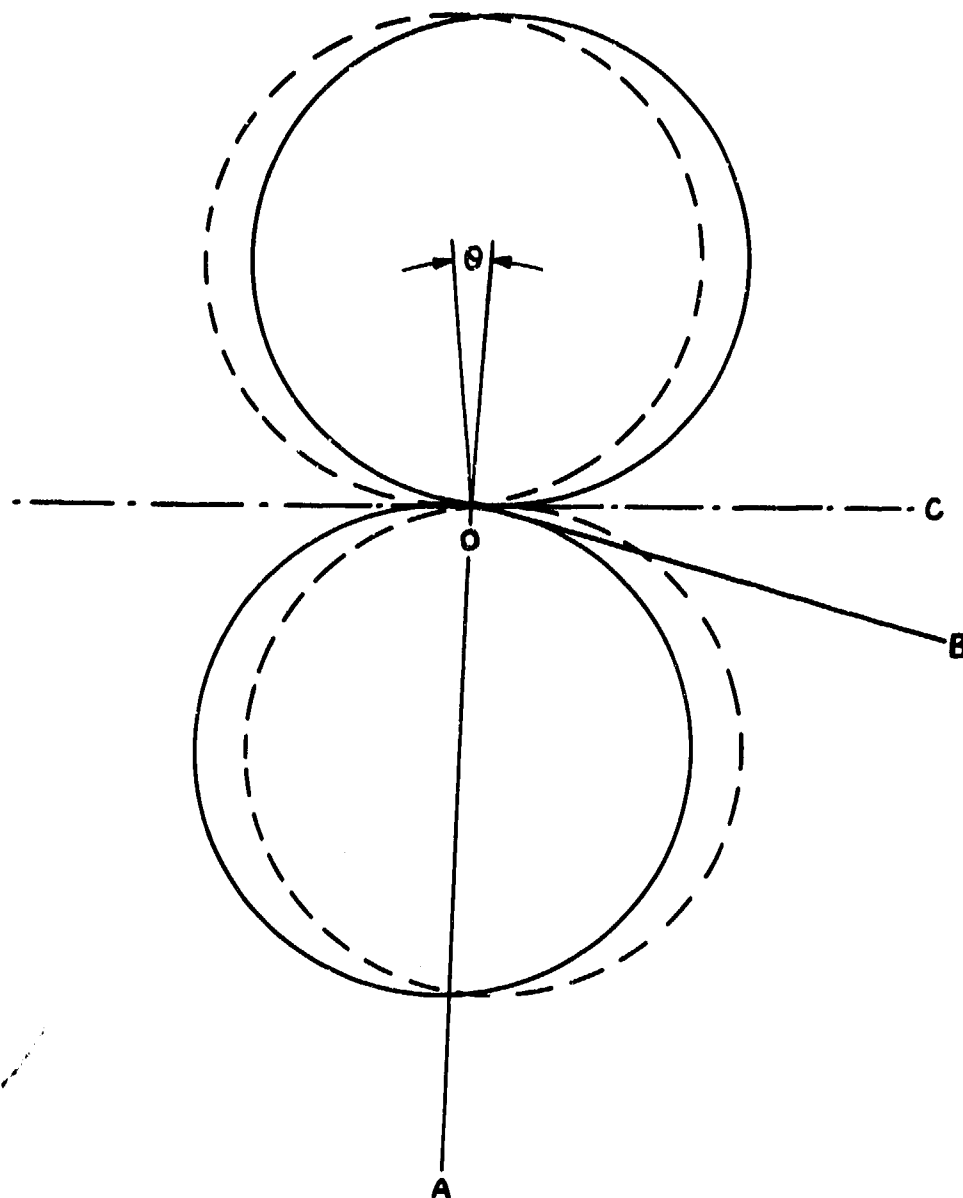


Fig.3 The geometry of rotor modulation

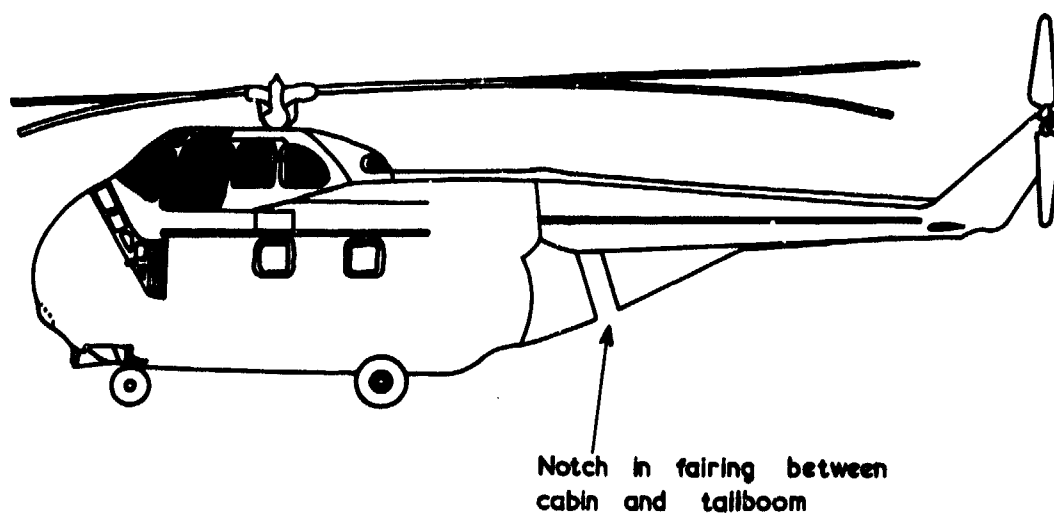


Fig.4 The siting of the notch antenna on the model helicopter

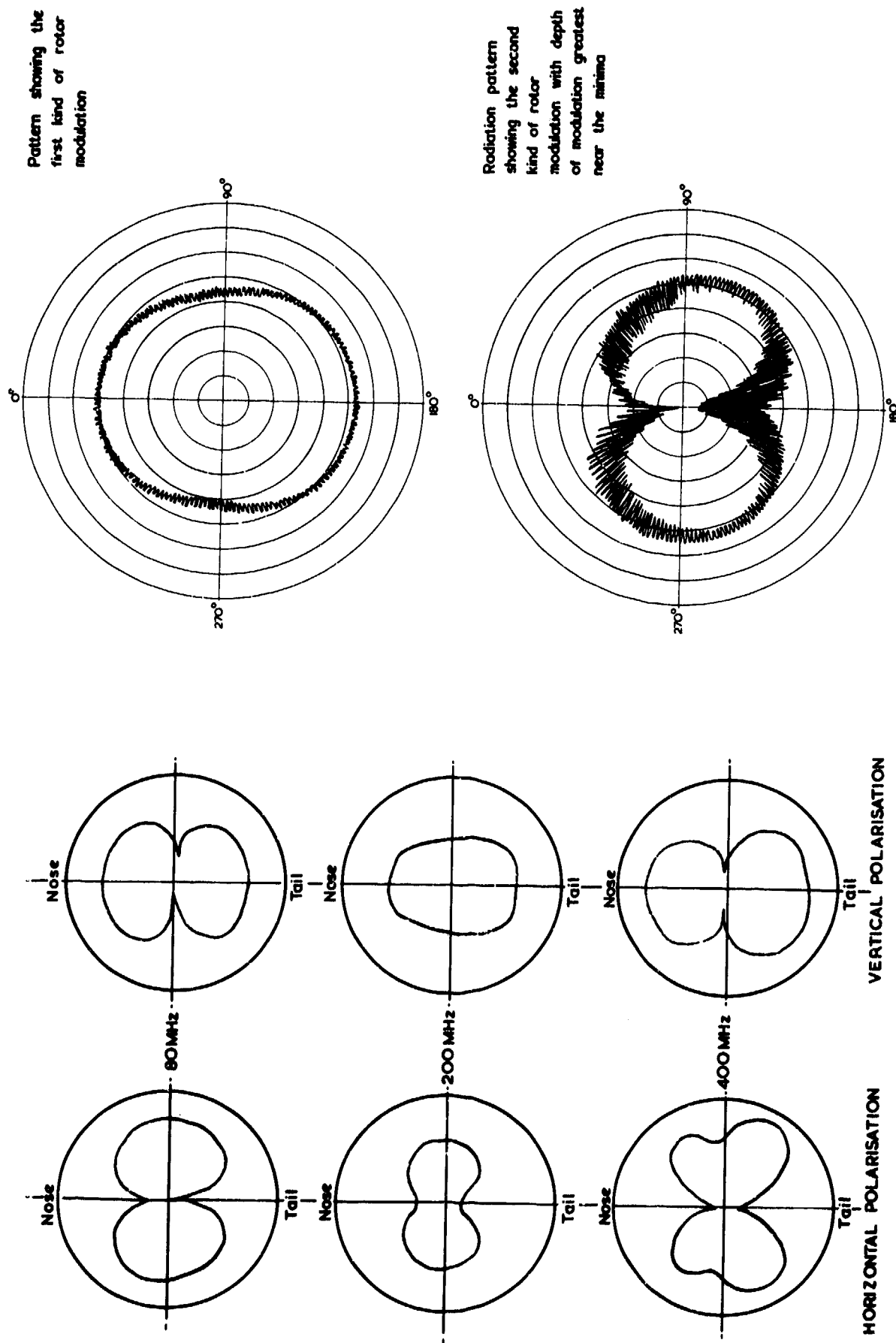


Fig.5 Measured radiation pattern of the notch on the model helicopter

Fig.6 Rotor modulation

RADIATION CHARACTERISTICS OF THINNED ARRAY ANTENNAS

W. Söntgerath
FORSCHUNGSINSTITUT FÜR
HOCHFREQUENZPHYSIK
D-5307 Wbg.-Werthhoven
Germany

SUMMARY

The advantages of phased array antennas are evident but they have to be paid for by considerable technical and financial expense. It may be reduced by "thinning" the array, i.e. by distributing only a few elements in an extended regular grid of a conventional "filled" array with one-half wavelength spacing.

In designing large arrays statistical methods for the element arrangement are used and from these only statistical information can be obtained with regard to resulting radiation patterns.

The paper commences with a survey of the well-known statistical relations between element distribution and radiation pattern of density-tapered arrays. Following a discussion of the statistical distribution of the signal energy in sidelobe directions, the effects on the radiation pattern of a special element distribution, i.e. the minimum distance of half a wavelength between adjacent elements is increased to one wavelength, are also treated. The paper concludes with a brief study concerning the problems which are caused by the digitally controlled phase shifters commonly used in phased array technique.

1. INTRODUCTION

For several applications, e.g. in radar and navigation, an increasing popularity can be noted for phased arrays, i.e. antenna arrays whose radiation patterns can be scanned by phase control of discrete antenna elements.

Experimental systems developed so far vary considerably in structure and dimensions. There are arrays with a few elements placed in a line, up to arrays with some thousand elements arranged on flat or curved apertures. All systems principally consist of three essential parts, i.e. radiating elements, phase shifters, and feeding network. The advantages of such antenna systems for radar technique originate from the lack of any mechanically moved parts. This allows an extremely fast beam scanning and thus special kinds of target tracking. The enormous costs however are a disadvantage of such a system.

A regular array with a radiation pattern of small beamwidth for a surveillance- or target-tracking radar has a large number of elements, which must be arranged at $\lambda/2$ -distance to avoid the occurrence of grating lobes, also in case of beam scanning. To get a beamwidth of 1° it is necessary to arrange about 10000 elements on an aperture.

By "thinning" the array, i.e. by distributing only a few elements on an extended regular grid of a conventional "filled" array one can considerably reduce the expense without loss of resolution, i.e. without enlarging the beamwidth of the antenna. Furthermore a decrease of the rather disturbing effects of mutual coupling can be expected. A disadvantage, however, results from the thinning by a loss of gain according to the smaller number of elements and an increase of the sidelobe level.

So far no methods have become known for an optimal distribution of the elements of a thinned array with respect to the radiation pattern. Only for small arrays there are iterative numerical approximations (Baklanov, Y.V., et al., 1962), (Skolnik, M.I., et al., 1964a). With larger arrays only statistical methods can be used, naturally yielding only statistical information of the expected radiation pattern (Lo, Y.T., 1968), (Lo, Y.T., 1964), (Willey, R.E., 1962), (Skolnik, M.I., et al., 1964b).

Statistically thinned antenna arrays (density tapered arrays) will now be considered; their elements are distributed on a $\lambda/2$ -grid. First a survey of the well-known statistical relations between element distribution and radiation pattern of such antenna arrays is given.

Furthermore the energy from sidelobe directions and problems due to the digital phase shifters, which in most cases are used for such arrays, will be treated. Finally a discussion of arrays with a modified element distribution is presented. These arrays have a minimum distance of λ between adjacent elements, while the elements are distributed on a $\lambda/2$ -grid. Most of the studies will be done

with linear and planar arrays. Only the array factor resulting from the geometric distribution of the elements will be investigated. The influence of mutual coupling between the elements will be neglected.

2. MAIN BEAMWIDTH AND SIDELobe LEVEL

Fig. 1 shows an array whose elements are arranged on a grid in the xy -plane of a Cartesian coordinate system. The direction of the observed point is given by the usually used angles θ and φ of a spherical coordinate system. The sum of the elements in the positions ν, μ with the amplitudes $I_{\nu\mu}$ and the phases depending on the scan angle θ_0, φ_0 yields the array factor

$$M = \frac{1}{\sum_{\nu} \sum_{\mu} I_{\nu\mu}} \sum_{\nu} \sum_{\mu} I_{\nu\mu} e^{i[\nu(u-u_0) - \mu(v-v_0)]} \quad (1)$$

with
$$\varphi_{\nu\mu} = -(\nu u_0 + \mu v_0) = -2\pi(\nu d/\lambda \sin \theta_0 \cos \varphi_0 + \mu d/\lambda \sin \theta_0 \sin \varphi_0)$$

$$u - u_0 = 2\pi d/\lambda (\sin \theta \cos \varphi - \sin \theta_0 \cos \varphi_0), \quad v - v_0 = 2\pi d/\lambda (\sin \theta \sin \varphi - \sin \theta_0 \sin \varphi_0)$$

In distributing the elements of statistically thinned arrays one generally tries to get a good approximation of the aperture illumination of a favourable amplitude tapered reference array, e.g. the current distribution for a Dolph-Chebyshev pattern. This approximation is shown in fig. 2 using a linear array with elements distributed on the x -axis. The current distribution of the reference array (solid curve in fig. 2), referred to its maximum value, is taken as probability of placing an element at a grid position. The probability of placing an element at position ν is:

$$p_{\nu} = \alpha \cdot I_{\nu} \quad (2)$$

where α is an additional thinning factor, responsible for the average number \bar{N} of elements

$$\bar{N} = \alpha \sum_{\nu} I_{\nu} \quad (3)$$

in the array. A random experiment assigns a number $0 \leq Z_{\nu} \leq 1$ to each grid point and an antenna element with amplitude $A_{\nu} = 1$ if $Z_{\nu} \leq p_{\nu}$. Taking a sufficient number of element distributions generated in this way the average element density of a grid point is:

$$\bar{A}_{\nu} = p_{\nu} = \alpha I_{\nu} \quad (4)$$

and the average array factor

$$\bar{M} = \frac{1}{N} \sum_{\nu} \bar{A}_{\nu} e^{i\nu(u-u_0)} \quad (5)$$

equals the favourably chosen array factor of the reference array.

The array factor of thinned arrays has been studied in a considerable number of papers using statistical methods (Skolnik, M.I., et al., 1964b), (Lo, Y.T., 1964), (Lo, Y.T., 1968). Thus we may restrict ourselves to the more important results. The main beamwidth of thinned arrays mainly depends on the geometric dimensions of the array and much less on the chosen reference aperture illumination, so that it can be determined from the antenna length L in the respective plane and a factor $\beta \approx 1$, which depends on the reference array:

$$\theta_{3dB} = \beta \cdot \frac{1}{L/\lambda} \quad (6)$$

The directivity of regular filled, planar arrays can be calculated under certain conditions, by integrating over the array factor (Hansen, R.C., 1966). For large statistically thinned arrays the following good approximation formula for the directivity as a function of the scan angle may be obtained:

$$D_a = \frac{N \cdot D_e \cdot c^2(\theta_0, \varphi_0)}{1 - \alpha \frac{\sum_{\nu} \sum_{\mu} I_{\nu\mu}^2}{\sum_{\nu} \sum_{\mu} I_{\nu\mu}} + \alpha \frac{\sum_{\nu} \sum_{\mu} I_{\nu\mu} \cdot c^2(\theta_0, \varphi_0) D_e}{D_{a0} \cos \theta_0}} \quad (7a)$$

As an exception in (7a) the pattern $c(\theta, \varphi)$ and the directivity D_e of the elements are considered. A necessary condition for (7a) to apply is that the single element patterns are not disturbed by mutual coupling effects. At high thinning ($\alpha \ll 1$) the

dependence of the directivity as a function of the scan angle and the element distribution, represented in the value D_0 , the directivity of the unscanned reference array, is low and for the limiting case results in:

$$D_0 = N \cdot D_e \cdot c^2(\beta_0, \varphi_0) \quad (7b)$$

whereas for filled arrays ($\alpha=1, I_{\nu\mu}=1$) the well-known relation

$$D_0 = D_e \cdot \infty \varphi_0^2 \quad (7c)$$

is valid.

The sidelobe level is affected by both, the degree of thinning and the positioning of the elements. For the average sidelobe attenuation we obtain

$$\overline{|M|^2} = \frac{1}{\alpha \sum_{\nu} \sum_{\mu} I_{\nu\mu}} \left(1 - \alpha \frac{\sum_{\nu} \sum_{\mu} I_{\nu\mu}^2}{\sum_{\nu} \sum_{\mu} I_{\nu\mu}} \right), \quad (8a)$$

and for a high degree of thinning ($\alpha \ll 1$), equation (8a) is simplified to (8b)

$$\overline{|M|^2} = \frac{1}{N}, \quad (8b)$$

i.e. the average sidelobe attenuation is inversely proportional to the number of remaining elements. For practical use not only the mean value of the array factor in the sidelobe region but also its distribution function is of interest. For a high degree of thinning ($\alpha \ll 1$) and a symmetric reference illumination with sufficiently high sidelobe attenuation ($|M| \ll \sigma$) the well-known Rayleigh distribution function is obtained

$$P(|M| \leq |M'|) = \left(1 - e^{-\frac{|M'|^2}{2\sigma^2}} \right) \quad (9)$$

with a non-directional variance

$$\sigma^2 \approx \frac{1}{2N} \left(1 - \alpha \frac{\sum_{\nu} \sum_{\mu} I_{\nu\mu}^2}{\sum_{\nu} \sum_{\mu} I_{\nu\mu}} \right) \quad (10)$$

The distribution function for the whole sidelobe region is the product of discrete distribution functions, according to (9) in m independent directions:

$$P(|M| \leq |M'|) = \left(1 - e^{-\frac{|M'|^2}{2\sigma^2}} \right)^m \quad (11)$$

A considerable disadvantage of thinned arrays compared with regular amplitude tapered arrays is the small sidelobe attenuation. Fig. 3 shows as an example the average and peak sidelobe level for thinned circular planar arrays with diameter $D = 40\lambda$. According to (8b) the average sidelobe level is shown as a function of the number of elements in the arrays. The curve above shows the theoretical limit of the maximum sidelobe attenuation, which can be realized (Mattson, E., 1971), (Andreasen, M.G., 1962):

$$|M| = \frac{4}{N} \left(1 - \frac{N \cdot \lambda^2}{4D^2} \right). \quad (12)$$

In practice the peaks of the sidelobes of a thinned array belong to the hatched region of fig. 3. According to (11) the probability for the peaks not exceed this region is 99% and 1% in the opposite direction. Because of the small influence of the element distribution on the main beamwidth and directivity the following studies are limited to the sidelobe region.

3. SIGNAL ENERGY FROM SIDELOBE DIRECTIONS

Because of their small sidelobe attenuation thinned arrays are considerably responsive to clutter and interference over the sidelobes. In the following, therefore, consideration is given to signal energy received from sidelobes of thinned arrays, i.e. the ratio V of the signal energy and the respective value in the main beam direction (Ries, G., Söntgerath, W., 1973).

It is known that the array factor has a Rayleigh-distribution in the sidelobe region. If the facility only transmits or receives (one way mode of propagation), the signal energy from the sidelobe directions is proportional to $|M|^2$, and for the distribution function we obtain:

$$P_1(V) = \int_0^V P(|M|^2) d|M|^2 = 1 - e^{-\frac{V}{2\sigma^2}}, \quad (13a)$$

$$\bar{V} = 2\sigma^2 \approx \frac{1}{N}. \quad (13b)$$

This is the average sidelobe level according to (8b). Fig. 4 shows, according to (13a), the theoretical distribution function for an array with a diameter of 40λ and 500 elements. The curve is well approximated by the frequency distribution curve, also shown in fig. 4, which has been found for such an array by classification of calculated values of attenuation in about 1000 independent sidelobe directions.

An especially critical role is played by the high sidelobe level of thinned arrays in case of radar at intensive disturbances due to echo. In the usual case of using one antenna for transmitting and receiving, for the distribution function of the signal energy from sidelobe regions follows:

$$P_2(V) = \int_0^V P(M^4) dM^4 = 1 - e^{-\frac{V}{2\sigma^2}} \quad (14a)$$

with

$$\bar{V} = 2\sigma^2, \quad (14b)$$

The distribution function according to (14a) and a respective frequency distribution curve, calculated from experimental data, are also shown in fig. 4 and agree sufficiently with each other.

If different antennas are used for transmitting and receiving, the distribution function of the signal energy from the sidelobe directions is:

$$P_3(V) = \int_0^V \int_0^V P_S(M_S^2) \cdot P_E\left(\frac{V'}{M_E^2}\right) \frac{dM_S^2}{M_S^2} dV' = 1 - \frac{\sqrt{V}}{\sigma_S \sigma_E} K_1\left(\frac{\sqrt{V}}{\sigma_S \sigma_E}\right), \quad (15a)$$

$$\bar{V} = 4 \sigma_S^2 \cdot \sigma_E^2, \quad (15b)$$

$$\sigma_E^2 = \frac{1}{2N_E} \left(1 - \alpha_E \frac{\sum_{\nu} \sum_{\mu} I_{\nu\mu E}^2}{\sum_{\nu} \sum_{\mu} I_{\nu\mu E}}\right), \quad \sigma_S^2 = \frac{1}{2N_S} \left(1 - \alpha_S \frac{\sum_{\nu} \sum_{\mu} I_{\nu\mu S}^2}{\sum_{\nu} \sum_{\mu} I_{\nu\mu S}}\right)$$

M_S , M_E and N_S , N_E respectively are the array factors and numbers of elements of the transmitting and the receiving antenna. K_1 is the modified first order Bessel-function of the second kind. Compared with the case above, where the same antenna was used for both transmitting and receiving, a reduction of the average signal energy of 3 dB results ($N_E = N_S = N$), if the correction factors in σ_E , σ_S are neglected, as equations (14b) and (15b) show. If, however, the total number of elements is not increased and $N_E = N_S = N/2$, the average signal energy is enhanced by 3 dB. The distribution function according to (15a) with $N_E = N_S = 250$ elements and the already introduced array parameter is shown in fig. 4, together with a calculated frequency distribution.

As a summary of the discussion above we can say that with a given number of elements the expected average signal energy from the sidelobe directions will just be minimal if all elements are used for transmitting as well as for receiving. Distributing the available elements onto two separate antennas a minimum enhancement of 3 dB is obtained.

4. ARRAYS WITH ENLARGED MINIMUM ELEMENT DISTANCE

The elements of an array antenna are usually distributed on a $\lambda/2$ -grid, so that the minimum distance of adjacent elements is $\lambda/2$. In some cases a larger distance may be necessary, e.g. if elements with geometric dimensions greater than $\lambda/2$ are used. In this case an additional condition on the element distribution at the $\lambda/2$ -grid has to be introduced, which guarantees a minimum element distance of one wavelength. The influence of this additional requirement on the array factor will be discussed below. This method of thinning does not lead to grating lobes. However, an increase of the sidelobe level cannot be avoided in the direction in which grating lobes in not thinned arrays with λ -element distance would appear. Fig. 5 shows the array factor of an array modified accordingly. The sidelobe level is raised in the region $(u-u_0) \approx \pi$ i.e. $\theta \approx 90^\circ$.

For the theoretical investigation of thinned arrays with enlarged minimum element distance the same statistical methods are used, as described above. To get a simplification of the problem linear arrays are investigated. The distribution of the elements is done by the already known random experiment, taking into account, however, the additional condition of a minimum element distance of λ . To get in the mean the given excitation for each position according to equation (2) the initial probability for the random experiment must be modified to:

$$P'_j = \frac{P_j}{1 - P_{j-1}} \quad (16)$$

Real and imaginary components of the array factor are asymptotically normally distributed. In this special case the variances depend upon the direction ($u-u_0$). We obtain for those variances in the sidelobe region (Ries, G., Söntgerath, W., 1972):

$$\sigma^2 = \sigma^2 - \sigma^2(u-u_0) = \frac{1}{2N} \left[1 - \alpha \frac{\sum I_p^2}{\sum I_p} - 2\alpha \cos(u-u_0) \frac{\sum I_p^2}{\sum I_p} + \sum_{s=0}^{\infty} 2^{s+1} \alpha^{s+2} \cos^2 \frac{(u-u_0) - \pi}{2} \cdot \cos \frac{(u-u_0) - \pi}{2} \frac{\sum I_p^{2s+2}}{\sum I_p} \right] \quad (17)$$

For a high degree of thinning, the part in (17) depending on the direction vanishes and equation (17) is reduced to (10). As an example fig. 6 shows the variance for different degrees of thinning of a linear array with 101 grid positions and a reference excitation according to Dolph-Chebyshev. Also shown is the respective mean value of σ^2 equalling the variance according to (10), i.e. no dependence on the direction for arrays without additional requirement. Thus, at a high degree of thinning, σ^2 remains almost constant over ($u-u_0$), whereas at a lower degree a considerable raise towards ($u-u_0$) results. For ($u-u_0$) = π the imaginary component of the array factor vanishes. The real component is normally distributed in this direction and its variance - by a factor 2 - greater than the variance, resulting from (17) with ($u-u_0$) = π . The variance which has been calculated by numerical computer experiments, is also shown in fig. 6 for $N = 25$ and a sample size of 300 different arrays and is quite close to the theoretical function resulting from (17).

Under the assumption of a favourably chosen reference excitation ($\sigma \gg |\bar{M}|$) the bivariate normal distribution of the array factor can in this case also be transformed into a Rayleigh-distribution according to (9), and for the total distribution function resulting from the product of the respective discrete distribution functions from all independent directions m we obtain:

$$P(|M| \leq |\bar{M}|) = \prod_{m=0}^m \left[1 - e^{-\frac{|\bar{M}|^2}{2\sigma^2(u,y)}} \right] \quad (18)$$

Fig. 7 shows the frequency distribution curve of the minimum sidelobe attenuation for the whole sidelobe region, calculated from the array factors of 400 different arrays with a minimum element distance of λ . It is a good approximation of the distribution function resulting from (18). To have a comparison, the distribution function according to (11) is also shown. An extension of the theory to planar arrays is done approximately in (Ries, G., Söntgerath, W., 1972).

5. EFFECTS DUE TO PHASE QUANTIZATION

Additional changes - especially in the sidelobe region - result from the phase steering. Phase steering by digital phase shifters leads to maximum phase errors

$$|\delta_p| = \frac{\pi}{2^b} \quad (19)$$

where b is the number of bits of the phase shifter. These errors must be taken into account with respect to equation (1). A phase error with a saw-tooth shaped changing over the array (fig. 8a) resulting from electronic pattern scanning with simple phase computers, leads, also for thinned arrays, to the well-known quantization lobes (Cheston, T.C., Frank, I., 1968) with the following amplitudes:

$$c_x = \frac{(-1)^x}{2^b \cdot x} \quad (20a)$$

and positions:

$$u_x = u_0 (1 + x \cdot 2^{-b}) \quad (20b)$$

Fig. 9 shows a calculated example together with the theoretical positions and amplitudes of the quantization lobes according to (20a,b). Means to reduce such pattern disturbances have also been suggested (Miller, C.J., 1964). By superposing a random phase error one has the possibility of varying the resulting phase error, equally distributed in a limited region, about the nominal phase, as sketched in fig. 8b. Here we shall show the resulting rest effects (Ries, G., Söntgerath, W., 1970). The respective phase control should be a random choice, so that the phase errors of all elements are mutually independent and, with frequent repetition equally distributed - region ($\Delta = 2\pi/2^b$) - about the nominal phase. The array factor of the array above with such a phase shape is also shown in fig. 9.

For a large number of statistically chosen phases of an array the Central Limit Theorem guarantees a bivariate normal distribution of the array factor. The average array factor equals the array factor in case of the nominal phase M_0 , with the exception of a constant factor

$$\bar{M} = \overline{\cos \delta_p} \cdot M_0 \quad (21)$$

The variances of the real and imaginary parts of the array factor are approximately equal to

$$\sigma_r^2 \approx \sigma_i^2 = \sigma_N^2 = \frac{\pi^2}{6} \frac{1}{2^{2b}} \frac{1}{N} \quad (22)$$

whereas the covariance can be neglected, so that a Rice-distribution results. In the interesting case of sidelobe peaks $|M| \gg \sigma_N$ approximately a one dimensional normal distribution results:

$$p(|M|) = \frac{1}{\sqrt{2\pi} \sigma_N} e^{-\frac{(|M| - \overline{|M|})^2}{2\sigma_N^2}} \quad (23)$$

The standardized distribution function according to (23) is shown in fig. 10. Also shown is the respective frequency distribution. Ad hoc the array factor of a thinned array has been calculated in one direction with 400 different statistically distributed phase errors. The theoretical mean value from (21) was 0.3690 and 0.3711 from 400 trials.

Because of the already high sidelobes the phase shifter digitizing effects together with a statistical additional phase are very small. This is different in case of filled arrays. In spite of an extremely high sidelobe attenuation in case of nominal phase, the average attenuation of these statistically distributed sidelobes caused by quantization amounts only to the double of the variance according to (22), i.e. near 43 dB for an array with 1000 elements and 3-bit phase shifters. This effect should always be taken into account to avoid a too negative judgement on thinned arrays because of their high sidelobes. For the array above the average sidelobe attenuation is, according to (8b), 30 dB.

The influence of the investigated phase behaviour on the main beam, results in a directivity reduction and a beam pointing error (Ries, G., 1970). This effect is small and has not been dealt with in this paper.

6. REFERENCES

- Andreasen, M.G., 1962, "Linear arrays with variable interelement spacing", Transact. IRE AP-10, 137-143.
- Baklanov, Y.V., Pokrovskiy, V.L., Surdutovich, G.I., 1962, "A theory of linear antennas with unequal spacing", Radio Engineering and Electronic Physics 7, 905-913.
- Cheston, T.C., Frank, J., 1968, "Array Antennas", Techn. Memo T6-958 Jo Hopkins Univ. Silver Springs.
- Hansen, R.C., 1966, "Microwave scanning antennas II", Academic Press, New York.
- Lo, Y.T., 1964, "A mathematical theory of antenna arrays with randomly spaced elements", IEEE Transact. AP-12, 257-268.
- Lo, Y.T., 1968, "Random periodic array", Radio Science 3, 425-436.
- Mattsson, E., 1971, "Designing thinned phased arrays", European Microwave Conference, Stockholm.
- Miller, C.J., 1964, "Minimizing the effects of phase quantization errors in an electronically scanned array", Symp. on electr. scanned array techniques and application, Rome, RADC-TDR-64-225-1.
- Ries, G., Söntgerath, W., 1970, "Einflüsse von Quantisierungsphasenfehlern auf die Strahlungscharakteristik ebener Antennengruppen", FHP-Forschungsbericht Nr. 4-70.
- Ries, G., Söntgerath, W., 1972, "Gruppenfaktor von statistisch verdünnten Antennen mit vergrößertem Elementmindestabstand", AEU Band 26, 542-550.
- Ries, G., Söntgerath, W., 1973, "Signalenergie aus Nebenzipfelrichtungen bei verdünnten Antennengruppen", FHP-Arbeitsbericht 1973.
- Skolnik, M.I., Neuhauser, G., Sherman III, J.W., 1964a, "Dynamic programming applied to unequally spaced arrays", Transact. IEEE AP-12, 35-43.
- Skolnik, M.I., Sherman III, J.W., Ogg, F.C., 1964b, "Statistically designed density-tapered arrays", Transact. IEEE AP-12, 408-417.
- Willey, R.W., 1962, "Space tapering of linear and planar arrays", Transact. IRE AP-10, 369-377.

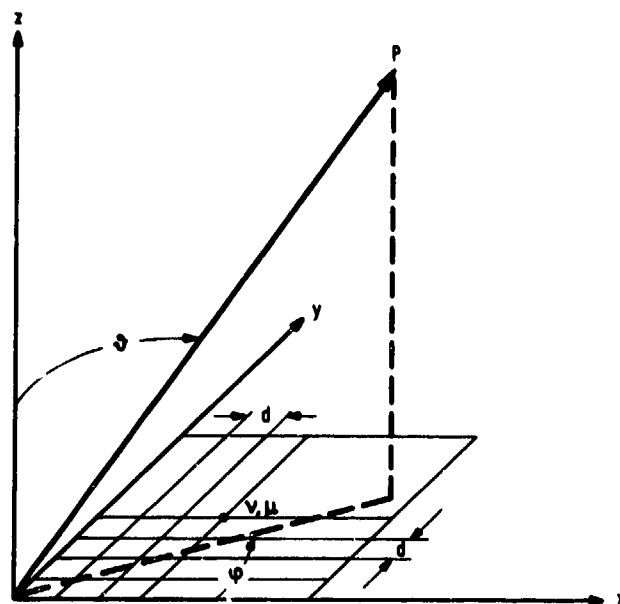


Fig.1 Coordinate system

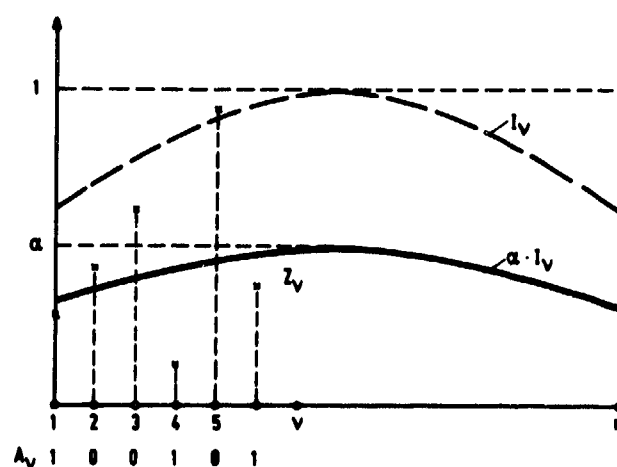


Fig.2 Element distribution of a linear array

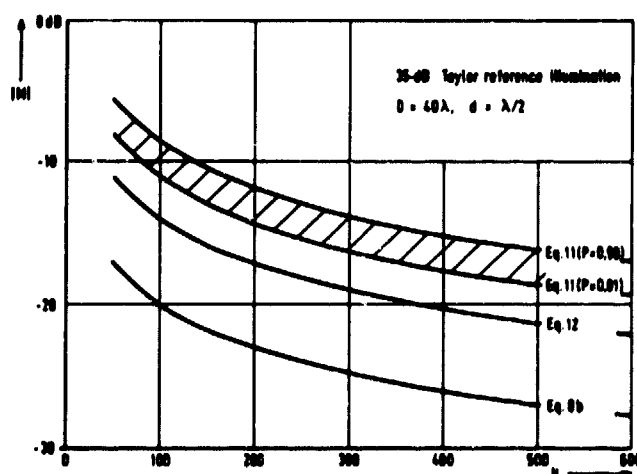


Fig.3 Average and minimum sidelobe attenuation of planar circular arrays

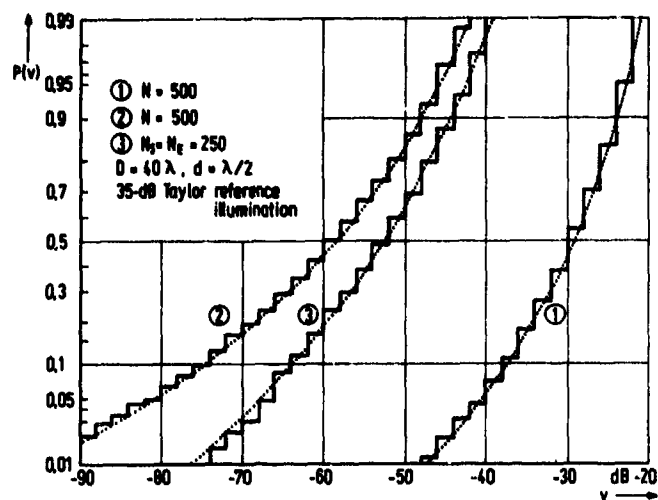


Fig.4 Distribution functions and frequency distribution of the signal energy from sidelobe directions

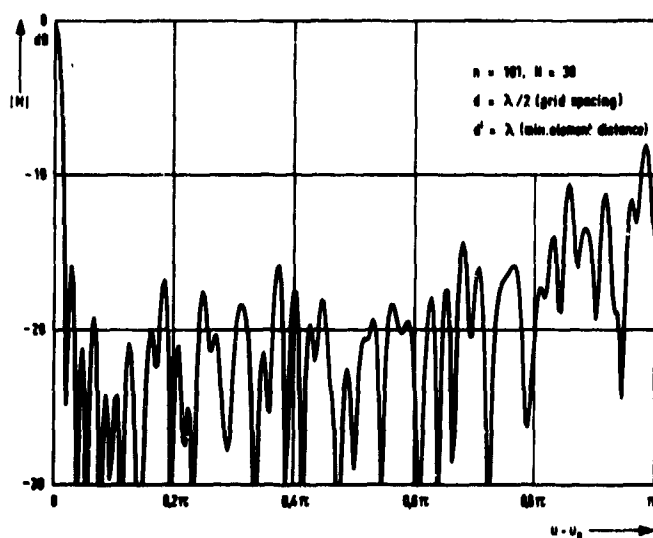


Fig.5 Array factor of a linear array with enlarged element distance

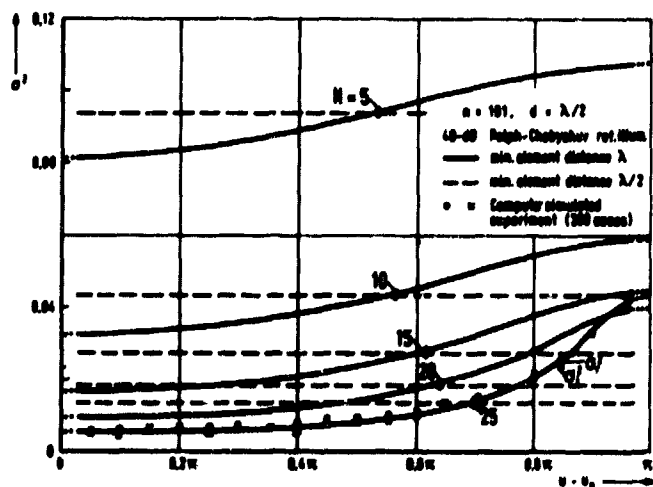


Fig.6 Variance of the sidelobe level of linear arrays with enlarged element distance

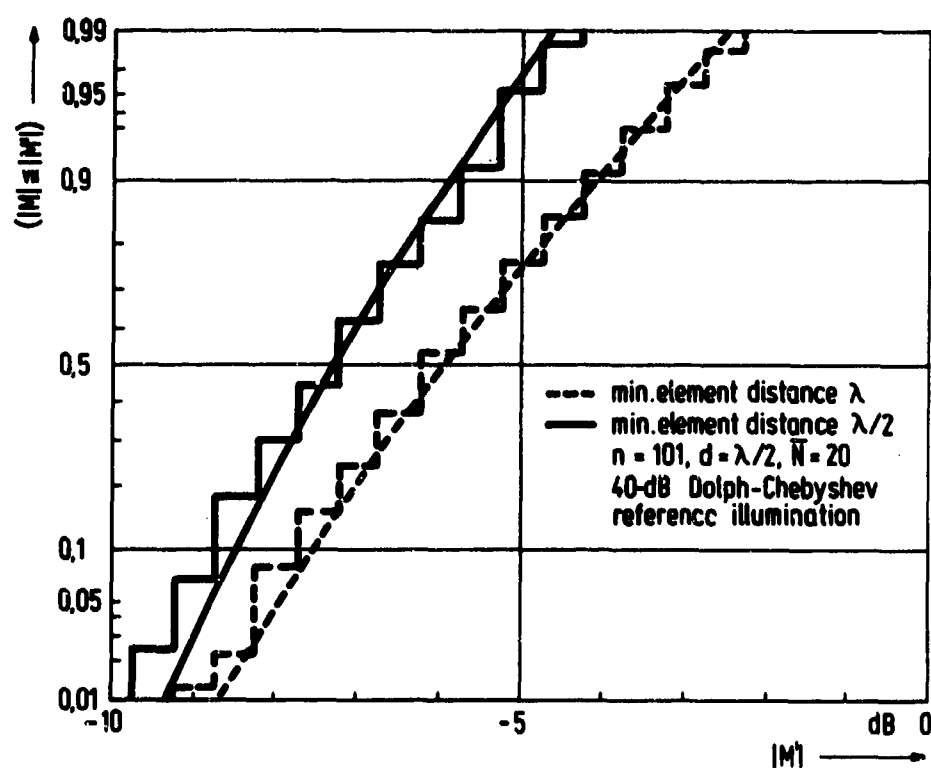


Fig.7 Distribution function and frequency distribution of the minimum sidelobe attenuation of linear arrays (Rayleigh distribution)

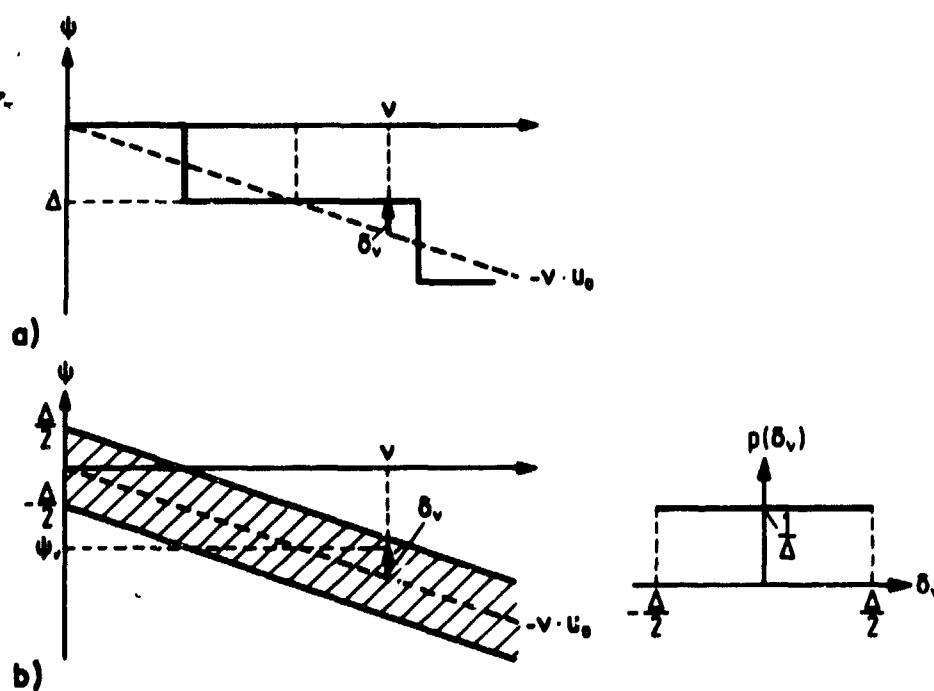


Fig.8 Periodic (a) and irregular (b) phase errors

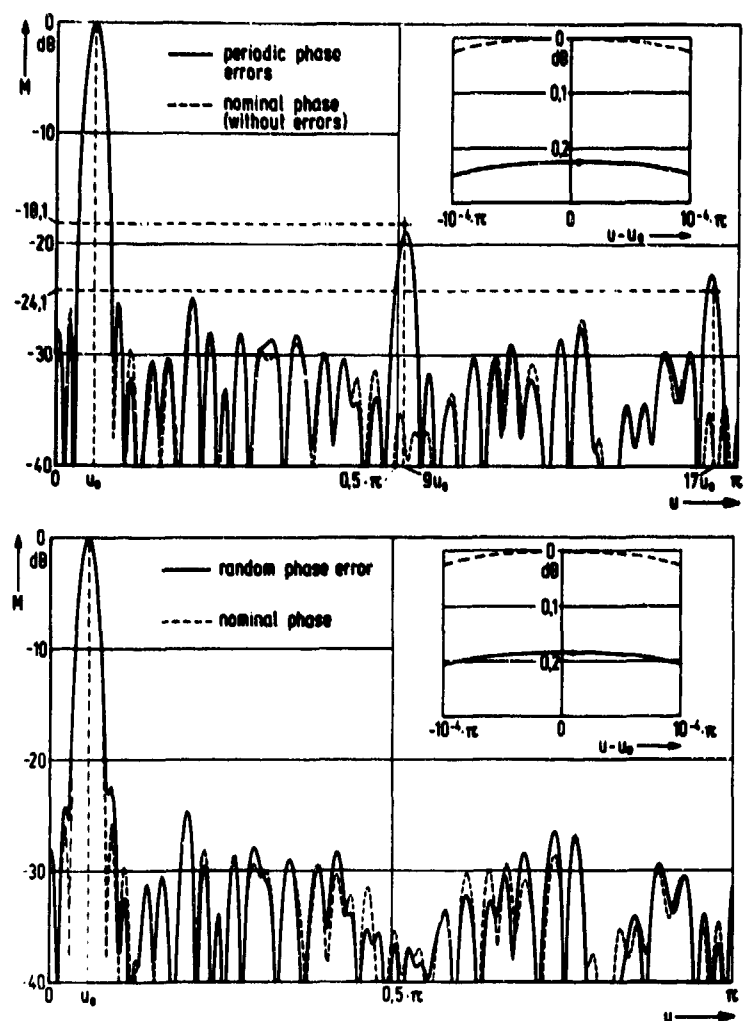


Fig.9 Array factor in the plane $\varphi = 0$ with (a) periodic phase errors (Fig.8(a) and (b) irregular phase errors (Fig.8(b)). Array lengths projected on the X-axis: 50λ , $N = 644$ random distributed elements.)

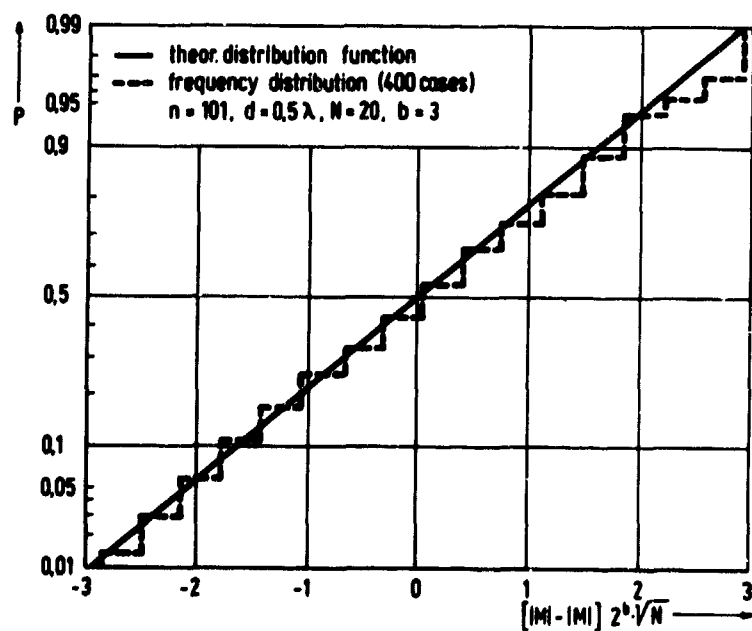


Fig.10 Distribution function and frequency distribution of the difference between the sidelobe level and its mean value (Normal distribution)

IN-FLIGHT MEASUREMENT OF AIRCRAFT ANTENNAE RADIATION PATTERNS

by

Helmut Bothe

Deutsche Forschungs- und Versuchsanstalt für Luft- und Raumfahrt e.V. (DFVLR)
 Institut für Flugführung
 33 Braunschweig, Flughafen
 Germany

SUMMARY

Building antennas into an aircraft is frequently optimized by electromagnetic modeling. Nevertheless official registration will depend on proving a certain coverage by in-flight measurements of radiation patterns from the actual aircraft. Moreover if additional antennas have to be attached to an aircraft later on, in-flight radiation measurements might be a more economical solution.

This paper deals with an in-flight measuring system which is completely independent from ground-based position finding equipment like radar and kine theodolites. The measuring method is based on VOR (Very High Frequency Omnidirectional Range System) and DME (Distance Measuring Equipment) information obtained on board the aircraft. This information is telemetered together with the other necessary parameters like heading, altitude, pitch and roll angles. These parameters are used to calculate the aspect angle and the distance of the aircraft from the ground based field intensity measuring device.

Real time calculation is done on a digital computer. The computer output supplies aspect angle and distance corrected field intensity as well as flight-path parameters in analog voltages for graphic presentation.

After a detailed description of the measuring method and system some examples of measured patterns are shown. In addition the magnitude of possible errors in the plotted radiation patterns are discussed.

INTRODUCTION

Antenna radiation patterns are normally measured in a test range, where the antenna under test can be rotated in two planes simultaneously. Thus a coverage of the whole sphere is achieved. Attached to an aircraft movements of the antenna are restricted to possible maneuvers of the aircraft. Horizontal patterns can be caught by flying the aircraft on a horizontal circle. If the circle is flown with different angles of roll, radiation patterns in the corresponding inclined planes through the aircraft's roll axis are caught. If the antenna under test is acting as a transmitter, a receiving antenna has to be located in the plane of the circle flown. In flat country this requirement cannot exactly be met with a ground based receiving antenna. But a distance of 40 km between flight path and receiver results in a deviation of only a few degrees. Vertical patterns are achieved by flying across the receiving antenna. These patterns are normally restricted to a range of 180° (below the fuselage of the aircraft) and may be slightly extended by the maximum allowable in-flight angle of pitch of the aircraft.

As will be shown later on, the locating of the aircraft must permanently be known during radiation pattern recording. VOR/DME is a well known position finding system installed in almost every well-equipped civil aircraft. On board the aircraft this system measures the angle θ between the north direction and the line aircraft-VORTAC station (TAC for TACTical air navigation system, the distance measuring part of which is used) as well as the distance ρ from aircraft to station (Figure 1). This equipment has been chosen because an available radar set did not suffice in range and the VOR/DME equipment is much less sophisticated.

In the VOR part of this navigation system angle information is obtained by amplitude modulating a VHF carrier (108 - 118 MHz) with a 30 Hz signal. The phase of this signal depends on the azimuth angle θ . Reference phase is transmitted by an additional 10 kHz subcarrier, which is frequency modulated by 30 Hz. In the DME part the distance from aircraft to VORTAC-station is measured by the travel time of 3.5 μ s double pulses with a pulse distance of 12 μ s modulating a UHF carrier in the 962 to 1213 MHz band. The responding frequency has a 64 MHz offset (Reference [1]).

HORIZONTAL PATTERN ANGLE OF ASPECT

The horizontal radiation pattern of an aircraft antenna is the radiation intensity versus the angle of aspect ϕ in Figure 1. ϕ is the angle between the axis of roll of the aircraft and the axis of sight d , if the radiation intensity is measured at test point M. Several other parameters denoted in Figure 1 are needed to determine ϕ . The angle of heading ψ oriented to north is normally derived from a gyro system on board the aircraft. The angle θ is delivered by the VOR equipment. Determining the distance e from test point M and VORTAC station as well as angle α is a problem of geodesy if the geographical coordinates of point M and the VORTAC station are known. The distance d between aircraft and test point M results from application of cosine law to Figure 1

$$(1) \quad d^2 = \rho^2 + e^2 - 2\rho e \cos(\alpha - \theta)$$

The angle γ can be derived by applying sine law to Figure 1

$$(2) \quad \gamma = \arcsin \left[(\sin(\alpha - \theta))e/d \right]$$

Now the angle of aspect ϕ is determined by the following relationship

$$(3) \quad \phi = 180^\circ - (\gamma - \theta) - \psi$$

As has been shown in Reference [2] this angle of aspect must be corrected if the angle of roll of the aircraft exceeds certain limits. The reason is that the angle of aspect must be determined in an aircraft oriented co-ordinate system while angles of heading and VOR are expressed in a ground based co-ordinate system. If ϕ is computed by Eq (3) and the angle of roll is denoted by φ the corrected angle of aspect is

$$(4) \quad \phi_c = \arccos \left((\cos \phi) / \sqrt{1 - (\sin \varphi \sin \phi)^2} \right)$$

Up to an angle φ of 20° the angle of aspect is in error by less than 2° . With larger angles of roll correction becomes inevitable as is shown by Figure 2.

Due to the altitude h of the aircraft the distances ρ and d in Figure 1 are slant ranges. This must be taken into account in Eq (1) and (2) for values of ρ and $d \leq h^2/0.2$ km if the maximum error is to be ≤ 0.1 km.

The flight path in Figure 1 need not be a circle. Any flight path with constant altitude is possible. The only condition is that the aircraft must fly a complete 360° turn.

VERTICAL PATTERN ANGLE OF ASPECT

The vertical radiation pattern of an aircraft antenna is the radiation intensity versus the angle of aspect θ measured between the axis of roll and the axis of sight d with respect to test point M in Figure 3. Again some more parameters are needed for computing θ . The angle of pitch δ is measured between the axis of roll and a horizontal line and is derived on board the aircraft from a vertical gyro.

The altitude h is computed from static pressure p_s , which is also measured on board the aircraft. Denoting static ground pressure by p_0 and the absolute ground temperature by T_0 h becomes (Reference [3])

$$(5) \quad h = \frac{1}{6.5} T_0 \left\{ 1 - \left(\frac{p_s}{p_0} \right)^{0.1903} \right\} \text{ km}$$

The distances ρ and e have already been mentioned in the horizontal pattern description. The distance a in Figure 3 is given by

$$(6) \quad a = \sqrt{\rho^2 - h^2} - e$$

and the angle ζ becomes

$$(7) \quad \zeta = \arctan (a/h)$$

Now the aspect angle θ is simply

$$(8) \quad \theta = 90^\circ + \delta - \zeta$$

The distance d between aircraft and test point M is also needed for correction of field intensity

$$(10) \quad d = \sqrt{h^2 + a^2}$$

MEASUREMENT OF FIELD INTENSITY

The field intensity measured at point M in Figures 1 and 3 depends on the transmitter power on board the aircraft, the aircraft antenna radiation pattern, the distance d , the ground reflections, the radiation pattern of the field-intensity test antenna and the polarization efficiency of the link. The radiation pattern of the aircraft antenna is the only desired parameter. All other parameters have to be made ineffective or compensated.

The transmitter power on board the aircraft can be kept constant by a stabilized power supply.

Variations in distance d are corrected by the link attenuation factor D

$$(11) \quad D = 20 \log \left(\frac{d}{\text{km}} \right)$$

For recording of horizontal patterns in the VHF range ground reflections are taken into account by operating the test antenna in the "ground reflection" mode (Reference [4]). This means, that the radiation pattern of the test antenna mounted a small distance above ground consists of a series of lobes in the vertical plane due to interferences between the direct ray and ground reflected rays. The antenna height above ground must be adjusted so that nulls are avoided in the area of the elevation angle in question. In the UHF range the directivity of the test antennas can easily be increased avoiding interfering reflections. For the measurement of vertical patterns steerable antennas with high directivity are preferred because the elevation angle has to cover a range of nearly 180° without nulls. Another approach mainly applied to low frequencies is a dipole close to the reflecting ground. In this case the received signal has

to be corrected by the radiation pattern of the receiving antenna.

Aircraft antennas are normally polarized vertically or horizontally. Variations in angle of roll of the aircraft will cause variations in polarization angle at the receiving station. If a linearly polarized receiving antenna is used, the correction factor k in received power depends on angle of roll φ and corrected angle of aspect ϕ_c (Reference [2])

$$(12) \quad k = \cos^2 \varphi + (\sin \phi_c \sin \varphi)^2$$

A more convenient method is to use a circularly polarized ground antenna. No correction is needed if exact circular polarization can be achieved. The short helical antenna shown in Figure 4 achieves an axial ratio of 1 if a conducting disc is arranged at the free end of the helix. Without disc the axial ratio of this antenna falls below 0.6. A more detailed description is given in Reference [5].

INSTALLATION OF THE MEASURING SYSTEM

With one exception all parameters in this system are obtained on board the aircraft. To process this information on ground and to synchronize the on-board derived data with the ground-measured field intensity a telemetry system must be used. Normally the required accuracy of less than 1 % error in some channels would have led to a PCM system. On the other hand much cost could be saved using an available IRIG telemetry system (Reference [6]) with proportional-bandwidth FM subcarrier channels. The accuracy problem has been solved by splitting up signals with allowable errors below 1 % into a coarse and a fine component. A disadvantage of the coarse-fine transmission is the large required bandwidth due to the steps occurring in the coarse and fine channel simultaneously, when the fine channel falls from maximum deflection to zero or vice versa.

The complete airborne system is shown in Figure 5. It consists of the necessary transducers and transducer systems, the coarse-fine splitting and signal-conditioning circuits matching the transducer outputs (potentiometers for pitch, roll and altitude, voltages for DME and synchros for heading and VOR) to the inputs of the voltage controlled frequency modulated subcarrier oscillators (VCO). The VCO outputs are now mixed and the composite signal frequency modulates the telemetry transmitter. Transmission is possible in the VHF and UHF telemetry bands. Small airborne transmitters exciting the antennas under test in question have been built. They are covering the frequency ranges of currently installed radio aids in civil and military aircraft.

Though the whole airborne system including VOR and DME is constructed as a black box (Size 0.3 m^3 , weight 75 kg, power consumption 300 VA) the aircraft's VOR and DME antennas are needed and a telemetry antenna must be installed. If the radiation pattern of the VOR antenna itself has to be measured, this antenna can be excited via duplex equipment at the same time. Moreover this duplexer operates the VOR system in the cockpit of the aircraft if the VOR antenna is not excited. During pattern recording of the DME antenna the DME equipment can be switched to the secondary radar transponder, which has to be turned off. During the measurement of radiation patterns the aircraft's own DME equipment is inoperable if it is equipped with only one DME antenna.

In the ground station (Figure 6) the received telemetry signal is heterodyned down to a low intermediate frequency, that can be directly recorded on magnetic tape (predetection recording) parallel with the field-intensity signal. So all information is stored even if the equipment fails in the subsequent part of the system. After demodulation of the radio frequency carrier the individual subcarriers in the composite signal are separated and demodulated by the subcarrier discriminators. The outputs of the discriminators as well as the output of the field-intensity meter are sampled by a commutator and digitized by a PAM to PCM converter 10 times per second each. The composite subcarrier signal, the PAM pulse train at the commutator output and the field-intensity signal are recorded on a second magnetic tape recorder (postdetection recording) for reproduction purposes of the measurement results.

All digitized data is transferred to a computer. First of all the coarse-fine channels are recombined. Then the horizontal angle of aspect ϕ is computed 30 times per second according to Eq (1), (2) and (3) or the vertical angle of aspect θ according to Eq (5), (6), (7) and (8). Furthermore the above mentioned corrections are made in accordance with Eq (4), (10) and (11). Limit exceedances for instance in angle of roll or pitch, are checked and printed out. Finally flight-path and radiation-pattern information which are present in polar co-ordinates are transformed to Cartesian co-ordinates by the computer. After digital to analog conversion real time recording of radiation pattern and flight path is done by two analog x-y-recorders. Each x- and y-output parameter is calculated 30 times per second.

ERRORS OF THE SYSTEM

The measured radiation intensity is normalized to its maximum value. Recording of one pattern will last only a short period of time. Therefore the gain stability of the field intensity measuring device including exciter transmitter is not critical. The main errors are caused by the amplitude characteristic of the logarithmic amplifier, which is specified to $\pm 1.5 \text{ dB}$ error over a full range of 70 dB.

In horizontal pattern recording angle of aspect errors are caused by different influences. Errors in angle of heading ψ will fully enter into the aspect angle ϕ . They can be kept below 1° if an airline quality gyro is used. VOR/DME errors in the order of $\pm 3^\circ$ or 0.2 km enter into the aspect angle to a degree, which depends on the position of the aircraft compared to the VORTAC station in question and to the measuring point M in Figure 1. Optimum conditions are achieved, if the points M, VORTAC and aircraft position in Figure 1 are shaping a right triangle with the right angle at the aircraft's position. Then a very small DME error of only 0.3° (at $d = 40 \text{ km}$) enters into the angle of aspect. Under this condition the VOR error primarily enters into distance d only with a value $\leq \pm 1.5 \text{ km}$ if $\rho \leq 30 \text{ km}$. Under these circumstances the error in distance correction of field intensity remains $\leq 0.3 \text{ dB}$.

When vertical patterns are recorded the error in angle of pitch fully enters into the angle of aspect θ . It is caused by the vertical gyro and can be kept well below 1° . Errors in altitude h and distance ρ measured by DME are more severe. After Figure 7 the error in angle of aspect depends on θ and becomes at most 1.2° , if an altitude of 6 km is measured with an error of 0.2 km, which is realistic. Under the same altitude condition a maximum error of $\Delta\theta = 2^\circ$ results from a DME error of $\Delta\rho = 0.2$ km (Figure 8). Fortunately the maximum errors caused by inaccurate altitude and distance measurements do not occur at the same angle θ .

MEASUREMENT RESULTS

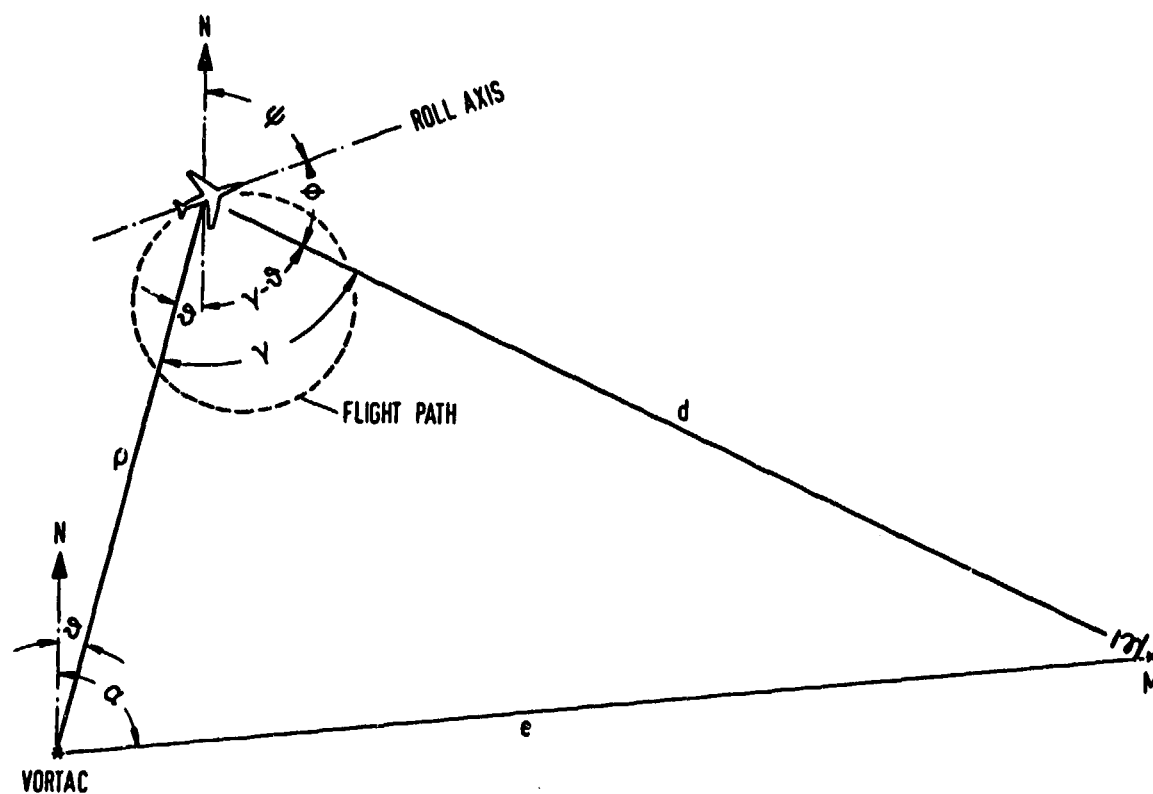
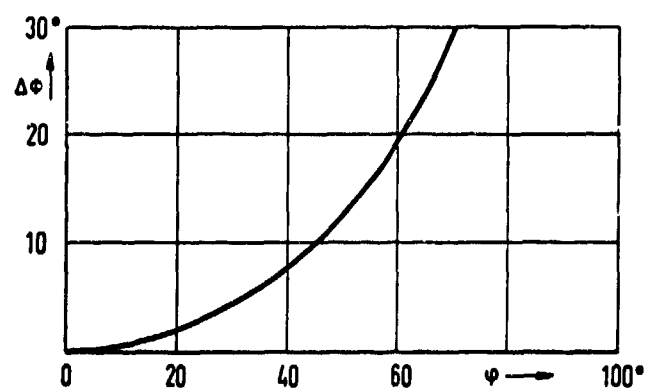
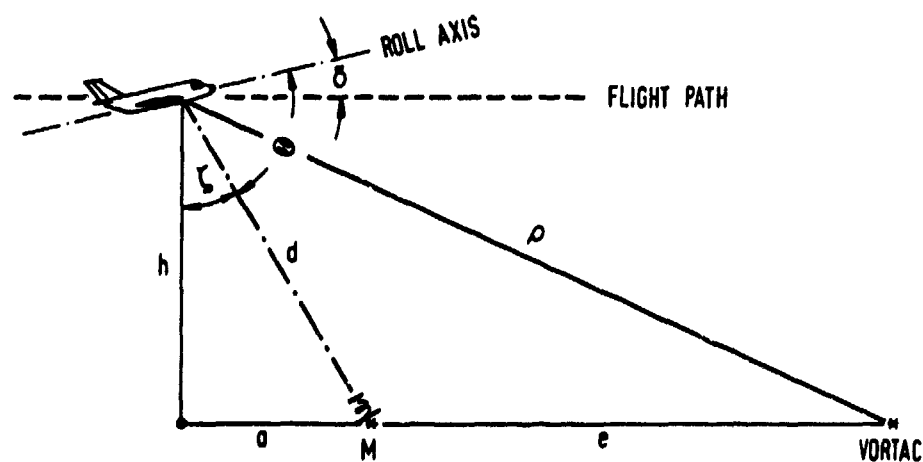
In Figure 9 the measured horizontal radiation pattern of a UHF telemetry antenna is shown, consisting of a one-quarter wavelength rod attached to the lower side of the fuselage of a small aircraft (Piaggio P 149 D). The exciting frequency has been 1.475 GHz. Variations in radiation intensity over a range of 10 dB can be observed. In Figure 10 the pattern of the same antenna is given measured during a left turn of the aircraft with a roll angle of 20° . In this case the variations in radiation pattern are up to 30 dB, mainly caused by reflexions from the aircraft's wings.

REFERENCES

- [1] BRANDT, L., "Funkortungssysteme für Luft- und Seefahrt", Dortmund: Verkehrs- und Wirtschaftsverlag, 1962.
- [2] MATTES, H., HINZPETER, U., "Ermittlung der Strahlungscharakteristiken von Flugzeugbordantennen im Fluge", Nachrichtentechnische Fachberichte Band 45, S. 180 - 185, Berlin: VDE-Verlag, 1972.
- [3] DIN 5450 (May 1937)
- [4] FORD, E.T., "The Antenna Test Range at ESTEC", Technical note TN 97 (ESTEC), Neuilly (France): ESRO, 1969.
- [5] BOTHE, H., "Kurze Wendelantennen mit exakt zirkularem Polarisationsverhalten durch eine Leitscheibe am Wendelende", DLR-FB 73-46, Porz-Wahn: DFVLR, 1973.
- [6] "Telemetry Standards Document 106-71, Appendix A" in Proceedings of the 1971 International Telemetry Conference, Instrument Society of America (ISA).

ACKNOWLEDGEMENT

The author wishes to acknowledge the assistance of W. Benecke, B. Bieger, H. Keese and P. Schulz during the development of this system.

Figure 1: Determination of horizontal angle of aspect ϕ Figure 2: Error $\Delta\phi$ in angle of aspect caused by angle of roll ψ Figure 3: Determination of vertical angle of aspect θ

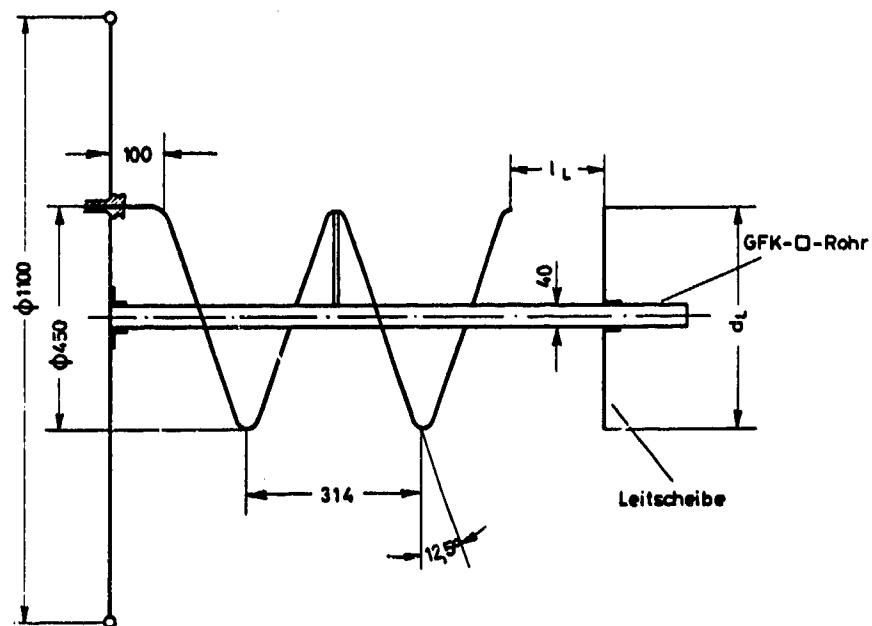


Figure 4: Circularly polarized receiving antenna

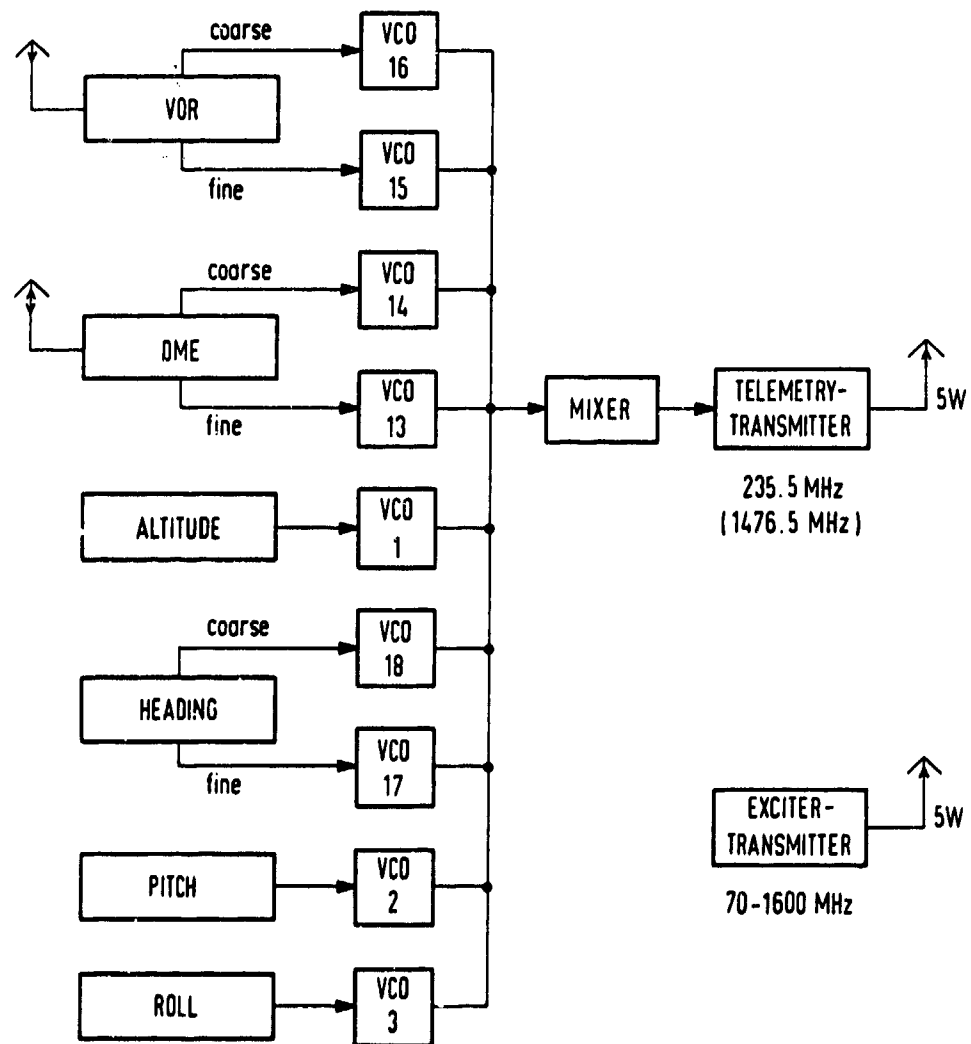


Figure 5: Airborne part of the measuring system (VCO numbers indicating IRIG-subcarrier channel numbers)

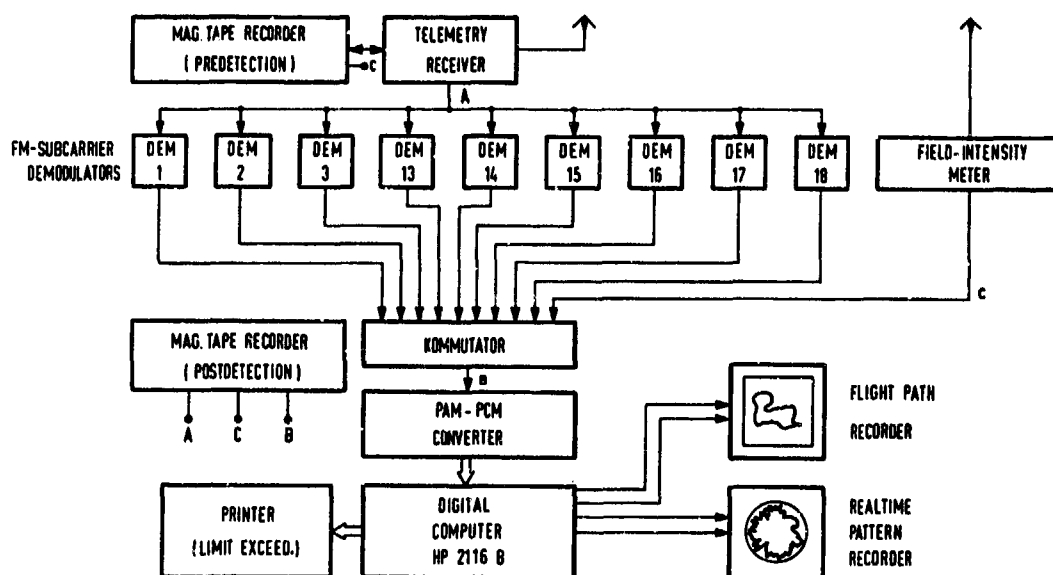


Figure 6: Ground part of the measuring system

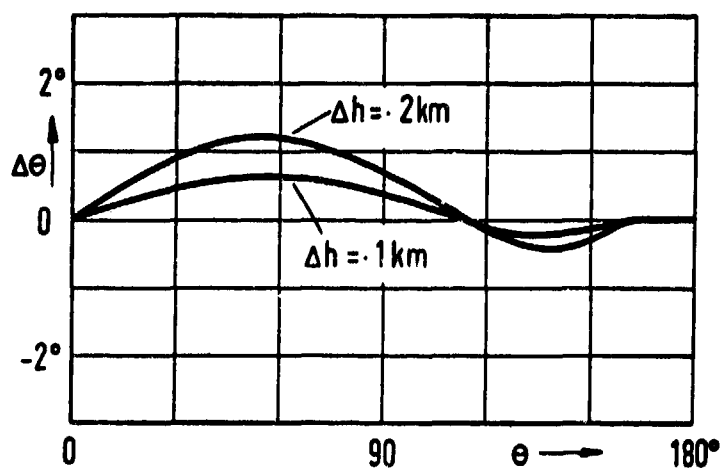


Figure 7: Error $\Delta\theta$ in vertical angle of aspect θ due to altitude errors Δh
 $h = 6 \text{ km}$ $e = 16,67 \text{ km}$

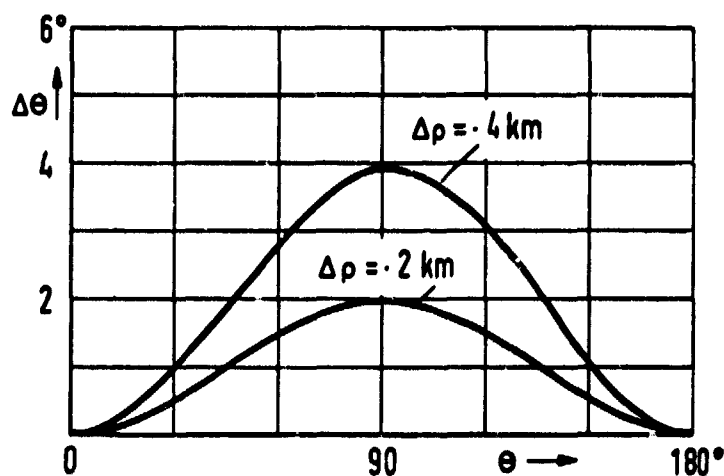


Figure 8: Error $\Delta\theta$ in vertical angle of aspect θ due to DME errors $\Delta\rho$
 $h = 6 \text{ km}$ $e = 16,67 \text{ km}$

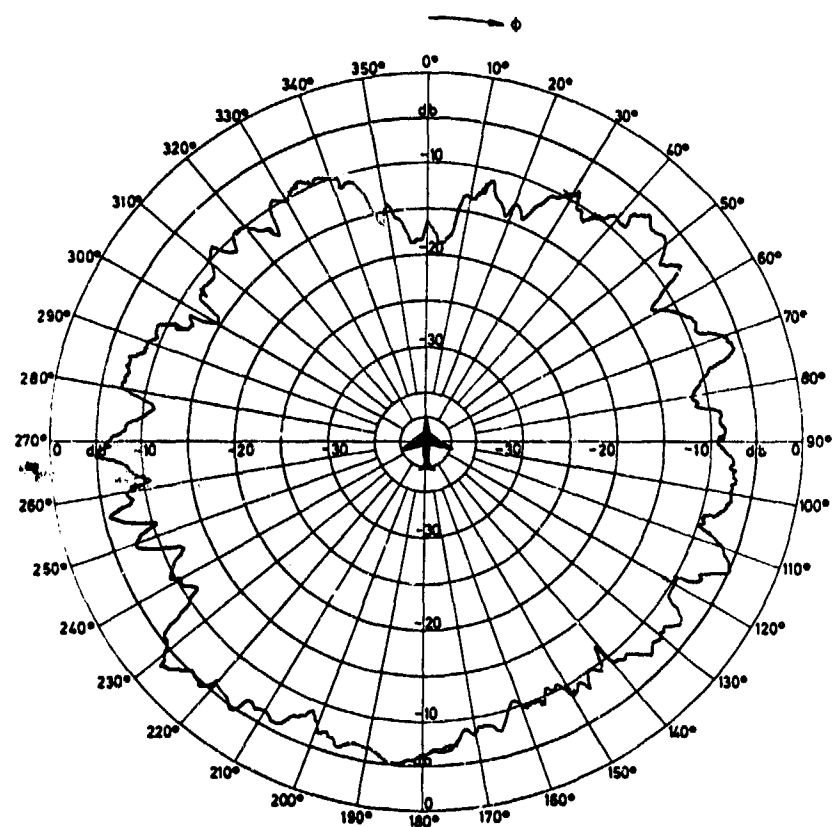


Figure 9: Horizontal radiation pattern of a UHF-telemetry antenna
angle of roll $\phi = 0^\circ$

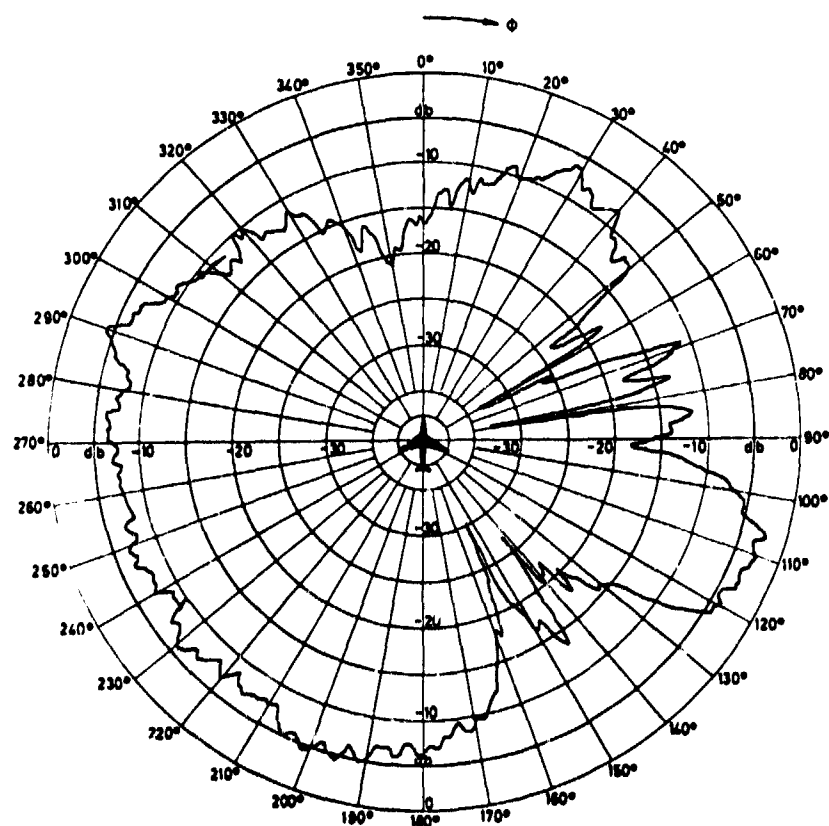


Figure 10: Horizontal radiation pattern of a UHF-telemetry antenna
angle of roll $\phi = 20^\circ$

DISCUSSION

R.H.J. CARY: I notice in Fig. 9 a 10dB difference in one side and the other at some angles. I comment that apparent differences are often unpredicted and difficult to explain. How do you ascertain the gain or efficiency of the antenna. Do you solve this using the propagation equation?

H. BOTHE: In this case these differences can be caused by an asymmetrical mounting of the L-Band telemetry antenna under test to the lower side of the fuselage. Besides that, some other antennas near the antenna under test probably influence the radiation pattern. The gain or efficiency is not measured. We only measure the relative radiation characteristics.

DYNAMIC MEASUREMENT OF AVIONIC ANTENNAS

I.D. OLIN
E. E. Maine, Jr.
U.S. Naval Research Laboratory
Washington, D.C., 20375, USA

SUMMARY

The equipment, data handling, flight control and some of the results obtained with a system specifically designed for dynamic measurements is described. The determination of aircraft aspect angle uses an approach based on measurements made at the ground radar site with the aircraft flying straight-line courses. Then making certain assumptions regarding flight attitude, a proper coordinate transformation can be effected and principal plane measurements plotted. The antenna signal source is provided by a delayed beacon triggered by an illuminating radar and driving the antenna under tests. To illustrate the results patterns for a X-band installation are shown. Coverage can be provided for an azimuth profile from nose-on (0°) to tail-on (180°) and for an elevation profile beam 0° to 30° below the aircraft for fixed azimuth aspects of nose-on and tail-on. Angle accuracy is ± 2 degrees and the accuracy of antenna gain measurements is estimated to be ± 2 dB.

1. INTRODUCTION

Techniques for the measurement of antenna characteristics are well known but often the results describe an idealized performance, especially with regard to the installation environment. In the case of avionic antennas factors such as ground planes, coupling with other antennas and blockage by the aircraft structure itself all introduce variations to the original design performance. Measurements of antenna characteristics in situ has been described elsewhere, (SCHEMITT, O.H., 1947; SINCLAIR, G., 1947), but has involved large scale model ranges in connection with missile vehicles or only effectively modeled portions of the aircraft structure. Dynamic measurement of in-flight aircraft, although offering a means to include all the appropriate environmental effects, has not been widely used, probably because of the somewhat inflexible angular coverage, difficulties in defining the measurement angles and in maintaining suitable calibration. Nonetheless, dynamic measurements properly executed can provide the final confirmation of antenna performance and are, therefore, an important adjunct to the conventional measurement procedures used in design.

Since 1963 the U.S. Naval Research Laboratory has operated a dynamic measurement facility utilizing radar equipment and procedures of original design. Initially intended for measurement of radar cross section (RCS) of in-flight aircraft, subsequent changes and additions have extended this capability to provide simultaneous measurement of both RCS and avionic antenna patterns. In this paper the techniques and approaches which are currently being used will be presented and some illustrations of the results shown. Generally the work involves four main areas of concern: (1) multi-band radar equipment of wide dynamic range and good stability, (2) antenna signal sources and calibration for both the test antenna and the radar equipment, (3) control and determination of aircraft aspect angles, (4) efficient data handling.

2. EQUIPMENT

Equipment includes the antennas, transmitters, receivers and data recorders required to measure antenna patterns as well as RCS. Measurements can be conducted in four bands: L, S, C, X corresponding to 22 cm, 10 cm, 5 cm and 3 cm ranges, respectively. In the case of RCS, measurements are generally conducted in all bands simultaneously. When antenna pattern measurements are made these have been confined to one of the bands using an aircraft installed beacon driving the antenna and following a fixed delay period triggered by the illuminating radar beam. Under these conditions RCS and pattern measurements can be performed together.

The approach followed in the ground system design was to use conventional pulsed magnetron transmitters driving polarization flexible antennas together with receivers of high stability and wide dynamic range. Data recording of the several channels is by means of digital magnetic tape which is subsequently reformatted for computer processing. In determining aircraft aspect angle, an approach based on in-flight recording of aircraft attitude was rejected due to cost and installation time in favor of measurements made at the ground site with the aircraft flying straight-line courses.

A photograph of the ground site is shown in Fig. 1 with the principal components noted. Table I indicates some of the basic system characteristics. The current system, installed at the Chesapeake Bay Division of NRL, represents considerable improvement over the one described earlier, (OLIN, I.D., 1965). In operation all transmitters are pulsed simultaneously with the L-and S-band system using coaxial feeds operating into a single eight-foot diameter reflector and the C-and X-band systems using separate 48-and 32-inch diameter reflectors. Polarization of the L-S band antenna is changed by physically rotating the feed through 90 degrees. At C-and X-bands the transmitted polarization is changed by switching the excited port of a dual-mode transducer and by rotating a quarter-wave plate, depending upon the required component. During operation the single pedestal supporting all the antennas is servo-slaved to the optical handstand. As an aid in acquisition, however, the operator can use an X-band monopulse receiver which displays error signals on a meter of the handstand. The receiver is mounted between the C-and X-band reflectors and uses a four-horn cluster polarized at 45° so that, regardless of transmitter polarization, a useable signal is received.

TABLE I
SYSTEM CHARACTERISTICS

Band	L	S	C	X
Frequency, Mhz	1300	2800	5500	9225
Peak Radiated Power, kW	250	250	250	250
Pulse Width, μ sec	1	1	1	1
Pulse Rate, Hz	500	500	500	500
Beamwidth, (E&H plane) deg	7.5 x 6	3.5 x 3	3 x 3	3 x 3
Antenna Gain, dB	28	33	34	34
Transmitted polarisation	H, V	H, V	RC, LC, H, V	RC, LC, H, V
Received Polarization	same as transmitted		simultaneous reception of parallel and orthogonal components	

H - horizontal
V - vertical
RC - right circular
LC - left circular

The L- and S-band systems are similar and a block diagram is shown in Fig. 2. With the 3-dB hybrid duplexer half the power is radiated, half is absorbed in a load, and a receiver port is provided with about 30-dB isolation. This degree of isolation permits the transmit-receiver (T.R.) tube used for mixer crystal protection to deionise rapidly, thus allowing the close-in target tracking required for the optical tracker. Data can be taken within the interval of 2000 to 20,000 yd. The receiver system uses no automatic gain control in the usual sense and operates with a linear instantaneous dynamic range of 40 dB. Since RCS measurements are performed as well as recording aircraft antenna patterns, much more dynamic range is needed for most targets. For this purpose an automatically operated switched attenuator system is employed. As shown in Fig. 2 a series of fixed attenuators is controlled by the video output level to produce an additional 65 dB range. Two isolator-matched 20-dB steps are used at r-f to prevent mixer saturation effects with the remaining 25 dB at i-f before the amplifier. With the total 105 dB range provided, all antenna and most RCS measurements can be accommodated over the 10:1 range interval. Local oscillator power is supplied by fixed oscillators rather than a klystron using afc, since normal frequency excursions operating with a limited receiver pass-band can produce undesirable pulse-to-pulse amplitude fluctuations. Some drift is inevitable however, and since it was desired to reproduce the transmitted pulse shape, the overall receiver pass-band is flat within $\pm 1/2$ dB over 5 MHz centered at 30 MHz. A block diagram of the microwave portion of the C- or X-band system is shown in Fig. 3. T.R. tube recovery time problems do not occur and a conventional duplexer is used. The i-f sections are identical for all bands.

Target range gating is provided by a conventional early-late gate tracker which can be connected to any of the receiver outputs. Ranging enables a 5 μ sec wide i-f gate in each receiver. Thus, assuming only the target of interest is present, range jitter effects are eliminated from the data by the use of a peak detection circuit. When antenna pattern measurements are made a separate i-f and recording channel with a second 5 μ sec gate delayed 10 μ sec from the reflected signal gate is used.

Fig. 4 shows a photograph of one of the beacon assemblies for aircraft installation. These have been built for operation in S-, C- or X-bands and typically use a 400 W peak rated tunable magnetron as the transmitter. The assembly consists of a commercial transponder, power supply and control box. Operation at 28V or 115V a-c is provided. Signal output is adjusted by varying the attenuator pad in the output line prior to flight. A variety of keying frequencies have been used for antenna stations available on the aircraft and since the illuminating radar spans several bands, one is usually selected for receiving antenna performance or consistency with the total measurements required of the aircraft. S-band has been keyed from the X- and S-band, C-band from C-band, and X-band from X-band.

Preparation for measurements at the radar include calibration of r-f and i-f attenuators, transmitter and local oscillator frequencies, data-system and receiver sensitivity. R-F signals are furnished by a calibrated ground site remote beacon so that system sensitivities are monitored at intervals during the measurements. Primary system calibration is accomplished before and after flights by tracking a balloon-borne 6-inch diameter metal sphere. Appropriate data corrections are applied to allow for differences between the optics region RCS and the actual measurement frequencies used. Radar beacon calibration includes a pre-flight and post-flight check of the frequency and peak power level, and a measurement of the attenuator pads.

Data recording is primarily by digital recording of pulse-to-pulse received signals. Six channels are available with receiver outputs stretched (held) to their peak values, quantized to 10 bits and recorded on a 1-in., 16-track recorder. Target range, azimuth, elevation and run number are recorded on the same tape at reduced rate. In addition, each radar trigger is counted and recorded for use in a tape search system in the laboratory reformatting process. Attenuator values are recorded in the bit locations used for video during the switching interval. Additional recordings are made as follows: A multi-channel pulse-to-pulse video record on 35-mm film, 16-mm bore-sight film from a collimated camera, a chart recording of the detected and stretched video, and a simultaneous voice commentary from all three operator stations during measurements.

Data from each of the many runs necessary to describe the patterns and/or RCS are recorded in a continuous stream on tape. Preparatory to reduction, data are selected and reformatted onto two IBM compatible

1/2-in. tapes containing proper record gaps. Reformat equipment shown in Fig. 5 enables tape search and recording of four pulse-to-pulse data channels simultaneously on one tape and the aircraft track data on another. Selection is based on confirmation of valid data runs and sections after inspection of boresight film and chart recordings, and checking recorded commentary of the operators and pilot.

3. DATA HANDLING

Data reduction is performed using a high-speed digital computer. Fig. 6 outlines the procedure which is used for the RCS measurements; antenna pattern data are reduced essentially according to the same flowchart. The line-of-sight (LOS) is first determined as a function of time for each of the data runs. Input data consist of the aircraft position in radar-oriented coordinates sampled twice per second. The position data and constraints on the aircraft courses then permit generating a coordinate transformation from the ground-based radar system to a new system erected about the aircraft. Once the transformation is complete the LOS is established in aircraft oriented coordinates and time dependent range azimuth and elevation angles are printed via a line printer and recorded on magnetic tape for use in later steps in the processing.

The second step is the generation of a pulse-to-pulse calibrated tape of received signals. The data inputs to the computer are (a) a magnetic tape containing voltage amplitudes for up to four selected data channels and coded levels for the accompanying attenuation values (b) a magnetic tape containing range and aspect data, and (c) punched cards containing various calibration factors and information for evaluation of the data. For the antenna pattern measurements, values of the radar and beacon transmitted power and radar antenna gain are supplied for each channel so that the sphere calibrations can be interpreted in terms of a receiver system calibration. The voltage values are corrected to a 0-dB level by removing step attenuation values present at the time of measurements, correcting for nonlinearities in the receiver transfer function, compensating for range, and applying calibrations appropriate to RCS and/or antenna pattern measurement. The final result of this part of the analysis is the pulse-to-pulse signal as a function of time on magnetic tape. This tape now becomes an input to the next step in the processing.

The third step is the subdivision of the data according to azimuth x elevation aspect cells. For the antenna pattern measurements $5^\circ \times 5^\circ$ cells are used, whereas for RCS $10^\circ \times 10^\circ$ cells are formed. Average antenna gains for data in each $5^\circ \times 5^\circ$ cell are generally calculated, or in the case of RCS, the 20th, 50th, and 80th percentiles of the cross-section distribution are calculated for the $10^\circ \times 10^\circ$ cells. The inputs are the aspect information from the first part of the processing and the calibrated signals tape from the second part of the processing. Outputs are punched on cards together with the number of sample values used in forming the distribution function or average.

The final processing step merges the cards for a single channel and for each aspect cell and prints and plots the results. This is done by a computer routine which accepts punched cards containing averages and percentile values and aspect-cell information, sorts according to aspect cell and merges values from like cells. The merging is accomplished by an averaging procedure in which each value is weighted according to the number of samples from which it was determined.

4. MEASUREMENTS

The radar equipment is sited near the edge of a 90-ft cliff, overlooking the Chesapeake Bay. Fig. 7 shows an outline of the area with ground projections of the courses used for measurements. Data are taken over water with maximum ranges of 10,000 to 20,000 yds. To minimize the effects of ground illumination the elevation angle of the radar is at least 5 degrees. Twelve different straight line courses of various altitudes and directions are used. Ten of these are in level flight, while two use a shallow climb and dive (12.5 degrees). The level flight courses are each designed to provide sufficient data within prescribed aspect angle intervals. Using 2500 and 5000-ft altitudes, the courses passing directly over the measurement site provide data between 5 and 40 degrees beneath the nose or tail of the aircraft to form an elevation cut. Most of the azimuth cut is plotted for data at a nominal -10 degrees elevation using the parallel offset courses which are flown at an altitude of 3000 ft. To cover the azimuthal angles near nose and tail (data between 5 and 15 degrees, and between 165 and 175 degrees) an offset course flown over the TACAN at 2500 ft altitude is used. Courses are flown in two directions and in a sequence which maximizes the data yield. By allowing the optical tracker operator to communicate directly with the pilot, details on run sequence, start and stop can be worked out efficiently. To obtain sufficient data for a repeatable RCS pattern using one polarization, a total of about twenty-six runs are required. If antenna patterns alone are measured, experience indicates only about twelve runs are needed.

5. ASPECT ANGLE ESTIMATES

The control and estimate of the aircraft aspect angle represents the most difficult problem in conducting the measurements. By using straight-line courses and maintaining their alignment with a site located TACAN, sufficient information is available from the target track to solve the coordinate transformation problem which is posed.

Fig. 8 illustrates an aircraft-oriented coordinate system centered at Q, in which a solution for the LOS to the radar centered at O is required. The three mutually perpendicular axes QU, QV, and QW are aligned in accordance with the following assumptions:

1. The QU axis coincides with the aircraft velocity vector.
2. The QV axis is parallel to the ground plane XOY of the radar.

A solution in which line-of-sight from the radar is transformed to aircraft-oriented coordinates is found which ignores any aircraft crab or roll angle. During final processing of the data these values can be inserted as appropriate to correct for this "idealized" solution. In order to satisfy the two conditions, measurements will need to be performed under favorable weather conditions and along straight flight courses. Note, however, that the second condition permits the aircraft to climb or dive in alignment with the radar and this trajectory is used in obtaining measurements directly nose-on and tail-on.

In accordance with the first assumption previously stated, the QU axis of the aircraft coordinate system coincides with the aircraft velocity vector. Denoting this by a unit vector \bar{U} , its components are given by

$$\bar{U} = 1/\dot{s} \{ \dot{x}, \dot{y}, \dot{z} \}$$

$$\text{where } \dot{s}^2 = \dot{x}^2 + \dot{y}^2 + \dot{z}^2.$$

Next \bar{V} and \bar{W} are used to represent unit vectors along the axes QV and QW, respectively and \bar{Z} represents a unit vector along the direction OZ of the radar coordinate system. The second assumption then implies that $\bar{V} \perp \bar{Z}$. Since the aircraft coordinate system forms an orthogonal set, $\bar{V} \perp \bar{U}$. This leads to the following constraints on \bar{V} , from which its components can be determined:

$$\bar{V} \cdot \bar{Z} = \bar{V} \cdot \bar{U} = 0, \bar{V} \cdot \bar{V} = 1$$

Having determined the components of both \bar{U} and \bar{V} , the components of \bar{W} are simply solved using:

$$\bar{W} \cdot \bar{U} = \bar{W} \cdot \bar{V} = 0, \bar{W} \cdot \bar{W} = 1$$

Once the location of each of the aircraft axes has been determined, the required coordinate transformation can be completed. Let \bar{B} represent a unit vector along the LOS direction from the radar and defined in radar oriented coordinates. Then the direction cosines of \bar{B} with respect to aircraft coordinates are:

$$\cos \alpha = \bar{B} \cdot \bar{U},$$

$$\cos \beta = \bar{B} \cdot \bar{V},$$

$$\text{and } \cos \gamma = \bar{B} \cdot \bar{W}.$$

with reference to Fig. 8 the required azimuth and elevation angles A and E are given by

$$A = \tan^{-1} \frac{\cos \beta}{\cos \alpha},$$

$$E = 90^\circ - \gamma.$$

Performing all indicated operations the resulting solution is:

$$A = \tan^{-1} \left[\sqrt{1 + \frac{\dot{z}^2}{\dot{x}^2 + \dot{y}^2}} \left(\frac{\dot{x}b_y - \dot{y}b_x}{\dot{x}b_x + \dot{y}b_y + \dot{z}b_z} \right) \right]$$

$$E = 90^\circ - \cos^{-1} \left\{ \frac{1}{\sqrt{1 + \frac{\dot{z}^2}{\dot{x}^2 + \dot{y}^2}}} \left[\frac{z(\dot{x}b_x + \dot{y}b_y)}{\dot{x}^2 + \dot{y}^2} - b_z \right] \right\}, \text{ where}$$

the b_x, b_y, b_z are the coordinates of \bar{B} .

Data used for the computation consists of spherical coordinates range, azimuth, and elevation sampled twice each second. Since numerical differentiation is required, the answers are very sensitive to random variations in the input data. These variations are caused by range jitter in the range tracker and by operator and servo errors in optically tracking the target and slaving the radar pedestal to the handstand. To remove these variations, input data are smoothed using an eleven-point interpolative routine, repeated three times. The defining equation of the i 'th point is

$$x_i = \frac{1}{11} \sum_{n=-5}^{+5} x_{i+n}$$

The effect of this smoothing process is to pass raw data through a low pass filter with a -3 dB bandwidth of approximately 0.3 radians/sec. This has been found adequate for the range of courses, speeds and system inaccuracies. Following smoothings and conversion to rectangular coordinates, the required velocities are obtained using a simple three-point formula. For 1/2 second samples, this becomes:

$$\dot{x}_i = x_{i+1} - x_{i-1}$$

6. MEASUREMENT ACCURACY

Regarding the measurement of signal levels from which both antenna patterns and RCS are derived, the three main sources of inaccuracy are due to (1) linearity errors, (2) frequency drift errors, (3) temperature effects. Calibration of the switched attenuators and measurements of the receiver transfer functions are performed and corrections applied during data reduction, but still contribute errors of about ± 0.5 dB. Short-term frequency drifts between the transmitter and receiver local oscillator, other than the nominal 30 MHz i-f, cause an error of ± 1.0 dB due to amplifier passband ripple. Temperature changes within the equipment cause offset errors in some of the circuits in addition to slightly detuning the bandpass amplifiers. These changes in addition to others cause differences in pre-flight and post-flight calibration to about ± 0.5 dB. The combined effect of the errors is to restrict measurement accuracy to about ± 2.0 dB.

One other factor, not related directly to measurement accuracy, but rather to measurement repeatability is that of aspect determination. As discussed earlier, the aspect solution employed ignores the effects of roll and crab. In all but the calmest of weather, however, some crabbing will be experienced and corrections made in order to define the aspect angle as accurately as possible. A technique used for determining crab angles is that of time correlation between bore-sight film and aspect solution in conjunction with some observable alignment feature on the aircraft. The most often used feature is that of opposite wing tips being aligned. Another technique is to key on some characteristic observable in the aircraft reflectivity pattern such as the specular return from the leading edge of the wing and again time correlate with the aspect solution. These observables can lead to accuracies of the order of $\pm 1^\circ$ for passing courses.

On radial courses heading reports from the pilot of the aircraft can be correlated with ground track projections and the crab angle determined by differencing the two. This particular technique can result in errors of up to 3 degrees.

7. TYPICAL RESULTS

Fig. 9 shows the reduced data for a single run of an aircraft past the measurement system. In this instance the aircraft was flying a crossing course at 5000 yds. offshore heading 180 degrees true with the antenna positioned with the center of the beam to starboard (90°). The resulting plot of the mean values from 5 degree cells shows the beam peaked at 85 degrees, but with five degree resolution the peak could have occurred between 85 and 90 degrees. The pattern 3 dB points, if symmetry is assumed, indicates a beam center 1.5 - 2 degrees forward of 90 degrees. There is, as mentioned earlier, an indeterminacy in actual aspect angle measurement which can also contribute to the peak of the beam plotting someplace other than its actual position. This pattern also shows clearly the first sidelobes of the antenna at approximately -15 dB.

Fig. 10 shows the results of a similar course, included here to show the somewhat deeper nulls and better defined sidelobes than the previous figure. This average data can be supplemented by examining the percentiles of the distribution of received signals in a manner similar to the RCS measurement, Fig. 11. Shown are the 10, 50, and 90 percentiles from which the mean values of Fig. 10 are drawn. The 50 percentile curve is nearly identical to the mean value curve but the 10 percentile curve shows more structure in the null region than either of these. In comparing the spread among the three percentiles from cell to cell, the signal falls significantly at the 120 degree and 125 degree points, the region of this first null in the pattern. The comparable null on the opposite side of the pattern occurs in the 55 degree to 60 degree region but does not exhibit the significantly lower signal. This could be a consequence of perturbation of the pattern by aircraft structure, basic non-symmetry in the pattern, or flight characteristics of the aircraft on this particular run not giving visibility to the null depth.

Fig. 12 is a plot of mean values, again from 5 degree cells but with the aircraft passing overhead and sweeping in elevation rather than azimuth. This plot actually shows the results from two such passes of the aircraft, one inbound during which the values in the forward region are determined and the other outbound during which the values in the after region are determined. The coverage in elevation, however is insufficient to capture the null detail of the pattern in that plane.

Fig. 13 illustrates the same antenna described in Fig. 10, but now emplaced so that the axis is directed at a nominal 45 degrees to the airframe. A comparison of the two figures reveals that the patterns in the two cases are not significantly different, thus the change in emplacement has not introduced any perturbations into the pattern of the antenna.

Fig. 14 is the plot of mean values from a course designed to provide measurements of azimuth pattern near the nose region. This particular run provided 30 degrees coverage and mapped the pattern into the first null region at 330 degrees. For this course the antenna was positioned pointing forward. There is structural blockage which spoils the pattern and produces a local null at zero degrees. A course which is the reciprocal of this provides comparable coverage near the tail of the aircraft.

All the patterns illustrated here were achieved by positioning an antenna of approximately 30 degree beamwidth at various angles with respect to the airframe and running designed courses to map the azimuth and elevation coverage desired. In the general case of an omnidirectional antenna, these courses would define the pattern over the total azimuth coverage which could then be presented in composite form.

8. CONCLUSIONS

The design of a system for making dynamic measurements has resulted in a stable multifrequency measurement tool. Using this system, it has been possible to perform accurate measurements of antenna patterns and gains of avionic antennas installed aboard aircraft. Such measurements have the advantage of providing a true pattern of an antenna in its operational environment, complete with pattern distortions and blockages as may exist. Furthermore such measurements may be made without an instrumented aircraft for aspect determination provided a controlled set of courses are used and the aircraft is equipped with a known stable power source driving the antenna being measured.

REFERENCES

OLIN, I.D. and QUEEN, F.D., "Dynamic Measurement of Radar Cross Sections," Proc. IEEE, Vol. 53, No. 8, pp 954-961, August, 1965.

SCHMITT, O.H. and PEYSER, W.P., "Aircraft Antenna Pattern Plotter," Electronics, Vol. 20, pp 88-91, May, 1947.

SINCLAIR, G., Et.al., "Measurement of Aircraft-Antenna Patterns Using Models," Proc. IRE, Vol. 35, No. 12, pp 1451-1462, December, 1947.

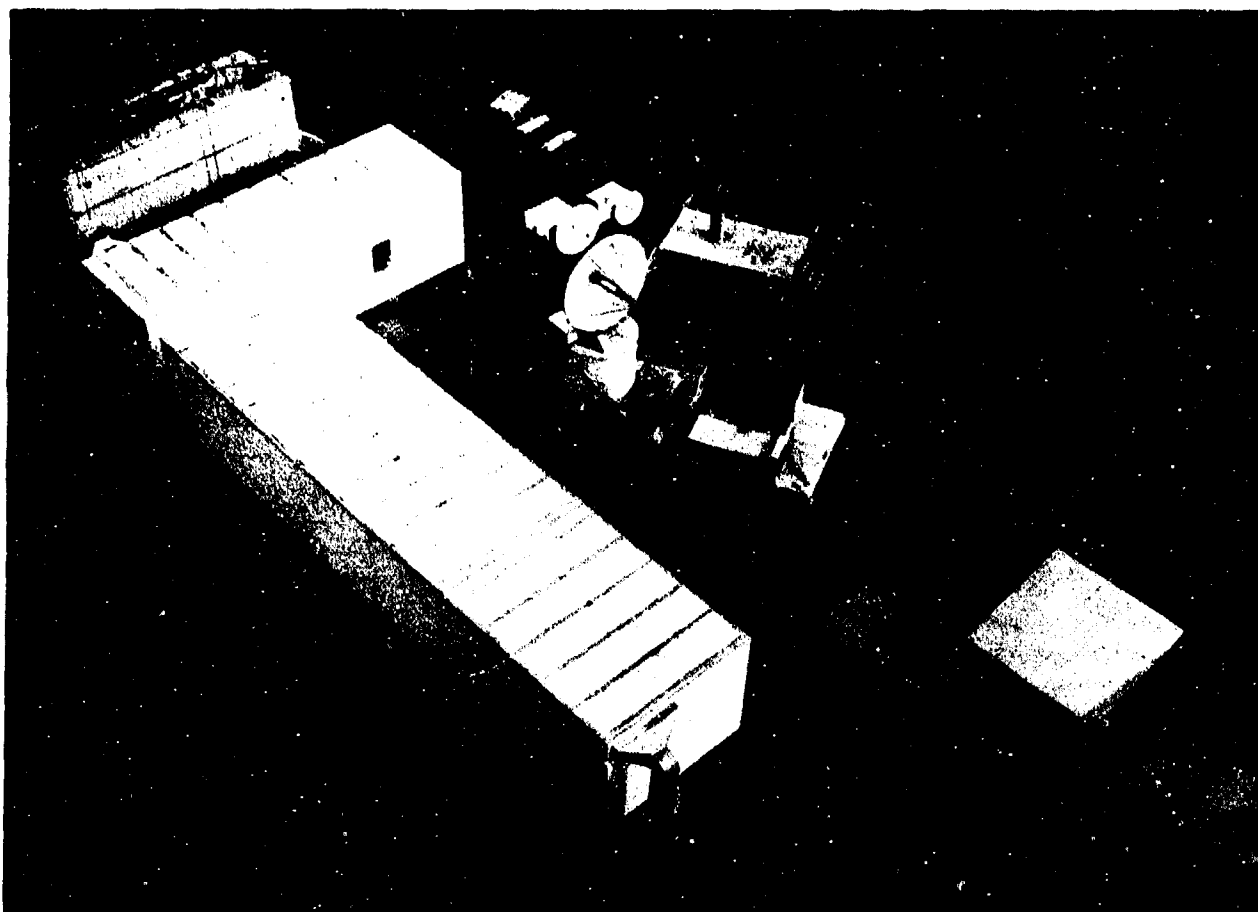


Fig. 1. Ground site equipment. A single antenna pedestal is used for four-band operation and is controlled by the adjacent optical handstand-tracker.

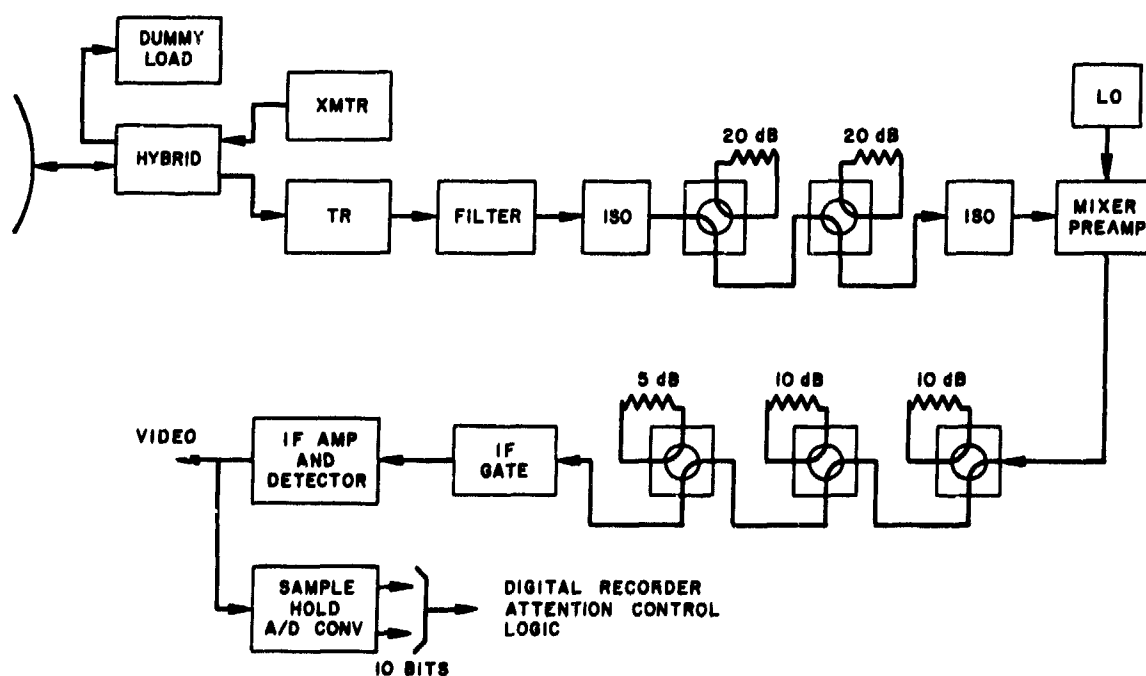


Fig. 2. L-or S-band system block diagram.

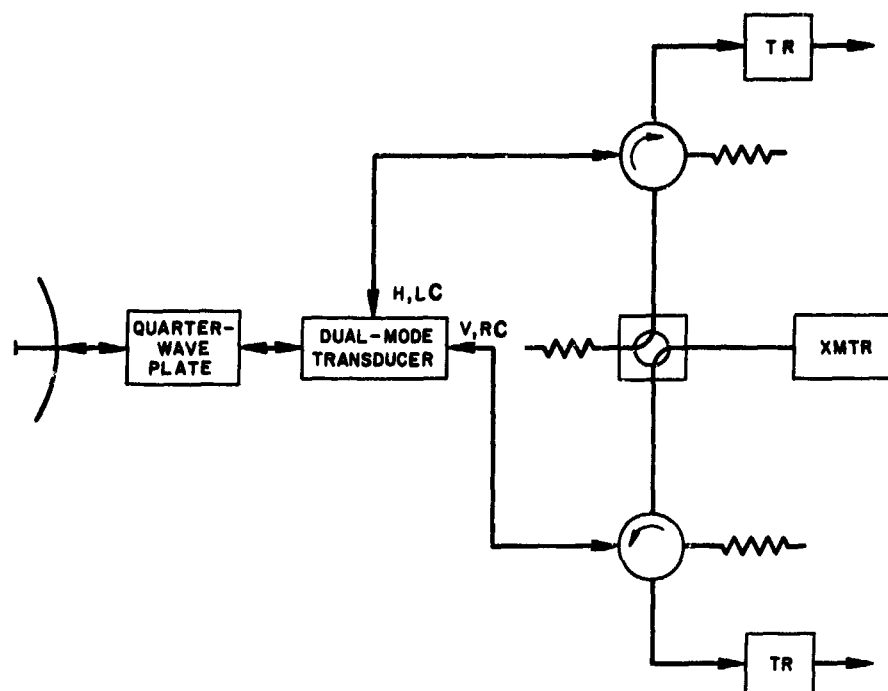


Fig. 3. X-band microwave section block diagram.

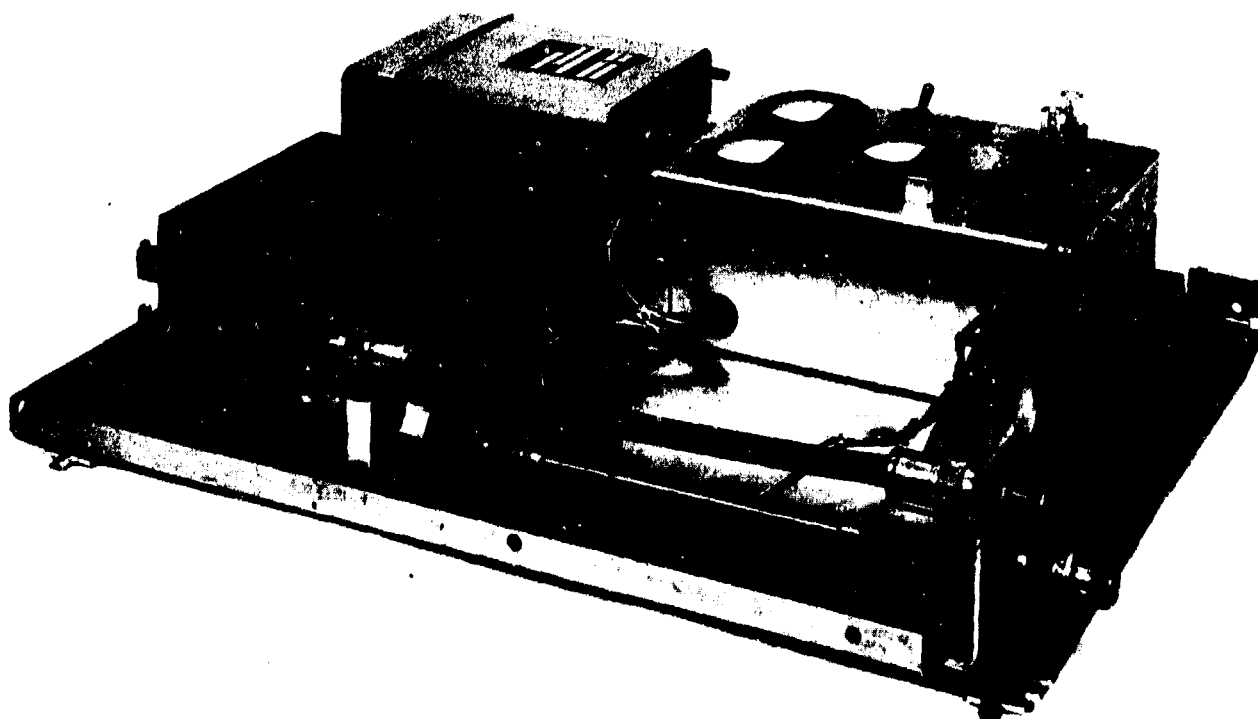


Fig. 4. Beacon assembly used for aircraft installation.

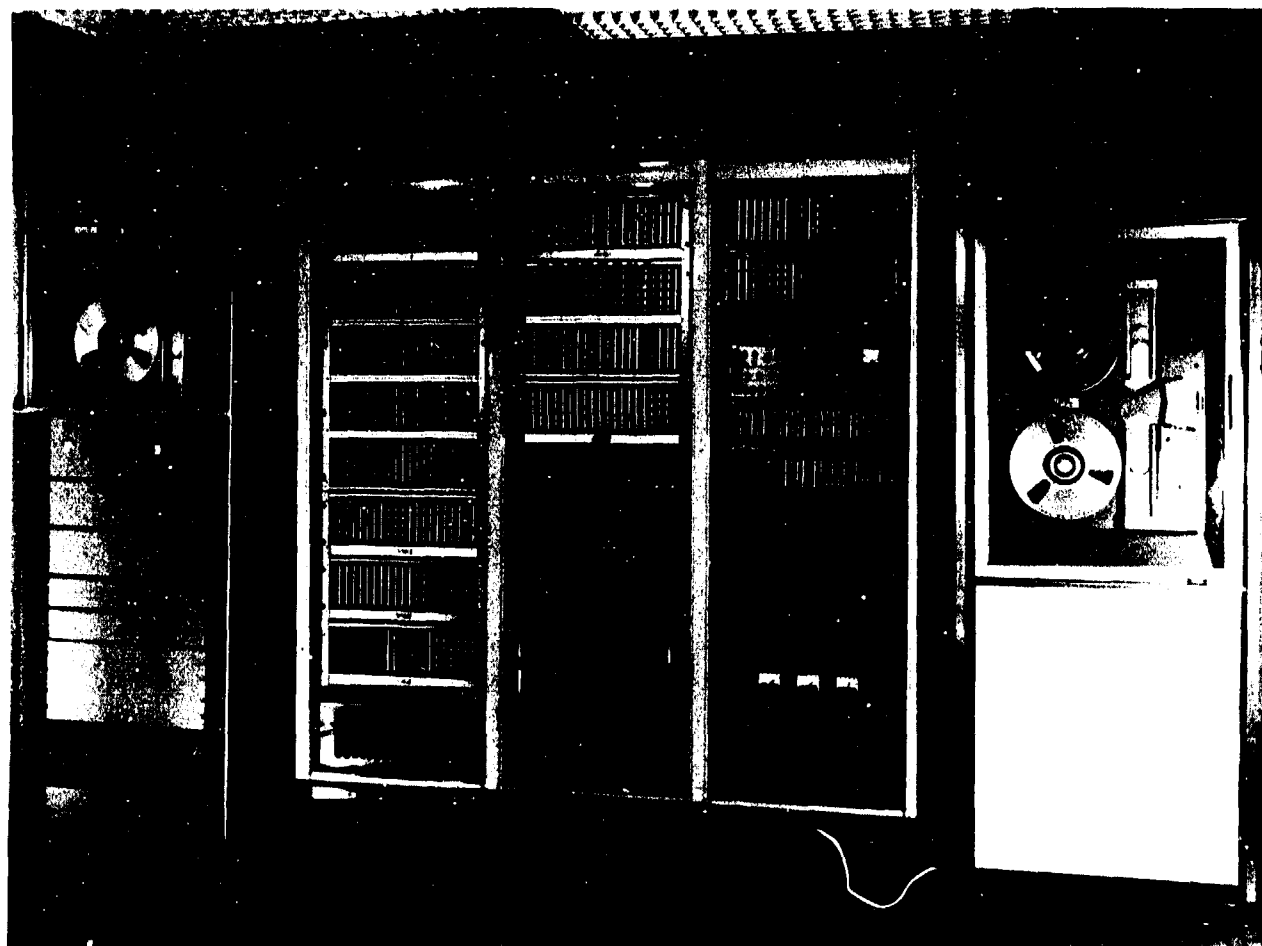


Fig. 5. Magnetic tape reformatting equipment.

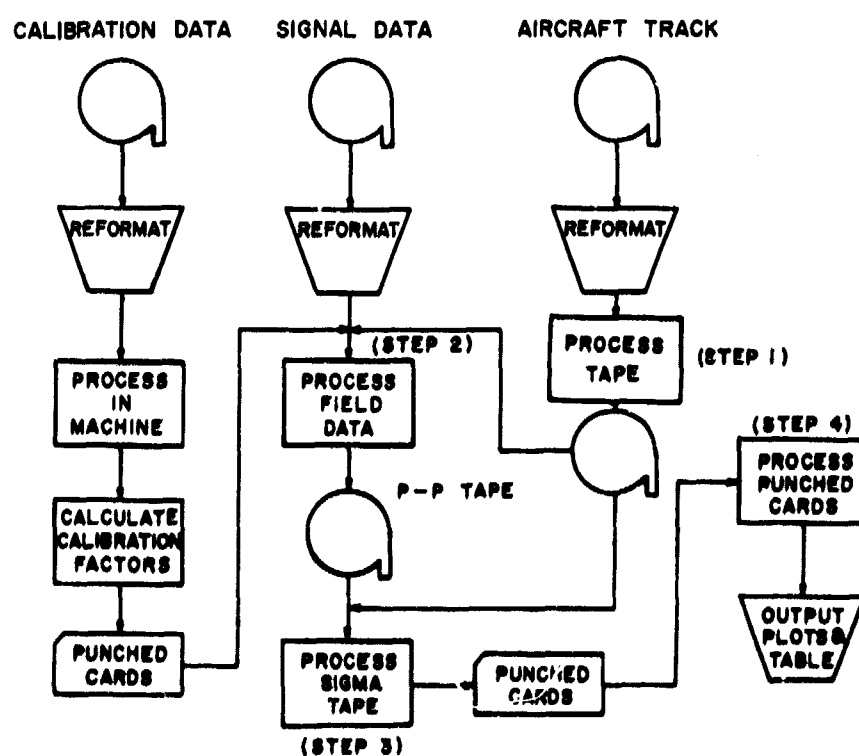


Fig. 6. Flow chart of the data reduction process.

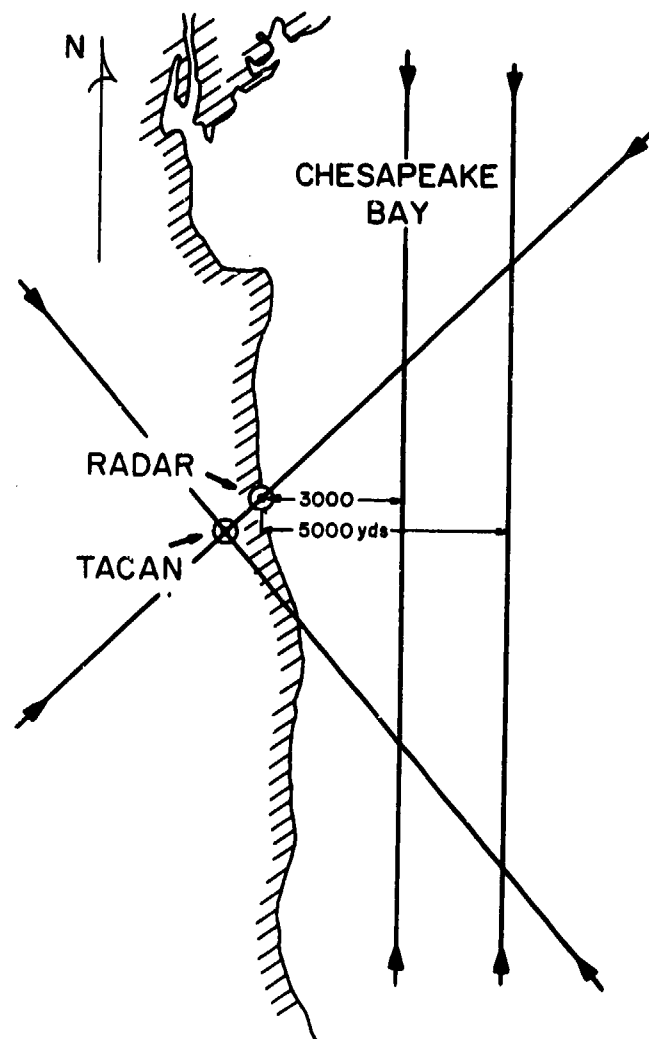


Fig. 7. Ground tracks of flight courses at the Chesapeake Bay area test site.

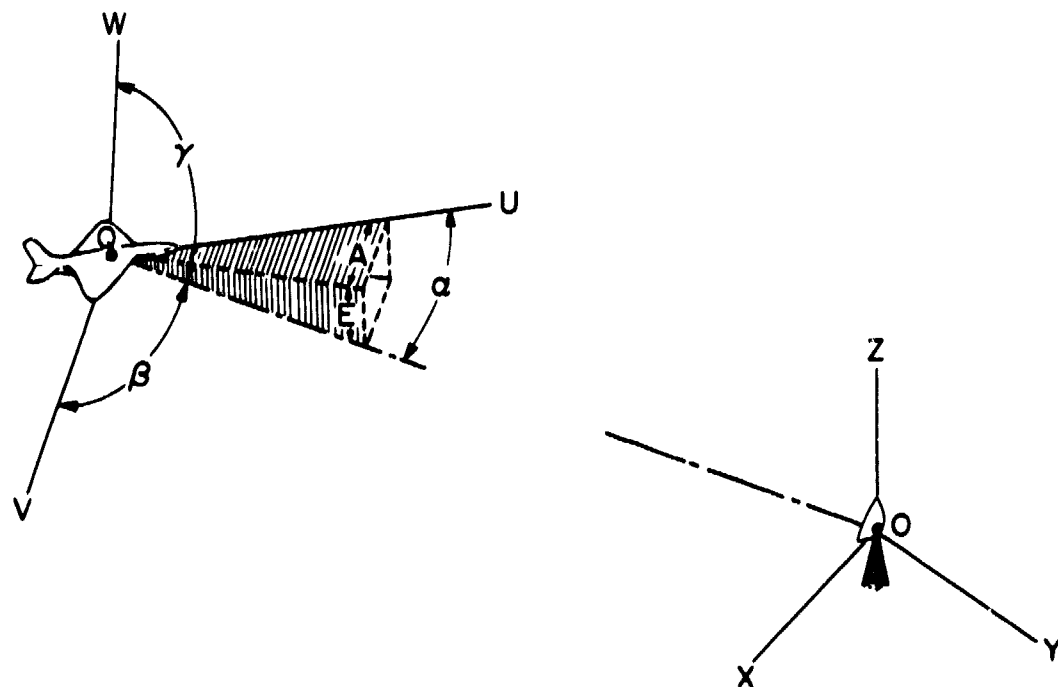


Fig. 8. Coordinate systems used for aspect angle problem solution.

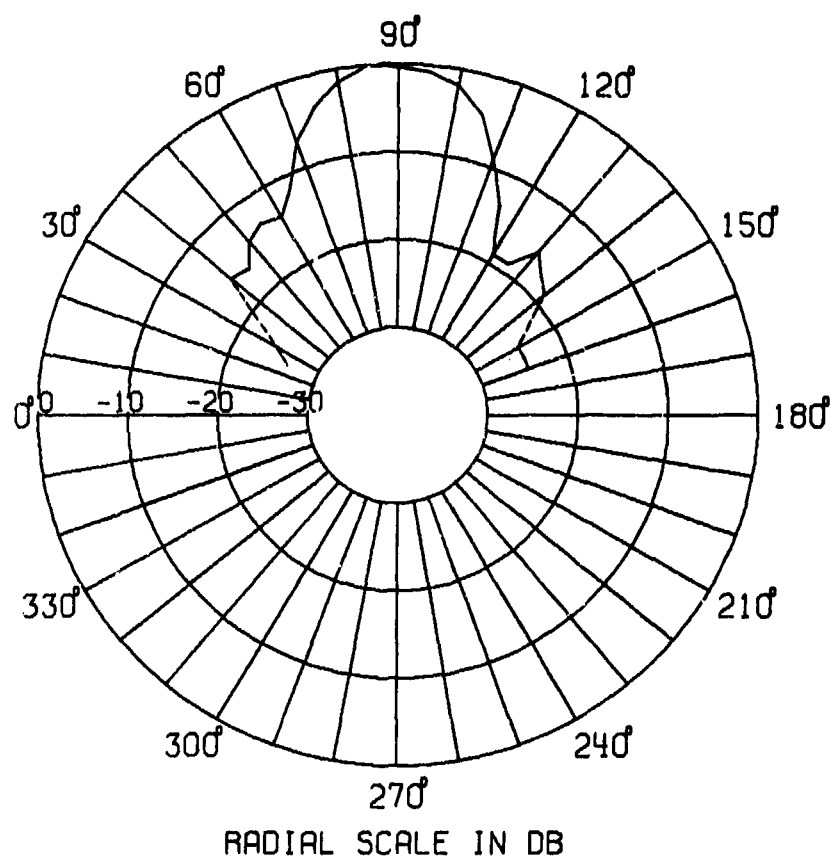


Fig. 9. Resultant azimuth pattern of antenna directed at 90 degrees.

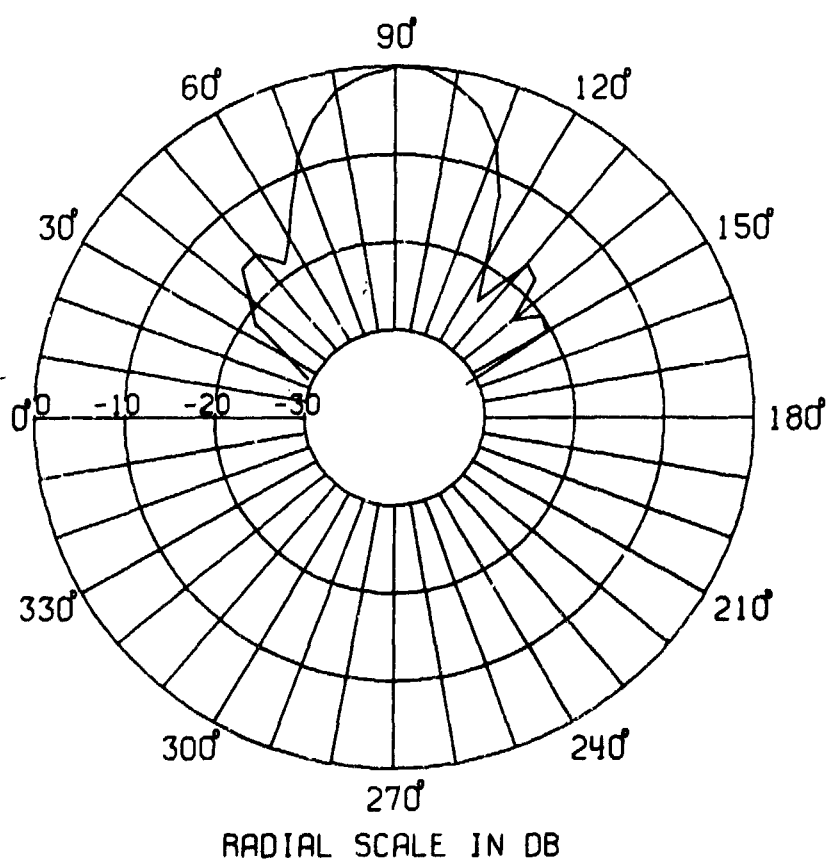


Fig. 10. Azimuth pattern of antenna directed at 90 degrees showing deeper null structure.

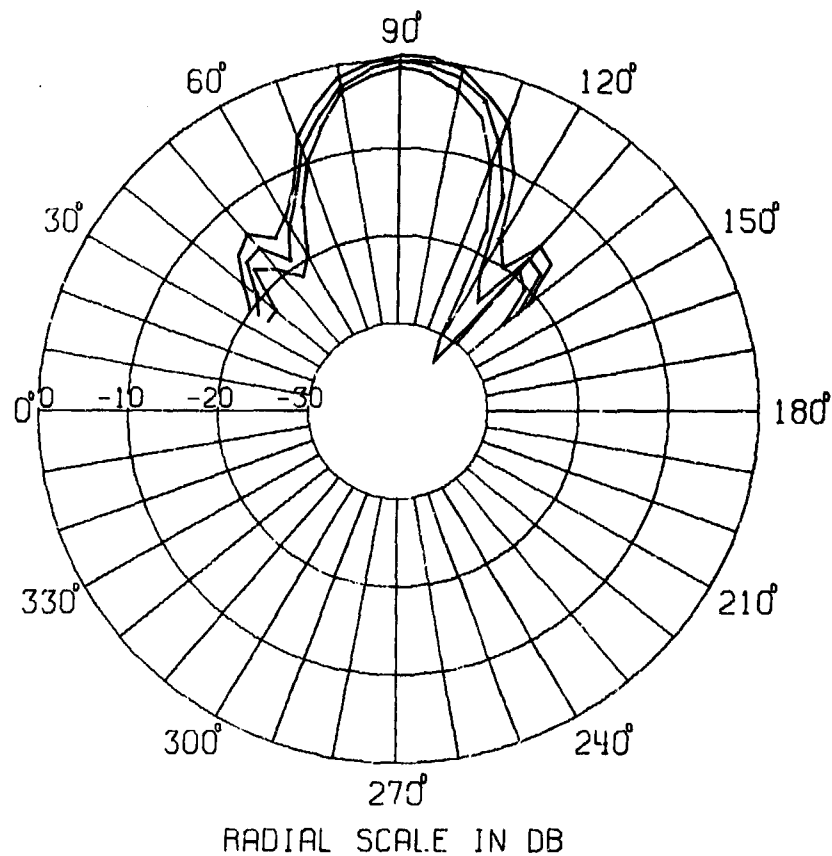


Fig. 11. Azimuth pattern of Fig. 10 showing 10, 50, and 90 percentile values from 5 degree cells.

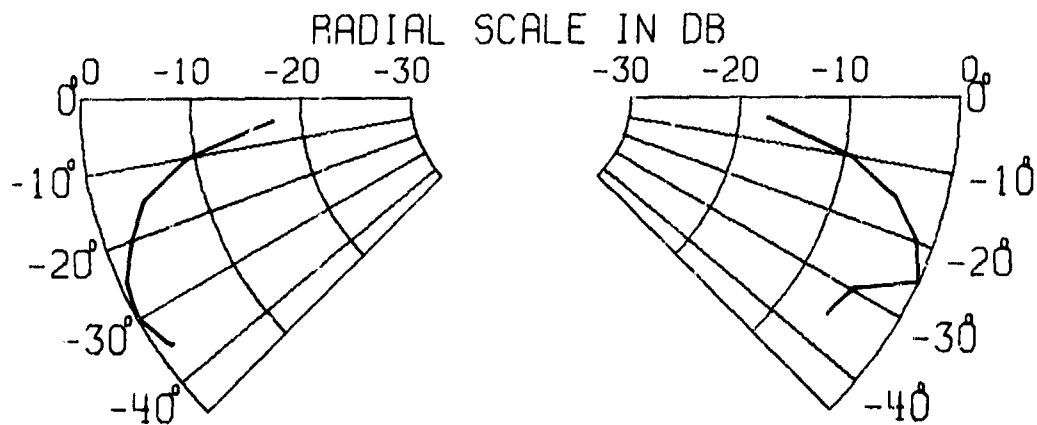


Fig. 12. Elevation pattern of antenna directed forward, then left. Patterns are shown at azimuth values of zero degrees and 180 degrees.

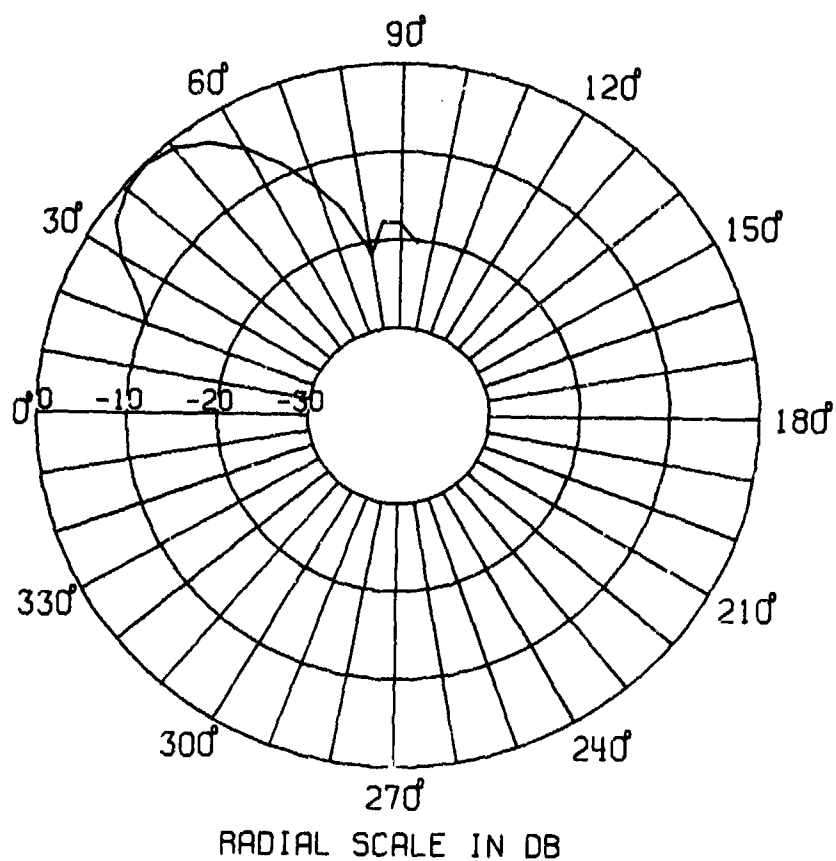


Fig. 13. Azimuth pattern of antenna directed at 45 degrees relative to the airframe.

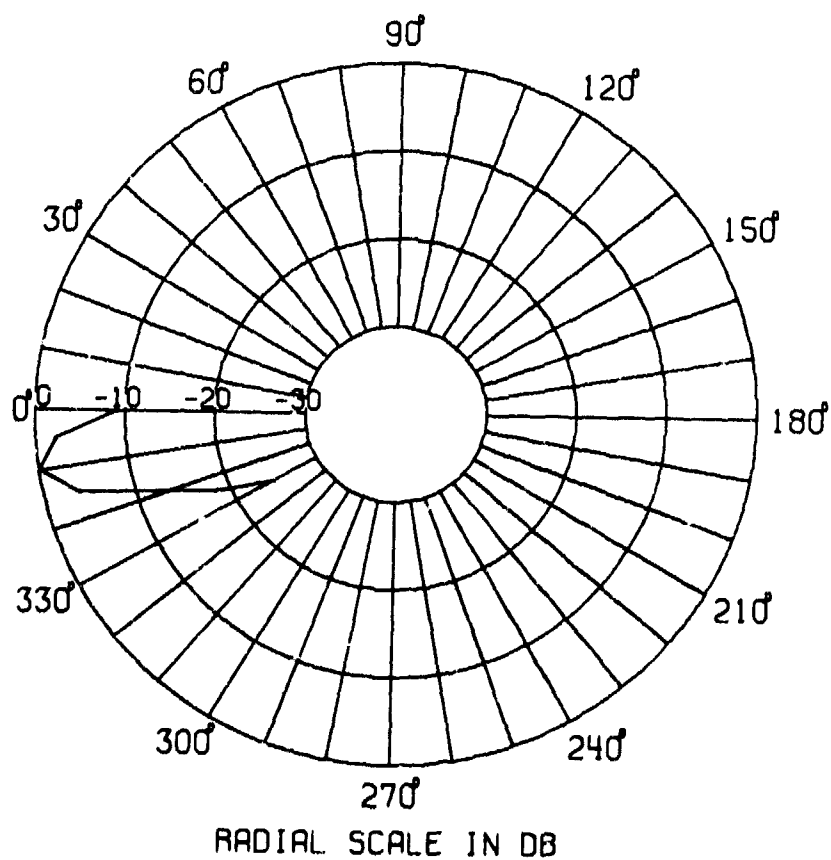


Fig. 14. Azimuth pattern of antenna directed at zero degrees relative to the airframe.

DISCUSSION

F.S. STRINGER: Assumptions of aircraft attitude have been made in the technique described. Would not improvements in accuracy be achieved by a measurement of attitude synchronized with the ground recordings? If improvements are likely, why have not such attitude records been obtained?

I.D. OLIN: Synchronized attitude measurements would indeed improve the aircraft aspect measurement accuracy. Moreover, it would somewhat reduce the restrictions regarding flight courses. But if flying time is to be kept reasonable only principal plane measurements, (implying little aircraft roll) may be made anyway.

In the approach described such measurements were not made because of the installation complexity and the time involved. A large variety of aircraft were to be measured and it was felt that all of them would be available for the necessary ground installation. The beacon installation is simple and performed by the general crew, so that our actual involvement with the aircraft was essentially restricted to flight time.

AN IMPROVED MEASURING TECHNIQUE FOR INVESTIGATIONS OF THE NEAR FIELD REGION OF ANTENNAS

Rüdiger Anders
Institute for Technical Electronics
Technical University Aachen
D 51 Aachen, Templergraben 55, Germany

SUMMARY

A new scattering technique for low reaction measurements of electromagnetic fields is presented using a small diode probe without any conductive feeder. The basic principle of this technique makes use of the frequency mixing property of a microwave diode as scatterer to convert the probe signal to the x-band microwave range where it easily can be transmitted and picked up by a remote auxiliary antenna. The theoretical background is given and several measurement set-ups for different operation conditions are discussed.

1. INTRODUCTION

During the last ten years measurements of the near field region of antennas have become increasingly important for the determination of the fundamental characteristics of antennas and for the purpose of deeper insight into the radiation mechanism of some complicated antennas as log-periodic and log-spiral antennas surface wave antennas and phased arrays. If detailed near field data are known from near field measurements, far-field radiation patterns, polarisation characteristics and phase characteristics as well as phase center locations and gain functions can easily be obtained from that data by computational methods [1],[2].

The striking advantage of near field measurements is the fact that in nearly all cases they can be done by laboratory experiments and thus help to save costs and time. On the other hand it is known as a troublesome drawback of all near field probing techniques that the probe disturbs the field distribution particularly in the vicinity of the antenna surface when picking up energy from the field for measuring purposes. This may cause inaccuracies in the experimental data and at least in the desired antenna characteristics.

In order to provide minimum disturbance of the field distribution by the measuring probe several ingenious and sophisticated techniques have been developed by different authors and recently summarized in an excellent review given by J. D. Dyson [3]. According to this the probing techniques may be divided into those for direct measurement and those for indirect measurement. The former give increased sensitivity and direct reading of the near field distribution as

$$U_{PT} = K_{PT} E_T C_T(r, \theta, \phi_r) \cos(\Omega_T t + \psi_r) \quad (1)$$

where U_{PT} is the signal voltage at the input of the probe feeder, K_{PT} denotes a constant depending on the effective aperture of the probe, E_T , Ω_T , and ψ_r are the maximum amplitude, the angular frequency, and the relative phase of the signal received by the probe and C_T stands for the desired relative radiation characteristic of the antenna under test.

The latter are known as scattering techniques. They make use of measuring the reradiated or scattered field of a small probe when it is moved in the field of interest. The quantity to be measured will be received simultaneously by the antenna under test and is given by

$$U_{ST} = K_{ST} E_T^2 C_T^2(r, \theta, \phi_r) \cos(\Omega_T t + 2\psi_r) \quad (2)$$

where U_{ST} is the voltage of the scattered signal at the antenna termination and K_{ST} a similar constant to K_{PT} . Equation (2) shows as main drawbacks of the scattering techniques reduced sensitivity and a quadratic proportionality between the output signal and the field distribution function C_T instead of a linear one in (1). As a consequence of this, given a limited dynamic input range of the measurement receiver, the scattering techniques only allow for a readout of half the dynamic range of the field distribution that can be covered by the direct probing techniques. Nevertheless on account of minimum field disturbance which mostly is of particular importance the scattering techniques are of major significance because of the absence of any conductive feeder to the probe.

This paper now deals with an improved measuring technique for probing electromagnetic fields which combines the advantages of both probing methods and avoids their drawbacks. In making use of the "SSBSC Homodyne" system for real-time measurements the measurement system to be presented guarantees high sensitivities up to -100 dBm with a dynamic range of 80 dB.

2. PRINCIPLE OF THE MEASURING TECHNIQUE

The basic principle of this new measurement system is to use a microwave mixing diode in a common glass or pill package with leads as scattering probe. The leads will act as the wire arms of a short electric or magnetic dipole with the diode junction as non-linear terminating impedance. When this probe is placed into the field of the antenna under test and in addition to this illuminated by an auxiliary signal radiated by a second transmitting antenna sufficient far away as is shown in Fig. 1 the probe will receive both signals different in frequency and feed a certain amount of them into the diode termination.

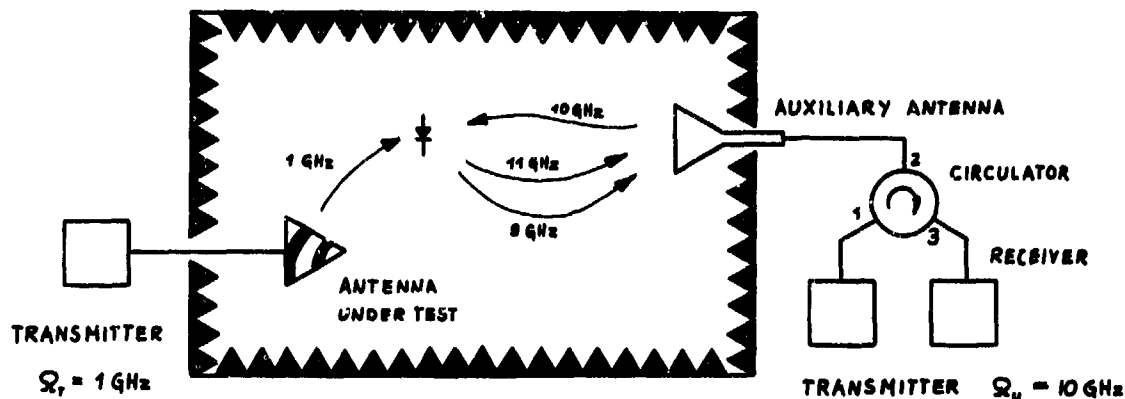


Fig. 1 Principle of the measuring technique

Due to the mixing property of the microwave diode additional sideband signals are generated and reradiated by the probe dipole. These sideband signals carry all information of the radiation fields of both antennas at the position of the scattering probe. They can be picked up simultaneously by the auxiliary antenna and then fed into a receiver for amplitude and phase determination. In order to make sure that only the spatial field distribution of the antenna under test is analysed some special steps must be adopted that eliminate the influence of the auxiliary antenna. These will be discussed later on.

While the signal frequency of the antenna under test is fixed by the test conditions (for example $\Omega_T = 1$ GHz) the frequency of the auxiliary signal may be chosen arbitrary but should be in the order of ten times the test frequency or larger in this particular field of application (e.g. $\Omega_M = 10$ GHz). If the probe length and diameter then are matched conveniently to the upper sideband signal ($\Omega_M + \Omega_T = 11$ GHz) as a resonant halfwave dipole or loop (which results in a 1.36 cm probe length or a 0.435 cm loop diameter) low transmission loss is provided on the transfer of the reradiated signals between probe and auxiliary antenna. Thus the probe size regarding to the wavelength of the test signal will be reduced to the order of 0.023λ . This small scattering probe gives sufficient resolution and brings out only negligible disturbance of the fields of interest. If smaller probes are required the probe size may be reduced far beyond the matching condition as far as the power of the signal generators and the sensitivity of the receiver make sure that the decreasing scattered signal can be indicated.

3. THEORETICAL BACKGROUND

Although the principle of this measuring technique is not restricted to the near field of antennas there is a significant difference in the measurement set-up if the field distribution in the vicinity of the antenna under test or at a more distant range is considered. As can be seen from Fig. 1 if the probe is positioned in the very near field the auxiliary antenna will not only illuminate the scatterer but also the antenna under test. In case of this an additional back-scattered signal from the antenna under test arises that interferes with the direct signal originating from the auxiliary antenna. As a matter of fact the carrier signal at the scatter termination is no more independent of the position of the antenna under test which is true for the distant field.

3.1 Theory without Back-Scattering at the Antenna Under Test

The observable voltage U_{PT} of the test signal was defined by (1) e.g.

$$U_{PT} = k_{PT} E_T C_T(r_T, \theta_T, \phi_T) \cos(\Omega_T t + \psi_T)$$

Similar to this the voltage U_{PH} of the auxiliary signal at the probe termination is given by

$$U_{PH} = k_{PH} E_M C_H(r_H, \theta_H, \phi_H) \cos(\Omega_M t + \psi_H) \quad (3)$$

where K_{PH} denotes a constant. E_H , Ω_H and ψ_H are the maximum amplitude the angular frequency and the relative phase respectively. C_H denotes the spatial radiation characteristic of the auxiliary antenna.

Assuming square law conversion for the scatter diode where no regard is made to input or output impedances or sensitivity of the diode the transfer characteristic can be represented by

$$U_{OUT} = a_0 + a_1 U_{IN} + a_2 U_{IN}^2 \quad (4)$$

where

$$U_{IN} = U_{PT} + U_{PH} \quad (5)$$

Equation (5) put into (4) yields the frequency spectrum

$$\begin{aligned} U_{OUT} = & a_0 + 0.5 a_2 (k_{PT} E_T C_T(r_T \theta_T \phi_T) + k_{PH} E_H C_H(r_H \theta_H \phi_H)) + \\ & + a_1 k_{PT} E_T C_T(r_T \theta_T \phi_T) \cos(\Omega_T t + \psi_T) + \\ & + a_1 k_{PH} E_H C_H(r_H \theta_H \phi_H) \cos(\Omega_H t + \psi_H) + \\ & + 0.5 a_2 k_{PT}^2 E_T^2 C_T^2(r_T \theta_T \phi_T) \cos(2\Omega_T t + 2\psi_T) + \\ & + 0.5 a_2 k_{PH}^2 E_H^2 C_H^2(r_H \theta_H \phi_H) \cos(2\Omega_H t + 2\psi_H) + \\ & + a_2 k_{PT} E_T C_T(r_T \theta_T \phi_T) k_{PH} E_H C_H(r_H \theta_H \phi_H) \cos((\Omega_H - \Omega_T)t + \psi_H - \psi_T) + \\ & + a_2 k_{PT} E_T C_T(r_T \theta_T \phi_T) k_{PH} E_H C_H(r_H \theta_H \phi_H) \cos((\Omega_H + \Omega_T)t + \psi_H + \psi_T) \end{aligned} \quad (6)$$

Fig. 2 gives a schematic sketch of that spectrum

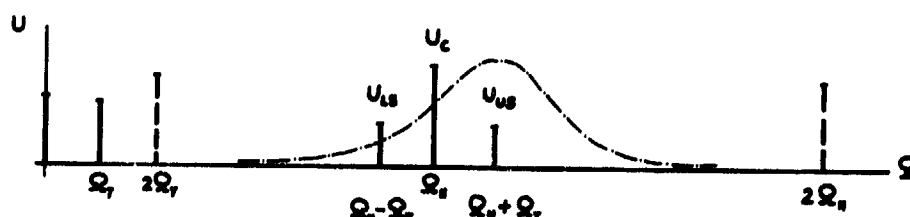


Fig. 2 sketch of the frequency spectrum

Now if the back-scattering frequency-response of the resonant scatterer is taken into account (dashed line in Fig. 2) the probe reradiates mainly the third and the last two terms of (6) with significant efficiency. These signals will be picked up by the auxiliary antenna acting simultaneously as receiving antenna. Due to the reception characteristic of the auxiliary antenna the associated receiver input signals are

$$U_C = b_C a_1 k_{PH} E_H^2 C_H^2(r_H \theta_H \phi_H) \cos(\Omega_H t + \psi_H) \quad (7)$$

$$U_{LS} = b_{LS} a_2 k_{PT} E_T C_T(r_T \theta_T \phi_T) k_{PH} E_H^2 C_H^2(r_H \theta_H \phi_H) \cos((\Omega_H - \Omega_T)t + \psi_H - \psi_T) \quad (8)$$

$$U_{US} = b_{US} a_2 k_{PT} E_T C_T(r_T \theta_T \phi_T) k_{PH} E_H^2 C_H^2(r_H \theta_H \phi_H) \cos((\Omega_H + \Omega_T)t + \psi_H + \psi_T) \quad (9)$$

where U_C , U_{LS} , and U_{US} denote the voltages of the carrier signal and the lower and upper sideband signals, while the constants b_C , b_{LS} and b_{US} regard to the transmission characteristic between probe and auxiliary antenna.

For the quantity $C_T(r_T \theta_T \phi_T)$ that is the desired relative spatial field distribution of the antenna under test only the signals U_{LS} and U_{US} are relevant. To evaluate the steps must be taken to guarantee that the radiation characteristic of the auxiliary antenna has no effect on the result. This can be accomplished in two different ways.

3.1.1. Analysis of One Sideband Signal

In (8) or (9) the only factor except C_T that may not retain constant when the scattering probe is moved in the field of interest is the relative radiation characteristic of the auxiliary antenna. This can be forced to become constant if the mutual position of the probe and the auxiliary antenna is kept fixed while the antenna under test is moved against the probe. As a matter of consequence Fig. 3 shows a simplified version of the necessary measurement set up.

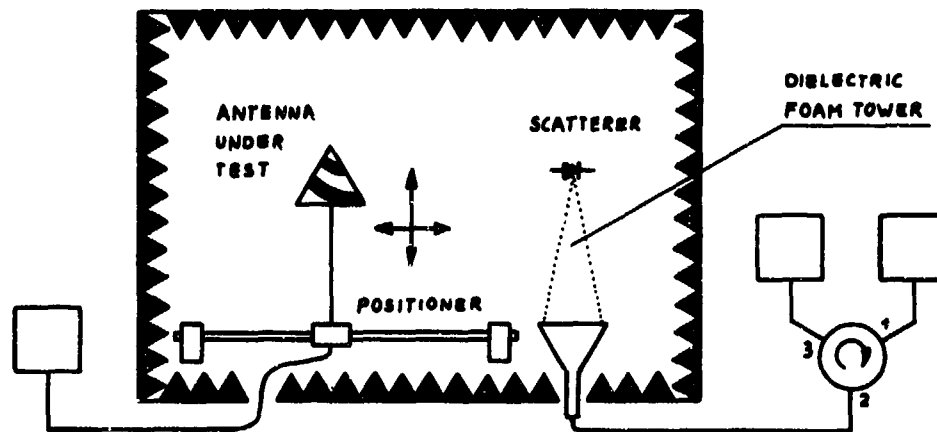


Fig. 3 Simplified set-up for measurements when back-scattering from the antenna under test need not to be taken into account

3.1.2. Analysis of Carrier and One Sideband Signal

Instead of keeping C_H constant the falsifying influence of C_H can be eliminated by detecting the carrier signal U_c and one sideband signal U_{LS} or U_{US} separately and taking the ratio of both signal outputs. If for example the upper sideband and the carrier signal are considered the ratio may be derived from (7) and (9) as

$$U_R = \frac{U_{US}}{U_c} \quad (10.1)$$

$$U_R = \frac{K_{OU} b_{US} a_2 k_{PT} E_T C_T (r_T \theta_T \phi_T) K_{PH} E_H^2 C_H^2 (r_H \theta_H \phi_H) |(\Omega_H + \Omega_T)t}{K_{OC} b_c a_1 K_{PH} E_H^2 C_H^2 (r_H \theta_H \phi_H) | \Omega_H t} \quad (10.2)$$

$$U_R = K_0 E_T C_T (r_T \theta_T \phi_T) \quad (10.3)$$

where K_{OU} and K_{OC} indicate the different detection efficiency of both signals and is a resultant constant. Opposite to the above mentioned analysis of only one sideband signal there is no restraint on a fixed position of the antennas used and the scatterer.

3.2 Theory Considering Back-Scattering at the Antenna Under Test

In a more general case especially when the scattering probe is moved in the vicinity of the antenna under test a back-scattering signal arises from direct illumination of the antenna under test by the auxiliary antenna. This undesired echo signal may cause errors because of interference with the carrier signal and a direct reradiation to the auxiliary antenna. Regarding to (5) U_{SN} is to be replaced by

$$U_{SN} = U_{PT} + U_{PH} + U_{PB} \quad (11)$$

where

$$U_{PB} = K_{PB} E_S C_S (r_S \theta_S \phi_S) \cos(\Omega_H t + \psi_S) \quad (12)$$

U_{PB} denotes that portion of the back-scattered auxiliary signal to interfere with the direct radiated auxiliary signal at the probe termination. All other factors and functions with subscript B are similar to (3) but refer to the back-scattered auxiliary signal. As a matter of consequence to (11), (7), (8) and (9) are to be replaced by

$$U_c = b_c a_1 C_H (r_H \theta_H \phi_H) \left[K_{PH} E_H C_H (r_H \theta_H \phi_H) \cos(\Omega_H t + \psi_H) + K_{PB} E_S C_S (r_S \theta_S \phi_S) \cos(\Omega_H t + \psi_S) \right] \quad (13)$$

$$U_{LS} = b_{LS} a_2 C_S (r_S \theta_S \phi_S) k_{PT} E_T C_T (r_T \theta_T \phi_T) \left[K_{PH} E_H C_H (r_H \theta_H \phi_H) \cos((\Omega_S - \Omega_T)t + \psi_H - \psi_T) + K_{PB} E_S C_S (r_S \theta_S \phi_S) \cos((\Omega_S - \Omega_T)t + \psi_S - \psi_T) \right] \quad (14)$$

$$U_{US} = b_{US} a_2 C_S (r_S \theta_S \phi_S) k_{PT} E_T C_T (r_T \theta_T \phi_T) \left[K_{PH} E_H C_H (r_H \theta_H \phi_H) \cos((\Omega_H + \Omega_T)t + \psi_H + \psi_T) + K_{PB} E_S C_S (r_S \theta_S \phi_S) \cos((\Omega_H + \Omega_T)t + \psi_S + \psi_T) \right] \quad (15)$$

Because of the impossibility to keep the radiation characteristics C_M and C_0 unchanged at the same time a determination of C_T similar to the method given in 3.1.1. fails in this more general case. If the second method is used (10.1) comes to the form

$$U_R = \frac{U_{us}}{U_c + b_0 U_0 C_0 (r_0 \omega_0 \phi_0)} \quad (16)$$

which seems to be useless too on account of the additional term in the denominator arising from the directly reradiated auxiliary signal to the auxiliary antenna. Fortunately this residual scattered auxiliary signal can be suppressed by means of a compensating technique. If the mutual position of the antenna under test and the auxiliary antenna remain unchanged when the probe is moved the signal corresponding to the second term in the denominator of (16) will be independent of the probe position too and thus can be canceled by adding a coherent signal at the receiver input equal in amplitude and opposite in phase.

4. MEASURING EQUIPMENT

Regarding to the theoretical results there are three different measurement set-ups for the experimental investigation of electromagnetic field distributions. Each of them makes use of the same scattering technique but differs in instrumentation.

4.1 Scatterer

As scattering probes conventional microwave semiconductor diodes in picomin-glass packages are used with straight wire leads as electrical field probe and bent leads for loop probes cut to the proper length. If diodes only in pillbox packages are available thin wires should be bonded onto the centres of the top plates to act as dipole arms. As for the type of diode schottky barrier diodes, point contact diodes as well as backward diodes have been tested successfully. The best results were obtained from backward diodes because of their high tangential sensitivity at zero bias operation and their low impedance. But also point contact diodes give satisfactory performance. In addition to this they are at lower price. Schottky barrier diodes do not reach their optimum operation properties in this special field of application because there is no bias available.

For the purpose of motion the scatter probes are mounted on top of a pyramidal dielectric foam tower which itself is put to a cartesian coordinate positioner.

4.2 Instrumentation

The expenditure of instrumentation depends largely on what one wants to measure. If data are desired of the extended near field only, where there is no significant back-scattering from the antenna under test two instrumentations are recommended.

4.2.1. Set-up Regarding to 3.1.1. Using Zero-Indication Method

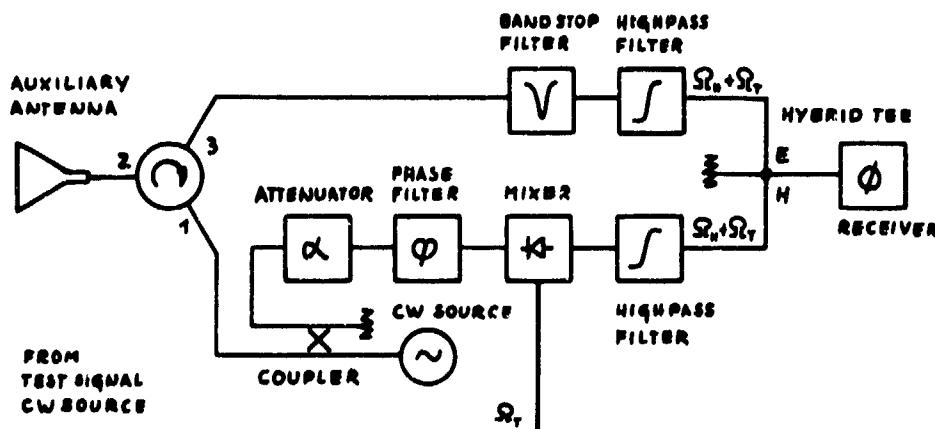


Fig. 4 Instrumentation for Zero-Indication Method

The basic measurement system is shown in Fig. 4. The antenna under test for example a conical log-spiral antenna is supplied by a signal source at test frequency $\Omega_T = 1.0$ GHz. At the same time a source signal at $\Omega_M = 10.0$ GHz is fed to an x-band horn acting as auxiliary antenna by means of a circulator. Both signals are radiated to the diode scatterer where they are mixed generating sideband signals at $\Omega_M \pm \Omega_T = 9$ GHz and 11 GHz, that will be reradiated and picked up by the auxiliary antenna. The received signals carrying the desired information travel clockwise through the circulator to the information channel in which a variable attenuator and a phase shifter as well as a band-stop filter with center frequency at 10.0 GHz are inserted. In addition to that reference

signals are edited by mixing a 10 GHz signal derived from the auxiliary power source by means of a directional coupler with a portion of the test signal derived in a similar manner. As the information signals and the reference signals are given to the E-arm and to the H-arm of a hybrid tee they will interfere at the input of an indicating receiver connected to a side arm of the hybrid tee. The receiver input signals will be of the form:

$$U_{RD} = K_R E_T C_T(r_T \theta_T \phi_T) E_H^2 C_H^2(r_H \theta_H \phi_H) \cos(\psi_H \mp \psi_T) \cos((\Omega_H \mp \Omega_T)t) \quad (17)$$

By appropriate adjustment of the attenuator and the phase shifter the receiver input signal can be made to vanish. Amplitude and phase variation of the desired field distribution then are obtained from the corresponding readouts.

If only amplitude measurements are of interest the information channel may be cut open behind the band-stop filter and connected directly to the receiver. Although the band-stop filter is not necessary for the measurement set-up in principle it is of significant importance to protect the receiver input against the power travelling counter clockwise from the 10 GHz signal source to the information channel because of the limited isolation of the circulator.

4.2.2. Set-up Regarding to 3.1.1. Using SSBSC Homodyne System

Despite its high dynamic range performance and its in principle simple instrumentation for point by point measurements when the field probe is moved it takes a large effort to set up a self-balancing microwave bridge for real-time measurements. In case of continuously moving the probe through the field of interest it seems very profitable to make use of the SSBSC homodyne system. For detailed information the reader is referred to an excellent survey given by R. J. King 4. The appropriate instrumentation using this single-sideband modulation technique is shown in Fig. 5.

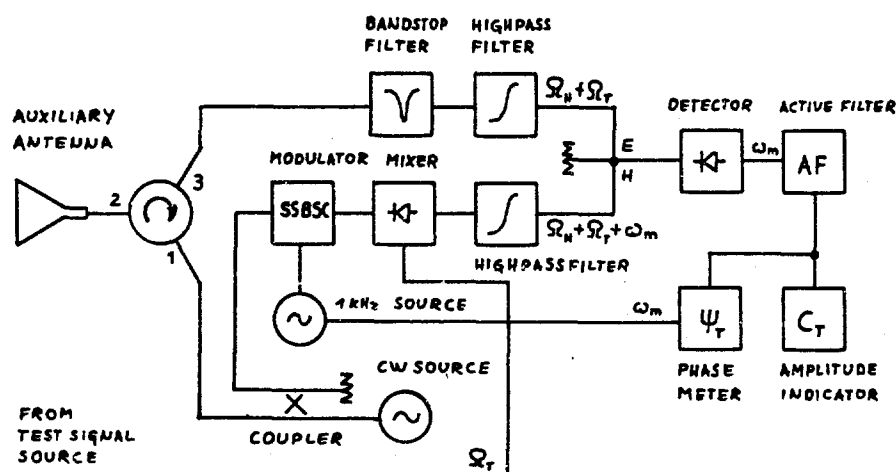


Fig. 5 Instrumentation with SSBSC Homodyne System

As a significant difference with respect to Fig. 4 it can be seen from Fig. 5 that the coherent 11.0 GHz signal of the reference channel has been replaced by an 11.000001 GHz SSBSC signal. This reference signal is generated by feeding a small signal derived from the 10 GHz auxiliary power source into a 10 GHz SSBSC-modulator and mixing the output signal up to 11 GHz with help of the test signal. As for the design of an effective SSBSC-modulator operating in the x-band a novel approach has been given by P. G. Brooker and J. D. E. Beyon 5. After passing the hybrid tee (to achieve good decoupling of both channels) the information and the reference signal are demodulated into the 1 kHz difference-frequency signal by means of a low-noise detector. To give a high sensitivity the detector is followed by a narrow band active RC-filter. Finally the output signal, which in contrast to (17) reads as

$$U_{RD} = K_D E_T C_T(r_T \theta_T \phi_T) E_H^2 C_H^2(r_H \theta_H \phi_H) \cos(\omega_m t + \psi_H \mp \psi_T) \quad (18)$$

where K_D is a constant and ω_m is the angular frequency of the demodulated 1 kHz signal, is given to an amplitude indicator and an AF-phase meter to read out the desired field quantities.

4.2.3. Set-up Regarding to 3.2. for Measurements in the Very Near Field of Antennas

As mentioned in 3.2. steps must be taken to eliminate the influence of the unavoidable back-scattering of the antenna under test. A measurement set-up to accomplish this is given by Fig. 6.

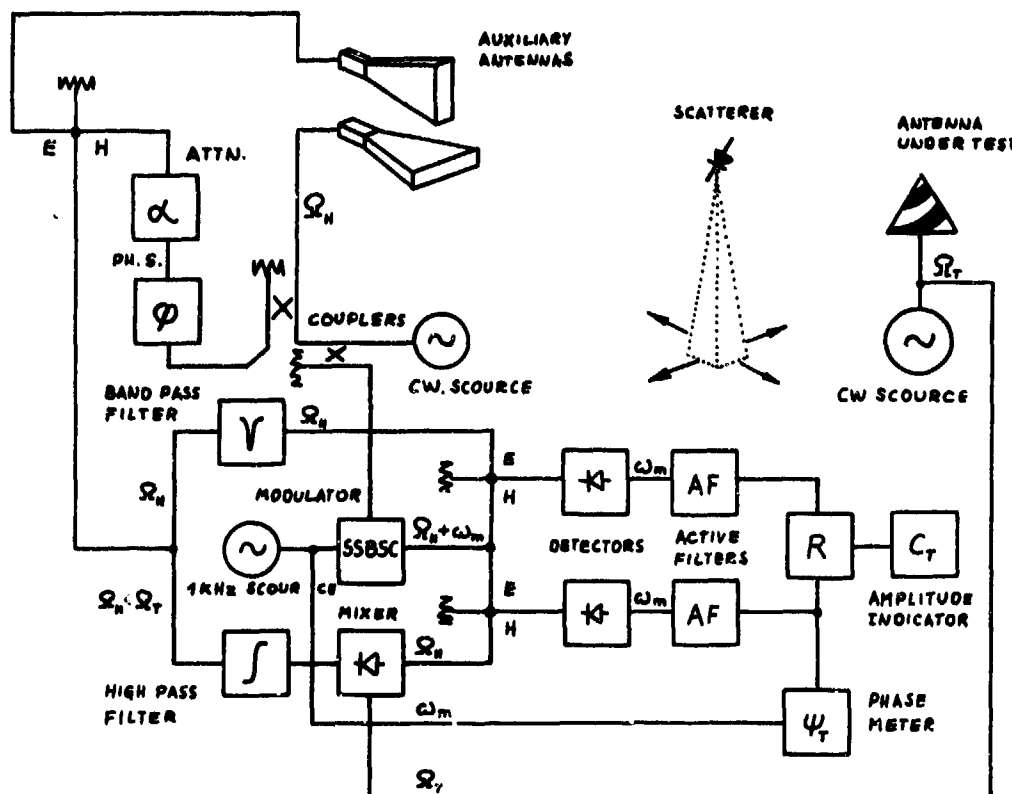


Fig. 6 Instrumentation with respect to the presence of back-scattering from the antenna under test

In opposite to the preceding instrumentations two separate linear polarized horns are used for transmission and reception. In consequence to the perpendicular orientation of both horns the receiving horn may be arranged to become decoupled from the transmitting horn in the order of 40 - 50 dB. Due to the residual coupling and to the back-scattering from the antenna under test two coherent small 10 GHz signals will read the receiving horn independently of the position of the scatter probe. Because of remaining unchanged if the antenna under test and the auxiliary horn are fixed these spurious signals, which represent the falsifying second term in the denominator of (16), can be eliminated from the measuring equipment, if an appropriate compensating signal is added by means of a hybrid tee. There needs to be no detailed further comment on the rest of the instrumentation, except that there are two separate SSU-modulated channels regarding to the carrier and to the upper sideband of the required scatter-signal. Finally the corresponding output signals are fed into a ratiometer for readout.

At least it should be emphasized that the plane of polarization of the scatter probe and that of the horns have to be inclined by 45°.

Extensive investigations of the different types of instrumentation are on test and have not been finished so far. Thus the outstanding final results will be object to future publication.

5. CONCLUSION

The scattering technique has been considered to be that measuring method for sampling the entire field characteristic of antennas to have the lowest reactive effect on the desired field distribution. Based on this technique a novel scattering method was introduced that makes use of a microwave diode scatterer to convert the required information of the field characteristic to the x-band, where it can be transmitted to a remote antenna and easily separated from the signal of the antenna under test. This method happens to give rise to errors if the probe is moved to the vicinity of the antenna surface because of unavoidable back-scattering from the antenna under test. In order to eliminate the erroneous back-scattering influence an evaluation method has been suggested which relates to the modulation factor of the scatter signal, e. g. the ratio of its carrier to its sideband signal. By the way this evaluation method removes the most significant disadvantage of the scattering techniques used so far, that is half the dynamic range capability of the direct reading probe methods. The corresponding theoretical background has been discussed and three measurement set-ups were presented for different operational conditions.

6. REFERENCES

1. J. Brown, E. V. Jull, "The prediction of radiation patterns from near-field measurements", Proc. Inst. Elec. Eng. vol. 10 S, pt. B, no 42, pp 635 - 644, Nov. 1961
2. W. M. Leach, Jr., D. T. Paris, "Probe compensated near-field measurements on a cylinder", IEEE Trans. AP, vol. AP-21, no 4, pp 435 - 445, July 1973
3. J. D. Dyson, "Measurements of near fields of antennas and scatterers", IEEE Trans. AP, vol. AP-21, no 4, pp 446 - 460, July 1973
4. R. J. King, "Real-time measurements of microwave parameters and EM fields", IEEE Trans. IM, vol. IM-21, pp 2 - 11, Febr. 1972
5. P. G. Brooker, J. D. E. Beyon, "A 10-GHz single sideband modulator with 1-kHz frequency shift", IEEE Trans. MTT, vol. MTT-19, pp 829 - 834, Oct. 1971

DETERMINATION OF THE MOVEMENT OF THE
APPARENT PHASE CENTRES OF AIRCRAFT
ANTENNAS FOR CALIBRATING THE ZDBS
INTERFEROMETER

A. Schrott and S. Modabber
 Institut für Flugfunk und Mikrowellen
 Deutsche Forschungs- und Versuchsanstalt für Luft- und Raumfahrt
 8031 Oberpfaffenhofen, Germany

SUMMARY

A new method for the determination of the curve on which the apparent phase centres of an aircraft antenna move with respect to the aspect angles is presented in this paper. The definition of the apparent phase centre is discussed.

The test equipment is explained by means of a schematic diagram. The sources of error of the measuring method and the accuracy of the approximation method for the analytical determination of the phase function are also discussed.

For the calculation of the apparent phase centres from the measured data an ALGOL computer program was developed.

Finally, the development and the optimization of the radiators meeting the requirements is described

1. INTRODUCTION

The motive for this work was the problem of calibrating the interferometer of the Zentrale Deutsche Bodenstation (ZDBS) (ÜTTL, H., GÜSSL, H., 1972).

All unpredictable influences like unevenness of the ground, mechanical tolerances etc. are eliminated by the calibration. During actual measurements the results will be corrected using the calibration data.

The position in space of a flash light mounted on the aircraft seen from the interferometer is determined by a photographic measuring system supported by a precision radar.

Ideal conditions would exist if it were possible to construct an aircraft antenna so that the phase centre from which the radiation seems to emanate is at the centre of the flash light for all aspect angles. To obtain the desired calibration accuracy for the interferometer for a distance of 10 km between aircraft and interferometer it is necessary to know the position of the apparent phase centre to an accuracy of 10 cm. At a frequency about 137 MHz it isn't possible to obtain a phase centre which is nearly at the same place for all aspect angles.

For the calibration of the interferometer, radial and circular flights are required. During the flights for the calibration the same profile of the aircraft is seen by the interferometer. With radial flights, for instance, only the phase characteristic of the section through the longitudinal axis of the aircraft is of interest. Due to the different influences of the ground reflections with horizontal or vertical polarization the aircraft antenna shall radiate circular polarization.

Radiators which meet the electrical, mechanical and flow demands are the crossed-slot antenna and the Archimedian spiral antenna. The crossed-slot antenna is used for the radial flights and is mounted in the middle part of the fuselage. The spiral antenna is used for the circular flights and is mounted in the left tip tank. Model measurements were carried out on a one-tenth scale model to find the best possible installation point for the antennas in the aircraft, namely an 'English Electric Canberra'. Because of the physically restricted conditions of installation both antennas had to be electrically

extended. For the crossed-slot antenna this was realized by capacitive reduction of the slots. The Archimedian spiral antenna was electrically extended by using a dielectric.

For the determination of the curve on which the apparent phase centres move with respect to the aspect angles a new method was evolved. In an iterative approach the shape of the wave front is determined. As the wave front is known, its evolute (locus of the apparent phase centre) may be constructed with the help of differential geometry. The method permits the determination of the wave front of radiators with large aperture, utilising a conventional antenna test range in connection with a phase measuring system.

2. APPARENT PHASE CENTRES

2.1. Definition of the Locus of the Apparent Phase Centres of Radiators on Bodies of Complicated Structure

If the wave front is approximated by the surface of a sphere, normals can be constructed to the surface and their point of intersection is defined as the radiator phase centre. In most cases, only in particular directions may the wave front be approximated by the surface of a sphere. In this case, the point of intersection of the normals is called the 'apparent phase centre'.

For radiators which are mounted on bodies of complicated structure and which excite the body, it is difficult to define, even for small zones of the solid angle, an apparent phase centre. Depending on the aspect angle the apparent phase centre appears to move. To describe this phenomenon apparent phase centres are defined for infinitesimally small zones of the aspect angle. The phase centre curve is obtained by connecting all the apparent phase centres for various angles.

2.2. Curvature of a Surface, Determination of the Main Radii of Curvature

For a plane section in the local coordinate system of a radiator, the curve on which the apparent phase centres move depending on aspect angle is the evolute of the wave front. For a point M on the wave front, the apparent phase centre is situated at the centre of the circle of curvature for the point M. In the general case, the three dimensional wave front at the point M may not be approximated by the surface of a sphere.

Depending on the section chosen through M on the three dimensional wave front different centres of curvature and radii of curvature result. Only for normal sections may physically significant results be obtained. For each normal section through M a different apparent phase centre occurs. All these apparent phase centres lie, however, on a line between two extreme points, the so called main radii of curvature. The direction from which the radiation at the point M emanates, may be determined by taking any normal section through M (see figure 1).

The curvature of a normal section C_{norm} is:

$$(1) \quad \frac{1}{R} = \frac{\cos^2 \alpha}{R_1} + \frac{\sin^2 \alpha}{R_2}.$$

R_1 and R_2 are the main radii of curvature. α is the angle between the sections C and C_1 (see figure 2).

3. METHODS FOR DETERMINING APPARENT PHASE CENTRES FROM MEASURED DATA

For the determination of apparent phase centres there are two basic methods, the phase reference method and the interferometer method (JONES, I.L., 1967). With the phase reference method, a single receiving antenna is used, the phase of the radiated wave being compared with a reference signal propagated via a coaxial cable from the antenna under test to the phase measuring receiver. From figure 3 it may be seen that this method is most sensitive to movements of the apparent phase centre parallel to a line joining the model and the phase measuring receiver.

For $l \gg d$

$$(2) \quad \Delta \varphi \approx \frac{2\pi}{\lambda} d \sin \theta$$

holds.

Within the interferometer method, the relative phase of the signal arriving at a pair of antennas is measured. The interferometer method is most sensitive to movements of the apparent phase centre at right angles to a line joining the antenna under test and the interferometer antennas (see figure 4).

If $l \gg d$

$$(3) \quad \Delta\varphi = \frac{4\pi}{\lambda} d \sin \gamma \cos \beta.$$

For the determination of the curve on which the apparent phase centres move with respect to the aspect angles a new method was evolved. The method permits the determination of the wave front of radiators with large aperture, utilising a conventional antenna test range in connection with a phase measuring system.

The antenna under test is mounted on a dielectric rotating tower (see figure 5). The position of the antenna under test with respect to the rotating axis, which must be known very exactly, is determined with the help of an optical system. As the ground reflections and the back scattering from obstacles may be neglected, the rotation of the antenna under test is analogous to a movement of the sonde on a circle in a plane perpendicular to the axis of rotation (see figure 6). The phase is measured by the phase reference method.

If the antenna under test has a fixed phase centre, and if this phase centre is in the point of rotation (dimensional problem), the relative phase is constant in the whole measuring range.

To determine the curve on which the apparent phase centres move, the wave front must be known. From a phase diagram measured on a circle with radius R , centre O , (see figure 6) the shape of the wave front in the plane of the section is obtained, if one draws from each measuring point the equivalent length l_v for the relative phase in the direction of the appropriate apparent phase centre. Providing all apparent phase centres seen from each aspect angle α are within a not too large angular range $\pm \epsilon$, the wave front may be determined in an iterative way. To a first approximation the lengths corresponding to the relative phase are drawn in the direction of the point of rotation. This wave front of first order calculated point by point is approximated by a polynomial using the least squares method. The locus of the apparent phase centres of first order is obtained by constructing the evolute. In the next iterative step, the l_v components are drawn in the direction of the apparent phase centres of first order, so obtaining the wave front of second order. The convergence of the method is very good because of ϵ being small in practical cases.

4. MATHEMATICAL TREATMENT OF THE PROBLEM

For the approximate reproduction of empirical functions whole rational functions, polynomials, are used. Because of simple mathematical operations the polynomials are best suitable for numerical analysis. The representation of a function by means of a polynomial is possible in various ways (MEINARDUS, G., 1964). One kind of approximation, which is very suitable for the reproduction of empirical functions, is curve fitting by means of equalizing polynomials. The desired close approximation over a fixed interval is achieved for a minimum of the sum of the squares of the deviations (ZURMOHL, R., 1965).

The empirical function $y = f(x)$ or $r = f(\alpha)$ respectively is given by measured data $y_i = f(x_i)$ ($r_i = f(\alpha_i)$). These values of the function are subject in general to errors. An interpolation polynomial which approximates the imperfect values y_i at the points x_i exactly is therefore not applicable. The result of the approximating function should be similar to a hand-drawn curve which suppresses the fluctuations. This is obtained with the aid of the balancing procedure. The order of the polynomial is lower than the number of measurement values. The surplus values are used for the suppression of the fluctuations. Correct selection of the order of the polynomial is essential.

The system of equations for the determination of the coefficients of a second order polynomial

$$(4) \quad y(x) = a_0 + a_1 x + a_2 x^2$$

is derived in the following.

The sum of the squares of the deviations of all ordinates y_i shall be a minimum, therefore

$$(5) \quad Q = \sum_{i=1}^N (\bar{y}_i - y_i)^2 = \min.$$

with

$$(6) \quad \bar{y}_i = \bar{y}(x_i) = a_0 + a_1 x_i + a_2 x_i^2.$$

From the three necessary conditions for (5)

$$(7) \quad \frac{dQ}{da_j} = 0 \quad (j = 0, 1, 2)$$

and the derivations

$$\frac{\partial \bar{y}_i}{\partial a_0} = 1, \quad \frac{\partial \bar{y}_i}{\partial a_1} = x_i, \quad \frac{\partial \bar{y}_i}{\partial a_2} = x_i^2$$

the following equations are obtained:

$$\frac{1}{2} \frac{\partial Q}{\partial a_0} = \sum (\bar{y}_i - y_i) \cdot 1 = 0$$

$$\frac{1}{2} \frac{\partial Q}{\partial a_1} = \sum (\bar{y}_i - y_i) x_i = 0$$

$$\frac{1}{2} \frac{\partial Q}{\partial a_2} = \sum (\bar{y}_i - y_i) x_i^2 = 0.$$

Or with the usual abbreviation of Gauß, representing sums by means of brackets, finally:

$$(8) \quad \begin{aligned} N a_0 + [x] a_1 + [x^2] a_2 &= [y] \\ [x] a_0 + [x^2] a_1 + [x^3] a_2 &= [xy] \\ [x^2] a_0 + [x^3] a_1 + [x^4] a_2 &= [x^2 y]. \end{aligned}$$

This is a linear system of equations with a symmetrical scheme of coefficients. The sums are extended over the N observations x_i, y_i .

The explained procedure for a parabola of second order may be used without difficulty for polynomials of arbitrary order. The normal equations are:

$$(9) \quad \begin{aligned} N a_0 + [x] a_1 + \dots + [x^n] a_n &= [y] \\ [x] a_0 + [x^2] a_1 + \dots + [x^{n+1}] a_n &= [xy] \\ \dots &\dots \\ [x^n] a_0 + [x^{n+1}] a_1 + \dots + [x^{2n}] a_n &= [x^n y]. \end{aligned}$$

After curve fitting the wave front points, the evolute can be determined with the following formulae (BRONSTEIN, I.N., 1964):

a) cartesian coordinates

$$(10) \quad \begin{aligned} y &= f(x) \\ x_c &= x - \frac{\frac{dx}{dy} \left[1 + \left(\frac{dy}{dx} \right)^2 \right]}{\frac{d^2 y}{dx^2}}, \quad y_c = y + \frac{1 + \left(\frac{dy}{dx} \right)^2}{\frac{d^2 y}{dx^2}} \end{aligned}$$

b) polar coordinates

$$(11) \quad \begin{aligned} r &= f(\alpha) \\ x_c &= r \cos \alpha - \frac{(r^2 + r'^2)(r \cos \alpha + r' \sin \alpha)}{r^2 + 2r'^2 - rr''} \\ y_c &= r \sin \alpha - \frac{(r^2 + r'^2)(r \sin \alpha - r' \cos \alpha)}{r^2 + 2r'^2 - rr''} \end{aligned}$$

x_c and y_c are the coordinates of the centres of curvature.

5. TEST EQUIPMENT, COMPUTER PROGRAM

The measurement of the phase diagrams and the directivity of the investigated antennas was carried out on antenna test range 2 of the Institut für Flugfunk und Mikrowellen of the DFVLR on a one-tenth scale model (see figure 7) (MATTE, H., 1972). The block diagram of the test equipment for the measurement of the relative phase and the directivity of an antenna is shown in figure 8.

For the calculation of the position of the apparent phase centres depending on aspect angles an ALGOL computer program was written (SCHROTT, A., FORSTER, H., 1973).

6. SOURCES OF ERROR

The method of the determination of the apparent phase centres from the phase characteristic is very sensitive to phase errors. For instance a phase error of 1° at the frequency of 1.37 GHz between two measuring points with an aspect angle difference of 5° causes an error of 7 mm in the lateral coordinate of the apparent phase centre.

Sources of error are: ground reflections, reflections from the dielectric tower, the model attachment and the phase reference cable, vibrations of the tower and changes in the cable delay because of temperature fluctuations.

The accuracy of the analytical construction of a function known point for point is shown by means of two mathematical models. Figure 9 represents the evolute of the approximated curve of a calculated wave front of a point source with the coordinates $x = 8.66$, $y = -5$ (cm). The transient errors in the approximated curve are clearly seen. To avoid transient errors in the actual zone of aspect angles, overlapping zones are added to this zone. Figure 10 represents the evolute of an elliptical wave front. The marked points are the nominal values.

The use of polynomials with the order $n \geq 15$ leads, due to the restricted accuracy of the computer (for short computer time single precision was used) to numerical problems so that the maximal order of the polynomials used was 14. For the approximation of phase characteristics with numerous points of inflection due to the limitation of the order of the polynomials the actual zone must be subdivided.

7. AIRCRAFT ANTENNAS FOR THE CALIBRATION OF THE ZDBS INTERFEROMETER

For the calibration of the interferometer of the "Zentrale Deutsche Bodenstation" (ZDBS) in Weilheim-Lichtenau with the help of an aircraft special antennas for the frequency range 136 - 138 MHz were developed and optimized.

Due to the different influences of the ground reflections with horizontal or vertical polarization, the aircraft antenna shall radiate circular polarization. Radiators which meet the electrical, mechanical and flow demands are the crossed-slot antenna and the Archimedian spiral antenna. The crossed-slot antenna, which is mounted in the middle part of the fuselage, is used for the radial flights and the Archimedian spiral antenna, which is mounted in the left tip-tank, for the circular flights. The models of the crossed-slot antenna and the Archimedian spiral are shown in figures 11 and 12.

Model measurements were carried out on a one-tenth scale model to find the best possible installation point for the antennas in the aircraft, namely an 'English Electric Canberra' (see figure 13). Because of the physically restricted conditions of installation both antennas had to be electrically extended. For the crossed-slot antenna this was realized by capacitive reduction of the slots. The Archimedian spiral antenna was electrically extended by using a dielectric. In figures 14 and 15 sketches of the crossed-slot antenna, the Archimedian spiral antenna and their feed networks are shown.

The crossed-slot antenna can be matched with the following methods:
Change of the position of the feed points, increasing capacitive reduction of the slots and variation of the depth or the resonator (the other dimensions of the resonator are physically restricted). The antenna

was matched so that the bandwidth of the antenna was a maximum, the depth of the resonator a minimum and the adjustment of the capacitive loads and the feeding points uncritical.

For good circular polarization the ends of the Archimedian spiral antenna are terminated with a matched load. The optimum phase difference between both arms of the antenna is achieved by adjusting a phase shifter at the feed point. The energy radiated from the back is absorbed with a high quality broad band absorber material. Therefore the depth of this antenna is also very small.

In the centre of both antennas the flash light for the optical ranging system will be mounted.

The coordinate system for the representation of the radiation patterns is shown in figure 16. For radiation patterns of the crossed-slot antenna see figures 17 - 22. The radiation patterns of the Archimedian spiral antenna are presented in figures 36 - 41. The beam of the Archimedian spiral antenna locks upwards to compensate the average roll angle of the aircraft in the circular flights.

The coordinate systems for the representation of the phase characteristic and the apparent phase centres are shown in figure 23 (crossed-slot antenna) and figure 42 (Archimedian spiral antenna). For the crossed-slot antenna, the origin of the coordinate system is in the point of intersection of the slots. For the Archimedian spiral antenna the origin of the coordinate system is in the feed point of this antenna.

In figures 24 - 35 the measured phase characteristic, the approximated phase characteristic and the x- and y-components of the apparent phase centres of the crossed-slot antenna for the polarizations E_θ , E_ϕ and left-hand circular are presented (great circle section $\phi = 0^\circ$). The normalized electrical field strength is drawn on a linear scale.

In the figures 43 - 54, the approximated phase characteristic and the x- and y-components of the apparent phase centres of the Archimedian spiral antenna for the polarizations E_θ , E_ϕ and left-hand circular are presented (great circle sections $\theta = 90^\circ$ for figures 43 - 51 and $\theta = 90^\circ$ for figures 52 - 54). In contrast to the crossed-slot antenna, because of mechanical restrictions of the positioner, the centre of rotation was not in the origin of the coordinate system.

In the actual zones of the aspect angles for the calibration

$(115^\circ \leq \theta \leq 135^\circ, \phi = 0^\circ)$ crossed-slot antenna,

$(80^\circ \leq \phi \leq 100^\circ, \theta = 90^\circ)$ Archimedian spiral antenna)

the movement of the apparent phase centre is relatively small.

8. CONCLUSIONS

The position of the apparent phase centres with respect to the aspect angle of two aircraft antennas for the calibration of the interferometer of the "Zentrale Deutsche Bodenstation" was determined. For the analysis of the measuring data a computer program was written. For the determination of the curve on which the apparent phase centres move with respect to the aspect angles a new method was evolved. In an iterative approach the shape of the wave front is determined. As the wave front is known its evolute may be constructed with the help of differential geometry.

Two special aircraft antennas were developed and optimized. Model measurements were carried out on a one-tenth scale model to find the best possible installation point for the antennas in the aircraft, namely an "English Electric Canberra". The achieved directivity as well as the position of the apparent phase centres with respect to the aspect angles is satisfactory.

Acknowledgements

The authors wish to acknowledge the assistance of their colleagues Mr. Forster and Mr. Hounam.

REFERENCES

- BRONSTEIN, I.N., 1964, "Taschenbuch der Mathematik", Verlag Harri Deutsch, Frankfurt/M, Zürich.
- JONES, I.L., 1967, "Movements of the Phase Centre of I.L.S Airborne Localizer Aerials on a Varsity Aircraft", AGARD Convergence Proceedings No. 15, pp. 67 - 96.
- MATTES, H., 1972, "Neue Meßanlage für Bordantennen in Oberpfaffenhofen", DFVLR Nachrichten No. 6, April 1972, pp. 226 - 229.
- MEINARDUS, G., 1964, "Approximation von Funktionen und ihre numerische Behandlung", Springer Verlag, Berlin, Göttingen, Heidelberg, New York.
- OTTL, H., GUSSL, H., 1972, "Ein Radio-Interferometer für 136 bis 138 MHz mit beweglichen Richtantennen im Bau", NTZ No. 6, pp. 300 - 304.
- SCHROTT, A., FORSTER, H., 1973, "Rechenprogramm zur Bestimmung der Ortskurve der scheinbaren Phasenzentren von Strahlern auf Körpern komplizierter Struktur aus Meßdaten", DFVLR Oberpfaffenhofen, intern report 003 (551)-73/7.
- ZURMOHL, R., 1965, "Praktische Mathematik für Ingenieure und Physiker", Springer Verlag, Berlin, Heidelberg, New York.

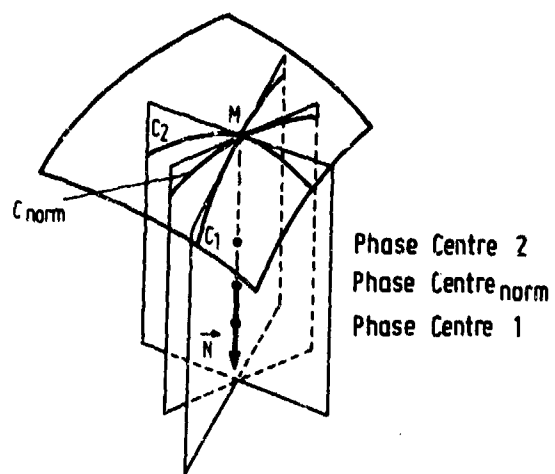


Fig.1 Position of the apparent phase centres of the point M due to several plane sections

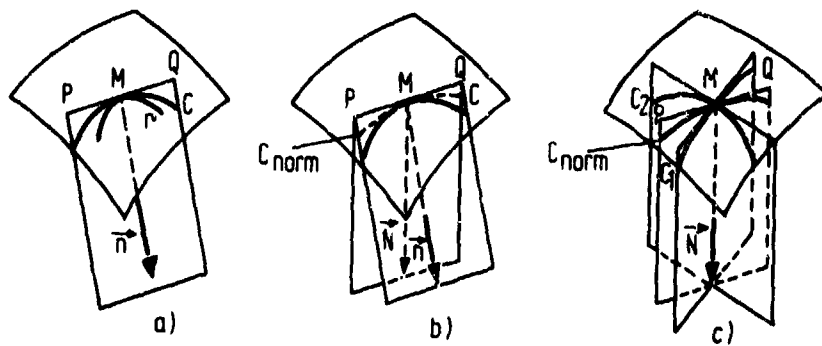


Fig.2 The construction of the radii of curvature

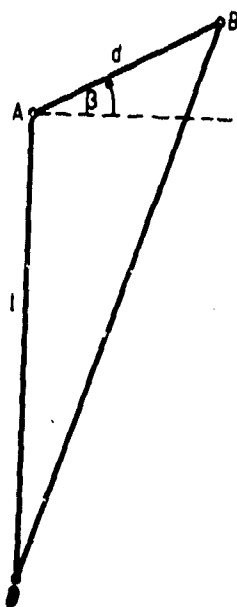


Fig.3 The phase reference method

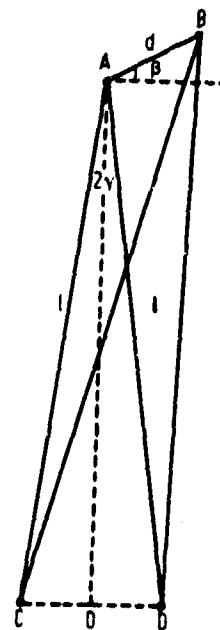


Fig.4 The interferometer method

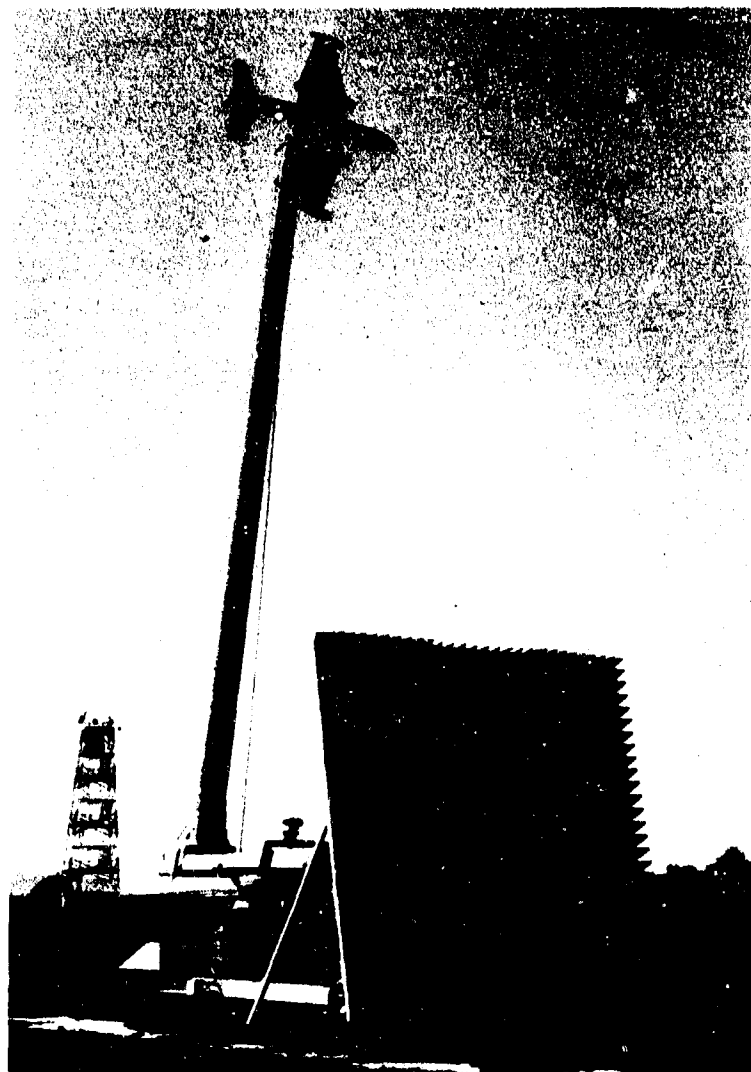


Fig.5 Positioner of the antenna test range II of the Institut für Flugfunk und Mikrowellen of the DFVLR

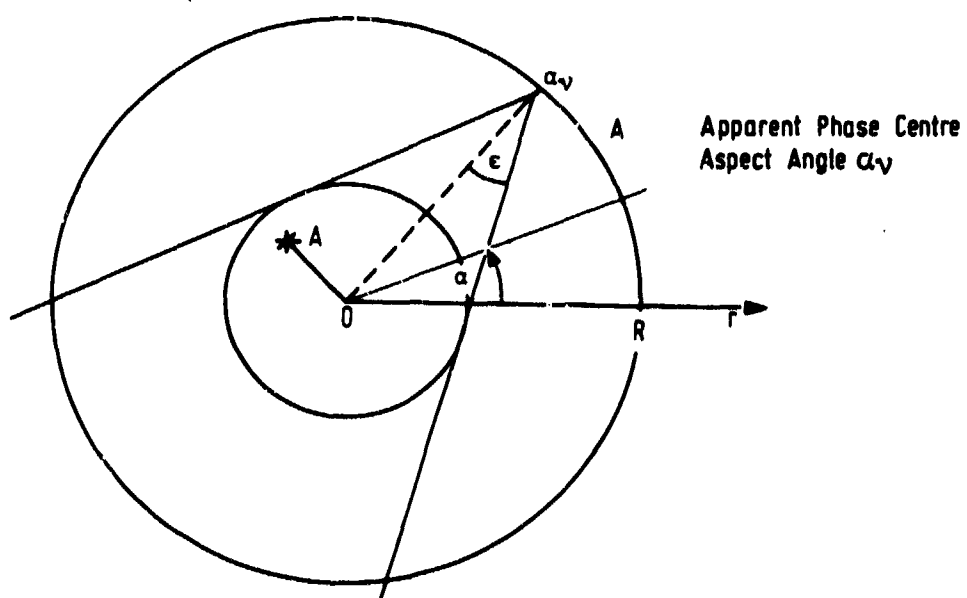


Fig.6 Representation of the measuring method

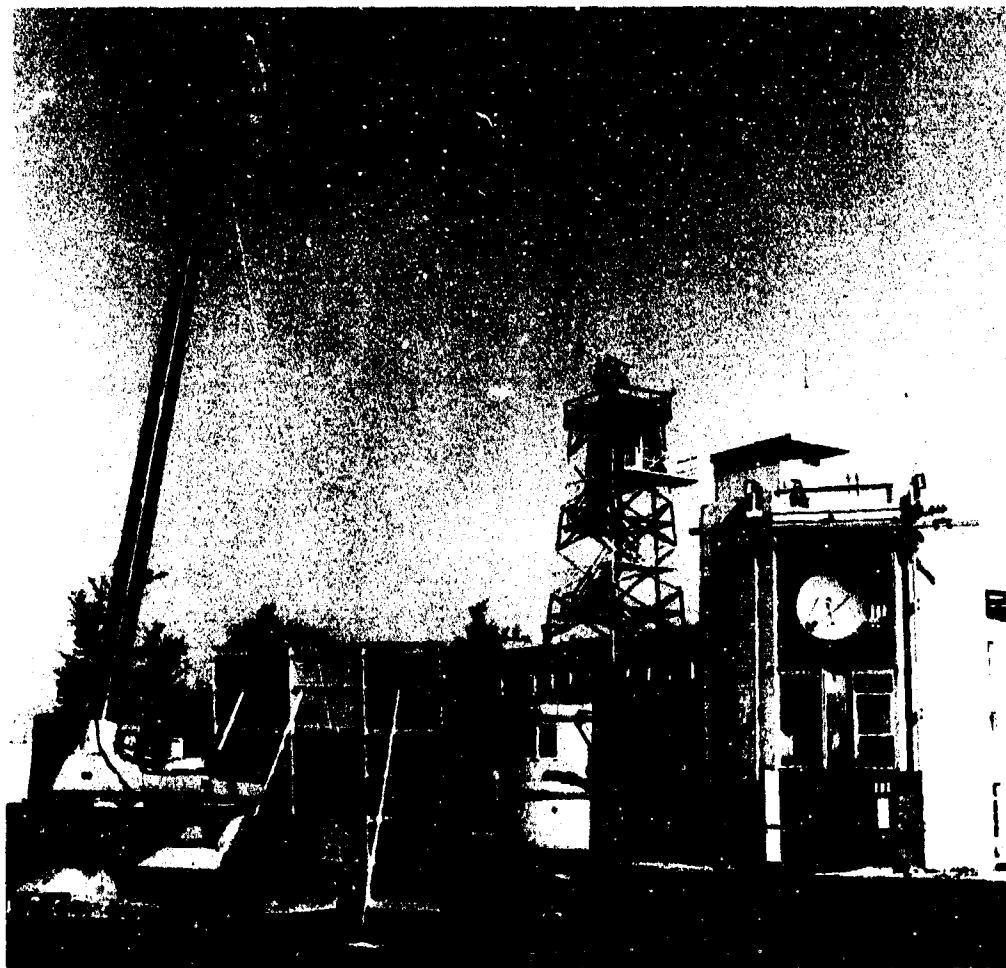


Fig.7 Antenna test range II

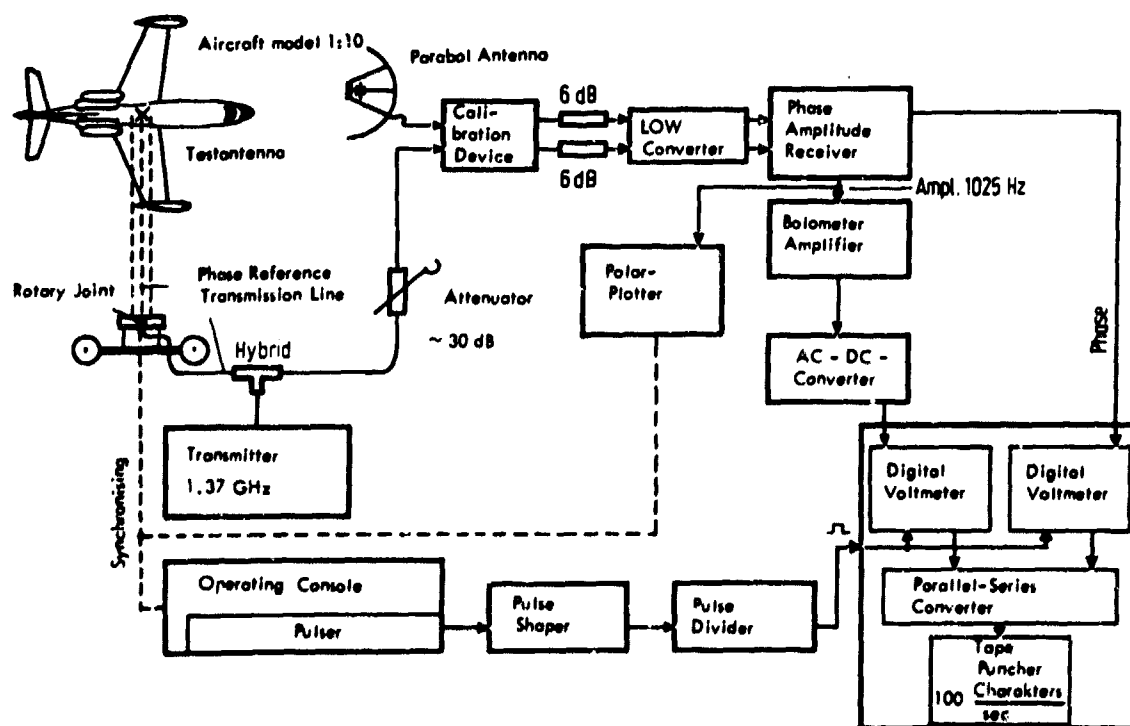


Fig.8 Phase and amplitude measuring system

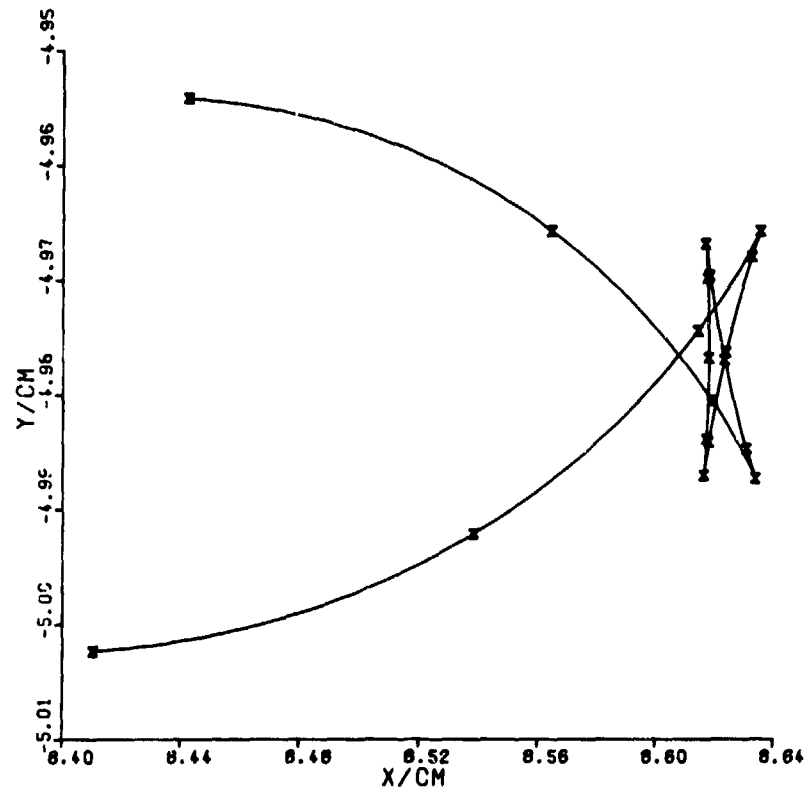


Fig.9 Approximation of a point source. Order of polynomial 6

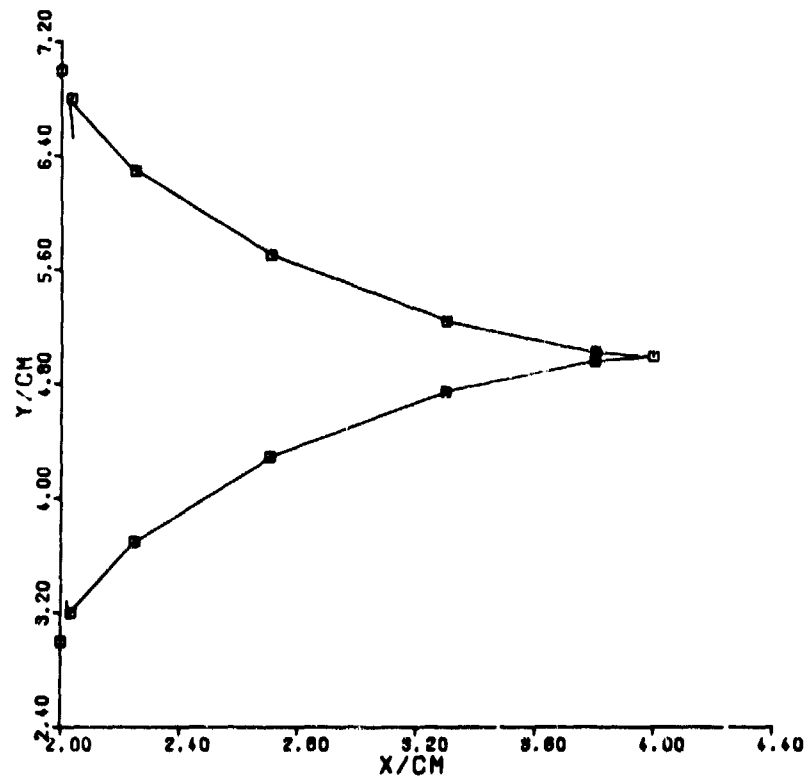


Fig.10 Evolute of an elliptical wavefront. Order of polynomial 6

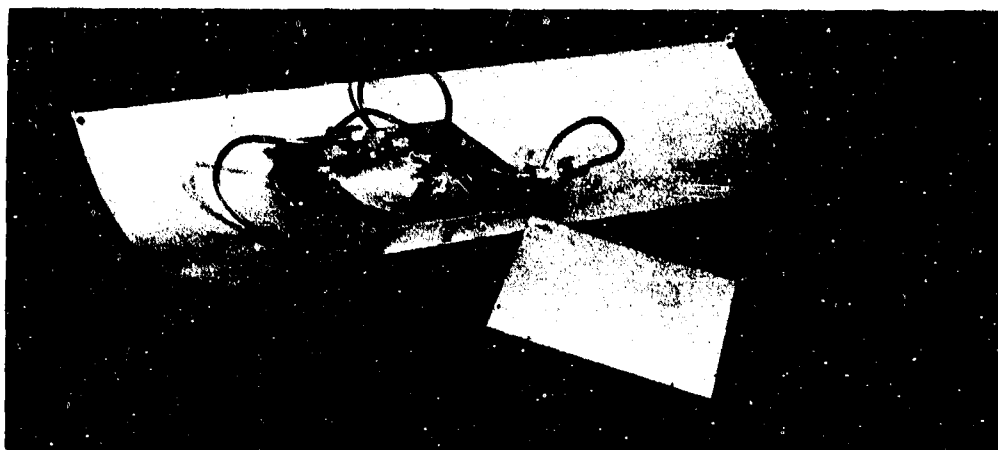


Fig.11 Crossed-slot model antenna



Fig.12 Archimedian spiral model antenna



Fig.13 English Electric Canberra

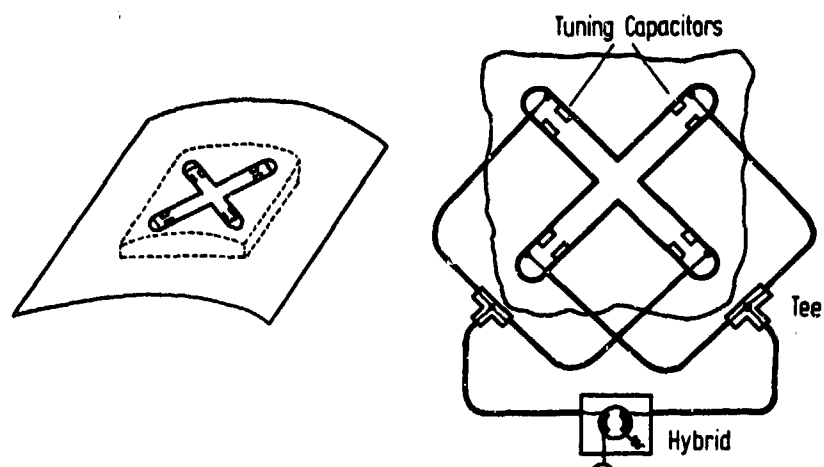


Fig.14 Crossed-slot antenna assembly. Schematic diagram

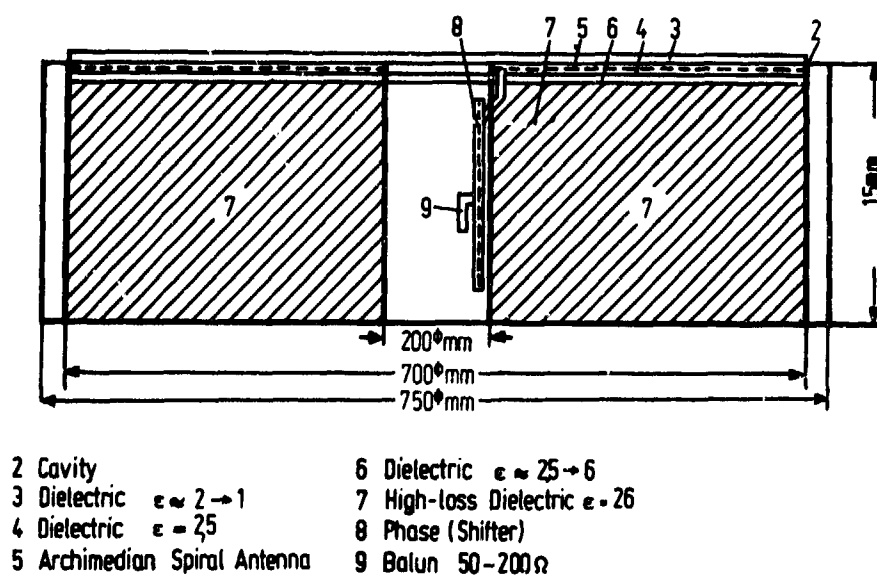


Fig.15 Archimedean spiral antenna assembly. Schematic diagram

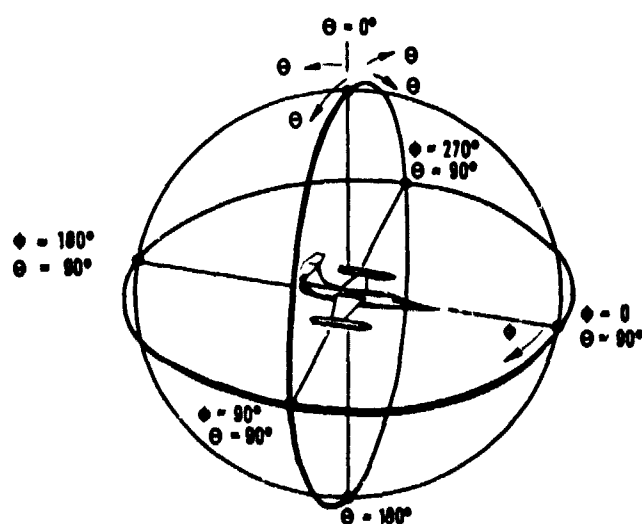


Fig.16 Coordinate system for the representation of the radiation patterns

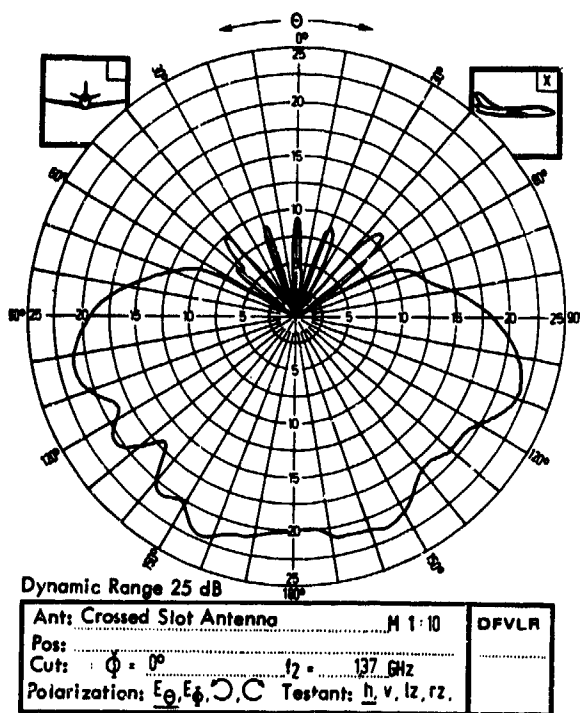


Fig.17 Great circle section $\Phi = 0^\circ$,
polarization E_θ

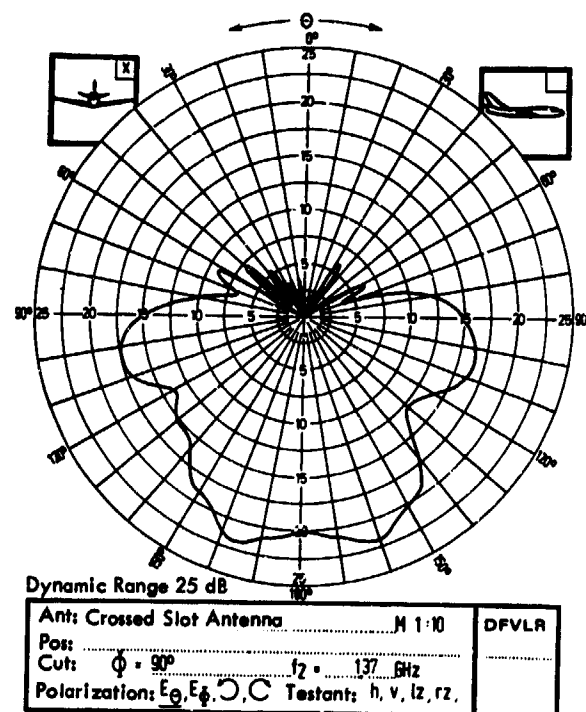


Fig.18 Great circle section $\Phi = 90^\circ$,
polarization E_θ

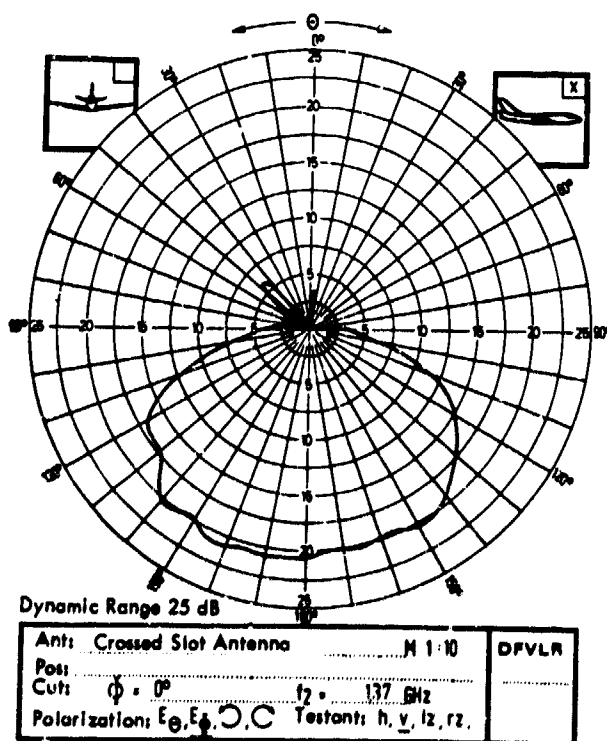


Fig.19 Great circle section $\Phi = 0^\circ$,
polarization E_ϕ

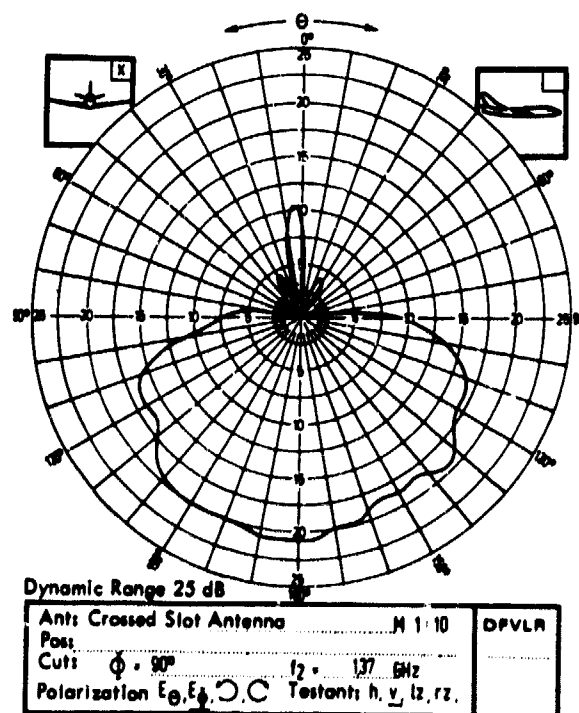


Fig.20 Great circle section $\Phi = 90^\circ$,
polarization E_ϕ

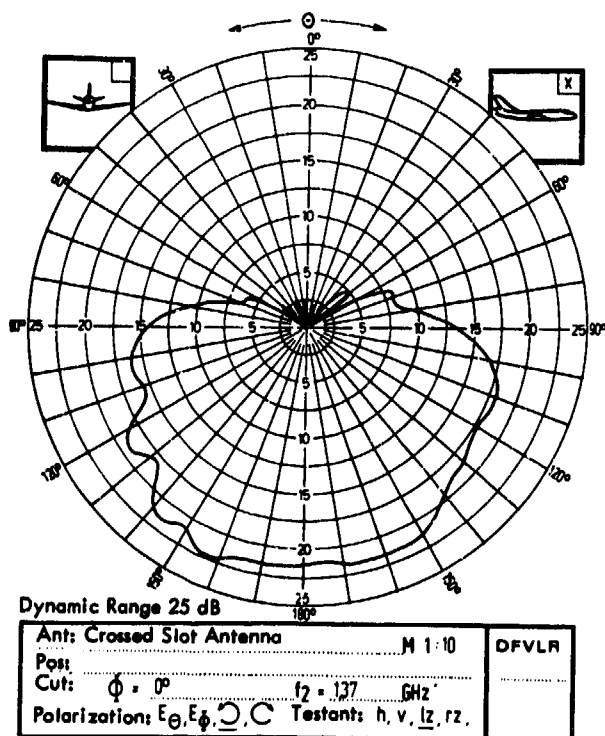


Fig.21 Great circle section $\phi = 0^\circ$,
left-hand polarization

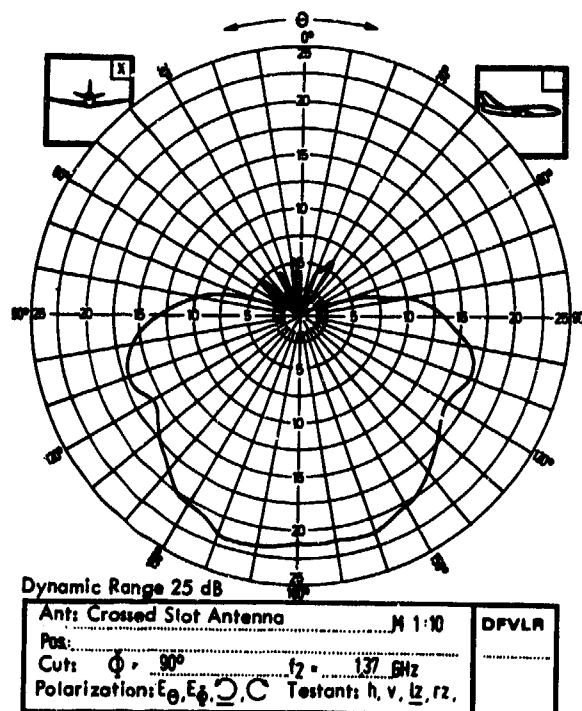


Fig.22 Great circle section $\phi = 90^\circ$,
left-hand polarization

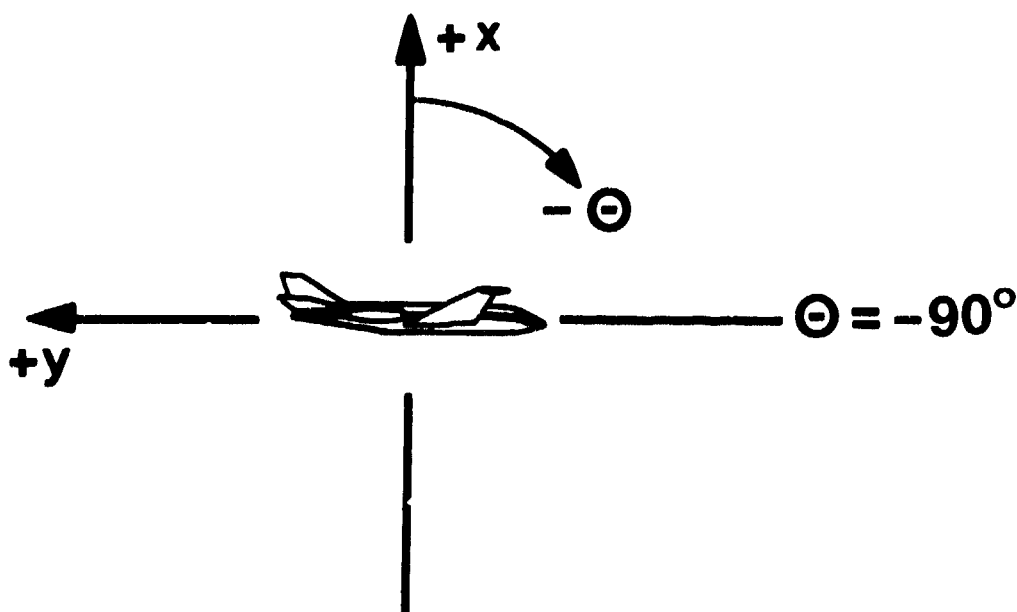


Fig.23 Coordinate system for the representation of the apparent phase centres of the crossed-slot antenna

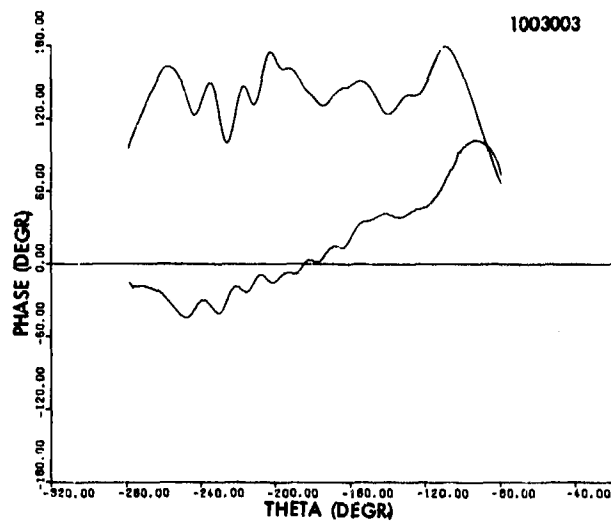


Fig.24 Relative phase and field strength with respect to the aspect angles, polarization E_{θ}

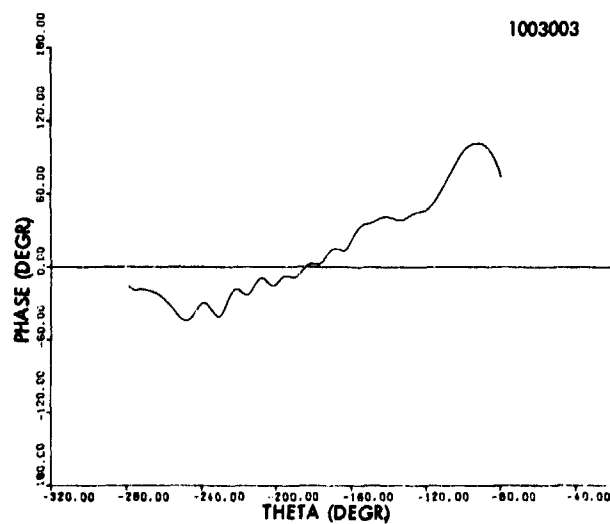


Fig.25 Approximated phase diagram, polarization E_{θ}

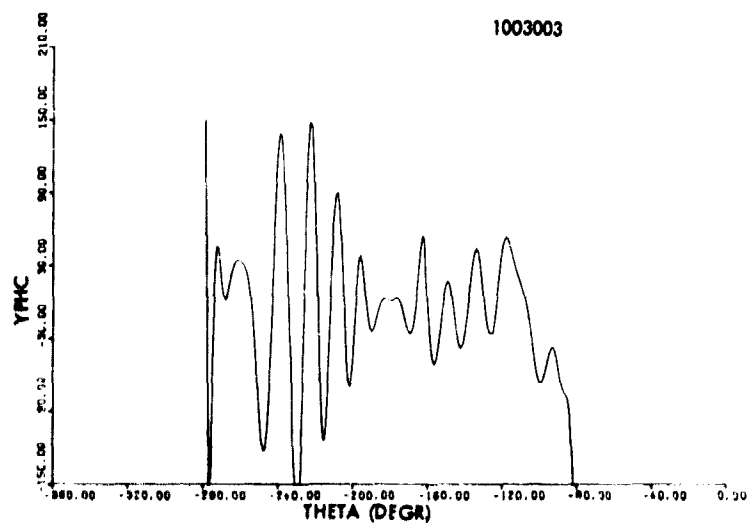


Fig.26 Y-component of the apparent phase centres, polarization E_{θ}

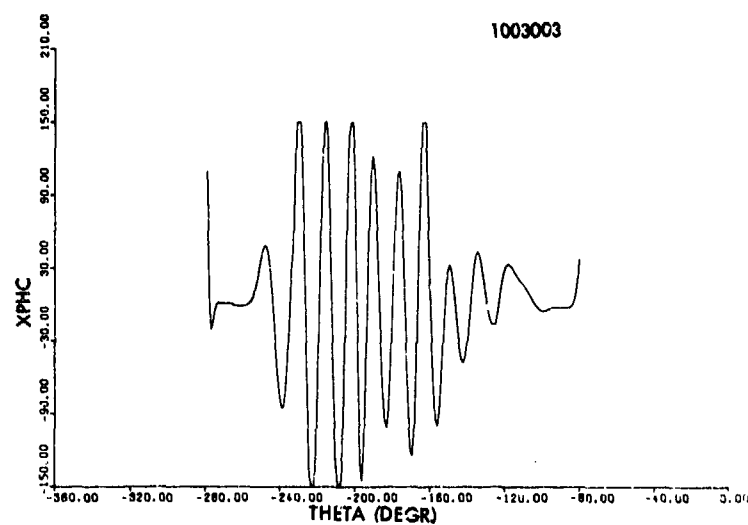


Fig.27 X-component of the apparent phase centres, polarization E_θ

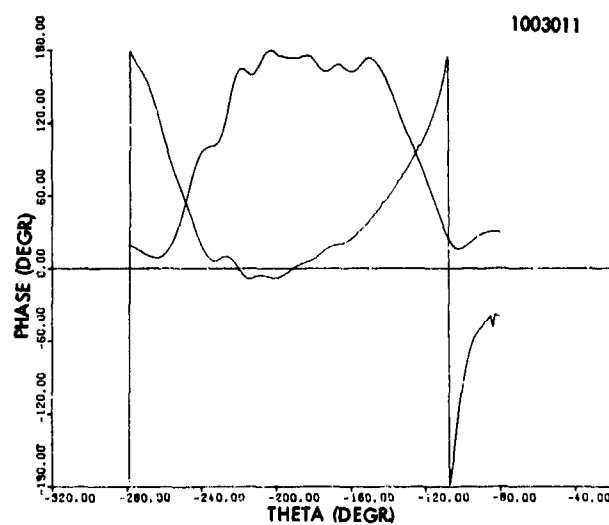


Fig.28 Relative phase and field strength with respect to the aspect angles, polarization E_ϕ

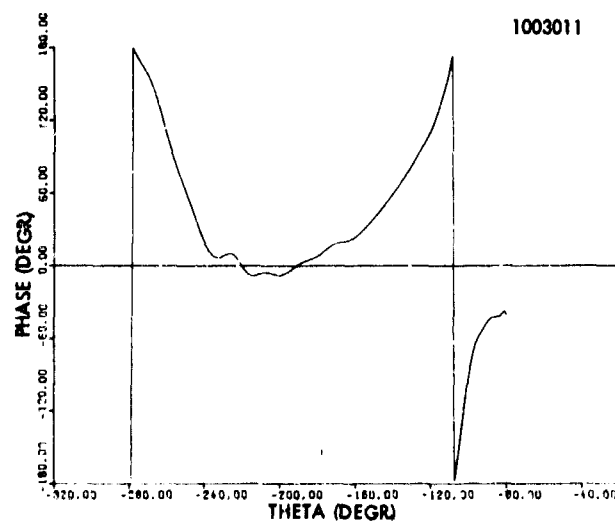


Fig.29 Approximated phase diagram, polarization E_ϕ

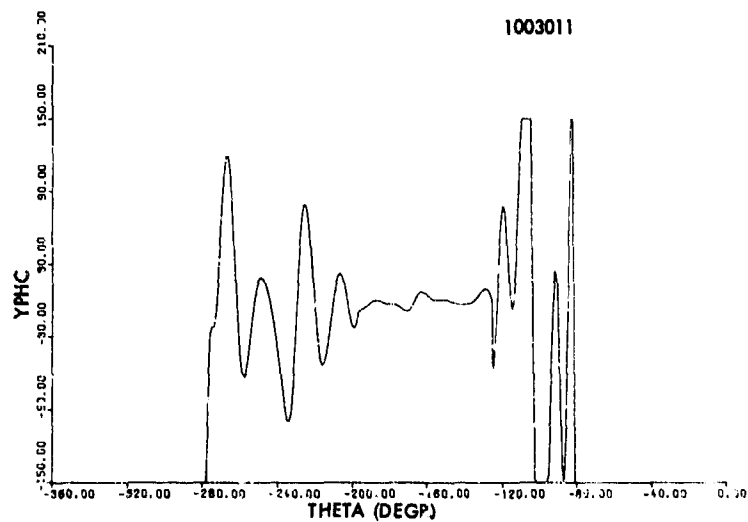
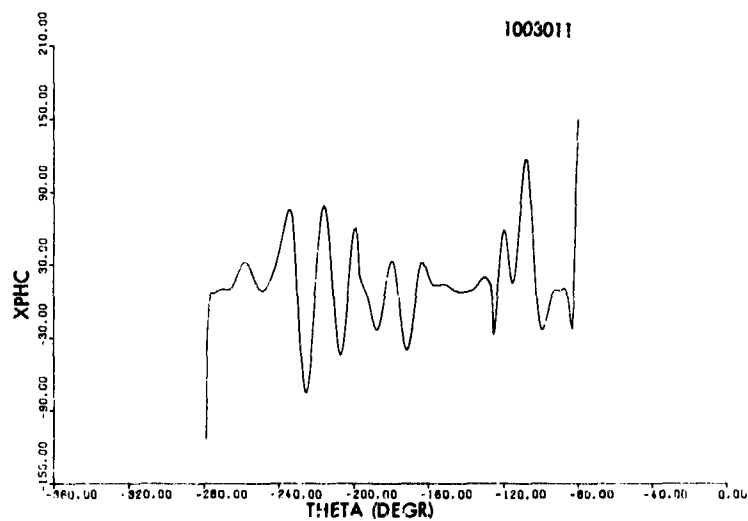
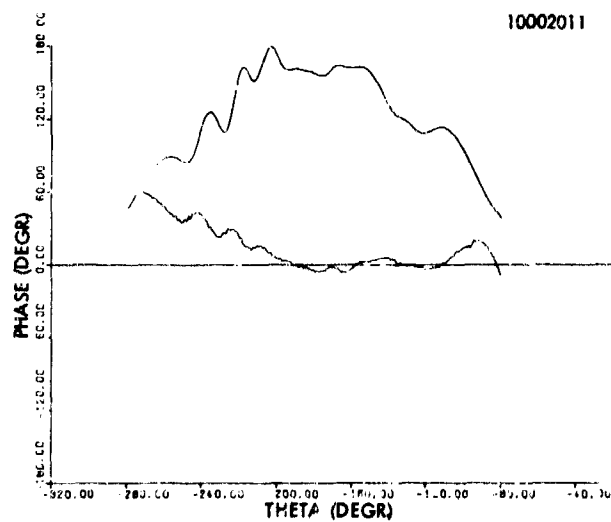
Fig.30 Y-component of the apparent phase centres, polarization E_ϕ Fig.31 X-component of the apparent phase centres, polarization E_ϕ 

Fig.32 Relative phase and field strength with respect to the aspect angles, left-hand polarization

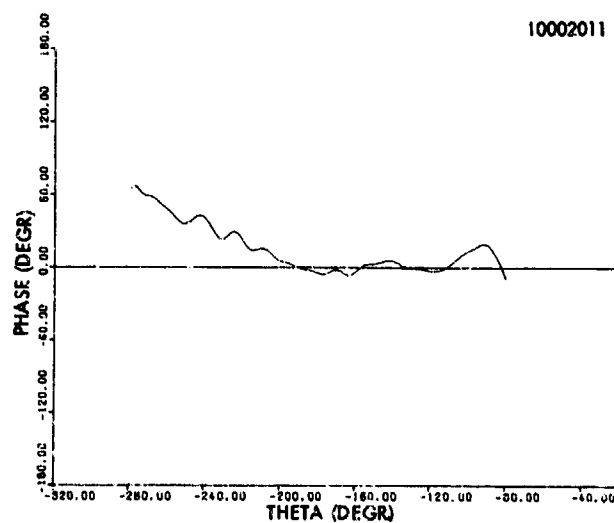


Fig.33 Approximated phase diagram, left-hand polarization

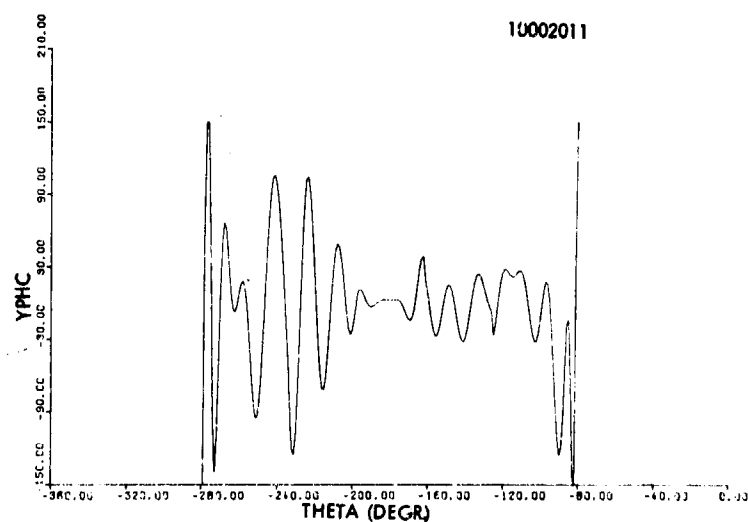


Fig.34 Y-component of the apparent phase centres, left-hand polarization

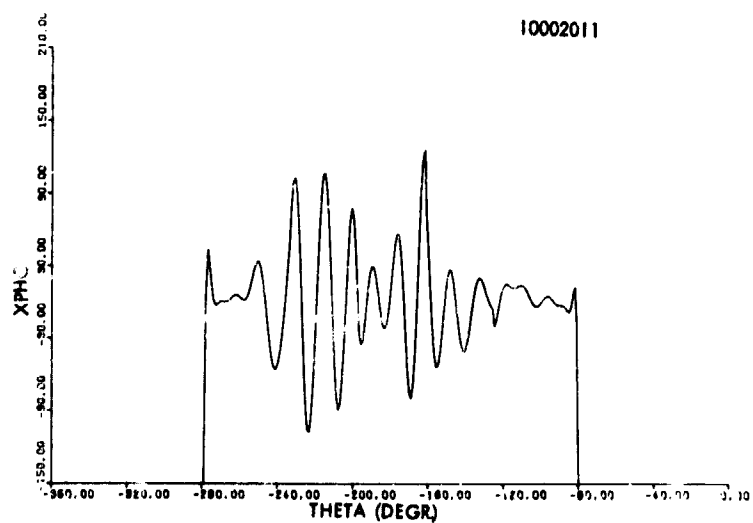


Fig.35 X-component of the apparent phase centres, left-hand polarization

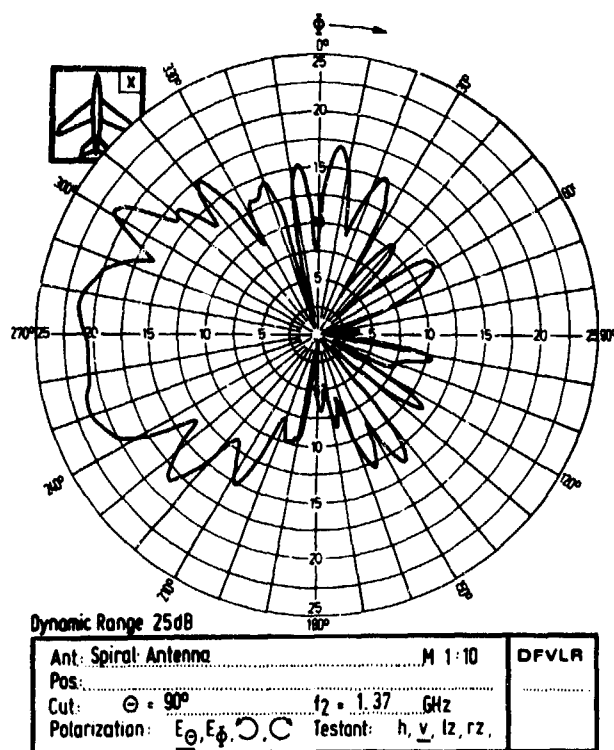


Fig.36 Great circle section $\Theta = 90^\circ$,
polarization E_Θ

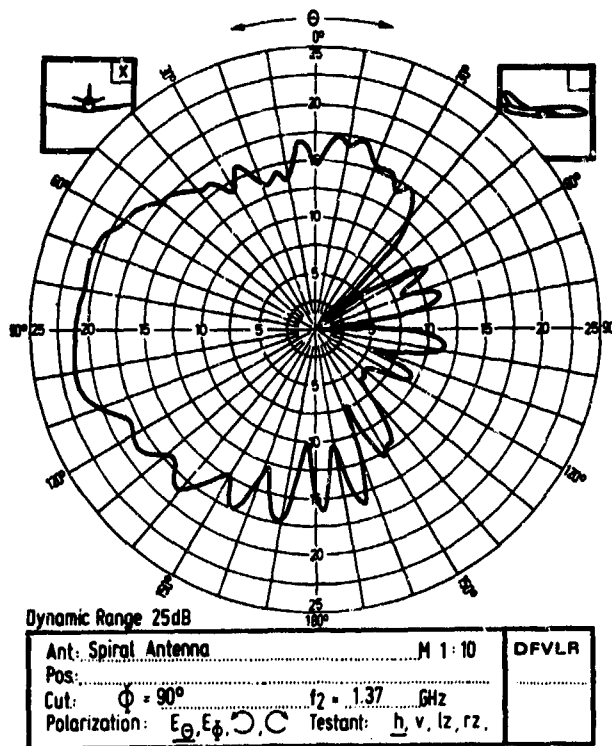


Fig.37 Great circle section $\Phi = 90^\circ$,
polarization E_Θ

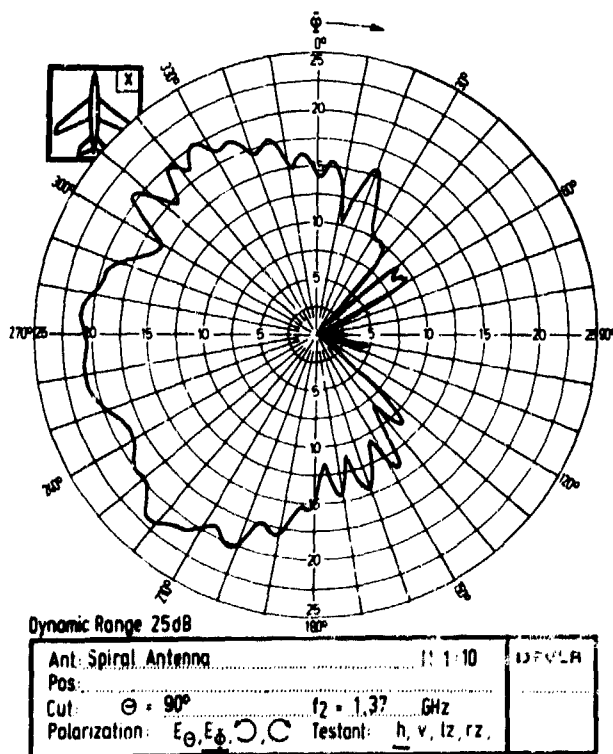


Fig.38 Great circle section $\Theta = 90^\circ$,
polarization E_Φ

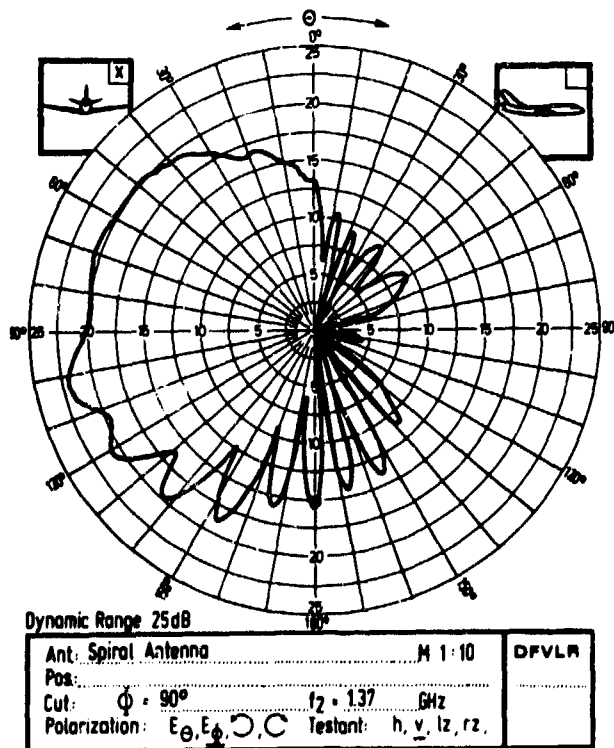


Fig.39 Great circle section $\Phi = 90^\circ$,
polarization E_Φ

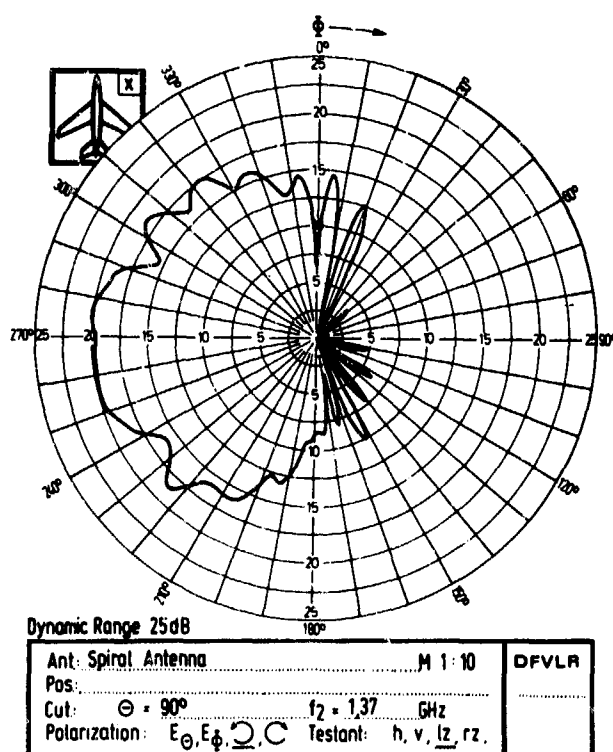


Fig.40 Great circle section $\Theta = 90^\circ$, left-hand polarization

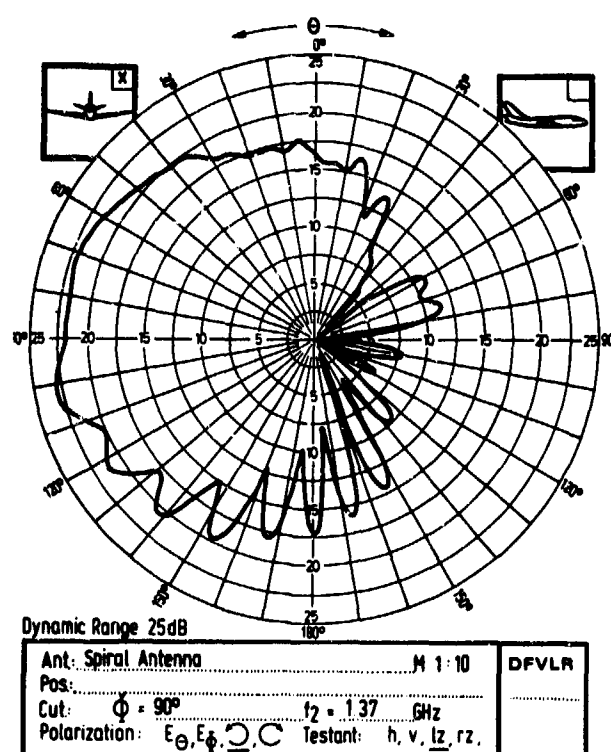


Fig.41 Great circle section $\Phi = 90^\circ$, left-hand polarization

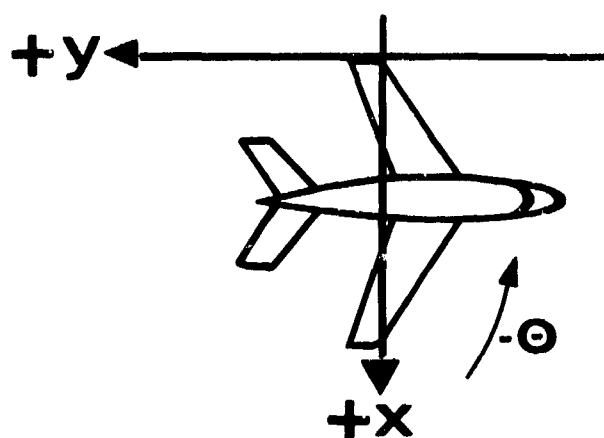


Fig.42 Coordinate system for the representation of the apparent phase centres of the Archimedian spiral antenna

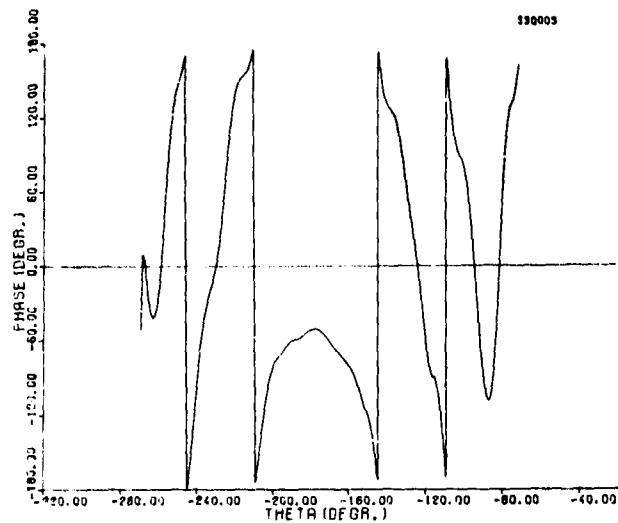


Fig.43 Approximated phase diagram, polarization E_{θ} , section $\theta = 90^{\circ}$

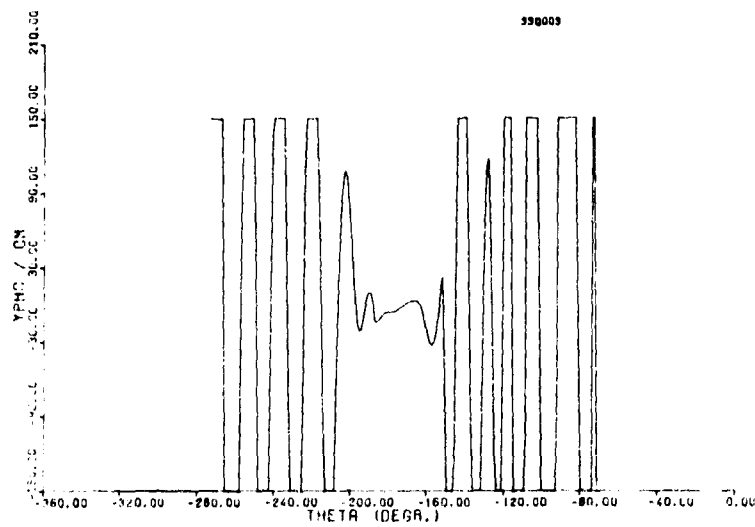


Fig.44 Y-component of the apparent phase centres, polarization E_{θ} , section $\theta = 90^{\circ}$

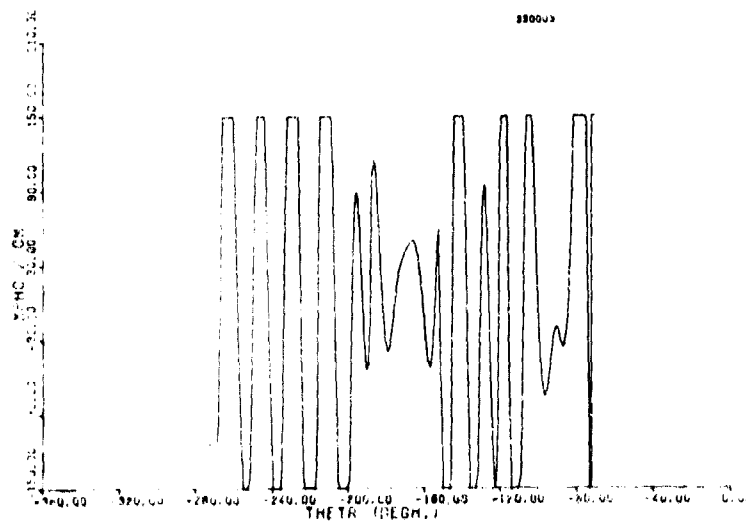


Fig.45 X-component of the apparent phase centres, polarization E_{θ} , section $\theta = 90^{\circ}$

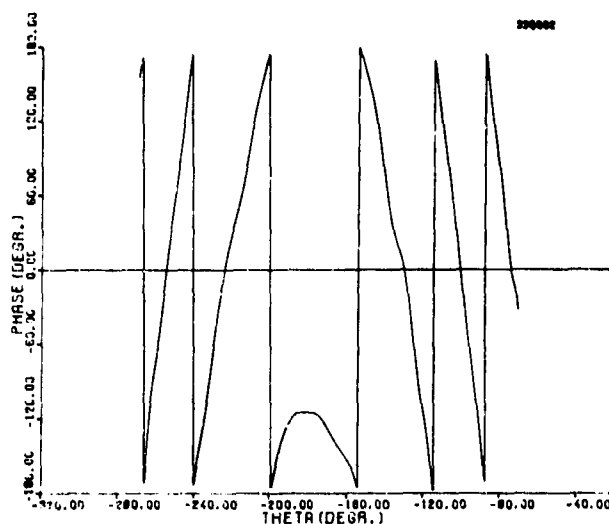


Fig.46 Approximated phase diagram, polarization E_ϕ , section $\Theta = 90^\circ$

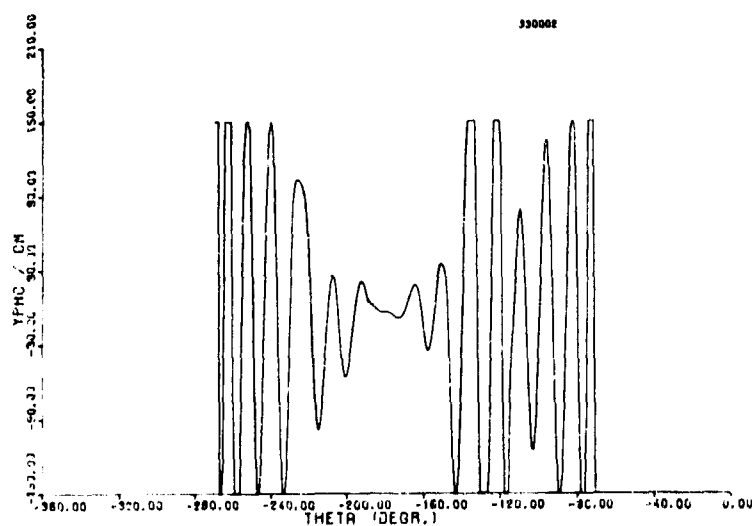


Fig.47 Y-component of the apparent phase centres, polarization E_ϕ , section $\Theta = 90^\circ$

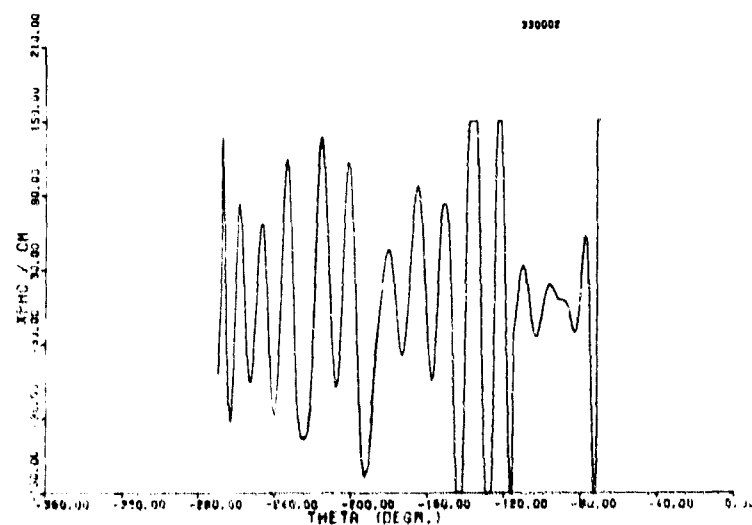


Fig.48 X-component of the apparent phase centres, polarization E_ϕ , section $\Theta = 90^\circ$

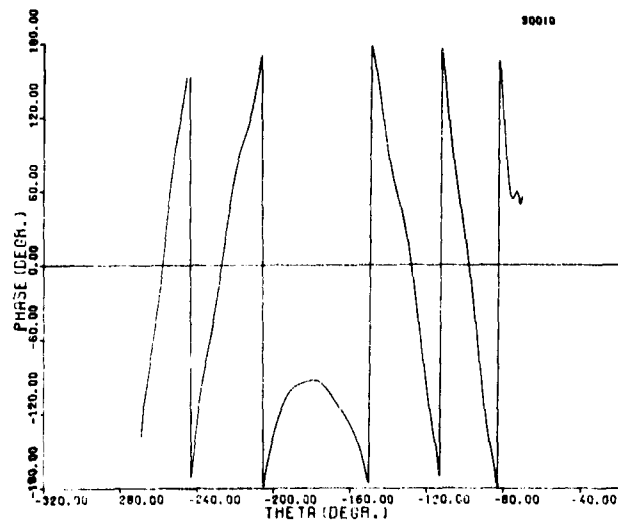


Fig.49 Approximated phase diagram, left-hand polarization, section $\Theta = 90^\circ$

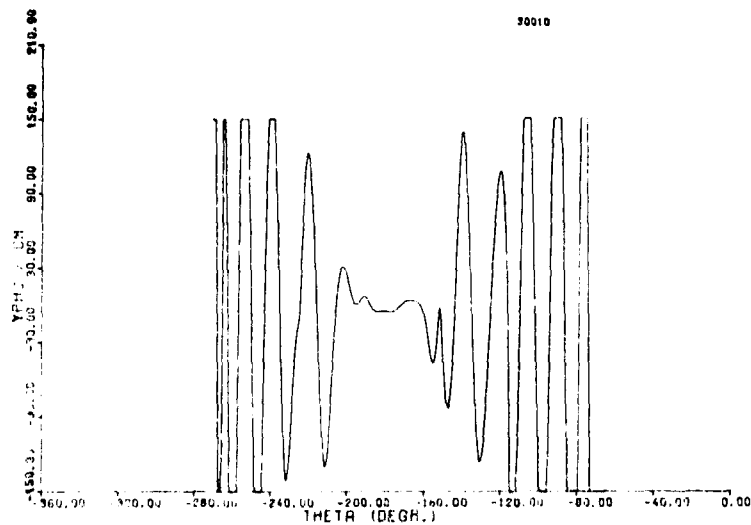


Fig.50 Y-component of the apparent phase centres, left-hand polarization, section $\Theta = 90^\circ$

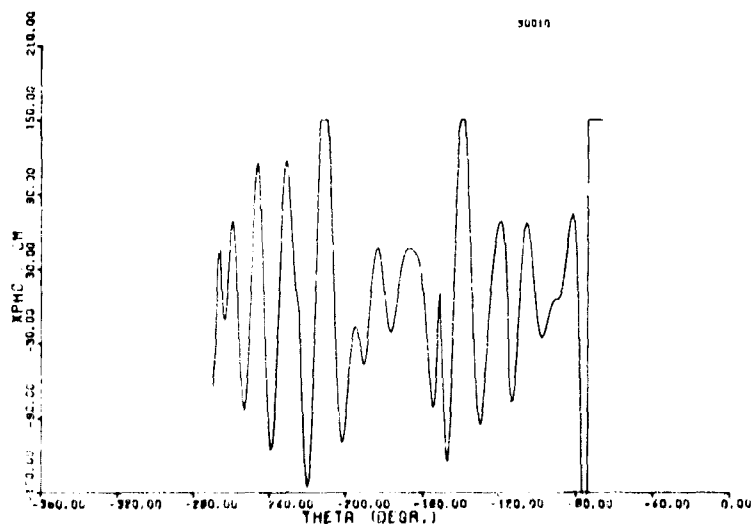


Fig.51 X-component of the apparent phase centres, left-hand polarization, section $\Theta = 90^\circ$

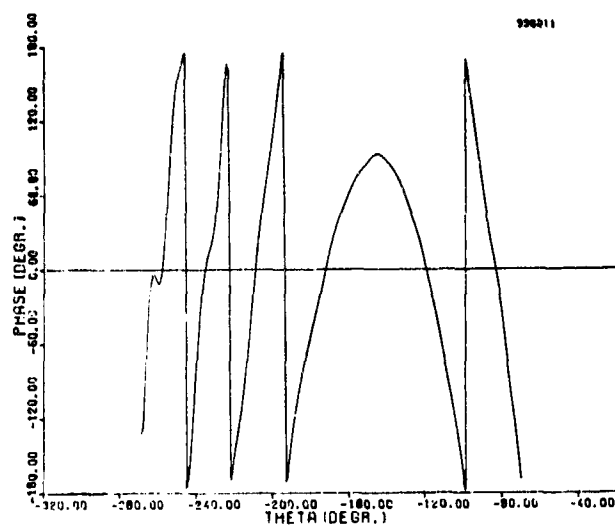


Fig.52 Approximated phase diagram, left-hand polarization, section $\Phi = 90^\circ$

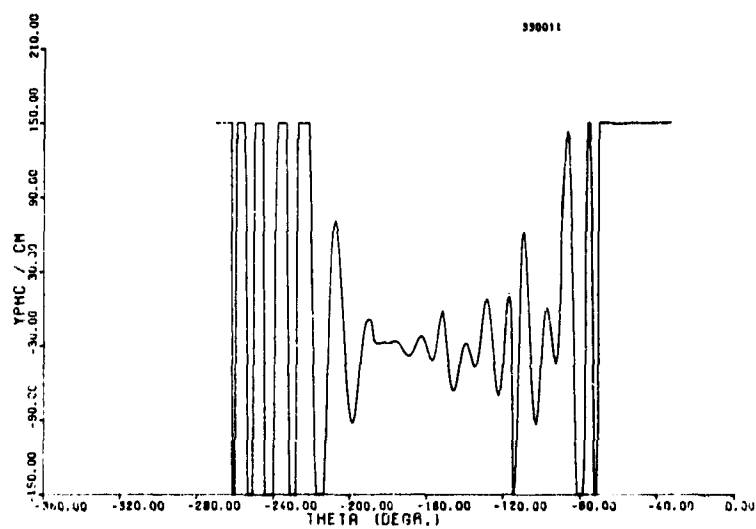


Fig.53 Y-component of the apparent phase centres, left-hand polarization, section $\Phi = 90^\circ$

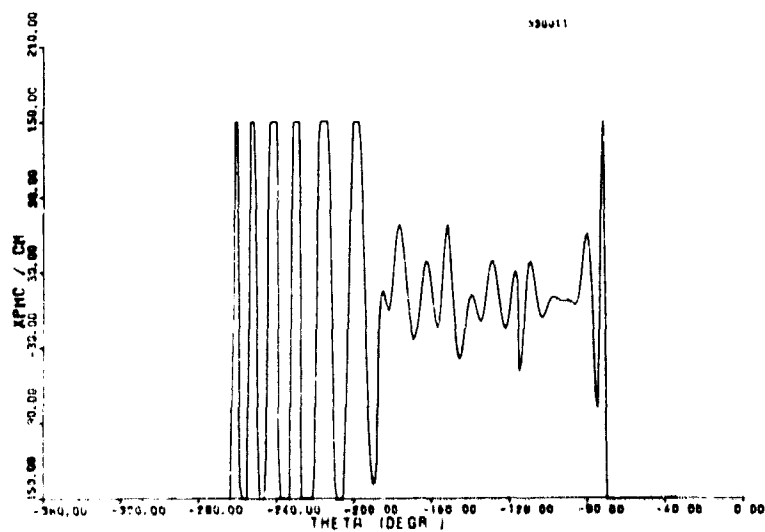


Fig.54 X-component of the apparent phase centres, left-hand polarization, section $\Phi = 90^\circ$

DISCUSSION

J.A. MARK: Can you explain why the apparent phase centre movement is so much greater with the spiral antenna than with the crossed slot antenna.

A.SCHROTT: This movement of the phase centre was a result of the different points of installation of the two antennas rather than any difference between spiral and crossed slot.

R.H.J. CARY: At Lichtenau there is a tower used to calibrate the interferometer arrays. Have any flights been done with an aircraft to compare the model experiments and the tower calibration?

H. OTTL: The boresight tower in the Lichtenau is only needed for amplitude and phase pattern measurements of the interferometer ground antennas.

The airplane with the crossed slot antenna and the archimedian spiral acts as an artificial satellite for calibrating purposes of the whole interferometer system (including antennas, pedestals, delays in the connecting cables, receiving system etc.).

The flight path of the plane will be photographed and compared against star position. So a calibration of interferometer is possible.

OFF-BORESIGHT ANGLE ESTIMATION
WITH A PHASE COMPARISON MONOPULSE SYSTEM

W. Sander
 Forschungsinstitut für Funk und Mathematik
 D 5307 Wachtberg-Werthhoven, Königstr. 2
 Germany

SUMMARY

This paper deals with the problem of estimating the angle of arrival with a phase comparison monopulse (PCM) system in the presence of internally generated thermal noise. A maximum likelihood analysis produces the form of the estimate which does not differ essentially from that found earlier for an amplitude comparison monopulse (ACM) system. In deriving the probability density function (pdf) of the estimate, no approximations of the nonlinear monopulse error curve are made. Therefore mean and variance of the estimate computed by numerical integration are valid at any signal-noise-ratio (SNR) and at any angle.

The bias of the estimate at low and moderate SNR is higher than known by other theories. A computer simulation proves the correctness of the results.

A comparison between radar and passive beacon tracking mode is made, and the problem of bidimensional angle measurement is mentioned.

1. INTRODUCTION

At the Forschungsinstitut für Funk und Mathematik (FFM) an experimental, ground-based, electronic radar system (ELRA) is designed and set up with the emphasis on the signal processing area. This project includes both the hardware:

- the electronic antenna (ELAN) consisting of separate active transmitting and receiving phased arrays in the S-band,
- the common phase shift arithmetic unit,
- coherent and incoherent signal processors, e.g. doppler filter and sequential detector,
- two process control computers TELEFUNKEN TR86,
- the main computer SIEMENS 4004/150,
- units for control and maintenance,

and the software:

- automatic test and diagnostic routines,
- search, acquisition and track procedures,
- air-traffic records, and synthetic air-traffic displays.

The active antenna ELAN has the following design features which have been presented in detail by WIRTH (1972). The transmitting antenna can be characterized by

- 500 printed folded-dipoles which are located on a circular $\lambda/2$ -grid with a diameter of about 43λ in a space-taper configuration (SÖNTGERATH, 1973),
- disc-seal triode amplifiers with 700 watts peak pulse power each,
- 3 bit PIN-diode phase shifter
- constrained feed.

The receiving antenna:

- 1300 channels consisting of a dipole followed by a balanced Schottky diode mixer, a low-noise IF-amplifier, a 3 bit phase shifter and a quadrature synchronous detector,
- five sum beams which are independently steerable by time multiplex switching in the search mode,
- a cluster of coherently formed beams (sum and difference) in the track mode.

A small version of the antenna with 25 transmitting and 39 receiving elements (ELAN 25/39) has been driven successfully. It has been described by GRÖGER (1972) and served mainly to test the components and their co-operation. The system will be expanded to 100/100 elements till the end of the year. Figure 1 shows the antenna cabins and the building which contains the signal processing units and the computers.

The antenna is to be used in an open-loop tracking scheme so that the question of the off-boresight angle measurement accuracy arises. Literature on this subject is sparse especially on PCM systems. The problem has been treated here in a more general way so that the results are extendable to other systems.

1.1 Some preliminaries

The cosines (u,v) of the angles between the direction of an incoming signal and the axis of a Cartesian co-ordinate system (x,y), which is based on the plane of the aperture, have been chosen as angular co-ordinates. That has the advantage, that the beamwidth expressed in these direction cosines does not change if the direction of the phased array is scanned away from the antenna normal. All numerical results are normalized to the 3dB-beamwidth of the sum beam. To get the informations in other co-ordinate systems, e.g. azimuth and elevation, the known transformation formulas have to be used (e.g. VON AULOCK, 1960).

The problem of angle measurement has been restricted to the unidimensional case. Deviations with bidimensional angle measurements are discussed at the end of the paper.

By "boresight" the electrical direction of the antenna is meant, which is given by the zero of the difference beam resp. by the peak of the sum beam and which may not correspond to the physical normal of the aperture of a phased array. Consequently off-boresight angles are those which differ from this direction but lie within the main beam of the sum pattern.

Numerical results are presented for the beacon track mode, that is, only the parameters of the receiving antenna are used. At the end of the paper the radar working mode is discussed.

2. ANGLE MEASUREMENT

2.1 Coherent beam forming

At the output of each channel of the receiving antenna the in-phase z_c and quadrature z_s components of the received signal are available. By summing them with equal weights the in-phase s_c and quadrature s_s components of the sum signal are generated.

$$s_c = \frac{1}{N} \sum_{i=1}^N z_{ci} = S(u) A \cos \varphi + n_1 \quad (1a)$$

$$s_s = \frac{1}{N} \sum_{i=1}^N z_{si} = S(u) A \sin \varphi + n_2 \quad (1b)$$

with

$A = \text{magnitude}$
 $\varphi = \text{phase}$ } of the received signal

$N = \text{number of elements}$

$S(u) = \text{real one-way sum pattern}$

$u = \text{direction cosine}$

$n_1, n_2 = \text{noise samples generated by thermal noise.}$

The main region of the sum pattern may be approximated by

$$S(u) = \frac{\sin(c_1 u)}{c_1 u} \quad (2)$$

with

$$c_1 = 2.78$$

Variable weights c_i are used to form the components d_c and d_s of the difference signal

$$d_c = \frac{1}{N} \sum_{i=1}^N c_i z_{ci} = -D(u) A \sin \gamma + n_3 \quad (3a)$$

$$d_s = \frac{1}{N} \sum_{i=1}^N c_i z_{si} = D(u) A \cos \gamma + n_4 \quad (3b)$$

with $D(u)$ = real one-way difference pattern.

A phase shift of $\pi/2$ occurs between sum and difference signal. The optimum weighting factors c_i have been found by ML analysis. They are proportional to the distance of the antenna element from the co-ordinate axis and normalized so that sum and difference beams give the same noise power output. BRENNAN(1962) has derived it in the special case of a linear array with equally spaced elements.

$$c_i = \frac{x_i}{\sqrt{\frac{1}{N} \sum_{i=1}^N x_i^2}} \quad x_i = \text{co-ordinate of the } i\text{-th element} \quad (4)$$

The main region of the difference pattern may be approximated by

$$D(u) = \frac{1 - \cos(c_2 u)}{c_2 u} \quad (5)$$

with

$$c_2 \approx 3.24$$

This manner to get the difference signal belongs to the phase comparison monopulse system. Since all antenna elements are arranged with their electrical axis parallel, an incoming signal causes the same amplitudes at all channel outputs but different phase shifts, which contain the angle information. Using a high number of elements, the main disadvantage of a PCM system, namely the sensitivity against relative phase shifts occurring in the mixer and IF-amplifier stages of the individual channels, has been avoided.

The four components of the sum and difference signal are combined to produce the normalized difference signal \hat{w} .

$$\hat{w} = \frac{s_c d_s - s_s d_c}{s_s^2 + s_c^2} \quad (6)$$

The signal w is corrupted by noise.

$$\hat{w} = w + n_5 \quad (7)$$

$$\text{with } w = w(u) = \frac{D(u)}{S(u)} \quad (8)$$

w is an odd function of the off-boresight angle u and has a pole at the first zero of the sum beam. Due to this pole the slope of the function becomes steeper with increasing angle.

2.2 The angle estimation procedure

A ML analysis demands to vary the angular position of the antenna until the normalized difference reaches zero. This very angle \hat{u} is the ML estimate in the case of a single hit system with amplitude and phase of the received signal unknown.

$$w(u) \Big|_{u=\hat{u}} = 0 \quad (9)$$

This procedure is unbiased but proves to be a closed-loop system which should be excluded in this analysis.

A suboptimum procedure uses the relationship between the normalized difference signal and the off-boresight angle.

$$\hat{u} = f(\hat{w}) \quad (10)$$

In the vicinity of the boresight (10) may be approximated by a straight line

$$\hat{u} = k_1 \hat{w} \quad (11)$$

or at greater off-boresight angles

$$\hat{u} = k_1 \hat{w} (1 + k_2 \hat{w}^2) \quad (12)$$

with k_1, k_2 constants.

In an analog manner the sum beam function (2) is replaced by a constant that does not take into account the decrease of the SNR when the target moves away from boresight. The estimate given by (11) or (12) is optimum only at $w=0$ that is for targets which happen to be at or near boresight.

With ELAN it is possible to form squinted sum beams by suitable choice of the weighting function of the beam forming network to simulate an ACM system, too. In this case the ML estimator has essentially the same form found in the PCM case with the difference that the components of the beams are no longer independent variables. The normalized correlation coefficient depends on the beam forming weighting function and decreases with increasing squint angle. It amounts about 0.77 at a squint angle of 0.5 bw (resp. 0.3 at 1.0 bw) and may not be neglected. In the PCM case the weighting functions are orthogonal resulting in a negligible small correlation.

So the results of this PCM system may be compared with those found by MOSCA (1968), who analysed an ACM system with no correlation between the beams. But compared to that work we succeeded in deriving the pdf of the estimate what gives more precise results in determining mean and variance of the estimate.

2.3 The probability density function of the estimate

At first we derive the pdf of the normalized difference signal \hat{w} , which is equivalent to the pdf of the off-boresight angle estimate \hat{u} , if (11) is used as angle estimator.

The four noise samples of the components of sum and difference signals are real, independent, Gaussian, random variables with zero mean and equal variance σ . Therefore the joint probability density function of the components conditioned on a signal source being at an angle u is given by

$$p_1(s_c, s_s, d_c, d_s | u) = \frac{1}{(2\pi\sigma^2)^2} \exp \left[-\frac{(s_c - SA \cos \varphi)^2 + (s_s - SA \sin \varphi)^2 + (d_c + DA \sin \varphi)^2 + (d_s - DA \cos \varphi)^2}{2\sigma^2} \right] \quad (13)$$

We transform these variables into an other space by the following one-to-one mapping.

$$\begin{aligned} w_1 &= s_c \\ w_2 &= s_s \\ w_3 &= d_c \\ \hat{w} &= \frac{s_c d_s - s_s d_c}{s_c^2 + s_s^2} \end{aligned} \quad (14)$$

The inverse transformation formulas are:

$$\begin{aligned} s_c &= w_1 \\ s_s &= w_2 \\ d_c &= w_3 \\ d_s &= \frac{w_2 w_3 + \hat{w} (w_1^2 + w_2^2)}{w_1} \end{aligned} \quad (15)$$

The Jacobian J of (15) is simply

$$J = \left| \frac{\partial d_s}{\partial \hat{w}} \right| = \frac{w_1^2 + w_2^2}{w_1} \quad (16)$$

The joint probability density functions of the old and new variables are related by (DAVENPORT, ROOT, 1958)

$$p_2(w_1, w_2, w_3, \hat{w} | w) = |J| \cdot p_1(s_c = w_1, s_s = w_2, d_c = w_3, d_s = \frac{w_2 w_3 + \hat{w} (w_1^2 + w_2^2)}{w_1}) \quad (17)$$

To get the wanted pdf of \hat{w} we must carry out an integration

$$p_3(\hat{w} | w) = \iiint_{-\infty}^{\infty} p_2(w_1, w_2, w_3, \hat{w} | w) dw_1 dw_2 dw_3 \quad (18)$$

From (18), (17), (16), and (13) we find after some tedious calculations

$$p_3(\hat{w} | w) = \frac{\exp(t - s')}{2(1 + \hat{w})^{1.5}} \left\{ I_0(t) + (2t + s'w^2)[I_0(t) + I_1(t)] \right\} \quad (19)$$

where

$$t = 0.5 s' \left(\frac{(1 + w \hat{w})^2}{1 + \hat{w}^2} - w^2 \right)$$

I_0, I_1 = modified Bessel functions of order zero and one

$$s = \frac{A^2}{2\sigma^2} = \text{SNR at the top of the sum beam}$$

$$s' = s \cdot S^2(u) = \text{SNR at the actual angle } u$$

A second unidimensional transformation leads to the wanted pdf. If we use the linear approximation method (11), the pdf is merely

$$p_4(\hat{u} | u) = \frac{1}{K_1} p_3(\hat{w} = \hat{u}/K_1 | w = u/K_1) \quad (20)$$

If we want to know the exact pdf of u without any approximation the complete relationship (10) has to be used. In general this function is unknown, but we know the inverse function

$$w = g(u) \quad (21)$$

The difference signal w is a single valued, nonlinear, but differentiable function of u . These properties are sufficient to compute the pdf of \hat{u} by the following formula.

$$p_5(\hat{u}|u) = \frac{\partial g(\hat{u})}{\partial \hat{u}} \cdot p_3(\hat{w} = g(\hat{u}) | w = g(u)) \quad (22)$$

This pdf has been plotted in figure 2 for a target at different positions with a SNR = 6dB at boresight. We used the exact sum and difference beams of the above mentioned small version of ELAN with 39 receiving elements which can be represented by (2) and (5) with a good accuracy. So other antennas with $\sin x/x$ patterns will obtain comparable results.

The pdf becomes more and more unsymmetrical at increasing off-boresight angle with a decreasing maximum. The most probable angle does not correspond to the actual angle. Figure 3 shows how the unsymmetry decreases while the SNR increases.

The form of the pdf remembers the pdf MOSCA (1968, fig 1) has plotted, which corresponds to the pdf of the ratio of two Gaussian random variables.

2.4 Mean of the estimate

Mean and variance of the estimate can be found by computing the first (23) and second (24) moment

$$E\{\hat{u}\} = \int_{-\hat{u}_{max}}^{\hat{u}_{max}} \hat{u} p(\hat{u}|u) d\hat{u} \quad (23)$$

$$E\{\hat{u}^2\} = \int_{-\hat{u}_{max}}^{\hat{u}_{max}} \hat{u}^2 p(\hat{u}|u) d\hat{u} \quad (24)$$

The limits of integration are given by the first zero of the sum beam where the normalized difference signal has a pole

$$\hat{u}_{max} \approx 1.18 \quad (25)$$

These moments could not be derived analytically but due to the good-natured behaviour of the integrand a calculation by numerical methods is possible without difficulty. So we can avoid the usual trouble in finding a measure of dispersion which arises when the pdf is unknown.

At low and moderate SNR the estimate is biased at off-boresight that is, the mean of the angle estimate differs from the actual angle by the bias $b_{\hat{u}}$

$$b_{\hat{u}} = u - E\{\hat{u}\} \quad (26)$$

This bias has been computed by use of (26), (23) and (22) and plotted in figure 4. It shows the growth of the bias of an on-boresight target with a distinct SNR when it moves off-boresight. To prove the correctness of these results a computer simulation has been performed. Crosses represent values found by a simulation with 1000 trials. At this small number of trials, which could not be increased by reason of lacking computing time, the properties of the internally generated random variables do not yet agree exactly with the imagined normal variables, though the correlation between computed and simulated values is good. In spite of the less precise results the simulation consumes much more computing time than the numerical calculation.

MOSCA (1968) has computed the bias of the estimate in the linear approximation case (11).

$$b_{\hat{u}} = u \exp[-\rho] \quad (27)$$

This and the exact computed function are compared in figure 5. By changing the SNR in (27) both curves can be made coinciding over a sufficiently great range

$$b_{\hat{u}} = u \exp[-\rho'] \quad (28)$$

with

$$\rho' = \rho \cdot S^2(u) \cdot \beta(u) \quad \rho' \leq 1$$

The first term takes into account the decrease of the SNR at the sum beam, the second term depends on the nonlinearity of the normalized difference signal. From figure 5 we find

$$\rho'' = \rho - \begin{cases} 2 \text{ dB} \\ 4 \text{ dB} \end{cases} \quad \text{at} \quad u = \begin{cases} 0.1 \\ 0.5 \end{cases}$$

At SNR ≤ -10 dB the angle information has been almost totally suppressed. This confirms the known rule to increase the SNR by integrating the signals of several hits and then to estimate the angle rather than to integrate the angle estimates of several hits.

2.5 Variance of the estimate

The variance of the estimate increases at off-boresight, too (fig.6). The Cramér-Rao lower bound of the ML estimate is given by

$$\sigma_0 \geq \frac{1}{K_3 \sqrt{2f}} \quad (29)$$

with

$$K_3 = c_2 / 2 \approx 1.62$$

From this we would deduce that at $u = 0.5$ where the SNR is halved the variance would be increased by the factor $\sqrt{2}$. But due to the nonlinearity of w this increase is smaller. Crosses represent again values of the computer simulation.

The variances of both methods are compared in figure 7 with the Cramér-Rao lower bound (29). In the case of $u = 0$ this lower bound is reached for SNR > 4 dB. At $u > 0$ the same relation is valid if the SNR is changed taking account of the declining SNR at off-boresight and the nonlinearity of the difference signal.

$$\sigma_0 \geq \frac{1}{K_3 \sqrt{2\rho''}} \quad (30)$$

with the empiric magnitude of

$$\rho'' = \rho - \begin{cases} 0.1 \text{ dB} \\ 2.3 \text{ dB} \end{cases} \quad \text{at} \quad u = \begin{cases} 0.1 \\ 0.5 \end{cases}$$

At a SNR < 4 dB the signal compression effect begins, and no simple relationship between the variance on the one hand and SNR and off-boresight angle on the other hand could be found.

3. EXTENSION TO OTHER SYSTEMS

3.1 Radar mode

In chapter 2 only the properties of the receive antenna have been considered. Therefore the results are valid in those cases where the power reradiated by the signal source does not depend on the direction of the receiving antenna, for instance

- in tracking an active source (beacon),
- bistatic radars,
- monostatic radars with a considerably broader sum beam of the transmitting antenna
- monostatic radars with independly steerable receiving and transmitting beams the latter being fixed.

In a normal monostatic radar, where receiving and transmitting antenna look into the same direction, the SNR is worsened additionally by the influence of the transmitting antenna. In equations (1) and (3) the one-way gain patterns of the receiving antenna have to be multiplied with that of the transmitting antenna.

$$S = S_T \cdot S_R$$

$$D = S_T \cdot D_R$$

(31)

with S_T = sum beam of the transmitter
 S_R = " " " " receiver
 D_R = difference beam of the receiver

When forming the ratio (6) we get the same normalized difference signal as in the beacon mode for S_T can be reduced. The only difference is the more rapid decay of the SNR at off-boresight angles. But if we take account of the fact that the total 3dB-beamwidth of both antennas is smaller than the beamwidth of a single antenna and that all numerical results are related to this beamwidth we can transfer all results into the radar mode without change.

3.2 Bidimensional angle measurement

By forming a second orthogonal difference beam a bidimensional angle measurement is possible. The correlation between both the angle estimates is very small so that their variances may be summed by vector addition. The sum beam has a radial pattern so that the SNR associated with the sum pattern depends on both angles u and v . The previous results are valid only in the case $v=0$. For $v \neq 0$ the definition of the SNR in (19) must be changed to

$$\rho' = \rho \cdot \sqrt{u^2 + v^2}$$

4. CONCLUSION

The nonlinearity of the normalized difference signal increases the bias and decreases slightly the variance at off-boresight angles.

To determine the bias of the estimate an earlier known relation (28) between bias, angle, and SNR may be used. The inserted SNR must be reduced by two terms. One term takes account of the worsened SNR of the sum beam at off-boresight angles, the other of the above mentioned effect.

At $\text{SNR} > 4\text{dB}$ the variance of the estimate is given by the Cramér-Rao lower bound (30). At off-boresight angles the inserted SNR has to be changed by two terms, the first being the same as above. The second term magnifies the SNR.

5. REFERENCES

- BRENNAN, L.E., 1961
 "Angular accuracy of a phased Array Radar"
 IRE Transactions on Antennas and Propagation
 (May, 1961) pp 268-75
- DAVENPORT, W.B.; ROOT, W.L., 1958
 "Random Signals and Noise"
 McGraw-Hill Book Company, New York
- GRÜGER, I., 1972
 "Aufbau und Ergebnisse einer elektronisch gesteuerten Antenne"
 Report No. 7 held at the DGON "Symposium über Radartechnik" at Ulm, Germany (Nov.1972)
- MOSCA, E., 1968
 "Maximum Likelihood Angle Estimation in Amplitude Comparison Monopulse Systems
 Operating on a Single Pulse Basis"
 Alta Frequenza, Vol. 37, No 5 pp 408-414
- SÖNTGERATH, W., 1973
 "Radiation Characteristics of Thinned Array Antennas"
 Report No 34 of this Meeting
- VON AULOCK, W.H., 1960
 "Properties of Phased Arrays"
 Proc. of the IRE, Vol. 48 (Oct., 1960) pp 1715-1727
- WIRTH, W.D., 1972
 "Elektronisch gesteuertes Radar - Aufbau eines Experimentalsystems"
 Report No 6 held at the DGON "Symposium über Radartechnik" at Ulm, Germany (Nov.1972)

6. ACKNOWLEDGMENT

The assistance of Mrs. G. Gniss, who wrote the computer programs and prepared the illustrations, is gratefully acknowledged.

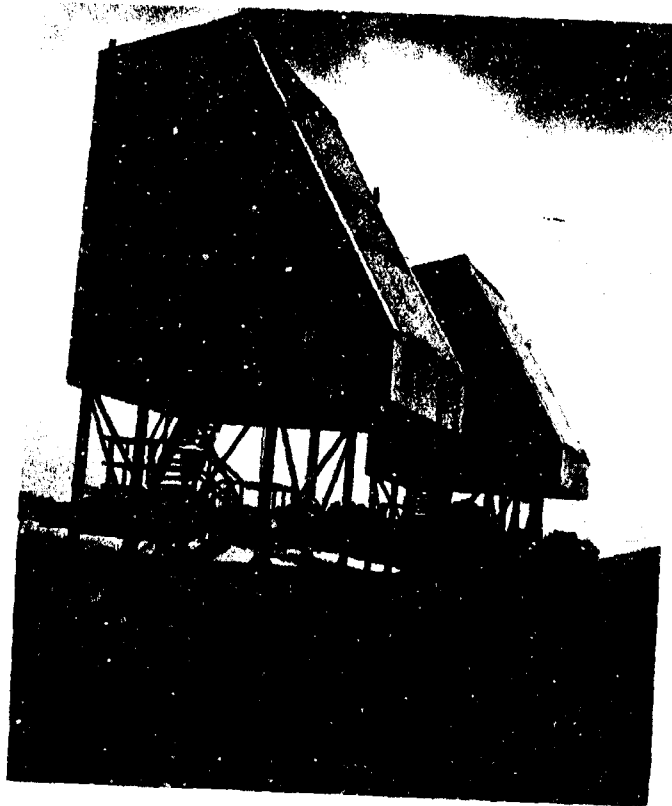


Fig. 1 Antenna site

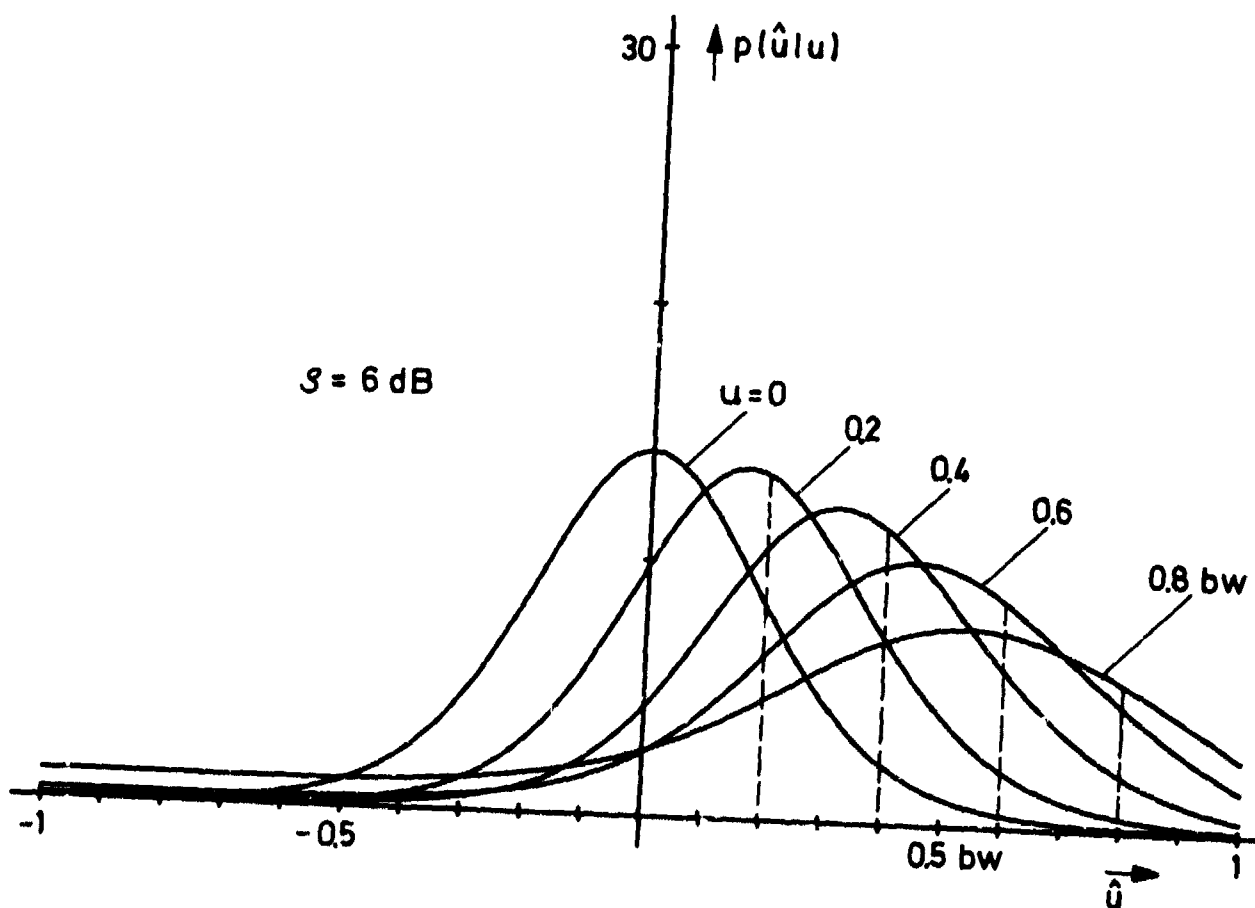


Fig. 2 Probability density function of the estimated angle with a target at 0, 0.2, 0.4, 0.6, and 0.8 beamwidth

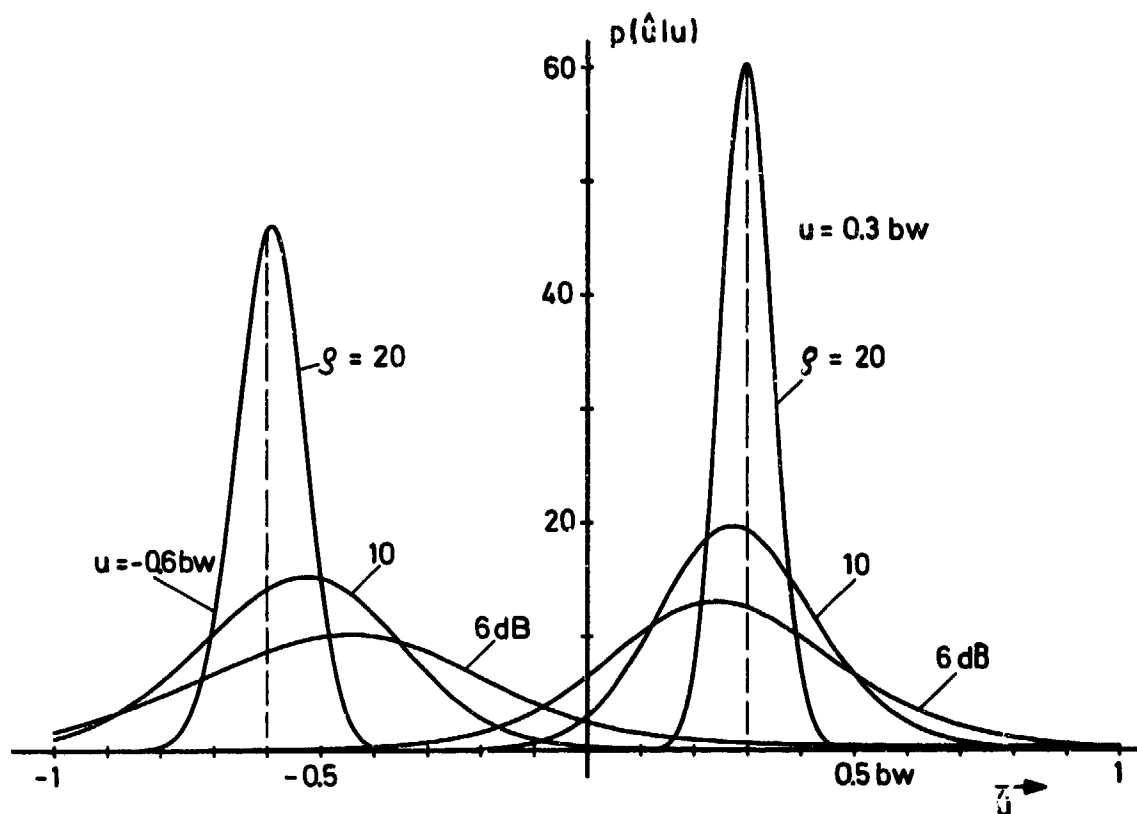


Fig. 3 Probability density function of the estimated angle at various signal-noise-ratios

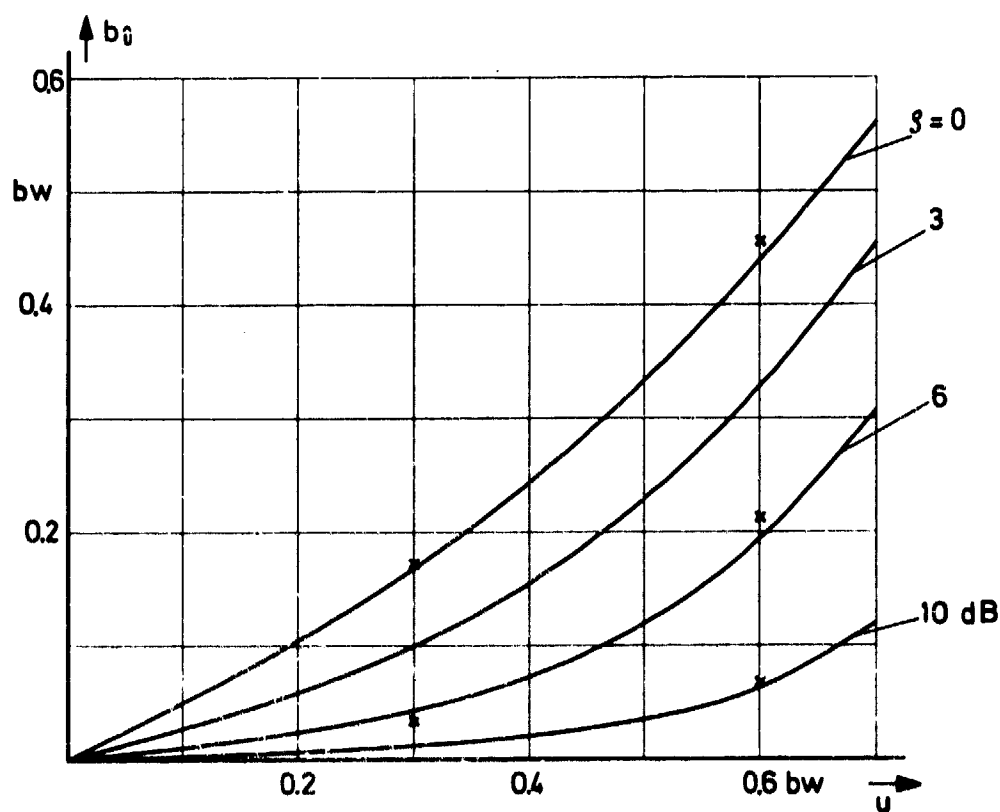


Fig. 4 Bias of the angle estimate
(crosses represent values found by computer simulation)

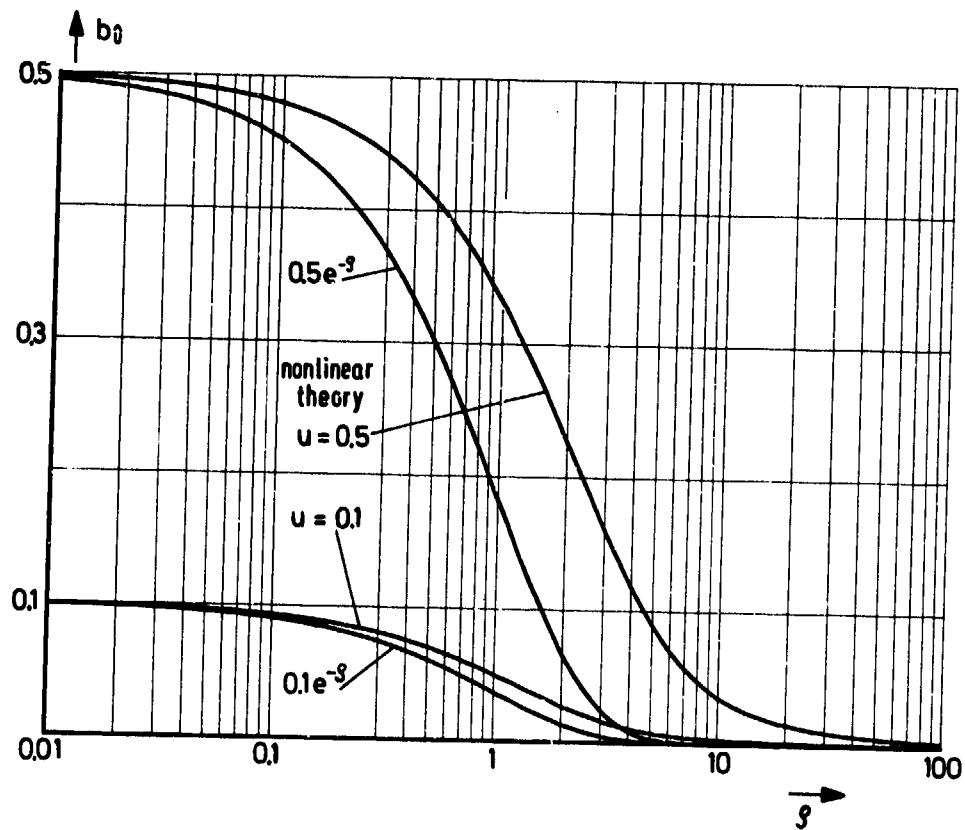


Fig. 5 Bias of the angle estimate
Comparison between linear approximation and
nonlinear theory

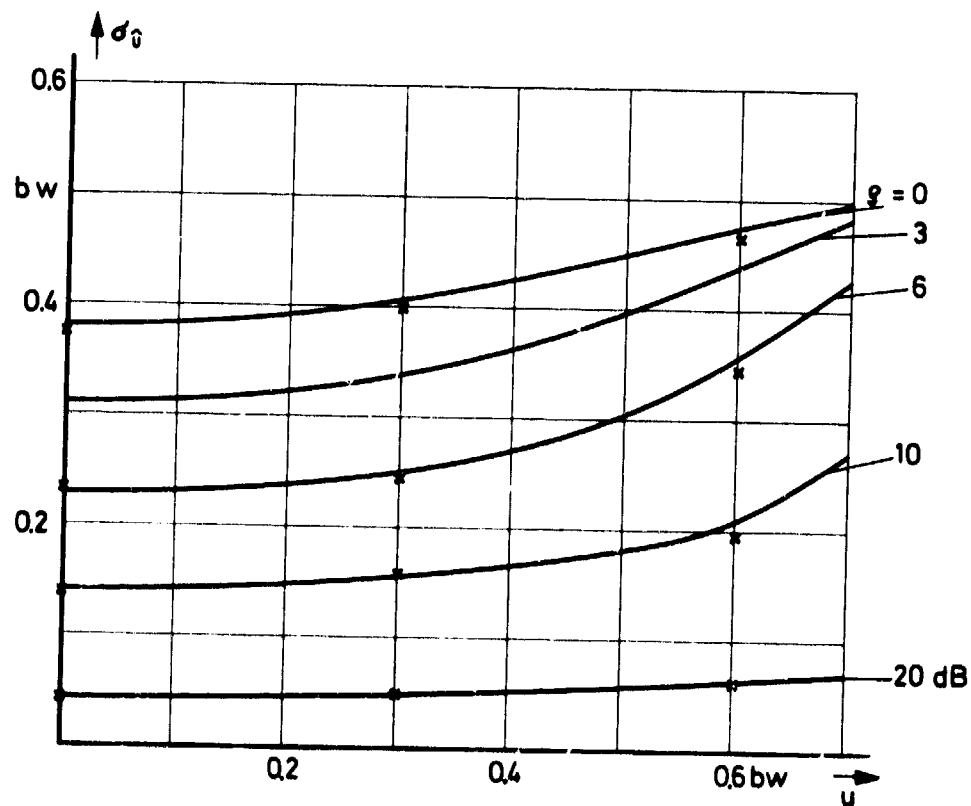


Fig. 6 Variance of the angle estimate
(crosses represent values found by computer
simulation)

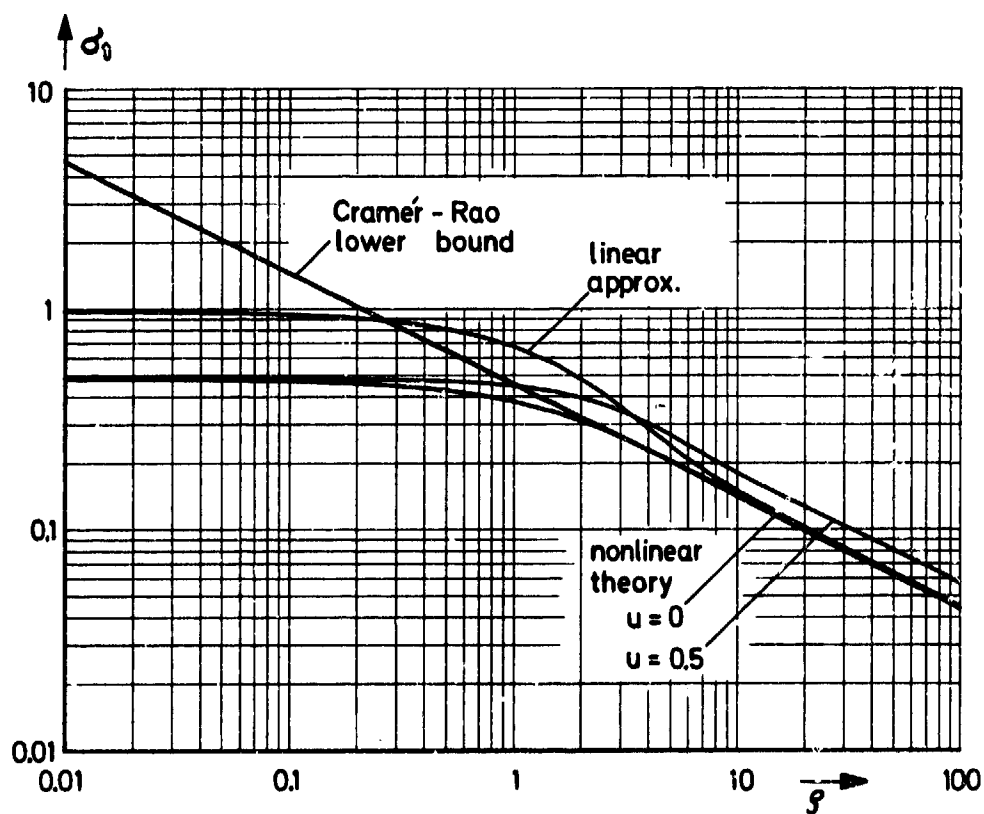


Fig. 7 Variance of the angle estimate.
Comparison between linear approximation and
nonlinear theory

ROLL PLANE ANALYSIS OF ON-AIRCRAFT ANTENNAS*

by
W.D. Burnside
R.J. Marhefka
C.L. Yu

The Ohio State University ElectroScience Laboratory
Department of Electrical Engineering
Columbus, Ohio 43212
28 June 1973

ABSTRACT

The roll plane radiation patterns of on-aircraft antennas are analyzed using high frequency solutions. This is a basic study of aircraft-antenna pattern performance in which the aircraft is modelled in its most basic form. The fuselage is assumed to be a perfectly conducting elliptic cylinder with the antennas mounted near the top or bottom. The wings are simulated by arbitrarily many sided flat plates and the engines by circular cylinders. The patterns in each case are verified by measured results taken on simple models as well as scale models of actual aircraft.

I. INTRODUCTION

This paper presents a basic theoretical study of roll-plane aircraft-antenna patterns for the UHF and microwave frequencies in which the antenna is mounted on the fuselage near the top or bottom. Since it is a study of general-type aircraft, the aircraft is modelled in its most basic form. The fuselage is assumed to be a perfectly conducting infinitely long elliptic cylinder. The wings and horizontal stabilizers are modelled by n -sided flat plates which lie in a plane that is parallel to the fuselage axis. The engines are approximated by circular cylinders.

The need for this type of solution is basically two-fold. First, there may be upwards to 200 antennas mounted on a single aircraft. If these antennas can be located on the aircraft at the design stage, then one can expect better performance in that optimum locations and necessary structural changes can be anticipated. Secondly, antenna systems are normally added or changed in the course of an aircraft's useful lifetime. Such relocation or addition of antennas has always required a great deal of engineering time and money.

Some of the first solutions used to compute on-aircraft antenna patterns were the modal solutions for infinitely long circular (Carter, P.S., 1943) and elliptical (Sinclair, G., 1951) cylinders. The fuselage was modelled by a cylinder whose cross-section approximated the fuselage cross-section at the antenna location. Arbitrary antennas were considered, and the antenna could be mounted on or above the fuselage. Results were quite adequate provided the aircraft structure was not illuminated too strongly. In fact, these solutions have provided the primary high frequency analysis to date. However, with the desire to improve system performance, versatility, and coverage the antenna pattern must be shaped for the desired application in such a way that it may actually illuminate the structure quite strongly. In many cases the system's performance is dependent on the pattern effects of the secondary contributors.

Another approach that has found great success at solving this type of problem is the Geometrical Theory of Diffraction (GTD). GTD is basically a high frequency solution (object large in terms of wavelength) which is divided into two basic problems; these being wedge or tip diffraction and curved surface diffraction. The only limitation of these solutions is that the source and various scattering centers be separated by at least a wavelength. In some cases even this requirement can be relaxed. Using this approach one applies a ray optics technique to determine the fields incident on the various scatterers. The fields diffracted are found using the GTD solutions in terms of rays which are summed with geometrical optics terms in the far zone. The scattered energy, which is analyzed in terms of rays, from a given structure tends to illuminate the other structures causing various higher-order scattered terms. Using the ray optics approach, one can trace out the various possible combinations of rays that interact between various scatterers and include only the dominant terms. Thus, one need only be concerned with the dominant scattering structures and neglect the secondary structures in the theoretical model. This makes the GTD approach ideal for a general high frequency study of on-aircraft antenna patterns.

II. WEDGE DIFFRACTION

The three dimensional wedge diffraction problem is pictured in Fig. 1. A source whose radiated E field is given by $E^i(s)$ is located at point $s^i(\rho^i, \phi^i, z^i)$. It can be an arbitrary electric or magnetic source causing plane, cylindrical, conical, or spherical wave incidence on the wedge tip. The diffracted vector field at point $s(\rho, \phi, z)$ can be written in terms of a dyadic diffraction coefficient. Kouyoumjian and Pathak (1970) have given a more rigorous basis for the GTD formulation and have shown that the diffracted fields may be written compactly if they are in terms of a ray-fixed coordinate system. The ray-fixed coordinate system is centered at the point of diffraction Q_E , (or points of diffraction in the case of plane wave incidence). Q_E is a unique point or points for a given source and observation point. The incident ray diffracts as a cone of rays such that $\rho_0 = \rho'_0$ (see Fig. 1).

*The work reported in this paper was supported in part by Grant NGR 36-008-144 between National Aeronautics and Space Administration, Langley Research Center, and The Ohio State University Research Foundation.

For our purpose, it is more convenient to write the diffracted field in terms of the V_B function (Hutchins, D.L., 1967) as

$$(1) \begin{bmatrix} E_H^d(s) \\ E_I^d(s) \end{bmatrix} \sim \begin{bmatrix} -V_B^- & 0 \\ 0 & -V_B^+ \end{bmatrix} \begin{bmatrix} E_H^i(Q_E) \\ E_I^i(Q_E) \end{bmatrix} \sqrt{\frac{L}{\sin \beta_0}} e^{jkL} A(s) e^{-jks}$$

where

$$V_B^\mp = V_B(L, \gamma^\mp, n) \mp V_B(L, \gamma^+, n).$$

The time dependence factor ($e^{j\omega t}$) is suppressed throughout this paper. The minus sign (V_B^-) applies for the E-field component parallel to the edge and the plus sign (V_B^+) applies for the E-field component perpendicular to the edge. The angular relations are expressed by

$$\gamma = \gamma^\mp = \phi \mp \phi' \quad \text{for } 0 \leq \phi, \phi' \leq \pi,$$

where the minus sign (γ^-) is associated with the incident field and the plus sign (γ^+) with the reflected field. The quantity $A(s)$ is a ray divergence factor given by (Pathak, P.K. etc., 1970)

$$A(s) = \begin{cases} \frac{1}{\sqrt{s}} & \text{plane, cylindrical (s=\rho) and conical wave incidence} \\ \frac{s'}{\sqrt{s(s'+s)}} & \text{spherical wave incidence} \end{cases}$$

and L is given by

$$L = \begin{cases} s \sin^2 \beta_0 & \text{plane wave incidence} \\ \frac{\rho' \rho}{\rho + \rho'} & \text{cylindrical wave incidence} \\ \frac{s's \sin^2 \beta_0}{s+s'} & \text{conical and spherical wave incidence.} \end{cases}$$

III. DIFFRACTION BY ELLIPTIC CYLINDER

The radiation from slots and monopoles mounted on smooth curved surfaces is pertinent to the design of flush-mounted antennas for aircraft and spacecraft. Recently, Pathak and Kouyoumjian (1972) have extended the GTD technique for plane wave diffraction by perfectly conducting convex surfaces to treat the radiation problem. This extension of GTD has been successfully applied to circular and elliptic cylinders, spheres, and spheroids (Burnside, W.D., 1972).

The GTD solution for the radiation by antennas mounted on convex surfaces employs the reciprocity theorem. Using this approach a plane wave field is assumed normally incident on a right circular cylinder. The antenna aperture field is, then, given by asymptotic solutions for exact expressions of the field on the cylinder surface. Employing the reciprocity theorem, one obtains the radiated field for that same antenna mounted on the cylinder. The geometrical optics solution is used to describe the radiated field in the lit region. The Fock approximation is used for the penumbra (transition) region; whereas in the deep shadow region, the GTD solution is applied. Using the GTD solution, a launch coefficient relates the antenna aperture field to the boundary layer surface waves which propagate around the surface along geodesic paths. Energy is continually diffracted by the surface wave in the tangent direction to the propagation path. This diffracted energy is given by a diffraction coefficient which is dependent on the surface geometry at the point of diffraction. The surface wave energy decays along the geodesic path in that energy is continually diffracted. This decay is expressed by an attenuation coefficient which is dependent on the surface geometry along the geodesic path.

The GTD solutions for infinitesimal slot and monopole antennas mounted on an elliptic cylinder as shown in Fig. 2 are given, neglecting torsional effects, by

A. Monopole case

Lit Region

$$(2) \quad \vec{E} = -\sin \theta_m \hat{\theta}_m F(\text{source})$$

Transition Region

a) Lit side

$$(3) \quad \vec{E} = \hat{n} \left\{ (\sin \theta_m)^{1/2} e^{jkL} g^* \left[-\left(\frac{k}{2\rho_g^2(r)} \right)^{1/3} d_L \right] \right\} \cdot F(\text{tangent})$$

b) Shadow side

$$(4) \quad \vec{E} = \hat{n} \left\{ \sqrt{\frac{d_{\psi 0}}{d_\psi}} e^{-jkL} g^* \left[\left(\frac{k}{2\rho_g^2(r)} \right)^{1/3} d_L \right] \right\} \cdot F(\text{tangent})$$

Deep Shadow

$$(5) \quad \vec{E} = \sum_j \hat{n}_j E_j^h F_j \text{ (tangent)}$$

B. Slot caseLit Region

$$(6) \quad \vec{E} = [(\hat{e}_1 \sin \beta - \hat{e}_2 \cos \beta) \cdot (\hat{b}'\hat{n}' + \hat{t}'\hat{b}')] \cdot F(\text{source})$$

Transition region

a) Lit side

$$(7) \quad \vec{E} = \left\{ \hat{n} \left[\frac{1}{2} e^{jk\ell} g^* \left(- \int \left(\frac{k}{2\rho_g^2(\ell)} \right)^{1/3} d\ell \right) \sin(\alpha_s + \beta) \right] + \right. \\ \left. \hat{b} \left[\frac{j}{2} e^{jk\ell} \tilde{g}^* \left(- \int \left(\frac{k}{2\rho_g^2(\ell)} \right)^{1/3} d\ell \right) \left(\frac{2}{k\rho_g} \right)^{1/3} \cos(\alpha_s + \beta) \right] \right\} \cdot F(\text{tangent})$$

b) Shadow side

$$(8) \quad \vec{E} = \left\{ \hat{n} \left[\frac{1}{2} \sqrt{\frac{d\psi_0}{d\psi}} e^{-jk\ell} g^* \left(\int \left(\frac{k}{2\rho_g^2(\ell)} \right)^{1/3} d\ell \right) \sin(\alpha_s - \beta) + \right. \right. \\ \left. \left. \hat{b} \left[-\frac{j}{2} \sqrt{\frac{d\psi_0}{d\psi}} e^{-jk\ell} \tilde{g}^* \left(\int \left(\frac{k}{2\rho_g^2(\ell)} \right)^{1/3} d\ell \right) \left(\frac{2}{k\rho_g} \right)^{1/3} \cos(\alpha_s - \beta) \right] \right\} \cdot F(\text{tangent})$$

Deep Shadow Region

$$(9) \quad \vec{E} = \sum_j \left[\hat{n}_j E_j^h \sin(\alpha_s - \beta) + \hat{b}_j E_j^s \cos(\alpha_s - \beta) \right] F_j(\text{tangent})$$

where

$$E^h = \sqrt{\frac{d\psi_0}{d\psi}} \sum_{m=0}^1 D_m^h L_m^h e^{-\int \gamma_m^h(\ell) d\ell}$$

$$E^s = \sqrt{\frac{d\psi_0}{d\psi}} \sum_{m=0}^1 D_m^s L_m^s e^{-\int \gamma_m^s(\ell) d\ell}$$

The functions $g^*()$ and $\tilde{g}^*()$ are the complex conjugates of the Fock function (Pathak, P.K., etc., 1972) for the hard and soft boundary conditions, respectively. The unit vectors \hat{n} and \hat{b} are, respectively, the normal and binormal to the geodesic curve at the diffraction (or tangent) point, and $F()$ is simply a phase factor to refer the phase to the origin of the coordinate system. The term $\sqrt{d\psi_0/d\psi}$ is the spread factor, which is related to the spread of the geodesic paths. In this case, $\sqrt{d\psi_0/d\psi}$ is unity. The longitudinal and transverse radii of curvature are given, respectively, by ρ_g and ρ_t . Note that the superscripts h and s indicate the hard and soft boundary conditions. The launch coefficients are given by

$$L_m^h = \left[\pi e^{j\frac{\pi}{2}} D_m^h \left(\frac{2}{k\rho_g} \right)^{1/3} A_1(-q_m) \right]_{\text{at the source}}$$

$$L_m^s = \left[\pi e^{-j\frac{\pi}{2}} D_m^s \left(\frac{2}{k\rho_g} \right)^{2/3} A_1'(-q_m) \right]_{\text{at the source}}$$

where D_m is defined in Table I. The subscript m refers to the m th mode of the boundary layer surface wave. Thus, γ_m is the propagation constant for the m th mode surface wave such that $\gamma_m = \alpha_m + jk$ where α_m is defined in Table I. The incremental arc length along the geodesic path is expressed by $d\ell$. The summation over " j " in the shadow region indicates that several terms can contribute in that region.

One must first find an efficient solution for the geodesic paths on the elliptic cylinder surface in order to analyze this problem successfully using GTD. A preferred coordinate system for the elliptic cylinder is illustrated in Fig. 3 and defined by

$$(10) \quad \begin{aligned} x &= d \cosh u \cos v = a_f \cos v \\ y &= d \sinh u \sin v = b_f \sin v \\ z &= z \end{aligned}$$

where $2d$ is the distance between the foci of the ellipse. Note that for $u = u_f$, where $u_f = \tanh^{-1}(b_f/a_f)$ [a constant], the above equations define an elliptical surface for $0 \leq v < 2\pi$. Thus, the elliptical surface shape is expressed by u_f , its size by d , and any point on the surface is defined by v .

Using the calculus of variations, the geodesic paths on an elliptical surface are given by

$$z = \frac{C}{\sqrt{1-C^2}} \int_{v_i}^{v_f} \sqrt{a_f^2 \sin^2 v + b_f^2 \cos^2 v} dv$$

Note that v_i and v_f are, respectively, the initial and final values of v along a given geodesic path. If one defines the geodesic starting direction by the angle (α_s) as shown in Fig. 2, then $C = -\cos \alpha_s$. The advantage of this geodesic solution lies in the fact that the integral can be quickly evaluated using numerical techniques. The important parameters of this problem are listed below:

$$z = \frac{-\cos \alpha_s}{|\sin \alpha_s|} \int_{v_i}^{v_f} \sqrt{a_f^2 \sin^2 v + b_f^2 \cos^2 v} dv \quad (\text{geodesic equation})$$

$$L = \frac{1}{|\sin \alpha_s|} \int_{v_i}^{v_f} \sqrt{a_f^2 \sin^2 v + b_f^2 \cos^2 v} dv \quad (\text{arc length})$$

$$\left. \begin{aligned} \hat{e}_1 &= \frac{-a_f \sin v \hat{x} + b_f \cos v \hat{y}}{\sqrt{a_f^2 \sin^2 v + b_f^2 \cos^2 v}} \\ \hat{e}_2 &= \hat{z} \end{aligned} \right\} \quad (\text{curvilinear coordinates})$$

$$\hat{t} = \sin \alpha_s \hat{e}_1 - \cos \alpha_s \hat{e}_2 \quad (\text{unit tangent vector})$$

$$\hat{n} = \frac{b_f \cos v \hat{x} + a_f \sin v \hat{y}}{\sqrt{a_f^2 \sin^2 v + b_f^2 \cos^2 v}} \quad (\text{unit normal vector})$$

$$\hat{b} = \hat{t} \times \hat{n} = +\cos \alpha_s \hat{e}_1 + \sin \alpha_s \hat{e}_2 \quad (\text{unit binormal vector})$$

$$\rho_g = \frac{(a_f^2 \sin^2 v + b_f^2 \cos^2 v)^{3/2}}{a_f b_f \sin^2 \alpha_s} \quad (\text{longitudinal radius of curvature})$$

Using the above relations, one can employ Eqs. (2-9) to determine the total radiated fields.

The principal plane radiation patterns (which correspond to roll plane patterns in the aircraft case) are shown in Fig. 4 for a circumferential slot, axial slot, and monopole mounted on a two wavelength radius circular cylinder. These patterns compare very favorably with the modal solutions (Sinclair, G., 1951) as shown in the same figures. The principal plane radiation patterns are shown in Fig. 5 for the same antennas mounted on an elliptic cylinder.

IV. NEAR FIELD SCATTERING BY A FINITE PLATE

The near field scattering by a finite flat plate is a relatively new topic at higher frequencies where the plate is large in terms of the wavelength. The solution presented here is a practical application of the three-dimensional wedge diffraction theory given earlier. The source is defined by its location and far-field pattern. The far-field pattern of the source is appropriate in that the plate is located at least $2D^2/\lambda$ away from the source where D is the maximum dimension of the source. The finite flat plate is simply specified by location of its n corners.

It is known that for a given scatter direction there is only one point along an infinitely long straight edge at which the diffracted field can emanate for a near zone source. Thus, this point must be found for each of the n edges that describe the flat plate. There are many ways of finding this diffraction point, one of which is described here. Since it is known that $\beta_0 = \beta'_0$ (see Fig. 1), it is obvious that

$$(11) \quad \hat{e}_m \cdot \hat{I} = \hat{e}_m \cdot \hat{d}$$

where \hat{e}_m , \hat{I} , and \hat{d} are, respectively, the m th edge unit vector, incident direction unit vector, and diffraction direction unit vector. Since the scatter direction is known (θ_s, ϕ_s), the value of $\hat{e}_m \cdot \hat{d} = c_m$ is easily computed for each edge. One need only search along the edge to find the point where $\hat{e}_m \cdot \hat{I} = c_m$.

Once the diffraction point is located, one must find the diffracted field value from the m th edge. The far field pattern of the source can be written as

$$(12) \quad \vec{E}_s(\theta, \phi) = [\hat{\theta} F(\theta, \phi) + \hat{\phi} G(\theta, \phi)] \frac{e^{-jks'}}{s'} = \vec{R}(\theta, \phi) \frac{e^{-jks'}}{s'}$$

where s' is the range from the source to the field point. Using the geometry illustrated in Fig. 1 and applying the results presented earlier one finds that

$$(13) \quad \begin{bmatrix} R_{||}^d \\ R_{\perp}^d \end{bmatrix} = \begin{bmatrix} -V_B^- & 0 \\ 0 & -V_B^+ \end{bmatrix} \begin{bmatrix} R_{||}^i \\ R_{\perp}^i \end{bmatrix} e^{-j[k(s'-\gamma) - k_{\rho}\rho]}$$

where

$$\begin{aligned} R_{||}^i &= \vec{R}(\theta_i, \phi_i) \cdot \hat{\beta}_0^i \\ R_{\perp}^i &= \vec{R}(\theta_i, \phi_i) \cdot \hat{\phi}_0^i \\ k_{\rho}\rho &= ks' \sin^2 \beta_0 \\ \gamma &= x_{dp} \sin \theta_s \cos \phi_s + y_{dp} \sin \theta_s \sin \phi_s + z_{dp} \cos \theta_s \\ V_B^{\pm} &= V_B(k_{\rho}\rho, \phi - \phi', 2) \pm V_B(k_{\rho}\rho, \phi + \phi', 2) \\ \hat{\phi}_0^i &= \hat{I} \times \hat{\beta}_0^i \end{aligned}$$

The coordinates (x_{dp}, y_{dp}, z_{dp}) define the point of diffraction.

Once these terms are determined the total diffracted field in ray form from a general m th edge is given by

$$(14) \quad \vec{R}_m^d(\theta_s, \phi_s) = R_{||}^d \hat{\beta}_0 + R_{\perp}^d \hat{\phi}_0$$

where $\hat{\phi} = \hat{d} \times \hat{\beta}_0$. Using the superposition principle the total singly diffracted field in ray form by the n edges of the flat plate is given using Eq. (14) by

$$(15) \quad \vec{R}^d(\theta_s, \phi_s) = \sum_{m=1}^n \vec{R}_m^d(\theta_s, \phi_s)$$

The first step in calculating the reflected field is to find the location of the image source, which is uniquely determined once the plane of the flat plate is defined relative to the source location. In fact, the image is located along a line which is orthogonal to the plate and positioned an equal distance on the opposite side of the plate.

With the image position known, one needs to determine if the reflected field contributes to the total scattered field using the geometrical optics approach. If the reflected field is a contributor, the ray from the image source in the scatter direction (θ_s, ϕ_s) must pass through the finite plate limits. Thus, one must find the location of the intersection point of this ray and the plane containing the flat plate. This can easily be accomplished using vector analysis. One can, then, predict within certain limits whether this intersection point falls within the bounds of the finite flat plate.

If reflections do occur, the reflected field from the image source can be written in ray form as

$$(16) \quad \vec{R}^r(\theta_s, \phi_s) = [\hat{\theta}^r F^r(\theta_s, \phi_s) + \hat{\phi}^r G^r(\theta_s, \phi_s)] \cdot e^{jk[x_1 \sin \theta_s \cos \phi_s + y_1 \sin \theta_s \sin \phi_s + z_1 \cos \theta_s]}$$

where $\hat{\theta}^r$ and $\hat{\phi}^r$ are related to the image source coordinate system with the image location defined by (x_1, y_1, z_1) . The functions $[F^r(\theta_s, \phi_s)$ and $G^r(\theta_s, \phi_s)]$ are found by employing the boundary conditions on the perfectly conducting flat plate. The total scattered field from the flat plate is, then, given by

$$(17) \quad \vec{R}^s(\theta_s, \phi_s) = \vec{R}^d(\theta_s, \phi_s) + \vec{R}^r(\theta_s, \phi_s)$$

In order to illustrate the versatility of this solution, it is used to approximate the scattering effect of a disc. This is done by computing the pattern of a monopole mounted on plates with increasingly many sides. In Fig. 6 the calculated results for plates with 4, and 6 sides are illustrated and compared with the measured result for the circular disk (Lopez, A.R., 1966). Note that as the number of sides is increased the closer the computed and measured results agree. Note also the agreement between measured and calculated patterns of a $\lambda/4$ dipole mounted above a square plate as illustrated in Fig. 7.

Even though the above results show good agreement one must realize the inherent approximations in this solution. It is based on edge diffraction with just singly diffracted edge rays being considered. Thus, it has been assumed that the plate is large in terms of the wavelength such that double diffraction is normally negligible. However, neglecting double diffraction may cause some error especially when the pattern is computed in the plane of the flat plate. Secondly, a diffraction term from each of the corners should be included, but it is not available in practical form at present. Nevertheless, the latter has little effect on the overall pattern except when a diffraction point (or points) approaches a corner. In these two cases our solution can be somewhat in error although only small angular regions are involved.

V. ROLL PLANE ANALYSIS

The basic aircraft to be analyzed in this study is composed of flat plates and cylinders. It is assumed that the source is mounted on the fuselage and restricted to the regions near the top or bottom of the aircraft. Arbitrary antennas can be considered simply by integrating these solutions for infinitesimal antennas over the equivalent aperture currents.

The lower frequency limit of these solutions is dictated by the ray optics format which requires that the various scattering centers be no closer than approximately a wavelength with the overall aircraft being large in terms of the wavelength. The upper frequency limit is dictated by the accuracy to which the model represents the actual aircraft considered.

The two-dimensional problem is considered initially in order to develop the necessary techniques to attack the much more difficult three-dimensional roll plane problem (Marhefka, R.J., 1971). The geometry of the two-dimensional problem is illustrated in Fig. 8 with and without the engines included. The fuselage and engines are assumed circular in cross-section and mounted symmetrically about the finite wing. Since wedge diffraction is applied to handle the finite length wing, the radiated field must be described in terms of rays. However, one of the nicer features of the GTD approach is that other solutions such as modal solutions can be cast into a ray form and then applied to a diffraction problem. Consequently, it was found that the modal solution (Sinclair, G., 1951) for an arbitrary antenna mounted on an infinite circular cylinder was satisfactory for treating the antenna mounted on the circular fuselage. In fact, this solution has been applied in past years as the sole solution for high frequency on-aircraft antenna analyses.

The radiation patterns for an axial slot are shown in Fig. 8a on a model without engines. The slot used for the measured patterns is simply an open-ended X-band waveguide. These solutions compare very favorably with measured results taken on a simulated two-dimensional aircraft model. The radiation patterns for the same configuration with the engines added are illustrated in Fig. 8b. Again very good agreement is obtained between our calculated and measured results. These results indicate that the scattering from the engines has little effect on the overall pattern except near $\phi \sim 90^\circ$ and $\phi \sim 270^\circ$. The same conclusion is true for the monopole and circumferential slot which were analyzed and measured although not shown here.

Since the roll plane cuts orthogonally across the fuselage, one should expect the fuselage cross-section to have a strong effect on the roll plane pattern. On the other hand, an aircraft fuselage is normally long and slender, such that its finite length effects are generally secondary. Consequently, the infinite elliptic cylinder representation of the fuselage for roll plane calculations appears to be a reasonable approximation in most cases. Since the antenna can be arbitrarily positioned on the fuselage with respect to the wings, one must consider the width of the wing as well as its length in order to obtain a practical analytic model. In order to accomplish this, the near field flat plate scattering solution is adapted to this new model such as illustrated in Fig. 9. Note that each wing can be located arbitrarily with any number of edges provided only that the wings are flat and horizontal.

Our model, now, consists of an infinitely long elliptic cylinder fuselage to which finite flat wings are attached. The various configurations analyzed are shown in Fig. 10 looking from the front of the aircraft with the antenna mounted in each case above the wings for the models illustrated. Using these models, one should be able to analyze a wide variety of aircraft shapes. This is verified by a comparison of results taken on actual aircraft scale models and presented later.

Let us first find the effective source location for the reflected field. Recall that in our flat plate result the source was imaged and the reflected field added to the total solution provided the image ray passed through the finite flat plate (wing) limits. So one must initially determine the effective source position and then the reflected field. With the source mounted on an infinitely long elliptic cylinder, the surface rays from the source propagate around the cylinder along geodesic paths, from which energy is continually diffracted tangentially. Now let us assume that the source does not illuminate the right wing directly (as illustrated in Fig. 9a) and proceed to determine the unique geodesic path that diffracts energy from a known tangent point which is then reflected off the wing in the desired radiation (or scatter) direction.

The effective source position for reflections from the right wing in terms of the radiation direction (θ_s, ϕ_s) is given by

$$\begin{aligned} x_e &= a_f \cos v_e \\ y_e &= b_f \sin v_e \\ z_e &= \cot \phi_s \int_{v_{so}}^{v_e} \sqrt{a_f^2 \sin^2 v + b_f^2 \cos^2 v} dv + z_{so} \end{aligned} \quad (18)$$

where $v_e = \tan^{-1}(b_f/a_f \cot \phi_s)$. These coordinates can, then, be used in the flat plate problem as the effective source location. Note that as the desired radiation direction is varied the effective source location changes. In addition, if the source directly illuminates the wing for a given reflection term then the effective source location is simply the actual source location (u_f, v_{so}, z_{so}) . A result similar to Eq. (18) can be found for the reflections from the left wing. Finally, the actual source field value used to compute the reflected term is determined from the GTD solutions of Section III.

Using a similar technique the effective source locations for the diffracted field components may be found. Our flat plate solution uses a search technique to find the diffraction point by computing the diffraction angles at selected test points along a given edge. Once a test point (x_d, y_d, z_d) is specified along the edge one can find the effective source location (x_e, y_e, z_e) using the geometry illustrated in Fig. 9b. Again it is assumed that the source does not directly illuminate the test point. One finds that the effective source is given by

$$\begin{aligned}
 x_e &= \frac{a_f^2 b_f^2 x_d + a_f^2 y_d \sqrt{a_f^2 y_d^2 + b_f^2 x_d^2 - a_f^2 b_f^2}}{(a_f^2 y_d^2 + b_f^2 x_d^2)} \\
 (19) \quad y_e &= \frac{a_f^2 b_f^2 y_d - b_f^2 x_d \sqrt{a_f^2 y_d^2 + b_f^2 x_d^2 - a_f^2 b_f^2}}{(a_f^2 y_d^2 + b_f^2 x_d^2)} \\
 z_e &= \frac{b_f x_e z_d I_V + a_f z_{so} (y_d - y_e) I_V'}{b_f x_e I_V + a_f (y_d - y_e) I_V'}
 \end{aligned}$$

where

$$I_V = \int_{v_{so}}^{v_e} \sqrt{a_f^2 \sin^2 v + b_f^2 \cos^2 v} dv,$$

$$I_V' = \sqrt{a_f^2 \sin^2 v_e + b_f^2 \cos^2 v_e}, \text{ and } v_e = \tan^{-1} \left(\frac{y_e / b_f}{x_e / a_f} \right).$$

Given the effective source location for the chosen test point, the search technique is applied to find the actual diffraction point along a given edge. Note that once the actual diffraction point is determined, the effective source of the diffracted field is specified by Eq. (19), and the source field value is, again, computed using the GTD solutions.

The total field is found by summing the directly radiated field with the scattered fields from the wings using the superposition principle. Several different configurations have been studied using this solution and compared with measured results. The patterns illustrated in Fig. 11 are based on a circular fuselage with the wings mounted in the central location. The roll plane pattern for $\lambda/4$ monopole is shown in Fig. 11a, with the antenna mounted directly above the wings. The pattern is shown in Fig. 11b for an axial slot mounted on the fuselage over the back limit of the wing. In Fig. 11c the pattern is shown for a circumferential slot mounted over the wings but rotated 45° from the straight up direction as considered in Fig. 11a. The patterns for a $\lambda/4$ monopole mounted on a circular fuselage wing above and below the central location are illustrated in Fig. 12. In Fig. 13 the roll plane patterns are illustrated for each of the three basic antennas mounted on an elliptic fuselage with the wings centrally attached. The patterns illustrated in Fig. 14 are for an axial slot mounted on an elliptic fuselage with the wings above and below the central position. Good agreement is obtained between the calculated and measured results in each case. The slight deviations are attributed primarily to the assumptions made in solving for the flat plate scattered field.

VI. CONCLUSIONS

The solutions that have been presented here provide a high-speed analytic tool for determining the type and location of antennas based on their roll plane performance. These programs typically compute a pattern in 30 seconds or less on a CDC 6600 digital computer. A 16 mm film has been developed which illustrates the advantages of a numerical solution for computing patterns for antennas on aircraft and is available upon request.

An additional feature of these solutions, which can be very important in certain critical cases, is that one can trace out the dominant pattern terms as they are scattered by the various parts of the aircraft structure. In this way one can quickly ascertain which structural scatterers are distorting the pattern in a critical region. This gives one the option of taking corrective action by changing the structure or by properly placing absorber. So these solutions not only provide fast pattern computations, but they also provide the antenna designer with a means of analytically considering several alternatives to improve the antenna's performance.

Each of the solutions developed have been verified by experimental results taken on a structure which approximates our analytic model. However, these results do not verify the general validity of our analytic model in representing an actual aircraft. There are no roll plane patterns published in the literature to our knowledge that would be suitable for our comparison. We appreciate the efforts of NASA personnel who measured the patterns of a $\lambda/4$ monopole mounted on an accurately scaled model of a KC-135 (Boeing 707); as well as, the effort of NADC personnel who measured two patterns on a scale model of a F-4 aircraft. The results are illustrated in Figs. 15 and 16 and the agreement in each case is very encouraging.

REFERENCES

- Burnside, W.D., "Analysis of On-Aircraft Antenna Patterns," Report 3390-1, August 1972, The Ohio State University ElectroScience Laboratory, Department of Electrical Engineering; prepared under Contract N62269-72-C-0354 for Naval Air Development Center.
- Carter, P.S., "Antenna Arrays Around Cylinders," Proc. IRE, Vol. 31, December, 1943, pp. 671-693.
- Hutchins, D.L., "Asymptotic Series Describing the Diffraction of a Plane Wave by a Two-Dimensional Wedge of Arbitrary Angle," Ph.D. Dissertation, The Ohio State University, Department of Electrical Engineering, (1967).
- Lopez, A.R., "The Geometrical Theory of Diffraction Applied to Antenna Pattern and Impedance Calculations," IEEE Transactions on Antennas and Propagation, Vol. AP-14, No. 1, (January 1966), p. 40.
- Marhefka, R.J., "Roll Plane Analysis of On-Aircraft Antennas," Report 3188-1, December 1971, The Ohio State University ElectroScience Laboratory, Department of Electrical Engineering; prepared under Contract N62269-71-C-0296 for Naval Air Development Center.
- Pathak, P.H. and Kouyoumjian, R.G., "The Dyadic Diffraction Coefficients for a Perfectly Conducting Wedge," Scientific Report No. 5, Report 2183-4, 5 June 1970, The Ohio State University ElectroScience Laboratory, Department of Electrical Engineering; prepared under Contract AF19(628)-5929 for Air Force Cambridge Research Laboratories.
- Pathak, P.H. and Kouyoumjian, R.G., "The Radiation from Apertures in Curved Surfaces," Report 3001-2, December 1972, The Ohio State University ElectroScience Laboratory, Department of Electrical Engineering; prepared under Grant NGR 36-003-144 for National Aeronautics and Space Administration.
- Sinclair, G., "The Patterns of Antennas Located Near Cylinders of Elliptical Cross Section," Proc. IRE, Vol. 39, No. 6, June 1951.

TABLE I
GENERALIZED DIFFRACTION COEFFICIENTS AND ATTENUATION CONSTANTS

Surface	Square of Diffraction Coefficient $C_{\theta}^2 = (\text{Column A}) \cdot (\text{Column B})$		Attenuation Constant $\alpha_{\theta} = (\text{Column C}) \cdot (\text{Column D})$	
	A. Keller's Result	B. Correction Terms	C. Keller's Result	D. Correction Terms
Soft Acoustic and Soft EM	$\frac{-1/2 \epsilon - 5/6 \epsilon_0^{1/3} \epsilon - j\pi/12}{k^{1/6} \epsilon_0^{1/6} (-\epsilon_0)^2}$	$1 \cdot \left(\frac{\epsilon}{\epsilon_0}\right)^{2/3} \epsilon_0 \left(\frac{1}{30} + \frac{\epsilon}{\epsilon_0} - \frac{\epsilon^2}{180}\right) e^{-j\pi/3}$	$\frac{\epsilon_0}{\epsilon} e^{j\pi/6} \left(\frac{\epsilon_0}{\epsilon}\right)^{1/3}$	$1 \cdot \left(\frac{\epsilon}{\epsilon_0}\right)^{2/3} \epsilon_0 \left(\frac{1}{30} - \frac{\epsilon}{\epsilon_0} \epsilon_0^2 + \frac{\epsilon^2}{180} \epsilon_0^2\right) e^{-j\pi/3}$
Hard Acoustic	$\frac{-1/2 \epsilon - 5/6 \epsilon_0^{1/3} \epsilon - j\pi/12}{k^{1/6} \epsilon_0^{1/6} (\epsilon_0)^2}$	$1 \cdot \left(\frac{\epsilon}{\epsilon_0}\right)^{2/3} \left(\epsilon_0 \left(\frac{1}{30} + \frac{\epsilon}{\epsilon_0} - \frac{\epsilon^2}{180}\right) - \frac{1}{\epsilon} \left(\frac{1}{10} + \frac{\epsilon}{\epsilon_0} - \frac{\epsilon^2}{180}\right)\right) e^{-j\pi/3}$	$\frac{\epsilon}{\epsilon_0} e^{j\pi/6} \left(\frac{\epsilon_0}{\epsilon}\right)^{1/3}$	$1 \cdot \left(\frac{\epsilon}{\epsilon_0}\right)^{2/3} \left(\epsilon_0 \left(\frac{1}{30} - \frac{\epsilon}{\epsilon_0} \epsilon_0^2 + \frac{\epsilon^2}{180} \epsilon_0^2\right) + \frac{1}{\epsilon} \left(\frac{1}{10} - \frac{\epsilon}{\epsilon_0} - \frac{\epsilon^2}{180}\right)\right) e^{-j\pi/3}$
Hard EM	$\frac{-1/2 \epsilon - 5/6 \epsilon_0^{1/3} \epsilon - j\pi/12}{k^{1/6} \epsilon_0^{1/6} (\epsilon_0)^2}$	$1 \cdot \left(\frac{\epsilon}{\epsilon_0}\right)^{2/3} \left(\epsilon_0 \left(\frac{1}{30} + \frac{\epsilon}{\epsilon_0} - \frac{\epsilon^2}{180}\right) - \frac{1}{\epsilon} \left(\frac{1}{10} - \frac{\epsilon}{\epsilon_0} - \frac{\epsilon^2}{180}\right)\right) e^{-j\pi/3}$	$\frac{\epsilon}{\epsilon_0} e^{j\pi/6} \left(\frac{\epsilon_0}{\epsilon}\right)^{1/3}$	$1 \cdot \left(\frac{\epsilon}{\epsilon_0}\right)^{2/3} \left(\epsilon_0 \left(\frac{1}{30} - \frac{\epsilon}{\epsilon_0} \epsilon_0^2 + \frac{\epsilon^2}{180} \epsilon_0^2\right) + \frac{1}{\epsilon} \left(\frac{1}{10} - \frac{\epsilon}{\epsilon_0} - \frac{\epsilon^2}{180}\right)\right) e^{-j\pi/3}$

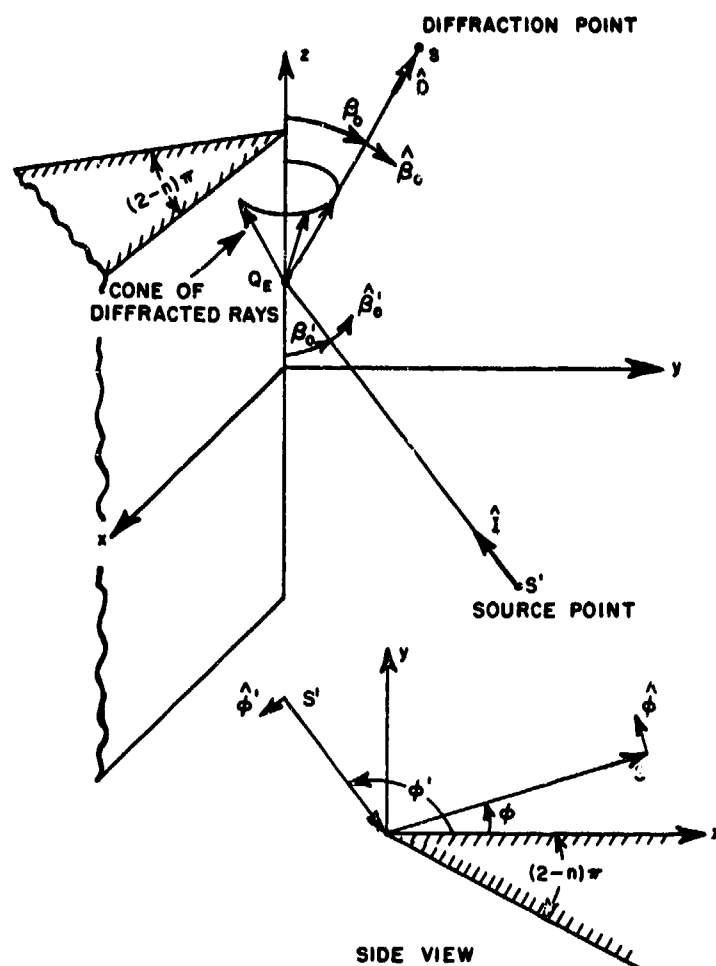
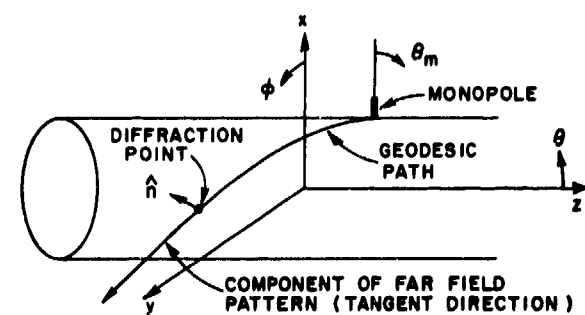
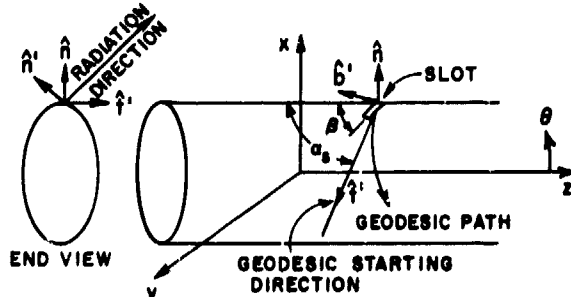


Fig. 1. Geometry for three-dimensional wedge diffraction problem.



(a) GEOMETRY OF MONOPOLE PROBLEM



(b) GEOMETRY OF SLOT PROBLEM

Fig. 2. Geometry of antennas mounted on an infinitely long elliptic cylinder.

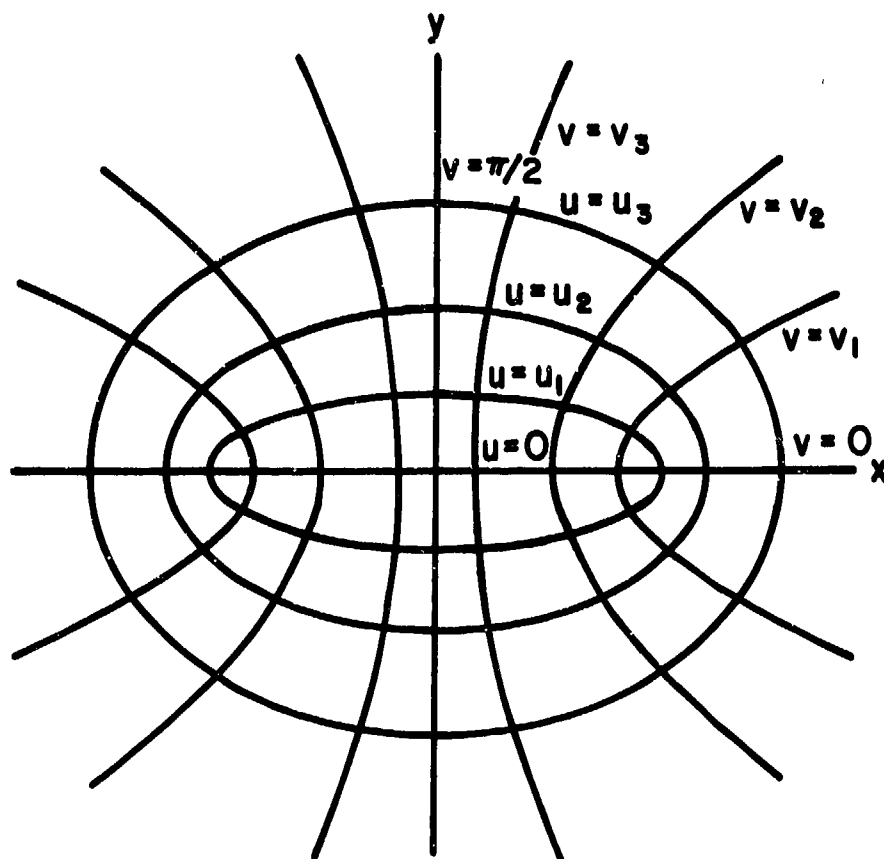


Fig. 3. Diagram showing the elliptic cylinder coordinate system.

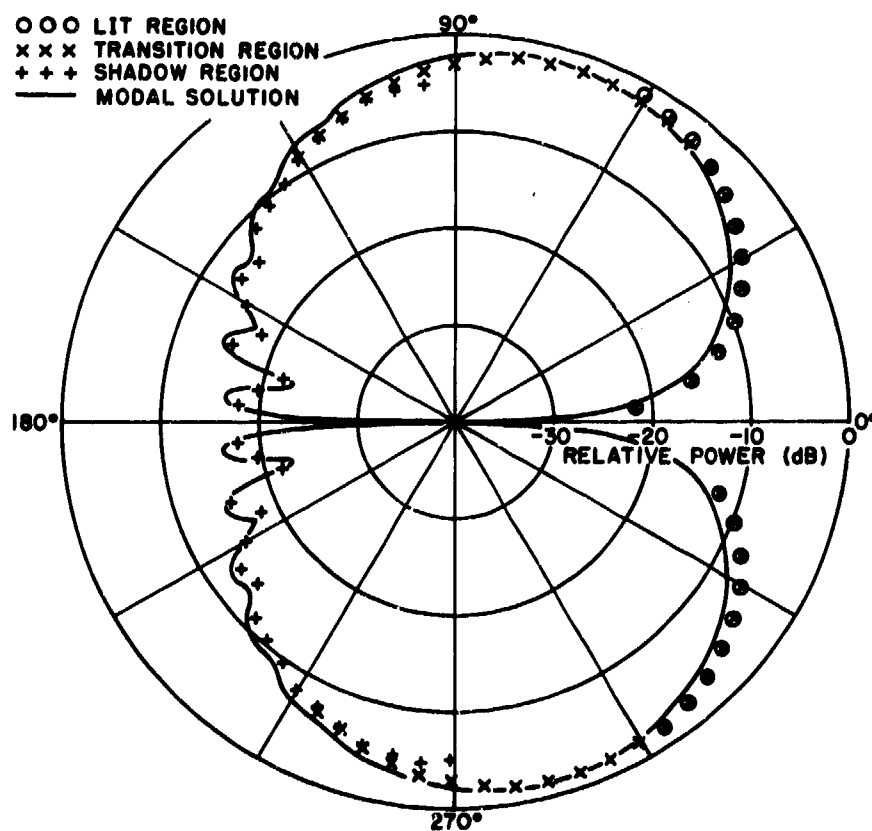


Fig. 4a. Principal plane pattern of a monopole mounted on a 2λ radius circular cylinder.

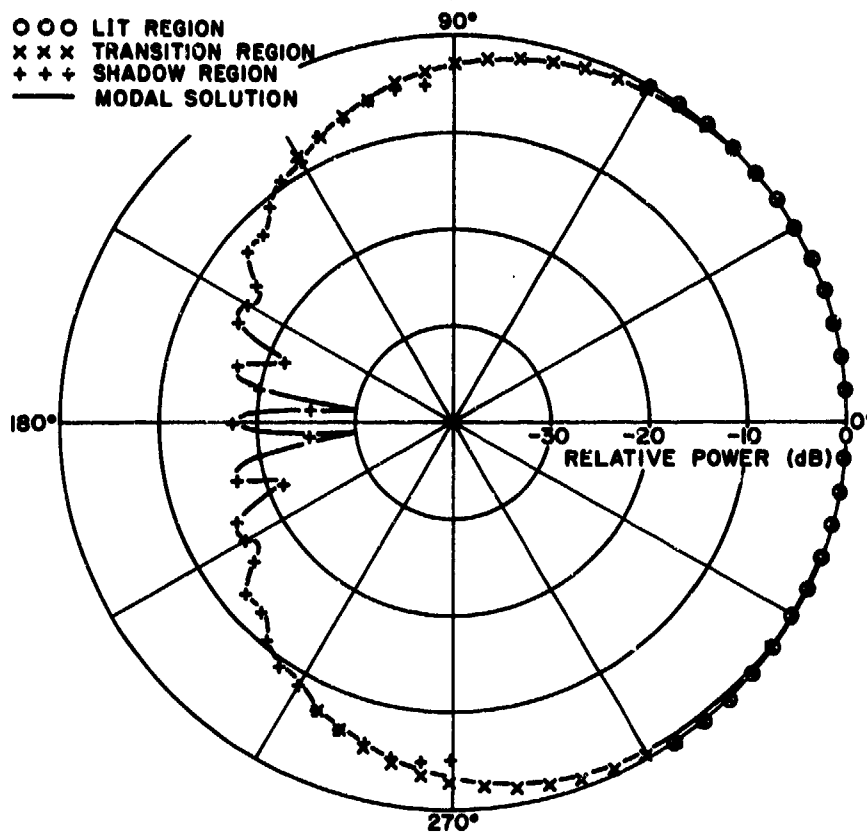


Fig. 4b. Principal plane pattern of an axial slot mounted on a 2λ radius circular cylinder.

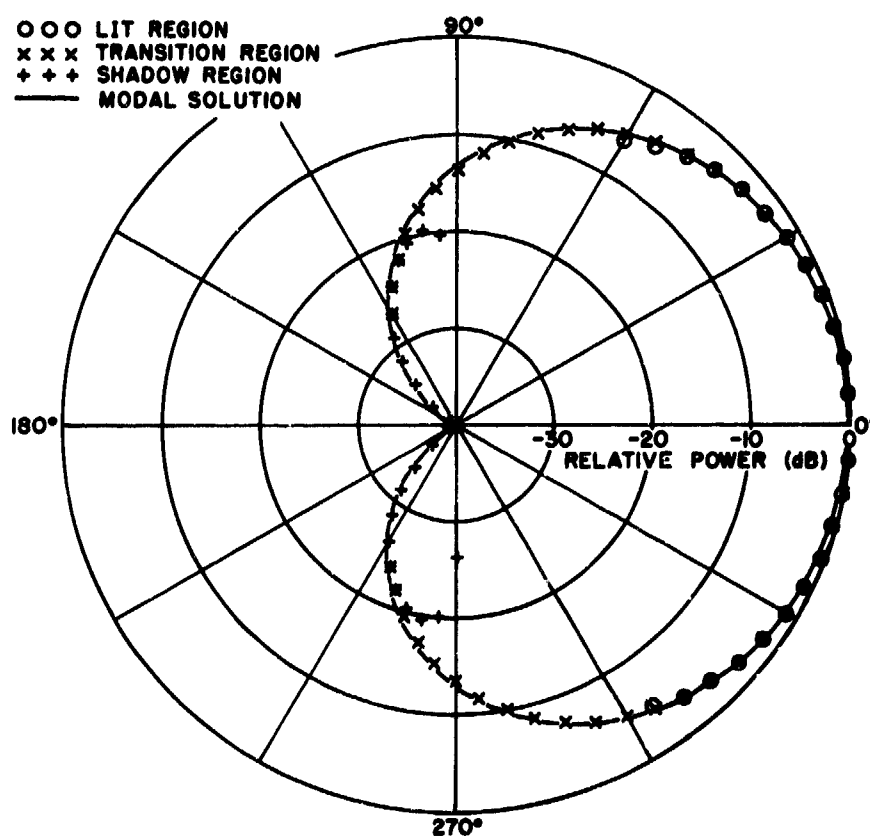


Fig. 4c. Principal plane pattern of a circumferential slot mounted on a 2λ radius circular cylinder.

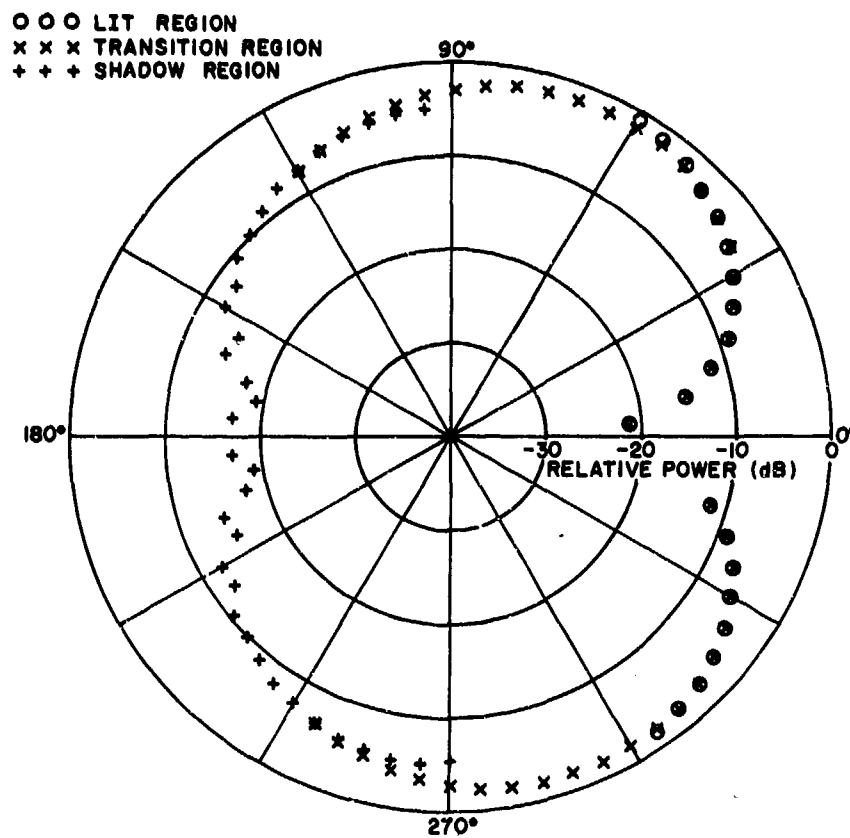


Fig. 5a. Principal plane pattern of a monopole mounted on an elliptic cylinder with $a_f = 4\lambda$ and $b_f = 2\lambda$.

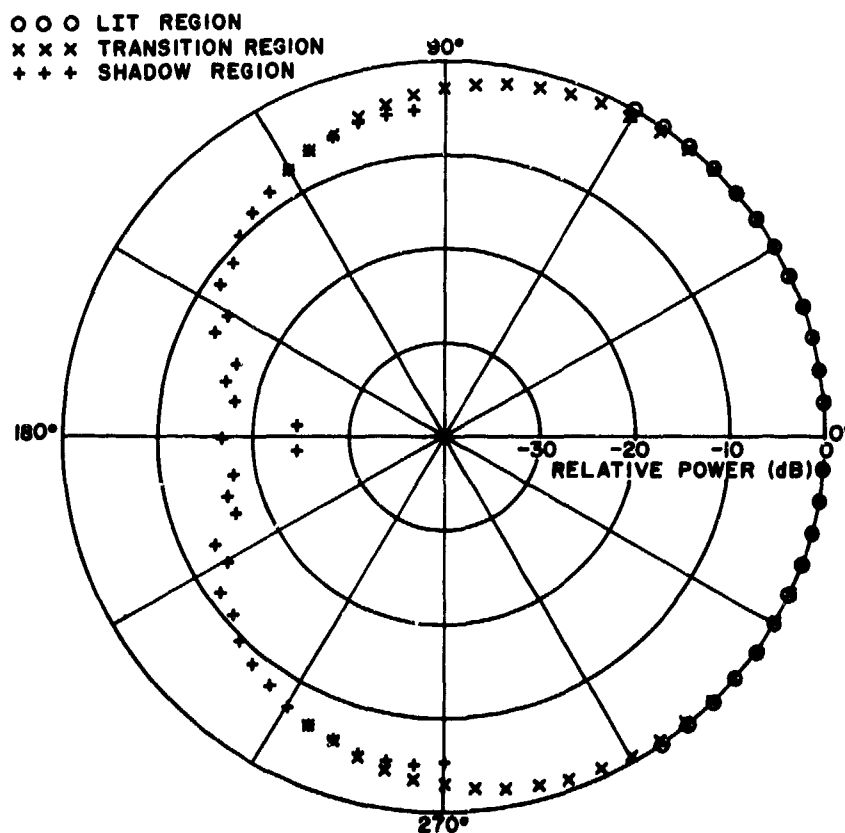


Fig. 5b. Principal plane pattern of an axial slot mounted on an elliptic cylinder with $a_f = 4\lambda$ and $b_f = 2\lambda$.

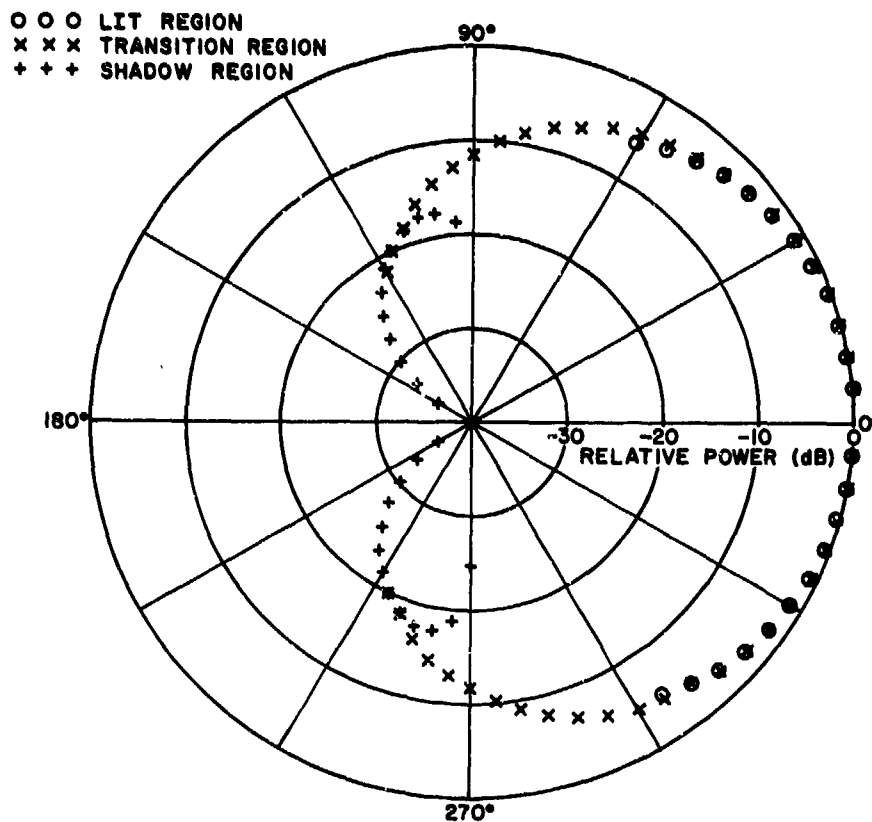


Fig. 5c. Principal plane pattern of a circumferential slot mounted on an elliptic cylinder with $a_f = 4\lambda$ and $b_f = 2\lambda$.

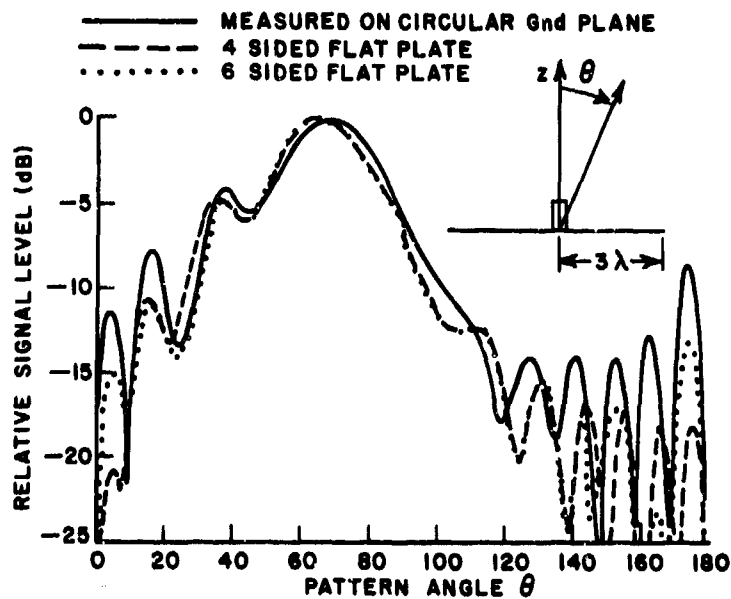


Fig. 6. Radiation pattern of a stub on a circular ground plane.

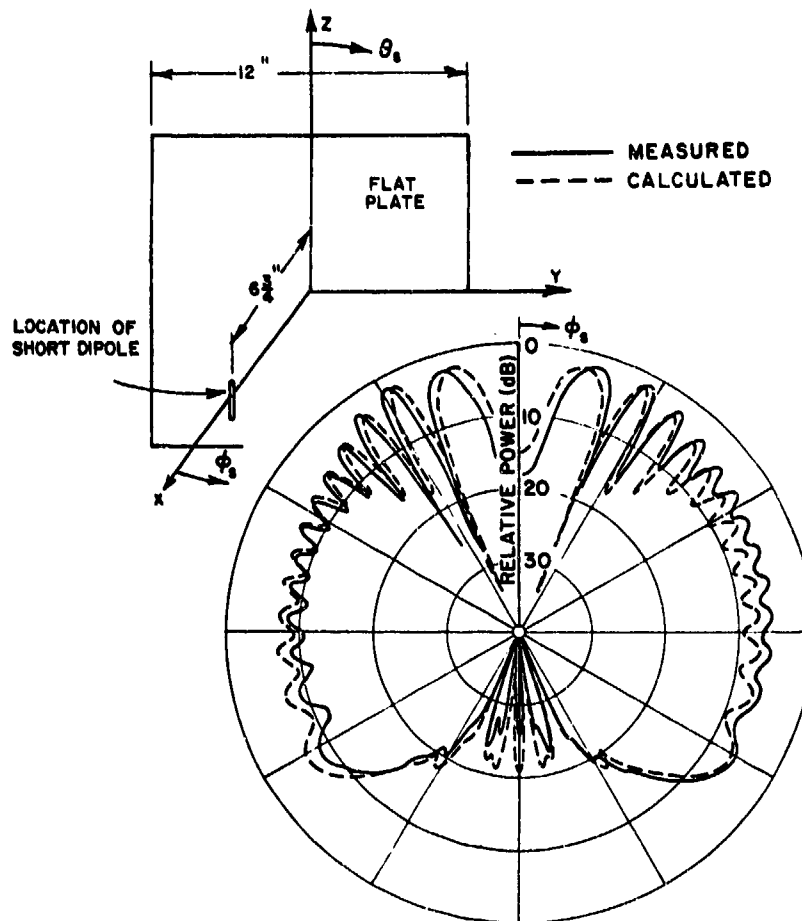


Fig. 7. E_ϕ radiation pattern for a small dipole mounted above a rectangular plate for $\theta_s = 90^\circ$ and $0^\circ < \phi_s < 360^\circ$ at $f = 10.43$ GHz.

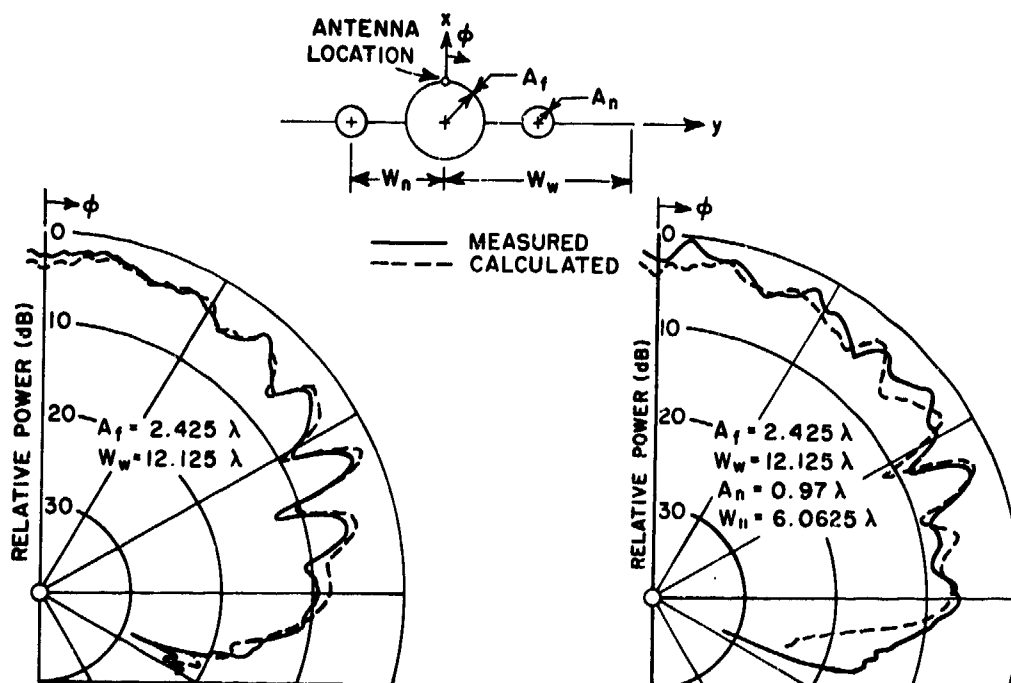


Fig. 8a. E_ϕ radiation pattern for an axial slot on a fuselage with finite length wing at $f = 11.45$ GHz.

Fig. 8b. E_ϕ radiation pattern for an axial slot on a fuselage with engine and finite length wing at $f = 11.45$ GHz.

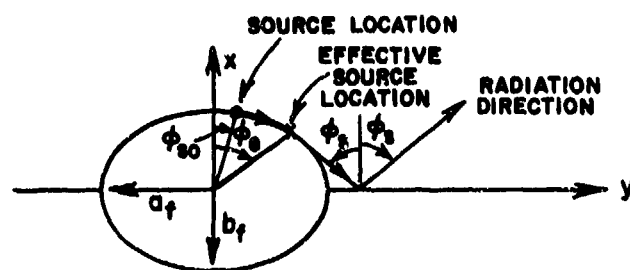


Fig. 9a. Reflection problem in x-y plane.

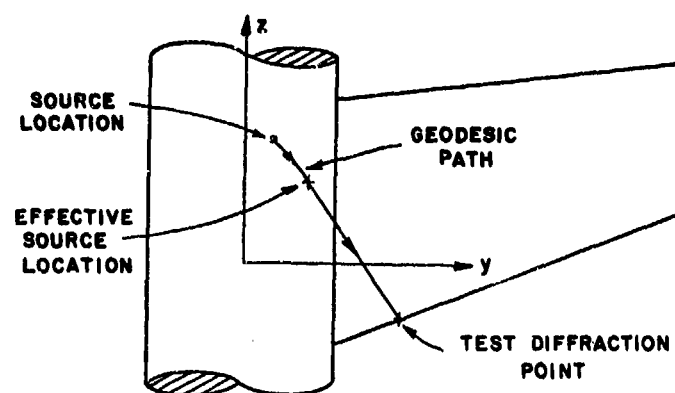


Fig. 9b. Diffraction problem in y-z plane.

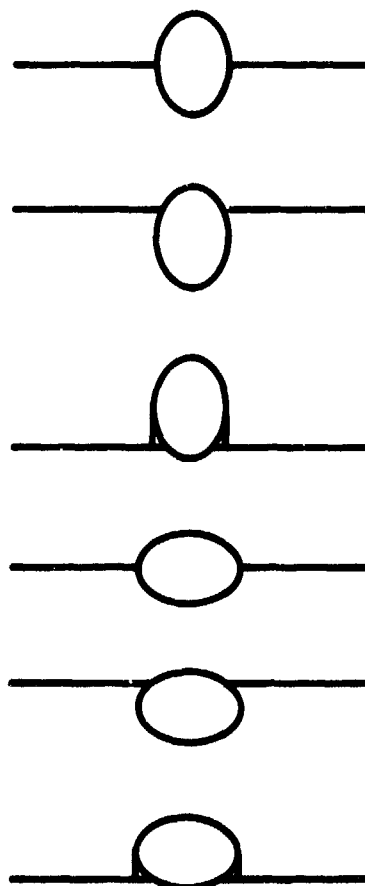


Fig. 10. Fuselage and wing geometry for theoretical aircraft model looking from the front.

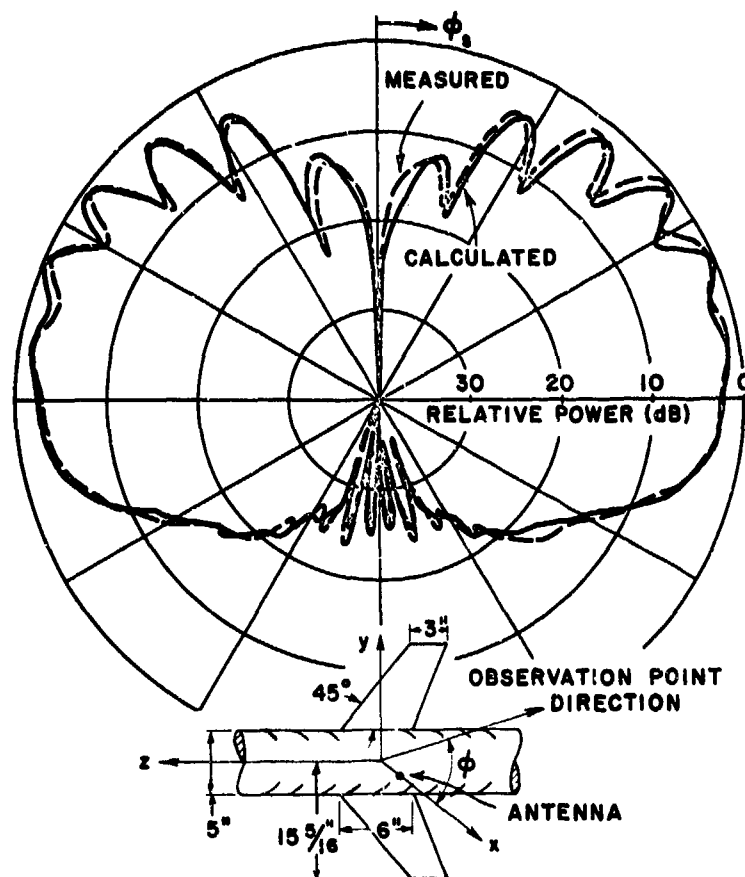


Fig. 11a. Roll plane pattern of monopole (E_ϕ) at $f = 11.45$ GHz.

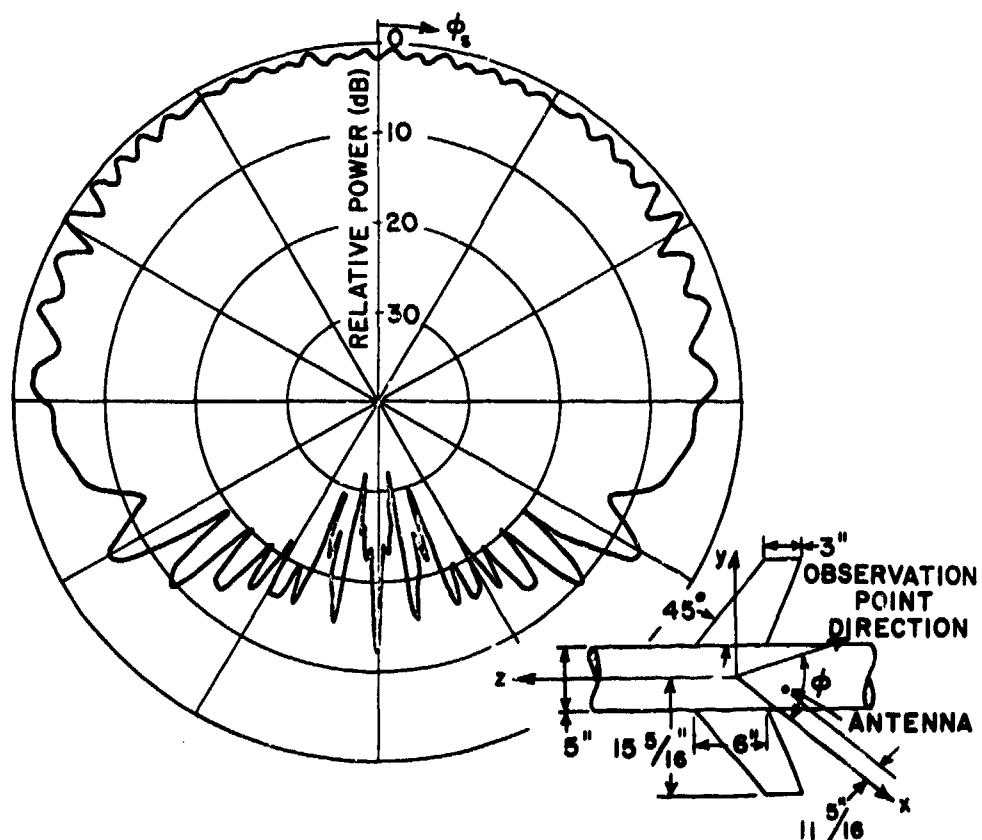


Fig. 11b. Roll plane pattern of axial slot (E_ϕ) at $f = 11.45$ GHz.

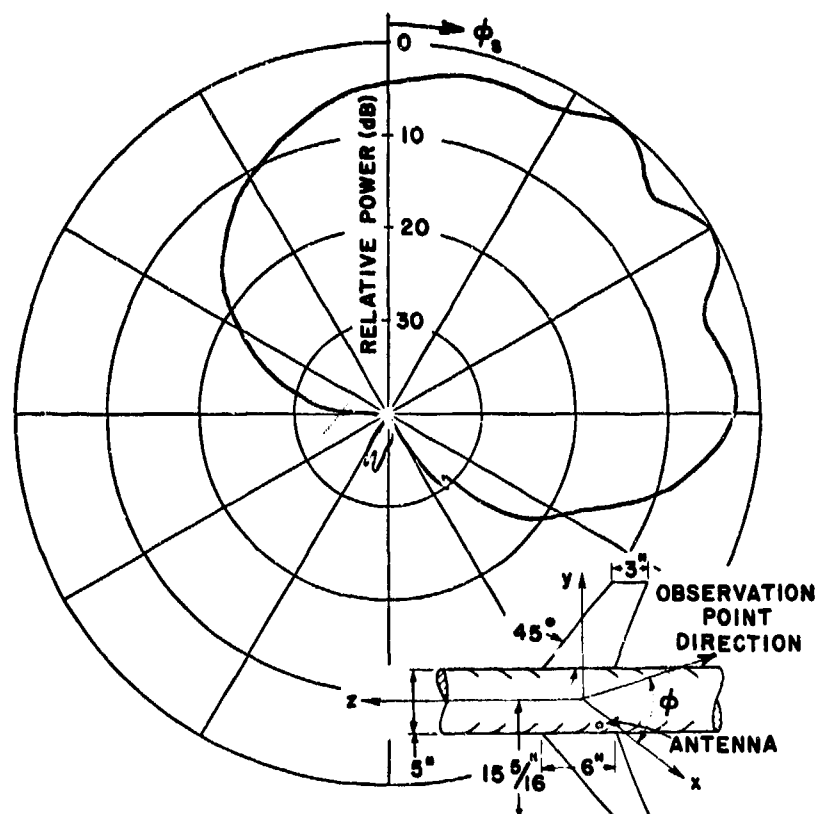


Fig. 11c. Roll plane pattern of a circumferential slot mounted over the wings but rotated 45° from the straight up direction of Fig. 11a.

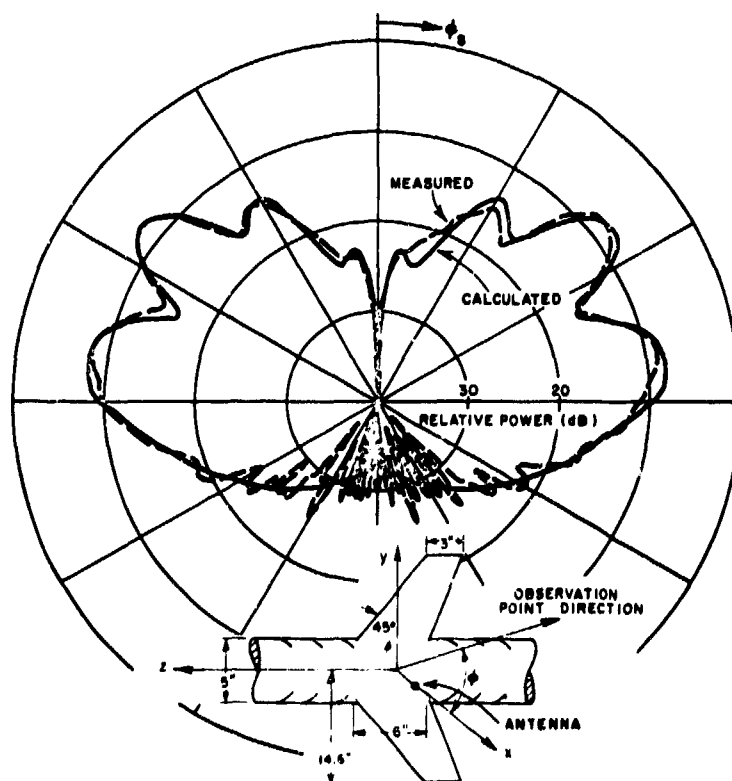


Fig. 12a. Roll plane pattern of a $\lambda/4$ monopole mounted on circular fuselage with wings attached at 45° above the central position.

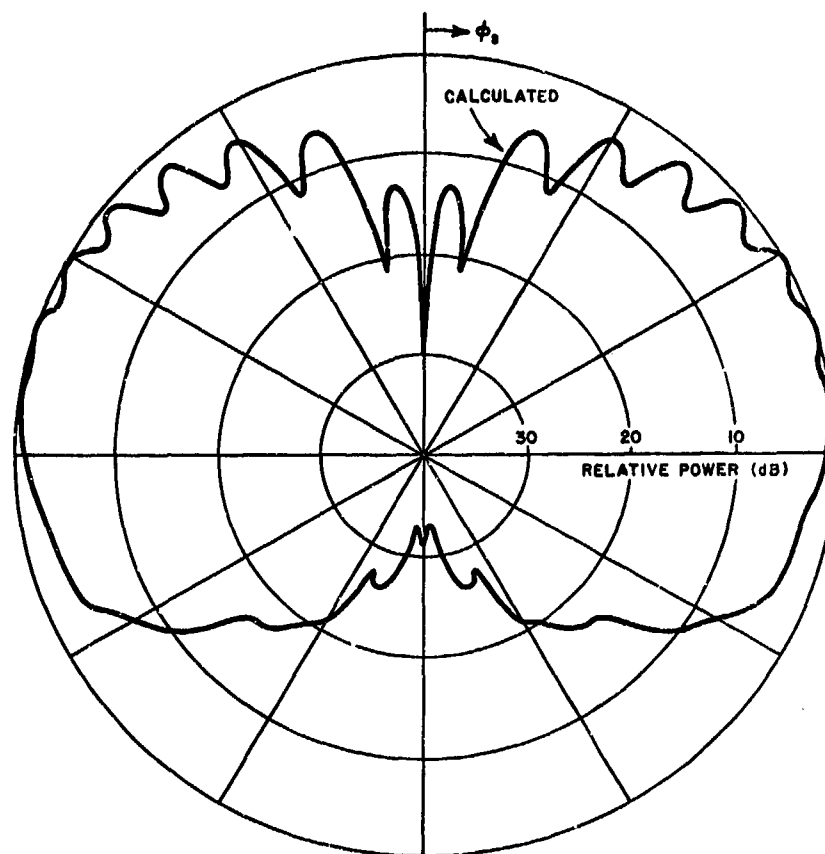


Fig. 12b. Roll plane pattern of a $\lambda/4$ monopole mounted on circular fuselage with wings attached at 45° below the central position, with same geometry as Fig. 12a otherwise.

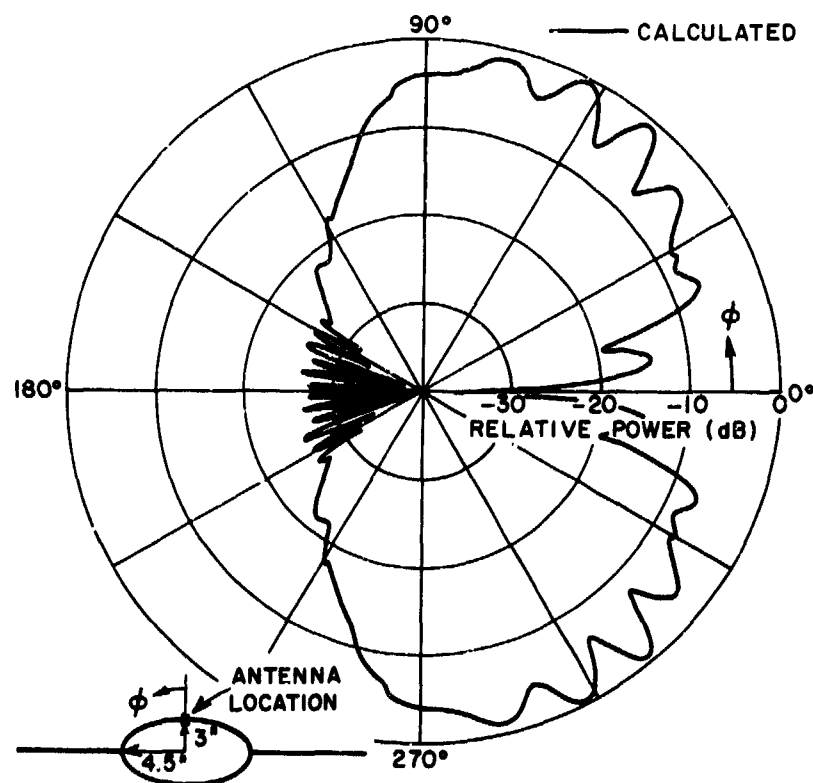


Fig. 13a. Roll plane pattern of a monopole mounted on an elliptic fuselage with centrally located wings at $f = 8$ GHz.

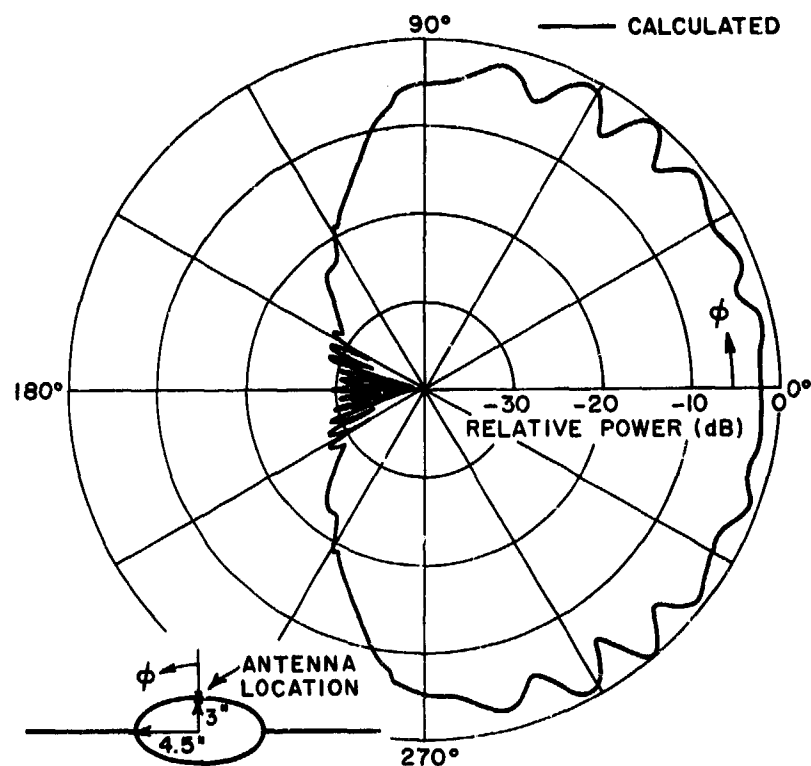


Fig. 13b. Roll plane pattern of an axial slot mounted on an elliptic fuselage with centrally located wings at $f = 8$ GHz.

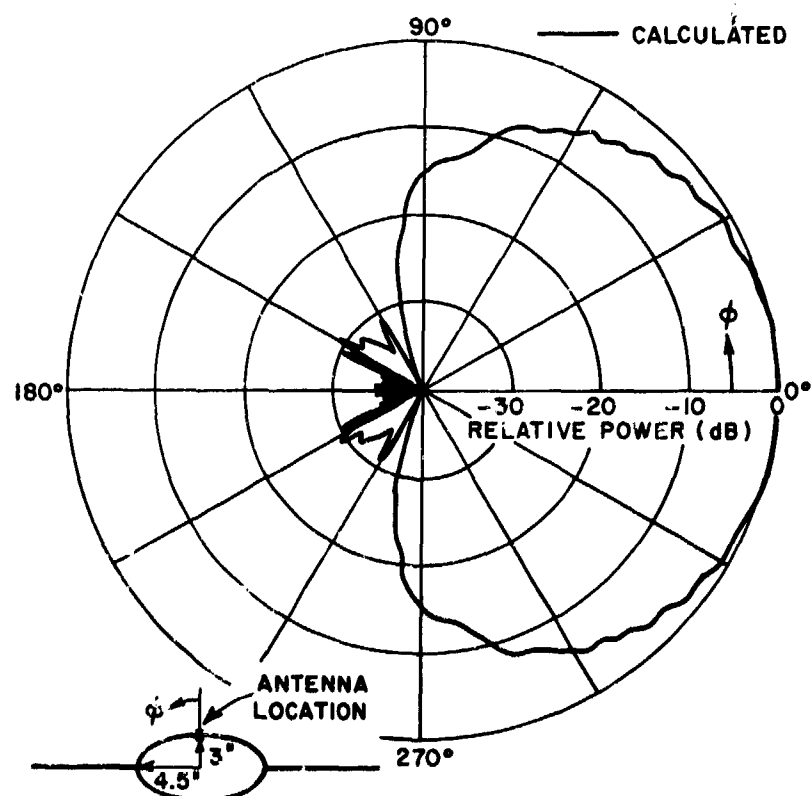


Fig. 13c. Roll plane pattern of a circumferential slot mounted on an elliptic fuselage with centrally located wings at $f = 8$ GHz.

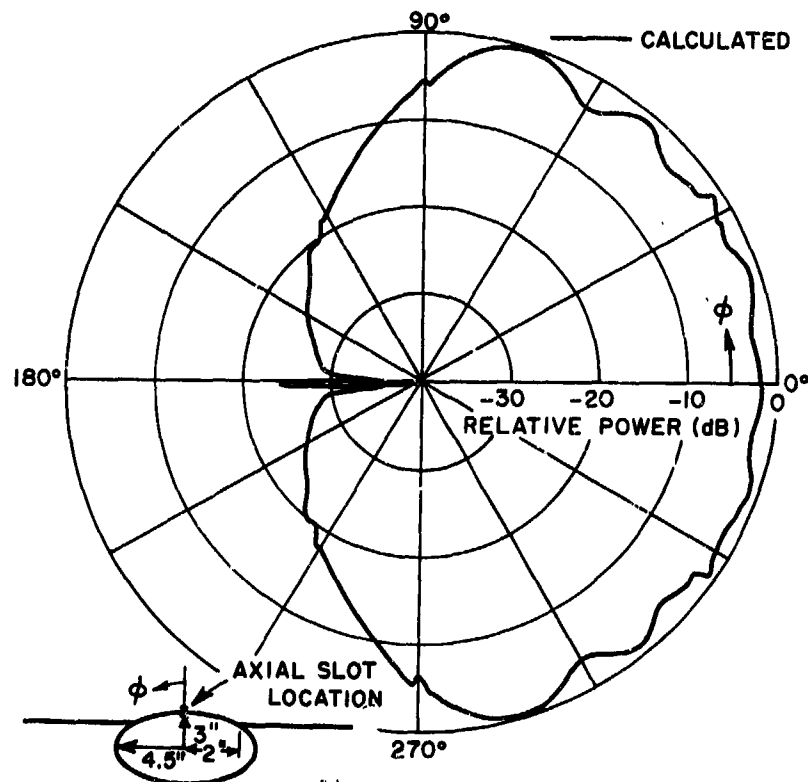


Fig. 14a. Roll plane pattern of an axial slot mounted on an elliptic fuselage with the wing attached above the central location at $f = 8$ GHz.

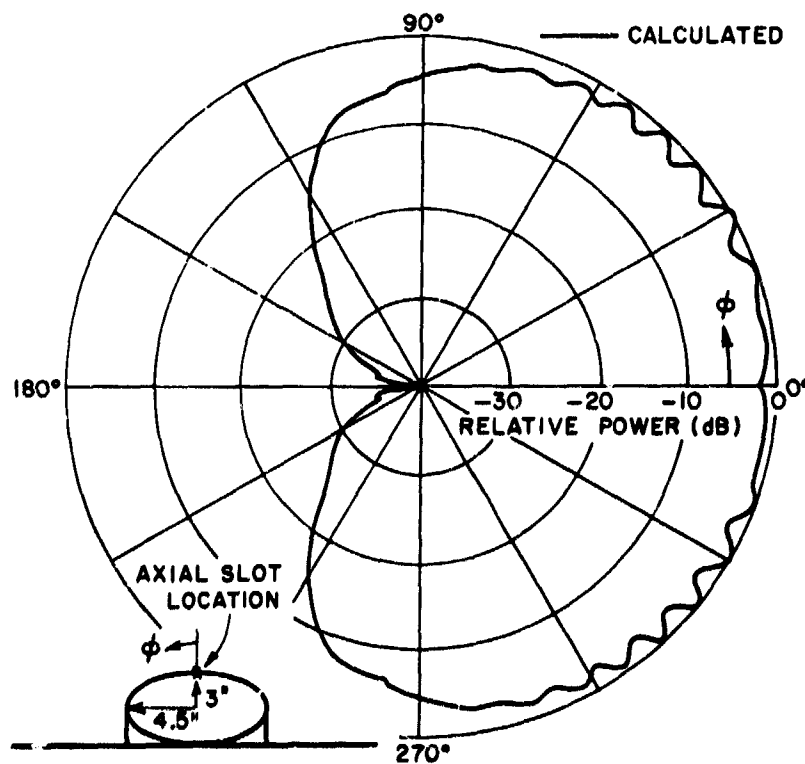


Fig. 14b. Roll plane pattern of an axial slot mounted on an elliptic fuselage with the wings attached below the central location at $f = 8$ GHz.

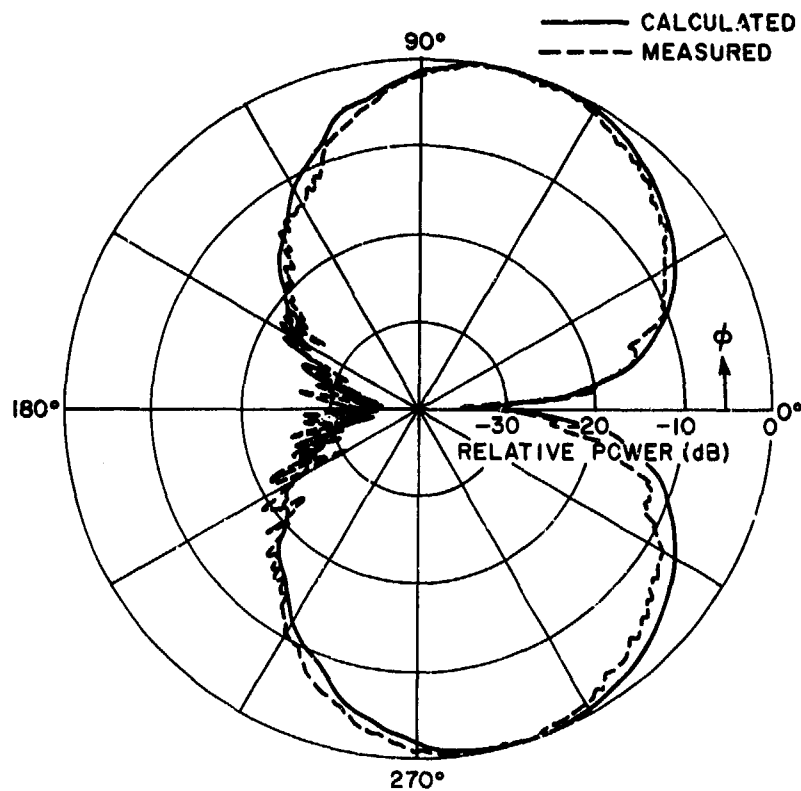


Fig. 15a. A $\lambda/4$ monopole mounted on the fuselage of a KC-135 forward of the wings.

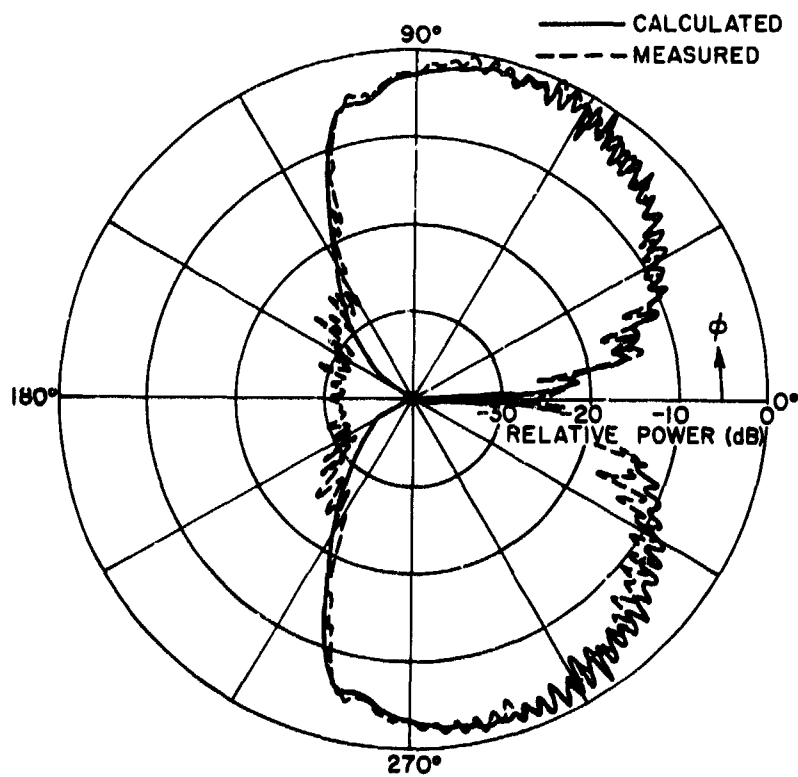


Fig. 15b. A $\lambda/4$ monopole mounted on the fuselage of a KC-135 over the wings.

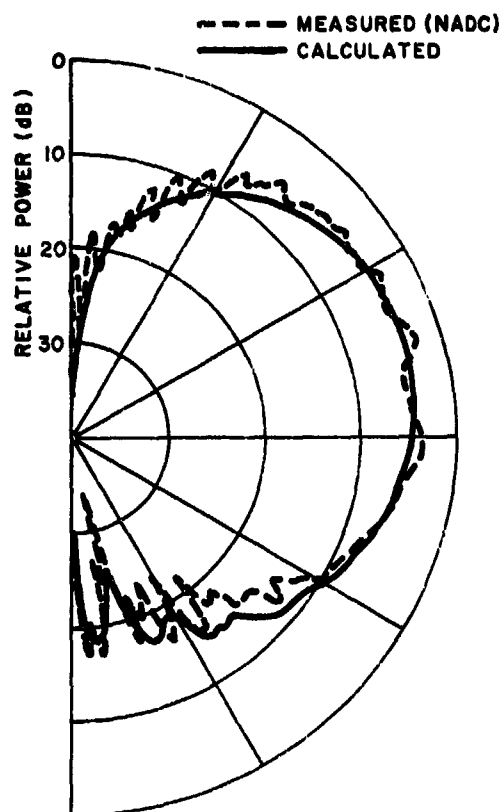


Fig. 16a. Roll plane pattern of a $\lambda/4$ monopole mounted 11" from the nose on the bottom of an 1/8 scale model of an F-4 aircraft at $f = 8.0$ GHz.

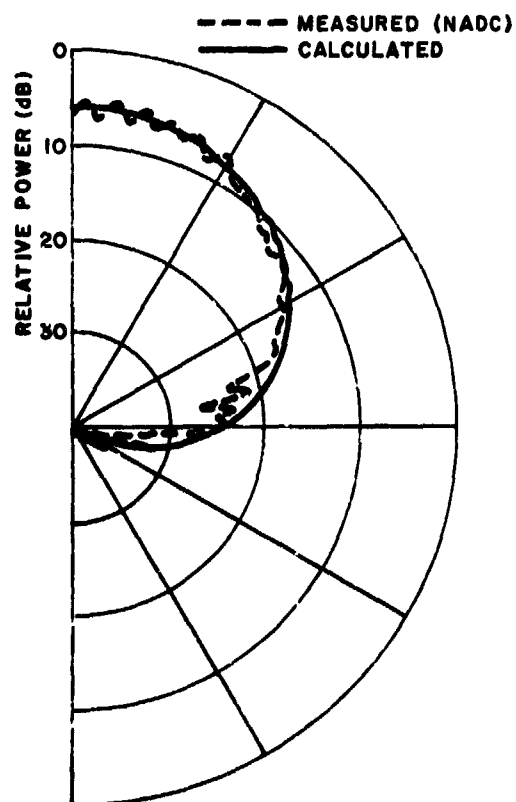


Fig. 16b. Roll pattern of a circumferential slot mounted 35-1/4" from the nose on the top of an 1/8 scale model of an F-4 aircraft at $f = 8.0$ GHz.

DISCUSSION

- A. SCHROTT:
- 1) Which method do you use in order to calculate the incident field?
 - 2) Do you consider multiple diffraction?
 - 3) Can you calculate the diffracted field of obstacles in the near field of your antenna?

W.D.BURNSIDE: 1) The incident fields are calculated using the standard GTD solutions of Professor Kouyoumjian of Ohio State University. If these reports are not available to you I might be able to assist. Basically three regions of field are considered:-

- a) the lit region (geometric optics)
- b) the transition region (Floek functions)
- c) the shadow region (creeping waves)

The edge diffracted fields are additionally included using wedge diffraction.

Multiple diffractions are not included in our solutions in that they are only strong in the plane of the wings and found to be rather weak. This is apparent in that our resulting patterns do not have jumps. Additionally multiple diffractions for arbitrary oriented edges is quite complex.

3) We can compute patterns up to a wavelength of the source or any scattering centre

W.HERSCH: There are several aspects that are of real importance when installing an antenna on an aircraft, particularly if one considers operation at microwave frequencies.

Can your programme take into account that typical aircraft surfaces are curved in two planes, that the phase centre of the antenna above the fuselage materially affects the elevation pattern and that the primary radiation pattern of any basic antenna is as a rule, seriously disturbed by protuberances from the aircraft, e.g., the proximity of other antennas or the cockpit window affecting the performance of a forward looking microwave antenna mounted on the nose of the aircraft.

J.E. HANSEN: Does your programme take into account multiply diffracted rays or do you consider single diffracted rays only?

W.D.BURNSIDE: The programme does not include multiply diffracted terms in that they only appear of any considerable magnitude in the vicinity of the plane of the flat plate. If these were important then we would have jumps in our calculated patterns in these regions. However, we have not seen jumps greater than about 1 dB in our patterns. Thus the results of neglecting multiple diffractions do not seem serious.

INVESTIGATION OF CHARACTERISTICS AND PRACTICAL IMPLEMENTATION OF ARBITRARILY POLARIZED RADIATORS IN SLOT ARRAYS†

J. S. Ajioka, D. M. Joe, R. Tang, N. S. Wong
Hughes Aircraft Company
Ground Systems Group
Fullerton, California 92634

SUMMARY

The feasibility of obtaining arbitrary polarization in both one and two dimensional arrays of slots in dual mode bifurcated waveguides has been demonstrated. The radiating element consists of a pair of crossed slots in the sidewall of a bifurcated rectangular waveguide that couple to even and odd waveguide modes. One linear polarization is excited by the even or "sum" mode and the orthogonal linear polarization is excited by the odd or "difference" mode. By superposing the sum and difference modes in the proper amplitude and phase, any arbitrary polarization can be synthesized.

A two-dimensional array consisting of eight waveguide linear arrays, ferrite phase shifters for scanning in the plane normal to the linear arrays and a feed network for power distribution and polarization control was constructed. Good radiation performance for various polarizations was obtained. In the case of linear polarization, the cross polarization component was down on the order of -25 dB and in the case of circular polarization, the axial ratio was on the order of 1 dB. The polarization was controlled with a phase shifter. Close in sidelobes of better than 20 dB were obtained for all polarizations. The above performance characteristics were obtained over a scan range of ± 20 degrees.

1. INTRODUCTION

Polarization agility is desirable for maximizing the signal to clutter or signal to jammer ratios for various target shapes. In principle, it is possible to suppress a jamming signal by using a polarization orthogonal to the jammer even when the jammer is within the main beam--an impossibility with coherent sidelobe cancelling techniques. Although circular polarization is effective for rain clutter rejection, it has a degrading effect in clear weather. Since it often rains in only certain sectors and may be clear in other directions, electronic polarization control is an obvious advantage. Other possible applications of polarization diversity is for minimizing friendly interference between radars operating in the same frequency band and it can also be used to minimize target glint problems because the nulls in a radar target cross section pattern are generally polarization dependent. Polarization versatility is generally unavailable in slot array antennas because of the difficulty in its implementation. The use of mechanically rotatable quarterwave plates in front of a conventional linearly polarized slot array aperture achieves limited success. However, this technique is cumbersome mechanically, and polarization cannot be changed on a pulse-to-pulse basis. This paper describes the theory, design, development and experimental performance of a slot array with electronically controlled polarization.

An arbitrarily polarized antenna is an antenna which can provide the most general elliptical polarization. This elliptical polarization includes linear and circular polarizations as special cases. In order to obtain polarization diversity, two orthogonal polarizations must be provided by the radiating element. The orthogonal polarizations can be dual linear or dual circular polarizations or they can be any two orthogonal elliptical polarizations. For instance, crossed slots, crossed dipoles, open-ended square or circular waveguide carrying the two dominant modes provide two orthogonal linear polarizations. Superpositioning of these orthogonal polarization components in the proper amplitude and phase can provide the most general elliptical polarization.

Hougardy and Shanks¹ have investigated an arbitrarily polarized linear slot array with crossed slots. One slot of the crossed slot pair couples to the TE_{10} mode and the other slot couples to the orthogonal TE_{01} mode of the square waveguide. By controlling the relative amplitude and phase of these two modes arbitrary polarization is achieved. Since the dimensions of the square waveguide are too large to be fitted into a two-dimensional array unless it is dielectrically loaded, it is not readily adaptable for two dimensional scanning arrays because of grating lobe formation. Ajioka has suggested that a rectangular waveguide loaded by a septum can possess two modes with equal phase velocities. Elliott² and Silvester³ have independently investigated this possibility and concurred in their findings. The septum waveguide will circumvent the space problem because the waveguide height can be made arbitrarily small without affecting the cutoff wavelength (see Figure 1). In addition to the septum waveguide, a rectangular waveguide with E-plane bifurcation which can support the sum or difference mode with exactly equal phase velocity is also a very attractive structure for the cross slot array design. Some of the methods of exciting the cross slots have been documented in a patent granted to Ajioka.⁴ A possible method of exciting cross slots in a bifurcated waveguide is shown in Figure 2. Since the partial septum waveguide has no advantage over the bifurcated waveguide for slot arrays and it possesses several disadvantages such as tighter fabrication tolerance requirements, poorer higher power handling and difficulty in equalizing the slot coupling to the two modes, it will not be discussed further in this paper.

2. PRINCIPLE OF OPERATION

The principle of operation of the antenna is based on a dual mode waveguide of such a geometry that each mode acts as an independent transmission line and independently excites orthogonal polarization fields in a dual polarizable element in a simple and convenient manner. By proper combination of these two orthogonal

†This work was supported by USAF Cambridge Research Laboratories, Office of Aerospace Research, L. G. Hanscom Field, Bedford, Massachusetts under Contract F19628-70-C-0142.

polarizations, any arbitrary polarization is realizable. Figure 2 shows a bifurcated waveguide operating in the sum and difference modes to give the orthogonal polarization. When the two halves of the bifurcated waveguide are excited in phase (sum mode) all R.F. currents on both sides of the septum flow in opposite directions and there is no field excited in the septum slot. In the sum mode, the bifurcated waveguide acts essentially as a single waveguide of twice the height operating in the dominant TE_{10} mode. Hence, any aperture cut in the sidewall will have a component of electric field (E-vector normal to the waveguide axis) excited in it due to the interruption of the transverse shunt currents in the waveguide. If the aperture is symmetrical about the axis normal to the waveguide axis, the sum mode will produce only a net polarization normal to the waveguide axis. Now if the two waveguide halves are excited in anti-phase, the R.F. currents in both sides of the septum will flow in the same direction and any aperture cut in the septum will have a component of field excited in it polarized in the same direction as the current that it interrupts. Also, the transverse currents in the sidewall flow in opposite directions; hence, their effects cancel in the sidewall aperture resulting in no radiation if the aperture is small enough to prevent the higher order odd mode from radiating. The slot in the septum is excited by the difference mode, this slot in turn excites the radiating sidewall aperture with polarization parallel to the waveguide axis. In short, the sum mode excites perpendicular polarization and the difference mode excites longitudinal polarization independently to produce the desired orthogonal polarizations.

3. METHOD OF CONTROLLING SLOT EXCITATION

In order to design an aperture distribution which gives the desired radiation pattern, the slot excitation must be controllable over a wide range of coupling coefficients for both polarization modes. Since the direction of the main beam depends on the phase velocity of the feeding wave, it is necessary that the loaded phase velocities of the sum and difference modes be equal so that their main beams coincide for all frequencies. Both the loaded phase velocities and slot excitation depend on the slot parameters. In the sum mode, the crossed slot is excited by transverse currents in the sidewall and is most simply represented by a shunt admittance. In the difference mode, the crossed slot is excited by the septum slot which is in turn excited by the longitudinal current in the septum and is most simply represented by a series impedance. The equivalent circuits are shown in Figure 3. If the admittance and impedance due to slot loading are real, the phase velocities would remain equal but since this is not the case in general, the slot admittances for one polarization mode and the slot impedances for the other polarization mode must be controllable to simultaneously satisfy the required admittance/impedance for aperture distribution control, equality of phase velocity and equality and minimization of power into the terminating load. Some of the crossed slot parameters for this control are:

1. Slot length
2. Slot width
3. Slot angle
4. Septum slot length
5. Septum slot width
6. Septum slot angle
7. Septum thickness
8. Waveguide width
9. Waveguide height

For the sum mode it is, in principle, possible to control the excitation by the slant angle of the crossed slots as is commonly done in linearly polarized sidewall slot arrays except that in the crossed slots, the longitudinal components of polarization oppose and only perpendicular polarization is radiated. This method of sum mode coupling was found to be impractical for low coupling values when near resonant length slots were used. For this reason, short non resonant slots were used and the coupling to the sum mode was controlled by slot length alone with the slot angle kept constant at about 50 degrees. For the difference mode, the slot coupling depends on the septum slot length and also on the radiating slot lengths as for the sum mode.

The impedance/admittance parameters of the nonresonant crossed slots as a function of slot length were determined by the "cavity" method⁵ of measurement. The measured data for a slot angle of 50 degrees is shown in Figures 4a and 4b. The conductance of the slots to the sum mode and the resistance of the slots to the difference mode can be controlled over a wide range (G/Y_0 , $R/Z_0 = .002$ to 0.15). This range is large enough to design any practical aperture distribution with minimum power lost in the terminating load. As shown in Figure 4a, the equivalent circuit for the sum mode consists of shunt elements (G and B) and the equivalent circuit for the difference mode consists of series elements R and X and also a shunt capacitance B_1 . The lengths of the non-resonant crossed slots were chosen to give the desired range of crossed slot coupling (G/Y_0) values for the sum mode. After this was done, the septum-slot length was adjusted to make the coupling of the difference mode to any crossed slot equal to that of the sum mode. That is, R/Z_0 is made equal to G/Y_0 . It was found that the septum slot length remained essentially constant for all slot lengths when the coupling coefficients of both modes were made equal. As a result, the desired range of coupling coefficients for both modes could be obtained by varying only one parameter; namely, the length of the crossed slots.

Although G/Y_0 is equal to R/Z_0 , there is a further requirement that the phase velocities of the sum and difference modes must be equal. The equivalent circuit for the sum mode is purely a shunt element and if the equivalent circuit to the odd mode were a purely series element, making B/Y_0 equal to X/Z_0 would insure equal phase velocities. However, the odd mode equivalent circuit is not purely a series circuit because of the shunt capacitance B_1 of Figure 3 and therefore must be represented by a tee or pi section. For this reason, the phase velocities of the two modes when loaded by the crossed slots are not equal. The inequality of phase velocities can be corrected by cutting non-radiating slots in the septum. Any aperture cut in the septum has negligible effect on the sum mode characteristics but, in general, does affect the difference mode. This property is used to make the difference mode phase velocity equal to that of the sum mode. This is accomplished by cutting a transverse slot in the septum in the region between the radiating crossed slots. The transverse slot extends across the entire width of the waveguide. The insertion phase is determined by the width of the slot. This insertion phase is leading which is required to compensate for the lagging phase due to the shunt capacitance (B_1) for the difference mode. These equalizing slots are used in pairs separated by $\lambda_g/4$ to minimize the mismatch effects. Measured insertion phase of the transverse slot as a function of slot width is shown in Figure 5.

4. EXPERIMENTAL RESULTS

In order to demonstrate the feasibility of this technique, a two dimensional array comprised of twelve linear arrays of 36 crossed-slots per array was fabricated and tested. A photograph of the array is shown in Figure 6. The central eight linear arrays were actively fed with a corporate feed and the outer four arrays were terminated in matched loads. Each of the eight active arrays had a dual ferrite phase shifter at the input--one phase shifter for each mode. The phase shifters are used for electronically steering the beam in the plane normal to the linear arrays and are also used for electronically controlling the polarization. A schematic diagram of one possible scheme to achieve polarization diversity by combining the two orthogonal polarizations of the array is shown in Figure 7.

4.1 Aperture Distributions

The amplitude and phase distributions across the aperture of each linear array were measured with and without mutual coupling from neighboring arrays. These measurements were made using a near field measuring facility as shown in Figure 8. A small dipole was used as a probe to sample the radiated field distribution from the slot array aperture. The dipole was moved along the linear array by sliding its carriage on a track installed parallel to the axis of the slot array.

Typical measured amplitude distributions for both the sum and difference mode excitations are shown in Figures 9 and 10. It can be seen that the near field probe can resolve the radiated field from the individual slots, and the peaks correspond to the relative power radiated by each slot. The envelope of the plot is, therefore, the measured aperture distribution. The plots show that the ideal design distribution was closely realized for both modes.

The measured phase distributions across the aperture of the slot array for both the sum and difference modes are shown in Figure 11. These phase measurements were made after compensating for the difference in phase velocities between the two modes. The measured phase distribution compared closely with the computed design.

The measured amplitude distributions across the array aperture with its neighboring arrays excited for both the sum and difference modes are shown in Figures 12 and 13 as a function of beam scan angle. The results show that the envelope still agrees closely with the theoretical distribution, and it remains fairly constant for all scan angles.

4.2 Radiation Patterns

The measured azimuth (plane of linear array) patterns at zero degree elevation (plane normal to linear arrays) are shown in Figures 14 and 15 for both polarization modes. It can be seen that the beam shapes of the two orthogonal linear polarizations are essentially identical. Also, since the phase velocities were equalized, the beams point in the same direction, this assures a good axial ratio over the main beam in the case of circular polarization. The main beam direction is 10 degrees from the array broadside as predicted in the array design. A sidelobe in the order of 21 dB appears at the opposite side making an angle of 10 degrees with respect to the array axis. This sidelobe is commonly referred to as the "reflection" lobe of the linear array. The reflection lobe in this case is more pronounced because of two reasons: (1) the cross slot is nonresonant, and (2) the number of elements in the linear array is small. This reflection lobe can be reduced by tuning the cross slots which is a well known technique in waveguide slot design. At about 46 degrees, another sidelobe can be observed in both patterns shown in Figures 14 and 15. This sidelobe is an uncanceled "grating lobe" and is caused by the fact that the number of linear arrays is too small. The problem is made more significant by the choice of element spacing. The mechanism for the formation of the extraneous sidelobe can be understood from the following reasoning. Consider a single linear array of slots, the element spacing is about 1.1λ . The pattern of one linear array consists of a main beam located at -10 degrees, and a grating lobe at +46 degrees. By the addition of another linear array with the elements offset by half of an element spacing in a staggered manner, the main beams of the two linear arrays reinforce each other, but the grating lobes cancel. The cancellation is only complete along the horizontal plane when the radiation phase of these two linear arrays is in antiphase. Away from the horizontal plane, the cancellation is imperfect because of phase center separation in elevation between the linear arrays and two residual grating lobes remain. One is directly above the other and the other one directly below the horizontal plane. This pair of grating lobes is analogous to an elevation difference pattern. As more pairs of linear arrays are added, the magnitude of these grating lobes is reduced until they disappear entirely. However, for the present case in which there are only a total of eight linear arrays, the suppression of these residual grating lobes is incomplete. The degree of cancellation is also dependent on manufacturing tolerance of various components. Obviously, the unbalance in either amplitude or phase between the linear arrays would produce a residual sidelobe. The reduction of this residual grating lobe is automatic when more linear arrays are employed in a typical two-dimensional array. An estimate of the residual grating lobe as a function of the number of linear arrays has been made. For a typical planar array antenna consisting of 40 linear arrays, the residual grating lobe is estimated to be below 40 dB.

Radiation patterns were also measured for various scan angles. Figure 16 shows the patterns for the two orthogonal linear polarization modes for a 20 degree elevation scan. The patterns are essentially the same as for 0 degree scan.

4.3 Axial Ratios

The experimental array was set for circular polarization, and the axial ratio was measured over various points within the main beam. As shown in Figure 17, the axial ratio between the 3 dB points is within 0.5 dB. This data verifies that the individual beams for vertical and horizontal polarizations are coincident.

4.4 Cross Polarization

The cross polarization level was measured to be about 30 dB at the main beam region and is generally much lower elsewhere. The cross polarization level at the grating lobe region appears to be significant for this experimental 2-D array. This is due to incomplete cancellation of the grating lobes among a small number of arrays. For a larger 2-D array, the residual grating lobe and its cross polarized energy are expected to be greatly diminished.

REFERENCES

1. Hougardy, H. H. and H. E. Shanks, "Arbitrarily Polarized Slot Array," 1958 IRE WESCON Convention Record, Part I, August 1958, pp. 157-160.
2. Elliott, R. S., "Two-Mode Waveguide for Equal Mode Velocities," IEEE Transactions on Microwave Theory and Techniques, Vol. MTF-16, No. 5, May 1968, pp. 282-286.
3. Silvester, P., "A General High-Order Element Waveguide Analysis Program," IEEE Transactions on Microwave Theory and Techniques, Vol. MTT-17, No. 4, April 1969, pp. 204-209.
4. Ajioka, J. S., "Two-Mode Waveguide Slot Array," Patent Number 3,503,073, 24 March 1970.
5. Lacy, P. D. and K. E. Miller, "An Improved Method for Measuring Losses in Short Waveguide Length," Hewlett Packard Journal, Vol. 9, December 1957.

ACKNOWLEDGEMENTS

The authors wish to thank Dr. R. Mack of AFCL for helpful discussions and suggestions during the course of this investigation.

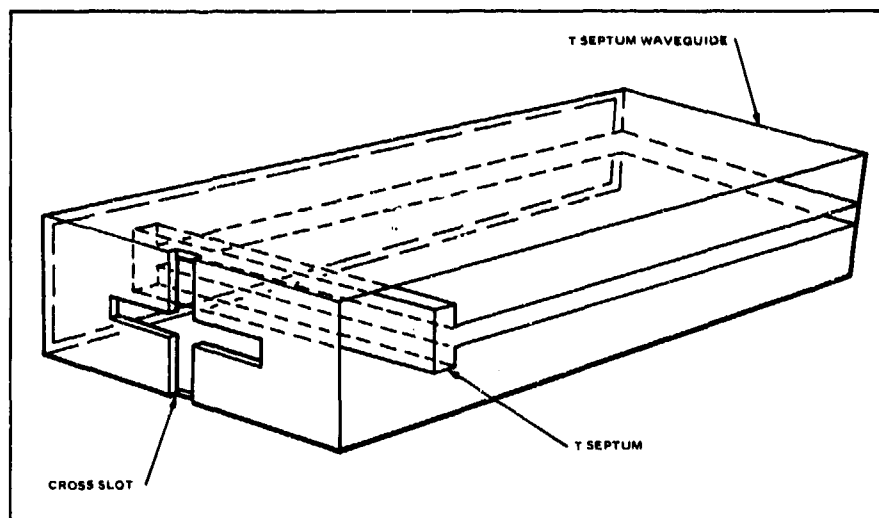


Fig.1 An arbitrarily polarized cross slot in the T-septum waveguide

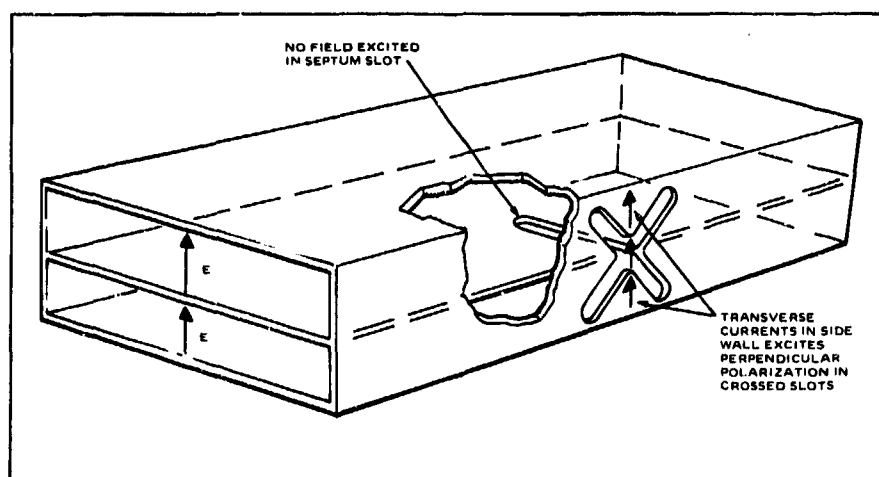


Fig.2(a) Sum (even) mode excites perpendicular polarization

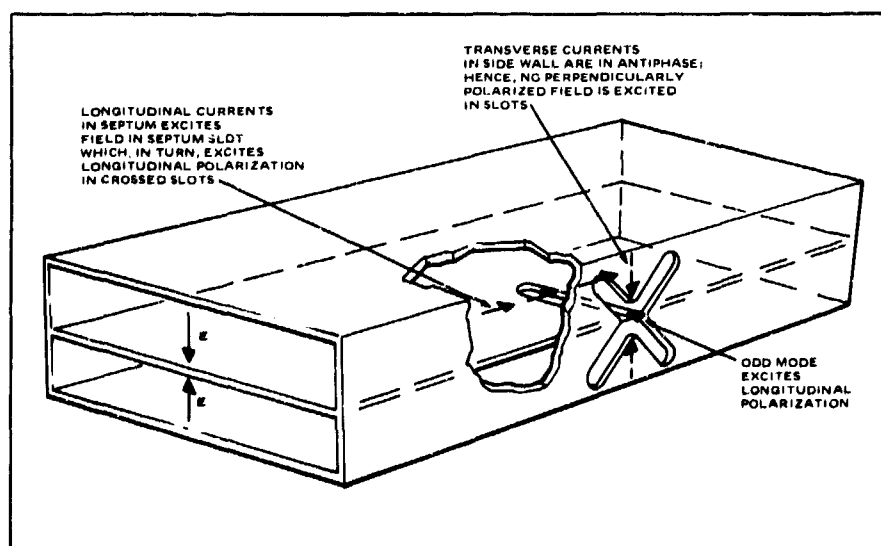


Fig.2(b) Difference (odd) mode excites longitudinal polarization in crossed slots

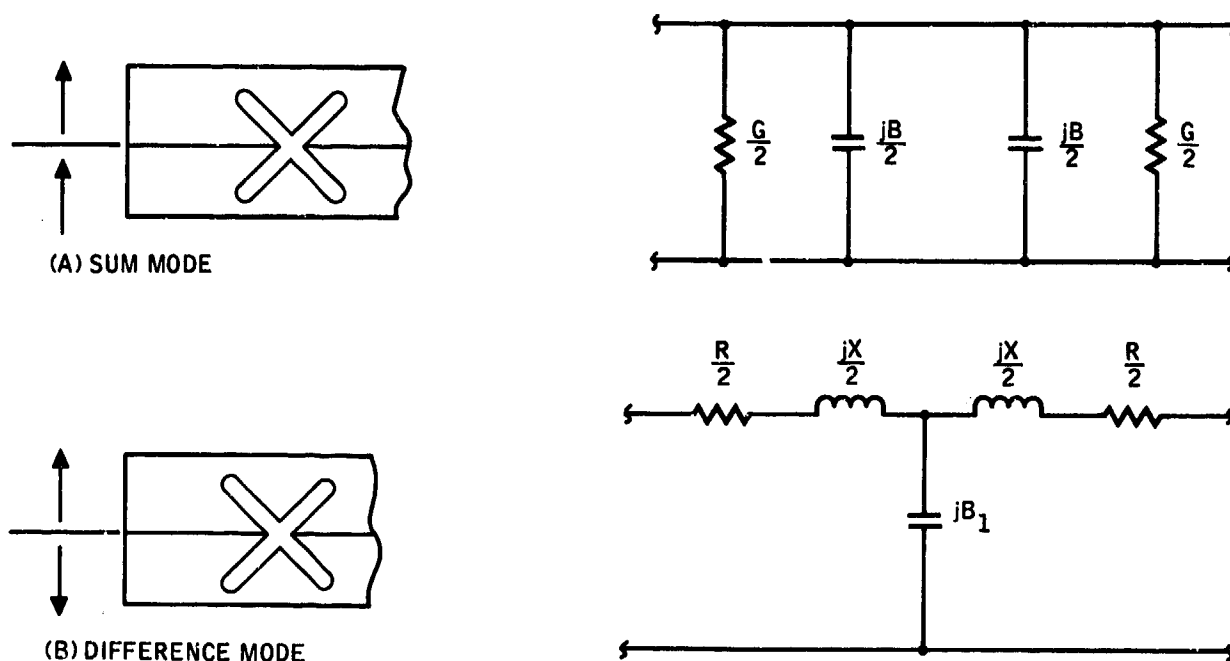


Fig.3 Equivalent circuit of cross slot in two modes of operation

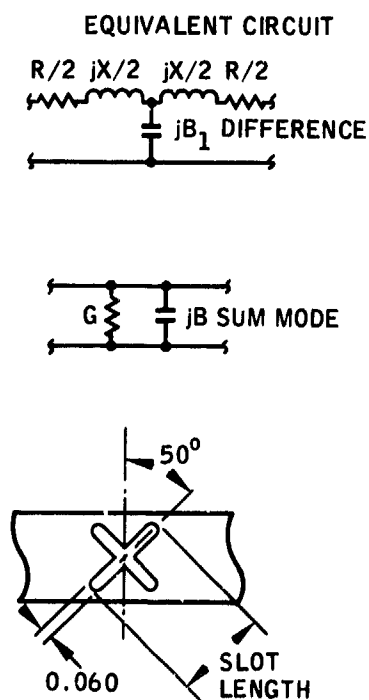
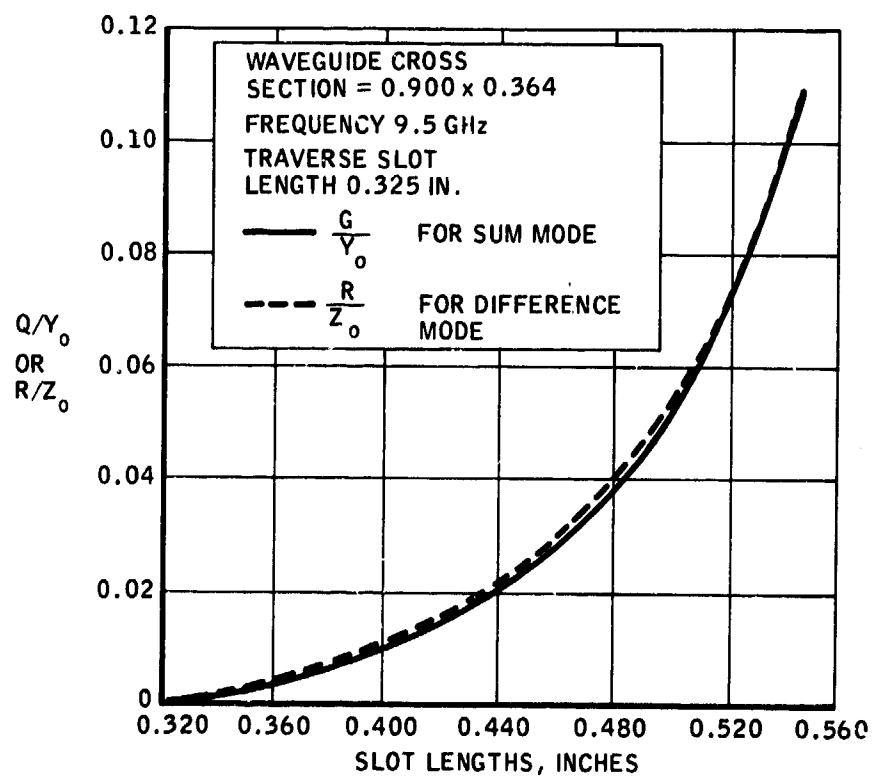


Fig.4(a) Normalized slot conductance or resistance

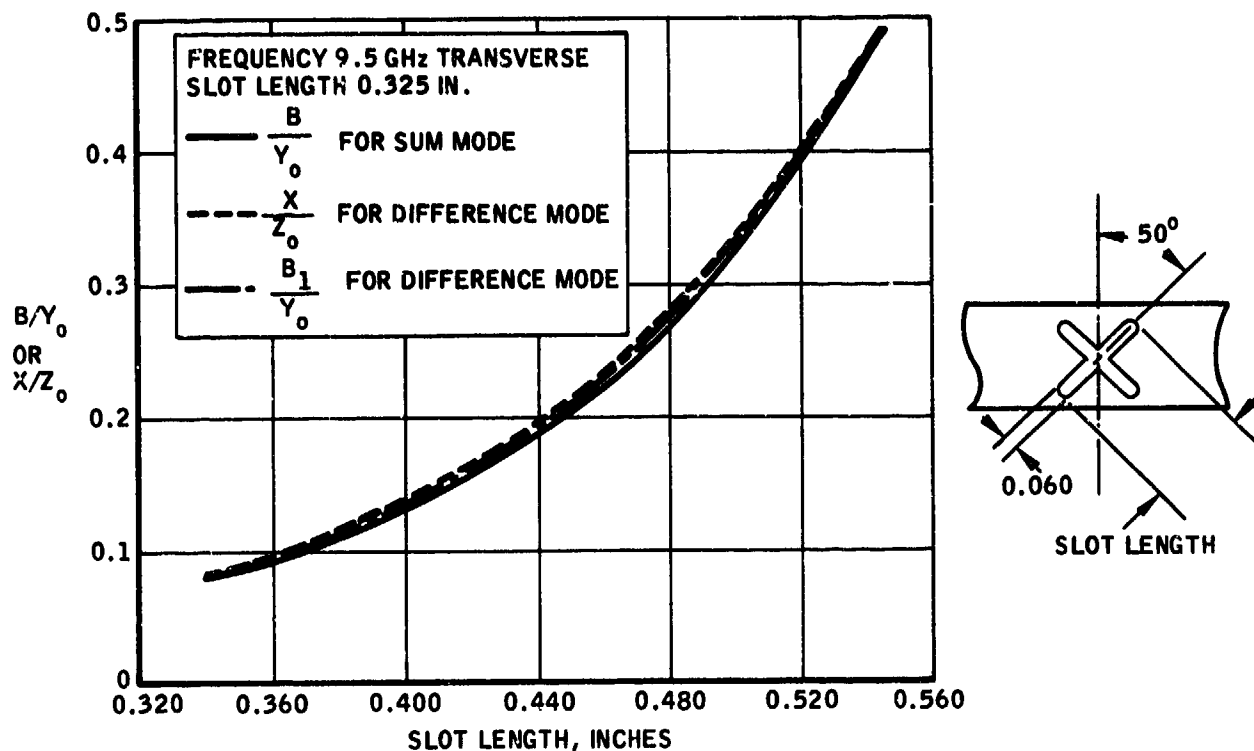


Fig.4(b) Normalized slot susceptance or reactance

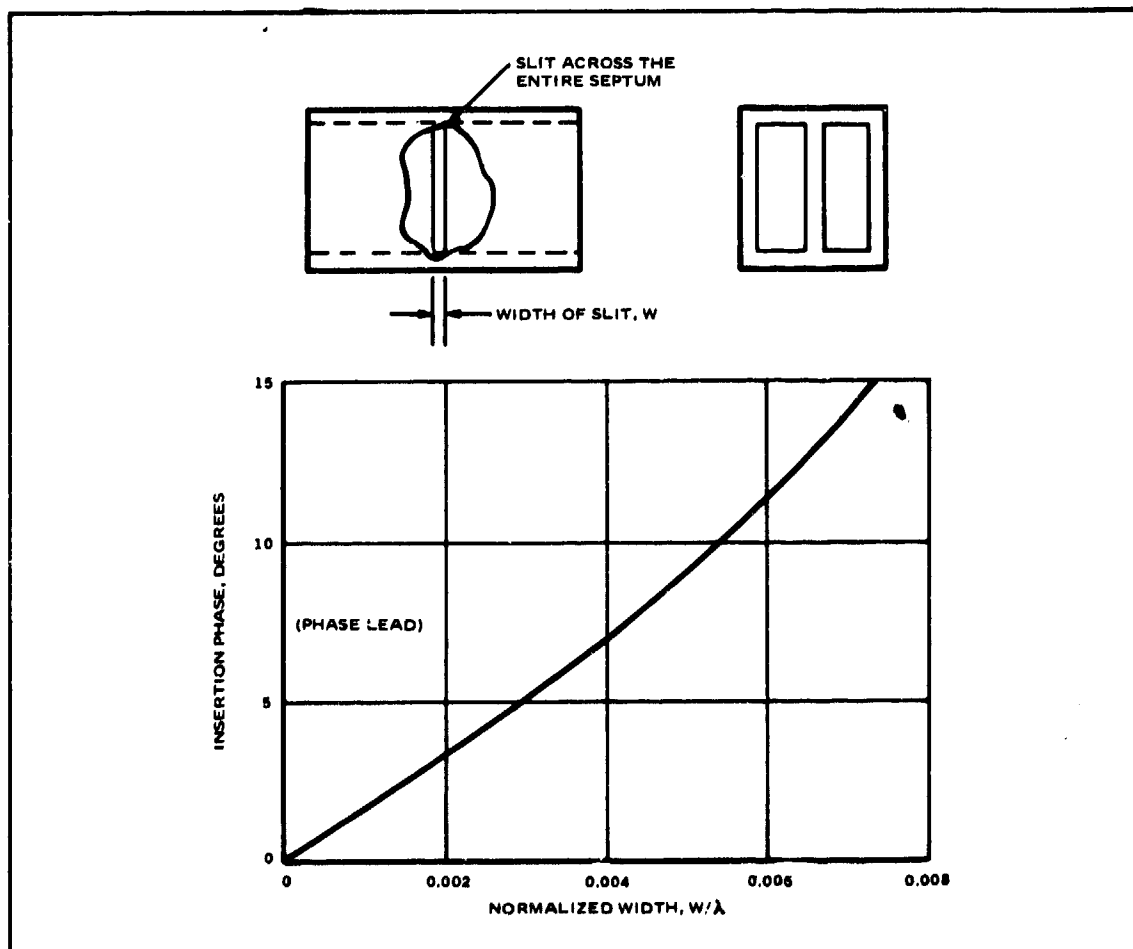


Fig.5 Insertion phase of transverse slit at septum

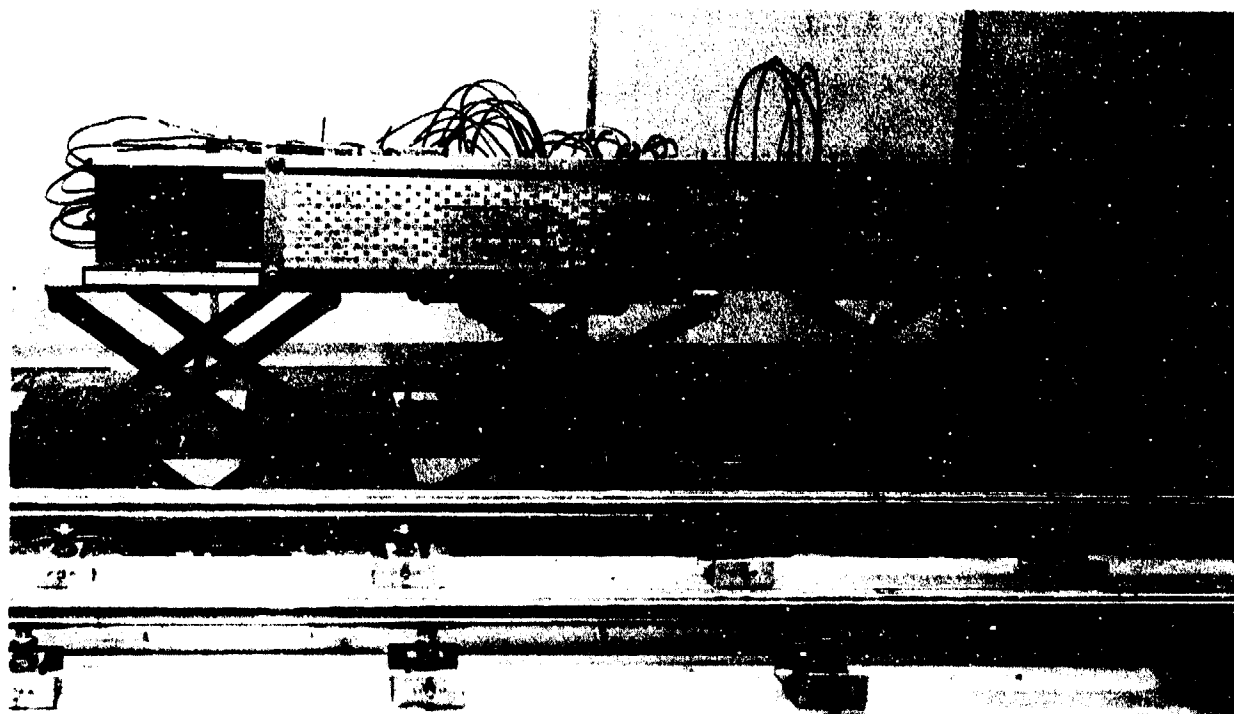


Fig.6 Photograph of the cross slot array

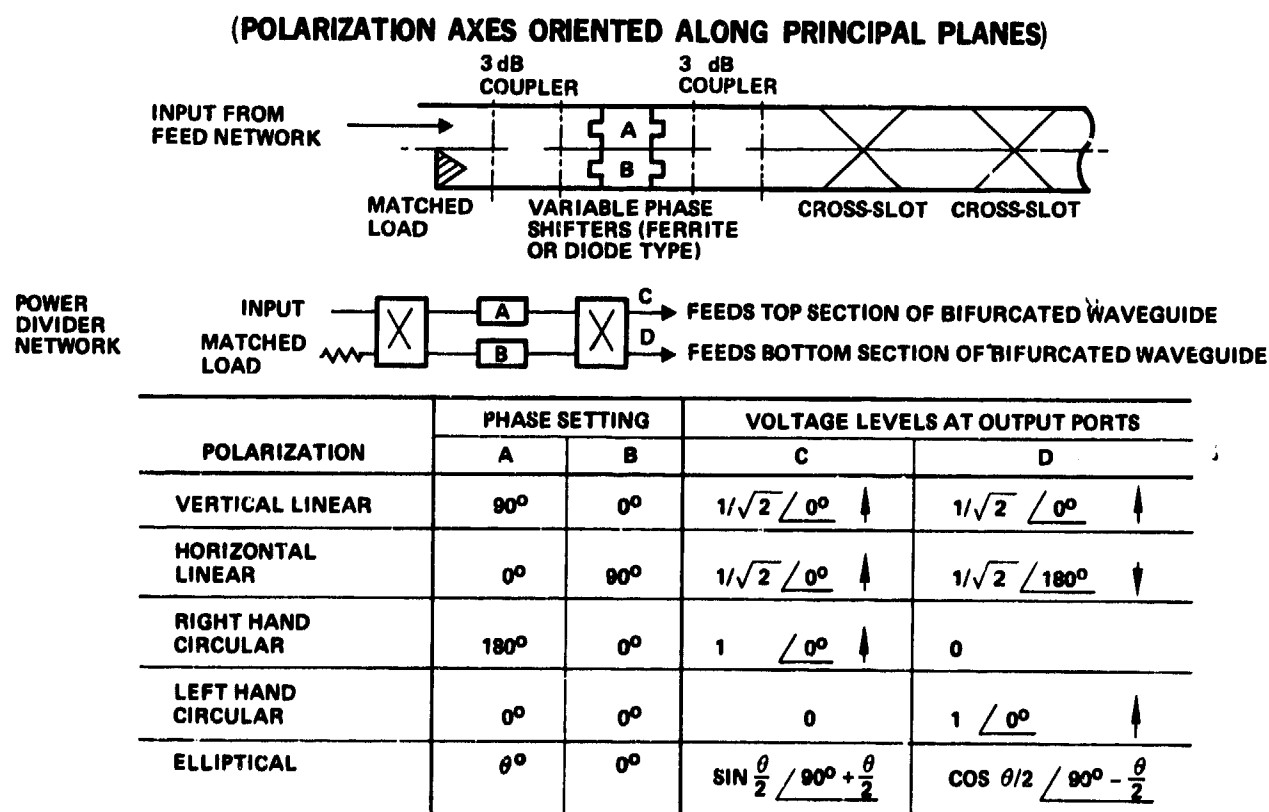


Fig.7 Method of polarization control

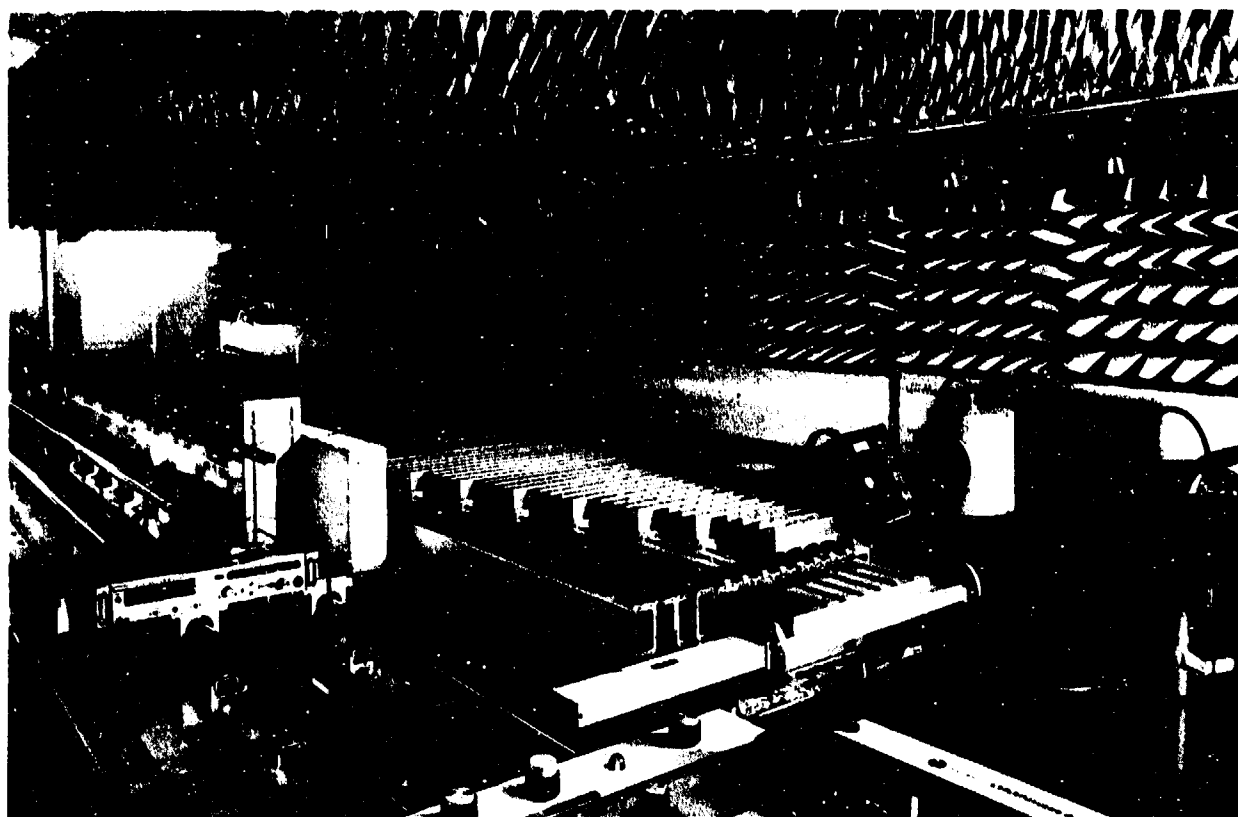


Fig.8 Near field probe room and antenna setup

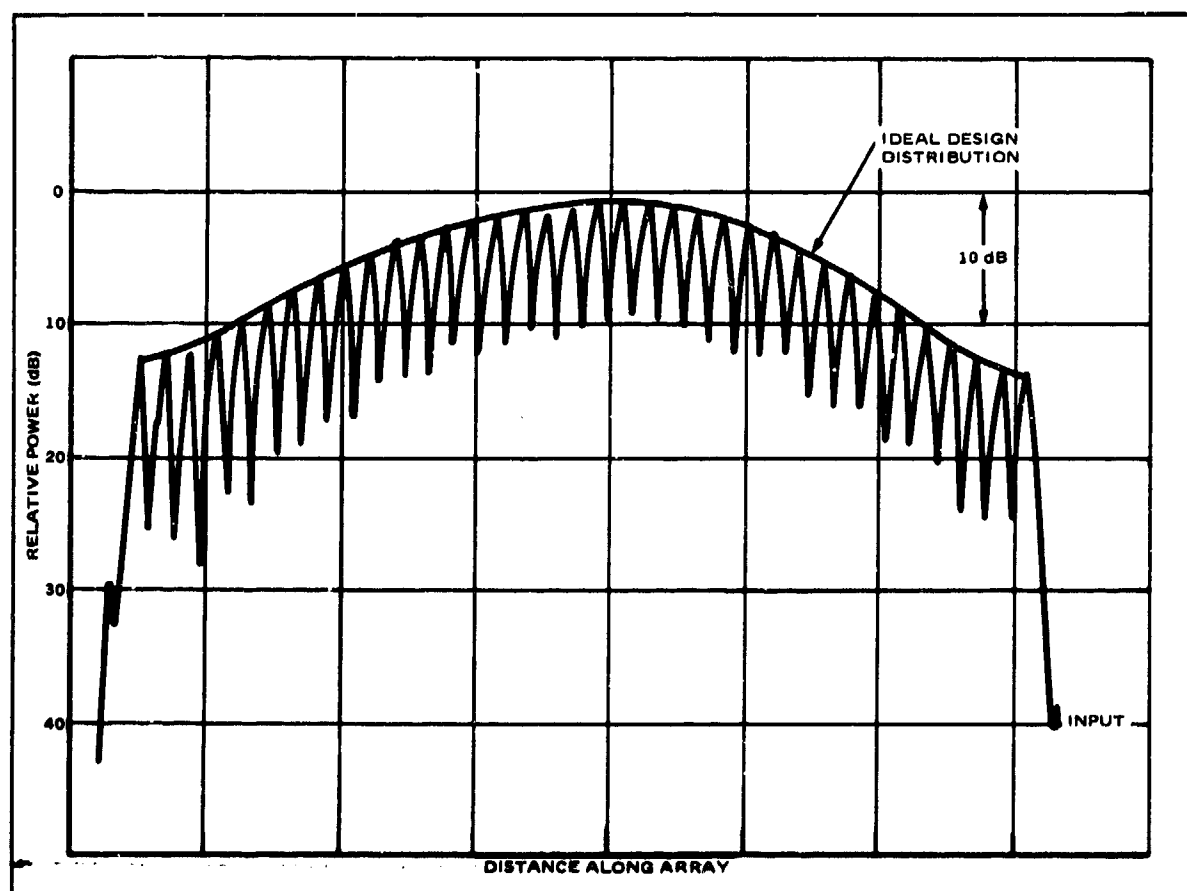


Fig.9 Measured aperture distribution for sum mode

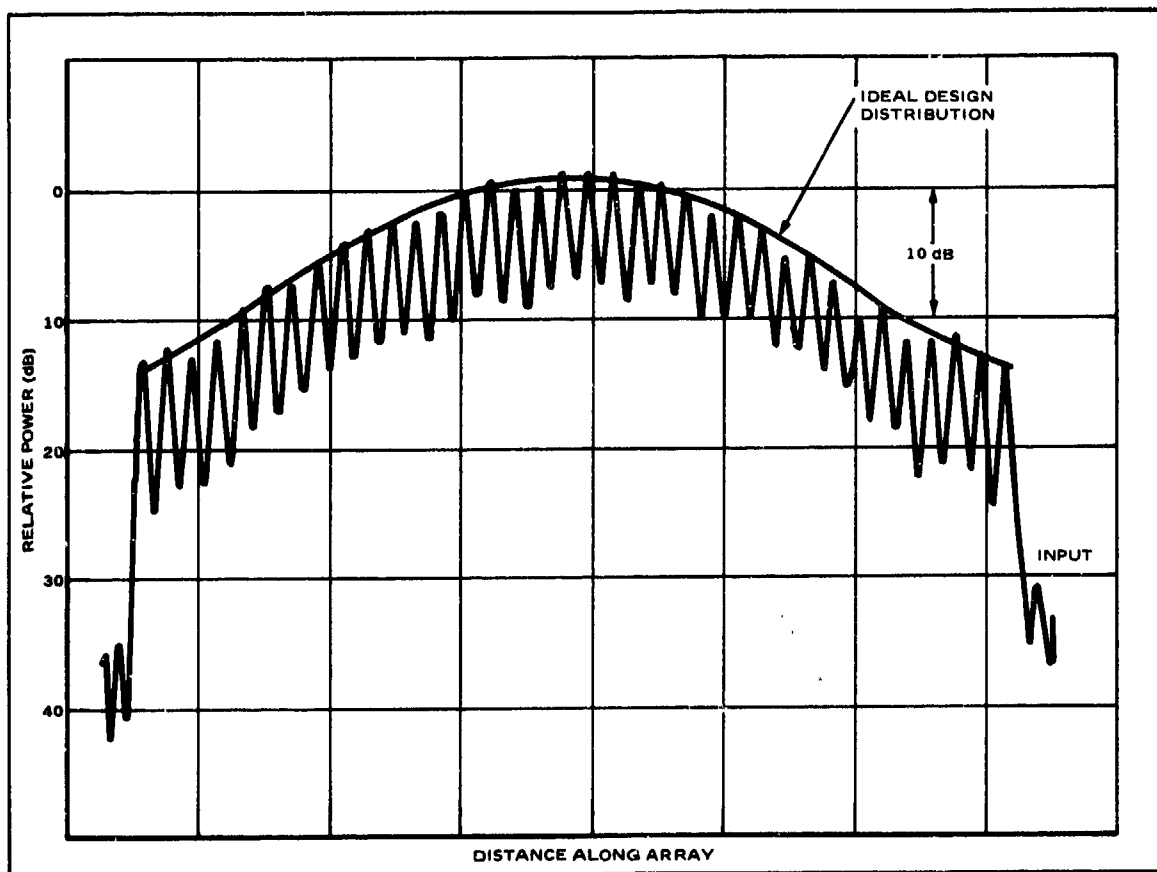


Fig.10 Measured aperture distribution for difference mode

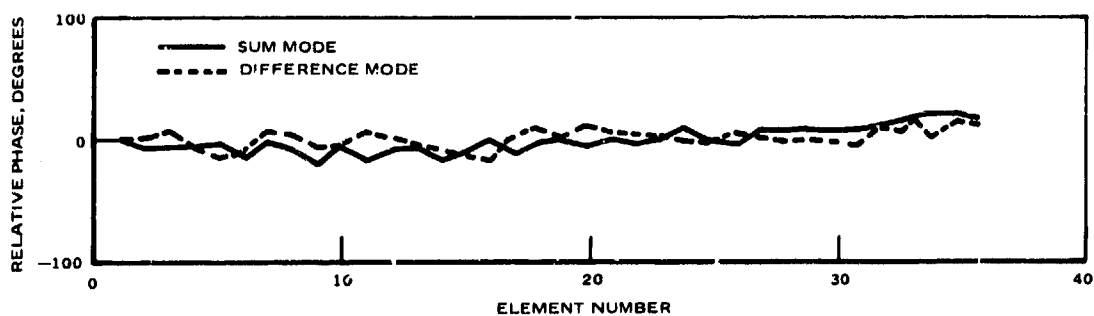


Fig.11 (a) Calculated residual aperture phase, after phase velocity compensation, after non-linear phase compensation

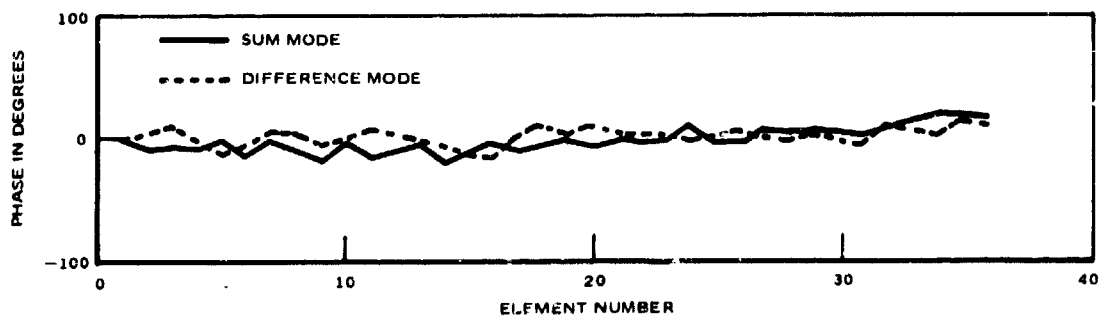


Fig.11(b) Measured aperture phase of a crossed slot array, after phase velocity compensation, after non-linear phase compensation

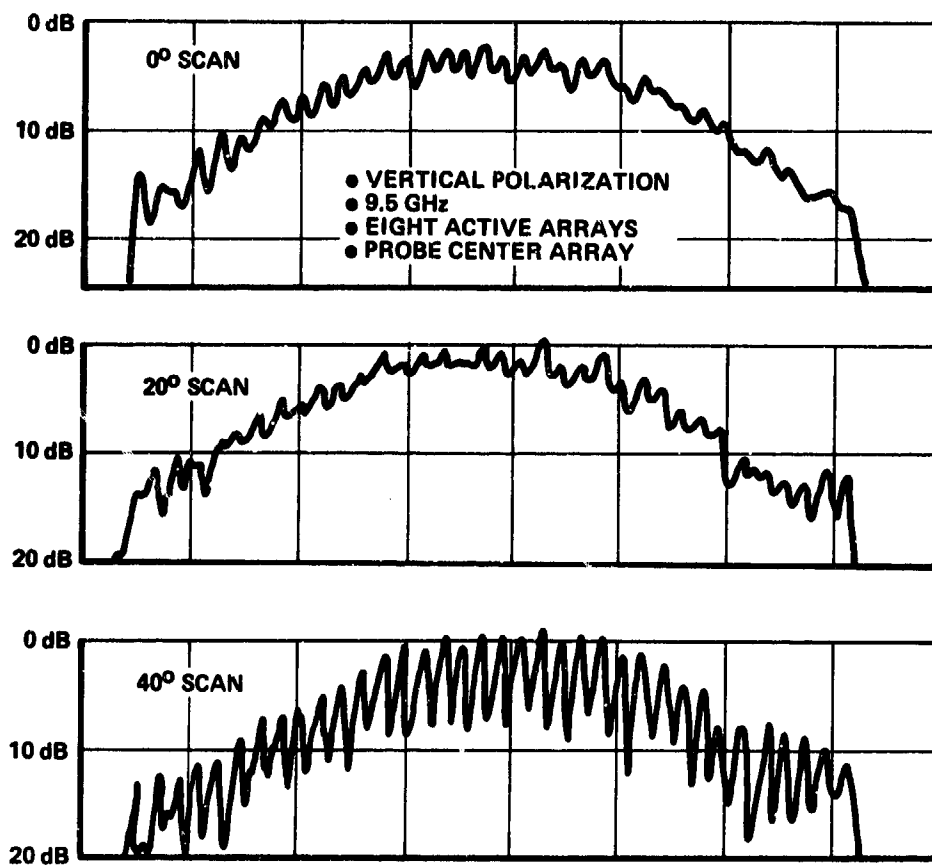


Fig.12 Measured amplitude distribution for typical array

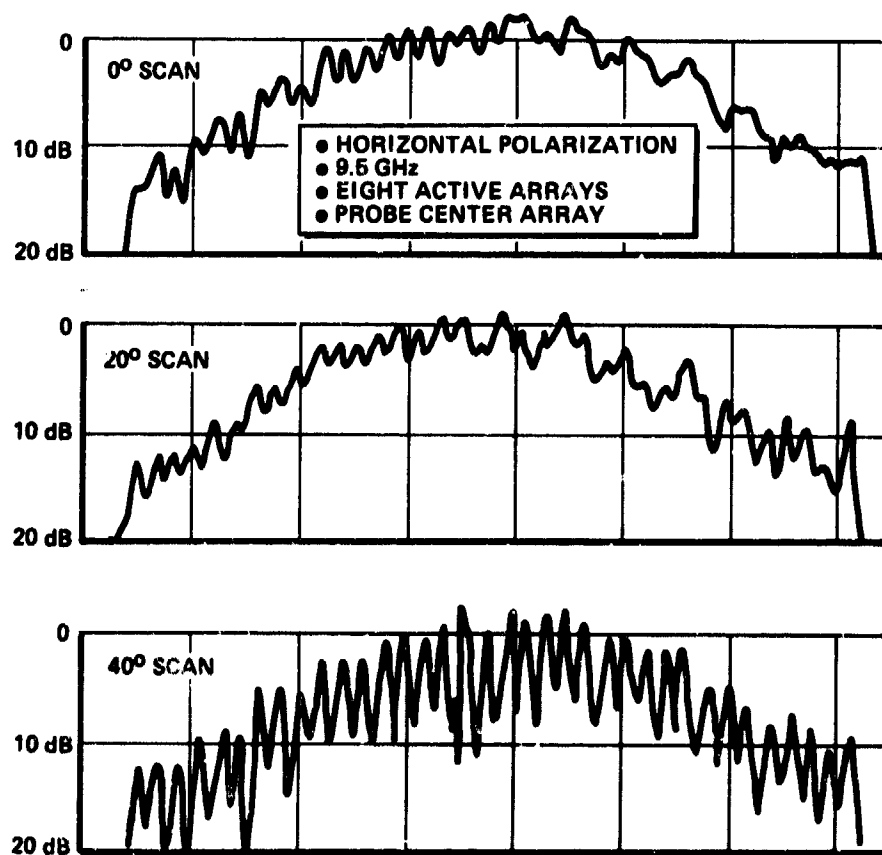


Fig.13 Measured amplitude distribution for typical array

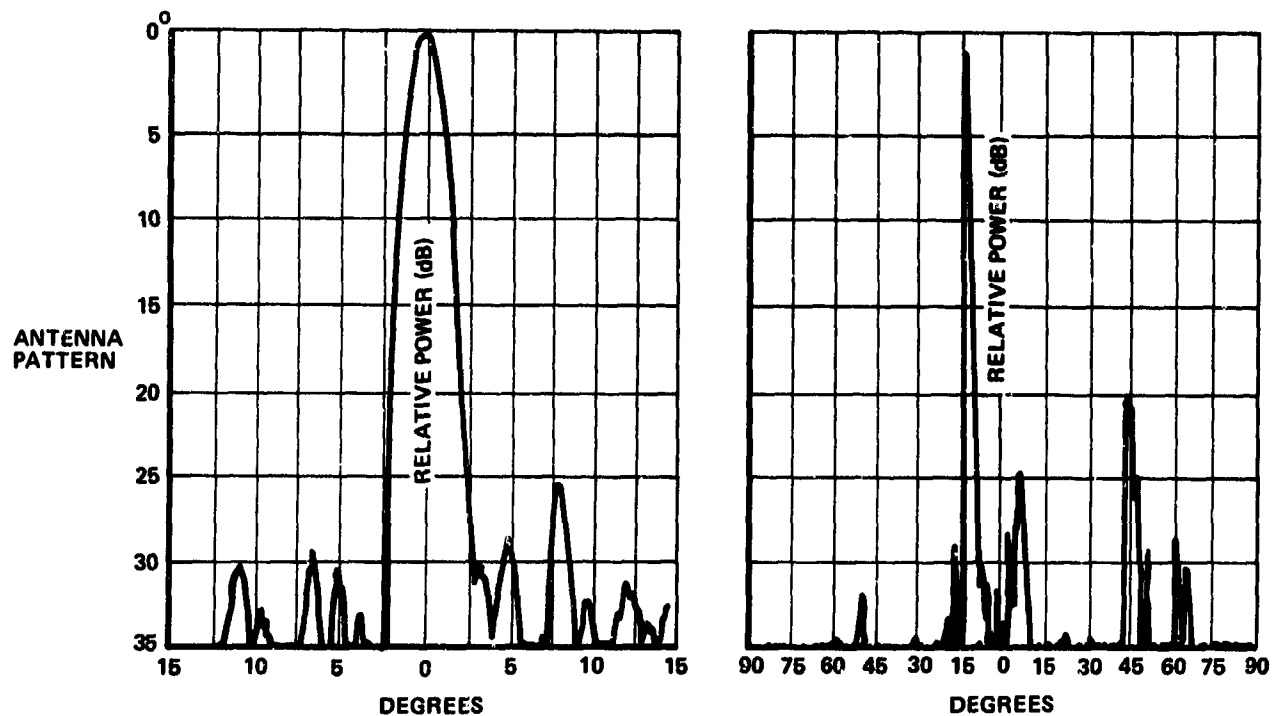


Fig.14 Radiation pattern for vertical polarization, 0° scan, 9.5 GHz

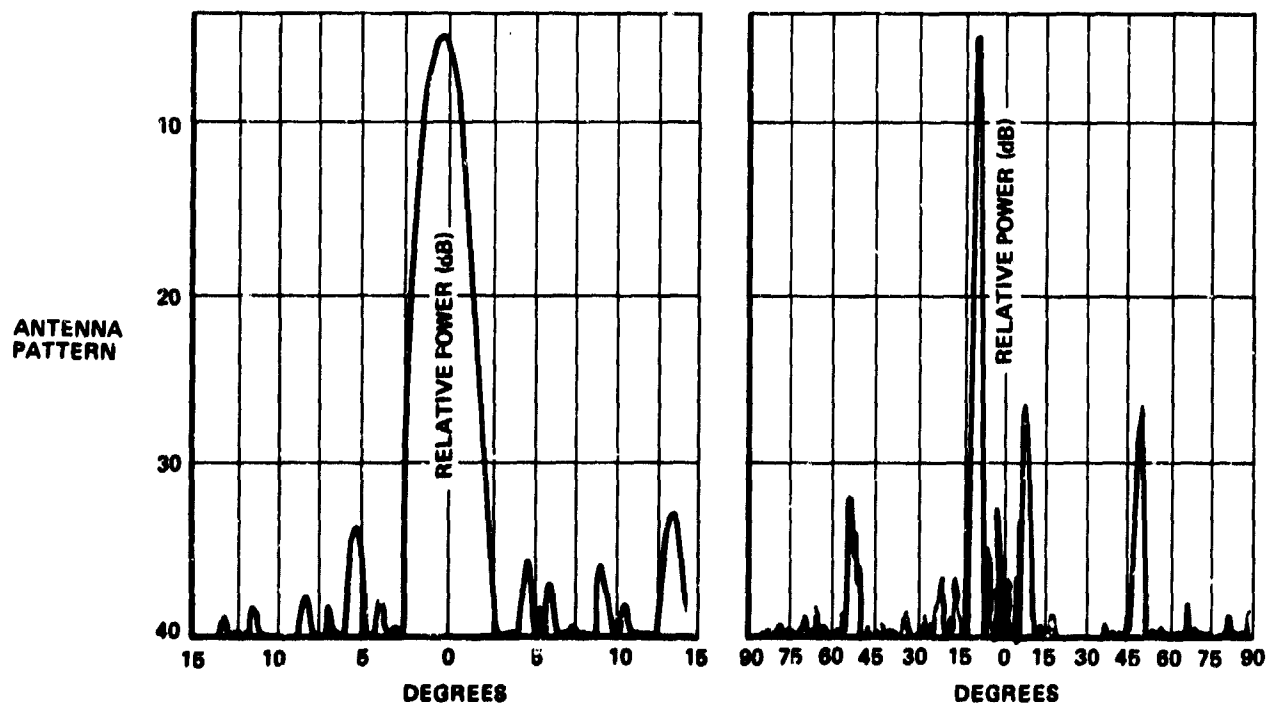


Fig.15 Radiation pattern for horizontal polarization 0° scan, 9.5 GHz

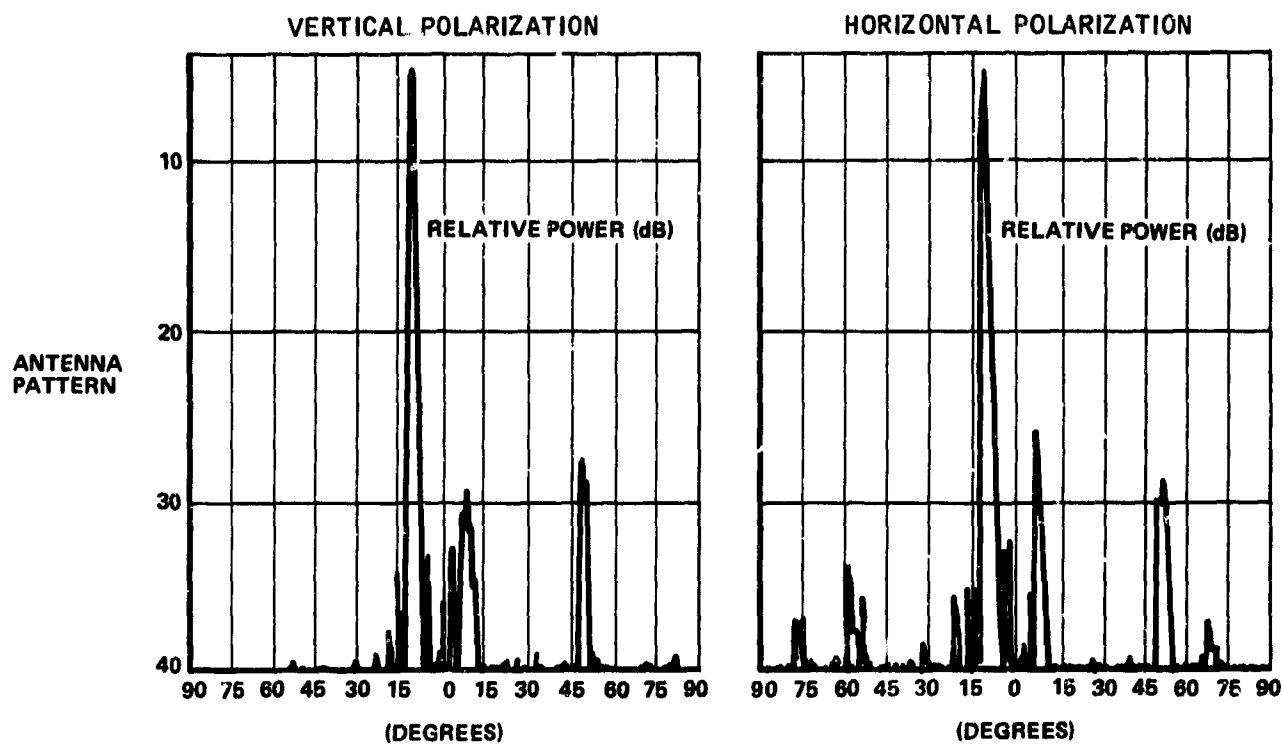


Fig.16 Radiation patterns at 20° scan, 9.5 GHz

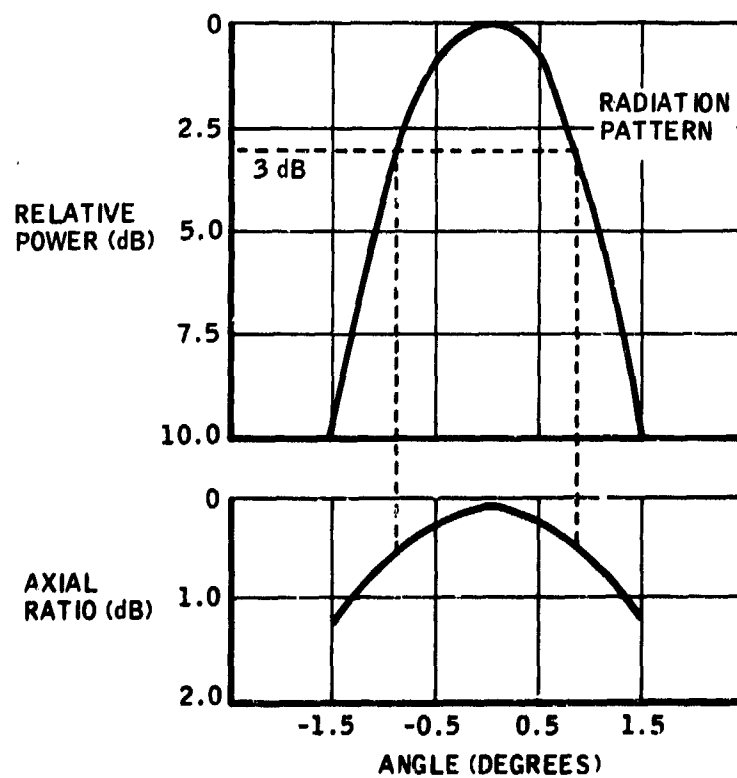


Fig.17 Measured axial ratio of two dimensional slot array

DISCUSSION

J.R. MARK: The suppression of grating lobes by means of staggering the arrays gives the best suppression in the broadside azimuth plane. When the array is scanned in elevation these grating lobes increase in level. What was the highest level over the elevation scan range, and what was the elevation scan range?

2. What caused the high level amplitude perturbations in the near field amplitude distribution for 40° scan.

J.S. AJIOKA: 1. For the triangular slot spacing of 1.366 inches base by 0.394 inch altitude, a grating lobe contour was calculated but was not given in the paper or viewgraphs, it is reproduced on page 42-15. This curve shows the scan position of the main beam when the first grating lobe occurs at some endfire position (generally not in the principal planes). For this array, the elevation scan limit is about 40 degrees from broadside.

2. The amplitude variation in the near field probe measurement shows the resolution of each individual slot. The envelope or peak values give the true aperture distribution.

J. THRIVES: I have three questions. (a) What process did you use to design the array which takes mutual coupling between the elements into account.

(b) Is each element matched to the waveguide.

(c) Could you not use the property of the slot in the common wall of the two wave guides to produce the antiphase between elements. This as I'm sure you know would of course reduce the grating lobes that at present exist.

J.S. AJIOKA: The practical method by which travelling wave waveguide slot arrays are designed taking mutual coupling into consideration is this:

1. Build a few linear arrays using the best data available that is qualitatively correct (it may be data taken on a single isolated slot). For example, in edge slot arrays with resonant slots, the slot angle is the governing factor for slot excitation -- the greater the slot angle, the greater the slot coupling whether it be isolated or in the active array environment.

2. Take this preliminary array of linear arrays (experience has shown that five linear arrays are sufficient) and probe the near field for amplitude, phase and power into the terminating load. Calculate or estimate the ohmic losses in the waveguide.

3. From these data, the slot parameters can be calculated. Now, one can make a table of slot admittance vs. slot angle which was taken in nearly the exact environment including aperture taper and, in shaped beam designs, approximately the correct non-linear phase environment.

4. From this empirically derived table of parameters, a new set of slot arrays is built. Experience has shown that this first iteration will result in a satisfactory design. If not, repeat the procedure. Antennas with better than -30dB sidelobe and high efficiency over a 12 per cent bandwidth have been designed and produced using this simple technique.

11. As to the question of each slot being matched to the waveguide, this is generally not a problem except when the main beam is at broadside to the linear array (resonance condition) because it is well known that the VSWR of long travelling wave arrays peak up at the broadside frequency and low VSWR at frequencies corresponding to off broadside scans. The VSWR vs. frequency plot resembles the antenna pattern -- the VSWR peak at broadside is analogous to the main beam of the antenna pattern. In practice, the broadside condition is avoided (usually by about three beamwidths minimum). In the present case, the main beam is always about 10 degrees off broadside to the linear arrays. If it is necessary to operate through broadside, then the elements should be matched to the waveguide and in practice, only the slots with large coupling need be matched and this has been done successfully by matching in groups with irises or posts between the slots.

In the case of the cross slot array which has non-resonant slots, the phase is compensated by reactive elements between slots as described in the written paper. See the near field amplitude and phase plots in the written paper.

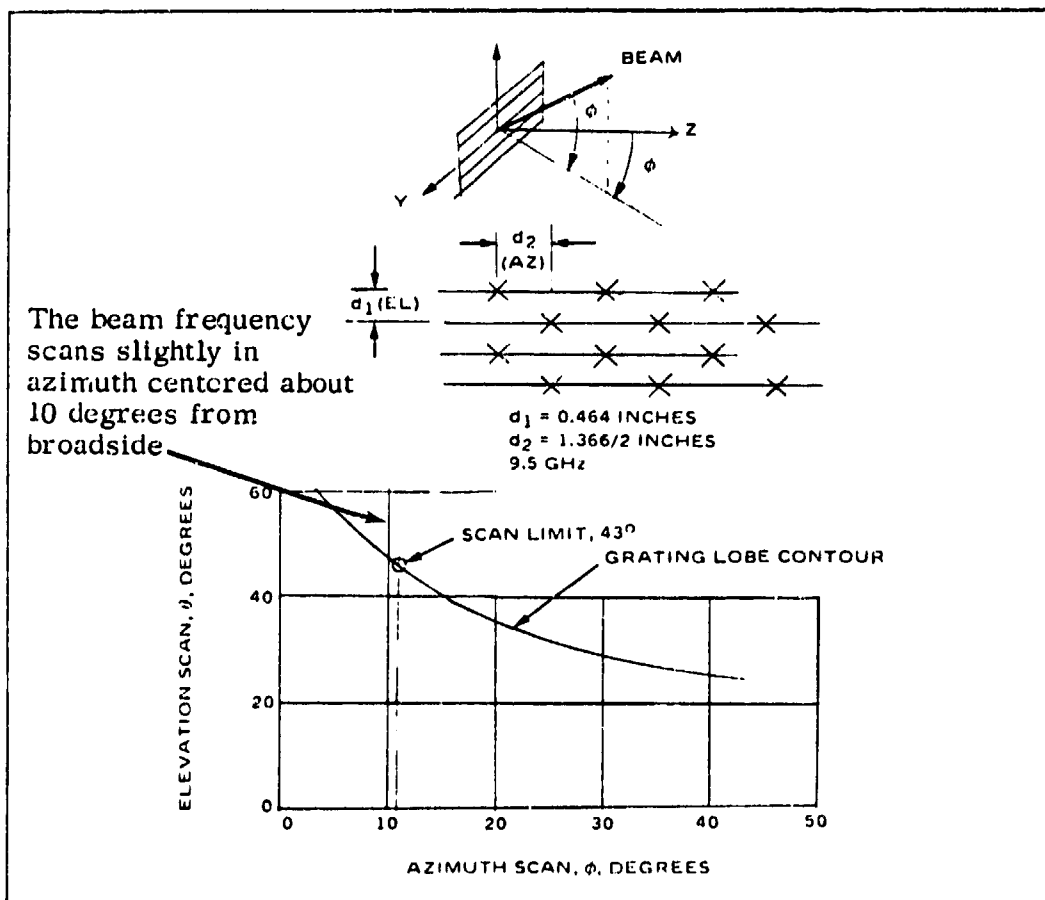
111. Antiphasing of alternate slots to make the slot spacing $\lambda/2$ instead of λ can be done for the odd mode but not for the even mode.

J. JACOBSEN: What is the bandwidth of the antenna?

2. How was the waveguide manufactured?

J.S. AJIOKA: The bandwidth was about 6-7%

2. The special waveguide was formed by combining two ordinary x-band waveguides.



Elevation Scan Limit for the Selected Element Spacing

Stepped Reflector Antenna with a Sector Shaped Main Beam

H. Thielen
Fernmeldetechnisches Zentralamt
der
Deutschen Bundespost,
Darmstadt, Germany

Summary

The optimum pattern of an antenna of telecommunication or television-broadcasting satellites consists in a sector-shaped main beam without any side lobes. In this case the "edge gain" (i.e. the gain function at the edges of the coverage area on earth) is 4.1 dB higher than that of a conventional antenna. Theory indicates that such a pattern is produced by a circular aperture illuminated by the oscillating Λ_1 -function. Measurements were made with a paraboloid reflector antenna containing a dielectric dish in its central zone. This dish effects a phase reversal of 180° between the central zone and the remaining ring zone of the reflector. The "edge gain" of this antenna is 1 dB higher than that of a conventional antenna. An increase of 1.4 dB would be obtained by a better feed system. It is also possible to achieve the phase reversal by an arrangement of metallic steps with a height of about one quarter-wavelength. If an antenna with two or more ring zones is used, a further increase of the "edge gain" can be obtained.

1. Introduction

For the purpose of saving transmitter power, it is desirable that the antenna of a telecommunication or television-broadcasting satellite has a maximum gain. The gain, however, cannot be increased beyond a certain value if the coverage area on the earth is a finite surface. In this case there is a theoretical maximum gain which depends on the geometrical dimensions of the coverage area and the distance of the satellite from the earth surface. An optimum illumination is achieved if there is a constant field strength within the coverage area. The transmitter antennas of telecommunication satellites used at present are mainly horn or paraboloid antennas. The main beam of these antennas is bell-shaped with the resulting disadvantageous effect that the edge of the coverage area on the earth is less intensely illuminated than the center. In addition, the radiated energy is partly wasted by by-passing the coverage area.

In the case of small coverage areas (Western Europe, for example), the optimum illumination resulting from a constant field strength pattern is achieved by means of an antenna having a sector shaped main beam without side lobes. If large areas of the earth or the whole earth is illuminated, the optimum antenna pattern deviates a little from the ideal sector shape and requires an increase of the level at the edges of the coverage area.

An Intelsat paper (N.N. 1966) published in 1966 included the statement that it was impossible to use antennas having shaped beams because these require too large a diameter. This statement was only correct as long as satellite transmitters were operated in the 4-GHz range. However, according to recent plans for operating telecommunication and television-broadcasting satellites at frequencies above 10 GHz, antennas will be reduced in size and, as a consequence, it will be possible to use antennas having shaped beams.

2. Theoretical aperture illuminations

An antenna pattern having a main beam in the shape of a circular sector and no side lobes at all is produced by an infinitely large circular aperture illuminated according to the Λ_1 -function (Koch, G.F., 1965). Fig. 1 shows the Λ_1 -function to the sixth zero ($\Lambda_1(x) = 2J_1(x)/x$). But even a finite aperture illuminated according to a truncated Λ_1 -function may provide a good approximation to the sectorial pattern. The approximation is the better the more "half-waves" of the Λ_1 -function there are in the aperture. If only multiples of integers are allowed for the number of "half-waves" of the illumination function in each aperture half, the illumination function may be written as follows:

$$h(r) = \Lambda_1(j_{1,m}r) = \frac{2J_1(j_{1,m}r)}{j_{1,m}r} \quad (1)$$

with $r = \rho/a$

is the radial component; a is the real aperture radius; r is the aperture radius normalized to the maximum value 1. $j_{1,m}$ are the zeros of the Bessel function of the first kind. Hence m indicates the number of zeros of the illumination in each radiator half. $m = 1$, for instance, denotes a constant phase illumination decreasing towards zero as the edge is approached; $m = 2$ means that there are 2 "half-waves" and $m = 3$ that there are 3 "half-waves" in each aperture half.

As the level is, in general, lowest at the edge of the coverage area, it is necessary to optimize the gain in this direction. Since there may be one or more minima in the main beam of an antenna with a Λ_1 -illumination, the following additional requirement has to be satisfied:

$$E(\vartheta) \geq E(\vartheta_0) \quad 0 \leq \vartheta \leq \vartheta_0 \quad (2)$$

In Eq. (2) ϑ denotes the radiation angle of the antenna as seen from the central axis; ϑ_0 is the angle between the central axis and the ray directed towards the edge of the coverage area; $E(\vartheta)$ and $E(\vartheta_0)$ are the values of the field strength produced on the earth.

A closer examination was made of the radiation characteristics of circular aperture antennas whose aperture field strengths satisfy the following functions:

$$h_0(r) = \Lambda_1(j_{1,1} r) \quad \text{for } 0 \leq r \leq 1 \quad (3a)$$

$$h_1(r) = \begin{cases} \Lambda_1(j_{1,2} r) & \text{for } 0 \leq r \leq \frac{j_{1,1}}{j_{1,2}} \\ k_0 \Lambda_1(j_{1,2} r) & \text{for } \frac{j_{1,1}}{j_{1,2}} < r \leq 1 \end{cases} \quad (3b)$$

$$h_2(r) = \begin{cases} \Lambda_1(j_{1,3} r) & \text{for } 0 \leq r \leq \frac{j_{1,1}}{j_{1,3}} \\ k_1 \Lambda_1(j_{1,3} r) & \text{for } \frac{j_{1,1}}{j_{1,3}} < r \leq \frac{j_{1,2}}{j_{1,3}} \\ k_2 \Lambda_1(j_{1,3} r) & \text{for } \frac{j_{1,2}}{j_{1,3}} < r \leq 1 \end{cases} \quad (3c)$$

k_0 , k_1 , and k_2 are constant factors. The calculation of the antenna pattern for the different values of k_0 , k_1 and k_2 was made according to the following formula:

$$C(\vartheta) = \int_0^1 f(r) J_0(ur) dr \quad (4a)$$

$$\text{with } u = \frac{D}{\lambda} \sin \vartheta \quad (4b)$$

D is the aperture diameter; λ the wavelength.

The gain may be calculated from the antenna pattern, using the equation.

$$G = \frac{2}{\int_0^{\vartheta_0} C^2(\vartheta) \sin \vartheta d\vartheta} \quad (5)$$

The gain function $G(\vartheta_0)$ - frequently $G(\vartheta_0)$ is also called "edge gain"-is obtained from the relation

$$G(\vartheta_0) = G \cdot C^2(\vartheta_0) \quad (6)$$

In the case of the illumination $h_0(r)$ (i.e. constant phase illumination to the first zero of the Λ_1 -function) the value obtained for the "edge gain" is

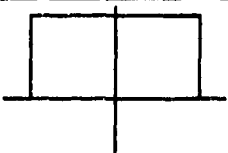
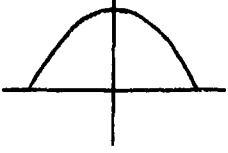
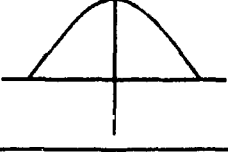
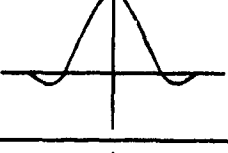
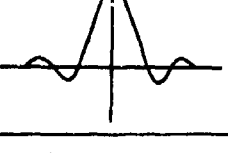
$$G(\vartheta_0) = \frac{1.56}{\sin^2 \vartheta_0} \quad (7)$$

The same value is obtained for antennas with the illumination $h(r) = \Lambda_0(r) = J_0(r)$. It is well-known that this function is the optimum illumination of circular apertures with constant phase illumination if a maximum "edge gain" is to be achieved (Rebhan, W., 1966, 1967).


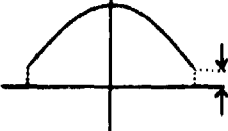
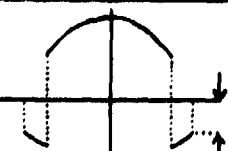
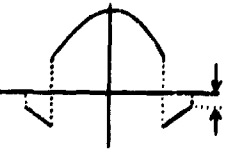
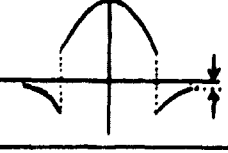
Table I

Geometric dimensions and radiation characteristics of circular aperture antennas

a) Theoretical aperture illuminations

Illumination	D/D_2	$(D/\lambda) \sin \theta_0$	u_0	$G(\theta_0) \sin^2 \theta_0$	η_F	$G'(\theta_0) \sin^2 \theta_0$
 const.	1	0,59	1,84	1,36	-	-
 $1 - r^2$	1	0,73	2,3	1,56	-	-
 $h_0(r)$	1	0,8	2,5	1,56	-	-
 $h_1(r)$	1,83	1,61	5,05	2,14	-	-
 $h_2(r)$	2,65	2,6	9,1	2,64	-	-

b) Practicable aperture illuminations

 -10 dB	1	0,66	2,08	1,53	0,9	1,38
 -14 dB	1	0,7	2,2	1,54	0,95	1,46
 Feed I -8,5 dB	1,36	1,23	3,86	1,66	0,85	1,41
 Feed II -17 dB	1,5	1,31	4,11	1,88	0,98	1,84
 Feed III -30 dB	1,76	1,46	4,59	1,94	0,995	1,93

In the case of the illumination function being $h_1(r)$ - i.e. 2 "half-waves" per aperture half - the optimum of an antenna is achieved at $k_0 = 0.65$ (Fig. 2). The "edge gain" is in this case

$$G(\vartheta_0) = \frac{2.14}{\sin^2 \vartheta_0} \quad (8)$$

It is true that the "edge gain" still increases with growing values of k_0 , but antenna patterns having illumination functions with $k_0 > 0.65$ do no longer satisfy the requirement of Eq. (2).

In the case of illuminations which are truncated at the third zero of the Λ_1 -function, the optimum is achieved at $k_1 = 0.9$ and $k_2 = 0.7$ (Fig. 2). The "edge gain" is

$$G(\vartheta_0) = \frac{2.64}{\sin^2 \vartheta_0} \quad (9)$$

The gain of an antenna having a sector-shaped pattern is

$$G = G(\vartheta_0) = \frac{2}{1 - \cos \vartheta_0} = \frac{4}{(2 \sin \vartheta_0 / 2)^2} \quad (10a)$$

For small values of ϑ_0 the relation holds that

$$G = G(\vartheta_0) = \frac{4}{\sin^2 \vartheta_0} \quad (10b)$$

Hence, the increase in the "edge gain" as compared with an aperture with constant phase illumination is 1.4 dB if the function is truncated at the second zero and 2.3 dB if the function is truncated at the third zero. An ideal sector shaped beam allows even an increase of 4.1 dB to be achieved.

Table I contains some data on the geometrical dimensions and the radiation characteristics.

3. Practicable aperture illuminations

As the illumination consists in a function oscillating from the center towards the edge with a decreasing amplitude, a phase reversal is required after each zero point. This phase reversal may be achieved by providing a paraboloidal reflector with suitable steps (Koch, G.F., 1965). Fig. 3 illustrates the basic features of this reflector. It consists of a paraboloidal reflector with the focal length f_1 whose surface is equipped with several ring-shaped metallic steps. The contour of these steps have the shape of a paraboloid of focal length f_2 .

The difference of the focal lengths is

$$f_1 - f_2 = \lambda/4 \quad (11)$$

A horn antenna may be used as a feed. Such feeds, however, cannot provide an exact reproduction of the Λ_1 -illumination. The Λ_1 -illumination is continuous whereas the aperture illumination of the stepped reflector has discontinuities at the zero points.

It is the purpose of the following passages to investigate the radiation characteristics of a stepped reflector consisting of the central zone and only one ring-shaped zone. As mentioned above, the radiation of this ring-shaped zone is reversed in phase with respect to the radiation of the central zone (Rothe, T., 1973).

If the pattern $C_F(\psi)$ of the feed is known, the pattern $C(\vartheta)$ of the stepped reflector antenna can be calculated as follows:

$$C(\vartheta) = \int_{\psi_1}^{\psi_2} C_F(\psi) J_0(k \cdot 2f_1 \cdot \sin \vartheta/2) \sin \psi/2 \, d\psi - \int_{\psi_1}^{\psi_2} C_F(\psi) J_0(k \cdot 2f_2 \cdot \sin \vartheta/2) \sin \psi/2 \, d\psi \quad (12)$$

In Equation (12) ψ is the radiation angle of the feed, $2\psi_2$ is the angular aperture of the central zone as seen from focus and $2\psi_1$ the angular aperture of the whole paraboloidal reflector; $k = 2\pi/\lambda$. For calculating the pattern of the stepped reflector antenna, the measured values of the patterns of different feeds were inserted into Eq. (12). These feeds have a pattern of approximate rotational symmetry (Fig. 4). Finally, the pattern of the stepped reflector antenna was used for calculating the gain and edge gain according to Eqs. (5) and (6).

The results of the calculations are listed in Table I. D_z is the diameter of the central zone of the reflector. $G(\vartheta_0)$ is the value of the "edge gain" without considering the spill-over, $G'(\vartheta_0)$ is the value of the "edge gain" including the spill-over. Consequently, $G'(\vartheta_0) = \eta_F G(\vartheta_0)$. The indicated values of the spill-over efficiency η_F are known from the experience of previous measurements. The other losses caused by aperture blocking, cross polarization, etc. are not taken into account. The illumination level at the edges of the reflector is also indicated in Table I.

The optimum "edge gain" $G(\vartheta_0)$ of a stepped reflector having a horn feed is only about 1 dB higher than the "edge gain" of a conventional paraboloidal antenna. In the case of the aperture illuminated according to the Λ_1 -function, which consists of the central zone and one ring zone, an increase of approximately 1.4 dB was achieved (see Table I and Eq. (8)). The reduction of the gain increase by 0.4 dB is mainly attributable to the high side lobe level of the stepped reflector antenna (see Figs. 6 and 7). The high side lobe level is caused by the unfavourable amplitude distribution of the aperture field. There is a possibility of changing the amplitude of the aperture field by developing other antenna types. The appropriate solution which suggests itself is a shaped Cassegrain antenna having a stepped main reflector. The use of shaped reflectors allows the amplitude distribution in the aperture of the main reflector to be improved (Galindo, V., 1964; Williams, W.F., 1965).

4. Experimental results

For experimental purposes a model was designed consisting of a paraboloidal reflector with a Plexiglas dish (Fig. 5). The propagation velocity of waves in a dielectric material is smaller than in air. The thickness of the dish was chosen in such a way that there is a delay time difference of $\lambda/2$ between the rays directly reflected by the reflector and those passing through the Plexiglas dish. The reflector has an angular aperture of $2 \times 50^\circ$ and a diameter of 60 cm (Rothe, T., 1973).

For the measurements two different dishes having the diameter $D_z = 44$ cm and $D_z = 40$ cm were used. In the first experiment (in which the diameter D_z was 44 cm) the feed was an open circular waveguide having the diameter of one wavelength and in the second case (the diameter D_z being 40 cm) a dual-mode horn having an aperture diameter of 1.7 wavelengths.

The deviation of the measurement results (Figs. 6 and 7) from the calculations is mainly attributable to the aperture blocking caused by the feed and the feed supports (increase of the first side lobe).

In the case of the stepped reflector antenna with the dual-mode feed, the measurements were made only at a frequency of 8.8 GHz. It was impossible to make broad-band measurements because the feed has a very narrow bandwidth. The pattern of the stepped reflector antenna with the open waveguide feed was investigated in the frequency range from 8.5 to 9.3 GHz (Fig. 8). The patterns measured at various frequencies do not differ very much from each other. In view of this, the stepped reflector antenna discussed here may be assumed to be usable at a relative bandwidth of approximately 9 percent.

There are plans for making experiments in the near future in order to test a stepped metal reflector having a diameter of 90 cm in the X-band. In this case the measurement results are expected to be better than those of the previous tests because large reflectors are less affected by aperture blocking.

5. Final remark

This paper did not investigate antennas with global beams. For the illumination of the whole earth horn antennas are more appropriate than reflector antennas because in this case the beamwidth need not be as narrow. For producing sector shaped radiation patterns with broader beamwidths, multimode and coaxial horns can be used. Several papers have already been published on these antennas (Rebhan, W., 1966; Scheffer, H., 1970; Thielen, H., 1970; Koch, G.F., 1973).

List of symbols

a	aperture radius
D_z	diameter of the central zone of the aperture
D	aperture diameter
f_1, f_2	focal lengths of paraboloidal reflectors
G	maximum gain of an antenna
$G(\vartheta_0)$	gain function in the direction ϑ_0
$h(r)$	illumination function of a circular aperture
$J_0(x), J_1(x)$	Bessel functions of the order zero and one, resp.
$J_{1,m}$	m-th zero of $J_1(x)$

$r = \rho / a$	radial compon. normalized to the max. value 1
η_F	spill-over efficiency
ϑ	radiation angle as seen from the central axis of the antenna
ϑ_0	angle between central axis and edge of the coverage area
$\bigwedge_1(x) = 2J_1(x)/x$	\bigwedge_1 -function
λ	free-space wavelength
ρ	radial component
ψ	radiation angle of the feed
ψ_1, ψ_2	angular apertures of paraboloidal antennas

References

1. Galindo, V., "Design of dual reflector antennas with arbitrary phase and amplitude distributions", IEEE Trans., vol. AP-12, pp. 403-408, July 1964.
2. Koch, G.F., "Parabolantennen mit geringer Rauschtemperatur", Nachrichtentechnische Z., vol 18 (1965), pp. 324-360.
3. Koch, G.F., "Ein Erreger für rauscharme Parabolantennen und andere Realisierungsmöglichkeiten einer \bigwedge_1 -Belegung", Nachrichtentechn. Z., vol. 18 (1965), pp. 374-379.
4. Koch, G.F., "A coaxial feed for high aperture efficiency and low spill-over of paraboloidal reflector antennas", IEEE Trans., AP-21, pp. 164-169, March 1973.
5. N.N., "Shaped-beam antennas", ICSC/T-24-14E W/3/68, March 8, 1968.
6. Rebhan, W., "Strahlungsdiagramme für Bordantennen von Nachrichtensatelliten", Frequenz, vol. 20 (1966), pp. 156-165.
7. Rebhan, W., "Theoretical analysis of antennas with sector shaped radiation pattern for communication satellites", AGARD conference proc. No. 15, Nov. 1967, pp. 353-363.
8. Rebhan, W., "Das optimale Strahlungsverhalten von Satellitenbordantennen zur Nachrichtenversorgung größerer Erdgebiete", Conference of NTG and URSI held in Darmstadt, Germany, Oct. 17-20, 1967, conference paper pp. 28-29.
9. Rothe, T., "Parabolspiegel mit dielektrischer Stufe zur Erzeugung einer sektorähnlichen Richtcharakteristik", diploma thesis of the Technische Hochschule Darmstadt.
10. Scheffer, H., "Optimale Dimensionierung von Koaxialerregern für Parabolantennen", Nachrichtentechn. Z., vol. 24 (1971), pp. 137-142.
11. Thielen, H., "Ein Mehrmoden-Koaxialerreger für Parabolantennen mit hohem Flächenwirkungsgrad und geringer Überstrahlung", Nachrichtentechn. Z., vol. 24 (1971), pp. 307-313.
12. Williams, W.F., "High efficiency antenna reflector", Microwave J., vol. 8, pp. 79-82, July 1965.

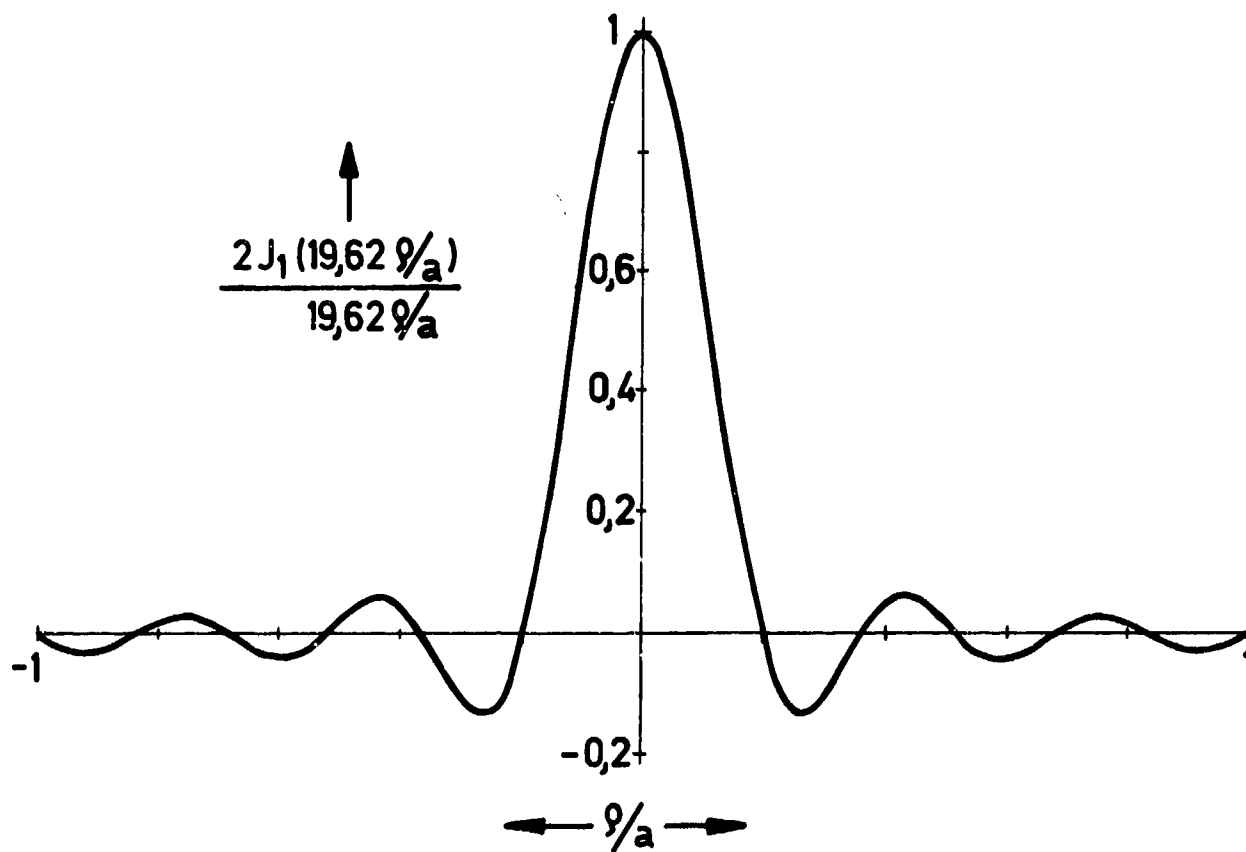


Fig. 1 Illumination of a circular aperture according to the J_1 -function

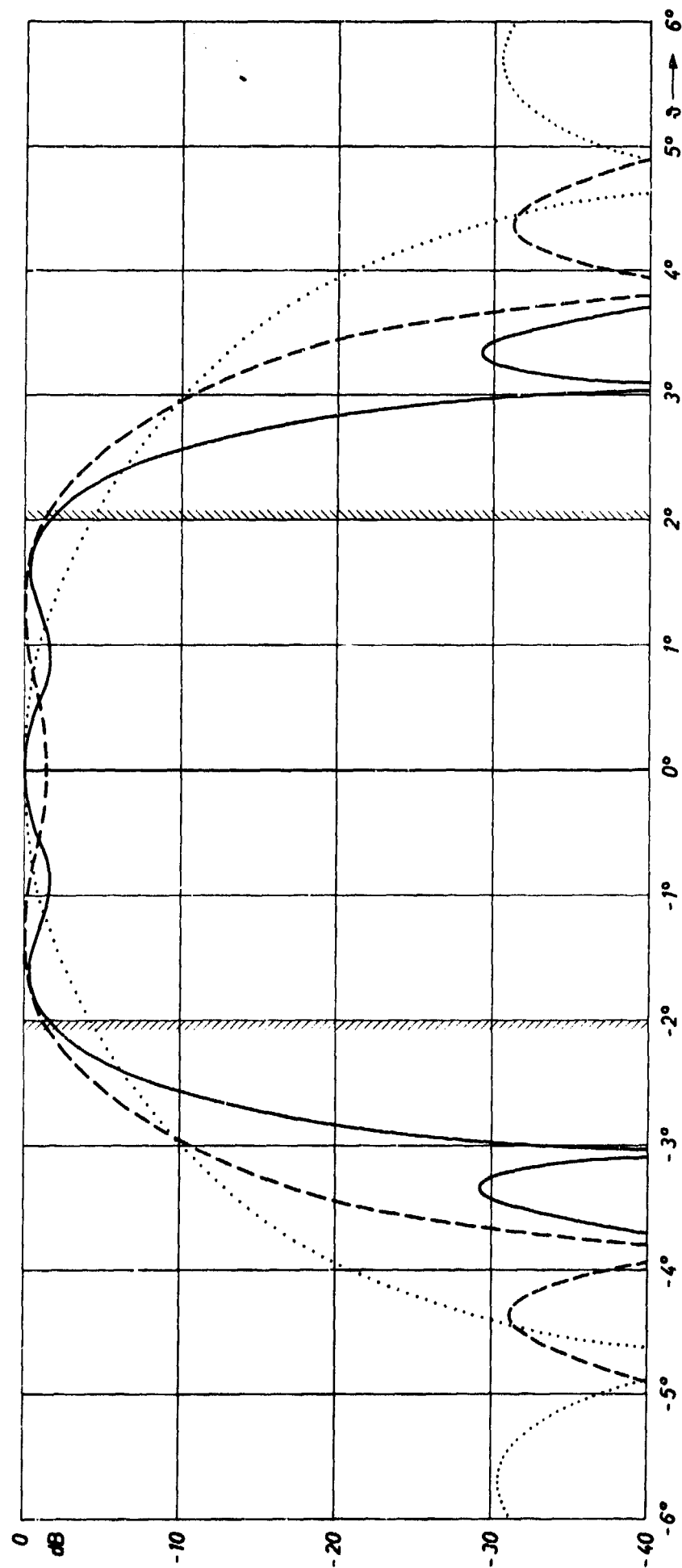


Fig. 2 Patterns of circular apertures illuminated according to truncated Δ_1 -functions. $2\theta_0 = 4^\circ$ (..... illum. $h_0(r)$; - - - illum. $h_1(r)$ with $k_0 = 0.65$; — illum. $h_2(r)$ with $k_1 = 0.9$ and $k_2 = 0.7$)

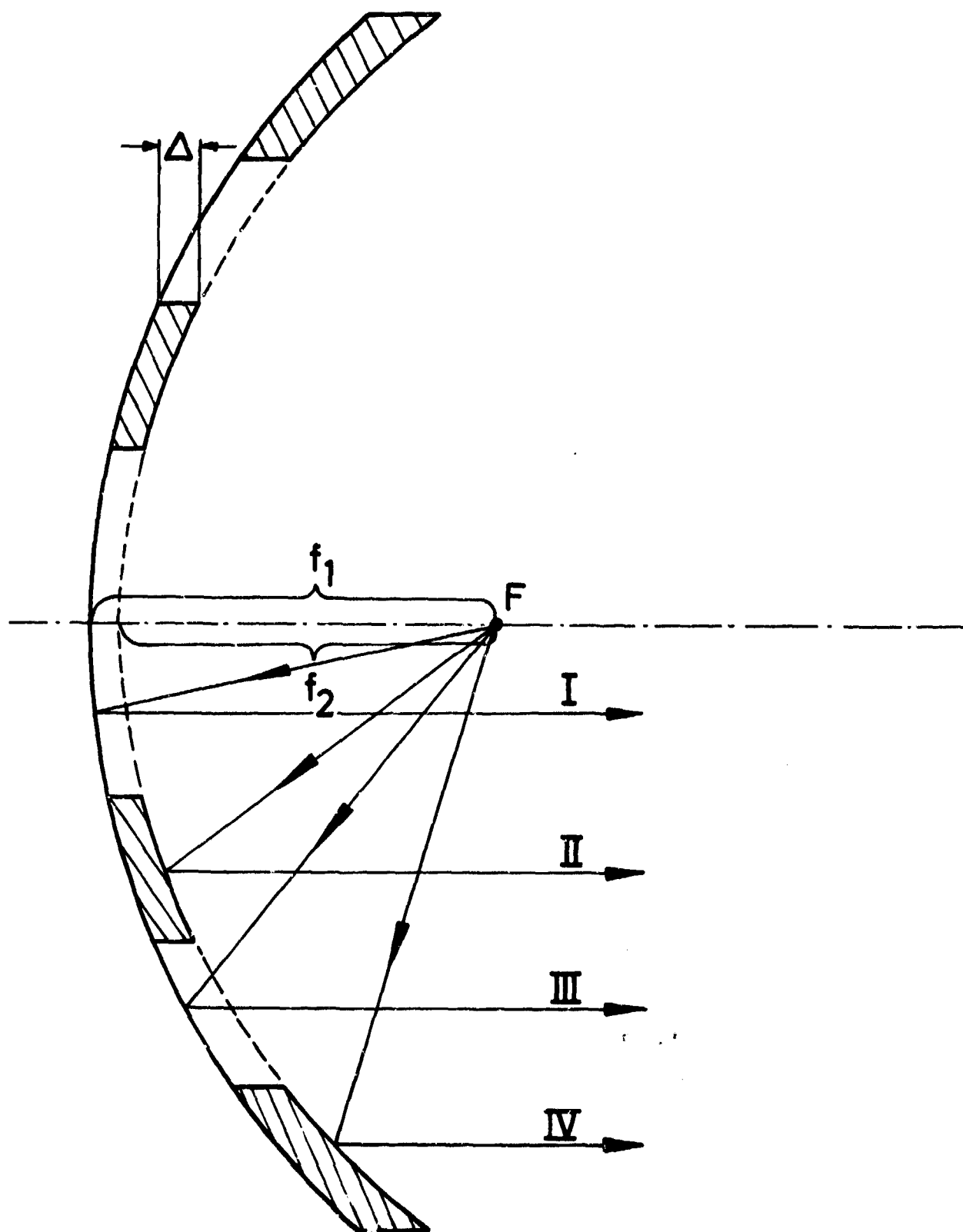


Fig. 3 Stepped reflector antenna with horn feed

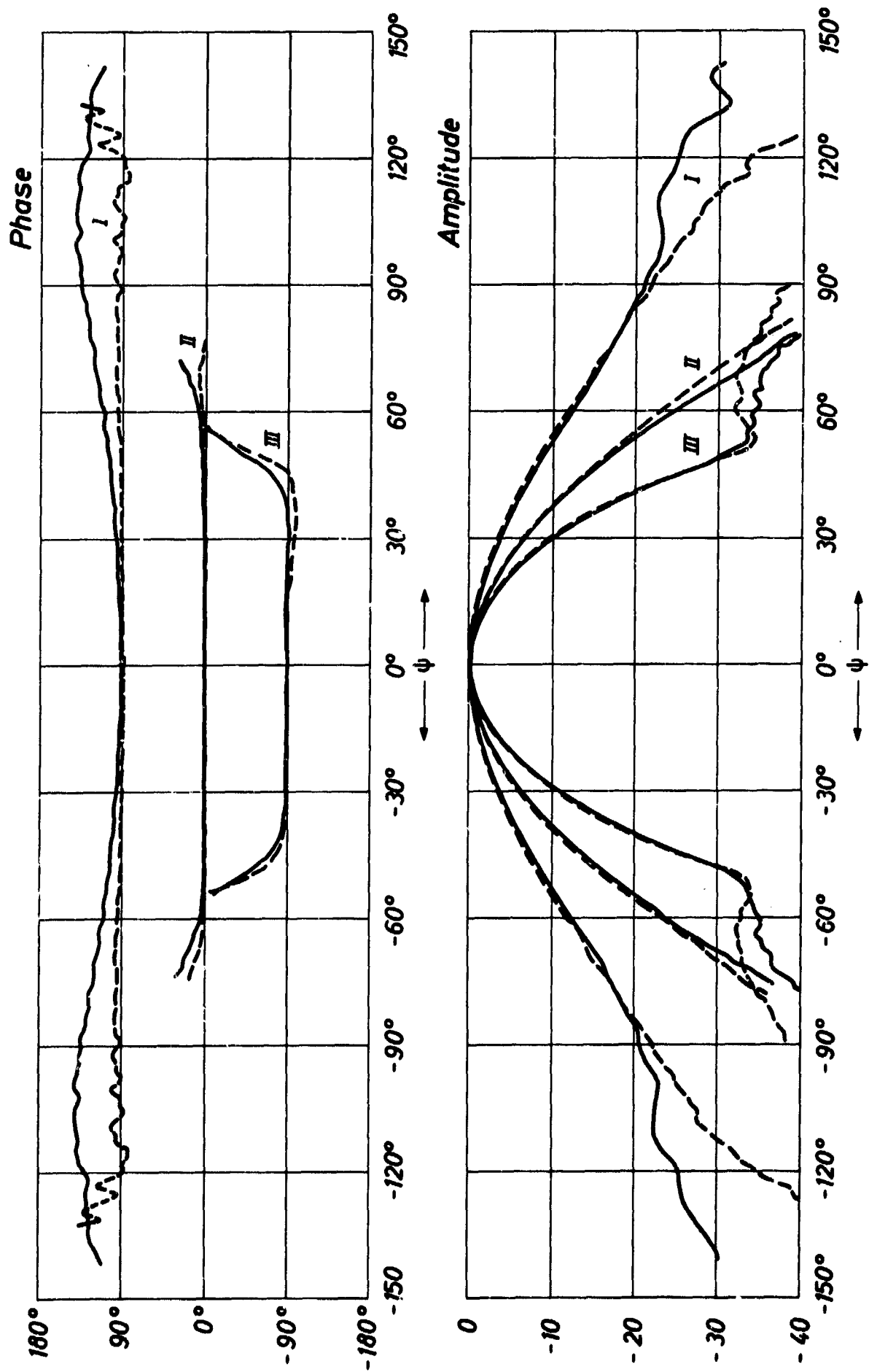


Fig. 4 Feed patterns (— E-plane; --- H-plane)

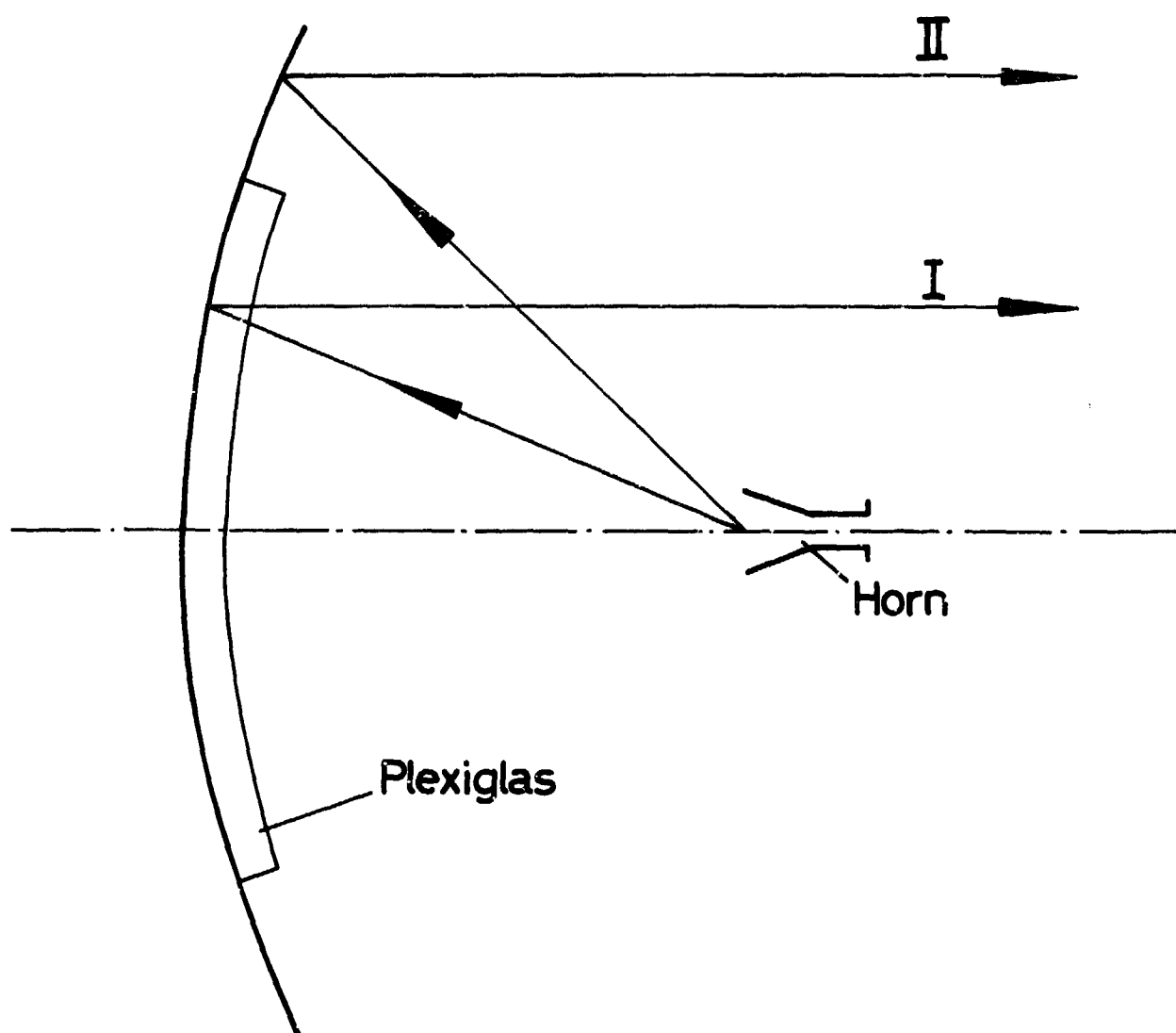


Fig. 5 Paraboloidal reflector antenna with dielectric dish

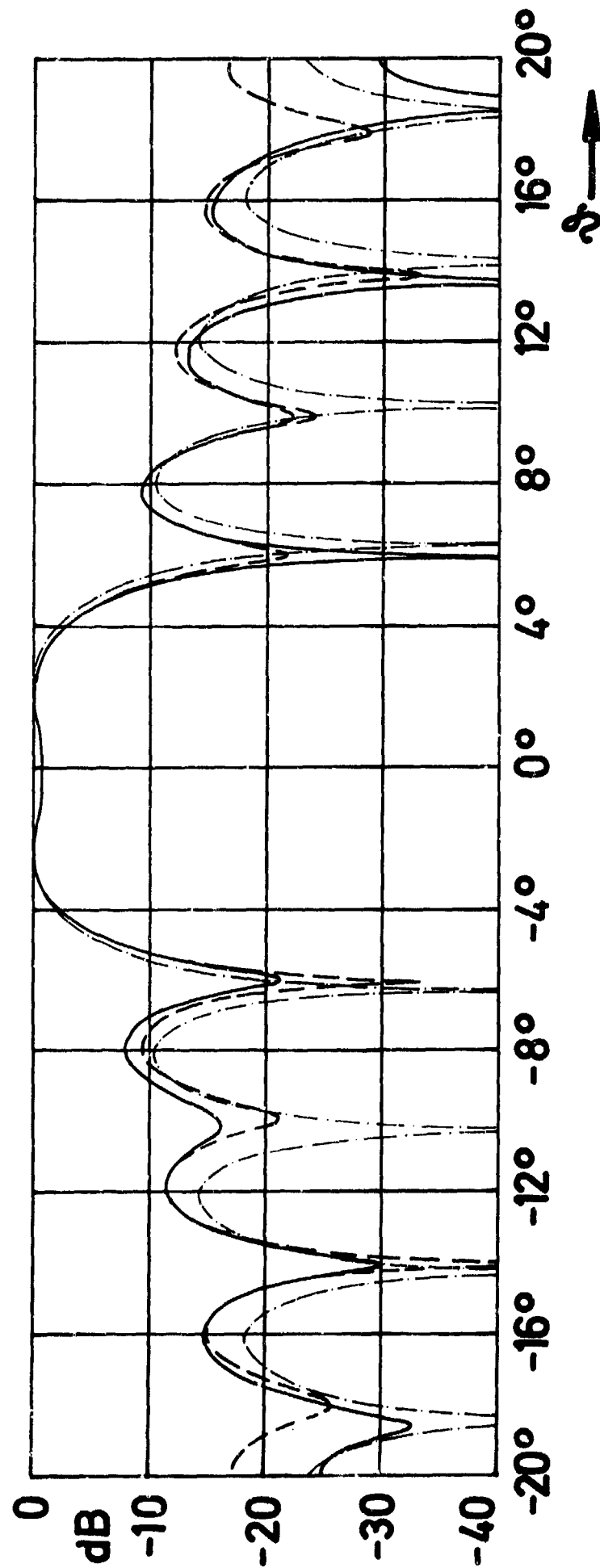


Fig. 6 Calculated and measured patterns of the paraboloidal antenna with dielectric dish. $D = 60$ cm; $D_2 = 44$ cm; $f = 8.8$ GHz
(..... calculated; — E-plane, measured; ---- H-plane, measured)

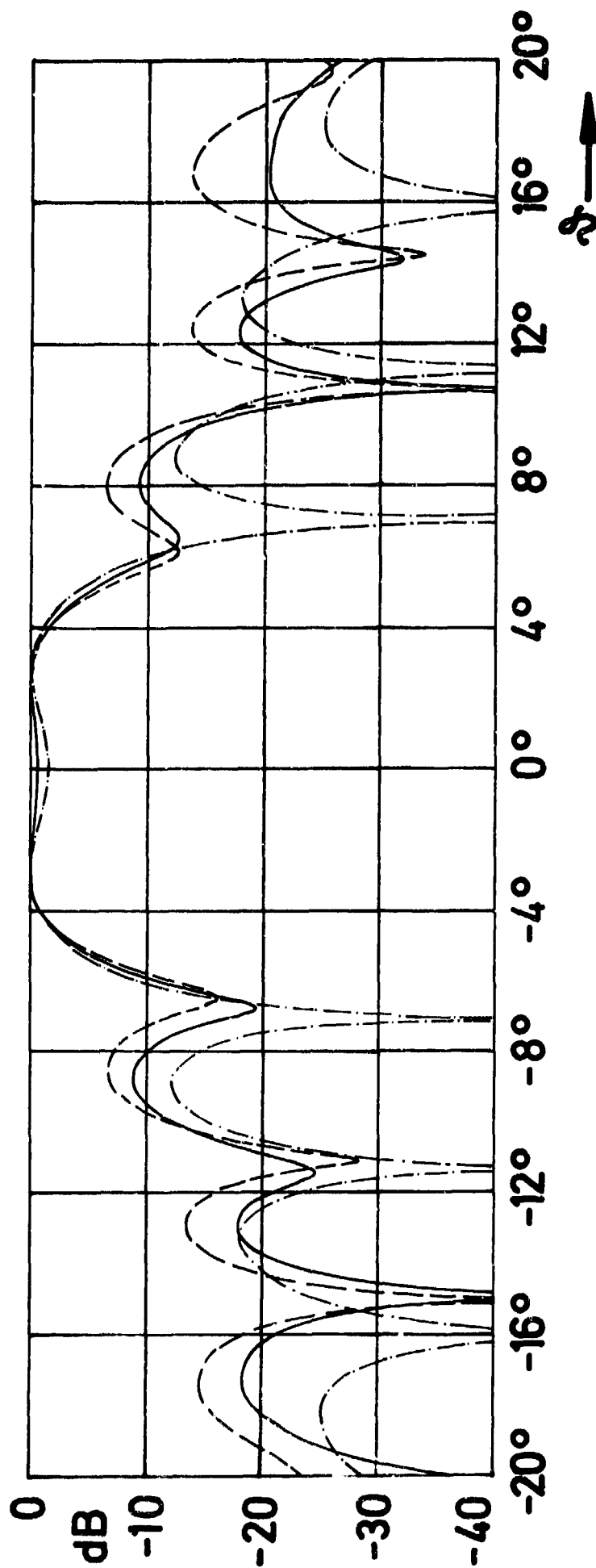


Fig. 7 Calculated and measured patterns of the paraboloidal antenna with dielectric dish. $D = 60$ cm; $D_z = 40$ cm; $f = 8.8$ GHz (--- calculated; — E-plane, measured; ---- H-plane, measured)

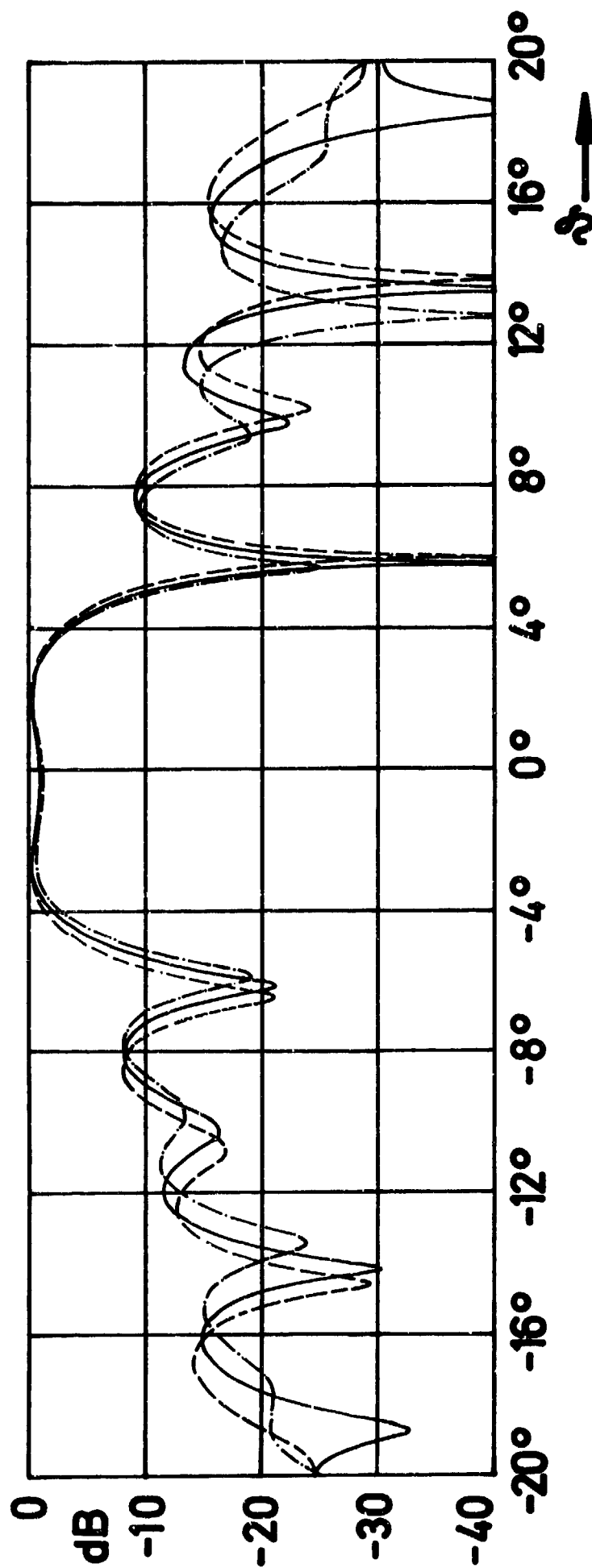


Fig. 8 Patterns (E-plane) of the paraboloidal antenna with dielectric dish measured at several frequencies. $D = 60$ cm; $D_g = 44$ cm
(----- 8.5 GHz; — 8.8 GHz; -.-.- 9.3 GHz)

DISCUSSION

A. SCHROTT: Do you think that the high sidelobe level in contrast to your theoretical investigations depends on the diffraction of the rays at the additional edges?

H. THIELEN: The increase of the side lobe level - e.g. the first side lobe is raised from 13.3dB (theoretical value) to 10dB (measured value) is mainly attributable to the aperture blocking caused by the feed and the feed supports. The effect of the aperture blocking is much higher than that of the diffraction at the edges. Moreover, the diameters of both the central zone and the whole reflector are relatively large (20λ and 30λ resp.) For that reason the influence of the edges is very small.

P. FROIDURE: Ne pensez vous pas qu'il peut y avoir une perturbation due à une réflexion parasite à la transition air plexiglass.

Pour limiter ce phénomène ne serait-il pas préférable de placer le déphaseur à diélectrique à la périphérie du miroir où les champs sont plus faibles.

H. THIELEN: 1. When we have determined the thickness of the dielectric dish, we have paid regard to the multiple reflection of the waves in that dish. Since there is a nearly vertical incidence of the waves we have no perturbation.

2. In the central zone the reflector is relatively flat. Therefore in this zone a better approach to the vertical incidence is achieved than in the outer zones of the reflector.

3. With the stepped metal reflector we obtained better results than with the reflector having plexiglass dish.